



Michael C. Gao · Jien-Wei Yeh
Peter K. Liaw · Yong Zhang
Editors

High-Entropy Alloys

Fundamentals and Applications

High-Entropy Alloys

Michael C. Gao • Jien-Wei Yeh
Peter K. Liaw • Yong Zhang
Editors

High-Entropy Alloys

Fundamentals and Applications



Editors

Michael C. Gao
National Energy Technology
Laboratory & AECOM
Albany, OR, USA

Peter K. Liaw
Department of Materials Science
and Engineering
The University of Tennessee
Knoxville, TN, USA

Jien-Wei Yeh
Department of Materials Science
and Engineering
National Tsing Hua University
Hsinchu, Taiwan, China

Yong Zhang
State Key Laboratory for Advanced
Metals and Materials
University of Science and Technology,
Beijing
Beijing, China

ISBN 978-3-319-27011-1
DOI 10.1007/978-3-319-27013-5

ISBN 978-3-319-27013-5 (eBook)

Library of Congress Control Number: 2016936877

© Springer International Publishing Switzerland 2016

This work is subject to copyright. All rights are reserved by the Publisher, whether the whole or part of the material is concerned, specifically the rights of translation, reprinting, reuse of illustrations, recitation, broadcasting, reproduction on microfilms or in any other physical way, and transmission or information storage and retrieval, electronic adaptation, computer software, or by similar or dissimilar methodology now known or hereafter developed.

The use of general descriptive names, registered names, trademarks, service marks, etc. in this publication does not imply, even in the absence of a specific statement, that such names are exempt from the relevant protective laws and regulations and therefore free for general use.

The publisher, the authors and the editors are safe to assume that the advice and information in this book are believed to be true and accurate at the date of publication. Neither the publisher nor the authors or the editors give a warranty, express or implied, with respect to the material contained herein or for any errors or omissions that may have been made.

Cover illustration: Image was prepared by Drs. Chun-Ming Lin and Jien-Wei Yeh.

Printed on acid-free paper

This Springer imprint is published by Springer Nature
The registered company is Springer International Publishing AG Switzerland

Preface

Scientific curiosity has driven Professors Jien-Wei Yeh and Brian Cantor to investigate multicomponent solid solution alloys in equal or near-equal molar ratios since 1995 and 1981, respectively. Both unconnectedly published their research in scientific journals in 2004. These unique alloys, in sharp contrast to traditional alloys based on one or two principal elements, have one striking characteristic: the unusually high entropy of mixing. Thus Prof. Yeh named these new alloys as high-entropy alloys (HEAs), and they soon have attracted the ever-rising interest from academia and industries all over the world. The history, definition, and progress of HEAs are introduced in Chap. 1, while their promising potential applications and perspectives are outlined in Chap. 15.

Since the first six journal papers published in 2004, there have been tremendous progress and development in both the fundamental understanding and applications of HEAs. This book is written in order to capture in time what have been understood, what attractive properties have been reported, and what challenges still remain pertaining to HEAs. In particular, this book attempts to tackle these questions: What kinds of physical and metallurgical aspects contribute to those superior material properties that are unique to HEAs? What are the entropy sources of HEAs? How can we accelerate the design and development of single-phase HEAs and high-performance multiphase HEAs? What are the proper modeling techniques available to mimic the disordered structures of HEAs at the atomic level, and how can they in turn help people understand the formation and properties of HEAs?

The 15 chapters cover very wide spectra of HEAs, ranging from manufacturing and processing, to advanced characterization, to mechanical and functional properties and from physical metallurgy to computational modeling on different time and length scales. This book mainly presents our own research work, including a great amount of unpublished results, but it also contains a minor amount of review of peers' work in order to be comprehensive. As a result, the review portion is not meant to be complete or impartial. The chapters are written by authors of varying backgrounds in experiments and/or modeling, who decide their preference in the

writing style and chapter contents. The intended readers of this book are students from colleges and graduate schools and research professionals from academia and industries.

Establishing the effective criteria to distinguish single-phase HEAs from multiphase HEAs and bulk metallic glasses (BMGs) has been an intense research topic. To date a number of empirical parameters have been proposed for this purpose, and they include enthalpies of mixing of liquid and solid solution phases, atomic size difference, electronegativity difference, valence electron concentration, Ω -parameter, ϕ -parameter, lattice topological instability, and the root mean square residual strain. Alternatively, one can design HEAs using the computational thermodynamic approach (i.e., CALPHAD (acronym of *CALculation of PHAse Dia-grams*)), experimental phase diagram inspection, ab initio molecular dynamics (AIMD) simulations, Monte Carlo simulations, and density functional theory (DFT) calculations. These theoretical efforts are all addressed in Chaps. 2 and 8, 9, 10, 11, 12 and 13, and hundreds of model-predicted single-phase HEAs with the face-centered cubic (FCC), body-centered cubic (BCC), and hexagonal close-packed (HCP) structures are provided in Chap. 11.

Detailed descriptions on the physical metallurgy of HEAs, which plays a center role in understanding their processing/structure/properties' relationships, are presented in Chap. 3. The impact on thermodynamics, kinetics, phase transformations, and properties from high entropy is evident, and the lattice distortion effect is regarded to be critical to the claimed properties unique to HEAs. Chapter 4 overviews advanced microstructure characterization tools, such as high-resolution scanning transmission electron microscopy (STEM), analytical transmission electron microscopy (TEM), three-dimensional atom probe, and neutron and synchrotron scattering for characterizing HEAs. Then fabrication routes via liquid, solid, and gas states are illustrated in Chap. 5, including ingot metallurgy, powder metallurgy, coating, rapid solidification, mechanical alloying, single-crystal preparation using the Bridgman method, laser cladding, and thin-film sputtering.

Mechanical properties of HEAs, which include tension, compression, hardness, wear, fracture, fatigue, and creep behavior, are reviewed in Chap. 6 in a comprehensive manner. Compositional, temperature, and temporal dependences of their mechanical behavior where available are also reviewed. Functional properties are reviewed in Chap. 7, including electrical, magnetic, electrochemical, and hydrogen storage properties of HEAs. As a special category of HEAs, the research progress in high-entropy BMGs is presented in Chap. 13, covering compositions, glass-forming ability, mechanical properties, and atomic structures and diffusion constants predicted from AIMD simulations. Chapter 14 describes the processing, microstructure, and properties of thick or thin HEA films on substrates for protection, function-enhancement, and/or decoration purposes.

It is worth mentioning that this book contains substantial amounts of pioneering unpublished computer modeling work, as presented in Chaps. 8–13. Chapter 8 first describes DFT calculations of phase stability of HEAs at zero temperature using the cluster expansion method, molecular dynamics simulations, and Monte Carlo simulations and then applies them to predict phase transformations in three

quaternary refractory BCC HEAs and, more importantly, their entropy sources. The applications of the coherent potential approximation (CPA) to HEAs are reviewed in Chap. 9, and the thermodynamic, magnetic, electronic, and elastic properties of selected HEAs are presented. Chapter 10 details the construction of special quasi-random structure (SQS) and their applications to determine structural stability, lattice vibrational property, electronic structure, elasticity, and stacking fault energy in quaternary and quinary FCC, BCC, and HCP HEAs. Both the positive and negative vibrational entropies of mixing are illustrated for selected FCC and BCC HEAs, respectively. The development and applications of CALPHAD thermodynamic databases for HEAs are detailed in Chap. 12, and the thermodynamic properties (entropy, enthalpy, and Gibbs energy) of FCC and BCC HEA systems are presented as a function of temperature and composition. The calculated entropies of mixing in selected FCC and BCC HEAs are consistent with the DFT calculations presented in Chaps. 8 and 10. Comparisons in the phase stability and solidification from model predictions with experiments are also highlighted.

We are very grateful for the following scientists who kindly reviewed one or more chapters of this book: Dan Dorescu, Sheng Guo, Shengmin Guo, Derek Hass, Jeffrey A. Hawk, Ursula Kattner, Laszlo J. Kecskes, Rajiv Mishra, Oleg Senkov, Zhi Tang, Fuyang Tian, Levente Vitos, Weihua Wang, Mike Widom, Quan Yang, Fan Zhang, and Margaret Ziomek-Moroz.

Finally we would like to thank all contributors for their effort and patience.

Albany, OR, USA
Hsinchu, Taiwan, Republic of China
Knoxville, TN, USA
Beijing, People's Republic of China
October 2015

Michael C. Gao
Jien-Wei Yeh
Peter K. Liaw
Yong Zhang

Contents

1	Overview of High-Entropy Alloys	1
	Jien-Wei Yeh	
2	Phase Formation Rules	21
	Yong Zhang, Sheng Guo, C.T. Liu, and Xiao Yang	
3	Physical Metallurgy	51
	Jien-Wei Yeh and Louis J. Santodonato	
4	Advanced Characterization Techniques	115
	Louis J. Santodonato and Peter K. Liaw	
5	Fabrication Routes	151
	Yong Zhang, Carl C. Koch, Sheng Guo Ma, Hui Zhang, and Ye Pan	
6	Mechanical Properties of High-Entropy Alloys	181
	Haoyan Diao, Xie Xie, Fei Sun, Karin A. Dahmen, and Peter K. Liaw	
7	Functional Properties	237
	Jien-Wei Yeh, Swe-Kai Chen, Han C. Shih, Yong Zhang, and Ting Ting Zuo	
8	Prediction of Structure and Phase Transformations	267
	Michael Widom	
9	Applications of Coherent Potential Approximation to HEAs	299
	Fuyang Tian, Yang Wang, Douglas L. Irving, and Levente Vitos	

10 Applications of Special Quasi-random Structures to High-Entropy Alloys	333
Michael C. Gao, Changning Niu, Chao Jiang, and Douglas L. Irving	
11 Design of High-Entropy Alloys	369
Michael C. Gao	
12 CALPHAD Modeling of High-Entropy Alloys	399
Chuan Zhang and Michael C. Gao	
13 High-Entropy Metallic Glasses	445
Akira Takeuchi, Michael C. Gao, Junwei Qiao, and Michael Widom	
14 High-Entropy Coatings	469
Jien-Wei Yeh, Su-Jien Lin, Ming-Hung Tsai, and Shou-Yi Chang	
15 Potential Applications and Prospects	493
Jien-Wei Yeh, An-Chou Yeh, and Shou-Yi Chang	
Index	513

Contributors

Shou-Yi Chang Department of Materials Science and Engineering, National Tsing Hua University, Hsinchu, Taiwan, Republic of China

Swe-Kai Chen Center for Nanotechnology, Materials Science, and Microsystems, National Tsing Hua University, Hsinchu, Taiwan, Republic of China

Karin A. Dahmen Department of Physics, University of Illinois at Urbana-Champaign, Urbana, IL, USA

Haoyan Diao Department of Materials Science and Engineering, The University of Tennessee, Knoxville, TN, USA

Michael C. Gao National Energy Technology Laboratory/AECOM, Albany, OR, USA

Sheng Guo Department of Materials and Manufacturing Technology, Chalmers University of Technology, Gothenburg, SE, Sweden

Douglas L. Irving Department of Materials Science and Engineering, North Carolina State University, Raleigh, NC, USA

Chao Jiang Thermo-Calc Software Inc., Pittsburgh, PA, USA

Carl C. Koch Department of Materials Science and Engineering, North Carolina State University, Raleigh, NC, USA

Peter K. Liaw Department of Materials Science and Engineering, The University of Tennessee, Knoxville, TN, USA

Su-Jien Lin Department of Materials Science and Engineering, National Tsing Hua University, Hsinchu, Taiwan, Republic of China

C. T. Liu Department of Mechanical and Biomedical Engineering, City University of Hong Kong, Kowloon Tong, Hong Kong, People's Republic of China

Sheng Guo Ma Institute of Applied Mechanics and Biomedical Engineering, Taiyuan University of Technology, Taiyuan, Shanxi Province, People's Republic of China

Changning Niu Department of Materials Science and Engineering, North Carolina State University, Raleigh, NC, USA

Ye Pan School of Material Science and Engineering, Southeast University, Nanjing, People's Republic of China

Junwei Qiao College of Materials Science and Engineering, Taiyuan University of Technology, Taiyuan, Shanxi Province, China

Louis J. Santodonato Division of Instrument and Source, Oak Ridge National Laboratory, Oak Ridge, TN, USA

Materials Science and Engineering Department, The University of Tennessee, Knoxville, TN, USA

Han C. Shih Institute of Nanomaterials, Chinese Culture University, Taipei, Taiwan, Republic of China

Fei Sun Department of Physics, University of Illinois at Urbana-Champaign, Urbana, IL, USA

Akira Takeuchi Institute for Materials Research, Tohoku University, Sendai, Japan

Fuyang Tian Institute for Applied Physics, University of Science and Technology Beijing, Beijing, China

Applied Materials Physics, Department of Materials Science and Engineering, Royal Institute of Technology, Stockholm, Sweden

Ming-Hung Tsai Department of Materials Science and Engineering, National Chung Hsing University, Taichung, Taiwan, Republic of China

Levente Vitos Applied Materials Physics, Department of Materials Science and Engineering, Royal Institute of Technology, Stockholm, Sweden

Division of Materials Theory, Department of Physics and Astronomy, Uppsala University, Uppsala, Sweden

Wigner Research Centre for Physics, Institute for Solid State Physics and Optics, Budapest, Hungary

Yang Wang Pittsburgh Supercomputing Center, Pittsburgh, PA, USA

Michael Widom Department of Physics, Carnegie Mellon University, Pittsburgh, PA, USA

Xie Xie Department of Materials Science and Engineering, The University of Tennessee, Knoxville, TN, USA

Xiao Yang State Key Laboratory for Advanced Metals and Materials, University of Science and Technology Beijing, Beijing, People's Republic of China

An-Chou Yeh Department of Materials Science and Engineering, National Tsing Hua University, Hsinchu, Taiwan, Republic of China

Jien-Wei Yeh Department of Materials Science and Engineering, National Tsing Hua University, Hsinchu, Taiwan, Republic of China

Chuan Zhang CompuTherm LLC, Madison, WI, USA

Hui Zhang School of Materials Science and Engineering, Anhui University of Technology, Ma'anshan, Anhui, People's Republic of China

Yong Zhang State Key Laboratory for Advanced Metals and Materials, University of Science and Technology Beijing, Beijing, People's Republic of China

Ting Ting Zuo State Key Laboratory for Advanced Metals and Materials, University of Science and Technology Beijing, Beijing, People's Republic of China

Chapter 1

Overview of High-Entropy Alloys

Jien-Wei Yeh

Abstract Alloys have evolved from simple to complex compositions depending on the ability of mankind to develop the materials. The resulting improved functions and performances of alloys enable advancements in civilizations. In the last century, significant evolution and progress have led to the invention of special alloys, such as stainless steels, high-speed steels, and superalloys. Although alloys composed of multiple elements have higher mixing entropy than pure metals, the improved properties are mostly due to mixing enthalpy that allows the addition of suitable alloying elements to increase the strength and improve physical and/or chemical properties. Since the turn of the century, more complex compositions with higher mixing entropies have been introduced. Such complex compositions do not necessarily guarantee a complex structure and microstructure, or the accompanied brittleness. Conversely, significantly higher mixing entropy from complex compositions could simplify the structure and microstructure and impart attractive properties to the alloys. Jien-Wei Yeh and Brian Cantor independently announced the feasibility of high-entropy alloys and equi-atomic multicomponent alloys in reports published in 2004. This breakthrough in alloying concepts has accelerated research on these new materials throughout the world over the last decade.

Keywords Binary alloys • Multicomponent alloys • Multi-principal-element alloys • High-entropy alloys (HEAs)

1.1 Historical Development of Alloys

The history of civilization is closely related with the development of new materials. During the Stone Age, natural materials used by ancient people included stone, wood, leather, bone, and native metals, such as gold, silver, and copper. These materials cover three basic material categories: ceramics, polymers, and metals. After the Stone Age, subsequent ages (i.e., Bronze, Iron, and Steel) successively

J.-W. Yeh (✉)

Department of Materials Science and Engineering, National Tsing Hua University,
Hsinchu, Taiwan 30013, Republic of China

e-mail: jwye@mx.nthu.edu.tw

came to be because of easier reduction of copper, tin, lead, mercury, and iron from their respective ores. This led to the development of the technology to produce these materials in large quantities. Alloying copper mainly with tin and lead and alloying iron mainly with the carbon from the combustion fuels created copper alloys, cast iron, and steels. Most have superior combinations of strength and toughness when compared with the ceramics and polymers of ancient times. These led to efficient applications for daily life, transportation, construction, and weapons.

The discovery of additional metal elements was slow due to poor deposits or great difficulty in reduction and extraction. However, significant progress occurred after the First Industrial Revolution, which began in England circa 1750. With the discovery and production of new elements by various technologies, new alloys were gradually developed and applied to common and special applications. This caused rapid advancements. Approximately 30 alloy systems, each based on one principal metal element, were developed and commercialized [1]. Well-known industrial alloys include high-speed steels, Stellite alloys, stainless steels, aluminum alloys, alnico alloys, permalloys, Cu-Be alloys, superalloys, and titanium alloys. Newly developed alloys from the mid-twentieth century include Ni-Al, Ti-Al, and Fe-Al intermetallic compounds and alloys and metallic glasses for special applications [2–4].

1.2 The Concept of Multicomponent Alloys

Traditionally, the utilization of native metals and artificial alloys from extractive elements is almost entirely based on one principal element or compound. Although pure metal elements with minimal impurities are used in jewelry, electrical, optical, and other special applications, alloying elements improves specific mechanical, physical, or chemical properties for specific applications. Thus, most practical alloys are multicomponent compositions. Making food by mixing or blending different ingredients is a comparable example, i.e., it is easy to blend fruit and vegetables to make mixed juices. Although some solid contents could be included for different taste and nutrition, mixed juice is typically homogenous, even when equal amounts of different fruit and vegetables are used. By similar thinking, metallurgists tried to synthesize new alloys by mixing many metal elements together, each in large proportions. However, this route is not encouraged because melting and casting the metals require a high temperature and the cast alloys often become hard and brittle. Franz Karl Archard, a German scientist and metallurgist in the late of eighteenth century, is possibly the only known researcher cited in literature as having studied multicomponent equi-mass alloys [5]. With five to seven elements selected from eight common elements at that time, including iron, copper, tin, lead, zinc, bismuth, antimony, and arsenic, his results showed that the properties of the alloys are diverse but not attractive. Clearly, this is the reason why

alloys with multiple principal alloying elements in high proportions were not realized during ancient times.

Even in modern times, the research and development of multicomponent alloys other than those based on one major element or one compound is not encouraged in physical metallurgy and materials science. The information based on binary or ternary phase diagrams perpetuates this fact [6]. Most phase diagrams show intermetallic compounds (IMs), which are ordered structures with compositions in stoichiometric ratio or near-stoichiometric ratio, or intermediate phases (IPs), which are compound-type solid solutions with relatively a wide composition range, also called as intermetallic phases [7]. For example, Al-Cu and Cu-Zn phase diagrams have 13 and 5 equilibrium phases of the IMs or IPs, respectively. Ternary phase diagrams are more complex in the variety of IMs or IPs than the binary phase diagrams. For example, the Al-Cu-Zn phase diagram has more than 20 equilibrium IMs or IPs in the solid state, including those extended from the Al-Cu and Cu-Zn binary phase diagrams. Quaternary phase diagrams cannot exist in a three-dimensional form except when one or more variables are fixed. Nevertheless, quaternary phase diagrams are expected to have a larger number of equilibrium IMs or IPs based on the upward trend from the binary to ternary systems. Besides this, alloys with a larger number of alloying elements typically have more equilibrium or nonequilibrium IMs or IPs. For example, adding different transition metals, such as Fe, Co, Ti, V, Sc, Mn, Cr, and Zr, in a small amount (e.g., ~4 wt%) into Al alloys, could form at least nine binary IMs or IPs (without counting possible ternary compounds) in the Al matrix according to their respective binary phase diagrams with Al. As a result, it is natural to expect that incorporating a larger number of components in high concentrations would lead to a complex microstructure with a large variety of IMs or IPs. Obviously, this discourages people from developing multicomponent alloys with higher contents of alloying elements. Therefore, the conventional concept still dominates the field of alloy development, including design, production, and applications. Any trial contrary to this concept is generally thought to be unreasonable and worthless. Thus, the possibility of discovering special microstructures, properties, and applications is still restricted in the traditional alloying concept. From a broader perspective, alloy information related to materials science and engineering and solid-state physics will be incomplete without a thorough understanding of alloys with multiple principal elements.

1.3 Ignition of the Research on High-Entropy Alloys

Two independent publications in 2004 by Jien-Wei Yeh in Taiwan and Brian Cantor in the United Kingdom, as well as a dependent publication in 2003 by S. Ranganathan in India, ignited research on the rarely touched alloy world [8–10]. A brand-new alloy concept, “high-entropy alloys (HEAs)” or “multi-principal-element alloys (MPEAs),” was brought into existence and investigated through increased experimental studies. This new concept placed a new milestone in the

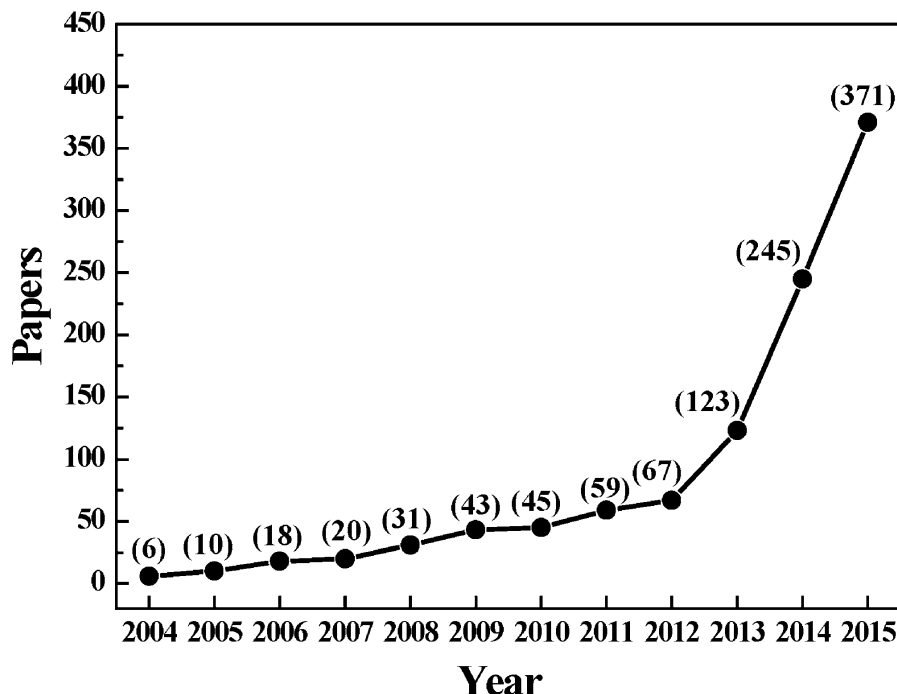


Fig. 1.1 Publications related with HEAs until the end of 2015

history of alloy development. During the following decade, extensive research has been conducted worldwide. This is reflected in Fig. 1.1, showing the increased number of journal publications related to HEAs.

1.3.1 Brian Cantor's Pioneering Work

In 1981, Cantor initiated research on equi-atomic multicomponent alloys with his undergraduate student Alain Vincent [11]. One of the experimental alloys had 20 components. They found that only one composition of $\text{Co}_{20}\text{Cr}_{20}\text{Fe}_{20}\text{Mn}_{20}\text{Ni}_{20}$, in atomic percentage, is of a single FCC phase, which means that all these five elements are mixed into a solid solution. The work was unpublished except in Vincent's thesis at Sussex University. Another undergraduate student, Peter Knight, at Oxford University in 1998, performed similar studies on a wider range of alloys. His work supported previous conclusions and presented new results, but it was also unpublished besides his thesis at Oxford. Circa 2002, Isaac Chang performed further research on such alloys at Oxford and presented the results at the Rapidly Quenched Metals conference in Bangalore in 2002. This was published in *Materials Science and Engineering A* in July 2004 [9].

In this paper, entitled *Microstructural development in equiatomic multicomponent alloys* [9], Cantor provided several important conclusions. First, equi-atomic alloys containing 20 components (i.e., 5 at.% of Mn, Cr, Fe, Co, Ni, Cu, Ag, W, Mo, Nb, Al, Cd, Sn, Pb, Bi, Zn, Ge, Si, Sb, and Mg) and another equi-atomic alloy composed of 16 elements (i.e., 6.25 at.% of Mn, Cr, Fe, Co, Ni,

Cu, Ag, W, Mo, Nb, Al, Cd, Sn, Pb, Zn, and Mg) are multiphase, crystalline, and brittle. This was observed for both the as-cast condition obtained by induction melting under Ar and the rapid-solidified condition obtained by melt spinning. Surprisingly, he found that the alloys consisted predominantly of a single FCC primary phase that contains many elements but is particularly rich in transition metals, notably Cr, Mn, Fe, Co, and Ni. Based on this observation, a five-component $\text{Co}_{20}\text{Cr}_{20}\text{Fe}_{20}\text{Mn}_{20}\text{Ni}_{20}$ alloy formed a single FCC solid solution with a typical dendritic structure in the as-cast condition. Further, based on this composition, a wide range of six- to nine-component alloys were examined through the addition other elements, such as Cu, Ti, Nb, V, W, Mo, Ta, and Ge. They all exhibited the primary dendrite of the FCC phase with substantial amounts of other transition metals, such as Nb, Ti, and V. In contrast, more electronegative elements, such as Cu and Ge, are rejected from dendrite regions into the interdendritic regions. He made an important conclusion that the total number of phases is always significantly less than the maximum equilibrium number allowed by the Gibbs phase rule and even less than the maximum number allowed under nonequilibrium solidification conditions.

1.3.2 Jien-Wei Yeh's Pioneering Work

In 1995, Yeh began exploring the world of MPEAs [12]. He believed that high mixing entropy could enhance mixing among components and reduce the number of phases. Figure 1.2 shows a solid solution forming a crystal structure with ten types of dissolved atoms and a solid solution forming an amorphous structure simulated by eight types of coins with large size differences. In this exploration, he first needed to ensure there was a possibility of synthesizing such alloys from raw elemental materials. With the help of Prof. S.K. Chen, his supervised graduate student, K.S. Huang, successfully produced the first whole-piece ingot, ~100 g, in a

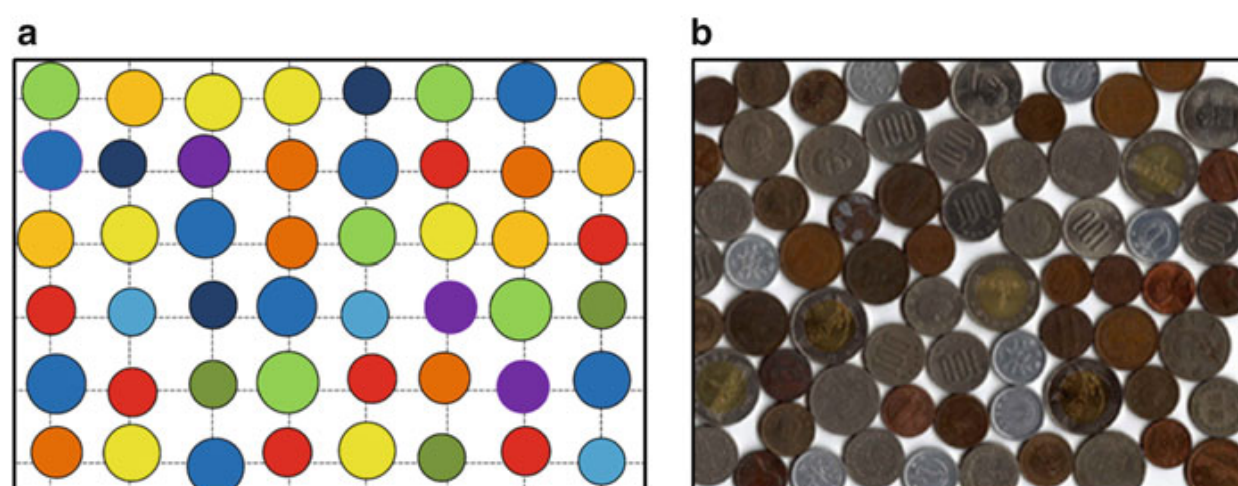


Fig. 1.2 (a) A schematic crystal structure with ten kinds of atoms and (b) a simulated amorphous structure with eight kinds of coins

bowl-shape water-cooled crucible using the arc-melting method [12]. After this success, around 40 equi-atomic alloys, each with 59 components, were prepared by arc melting. Investigations were then conducted on the microstructure, hardness, and corrosion resistance of the as-cast state and fully annealed state of these alloys. From this data, 20 experimental alloys based on Ti, V, Cr, Fe, Co, Ni, Cu, Mo, Zr, Pd, and Al (with or without 3 at.% B addition) were chosen and discussed in his master thesis at the National Tsing Hua University in 1996 [12]. They are categorized into three equi-atomic series differing in Cu, Al, and Mo. Each series varies from 6-components to 9-components, i.e., Cu, Al, or Mo + TiVFeNiZr + Co + Cr + Pd + 0 or 3 at.% B. Based on this study, the typical dendritic structure was observed in the as-cast structure. All alloys have a high hardness level in the range from 590 to 890 HV, depending on the composition and fabrication conditions, as-cast or fully annealed. The full annealing treatment generally retains a similar hardness level of the as-cast state. In each series, a higher number of components increase the hardness, but the nine-component alloys display a small decrease in hardness. Small additions of B could lead to an increase in hardness. In the discussion on these trends, a large lattice distortion and stronger bonding were proposed to explain the strong solid solution hardening. It is noteworthy that all X-ray diffraction (XRD) patterns of these alloys were unidentified and left without any indication of diffraction plane indices in the thesis. The unidentified patterns were due to the innocence at this initial stage of research. Yeh thought that their crystal structures might be new and unseen in the data bank of X-ray diffraction. In general, all of these alloys displayed very good corrosion resistance, which was assessed by their weight loss after immersion in four acidic solutions of HCl, H₂SO₄, HNO₃, and HF, each with 0.01 and 1M concentrations, for 24 h, respectively. The addition of effective passive elements, such as Cr and Mo, and the benefit of a low free energy due to high mixing entropy were thought to contribute to the corrosion resistance. This study also suggested that the high-entropy effect, lattice distortion effect, and slow diffusion effect would exist in such alloys.

After this study, two master theses were written covering similar HEA alloy concepts [13, 14]. Then, more colleagues, including S.J. Lin, T.S. Chin, J.Y. Gan, and T.T. Shun, were invited to join HEAs research. Nine different studies were performed from 2000 to 2003 [15–23]: five studies on HEAs bulk alloys concerning deformation behavior, wear behavior, and annealing behavior, two studies on HEA thin films deposited by magnetron sputtering, and two on HEA thermal spray coatings. As of 2014, Yeh has supervised 84 master students and 11 PhD students in this exciting area.

In Feb. 2004, the first HEA paper, entitled *Multi-principal-element alloys with improved oxidation and wear resistance for thermal spray coating*, was published in *Advanced Engineering Materials* [24]. In May 2004, the second HEA paper, entitled *Nanostructured high-entropy alloys with multi-principal elements - novel alloy design concepts and outcomes*, was also published in the same journal. This paper is the first to elucidate the concept of HEAs by providing experimental results and related theories [8]. In this paper, their promising properties were shown to be potentially suitable for many applications, such as tools, molds, dies, and

mechanical parts as well as anticorrosive high-strength parts in chemical plants, IC foundries, and even marine applications. In addition, coating technology could further expand the applications of HEAs to functional films, such as hard-facing and diffusion barriers. Thus, the HEAs concept is not simply a compositional concept, but may lead to a new and uncharted territory with many possible materials, new phenomena, new theories, and new applications.

Later in 2004, two papers, entitled *Wear resistance and high-temperature compression strength of FCC CuCoNiCrAl_{0.5}Fe alloy with boron addition* and *Formation of simple crystal structures in solid-solution alloys with multi-principal metallic elements*, were published in *Metallurgical and Materials Transactions A* [25, 26]. In addition, one paper, entitled *Nanostructured nitride films of multi-element high-entropy alloys by reactive DC sputtering*, was published in *Surface and Coatings Technology* in the same year [27]. This paper also marked the historical milestone of the initial development of high-entropy ceramics (HECs), such as HE nitrides, HE carbides, HE carbonitrides, and HE oxides. By the end of 2014, Yeh and his colleague published 111 journal articles related with HEAs. Using these HEAs concepts, developments in the materials world have been extended to high-entropy materials (HEMs) although high-entropy polymers (HEPs) have not yet been published.

1.3.3 *Srinivasa Ranganathan's Alloyed Pleasure in 2003*

S. Ranganathan is a significant scientist in the ignition of HEAs. Ranganathan is the Senior Scientist Platinum Jubilee Fellowship of the National Academy of Sciences, India. He has contributed to the understanding of the structure of interfaces, quasicrystals, bulk metallic glasses, and nanostructured materials. He also spent extensive time investigating novel multicomponent alloys. Through the communications and discussions on this unknown field with J.W. Yeh, his article entitled “Alloyed pleasures – multimetallic cocktails” was published in *Current Science* in Nov. 2003 [10]. In this article, he reviews three new alloy areas: bulk metallic glasses by A. Inoue, superelastic and superplastic alloys (or gum metals) by T. Saito, and HEAs by J.W. Yeh. Thus, this article is the first journal publication on HEAs.

In this article, Ranganathan described the limitations metallurgists face with multicomponent alloys in the following paragraphs:

Metallurgists confined themselves to systems where the number of alloying elements was limited in any one phase. This was partly because as alloys are made with an increasing number of component metals, the database necessary in terms of phase diagram information increases sharply. If the processing variables are superimposed leading to metastable phases and altered microstructures, the possibilities become astronomical. In fact, one German scientist estimated the possibilities to exceed the number of atoms in the entire universe! In the presence of such cornucopia metallurgists retreated to produce alloys with a few components and assume that incremental improvement is the only possible route.

He also said that *the multi-component alloys represent a new frontier in metallurgy. They require hyper-dimensions to visualize. If we use a coarse mesh of 10 at. % for mapping a binary system, the effort involved in experimental determination of phase diagrams rises steeply. Thus, the effort of experimental determination of a seven component system will be 10⁵ times that of a binary diagram and will alone need as much effort as has been spent over the last hundred years in establishing ~4000 binary and ~8000 ternary diagrams. While the computation of phase diagrams from first principles has made impressive progress in the last decade, the prospect of calculation of higher order systems is a daunting task. In this scenario we have explorers like A. Inoue, T. Saito and J.W. Yeh pointing to exciting new alloys with applications.*

In May 2004, Ranganathan traveled to Taiwan to visit Yeh in order to further understand and discuss HEAs. In Nov. 2005, he invited Yeh and his colleague S.K. Chen to attend the international symposium, “Frontiers in Design of Materials 2005,” held at the Indian Institute of Technology Madras in Chennai, India. Yeh gave a presentation with the topic “Novel Alloy Concept, Challenges, and Opportunities of High-Entropy Alloys”. In Jan. 2007, he again invited Yeh to give a talk, entitled “Molecular Dynamics Simulation for Multi-elemental Effects on the Glass Formability of Equal-mole Alloys,” in the workshop on Bulk Metallic Glasses: Science and Technology (BMG 2007) at the Indian Institute of Science in Bangalore, India. Through his invitation, high-entropy alloy concept quickly propagated to the large international attendance at the talks.

1.4 Definition of High-Entropy Alloys

Before introducing the definition of HEAs, an understanding is needed on the mixing entropy and configuration entropy of alloys, arising from the mixing of pure components. From statistical thermodynamics, Boltzmann’s equation [28, 29] calculates the configurational entropy of a system:

$$\Delta S_{\text{conf}} = k_B \ln w \quad (1.1)$$

where k_B is Boltzmann’s constant and w is the number of ways in which the available energy can be mixed or shared among the particles in the system. For a random n -component solid solution, in which the i th component has a mole fraction X_i , its ideal configurational entropy per mole is

$$\Delta S_{\text{conf}} = -R \sum_{i=1}^n X_i \ln X_i \quad (1.2)$$

where R is the gas constant, 8.314 J/K/mol.

Table 1.1 Ideal configurational entropies in terms of R for equi-atomic alloys with constituent elements up to 13 [31]

n	1	2	3	4	5	6	7	8	9	10	11	12	13
ΔS_{conf}	0	0.69	1.1	1.39	1.61	1.79	1.95	2.08	2.2	2.3	2.4	2.49	2.57

Consider an equi-atomic alloy in its liquid state or regular solid solution state. Its configurational entropy per mole is calculated as [8, 30]

$$\Delta S_{\text{conf}} = -k \ln w = -R \left(\frac{1}{n} \ln \frac{1}{n} + \frac{1}{n} \ln \frac{1}{n} + \cdots + \frac{1}{n} \ln \frac{1}{n} \right) = -R \ln \frac{1}{n} = R \ln n \quad (1.3)$$

Although the total mixing entropy has four contributions: configurational, vibrational, magnetic dipole, and electronic randomness, configurational entropy is dominant over the other three contributions [8] agreeing with theoretical predictions presented in Chaps. 8 and 10. Hence, the configurational entropy often represents the mixing entropy in order to avoid difficult calculations to determine the other three contributions. Table 1.1 lists the configurational entropies of equi-atomic alloys in terms of the gas constant R . The configurational entropy increases as the number of elements increases. The entropy change per mole, ΔS_f , from a solid to a liquid during melting is approximately one gas constant R for metals, which is defined as Richard's rule. Moreover, the enthalpy change or latent heat per mole during melting, ΔH_f , correlates with ΔS_f by the equation: $T_m \Delta S_f = \Delta H_f$ because the free energy change, ΔG_f , is zero. From the bond number difference in the solid and the liquid, ΔH_f is regarded as the energy required to destroy approximately one-twelfth of all bonds in the close-packed solid of one mole. Thus, $T_m R$ is approximately equal to one-twelfth of the bonding energy in the close-packed solid of one mole. This demonstrates that mixing entropy of R per mole of an alloy is significant and RT is comparable with the mixing enthalpy per mole arising from the bonding energy difference between the alloyed state and the unalloyed state. As a result, the mixing entropy of R per mole is significantly large in lowering the mixing free energy by an amount of RT , especially at high temperatures (e.g., $RT = 8.314 \text{ kJ/mol}$ at 1000 K).

If the strain energy effect due to the atomic size difference is not considered, the mixing enthalpy from chemical bonding and the mixing entropy are the two main factors that determine the equilibrium state. In contrast to negative mixing enthalpy (the driving force to form compounds) and positive mixing enthalpy (the driving force to form a segregated state), mixing entropy is the driving force to form a random solid solution. Thus, the actual equilibrium state depends on the competition among the relative values of different states. For example, dividing the formation enthalpies of two typical strong intermetallic compounds, NiAl and TiAl, by their respective melting points obtains $1.38R$ and $2.06R$, respectively [8]. This means the driving force for forming strong compounds is of this order. On the other hand, the formation enthalpy of Cr-Cu and Fe-Cu

are 12 and 13 kJ/mol, respectively. Dividing the formation enthalpies by the melting point of Cu obtains $1.06R$ and $1.15R$, respectively. Thus, it is reasonable to think that the mixing entropy of $1.5R$ per mole is relatively large to compete with the mixing enthalpy and there is a higher probability to form solid solutions. Shown in Table 1.1, the ideal configurational entropy of a 5-element alloy is $1.61R$ [31]. Hence, a system with at least five elements would have larger probability to form solid solutions. Although a random solid solution might not form in most cases, the solid solutions with a high degree of randomness are easier to obtain. Thus, high mixing entropy enhances mutual solubility among constituent elements and effectively reduces the number of phases, especially at high temperatures.

Based on the above considerations, there are two definitions for “high-entropy alloys” [31]. One is based on composition and the other is based on configurational entropy. For the former, HEAs are preferentially defined as alloys containing at least five principal elements, each with an atomic percentage between 5 and 35 %. The atomic percentage of each minor element, if any, is hence less than 5 %. This definition is expressed as

$$n_{\text{major}} \geq 5 \quad 5\% \leq X_i \leq 35\% \quad \text{and} \quad n_{\text{minor}} \geq 0 \quad X_j \leq 5\%, \quad (1.4)$$

where n_{major} and n_{minor} are the number of major elements and minor elements, respectively. X_i and X_j are the atomic percentages of major element i and minor element j , respectively.

For the later, HEAs are defined as alloys having configurational entropies at a random state larger than $1.5R$, no matter they are single phase or multiphase at room temperature. This is expressed as

$$\Delta S_{\text{conf}} \geq 1.5R \quad (1.5)$$

Although each definition covers a wide range of alloys, both definitions overlap for the most part. The compositions in non-overlapping regions are also regarded as HEAs. For example, $\text{CoCrCu}_{0.2}\text{Fe}_{0.2}\text{Ni}$ in atomic ratio (or molar ratio) is HEAs by the composition definition since it is also $\text{Co}_{29.4}\text{Cr}_{29.4}\text{Cu}_{5.9}\text{Fe}_{5.9}\text{Ni}_{29.4}$ in atomic percentage. However, their configurational entropy is approximately $1.414R$, which does not fit into the high-entropy definition. Under this condition, this alloy is still considered a HEA. Another example is an equimolar alloy with 25 elements. Although each element has a concentration of 4 at.% in the composition, this alloy is still a HEA since the configurational entropy is $3.219R$. Thus, an alloy with a composition fitting only one of the two definitions could be also regarded as a HEA. As for the quaternary equimolar alloy CoCrFeNi , it is sometimes considered a HEA in literature because its composition and configurational entropy are close to the lower limits of both definitions. Thus, the definitions of HEAs are guidelines, not laws.

From the two definitions of HEAs, it is realized that the basic principle behind HEAs with multiple principal elements is to have high mixing entropy in order to

enhance the formation of solid solution phases and inhibit the formation of intermetallic compounds. This principle is thus very important to avoid complicated structure and brittleness for HEAs. It further guarantees that most HEAs can be feasibly synthesized, processed, analyzed, manipulated, and used. Among various thermodynamic factors such as mixing enthalpy, mixing entropy, atomic size difference, valence electron concentration, and electronegativity, because mixing entropy is the only factor which increases with increasing the number of principal components, the name “high-entropy alloys” is pertinent for MPEAs.

As $1.5R$ is a lower limit for HEAs, we further define medium-entropy alloys (MEAs) and low-entropy alloys (LEAs) to differentiate the power of the mixing entropy effect. Here, $1R$ is the boundary between medium-entropy and low-entropy alloys since a mixing entropy less than $1R$ is expected to be much less competitive with a larger mixing enthalpy. That is,

$$\text{For MEAs: } 1.0R \leq \Delta S_{\text{conf}} \leq 1.5R \quad (1.6)$$

$$\text{For LEAs: } \Delta S_{\text{conf}} \leq 1.0R \quad (1.7)$$

Table 1.2 provides the configurational entropies calculated for typical traditional alloys at their liquid state or random state [31]. This table shows that most alloys have low entropies. Further, some concentrated alloys such as Ni-based, Co-based superalloys, and BMGs have medium entropies between 1 and $1.5R$. Figure 1.3 shows the types of alloys in the alloy world based on configurational entropy. This demonstrates that HEAs are an extension from LEAs and MEAs from the entropy viewpoint. The HEAs are not entirely alloys with complex structures and useless properties as predicted by traditional experiences and concepts.

Table 1.2 Configurational entropies calculated for typical traditional alloys at their liquid state or random state [31]

Systems	Alloys	ΔS_{conf} at liquid state
Low-alloy steel	4340	$0.22R$ low
Stainless steel	304	$0.96R$ low
	316	$1.15R$ medium
High-speed steel	M2	$0.73R$ low
Mg alloy	AZ91D	$0.35R$ low
Al alloy	2024	$0.29R$ low
	7075	$0.43R$ low
Cu alloy	7-3 brass	$0.61R$ low
Ni-based superalloy	Inconel 718	$1.31R$ medium
	Hastelloy X	$1.37R$ medium
Co-based superalloy	Stellite 6	$1.13R$ medium
BMG	$\text{Cu}_{47}\text{Zr}_{11}\text{Ti}_{34}\text{Ni}_8$	$1.17R$ medium
	$\text{Zr}_{53}\text{Ti}_5\text{Cu}_{16}\text{Ni}_{10}\text{Al}_{16}$	$1.30R$ medium

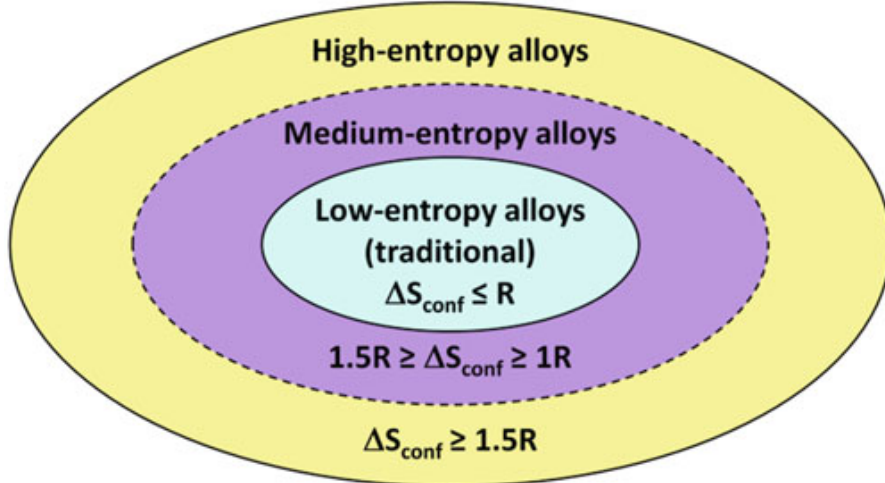


Fig. 1.3 Types of alloys in the alloy world based on configurational entropy [31]

1.5 Clarification on Some Misunderstandings

Historically, there exists a common misconception that compositions such as those of HEAs would have complex structure and be brittle by nature, as mentioned in Sect. 1.2. Even modern physical metallurgy carelessly consolidates this misconception, because adding larger amounts of an alloying element into an alloy often leads to an intermetallic compound or phase. A larger number of alloy elements in large proportion in an alloy tend to form more intermetallic compounds or phases between a host element and alloying elements (based on binary phase diagrams) and even between alloying elements (based on ternary phase diagrams). By the concept of HEAs, this misconception is overcome through the understanding that high mixing entropy could enhance the formation of solid solutions. However, new misunderstandings might arise if the definitions of HEAs and the literature on HEAs are not better understood. One predominant misconception is that HEAs would be easy to form metallic glasses. Another is that a HEA would be a simple multielement solid solution. In addition, some think that HEAs are unstable in nature, whereas some think that HEAs are actually very stable.

In fact, most HEAs processed through traditional melting-and-casting route are crystalline, and only special compositions could be amorphous. For example, $Pd_{20}Pt_{20}Cu_{20}Ni_{20}P_{20}$ was reported to be a high-entropy, bulk metallic glass (HE-BMGs) [32]. Special processes, such as mechanical alloying, rapid solidification, and thin-film deposition, also easily enhance the formation of an amorphous structure. However, it must be mentioned that increasing the number of elements has a stronger tendency to lead to topological disorder, like an amorphous structure or even a liquid-like one, as revealed by the molecular dynamics simulation results [33]. This is likely related to the confusion principle proposed by Turnbull [34, 35] and Greer [36]. This principle stipulates that more components constituting an alloy will lead to a lower chance of selecting viable crystal structures and thus have greater glass formability. This implies the manifestation of high-entropy effect and sluggish diffusion effect, both of which enhance the tendency to mix and

randomize the component atoms. If the atomic size difference is sufficient to cause topological instability, an amorphous structure is easier to form upon relatively higher cooling rates.

HEAs will not necessarily form single multi-element random (disordered) solid solutions. Besides high mixing entropy, there are other factors acting against the formation of random solid solution, including mixing enthalpy, atomic size difference, and valence electron concentration, which will be discussed in Chaps. 2 and 3. High mixing entropy enhances the formation of solid solutions but does not guarantee the formation of a single random solid solution. It was for this reason that Gao et al. developed an effective strategy for discovering single-phase HEAs, which combined ab initio molecular dynamics (AIMD) simulations, the CALPHAD (acronym of calculation of phase diagrams) method, and the inspection of existing phase diagrams [37]. In addition, Santodonato et al. elucidated the relative importance of configurational entropy through the structural evolution of the $\text{Al}_{1.3}\text{CoCrCuFeNi}$ alloy from a liquid state down to the solid state at room temperature. Various techniques, including scanning electron microscopy (SEM), transmission electron microscopy (TEM), energy dispersive spectroscopy (EDS), electron backscatter diffraction (EBSD), 3D atom probe tomography, and AIMD simulation, were conducted for the observation and verification [38]. Therefore, it was concluded that HEAs could be a single phase or multiple phases with different degrees of ordering, depending on their compositions and kinetic factors imposed by processing. From an engineering viewpoint, alloy development is not necessarily limited to single-phase HEAs since multiphase HEAs could also have practical applications [39].

Are HEAs thermodynamically unstable or stable in nature? HEAs could be in an equilibrium state if sufficiently annealed. However, this is generally a lengthy process when compared to conventional alloys due to their lower diffusion rate and phase transformation rate. Conversely, if the HEAs are not fully annealed, their phases and microstructure could be in a nonequilibrium metastable state. This phenomenon is also found in conventional alloys. Since practical production does not usually allow prolonged processing time to reach an equilibrium structure and metastable structure could also have good performance in applications, HEAs with a metastable structure would be applicable structures in applications.

Therefore, HEAs could have a broad range of compositions, phases, and microstructures and thus generate a wide range of physical, mechanical, and chemical properties. Certainly, controlling metastable structures to obtain the best performance for specific applications is an important research issue of HEAs.

1.6 Recent Activities for HEAs and HE-Related Materials

After Yeh, Cantor, and Ranganathan initiated the field of research into HEAs, 1038 journal articles related to HEAs were published by the end of 2015, as shown in Fig. 1.1. However, the research and understanding of HEAs are still very limited. A large territory of HEA research has yet to be explored and

Table 1.3 Special issues on HEAs

Special issue	Journal	Vol.	Year	Editors	Publisher	Country
Recent advances in high-entropy alloys	<i>Annales de Chimie Science des Matériaux</i>	31	2006	J.W. Yeh, A. Davison	Lavoisier	France
High-entropy alloys	<i>Entropy</i>	15	2013	J.W. Yeh	MDPI	Switzerland
High-entropy alloys	<i>JOM</i>	64	2012	M.C. Gao	Springer	Germany
High-entropy alloys	<i>JOM</i>	65	2013	M.C. Gao	Springer	Germany
High-entropy alloys	<i>JOM</i>	66	2014	M.C. Gao	Springer	Germany
High-entropy alloys	<i>JOM</i>	67	2015	M.C. Gao	Springer	Germany
High-entropy alloys	<i>Advances in Materials Science and Engineering</i>	–	2015	Y. Zhang, J.W. Yeh, I.F. Sun, J.P. Lin, K.F. Yao	Hindawi	USA
High-entropy alloys	<i>Materials Science and Technology</i>	–	2015	H.K. Bhadeshia	Maney	UK
High entropy alloy coatings		–	2015	T.M. Yue	MDPI	Switzerland

developed. Recently, in response to the interest from many groups and researchers, nine special issues on HEAs were published or processed, as listed in Table 1.3. In addition, five articles reviewing the research of HEAs were published in journals [30, 31, 40–42]. Meanwhile, several international symposiums and workshops on HEAs have been held, as listed in Table 1.4. As for the relative contribution of SCI (science citation index) papers on HE-related materials, Fig. 1.4a shows the proportions of contributions from Taiwan, Asia (excluding Taiwan), Europe, and America from 2004 to 2014. In addition, Asia, Europe, and America have an increased growth in the number of papers. These facts show remarkable and increasing attraction of the HEAs field to the materials community.

1.7 Research Fields in HEAs and HE-Related Materials

Although basic differences exist in the concept of alloy composition between HEAs and conventional alloys, the research fields in HEAs are similar to those in conventional alloys. For fabricating HEAs, three main routes are also applied: ingot metallurgy (IM), powder metallurgy (PM), and coating and deposition. For measuring properties and investigating microstructures of the HEAs, methods and

Table 1.4 International symposiums and workshops on HEAs

Symposium	Meeting ^a	Date	Place	Organizers
BMGs and HEAs	IUMRS-ICA conference	Sep. 25–28, 2010	Qingdao, China	Z. Lu, Y. Li, T. Zhang, X. Hui
BMGs and HEAs	IUMRS-ICA conference	Sep. 19–22, 2011	Taipei, Taiwan	J.C. Huang, J.W. Yeh
BMGs and HEAs	IUMRS-ICA conference	Aug. 26–31, 2012	Busan, Korea	E.S. Park, H. Kato, W.H. Wang, J.C. Huang
BMGs and HEAs	IUMRS-ICAM conference	Sep. 22–28, 2013	Qingdao, China	C.T. Liu, Z. Lu, P.K. Liaw
HEAs	MS&T-2012 meeting	Oct. 7–11, 2012	Pittsburgh, USA	M.C. Gao
HEAs (I)	TMS-2013 annual meeting	March 3–7, 2013	San Antonio, USA	P.K. Liaw, G.Y. Wang, M.C. Gao, S.N. Mathaudhu
HEAs (II)	TMS-2014 annual meeting	Feb. 16–20, 2014	San Diego, USA	P.K. Liaw, G.Y. Wang, M.C. Gao, S.N. Mathaudhu
HEAs	Workshop	Dec. 15–16, 2014	Quiyang, China	Z. P. Lu
HEAs (III)	TMS-2015 annual meeting	March 15–19, 2015	Orlando, USA	P.K. Liaw, G.Y. Wang, M.C. Gao, S.N. Mathaudhu
HEAs	Workshop	March 28–29, 2015	Madras, India	B.S. Murty, R.S. Kottada

MS&T Materials Science & Technology

TMS The Minerals, Metals & Materials Society

^aIUMRS-ICA International Union of Materials Research Societies – The IUMRS International Conference in Asia

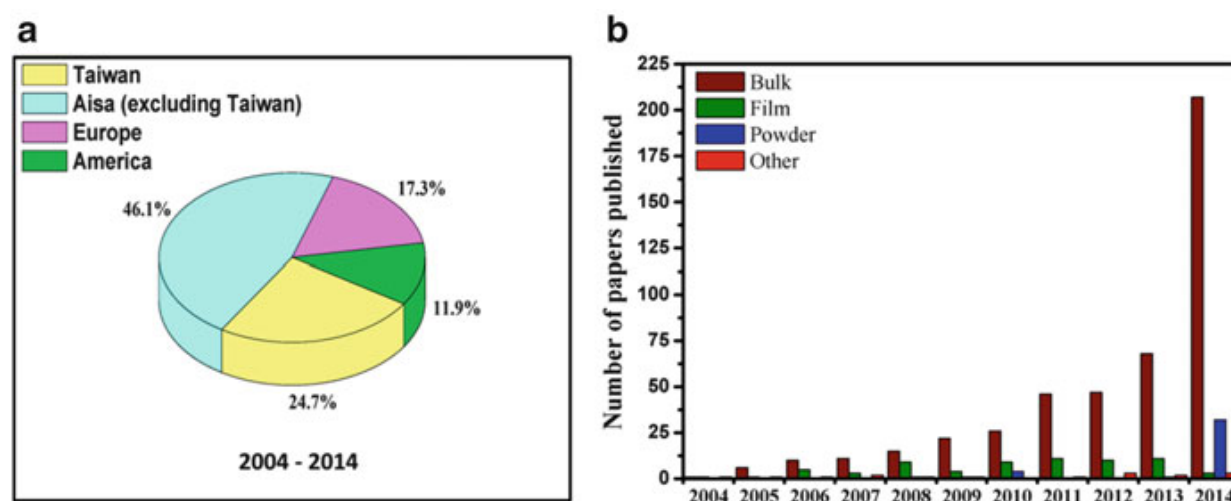


Fig. 1.4 (a) Contributions of HEAs papers from different areas and (b) growth of the number of papers in different research fields from 2004 to 2014

techniques used for conventional alloys are also useful to HEAs. However, different compositions lead to different microstructures and properties. As a result, correlations between composition, process, properties, and microstructure in HEAs provide unlimited research issues for both scientific curiosity and applied sciences.

For a simple classification of research fields based on the fabrication route, Fig. 1.4b illustrates that research on HEAs by number of SCI papers. Bulk HEAs prepared by melting-and-casting methods occupy the largest portion, thin-film and thick-film coatings are next, and powders and sintered products account for a small proportion. Furthermore, basic science studies, theoretical approaches, and simulations and modeling are very important but still on a small scale.

1.8 The Scope of This Book

Although research on HEAs is still in infancy, different research areas were explored over the last decade. Clearly, the main roads in this new world of research were paved to reach different areas from the world of conventional materials. These roads make it convenient for newcomers to enter this field of work. The efficiency in paving these roads is attributed to the aid from materials science and engineering, modern facilities, computerization, and information network. Significant reduction in time, effort, and resources would be impossible if research and development on HEAs was performed in earlier times when the aids mentioned above did not exist.

This book covers a wide spectrum. Chapter 2 (Formation Rules) details the existing criteria for the phase formation of HEAs and compares thermodynamic and topological parameters over wide ranges of materials, including HEAs, metallic glasses, and traditional metallic alloys. Chapter 3 (Physical Metallurgy) focuses on the relationship between composition, processing, microstructure, and properties. Both thermodynamics and kinetics will be analyzed to illustrate phase transformations in HEAs. Chapter 4 (Advanced Characterization Techniques) provides a brief introduction to some advanced microstructure characterization tools, such as high-resolution scanning transmission electron microscopy or analytical TEM, three-dimensional atom probe, and neutron scattering for characterizing HEAs. Chapter 5 (Fabrication Routes) illustrates the manufacturing routes in producing HEAs, including ingot metallurgy, powder metallurgy, coating, rapid solidification, mechanical alloying, single crystal preparation using the Bridgman method, laser cladding, and thin-film sputtering. Chapter 6 (Mechanical Properties of High-Entropy Alloys) emphasizes the mechanical properties of HEAs, including tension, compression, hardness, and wear tests. Fracture, fatigue, and creep behavior are also summarized. Chapter 7 (Functional Properties) introduces electrical, magnetic, electrochemical, and hydrogen storage properties of HEAs. Chapter 8 (Prediction of Structure and Phase Transformations) introduces first-principles methods into the HEA area for predicting phase stability in three quaternary systems at both $T=0$ K and finite temperatures. The method of hybrid Monte Carlo/molecular dynamics (MC/MD) simulations is introduced, and identifying entropy sources in the BCC HEAs is highlighted. Chapter 9 (Applications of Coherent Potential Approximation to High-Entropy Alloys) details the coherent potential approximation within the exact muffin-tin orbitals method to describe the chemically and magnetically disordered phases for systems of an arbitrary number of components.

Applications of this method to predict lattice stability, electronic and magnetic structure, and elasticity of single-phase HEAs are presented here. Chapter 10 (Applications of Special Quasi-Random Structures to High-Entropy Alloys) details the framework and tools available to generate special quasi-random structures (SQSs). Examples of SQSs for FCC, HCP, and BCC in 4- and 5-component alloys are presented. Comparisons between MC/MD, CPA, and SQS are discussed, and the entropy sources in FCC, BCC, and HCP HEAs are predicted. Chapter 11 (Design of High-Entropy Alloys) presents common methods for searching for single-phase HEAs in FCC, BCC, and HCP lattices. These methods include AIMD simulations, DFT calculations, CALPHAD modeling, and phase diagram inspection. New single-phase HEA compositions are suggested. Chapter 12 (CALPHAD Modeling of High-Entropy Alloys) emphasizes thermodynamic database development tailored for HEA systems and applications of CALPHAD to understand HEA formation and alloy design. Chapter 13 (High-Entropy Metallic Glasses) describes how to use the concept of high entropy to produce metallic glasses. High-entropy metallic glasses and their elastic/plastic properties are presented here. Chapter 14 (High-Entropy Coatings) describes thick HEA films or thin HEA films on substrates to provide protection, function enhancement, and/or decoration purposes. Chapter 15 (Potential Applications and Prospects) summarizes promising potential applications. It is perspective that numerous HE materials with improved properties will be successively developed in the future.

Acknowledgment J.W.Y. sincerely thanks Professors Ranganathan and Cantor for their great contributions from the beginning of high-entropy alloys era and also thanks four colleagues, Professors Su-Jien Lin, Swe-Kai Chen, Tsung-Shune Chin, and Han C. Shih for their continued research and contributions on high-entropy alloys. J.W.Y. would like to acknowledge the Ministry of Science and Technology, Ministry of Economic Affairs, and National Tsing Hua University, R.O.C., for their financial supports through different projects of high-entropy alloys. He also thanks Dr. Chun-Ming Lin for the collections and statistical analyses of papers on high-entropy alloys.

References

1. ASM International (1990) Metals handbook, vols 1 and 2, 10th edn. ASM International, Materials Park, OH
2. Westbrook JH, Fleischer RL (2000) Intermetallic compounds-structural applications of intermetallic compounds. Wiley, West Sussex
3. Westbrook JH, Fleischer RL (2000) Intermetallic compounds-magnetic, electrical and optical properties and applications of intermetallic compounds. Wiley, West Sussex
4. Suryanarayana C, Inoue A (2010) Bulk metallic glasses, 1st edn. CRC Press, West Palm Beach
5. Smith CS (1963) Four outstanding researchers in metallurgical history. American Society for Testing and Materials, Baltimore
6. Baker H (ed) (1992) ASM handbook, vol 3, Alloy phase diagrams. ASM International, Materials Park
7. Reed-Hill RE, Abbaschian R (1994) Physical metallurgy principles, 3rd edn. PWS Publishing Company, Boston, pp 353–358

8. Yeh JW, Chen SK, Lin SJ, Gan JY, Chin TS, Shun TT, Tsau CH, Chang SY (2004) Nanostructured high-entropy alloys with multiple principal elements: novel alloy design concepts and outcomes. *Adv Eng Mater* 6:299–303
9. Cantor B, Chang ITH, Knight P, Vincent AJB (2004) Microstructural development in equiatomic multicomponent alloys. *Mater Sci Eng A* 375–377:213–218
10. Ranganathan S (2003) Alloyed pleasures: multmetallic cocktails. *Curr Sci* 85:1404–1406
11. Cantor B (2014) Multicomponent and high entropy alloys. *Entropy* 16:4749–4768
12. Huang KH, Yeh JW (advisor) (1996) A study on the multicomponent alloy systems containing equal-mole elements. Master's thesis, National Tsing Hua University, Taiwan
13. Lai KT, Chen SK, Yeh JW (1998) Properties of the multicomponent alloy system with equal-mole elements. Master's thesis, National Tsing Hua University, Taiwan
14. Hsu YH, Chen SK, Yeh JW (2000) A study on the multicomponent alloy systems with equal-mole FCC or BCC elements. Master's thesis, National Tsing Hua University, Taiwan
15. Hung YT, Chen SK, Yeh JW (2001) A study on the Cu-Ni-Al-Co-Cr-Fe-Si-Ti multicomponent alloy system. Master's thesis, National Tsing Hua University, Taiwan
16. Chen KY, Shun TT, Yeh JW (2002) Development of multi-element high-entropy alloys for spray coating. Master's thesis, National Tsing Hua University, Taiwan
17. Tung CC, Shun TT, Chen SK, Yeh JW (2002) Study on the deformation microstructure and high temperature properties of Cu-Co-Ni-Cr-Al-Fe. Master's thesis, National Tsing Hua University, Taiwan
18. Chen MJ, Lin SS (2003) The effect of V, S, and Ti additions on the microstructure and wear properties of Al(0.5)CrCuFeCoNi high-entropy alloys. Master's thesis, National Tsing Hua University, Taiwan
19. Huang PK, Yeh JW (2003) Research of multi-component high-entropy alloys for thermal spray coating. Master's thesis, National Tsing Hua University, Taiwan
20. Hsu CY, Shun TT, Chen SK, Yeh JW (2003) Alloying effect of boron on the microstructure and high-temperature properties of CuCoNiCrAl_{0.5}Fe alloys. Master's thesis, National Tsing Hua University, Taiwan.
21. Lin PC, Chin TS, Yeh JW (2003) Development on the high frequency soft-magnetic thin films from high-entropy alloys. Master's thesis, National Tsing Hua University, Taiwan
22. Tsai CW, Shun TT, Yeh JW (2003) Study on the deformation behavior and microstructure of CuCoNiCrAl_xFe high-entropy alloys. Master's thesis, National Tsing Hua University, Taiwan
23. Tsai MH, Yeh JW, Gan JY (2003) Study on the evolution of microstructure and electric properties of multi-element high-entropy alloy films. Master's thesis, National Tsing Hua University, Taiwan
24. Huang PK, Yeh JW, Shun TT, Chen SK (2004) Multi-principal-element alloys with improved oxidation and wear resistance for thermal spray coating. *Adv Eng Mater* 6:74–78
25. Hsu CY, Yeh JW, Chen SK, Shun TT (2004) Wear resistance and high-temperature compression strength of FCC CuCoNiCrAl_{0.5}Fe alloy with boron addition. *Metall Mater Trans A* 35:1465–1469
26. Yeh JW, Chen SK, Gan JY, Lin SJ, Chin TS, Shun TT, Tsau CH, Chang SY (2004) Formation of simple crystal structures in Cu-Co-Ni-Cr-Al-Fe-Ti-V alloys with multiprincipal metallic elements. *Metall Mater Trans A* 35:2533–2536
27. Chen TK, Shun TT, Yeh JW, Wong MS (2004) Nanostructured nitride films of multi-element high-entropy alloys by reactive DC sputtering. *Surf Coat Tech* 188–189:193–200
28. Gaskell DR (1995) Introduction to the thermodynamics of materials, 3rd edn. Taylor & Francis Ltd, Washington, DC, pp 80–84
29. Swalin RA (1972) Thermodynamics of solids, 2nd edn. Wiley, New York, pp 35–41
30. Yeh JW (2006) Recent progress in high-entropy alloys. *Annales De Chimie – Science des Materiaux (Euro J Control)* 31:633–648
31. Yeh JW (2013) Alloy design strategies and future trends in high-entropy alloys. *JOM* 65:1759–1771

32. Takeuchi A, Chen N, Wada T, Yokoyama Y, Kato H, Inoue A, Yeh JW (2011) $\text{Pd}_{20}\text{Pt}_{20}\text{Cu}_{20}\text{Ni}_{20}\text{P}_{20}$ high-entropy alloy as a bulk metallic glass in the centimeter. *Intermetallics* 19:1546–1554
33. Kao SW, Yeh JW, Chin TS (2008) Rapidly solidified structure of alloys with two to eight equal-molar elements – a simulation by molecular dynamics. *J Phys Condens Matter* 20:145214
34. Turnbull D (1977) On the gram-atomic volumes of metal–metalloid glass forming alloys. *Scr Metall* 11:1131–1136
35. Turnbull D (1981) Metastable structure in metallurgy. *Metall Trans B* 12:217–230
36. Greer AL (1993) Confusion by design. *Nature* 366:303–304
37. Gao MC, Alman DE (2013) Searching for next single-phase high-entropy alloy compositions. *Entropy* 15:4504–4519. doi:[10.3390/e15104504](https://doi.org/10.3390/e15104504)
38. Santodonato LJ, Zhang Y, Feygenson M, Parish CM, Gao MC, Weber RJK, Neufeind JC, Tang Z, Liaw PK (2015) Deviation from high-entropy configurations in the atomic distributions of a multi-principal-element alloy. *Nat Commun* 6:5964. doi:[10.1038/ncomms69](https://doi.org/10.1038/ncomms69)
39. Miracle DB, Miller JD, Senkov ON, Woodward C, Uchic MD, Tiley J (2014) Exploration and development of high entropy alloys for structural applications. *Entropy* 16:494–525
40. Zhang Y, Zuo TT, Tang Z, Gao MC, Dahmen KA, Liaw PK, Lu ZP (2014) Microstructures and properties of high-entropy alloys. *Prog Mater Sci* 61:1–93
41. Tsai MH, Yeh JW (2014) High-entropy alloys: a critical review. *Mater Res Lett.* doi:[10.1080/21663831.2014.912690](https://doi.org/10.1080/21663831.2014.912690)
42. Samaei AT, Mirsayar MM, Aliha MRM (2015) The microstructure and mechanical behavior of modern high temperature alloys. *Eng Solid Mech* 3:1–20

Chapter 2

Phase Formation Rules

Yong Zhang, Sheng Guo, C.T. Liu, and Xiao Yang

Abstract This chapter gives an overview of existing active phase formation rules for high-entropy alloys (HEAs). A parametric approach using physiochemical parameters including enthalpy of mixing, entropy of mixing, melting points, atomic size difference, and valence electron concentration is used to delineate phase formation rules for HEAs, with a reference to other multicomponent alloys like bulk metallic glasses (BMGs). Specifically, rules on forming solid solutions, intermetallic compounds, and the amorphous phase are described in detail; formation rules of solid solutions with the face-centered cubic (fcc) or body-centered cubic (bcc) structure are also discussed. Some remaining issues and future prospects on phase formation rules for HEAs are also addressed at the end.

Keywords Solid solution • Enthalpy of mixing • Entropy of mixing • Atomic size difference • Electronegativity difference • Valence electron concentration • e/a ratio • Hume-Rothery rules • Empirical rules • Bulk metallic glasses • Single phase • Face-centered cubic (fcc) • Hexagonal close-packed (hcp) • Body-centered cubic (bcc) • Multiphase • High-entropy alloys (HEAs)

Y. Zhang (✉) • X. Yang

State Key Laboratory for Advanced Metals and Materials, University of Science and Technology Beijing, Beijing, People's Republic of China

e-mail: drzhangy@ustb.edu.cn; yangxiao_sky@163.com

S. Guo

Department of Materials and Manufacturing Technology, Chalmers University of Technology, Gothenburg, SE, Sweden

e-mail: sheng.guo@chalmers.se

C.T. Liu

Department of Mechanical and Biomedical Engineering, City University of Hong Kong, Kowloon Tong, Hong Kong, People's Republic of China

e-mail: chainliu@cityu.edu.hk

2.1 Introduction

The definition of HEAs has been quite controversial. Initially, HEAs were simply defined by their compositional complexity (i.e., composing of at least five major metallic elements, each with a concentration between 5 and 35 at.%) [1]. Recently, this notion has been challenged and the argument is that the microstructural complexity needs to also be considered when classifying HEAs. Particularly, this more strict definition of HEAs requires that the structure of HEAs has to be the single-phased disordered solid solution [2]. Indeed, the much narrower definition of HEAs is more physically justified. From the entropic point of view, the configurational entropies of the multi-principal-element alloys could be low (not really high entropy), if ordered solid solution or intermetallic compounds form. However, new problems also arise with this narrower definition of HEAs. The difficulties include but are not limited to the following situations: in cases where two solid solutions form and also no intermetallic compounds form, which are commonly seen in multi-principal-element alloys [3], can those alloys be classified as HEAs? What is the acceptable threshold configurational entropy (how high is high?) for alloys to be classified as HEAs? If the amorphous phase with a high configurational entropy is formed [4], can those alloys be called HEAs? Practically, it is more convenient to adopt the initial definition of HEAs (i.e., defined from the compositional complexity). [For more information on the history and development of HEAs, please refer to Chap. 1 for details.]

The configurational entropies of compositionally complex alloys are high in the liquid or fully random solid solution state. To avoid further confusions, a sort of arbitrary threshold of configurational entropy larger than $1.5R$ (where R is the gas constant) was suggested as an operational definition for HEAs [5]. Then one needs to be aware that different phase constitutions can occur to HEAs, including solid solutions, intermetallic compounds, or even the amorphous phase, depending on the alloy compositions and sometimes the cooling rate if they are prepared by the solidification route [6]. It is within this context that the phase selection among solid solutions, intermetallic compounds, and the amorphous phase in HEAs will be discussed. This will be done using a parametric approach, which utilizes parameters including the atomic size mismatch, mixing enthalpy, the mixing entropy, and melting points [7–10]. These physiochemical parameters [as will be introduced in Sect. 2.2] can reasonably be used to predict the formation of these different phases from the given compositions, although, notably, the occurrence of intermetallic compounds is still difficult to be predicted and controlled. Furthermore, considering the significance of solid solution type on the mechanical properties of HEAs, the phase selection between fcc- and bcc-type solid solutions is discussed in Sect. 2.3, where the electron concentration plays a critical role. Some outstanding issues and future prospects relevant to the phase formation rules for HEAs are addressed in Sect. 2.4, before a summary is given in Sect. 2.5.

2.2 Thermodynamics and Geometry Effect

If kinetic factors are not involved, phase formation is thermodynamically controlled by the Gibbs free energy, G , which is related to the enthalpy, H , and the entropy, S , via the following equation, in the case of forming alloys from mixing elemental components:

$$\Delta G_{\text{mix}} = \Delta H_{\text{mix}} - T\Delta S_{\text{mix}} \quad (2.1)$$

Here ΔG_{mix} is the Gibbs free energy of mixing, ΔH_{mix} is the enthalpy of mixing, ΔS_{mix} is the entropy of mixing, and T is the temperature at which different elements are mixed. Note that the term ΔS_{mix} includes all entropy sources such as configurational, vibrational, electronic, and magnetic contributions. [Please refer to Chaps. 8, 10, and 12 for quantification of the entropy sources in example HEA systems of Co-Cr-Fe-Mn-Ni, Al-Co-Cr-Fe-Ni, and Mo-Nb-Ta-Ti-V-W.] Naturally, it is the competition between ΔH_{mix} and $T\Delta S_{\text{mix}}$ that determines the phase selection in HEAs. This constitutes the thermodynamic consideration of phase formation rules. Another important effect when considering the phase formation is the geometry effect or, more specifically, the atomic size effect. The atomic size effect is clearly articulated both in the classic Hume-Rothery rules for forming binary solid solutions [11] and the famous Inoue's three empirical rules for the easy formation of BMGs [12]. When establishing phase formation rules for HEAs is addressed using the parametric approach, the descriptors [13] naturally are picked from parameters that are related to the thermodynamics and geometry considerations. Not surprisingly, effective phase formation rules normally comprise both these two considerations.

Figure 2.1 shows a phase selection diagram for multicomponent alloys, including HEAs and BMGs, based on the enthalpy of mixing, ΔH_{mix} , and the atomic size difference, Delta (δ). Here, δ is defined as [9]

$$\delta = \sqrt{\sum_{i=1}^N x_i \left(1 - d_i / \sum_{j=1}^N x_j d_j\right)^2} \quad (2.2)$$

where N is the number of elements, x_i or x_j is the composition of the i th or j th element, and d_i or d_j is the atomic diameter of the i th or j th component. The enthalpy of mixing, ΔH_{mix} , for the multicomponent alloys can be estimated by [9]

$$\Delta H_{\text{mix}} = \sum_{i=1, i \neq j}^N 4\Delta H_{\text{AB}}^{\text{mix}} x_i x_j \quad (2.3)$$

where $\Delta H_{\text{AB}}^{\text{mix}}$ is the enthalpy of mixing for the binary equiatomic AB alloys.

The calculated ΔH_{mix} and δ for HEAs and BMGs used in Fig. 2.1 are listed in Table 2.1. It is noted here that the listed phases in Table 2.1 are basically detectable from the X-ray diffraction and they do not necessarily comprise all phases existing in the listed alloys. Seen from Fig. 2.1, in the zone marked S, only disordered solid solution will form. In this zone, as the component atomic size difference is

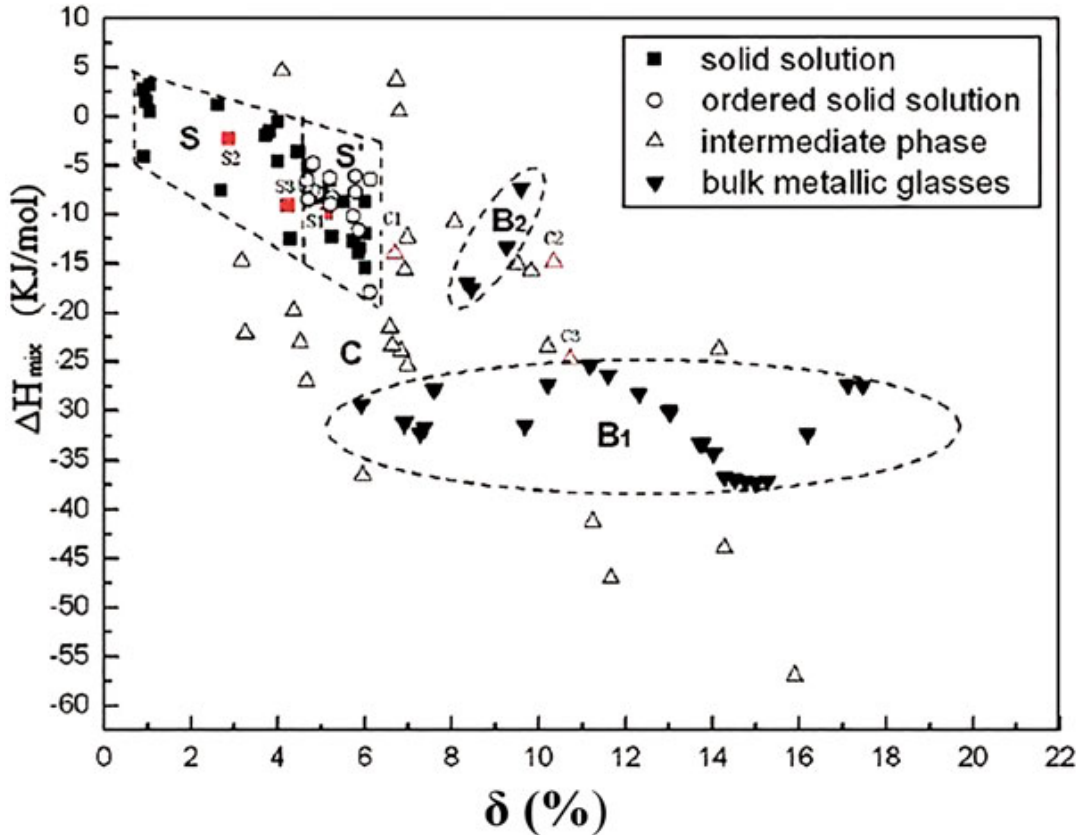


Fig. 2.1 Phase selection diagram of HEAs and BMGs based on the enthalpy of mixing, ΔH_{mix} , and the atomic size difference, Delta (δ) [9]

relatively small, the component atoms easily substitute for each other and have the similar probability to occupy the lattice sites to form solid solutions. At the same time, ΔH_{mix} is not negative enough for alloys to form a compound. In the zone marked **S'**, HEAs still have solid solution as the main phase, but a small amount of the ordered solid solution precipitates in some HEAs. Compared with zone **S**, δ increases which deepens the extent of ordering in HEAs. ΔH_{mix} also becomes more negative to promote the precipitation of ordered phases in certain HEAs in zone **S'**. BMGs are located in two zones marked **B1** and **B2**. The zone **B2** contains Mg- and Cu-based bulk metallic glasses, while the zone **B1** contains other kinds of BMGs, such as Zr-based bulk metallic glasses. Clearly, compared with HEAs, BMGs have larger δ and more negative ΔH_{mix} . Another zone in Fig. 2.1 is marked **C**, in which many intermediate phases will form.

According to Eq. 2.1, at elevated temperatures the high ΔS_{mix} can significantly lower the free energy and thus lower the tendency to order and segregate during the solidification process, which consequently makes solid solution more easily form and more stable than intermetallics or other ordered phases. Therefore, for some HEAs, due to the effect of high ΔS_{mix} , solid solution phases form prior to intermetallics, and the total number of phases is well below the maximum equilibrium number allowed by the Gibbs phase rule. To compare the effect of ΔS_{mix} , Fig. 2.1 is replotted in three dimensions by adding one axis of ΔS_{mix} , as shown in Fig. 2.2. It is apparent that all HEAs have a higher level of ΔS_{mix} than that of BMGs (marked by \blacktriangledown). The HEAs forming solid solution phases (marked by \blacksquare) have ΔS_{mix} in the range of 12–17.5 J/(mol · K) and with smaller values of δ . Intermetallic phases (marked by Δ) form at a

Table 2.1 Phase constitution; valence electron concentration, VEC ; enthalpy of mixing, ΔH_{mix} ; entropy of mixing, ΔS_{mix} ; average melting point, T_m ; Ω ($\Omega = T_m \Delta S_{\text{mix}} / (\Delta H_{\text{mix}})$); and atomic size difference, δ , for representative HEAs and BMGs. Three color codes are used to differentiate solid solutions, solid solutions plus intermetallic compounds, and the amorphous phase forming multicomponent alloys

Alloys	Major phases	VEC	ΔH_{mix} [kJ/mol]	ΔS_{mix} [J/(mol · K)]	T_m (K)	Ω	δ [%]	Refs.
$\text{Cr}_2\text{CuFe}_2\text{Mn}_2\text{Ni}_2$	fcc	8.11	0.10	13.14	1749.11	229.83	0.91	[10]
CoCrFeMnNi	fcc	8.00	-4.16	13.38	1792.40	5.77	0.92	[10]
$\text{CrCu}_2\text{Fe}_2\text{MnNi}_2$	fcc	8.88	3.88	12.97	1680.88	5.61	0.95	[10]
CoCrCuFeMnNi	fcc	8.50	1.44	14.90	1720.00	17.80	0.99	[10]
$\text{CrCuFeMn}_2\text{Ni}_2$	fcc	8.43	0.44	12.98	1713.00	50.53	0.99	[10]
$\text{CoCrCu}_{0.5}\text{FeNi}$	fcc	8.56	0.49	13.15	1804.67	48.44	1.06	[10]
CoCrFeNi	fcc	8.25	-3.75	11.53	1860.50	5.71	1.06	[10]
CoCrCuFeNi	fcc	8.80	3.20	13.38	1760.00	7.36	1.07	[10]
CuNi	fcc	10.50	4.00	5.76	1543.00	2.22	1.63	[10]
CoCuFeNiV	fcc	8.60	-1.78	14.90	1833.67	15.35	2.63	[10]
CrCuFeMoNi	fcc	8.20	4.64	13.38	1985.00	5.72	2.92	[10]
$\text{CoCrFeMo}_{0.3}\text{Ni}$	fcc	8.09	-4.15	12.83	1932.67	5.97	2.92	[10]
$\text{Al}_{0.25}\text{CrCuFeNi}_2$	fcc	8.71	0.36	12.14	1712.64	57.31	2.93	[16]
$\text{Al}_{0.25}\text{CoCrCu}_{0.75}\text{FeNi}$	fcc	8.40	-0.71	14.32	1738.78	35.07	3.00	[10]
$\text{Al}_{0.3}\text{CoCrCuFeNi}$	fcc	8.47	1.56	14.43	1713.22	15.85	3.15	[10]
$\text{Al}_{0.25}\text{CoCrFeNi}$	fcc	7.94	-6.75	12.71	1805.97	3.40	3.25	[10]
$\text{Al}_{0.3}\text{CoCrFeMo}_{0.1}\text{Ni}$	fcc	7.84	-7.26	13.44	1820.81	3.37	3.74	[10]
CoCrFeNiPd	fcc	8.60	-5.60	13.38	1853.80	4.43	3.76	[20]
$\text{Al}_{0.375}\text{CoCrFeNi}$	fcc	7.80	-7.99	12.97	1781.04	2.89	3.80	[10]
$\text{Al}_{0.5}\text{CoCrCuFeNi}$	fcc	8.27	-1.52	14.70	1684.86	16.29	3.82	[10]
$\text{Al}_{0.5}\text{CrCuFeNi}_2$	fcc	8.45	-2.51	12.60	1677.23	8.41	3.82	[16]
$\text{Al}_{0.5}\text{CoCrCuFeNiV}_{0.2}$	fcc	8.16	-2.50	15.44	1703.01	10.52	3.87	[10]
$\text{Al}_{0.5}\text{CoCrCu}_{0.5}\text{FeNi}$	fcc	8.00	-4.60	14.54	1717.55	5.43	4.00	[10]

(continued)

Table 2.1 (continued)

Alloys	Major phases	VEC	ΔH_{mix} [kJ/mol]	ΔS_{mix} [J/(mol · K)]	T_m (K)	Ω	δ [%]	Refs.
Al _{0.3} CoCrFeNiTi _{0.1}	fcc	7.80	-8.93	13.47	1799.24	2.72	4.06	[10]
CoCrFeNiPd ₂	fcc	8.83	-6.11	12.98	1849.33	3.92	4.33	[20]
CoCrCuFeNiTi _{0.5}	fcc	8.36	-3.70	14.70	1776.91	7.05	4.46	[10]
Co _{1.5} CrFeNi _{1.5} Ti _{0.5}	fcc	8.09	-10.74	12.86	1848.00	2.22	4.60	[10]
Co _{1.5} CrFeNi _{1.5} Ti _{0.5} Mo _{0.1}	fcc	8.05	-10.64	13.38	1866.70	2.35	4.72	[10]
Al _{0.2} Co _{1.5} CrFeNi _{1.5} Ti _{0.5}	fcc	7.91	-12.50	13.67	1815.91	1.98	5.00	[19]
Al _{0.25} CoCrCu _{0.75} FeNiTi _{0.5}	fcc	8.00	-7.28	15.55	1757.61	3.76	5.03	[10]
Mo _{25.6} Nb _{22.7} Ta _{24.4} W _{27.3}	bcc	5.53	-6.49	11.50	3177.60	5.62	2.27	[10]
Mo _{21.7} Nb _{20.6} Ta _{15.6} V ₂₁ W _{21.1}	bcc	5.43	-4.54	13.33	2950.49	8.67	3.18	[10]
Al _{0.3} CrFe _{1.5} MnNi _{0.5}	bcc	7.19	-5.51	12.31	1747.34	3.90	3.32	[10]
NbHfTaTiZr	bcc	4.40	2.72	13.38	2524.20	12.42	4.01	[21]
Al _{0.5} CrFe _{1.5} MnNi _{0.5}	bcc	7.00	-6.77	12.67	1711.17	3.20	4.03	[10]
AlCrCuFeMnNi	bcc	7.50	-5.11	14.90	1580.58	4.62	4.73	[10]
AlCoCrFeNiSi _{0.6}	bcc	6.86	-22.76	14.78	1676.38	1.09	4.98	[22]
AlCoCrCu _{0.5} FeNi	bcc	7.55	-7.93	14.70	1646.27	3.05	5.02	[10]
AlCoCrFeNiSi _{0.4}	bcc	6.96	-19.84	14.70	1675.98	1.24	5.07	[22]
AlCoCrCu _{0.25} FeNi	bcc	7.38	-9.94	14.34	1660.00	2.39	5.13	[10]
AlCoCrFeNiSi _{0.2}	bcc	7.08	-16.39	14.22	1675.56	1.45	5.15	[22]
AlCoCrFeNi	bcc	7.20	-12.32	13.38	1675.10	1.83	5.25	[10]
AlCoCrFeNiMo _{0.1}	bcc	7.18	-12.13	13.92	1699.02	1.95	5.30	[23]
AlCoCrFeNiNb _{0.1}	bcc	7.16	-13.32	13.92	1696.18	1.77	5.50	[17]
Al _{1.25} CoCrFeNi	bcc	7.00	-13.42	13.34	1639.79	1.62	5.55	[10]
Al _{2.0} CrCuFeNi ₂	bcc	7.29	-9.63	12.89	1517.86	2.03	5.71	[16]
AlCoCrCu _{0.5} Ni	bcc	7.44	-10.17	13.15	1609.67	2.08	5.74	[10]
Al _{1.5} CoCrFeFeNi	bcc	6.82	-14.28	13.25	1607.68	1.50	5.77	[10]

Al _{2.3} CoCrCuFeNi	bcc	6.97	-9.38	14.35	1499.60	2.29	5.84	[10]
Al _{2.5} CoCrCuFeNi	bcc	6.87	-9.78	14.21	1484.50	2.15	5.91	[10]
Al _{2.8} CoCrCuFeNi	bcc	6.72	-10.28	14.01	1463.31	1.99	5.99	[10]
Al ₂₀ (CoCrCuFeMnNiV ₂ Ti) ₈₀	bcc	7.36	-15.44	17.99	1633.50	1.91	6.01	[10]
Al ₂ CoCrFeNi	bcc	6.50	-15.44	12.98	1551.50	1.30	6.04	[10]
Al ₃ CoCrCuFeNi	bcc	6.63	-10.56	13.86	1450.06	1.90	6.09	[10]
Al _{2.5} CoCrFeNi	bcc	6.23	-16.09	12.63	1503.96	1.17	6.19	[10]
Al ₃ CoCrFeNi	bcc	6.00	-16.41	12.26	1463.21	1.10	6.26	[10]
AlCoCuNiTiZn	bcc	8.17	-17.89	14.90	1680.12	1.39	6.43	[10]
Al _{1.5} CoCrFeNiTi	bcc	6.38	-20.73	14.78	1659.73	1.18	6.64	[18]
Al ₂ CoCrFeNiTi	bcc	6.14	-21.63	14.53	1607.86	1.08	6.64	[18]
CoCrFeNiTi _{0.3}	fcc + hcp	7.95	-8.89	12.83	1866.47	2.69	4.06	[10]
CrCu ₂ Fe ₂ Mn ₂ Ni	bcc + fcc	8.50	4.69	12.97	1654.88	4.58	0.83	[10]
Cr ₂ CuFe ₂ MnNi	bcc + fcc	8.00	2.61	12.89	1784.86	8.82	0.84	[10]
CrCuFeMnNi	bcc + fcc	8.40	2.72	13.38	1710.00	8.41	0.92	[10]
Cr ₂ Cu ₂ Fe ₂ MnNi ₂	bcc + fcc	8.56	3.56	13.14	1729.33	6.38	0.94	[10]
Cr ₂ Cu ₂ FeMn ₂ Ni ₂	bcc + fcc	8.44	2.37	13.14	1697.00	9.40	0.97	[10]
CoCrFeGeMnNi	bcc + fcc	7.33	-15.17	14.90	1695.50	1.67	3.25	[10]
Al _{0.5} CoCrCuFeNiV _{0.4}	bcc + fcc	8.05	-3.34	15.76	1719.92	8.12	3.80	[10]
Al _{0.5} CoCrCuFeNiV _{1.2}	bcc + fcc	7.69	-5.73	15.98	1777.49	4.96	3.99	[10]
Al _{0.5} CoCrCuFeNiV ₂	bcc + fcc	7.40	-7.08	15.60	1822.77	4.01	3.99	[10]
Al _{0.5} CoCrCuFeNiV _{1.4}	bcc + fcc	7.61	-6.14	15.91	1789.79	4.64	4.00	[10]
Al _{0.5} CoCrCuFeNiV _{1.6}	bcc + fcc	7.54	-6.50	15.82	1801.40	4.38	4.00	[10]
Al _{0.5} CoCrCuFeNiV _{1.8}	bcc + fcc	7.47	-6.81	15.72	1812.38	4.19	4.00	[10]
Al _{0.5} CoCrFeNi	bcc + fcc	7.67	-9.09	13.15	1757.50	2.55	4.22	[10]
Al _{0.8} CoCrCuFeNi	bcc + fcc	8.00	-3.61	14.87	1646.00	6.78	4.49	[10]
AlCoCrCuFeNiSi	bcc + fcc	7.29	-18.86	16.18	1631.50	1.40	4.51	[10]

(continued)

Table 2.1 (continued)

Alloys	Major phases	VEC	ΔH_{mix} [kJ/mol]	ΔS_{mix} [J/(mol · K)]	T_m (K)	Ω	δ [%]	Refs.
AlCoCrCuFeNiV	bcc + fcc	7.43	-7.76	16.18	1705.07	3.56	4.69	[10]
Al _{0.75} CoCrCu _{0.25} FeNi	bcc + fcc	7.60	-8.47	14.32	1696.33	2.87	4.71	[10]
AlCrCuFeNi ₂	bcc + fcc	8.00	-5.78	12.98	1615.25	3.63	4.82	[16]
AlCoCrCuFeNi	bcc + fcc	7.83	-4.78	14.90	1622.25	5.06	4.82	[10]
Al _{0.75} CoCrFeNi	bcc + fcc	7.42	-10.90	13.33	1714.13	2.09	4.83	[10]
AlCo _{0.5} CrCuFeNi	bcc + fcc	7.73	-4.50	14.70	1608.82	5.26	4.91	[10]
AlCoCrCuFeNi _{0.5}	bcc + fcc	7.64	-3.90	14.70	1612.64	6.08	4.91	[10]
AlCoCrCuFeMo _{0.2} Ni	bcc + fcc	7.77	-4.47	15.60	1633.31	5.70	4.95	[10]
AlCoCrCuFe _{0.5} Ni	bcc + fcc	7.82	-5.55	14.70	1605.09	4.25	5.00	[10]
AlCoCr _{0.5} CuFeNi	bcc + fcc	8.00	-5.02	14.70	1572.82	4.61	5.02	[10]
Al _{0.875} CoCrFeNi	bcc + fcc	7.31	-11.66	13.37	1694.12	1.95	5.06	[10]
Al _{1.3} CoCrCuFeNi	bcc + fcc	7.60	-6.24	14.85	1589.45	3.78	5.19	[10]
AlCoCrCuNi	bcc + fcc	7.80	-6.56	13.38	1584.50	3.23	5.19	[10]
Al _{0.5} CoCeCu _{0.5} FeNiTi _{0.5}	bcc + fcc	7.09	-10.84	15.75	1738.32	2.52	5.25	[10]
Al _{1.5} CrCuFeNi ₂	bcc + fcc	7.62	-8.05	13.01	1562.81	2.53	5.38	[16]
Al _{1.5} CoCrCuFeNi	bcc + fcc	7.46	-7.04	14.78	1569.27	3.30	5.38	[10]
Al _{1.8} CoCrCuFeNi	bcc + fcc	7.26	-8.08	14.65	1541.22	2.79	5.54	[10]
AlCo ₃ CrFeNiTi _{0.5}	bcc + fcc	7.47	-14.93	13.49	1718.47	1.55	5.69	[10]
Al ₂ CoCrCuFeNi	bcc + fcc	7.14	-8.65	14.53	1523.86	2.56	5.71	[10]
AlCr ₃ CuFeNiTi	bcc + fcc	6.75	-9.31	13.86	1794.44	2.67	5.72	[10]
Al _{11.1} (CoCrCuFeMnNiVTi) _{88.9}	bcc + fcc	7.43	-12.74	18.27	1711.28	2.45	5.75	[10]
AlCoCuNi	bcc + fcc	8.25	-8.00	11.52	1447.40	2.08	5.77	[10]
AlCoCrCuFeNiTiV	bcc + fcc	7.00	-13.94	17.29	1735.19	2.15	5.87	[10]
AlCo ₂ CrFeNiTi _{0.5}	bcc + fcc	7.23	-16.43	14.23	1710.54	1.49	5.91	[10]
AlCr ₂ CuFeNiTi	bcc + fcc	6.86	-11.10	14.53	1746.07	2.29	5.99	[10]

$\text{AlCo}_{0.5}\text{CrFeNiTi}_{0.5}$	bcc + fcc	7.08	-17.17	14.54	1705.58	1.45	6.02	[10]
$\text{AlCr}_{1.5}\text{CuFeNiTi}$	bcc + fcc	6.92	-12.26	14.78	1716.31	2.08	6.14	[10]
AlCuNi	bcc + fcc	8.00	-8.44	9.13	1339.80	1.45	6.20	[10]
AlCrCuFeNiTi	bcc + fcc	7.00	-13.67	14.90	1681.58	1.83	6.29	[10]
$\text{AlCr}_{0.5}\text{CuFeNiTi}$	bcc + fcc	7.09	-15.40	14.70	1640.55	1.56	6.45	[10]
$\text{Al}_{0.75}\text{CoCrCu}_{0.25}\text{FeNiTi}_{0.5}$	bcc1 + bcc2	7.00	-15.26	15.55	1719.02	1.75	5.83	[10]
$\text{AlCoCrCu}_{0.5}\text{FeNiTi}_{0.5}$	bcc1 + bcc2	7.25	-13.42	15.86	1671.25	1.97	5.90	[10]
$\text{AlCoCrCu}_{0.25}\text{FeNiTi}_{0.5}$	bcc1 + bcc2	7.09	-15.50	15.54	1684.87	1.68	6.01	[10]
$\text{AlCoCrFeNiTi}_{0.5}$	bcc1 + bcc2	6.91	-17.92	14.70	1699.73	1.39	6.11	[10]
AlCoCrCuFeNiTi	bcc1 + bcc2 + fcc	7.29	-13.80	16.18	1668.50	1.95	6.23	[10]
AlCoCrFeNiTi	bcc1 + bcc2	6.67	-21.56	14.90	1720.25	1.19	6.58	[10]
$\text{Al}_{0.5}\text{CoCrCuFeNiV}_{0.6}$	bcc + fcc + σ -phase	7.95	-4.07	15.92	1735.73	6.79	3.94	[10]
$\text{Al}_{0.5}\text{CoCrCuFeNiV}_{0.8}$	bcc + fcc + σ -phase	7.86	-4.71	16.00	1750.53	5.95	3.97	[10]
$\text{Al}_{0.5}\text{CoCrCuFeNiV}$	bcc + fcc + σ -phase	7.77	-5.25	16.01	1764.42	5.38	3.98	[10]
AlCoCrCuFeMnNi	bcc + fcc + unknown phase	7.71	-5.63	16.18	1607.64	4.61	4.57	[10]
AlCoCrCuFeMnNi	bcc + fcc + unknown phase	7.71	-5.63	16.18	1607.64	4.61	4.57	[10]
AlCoCrFeNiSi	bcc + δ -phase	6.67	-27.33	14.90	1677.08	0.91	4.82	[22]
$\text{AlCoCrFeNiSi}_{0.8}$	bcc + δ -phase	6.76	-25.23	14.87	1676.74	0.99	4.90	[22]
AlCrMoSiTi	Ordered bcc + Mo_5Si_3	4.60	-34.08	13.38	1918.90	0.75	4.91	[10]
$\text{AlCoCrCuFeNiMo}_{0.4}$	bcc + α -phase	7.72	-4.20	15.91	1701.80	6.45	5.05	[10]
$\text{Co}_{1.5}\text{CrFeMo}_{0.5}\text{Ni}_{1.5}\text{Ti}_{0.5}$	fcc + σ -phase	7.92	-10.25	14.17	1935.25	2.67	5.09	[10]
$\text{AlCoCr}_2\text{FeMo}_{0.5}\text{Ni}$	bcc + σ	6.92	-10.27	14.23	1839.38	2.55	5.10	[24]
$\text{AlCoCrCuFeNiMo}_{0.6}$	bcc + α -phase	7.67	-3.95	16.08	1737.95	7.07	5.13	[10]
$\text{AlCoCrFe}_2\text{Mo}_{0.5}\text{Ni}$	bcc + σ -phase	7.23	-9.70	14.23	1789.85	2.63	5.15	[10]
CoCrCuFeMnNiTiV	fcc + bcc + σ -phase + unknown phase	7.50	-8.13	17.29	1808.50	3.85	5.19	[10]
$\text{AlCoCrCuFeNiMo}_{0.8}$	bcc + α -phase	7.62	-3.72	16.16	1771.99	7.69	5.20	[10]

(continued)

Table 2.1 (continued)

Alloys	Major phases	VEC	ΔH_{mix} [kJ/mol]	ΔS_{mix} [J/(mol · K)]	T_m (K)	Ω	δ [%]	Refs.
AlCoCrCuFeNiMo	bcc + α -phase	7.57	-3.51	16.18	1804.07	8.32	5.25	[10]
CoCrCuFeNiTi _{0.8}	fcc + Laves phase	8.14	-6.75	14.89	1785.66	3.95	5.26	[10]
AlCoCr _{1.5} FeMo _{0.5} Ni	bcc + σ	7.00	-10.83	14.53	1814.92	2.43	5.27	[24]
Co _{1.5} CrFeMo _{0.8} Ni _{1.5} Ti _{0.5}	fcc + σ -phase	7.83	-9.96	14.21	1980.95	2.83	5.28	[10]
AlCo ₂ CrFeMo _{0.5} Ni	bcc + fcc + σ -phase	7.38	-10.70	14.23	1783.54	2.37	5.29	[10]
AlCoCrFe _{1.5} Mo _{0.5} Ni	bcc + σ -phase	7.17	-10.50	14.53	1788.08	2.47	5.30	[10]
AlCoCrFeMo _{0.2} Ni	bcc + α -phase	7.15	-11.95	14.22	1722.02	2.05	5.35	[23]
AlCo _{1.5} CrFeMo _{0.5} Ni	bcc + σ -phase	7.25	-11.08	14.53	1784.67	2.34	5.39	[10]
AlCoCrFeMo _{0.3} Ni	bcc + α -phase	7.13	-11.78	14.43	1744.15	2.14	5.40	[23]
AlCoCrFeMo _{0.4} Ni	bcc + α -phase	7.11	-11.60	14.59	1765.46	2.22	5.44	[23]
AlCoCrFeMo _{0.5} Ni	bcc + σ -phase	7.09	-11.44	14.70	1786.00	2.29	5.47	[10]
AlCoCrFeMo _{0.5} Ni	bcc + σ	7.09	-11.44	14.70	1786.00	2.29	5.47	[24]
AlCoCrFeMo _{0.5} Ni	bcc + α -phase	7.09	-11.44	14.70	1786.00	2.29	5.47	[23]
AlCo _{0.5} CrFeMo _{0.5} Ni	bcc + σ -phase	6.90	-11.72	14.53	1787.60	2.22	5.54	[10]
AlCoCrFe _{0.6} Mo _{0.5} Ni	bcc + σ -phase	7.02	-12.32	14.61	1784.04	2.12	5.61	[10]
CoCrCuFeNiTi	fcc + Laves phase	8.00	-8.44	14.90	1791.00	3.17	5.65	[10]
AlCoCr _{0.5} FeMo _{0.5} Ni	bcc + σ	7.20	-12.08	14.53	1750.06	2.11	5.69	[24]
Al _{0.5} B _{0.2} CoCrCuFeNi	fcc + boride	8.09	-4.00	15.44	1708.73	6.60	5.77	[10]
AlCoCrFeNb _{0.25} Ni	bcc + Laves phase	7.10	-14.66	14.34	1726.29	1.69	5.83	[17]
Co _{1.5} CrFeNi _{1.5} Ti	fcc + η	7.75	-15.61	13.21	1856.17	1.57	5.83	[19]
AlCoFeMo _{0.5} Ni	bcc + σ	7.33	-12.74	13.15	1708.89	1.76	5.93	[24]
Al _{0.2} Co _{1.5} CrFeNi _{1.5} Ti	fcc + η	7.60	-17.12	13.97	1826.40	1.49	6.01	[19]
Al _{3.0} CrCuFeNi ₂	bcc + ordered bcc	6.75	-11.50	12.42	1444.81	1.56	6.03	[16]
Al ₄₀ (CoCrCuFeMnNiTiV) ₆₀	bcc + Al ₃ Ti + unknown phase	5.70	-18.29	15.97	1458.50	1.27	6.09	[10]
CoCrFeNiTi	fcc + bcc + CoTi ₂	7.40	-16.32	13.38	1877.60	1.54	6.13	[18]

AlAuCoCrCuNi	fcc + AuCu	8.33	-6.45	14.90	1543.42	3.57	6.14	[10]
AlCoCrFeNb _{0.5} Ni	bcc + Laves phase	7.00	-16.53	14.70	1772.82	1.58	6.24	[17]
Al _{0.5} CoCrFeNiTi	fcc + bcc + CoTi ₂ + FeTi	7.00	-16.79	14.70	1791.77	1.57	6.44	[18]
AlCoCrFeNb _{0.75} Ni	bcc + Laves phase	6.91	-18.03	14.85	1815.30	1.50	6.55	[17]
AlCoCrFeNiTi	fcc + bcc + CoTi ₂ + FeTi	6.67	-19.22	14.90	1720.25	1.33	6.58	[18]
AlCoCrFeNiTi _{1.5}	bcc1 + bcc2 + Laves phase	6.46	-23.91	14.78	1737.62	1.08	6.93	[10]
Al _{0.5} B _{0.6} CoCrCuFeNi	fcc + boride	7.75	-8.01	15.92	1751.76	3.48	8.07	[10]
Al _{0.5} BCoCrCuFeNi	fcc + ordered fcc + boride	7.46	-11.03	16.01	1789.50	2.60	9.52	[10]
CrCuFeNiZr	bcc + compounds	7.80	-14.40	13.38	1831.60	1.70	9.91	[10]
CoCrCuFeNiTi ₂	Compounds	7.43	-14.04	14.53	1813.14	1.87	6.69	[10]
AlCoCrCuNiTiY _{0.5}	Cu ₂ Y + AlNi ₂ Ti + Cu + Cr	6.85	-18.32	16.00	1935.38	1.68	7.53	[10]
CuFeHfTiZr	Compounds	6.20	-15.84	13.38	1949.40	1.64	9.84	[10]
CoCuHfTiZr	Compounds	6.40	-23.52	13.38	1941.20	1.11	10.21	[10]
AlTiVYZr	Compounds	3.80	-14.88	13.38	1802.10	1.62	10.35	[10]
BeCuNiTiVZr	Compounds	6.00	-24.89	14.90	1820.67	1.09	11.09	[10]
AlCoCrCuNiTiY _{0.8}	Cu ₂ Y + AlNi ₂ Ti + Cu + Cr	6.68	-19.00	16.16	1929.45	1.64	12.73	[10]
AlCoCrCuNiTiY	Cu ₂ Y + AlNi ₂ Ti + Cu + Cr + unknown phase	6.57	-19.37	16.18	1925.79	1.62	13.45	[10]
Cu ₄₇ Ti ₃₃ Zr ₁₁ Si ₁ Ni ₆ Sn ₂	Amorphous	7.65	-17.02	10.45	1645.17	1.01	8.36	[10]
Cu ₄₇ Ti ₃₃ Zr ₁₁ Si ₁ Ni ₈	Amorphous	7.77	-17.56	10.07	1669.63	0.96	8.46	[10]
Ti ₄₅ Cu ₂₅ Ni ₁₅ Sn ₃ Be ₇ Zr ₅	Amorphous	6.51	-21.22	11.90	1705.29	0.96	9.08	[10]
Mg ₆₅ Cu ₁₅ Ag ₅ Pd ₅ Y ₁₀	Amorphous	4.30	-13.24	9.10	1074.86	0.74	9.27	[10]
Mg ₆₅ Cu ₁₅ Ag ₅ Pd ₅ Gd ₁₀	Amorphous	4.30	-13.24	9.10	1053.49	0.72	9.27	[10]
Mg ₆₅ Cu _{7.5} Ni _{7.5} Zn ₅ Ag ₅ Y ₁₀	Amorphous	4.33	-7.35	9.96	1107.24	1.50	9.53	[10]
Zr ₅₇ Ti ₅ Al ₁₀ Cu ₂₀ Ni ₈	Amorphous	5.78	-31.50	10.18	1813.45	0.59	9.69	[10]
Co _{64.8} Fe _{7.2} B _{19.2} Si _{4.8} Nb ₄	Amorphous	7.38	-24.16	8.83	1922.41	0.70	10.02	[30]
Co _{57.6} Fe _{14.4} B _{19.2} Si _{4.8} Nb ₄	Amorphous	7.30	-24.27	9.88	1925.36	0.78	10.05	[30]

(continued)

Table 2.1 (continued)

Alloys	Major phases	VEC	ΔH_{mix} [kJ/mol]	ΔS_{mix} [J/(mol · K)]	T_m (K)	Ω	δ [%]	Refs.
$\text{Co}_{50.4}\text{Fe}_{21.6}\text{B}_{19.2}\text{Si}_{4.8}\text{Nb}_4$	Amorphous	7.23	-24.34	10.54	1928.31	0.83	10.08	[30]
$\text{Co}_{43.2}\text{Fe}_{28.8}\text{B}_{19.2}\text{Si}_{4.8}\text{Nb}_4$	Amorphous	7.16	-24.37	10.91	1931.26	0.86	10.12	[30]
CuNiHfTiZr	Amorphous	6.60	-27.36	13.38	1932.80	0.95	10.21	[10]
$\text{Ni}_{45}\text{Ti}_{20}\text{Zr}_{25}\text{Al}_{10}$	Amorphous	6.60	-45.41	10.46	1792.15	0.41	10.35	[27]
$\text{Ni}_{40}\text{Cu}_5\text{Ti}_{17}\text{Zr}_{28}\text{Al}_{10}$	Amorphous	6.65	-43.25	11.67	1779.11	0.48	10.48	[27]
$\text{Ni}_{39.8}\text{Cu}_{5.97}\text{Ti}_{15.92}\text{Zr}_{27.86}\text{Al}_{9.95}\text{Si}_{0.5}$	Amorphous	6.71	-43.58	11.97	1772.80	0.49	10.50	[27]
$\text{Ni}_{40}\text{Cu}_6\text{Ti}_{16}\text{Zr}_{28}\text{Al}_{10}$	Amorphous	6.72	-42.79	11.77	1773.23	0.49	10.52	[27]
$\text{Ti}_{55}\text{Zr}_{10}\text{Cu}_9\text{Ni}_8\text{Be}_{18}$	Amorphous	4.75	-25.43	10.70	1824.72	0.77	11.18	[10]
$\text{Ti}_{50}\text{Zr}_{15}\text{Cu}_9\text{Ni}_8\text{Be}_{18}$	Amorphous	4.75	-26.37	11.30	1833.82	0.79	11.64	[10]
$\text{Ti}_{40}\text{Zr}_{25}\text{Ni}_3\text{Cu}_{12}\text{Be}_{20}$	Amorphous	4.62	-25.88	11.60	2010.40	0.90	12.03	[10]
$\text{Ni}_{40}\text{Cu}_5\text{Ti}_{16.5}\text{Zr}_{28.5}\text{Al}_{10}$	Amorphous	6.65	-43.41	11.65	1780.02	0.48	12.07	[27]
$\text{Ti}_{40}\text{Zr}_{25}\text{Cu}_9\text{Ni}_8\text{Be}_{18}$	Amorphous	4.75	-28.26	11.98	1852.02	0.79	12.31	[10]
$\text{Mg}_{65}\text{Cu}_{20}\text{Zn}_5\text{Y}_{10}$	Amorphous	4.40	-5.98	8.16	1085.64	1.48	12.70	[10]
$\text{Fe}_{61}\text{B}_{15}\text{Mo}_7\text{Zr}_8\text{Co}_7\text{Y}_2$	Amorphous	6.76	-30.13	10.30	1992.27	0.68	13.20	[10]
$\text{Fe}_{61}\text{B}_{15}\text{Mo}_7\text{Zr}_8\text{Co}_5\text{Y}_2\text{Cr}_2$	Amorphous	6.70	-29.97	10.65	1999.53	0.71	13.20	[10]
$\text{Fe}_{61}\text{B}_{15}\text{Mo}_7\text{Zr}_8\text{Co}_6\text{Y}_2\text{Al}_1$	Amorphous	6.70	-30.30	10.54	1983.91	0.69	13.24	[10]
$\text{Zr}_{38.5}\text{Ti}_{16.5}\text{Cu}_{15.25}\text{Ni}_{9.75}\text{Be}_{20}$	Amorphous	5.25	-33.20	12.47	1828.35	0.69	13.36	[10]
$\text{Zr}_{39.88}\text{Ti}_{15.12}\text{Cu}_{13.77}\text{Ni}_{9.98}\text{Be}_{21.25}$	Amorphous	5.14	-34.27	12.34	1834.26	0.66	13.59	[10]
$\text{Er}_{20}\text{Tb}_{20}\text{Dy}_{20}\text{Ni}_{20}\text{Al}_{20}$	Amorphous	4.40	-37.60	13.38	1554.90	0.55	13.66	[25]
$\text{Dy}_{46}\text{Al}_{24}\text{Co}_{18}\text{Fe}_2\text{Y}_{10}$	Amorphous	4.18	-33.26	10.95	1533.60	0.50	13.71	[10]
$\text{Co}_{45.5}\text{Fe}_{2.5}\text{Cr}_{15}\text{Mo}_{14}\text{C}_{15}\text{B}_6\text{Er}_2$	Amorphous	6.88	-33.41	12.82	2327.43	0.89	13.79	[31]
$\text{Co}_{43}\text{Fe}_5\text{Cr}_{15}\text{Mo}_{14}\text{C}_{15}\text{B}_6\text{Er}_2$	Amorphous	6.85	-33.46	13.34	2369.44	0.94	13.80	[31]
$\text{Zr}_{41.2}\text{Ti}_{13.8}\text{Cu}_{12.5}\text{Ni}_{10}\text{Be}_{22.5}$	Amorphous	5.03	-36.72	12.18	1839.28	0.61	13.82	[10]
$\text{Zr}_{42.63}\text{Ti}_{12.37}\text{Cu}_{11.25}\text{Ni}_{10}\text{Be}_{23.75}$	Amorphous	4.91	-36.90	11.97	1844.44	0.60	14.05	[10]
$\text{Ce}_{65}\text{Al}_{10}\text{Ni}_{10}\text{Cu}_{10}\text{Nb}_5$	Amorphous	4.60	-19.86	9.32	1236.25	0.58	14.18	[26]

$Zr_{44}Ti_{11}Cu_{10}Ni_{10}Be_{25}$	Amorphous	4.80	-37.07	11.73	1849.48	0.59	14.27	[10]
$Zr_{45.38}Ti_{9.62}Cu_{8.75}Ni_{10}Be_{26.25}$	Amorphous	4.69	-37.23	11.46	1845.09	0.57	14.49	[10]
$Gd_{36}Y_{20}Al_{24}Co_{20}$	Amorphous	4.20	-34.26	11.26	1509.56	0.50	14.49	[32]
$Zr_{46.75}Ti_{8.25}Cu_{7.5}Ni_{10}Be_{27.5}$	Amorphous	4.58	-37.03	11.16	1848.95	0.56	14.70	[10]
$La_{68}Al_{14}(Cu_{5/6}Ag_{1/6})_8Ni_5Co_5$	Amorphous	4.29	-26.33	8.94	1224.51	0.42	14.93	[29]
$La_{32}Ce_{32}Al_{16}Ni_5Cu_{12}Co_3$	Amorphous	4.49	-27.96	12.74	1221.42	0.56	15.05	[33]
$La_{32}Ce_{32}Al_{16}Ni_5Cu_{10}Co_5$	Amorphous	4.45	-25.71	12.11	1229.66	0.62	15.11	[33]
$Sr_{20}Ca_{20}Yb_{20}Mg_{20}Zn_{20}$	Amorphous	4.20	-13.12	13.38	973.54	0.99	15.25	[25]
$Ce_{60}Al_{15}Ni_{15}Cu_{10}$	Amorphous	4.85	-30.60	9.19	1178.23	0.35	15.29	[26]
$La_{66}Al_{14}(Cu_{5/6}Ag_{1/6})_{10}Ni_5Co_5$	Amorphous	4.45	-26.73	9.35	1227.38	0.43	15.32	[29]
$La_{32}Ce_{32}Al_{16}Ni_5Cu_3Co_{12}$	Amorphous	4.31	-27.92	12.74	1258.50	0.57	15.33	[33]
$Sr_{20}Ca_{20}Yb_{20}(Li_{0.55}Mg_{0.45})_{20}Zn_{20}$	Amorphous	4.09	-12.15	14.53	922.03	1.10	15.49	[25]
$La_{62}Al_{14}Cu_{20}Ag_4$	Amorphous	4.92	-26.72	8.50	1191.97	0.38	15.49	[28]
$La_{65}Al_{14}(Cu_{5/6}Ag_{1/6})_{11}Ni_5Co_5$	Amorphous	4.53	-26.86	9.54	1228.82	0.44	15.51	[29]
$Ce_{57}Al_{10}Ni_{12.5}Cu_{15.5}Nb_5$	Amorphous	5.22	-22.06	10.39	1268.38	0.60	15.53	[26]
$La_{64}Al_{14}(Cu_{5/6}Ag_{1/6})_{12}Ni_5Co_5$	Amorphous	4.61	-27.06	9.72	1230.25	0.44	15.68	[29]
$La_{62}Al_{14}(Cu_{5/6}Ag_{1/6})_{20}Ni_2Co_2$	Amorphous	4.86	-26.89	9.48	1208.43	0.43	15.70	[28]
$Nd_{60}Al_{10}Ni_{10}Cu_{20}$	Amorphous	5.30	-27.48	9.05	1311.75	0.43	15.70	[32]
$La_{32}Ce_{32}Al_{16}Ni_5Cu_{15}$	Amorphous	4.55	-23.80	12.11	1209.06	0.62	15.72	[33]
$Pr_{60}Al_{10}Ni_{10}Cu_{20}$	Amorphous	5.30	-27.52	9.05	1260.75	0.41	15.94	[32]
$La_{62}Al_{14}(Cu_{5/6}Ag_{1/6})_{14}Ni_5Co_5$	Amorphous	4.77	-27.31	10.06	1233.12	0.45	16.02	[28]
$La_{55}Al_{25}Ni_5Cu_{10}Co_5$	Amorphous	4.45	-32.31	10.02	1200.78	0.37	16.19	[10]
$Sr_{20}Ca_{20}Yb_{20}Mg_{20}Zn_{10}Cu_{10}$	Amorphous	3.70	-10.60	14.53	1040.07	1.43	16.35	[25]
$(CeLaPrPd)_{65}Co_{25}Al_{10}$	Amorphous	5.64	-47.60	14.62	1396.78	0.43	16.78	[34]
$Nd_{60}Al_{15}Ni_{10}Cu_{10}Fe_5$	Amorphous	5.95	-27.37	9.99	1313.18	0.48	17.11	[10]
$Nd_{61}Al_{11}Ni_8Co_5Cu_{15}$	Amorphous	6.28	-27.43	9.82	1307.13	0.47	17.46	[10]

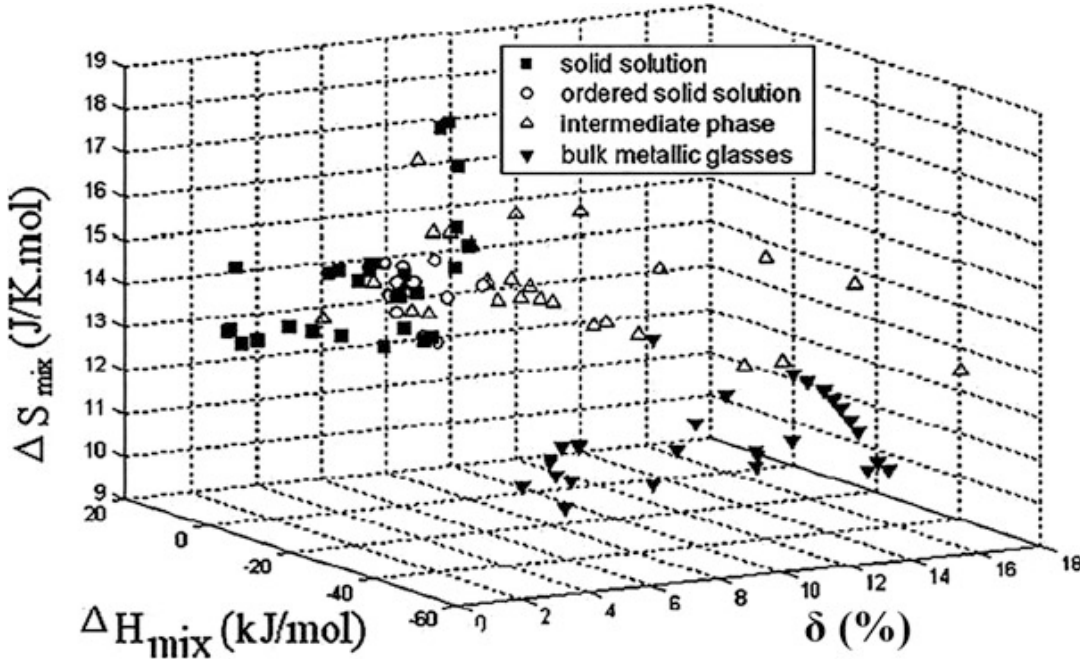


Fig. 2.2 Phase selection diagram of HEAs and BMGs based on ΔH_{mix} , Delta (δ), and ΔS_{mix} [9]

larger value of δ , but with the ΔS_{mix} in the range of 11–16.5 $\text{J}/(\text{mol} \cdot \text{K})$. There is a transition zone (marked by \circ) between the solid solution phase zone and the intermetallic compound zone, which contains ordered solid solution phases. It is noted that *all configuration entropies mentioned here are calculated for HEAs assuming they are in the liquid or fully random solid solution state (i.e., using the Boltzmann equation)*:

$$\Delta S_{\text{mix}} = -R \sum_{i=1}^N x_i \ln x_i \quad (2.4)$$

A new parameter, Ω , combining effects of ΔS_{mix} and ΔH_{mix} on the stability of multicomponent solid solution, was recently proposed by Yang and Zhang [10, 14, 15]. The parameter Ω is defined by

$$\Omega = \frac{T_m \Delta S_{\text{mix}}}{|\Delta H_{\text{mix}}|} \quad (2.5)$$

$$T_m = \sum_{i=1}^N x_i (T_m)_i \quad (2.6)$$

where T_m is the average melting temperature of the N -element alloy and $(T_m)_i$ is the melting point of the i th component of the alloy. By analyzing the phase formation using the parameters Ω and δ of various reported multicomponent alloys (shown in Fig. 2.3), new criteria for forming solid solution phases in HEAs were suggested: $\Omega \geq 1.1$ and $\delta \leq 6.6\%$. In contrast, intermetallic compounds and BMGs have larger values of δ and smaller values of Ω , and the value of Ω for BMGs is smaller than that of intermetallic compounds. Figure 2.4 replaces δ in Fig. 2.3 by the number of elements, N . It can be seen that solid solution forming HEAs appear at higher Ω and larger N , while BMGs appear at lower Ω and smaller N .

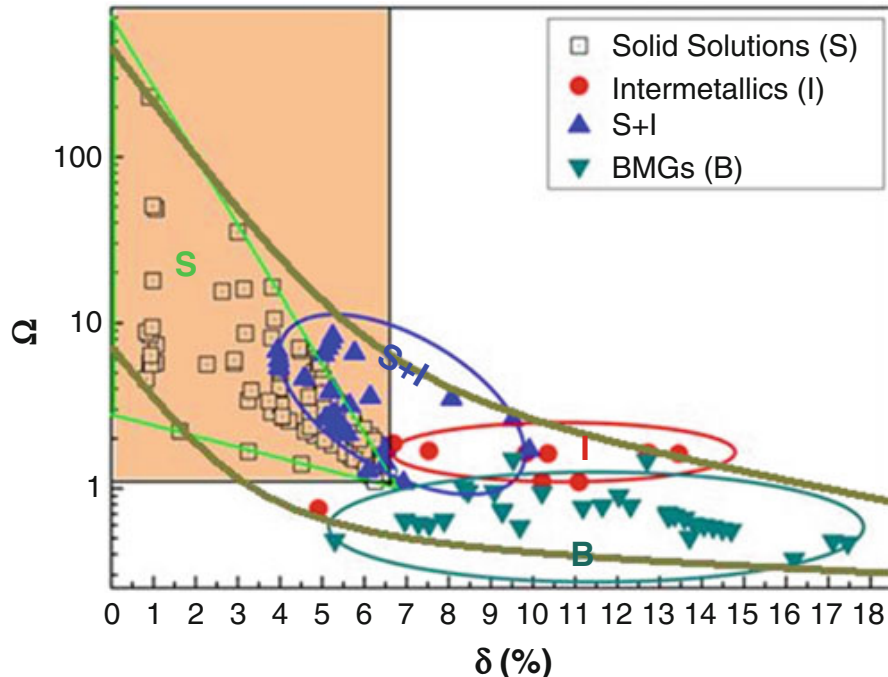


Fig. 2.3 Phase selection diagram of HEAs and BMGs based on Ω and δ [16]

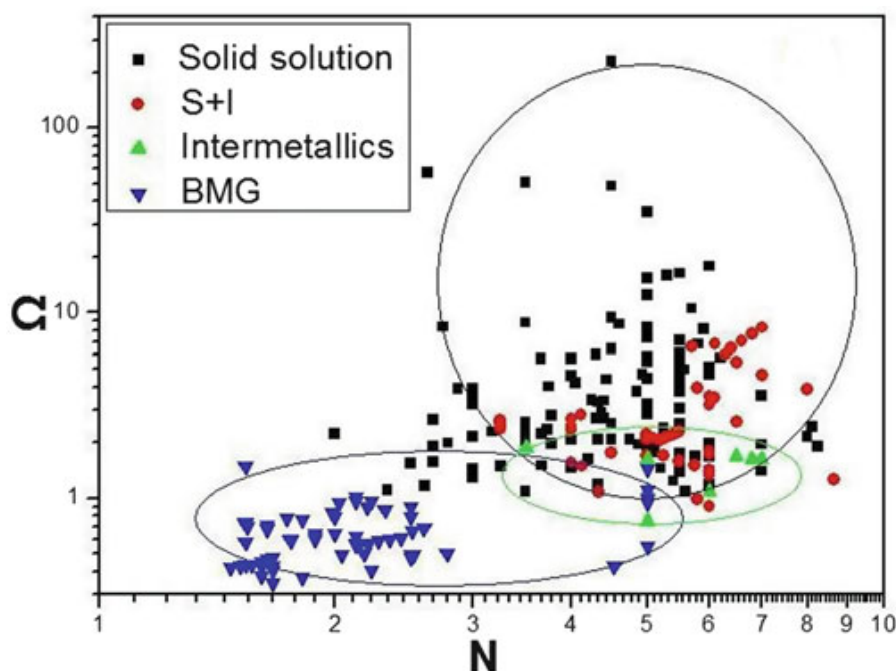


Fig. 2.4 Phase selection diagram of HEAs and BMGs based on Ω and the number of elements, N [16]

2.3 Electron Concentration

HEAs with solid solution structures are generally desired, since most, if not all, advantageous features like high hardness [1], sluggish diffusion kinetics [35], and high-temperature softening resistance [36] are related to the multi-principal-element solid solution structures. The formation of solid solutions in HEAs, as discussed previously, can be reasonably predicted using parametric approaches

based on physiochemical properties of constituent alloying elements, like atomic radii, mixing enthalpies between any two elements, and melting points [7–10]. However, these parametric approaches do not tell much information about the crystal structure of the achieved solid solutions. Since it has been widely known that, based on existing experimental evidences [37], the crystal structure significantly affects the mechanical behavior of HEAs, having the capability to design them with desirable crystal structure is crucial. [The energies of HEAs in fcc, bcc, and hcp structures are presented in Chaps. 7, 8, 9, 10, and 11 using predictive computational methods based on first-principles density functional theory (DFT) and in Chap. 12 using CALPHAD modeling. The $\Delta H_{\text{mix}}-\delta$ relation is reevaluated based on DFT calculations as presented in Chap. 11.]

The solid solutions formed in HEAs are normally of fcc, bcc, and hcp or a mixture of these structures [37]. fcc-structured HEAs are known to possess good ductility, but with relatively low strength [38]. bcc-structured HEAs can have much higher strength [39], but almost always at the cost of much decreased ductility, particularly in tension. Is it possible to control the formation of fcc- or bcc-structured solid solutions in HEAs? The $\delta-\Delta H_{\text{mix}}$ plot shown in Fig. 2.5 indicates that the fcc-type solid solutions form at sufficiently small δ , and bcc solid solutions form at larger δ [16], assuming ΔH_{mix} still satisfies the conditions to form solid solutions. However, the fcc-type solid solution forming δ range largely overlaps with that of the bcc solid solutions, which practically means δ has limited use in terms of controlling the formation of fcc- or bcc-structured HEAs. As such, new criteria or new parameters need to be established for this important purpose.

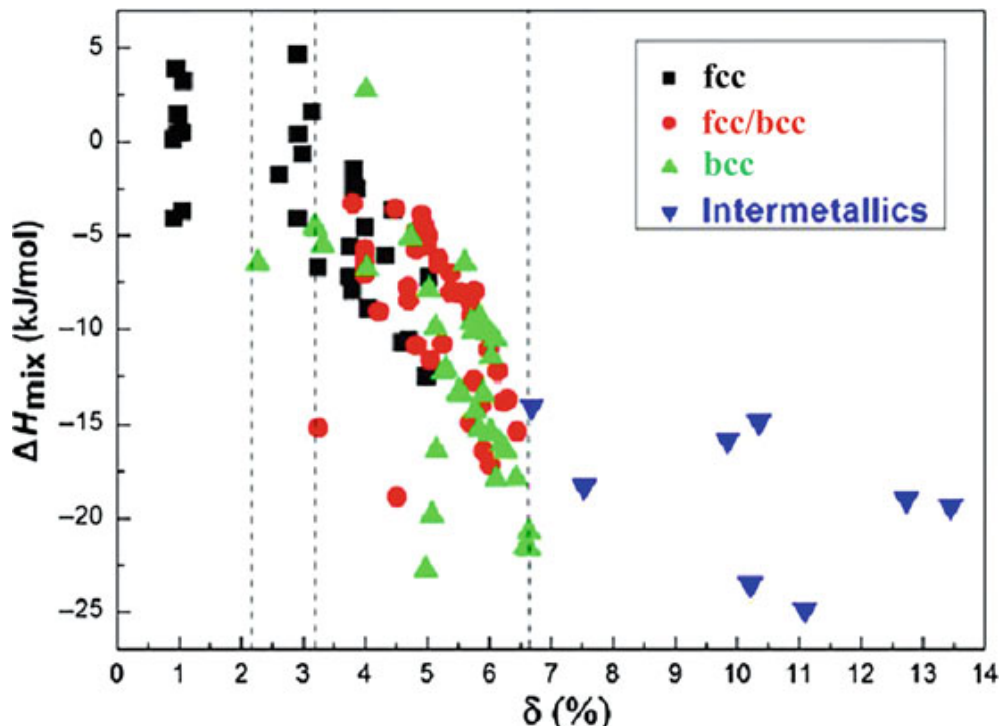


Fig. 2.5 Dependence of crystal structures on the enthalpy of mixing, ΔH_{mix} , and the atomic size mismatch, δ , in various HEAs [16]

Inspirations to address this issue came from the equivalency of alloying elements in stabilizing fcc- or bcc-type solid solutions. It has been widely confirmed by experiments that elements like Al and Cr are bcc phase stabilizers and Ni and Co are fcc phase stabilizers [40]. It was clearly shown that in the $\text{Al}_x\text{Co}_y\text{Cr}_z\text{Cu}_{0.5}\text{Fe}_v\text{Ni}_w$ alloy system, 1.11 portions of Co was equivalent to 1 portion of Ni as the fcc phase stabilizer, and 2.23 portions of Cr was equivalent to 1 portion of Al as the bcc stabilizer. When the equivalent Co % was greater than 45 at.%, the alloys had an fcc structure; when the equivalent Cr % was greater than 55 at.%, the alloys had a bcc structure [41]. Naturally, this equivalency of alloying elements in stabilizing a particular crystal structure reminds the well-known effect of electron concentration on the crystal structure in conventional alloys [42]. Before the effect of electron concentration on the crystal structure of solid solutions forming HEAs is discussed, two different notions of electron concentrations, valence electron concentration (*VEC*) and electrons per atom ratio (*e/a*), will be introduced first, as there exist subtle differences in their definitions and resulting applications.

2.3.1 *VEC and e/a*

Electron concentration has been known to play a critical role in controlling the phase stability and even physical properties of alloys [42]. It is pointed out that two different notions of electron concentration exist, one is the average number of itinerant electrons per atom ratio (*e/a*), and the other is the number of total electrons (*VEC*) (including d electrons involved in the valence band). For example, *e/a* and *VEC* for pure Cu ([Ar] 3d¹⁰4s¹) is 1 and 11, respectively. Basically, *e/a* is in connection with the Hume-Rothery electron concentration rule, and *VEC* is a key parameter in first-principles band calculations and is obtained by integrating the density of states (DOS) of the valence band from the bottom up to a given energy. Mizutani discussed different applications of *e/a* and *VEC* in depth in his monograph *Hume-Rothery Rules for Structurally Complex Alloy Phases* [42]. [Interested readers are suggested to refer to this book for more detailed information on the difference between *e/a* and *VEC*.] Some applications of *e/a* and *VEC* in terms of the crystal structure and phase stability are exemplified here, to facilitate the discussions that are followed.

The effect of *e/a* on the phase stability is articulated in the Hume-Rothery rules, where Hume-Rothery noted that similar structures occur at characteristic *e/a* [42]. As a classical example, Fig. 2.6 shows the *e/a* dependence of the phase stability in alloys based on noble metals (Cu-, Ag-, and Au-based alloys) [42]. Seen from Fig. 2.6, the α -, β -, γ -, ϵ -, and η -phases successively appear at particular *e/a* ranges, regardless of the solute element added to noble metals. The fcc α -phase exists at $e/a < 1.4$. Near $e/a = 1.5$, the bcc β -phase exists at high temperatures, which is replaced either by its ordered CsCl-type (B2) β -phase or by the hcp ζ -phase at low temperatures. Also around $e/a = 1.5$, the μ -phase containing 20 atoms in its β -Mn-type cubic unit cell occurs in certain alloy systems. The complex cubic

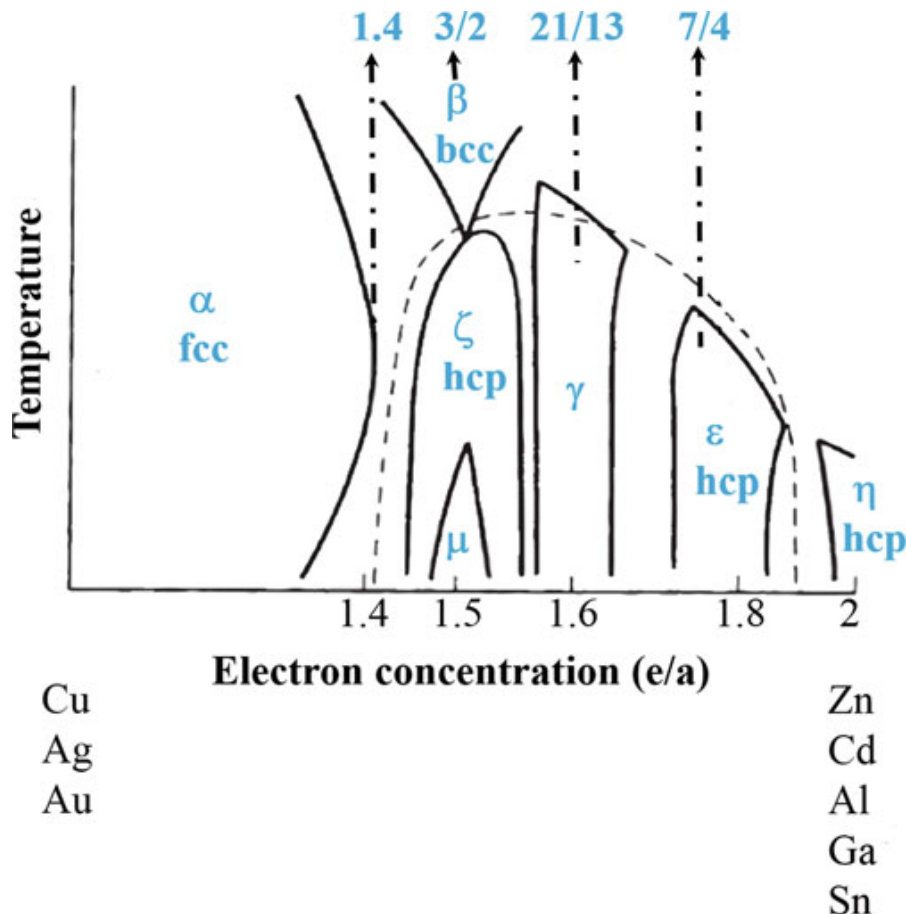


Fig. 2.6 Schematic phase diagram showing the Hume-Rothery electron concentration (e/a) rule in noble metal alloys [42]

γ -phase is stabilized at about $e/a = 1.6$ and the hcp ϵ -phase in the range $1.7 < e/a < 1.9$. The hcp η -phase appears as a primary solid solution of Zn and Cd and is centered at $e/a = 2.0$. This is the Hume-Rothery electron concentration rule. Because of their locations at particular electron concentrations, these alloys are called electron compounds or Hume-Rothery electron phases. Judging from its strong e/a dependence, it has been naturally thought that the interaction of the Fermi surface with the Brillouin zone must play a critical role in stabilizing these electron phases.

VEC has been proved to be quite effective in controlling the ordered crystal structures of Co_3V alloyed with Fe and Ni [43]. Ni, Co, and Fe have similar atomic sizes and electronegativities, but differ in VEC: 10, 9, and 8, respectively [37]. The stoichiometric Co_3V has a six-layer hexagonal ordered structure with the stacking sequence **ABCACB**. The stacking character of Co_3V is **hcchcc**, with a 33.3 % hexagonality. VEC of Co_3V can be increased by partial replacement of Co by Ni: $(\text{Ni}, \text{Co})_3\text{V}$. With increasing VEC, the hexagonality can increase from 33.3 to 100 % at a VEC of 8.54. Further increasing VEC to 8.75, when Ni completely replaces Co, results in a change in the basic layer structure from triangular (T) type to rectangular (R) type, and stacking of the R layers gives a tetragonal ordered structure similar to DO_{22} -type Ni_3V . VEC of Co_3V can also be reduced by

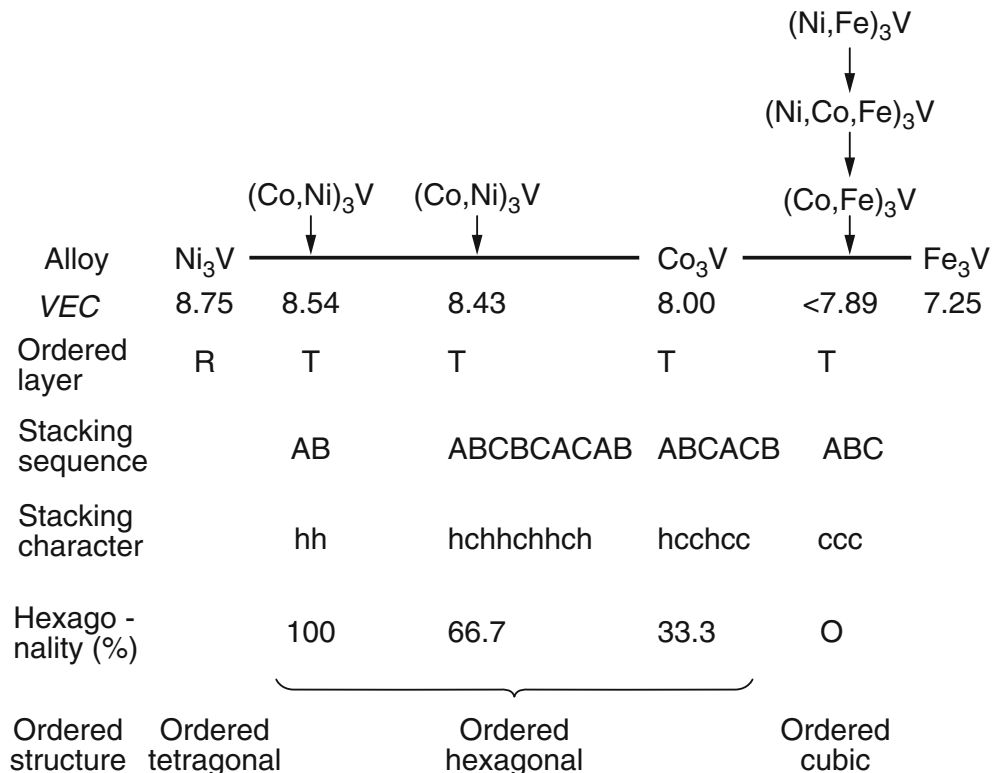


Fig. 2.7 Effect of the electron concentration (*VEC*) on the stability of ordered crystal structures in $\text{Ni}_3\text{V}-\text{Co}_3\text{V}-\text{Fe}_3\text{V}$ alloys [43]

partial replacement of Co by Fe: $(\text{Co}, \text{Fe})_3\text{V}$. With *VEC* below 7.89, the $\text{L}1_2$ ordered cubic structure having the stacking sequence **ABC** (**ccc**) is stabilized. Controlling the hexagonality of Co_3V alloys by the adjustment of *VEC* is very important to the room temperature ductility, as ordered hexagonal alloys are brittle due to the limited number of slip systems, while the deformation behavior of ordered cubic alloys is similar to that of ductile fcc alloys. Indeed, ordered cubic alloys of the compositions of $(\text{Fe}, \text{Co})_3\text{V}$, $(\text{Fe}, \text{Co}, \text{Ni})_3\text{V}$, and $(\text{Fe}, \text{Ni})_3\text{V}$ are all ductile, and ordered hexagonal alloys of the compositions of Co_3V and $(\text{Ni}, \text{Co})_3\text{V}$ are brittle. The *VEC* dependence of the phase stability in Co_3V alloys is shown in Fig. 2.7. Similarly, the *VEC* rule has been successfully applied to tune the phase stability (cubic C15 and hexagonal C14 and C36) in NbCr₂-based Laves phase alloys [44].

2.3.2 *VEC or e/a?*

As shown above, both *e/a* and *VEC* have been proved to be correlated to the phase stability and physical properties of alloys. One needs to be cautious in selecting *e/a* or *VEC* as an electron concentration parameter though, depending on the situation that is involved. Mizutani [42] showed that physical properties, including the saturation magnetization and the electronic specific heat coefficient in 3d transition metals, the superconducting transition temperature of TM (transition metal) alloys,

and the thermoelectric power in the Heusler ($L2_1$)-type Fe_2VAl alloys, all exhibit a universal behavior with respect to VEC . Mizutani noted that all these properties are clearly related to the total DOS at the Fermi level. Meanwhile, physical properties like the axial ratio, c/a , the magnetic susceptibility corrected for ionic contributions, and the electronic specific heat coefficient in noble metal alloys are all correlated to e/a , and not to VEC . These properties are known to be dominated by the FsBz (Fermi surface-Brillouin zone) interactions and therefore are unsurprisingly scaled in terms of e/a , which is introduced through the Fermi diameter $2k_F$ in the matching condition. When discussing the role of two electron concentration parameters VEC and e/a in designing new CMAs (complex metallic alloys), which are characterized by a pseudogap across the Fermi level, Mizutani concluded that VEC can be used as long as a rigid-band model holds, assuming that the electronic density of states of an alloy can be inferred from that of the host, whereas e/a or e/uc (electrons per unit cell) is also useful, only if sound e/a values for the TM elements are used. e/a values for transition metals have been quite controversial for a long time and no satisfied solutions have yet emerged. This difficulty has challenged the interpretations of the Hume-Rothery electron concentration rule for alloys containing TM elements. Mizutani evaluated different proposals for e/a , mainly analyzing those postulated by Raynor and by Haworth and Hume-Rothery [42], and then deduced a new set of e/a values for TM elements based on the Hume-Rothery plot, which is quite different to the previous proposals [42]. The work from Mizutani will not end the discussion on e/a values for TM elements though, since not all e/a have been determined, and e/a for each element even varies depending on the atomic environment. It should be noted that the e/a rule has also been used to design quasi-crystalline alloys [45, 46] and even amorphous alloys [47, 48], with some success. Nevertheless, the choice of e/a for TM elements was also ambiguous.

2.3.3 *The Effect of VEC on the Phase Stability of HEAs*

As said previously, the equivalency of alloying elements in stabilizing fcc- or bcc-type solid solutions in HEAs naturally leads one to correlate this equivalency to the electron concentration effect. Since currently developed HEAs comprise mainly TM elements, considering the difficulty of defining the e/a values for them, VEC seems to be a more straightforward electron concentration parameter. Meanwhile, it has been shown that in the $\text{Al}_x\text{Co}_y\text{Cr}_z\text{Cu}_{0.5}\text{Fe}_v\text{Ni}_w$ alloy system, 1.11 portions of Co was equivalent to 1 portion of Ni as the fcc phase stabilizer [41]. This further indicates that VEC has an effect on the phase stability in HEAs: a VEC of 9 for Co and 10 for Ni. To verify this, Guo et al. designed a series of $\text{Al}_x\text{CrCuFeNi}_2$ alloys [37], fully replacing Co with Ni in the widely studied $\text{Al}_x\text{CoCrCuFeNi}$ alloys. It was experimentally proved that the new $\text{Al}_x\text{CrCuFeNi}_2$ alloy system showed a very similar trend of phase stability to that of $\text{Al}_x\text{CoCrCuFeNi}$ alloys, with the increasing Al concentration. In addition, there seemed to exist threshold VEC values for forming different types of solid solutions at $VEC \geq 8.0$, where sole

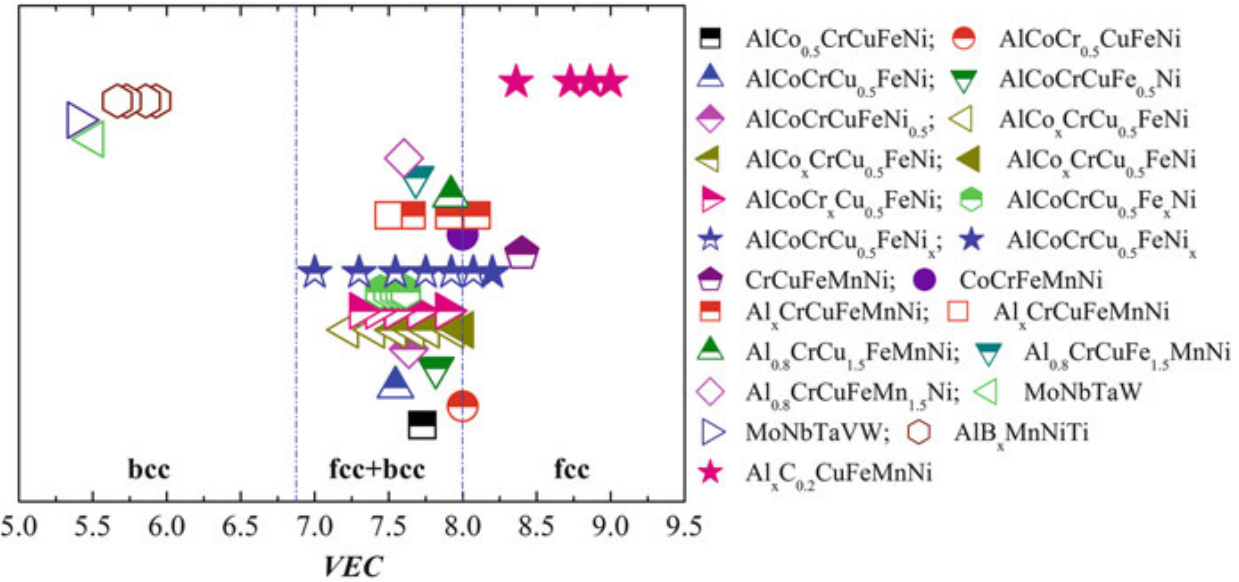


Fig. 2.8 Relationship between VEC and the phase stability for fcc and bcc solid solutions in various HEAs. Note on the legends: fully closed symbols for sole fcc phases, fully open symbols for sole bcc phases, and top-half closed symbols for mixed fcc and bcc phases [37]

fcc solid solution phases formed. Guo et al. then moved to scrutinize the VEC effect on the phase stability in various solid solution forming HEAs (where no intermetallic compounds or amorphous phase is formed), comprising different alloying elements. The result of this statistical analysis is shown in Fig. 2.8 [37], from which two important conclusions can be drawn. Firstly and qualitatively, in solid solution forming HEAs, bcc phases are stabilized at a lower VEC , while fcc phases are stabilized at a higher VEC . In the intermediate VEC , both fcc and bcc phases exist. Secondly and almost quantitatively, fcc phases occur at $VEC \geq 8.0$, bcc phases at $VEC < 6.87$, and a mixture of fcc and bcc phases at $6.87 \leq VEC < 8$. Some exceptions do exist, particularly for Mn-containing HEAs. The VEC rule provides a convenient way to design fcc- or bcc-structured HEAs containing mainly TM elements, from the electron concentration perspective, and its validity has been verified widely by subsequent experiments following its publication.

A few notes need to be added in terms of utilizing the VEC rule. First, the VEC rule was proposed based on the experimental results from cast alloys. Its validity to HEAs prepared by other routes (e.g., the powder metallurgy method) has not been evaluated. Second, the VEC rule only works on the premise that the solid solutions are the only alloying products (i.e., no intermetallic compounds or amorphous phase is formed). Third, when discussing the separation of fcc and bcc solid solutions, no distinction was made between disordered and ordered solid solutions. For example, B2-type ordered bcc phases and disordered bcc phases were both classified as bcc solid solutions. Fourth, forming the fcc or bcc solid solutions does not necessarily indicate the formation of one fcc or bcc phase. For example, this can mean the formation of two disordered fcc phases or one disordered fcc plus one ordered fcc phase. Fifth, the threshold VEC values of 6.87 and 8.0 are mainly for reference. They can vary in different alloy systems [37] and even vary for the same compositions that were cast with different cooling rates [6] or after subsequent heat

treatments at various temperatures [49]. The latter variations are understandable, considering that solid solution phases appearing in cast HEAs are actually frozen stable solid-state phases at elevated temperatures [50] and therefore affected by factors like kinetics and also the entropic contribution to the Gibbs free energy. However, so far there are no exceptions against the trend that a higher *VEC* favors the fcc phase and a lower *VEC* favors the bcc phase, in solid solution forming HEAs. From the published experimental results, the threshold *VEC* values of 6.87 and 8.0 still seem to be a reasonable guidance to design fcc- or bcc-structured HEAs, prepared from the direct casting. Again, it has to be emphasized that, so far this statement has mostly been verified for HEAs containing mainly TM elements.

In the second note that is given above, it is emphasized that the *VEC* rule for the formation of fcc- or bcc-type solid solutions only works when no intermetallic compounds form. In cases when entropic contribution in lowering the Gibbs free energy is not sufficient to surpass the very negative enthalpy among alloying elements, intermetallic compounds form [7]. Interestingly, Tsai et al. showed that *VEC* can also be used to predict the formation of σ -phase in cast Cr- and V-containing HEAs, and furthermore the *VEC* range of the formation of σ -phase was $6.88 < VEC < 7.84$ (Fig. 2.9). It is interesting to point out that this range almost overlaps with that for forming the mixture of fcc and bcc solid solutions proposed by Guo et al.: $6.87 \leq VEC < 8$ [51]. No σ -phase was found to form outside this range. Based on these results, it seems probable that the internal energy difference between the mixed fcc and bcc solid solutions and the σ -phase is small. The general applicability of the *VEC* rule to the formation of σ -phase in other alloy systems and to other type of intermetallic compounds is uncertain and still awaits further experimental evidences.

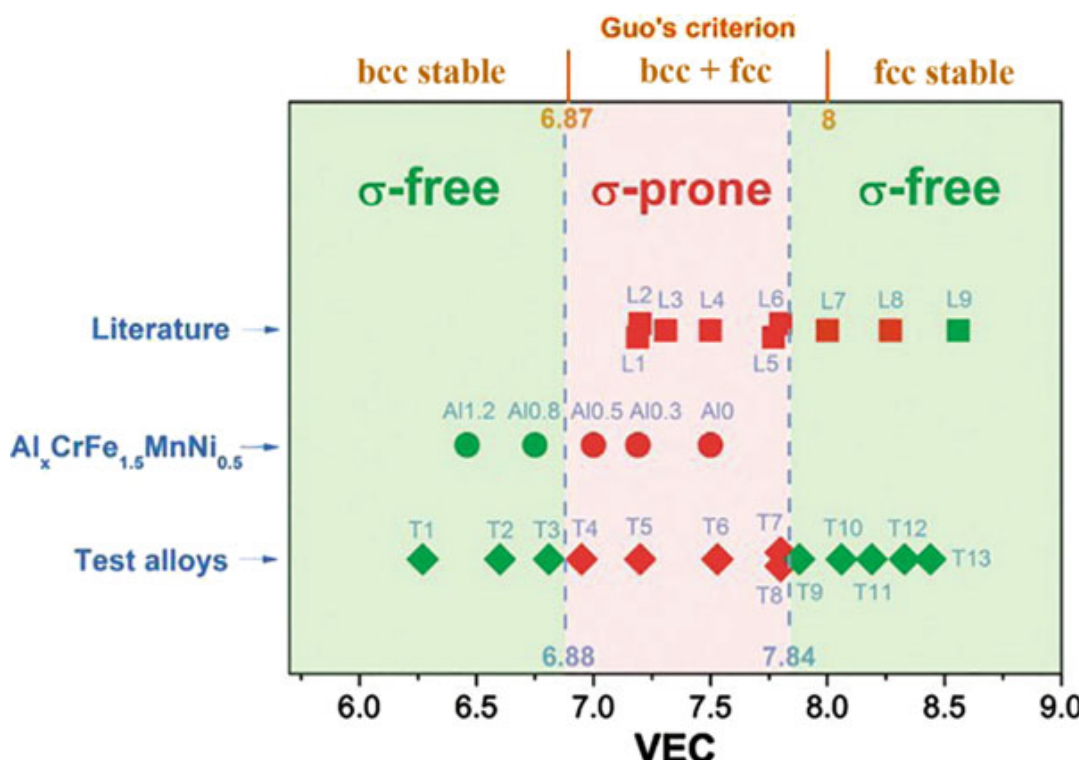


Fig. 2.9 Relationship between *VEC* and the presence of the σ -phase after aging for various HEAs [51]

2.4 Remaining Issues and Future Prospects

2.4.1 *Phase Formation Rules for HEAs Containing Mainly Non-TM Elements*

The phase formation rules proposed in Sect. 2.2 are basically based on HEAs containing mainly 3d and/or 4d TM elements. For low-density multicomponent HEAs containing high concentrations of Al, Mg, Li, Zn, Cu, and/or Sn, it was found that most previous phase formation rules fail to work effectively [15]. The configurational entropy seems not to be a dominant factor controlling the phase selection in low-density multicomponent alloys containing significant amounts of Al, Mg, and Li. Compared with HEAs containing mainly TM elements, low-density multicomponent alloys do not readily form solid solution phases with a simple crystal structure. As seen in Fig. 2.10, the threshold values of parametric criteria that are given in Sect. 2.2 need to be modified to be applicable for low-density HEAs containing mainly non-TM elements. Namely, solid solutions form at smaller value of δ ($<4.5\%$), larger value of ΔH_{mix} ($\sim -1 \text{ kJ/mol} < \Delta H_{\text{mix}} \leq 5 \text{ kJ/mol}$), and larger value of Ω ($>\sim 10$).

2.4.2 *Justification of the VEC Rule*

The validity of the *VEC* rule in controlling the fcc- or bcc-type solid solution phases in HEAs has been proved by a large amount of experiments. This indicates that the phase stability in HEAs is probably determined by the total DOS at the Fermi level, which can be predicted by first-principles calculations. Widom et al. used first-principles calculations to study the ordering issue in Mo-Nb-Ta-W refractory HEAs [53, 54]. Tian et al. studied the structural stability in CoCrFeNiAl_x HEAs and they found that at 300 K the fcc phase in these alloys is stable at $VEC \geq 7.57$ and the bcc phase is stable at $VEC \leq 7.04$ [55]. These threshold *VEC* values are not too far away from those proposed by Guo et al. [37]. Firstly, as discussed before, the threshold *VEC* values proposed by Guo et al. are mainly for reference only and variations among different alloy systems are expected. Secondly, in Tian et al.'s calculation, the relative stability of fcc and bcc phases was compared at 300 K. This would also cause some concerns, as these solid solution phases are not equilibrium phases at room temperature [50]. In order to physically justify the *VEC* rule, more work from the theoretical side needs to be carried out. For example, temperature may impact the chemical and structural ordering of HEAs to a large degree and consequently their electronic and thermodynamic properties. Furthermore, additional work is required to verify the *VEC* rule for HEAs not containing mainly TM elements.

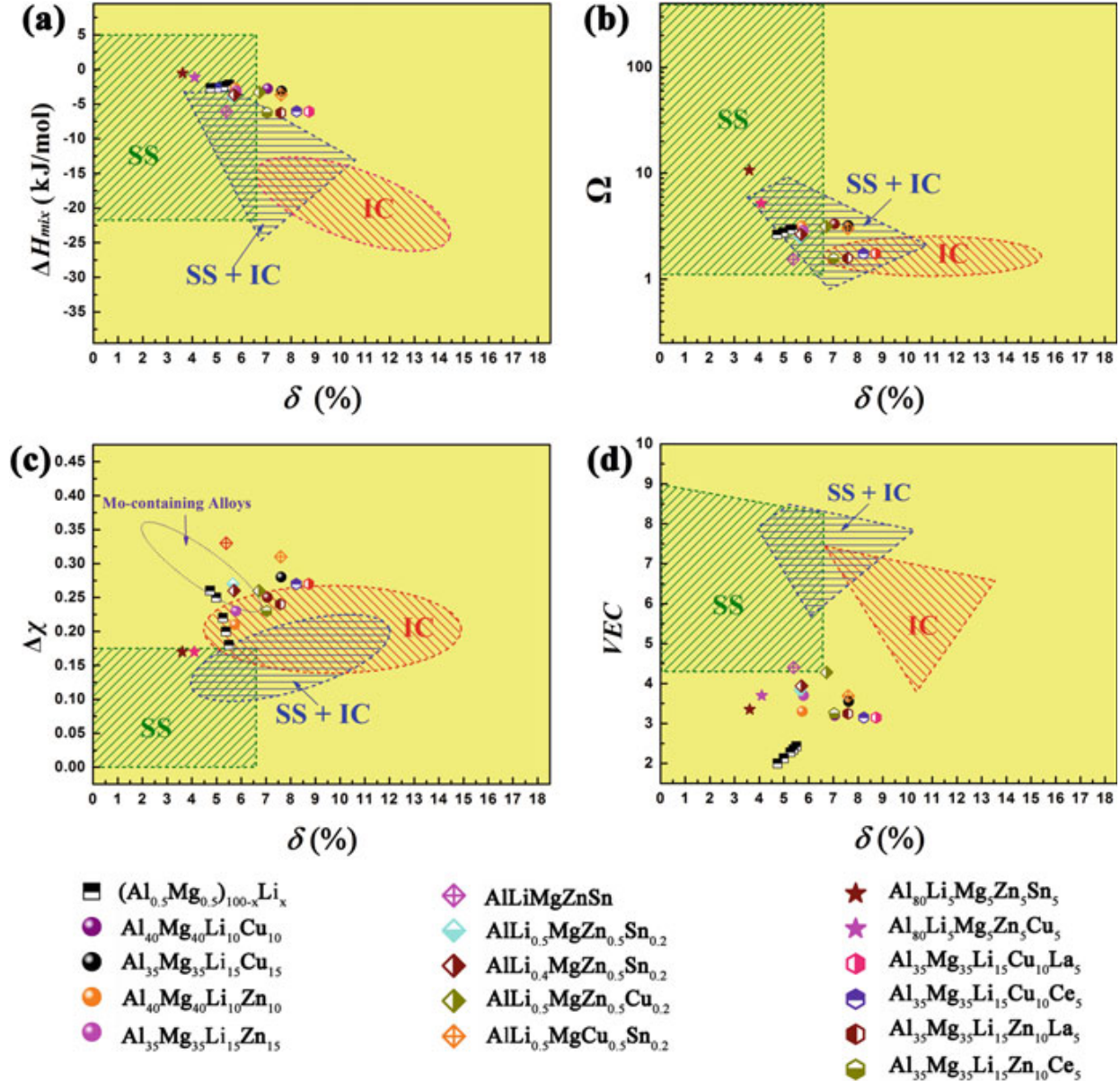


Fig. 2.10 (a) δ - ΔH_{mix} , (b) δ - Ω , (c) δ - $\Delta\chi$ ($\Delta\chi$ is the electronegativity difference among elements, defined in Ref. [52]), and (d) δ -VEC plots for low-density multicomponent alloys on crosshatched regions developed in previous HEA investigations. For $(\text{Al}_{0.5}\text{Mg}_{0.5})_{100-x}\text{Li}_x$, $x = 5, 10, 15, 25$, and 33.33 [15]

2.4.3 Beyond fcc and bcc Solid Solutions

In almost all available experimental results, if solid solutions are formed in HEAs, these solid solutions are fcc structured, bcc structured, or a mixture of these structures. However, some other types of solid solutions were also found. Recently, Lilenstein reported an orthorhombic structure in the $\text{Ti}_{35}\text{Zr}_{27.5}\text{Hf}_{27.5}\text{Ta}_5\text{Nb}_5$ alloy [56], although whether an alloy of such a composition can be classified as HEAs is debatable. However, hcp-type solid solutions have been experimentally observed or theoretically predicted in high-entropy alloy systems like DyGdHoTbY , DyGdLuTbY , DyGbLuTbTm , $\text{CoFeMnTi}_x\text{V}_y\text{Zr}_z$, CrFeNiTiVZr , CoFeNiTi , and

CoOsReRu [57–62]. These alloys pose challenges to the *VEC* rule that was initially established to control the formation of fcc- and bcc-type solid solutions in HEAs. The phase stability dependence on the electron concentration needs to be further understood along with the discovery of new HEAs containing different phase constitutions.

2.4.4 *On e/a*

The difference between *VEC* and *e/a*, in terms of both definitions and applications, has been discussed (more details in Ref. [42]). Due to the difficulty in defining the *e/a* values for TM elements, the use of *VEC* is more convenient for predicting the phase selection in HEAs. However, based on the historical contribution of *e/a* to understand the phase stability in alloys, efforts to study the effect of *e/a* on the phase stability in HEAs are still necessary. Poletti and Battezzati recently evaluated the phase stability of HEAs using both *e/a* and *VEC* [63]. They claimed that fcc phases are stabilized at $VEC > 7.5$ and $1.6 < e/a < 1.8$ and bcc phases are stabilized at $VEC < 7.5$ and $1.8 < e/a < 2.3$. If such a correlation between *e/a* and the phase stability does exist, then it provides a new perspective to design HEAs. However, it needs to be noted that when calculating *e/a*, they counted the electrons on the *s* and *p* orbital for all elements, even for TM elements, such as an *e/a* of 1 for Cr ([Ar] 3d⁵4s¹) and 2 for Fe ([Ar] 3d⁶4s²) and Ni ([Ar] 3d⁸4s²). The choice of *e/a*, and hence the soundness of this *e/a* dependence of the phase stability, needs more justifications. Nevertheless, it is expected that future work along this line of thinking will help to gain a deeper understanding into the effect of electron concentration on the phase stability of HEAs.

2.5 Summary

The phase formation rules in HEAs have been formulated using a parametric approach, utilizing parameters based on two considerations, i.e., thermodynamics and geometry effect. A couple of criteria are proposed to predict and control the phase selection, among solid solutions, intermetallic compounds, and the amorphous phase, in HEAs containing mainly transition metals. These criteria include the enthalpy of mixing, ΔH_{mix} ; the atomic size difference, δ ; and the Ω parameter. Particularly, $\Omega \geq 1.1$ and $\delta \leq 6.6\%$ proved to be quite effective in predicting the solid solutions in HEAs. The formation of intermetallic compounds tends to complicate the phase formation rules, and this still constitutes a challenge to formulate sufficient conditions (i.e., not just necessary conditions) to form solid solutions in HEAs. The applicability of current phase formation rules to HEAs containing mainly non-TM elements needs further inspections.

Inspired by the equivalency of stabilizing elements and also the well-established knowledge on physical metallurgy, the valence electron concentration, *VEC*, has been found to be a good criterion to control the fcc and bcc solid solutions, the two

most common types of solid solutions seen in HEAs. The *VEC* rule enables one to refine the design of HEAs with desired crystal structures, based on the parametric approaches to design solid solution forming HEAs. Essentially, elements with a higher *VEC* tend to stabilize the fcc phase and elements with a lower *VEC* tend to stabilize the bcc phase, and the threshold values of 8.0 and 6.87 can be a quite reasonable guidance. Since the *VEC* rule was proposed, its effectiveness has been verified by a large amount of experiments and awaits further inspections. Its applicability to HEAs prepared by routes other than casting also needs to be evaluated. Theoretical analyses, mainly based on first-principles calculations, are required to elevate the electron concentration dependence of the phase stability in HEAs, from empirical rules to scientific theories. Meanwhile, new developments are necessary to tackle challenges like the formation of solid solutions other than fcc and bcc structures. Another important electron concentration parameter, electrons per atom ratio, *e/a*, is worthy of more attention.

Acknowledgments Y.Z. and X.Y. would like acknowledge the financial supports from the National Natural Science Foundation of China (NSFC) with grant nos. of 51210105006, 50971019, 50571018, and 51471025 and National High-Tech R&D (863) Program with grant no. of 2009AA03Z113. S.G. thanks the Area of Advance Materials Science from Chalmers University of Technology, for the start-up funding. C.T.L. acknowledges the financial support from the Research Grants Council (RGC) of the Hong Kong government, through the General Research Fund (GRF) with the account number CityU 521411.

References

1. Yeh JW, Chen SK, Lin SJ, Gan JY, Chin TS, Shun TT, Tsau CH, Chang SY (2004) Nanostructured high-entropy alloys with multiple principal elements: novel alloy design concepts and outcomes. *Adv Eng Mater* 6(5):299–303. doi:[10.1002/adem.200300567](https://doi.org/10.1002/adem.200300567)
2. Otto F, Yang Y, Bei H, George EP (2013) Relative effects of enthalpy and entropy on the phase stability of equiatomic high-entropy alloys. *Acta Mater* 61(7):2628–2638. doi:[10.1016/j.actamat.2013.01.042](https://doi.org/10.1016/j.actamat.2013.01.042)
3. Tong CJ, Chen YL, Chen SK, Yeh JW, Shun TT, Tsau CH, Lin SJ, Chang SY (2005) Microstructure characterization of $\text{Al}_x\text{CoCrCuFeNi}$ high-entropy alloy system with multiprincipal elements. *Metall Mater Trans A* 36(4):881–893. doi:[10.1007/s11661-005-0283-0](https://doi.org/10.1007/s11661-005-0283-0)
4. Wang WH (2014) High-entropy metallic glasses. *JOM* 10(66):2067–2077. doi:[10.1007/s11837-014-1002-3](https://doi.org/10.1007/s11837-014-1002-3)
5. Miracle DB, Miller JD, Senkov ON, Woodward C, Uchic MD, Tiley J (2014) Exploration and development of high entropy alloys for structural applications. *Entropy* 16(1):494–525. doi:[10.3390/e16010494](https://doi.org/10.3390/e16010494)
6. Singh S, Wanderka N, Murty BS, Glatzel U, Banhart J (2011) Decomposition in multi-component AlCoCrCuFeNi high-entropy alloy. *Acta Mater* 59(1):182–190. doi:[10.1016/j.actamat.2010.09.023](https://doi.org/10.1016/j.actamat.2010.09.023)
7. Guo S, Hu Q, Ng C, Liu CT (2013) More than entropy in high-entropy alloys: forming solid solutions or amorphous phase. *Intermetallics* 41:96–103. doi:[10.1016/j.intermet.2013.05.002](https://doi.org/10.1016/j.intermet.2013.05.002)
8. Guo S, Liu CT (2011) Phase stability in high entropy alloys: formation of solid-solution phase or amorphous phase. *Prog Nat Sci:Mater Int* 21(6):433–446. doi:[10.1016/S1002-0071\(12\)60080-X](https://doi.org/10.1016/S1002-0071(12)60080-X)

9. Zhang Y, Zhou YJ, Lin JP, Chen GL, Liaw PK (2008) Solid-solution phase formation rules for multi-component alloys. *Adv Eng Mater* 10(6):534–538. doi:[10.1002/adem.200700240](https://doi.org/10.1002/adem.200700240)
10. Yang X, Zhang Y (2012) Prediction of high-entropy stabilized solid-solution in multi-component alloys. *Mater Chem Phys* 132(2–3):233–238. doi:[10.1016/j.matchemphys.2011.11.021](https://doi.org/10.1016/j.matchemphys.2011.11.021)
11. Cahn RW, Hassen P (1996) Physical metallurgy, vol 1, 4th edn. North Holland, Amsterdam
12. Inoue A (2000) Stabilization of metallic supercooled liquid and bulk amorphous alloys. *Acta Mater* 48(1):279–306, [http://dx.doi.org/10.1016/S1359-6454\(99\)00300-6](http://dx.doi.org/10.1016/S1359-6454(99)00300-6)
13. Curtarolo S, Hart GLW, Nardelli MB, Mingo N, Sanvito S, Levy O (2013) The high-throughput highway to computational materials design. *Nat Mater* 12(3):191–201. doi:[10.1038/nmat3568](https://doi.org/10.1038/nmat3568)
14. Zhang Y, Yang X, Liaw PK (2012) Alloy design and properties optimization of high-entropy alloys. *JOM* 64(7):830–838. doi:[10.1007/s11837-012-0366-5](https://doi.org/10.1007/s11837-012-0366-5)
15. Yang X, Chen SY, Cotton JD, Zhang Y (2014) Phase stability of low-density, multiprincipal component alloys containing aluminum, magnesium, and lithium. *JOM* 10(66):2009–2020. doi:[10.1007/s11837-014-1059-z](https://doi.org/10.1007/s11837-014-1059-z)
16. Zhang Y, Lu ZP, Ma SG, Liaw PK, Tang Z, Cheng YQ, Gao MC (2014) Guidelines in predicting phase formation of high-entropy alloys. *MRS Commun* 4(2):57–62. doi:[10.1557/mrc.2014.11](https://doi.org/10.1557/mrc.2014.11)
17. Ma SG, Zhang Y (2012) Effect of Nb addition on the microstructure and properties of AlCoCrFeNi high-entropy alloy. *Mater Sci Eng A* 532:480–486. doi:[10.1016/j.msea.2011.10.110](https://doi.org/10.1016/j.msea.2011.10.110)
18. Zhang KB, Fu ZY (2012) Effects of annealing treatment on phase composition and microstructure of CoCrFeNiTiAl_x high-entropy alloys. *Intermetallics* 22:24–32. doi:[10.1016/j.intermet.2011.10.010](https://doi.org/10.1016/j.intermet.2011.10.010)
19. Chuang MH, Tsai MH, Wang WR, Lin SJ, Yeh JW (2011) Microstructure and wear behavior of Al_xCo1.5CrFeNi1.5Ti_y high-entropy alloys. *Acta Mater* 59(16):6308–6317. doi:[10.1016/j.actamat.2011.06.041](https://doi.org/10.1016/j.actamat.2011.06.041)
20. Lucas MS, Mauger L, Munoz JA, Xiao YM, Sheets AO, Semiatin SL, Horwath J, Turgut Z (2011) Magnetic and vibrational properties of high-entropy alloys. *J Appl Phys* 109(7):07E307. doi:[10.1063/1.3538936](https://doi.org/10.1063/1.3538936)
21. Senkov ON, Scott JM, Senkova SV, Miracle DB, Woodward CF (2011) Microstructure and room temperature properties of a high-entropy TaNbHfZrTi alloy. *J Alloys Compd* 509(20):6043–6048. doi:[10.1016/j.jallcom.2011.02.171](https://doi.org/10.1016/j.jallcom.2011.02.171)
22. Zhu JM, Fu HM, Zhang HF, Wang AM, Li H, Hu ZQ (2010) Synthesis and properties of multiprincipal component AlCoCrFeNiSi_x alloys. *Mater Sci Eng A* 527(27–28):7210–7214. doi:[10.1016/j.msea.2010.07.049](https://doi.org/10.1016/j.msea.2010.07.049)
23. Zhu JM, Fu HM, Zhang HF, Wang AM, Li H, Hu ZQ (2010) Microstructures and compressive properties of multicomponent AlCoCrFeNiMo_x alloys. *Mater Sci Eng A* 527(26):6975–6979. doi:[10.1016/j.msea.2010.07.028](https://doi.org/10.1016/j.msea.2010.07.028)
24. Hsu CY, Juan CC, Wang WR, Sheu TS, Yeh JW, Chen SK (2011) On the superior hot hardness and softening resistance of AlCoCr_xFeMo_{0.5}Ni high-entropy alloys. *Mater Sci Eng A* 528(10–11):3581–3588. doi:[10.1016/j.msea.2011.01.072](https://doi.org/10.1016/j.msea.2011.01.072)
25. Gao XQ, Zhao K, Ke HB, Ding DW, Wang WH, Bai HY (2011) High mixing entropy bulk metallic glasses. *J Non Cryst Solids* 357(21):3557–3560. doi:[10.1016/j.jnoncrysol.2011.07.016](https://doi.org/10.1016/j.jnoncrysol.2011.07.016)
26. Zhang B, Wang RJ, Zhao DQ, Pan MX, Wang WH (2004) Properties of Ce-based bulk metallic glass-forming alloys. *Phys Rev B* 70(22):224208. doi:[10.1103/PhysRevB.70.224208](https://doi.org/10.1103/PhysRevB.70.224208)
27. Xu DH, Duan G, Johnson WL, Garland C (2004) Formation and properties of new Ni-based amorphous alloys with critical casting thickness up to 5 mm. *Acta Mater* 52(12):3493–3497. doi:[10.1016/j.actamat.2004.04.001](https://doi.org/10.1016/j.actamat.2004.04.001)
28. Jiang QK, Zhang GQ, Chen LY, Wu JZ, Zhang HG, Jiang JZ (2006) Glass formability, thermal stability and mechanical properties of La-based bulk metallic glasses. *J Alloys Compd* 424(1–2):183–186. doi:[10.1016/j.jallcom.2006.07.109](https://doi.org/10.1016/j.jallcom.2006.07.109)

29. Jiang QK, Zhang GQ, Yang L, Wang XD, Saksl K, Franz H, Wunderlich R, Fecht H, Jiang JZ (2007) La-based bulk metallic glasses with critical diameter up to 30 mm. *Acta Mater* 55 (13):4409–4418. doi:[10.1016/j.actamat.2007.04.021](https://doi.org/10.1016/j.actamat.2007.04.021)
30. Chang CT, Shen BL, Inoue A (2006) Co-Fe-B-Si-Nb bulk glassy alloys with superhigh strength and extremely low magnetostriction. *Appl Phys Lett* 88(1):011901. doi:[10.1063/1.2159107](https://doi.org/10.1063/1.2159107)
31. Zhang T, Yang Q, Ji YF, Li R, Pang SJ, Wang JF, Xu T (2011) Centimeter-scale-diameter Co-based bulk metallic glasses with fracture strength exceeding 5000 MPa. *Chin Sci Bull* 56 (36):3972–3977. doi:[10.1007/s11434-011-4765-8](https://doi.org/10.1007/s11434-011-4765-8)
32. Li S, Xi XK, Wei YX, Luo Q, Wang YT, Tang MB, Zhang B, Zhao ZF, Wang RJ, Pan MX, Zhao DQ, Wang WH (2005) Formation and properties of new heavy rare-earth-based bulk metallic glasses. *Sci Techno Adv Mater* 6(7):823–827. doi:[10.1016/j.stam.2005.06.019](https://doi.org/10.1016/j.stam.2005.06.019)
33. Jiang QK, Zhang GQ, Chen LY, Zeng QS, Jiang JZ (2006) Centimeter-sized ($\text{La}_{0.5}\text{Ce}_{0.5}$)-based bulk metallic glasses. *J Alloys Compd* 424(1–2):179–182. doi:[10.1016/j.jallcom.2006.07.007](https://doi.org/10.1016/j.jallcom.2006.07.007)
34. Li R, Pang SJ, Men H, Ma CL, Zhang T (2006) Formation and mechanical properties of (Ce-La-Pr-Nd)-Co-Al bulk glassy alloys with superior glass-forming ability. *Scr Mater* 54 (6):1123–1126. doi:[10.1016/j.scriptamat.2005.11.074](https://doi.org/10.1016/j.scriptamat.2005.11.074)
35. Tsai KY, Tsai MH, Yeh JW (2013) Sluggish diffusion in Co-Cr-Fe-Mn-Ni high-entropy alloys. *Acta Mater* 61(13):4887–4897. doi:[10.1016/j.actamat.2013.04.058](https://doi.org/10.1016/j.actamat.2013.04.058)
36. Wu WH, Yang CC, Yeh JW (2006) Industrial development of high-entropy alloys. *Ann Chimie Sci Materiaux* 31(6):737–747. doi:[10.3166/acsm.31.737-747](https://doi.org/10.3166/acsm.31.737-747)
37. Guo S, Ng C, Lu J, Liu CT (2011) Effect of valence electron concentration on stability of fcc or bcc phase in high entropy alloys. *J Appl Phys* 109(10):103505. doi:[10.1063/1.3587228](https://doi.org/10.1063/1.3587228)
38. Wang FJ, Zhang Y, Chen GL, Davies HA (2009) Tensile and compressive mechanical behavior of a CoCrCuFeNiAl_{0.5} high entropy alloy. *Int J Mod Phys B* 23(6–7):1254–1259. doi:[10.1142/S0217979209060774](https://doi.org/10.1142/S0217979209060774)
39. Senkov ON, Wilks GB, Miracle DB, Chuang CP, Liaw PK (2010) Refractory high-entropy alloys. *Intermetallics* 18(9):1758–1765. doi:[10.1016/j.intermet.2010.05.014](https://doi.org/10.1016/j.intermet.2010.05.014)
40. Tung CC, Yeh JW, Shun TT, Chen SK, Huang YS, Chen HC (2007) On the elemental effect of AlCoCrCuFeNi high-entropy alloy system. *Mater Lett* 61(1):1–5. doi:[10.1016/j.matlet.2006.03.140](https://doi.org/10.1016/j.matlet.2006.03.140)
41. Ke GY, Chen SK, Hsu T, Yeh JW (2006) FCC and BCC equivalents in as-cast solid solutions of $\text{Al}_x\text{Co}_y\text{Cr}_z\text{Cu}_{0.5}\text{Fe}_v\text{Ni}_w$ high-entropy alloys. *Ann Chimie Sci Materiaux* 31(6):669–683. doi:[10.3166/acsm.31.669-684](https://doi.org/10.3166/acsm.31.669-684)
42. Mizutani U (2011) Hume-Rothery rules for structurally complex alloy phases. CRC Press, Boca Raton
43. Liu CT, Stiegler JO (1984) Ductile ordered intermetallic alloys. *Science* 226(4675):636–642. doi:[10.1126/science.226.4675.636](https://doi.org/10.1126/science.226.4675.636)
44. Zhu JH, Liaw PK, Liu CT (1997) Effect of electron concentration on the phase stability of NbCr₂-based Laves phase alloys. *Mater Sci Eng A* 239–240:260–264. doi:[10.1016/S0921-5093\(97\)00590-X](https://doi.org/10.1016/S0921-5093(97)00590-X)
45. Tsai AP, Inoue A, Yokoyama Y, Masumoto T (1990) Stable icosahedral Al-Pd-Mn and Al-Pd-Re alloys. *Mater Trans JIM* 31(2):98–103. doi:[10.2320/matertrans1989.31.98](https://doi.org/10.2320/matertrans1989.31.98)
46. Yokoyama Y, Tsai AP, Inoue A, Masumoto T, Chen HS (1991) Formation criteria and growth-morphology of quasi-crystals in Al-Pd-TM (TM = transition metal) alloys. *Mater Trans JIM* 32(5):421–428. doi:[10.2320/matertrans1989.32.421](https://doi.org/10.2320/matertrans1989.32.421)
47. Chen W, Wang Y, Qiang J, Dong C (2003) Bulk metallic glasses in the Zr-Al-Ni-Cu system. *Acta Mater* 51(7):1899–1907. doi:[10.1016/s1359-6454\(02\)00596-7](https://doi.org/10.1016/s1359-6454(02)00596-7)
48. Dong C, Wang Q, Qiang JB, Wang YM, Jiang N, Han G, Li YH, Wu J, Xia JH (2007) From clusters to phase diagrams: composition rules of quasicrystals and bulk metallic glasses. *J Phys D Appl Phys* 40(15):R273–R291. doi:[10.1088/0022-3727/40/15/r01](https://doi.org/10.1088/0022-3727/40/15/r01)

49. Wang Z, Guo S, Liu CT (2014) Phase selection in high-entropy alloys: From nonequilibrium to equilibrium. *JOM* 10(66):1966–1972. doi:[10.1007/s11837-014-0953-8](https://doi.org/10.1007/s11837-014-0953-8)
50. Ng C, Guo S, Luan JH, Shi SQ, Liu CT (2012) Entropy-driven phase stability and slow diffusion kinetics in $\text{Al}_{0.5}\text{CoCrCuFeNi}$ high entropy alloy. *Intermetallics* 31:165–172. doi:[10.1016/j.intermet.2012.07.001](https://doi.org/10.1016/j.intermet.2012.07.001)
51. Tsai MH, Tsai KY, Tsai CW, Lee C, Juan CC, Yeh JW (2013) Criterion for sigma phase formation in Cr- and V-containing high-entropy alloys. *Mater Res Lett* 1(4):207–212. doi:[10.1080/21663831.2013.831382](https://doi.org/10.1080/21663831.2013.831382)
52. Fang SS, Xiao X, Lei X, Li WH, Dong YD (2003) Relationship between the widths of supercooled liquid regions and bond parameters of Mg-based bulk metallic glasses. *J Non Cryst Solids* 321(1–2):120–125. doi:[10.1016/s0022-3093\(03\)00155-8](https://doi.org/10.1016/s0022-3093(03)00155-8)
53. Widom M, Huhn WP, Maiti S, Steurer W (2014) Hybrid Monte Carlo/molecular dynamics simulation of a refractory metal high entropy alloy. *Metall Mater Trans A* 45(1):196–200. doi:[10.1007/s11661-013-2000-8](https://doi.org/10.1007/s11661-013-2000-8)
54. Huhn WP, Widom M (2013) Prediction of A2 to B2 phase transition in the high-entropy alloy Mo-Nb-Ta-W. *JOM* 65(12):1772–1779. doi:[10.1007/s11837-013-0772-3](https://doi.org/10.1007/s11837-013-0772-3)
55. Tian FY, Delczeg L, Chen NX, Varga LK, Shen J, Vitos L (2013) Structural stability of NiCoFeCrAl_x high-entropy alloy from ab initio theory. *Phys Rev B* 88(8):085128. doi:[10.1103/PhysRevB.88.085128](https://doi.org/10.1103/PhysRevB.88.085128)
56. Lilensten L, Couzinié JP, Perrière L, Bourgon J, Emery N, Guillot I (2014) New structure in refractory high-entropy alloys. *Mater Lett* 132:123–125. doi:[10.1016/j.matlet.2014.06.064](https://doi.org/10.1016/j.matlet.2014.06.064)
57. Kao YF, Chen SK, Sheu JH, Lin JT, Lin WE, Yeh JW, Lin SJ, Liou TH, Wang CW (2010) Hydrogen storage properties of multi-principal-component $\text{CoFeMnTi}_x\text{V}_y\text{Zr}_z$ alloys. *Int J Hydrogen Energy* 35(17):9046–9059. doi:[10.1016/j.ijhydene.2010.06.012](https://doi.org/10.1016/j.ijhydene.2010.06.012)
58. Kunce I, Polanski M, Bystrzycki J (2013) Structure and hydrogen storage properties of a high entropy ZrTiVCrFeNi alloy synthesized using Laser Engineered Net Shaping (LENS). *Int J Hydrogen Energy* 38(27):12180–12189. doi:[10.1016/j.ijhydene.2013.05.071](https://doi.org/10.1016/j.ijhydene.2013.05.071)
59. Tsau C-H (2009) Phase transformation and mechanical behavior of TiFeCoNi alloy during annealing. *Mater Sci Eng A* 501(1–2):81–86. doi:[10.1016/j.msea.2008.09.046](https://doi.org/10.1016/j.msea.2008.09.046)
60. Gao MC, Alman DE (2013) Searching for Next Single-Phase high-entropy alloy compositions. *Entropy* 15(10):4504–4519. doi:[10.3390/e15104504](https://doi.org/10.3390/e15104504)
61. Takeuchi A, Amiya K, Wada T, Yubuta K, Zhang W (2014) High-entropy alloys with a hexagonal close-packed structure designed by equi-atomic alloy strategy and binary phase diagrams. *JOM* 10(66):1984–1992. doi:[10.1007/s11837-014-1085-x](https://doi.org/10.1007/s11837-014-1085-x)
62. Feuerbacher M, Heidelmann M, Thomas C (2014) Hexagonal high-entropy alloys. *Mater Res Lett* 3:1–6. doi:[10.1080/21663831.2014.951493](https://doi.org/10.1080/21663831.2014.951493)
63. Poletti MG, Battezzati L (2014) Electronic and thermodynamic criteria for the occurrence of high entropy alloys in metallic systems. *Acta Mater* 75:297–306. doi:[10.1016/j.actamat.2014.04.033](https://doi.org/10.1016/j.actamat.2014.04.033)

Chapter 3

Physical Metallurgy

Jien-Wei Yeh

Abstract Physical metallurgy is a branch of materials science, especially focusing on the relationship between composition, processing, crystal structure and microstructure, and physical and mechanical properties. Because all properties are the manifestation of compositions, structure and microstructure, thermodynamics, kinetics, and plastic deformation, factors as encountered in processing control become very important to control phase transformation and microstructure and thus properties of alloys. All the underlying principles have been well built and physical metallurgy approaches mature. However, traditional physical metallurgy is based on the observations on conventional alloys. As composition is the most basic and original factor to determine the bonding, structure, microstructure, and thus properties to a certain extent, physical metallurgy principles might be different and need to be modified for HEAs which have entirely different compositions from conventional alloys. The most distinguished effects in HEAs are high-entropy, severe lattice distortion, sluggish diffusion, and cocktail effects. This chapter will present and discuss the corresponding subjects of physical metallurgy based on these effects.

Keywords Physical metallurgy • High-entropy effect • Severe lattice distortion effect • Sluggish diffusion and cocktail effect • Cocktail effect • High-entropy alloys (HEAs)

3.1 Introduction

Physical metallurgy is a science focusing on the relationships between composition, processing, crystal structure and microstructure, and physical and mechanical properties [1, 2]. Figure 3.1 shows the scheme of physical metallurgy, in which straightforward correlations can be seen. Composition and processing determine

J.-W. Yeh (✉)

Department of Materials Science and Engineering, National Tsing Hua University,
Hsinchu, Taiwan 30013, Republic of China
e-mail: jwye@mx.nthu.edu.tw

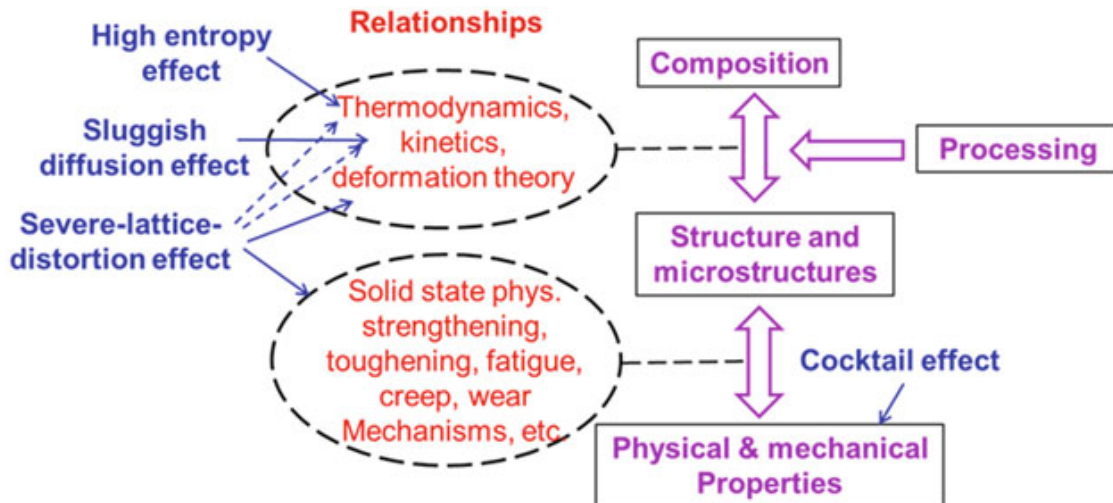


Fig. 3.1 The scheme of physical metallurgy in which those areas influenced by four core effects of HEAs are indicated

structure and microstructure, which in turn determine properties. The relationships between composition, processing, and crystal structure and microstructure are thermodynamics, kinetics, and deformation theory. Those between crystal structure, microstructure, and physical and mechanical properties are solid-state physics and theories for strengthening, toughening, fatigue, creep, wear, etc. Therefore, the understanding of physical metallurgy is very helpful to manipulate, develop, and utilize materials. Physical metallurgy has been gradually built over 100 year since using optical microscope to observe the microstructure of materials. The underlying principles were thought to become mature [2]. However, traditional physical metallurgy is based on the observations on conventional alloys. As compositions of high-entropy alloys (HEAs) are entirely different from those of conventional alloys, physical metallurgy principles might need to be modified for HEAs and thus require more future research.

Because of their uniqueness, four core effects of HEAs were proposed in 2006 [3]. They are high-entropy effect for thermodynamics, sluggish diffusion effect for kinetics, severe lattice distortion effect for structure, and cocktail effect for properties, respectively. Figure 3.1 also shows the influence positions of these four core effects in the scheme of physical metallurgy. High-entropy effect should be involved in thermodynamics to determine the equilibrium structure and microstructure. Sluggish diffusion effect affects kinetics in phase transformation. Severe lattice distortion effect not only affects deformation theory and all the relationships between each property, structure, and microstructure but also affects thermodynamics and kinetics. As for the cocktail effect, it is the overall effect from composition, structure, and microstructure. Properties of HEAs are not as simple as those predicted from the rule of mixture, but mutual interactions between unlike atoms and the feature of phases and microstructure would give excess quantity to each property. Therefore, physical metallurgy principles of HEAs might be different from those of current physical metallurgy because of these influences. We need to

review every aspect of physical metallurgy through the four core effects of HEAs. It can be expected that when physical metallurgy encompasses all alloys including tradition alloys and HEAs, the whole understanding of the alloy world becomes realized.

3.2 Four Core Effects of HEAs

3.2.1 *High-Entropy Effect*

As the name of HEAs implies, high entropy is the first important core effects [4]. This effect could enhance the formation of solution phases and render the microstructure much simpler than expected before. This effect thus has the potential to increase the strength and ductility of solution phases due to solution hardening. Why high entropy could enhance the formation of solution phases? Before answering this, it is necessary to know that there are three possible categories of competing states in the solid state of an alloy: elemental phases, intermetallic compounds (ICs), and solid solution phases [4]. Elemental phase means the terminal solid solution based on one metal element as seen in the pure component side of a phase diagram. Intermetallic compound means stoichiometric compounds having specific superlattices, such as NiAl having B2 structure and Ni₃Ti having D₀₂₄ structure, as seen at certain concentration ratios in phase diagrams. Solid solution phase could be further divided into random solid solution and ordered solid solution. Random solid solutions are those with crystal structure in which different components occupy lattice sites by probability although short-range ordering might exist. They could be the phases with the structures of BCC, FCC, or HCP. Ordered solid solutions are intermetallic phases (IPs) or intermediate phase. They are solid solutions with the crystal structure based on intermetallic compounds, as seen in the broader composition ranges around different stoichiometric compounds in phase diagrams [5, 6]. In such phases, different constituent elements tend to occupy different sets of lattice sites. Their degree of ordering is smaller than that of completely ordered structure and thus they can be called partially ordered solid solutions. Although they have the structure of intermetallic compounds and might be classified to intermetallic compounds, they are classified as solid solution phases here with the emphasis on their significant solubility between constituent elements. This is the same thing to separate random solid solutions from terminal phases.

1. General trend in phase competition

According to the second law of thermodynamics, a system reaches its thermodynamic equilibrium when its Gibbs free energy is the lowest at given temperature and pressure. In order to elucidate high-entropy effect in enhancing the formation of

Table 3.1 Comparisons of ΔH_{mix} , ΔS_{mix} , and ΔG_{mix} between elemental phases, compounds, and solid solutions. Strain energy from atomic size difference is not included in ΔH_{mix}

Possible states	Elemental phases	Compounds	Random solid solutions	Partially ordered solid solutions
ΔH_{mix}	~0	Large negative	Medium negative	Medium negative
$-T\Delta S_{\text{mix}}$	~0	~0	$-RT\ln(n)$	$<-RT\ln(n)$
ΔG_{mix}	~0	Large negative	Large negative	Large negative

solid solution phases and inhibiting the formation of IMs, HEAs composed of constituent elements with stronger bonding energies between each other are considered first. If strain energy contribution to mixing enthalpy due to atomic size difference is not considered for simplicity, as shown in Table 3.1, elemental phases based on one major element would have small-negative ΔH_{mix} and small ΔS_{mix} , compound phases would have large-negative ΔH_{mix} but small ΔS_{mix} , and solid solution phases containing multi-elements would have medium-negative ΔH_{mix} and high ΔS_{mix} . As a result, solid solution phases become highly competitive with compound phases for attaining the equilibrium state especially at high temperatures.

Why multi-principal-element solid solutions have medium ΔH_{mix} ? This is because there has a proportion of unlike atomic pairs in solution phases [4]. For example, by taking a mole of atoms, N_0 , a binary intermetallic compound (B2) NiAl in complete ordering would have $(1/2) \times 8N_0$ Ni-Al bonds as the coordination number is 8, whereas a mole of NiAl random solid solution would have $(1/2) \times (1/2) \times 8N_0$ Ni-Al bonds. Thus, the mixing enthalpy in the random state is one-half of that of the completely ordered state. Similarly, for a five-element equimolar alloy, that in the random solid solution state is $4/5$ of that in binary compounds assuming each compound of the ten possible binary compounds has the same mixing enthalpy, i.e., all heats of mixing for unlike atom pairs are the same. Similarly, for an eight-element equimolar alloy, the ratio becomes $7/8$. Therefore, higher number of element would allow the random state to have the mixing enthalpy closer to that of the completely ordered state and to become even more competitive with the ordered state under the aid of its high mixing entropy.

If the average of the mixing enthalpy of unlike pairs (28 unlike pairs in total) in an equiatomic eight-element alloy ABCDEFGH is assumed to be -23 kJ/mol, ΔH_{mix} of completely ordered structure, i.e., forming 28 intermetallic compounds (each has $N_0/8$ atoms), is -46 kJ/mol, and that of complete disordered structure, i.e., random solid solution, is $-46 \times 7/8 = -40.25$ kJ/mol. On the other hand, the configurational entropy (ΔS_{conf}) of completely ordered structure is 0 and that of complete disordered structure is 17.29 J/Kmol. At 1473 K, which is often lower than the melting points of most HEAs, ΔG_{mix} of completely ordered structure is thus equal to -46 kJ/mol and that of completely disordered structure is equal to -65.72 kJ/mole. Therefore, completely disordered structure is the stable phase at

1473 K. Furthermore, completely disordered structure is also stable at temperature down to 333 K since the temperature of free energy equivalence between these two states can be calculated to be 333 K. However, it should be mentioned that due to the difference of mixing enthalpy between different unlike pairs and the effect of strain energy, partially ordered state might have lower mixing free energy than the random state and form at 1473 K or become the stable state by phase separation. Obviously, the assumption of the 10 or 28 binary compounds having the same or similar mixing enthalpies is almost impossible from the elements in the periodical table. They are hypothetical alloy systems which are used to emphasize the fact that there are lots of unlike pairs with strong bonding and have medium-negative mixing enthalpy in the random solutions or partially ordered solid solutions. They still have low free energy of mixing because some loss of mixing enthalpy could be compensated by higher mixing entropy.

2. The effect of the diversity of mixing enthalpy between unlike atom pair

In general, if mixing enthalpies for unlike atomic pairs do not have large difference, solid solution phases would be dominant in the equilibrium state [4]. For example, CoCrFeMnNi alloy can form a single FCC solution even after full-annealing treatments [7, 8]. Ductile refractory HfNbTaTiZr alloy has single BCC phase in the as-cast state [9] and in the as-homogenized state. Conversely, large difference might generate more than two phases. For example, Al has stronger bonding with transition metals but Cu has no attractive bond with most transition metals. As a result, AlCoCrCuFeNi alloy forms Cu-rich FCC + multi-principal-element FCC + multi-principal-element BCC (A2) at high temperatures above 600 °C and have B2 precipitates in the Cu-rich FCC and spinodally decomposed structure of A2 + B2 phases from A2 phase during cooling. B2 solid solution containing multi-principal-elements is in fact derived from the NiAl-type compound [10]. Even larger difference in mixing enthalpies for unlike atomic pairs in those alloys containing O, C, B, or N would generate oxides, carbides, borides, or nitrides in the microstructure. However, it can be found that these strong phases often have certain solubilities of other elements with similar strong bonding due to mixing entropy effect, for example, in $\text{Al}_{0.5}\text{B}_x\text{CoCrCuFeNi}$ ($x = 0-1$) alloys, strong boride phase rich in Cr, Fe, and Co forms [11].

3. The effect of atomic size difference

To include the effect of atomic size difference on the phase formation, Zhang et al. [12] first proposed the forming trend of disordered solid solutions, ordered solid solution, intermediate phases, and bulk metallic glass (BMG) by comparing ΔS_{mix} , ΔH_{mix} , and atomic size difference (δ). The former three are commonly found in HEAs, in which disordered solid solutions and ordered (or partially ordered) ones are those with BCC, FCC, or HCP structures, and intermediate phases are those with more complex compound structures. Guo et al. [13] also used these factors to lay out the phase selection rule for such kinds of phase.

Moreover, Yeh [14], Chen et al. [15], and Yang et al. [16] used δ and the ratio of $T\Delta S_{\text{mix}}$ to ΔH_{mix} to describe the order-disorder competition in HEAs and also the existing range of intermetallics and BMG. All these have been discussed in Chap. 2. The main point is that solution-type phases tend to form in highly alloyed multicomponent alloys. Disordered solutions preferentially form under smaller δ , smaller $|\Delta H_{\text{mix}}|$, and higher ΔS_{mix} .

In summary, high-entropy effect is the first important effect for HEAs because it can inhibit the formation of many different kinds of stoichiometric compounds which have strong ordered structures and are usually brittle. Conversely, it enhances the formation of solution-type phases and thus reduces the number of phases much lower than the maximum number (i.e., $n+1$, n is the number of components) of phases predicted by Gibbs' phase rule. This renders the microstructure simpler than expected before, with the positive expectation in displaying better properties.

3.2.2 Severe Lattice Distortion Effect

Because of high-entropy effect, a solid solution phase in HEAs is often a whole-solute matrix no matter its structure is BCC, FCC, HCP, or other more complex compound structures [17]. Thus, every atom in the multi-principal-element matrix is surrounded by different kinds of atom and suffers lattice strain and stress as shown in the right side of Fig. 3.2. In addition to the atomic size difference, different bonding energies and crystal structure tendencies among constituent elements are expected to cause even higher lattice distortion since the nonsymmetrical neighboring atoms, i.e., nonsymmetrical bindings and electronic structure, around an atom, and the variation of such non-symmetry from site to site

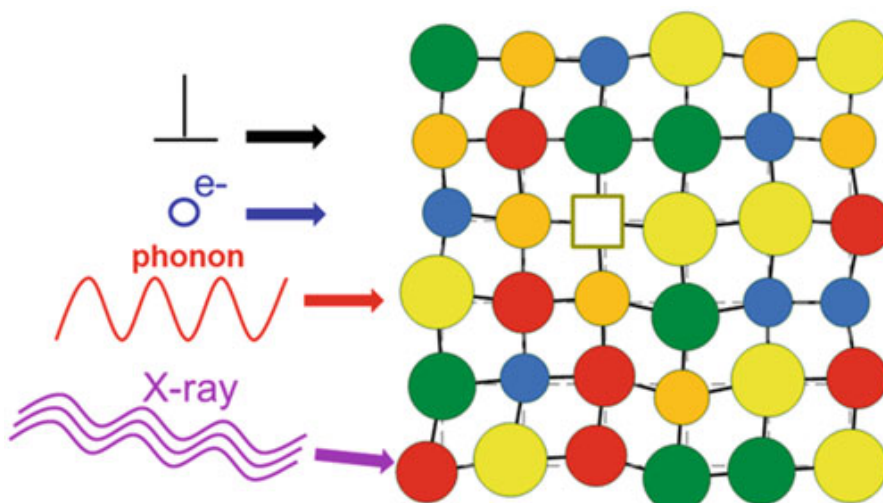


Fig. 3.2 Schematic diagram showing the severely distorted lattice and the various interactions with dislocations, electrons, phonons, and x-ray beam

would affect the atomic position [8, 18]. In conventional alloys, most matrix atoms (or solvent atoms) have the same kind of atoms as their neighbors. The overall lattice distortion is much smaller than that in HEAs.

1. Crystal structure effect on lattice distortion

Wang has used Monte Carlo method in combination with MaxEnt (the principles of maximum entropy) to demonstrate the entropy force to maximize mixing entropy for single-phase solid solution [19]. He built atomic structure models of bulk equiatomic alloys with BCC and FCC lattices from four to eight principal elements. Based on the built models, the atomic structure features are analyzed. Table 3.2 shows the information on the structure analyses of these models. The shortest distance of an atom is the distance of the atom to its nearest-same-element atom. It is surprising to note that an atom to have another atom of same element (like-pair) in the first nearest neighbor can all be avoided for those BCC alloys with five or more elements, and most of the same elements in quaternary and quinary BCC are found in the second nearest-neighbor shell. This peak region providing highest number of like-pairs moves to the third nearest-neighbor shell as the element number increases. On the other hand, there are still a larger proportion of same elements in the first shell in quaternary (74.3 %) and quinary FCC alloys (47.3 %). Because larger proportion of unlike pairs between the center atom and dissimilar atoms in the first shell would give larger distortion (contributions from second and higher shell are diminishingly minor), it can be expected from Table 3.2 that larger number of elements would tend to give larger distortion, and BCC structure has larger distortion than FCC if constructed by the same set of elements with same proportion. This might suggest that BCC solid solution could have larger solution hardening effect than FCC solid solution by the same set of elements with same proportion. This will be discussed in Sect. 3.6.4.

Table 3.2 Distribution of the shortest distances between the same-element atoms on the nearest-neighbor lattice sites in the created BCC and FCC MaxEnt models

Phase	Cell type	Distance distribution in nearest-neighbor sites (%)					
		1	2	3	4	5	6
Quaternary phase	BCC	8.5	83.0	6.9	1.6	0.0	0.0
	FCC	74.3	23.8	1.9	0.0	0.0	0.0
Quinary phase	BCC	0.0	65.5	30.6	3.4	0.5	0.0
	FCC	47.3	45.0	7.5	0.2	0.0	0.0
Senary phase	BCC	0.0	41.4	52.4	6.0	0.2	0.0
	FCC	17.2	64.9	17.7	0.2	0.0	0.0
Septenary phase	BCC	0.0	19.2	65.3	15.0	0.3	0.2
	FCC	3.9	50.4	44.4	1.1	0.2	0.0
Octonary phase	BCC	0.0	2.5	70.9	24.3	2.1	0.2
	FCC	0.2	27.1	69.8	2.7	0.2	0.0

The distances for the successive nearest-neighbor sites in BCC and FCC lattices are $\sqrt{3}a_0/2$, a_0 , $\sqrt{2}a_0, \dots$; and $\sqrt{2}a_0/2$, a_0 , $\sqrt{3/2}a_0, \dots$, respectively [19]

2. Factors on lattice distortion and relaxation

Lattice distortion might be described by different ways but the most common way only considers atomic size factor [16, 20, 21]. That is, lattice distortion could be directly related to differences in atomic size (δ) by the following equation for a multiple-element matrix:

$$\delta = 100 \sqrt{\sum_{i=1}^n c_i (1 - r_i/\bar{r})^2} \quad (3.1)$$

where $\bar{r} = \sum_{i=1}^n c_i r_i$ and c_i and r_i are the atomic percentage and atomic radius of the i th element, respectively. This equation is based on the assumption similar to conventional assumption for the misfit strain of a solute in a matrix, in which the solute atom occupies the exact lattice site. In the multiple-element matrix, pseudo-unary matrix with solvent atoms with an average radius \bar{r} is used. Therefore, this equation gives the average misfit strain in the pseudo-unary matrix. Apparently, this equation is still not accurate since positions of solute atoms in the multiple-element matrix would have some deviations from the exact site of the average lattice. Therefore, better descriptions of lattice distortion are still the issue in the future. Furthermore, it should be mentioned that the lattice distortion is not only from atomic size difference but also from bonding difference and crystal structure difference among components. Assuming a case that distortion strain is only 1 %, the local atomic stress could be estimated to be around 0.01E (or $\sim 0.01 \times 8G/3 = 0.027 G$) in tension and 0.0135G in shear for isotropic solid at every lattice site where E and G are Young's modulus and shear modulus, respectively. As the theoretical shear strength is about 0.039–0.11G and actual (or observed) shear strength is orders of magnitude below that [22], in general lower than 0.001G [22], it can be realized that such a small distortion strain is still not negligible. Furthermore, it is easy to find that the critical lattice distortion above which local atomic stress exceeds theoretical shear strength ($\sim G/15$) is $\sim 5\%$, supposing that Hooke's law is still valid. This suggests that higher distortion would cause instability in forming random or disordered solid solution. But this is underestimated since the lattice distortion of 6.6 % is empirically found to be the borderline between disordered solid solution and other complex crystal structures, as discussed in Chap. 2. This indicates that the final lattice distortion would be resulted from some relaxation by adjusting relative atom positions in the lattice sites for the sake of reducing the distortion energy and maintaining the local atomic stress balance. By this, the critical lattice distortion just for maintaining disordered solid solution, calculated by misfit strain concept, is relaxed to 6.6 %.

3. Evidences of lattice distortion effect

Severe lattice distortion not only affects properties but also reduces the thermal effect on properties. Figure 3.2 also shows that interactions will occur when dislocations, electrons, phonons, and x-ray beams passing through the distorted lattice. In general, it can effectively increase hardness and strength by large solution

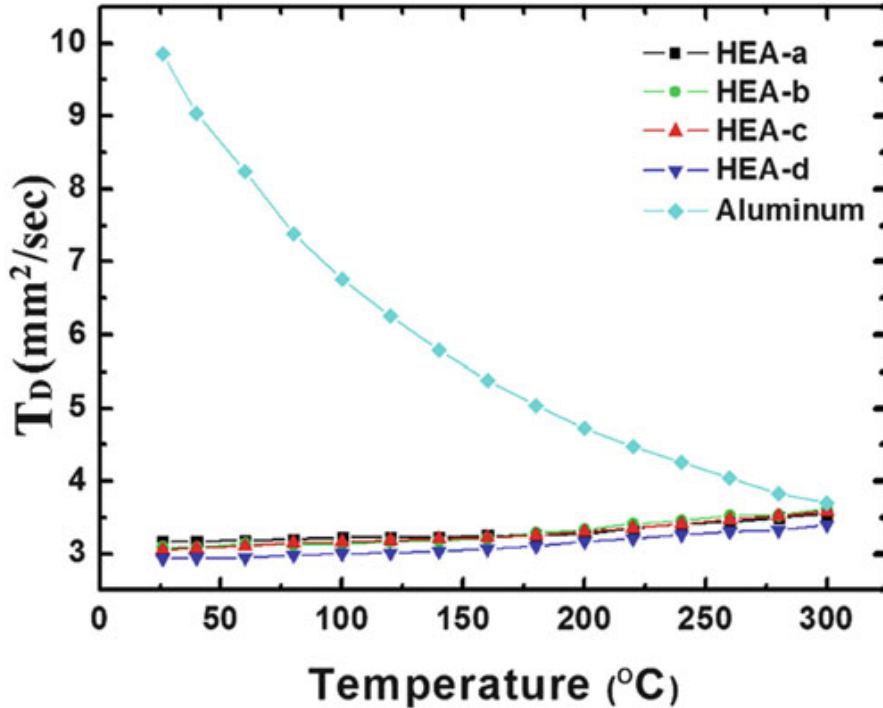


Fig. 3.3 Thermal diffusivities as a function of temperature for pure aluminum and HEA-a ($\text{Al}_{0.3}\text{CrFe}_{1.5}\text{MnNi}_{0.5}$), HEA-b($\text{Al}_{0.5}\text{CrFe}_{1.5}\text{MnNi}_{0.5}$), HEA-c($\text{Al}_{0.3}\text{CrFe}_{1.5}\text{MnNi}_{0.5}\text{Mo}_{0.1}$), and HEA-d($\text{Al}_{0.5}\text{CrFe}_{1.5}\text{MnNi}_{0.5}\text{Mo}_{0.1}$) [25]

hardening. For example, refractory MoNbTaW alloy and MoNbTaVW alloy have Hv 4455 MPa and 5250 MPa, respectively. Their hardness values are three times that obtained by the mixture rule [23]. In addition, severe lattice distortion significantly decreases electrical and thermal conductivity since it can markedly scatter free electrons and phonons [24]. For example, Lu et al. studied the thermal diffusivity as a function temperature for four HEAs and pure Al as shown in Fig. 3.3. It was found that the slopes of thermal diffusivities of HEAs with respect to temperature are positively small and thus insensitive to temperature whereas those of conventional metal Al are negatively large and sensitive to temperature [25]. In x-ray diffraction, peak intensity largely decreases due to diffuse scattering on the distorted atomic planes [18]. Lots of x-ray cannot fulfill Bragg's law during diffraction and are scattered to the background. It is also noted that all these properties in HEAs become quite insensitive to temperature. This is explainable since the lattice distortion caused by thermal vibration of atoms is relatively small as compared with the severe lattice distortion [4, 18].

3.2.3 Sluggish Diffusion Effect

Phase transformations in HEAs would require cooperative diffusion of many different kinds of atoms to accomplish the partitioning of composition between phases. However, the vacancy concentration for substitutional diffusion is still limited in HEAs as found in traditional alloys since each vacancy in crystalline HEAs is also associated with a positive enthalpy of formation and an

Table 3.3 The concentrations of end members of three diffusion couples [8]

Couple	Alloy	Composition (at.%)				
		Co	Cr	Fe	Mn	Ni
Cr – Mn	1	22	29	22	5	22
	2	22	17	22	17	22
Fe – Co	3	33	23	11	11	22
	4	11	23	33	11	22
Fe – Ni	5	23	24	30	11	12
	6	23	24	12	11	30

excess mixing entropy. The competition between these two factors yields a certain equilibrium vacancy concentration with minimum free energy of mixing at a given temperature [26]. A vacancy in the whole-solute matrix is in fact surrounded and competed by different element atoms during diffusion. Either a vacancy or an atom would have a fluctuated diffusion path to migrate and have slower diffusion and higher activation energy. As a result, diffusional phase transformation would be slower in HEAs. In brief, the sluggish diffusion effect implies slower diffusion and phase transformation.

1. Diffusion couple experiment on HEAs

Although there are many indirect evidences of sluggish diffusion effect, direct diffusion measurement is more persuasive. In order to verify this effect, a near-ideal solution system of Co-Cr-Fe-Mn-Ni with stable single FCC solid solution was selected by Tsai et al. to do diffusion experiment [8]. Four quasi-binary diffusion couples were made as listed in Table 3.3. In the two end members of each couple, only two elements differed in concentration. The diffusion couple was tightly fixed in a molybdenum tube which was then sealed in a vacuum quartz tube. From the concentration profiles obtained after diffusion at 1173, 1223, 1273, and 1323 K, diffusion coefficients and activation energy were calculated. Figure 3.4 shows the temperature dependence of the diffusion coefficient of a different element, revealing that the sequence of elements in the order of decreasing diffusion rate was Mn, Cr, Fe, Co, and Ni. It was also found that diffusion coefficients of each elements at T/T_m in the Co-Cr-Fe-Mn-Ni alloy system were the smallest in similar FCC matrices including Fe-Cr-Ni(-Si) alloys and pure Fe, Co, and Ni metals (see Fig. 3.5). In addition, the melting-point-normalized activation energies, Q/T_m , in the HEA were the largest as shown in Fig. 3.6. It was also noted that for the same element, the degree of sluggish diffusion is related to the number of principal elements in the matrix. For example, the Q/T_m values in the present HEAs are the highest; those in Fe-Cr-Ni(-Si) alloys are the second; and those in pure metals are the lowest. In brief, all these are direct evidences for the sluggish diffusion effect in HEAs.

2. Positive benefits from sluggish diffusion effect

Sluggish diffusion effect might provide several important advantages as found in many related researches [10, 27–34]. They include easiness to get supersaturated

Fig. 3.4 Temperature dependence of the diffusion coefficients for Co, Cr, Fe, Mn, and Ni obtained from Co-Cr-Fe-Mn-Ni diffusion couple experiments [8]

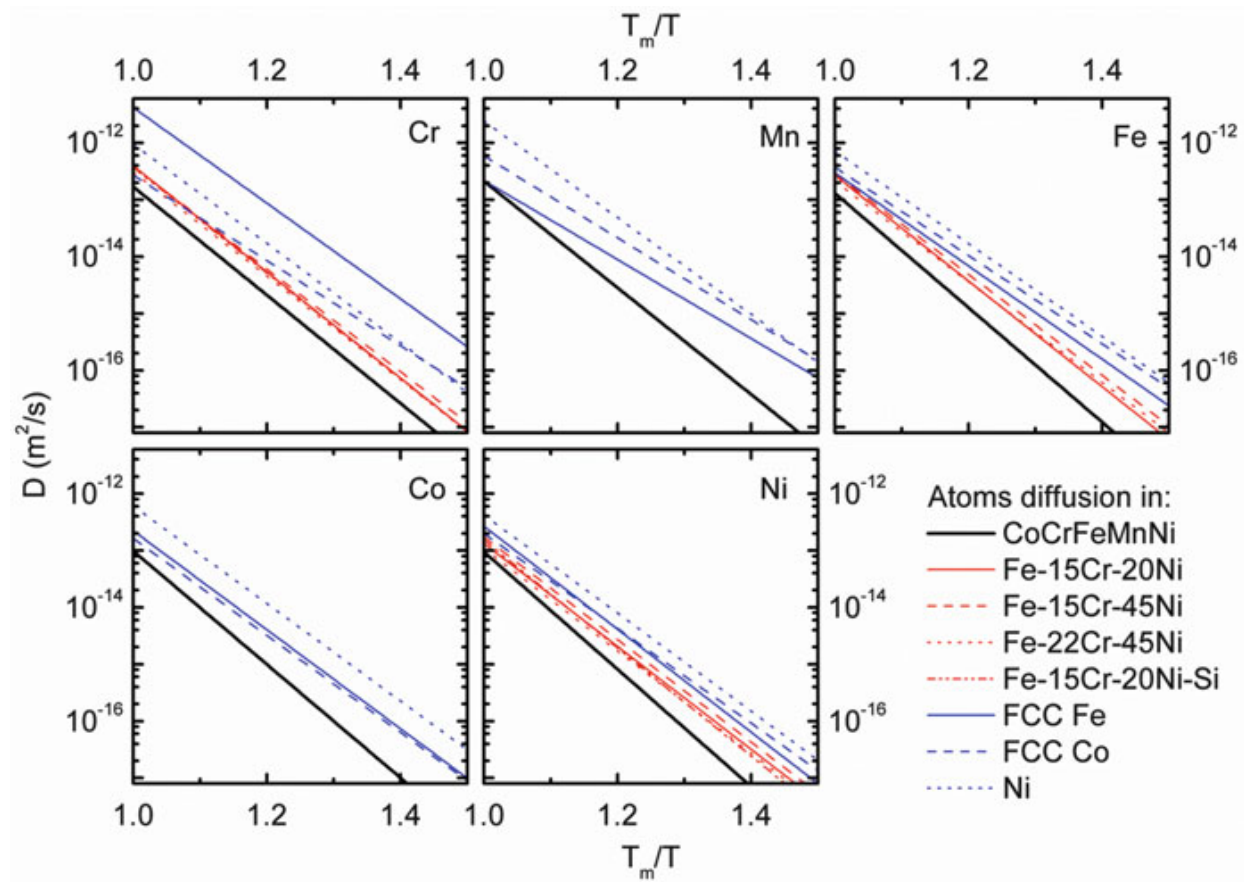
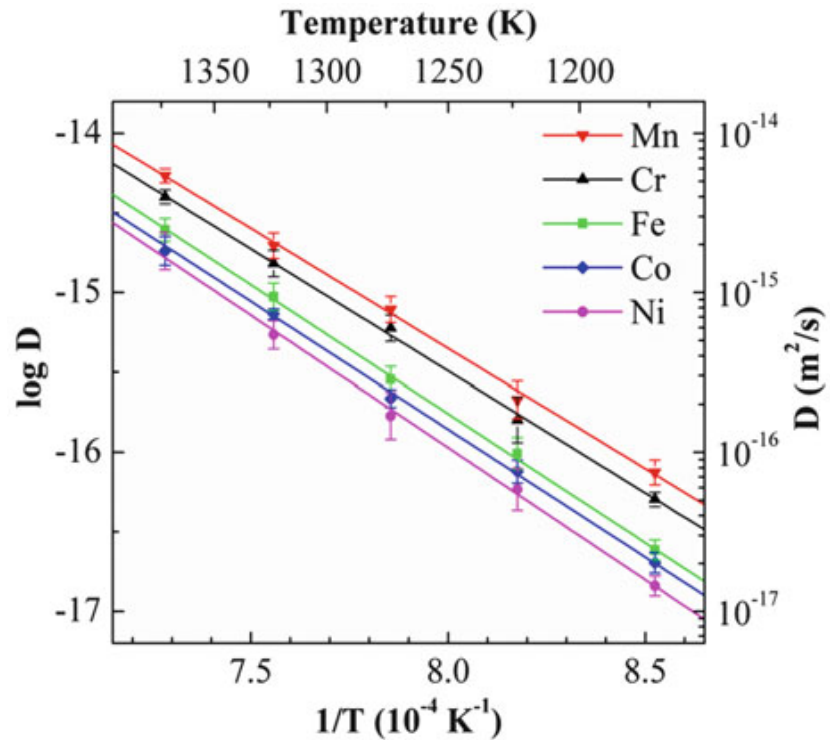
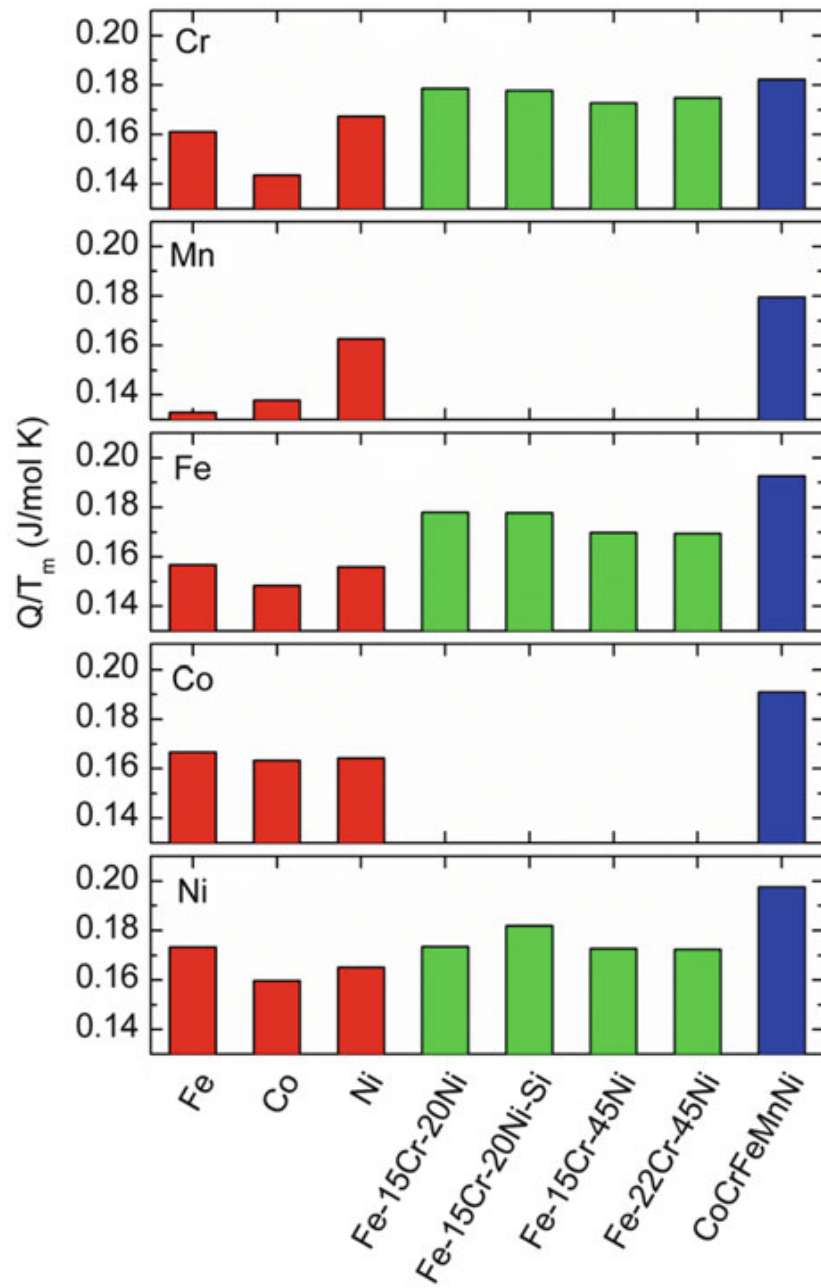


Fig. 3.5 Temperature dependence of the diffusion coefficients for Cr, Mn, Fe, Co, and Ni in different matrices

Fig. 3.6 Melting-point-normalized activation energy of diffusion for Cr, Mn, Fe, Co, and Ni in different matrices [8]



state and fine precipitates, increased recrystallization temperature, slower grain growth, reduced particle coarsening rate, and increased creep resistance. These advantages might benefit microstructure and property control for better performance. For example, Liu et al. studied the grain growth of cold-rolled and annealed sheet of CoCrFeMnNi HEA and found that activation energy is much higher than AISI 304LN stainless steels, which is consistent with the sluggish diffusion effect [33].

3.2.4 *Cocktail Effect*

The term “multimetallic cocktails” was first proposed by Ranganathan to emphasize alloy pleasures in alloy design and development [35]. Although this effect is also possessed by conventional alloys, cocktail effect is emphasized in HEAs

because at least five major elements are used to enhance the properties of materials. As stated above, HEAs might have simple phase, two phases, three phases, or more depending on the composition and processing. As a result, the whole properties are from the overall contribution of the constituent phases by the effect of grain morphology, grain-size distribution, grain and phase boundaries, and properties of each phase. However, each phase is a multi-principal-element solid solution and can be regarded as atomic-scale composites. Its composite properties not only come from the basic properties of elements by the mixture rule but also from the mutual interactions among all the elements and from the severe lattice distortion. Interaction and lattice distortion would bring excess quantities to the quantities predicted by the mixture rule. As a whole, “cocktail effect” ranges from atomic-scale multi-principal-element composite effect to microscale multi-phase composite effect. Therefore, it is important for an alloy designer to understand related factors involved before selecting suitable composition and processes based on the cocktail effect [4]. For example, refractory HEAs developed by Air Force Research Laboratory have melting points very much higher than those of Ni-base and Co-base superalloys [23, 29]. This is simply because refractory elements were selected as constituent elements. By the mixture rule, quaternary alloy MoNbTaW and quinary alloy MoNbTaVW have melting point above 2600 °C. As a result, both alloys display much higher softening resistance than superalloys and have yield strength above 400 MPa at 1600 °C as shown in Fig. 3.7 [29]. Such refractory HEAs are thus also expected to have potential applications at very high temperatures. In another example, Zhang et al. studied FeCoNi(AlSi)_{0.8} alloys for finding the composition with the optimum combination of magnetic, electrical, and mechanical properties. The best was achieved in alloy FeCoNi(AlSi)_{0.2} with saturation magnetization (1.15 T), coercivity (1400 A/m), electrical resistivity (69.5 $\mu\Omega\text{cm}$), yield strength

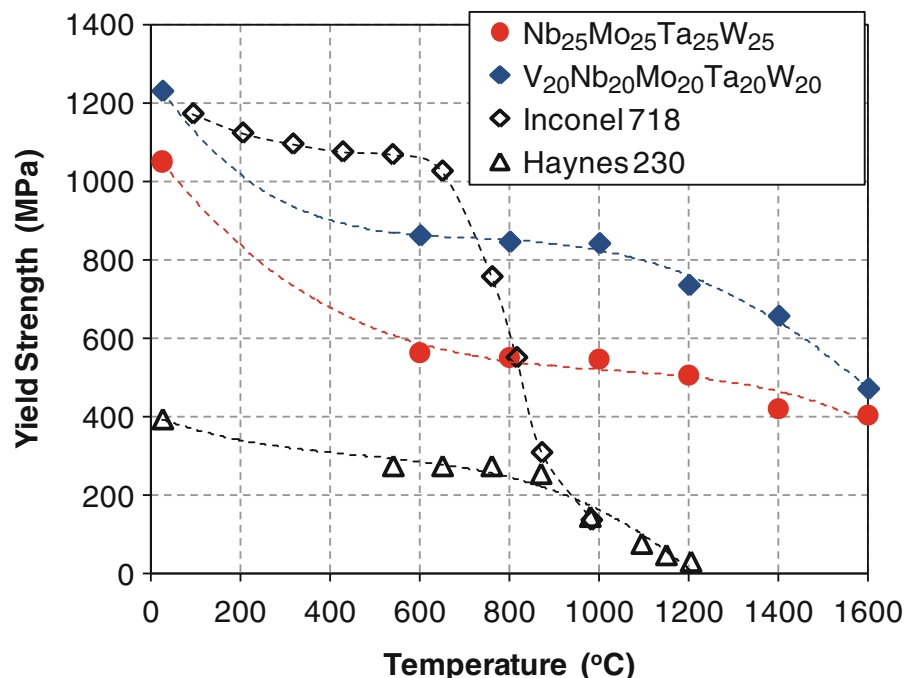


Fig. 3.7 Temperature dependence of the yield stress of Nb₂₅Mo₂₅Ta₂₅W₂₅ and V₂₀Nb₂₀Mo₂₀Ta₂₀W₂₀ HEAs and two superalloys, Inconel 718 and Haynes 230 [29]

(342 MPa), and strain without fracture (50 %), which makes the alloy an excellent soft magnetic materials for many potential applications [36]. Obviously, this alloy design relied on the selection of equimolar ferromagnetic elements (Fe, Co, and Ni) for forming ductile FCC phase with higher atomic packing density than BCC and suitable addition of nonmagnetic elements (Al and Si having slightly antiparallel magnetic coupling with Fe, Co, and Ni) to increase lattice distortion. It led to a positive cocktail effect in achieving high magnetization, low coercivity, good plasticity, high strength, and high electrical resistance.

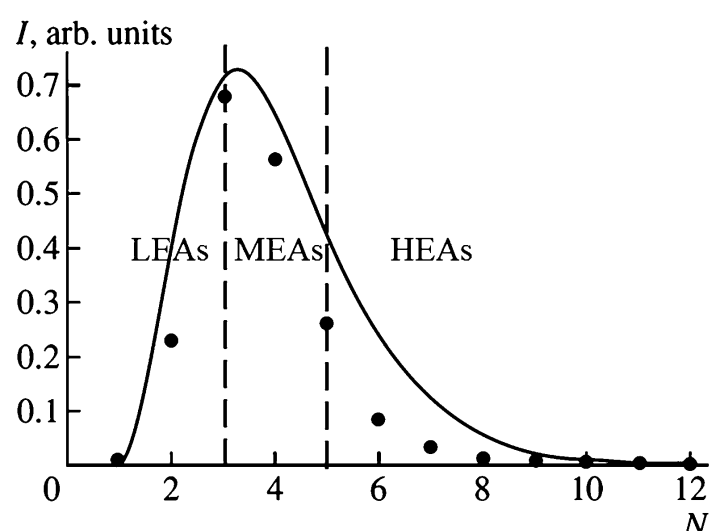
3.3 Crystal Structures and Phase Transformation in HEAs

3.3.1 *The Number of Crystal Structures in Alloy World*

1. Mackey's statistical analysis on crystal number

In the periodic table, there are 80 metal elements and most of them are of three simple structures: FCC, HCP, and BCC. However, there exist different kinds of ICs and IPs in binary alloys, as seen in binary phase diagrams. Moreover, more ternary ICs or IPs exist in lots of ternary alloy systems. Thus, it is easy to have the concept that higher-order alloy systems would generate more ICs or IPs and an alloy with a large number of elements would have many different kinds of ICs and IPs in equilibrium although Gibbs' phase rule places the limitation for the maximum number of phases. Is this right? Mackay has reported the statistics of inorganic crystal structures in his paper entitled “On Complexity” [37]. He wrote “The Inorganic Crystal Structure Database contains some 50,000 structures (many of which are duplicated), which can be searched according to various parameters. Figure 3.1 (i.e., Fig. 3.8 in this chapter) shows a plot of the numbers of structures containing 1, 2, 3, ..., N different elements. A cursory examination shows that many of the structures with large values of N contain solid solutions, different

Fig. 3.8 Points denote the numbers of inorganic crystal structures with 1, 2, 3, ..., N different elements. $N = 3$ has a maximum of 19,000. The line follows the Planck distribution of energy in an absolutely black body [34]. Three alloy regions, LEAs, MEAs, and HEAs, are indicated



elements occupying the same sites, but the result is nevertheless clear. There is a sharp limit to complexity.” He tried to explain this phenomenon by two approaches. One is “The problem could be considered thermodynamically. For example, a soup of many elements does not produce very complex crystals but minimizes the configurational entropy by forming ordered crystal of several simpler compositions.” The other is based on the similarity between Planck distribution of energy in an absolutely black body and the distribution of numbers of crystal structure: “In fact, in a one-dimensional crystal, the number of atoms in a repeat must be an integer and similar effects are to be expected in three-dimensions. Space is “quantized” by atomicity, and not all dimensions of unit cells are possible.” As a result, the explanations for the distribution are still not clear and require further confirmation. On the other hand, if we select 2 elements from 80 metal elements in the periodic table, there are 3160 combinations. Furthermore, the selection of 40 elements from 80 metal elements give possible combinations with a number 1.075×10^{23} , which is about one-sixth of an Avogadro’s number. As there are around 6500 inorganic crystal structures found from binary systems and 19,000 structures from ternary systems (see Fig. 3.8), it could be expected that the number of crystal structure would be huge by extrapolation. It has been estimated that the number of compounds for metal systems could be up to 10^{90} , which exceed the number of atoms, around 10^{80} , in the universe. Thus, the number of compounds is inconceivable except some factors interfere with this extrapolation.

2. Entropy and dilution effects on the statistical distribution of crystal number

What are the interfering factors? Considering the high-entropy effect in HEAs, high entropy is thought to be one important factor to interfere those factors which cause the formation of compounds such as larger atomic size difference which promotes size-factor compounds with highest-neighboring atoms to maximize bond number and also lower the strain energy, valence bonding which promotes valence compounds to maximize the ionic and/or covalent bond strength and satisfy the valence balance, and certain valence electron concentration (e/a) ranges which stabilize electron phases [38, 39]. Entropy effect can be seen in binary and ternary systems. It can enhance the substitution in compounds between different elements with similar chemical features. As the electronegativity and valence of elements in the same group or close groups of the periodic table generally have close chemical feature, the substitution is common. It is apparent that this partial substitution is favored by increasing mixing entropy with some gain or loss in mixing enthalpy depending on the substituting element. For example, NiAl compound (with B2 crystal structure) has a range of composition (also called as NiAl intermediate phase) in Ni-Al phase diagram. By alloying, Co and Pt can substitute a portion of Ni, and Ti and Ta can substitute a portion of Al in the compounds. By the same reason, even high mixing entropy in high-order compositions could enhance the substitution and the mixing in the compounds. This means the ability to accommodate more elements in compounds to form IPs could consume a portion of components. Besides compounds, similar substitution and consumption also occur in the terminal phases based on the component’s structures. Furthermore, there is a

dilution effect in high-order alloy such as HEAs. For equiatomic quinary alloys in which each component possesses 20 % in atomic concentration, its tendency to form compounds is lower since the ratio in A_xB_y -type compounds is often 2:5, 3:4, 1:1, 4:3, or 2:5. Only the ratios, 2:5 and 5:2, are possible except the cases in which the components could be grouped into two and form pseudo-binary alloys. Even for this, solution-type compounds (or IPs) are formed due to high-entropy effect. Therefore, in high-order alloys such as HEAs, high-entropy and dilution effect could enhance the formation of solution-type phase including terminal solid solutions or IPs. This is the main reason, as referred to Fig. 3.8, why there are a sharp decrease in the number of crystal structures with four elements and a further decrease with elements more than four. It is noted that the number of crystal structure with more than eight elements is nearly at the same level of that with one element. As observed by Mackay, many of the structures with large values of N contain solid solutions, different elements occupying the same sites. This is clearly the evidence to support the above explanation based on high-entropy and dilution effects.

What is the entropy effect on the shape of crystal number distribution? The large decrease in the number of crystal structures in fact echoes the definition of HEAs emphasizing the number of major elements being at least five. Two lines are set in the plot of Fig. 3.8 to mark the degree of entropy effect. Mixing entropy is pronounced for crystal structures with at least five elements, moderately pronounced for those with three to five elements and less pronounced for those with one or two elements. As a result, the fast increase of crystal structure number from one element to three elements is due to weaker entropy effect, the slowdown and concave-down are due to increased entropy effect from three to five elements, and further decrease to small number after five elements is related to strong entropy effect. In brief, the distribution curve can be related to entropy effect. This correlation explains the classification of alloy world into HEAs, MEAs, and LEAs based on the number of major elements [3]. Based on the above reasons, it can be expected that most crystal structures in HEAs are also found in LEAs or MEAs. Furthermore, a lot of crystals are of BCC, FCC, and HCP solid solutions since terminal phases of 80 elements almost belong to three kinds of structures: FCC, HCP, and BCC.

3.3.2 *Factors Affecting Solubility Between Metal Elements*

According to crystallography [40], a lattice is a regular periodic array of points in space. The crystal structure is formed when a basis of atoms (atom or a group of atoms or ions) is attached identically to every lattice point. This can be expressed as

$$\text{Lattice} + \text{basis} = \text{crystal structure} \quad (3.2)$$

where every basis is identical in composition, arrangement, and orientation.

Hume-Rothery (H-R) rules are rules in judging the mutual solubility of the two elements at high temperatures in substitutional solid solution of a binary alloy. For example, the solubilities of Ni, Co, Cr, Mo, and Si in Fe are regarded as larger than 15 at.% although their solubility is much lower than 15 at.% at room temperature [41]. He is the first to propose three empirical rules to explain the formation of solid solutions in 1920s. [42, 43]: (1) the atomic sizes of the solvent and solute must not differ by more than 15 %, (2) the electrochemical nature of the two elements must be similar, and (3) a higher-valent metal is more soluble in a lower-valent metal than vice versa. Through a number of latter research, H-R rule are generally stated as [44]:

1. The radii of the solute and solvent atoms must not differ by more than about 15 %: For complete solubility, the atomic size difference should be less than 8 %.
2. The crystal structures of the two elements must be the same for extended solid solubility.
3. Extended solubility occurs when the solvent and solute have the same valency.
4. The two elements should have similar electronegativity so that intermetallic compounds will not form.

Therefore, the similarity and difference of crystal structure, valence, electronegativity, and atomic size are considered to affect the maximum solubility which occurs in the high temperature range below solidus line as seen in phase diagrams. For example, Cu-Ag system has an atomic size difference of 12.5 % ($r_{\text{Cu}} = 0.128 \text{ nm}$, $r_{\text{Ag}} = 0.145 \text{ nm}$ [40]), same electronegativity (Cu and Ag are both 1.9), same crystal structure (both are FCC), and small difference in valences (+1 for Ag and +1 and +2 for Cu). Thus, due to its atomic size difference larger than 8 %, the maximum solubility of Ag in Cu at 779 °C is 8 wt.% (~5 at.%) and that of Cu in Ag is 8.8 wt.% (~14.3 at.%).

Alonso and Simozar [41] have correlated the mixing enthalpy, atomic size difference, and maximum solubility quite well. In fact, mixing enthalpy can be regarded as the result of interaction between two elements, which have been more precisely treated by Miedema model using work function, the electron density of the Wigner-Seitz cell, and molar volume of the two elements. This parameter is obviously better than crystal structure, electronegativity, and valence between two elements in the solubility prediction [41, 45]. However, mixing entropy hasn't been considered as a factor in the solubility prediction although it is known to have a contribution of $-T\Delta S$ to the mixing free energy. This neglect might be due to the thinking that binary alloys have low mixing entropy as compared with mixing enthalpy. In fact, mixing entropy is still important at high temperatures. Co-Cr binary system is an example. Although Co is FCC at above 810 °C and Cr is BCC, the mutual solubility is very high (37 wt.%Cr in Co side and 56.1 wt.%Co in Cr side at 1395 °C). This could not be explained adequately with H-R rules since they are different in crystal structure, atomic size (Co, 0.125 nm, and Cr, 0.128 nm), and electronegativity (Co, 1.7, and Cr, 1.6) and quite different in valence (Co, +2 and +3; Cr, +3, +4, and +6). Obviously, mixing entropy could relax the strictness of H-R rules. In HEAs, there are many examples which reveal the relaxation of H-R rules.

That means large mutual solubilities in BCC and FCC solid solutions and partially ordered solid solutions with compound structures at high temperatures are often found in those alloys not fulfilling the rules, such as in AlCoCrCuFeNi [10], AlCrCuFeMnNi [46], CoCrFeMnNi [7, 8], and HfNbTaTiZr [9]. This is also why most of the phase formation criteria for HEAs discussed in Chap. 2 already consider high-entropy effect for the extended solubility.

3.3.3 Phase Transformation in Different Processing for HEAs

1. High-entropy effect on phase evolution from liquid state

High-entropy effect plays an important role on the phase transformation of HEAs. It should be reminded that mixing entropy is compared at the liquid solution or random solid-solution state in the definition of HEAs. That means HEAs have high mixing entropy at such states as compared with those of conventional alloys. Why high mixing entropy at such states is emphasized? Figure 3.9 shows the typical phase evolution during solidification and cooling [4]. If an alloy has high mixing entropy, simple solid-solution phases will form at high temperatures due to the large $T\Delta S_{\text{mix}}$. During subsequent cooling, mixing entropy become less important and short-range ordering, long-range ordering, or even precipitation of second phases might occur. But sluggish diffusion effect may either yield fine precipitates or inhibit precipitation depending on alloys and processing, which is important for improving mechanical properties. Santodonato et al. studied the evolution of structure, microstructure, phase composition, long-range ordering, short-range ordering, and configurational entropy of $\text{Al}_{1.3}\text{CoCrCuFeNi}$ HEA from room temperature to above 1315 °C by using atom probe tomography, SEM, TEM, EDS, EBSD, neutron diffraction, synchrotron x-ray powder diffraction, and ab initio molecular dynamics simulation [10, 47]. At above 1315 °C, the alloy becomes 100 % liquid, with some preferred nearest-neighbor pair correlations: Al-Ni, Cr-Fe, and Cu-Cu. At 1230–1315 °C, Cu-rich liquid plus BCC crystals ($\text{Al}_{1.3}\text{CoCrCu}_{1-z}\text{FeNi}$) with chemical short-range order are obtained. Total configurational entropy of

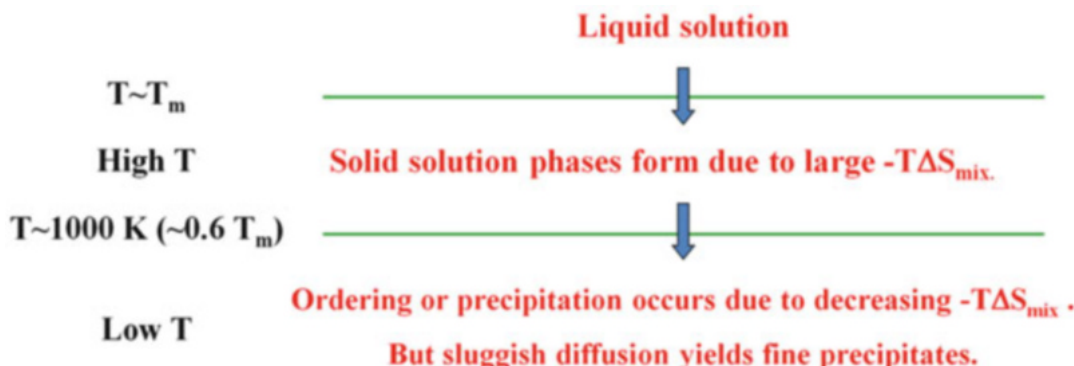


Fig. 3.9 Phase evolution during solidification and cooling of HEAs [4]

BCC phase is $1.73R \leq \Delta S_{\text{conf}} \leq 1.79R$ calculated by the phase composition and degree of ordering. At 1080–1230 °C, 95 % B2 phase ($\text{Al}_{1.3}\text{CoCrCu}_{0.7}\text{FeNi}$) and 5 % Cu-rich liquid are obtained. The total configurational entropy of B2 phase is $1.63R \leq \Delta S_{\text{conf}} \leq 1.73R$. At 600–1080 °C, 85 % B2 phase ($\text{Al}_{1.3}\text{CoCrCu}_{0.1}\text{FeNi}$) plus 10 % Cu-rich rod FCC phase and 5 % Cu-rich interdendrite are obtained. The total configurational entropy of B2 phase is $\Delta S_{\text{conf}} = 1.50R$. At room temperature to 600 °C, 84 % spinodal BCC/B2 ($\text{Co}_{0.2}\text{CrFe}_{0.5}/\text{Al}_{1.3}\text{Co}_{0.8}\text{Fe}_{0.5}\text{Ni}$) plus 16 % various Cu-rich FCC phases are obtained. The total configurational entropy is $0.89R$. They concluded that when the alloy undergoes elemental segregation, precipitation, chemical ordering, and spinodal decomposition with decreased temperature, a significant amount of disorder remains due to the distributions of multiple elements in the major phases. That means an enhancement of the overall disorder due to the entropy effect still exists at room temperature as reflected by the multi-principal-element composition in most phases.

Conversely, if multi-principal-element alloys do not have high mixing entropy at high temperatures, intermetallic phases would form at high temperatures. And in subsequent cooling, the microstructure would become even more complex. Such complex microstructures obviously become very difficult to understand and manipulate and very brittle to be utilized. Therefore, the fortune to avoid the complexity at low temperatures essentially comes from the high-entropy effect which is amplified by high temperature and becomes stronger in competing with mixing enthalpies of intermetallic compounds.

How about the phase diagrams of HEAs? Due to high-entropy effect involved, phase diagram of a HEA system in the composition hyperspace may not be too complicated. Single-phase region, two-phase region, and three-phase region might exist. Each region has their composition and temperature range. Thus, if the phase diagram of a HEA system is known, the equilibrium phases of a composition in the system can be predicted. Figure 3.10 shows the approximate phase diagrams of different alloy series of Al-Co-Cr-Fe-Mo-Ni system [48]. Each diagram was obtained by investigating an alloy series varied with the content of one element with SEM, TEM, room-temperature and high-temperature x-ray diffractometer, and differential thermal analyzer (DTA). Taking the $\text{AlCoCrFeMo}_{0.5}\text{Ni}$ as an example, three phases, FCC + B2 + σ , coexist at 1000 °C and two phases, B2 + σ , coexist at 400 °C. From the viewpoint of thermodynamics, the two and three solid solutions would have lower free energies than that of the single random solid-solution phase. Figure 3.11 shows the schematic curves of mixing Gibbs' free energy at 400 and 1000 °C, respectively, for such a comparison. Although the mixing free energy for each solid solution and thus the overall mixing free energy were not calculated due to their complexity and almost impossible to take a common tangent plane for the equilibrium compositions in the hyperspace, the role of high mixing entropy in further lowering free energy of solution-type phase from pure elements or compounds is obvious in the figure. That is to say that an existence of a mixture of several multi-principal-element solution phases in equilibrium is still a result of high-entropy effect.

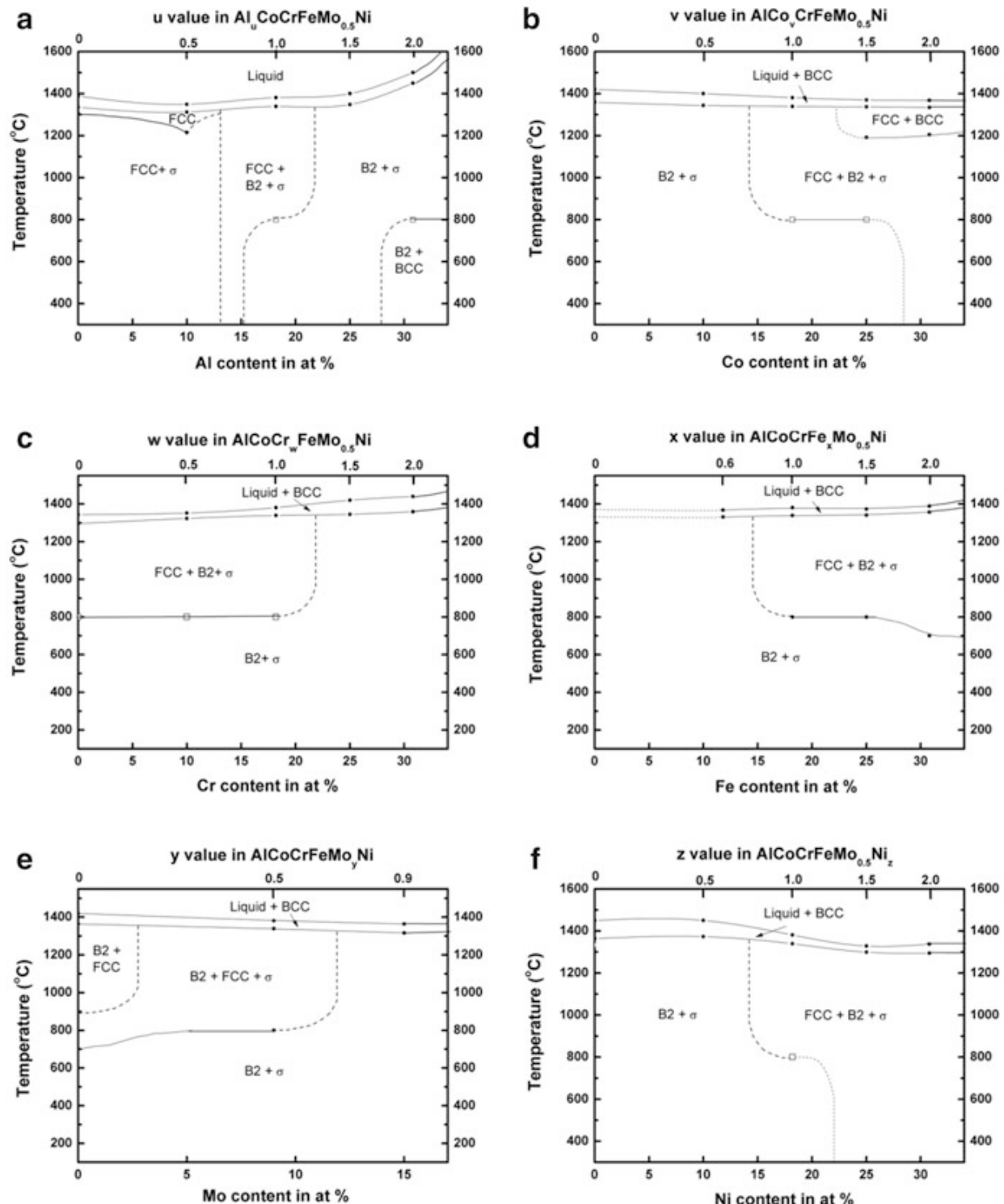


Fig. 3.10 Schematic phase diagrams of different alloy systems: (a) $\text{Al}_u\text{CoCrFeMo}_{0.5}\text{Ni}$, (b) $\text{AlCo}_v\text{CrFeMo}_{0.5}\text{Ni}$, (c) $\text{AlCoCr}_w\text{FeMo}_{0.5}\text{Ni}$, (d) $\text{AlCoCrFe}_x\text{Mo}_{0.5}\text{Ni}$, (e) $\text{AlCoCrFeMo}_y\text{Ni}$, and (f) $\text{AlCoCrFeMo}_{0.5}\text{Ni}_z$ alloys [48]

2. Lattice distortion and sluggish diffusion effects on solid-state transformation

What factors affect phase transformation? Phase transformation has two categories: diffusional type and diffusionless type. Diffusion type one includes solidification, eutectic reaction, eutectoid reaction, precipitation, spinodal decomposition, ordering transformation, and dissolution as found in phase diagram when cooling or heating is exerted. In addition, long holding time at high temperatures

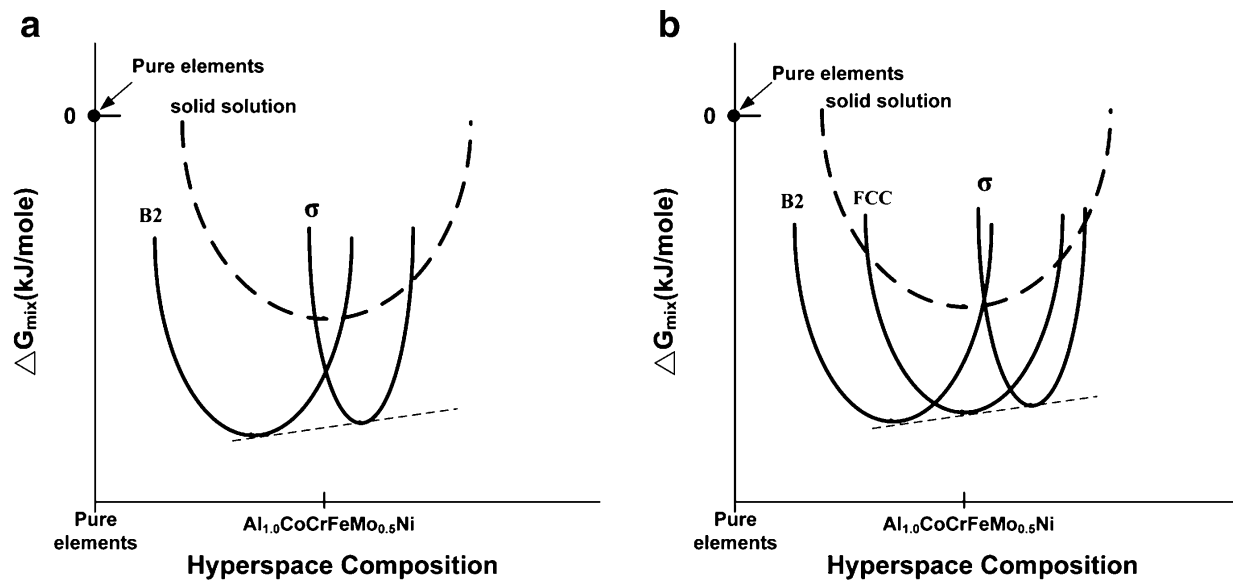


Fig. 3.11 Schematic curves of mixing Gibbs' free energy for the AlCoCrFeMo_{0.5}Ni alloy at (a) 673 K and (b) 1273 K [49]

will cause grain coarsening and Oswald ripening of second phase particles. One example of diffusionless type one is martensitic transformation. Up to 2015, HEAs have provided many examples for different diffusional phase transformations in the literature. However, examples for martensitic transformation are still rare. Nucleation and growth are commonly seen in addition to spinodal transformation. In nucleation-and-growth transformation process, surface energy required to form a nucleus results in the nucleation energy barrier for an embryo to become a stable nucleus. In addition, free energy difference between new and old phases (or new state and old state) provides driving force for the transformation. Because lattice distortion affects interfacial energy and driving force, and sluggish diffusion affects nucleation rate and growth rate, their detailed effects need to be considered for each HEA. But, the general trend of these effects will be considered and explained in Sects. 3.4, 3.5, 3.6 and 3.7.

3. Lattice distortion and sluggish diffusion effects under severe deformation or extremely high cooling rate

What is the lattice distortion and sluggish diffusion effects under severe deformation and extremely high cooling rate? Mechanical alloying and sputtering deposition are easy ways to obtain non-equilibrium simple solid solutions due to the kinetic reason by which sufficient long-range diffusion is inhibited. In addition to crystalline structures, amorphous structure is especially easy to form either by mechanical alloying [49–52] and by sputtering deposition from HEA targets [31, 53] since atomic size difference required to form amorphous structure is smaller than that required for solidification route. Egami's criterion based on topological instability is suitable to explain which compositions tend to form amorphous solid because the alloy synthesized by mechanical alloying or sputtering deposition is directly formed from elemental state [51]. His criterion is that topological instability would happen when the critical volume expansion, 6.3 %,

by atoms of different sizes is exceeded [51, 54, 55]. It has been found that diverse atomic size in HEAs enhances the topological stability and sluggish diffusion of HEAs is helpful in freezing the atom configuration and avoiding crystallization. The combination of a deposition temperature at 400–500 °C and a deposition time 1 h is still easy to obtain the HEA amorphous films with lesser atomic size difference. On the other hand, by solidification route, stricter alloy design is required for obtaining amorphous structure by rapid solidification with at least one dimension very small in thickness or by moderate cooling with bulk forms. Because nucleation and growth of solid phases should be involved during the cooling through freezing range, compositions near deep eutectic composition and fulfilling Inoue's rules tend to have high glass formability [56]. Another viewpoint to increase the glass formability relates with confusion principle which says more components will have a lower chance to select viable crystal structures and thus have greater glass formability [57–60]. To summarize the general factors for forming amorphous structure, increased atomic size difference, negative mixing enthalpy, number of components, and deviation in crystal structures could increase the glass formability of a solid solution [54–60].

3.4 Defects and Defect Energies in HEAs

3.4.1 *Defects in Distorted Lattice and Origin of Defect Energy*

It is well known that even in very pure crystals, it is inevitable to have a certain amount of crystal defects such as vacancies and impurity atoms, which exist at least because of their contribution in mixing entropy. In addition, during preparation of materials, dislocations and grain boundaries and even voids are easily to be introduced into the materials. In HEAs, their structure could be either amorphous structure or crystal structure which depends on the composition and process used. In amorphous structure with multiple elements, residual strain energy might exist since atoms in the structure could suffer from atomic-scale compressive or tensile stress although there is no net stress to cause plastic flow. This stress is different from the external applied stress or residual stress balanced in a long-range scale. Residual distortion energy in amorphous structure could be relaxed to a lower level if suitable thermal energy is provided, such as annealing at below glass transition temperature. In crystal structure with multiple elements, the crystal lattice is distorted due to the difference in atomic size, crystal structure tendency, and chemical bonding as discussed in Sect. 3.2.2. Any atom at a lattice site might have position deviation from exact lattice site. In addition, the electron configuration around the atom has no symmetry as compared with that of crystal structure of pure component. All the deviation and non-symmetry depends on its neighboring atoms. Apparently, such a severe lattice distortion, i.e., distortion exists everywhere, affects phase stability, microstructure, and properties.



Fig. 3.12 A portion of material is shown, which contains an interface with interface area A . Total free energy G is equal to $G_0 + \gamma A$, where γ is the excess free energy per unit interface area arising from the generation of the interface

Topologically, strain and strain energy might be used to describe the degree of lattice distortion in the whole-solute lattice. Because vacancies, dislocations, stacking faults, twins, and grain boundaries are all formed from the lattice, the atomic configuration of these defects would be different between pure lattice and whole-solute lattice with distortion. In addition, the energy level of distorted lattice would be higher than pure lattice without distortion if average chemical bonding is the same. In other words, the deviation of energy level of a kind of defect from the energy level of distorted lattice would be smaller than its deviation from that of pure lattice. This concept could be realized from the typical textbook on phase transformation [61]. The origin of interface energy is discussed in the book. It says, as shown in Fig. 3.12, “The free energy of a system containing an interface of area A and free energy γ per unit area is given by $G = G_0 + A\gamma$ where G_0 is the free energy of the system assuming that all material in the system has the properties of the bulk— γ is therefore the excess free energy arising from the fact that some material lies in or close to the interface. It is also the work that must be done at constant T and P to create unit area of interface.” Another textbook on thermodynamics of solids [62] also says, “The interface is a site of disturbance on an atomic scale, since the environment of atoms at the interface is not regular as it is in the interior of the phase. As a result, to increase the area of an interface, work must be expended by the system.” Although this concept is for interfacial energy, it is similarly applied to the energy of other defects since all these other defects are generated by doing work from the distorted lattice.

The energies of vacancies, dislocations, stacking faults, twin boundaries, and high-angle grain boundaries in most pure metals have been well established in the literature. Table 3.4 selects typical examples of FCC metals, Al, Cu, Ag, Au, and Ni and lists their values for comparison. In the multiple-principal-element matrix, the lattice distortion energy would increase the energy level of the distorted lattice and thus reduce the defect energy from the undistorted lattice to a lower level. Therefore, it is important to estimate the distortion energy so that the importance of distortion energy in affecting defect energy could be determined. The estimation will be presented in the next section.

Table 3.4 The energies of vacancies, dislocations, stacking faults, twin boundaries, and high-angle grain boundaries in FCC metals: Al, Cu, Ag, Au, and Ni

Element	Vacancies (kJ/mole) [63, 64]	Dislocation Gb^2 [65]			Stacking fault (mJ/m ²) [66]	Coherent twin boundary (mJ/m ²) [66]	High-angle grain boundary (mJ/m ²) [66]
		G (GPa)	b (nm)	Gb^2 (10 ⁻⁹ J/m)			
Al	72.5	26.1	0.286	2.1	166	75	324
Cu	96.1	48.3	0.255	3.1	78	24	625
Ag	105	30.3	0.289	2.5	22	8	375
Au	92.5	27.0	0.288	2.2	45	15	378
Ni	138	76.0	0.249	4.7	128	43	866

3.4.2 Lattice Distortion and Distortion Energy

In Sect. 3.2.2, it was discussed that besides atom size difference, different bonding energies and crystal structure tendencies among constituent elements also increase lattice distortion. The lattice distortion energy due to atomic size difference has been formulated in the literature. However, the effects of crystal structure difference, bonding difference, and the extent of lattice relaxation on distortion energy are still difficult to estimate in a quantitative way. Nevertheless, the lattice distortion energy could increase the lattice energy level due to chemical bonding energy. In other words, lattice energy level per mole is equal to the sum of that contributed by chemical bonding and lattice strain per mole:

$$U_{\text{lattice, per mole}} = U_{\text{bonding, per mole}} + U_{\text{strain, per mole}} \quad (3.3)$$

The common calculation of distortion strain is the average misfit strain by using Eq. 3.1. It was also mentioned that actual lattice distortion is not as large as predicted by misfit strain. There would have relaxation process to adjust the atomic configuration in the lattice so that local stress balance and overall minimum free energy could be reached at the equilibrium state. The lattice for such an atomic configuration is just the average lattice as measured by XRD method. Therefore, the lattice strain of this atomic configuration should be based on the average lattice. The calculation of lattice distortion strain and strain energy was proposed by Huang et al. who investigated inhibition mechanism why original grain-size strengthening of high-entropy AlCrNbSiTiV nitride film with NaCl-type structure in the as-deposited state changes little, even after annealing at 1000 °C for 5 h [20]. They calculated the strain and strain energy based on the average lattice constant of average lattice measured by XRD. The strain caused by a component is the deviation between its lattice constant at the pure component state and the experimental average lattice constant. This calculation is based on the tendency that each component would take their original lattice if no constraint for local atomic stress balance and minimum free energy is exerted. The fitting of their original lattices to

average lattice brings about the strain energy. Thus, by assuming average strain energy per unit volume is U_0 , and per atom, $U_{0, \text{per atom}}$, the following equations could be obtained under the hypothesis of isotropic elastic solids:

$$U_0 = \frac{1}{2} \varepsilon_x^2 E + \frac{1}{2} \varepsilon_y^2 E + \frac{1}{2} \varepsilon_z^2 E, \quad (3.4)$$

$$\varepsilon_x^2 = \varepsilon_y^2 = \varepsilon_z^2 = \sum_i x_i \varepsilon_i^2, \quad (3.5)$$

$$\varepsilon_i = \frac{a_i - a_{\text{exp}}}{a_{\text{exp}}}, \quad (3.6)$$

and

$$U_{0, \text{per atom}} = \frac{U_0}{\rho_v}, \quad (3.7)$$

where E is Young's modulus; ε_x , ε_y , and ε_z are strains in the [100], [010], and [001] directions, respectively; ε_i is the lattice strain from component i ; x_i is the molar fraction of component i ; a_i is the lattice constant of component i ; a_{exp} is average lattice constant of the whole-solute lattice obtained by XRD method; and ρ_v is the mole number density.

By using the above equation to calculate the distortion energy of AlCrNbSiTiV nitride film with NaCl-type structure, it is successful to explain low driving force for subgrain growth and grain growth and also the actual subgrain size and grain size observed with TEM. The agreement suggests the distortion energy calculation is persuasive.

As an example for the calculation, an equimolar alloy series from Ni, NiCo, NiCoFe, NiCoFeCr, and CoNiFeCrMn alloy with single FCC structure is used. The basic features of the elements used in this alloy series are listed as Table 3.5 [67]. In the table, the atomic radius and lattice constants are of FCC structure, in which those of non-FCC Cr and Mn, although not found directly in the literature, have been calculated using the equation: $a_{\text{FCC}} = 4r_i/\sqrt{2}$, where r_i is the atomic radius of element i in 12-coordinated metals as listed in the table. Average lattice constants measured by XRD and Burgers' vector, Young's modulus measured by tensile test, and density measured by Archimedes' method for the alloy series are listed in

Table 3.5 Properties of constituent elements in Ni-Co-Fe-Cr-Mn alloy series [67]

Element	Ni	Co	Fe	Cr	Mn
Crystal structure (20 °C)	FCC	HCP	BCC	BCC	SC
Atomic radius, r_i (Å)	1.25	1.25	1.27	1.28	1.26
Lattice constant, a_i (Å)	3.524	3.544	3.555	3.620	3.564
Melting point (°C)	1455	1495	1538	1863	1244

Table 3.6 Related data of Ni-Co-Fe-Cr-Mn alloy series

Metals	Ni	NiCo	NiCoFe	NiCoFeCr	NiCoFeCrMn
Lattice constant, a_{avg} (Å)	3.524	3.534	3.541	3.561	3.561
Lattice constant, a_{exp} (Å)	3.524	3.532	3.569	3.589	3.612
Burgers' vector, b (Å)	2.492	2.498	2.524	2.538	2.554
Young's modulus, E (GPa)	199.5	183.4 ± 5.4	162.3 ± 2.2	232.9 ± 3.2	168.4 ± 5.8
Shear modulus, G (GPa)	76.0	69.6	62.1	90.8	66.0
Density, ρ_v (mole/cm ³)	0.150	0.149	0.146	0.144	0.140
$\sum_i x_i \varepsilon_i^2 (\times 10^{-4})$	0	0.08	0.74	1.63	2.76
U_0 per mole (J)	0	15.4	123	396	500
U_0 per atom ($\times 10^{-22}$ J)	0	0.26	2.0	6.6	8.3

Table 3.6 [68]. Based on this and Eqs. 3.4 and 3.7, we can calculate the distortion energies also listed in Table 3.6. It can be seen that the distortion energy increases with increased addition of element. Although Mn does not have the largest lattice constant, distortion energy still increases after its addition.

3.4.3 Vacancies

In HEAs, what is the formation enthalpy of vacancy? Is the vacancy concentration influenced by high mixing entropy? How about the diffusivity of vacancy? All these answers are important for understanding the kinetics of phase transformation and creep behaviors.

It is well known that vacancies are inevitable in materials because of entropy reason. The formation of a vacancy by removing an atom would destroy the bonds with its neighboring atoms and thus raise the energy state with an increase, ΔH_v , in enthalpy although some relaxation would occur. Besides, the formation would also be associated with an excess entropy ΔS_v mainly by vibrational randomness around vacancy. However, an amount of vacancy would increase the configuration entropy by configurational randomness. For a pure metal, it can be derived that there exists a critical concentration at which the total free energy of mixing is minimum [26]. Consider a crystal containing N_0 atoms and N_v vacancies, the free energy change from perfect crystal without vacancies could be written as

$$G - G_0 = N_v \Delta H_v - kT \ln[(N_0 + N_v)! / N_0! N_v!] - N_v T \Delta S_v \quad (3.8)$$

where k is Boltzmann's constant. Using Stirling's approximation and rearrangement,

$$G - G_0 = N_v \Delta H_v - kT[(N_0 + N_v) \ln(N_0 + N_v) - N_0 \ln N_0 - N_v \ln N_v] - N_v T \Delta S_v \quad (3.9)$$

Since $d(G - G_0)/dN_v = 0$ at equilibrium and N_0 is very small, it leads to the equilibrium vacancy concentration

$$X_v = N_v/(N_0 + N_v) = e^{\Delta S_v/kT} e^{-\Delta H_v/kT} = e^{-\Delta G_v/kT} \quad (3.10)$$

How about the vacancy concentration in HEAs? Consider the simplest case, an equimolar random ideal solid solution with n metal elements which have the same atomic size, then the above equation becomes

$$G_h - G_{0h} = N_{vh} \Delta H_{vh} - kT[(N_0 + N_{vh}) \ln(N_0 + N_{vh}) - N_0 \ln(N_0/n) - N_{vh} \ln N_{vh}] - N_{vh} T \Delta S_{vh} \quad (3.11)$$

Since $d(G_h - G_{0h})/dN_v = 0$ at equilibrium and N_0 is very small, it leads to the equilibrium vacancy concentration

$$X_{vh} = N_{vh}/(N_0 + N_{vh}) = e^{\Delta S_{vh}/kT} e^{-\Delta H_{vh}/kT} = e^{-\Delta G_{vh}/kT} \quad (3.12)$$

Therefore, the number of elements does not alter the equation form of vacancy concentration for pure metal. For a non-equimolar and non-ideal solid solution in which atomic size and bonding are different between elements, the equation form is still the same except using its own excess enthalpy, excess entropy, and excess free energy. This demonstrates that the equation of vacancy concentration for each solid-solution phase of HEAs is essentially the same as that for pure metals. Does lattice distortion of multiple-element matrix affect the excess enthalpy? The answer is that lattice distortion would be very small and negligible since lattice distortion energy per mole of atoms as shown in Table 3.6 is far below the heat of formation of vacancy per mole. The largest distortion energy, 500 J/mole, of quinary alloy is about five thousandth of the formation enthalpy of vacancy as seen in Table 3.4. This is reasonable because the formation of a vacancy needs to break chemical bonds with its neighboring atoms whereas lattice distortion only changes bond length or angle. In brief, the concept of vacancy concentration for conventional alloys still holds for HEAs.

3.4.4 Solutes

Solute atoms come from the impurity inherent from the extraction and fabrication processes or intended alloying from initial alloy design for improving properties. In HEAs, most phases are of solid solutions (disordered or partially ordered). In each

solid solution, a variety of elements are mixed in the matrix which can be regarded as a whole-solute matrix. Larger atoms are mostly in compressive strain or stress whereas smaller atoms mostly are in tensile strain or stress. Thus, each lattice point of the whole-solute matrix has atomic-scale lattice strain and the whole lattice suffers severe lattice distortion as compared with conventional lattice with a major element. As mentioned previously, besides atomic size effect, different crystal structure tendencies and different bondings among unlike neighboring atoms would influence atomic position and cause further distortion. However, due to the tendency to lower the total free energy, lattice strain at each site would be relaxed by adjusting the relative positions of neighboring atoms.

1. Stress field around an atom

Despite the relaxation, the atomic-scale stresses exist in the whole-solute matrix. Egami has pointed out the existence [54, 55]. Even in amorphous structure, such atomic-scale stresses still exist. Although such atomic-scale stress varies from site to site in the lattice, some in compression and some in tension, local balance between their stresses should be attained in the steady state. That is, their overall contribution to microscale or macroscale stress is zero on average basis. Because the stress field around a solute atom would be shielded or eliminated by the stress field of surrounding atoms, the long-range atomic stress of any atom would be small. That is, the stress around an atom is atomic scale or short range.

2. Distortion effect on lattice constant

As the whole-solute matrix of HEA solid solution is a mixture of various elements, the lattice constant of the real crystal structure would have some relation with the lattice constant of pure element. For the simplest case of random solid solution, is Vegard's law valid? Vegard's law in a binary A-B solid solution can be expressed as

$$a_{AB} = (1 - x)a_A + xa_B \quad (3.13)$$

where x is the fraction of component B. Vegard's law can be regarded as the rule of mixtures, which was proposed based on his observation on continuous solid solution of ionic salts, such as KCl-KBr. However, this law is not strictly obeyed by metallic solid solutions [6]. But the reason for the deviation is still unclear. For this, we need to consider the effects of lattice distortion and excess chemical bonding. It is proposed that lattice distortion could expand the average lattice predicted by Vegard's law and stronger excess chemical bonding would give shorter bond length and thus smaller lattice constant. The superposition of these two main effects determines the real lattice constant. For the first effect, let's consider the equilibrium structure without lattice distortion and used pure Ni as example. Figure 3.13a shows the equilibrium case in which atoms in pure Ni are in their equilibrium positions at the minimum of potential well, bond strengths are maximized, and its lattice constant attains the minimum. Figure 3.13b shows the perturbation case. In

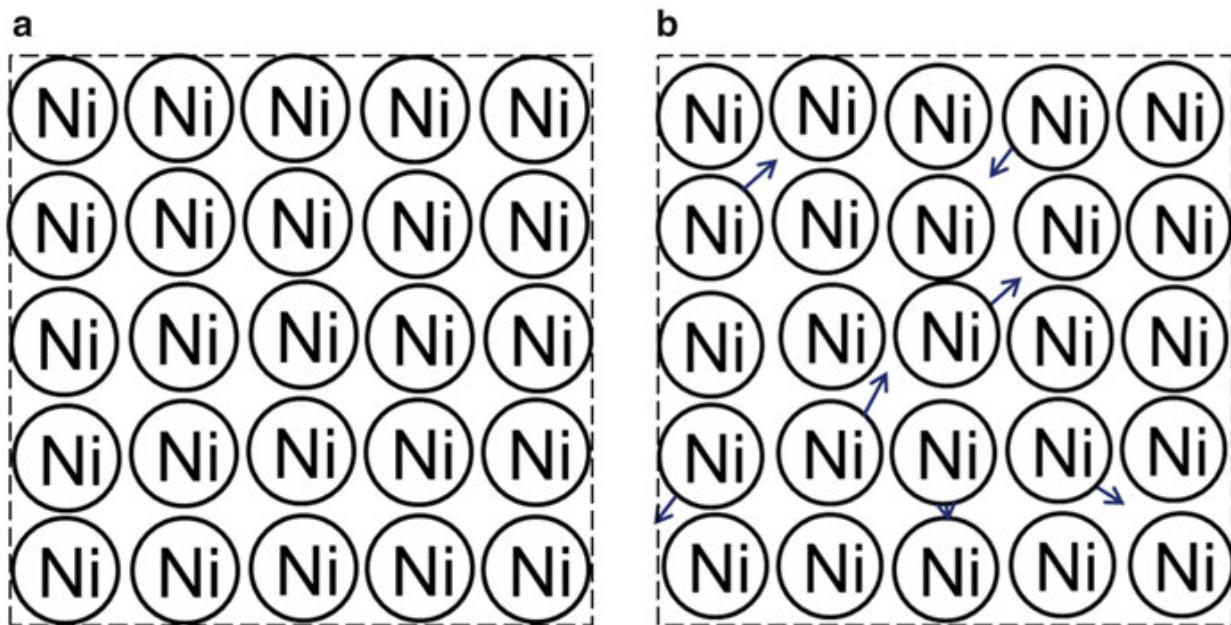


Fig. 3.13 (a) Equilibrium structure of pure Ni without lattice distortion and (b) expanded structure of pure Ni with lattice distortion

this structure, any offset of an atom from the minimum of potential well would decrease local bond strength and increase overall bond length or lattice constant. In other words, a distorted lattice with zigzag atomic directions and planes would disturb the original equilibrium lattice to have a certain expansion of volume. In the extreme case, amorphous solid could have a lower density than crystalline solid by 0.3–0.5 %.

This thinking could be applied to binary solid solution. Because the average lattice predicted by Vegard's law is a linear combination of two component lattices and total free energy would be raised by atomic size difference or other differences in electrochemical properties, a certain offset from the composite minimum position of potential well is needed in order to relax total free energy. Under such a lattice distortion, the effective bond strength is reduced and lattice constant is increased. Similarly, for Ni-Co-Fe-Cr-Mn alloy series which is near-ideal FCC solid solution, the lattice distortion $\varepsilon_x^2 = \varepsilon_y^2 = \varepsilon_z^2 = \sum_i x_i \varepsilon_i^2$ increases with

increased number of elements explaining why the lattice constant of real crystal structure generally has more deviation from that predicted by Vegard's law. The deviations from binary to quinary alloys are -5.66×10^{-4} , 7.91×10^{-3} , 7.86×10^{-3} , and 1.43×10^{-2} , respectively (see Table 3.6). It should be mentioned that the quinary alloy has a negative mixing enthalpy $-4.16 \text{ kJ mol}^{-1}$ which would reduce bond length and thus lattice constant. Hence, the increased lattice constants as compared with ideal average lattice constant indeed give a strong suggestion that lattice distortion has the effect to expand the lattice (see the quinary alloy in Fig. 3.14).

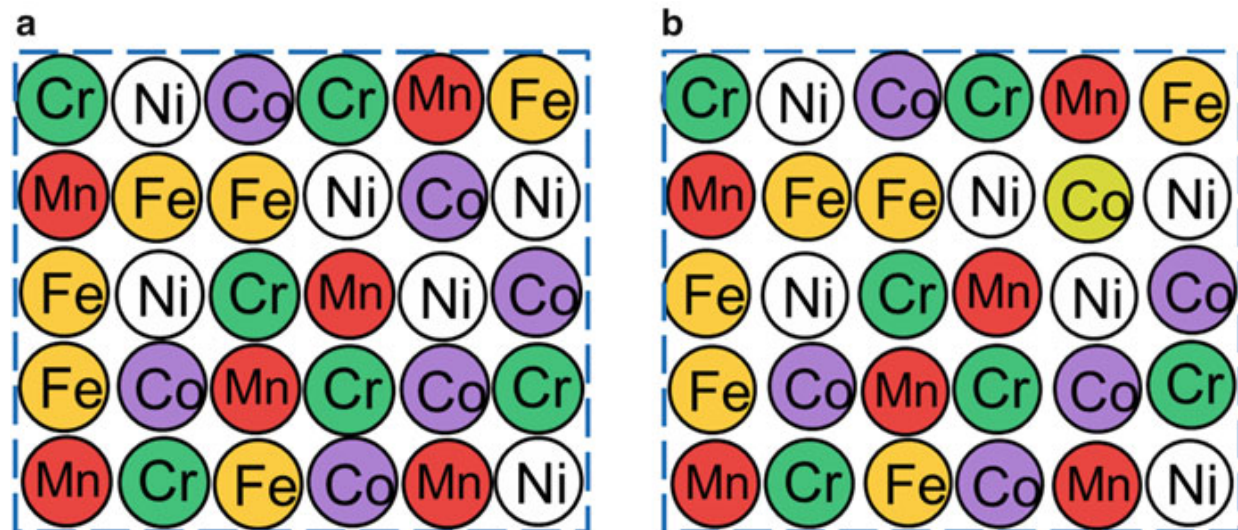


Fig. 3.14 (a) Equilibrium structure of CoCrFeMnNi without lattice distortion and (b) expanded structure of CoCrFeMnNi with lattice distortion

3.4.5 Dislocations

1. Lattice distortion and pinning effect on dislocation energy

Dislocations exist in metals by various sources including nucleation and growth of solid during solidification and cooling, collapse of quenched vacancies, stress concentration, and multiplication of dislocation sources [69]. However, due to severe lattice distortion in the whole-solute matrix, dislocation energy, typically written as Gb^2 for conventional alloys (G , shear modulus; \mathbf{b} , Burgers' vector), needs to be modified by considering two factors: the interaction between dislocations and surrounding atoms and lattice distortion energy level. If no interaction occurs between dislocations and nearby atoms, the stress field equations are the same as that in a perfect lattice in the literature [69]. However, interaction would occur for the sake of reducing total energy if thermal activation and time are sufficient to let flexible dislocation and nearby atoms to adjust their relative position to lower total energy and form dislocation atmosphere. Since this adjustment does not require long-range diffusion and could be achieved by pipe diffusion in the core with the abundant solutes everywhere, such an adjustment within several atomic distances is possible at relatively lower temperature than that for conventional alloys. This is unique for HEAs since conventional matrix with one major element would require long-range diffusion to attract solutes from faraway regions toward dislocation cores and thus higher temperature to enhance the diffusion to form atmospheres.

The core radius of a dislocation, in which stress and strain do not follow linear elastic mechanics, is usually thought to be $5\mathbf{b}$ (i.e., 5 atoms in the radius), and the stress built up in the core is theoretical stress which is around $Gb/30$ [70]. This core energy could account for one-tenth of dislocation energy [69, 70]. In the core, large atoms such as Cr and Fe could migrate into tensile region beneath the edge dislocation whereas smaller atoms could diffuse into compressive region just

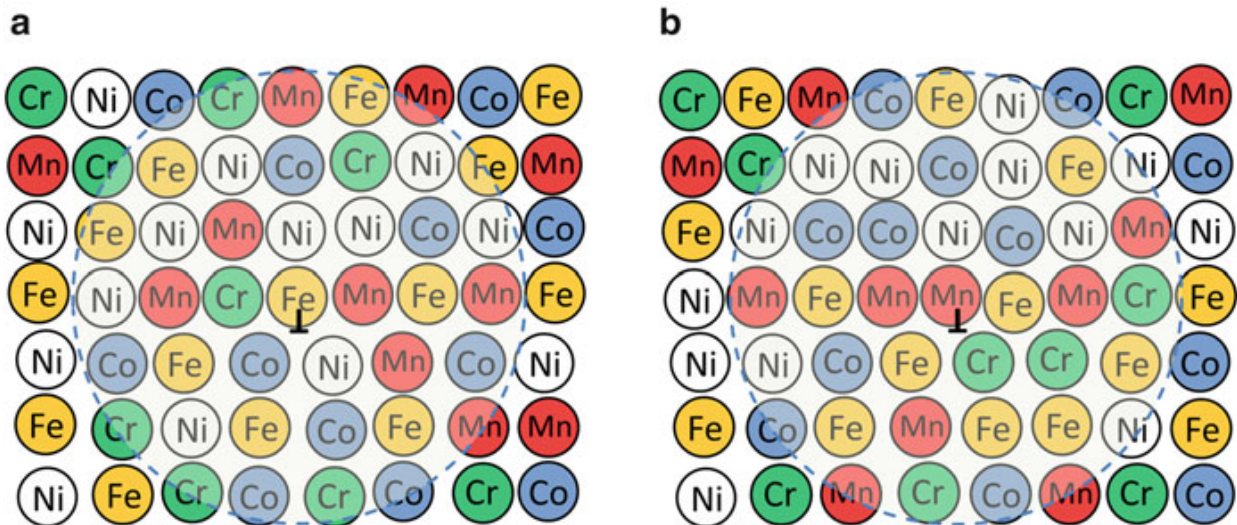


Fig. 3.15 Atomic configurations around a dislocation: (a) before relaxation and (b) after relaxation. Relaxation means that overall strain energy is lowered by rearrangement of different atoms. Dashed circle presents the range of dislocation core

above dislocation line through fast dislocation-pipe diffusion, as shown in Fig. 3.15. Although such a rearrangement could release the overall energy, the stress field around a dislocation is essentially unchanged because it is a long-range field formed initially with dislocation and not affected by the short-range interaction in the core.

On the other hand, lattice distortion could reduce the effective energy of dislocations since the defect energy is a relative difference of the energy level between defects (vacancy, dislocation, grain boundary, and surface) and lattice. This means when we create the defect by doing work, the work would be smaller in distorted lattice than in perfect lattice without distortion energy. Alternately, when two opposite dislocations cancel with each other and return to distorted lattice, the energy release would be lower. Therefore, the dislocation energy is reduced and becomes smaller than the expected Gb^2 . Here, quinary alloy CoCrFeMnNi is chosen for the estimation. As seen in Table 3.6, the core volume per unit length (m) of a dislocation in this alloy is

$$\text{Core volume per unit length} = (5b)^2 \pi \times 1 \text{ m} = 5.12 \times 10^{-18} \text{ m}^3 \quad (3.14)$$

The distortion energy of the same volume in the distorted lattice without dislocations is

$$\begin{aligned} \text{Equivalent distortion energy/m} &= 5.12 \times 10^{-18} \text{ m}^3 \times \rho_v \times U_{0\text{per mole}} \\ &= 3.58 \times 10^{-10} \text{ J/m} \end{aligned} \quad (3.15)$$

$$\begin{aligned} \text{Dislocation energy/m} &= Gb^2 - 3.58 \times 10^{-10} \text{ J/m} \\ &= 4.3 \times 10^{-9} \text{ J/m} - 3.58 \times 10^{-10} \text{ J/m} \\ &= 3.94 \times 10^{-9} \text{ J/m} \end{aligned} \quad (3.16)$$

Thus, lattice distortion in the quinary alloy CoCrFeMnNi reduces about one-tenth of the dislocation energy. In brief, the two factors could lower dislocation energy to a certain extent: easy relaxation effect to lower the overall strain energy (but un-estimated) by forming atmosphere and distorted lattice effect to lower the dislocation energy by increasing the energy level of lattice. For other systems with larger atomic size difference and thus U_0 per mole, the dislocation energy would be significantly lower. It should be mentioned that the stress required to form a dislocation is similar to the theoretical shear stress to shear a crystal along slip plane. The theoretical stress is about $G/15$. In real crystals having dislocations to aid the slip deformation, the actual stress required to shear only ranges from 1/100 to 1/10,000 of theoretical shear stress. This means, even if the above two factors result small energy reduction of dislocation energy, their effects on real strength can be significant. Therefore, compared to the undistorted lattice, dislocations in the whole-solute matrix have a relatively lower energy state which are more difficult to move in the slip plane, not only to overcome strong atmospheres but also to overcome the abundant solute obstacles even after releasing from atmospheres. This will be further discussed in the later section of solution hardening. However, it should be pointed out that more fundamental research to derive exact dislocation energy by simulation or theoretical calculation is required in the future. Direct observations or indirect evidences are also required to check the existence of strain aging (solute pinning on dislocations).

2. Virtual force on dislocations under applied stress

The virtual force that results from a shear stress applied to a conventional crystal needs to be checked for HEA crystal. Since the virtual force is derived by equating the external work done by applied stress with the internal work done by the virtual force, which does not concern with lattice distortion, the virtual force equation for dislocations in HEAs is the same as that in conventional alloys. That is, all the virtual force per unit length on screw, edge, or mixed dislocations in the slip plane is

$$F = \tau_o b \quad (3.17)$$

where τ_o is the applied shear stress in parallel with Burgers' vector. If the stress is not parallel with Burgers' vector, the virtual force could be calculated by a general equation called Peach-Koehler equation: the cross product of stress tensor and Burgers' vector [69, 70].

3.4.6 Stacking Faults

1. Lattice distortion and Suzuki effect on stacking fault energy

Stacking faults relate with dislocations. Discontinuities in the stacking order of atomic planes are called stacking faults. If a stacking fault terminates in the crystal, its boundary is a partial dislocation. In FCC, it could be Shockley partial

dislocations or Frank partial dislocations [69]. Stacking fault can be regarded as a planar defect and have a surface energy because the atoms on either side of a stacking fault are not in normal positions and lose some bonding energy. The stacking fault is in fact a HCP layer with four atomic layers. However, strain fields and chemical tendency in FCC or HCP structure of those atoms near or along stacking fault could be used to lower the stacking fault energy (SFE) by segregation and adjusting their positions if suitable thermal energy is provided. This is the so-called Suzuki interaction. Conventionally Suzuki interaction is used for explaining the reduction of SFE due to alloying effect. For HEAs, this interaction also holds true and can be considered as one factor in lowering SFE. In the whole-solute matrix, this local adjustments or rearrangements of atoms will change the composition in atomic-scale range (without long-range diffusion as in the conventional matrix) but might not change it when measured in nanoscale or larger range. Therefore, the proof on such an interaction requires very careful analysis on identifying the segregation.

Besides Suzuki interaction, there is in fact another factor, lattice distortion energy, in reducing SFE for HEAs. Figure 3.16 shows the schematic diagram for the effect of Suzuki interaction and lattice distortion, in which different free energy levels of stacking fault, perfect lattice without distortion, and distorted lattice are shown. The hypothetical lattice without distortion means solute atoms simply occupy lattice sites and do not cause the lattice distortion. The energy level of stacking fault is assumed to be constant although it could be somewhat lower by relaxation in distorted lattice. The stacking fault energy in such a lattice is γ_{perfect} . After Suzuki interaction which releases some energy, U_{suzuki} , of stacking fault, the stacking fault energy is reduced. In reality, lattice is distorted by solute atoms and has a higher energy level due to distortion energy. As a result, real SFE, γ_{real} , is even lower than $\gamma_{\text{perfect}} - U_{\text{suzuki}}$. Therefore, as all atoms in the HEA matrix are solutes, the SFE in HEA matrix is inherently low because of Suzuki interaction and lattice distortion energy. However, Suzuki interaction occurs when thermal energy is suitably provided to cause the diffusion for segregation. Thus, suitable temperature is required. Low temperature could not afford the diffusion for segregation whereas high temperature would destroy the interaction or segregation toward randomness.

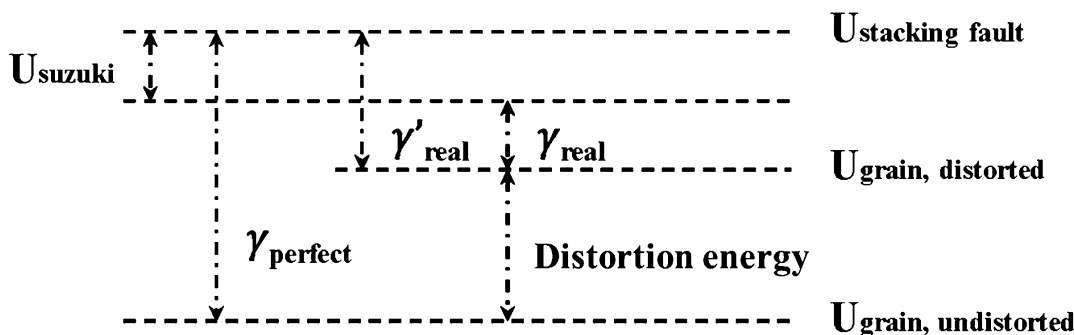


Fig. 3.16 Diagram shows the effect of Suzuki interaction and lattice distortion on stacking fault energy. Different free energy levels of stacking fault, perfect lattice without distortion, and distorted lattice are compared

If a specimen is processed to avoid the suitable temperature range for Suzuki interaction, SFE becomes γ'_{real} which is larger than γ_{real} by U_{suzuki} .

As Suzuki interaction and lattice distortion energy depend on the constituent elements in the matrix, the relative positions of energy levels and thus real SFE also depend on compositions.

It should be pointed out that lattice distortion energy effect should be also considered as the second factor in reducing SFE of conventional alloys such as FCC Cu-Al bronze and FCC Cu-Zn brass in considering the origin of interface energy mentioned above. The additions of Al and Zn into the copper matrix have been found to effectively lower SFE. In view of the second factor, the significant atomic size difference between Al (1.43 Å) and Cu (1.28 Å) and between Zn (1.39 Å) and Cu and other differences in crystal structure tendency and chemical bonding can cause lattice distortion and decrease SFE.

2. Stacking fault energies measured for HEAs

By using XRD patterns taken from powder samples, stacking fault energy of the equiatomic alloy series with single FCC structure, Ni, NiCo, NiCoFe, NiCoFeCr, and NiCoFeCrMn has been measured [68]. The powders were obtained from two bulk samples by using a high-speed steel rasp. One is cold-rolled sample obtained by cold-rolling the sheet homogenized at 1100 °C for 6 h and quenched. The cold reduction is 70 % so that fully work hardening is ensured. The other is full-annealed sample which is obtained by heat-treating the cold-rolled sample at 1100 °C for 10 min. Table 3.7 shows the related data for deriving stacking fault energy by using related equations as reported in the literature [71]. The SFE, 108 mJ/m², of pure Ni obtained by this XRD method agrees well with that, 128 mJ/m², obtained by TEM node method in the literature [72, 73]. Figure 3.17 shows the variation of SFE with the number of composing elements. Stacking fault energy decreases with increasing number of elements. It is noted that there is a large reduction of SFE from Ni to NiCo and NiCoFeCrMn has the lowest SFE, 6.2 mJ/m². As SFE of FCC Co is 15 mJ/m² [73], the SFE value, 40.8 mJ/m², of NiCo in Table 3.7 is reasonable since the SFE predicted by the rule of mixture is 71.5 mJ/m². Suzuki interaction and lattice distortion energy in NiCo alloy would cause a further reduction of SFE. In fact, the value is similar to that found for NiCo in the literature [72].

Koch's group used mechanical alloying method to prepare another equiatomic alloy series and derived stacking fault energy by using XRD method and different

Table 3.7 Related data and related equations for deriving stacking fault energy by XRD method [61]

Alloys	Ni	NiCo	NiCoFe	NiCoCrFe	NiCoFeCrMn
$\Delta 2\theta$ (degrees)	0.02	0.02	0.02	0.05	0.156
$\alpha(\times 10^{-3})$	3.66	3.69	3.71	9.32	29.2
$<\varepsilon^2_{50}>_{111} (\times 10^{-5})$	7.84	7.92	6.71	9.31	9.89
G (GPa)	76	69.6	62.1	90.8	66.1
γ (mJ/m ²)	108	40.8	31.3	25.3	6.2

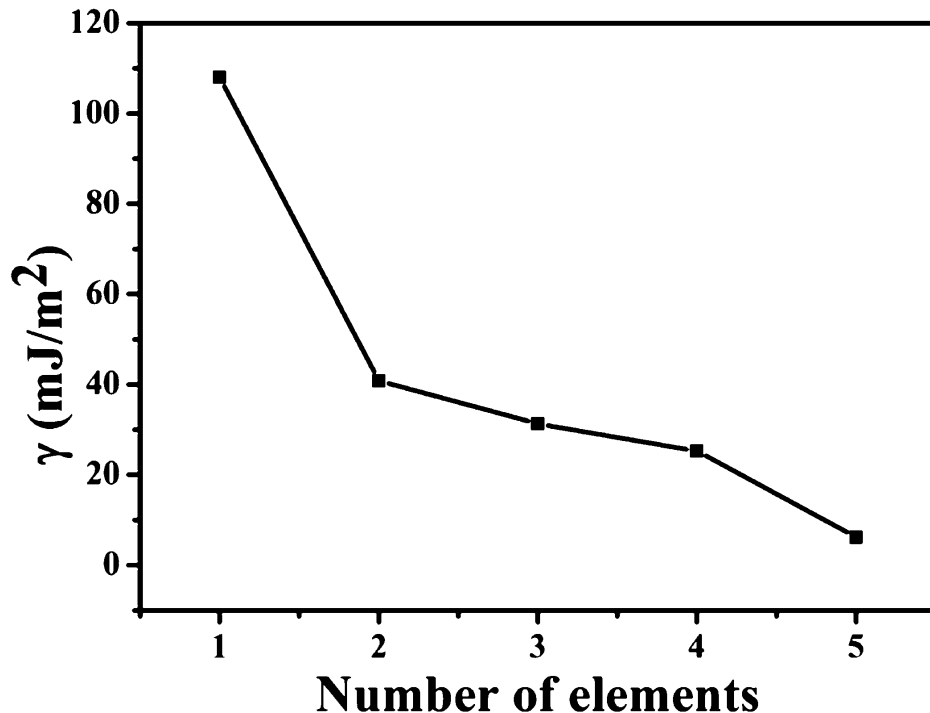


Fig. 3.17 SFE as a function of the number of composing elements from Ni to NiCoFeCrMn alloy [68]

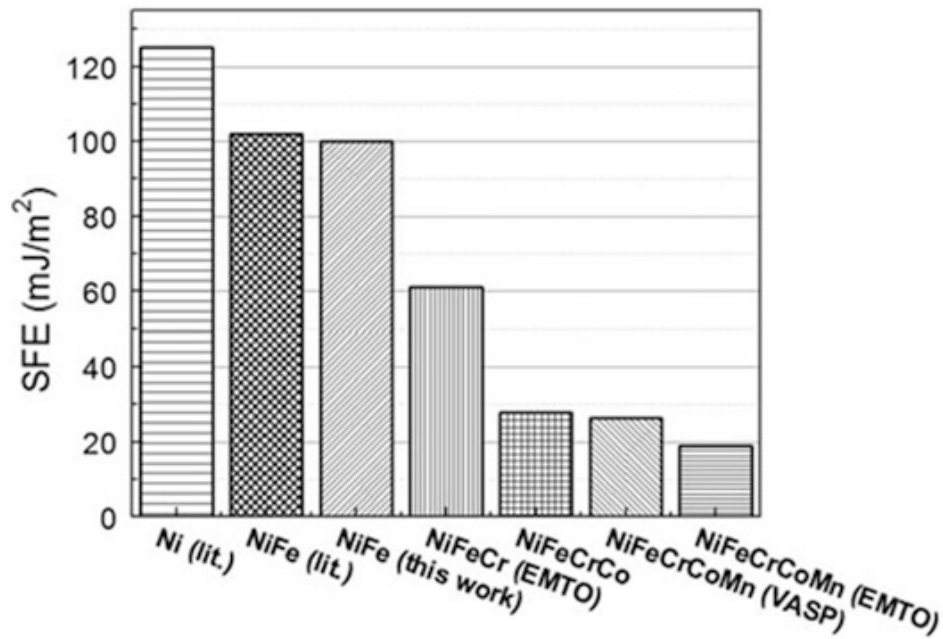


Fig. 3.18 Stacking fault energies of equiatomic FCC metals from pure Ni to NiFeCrCoMn measured by XRD methods combined with different simulations [74]

simulations [74]. They found that SFE decreases with increased number of elements, and five-element alloy has the lowest SFE (see Fig. 3.18). However, there exists a larger difference between the SFEs of equiatomic CoCrFeMnNi in Figs. 3.17 and 3.18. Hence, further research is required for clarification. In addition, by varying Ni content and Cr content, Kock's group found that $\text{Ni}_{14}\text{Fe}_{20}\text{Cr}_{26}\text{Co}_{20}\text{Mn}_{20}$ alloy has an extremely low SFE 3.5 mJ/m^2 [74]. If one plots

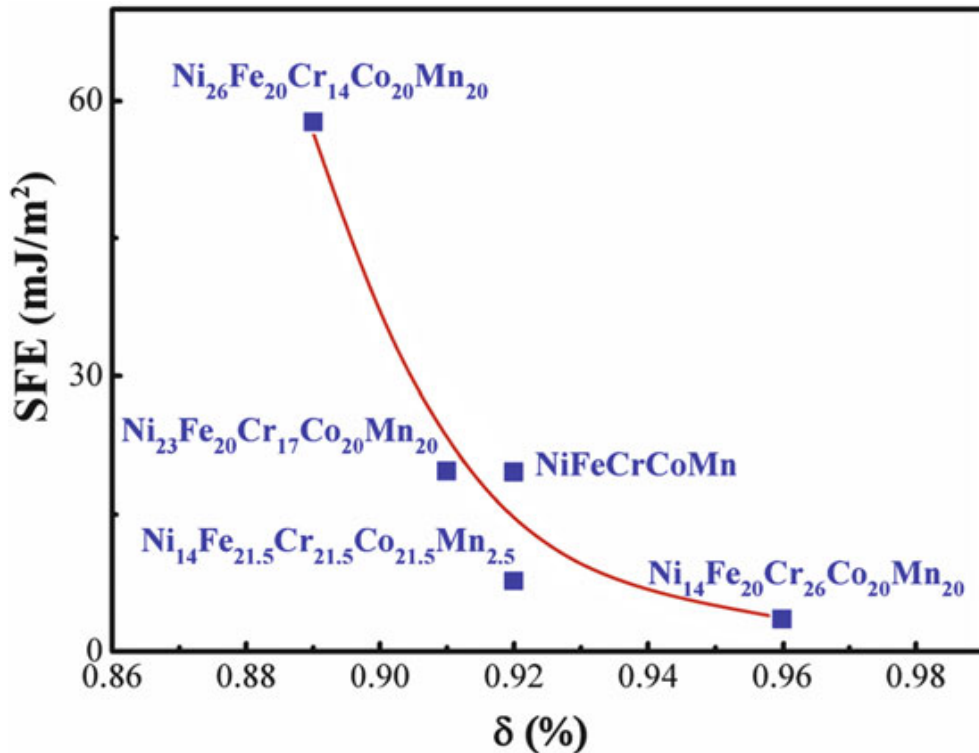


Fig. 3.19 Stacking fault energies [74] and atomic size differences of non-equiautomic and equiautomic Co-Cr-Fe-Mn-Ni alloys

SFEs as a function of atomic size difference (see Eq. 3.1) for these Co-Cr-Fe-Mn-Ni alloys, Fig. 3.19 is obtained revealing the trend which rationalizes the combined effect of increased energy level of the distorted matrix and the increased strain energy relief of stacking fault by in situ atom position adjustment since larger atomic size difference could enhance these two factors. However, all these phenomena require new model and theory to explain the mechanisms.

3. Effect of stacking fault energy on slip bands

Stacking fault energy is very important in affecting dislocation movement, dislocation substructure, twinning, strength, strain hardening, ductility, climb, creep, stress corrosion, and hydrogen embrittlement. For example, low SFE will give larger separation between partial dislocations. For the stacking fault bounded by Shockley partial dislocations in FCC structure, the cross-slip or double cross-slip process becomes more difficult since far-spaced partial dislocations need to combine into complete screw dislocations for finishing such processes. The resulting dislocation structure will be more uniform in planar array and slip bands are finer and more uniform. In addition, both the stress and energy required to form twins is lower because a coherent twin boundary is basically half-thickness of a stacking fault. Figure 3.20 shows the optical micrographs of the slip bands in grains after cold-rolling with a reduction of 50 % from Ni to NiCoFeCrMn alloy [68]. It can be seen under such a reduction that there is essentially one slip system operated. However, the average spacing between slip bands first decreases and then increases with increasing number of elements. Their spacings are 15.8, 9.0, 3.3, 5.4,

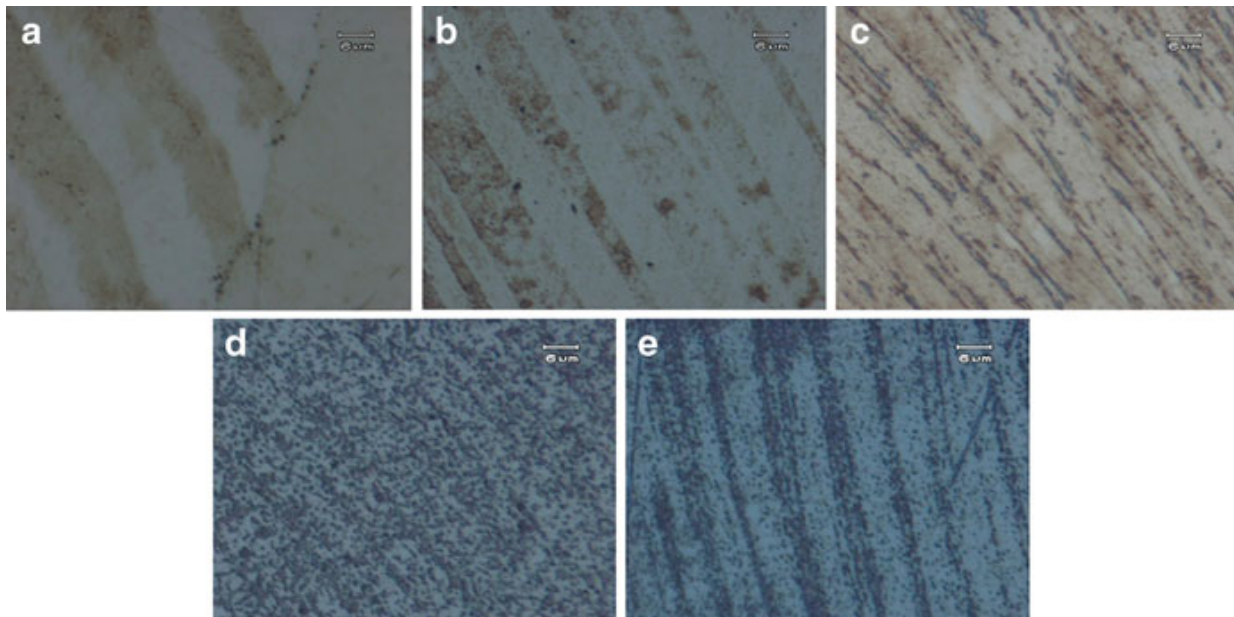


Fig. 3.20 Slip bands observed in the grains after cold-rolling with a reduction of 50 %: (a) Ni, (b) NiCo, (c) NiCoFe, (d) NiCoFeCr, and (e) NiCoFeCrMn [68]

and 6.0 μm . As dislocation etching pits represent dislocation, dark slip bands in Ni, NiCo, and NiCoFe suggest that dislocation density in slip bands is high enough to let pits seen under optical microscope. This means the plastic strain in their slip bands is also large. However, NiCoFe has the densest slip bands, which is helpful to release the strain concentration in each slip band and helpful to enhance ductility. It is noted that NiCoFeCr and NiCoFeCrMn alloys have discrete etching pits in slip bands and between slip bands. The spreading of etching pits is obviously large in NiCoFeCr as compared with NiCoFeCrMn alloy. However, because NiCoFeCrMn alloy has much smaller SFE than that of NiCoCrFe, nanotwinning deformation is much easier to operate especially between slip bands. To sum up, decreased SFE from Ni to NiCoFeCr could increasingly inhibit cross-slip and double cross-slip and thus enhance strain hardening and the activation for other slip bands. Higher strain hardening and lesser strain concentration in turn delay the fracture and improve the ductility. On the other hand, low SFE of NiCoFeCr and NiCoFeCrMn is expected to induce nanotwinning deformation, in which NiCoFeCrMn would be much easier than NiCoFeCr. So, a portion of strain is expended in nanotwinning which is expected to form between slip bands. Similar phenomena could be observed in low SFE stainless steel such as 310S (Fe-25Cr-19Ni) having a SFE of $14/\text{m}^2$ [71, 75]. This is why etching pits of NiCoFeCrMn are not so dense in between slip band. The large formation of nanotwinning (during rolling or tensile deformation at low temperatures) is especially beneficial for ductility due to large strain hardening and induced plasticity.

As the cold-rolling reduction is increased up to 90 %, second slip systems are induced in deformed grains [68]. Coarse slip bands in Ni and NiCo become intersected and wavy. Fine slip bands in NiCoFe are also found to be interwoven. NiCoFeCr alloy has even fine and dense interwoven structure of slip lines.

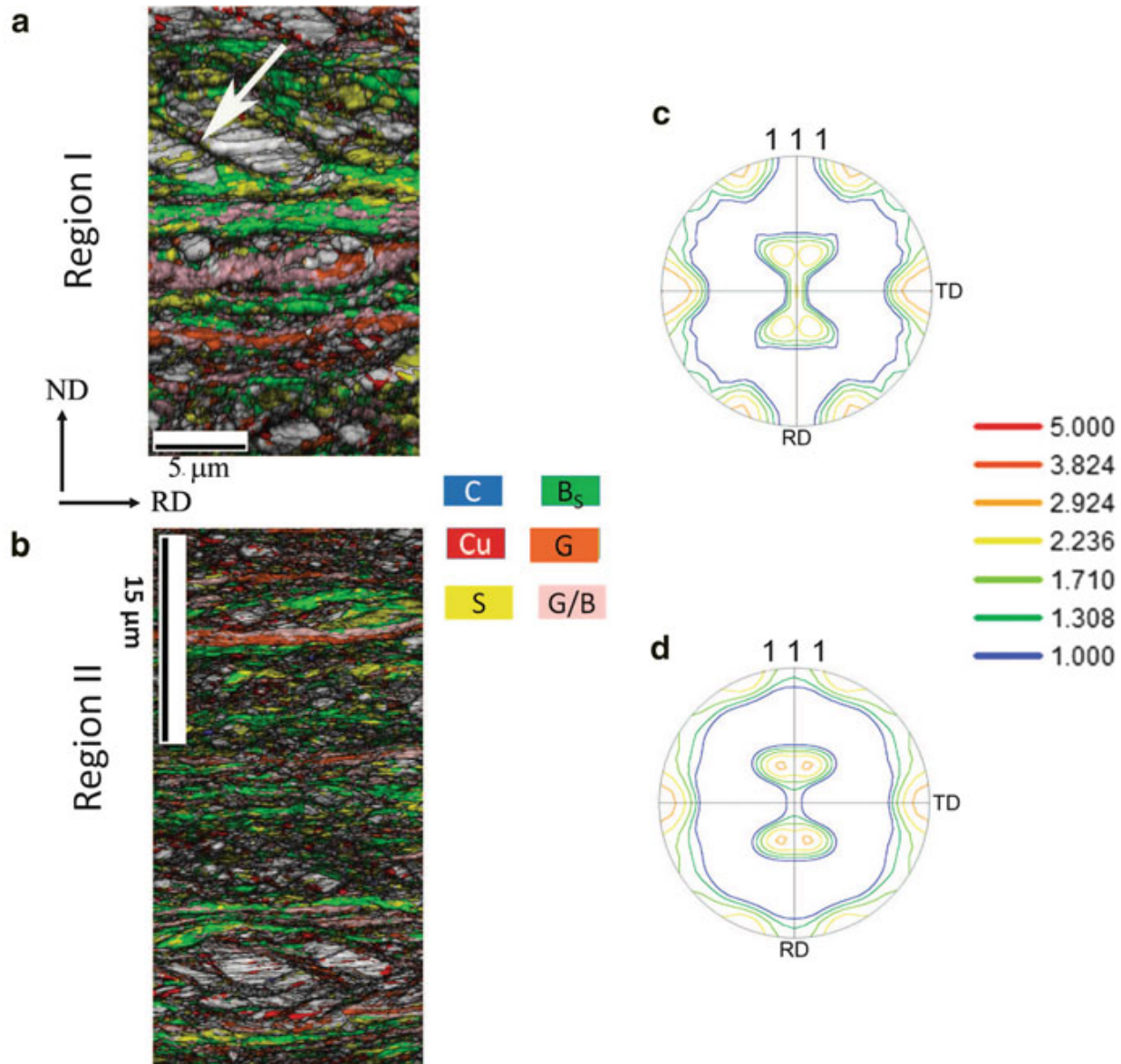


Fig. 3.21 (a) and (b) are IQ maps with overlaid orientations obtained from two different regions of 90 % cold-rolled NiCoFeCrMn; (c) and (d) are the corresponding (111) pole figures [76]

NiCoFeCrMn alloy has very fine network structure in which substructures with deformed subgrains and nanograins exist.

4. Texture of FCC NiCoFeCrMn alloy

Figure 3.21 shows the cross-sectional microstructure and texture of the NiCoFeCrMn after 90 % cold-rolling [76]. Figure 3.21a, b shows the EBSD (electron backscatter diffraction) image quality (IQ) maps overlaid with the typical FCC rolling texture components while Fig. 3.21c, d shows the (111) pole figures for two different regions, respectively. The IQ maps show submicron-cell structure. Thin shear band (marked by the arrow) inclined to the rolling direction (RD) about $\sim 25^\circ$ could be observed in region I. The HAGB (high-angle grain boundary) fractions in the two regions are similar. The orientation maps show strong presence of the brass ($\{110\} <112>$; designated as B_S and highlighted in green), S ($\{123\} <634>$; highlighted in yellow), and Goss ($\{110\} <001>$; designated as G and

highlighted in orange) components but very little presence of the copper orientation ($\{112\} <111>$; designated as Cu and highlighted in red). The appearance of the (111) pole figures (Fig. 3.21c, d) clearly reveals the development of a predominantly B_S texture after 90 % cold-rolling. The volume fractions of the different texture components obtained from the two regions are very similar, which indicate that the microtexture in the HEA following heavy deformation is reasonably homogeneous brass texture. Besides the volume fraction of random components is 42 %, and that of brass component is the largest, around 22 %, among the rest components.

3.4.7 Grain Boundaries

1. Lattice distortion and local rearrangement effect on grain boundary energy

Grain boundaries are the interface between adjacent grains with different orientations. There are low-angle boundaries constructed with dislocation arrays, high-angle boundaries with disordered structure along with it, and coincident boundaries at specific misorientation angles. They all have interface energy because the energy level is higher than that of the matrix. Similar to stacking fault discussed in Sect. 3.4.6, the effective boundary energy of all kinds of grain boundary could be lowered by the segregation layer of solute atoms along boundaries and by the higher energy level of the distorted matrix as compared with the pure matrix. This means grain boundaries in HEAs are smaller in boundary energy and thus become more stable and difficult to migrate than that in conventional alloys during annealing. Furthermore, the driving force for grain coarsening is also lower in HEAs. All these are beneficial to have more stable grain structure at high temperatures. To understand the distortion energy effect on grain boundary energy, an extreme case of distorted matrix, that is, amorphous structure, could be used as an example. As high-angle boundaries except those specific orientations could be regarded as disordered interface layer in the matrix, any boundary line in amorphous structure would be completely disordered in atomic configuration and equivalent to other disordered structure besides boundary line. Thus, no boundary energy of the boundary line could exist. This is why amorphous structure has no grain boundaries.

2. Factors affecting grain and particle coarsening in HEAs

Consider a metal with an average grain size D and assume the polyhedral grains to be spherical for simplifying the calculation. Then for one unit volume, the total grain boundary area is

$$A_g = (1/2)D^2\pi(1/(D^3\pi/6)) = 3/D. \quad (3.18)$$

Thus, the total grain boundary energy per unit volume is

$$U_g = 3\gamma/D. \quad (3.19)$$

Assume grains grow with an incremental size dD , the loss of U_g will be

$$dU_g = (3\gamma/D^2)dD. \quad (3.20)$$

Assume the virtual driving force on unit grain boundary area is F_g , then the work done by driving force is equal to the loss of U_g :

$$(3/D) F_g dD/2 = (3\gamma/D^2)dD. \quad (3.21)$$

This gives

$$F_g = 2\gamma/D. \quad (3.22)$$

Since this derivation is only based on grain size and boundary energy, the result is equally applied to single-phase HEAs. It implies that driving force of grain growth is proportional to grain boundary energy and inversely proportional to grain size.

In reality, grain growth concerns with boundary migration. Assuming the mobility is M_g and grain growth rate is ν_g , the phenomenological equation becomes

$$\nu_g = M_g F_g. \quad (3.23)$$

The mobility of boundary is determined by the successful jumping rate of atoms across the boundary which has an energy barrier to overcome and thus lower energy barrier and higher temperature would result in higher mobility [61]. Besides these two factors in affecting mobility and growth rate, other structural factors solute segregation and precipitates along grain boundary also drag the boundary directly. The drag force F_d will cancel a portion of driving force and the above equation becomes

$$\nu_g = M_g (F_g - F_d). \quad (3.24)$$

Because driving force is inversely proportional to grain size, it is apparent that a stable grain size is attained at the treating temperature when driving force is equal to drag force. This also implies smaller grain boundary energy and larger drag force would get a smaller grain size. It is well known that higher temperature could eliminate the segregation and second phase along boundaries (except oxides or similar stable phases) and might lead to abnormal grain growth. All these phenomena and phenomenological relations also hold true for single-phase HEAs.

However, there is something different between conventional matrix and the whole-solute matrix in HEAs. First, the grain boundary energy is inherently low

in HEAs as discussed above. This would reduce the driving force and thus lower the growth rate. Second, the successful jumps across grain boundary would be more difficult in HEAs since many kinds of component are involved and need to cooperate to make the same composition of adjacent grains. This in turn lowers the mobility of boundary. Third, segregation along grain boundary is easy in HEAs since grain boundary has relatively higher diffusion rate than grain interiors and segregation to lower grain boundary energy could be obtained by atomic-scale rearrangement of solutes along grain boundaries, which might be accomplished even at room temperature within a suitable aging time. As a result, drag force is easy to be attained during grain growth and retard grain growth. In brief, the grain growth is effectively slower than conventional alloys with similar melting points. Several researches also reported such an observation on a typical FCC CoCrFeMnNi HEA [33, 76]. Liu et al. found the growth kinetics could be described by a power law of 3 (see Fig. 3.22), suggesting that grain boundary motion is controlled by a solute-drag mechanism. The activation energy for growth was about $321.7 \text{ kJ mol}^{-1}$ which is close to the highest activation energy, $317.5 \text{ kJ mol}^{-1}$ of Ni among the five elements as described in Sect. 3.2.3 [8]. This demonstrates that the grain boundary migration during grain growth is rate-controlled by the diffusion of slowest Ni atoms through lattice diffusion, instead of grain boundary diffusion as seen for conventional alloys. This is very particular in consideration of the smaller activation energy of AISI 304LN stainless steels, which is only about 150 kJ mol^{-1} [33].

In binary alloys, if an impurity has small solubility in the matrix, the relative segregation (or enrichment ratio) to grain boundary is large and causes slow grain growth rate. If an impurity has large solubility, the inhibiting effect on grain growth becomes small at the same content due to lesser segregation [61]. However, this phenomenon is not applied to HEAs with the whole-solute matrix, since grain boundaries in HEAs already have many different components to rearrange the best segregation to lower overall free energy. The rearrangement is mainly confined in the grain boundary layer with a typical width about 0.5 nm. That means the average composition in this layer would be similar to that in the grain interiors. For the case with minor impurity and alloying elements, the observation in binary alloy mentioned above could be applied if the whole-solute matrix is regarded as a pseudo-unary matrix. The minor elements having low solubility in the pseudo-unary matrix would segregate a large portion to enrich grain boundaries. But, they might bring brittleness to HEAs and need our precaution.

Phase boundary is the interface between two phases. In equilibrium, chemical potential of each component in both phases and their phase boundary are equal. But, the free energy level of both phases could be different with each other. Thus, the phase boundary energy could be regarded as the energy difference between the energy level of phase boundary and the arithmetic average of the energy levels of both phases. Similarly, lattice distortion in both phases raises their energy level and also might lower the phase boundary energy under no distortion effect. This would also affect the particle coarsening or phase coarsening in two-phase alloys.

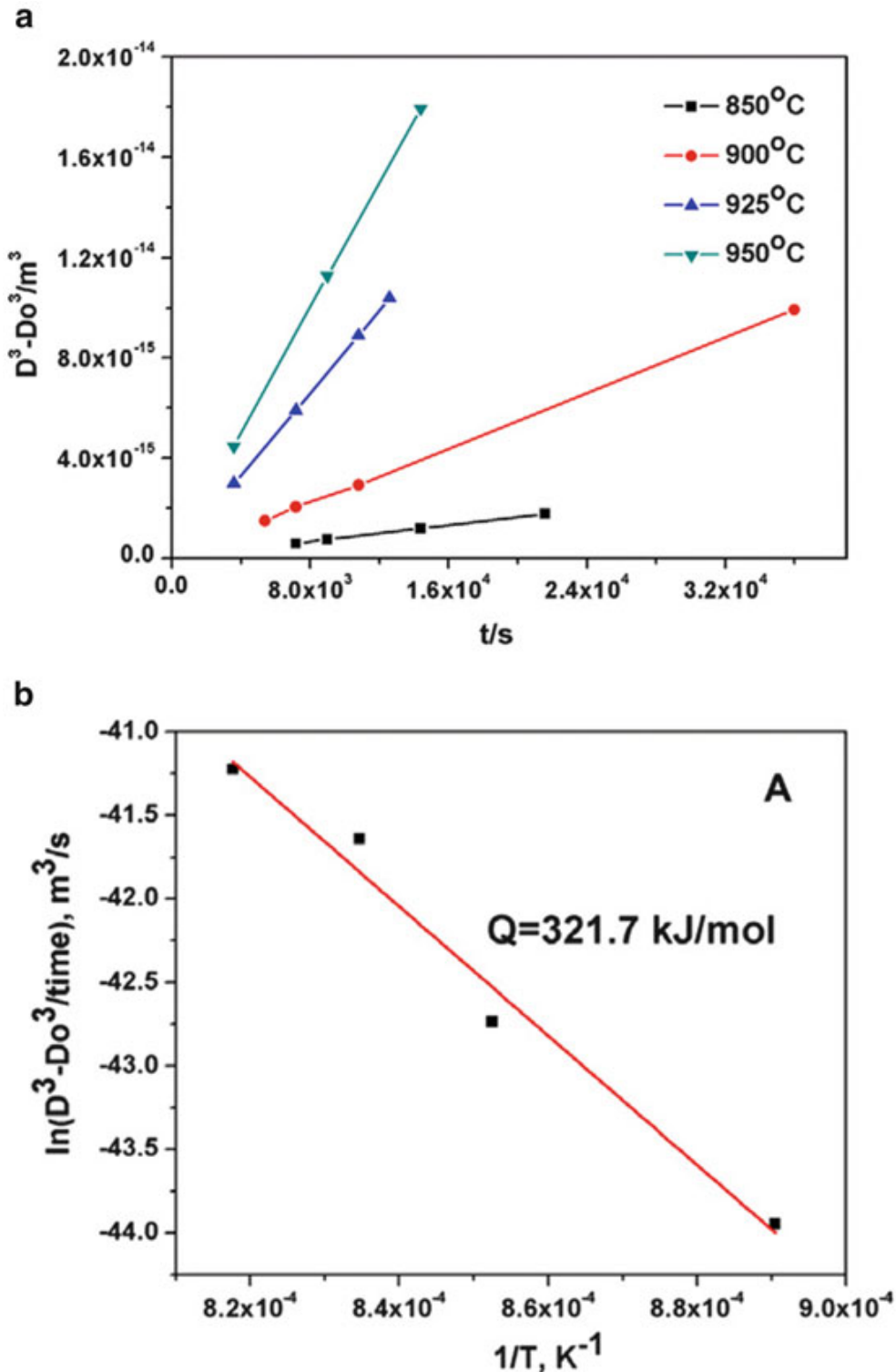


Fig. 3.22 (a) Grain size as a function of the annealing time for the CoCrFeMnNi alloy specimens at different temperatures; a linear relation between the cube of the grain size and time is observed. (b) Grain-growth constant, C , as a function of the reciprocal of absolute temperature. Activation energy is calculated [33]

3.5 Basic Mechanism of Sluggish Diffusion

For a multi-principal-element solid solution, the mechanism of substitutional diffusion is still vacancy mechanism except that the diffusion is sluggish and the kinetic process is lower due to larger activation energy of diffusion. This sluggish diffusion effect has been confirmed with the diffusion couple experiment on

Fig. 3.23 Illustration of an atom-vacancy pair ($A-V$) and their neighboring atoms in an FCC lattice: A_{1-7} , atoms adjacent to A only, type 1; V_{1-7} , atoms adjacent to V only, type 2; and S_{1-4} , atoms adjacent to both A and V , type 3 [8]

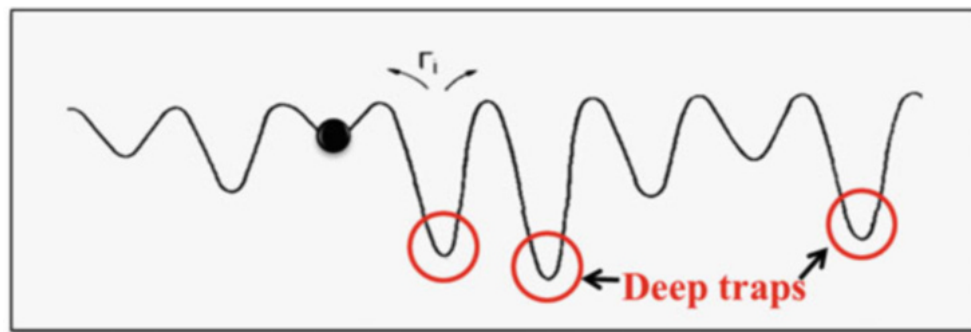
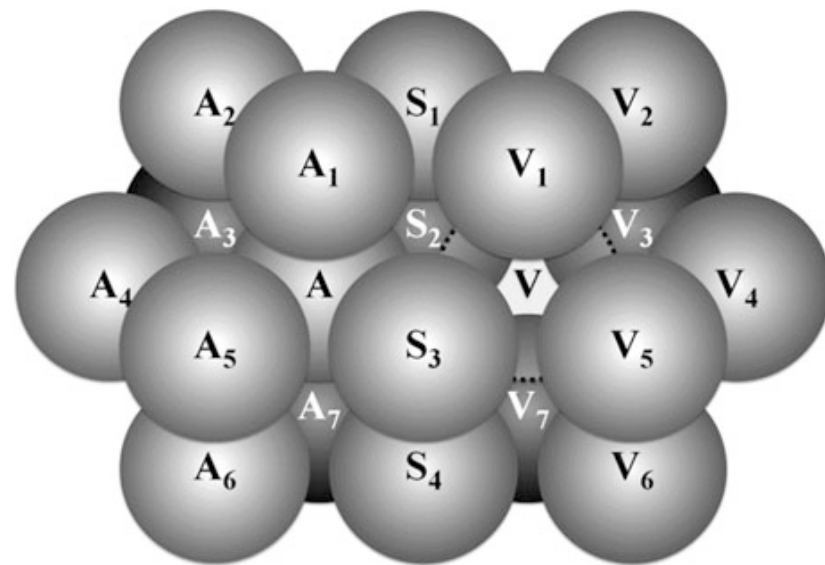


Fig. 3.24 Schematic diagram showing the fluctuation of lattice potential energy along the diffusion path for an atom in the lattice. *Deep traps* are indicated

Co-Cr-Fe-Mn-Ni HEA system as discussed in Sect. 3.2.3 [8]. In this section, the sluggish diffusion was explained based on the distorted lattice. The distorted multi-principal-element lattice would have fluctuated lattice potential energy (LPE) for the migration of an atom from one site to site because each site is surrounded by different kinds of atoms and has different types of bonds. Consider an atom-vacancy pair ($A-V$) and their nearest-neighboring atoms in an FCC lattice, as shown in Fig. 3.23. The nearest-neighboring atoms of the $A-V$ pair can be divided into three types. Type-1 (T1) atoms are adjacent to A (A_{1-7}), type-2 (T2) atoms are adjacent to V (V_{1-7}), and type-3 (T3) atoms are adjacent to both A and V (S_{1-4}). When atom A exchanges with vacancy V , four T3 atoms remain to be the neighbors of A , but the seven $A - T1$ bonds are broken and seven new $A - T2$ bonds are established instead. Therefore, when an atom migrates, the change in LPE comes from the interaction energy difference between $A - T1$ bonds and $A - T2$ bonds. As a result, this fluctuated LPE would let the diffusion of atoms be more difficult than that in the lattice with uniform LPE, as shown in Fig. 3.24. This is analogue to the driving of a car along a rugged road. The barrier is higher and the speed is lower than those along a smooth road. As for the self-diffusion of vacancies, the activation energy required is also lower than that in undistorted lattice with uniform lattice potential energy. By the same thinking, the interstitial diffusion of small atoms

would be slowed down and its activation energy is higher in the distorted lattice although vacancy aid is not required.

High diffusion paths along dislocations and grain boundaries also exist in the whole-solute matrix in HEAs. In conventional alloy matrix, the diffusivity along dislocation, D_p , and that along high-angle grain boundaries, D_g , have similar order in magnitude because high-angle grain boundaries could be regarded as an array of dislocations with very small spacing between two neighboring dislocations. But both diffusivities are larger than those through defect-free lattice, D_l , at any temperature. For example, at 500 °C, D_p/D_l and D_g/D_l in silver are 2×10^6 and at 1×10^6 , respectively [77, 78]. Moreover, its activation energy of diffusion in grain boundary is about 0.45 of that in the lattice. The increased diffusivity could be explained with the increased degree of opening in the defect structure. That means the jumping frequency of an atom in these defect structures is much higher than that of an atom in the lattice. Similar trend of diffusivity for lattice, dislocation, and grain boundary holds for the whole-solute matrix in HEAs although atom diffusion in such a distorted lattice is more difficult than that in undistorted lattice.

However, all the above discussions still need to be justified by more researches on different-structured HEAs, such as BCC and HCP. More rigorous mechanisms are also required. In addition, isotopic elements should be also incorporated in the diffusion couples for non-ideal solutions in order to get diffusion coefficients of each component and assist the understanding of mechanisms.

3.6 Plastic Deformation in HEAs

All basic processes for plastic deformation such as dislocation slip, twinning, and grain boundary sliding in conventional alloys are also seen in HEAs but their detailed mechanisms might be significantly different between conventional alloys and HEAs. This is at least because the whole-solute matrices in HEAs are distorted at all lattice points which directly affect the behaviors of plastic deformation.

3.6.1 Yielding and Serration Phenomenon

As discussed in Sect. 3.4.5, there are two factors in lowering dislocation energy: easy relaxation effect to lower the overall strain energy by forming atmosphere and distorted lattice effect to lower the dislocation energy by increasing the energy level of lattice. Compared with the undistorted lattice, dislocations require extra stress to overcome atmospheres and to overcome the whole-solute obstacles even after releasing from atmospheres. This lattice distortion effect is the structural factor contributing to solution hardening, in addition to other factors relating to excess chemical bonding, shear modulus difference, short-range order, and dipole interaction. If temperature is sufficiently low in inhibiting pipe diffusion, atmosphere

could not automatically form around dislocations through aging. The extra stress to overcome atmosphere is absent. As diffusion increases with increasing temperature, the relaxation effect to form atmosphere becomes easier because of abundant solutes everywhere. This aging might increase the yield strength by an extra stress for dislocations releasing from atmospheres at room temperature. This might be used to explain the small load drops after yielding observed at 77 K, 293 K, and 473 K (not at higher temperatures) for fine-grained FCC CoCrFeMnNi alloy which received a recrystallization treatment at 1073 K for 1 h for obtaining a grain size of 4.4 μm [79]. In addition, the relaxation effect at higher temperatures could result in serration phenomena (dynamic strain aging) during deformation. However, at much higher temperatures, thermal vibration becomes too large to make successful structural relaxation, and serration behavior would disappear. This also explains why CoCrFeMnNi alloy displayed serration behavior on stress-strain curves at 673 K for three grain sizes: 4.4, 50, and 155 μm [79]. So, the relaxation behavior of HEAs is different from that in conventional alloys in which solutes are limited in concentration and require long-distance diffusion to release the strain energy and pin the dislocations.

3.6.2 Effect of Low Stacking Fault Energy on Ductility and Toughness

In fact, a perfect dislocation would tend to decompose itself into two Shockley partial dislocations with wide stacking fault in FCC HEA solid solution which generally has low stacking fault energy. As discussed in Sect. 3.4.6, this feature causes the cross-slip and double cross-slip of screw dislocations to be more difficult and tend to form a substructure characterized by banded, linear arrays of dislocations. This is because each double cross-slip could form a Frank-Reed source which in turn generates new dislocation loops in the slip plane. In contrast, high stacking fault metals tend to exhibit tangled dislocations and dislocation cell structure after deformation. Thus, deformation in HEA solid solution tends to be more uniform with more planar slips. This tendency gives an advantage in enhancing ductility because stress concentration on interface between the matrix and inclusions or on grain boundaries becomes smaller without coarse slip band impingement. In addition, less cross-slip gives smaller dynamic recovery and strain hardening. Both effects could be beneficial for the good ductility of FCC HEAs.

The inherent low stacking fault energy of FCC HEAs also enhances the nanotwinning deformation mechanism which benefits strain hardening rate and overall ductility. Basically, low SFE in FCC means that coherent twin boundary energy (one-half of SFE because a coherent twin boundary, e.g., C in ABCABCACBA... stacking sequence, is similar to one-half of an intrinsic stacking fault, ABCABCBCABC... bounded by Shockley partial dislocations) and thus the critical stress for nucleation and growth are also low. On the other

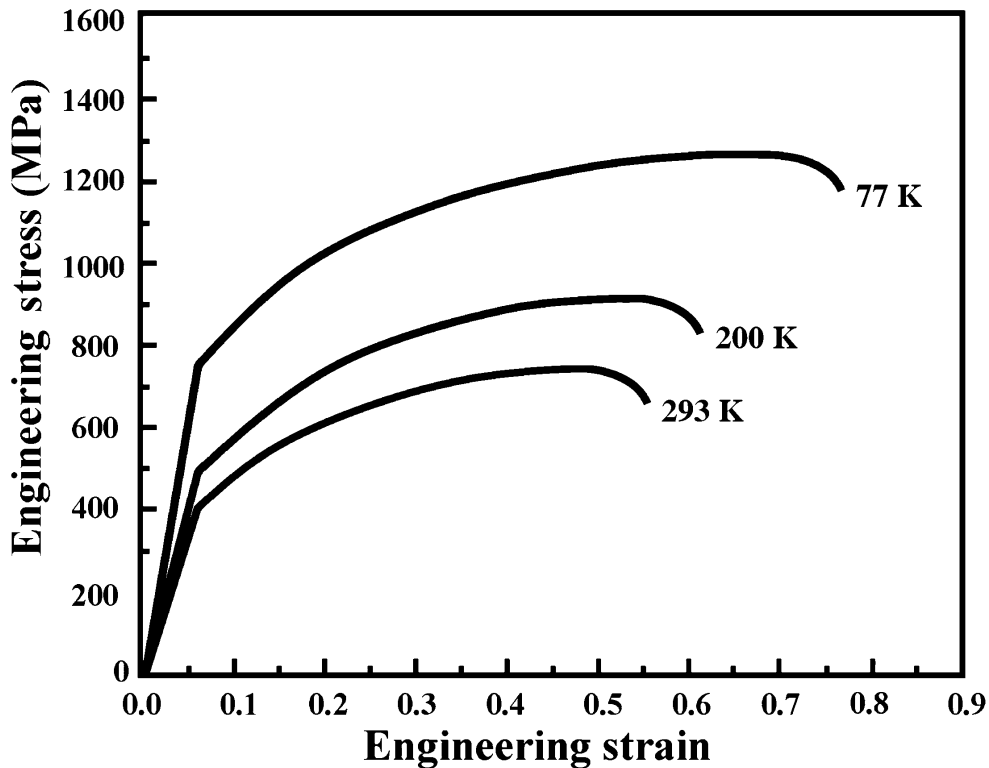


Fig. 3.25 Typical stress-strain curves obtained by tensile testing at 77, 200, and 293 K. Yield strength, ultimate tensile strength, and ductility (strain to failure) all increase with decreasing temperature [80]

hand, the yield stress of FCC HEAs is increased by solution hardening and other strengthening mechanism, which make the movement of dislocation more difficult. As a result, the formation of deformation twinning becomes easier in FCC HEA solid solution under the competition between the two critical stresses required for twinning and slip deformations, respectively. By this competition, both low temperatures and high strain rates will enhance the nanotwinning deformation since the yield strength increases faster than critical stress for twinning. Twinning during deformation is very important to induce higher plasticity. Twin-induced plasticity steels (TWIP steels) are a famous example in which twinning causes high strain hardening rate and lets the onset of necking delayed to occur at higher strain according to Considere's criterion. Therefore, FCC HEA solid solution generally has an excellent combination of strength and toughness. Otto et al. [79] observed the temperature effect on the mechanical properties of FCC CoCrFeMnNi HEA and found that yield strength, strain hardening, and ductility are increased as temperature decreases from 293 to 77 K. Moreover, Gludovatz et al. reported similar results as shown in Fig. 3.25 [80]. They also showed that CoCrFeMnNi HEA displays remarkable fracture toughness properties at tensile strengths of 730–1280 GPa, which exceed $200 \text{ MPa} \cdot \text{m}^{1/2}$ at crack initiation and rise to $>300 \text{ MPa} \cdot \text{m}^{1/2}$ for stable crack growth at cryogenic temperatures down to 77 K. The alloy has toughness levels that are comparable to the very best cryogenic steels, specifically certain austenitic stainless steels and high-Ni steels. Wu et al. reported the temperature dependence of the mechanical properties of various equiatomic alloys which are subsets of the CoCrFeMnNi HEA [81]. The UTS and uniform elongation to

fracture of all the equiatomic alloys such as CoCrNi, CoCrMnNi, and CoCrFeNi also increase with decreasing temperature, with the largest increase occurring between 77 and 293 K. To sum up, this phenomenon was attributed to a transition from planar-slip dislocation activity at room temperature to deformation by mechanical nanotwinning with decreasing temperature, which results in continuous steady strain hardening at cryogenic temperatures.

Easy twinning has another advantage in producing abundant twins which will effectively reduce the grain size and increase the grain-size strengthening approximately at below recrystallization temperatures. Also, fine grain size could enhance superplasticity at above recrystallization temperatures by grain boundary sliding. Thus, low stacking fault energy of FCC HEAs is very beneficial for microstructure refining and property enhancement.

3.6.3 Deformation Mechanisms in BCC or HCP HEAs

The last two sections concern with the deformation behaviors in FCC HEAs. As for the dislocation behavior in BCC HEAs, the study is quite lack. This is because most BCC HEAs have high strength but brittle. The dislocation structure has been found in refractory BCC HEA HfNbTaTiZr in the as-cast state, as shown in Fig. 3.26 [82]. There is the presence of numerous dislocations, the majority of which are arranged in subgrain boundaries. In addition, pileups are observed and some dislocation reactions have led to the formation of hexagonal networks. This indicates that dislocations exist in the as-cast alloys, which suggests that plastic deformation could assist by dislocation movement. Senkov et al. reported that refractory BCC HEA HfNbTaTiZr has compressive fracture strain higher than 50 %. The microstructure observation on the cross section of compression-tested specimen revealed deformation twins and cracking along some grain boundaries as shown in Fig. 3.27 [9]. This further demonstrates that twinning is also a possible deformation mechanism. Although lesser investigations could be found for HCP HEAs, it is believed that basic deformation mechanisms are similar to conventional HCP alloys except suitable modifications mentioned above.

3.6.4 Strengthening Mechanisms in HEAs

Strengthening mechanisms in physical metallurgy include solution hardening, strain hardening, grain-size strengthening, precipitation hardening, dispersion hardening, martensitic strengthening, and composite strengthening. Except martensitic strengthening, they have been also found in the literature on HEAs and HEA-related composites.

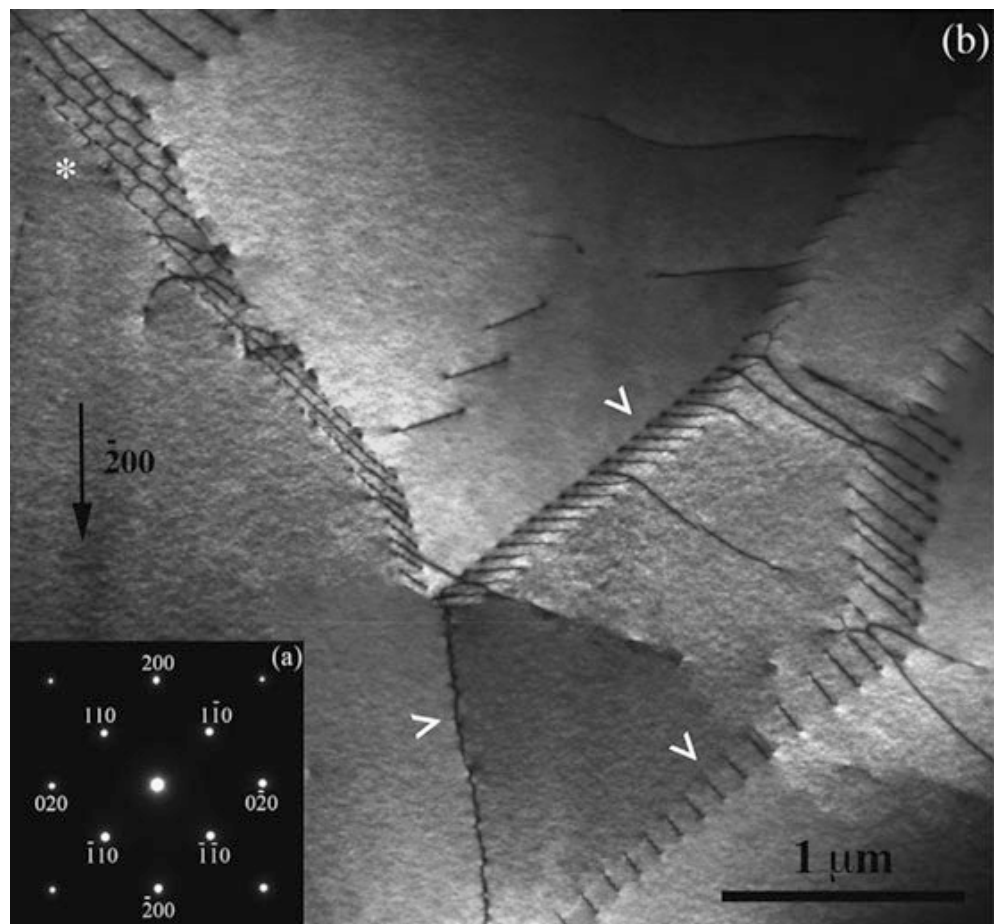
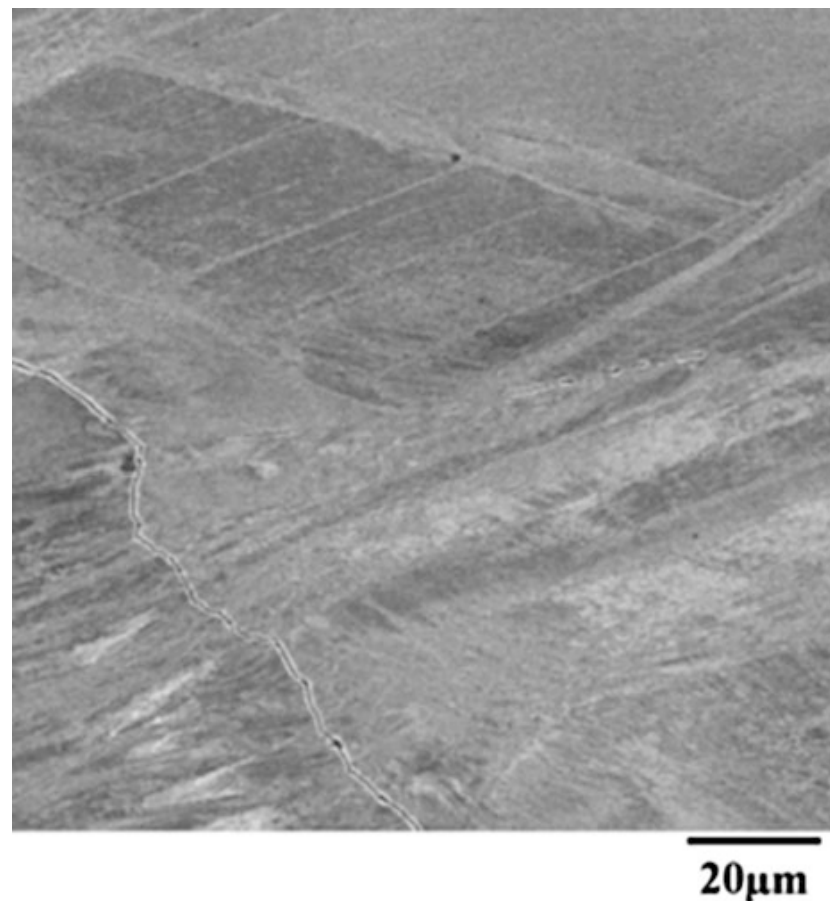


Fig. 3.26 TEM observations on refractory BCC HfNbTaTiZr HEA: (a) selected area diffraction (inset) indicating the [001] zone-axis pattern; (b) bright-field micrograph of the as-cast microstructure. Symbols highlight the presence of subgrain boundaries and hexagonal dislocation network [82]

Fig. 3.27 SEM backscatter electron image of a longitudinal cross section of the HIP'd $\text{Ta}_{20}\text{Nb}_{20}\text{Hf}_{20}\text{Zr}_{20}\text{Ti}_{20}$ alloy after compression deformation at room temperature [9]



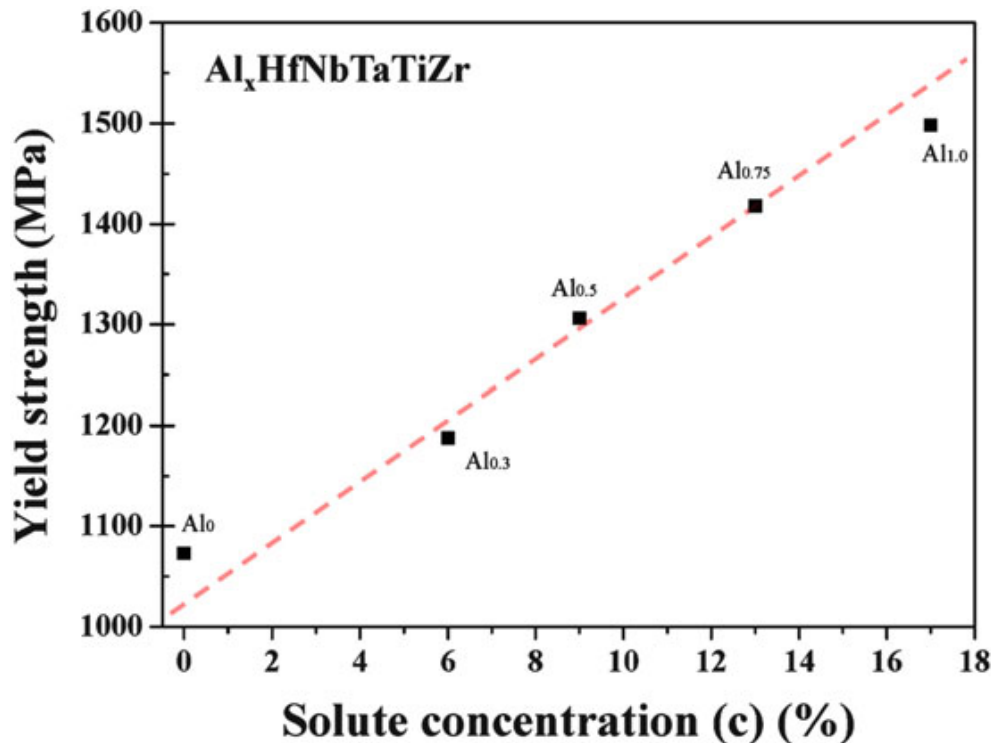


Fig. 3.28 Effects of solute concentration of Al on the yield strength of the Al_xHfNbTaTiZr HEAs [83]

1. Solution hardening

For solution hardening, the whole-solute matrix inherently has a very large solution hardening effect when real strength (or hardness) and rule-of-mixture strength (or hardness) are compared. The ratio could be as high as 3–4 for HfNbTaTiZr [9] and NbMoTaW and VNbMoTaW [23]. This is surprising because such high strength could be attained only by solution hardening. However, the ratio is about 1–2 for FCC HEAs. This might be related to the fact that the distortion in FCC HEA is smaller than that in BCC HEA as discussed in Sect. 3.2.2. In the strengthening through the addition of one component to the whole-solute matrix, Lin et al. studied a series of refractory Al_{0–1}HfNbTaTiZr HEA and found the linear relation, $\sigma = 1031 + 26.1 c$ (MPa), between yield strength and atomic percentage, c , of Al, as shown in Fig. 3.28 [83]. They proposed that the strengthening effect of a certain element in a single-phase HEA alloy can be explained based on quasi-binary alloy concept. The fact of linearity is thus originated from the strengthening contribution per Al atom. Strong bonding factor in combination with atomic-size-difference factor (or lattice distortion) is the main contributor of Al addition to strengthening. However, a number of metals follow the less-effective $c^{1/2}$ dependence of solution hardening with substitutional solutes and interstitial ones [84]. Although exponent from 1/3 to 1 was also observed in conventional metals, theoretical models for HEAs are required to be established.

2. Grain-size strengthening

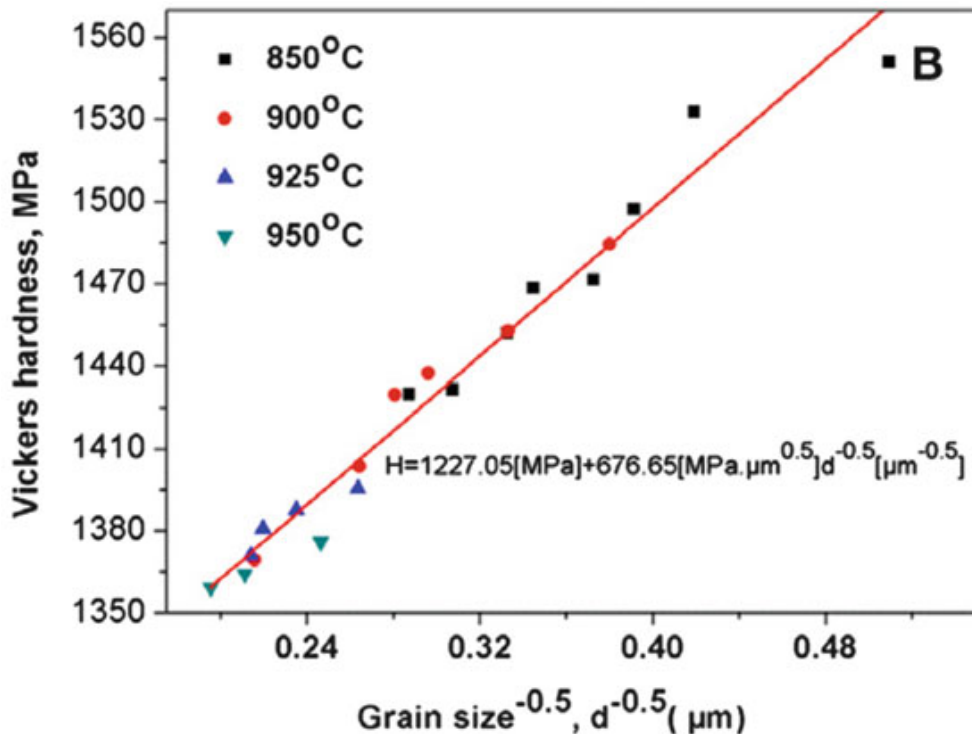


Fig. 3.29 Hardness as a function of grain size in the CoCrFeMnNi alloy [33]

In grain-size strengthening, Liu et al. systematically investigated the grain growth behavior of FCC CoCrFeMnNi equiatomic HEA by cold-rolling and subsequently annealing at different temperatures [33]. One can see from Fig. 3.29 [33] that Hall-Petch relation also holds for this alloy. But it is noted that the hardening coefficient, $677 \text{ MPa } \mu\text{m}^{-0.5}$, is quite large since the upper bound of hardening coefficient in BCC, FCC, and HCP metals is about $600 \text{ MPa } \mu\text{m}^{-0.5}$. This suggests that grain boundary hardening efficiency in the current CoCrFeMnNi alloy is much higher. The reason might relate to the large strain hardening of this alloy [80]. Furthermore, $\text{Al}_{0.2}\text{CoCrFeMnNi}$ alloy has even larger hardening coefficient, $2199 \text{ MPa } \mu\text{m}^{-0.5}$, because addition of Al provides larger lattice distortion and stronger bonding and thus larger work hardening [85]. This might be explained with Li's theory. He explained that grain-size strengthening in fact arises from the strain hardening of the near-grain boundary regions due to the dislocation pumping from grain boundary ledges under the elastic incompatibility stresses between adjacent grains before macroyielding [86]. Therefore, larger strain hardening such as FCC HEAs would imply larger hardening coefficient.

3. Strain hardening

Strain hardening is commonly observed in the deformation of HEAs. In FCC HEAs, slip and nanotwinning could be the main mechanisms because their stacking fault energies are effectively lower. Higher temperature and lower strain rate enhance the deformation by dislocation motion whereas lower temperature such as at subzero and higher strain rate such as forging and rolling, nanotwins are more pronounced in the deformed structure. It can be observed that both mechanisms can give high strain hardening. In the slip mechanism, low stacking fault energy makes

dislocation cross-slip more difficult and thus delay dynamic recovery to cause softening. In the nanotwinning mechanism, grain-size strengthening due to the formation of nanotwins is involved during deformation. Both factors increase large strain hardening and thus result in enhanced ductility based on Considere's criterion [79–81]. In BCC HEAs, twinning is less found during deformation suggesting its formation is difficult as compared with slip. Strain hardening is generally smaller than that of FCC HEAs [9]. This could be attributable to three factors: (1) high strength due to large solution hardening, (2) easy cross-slip to cause dynamic recovery, and (3) difficult twinning. The first factor relates to large lattice distortion which is similar to severe cold-work structure. The second and third factors relate to the lack of partial dislocations and many slip systems for cross-slip. Cryo-rolling might enhance twinning because the stress for dislocation glide is significantly increased. However, more researches for taking more data (including HCP HEAs and other structures) and building rigorous theories are required.

4. Precipitation, dispersion, and composite hardenings

Precipitation hardening is often observed in HEAs. To the first approximation, conventional theories on these are also applicable to HEAs. Precipitate shape, size, coherency, degree of ordering, shear modulus, and volume fraction are factors affecting the strengthening [86]. But, in HEAs, multi-principal-element matrix and multi-principal-element precipitates might be stronger than conventional ones and have higher strength level. Interface energy and strain field between precipitates and the matrix should be further considered. Dispersion hardening is obtained by adding hard particles to the alloy in the molten liquid, to the alloy by powder metallurgy, or to the alloy by internal oxidation [86]. Their strengthening mechanism is essentially similar to precipitation hardening for HEAs. Composite strengthening is obtained by in situ phase formation such as eutectic and eutectoid structure or by extrinsically adding large amount of second phases or reinforcements. Finer lamellae, fine particles, and fine fibers would provide higher strength. HEA-related hard metals such as sintered carbides and cermets with HEA binders have been reported [87, 88]. Wettability, interface bonding, morphology, grain size, distribution, volume fraction, and binder strength are needed to be considered. It is noted that HEA binders might change all these factors and thus properties. Understanding of the mechanisms is very important for improving properties.

3.7 Creep and Creep Mechanisms in HEAs

3.7.1 *Creep Behavior and Extrapolation Method to Predict Creep*

Creep deformation is a very important aspect for the materials used at high temperatures [84, 89–91]. A number of high-temperature failures are due to creep

or creep plus fatigue since failures and insufficient yield strength and tensile strength could be observed instantly or in the early stage failure. A material creep at high temperatures means its dimension changes with time under a load. Creep test at constant load could give a creep curve, i.e., strain (ε) as a function of time (t). It typically displays three distinct stages after the initial rapid elongation: I (primary), II (secondary), and III (tertiary). The slope, $d\varepsilon/dt$, of the curve is creep rate. In primary stage, the creep rate decreases with time; in secondary stage, the creep rate changes little and remains constant; and in tertiary stage, the creep rate increases rapidly with time until fracture occurs. In general, higher load will result in higher creep rate and shorten the time to rupture. In the intermediate stress range ($10^{-4} < \sigma/G < 10^{-2}$; σ is applied stress and G is shear modulus), constant creep rate in stage II could be described by power law:

$$d\varepsilon/dt = A \sigma^n e^{-Qc/RT} \quad (3.25)$$

where A and n are constants depending on creep mechanism and Qc the activation energy for creep. It should be noted that Qc is approximately equal to the activation energy for self-diffusion for pure metals and solid-solution alloys if $T > 0.5 T_m$.

Usually, an industrial equipment is designed to have a reasonable life for customers. For jet turbine, power plant turbine, and nuclear reactors, the reasonable lives are 10,000 h (~1 year), 100,000 h (~10 years), and 350,000 h (~40 years), respectively. To avoid the lengthy tests, the extrapolation methods have been developed. The Larson-Miller equation with the following form has been commonly accepted and used for the extrapolation:

$$T(\log t_r + C) = m, \quad (3.26)$$

where C is the Larson-Miller constant depending on the alloy, t_r is the time to failure, and m is the Larson-Miller parameter depending on stress. Thus, one can use the shorter rupture time obtained by creep testing at higher temperature to predict rupture time at lower temperatures under the same stress. It is noted that higher m would be better by giving longer rupture time under the same stress.

3.7.2 Creep Mechanisms

The creep deformation mechanisms have been well-established and can be approximately grouped into four kinds [84, 89–91]:

1. Diffusion creep: $\sigma/G < 10^{-4}$

This involves a flow of vacancies and atoms through the material. Two mechanisms are possible. Nabarro and Herring mechanism states that the vacancies move in such a way to produce an increase in length under the direction of applied stress. The grain boundaries could act as sources or sinks. Coble proposed another

mechanism which is based on the diffusion along grain boundaries. The activation energies of both creep mechanisms are the self-diffusion activation energy in lattice and grain boundary, respectively. Coble mechanism is predominant for lower temperatures and small grain size where grain boundary is more important than bulk diffusion. Both mechanisms could be operated in parallel and creep rate is the summation of both creeps. The summation equation is [84]

$$d\varepsilon/dt = A_{\text{NH}}(D_L/d^2)(\sigma\Omega/kT) + A_C(D_{\text{GB}}/\delta/d^3)(\sigma\Omega/kT) \quad (3.27)$$

where D_L and D_{GB} are diffusion coefficients of lattice and grain boundary, respectively. Ω is the atomic volume, d is grain size, and δ is grain boundary thickness. Thus, Coble creep is more sensitive to grain size.

2. Dislocation creep: $10^{-4} < \sigma/G < 10^{-2}$

This also involves vacancy diffusion which assists dislocations to overcome obstacles by climb during their glide, called climb-plus-glide mechanism. Since the rate of climb is determined by the rate at which the vacancies arrive at (as vacancy sinks) or leave (as vacancy sources) the dislocation, higher rate of climb process enhanced by larger stress and higher temperature would enhance dislocation climb and glide and cause higher creep rate. The creep rate in this stage is described by power law as mentioned above. For pure metals in which dislocation climb is easier, glide contributes most of creep strain and becomes the rate-controlling process; n is commonly about 5 and can be derived as in the following formula based on the balance between softening mode and hardening mode [91]:

$$d\varepsilon/dt = A'(\gamma_{\text{SF}}/Gb)^3(\sigma/G)^5 e^{-Q_c/RT} \quad (3.28)$$

where A' is a constant and γ_{SF} is the stacking fault energy (SFE). This mechanism is also evidenced by the formation of dislocation cell substructure observed by TEM and same cell size remains during stage II creep but inversely proportional to applied stress.

Sherby and Burke further divided solid-solution alloys into two classes with different mechanisms [89, 91]. In class I alloys, dislocation glide is controlled by the drag of solutes and n is about 3, such as in Ni-Au binary system with larger atomic size difference. In class II alloys with small atomic size difference such as Ni-Fe, Ni-Co, and Ni-Cr, the creep is controlled by dislocation climb as in pure metals; thus n is also about 5.

3. Dislocation glide: $\sigma/G > 10^{-2}$

At high stress, power law breaks down and dislocation climb is replaced by dislocation glide which does not involve diffusion. Thermally activated dislocation glide is the rate-controlling step. When a dislocation encounters the obstacles, thermal energy is required to overcome the obstacles with energy barrier U_0 . Applied stress could provide a work to reduce the thermal energy required to

overcome the barriers. Thus larger stress and higher temperature could increase such “dislocation glide” creep. This process occurs from low temperature to high temperature [84, 89, 90].

4. Grain boundary sliding

Grain boundary sliding occurs during the stage II to accommodate the grain shape change under creep strain. Smaller steady-state creep rate in stage II also has smaller grain boundary sliding. But, it becomes important in stage III with higher creep rate because it causes intergranular crack initiation and propagation. As grain boundary slides, diffusional mass flow is required to accommodate the incompatibility between grains. When this is not sufficient, voids at grain boundaries will form. However, single-crystal components do not have grain boundary sliding and have improved creep resistance [84, 89, 90].

3.7.3 Potential of HEAs to Have Improved Creep Resistance

Based on the above creep mechanisms, different factors could be considered to increase creep resistance and rupture life. Combining the positive factors would have superposition effect on creep resistance. Following factors are thus discussed to find the potential of HEAs to get improved creep resistance.

1. Sluggish diffusion factor

As mentioned above, for both diffusion and dislocation creeps, steady-state creep rate is directly related to the diffusion rate in the alloy. Activation energy for creep is essentially equal to that for diffusion. In this regard, sluggish diffusion in HEAs has the benefit to have a better resistance to creep. Similarly, grain boundary sliding is also inhibited because diffusion in the vicinity of grain boundaries to support the diffusion and dislocation creeps is sluggish. This leads to enhanced resistance to creep. In addition, the component having the slowest diffusion rate could become the rate-determining component in creep. This demonstrates the benefit from HEA composition which contains appreciable amounts of major elements. If the slowest component is added, its power to determine the creep rate would be significant. In refractory BCC-type HEAs which have a common melting point over 2000 °C, all these sluggish diffusion effects might compensate the higher diffusion rate in the open-packed structure of BCC matrix.

2. Low stacking fault energy factor

Solute addition has been found to lower the SFE such as Cu-Al bronze and Cu-Zn brass due to interactions between solutes and stacking fault. It is well known that low stacking fault energy of pure metals and solid-solution-strengthened alloys have low creep rate [91, 92]. This trend can be explained because low SFE causes the dislocation difficult to overcome obstacles by cross-slip. This makes the dislocation mainly use climb process to overcome the obstacles. Although the actual

model/mechanism is still not clear, this trend suggests that low stacking fault energy has the advantage in reducing creep rate. As FCC-HEAs have quite low stacking fault energy, they have the potential to have a better creep resistance.

3. Atomic size difference factor

In polycrystalline nickel, solid-solution strengthening has been found to increase the time to fracture under the same stress. In addition, larger atomic size difference gives larger creep resistance (higher stress at the same stage-II strain rate). Even larger atomic size difference could reduce stress component from five to three as mentioned above. Furthermore, higher content of solutes gives smaller creep rate [91]. Based on the same trend, it appears that multi-principal-element solid-solution phases in HEAs would be beneficial to the creep resistance because they essentially possess the whole-solute matrix and have solute-dislocation interaction everywhere.

4. Precipitate factor

In nickel alloys, γ' phase not only enhances high-temperature strength but also increases creep resistance [91]. Higher volume fraction of γ' phase could increase creep resistance. For example, the Nimonic 80A, 90, 105, and 115 alloys having γ' fractions of 0.17, 0.18, 0.32, and 0.62, respectively, also have improved creep resistance. The temperature of the last alloy for 1000 h creep life at 137 MPa is higher than the first by about 120 °C. In addition, lattice misfit between γ' phase and γ matrix and solvus temperature of γ' phase are important factors for creep resistance [91]. Small lattice misfit means less coarsening rate of γ' precipitates and higher solvus temperature means higher thermal stability of γ' phase at higher working temperature. As different solute elements have different partitions between γ' phase and γ matrix affecting lattice misfit, shear modulus, coherency, and stability, how to design high-entropy superalloys based on conventional superalloys is a good research topic to obtain improved properties.

5. Carbide and boride factors

Small addition of boron and carbon for forming boride and carbide particles could increase the resistance of grain boundary sliding and thus improve creep resistance. For example, Che and Knowles [91] tested an experimental second-generation superalloy in creep at 950 °C and 290 MPa; addition of 0.09 wt.%C and 0.01 wt.%B could improve the rupture life from 10 h to 100 h. This is due to small carbide $M_{23}C_6$ formed along grain boundaries. This method is also required for improving creep resistance of polycrystalline HEAs.

Up to 2015, direct data on creep properties of HEAs are lack in the literature. He et al. reported the steady-state flow behavior of CoCrFeMnNi HEA in strain-rate jump tension tests at temperatures ranging from 1023 to 1123 K ($\sim 0.65\text{--}0.7 T_m$) [93]. They used the power law Eq. 3.24 to fit flow behavior with stress and temperature shown in Fig. 3.30. Two regions, region I with a low stress exponent at the low strain rates (or stresses) and region II with a high stress exponent at the high strain rates (or stresses), are observed. The activation energies are 284 kJ/mol

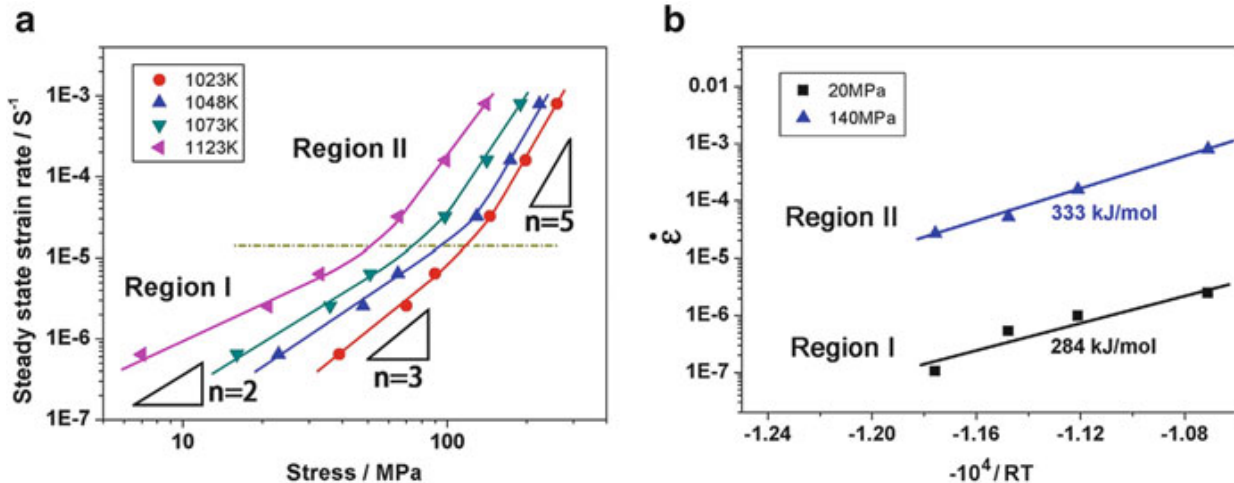


Fig. 3.30 (a) Steady-state strain rate as a function of the true stress on a double logarithmic plot shows apparently two deformation regions (marked as region I and region II) and (b) the steady-state strain rate vs. the inverse of temperature on an Arrhenius plot showing the apparent activation energy of ~ 280 kJ/mol for region I and ~ 330 kJ/mol for region II, respectively

in region I and 333 kJ/mol in region II. They emphasized that these values are comparable to the activation energies for lattice diffusion in the FeCoNiCrMn alloy [8], for example, Ni (317.5 kJ/mol), Cr (292.9 kJ/mol), and Mn (288.4 kJ/mol). The stress exponent about 5 in region II suggests that the dominant deformation process is dislocation climb. The activation energy around 330 kJ/mol can be rationalized by that (317.5 kJ/mol) of the slowest-diffusing species Ni which controls the rate process. On the other hand, the stress exponent about three in region I suggests that the mechanism is the drag of gliding dislocations. However, the lower activation energy, 284 kJ/mol, is difficult to rationalize by the slowest Ni. But when region I in Fig. 3.30 is rechecked, an activation energy same as region I might be expected. This again confirms that rate controlling is still the slowest Ni.

Besides, the measurement of hot hardness to see the softening resistance at high temperatures could provide an indicator to compare creep resistance between materials [94]. In addition, indentation creep test is also a way to compare the creep resistance [94–96]. Figure 3.31 shows the plots of hot hardness vs. temperature for Al_xCoCrFeNi cast alloys ($x = 0\text{--}1.8$) from room temperature to 1273 K [94]. In this alloy series, Al_{0–0.3} alloys form single FCC structure. Al_{0.5–0.9} alloys form FCC plus BCC mixture in which BCC phase further decomposes into modulated spinodal structure. Al_{0.9–1.8} alloys form complete spinodal structure [94, 97].

Although hot hardness represents the strength at high temperatures, their variation could provide information about deformation mechanism. The hot hardness as a function of temperature can be represented by the following equation suggested by Westbrook [94, 95, 98–100]:

$$H = A \exp(-BT) \quad (3.29)$$

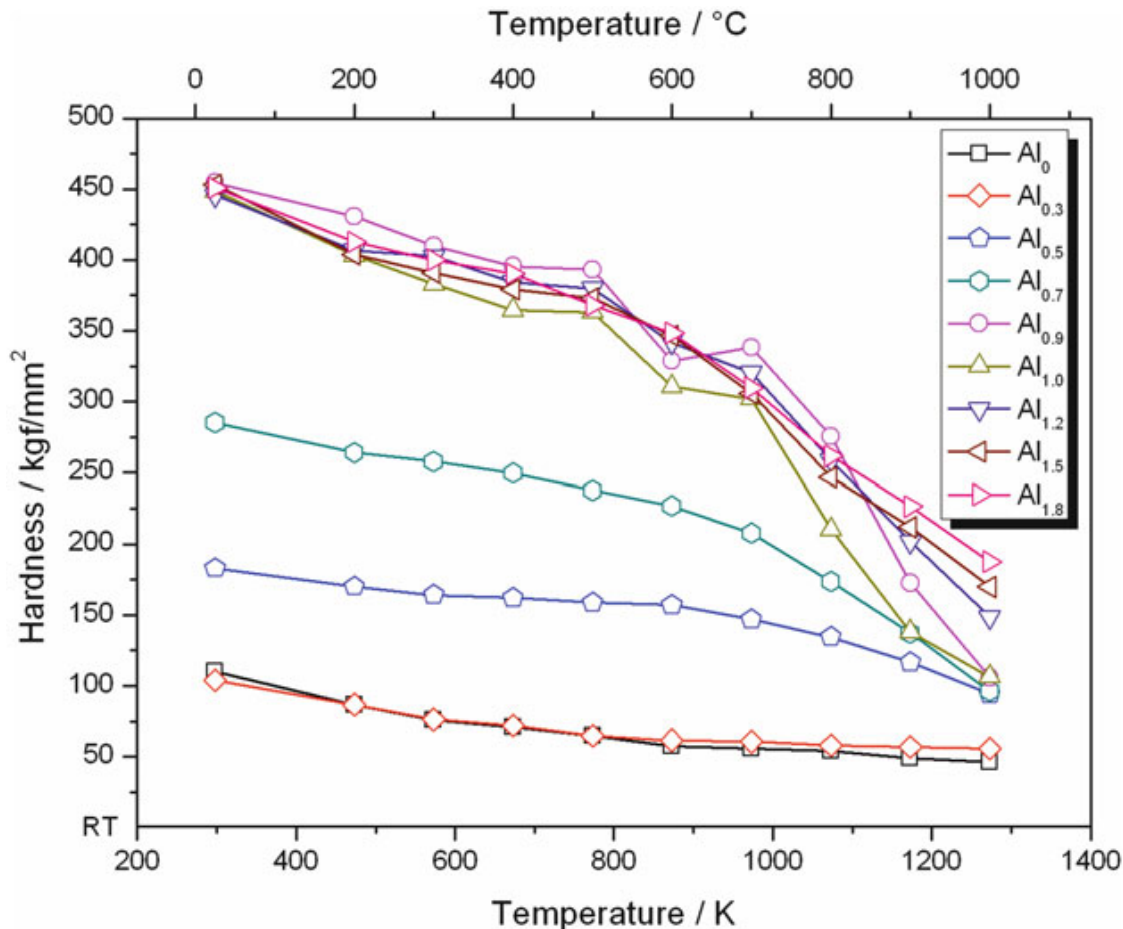


Fig. 3.31 Hot hardness vs. temperature plots for $\text{Al}_x\text{CoCrFeNi}$ alloys ($x = 0\text{--}1.8$) from room temperature to 1273 K [94]

where A is the intrinsic hardness or the value of hardness at 0 K and B is called softening coefficient. There are two set of constants A and B in low-temperature and high-temperature regions, respectively, suggesting a change in the deformation mechanism. In most metals and alloys, the transition temperature T_T is known to occur at about $0.5 T_m$, where T_m is the melting point. It has been suggested that the deformation mechanism for low temperatures is slip and that for high temperatures ($>0.5 T_m$) is dislocation climb and glide [95, 99, 100]. The activation energy is also same as that of lattice diffusion. This is reasonable since at temperatures above T_T the indentation size does not attain a constant value after a certain time but continues to increase with time [99]. Because the plastic zone gradually built beneath the indenter, dislocations are generated in the interface and multiplied in the zone. As the diffusion is high, dynamic recovery occurs during indenter descending. This is mainly due to the climb of edge dislocations to overcome obstacles and the movement of jogged screw dislocations to facilitate cross-slip. If dwell time increases, creep deformation continues and hardness decreases.

Table 3.8 lists and compares hot-hardness transition temperature (T_T), homologous temperature (T_T/T_m), and two sets of intrinsic hardness (A) and softening coefficient (B): A_I and B_I for low temperatures and A_{II} and B_{II} for high temperatures, for $\text{Al}_x\text{CoCrFeNi}$ cast alloys and three commercial alloys, T-800, In718, and In718H [94]. One can see that all the homologous temperatures are about 0.5

Table 3.8 Transition temperature (T_T), intrinsic hardness (A), softening coefficient (B), melting point, and homologous temperature of the $\text{Al}_x\text{CoCrFeNi}$ alloys and commercial alloys T-800, In718, and In718H [94]

Alloy	K	Transition temperature (T_T)	Below T_T		Above T_T		Melting point (T_m)	T_T/T_m	Homologous temperature
			A_I	B_I	A_{II}	B_{II}			
Al_0	815	148	1.09×10^{-3}		97	5.77×10^{-4}	1690	0.48	
$\text{Al}_{0.3}$	823	134	9.28×10^{-4}		79	2.82×10^{-4}	1655	0.50	
$\text{Al}_{0.5}$	938	194	2.60×10^{-4}		491	1.25×10^{-3}	1631	0.58	
$\text{Al}_{0.7}$	914	320	3.86×10^{-4}		1575	2.13×10^{-3}	1621	0.56	
$\text{Al}_{0.9}$	844	539	4.88×10^{-4}		3888	2.83×10^{-3}	1635	0.52	
$\text{Al}_{1.0}$	823	532	5.67×10^{-4}		3234	2.68×10^{-3}	1635	0.50	
$\text{Al}_{1.2}$	903	503	4.08×10^{-4}		2381	2.13×10^{-3}	1643	0.55	
$\text{Al}_{1.5}$	888	504	4.22×10^{-4}		1699	1.79×10^{-3}	1660	0.53	
$\text{Al}_{1.8}$	884	511	4.28×10^{-4}		1379	1.55×10^{-3}	1680	0.53	
T-800 ^a	818	791	2.84×10^{-4}		8041	3.12×10^{-3}	1563	0.52	
In718 ^b	1069	268	3.10×10^{-4}		11,766	3.55×10^{-3}	1609	0.66	
In718H ^c	1037	487	5.29×10^{-4}		13,778	3.74×10^{-3}	1609	0.64	

^aComposition of T-800: Co, 47.6 %; Mo, 28 %; Cr, 18 %; Si, 3.4 %; Fe, 1.5 %; and Ni, 1.5 %

^bComposition of In 718: Ni, 53 %; Cr, 19 %; Fe, 18.5 %; Nb, 5.1 %; Mo, 3 %; Ti, 0.9 %; and Al, 0.5 %

^cAnnealed at 1253 K for 30 min, air-cooled, and aged at 1033 K for 8 h, furnace-cooled at a rate of 55 K, heated to 893 K for 8 h, and air-cooled

except that 0.66 of In718. Furthermore, the softening coefficients, B_I , are similar to those of the comparing alloys, whereas the softening coefficients, B_{II} , are in general smaller than those of the compared commercial alloys. This suggests that the present alloy system has a higher softening resistance than compared alloys at above T_T . The explanation is related to sluggish diffusion effect in the multi-principal-element solid-solution phases such as ordered BCC, disordered BCC, FCC, and sigma phases in the alloy series. It is noted that Al_0 and $\text{Al}_{0.3}$ alloys with single FCC phase have the lowest B_{II} values. This demonstrates the combined effects of the lower diffusion rate of FCC structure than other structures and the sluggish diffusion in the multi-principal-element matrix.

Indentation creep test was also used for measuring the hot hardness as a function of dwell time (5, 10, and 30 s) on $\text{Al}_{0.3}$, $\text{Al}_{0.5}$, $\text{Al}_{0.7}$, $\text{Al}_{0.9}$, and $\text{Al}_{1.5}$ alloys at 773, 873, 973, 1073, and 1173 K [94]. The results also confirm that the FCC $\text{Al}_{0.3}$ alloy has negligible creep and the Al_x alloys with $x \geq 0.5$ display some creep at above T_T . This is consistent with the variation of the B_{II} values with aluminum content.

3.8 Conclusions and Perspective

This chapter emphasizes the four core effects of HEAs, which influence many aspects of physical metallurgy. By these core effects, many aspects have been discussed as detailed as possible with the author's knowledge. One can see that their effects on microstructure and properties are mostly positive and encouraging. Alloy design utilizing these positive effects becomes very promising to develop application-oriented HEAs. Nevertheless, the discussion and explanation are still far from completeness. More experimental data and evidences and clear mechanisms and theories are required for HEAs in the future. When physical metallurgy from conventional alloys to HEAs is built, the whole understanding of the alloy world becomes realized.

Acknowledgments J.W.Y. would like to acknowledge all the financial supports from the Ministry of Science and Technology, Ministry of Economic Affairs, and National Tsing Hua University, R.O.C.

References

1. Reed-Hill RE, Abbaschian R (1994) Physical metallurgy principles, 3rd edn. PWS Publishing Company, Boston, pp xiii–xv
2. Cahn RW, Haasen P (eds) (1983) Physical metallurgy, 3rd revised and enlarged ed. Elsevier Science publishers BV, Amsterdam, pp 1–35
3. Yeh JW (2006) Recent progress in high-entropy alloys. Ann Chimie Sci Materiaux (Eur J Control) 31:633–648
4. Yeh JW (2013) Alloy design strategies and future trends in high-entropy alloys. JOM 65:1759–1771
5. Reed-Hill RE, Abbaschian R (1994) Physical metallurgy principles, 3rd edn. PWS Publishing Company, Boston, pp 353–358
6. Cullity BD, Stock SR (2001) Elements of X-ray diffraction, 3rd edn. Prentice-Hall Inc, Upper Saddle River, pp 327–340
7. Otto F, Yang Y, Bei H, George EP (2013) Relative effects of enthalpy and entropy on the phase stability of equiatomic high-entropy alloys. Acta Mater 61:2628–2638
8. Tsai KY, Tsai MH, Yeh JW (2013) Sluggish diffusion in Co-Cr-Fe-Mn-Ni high-entropy alloys. Acta Mater 61:4887–4898
9. Senkov ON, Scott JM, Senkova SV, Miracle DB, Woodward CF (2011) Microstructure and room temperature properties of a high-entropy TaNbHfZrTi alloy. J Alloys Compd 509:6043–6048
10. Tong CJ, Chen YL, Chen SK, Yeh JW, Shun TT, Tsau CH, Lin SJ, Chang SY (2005) Microstructure characterization of $\text{Al}_x\text{CoCrCuFeNi}$ high-entropy alloy system with multi-principal elements. Metall Mater Trans A 36A:881–893
11. Hsu CY, Yeh JW, Chen SK, Shun TT (2004) Wear resistance and high-temperature compression strength of FCC CuCoNiCrAl 0.5Fe alloy with boron addition. Metall Mater Trans A 35A:1465–1469
12. Zhang Y, Zhou YJ, Lin JP, Chen GL, Liaw PK (2008) Solid-solution phase formation rules for multi-component alloys. Adv Eng Mater 10:534–538

13. Guo S, Liu CT (2013) Phase selection rules for complex multi-component alloys with equiatomic or close-to-equiatomic compositions. *Chin J Nat* 35:85–96
14. Yeh JW (2009) Recent progress in high-entropy alloys, the 2009 cross-strait conference on metallic glasses. National Taiwan University of Science and Technology, Taipei
15. Chen ST, Yeh JW (2009) Effect of mixing enthalpy, mixing entropy and atomic size difference on the structure of multicomponent alloys. Master's thesis, National Tsing Hua University
16. Yang X, Zhang Y (2012) Prediction of high-entropy stabilized solid-solution in multi-component alloys. *Mater Chem Phys* 132:233–238
17. Yeh JW, Chen SK, Gan JY, Lin SJ, Chin TS, Shun TT, Tsau CH, Chang SY (2004) Formation of simple crystal structures in solid-solution alloys with multi-principal metallic elements. *Metall Mater Trans A* 35A:2533–2536
18. Yeh JW, Chang SY, Hong YD, Chen SK, Lin SJ (2007) Anomalous decrease in X-ray diffraction intensities of Cu-Ni-Al-Co-Cr-Fe-Si alloy systems with multi-principal elements. *Mater Chem Phys* 103:41–46
19. Wang S (2013) Atomic structure modeling of multi-principal-element alloys by the principle of maximum entropy. *Entropy* 15:5536–5548
20. Huang PK, Yeh JW (2010) Inhibition of grain coarsening up to 1000 °C in (AlCrNbSiTiV)N superhard coatings. *Scr Mater* 62:105–118
21. Guo S, Liu CT (2011) Phase stability in high entropy alloys: formation of solid-solution phase or amorphous phase. *Proc Natl Acad Sci U S A* 21:433–446
22. Meyers MA, Chawla KK (1984) Mechanical metallurgy: principles and applications. Prentice-Hall, Inc, Englewood Cliff, New Jersey, pp 188–199
23. Senkov ON, Wilks GB, Miracle DB, Chuang CP, Liaw PK (2010) Refractory high-entropy alloys. *Intermetallics* 18:1758–1765
24. Kao YF, Chen SK, Chen TJ, Chu PC, Yeh JW, Lin SJ (2011) Electrical, magnetic, and hall properties of $\text{Al}_x\text{CoCrFeNi}$ high-entropy alloys. *J Alloys Compd* 509:1607–1614
25. Lu CL, Lu SY, Yeh JW, Hsu WK (2013) Thermal expansion and enhanced heat transfer in high-entropy alloys. *J Appl Crystallogr* 46:736–739
26. Swalin RA (1972) Thermodynamics of solid, 2nd edn. Wiley, New York, pp 263–266
27. Tsai CW, Chen YL, Tsai MH, Yeh JW, Shun TT, Chen SK (2009) Deformation and annealing behaviors of high-entropy alloy $\text{Al}_{0.5}\text{CoCrCuFeNi}$. *J Alloys Compd* 486:427–435
28. Hsu CY, Juan CC, Wang WR, Sheu TS, Yeh JW, Chen SK (2011) On the superior hot hardness and softening resistance of $\text{AlCoCr}_x\text{FeMo}_{0.5}\text{Ni}$ high-entropy alloys. *Mater Sci Eng A* 528:3581–3588
29. Senkov ON, Wilks GB, Scott JM, Miracle DB (2011) Mechanical properties of $\text{Nb}_{25}\text{Mo}_{25}\text{Ta}_{25}\text{W}_{25}$ and $\text{V}_{20}\text{Nb}_{20}\text{Mo}_{20}\text{Ta}_{20}\text{W}_{20}$ refractory high entropy alloys. *Intermetallics* 19:698–706
30. Tsai MH, Wang CW, Tsai CW, Shen WJ, Yeh JW, Gan JY, Wu WW (2011) Thermal stability and performance of NbSiTaTiZr high-entropy alloy barrier for copper metallization. *J Electrochem Soc* 158:H1161–H1165
31. Tsai MH, Yeh JW, Gan JY (2008) Diffusion barrier properties of AlMoNbSiTaTiVZr high-entropy alloy layer between copper and silicon. *Thin Solid Films* 516:5527–5530
32. Shun TT, Hung CH, Lee CF (2010) Formation of ordered/disordered nanoparticles in FCC high entropy alloys. *J Alloys Compd* 493:105–109
33. Liu WH, Wu Y, He JY, Nieh TG, Lu ZP (2013) Grain growth and the hall-petch relationship in a high-entropy FeCrNiCoMn alloy. *Scr Mater* 68:526–529
34. Juan CC, Hsu CY, Tsai CW, Wang WR, Sheu TS, Yeh JW, Chen SK (2013) On microstructure and mechanical performance of $\text{AlCoCrFeMo}_{0.5}\text{Ni}_x$ high-entropy alloys. *Intermetallics* 32:401–407
35. Ranganathan S (2003) Alloyed pleasures: multimetallic cocktails. *Curr Sci* 85:1404–1406
36. Zhang Y, Zuo TT, Cheng YQ, Liaw PK (2013) High-entropy alloys with high saturation magnetization, electrical resistivity, and malleability. *Sci Rep* 3:1455

37. Mackay AL (2001) On complexity. *Crystallogr Rep* 46:524–526
38. Cahn RW, Haasen P (eds) (1983) Physical metallurgy, 3rd revised and enlarged ed. Elsevier Science publishers BV, Amsterdam, pp 219–248
39. Porter DA (1992) Phase transformations in metals and alloys. Chapman & Hall, New York, pp 1–59
40. Kittel C (1996) Introduction to solid state physics, 7th edn. Wiley, Hoboken, pp 3–26
41. Alonso JA, Simozar S (1980) Prediction of solid solubility in alloys. *Phys Rev B* 22:5583–5588
42. Hume-Rothery W (1967) Factors affecting the stability of metallic phases. In: Rudman PS, Stringer J, Jaffee RI (eds) Phase stability in metals and alloys. McGraw-Hill, New York
43. Hume-Rothery W, Smallman RE, Haworth CW (1969) Structure of metals and alloys, 5th edn. Institute of Metals, London
44. Smith WF, Hashemi J (2006) Foundations of materials science and engineering, 4th edn. McGraw-Hill, Inc., New York
45. De Boer FR, Boom R, Mattens WCM, Miedema AR, Niessen AK (1988) Cohesion in metals: transition metal alloys. North-Holland Physics Publishing/Elsevier Science Publisher B.V, Amsterdam
46. Chen HY, Tsai CW, Tung CC, Yeh JW, Shun TT, Chen HC, Chen SK (2006) The effect of the substitution of Co by Mn in Al-Cr-Cu-Fe-Co-Ni high-entropy alloys. *Ann Chimie Sci Materiaux* 31:685–698
47. Santodonato LJ, Zhang Y, Feygenson M, Parish CM, Gao MC, Weber RJK, Neufeld JC, Tang Z, Liaw PK (2015) Deviation from high-entropy configurations in the atomic distributions of a multi-principal-element alloy. *Nat Commun* 6:5964:1–13. doi:[10.1038/ncomms6964](https://doi.org/10.1038/ncomms6964)
48. Hsu CY, Juan CC, Chen ST, Sheu TS, Chen ST, Yeh JW, Chen SK (2013) Phase diagrams of high-entropy alloy system Al-Co-Cr-Fe-Mo-Ni. *J Appl Meteorol* 65:1829–1839
49. Chen YL, Hu YH, Tsai CW, Hsieh CA, Kao SW, Yeh JW, Chin TS, Chen SK (2009) Alloying behavior of binary to octonary alloys based on Cu-Ni-Al-Co-Cr-Fe-Ti-Mo during mechanical alloying. *J Alloys Compd* 477:696–705
50. Chen YL, Hu YH, Hsieh CA, Yeh JW, Chen SK (2009) Competition between elements during mechanical alloying in an octonary multi-principal-element alloy system. *J Alloys Compd* 481:768–775
51. Chen YL, Hu YH, Tsai CW, Yeh JW, Chen SK, Chang SY (2009) Structural evolutions during mechanical milling and subsequent annealing of Cu-Ni-Al-Co-Cr-Fe-Ti alloys. *Mater Chem Phys* 118:354–361
52. Chen YL, Tsai CW, Juan CC, Chuang MH, Yeh JW, Chin TS, Chen SK (2010) Amorphization of equimolar alloys with HCP elements during mechanical alloying. *J Alloys Compd* 506:210–215
53. Chang HW, Huang PK, Davison A, Yeh JW, Tsau CH, Yang CC (2008) Nitride films deposited from an equimolar Al-Cr-Mo-Si-Ti alloy target by reactive DC magnetron sputtering. *Thin Solid Films* 516:6402–6408
54. Egami T (1996) The atomic structure of aluminum based metallic glasses and universal criterion for glass formation. *J Non Cryst Solids* 205–207:575–582
55. Egami T, Waseda Y (1984) Atomic size effect on the formability of metallic glasses. *J Non Cryst Solids* 64:113–134
56. Inoue A (2000) Stabilization of metallic supercooled liquid and bulk amorphous alloys. *Acta Mater* 48:279–306
57. Kao SW, Yeh JW, Chin TS (2008) Rapidly solidified structure of alloys with two to eight equal-molar elements – a simulation by molecular dynamics. *J Phys Condens Matter* 20:145214
58. Turnbull D (1977) On the gram-atomic volumes of metal-metalloid glass forming alloys. *Scr Metall* 11:1131–1136
59. Turnbull D (1981) Metastable structures in metallurgy. *Metall Trans B* 12B:217–230

60. Greer AL (1993) Confusion by design. *Nature* 366:303–304
61. Porter DA (1992) Phase transformations in metals and alloys. Chapman & Hall, New York, pp 110–142
62. Swalin RA (1972) Thermodynamics of solids, 2nd edn. Wiley, New York, pp 220–223
63. www.materials.ac.uk/elearning/.../vacancies/enthalpy.html
64. Swalin RA (1972) Thermodynamics of solids, 2nd edn. Wiley, New York, pp 267–289
65. Meyers MA, Chawla KK (1984) Mechanical metallurgy: principles and applications. Prentice-Hall, Inc, Englewood Cliff, New Jersey, pp 52–59, and 247–256
66. Humphreys FJ, Hatherly M (2004) Recrystallization and related annealing phenomena, 2nd edn. Elsevier, Oxford, pp 102–104
67. Kittel C (1996) Introduction to solid state physics, 7th edn. Wiley, Hoboken, p 78
68. Lee C, Yeh JW (2013) Study on deformation behaviors of equimolar alloys from Ni to CoCrFeMnNi. Master's thesis, National Tsing Hua University
69. Meyers MA, Chawla KK (1984) Mechanical metallurgy: principles and applications. Prentice-Hall, Inc, Englewood Cliff, New Jersey, pp 226–270
70. Weertman J, Weertman JR (1964) Elementary dislocation theory. Macmillan, New York, pp 22–83
71. Schramm RE, Reed RF (1975) Stacking fault energies of seven commercial austenitic stainless steels. *Metall Trans A* 6A:1345–1351
72. Gallagher PCJ (1970) The influence of alloying, temperature, and related effects on the stacking fault energy. *Metall Trans* 1:2429–2461
73. Humphreys FJ, Hatherly M (2004) Recrystallization and related annealing phenomena, 2nd edn. Elsevier Science Ltd, Oxford, pp 24–26
74. Zaddach AJ, Niu C, Kock CC, Irving DL (2013) Mechanical properties and stacking fault energies of NiFeCrCoMn high-entropy alloy. *J Appl Meteorol* 65:1780–1789
75. Morikawa T, Higashida K (2010) Deformation microstructure and texture in a cold-rolled austenitic steel with low stacking-fault energy. *Mater Trans* 51:620–624
76. Bhattacharjee PP, Sathiaraj GD, Zaid M, Gatti JR, Lee C, Tsai CW, Yeh JW (2014) Microstructure and texture evolution during annealing of equiatomic CoCrFeMnNi high-entropy alloy. *J Alloys Compd* 587:544–552
77. Shewmon PG (1963) Diffusion in solids. McGraw-Hill, New York, pp 164–178
78. Reed-Hill RE, Abbaschian R (1994) Physical metallurgy principles, 3rd edn. PWS Publishing Company, Boston, pp 390–394
79. Otto F, Dlouhy A, Somsen C, Bei H, Eggeler G, George EP (2013) The influences of temperature and microstructure on the tensile properties of a CoCrFeMnNi high-entropy alloy. *Acta Mater* 61:5743–5755
80. Gludovatz B, Hohenwarter A, Catoor D, Chang EH, George EP, Ritchie RO (2014) A fracture-resistant high-entropy alloy for cryogenic applications. *Science* 345:1153–1158
81. Wu Z, Bei H, Pharr GM, George EP (2014) Temperature dependence of the mechanical properties of equiatomic solid solution alloys with face-centered cubic crystal structures. *Acta Mater* 81:428–441
82. Couzinié JP, Dirras G, Perrière L, Chauveau T, Leroy E, Champion Y, Guillot I (2014) Microstructure of a near-equimolar refractory high-entropy alloy. *Mater Lett* 126:285–287
83. Lin CM, Juan CC, Chang CH, Tsai CW, Yeh JW (2015) Effect of Al addition on mechanical properties and microstructure of refractory $\text{Al}_x\text{HfNbTaTiZr}$ alloys. *J Alloys Compd* 624:100–107
84. Courtney TH (1990) Mechanical behavior of materials, international ed. McGraw-Hill, New York, pp 162–219 & 263–324
85. Tsai BS, Yeh JW (2015) Microstructure and mechanical properties of $\text{Al}_x\text{CoCrFeMnNi}$ ($x = 0 \sim 1$). Master's thesis, National Tsing Hua University
86. Meyers MA, Chawla KK (1984) Mechanical metallurgy: principles and applications. Prentice-Hall, Inc, Englewood Cliff, New Jersey, pp 402–413, & 494–514

87. Chen CS, Yang CC, Chai HY, Yeh JW, Chau JLH (2014) Novel cermet material of WC/multi-element alloy. *Int J Refract Met Hard Mater* 43:200–204
88. Lin CM, Tsai CW, Huang SM, Yang CC, Yeh JW (2014) New TiC/Co_{1.5}CrFeNi_{1.5}Ti_{0.5} cermet with slow TiC coarsening during sintering. *J Appl Meteorol* 66:2050–2056
89. Meyers MA, Chawla KK (1984) Mechanical metallurgy: principles and applications. Prentice-Hall, Inc, Englewood Cliff, New Jersey, pp 659–687
90. Dieter GE (1988) Mechanical metallurgy, SI metric ed. McGraw-Hill, New York, pp 432–470
91. Reed RC (2006) The superalloys: fundamentals and applications. Cambridge University Press, Cambridge, pp 1–120
92. Mohamed FA, Langdon TG (1974) The transition from dislocation climb to viscous glide in creep of solid solution alloys. *Acta Metall* 30:779–788
93. He JY, Zhu C, Zhou DQ, Liu WH, Nieh TG, Lu ZP (2014) Steady state flow of the FeCoNiCrMn high entropy alloy at elevated temperatures. *Intermetallics* 55:9–14
94. Wang WR, Wang WL, Yeh JW (2014) Phases, microstructure and mechanical properties of Al_xCoCrFeNi high-entropy alloys at elevated temperatures. *J Alloys Compd* 589:143–152
95. Khana KB, Kutty TRG, Surappa MK (2006) Hot hardness and indentation creep study on Al-5% Mg alloy matrix-B₄C particle reinforced composites. *Mater Sci Eng A* 427:76–82
96. Kutty TRG, Jarvis T, Ganguly C (1997) Hot hardness and indentation creep studies on Zr-1Nb-1Sn-0.1Fe alloy. *J Nucl Mater* 246:189–195
97. Wang WR, Wang WL, Wang SC, Tsai YC, Lai CH, Yeh JW (2012) Effects of Al addition on the microstructure and mechanical property of Al_xCoCrFeNi high-entropy alloys. *Intermetallics* 26:44–51
98. Dieter GE (1988) Mechanical metallurgy, SI metric ed. McGraw-Hill, New York, pp 336–337
99. Merchant HD, Murty GS, Bahadur SN, Dwivedi LT, Mehrotra Y (1973) Hardness-temperature relationships in metals. *J Mater Sci* 8:437–442
100. Kutty TRG, Ravi K, Ganguly C (1999) Studies on hot hardness of Zr and its alloys for nuclear reactors. *J Nucl Mater* 265:91–99

Chapter 4

Advanced Characterization Techniques

Louis J. Santodonato and Peter K. Liaw

Abstract This chapter first provides a brief introduction to some advanced microstructure characterization tools, such as three-dimensional (3D) atom probe tomography, high-resolution transmission electron microscopy, and neutron scattering. Applications of these techniques to characterize high-entropy alloys (HEAs) are illustrated in model alloys. Utilization of these advanced techniques can provide extremely useful structural and chemical information at the nanoscale. For example, the identification of nano-twins in the fracture-toughness crack region of an HEA may explain the anomalous increases in strength and ductility at cryogenic temperatures. Another striking feature of HEAs is the large local strain among neighboring atoms, which, in general, are arranged in a crystal structure with long-range order. Our understanding of these types of features, and their effect on material properties, will increase as the microstructural characterization techniques described here are further developed and applied to HEA research.

Keywords Microstructure characterization • Three-dimensional atom probe tomography • High-resolution transmission electron microscopy • Neutron scattering • Nanoscale • Microstructure • Nano-twins • Local strain • Solid solution • Atomic scale • High-entropy alloys (HEAs)

Characterization techniques included in this chapter:

- Scanning electron microscopy (SEM)
- Transmission electron microscopy (TEM)

L.J. Santodonato

Division of Instrument and Source, Oak Ridge National Laboratory,
Oak Ridge, TN 37831, USA

Materials Science and Engineering Department, The University of Tennessee,
Knoxville, TN 37996, USA
e-mail: Santodonatol@ornl.gov

P.K. Liaw (✉)

Department of Materials Science and Engineering, The University of Tennessee,
Knoxville, TN 37996, USA
e-mail: pliaw@vols.utk.edu

- High-angle annular dark-field (HAADF) imaging
- Selected area electron diffraction (SAED)
- Energy-dispersive X-ray spectroscopy (EDX)
- Backscattered electron (BSE) imaging
- Atom probe tomography (APT)
- Electron backscatter diffraction (EBSD)
- X-ray diffraction (XRD)
- High-energy synchrotron X-ray diffraction
- Anomalous X-ray diffraction (AXRD)
- Neutron scattering, including diffraction and pair-distribution function analysis (PDF)

4.1 Overview of Advanced Characterization Techniques

The experimental studies of high-entropy alloys (HEAs) most often begin with standard techniques, which are later integrated with more advanced techniques. For example, the crystal structures of many HEAs may be determined, using the conventional X-ray diffraction facilities available in many university laboratories. Typical HEA diffraction patterns are quite simple and may be indexed to the body-centered cubic (BCC), face-centered cubic (FCC), and hexagonal close packed (HCP) structures [1–6]. The only way that the multiple principal elements can produce such simple structures is by randomly occupying the lattice sites. Thus, the solid-solution microstructures are inferred, simply by indexing the diffraction peaks, and the phases are often referred to as the “disordered” FCC, BCC, or HCP phases. More detailed examinations, however, may reveal that the structures are not completely disordered (e.g., small “superstructure” peaks may be present). Furthermore, the crystal structures may have significant local distortions. In such cases, additional studies using synchrotron X-ray and/or neutron scattering may be needed, in order to determine the details of the atomic structures. The scientific community has access to several advanced techniques, such as synchrotron X-ray scattering, neutron scattering, and the microscopy techniques described below, by submitting peer-reviewed proposals to major user facilities (Table 4.1).

Electron microscopy techniques, such as transmission electron microscopy (TEM) and scanning electron microscopy (SEM), are the primary tools for studying HEA microstructures. Note that many HEAs, especially when studied in the as-cast condition, have complex microstructures with multiple phases. Because the microstructures contain multiple principal elements, phase-specific elemental analyses should be an integral part of the microscopy studies, using techniques such as energy-dispersive X-ray spectroscopy (EDX). Furthermore, phase-specific diffraction techniques, such as the electron backscatter diffraction (EBSD) and selected area electron diffraction (SAED), are often part of the microscopy studies. EBSD is typically used to obtain a large-scale map (tens or hundreds of microns) of the crystal structures, grain sizes, and grain orientations and correlates them with

Table 4.1 Major user facilities providing access to neutron scattering and synchrotron X-ray diffraction

Technique	Facility
Neutron scattering	<i>North America</i>
	Oak Ridge Neutron Facilities (SNS/HFIR)
	NIST Center for Neutron Research
	Los Alamos Neutron Science Center (LANSCE)
	University of Missouri Research Reactor Center
	Canadian Neutron Beam Centre, Chalk River, Canada
	Indiana University Cyclotron Facility
	<i>Europe</i>
	ISIS-Rutherford-Appleton Laboratories, United Kingdom
	Institut Laue-Langevin, Grenoble, France
	Leon Brillouin Laboratory, Saclay, France
	Berlin Neutron Scattering Center, Germany
	GEMS at Helmholtz-Zentrum Geesthacht, Germany
	Juelich Center for Neutron Science, Germany
	FRM-II, Munich, Germany
	Budapest Neutron Centre, Hungary
	RID, Delft, The Netherlands
	SINQ, Paul Scherrer Institut (PSI), Switzerland
	Frank Laboratory of Neutron Physics, Dubna, Russia
	St. Petersburg Neutron Physics Institute, Gatchina, Russia
	<i>Asia and Australia</i>
	ISSP Neutron Scattering Laboratory, Tokai, Japan
	JAEA Research Reactors, Tokai, Japan
	KENS Neutron Scattering Facility, Tsukuba, Japan
	Hi-Flux Advanced Neutron Application Reactor, Korea
	Bhabha Atomic Research Centre, Mumbai, India
	Bragg Institute, ANSTO, Australia
Synchrotron X-ray	<i>North America</i>
	ALS: Advanced Light Source (Berkeley, CA USA)
	APS: Advanced Photon Source (Argonne, IL USA)
	CHESS: Cornell High Energy Synchrotron Source (Cornell, Ithaca, NY USA)
	NSLS: National Synchrotron Light Source (Brookhaven, Upton, NY USA)
	SSRL: Stanford Synchrotron Radiation Laboratory (SLAC, Stanford, CA USA)
	SURF: NIST SURF-II UV synchrotron (NIST, Gaithersburg, MD USA)
	Synchrotron Radiation Center (Stoughton, WI USA)
	<i>Europe</i>
	Daresbury Laboratory SERC (Daresbury, England)
	ESRF: European Synchrotron Radiation Facility (Grenoble, France)
	LURE (Orsay, France)
	DELTA: Dortmund Electron Test Accelerator (Dortmund, Germany)
	ELSA: Electron Stretcher and Accelerator (Bonn, Germany)
	HASYLAB (DESY, Hamburg, Germany)
	Elettra (Trieste, Italy)

(continued)

Table 4.1 (continued)

Technique	Facility
	MAXLAB (Lund, Sweden)
	SLS: Swiss Light Source (PSI, Villigen, Switzerland)
	<i>Asia</i>
	BSRF: Beijing Synchrotron Radiation Facility (Beijing, China)
	The Photon Factory (KEK, Tsukuba, Japan)
	SPring-8 (Riken Go, Japan)
	SRRC: Synchrotron Radiation Research Center (Hsinchu City, Taiwan)

Source: www.ncnr.nist.gov

microstructural features. SAED may focus on a smaller region of the microstructure and is often used to determine subsequent dark-field TEM studies, providing a nanoscale map of the crystal structures.

The atomic-level homogeneity and structural features are important issues in HEAs. The atomic configurations are directly related to the configurational entropy of mixing, which forms the basis of the HEA design strategy. Atomic-level features are beyond the resolution of many techniques. However, the specialized TEM technique of high-angle annular dark-field (HAADF) imaging is capable of capturing atomic-level details. APT is another powerful technique, capable of detecting individual atoms within a selected volume and constructing detailed maps of the atomic distribution.

Advanced characterization techniques are not simply a matter of using advanced equipment. The integration of several techniques, and clever experimental design, is a crucial factor. The examples given below, taken from a review of the literature, illustrate these strategies.

4.2 Microstructural Features of the $\text{Al}_x\text{CoCrCuFeNi}$ System: Integrated SEM, TEM (Bright and Dark Field), SAED, EDX, and XRD

The tendency of HEAs to form simple solid-solution structures was established from the early work on the $\text{Al}_x\text{CoCrCuFeNi}$ alloys, with varying aluminum contents (molar ratios from $x = 0$ to 3.0) [1, 2]. Conventional XRD was used to identify the FCC and BCC crystal structures in this system and to establish the trend that the FCC-dominated microstructure changes to a BCC-dominated microstructure as the aluminum content increases (Fig. 4.1). The effect of aluminum content on the HEA microstructure continues to be studied to the present [5].

Because the alloy contains multiple principal elements, the simple FCC and BCC crystal structures may be interpreted as substitutional solid solutions, where each lattice site is statistically populated by several elements. However, a deviation from the simple FCC/BCC structure is indicated by the presence of “ordered BCC”

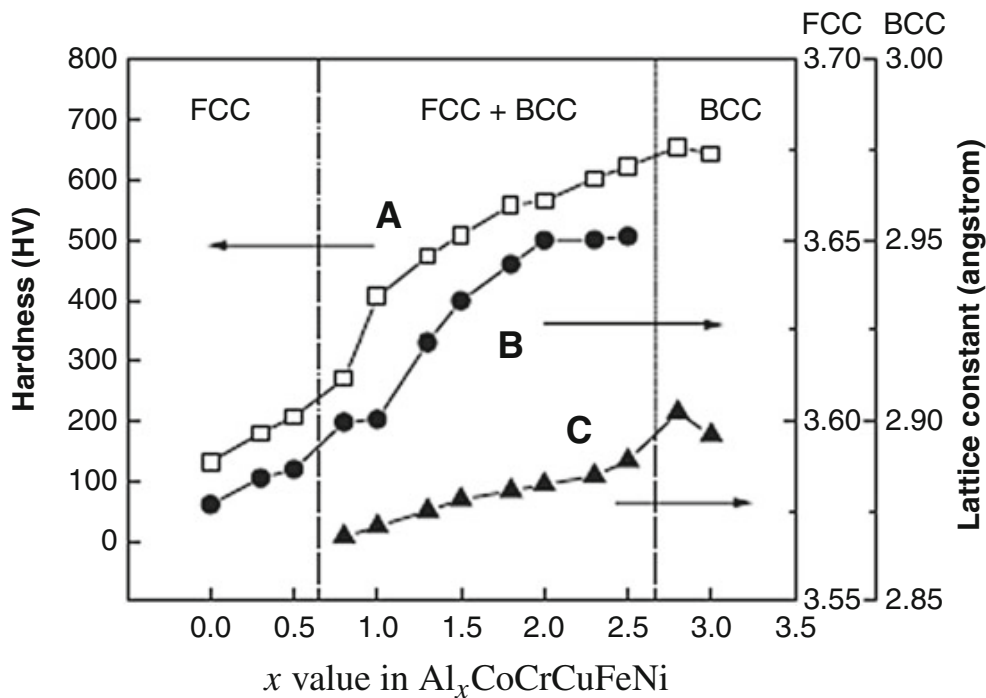


Fig. 4.1 FCC/BCC crystal structure trend in the $\text{Al}_x\text{CoCrCuFeNi}$ system (From Ref. [1])

peaks in the diffraction scans (Fig. 4.2). These peaks are systematically absent in a true BCC structure (i.e., peaks where the sum of the Miller indices, $h + k + l$, is odd). Their presence indicates that the solid solution is at least partially ordered, such that the site at the center of the unit cell does not have the same atomic occupation as the site at the origin (Fig. 4.3). The detailed nature of this type of ordering has been the subject of subsequent studies [7–9] and is discussed later in the chapter (Sect. 4.8).

The microstructures of the as-cast $\text{Al}_x\text{CoCrCuFeNi}$ alloys progress from the simple to complex structures, as the aluminum content is increased. A thorough characterization was obtained [1, 2], using a combination of SEM and TEM studies. Dendrite and interdendrite structures were observed using SEM (Fig. 4.4). The SEM studies included EDX to determine, for example, that the interdendrites are Cu rich. Despite the Cu segregation in the small volume fraction of the interdendrites, the EDX results showed that the dendrites were composed of multiple principal elements, particularly for low Al contents ($x < 0.8$). As the Al content increases to $x = 1$, the dendrites develop a spinodal microstructure (i.e., a periodic microstructure, arising from composition fluctuations). The changes in the SEM microstructures may be correlated with the XRD studies, such that the alloy phases for the low aluminum content are FCC (a Cu-rich FCC phase in the interdendrites and a multi-principal element FCC phase in the dendrites) and mixed-phase FCC/BCC/B2 at higher aluminum contents. However, further information from the TEM studies is needed for a more detailed picture.

The TEM bright-field imaging, SAED, confirms the correlation between the XRD crystal structures and the microstructures. Both the dendrites and interdendrites of the as-cast $\text{Al}_x\text{CoCrCuFeNi}$ alloys, with aluminum contents from $x = 0$ to 0.5, were composed of FCC structures. Within the dendrites and interdendrites, a homogeneous TEM microstructure was observed.

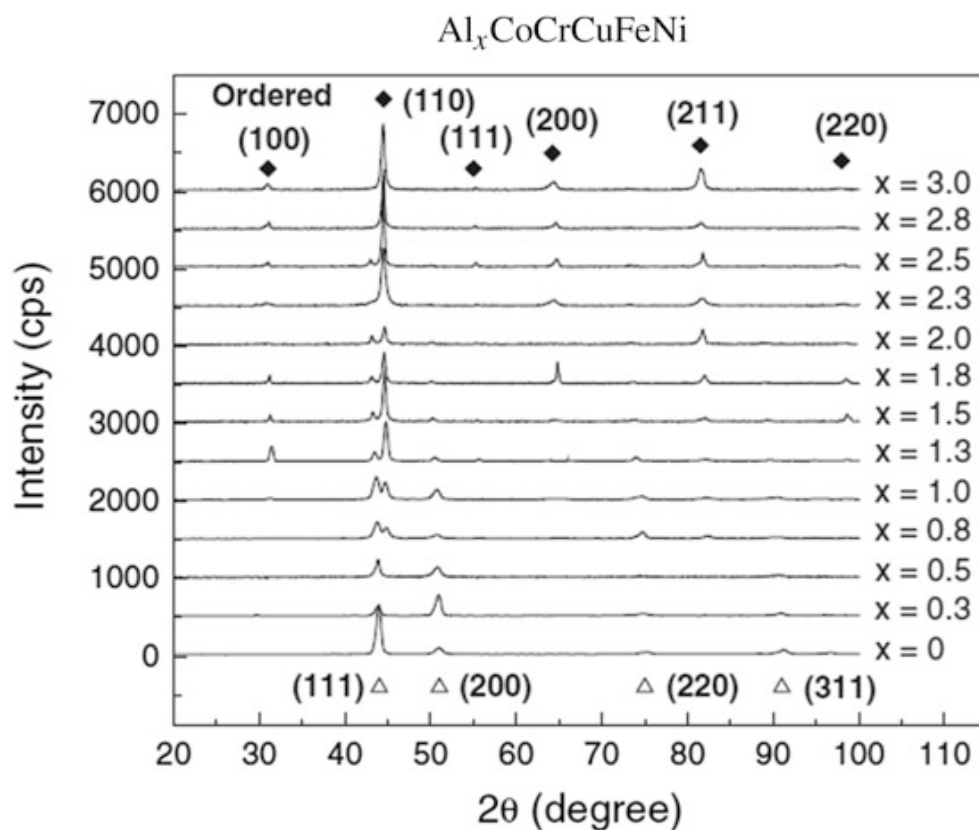


Fig. 4.2 XRD analyses of the $\text{Al}_x\text{CoCrCuFeNi}$ alloy system with different aluminum contents (x values). The patterns are indexed to FCC (open triangles) and BCC (solid diamonds) phases. Ordered peaks of the B2 phase are also indicated (From Ref. [2])

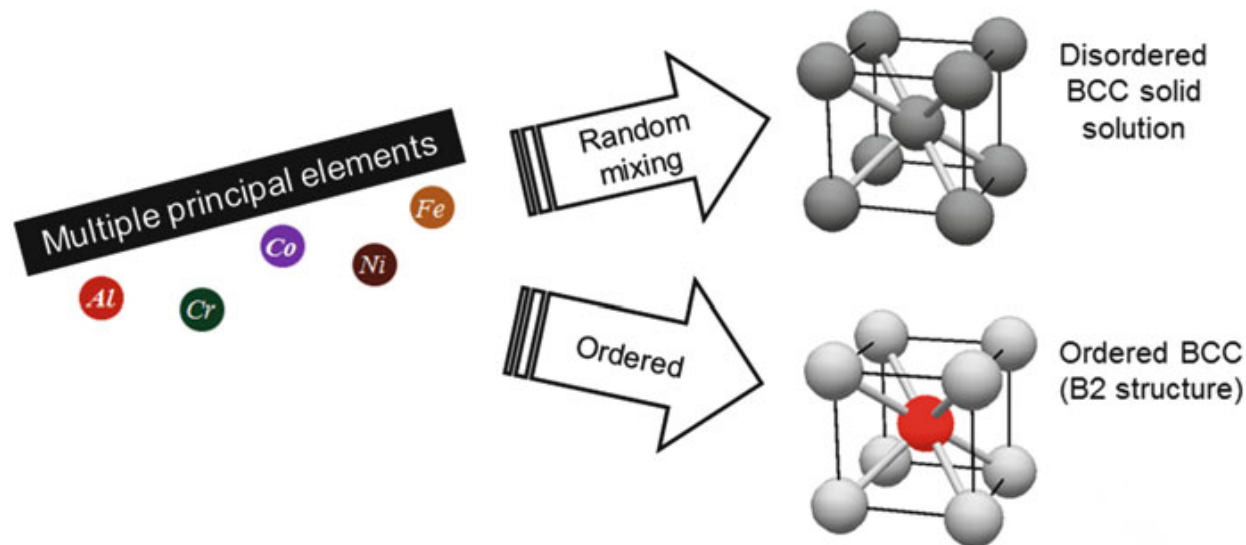


Fig. 4.3 Schematic illustration of disordered versus ordered BCC structures in HEAs. The gray spheres represent crystal sites that are occupied by a random or nearly random mixture of elements. The colored sphere, in the center of the B2-ordered unit cell, represents a site that is preferentially occupied, by Al, for example. Note that there are several different mixing scenarios that could lead to a B2-ordered structure

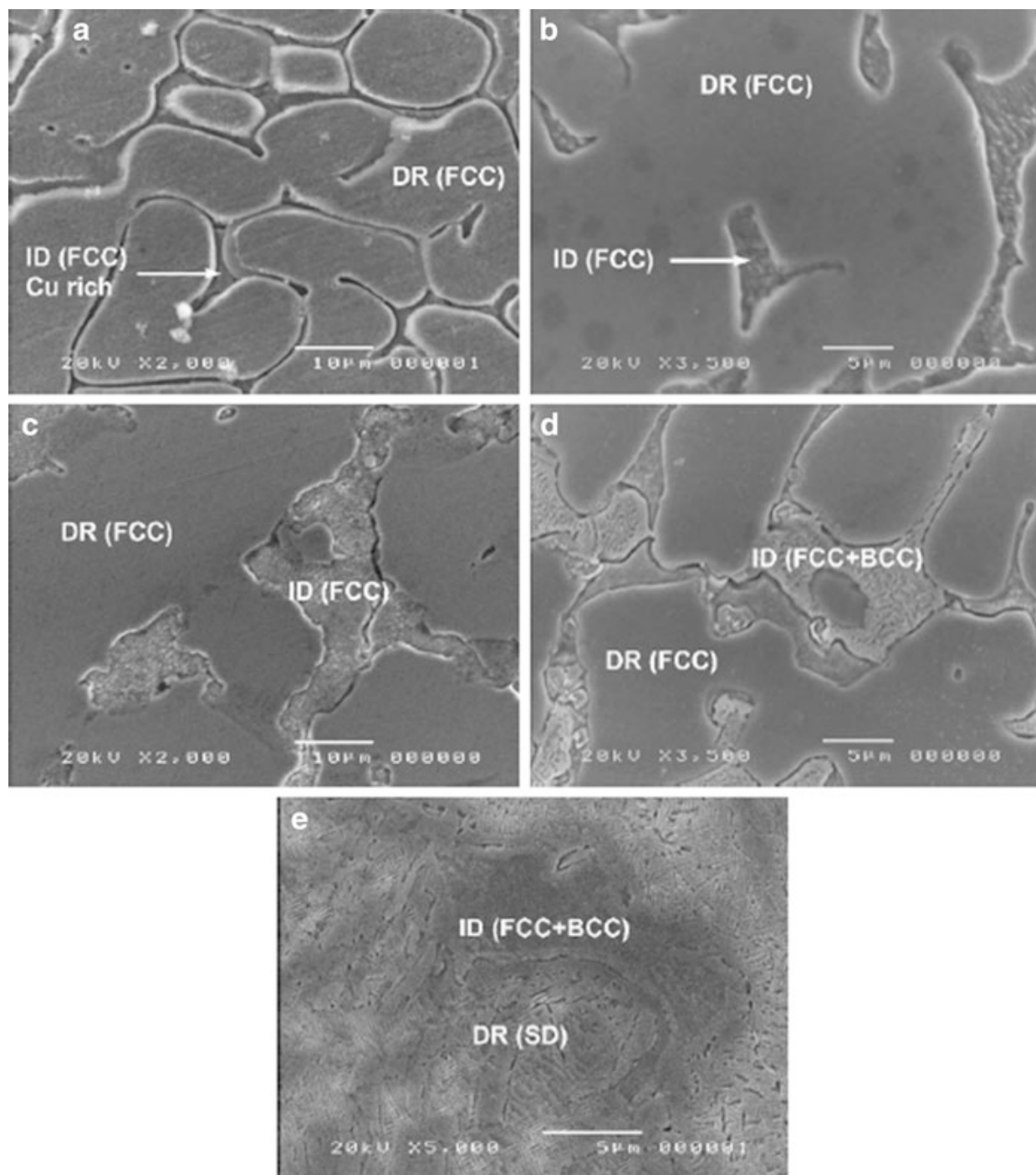


Fig. 4.4 SEM microstructures of the as-cast $\text{Al}_x\text{CoCrCuFeNi}$ alloys with different aluminum contents (x values): (a) 0, (b) 0.3, (c) 0.5, (d) 0.8, and (e) 1.0 [(dendrite (DR), interdendrites (ID), and spinodal decomposition (SD)] (From Ref. [2])

The TEM examinations of the dendrites in the $\text{Al}_{0.8}\text{CoCrCuFeNi}$ composition show only a simple FCC phase, as in the lower Al-content compositions. However, the interdendrites were composed of mixed FCC and BCC phases, resulting from a eutectic reaction, corresponding to the two main groups of XRD peaks at the $x = 0.8$ composition (Fig. 4.2). As the Al content is further increased to $x \geq 1$, the BCC structures dominate. The TEM and SAED analyses (Fig. 4.5) further elucidate the phase decomposition seen in the SEM micrographs (Fig. 4.4). Superstructure reflections are clearly observed in the SAED (an inset on the bright-field image of

Fig. 4.5a), indicating that the spinodal microstructure contains an ordered BCC phase. A more precise pinpointing of the ordered phase was achieved, using the dark-field TEM analysis [2].

In dark-field TEM, the image is produced by the portion of the electron beam that is diffracted at a particular scattering vector, \mathbf{Q}_{hkl} . The dark-field TEM images of the equimolar AlCoCrCuFeNi alloy (Fig. 4.5b), based upon the (0 1 0) superstructure reflection seen in the SAED pattern (Fig. 4.5a, inset), reveal that the ~100-nm thick plates have an ordered BCC (B2) structure and the ~70-nm thick interplates have a disordered BCC structure. Thus, a combination of bright-field (i.e., a transmitted beam) and dark-field (i.e., a diffracted beam) TEM examinations allows a nanometer-scale mapping of the crystallographic features of the alloy.

The equimolar AlCoCrCuFeNi alloy contains various nanoprecipitates, visible in Figs. 4.5c–e. A SAED pattern of one of the nanoprecipitates (Fig. 4.5c, inset) corresponds to the FCC structure. In the dark-field TEM image, based upon one of the FCC reflections (Fig. 4.5d), nanoprecipitates of various sizes appear bright, indicating that they have similar FCC structures. The BCC/B2 matrix appears dark, because it does not produce any significant scattering in the vicinity of the FCC

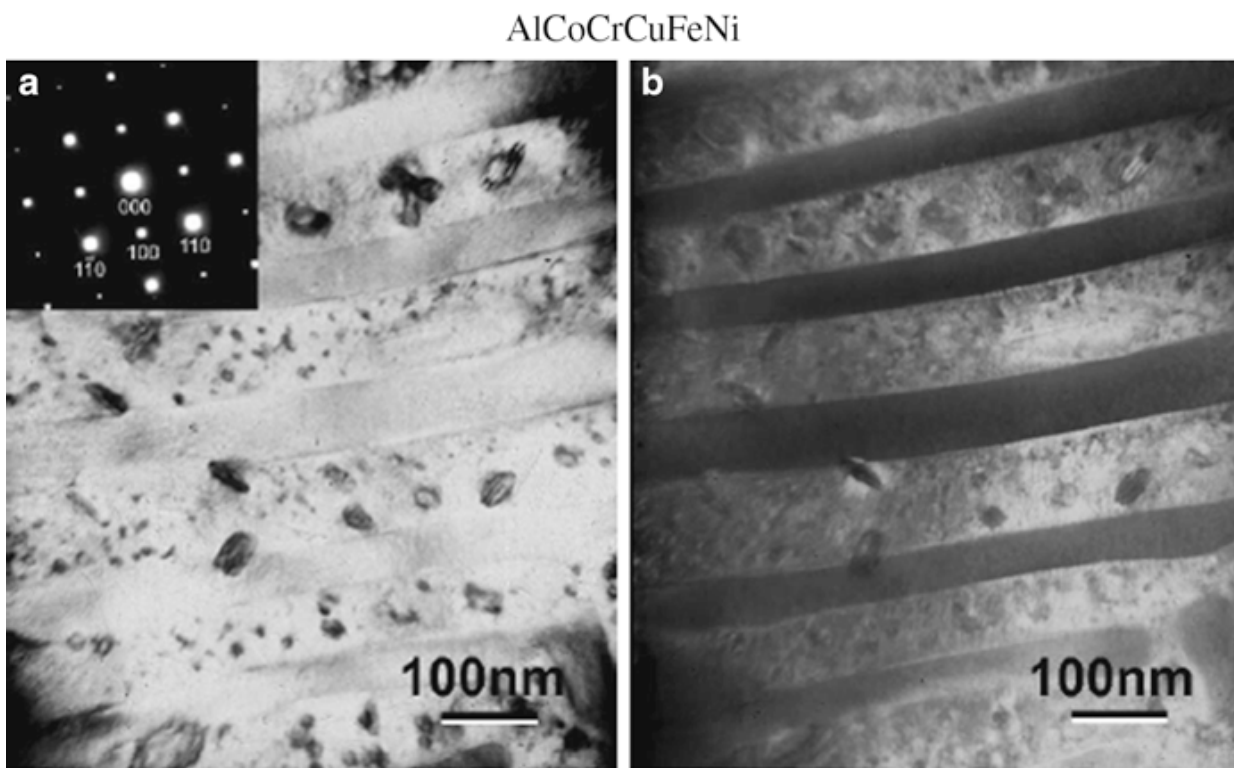


Fig. 4.5 TEM microstructures of the dendrite of the as-cast $\text{Al}_{1.0}\text{CoCrCuFeNi}$ alloy: (a) bright-field image of modulated plates and interplates with the SAED pattern of the BCC [0 0 1] zone axis; (b) dark-field image corresponding to the (0 1 0) superlattice spot of the SAED pattern shown in (a); parts (c) through (e) shown on the next page. (c) Bright-field image with the SAED pattern of the arrowed precipitate close to the FCC zone axis; (d) dark-field image corresponding to the circled spot of the SAED pattern shown in (c); and (e) enlarged bright-field image of the modulated plates and interplates with the same SAED pattern of the BCC [0 0 1] zone axis shown in (a); α , interplate, 70-nm wide, disordered BCC phase (A2), of lattice constant 2.89 Å; β , plate, 100-nm wide, ordered BCC phase (B2), lattice constant of 2.89 Å; ϵ , nanoprecipitation in plate, 7–50 nm in diameter, close to the FCC phase; and δ , contrast in the interplate due to the surface roughness effect of the TEM foil (From Ref. [2])

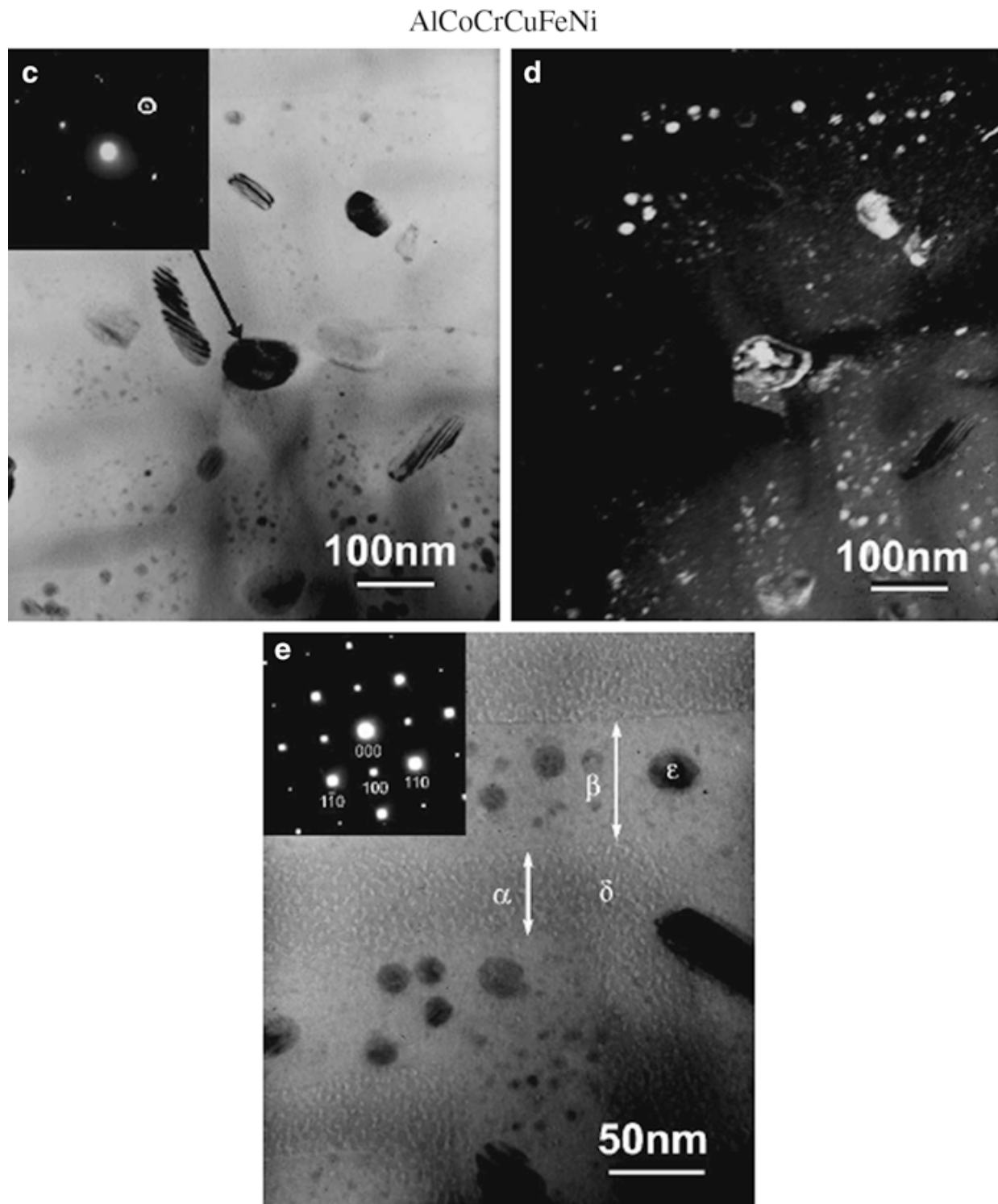


Fig. 4.5 (continued)

reflection. Finally, the enlarged bright-field TEM image (Fig. 4.5e) shows more details of the spinodal microstructure and the various nanoprecipitates.

The early studies [1, 2] of the $\text{Al}_x\text{CoCrCuFeNi}$ alloys, summarized here, established that the HEA design strategy promotes the formation of simple, solid-solution microstructures. These studies also showed how the disordered solid-solution microstructures may decompose into a mixture of ordered and disordered phases and that a variety of nanoprecipitates are present. These studies integrated XRD, SEM, and TEM. The TEM studies included bright-field imaging, SAED, and dark-field imaging, based upon particular SAED reflections, in order to correlate

the crystal structures with the nanoscale features of the microstructure. These detailed, early studies set the foundation for the field of the HEA research. The strategic use of conventional XRD, SEM, bright-field and dark-field TEM continue to advance our understanding of HEAs.

4.3 Understanding the Fracture-Resistant Behavior of the CoCrFeMnNi Alloy: BSE Imaging, EBSD, EDX, and Stereomicroscopy

XRD studies indicate that the CoCrFeMnNi alloy forms a single-phase FCC solid solution and EDX verifies the nearly homogeneous CoCrFeMnNi composition of the solid solution [10, 11]. This alloy exhibits excellent damage tolerance, with fracture-toughness values [11] exceeding $200 \text{ MPa} \cdot \text{m}^{1/2}$. Moreover, both the strength and ductility increase at cryogenic temperatures, contrary to the trend in most alloys, where ductility typically decreases as strength increases. When CoCrFeMnNi was cooled from room temperature to 77 K, the ultimate tensile strength was found to increase by 70 %, reaching 1280 MPa, while the tensile ductility (strain at failure) increased by 25 %, such that $\epsilon > 0.7$ [11]. The nature of this interesting behavior in CoCrFeMnNi was uncovered using microscopy to examine the sample regions surrounding a fracture-toughness crack tip. The complementary techniques included stereomicroscopy, SEM, EBSD, EDX, and BSE imaging.

Sample preparation and fatigue-cracking procedures were important aspects of the CoCrFeMnNi study, and were crucial for obtaining relevant microscopy results, which revealed the underlying mechanisms of the fracture resistance. The CoCrFeMnNi alloys were prepared by arc melting and drop casting into a rectangular cross-section mold (25.4 mm × 19.1 mm × 127 mm). The specimens were further processed by cold forging, cross rolling (producing a 60 % reduction in thickness), and annealing at 800 °C for one hour in air. The annealing process produced fully recrystallized, equiaxed grains of ~6 µm size, as shown on the BSE micrograph (Fig. 4.6). The Cr-rich and Mn-rich particles, ~2 µm in diameter, are dispersed throughout the solid-solution matrix. These particles may serve as the initiation sites for microvoids that form during cracking [11], as described further below.

The annealed CoCrFeMnNi specimens were cut into the compact-tension geometry (ASTM International, formerly known as the American Society of Testing and Materials, Standard E18200) [12], of a nominal width, $W = 18 \text{ mm}$, and thickness, $B = 9 \text{ mm}$, and notched (6.6 mm in length with notch root radii of ~100 µm) using electrical discharge machining (EDM). The specimens were then fatigue cracked by applying a cyclic load, using a commercial load frame, until the crack propagated to a length of about 10 mm. Finally, some of the cracked samples were sliced in half, such that their final thickness was $B/2$. This slicing procedure exposed new

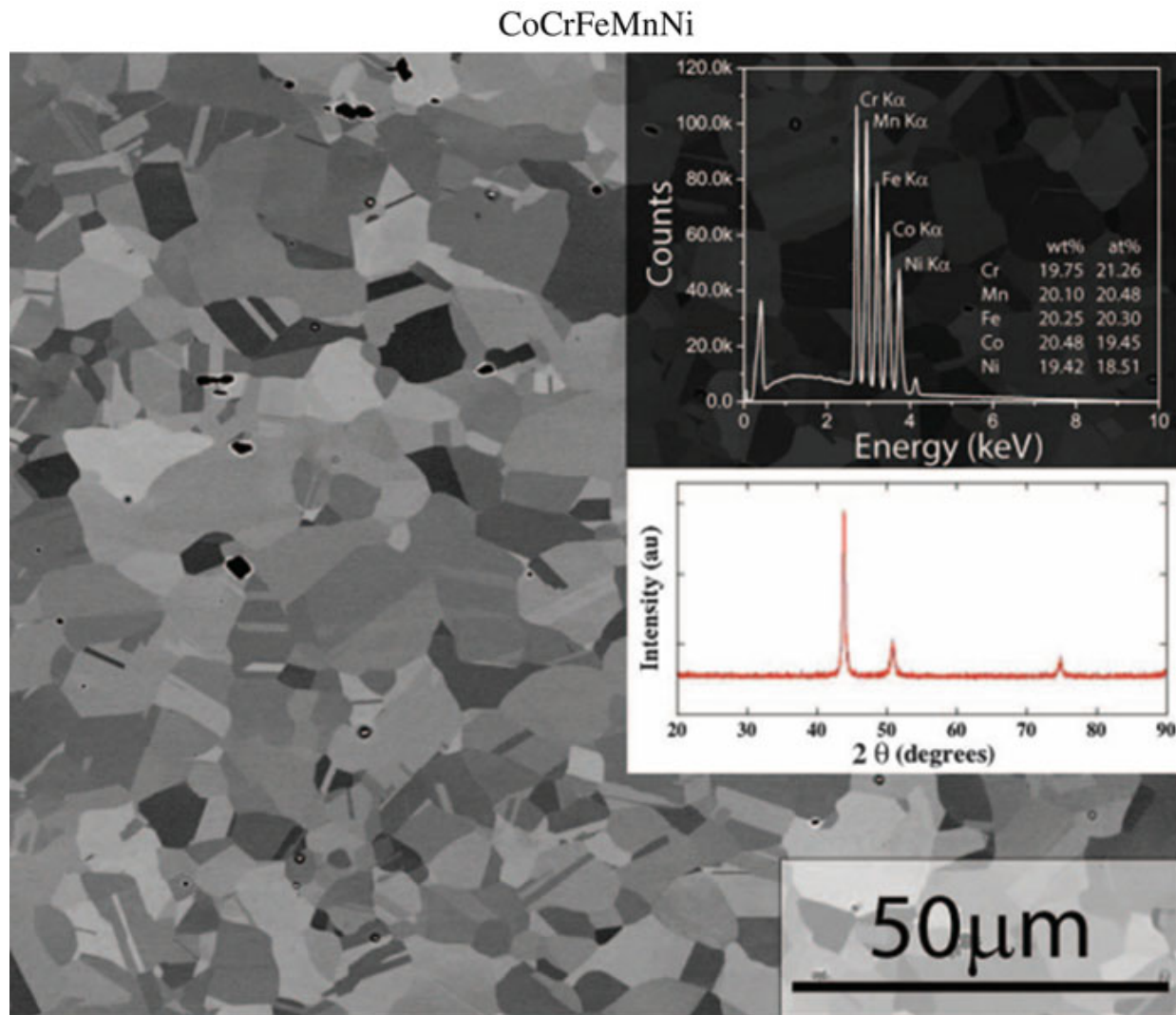


Fig. 4.6 Backscattered electron (BSE) micrograph of the annealed CoCrFeMnNi, showing $\sim 6 \mu\text{m}$ grains containing several recrystallization twins. The inset on the top right shows the EDX result, verifying the equimolar composition of the solid solution. The inset on the middle right shows the simple X-ray diffraction pattern, which corresponds to the FCC structure (From Ref. [11])

surfaces, which were representative of the interior of the sample during the fatigue-cracking process, including the regions in the immediate vicinity of the crack tip, where plane-strain conditions prevail. The slicing provided pairs of closely related samples for control tests, such as those used to verify that the microscopy preparation, where specimens were embedded at 180 °C in a conductive resin, did not introduce any structural damage. Thus, the microscopy studies of the carefully prepared fatigue-cracked specimens provided the reliable and relevant information about the mechanisms of the fracture-resistant behavior in the CoCrFeMnNi alloy.

Low-magnification SEM images of surfaces containing the fatigue cracks (Fig. 4.7a) show many irregular-shaped voids along the crack path, indicating that ductile fracture occurs by microvoid coalescence. Signs of ductile fracture are present for both the room-temperature and 77 K fatigue cracks, based upon the low-magnification SEM. Higher-magnification EBSD and BSE images, however, reveal important details and distinctions between the room-temperature and cryogenic deformation and fracture behaviors.

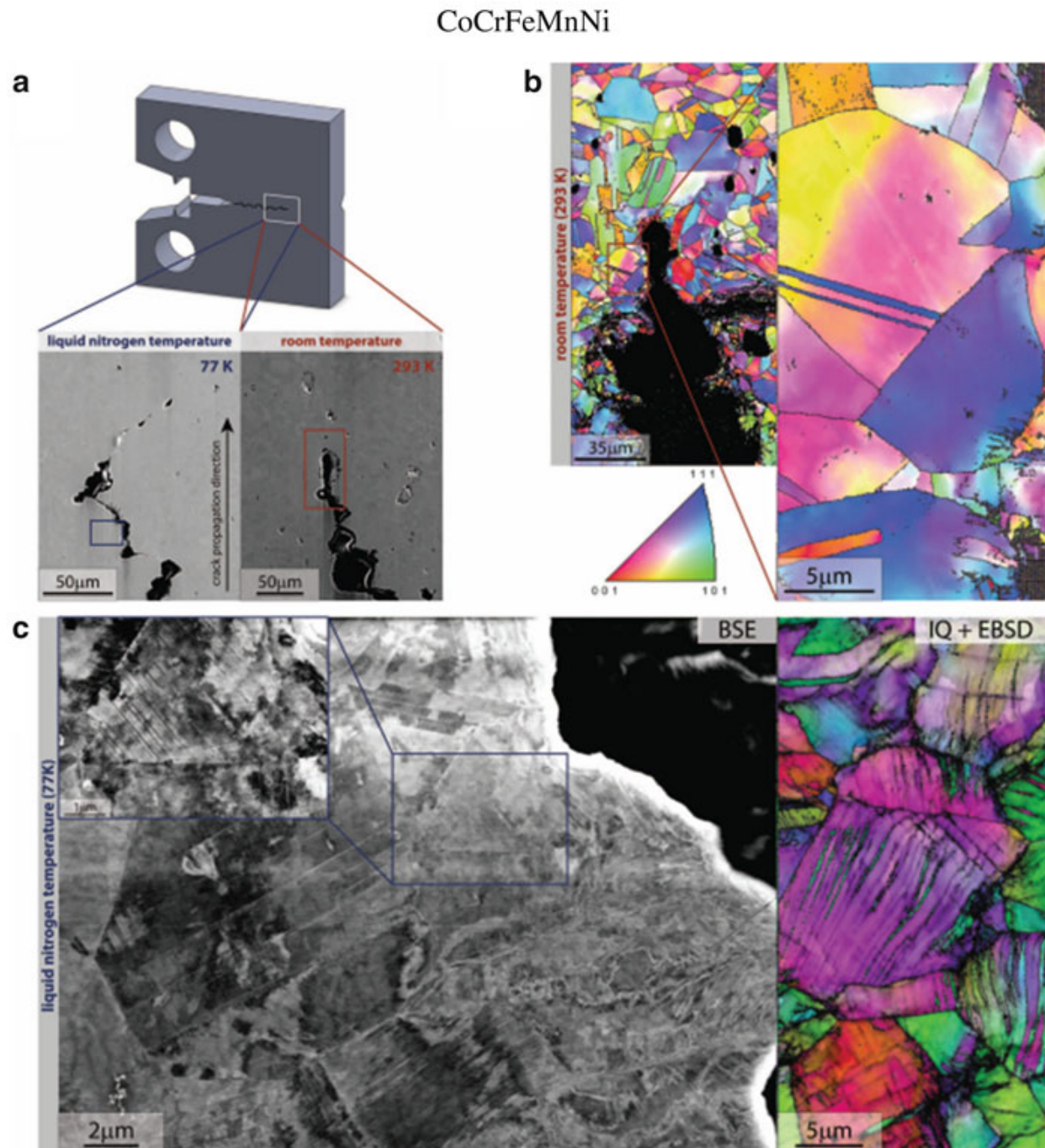


Fig. 4.7 Deformation mechanisms near the crack tip at the center (plane-strain) section of CoCrFeMnNi HEA samples. (a) Low-magnification SEM images of samples tested at room temperature and 77 K show ductile fracture by the microvoid coalescence. (b) EBSD images of the room-temperature sample show grain misorientations due to dislocations, representing the dominant deformation mechanism. Annealing twins are also present, as in the crack-free regions. (c) At 77 K, nano-twinning is seen on the BSE and EBSD images (the “IQ + EBSD” label indicates that the EBSD image is an overlay to an image quality [IQ] map). The low-temperature nano-twinning provides the enhanced ductility (tensile engineering strain >0.7 at failure stress of 1280 MPa). The cell structures (dark patches) seen throughout the BSE image, and especially on the inset, are due to the dislocation activity (From Ref. [11])

The EBSD images of the room-temperature crack tip show pronounced grain misorientations (Fig. 4.7b), which are attributed to the glide of dislocations on the $\{111\}$ crystal planes, and may serve as the primary room-temperature deformation mechanism. Several twins are also visible near the room-temperature crack tip,

which are identified as annealing twins, because they are present throughout the bulk of the annealed CoCrFeMnNi samples. In the immediate vicinity of the crack formed at 77 K, however, EBSD and BSE images show nano-twinning (i.e., closely spaced twins, on the nanometer scale). The nano-twins appear in addition to the dislocation cell structures, which are associated with the abovementioned dislocation glide (Fig. 4.7c). It is concluded, therefore, that nano-twinning provides an extra deformation mechanism at cryogenic temperatures and is responsible for the enhanced ductility and exceptional toughness of the CoCrFeMnNi HEA.

The nano-twinning in the CoCrFeMnNi alloy was observed using EBSD on highly polished surfaces (progressively polished to a 0.05- μm surface finish, followed by a final polishing step using colloidal silica) [13]. These surfaces intersected the actual crack surfaces, providing the crucial information about the deformation behavior around the crack. Additional information was obtained by directly examining the crack surfaces of fully separated compact-tension samples, using optical stereomicroscopy, EDX, and SEM stereo image pairs. The results helped determine that the high toughness was associated with ductile fracture by microvoid coalescence.

SEM shows that the CoCrFeMnNi crack surfaces are covered with ductile fracture dimples (Fig. 4.8a). Distinct particles are observed within the dimples, which were shown to be Mn rich and Cr rich, using EDX. These particles were identified as microvoid-initiation sites. These microvoids grow and coalesce, when a sufficient tensile stress is applied, ultimately leading to ductile fracture. Three-dimensional fracture surface models were constructed from SEM stereo image pairs (Fig. 4.8b), which show distinct differences between the fatigue pre-crack regions, and the final ductile fracture zone, where the dimples become most pronounced.

The CoCrFeMnNi fracture-toughness study [11] demonstrates the value of an integrated mechanical testing and microscopy experiment plan. Here, the microscopy studies were performed on carefully prepared compact-tension specimens. Microstructural features were examined across many length scales, from millimeters (optical microscopy) to nanometers (BSE and EBSD). Nano-twinning was identified as the underlying mechanism for the exceptional cryogenic ductility and fracture enhancement.

4.4 Phase Decomposition in AlCoCrCuFeNi: High-Resolution TEM and APT

Although HEAs have a tendency to form solid solutions with simple crystal structures, detailed examinations of the microstructures sometimes reveal significant complexity. The AlCoCrCuFeNi HEA is an excellent example. A comparison of splat-quenched versus conventional cast samples was made, using the high-resolution electron microscopy and atom probe tomography as the main analytical techniques [8]. XRD was also used to identify the major phases. Advanced sample

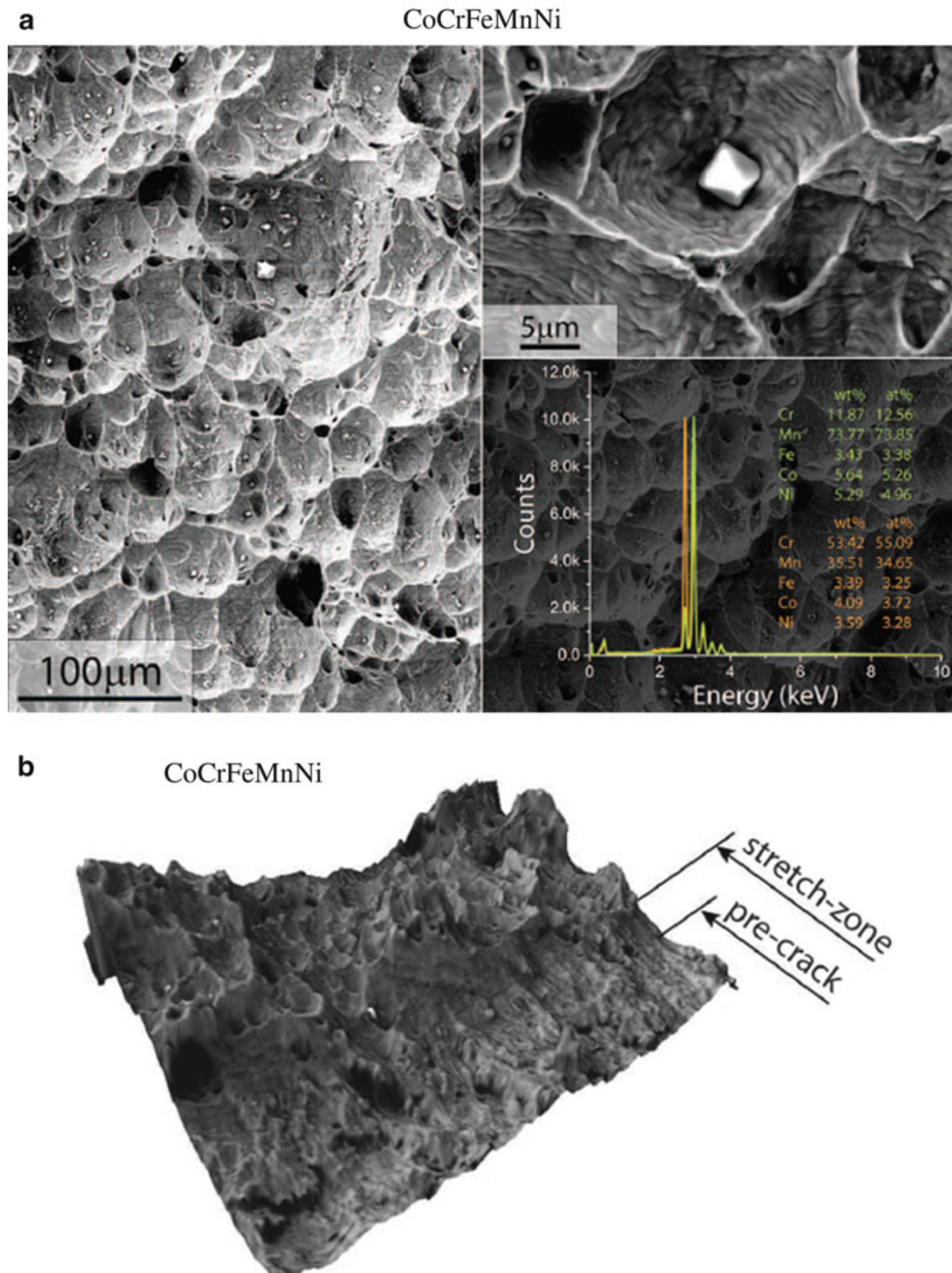


Fig. 4.8 (a) SEM micrograph of a room-temperature crack surface covered with dimples, indicating a ductile fracture mode. The particles seen within the dimples served as microvoid-initiation sites. These particles were determined to be Cr rich and Mn rich from EDX analyses (inset). (b) A three-dimensional fracture surface was rendered using SEM stereo image pairs. The different morphologies of the fatigue pre-crack zone, stretch zone (transitional region), and ductile fracture zone are visible (From Ref. [11])

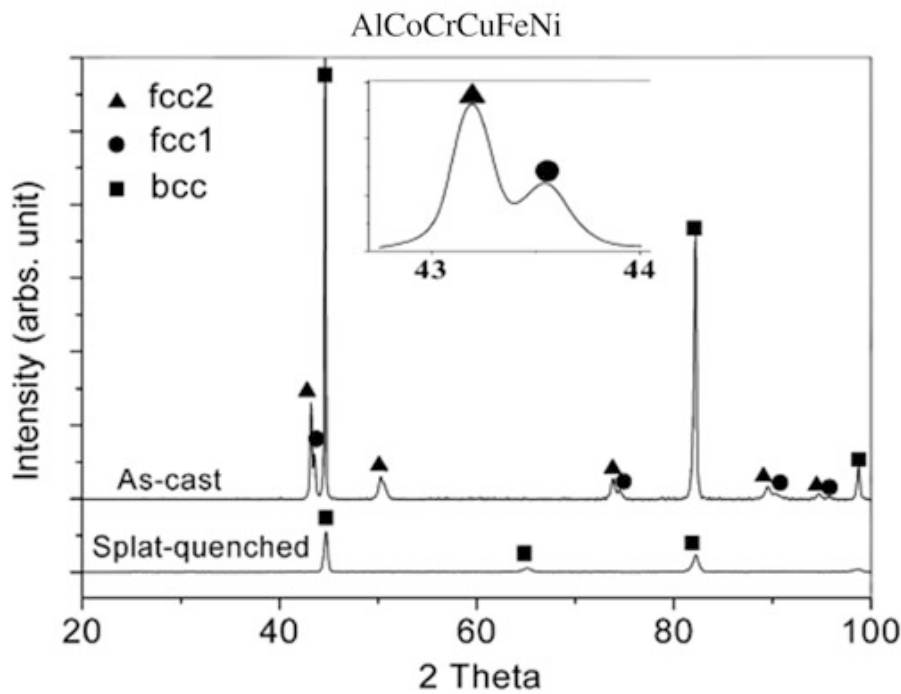


Fig. 4.9 Comparison of XRD patterns of as-cast and splat-quenched AlCoCrCuFeNi samples. The as-cast samples separate into three different phases (fcc1, fcc2, and bcc), while the splat-quenched samples appear to be of a single phase (From Ref. [8])

preparation techniques, particularly splat quenching, which produced cooling rates on the order of 10^6 K/s, played a key role in this study. It was shown that the quenched samples consisted of a single-phase, imperfectly ordered solid solution, while the cast samples formed complex, multiphase microstructures.

The XRD patterns of the as-cast samples were indexed to three phases: FCC1 (a lattice parameter, $a_{\text{fcc}1} = 3.59$ Å), FCC2 ($a_{\text{fcc}2} = 3.62$ Å), and BCC ($a_{\text{bcc}} = 2.87$ Å). The splat-quenched samples, however, produced only the BCC reflections (Fig. 4.9). The details of the microstructure, and the atomic structure, were revealed using the high-resolution TEM and APT.

A bright-field TEM image shows the polycrystalline microstructure of the splat-quenched alloy (Fig. 4.10a), which has ~ 1.5 μm grain sizes. The dark-field TEM (Fig. 4.10b) reveals a domain-like structure within the crystal grains, seen as bright spots throughout the image. The SAED pattern corresponds to an ordered BCC, or B2 structure, and the dark-field image is produced, using the [1 0 0] superlattice reflection. Thus, the spots on the dark-field image are ultimately interpreted as an imperfectly ordered B2 phase, consisting of a mixture of B2 and BCC domains within a coherent crystal structure.

The as-cast samples show a phase-separated microstructure, similar to the results of the earlier study [2] presented in Fig. 4.5. However, new details of the atomic-level phase decomposition were obtained using APT, a technique where individual atoms are stripped from a specimen that is specially prepared in the form of a sharp tip (Fig. 4.11). The as-cast AlCoCrCuFeNi samples were sharpened, using a two-step process: mechanical polishing and focused ion beam (FIB) milling. The subsequent APT studies provided atom maps (Fig. 4.12) within various

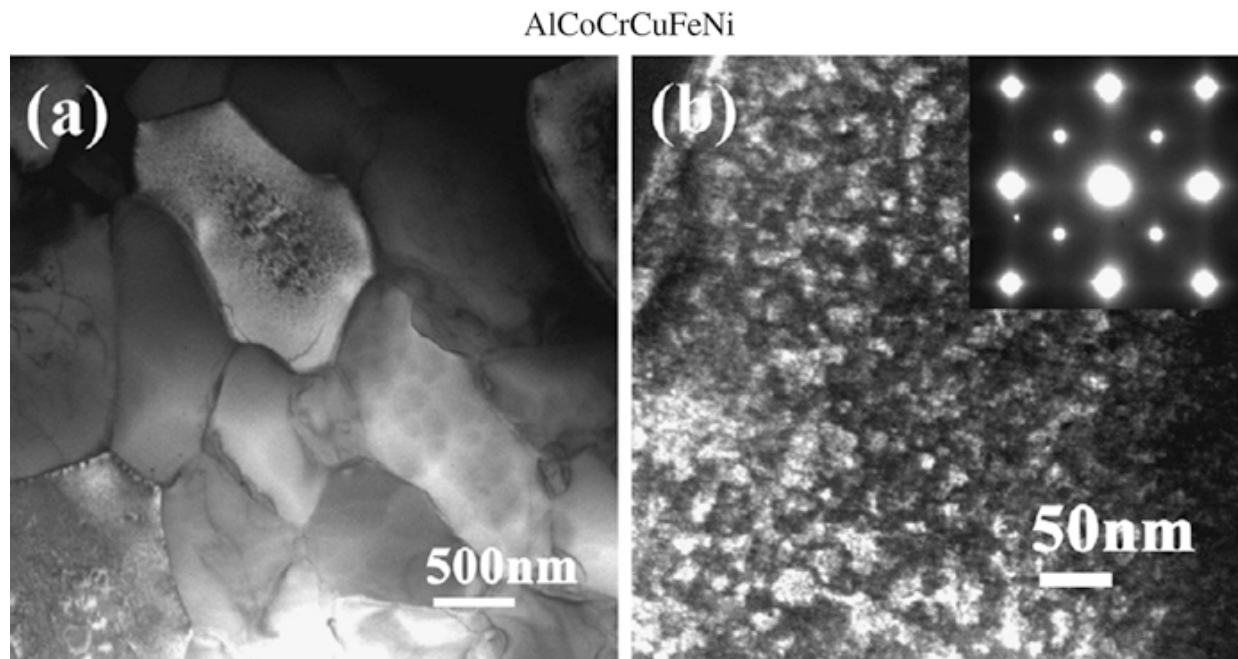
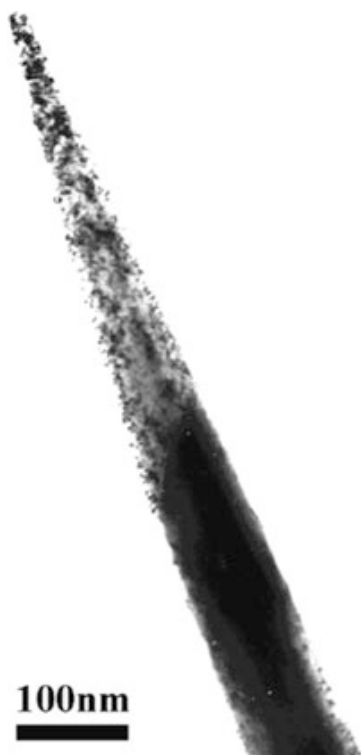


Fig. 4.10 TEM images of the splat-quenched AlCoCrCuFeNi. **(a)** Bright-field micrographs show the polycrystalline microstructure. **(b)** A dark-field image, using the (1 0 0) superlattice reflection, reveals a domain-like structure within the grains. The inset shows the SAED pattern (From Ref. [8])

Fig. 4.11 TEM image of an AlCoCrCuFeNi needle-tip sample prepared for the APT study (From Ref. [8])



microstructural features, such as the Al-Ni-enriched B2-ordered plates, the Fe-Cr-enriched BCC interpolates, and the Cu-rich plate precipitates.

By correlating the APT and high-resolution microscopy results, a very detailed picture of the extensive phase decomposition in the as-cast AlCoCrCuFeNi emerged. The splat-quenched samples had a single-phase, solid-solution character.

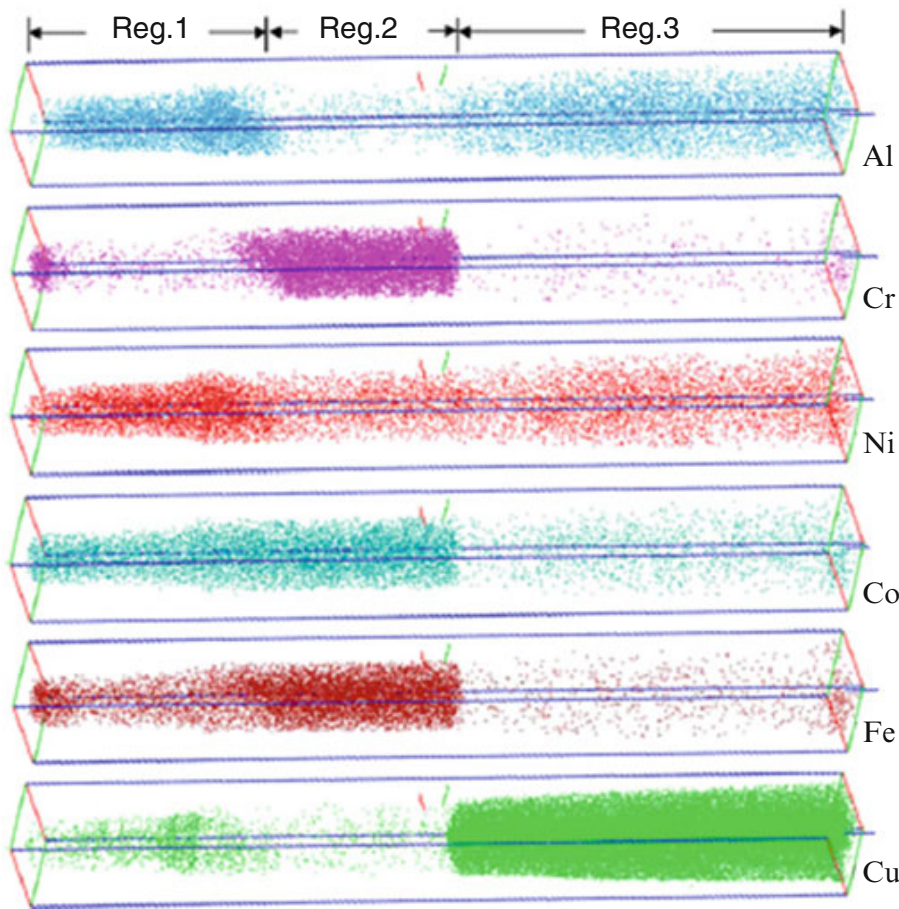


Fig. 4.12 Atom maps from an APT study of the as-cast AlCoCrCuFeNi. The numbered regions correspond to (1) an Al-Ni-enriched region, (2) a Cr-Fe-enriched region, and (3) a Cu-rich plate precipitate (From Ref. [8])

The single-phase character was especially apparent on the XRD and bright-field TEM images. However, the high-resolution dark-field TEM studies revealed a domain-like structure, produced by the local segregation of elements. The strong tendency for elemental segregation thus became apparent.

4.5 Nature of the Phase Interfaces in $\text{Al}_{1.5}\text{CoCrCuFeNi}$: HAADF Imaging

Phase separation in the $\text{Al}_x\text{CoCrCuFeNi}$ system (Figs. 4.4 and 4.5) has been thoroughly studied [1, 2, 7, 8, 14]. This section highlights the use of HAADF to study the nanoscale microstructural features and even the atomic-level details of the interfaces between the B2 and BCC phases in $\text{Al}_{1.5}\text{CoCrCuFeNi}$. The work was performed at the Center for Electron Microscopy and Analysis (CEMAS) at the Ohio State University [15].

The high-angle annular dark-field (HAADF) imaging is a technique where high-angle scattered electrons are collected, using an annular detector in a scanning transmission electron microscope [16]. When combined with EDX, nanoscale

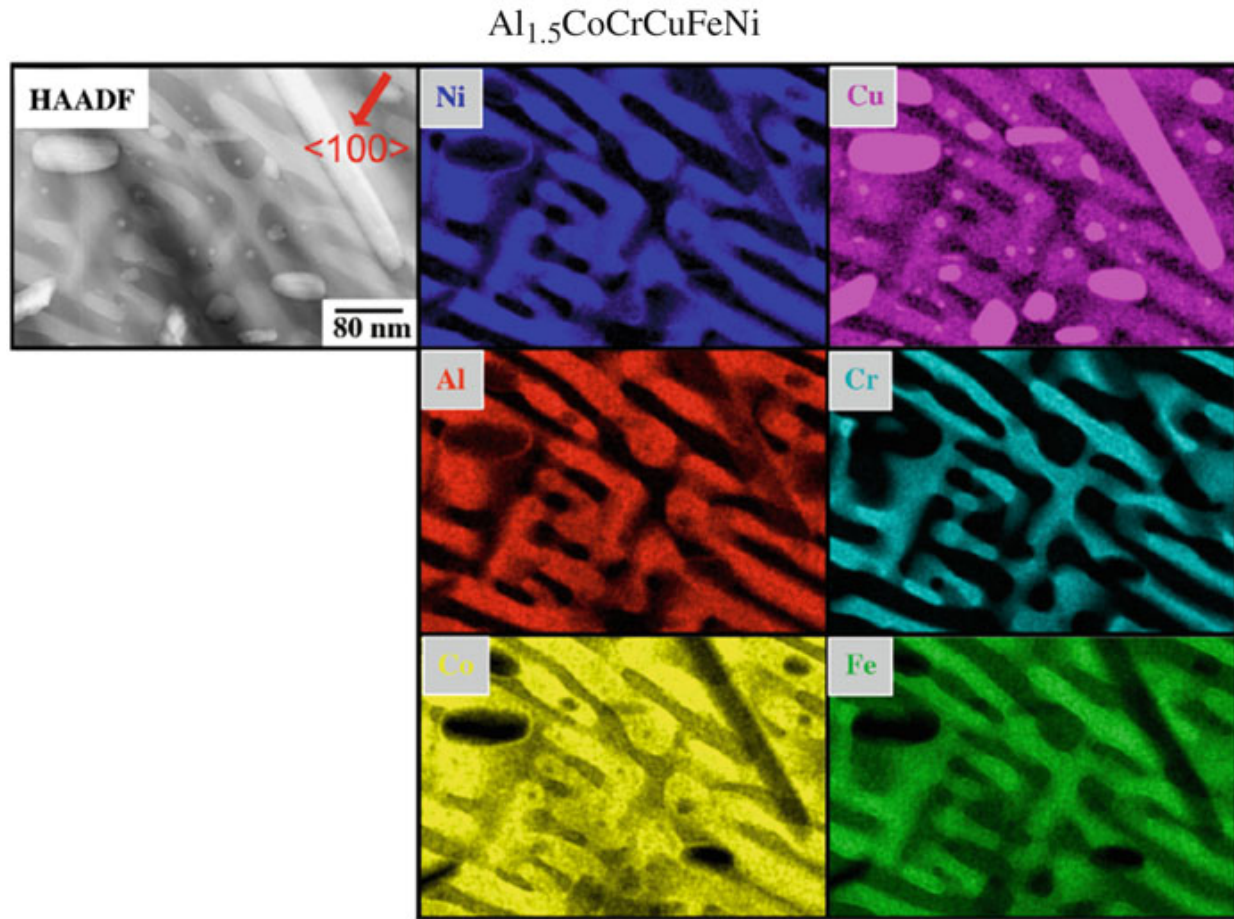


Fig. 4.13 HAADF and EDX maps of the nanoscale elemental segregation in the $\text{Al}_{1.5}\text{CoCrCuFeNi}$ alloy (From Ref. [15])

segregation of elements may be detected. In the case of $\text{Al}_{1.5}\text{CoCrCuFeNi}$ (Fig. 4.13), the elements, Ni, Al, Co, and small amounts of Fe and Cu, tend to partition to one of the platelike phases. The elements, Cr, Fe, and small amounts of Co, tend to partition to the other of the two platelike phases. In addition to the two main platelike phases, Cu-rich precipitates are seen on the EDX images.

At higher magnifications, individual columns of atoms can be resolved, and the coherent lattice structure of the different phases can be directly observed (Fig. 4.14). Sample orientation was an important consideration on these high-resolution HAADF images. It was determined that the interfacial planes (planes separating the BCC and B2 plates) have normals in the $<0\ 0\ 1>$ direction. The sample could thus be tilted about the $<0\ 0\ 1>$ axis without significantly changing the projection of the interfaces. When the sample was tilted such that the electron beam direction was near $<1\ 1\ 0>$, a pronounced contrast was found between the B2 and BCC regions. In particular, the spots (i.e., atom columns) in the B2 region have alternating intensities, forming rows of above-average and rows of below-average intensities (the top left portion of Fig. 4.14). These alternating intensities are consistent with the B2 structure, particularly, if the Al atoms preferentially occupy one sublattice, giving it a lower average atomic number, Z, compared to the other sublattice, which has more Ni, Co, and Fe. As expected, the atom column intensities

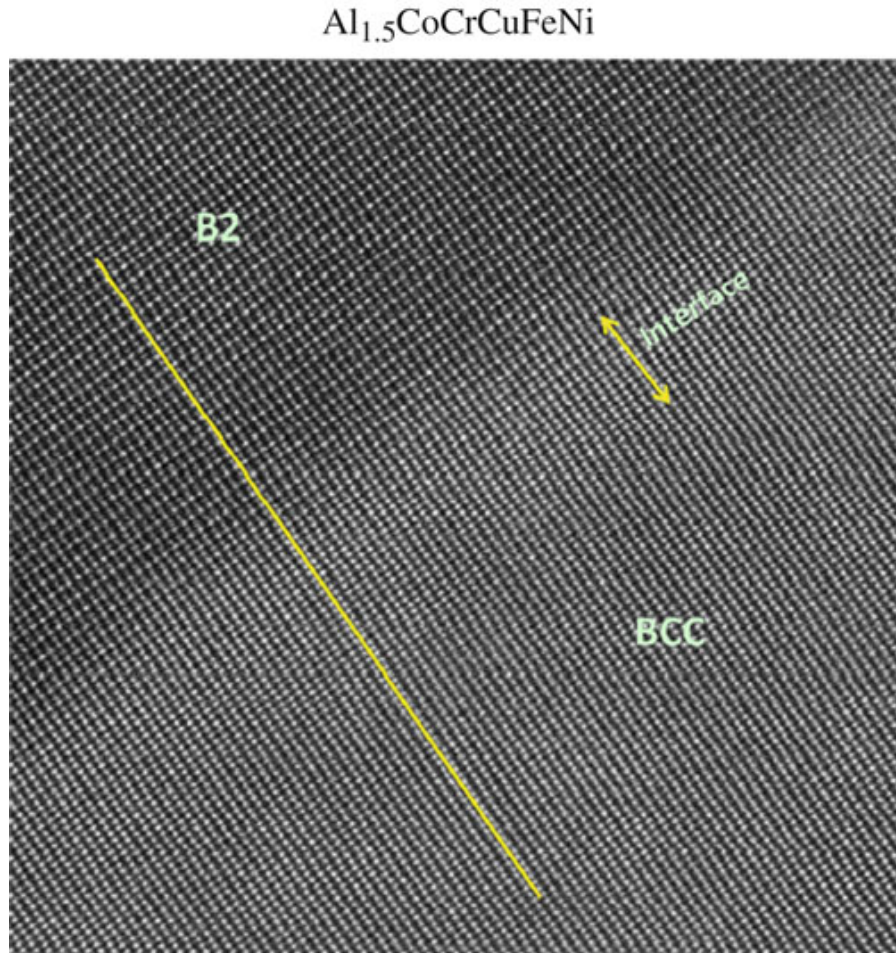


Fig. 4.14 High-resolution HAADF image showing individual atom columns in $\text{Al}_{1.5}\text{CoCrCuFeNi}$. The electron beam is aligned along the $<1\ 1\ 0>$ direction, and the interface normal is along $<0\ 0\ 1>$. As emphasized by the yellow line, the lattices of the phases are aligned and registered. The B2 phase has alternating intensities, and the BCC phase has much more uniform atom column intensities. An interface region, about 2-nm thick, has a different intensity profile than either the BCC or B2 regions. Each region is associated with a particular composition and structure (i.e., a distinct phase) (From Ref. [15])

in the BCC region (lower right) are nearly uniform, due to the disordered mixing of the elements in this phase, giving each atom column the same average Z.

The presently described HAADF study identified, for the first time, a distinct interface region between the B2 and BCC phases. The interface region is about 2-nm thick, and it has an intensity profile different from either the main B2 or the BCC phase. The interface is actually a secondary B2 phase, with a different composition than the main B2 phase. In particular, the interface phase is FeCo enriched and is similar to the binary FeCo intermetallic compound.

The atomic-scale resolution and Z-sensitivity of the HAADF measurements were crucial factors in identifying the interface phase, which may play an important role in the mechanical properties of the $\text{Al}_{1.5}\text{CoCrCuFeNi}$ HEA. In general, HAADF may play a critical role in determining the detailed microstructures of many HEAs.

4.6 Chemical Disorder Verified Using Anomalous X-Ray Diffraction and Neutron Scattering

Ordered structures (Fig. 4.3) have been detected in many HEAs, such as $\text{Al}_x\text{CoCrCuFeNi}$, based on the appearance of superstructure reflections in the XRD patterns (Fig. 4.2). The detection of the XRD superstructure reflections, however, is possible only when there is a sufficient difference in the X-ray scattering factors (f) of the elements in the ordered HEA phase. The same requirement applies to neutron diffraction, where the neutron scattering lengths (b) among the elements must be sufficiently different to be sensitive to ordered versus disordered distributions. It is important to note that the f and b follow very different trends across the periodic table, which is a great motivation for conducting complementary X-ray and neutron scattering studies.

In the case of the conventional XRD, using $\text{Cu K}\alpha$ radiation, for example, there are small differences in f for elements that are close in atomic numbers. Consequently, the conventional XRD cannot distinguish between ordered and disordered distributions of the transition metals, such as the possible configurations shown in Fig. 4.15. Aluminum, however, has a significantly lower f than the 3-d transition metals. Therefore, B2 order has been readily detected in the $\text{Al}_x\text{CoCrCuFeNi}$ family, even using the conventional XRD (Fig. 4.2). Despite the detection of the B2 order in the Al-containing HEAs, a detailed knowledge of the atomic distributions is not feasible, based upon the conventional XRD alone. The anomalous X-ray diffraction (AXRD), however, may be used to create the scattering contrast needed to detect ordering in HEAs.

Lucas et al. [17] applied AXRD (using the beamline, 33BM, at the Advanced Photon Source of the Argonne National Laboratory) and neutron scattering (using the ARCS spectrometer at the Spallation Neutron Source, Oak Ridge National Laboratory) to demonstrate that the CoCrFeNi alloy lacks the

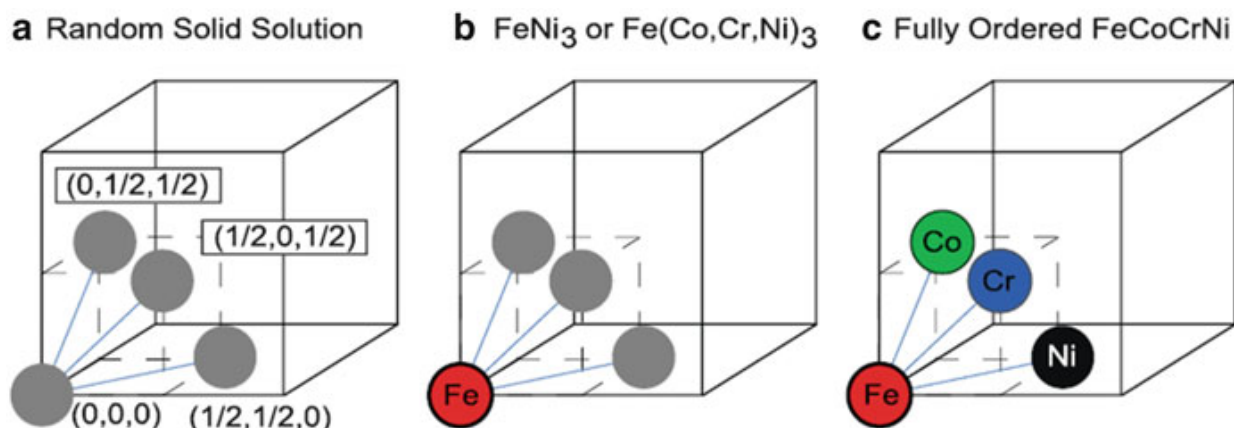


Fig. 4.15 Different atomic distributions on a simple cubic lattice (*solid box*) with the face-centered cubic atomic basis. (a) The random solid solution where gray atoms represent an average atom. (b) The L12-ordered structure where the gray atoms represent Ni atoms for FeNi_3 or a random mixture of Co, Cr, and Ni atoms for $\text{Fe}(\text{Co,Cr,Ni})_3$. (c) A fully ordered CoCrFeNi alloy (From Ref. [17])

long-range chemical order. The applicability of AXRD to this problem is best understood by examining expressions for the structure factor, F_{hkl} . The Bragg intensity of the hkl family of planes is proportional to $|F_{hkl}|^2$, where F_{hkl} is given by

$$F_{hkl} = \sum_{j=1}^N f_j \exp \left[2\pi i \left(hx_j + ky_j + lz_j \right) \right]. \quad (4.1)$$

Here, the unit cell contains N atoms, identified by $j = 1$ to N , located at positions, x_j , y_j , and z_j , and having atomic scattering factors, f_j . For the case of a CoCrFeNi alloy with a random FCC solid-solution structure, Eq. 4.1 may be written as [17]

$$F_{hkl}^{\text{rss}} = \langle f \rangle \left[1 + (-1)^{h+k} + (-1)^{h+l} + (-1)^{l+k} \right], \quad (4.2)$$

where $\langle f \rangle$ represents the concentration-weighted average scattering factor for the Co, Cr, Fe, and Ni atoms and the “rss” superscript identifies the random solid-solution phase. The rss structure factor of Eq. 4.2 gives the familiar FCC selection rule, allowing only non-mixed reflections (i.e., h , k , and l are all even or all odd). If the alloy is ordered, however, the elements will preferentially occupy certain sites, and the average scattering factor $\langle f \rangle$ will be replaced by the element-specific scattering factors in a structure factor. For example, if the ordering behavior is similar to the scheme shown in Fig. 4.15, then Eq. 4.1 may be written as

$$F_{hkl}^{\text{ord}} = \left[f_{\text{Fe}} + f_{\text{Ni}}(-1)^{h+k} + f_{\text{Cr}}(-1)^{h+l} + f_{\text{Co}}(-1)^{l+k} \right]. \quad (4.3)$$

For the conventional XRD with the CuK α radiation, $f_{\text{Fe}} \approx f_{\text{Ni}} \approx f_{\text{Cr}} \approx f_{\text{Co}}$, and the structure factors given in Eqs. 4.2 and 4.3 are nearly equivalent. Thus, no superstructure reflections will be detected, even if the alloy is ordered.

Using AXRD, the incident photon energies are tuned to the K-edge of a selected element, significantly reducing its scattering factor (Fig. 4.16). The sensitivity to chemical ordering is, thus, greatly enhanced. Lucas et al. [17] included the ordered FeNi_3 compound as a control sample in their study of the CoCrFeNi alloy to verify that their measurement was sensitive to the chemical order. Thus, when the CoCrFeNi alloy showed no signs of order in the AXRD measurements (Fig. 4.17), it made a convincing case that the alloy indeed lacked the long-range chemical order. The authors were careful to specify that the diffraction results address only the long-range order, and, therefore, short-range order could not be ruled out.

In the case of neutron diffraction, the scattering lengths, b_{Fe} , b_{Ni} , b_{Cr} , and b_{Co} , will replace the scattering factors, f , in Eq. 4.3. These neutron scattering lengths have a significant variation (Table 4.2) and, thus, provide a modest sensitivity to ordering. The CoCrFeNi study [17] included both neutron diffraction and AXRD measurements, with consistent results (i.e., the lack of the long-range order). Furthermore, the vibrational density of states was obtained from the inelastic

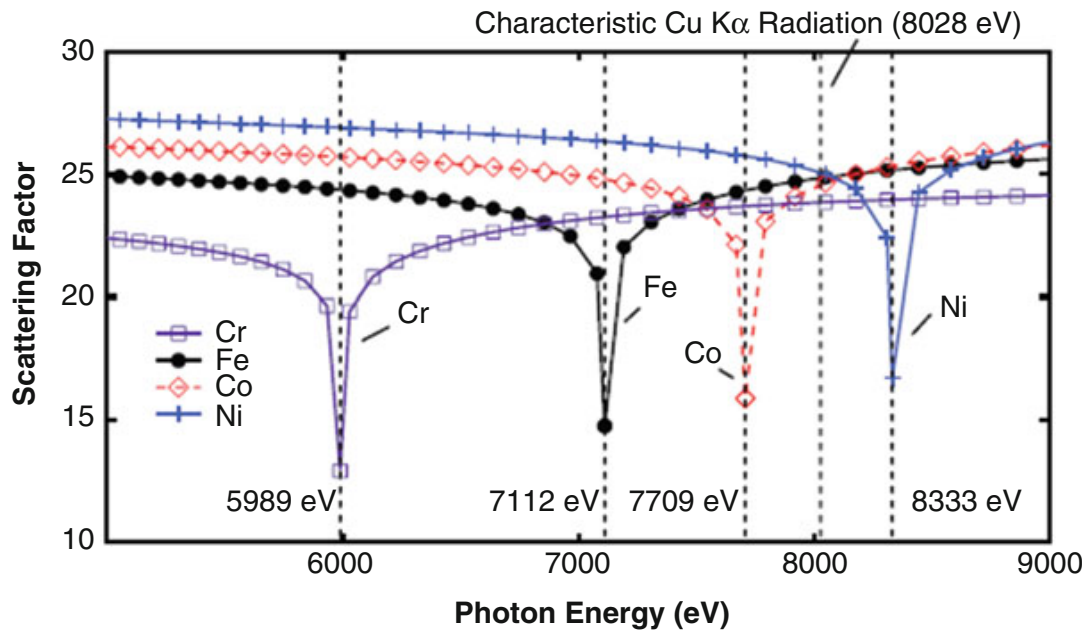


Fig. 4.16 The basis for AXRD. The real part of the scattering factor, f , as a function of photon energy, shows sharp dips. The dashed vertical lines are the energies used in AXRD experiments on the CoCrFeNi HEA (From Ref. [17])

scattering of neutrons. The inelastic neutron results demonstrated that the average forces on the Fe and Ni atoms are similar, providing more evidence of the disordered solution structure, independent of the diffraction results. Note that the inelastic measurements were less sensitive to the Co and Cr vibrational modes than the Fe and Ni modes. Therefore, it could not be concluded that all of the atoms experienced similar atomic forces.

The CoCrFeNi study summarized above demonstrates the great potential of techniques, such as AXRD and neutron scattering (both diffraction and inelastic scattering), for characterizing HEAs. Another complementary use of neutron and X-ray scattering is given in the next section.

4.7 Local Atomic Structure in the Ternary HfNbZr Alloy

Most HEAs [18] have a long-range crystal order, i.e., the atoms occupy positions on a periodic lattice. However, the atoms may fill the lattice sites in a disordered fashion, causing local distortions in the lattice structure, due to the different sizes of the atoms. These local distortions are an important feature of HEAs, potentially strengthening the material.

An important technique for studying the local atomic structure is the pair-distribution function (PDF) [19] analysis. The reduced PDF may be calculated from the Fourier transform of the structure function, $S(Q)$, experimentally determined from diffraction measurements, such that

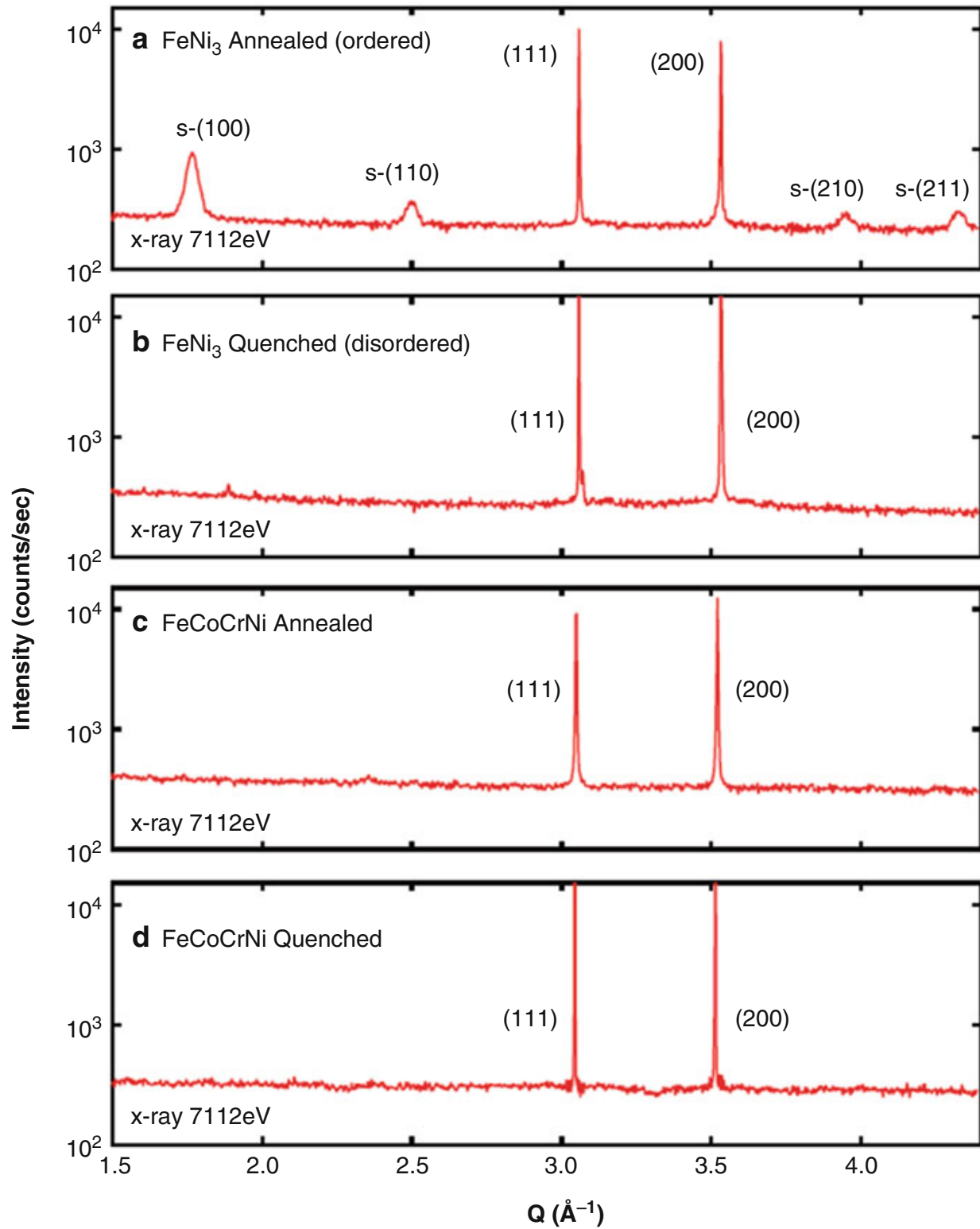


Fig. 4.17 Anomalous X-ray diffraction (AXRD) patterns comparing FeNi₃, which has a strong tendency to order, with the equimolar CoCrFeNi, which show no tendency to order. Both materials were measured in the annealed and quenched conditions (From Ref. [17])

Table 4.2 Neutron scattering lengths of selected elements

Element	b (fm)
Al	3.45
Co	2.49
Cr	3.64
Cu	7.72
Fe	9.45
Ni	10.3

A complete listing of neutron scattering lengths may be found in Ref. [28]

$$G(r) = \frac{2}{\pi} \int_0^{\infty} Q[S(Q) - 1] \sin(Qr) dQ, \quad (4.4)$$

where Q is the magnitude of the scattering vector in a reciprocal space and r is the interatomic distance. Software applications, such as PDFgui [20] and PDFgetN [21], may be used to obtain the PDF, which gives a real-space map of the atomic structure. The “pairs” in the PDF refer to the nearest neighbor, second neighbor, etc. pairs of atoms in the structure. The peaks in a PDF profile give the distances between these pairs. The PDF studies are often conducted, using optimized diffractometers at high-energy synchrotron X-ray and/or neutron user facilities (Table 4.1).

The HfNbZr alloy, containing only three elements, has been used as a test case to study the local structure of HEAs, in order to simplify sample preparation and data analysis [22]. Complementary PDF measurements were made using high-energy synchrotron X-rays (beamline ID6-C, Advanced Photon Source, Argonne National Laboratory, IL.) and neutrons (high-intensity powder diffractometer [HIPD] at the Los Alamos National Laboratory, NM).

Diffraction studies show that the HfNbZr alloy has a BCC structure in both bulk sample and in a thin film ~ 1.5 μm thick. The model PDF was calculated, using PDFgui [20], based upon the BCC structure obtained from the Rietveld refinement [23] of the neutron scattering intensities. The experimental neutron and synchrotron X-ray PDFs are plotted, along with the model calculation, in Fig. 4.18.

PDFs obtained from X-ray diffraction and neutron diffraction agree well with each other. The measured PDFs differ from the calculated PDF, particularly in the peak shape of the first two peaks, indicating local lattice distortion due to different atomic sizes in the solid solution (the metallic radii of Hf, Nb, and Zr are 1.59, 1.46, and 1.60 \AA , respectively).

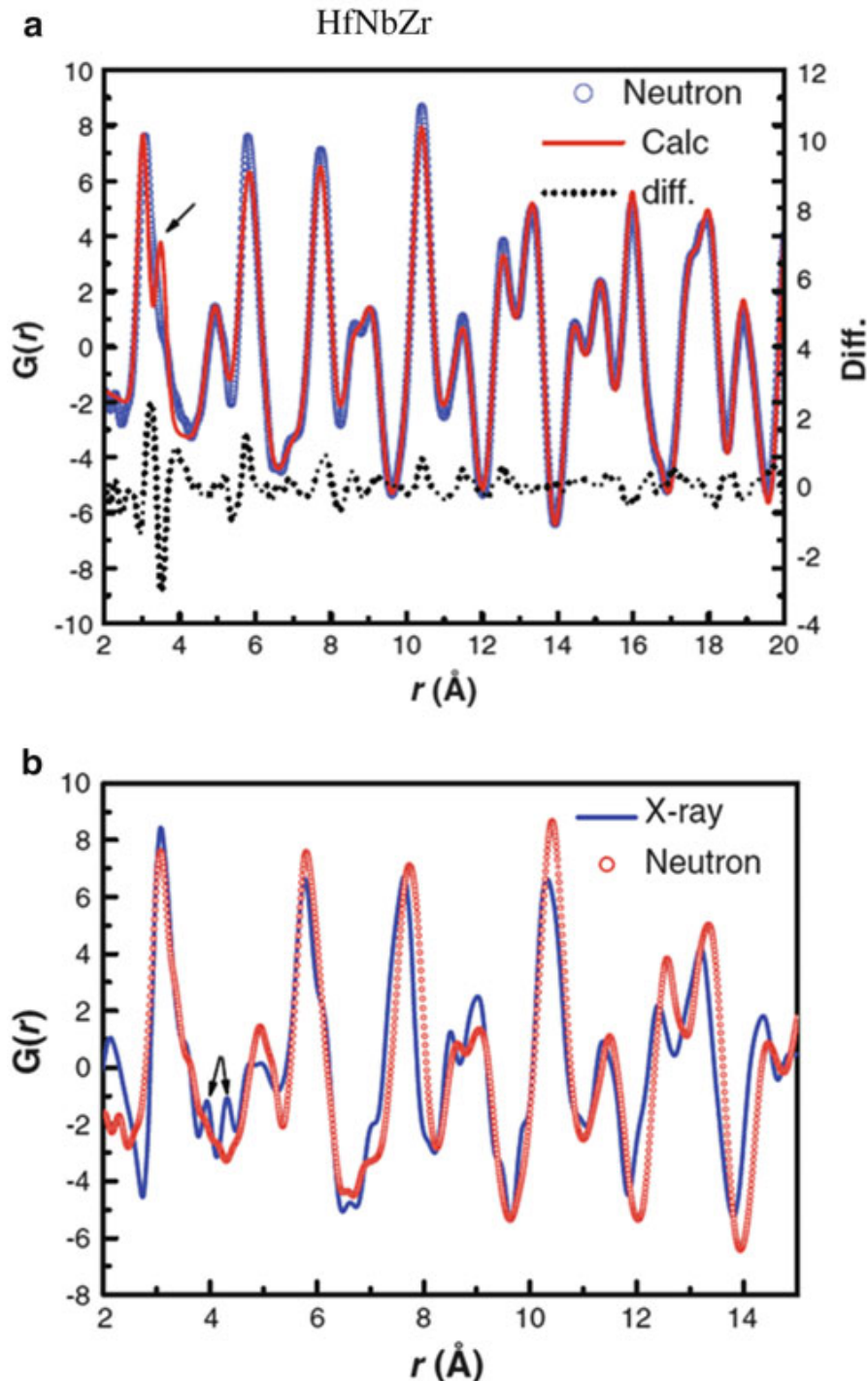


Fig. 4.18 Comparison of observed and calculated PDF (pair-distribution function) for HfNbZr. **(a)** The PDFs obtained from the neutron and the calculation agree well. The difference in the first two peaks (see arrow) originates from the size difference of the atoms in the lattice, which makes the second peak shadowed by the first peak in the neutron data. **(b)** In a comparison, the X-ray and neutron PDF agree in the main features. Some features, such as the X-ray peaks noted by the arrows, are attributed to noise (From Ref. [22])

4.8 Deviations from High-Entropy Atomic Configurations Characterized Using Complementary Neutron and X-Ray Diffraction Techniques

HEAs have a tendency to form solid solutions because of the high configurational entropy of mixing ($\Delta S_{\text{mix}}^{\text{conf}}$). Although disordered solid solutions are especially favored at high temperatures, as temperature decreases, the entropy effect is diminished in relation to the enthalpy effect, and phases with a higher degree of order may form. However, even when “ordered” phases form in HEAs, these phases may be only partially ordered, such that a persistent entropy effect influences the material properties. Thus, the HEA strategy applies not only to single-phase solid-solution structures but also to more complex alloys containing partially ordered intermetallic phases; see, for example, [9]. It is important, therefore, to study the detailed atomic distributions within HEAs and to quantify the $\Delta S_{\text{mix}}^{\text{conf}}$. Calculations of the entropy sources of HEAs, including configurational, vibrational, and electronic contributions, are presented in Chap 8 and 10 based on first-principles methods, while the total entropy and entropy of mixing of HEAs are also determined using the CALPHAD (acronym of *CALculation of PHAse Diagrams*) method as presented in Chap 12.

The ordered HEA phases often have seemingly simple crystal structures, such as the B2 structure (Fig. 4.3), which is best known in the context of binary intermetallic compounds. Experimentally, B2 ordering is easily detected by the presence of superlattice reflections in diffraction patterns that otherwise resemble BCC patterns (Fig. 4.2). The complexity arises, in the case of multi-element B2 phases, in determining the particular atomic arrangement associated with the B2 order. In principle, the atomic distribution may be directly solved by applying Rietveld refinements [23] to match multi-element structural models to the observed diffraction profiles. Such refinements have several fitting parameters, which may not strongly converge. The problem may be greatly simplified, however, by introducing a single parameter (δ) to represent the scattering contrast between the two sites in the B2 unit cell [9]. As shown below, the δ -parameter model may be used to interpret the observed diffraction data and ultimately to experimentally determine the $\Delta S_{\text{mix}}^{\text{conf}}$ of the B2-ordered structure. The approach may be adapted to other types of ordered, multi-element structures.

The HEA lattice sites are statistically populated by several elements, each with different neutron and X-ray scattering lengths. These sites may be characterized in terms of their average scattering lengths, which are generally different for neutrons versus X-rays. Therefore, complementary information may be obtained by combining the experimental techniques. Using the case of neutron scattering as an example, the average scattering length of an elemental distribution may be defined by [9]

$$b_{\text{av}} = \sum_{i=1}^n x_i b_i, \quad (4.5)$$

where x_i is the molar fraction and b_i is the neutron scattering length of the i th element. The B2 structure is characterized by two sublattices, α and β , which generally have different elemental distributions. The average scattering lengths associated with the α and β sublattices, respectively, may be written as

$$b_\alpha = b_{\text{av}} \times (1 + \delta) \quad (4.6)$$

and

$$b_\beta = b_{\text{av}} \times (1 - \delta). \quad (4.7)$$

The δ may be incorporated into Rietveld refinements as a unitless parameter, which is directly related to the neutron structure factors:

$$F_{hkl}^{\text{fund}} = b_\alpha + b_\beta, \quad (4.8)$$

$$F_{hkl}^{\text{super}} = b_\alpha - b_\beta, \quad (4.9)$$

where F_{hkl}^{fund} applies to the B2 fundamental reflections (those where the sum of the Miller indices, $h + k + l$, is an even number) and F_{hkl}^{super} to the superstructure reflections ($h + k + l$ is an odd number). Thus, the δ parameter is equal to the ratio of the superstructure and fundamental structure factors:

$$\delta = \frac{F_{hkl}^{\text{super}}}{F_{hkl}^{\text{fund}}} \quad (4.10)$$

The δ parameter may be determined experimentally by measuring the ratio of superstructure and fundamental peak intensities. The parameter has little significance, however, unless it can be associated with an actual structure. Fortunately, this relationship becomes apparent when the B2 structure is represented in terms of order parameters. In particular, let $x_{i\alpha}$ and $x_{i\beta}$ represent the molar fractions of the element, i , on the α and β sublattices, respectively, expressed as

$$x_{i\alpha} = x_i(1 + \eta_i) \quad (4.11)$$

and

$$x_{i\beta} = x_i(1 - \eta_i), \quad (4.12)$$

where η_i is the order parameter of the element, i . The η_i value may range from -1 to 1 , such that $\eta_i = 1$ represents an exclusive occupation of the α sublattice, $\eta_i = 0$ represents the random occupation of both sublattices, and $\eta_i = -1$ represents an

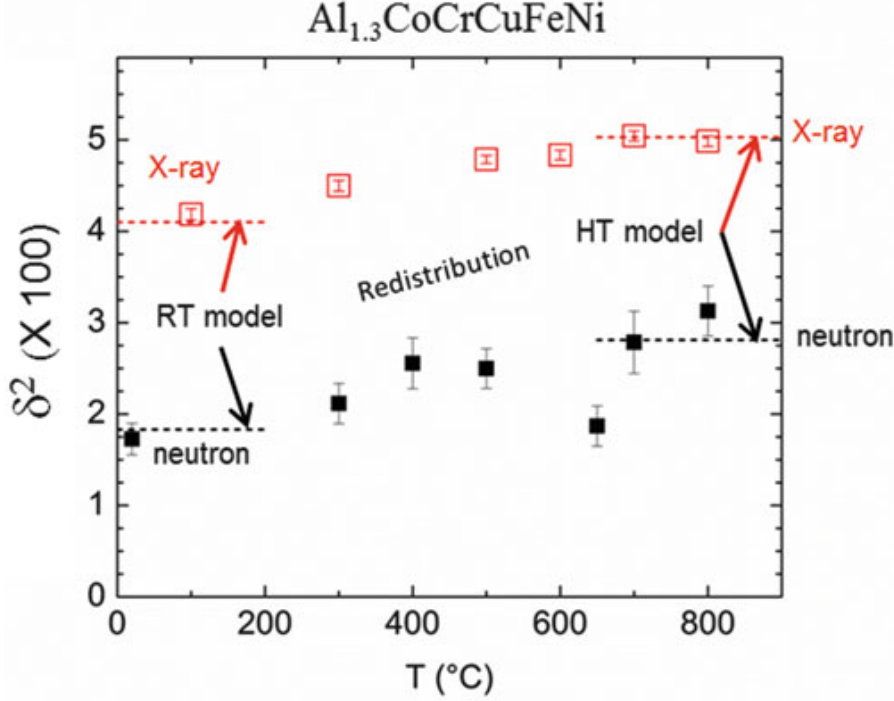


Fig. 4.19 Atomic distribution analysis. Based upon the integrated intensity ratios of the B2 (1 0 0) superstructure and (1 1 0) fundamental reflections, δ^2 values are plotted versus temperature, for both the synchrotron X-ray and neutron diffraction results. The values are determined from the least squares fitting of Gaussian curves to the observed peaks and the error bars from the standard errors of the Gaussian fits. The fitted values are compared to the model calculations, indicated by the dashed black (neutron calculations) and red (X-ray calculations) lines. Calculations for a room-temperature model (RT model) and high-temperature model (HT model) are shown. Atomic redistributions occur in the temperature region associated with the spinodal transformation in the $\text{Al}_{1.3}\text{CoCrCuFeNi}$ alloy. A spinodal BCC phase coexists at room temperature (Adapted from Ref. [9])

exclusive occupation of the β sublattice. The relationship between δ and the order parameters is given by

$$\delta = \frac{1}{b_{\text{av}}} \sum x_i \eta_i b_i \quad (4.13)$$

Using Eq. 4.13, atomic distribution models consistent with complementary neutron and X-ray diffraction results (Fig. 4.19) were identified for the complex $\text{Al}_{1.3}\text{CoCrCuFeNi}$ alloy [9]. At high temperatures, for example, the primary B2 phase was characterized by Al atoms preferentially occupying one sublattice, while all of the remaining transition-metal atoms were distributed on both sublattices. As temperature decreases, phase separation occurs, and the atomic distributions associated with the B2 phase undergo significant change. Despite all of the complex details, the $\Delta S_{\text{mix}}^{\text{conf}}$ of the multi-element B2 phase was quantified, according to

$$\Delta S_{\text{mix}}^{\text{conf}} = -\frac{R}{2} \sum_{i=1}^n \{x_i(1 + \eta_i)\ln[x_i(1 + \eta_i)] + x_i(1 - \eta_i)\ln[x_i(1 - \eta_i)]\}. \quad (4.14)$$

The previously used “ordered” versus “disordered” classifications were thus replaced by quantitative characterizations, and a persistent entropy effect was demonstrated [9].

4.9 In Situ Neutron Diffraction Study of the Deformation Behavior of the CoCrFeNi HEA

Using a specialized engineering diffractometer (Fig. 4.20), the deformation behavior of HEAs may be examined by applying stress to a sample mounted in a load frame, while simultaneously collecting neutron diffraction data. The applied stress leads to changes in the lattice constants (i.e., elastic lattice strains), which are determined by precisely tracking the positions of the Bragg reflections during loading. The lattice strain, ε_{hkl} , which may be strongly dependent on the crystal grain orientation, $h k l$, is calculated by

$$\varepsilon_{hkl} = \frac{d_{hkl} - d_{hkl,0}}{d_{hkl,0}}, \quad (4.15)$$

where d_{hkl} is the d-spacing for a given hkl reflection at a load and $d_{hkl,0}$ is the value at zero load. In addition to the peak positions, the relative intensities may change during loading, which often indicate changes in texture caused by plastic deformation. Another important aspect of the in situ neutron diffraction study is the simultaneous measurement of the macroscopic strain, determined by the load frame displacements and/or strain gauges on the sample. Ultimately, the combined observations of the lattice strain, macroscopic strain, and texture evolution may lead to a detailed understanding of the HEA deformation behavior.

The CoCrFeNi HEA was studied using the Spallation Neutron Source (SNS, Oak Ridge National Laboratory, TN, USA) VULCAN diffractometer [24], which has a high resolution ($\Delta d/d = 0.2\%$) over a wide range of d-spacings, and is equipped with a multi-axis load frame. The CoCrFeNi HEA consists mostly of a single FCC phase and therefore serves as an interesting comparison to conventional FCC metals [25]. One important comparison concerns the elastic lattice strain behavior, which, in conventional FCC metals, is anisotropic, with soft $<1\ 0\ 0>$ directions, attributed to the low atomic packing density and the large interplanar distance of the $(1\ 0\ 0)$ planes [26]. In the FCC CoCrFeNi alloy, however, the atomic separations and interactions vary from atom to atom. The VULCAN study shed some light on the impact of these local fluctuations on the deformation behavior of the CoCrFeNi alloy.

The neutron diffraction pattern (Fig. 4.21a) verified the FCC structure, and the tensile stress–strain curve (Fig. 4.21b) showed that the macroscopic deformation behavior of the CoCrFeNi alloy is similar to that of conventional FCC metals. In particular, the CoCrFeNi alloy has a low yield strength (~200 MPa), large tensile

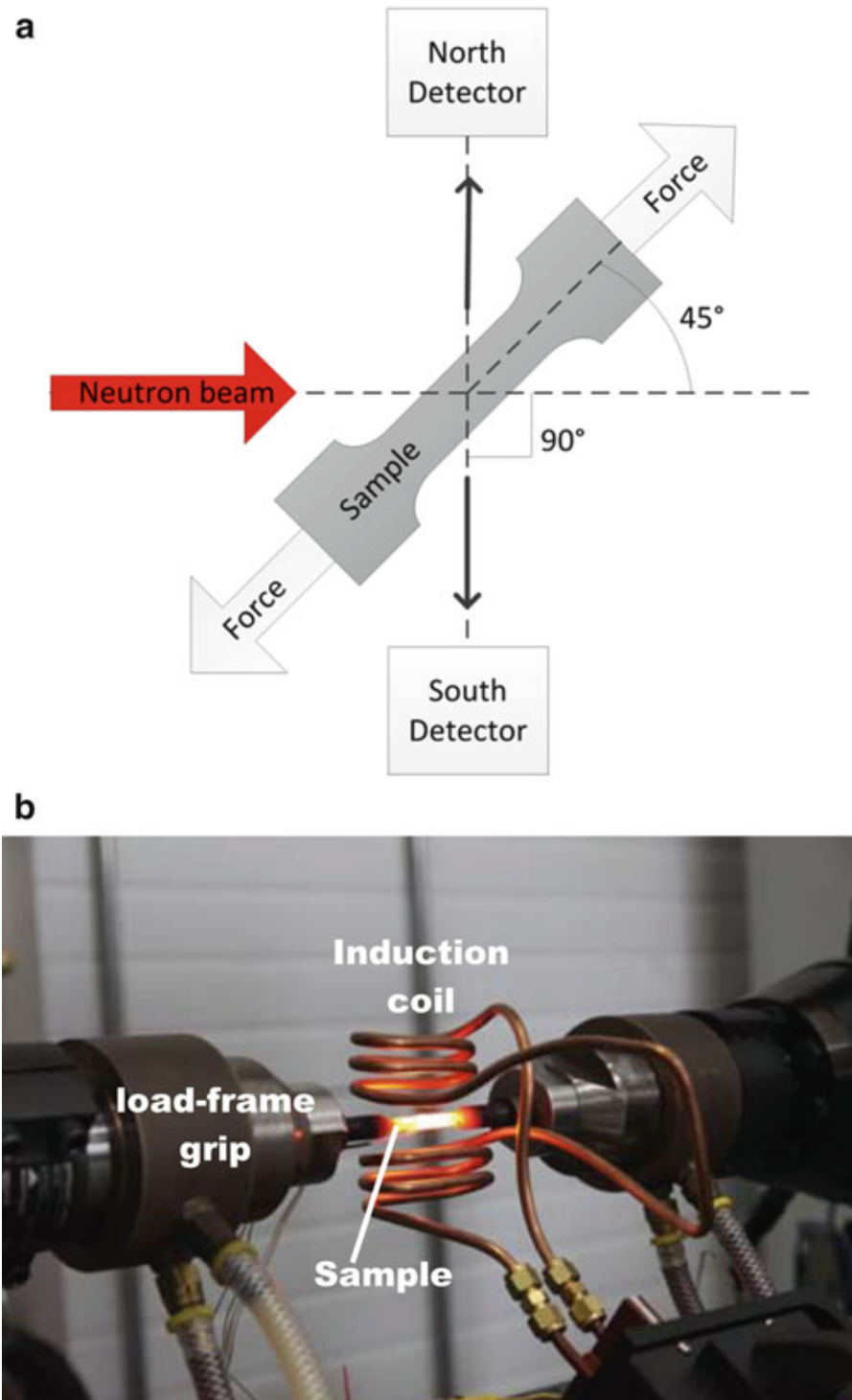


Fig. 4.20 Diffraction geometry for measuring lattice strains due to applied tensile loads. (a) Schematic diagram showing a sample oriented at 45° to the incident neutron beam and two detectors at 90° to the beam direction. The scattering vectors of the diffracted beams collected on the North and South detectors are transverse and parallel to the sample axis, respectively. Thus, transverse and parallel lattice strains are detected separately. (b) [From the SNS website, <http://neutrons.ornl.gov>] A photograph of a sample mounted on a load frame, and heated by an induction coil, at the SNS VULCAN instrument

plasticity (~40 %), and a work-hardening coefficient of 0.47, which is similar to that of FCC copper. The lattice strains (Fig. 4.22a) and the deformation-induced changes in peak intensities (Fig. 4.22b) provide further indications that the CoCrFeNi alloy has deformation behavior similar to conventional FCC metals.

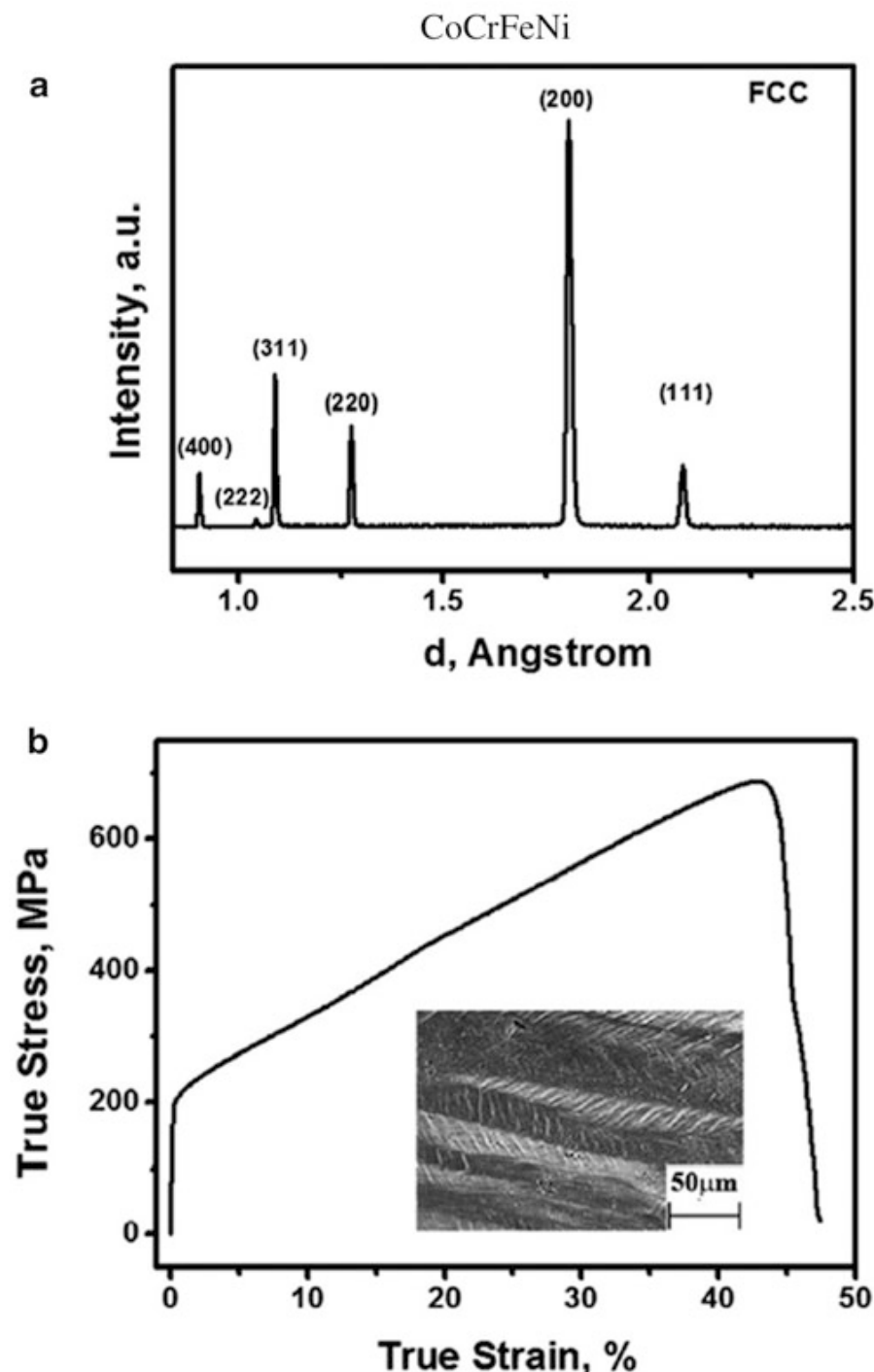


Fig. 4.21 (a) The diffraction pattern of CoCrFeNi confirms that the alloy is mostly a single FCC phase. (b) The tensile stress-strain curve shows the same features as conventional FCC metals, such as low yield strength (~ 200 MPa), large tensile plasticity, and considerable work hardening. The inset shows an SEM image of the lateral fracture surface, with typical FCC features, such as the numerous slip bands (From Ref. [25])

The $[2\ 0\ 0]$ grains have a significantly larger elastic strain than the other orientations ($[1\ 1\ 1]$, $[2\ 2\ 0]$, $[3\ 1\ 1]$, and $[3\ 3\ 1]$), based upon d -spacing shifts (Eq. 4.15), which is expected in FCC metals. The ratio of the elastic stiffness (i.e., the slope of stress–lattice strain curves) in the $<1\ 1\ 1>$ and $<1\ 0\ 0>$ directions was found to be 1.98, close to pure nickel [25]. Finally, the deformation-induced intensity changes

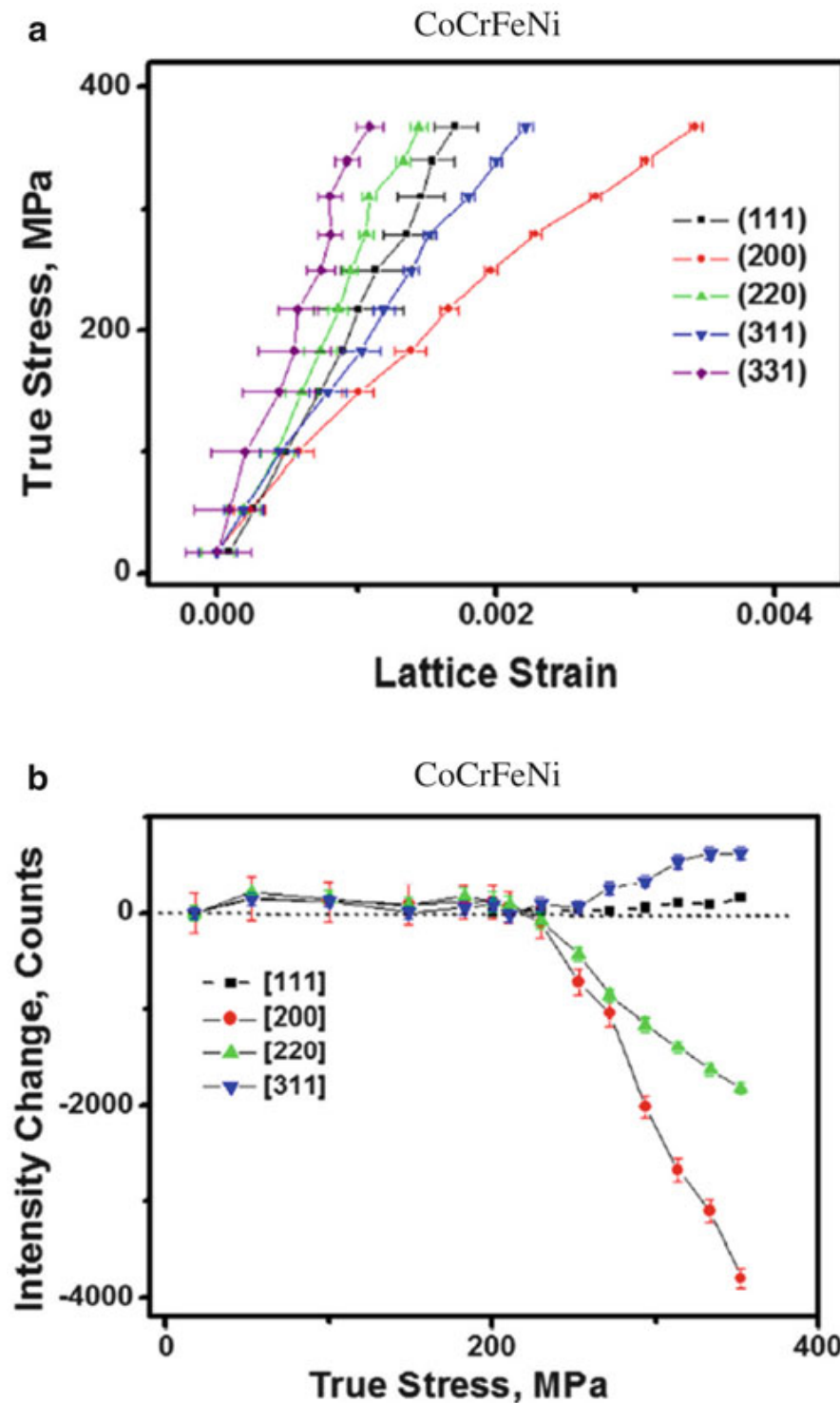


Fig. 4.22 (a) The evolution of lattice strain shows a strong, anisotropic strain response, typical of an FCC structure. (b) The peak intensities begin to change above the yield stress (~ 200 MPa) due to plastic deformation-induced texture development (From Ref. [25])

(Fig. 4.22b) are similar to those observed in FCC metals and conventional FCC alloys, in which the textured structure forms during tensile elongation.

The technique of in situ neutron diffraction during loading provides both macroscopic and microscopic information about the deformation behaviors and mechanisms in HEAs. In the case of the CoCrFeNi alloy, the technique provided a rigorous verification that the room-temperature deformation behavior was similar to that of conventional FCC metals. Of course, this similarity does not necessarily

hold for all HEAs and for different temperature ranges. This neutron technique will likely be employed on many other HEAs and under a variety of environmental conditions.

4.10 Future Work

The experimental studies of HEAs are becoming more thorough and challenging, as the field advances. For example, there is a growing need to move beyond room-temperature experiments and conduct structural and mechanical characterizations over wide temperature ranges, as exemplified in recent high-impact HEA research [11]. Given that the influence of entropy is linked to temperature, it may be expected that HEA characterizations increasingly involve temperature as a variable and that they become better integrated with theoretical studies. For the most part, the technology to perform *in situ* structural and mechanical characterizations throughout wide temperature ranges already exists. As shown in Fig. 4.20b, for example, the combination of loading, heating, and neutron diffraction is available at major user facilities. However, the capabilities must continue to advance and keep pace with new trends in HEA characterization, such as the study of serration behavior [4, 27].

Microscopy studies will continue to play a large role in HEA research, with perhaps increased emphasis on understanding how the microstructures can be manipulated by fabrication methods and processing techniques [4]. Thus, an increased integration of the fabrication, processing, and microstructural studies is needed. Furthermore, a greater understanding of how plastic deformation affects the microstructure, and even the nanostructure, is required. Features must be characterized across many length scales and in three dimensions. Advances in three-dimensional microstructure characterization should be applied to HEAs in order to learn more about properties such as fracture toughness and fracture mechanisms [4, 11]. Quite literally, researchers will dig beneath the surface when studying HEA microstructures and properties.

The presence and influence of local lattice strains, as a potential strengthening mechanism, for example, has been postulated from the early days of the HEA research. Yet, few studies have directly addressed this important aspect of HEAs. Perhaps the first local structure study of HEAs was described above, in which the pair-distribution-function (PDF) analysis was applied to the ternary HfNbZr alloy [22]. The presence of local lattice distortions was indeed verified. However, the detailed nature and influence of the local lattice distortions are still not well understood. Therefore, there is much work to be done in the area of local HEA structures and great opportunities to conduct groundbreaking research.

One theme that emerges from the advanced characterization examples described in this chapter is the importance of integrating different techniques, such as neutron and X-ray scattering, and multiple imaging techniques, ranging from the optical examination of fracture surfaces to the atom probe tomography studies of the

nanoscale structures. An advanced understanding of HEAs must encompass features across several length scales and behaviors under a wide range of environmental conditions. A growing number of scientists will likely be attracted to HEA research, in pursuit of many exciting questions.

4.11 Conclusion

Advanced characterization techniques, as applied to HEAs, often involve an integration of many methods and experimental equipment, such as SEM, TEM (with bright- and dark-field techniques), SAED, and APT. In other cases, novel techniques are used, such as the splat-quenched sample preparation [8]. In general, the advanced experimental characterizations are difficult and require considerable resources. Many researchers take advantage of the instruments operated at the major user facilities (Table 4.1), which are typically available through a peer-reviewed proposal process. Although great efforts are required to conduct the high-impact research in the area of HEAs, the potential reward is great. Many major questions remain to be answered: What are the best ways to characterize local lattice strains and determine their effect on the strength and deformation behavior of HEAs? How does the deformation behavior of HEAs differ from that of conventional alloys, and what microstructural characterization techniques will we use to better understand it? What microstructural features (grain size, twinning, dislocation structures, chemical homogeneity, etc.) are most crucial for producing HEAs with exceptional properties? Significant discoveries will likely be made, as these questions are studied.

Acknowledgments The authors acknowledge the financial supports by Department of Energy (DOE) Office of Nuclear Energy's Nuclear Energy University Programs (NEUP, grant #00119262), the DOE Office of Fossil Energy, NETL (DE-FE0008855 and DE-FE-0011194), and the US Army Office Project (W911NF-13-1-0438).

References

1. Yeh JW, Chen SK, Lin SJ, Gan JY, Chin TS, Shun TT, Tsau CH, Chang SY (2004) Nanostructured high-entropy alloys with multiple principal elements: novel alloy design concepts and outcomes. *Adv Eng Mater* 6(5):299–303. doi:[10.1002/adem.200300567](https://doi.org/10.1002/adem.200300567)
2. Tong CJ, Chen YL, Chen SK, Yeh JW, Shun TT, Tsau CH, Lin SJ, Chang SY (2005) Microstructure characterization of Al_xCoCrCuFeNi high-entropy alloy system with multiprincipal elements. *Metall Mater Trans A Phys Metall Mater Sci* 36A(4):881–893. doi:[10.1007/s11661-005-0283-0](https://doi.org/10.1007/s11661-005-0283-0)
3. Takeuchi A, Amiya K, Wada T, Yubuta K, Zhang W (2014) High-entropy alloys with a hexagonal close-packed structure designed by equi-atomic alloy strategy and binary phase diagrams. *JOM* 66(10):1984–1992. doi:[10.1007/s11837-014-1085-x](https://doi.org/10.1007/s11837-014-1085-x)

4. Zhang Y, Zuo TT, Tang Z, Gao MC, Dahmen KA, Liaw PK, Lu ZP (2014) Microstructures and properties of high-entropy alloys. *Prog Mater Sci* 61 (0):1–93. <http://dx.doi.org/10.1016/j.pmatsci.2013.10.001>
5. Tang Z, Gao MC, Diao HY, Yang TF, Liu JP, Zuo TT, Zhang Y, Lu ZP, Cheng YQ, Zhang YW, Dahmen KA, Liaw PK, Egami T (2013) Aluminum alloying effects on lattice types, microstructures, and mechanical behavior of high-entropy alloy systems. *JOM* 65 (12):1848–1858. doi:[10.1007/s11837-013-0776-z](https://doi.org/10.1007/s11837-013-0776-z)
6. Zhang Y, Lu ZP, Ma SG, Liaw PK, Tang Z, Cheng YQ, Gao MC (2014) Guidelines in predicting phase formation of high-entropy alloys. *MRS Communications* 4(02):57–62. doi:[10.1557/mrc.2014.11](https://doi.org/10.1557/mrc.2014.11)
7. Wang YP, Li BS, Fu HZ (2009) Solid solution or intermetallics in a high-entropy alloy. *Adv Eng Mater* 11(8):641–644. doi:[10.1002/adem.200900057](https://doi.org/10.1002/adem.200900057)
8. Singh S, Wanderka N, Murty BS, Glatzel U, Banhart J (2011) Decomposition in multi-component AlCoCrCuFeNi high-entropy alloy. *Acta Mater* 59(1):182–190. doi:[10.1016/j.actamat.2010.09.023](https://doi.org/10.1016/j.actamat.2010.09.023)
9. Santodonato LJ, Zhang Y, Feygenson M, Parish C, Neufeld J, Weber RJR, Gao MC, Tang Z, Liaw PK (2015) Deviation from high-entropy configurations in the atomic distributions of a multi-principal-element alloy. *Nat Commun* 6:1–64. doi:[10.1038/ncomms6964](https://doi.org/10.1038/ncomms6964)
10. Cantor B, Chang ITH, Knight P, Vincent AJB (2004) Microstructural development in equiatomic multicomponent alloys. *Mater Sci Eng A Struct Mater Prop Microstruct Process* 375:213–218. doi:[10.1016/j.mesa.2003.10.257](https://doi.org/10.1016/j.mesa.2003.10.257)
11. Gludovatz B, Hohenwarter A, Cattoor D, Chang EH, George EP, Ritchie RO (2014) A fracture-resistant high-entropy alloy for cryogenic applications. *Science* 345(6201):1153–1158. doi:[10.1126/science.1254581](https://doi.org/10.1126/science.1254581)
12. International A (2013) Standard test method for measurement of fracture toughness. ASTM International, West Conshohocken, PA, pp E1820–E1821
13. Online supplementary materials to ref. 7
14. Liu Z, Guo S, Liu X, Ye J, Yang Y, Wang X-L, Yang L, An K, Liu CT (2011) Micromechanical characterization of casting-induced inhomogeneity in an Al0.8CoCrCuFeNi high-entropy alloy. *Scr Mater* 64(9):868–871. doi:[10.1016/j.bbr.2011.03.031](https://doi.org/10.1016/j.bbr.2011.03.031)
15. Welk BA, Williams REA, Viswanathan GB, Gibson MA, Liaw PK, Fraser HL (2013) Nature of the interfaces between the constituent phases in the high entropy alloy CoCrCuFeNiAl. *Ultramicroscopy* 134:193–199. doi:[10.1016/j.ultramic.2013.06.006](https://doi.org/10.1016/j.ultramic.2013.06.006)
16. Liu J, Cowley JM (1991) Imaging with high-angle scattered electrons and secondary electrons in the STEM. *Ultramicroscopy* 37(1–4):50–71. [http://dx.doi.org/10.1016/0304-3991\(91\)90006-R](http://dx.doi.org/10.1016/0304-3991(91)90006-R)
17. Lucas MS, Wilks GB, Mauger L, Muñoz JA, Senkov ON, Michel E, Horwath J, Semiatin SL, Stone MB, Abernathy DL, Karapetrova E (2012) Absence of long-range chemical ordering in equimolar FeCoCrNi. *Appl Phys Lett* 100 (25):2519071–2519074. <http://dx.doi.org/10.1063/1.4730327>
18. Takeuchi A, Chen N, Wada T, Yokoyama Y, Kato H, Inoue A, Yeh JW (2011) Pd20Pt20Cu20Ni20P20 high-entropy alloy as a bulk metallic glass in the centimeter. *Intermetallics* 19(10):1546–1554
19. Proffen T, Billinge SJL, Egami T, Louca D (2003) Structural analysis of complex materials using the atomic pair distribution function - a practical guide. *Zeitschrift Fur Kristallographie* 218(2):132–143. doi:[10.1524/zkri.218.2.132.20664](https://doi.org/10.1524/zkri.218.2.132.20664)
20. Farrow CL, Juhas P, Liu JW, Bryndin D, Bozin ES, Bloch J, Proffen T, Billinge SJL (2007) PDFfit2 and PDFgui: computer programs for studying nanostructure in crystals. *J Phys Condens Matter* 19(33):335219. doi:[10.1088/0953-8984/19/33/335219](https://doi.org/10.1088/0953-8984/19/33/335219)
21. Peterson PF, Gutmann M, Proffen T, Billinge SJL (2000) *J Appl Crystallogr* 33:1192
22. Guo W, Dmowski W, Noh J-Y, Rack P, Liaw P, Egami T (2013) Local atomic structure of a high-entropy alloy: an X-ray and neutron scattering study. *Metall Mater Trans A* 44:1994–1997

23. Rietveld H (1969) A profile refinement method for nuclear and magnetic structures. *Journal of Applied Crystallography* 2(2):65–71. doi:[10.1107/S0021889869006558](https://doi.org/10.1107/S0021889869006558)
24. Wang XL, Holden TM, Rennich GQ, Stoica AD, Liaw PK, Choo H, Hubbard CR (2006) VULCAN—The engineering diffractometer at the SNS. *Phys B: Condens Matter* 385–386, Part 1 (0):673–675. <http://dx.doi.org/10.1016/j.physb.2006.06.103>
25. Wu Y, Liu WH, Wang XL, Ma D, Stoica AD, Nieh TG, He ZB, Lu ZP (2014) In-situ neutron diffraction study of deformation behavior of a multi-component high-entropy alloy. *Appl Phys Lett* 104(5). <http://dx.doi.org/10.1063/1.4863748>
26. An K, Skorpenske H, Stoica A, Ma D, Wang X-L, Cakmak E (2011) First In Situ lattice strains measurements under load at VULCAN. *Metall Mater Trans A* 42(1):95–99. doi:[10.1007/s11661-010-0495-9](https://doi.org/10.1007/s11661-010-0495-9)
27. Antonaglia J, Xie X, Tang Z, Tsai CW, Qiao JW, Zhang Y, Laktionova MO, Tabachnikova ED, Yeh JW, Senkov ON, Gao MC, Uhl JT, Liaw PK, Dahmen KA (2014) Temperature effects on deformation and serration behavior of high-entropy alloys (HEAs). *JOM* 66 (10):2002–2008. doi:[10.1007/s11837-014-1130-9](https://doi.org/10.1007/s11837-014-1130-9)
28. Shirane G, Shapiro SM, Tranquada JM (2002) Neutron Scattering with a triple-axis spectrometer. Cambridge University Press, Cambridge, UK

Chapter 5

Fabrication Routes

Yong Zhang, Carl C. Koch, Sheng Guo Ma, Hui Zhang, and Ye Pan

Abstract The high-entropy alloys (HEAs) are essentially solid-solution alloys that contain multiprincipal elements in simple crystal structure such as body-centered cubic (BCC), face-centered cubic (FCC), and hexagonal close-packed (HCP) lattices. The typical manufacturing routes for traditional materials can be applied to producing HEAs. Depending on how the constituent elements are mixed, the processes are divided into liquid melting, solid-state mechanical alloying, and gas-state mixing. This chapter reviews those typical manufacturing routes in producing HEAs, including ingot metallurgy, powder metallurgy, coating, rapid solidification, mechanical alloying, single crystals prepared by using the Bridgman method, laser cladding, and thin film sputtering. Comparisons between these methods and the resulting structures are provided.

Keywords Fabrication routes • Liquid melting • Mechanical alloying • Vapor deposition • Micro-segregation • Single crystal • Bridgman method • Laser cladding • Thin film • Nanostructure • Microstructure • High-entropy alloys (HEAs)

Y. Zhang (✉)

State Key Laboratory for Advanced Metals and Materials, University of Science and Technology Beijing, Beijing, People's Republic of China
e-mail: drzhangy@ustb.edu.cn

C.C. Koch

Department of Materials Science and Engineering, North Carolina State University, 911 Partners Way, suite 3002, Raleigh, NC 27606, USA
e-mail: ckoch@ncsu.edu

S.G. Ma

Institute of Applied Mechanics and Biomedical Engineering, Taiyuan University of Technology, Taiyuan, Shanxi Province 030024, People's Republic of China
e-mail: mashengguo@tyut.edu.cn

H. Zhang

School of Materials Science and Engineering, Anhui University of Technology, Ma'anshan, Anhui 243002, People's Republic of China
e-mail: huihang@ahut.edu.cn

Y. Pan

School of Material Science and Engineering, Southeast University, Nanjing 211189, People's Republic of China
e-mail: panye@seu.edu.cn

5.1 Introduction

The fabrication processes of high-entropy alloys can be categorized into three major routes, as shown in Fig. 5.1. The first route is from the liquid state, which includes arc melting, electric resistance melting, inductive melting, laser melting, laser cladding, and Laser Enhanced Net Shape (LENS) forming. The second route is from the solid state, which mainly includes mechanical alloying and subsequent consolidation process. We can also mix the elements from the vapor state. This route includes sputter deposition, pulse laser deposition (PLD), atomic layer deposition (ALD), molecular beam epitaxy (MBE), and vapor phase deposition to prepare the films on substrates.

5.2 Liquid-State Route

5.2.1 Arc Melting

Arc melting is the most common technique to prepare HEAs [1, 2], by which all the constituent elements are fully mixed in the liquid state and then solidified in the copper crucible. Multiple repetitive melting and solidification are often carried out to ensure the chemical homogeneity of the alloys. The shape of solidified ingots is button-like in the bowl-like copper crucible. Another version is to let the melt drop

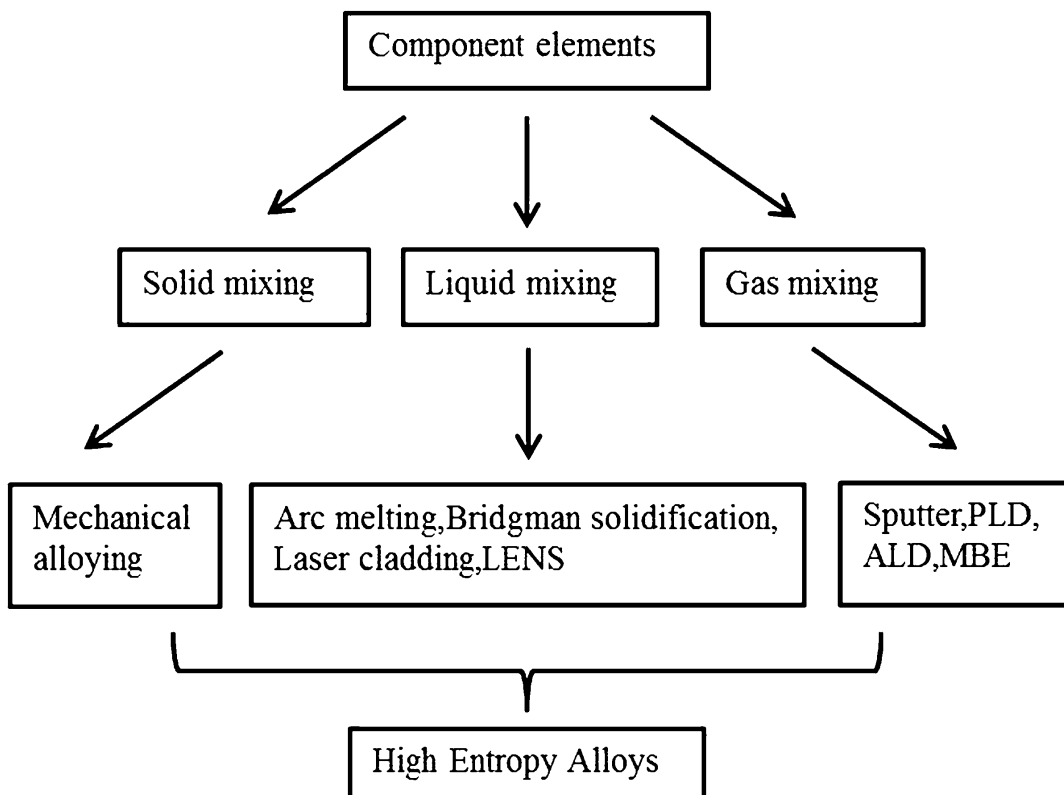


Fig. 5.1 Summary of the fabricating routes for HEAs

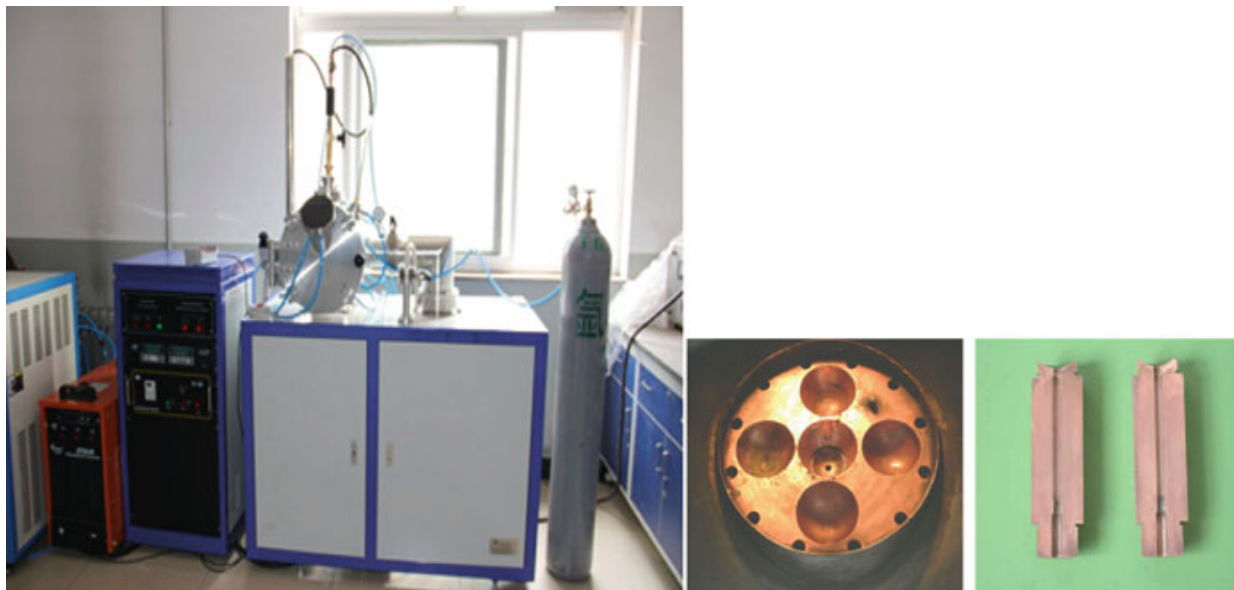


Fig. 5.2 Photograph of the arc-melting and casting equipment (the right two are the copper crucible and copper mold)

into a copper mold through the hole pre-machined in the bottom of the copper crucible. Figure 5.2 shows the picture of such an arc-melting and copper-mold-casting equipment. The copper crucible and split copper mold are also shown. By this method, cylindrical ingots can be achieved with higher cooling rate. The samples are also convenient to be machined into specimens for tensile/compressive testing. Based on this casting method, a series of HEAs with unique properties have been found. For instance, Zhou et al. [3] have applied this technique to prepare AlCoCrFeNiTi_x (x in molar ratio) HEAs, which exhibited body-centered cubic (BCC) solid-solution structures and excellent compressive properties such as ultrahigh fracture strength and significant work-hardening capability. Wang et al. [4] found that the alloy strength and plasticity of the AlCoCrFeNi HEAs were enhanced significantly by decreasing the diameter of cast samples and thus increasing the cooling rate during solidification.

However, the problem with this technique is that the solidification process cannot be easily controlled due to the nature of rapid solidification, which thus leads to a varying microstructure characteristic from the surface to the center of alloy samples, e.g., inhomogeneous distribution of the as-cast dendrites in morphology and size, ranging from fine grains (label A) to columnar dendrites (label B) and then to coarse equiaxed dendrites (label C), as shown in Fig. 5.3, and hence an uncontrollable macroscopic property [5]. In addition, a series of inevitable as-cast defects, including elemental segregation, suppression of equilibrium phases, microscopic and macroscopic residual stresses, cracks, and porosities, may also have a negative effect on the mechanical properties of HEAs. Measures should be taken to reduce or eliminate these defects in the HEAs. Therefore, in the following sections, a series of fabricating routes that can provide an improved balance of strength and damage tolerance are introduced.

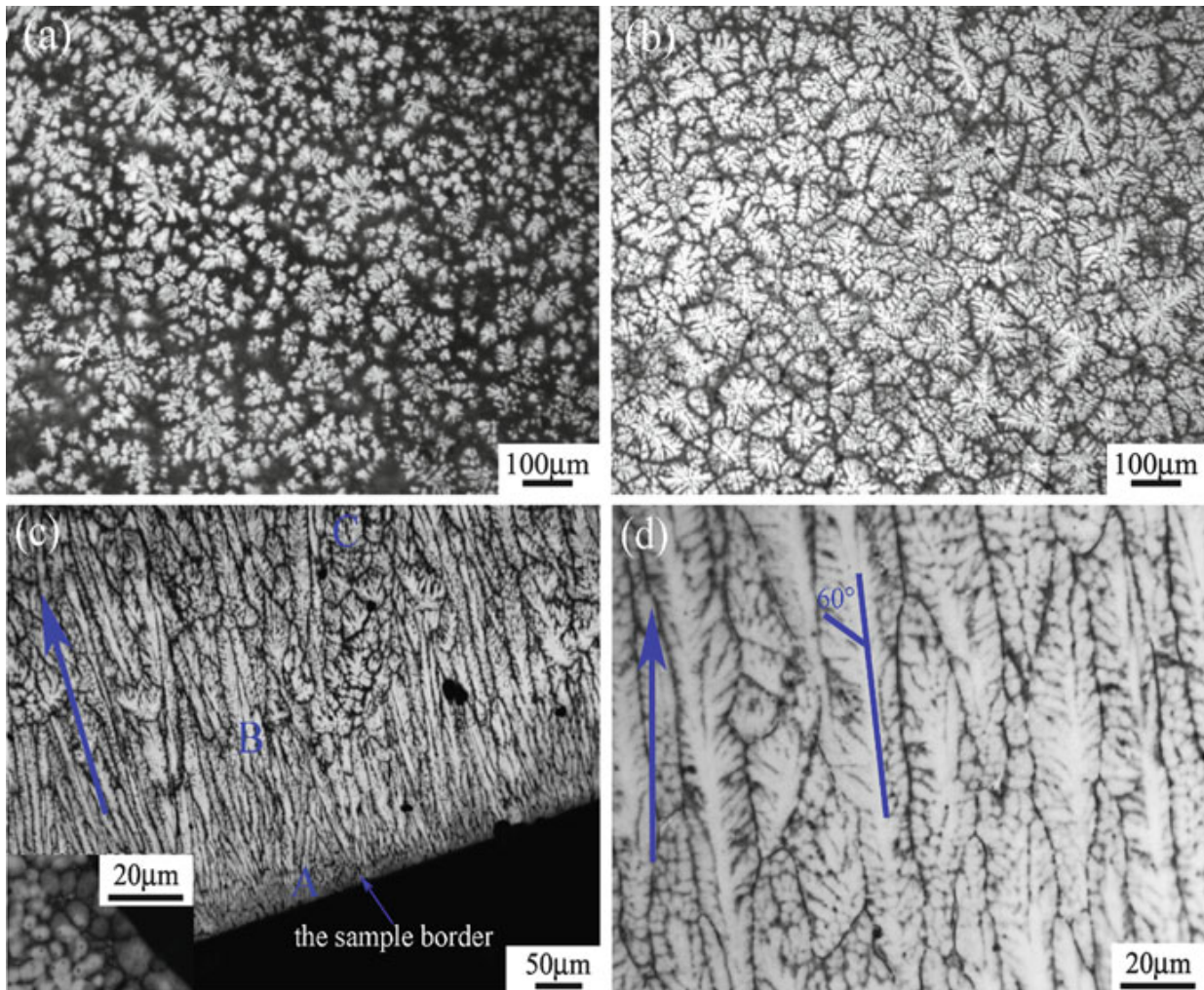


Fig. 5.3 The optical micrographs of the AlCoCrFeNi HEA cylindrical samples by the arc-melting and copper-mold casting: **(a)** and **(b)** central equiaxed dendrites; **(c)** typical as-cast structure with fine grains viewed in the inset; **(d)** transitional columnar dendrites [5]

5.2.2 Bridgman Solidification Casting

Compared with the common casting, the Bridgman solidification technique (BST) can be effectively used for the microstructure control and property optimization of HEAs. Specifically, the direction of the thermal conduction and extraction for rod-shaped samples obtained by BST is intensively along the longitudinal direction, which assures the microstructural growth direction; two important processing parameters, namely, the temperature gradient and growth rate, can be precisely controlled by adjusting the heating power and withdrawal velocities, which ensures the microstructural morphology and size. The two factors finally yield controllable microstructures and properties of HEAs. Among successful cases, the Ti-Al-Nb intermetallics [6] and nickel-based superalloys [7] are two typical alloys. The former applies the BST to control the lamellar structure and the latter to optimize the coherent γ - γ' structure in order to improve their high-temperature performances. In addition, it is also reported that dendrites/bulk metallic glass (BMG) composites are successfully tailored by BST, during which the dendrites are homogeneously



Fig. 5.4 Photograph of the Bridgman solidification equipment

distributed within the BMG matrix, and the dendrite spanning length has a strong dependence on the temperature gradient and growth rates [8]. Figure 5.4 shows the photograph of the BS equipment.

Figure 5.5 schematically illustrates the BST processing and the sample location. Firstly, the target alloys are cast into rod-shaped samples by the common casting method. Then, the synthesized samples are crashed into pieces and placed in an alumina tube with an internal diameter of 3 mm and a wall thickness of ~1 mm, which are inductively heated to the fully melted condition by adjusting proper heating power and holding time. Subsequently, the BS processing is performed by assigning a withdrawal velocity R ranging from 5 to 2000 $\mu\text{m/s}$ and a temperature gradient G of ~45 K/mm. The liquid alloys are directionally put into the water-cooled Ga-In-Sn liquid agents, where three regions of the sample location can be definitely demonstrated including region A, unremelted region; region B, transition region; and region C, fully remelted or directionally growth region [9].

Figure 5.6 shows the optical micrographs of the AlCoCrFeNi HEAs by BST with different withdrawal velocities. Note that by BS processing, apparent morphology transition from flowery dendrites to equiaxed grains is observed, as shown in Fig. 5.6a–d, and the average grain size is about 100–150 μm [5].

Furthermore, Fig. 5.7 shows the corresponding scanning electron microscopy (SEM) images. Honeycomb-like structures with uniform dispersion of nanoscale spherical particles can be seen in Fig. 5.7a–d. These nanoscale precipitations with sizes of ~50–100 nm may originate from the spinodal decomposition, which leads to a modulated structure composed of ordered (B2) and disordered (A2) phases, as marked by 1 and 2, respectively [5].

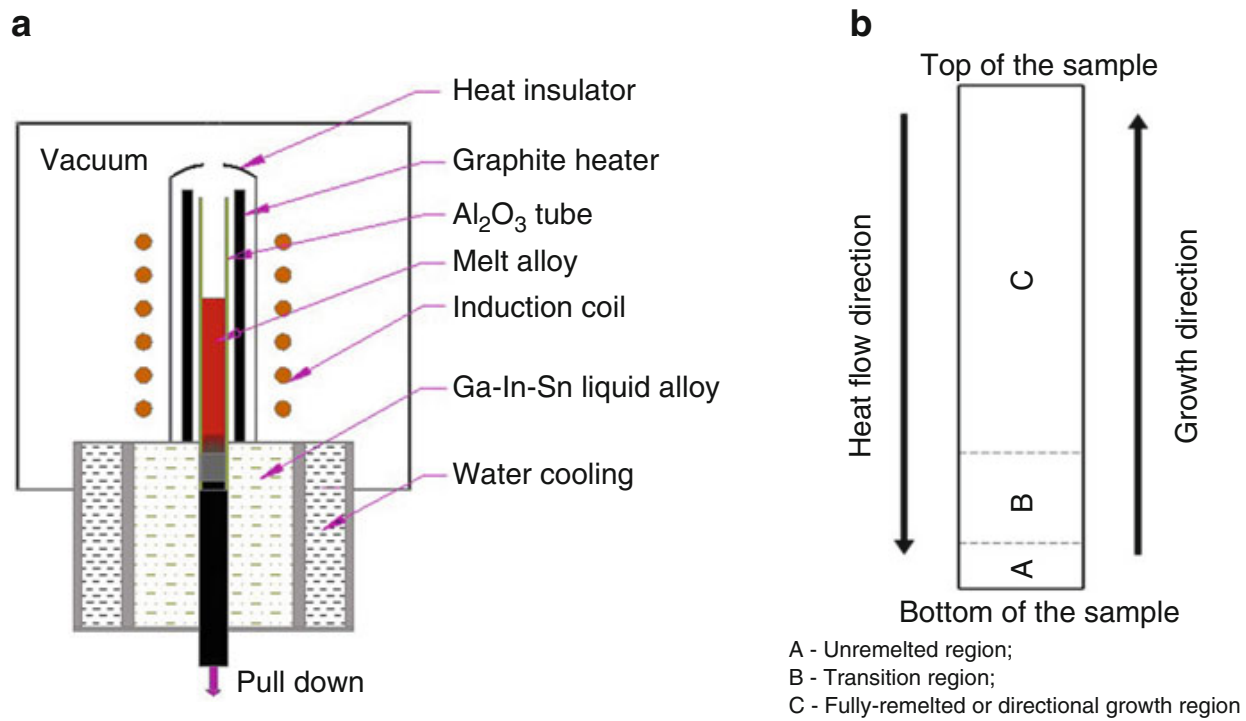


Fig. 5.5 A schematic diagram of the BST: (a) the BS processing and (b) the sample location [9]

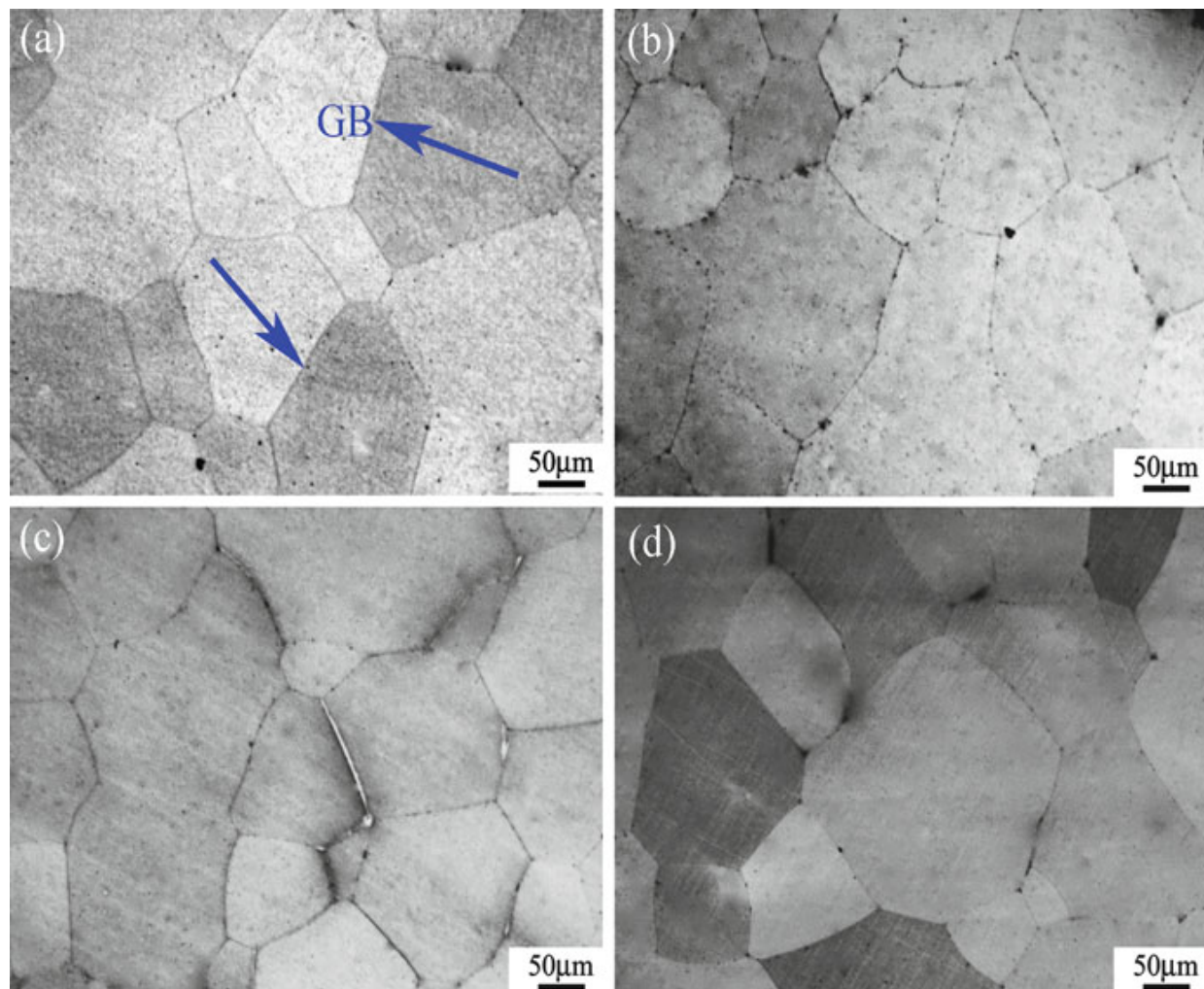


Fig. 5.6 The optical micrographs of the AlCoCrFeNi HEAs by BST with withdrawal velocities of (a) 200, (b) 600, (c) 1000, and (d) 1800 μm/s [5]

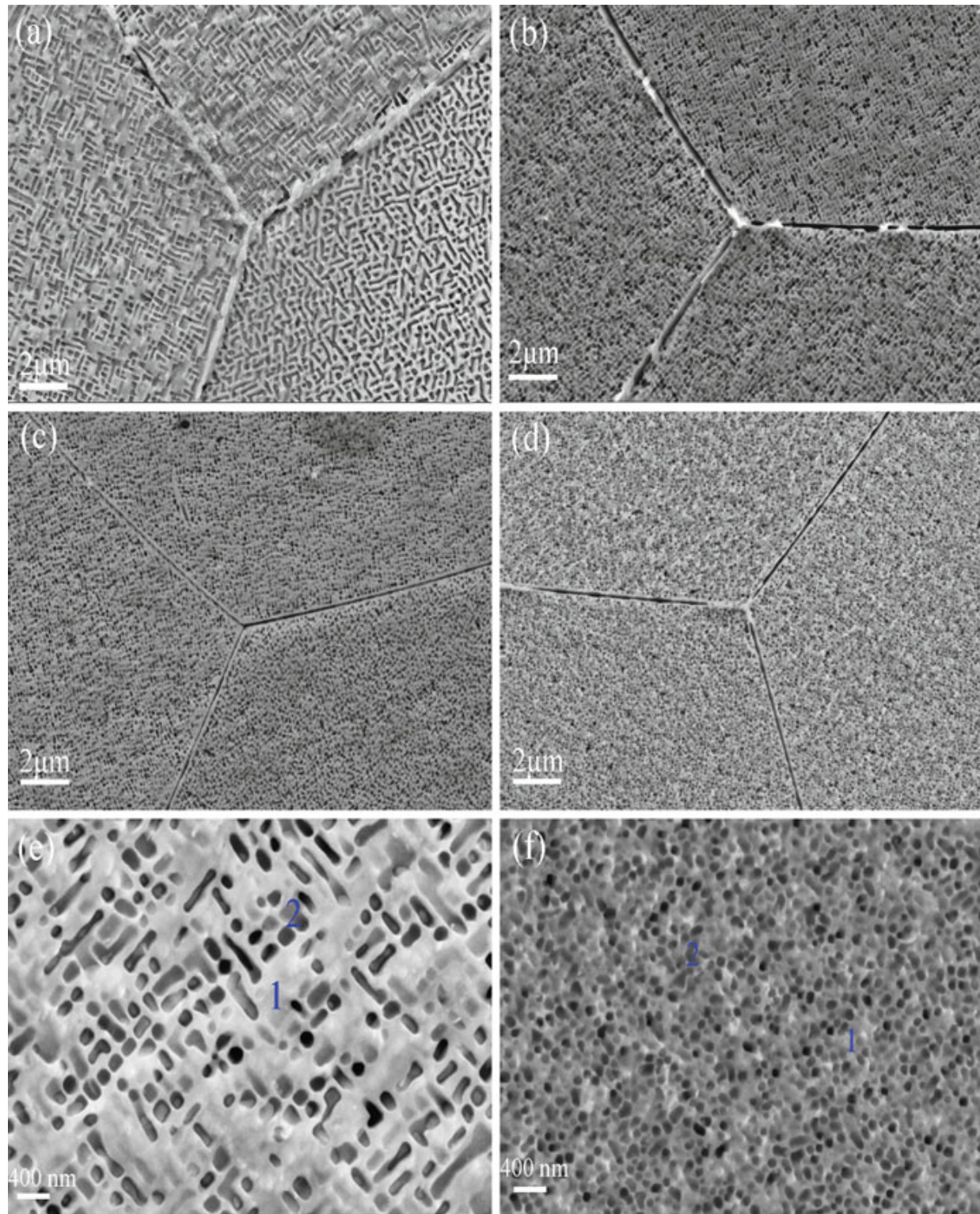


Fig. 5.7 The SEM secondary electron images of the AlCoCrFeNi HEAs by BST with withdrawal velocities of (a) 200, (b) 600, (c) 1000, and (d) 1800 $\mu\text{m/s}$. (e) and (f) are the magnifications of (a) and (d), respectively [5]

5.2.3 Synthesis of Single-Crystal HEA by BST

Since the mid-twentieth century, metal single crystals have been developed, in terms of the synthesis of single crystals and the growth mechanisms of single crystals from their melts, on the consideration of the requirements of their

mechanical and physical properties especially for the high-temperature performances [10]. From the viewpoint of solidification theory, the production of a single crystal has in fact required the atoms of a melt solidifying into a nucleus or seed that further grows into a whole single crystal. However, the seed crystal is not so easy to be fabricated because a large number of nuclei are formed initially in the common casting methods such as the copper-mold casting. In other words, upon solidification, competitive growth with preferred crystallographic orientation has to be done, and finally one nucleus will extend for any distance into the crystal [10]. The fundamental task to obtain the seed crystal can be realized by BST and proper G/R ratios, which will be stated in the following sections.

The superior high-temperature properties of HEAs hold great potential for high-temperature applications (as an example for the turbine blades in aircraft engines [7]). In addition, as mentioned above, almost all reported HEAs microstructures are polycrystalline regardless of whether they have a single-phase or multiple-phase state [1, 2]. As we know, grain boundary (GB) often plays a negative or even fatal role in the high-temperature performances of materials, which acts as shortcut paths for diffusivity of atoms (thermodynamic instability) and easy nucleation sites for cracks (more sensitive to fracture). Also compositional segregation or impurities tend to locate at GB that easily yields the brittle tendency of materials. These intrinsic defects associated with GB have led to the rapid development of single-crystal alloys, such as the single-crystal nickel-based superalloys and Ni_3Al -based alloys [7, 11]. Therefore, there is an urgent need in producing single-crystal HEAs for which the composition is homogeneous and property characterization could truly represent HEAs from a viewpoint of fundamental understanding.

Figure 5.8 shows the microstructure evolution and schematic illustration of the $\text{CoCrFeNiAl}_{0.3}$ HEA by BS processing. Here, it needs to be noted that the designated R value is about $5 \mu\text{m/s}$ and two BS steps as described in Fig. 5.5 are repeatedly conducted upon the present system. As shown in the middle schematic diagram, based on the growth direction of the sample, the $\text{CoCrFeNiAl}_{0.3}$ HEA undergoes an obvious microstructural transition from dendrites to equiaxed grains and then to columnar grains and last to a single-crystal structure. Specifically, typical network-like dendrites and interdendrites morphology stem from region A of the sample (a region close to the Ga-In-Sn liquid alloy surface) and thus remain in the as-cast microstructure. Along the solidification direction or the transition region B, numerous equiaxed grains with a wide size range of $\sim 50\text{--}300 \mu\text{m}$ are obtained, accompanied by some twinning crystals with a width of several tens micrometer possibly due to the annealing-like effect. As the solid/liquid interface advances into the fully remelted region C, the bulky columnar grains with a millimeter scale are formed due to the significantly preferential growth of grains with the crystallographic orientation inclining to the growth direction. As a result, in the upmost part of the sample, only one grain or the seed crystal with preferential crystallographic orientation is obtained. In other words, a single-crystal growth is achieved via planar interface through a controlled BS processing. Relying on the second BS processing, the growth of a whole single crystal proceeds from the seed crystal at the end of the rod, and a single-crystal $\text{CoCrFeNiAl}_{0.3}$ HEA sample with 3 mm in diameter and 50 mm in length is finally acquired [9].

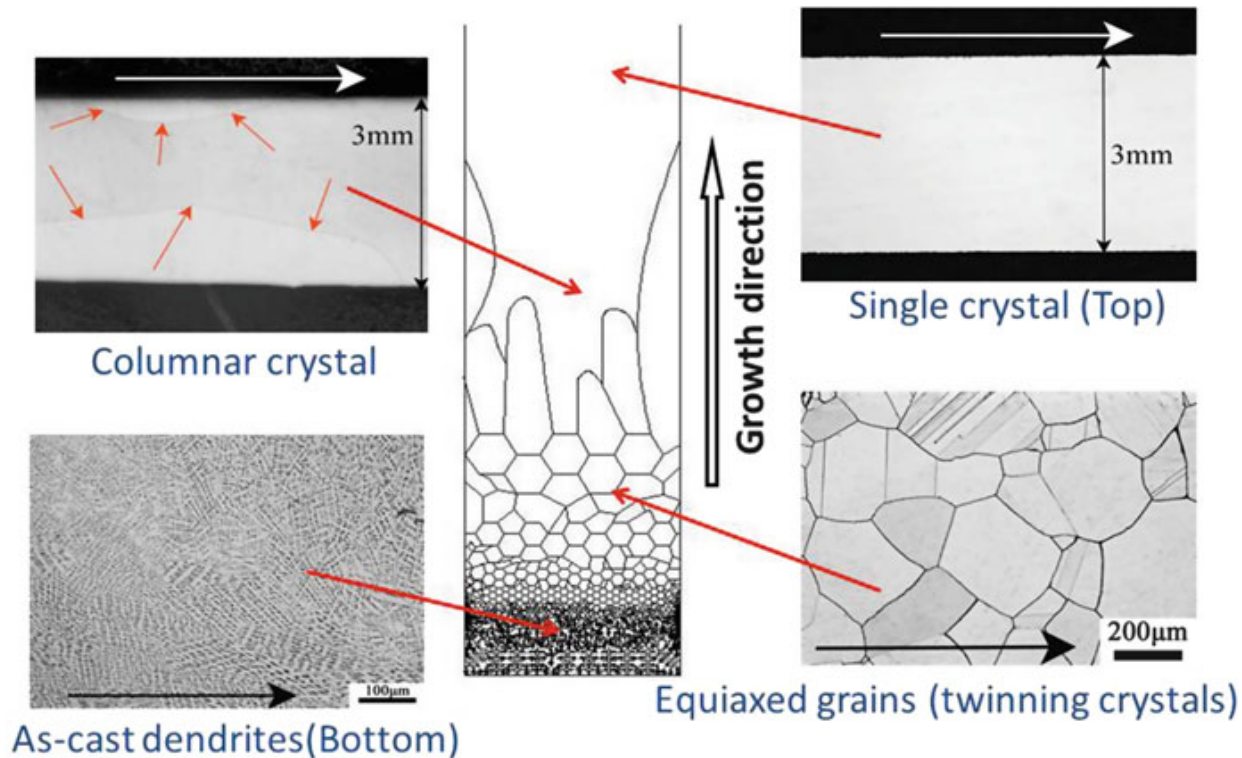


Fig. 5.8 Microstructure evolution and systematic illustration of the CoCrFeNiAl_{0.3} HEA prepared by BST [9]

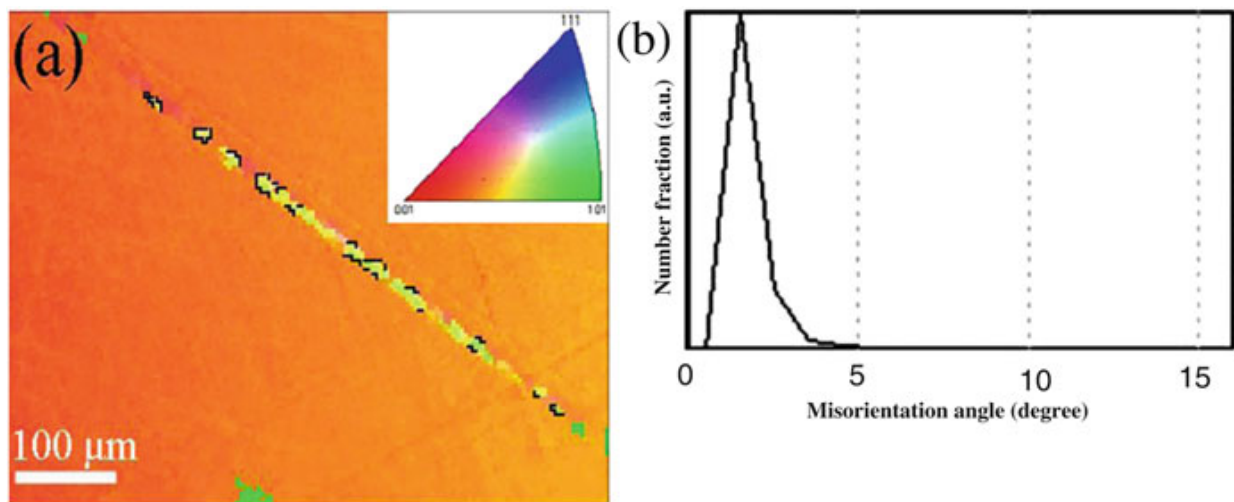


Fig. 5.9 The EBSD analyses of the single-crystal CoCrFeNiAl_{0.3} HEA: (a) crystallographic orientation and (b) misorientation angle [12]

For the scientific validity of the single-crystal product, Fig. 5.9 displays the electron backscattered diffraction (EBSD) mapping of the single-crystal CoCrFeNiAl_{0.3} HEA. As indicated in Fig. 5.9a, the crystallographic orientation of the single-crystal sample mainly focuses on the <001> direction. Figure 5.9b presents the misorientation distribution of the single-crystal product. Note that the misorientation curve is very narrow and close to a Gaussian distribution and very low-angle grain boundaries (generally, grain boundaries with an angle less than 15° are referred to as low-angle grain boundaries) basically within 2° are detected,

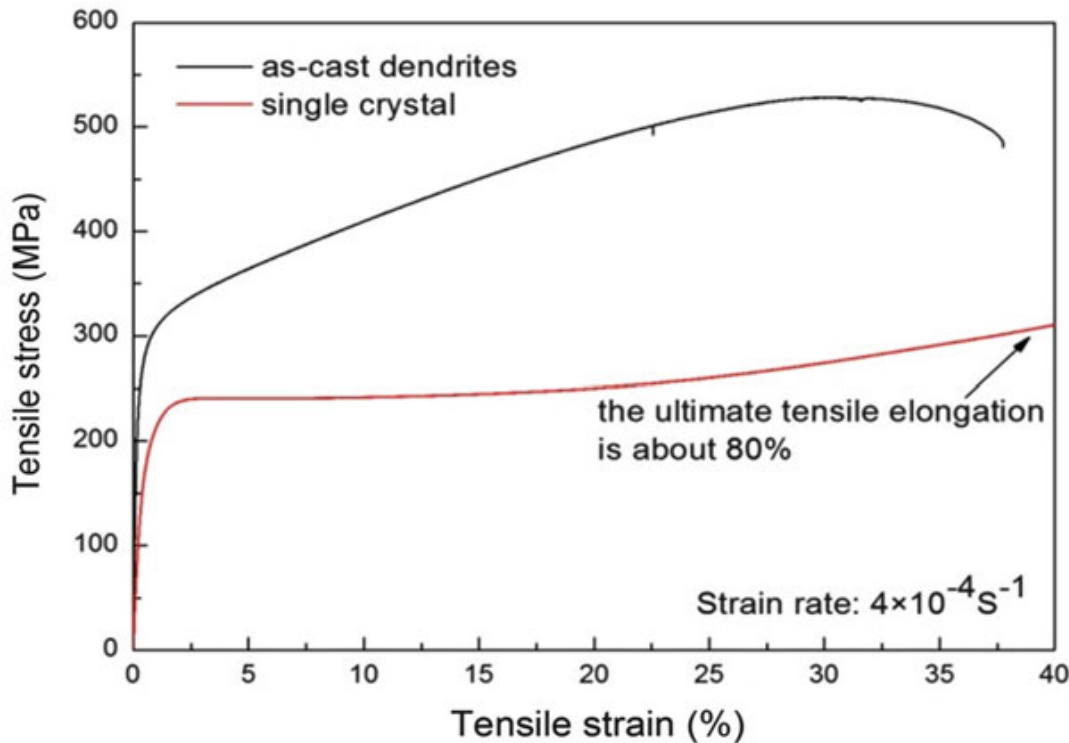


Fig. 5.10 Tensile stress–strain curves of the CoCrFeNiAl_{0.3} HEA for both as-cast and single-crystal states [12]

indicating that the scattering level of the crystallographic orientation for the single crystal is within acceptable limits [12].

Figure 5.10 shows the engineering tensile stress–strain curves of the CoCrFeNiAl_{0.3} HEAs for both as-cast and single-crystal states. It can be seen that the single-crystal alloy exhibits an ultimate tensile elongation value of about 80 %, which is much higher than the as-cast sample, while the yielding tensile strength and ultimate tensile strength values of the former case are also lower than that of the latter case by 32.7 % and 24.4 %, respectively [12]. This feature indicates that the classic Hall–Petch relationship still conforms to the current HEA and the single-crystal product demonstrates a larger homogenous deformation capability than the as-cast sample.

5.2.4 Laser Melting and Laser Cladding

Laser cladding uses a concentrated beam of energy from the laser as the heat source and can keep the heat-affected zone of the substrate very shallow by focusing to a very small area. This feature minimizes the chance of cracking, voids, and deformation and results in fine microstructure and a metallurgical bond that have superior bond strength over thermal spray. So far, coating materials for the laser cladding are primarily focused on Co- or Ni-based superalloys, such as Inconel and Stellite alloys, which however are considerably expensive with a relatively low hardness. The newly designed HEAs have shown great potentials in applications

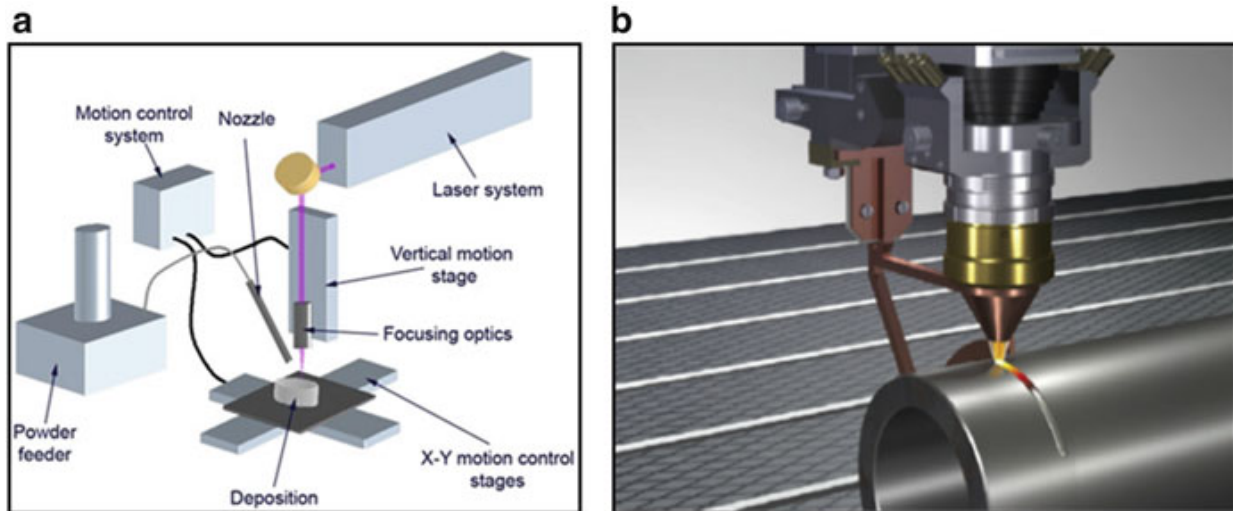


Fig. 5.11 (a) Schematic diagram and (b) operation of laser cladding process [13, 14]

where high strength, high hardness, high wear resistance, or high-temperature softening resistance is required. Some of these promising properties match those of the widely used Co- and Ni-based coatings with the advantage of low cost.

The schematic drawing of the laser cladding process is illustrated in Fig. 5.11a [13]. The basic system consists of a laser source to generate the beam, a set of optics to direct and focus the beam, a powder feeder, and a part manipulator. The laser and optics stay stationary and the specimens move with respect to the laser. Laser cladding systems are fully automated providing precise control of the cladding process. The melt pool produced by the laser beam rapidly solidifies as the beam and powder injection are moved away and becomes a fully dense weld bead. Figure 5.11b is the laser cladding process by filling cladding materials in synchronous feeding way [14]. A single and overlapped multi-passed layer can be formed to protect the material's surface after cladding. Therefore, it can be applied to all kinds of product with a variety of sizes and shapes and continues to gain market.

Zhang et al. delicately studied the influences of laser rapid solidification on the microstructure and phase structure in the HEA coatings [15–18]. They calculated the nucleation incubation time for various competing phases and indicated that the growth of intermetallic compounds will be hampered if the solidification rate is sufficiently high, because different atomic radii in the HEA composition leads to the increase of the solid–liquid interface energy and the difficulty of the long-range diffusion of atoms in the crystal lattice, thus favoring the nucleation of solid solution and decreasing growth rate of intermetallic compounds [19]. Meanwhile, they found there are lots of nano- or submicron-size precipitates in their fabricated HEA coatings. Qiu et al. also found many Ti-rich nanocrystals distributed in the solid-solution matrix in the laser cladding Al₂CoCrCuFeNi_{1.5}Ti coating [20]. Ideally, the HEAs generally refer to single-phase solid solutions, and there exist concerns that precipitates in HEA coatings may deteriorate the toughness. However, if we noted the widely used commercial Ni- and Co-based alloy coatings, which always contain various types and high content of brittle precipitates, such as CrNi, Co₇W₆, Cr₂₃C₆, and Ni₃B [21, 22], there is no need to worry about such

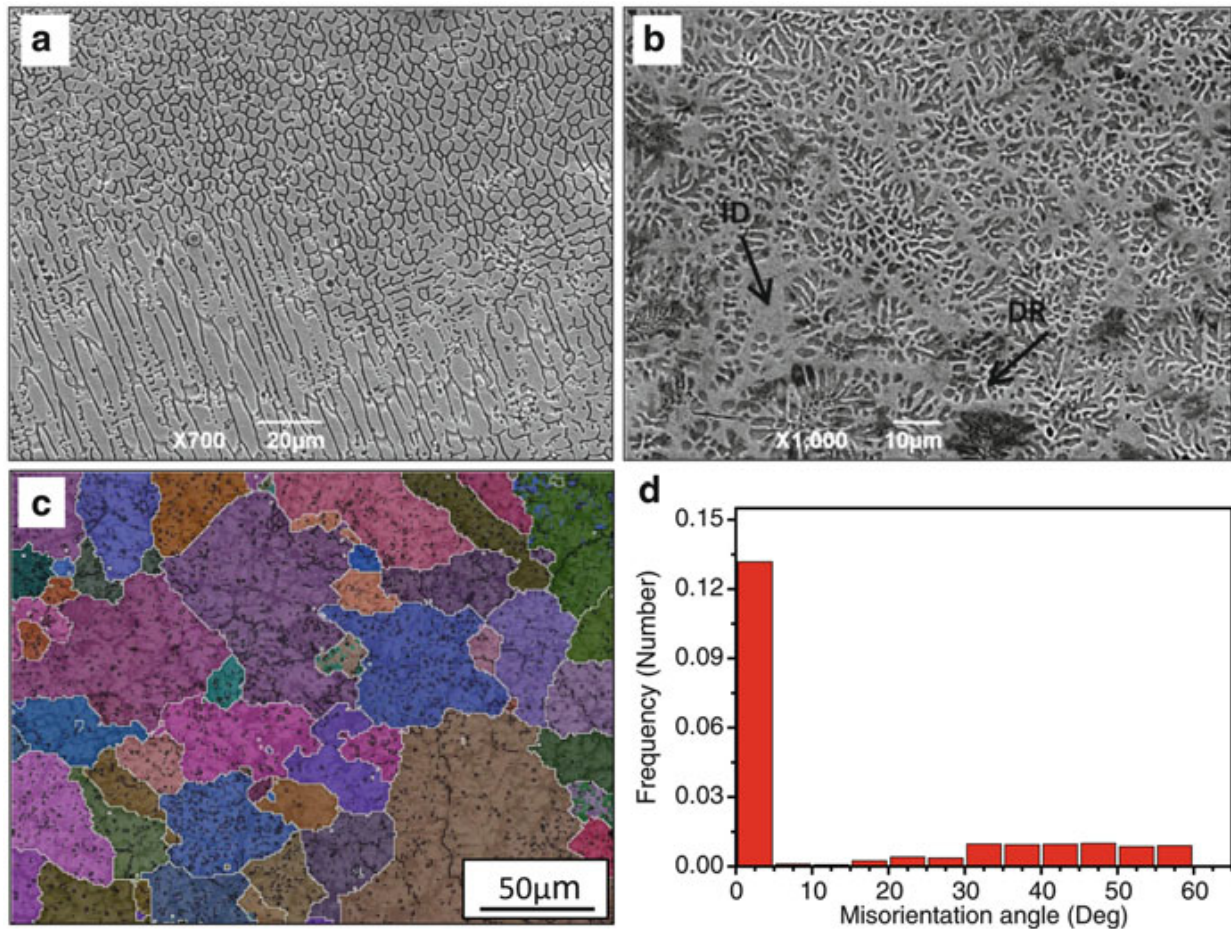


Fig. 5.12 Microstructure of the HEA coatings: (a) CoCrCuFeNi [16]; (b–d) SEM, EBSD, and angle distribution of grain boundaries in the Al₂CoCrFeNiSi coating, respectively [19]

precipitates possibly ruining the toughness of the HEA coatings. On the contrary, the precipitate content should be minor in the rapidly solidified HEA coatings and is generally in nanoscale dimensions. As a consequence, it is deemed that more attention should be paid to the brittleness of the solid-solution phase in the HEA coatings.

As for the microstructure features in the laser rapidly solidified HEA coatings, it is believed that the microstructure and component segregation are mainly influenced by laser-processing parameters and coating component. Figure 5.12a presents the columnar and equiaxed grains in the CoCrCuFeNi coating and shows a typical morphology of single-phase alloys [16], while energy-dispersive X-ray spectroscopy (EDS) analysis confirms that all alloying elements are almost uniformly distributed in the coating. Figure 5.12b shows typical dendrite microstructure with coarse interdendritic regions in the Al₂CoCrFeNiSi coating, which is mainly composed of a simple BCC solid-solution phase as identified by the X-ray diffraction (XRD) analysis [19]. The distinctive contrast between the dendritic and interdendritic regions is correspondent to two BCC phases with slightly different lattice constants. The formation of secondary arms is mainly caused by component segregation, which promotes the constitutional supercooling at the interface of liquid–solid during solidification. As shown in Fig. 5.12c by EBSD observation when using the lattice constant of α -Fe to calibrate the phase distribution in the

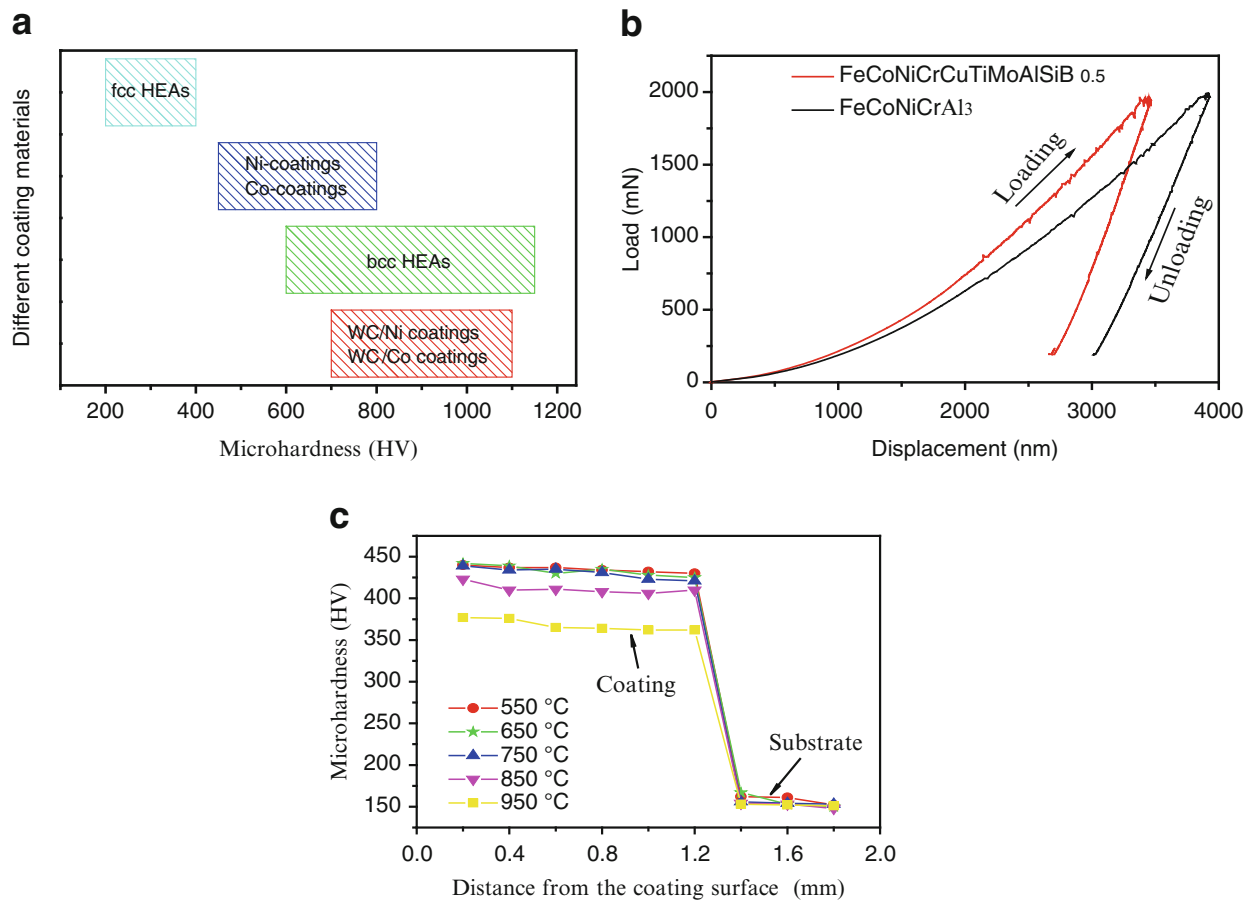


Fig. 5.13 Hardness of the HEA coatings. **(a)** Comparison of the hardness in different coating materials [18, 24]. **(b)** The nanoindentation curves [40]. **(c)** Effect of annealing treatment on the hardness in the CoCrCuFeNi coating [24]

coating, it is interesting to find that the microstructure of the coating has coarse equiaxed grains with the size about 100 μm , verifying that the coupled growth of dendritic and interdendritic microstructure observed in Fig. 5.12b has similar growth orientation and crystal lattice. Figure 5.12d presents the distribution of misorientations for the grain boundaries and confirms there exist lots of low-angle grain boundaries in the coating [19].

Figure 5.13a shows the hardness of the laser cladding HEA coatings compared with conventional Ni- and Co-based alloy coatings containing different amount of WC hard particles. Hardness of FCC-structured HEA coatings ranged from 200 to 400 HV, while BCC-structured HEA coatings reached 600–1150 HV [15, 17, 18], which was higher than the hardness of about 400–800 HV in Ni- and Co-based coatings [21, 22]. This indicated great advantages of HEA coatings over conventional alloy coatings, both in hardness and materials cost. Meanwhile, it should be noted that Qiu and Zhang et al., respectively, reported a hardness of about 1100 and 1150 HV in $\text{Al}_2\text{CoCrCuFeNi}_2\text{Ti}$ and $\text{AlCoCrCuFeMoNiSiTiB}_{0.5}$, which was almost four times that of the Q235 iron substrate [18, 23]. Zhang et al. further proved that laser clad HEA coatings have higher hardness than that of the similar composition alloy prepared by ordinary solidification process because of the rapid solidification influences, such as grain refinement, relief of component segregation, nano-size

precipitates, etc. [15–18]. Figure 5.13b depicts a serrated flow behavior in the load–displacement curves of $\text{Al}_3\text{CoCrFeNi}$ and $\text{AlCoCrCuFeMoNiSiTiB}_{0.5}$ coatings by nanoindentation, which were measured by sharp cube-corner indenter with large load force of 2 N. One possible explanation for the serrated flow behavior could be the repeated solute locking and unlocking of dislocations during plastic deformation in crystalline alloys. The high hardness of the HEAs may result from the stronger interaction between the dislocation and solute atoms, which is greater than those in the traditional alloys [18]. HEA coating also exhibits excellent resistance to high-temperature softening up to 1000 °C, which is similar with bulk HEAs prepared by the arc-melting technique [18, 24]. Figure 5.13c presents the effect of annealing treatment on the hardness in the laser clad CoCrCuFeNi coating [24]. The coating shows an impressive phase stability of up to 0.7 T_m (750 °C) and presents good potential to be used as high-temperature coating materials. Meanwhile, it was reported that lots of profuse stacking faults, which are known to be beneficial for the creep properties at elevated temperatures, formed in the coating after annealing treatment at 750 °C. The mechanical stability, together with the morphological and phase stability for the CoCrCuFeNi coating, makes it a good candidate coating material to be used at high temperatures, at least up to 750 °C.

As for corrosion resistant property of the HEA coatings, Yue et al. fabricated $\text{AlCoCrCu}_x\text{FeNiSi}_{0.5}$ coatings to protect AZ31 Mg substrate and found the corrosion current densities of the coatings were one order of magnitude lower than that of the un-clad magnesium [25]. The $\text{Al}_2\text{CoCrCuFeNi}_x\text{Ti}$ coating could play an important protective role in NaOH and NaCl environment on Q235 substrate. Meanwhile, it is found that the corrosion resistance of CoCrCuFeNi coating in NaCl solution is easier to be passivated and has higher corrosion resistance than that in Ni-based alloy coating [16, 20]. As for oxidation resistance, Huang et al. prepared AlCrSiTiV coating to protect the wear and oxidation of the Ti-6Al-V substrate [26]. They found that the weight gain of the Ti-6Al-V substrate after oxidization at 800 °C for 50 h is almost five times higher than the HEA coating owing to the formation of dense, adherent, and protective Cr_2O_3 and Al_2O_3 oxide layer on the surface of the HEA coating, thus reducing the interdiffusion of atoms across the oxide layer and the oxidation kinetics.

5.3 Solid-State Route

5.3.1 *Introduction: Description of Mechanical Alloying and Milling*

The milling of materials has been a major component of the ceramic processing and powder metallurgy industries. The objectives of milling include particle size reduction, mixing or blending, and particle shape changes. However, ball milling of powders can often accomplish solid-state alloying – mechanical alloying. The

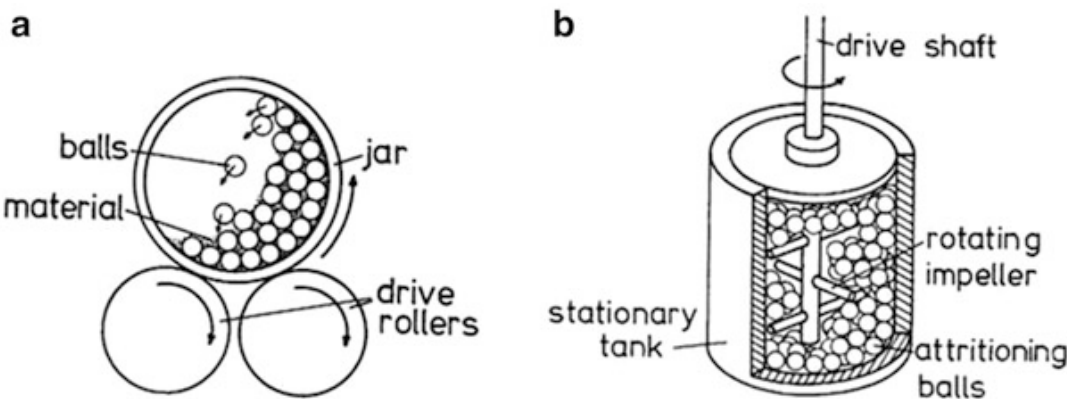


Fig. 5.14 (a) Schematic cross-section of a tumbler ball mill [29]. (b) Schematic of an attritor ball mill [29]

development of this process by J.S. Benjamin and his colleagues at the International Nickel Company has been described previously [27, 28]. Mechanical alloying has been defined as a dry, high-energy, ball milling process that produces composite metal alloy powders with controlled, extremely fine microstructures. In mechanical alloying, the resultant powder develops through the repeated cold welding and fracture of the powder particles until the final composition of the powders corresponds to the percentage of the respective constituents in the initial charge. While the first application of MA was the production of oxide dispersion strengthened alloys, it has subsequently been used as a nonequilibrium processing method to make a wide variety of metastable materials such as extended solid solutions, nanocrystalline metals and alloys, quasicrystalline materials, and amorphous materials. The large literature on this subject has been covered in several reviews [29, 30] in which the processing methods, mechanics/physics of mechanical attrition, the synthesis of “equilibrium” phases, and the variety of metastable phases formed have been documented. A schematic of two common devices for mechanical attrition is given in Fig. 5.14a (a tumbler ball mill) and Fig. 5.14b (an attritor mill) [29].

Mechanical attrition – the ball milling of powders – is often divided into “mechanical alloying” (MA) where compositional changes occur in the milling of dissimilar powders (alloying on the atomic level) and “mechanical milling”(MM) where structural changes can be induced on ball milling of single-component powders (elements or compounds) such as solid-state amorphization or production of nanocrystalline grain microstructures. Mechanical alloying (MA) will be the focus of this section.

The several advantages of the mechanical alloying process include its versatility. Almost any material can be produced by this method including ductile metal alloys, brittle intermetallic compounds, and composites. Mechanical alloying, which is typically carried out at room temperature or below, bypasses the potential problems with melting and casting methods and the segregation of chemistry the latter methods can produce. Thus, it can synthesize alloys with very different melting temperatures or vapor pressures that often pose a problem for solidification processing. The as-milled crystalline microstructures are typically very fine

grained, and this is one of the important processing routes for making nanocrystalline materials.

Disadvantages of mechanical alloying include possible contamination from the milling media or atmosphere and the fact that in most cases the product is powder which requires subsequent consolidation to bulk form. The contamination problem can be minimized or eliminated by proper choice of the milling media (composition of balls and vial) and by milling in a high-purity inert gas or vacuum environment. The consolidation process is most important if the as-milled structure needs to be retained and temperatures of consolidation cause changes (e.g., grain growth or crystallization).

In the following sections, examples of equilibrium phases, metastable phases, and high-entropy alloys prepared by mechanical alloying will be presented. The possible competition between formation of amorphous and solid-solution high-entropy alloys will be discussed.

5.3.2 Examples of “Equilibrium” Phases Produced by Mechanical Alloying

In this section several examples are given of material synthesis by mechanical alloying of elemental component powders which produce the phase predicted by the binary equilibrium phase diagram. The word “equilibrium” is put in quotation marks in the section heading to indicate that there may be some nonequilibrium features associated with the equilibrium phase product of mechanical alloying.

A number of equilibrium solid-solution alloys have been produced by mechanical alloying such as Ni-Cr [30], which first showed the true atomic-level alloying. Ge and Si exhibit complete solid solubility, and while both are brittle at room temperature, the solid solution of these elements across the phase diagram could be obtained by mechanical alloying [31]. Lattice parameters for Si and Ge powders and the solid-solution Ge – 72 at.% Si alloy are given as a function of milling time in Fig. 5.15 [31]. The intermetallic compound, Nb₃Sn, can be prepared by mechanical alloying of Nb and Sn powders. However, on continued milling after the compound has been formed, an amorphous phase is observed. The amorphization of a single-phase equilibrium structure will be discussed later in regard to the competition between amorphous and crystalline solid-solution HEAs.

5.3.3 Examples of Metastable Phases Produced by Mechanical Alloying

Mechanical alloying/milling as a nonequilibrium processing method to prepare metastable materials has been used widely since it was observed that mechanical alloying could produce an amorphous alloy by ball milling of elemental powders

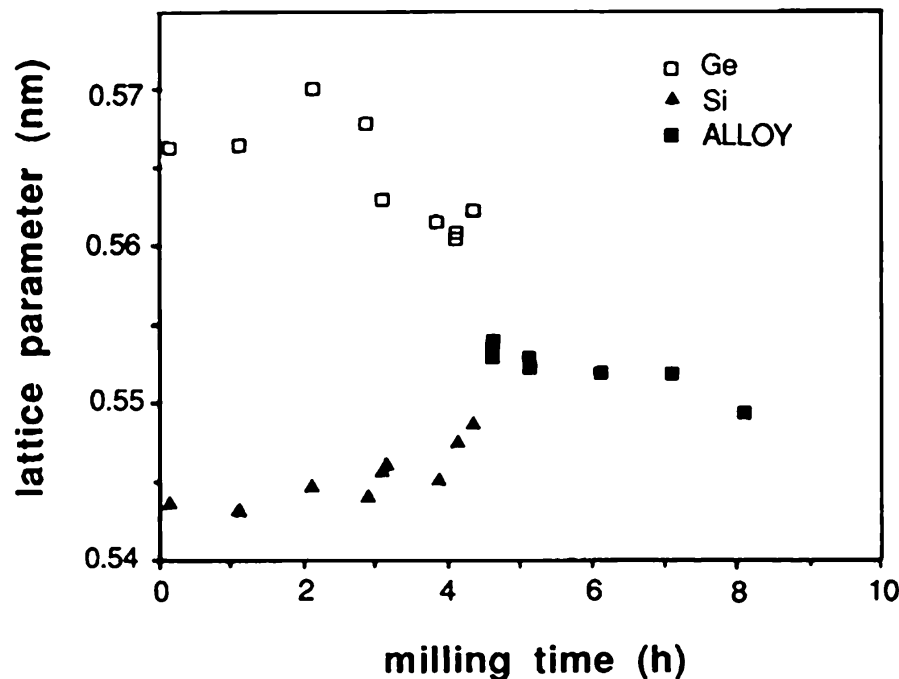


Fig. 5.15 Lattice parameter vs. milling time for Si and Ge powder for the composition Ge – 72 at. % Si [31]

[32] in 1983. Besides the synthesis of metallic glasses, it has been used to prepare extended solid solutions, nanocrystalline microstructures, quasicrystalline materials, and metastable crystalline compounds. Of particular interest with regard to making solid-solution HEAs are the examples of extended solid solutions in binary alloys, nanocrystalline microstructures, and metallic glasses. These will be briefly discussed in turn.

Extended – supersaturated – solid solutions have been obtained in many binary systems [29, 30]. Analogous to the results of rapid solidification from the liquid phase, mechanical alloying is capable of significantly extending solid solubilities. One example is the well-studied Ag-Cu binary where the equilibrium solubility of Cu in Ag is a maximum of 14.1 at.%. Both mechanical alloying and rapid solidification can extend this to 100 at.%, that is, complete solid solubility across the binary phase diagram. Many other examples are listed in Table 9.1 in Ref. [4]. Of concern to the production of solid-solution HEA phases by mechanical alloying is that metastable, supersaturated solid solutions may be produced in the as-milled powders. In order to assess the equilibrium structure of the HEA, elevated temperature annealing is necessary for times long enough to ensure the equilibrium state has been obtained.

Mechanical alloying/milling has been used extensively to produce metals, alloys, and intermetallic compounds with nanocrystalline microstructures. It is probable that the as-milled powders of HEAs will have a nanocrystalline microstructure. Such a microstructure, if maintained after powder consolidation, may offer enhanced properties, such as mechanical hardness and strength. It may also affect the stability of the phases formed due to the high energy of the large grain boundary areas in nanocrystalline materials.

Metallic glasses (amorphous alloys) are competitors with simple solid-solution structures in multicomponent HEAs. The empirical rules that distinguish between HEAs and metallic glasses made from the liquid state may not apply to those produced by mechanical alloying. That is, metallic glasses are favored by large negative heats of mixing and dissimilar atomic sizes of the components, while solid-solution HEAs typically require small (nearly ideal) heats of mixing and similar atomic sizes of the constituents. However, the mechanism for solid-state amorphization by mechanical alloying differs from that for amorphization by quenching from the liquid state. In the latter case, the kinetic constraint of cooling fast enough from the liquid state to miss the “nose” of a crystalline time–temperature–transformation (TTT) curve to reach the glass transition temperature is controlling. Factors such as large negative heats of mixing and dissimilar atomic sizes affect these kinetics. However, in solid-state amorphization by mechanical alloying or milling, different mechanisms are likely. While there are several possible explanations proposed for amorphization by ball milling of powders [30], it is generally recognized that amorphization during MA is not purely a mechanical process and that a solid-state reaction similar to that observed in amorphization of thin films (solid-state amorphization reaction) [33] occurs during MA also. During MM, however, destabilization of the crystalline phase is thought to occur by the increase in free energy through accumulation of structural defects such as vacancies, dislocations, grain boundaries, and antiphase boundaries. In order to raise the free energy of the crystalline state to that of the amorphous phase, the only such defects that provide enough free energy are grain boundaries or, in the case of an ordered structure, disordering energy. Therefore, one suggestion for solid-state amorphization by MM is that the creation of nanocrystalline grain sizes can destabilize the crystalline structure when the grain size is reduced to a critical value that provides sufficient free energy to transform to the amorphous structure. Whatever the mechanism may be, it is clear that ball milling of single-component (elemental, alloy, or compound) powders can induce solid-state amorphization in some materials which is invariably preceded by the formation of a fine nanocrystalline structure.

5.3.4 Examples of Solid-Solution HEAs Produced by Mechanical Alloying

The first examples of solid solution HEAs prepared by MA were given by Murty and coworkers. The Ph.D. thesis of S. Varalakshmi [34] reported on the preparation of equiatomic elemental powder blends in the AlFeTiCrZnCu, CuNiCoZnAlTi, FeNiMnAlCrCo, and NiFeCrCoMnW systems using mechanical alloying. The equiatomic binary to six-component compositions of all four systems was synthesized in the order of, for example, AlFe, AlFeTi, AlFeTiCr, AlFeTiCrZn, and

AlFeTiCrZnCu. The influence of composition on HEA formation was also followed in non-equiautomic compositions by varying one of the elements from 0 to 50 at.%. All the alloys in these systems had either the BCC or FCC phase as the major phase as determined by X-ray diffraction. The as-milled structures (either BCC or FCC) were maintained after annealing at 800 °C for 1 h. The as-milled structures exhibited nanocrystalline grain sizes (~10 nm), and the nanostructured grain size was retained after annealing at 800 °C. Several papers were published from this thesis work [35–37]. Subsequently Chen et al. [38] studied the alloying behavior of binary to octonary alloys based on Cu-Ni-Al-Co-Cr-Fe-Ti-Mo prepared by mechanical alloying. Binary and ternary alloys formed FCC phases or BCC phases, respectively. Quaternary to octonary alloys first formed FCC solid solutions which transformed to amorphous structures after prolonged milling.

Zhang et al. [39] milled equiautomic AlCoCrCuFeNi. The as-milled powders were solid solutions with the BCC (major phase) and FCC (minor phase) structures. The grain size was very fine nanoscale with estimated size of about 7 nm. Annealing at 600 °C gave BCC and FCC phases. After annealing at 1000 °C, another FCC phase appeared. This was comparable to the structures observed in arc-melted and cast AlCoCrCuFeNi.

Praveen et al. [40] prepared AlCoCrCuFe and CoCrCuFeNi equiautomic alloys by mechanical alloying followed by spark plasma sintering (SPS) at 900 °C to compact the powders. After mechanical alloying for 15 h, AlCoCrCuFe showed mostly BCC structure, with a minor FCC peak by X-ray diffraction. However, CoCrCuFeNi showed mostly the FCC phase with very small traces of BCC. The structures observed by X-ray diffraction after SPS were as follows: in AlCoCrCuFe on ordered BCC (B2) phase was dominant with small amounts of Cu-rich FCC phase and sigma phase, and in CoCrCuFeNi, FCC phases were dominant with small amounts of sigma phase present. The authors suggest that the additional phases formed in these alloys are attributed to the influence of enthalpies of mixing, and configurational entropy is not sufficient to suppress their formation.

Tariq et al. [41] synthesized AlCoCrCuFeNi, AlCoCrCuFeNiW, and AlCoCrCuFeNiWZr equiautomic alloys by mechanical alloying of the elemental powders. All the alloys were analyzed by X-ray diffraction and the as-milled structures were found to be mostly BCC, with small FCC peaks. The seven-component alloy containing W appeared to have somewhat more FCC phase.

Sriharitha et al. [42] studied phase formation in mechanically alloyed $\text{Al}_x\text{CoCrCuFeNi}$ with $x = 0.45, 1, 2.5, 5$. The lower Al-content ($x = 0.45, 1$) alloys showed a mixture of FCC phases (major) and BCC phase (minor). The Al-rich alloys ($x = 2.5, 5$) exhibited a single ordered BCC (B2) phase. After heating up to 1480 °C in a differential scanning calorimeter (DSC), the BCC phase disappeared from the lower Al-content alloys. The alloy with 2.5 mol Al showed FCC peaks along with the B2 peaks, while the alloy with 5 mol Al exhibited only B2 peaks. Fine grain sizes (nanocrystalline or submicron) were observed after heating in the DSC, suggesting the microstructure has good thermal stability.

Fu et al. [43] have studied the effect of Cr additions on the alloying behavior and structure of CoFeNiAl_{0.5}Ti_{0.5} prepared by mechanical alloying. After long milling times (42 h), the alloy without Cr showed only FCC peaks in X-ray diffraction. However, the Cr-containing alloy exhibited a mixed structure of FCC and BCC phases. However, after SPS at 1000 °C, the alloy without Cr now showed a mixture of FCC and BCC phases, while the Cr-containing alloy showed mainly FCC phases (with a small unidentified peak).

Praveen et al. [44] reported the phase evolution and densification behavior of nanocrystalline HEAs prepared by mechanical alloying and compacted by spark plasma sintering (SPS). They studied multicomponent alloys with the following equiatomic compositions: CoCrCuFeNi, CoCuFeNi, CoCrCuNi, CoCrFeNi, CoFeMnNi, and CoFeNi. The as-milled structures resulted in a major FCC phase and a minor BCC phase in Cr-containing alloys and a single FCC phase in the other alloys. After SPS, CoFeMnNi and CoFeNi remained FCC. However, CoCuFeNi transformed to two FCC phases, and CoCrFeNi had a major FCC phase with minor sigma phase.

In order to study the stacking fault energy in selected HEAs by experimental and computational methods, Zaddach et al. [45] prepared alloys with the following compositions by both arc-melting and casting and mechanical alloying methods: NiFe, NiFeCr, NiFeCrCo, NiFeCrCoMn, and off-stoichiometry alloys Ni₂₆Fe₂₀Cr₁₄Co₂₀Mn₂₀, Ni₂₃Fe₂₀Cr₁₇Co₂₀Mn₂₀, Ni₁₄Fe₂₀Cr₂₆Co₂₀Mn₂₀, and Ni₁₄Fe_{21.5}Cr_{21.5}Co_{21.5}Mn_{21.5}. All the alloys prepared by mechanical alloying contained a single-phase FCC structure. This is illustrated in Fig. 5.16 for the X-ray diffraction results of these alloys.

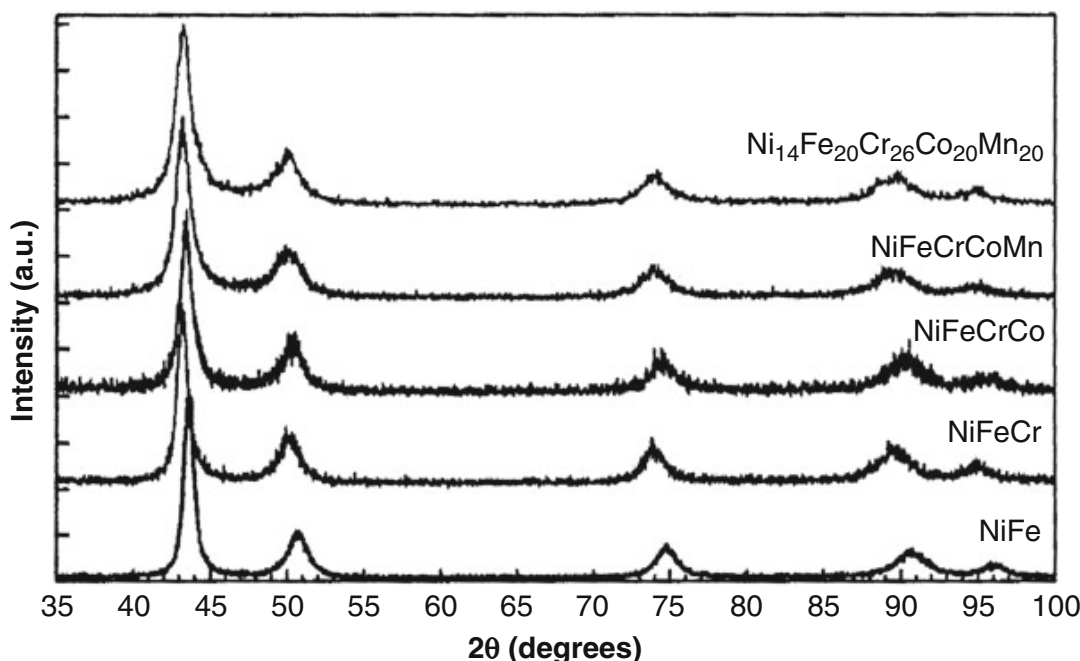


Fig. 5.16 XRD patterns of as-milled NiFe, NiFeCr, NiFeCrCo, and NiFeCrCoMn

5.4 Vapor-State Route

This subsection mainly reviews HEA thin film process via vapor deposition and then compares the resulting properties with traditional low-entropy films. More applications of vapor deposition to process HEA films in carbides and nitrides are detailed in Chap. 14.

5.4.1 Physical Vapor Deposition

Physical vapor deposition (PVD) presents a variety of vacuum deposition methods used to deposit thin films by the condensation of a vaporized form of the desired film material onto various workpiece surfaces. It includes cathodic arc deposition, electron beam physical vapor deposition, evaporative deposition, pulsed laser deposition, and sputter deposition [46].

Among them, magnetron sputtering deposition is the most popular method to fabricate HEA films, as shown in Fig. 5.17. Based on the ion or atom bombardment from the sputtering gas, sputtered atoms close to the atomic fractions of the deposited HEA are ejected from the sputtering target. These sputtered atoms are randomly deposited on the substrate, but the nucleation and growth and thus microstructure of the HEA film are determined by the parameters including the form of source material, power, base pressure, atmosphere composition, substrate bias voltage, and workpiece temperature. So far, this technique has been widely applied to the preparation of a series of HEA films. For example, Tsai et al. [47] successfully synthesized the AlMoNbSiTaTiVZr HEA layer and investigated its diffusion barrier properties between copper and silicon. Chang et al. [48] systematically investigated the influence of substrate bias, deposition temperature, and post-deposition annealing on the structure and properties of the (AlCrMoSiTi)N

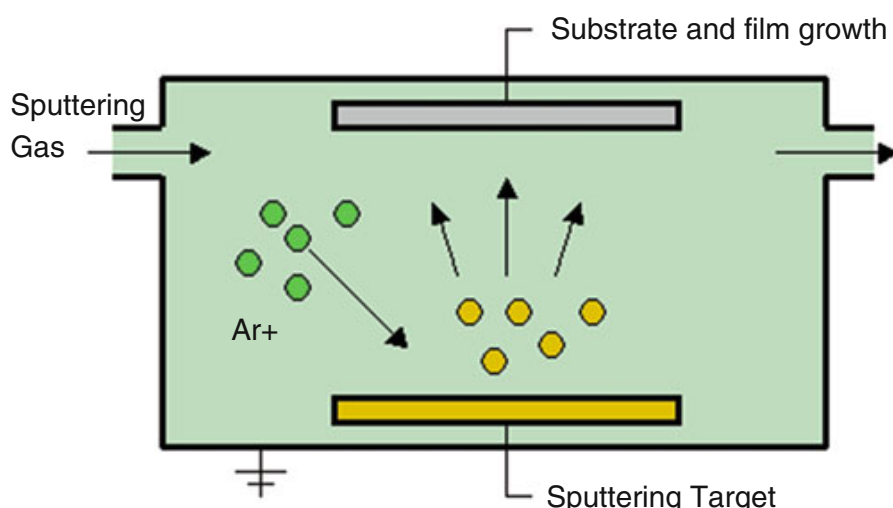


Fig. 5.17 A schematic showing the processing of sputtering deposition [46]

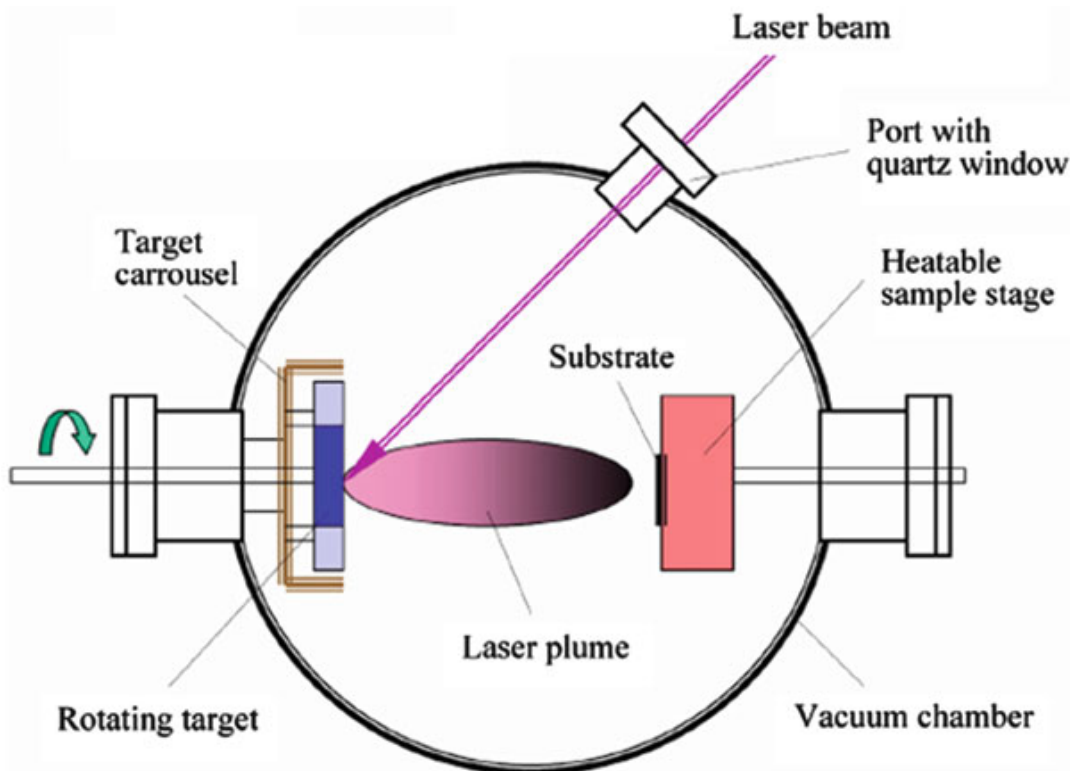


Fig. 5.18 A schematic showing the processing of pulse laser deposition [52]

coatings. Dolique et al. [49, 50] studied the relationship between structure and composition as well as its thermal stability (by *in situ* XRD analysis) of the AlCoCrCuFeNi thin film. Cheng et al. [51] found that the (AlCrMoTaTiZr)N nitride film exhibited a very high hardness of 40.2 GPa and a good wear resistance.

PLD, as another thin film deposition technique, has been effectively used in depositing materials with multielements or complex stoichiometry [52]. Figure 5.18 schematically shows the processing of PLD. A high-powered laser beam from the vacuum chamber strongly strikes the rotating target with required atomic fractions of the HEAs. Due to superheating, the vaporized energetic species from the target material, including atoms, ions, electrons, and otherwise, are in the form of plasma plume, which are further deposited as a thin film on the substrate surface.

Atomic layer deposition (ALD) can be used to effectively control over the atomic layer and film growth of the deposited material using sequential, self-limiting surface reactions, which belongs to a gas-phase chemical process [53]. As shown in Fig. 5.19, the conventional ALD reaction is commonly based on binary reaction sequences, where the reaction chemicals or gaseous species are referred to as precursors and the growth of the film is ascribed to expose its surface on these precursors. Moreover, the reaction between the precursor and the surface of the material is achieved sequentially (called as an ALD cycle) as exhibited in Fig. 5.18. Therefore, for the synthesis of the HEA film, multiple ALD cycles are necessary to be done due to the nature of multicomponent alloys.

Molecular beam epitaxy (MBE), as a thin film deposition technique, is widely used to grow thin, epitaxial films of a wide variety of materials [54]. Due to an

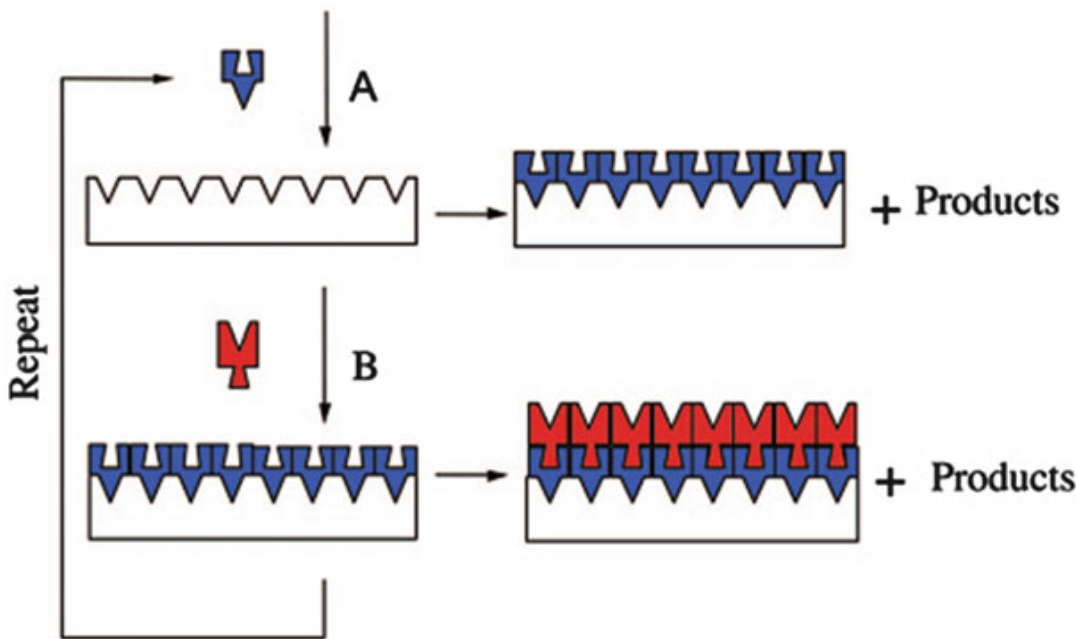


Fig. 5.19 A schematic showing the processing of atomic layer deposition [53]

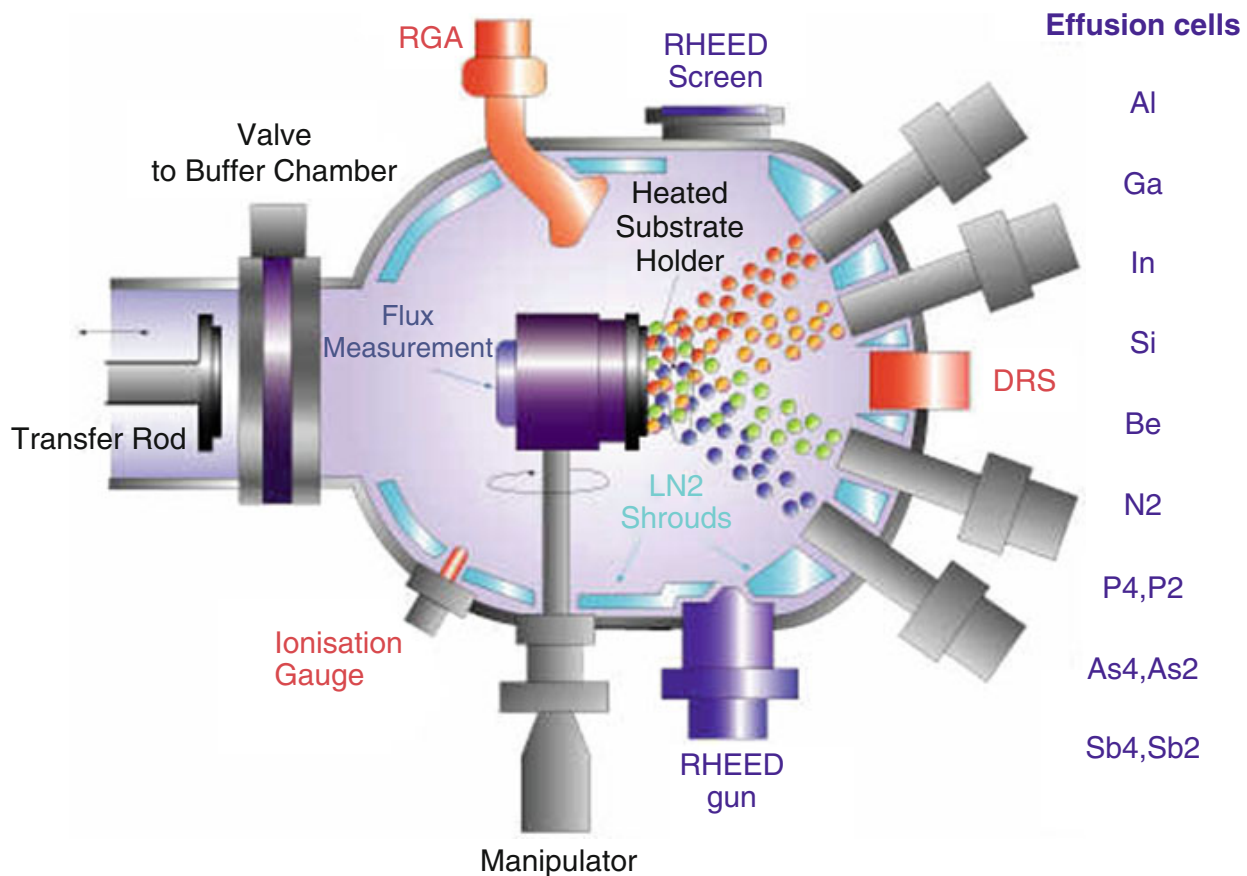


Fig. 5.20 A schematic showing the processing of molecular beam epitaxy [54]

ultra-high vacuum preparation environment and very low deposition rate, the highest purity of the grown films can be achieved such as depositing single crystals. Therefore, the MBE technique can be potentially used to prepare the HEA thin film with single-crystal status (Fig. 5.20).

5.5 Discussion

5.5.1 Mechanical Properties and Application Prospects

Mechanical properties of metallic materials are generally controlled by phase selection, grain size, alloying effect, component segregation, etc., which may be strongly influenced by the solidification rate. Zhang et al. [4] verified that the morphology of AlCoCrFeNi alloy changed from the dendrite prepared by copper-mold casting to the equiaxed grains by Bridgman solidification with improved plasticity by a maximum of 35 %. They believed the high-temperature gradient and solidification rate tend to decrease the constitutional undercooling (constitutional undercooling, which occurs during solidification, is due to compositional changes and results in cooling a liquid below the freezing point ahead to the solid–liquid interface) of the alloy, and thus it is possible to restrain the dendrite formation and leads to grain refinement. This provides a new idea to improve the mechanical properties of the HEAs by rapid solidification methods. Zhang et al. [15–18] found that the laser rapid solidification can effectively decrease the long-range diffusion rate of atoms and thus favor the formation of solid solutions rather than intermetallic compounds. Large solidification rates further lead to the formation of nano- or submicron-size precipitates in the HEAs coatings, which significantly contributes to the outstanding hardness of the HEAs coatings.

Mechanical alloying, as a classical nonequilibrium processing method, can make a wide range of extended solid solutions, nanocrystalline, quasicrystal, or even amorphous materials. Repeated cold welding makes it a perfect selection for synthesizing the alloys with very high melting temperatures, which is often a challenge for other solidification routes. The vapor decomposition, such as PVD, ALD, and MBE, exhibits a potential synthesis route for the HEA films in carbides and nitrides. Due to the significant sluggish diffusion effect, the AlMoNbSiTaTiVZr HEA films demonstrate outstanding diffusion barrier properties between copper and silicon [47]. On the basis of the multiprincipal cocktail effect, the (AlCrMoTaTiZr)N nitride film exhibited a very high hardness of 40.2 GPa and a good wear resistance, showing a huge application potential in the surface engineering field [51].

5.5.2 Thermodynamic Analysis of the Phase Formation

In the previous sections, we have presented three major fabrication routes to prepare HEAs. One apparent difference among them is that their mixing temperatures are very different. For the liquid mixing, the mixing temperature T is above the melting temperature T_m and below the boiling temperature T_b ($T_m < T < T_b$). For the vapor mixing, T is above T_b ($T > T_b$), while for the solid mixing, T is below T_m ($T < T_m$).

It is known that the cooling rates for both the liquid and gas-state routes impact the resulting microstructure substantially. For example, a more or less homogenous solid solution in the FCC structure was obtained in AlCoCrCuFeNi using the splat quenching, while multiphases formed when the sample cooled at a low rate from melt [56]. The cooling rates for vapor deposition are typically orders of magnitude higher than those for conventional arc-melting technique, and as a result, the gas-state route often results in much wider ranges of compositions that can form single solid solution with much finer grain sizes and more uniform elemental distribution in the solid than the liquid-state route. For instance, for the CoCrCuFeNi, noticeable Cu segregation is prevalent in the sample fabricated using the arc-melting technique [1], while using the sputter deposition technique, all alloying elements are almost uniformly distributed in the coating [39].

As for the solid mixing, e.g., the mechanical alloying, numerous reports have revealed that simple solid-solution or even amorphous lattices were dominated in the nanocrystalline structures in spite that minor ordered phases or precipitations such as sigma phase were still presented. For example, Lucas et al. [57] reported a single FCC solid solution without long-range chemical order in CoCrFeNi that was processed using the arc-melting technique, while Praveen et al. [44] reported σ phase formation in addition to the FCC solid solution in CoCrFeNi that was processed using the ball milling technique. It is generally recognized that the entropy effect cannot sufficiently overcome the enthalpy effect due to its lower reaction temperature ($T < T_m$), which thus leads to a lower level of disordered solid-solution phase. However, it needs to be pointed out that by using mechanical alloying, the mechanical energy W should not be ignored, since it contributes to the change of Gibbs free energy of the system (ΔG) by

$$\Delta G = \Delta H + W - T\Delta S \quad (5.1)$$

where ΔS (ΔH) is the change in the entropy (enthalpy) of the system between two states and T is the temperature.

From (5.1), one can see that the W can be a contributor to reduce the enthalpy effect besides the entropy. Moreover, Zhang et al. proposed a Ω criterion that was expressed as $\Omega = T\Delta S/|\Delta H|$ and found that a higher Ω or Ω/T value would predict a higher level of disordered solid-solution phase [55]. Subsequently, on the consideration of the mechanical energy for the mechanical alloying, the Ω criterion can be simply changed as

$$\Omega = T\Delta S/(|\Delta H| - |W|) \quad (5.2)$$

From Eq. (5.2), due to the introduction of the W , a higher Ω value can be still obtained even when the temperature is relatively small. In other words, a higher Ω/T value can be realized in this case, which confirms that the solid-solution phase rather than ordered phase tends to be formed by using mechanical alloying.

5.6 Summary

The arc-melting technique is the most widely reported method in the literature. The HEAs with multiprincipal alloying elements easily exhibit concentrated solid-solution structures and unique mechanical properties. A dendritic microstructure is often observed in the as-cast state, and thus annealing at higher temperatures is required to obtain equiaxed grains and eliminate chemical inhomogeneity. The Bridgman solidification technique successfully synthesizes the single-crystalline HEAs with exceptional tensile plasticity. Due to the significantly higher cooling rates used, the laser cladding HEA coatings demonstrate very fine microstructures and superior properties, such as high-temperature softening resistance, corrosion resistance, and oxidation resistance.

Mechanical alloying of elemental powders is a versatile method to prepare high-entropy alloys. The as-milled powders typically have a nanocrystalline grain structure. Annealing the as-milled powders may or may not lead to changes in the as-milled crystal structure dependent on the particular alloy. Caution in using mechanical alloying to study the competition between an amorphous structure and crystalline solid solutions should be considered since prolonged milling may convert a crystalline structure into an amorphous phase by the introduction of sufficient free energy of the defects – grain boundaries.

Physical vapor deposition is an effective method to prepare thin films from a wide variety of materials. Magnetron sputtering deposition, based on its easy availability, has been successfully applied to prepare the multicomponent HEA thin films with potentially promising properties. Compared with the sputtering deposition, the atomic layer deposition technique can easily realize the film growth with controllable atomic layers, while the molecular beam epitaxy exhibits a potential on the preparation of the single-crystalline HEA films.

Acknowledgments Y.Z. and S.G.M. acknowledge the financial supports from the National Science Foundation of China (NSFC) with granted No. of 51210105006, 50971019, 50571018, 51471025, and 51501123 and National High-tech R&D (863) program with granted No. of 2009AA03Z113. C.C.K. acknowledges the support by the National Science Foundation from the Metals and Metallic Nanostructures program under grant DMR-1104930. H.Z. and Y.P. thank the financial supports from the National Natural Science Foundation of China under Grant No. 51271001 and the Open Project of Jiangsu Key Laboratory of Advanced Metallic Materials under Grant No. AMM201201.

References

1. Yeh JW, Chen SK, Lin SJ, Gan JY, Chin TS, Shun TT, Tsau CH, Chang SY (2004) Nanostructured high-entropy alloys with multiple principal elements: novel alloy design concepts and outcomes. *Adv Eng Mater* 6(5):299–303. doi:[10.1002/adem.200300567](https://doi.org/10.1002/adem.200300567)
2. Zhang Y, Zuo TT, Tang Z, Gao MC, Dahmen KA, Liaw PK, Lu ZP (2014) Microstructures and properties of high-entropy alloys. *Prog Mater Sci* 61:1–93. doi:[10.1016/j.pmatsci.2013.10.001](https://doi.org/10.1016/j.pmatsci.2013.10.001)

3. Zhou YJ, Zhang Y, Wang YL, Chen GL (2007) Solid solution alloys of AlCoCrFeNiTix with excellent room-temperature properties. *Appl Phys Lett* 90:181904. doi:[10.1063/1.2734517](https://doi.org/10.1063/1.2734517)
4. Wang FJ, Zhang Y, Chen GL (2009) Cooling rate and size effect on the microstructure and mechanical properties of AlCoCrFeNi high entropy alloy. *J Eng Mater Technol* 131:034501. doi:[10.1115/1.3120387](https://doi.org/10.1115/1.3120387)
5. Zhang Y, Ma SG, Qiao JW (2012) Morphology transition from dendrites to equiaxed grains for AlCoCrFeNi high-entropy alloys by copper mold casting and Bridgman solidification. *Metall Mater Trans A* 43(8):2625–2630. doi:[10.1007/s11661-011-0981-8](https://doi.org/10.1007/s11661-011-0981-8)
6. Ding XF, Lin JP, Zhang LQ, Su YQ, Chen GL (2012) Microstructural control of TiAl-Nb alloys by directional solidification. *Acta Mater* 60(2):498–506. doi:[10.1016/j.actamat.2011.10.009](https://doi.org/10.1016/j.actamat.2011.10.009)
7. Pollock TM, Tin S (2006) Nickel-based superalloys for advanced turbine engines: chemistry, microstructure and properties. *J Propuls Power* 22(2):361–375. doi:[10.2514/1.18239](https://doi.org/10.2514/1.18239)
8. Qiao JW, Zhang Y, Liaw PK (2008) Tailoring microstructures and mechanical properties of Zr-based bulk metallic glass matrix composites by the Bridgman solidification. *Adv Eng Mater* 10(11):1039–1042. doi:[10.1002/adem.200800149](https://doi.org/10.1002/adem.200800149)
9. Ma SG, Zhang SF, Gao MC, Liaw PK, Zhang Y (2013) A successful synthesis of the CoCrFeNiAl_{0.3} single-crystal, high-entropy alloy by Bridgman solidification. *J Miner, Met Mater Soc* 65(12):1751–1758
10. Hurle DTJ (1963) Mechanisms of growth of metal single crystals from the melt. *Prog Mater Sci* 10:81–147. doi:[10.1016/0079-6425\(63\)90009-4](https://doi.org/10.1016/0079-6425(63)90009-4)
11. Aoki K, Izumi O (1978) On the ductility of the intermetallic compound Ni₃Al. *Trans JIM* 19:203–210. doi:[10.1007/s11837-013-0733-x](https://doi.org/10.1007/s11837-013-0733-x)
12. Ma SG, Zhang SF, Qiao JW, Wang ZH, Gao MC, Jiao ZM, Yang HJ, Zhang Y (2014) Superior high tensile elongation of a single-crystal CoCrFeNiAl_{0.3} high-entropy alloy by Bridgman solidification. *Intermetallics* 54:104–109. doi:[10.1016/j.intermet.2014.05.018](https://doi.org/10.1016/j.intermet.2014.05.018)
13. Wikipedia, free encyclopedia. http://en.wikipedia.org/wiki/Cladding_%28metalworking%29
14. Schnell A, Kurz W (2003) Epitaxial deposition of MCrAlY coatings on a Ni-base superalloy by laser cladding. *Scr Mater* 49(7):705–709. doi:[10.1016/S1359-6462\(03\)00369-5](https://doi.org/10.1016/S1359-6462(03)00369-5)
15. Zhang H, He YZ, Pan Y, Jiao HS (2011) Microstructure and properties of 6FeCoNiCrAlTiSi high-entropy alloy coating prepared by laser cladding. *Appl Surf Sci* 257(6):2259–2263. doi:[10.1016/j.apsusc.2010.09.084](https://doi.org/10.1016/j.apsusc.2010.09.084)
16. Zhang H, Pan Y, He YZ (2011) Synthesis and characterization of FeCoNiCrCu high-entropy alloy coating by laser cladding. *Mater Des* 32(4):1910–1915. doi:[10.1016/j.matdes.2010.12.001](https://doi.org/10.1016/j.matdes.2010.12.001)
17. Zhang H, Pan Y, He YZ (2011) Effects of annealing on the microstructure and properties of 6FeNiCoCrAlTiSi high-entropy alloy coating prepared by laser cladding. *J Therm Spray Technol* 20(5):1049–1055. doi:[10.1007/s11666-011-9626-0](https://doi.org/10.1007/s11666-011-9626-0)
18. Zhang H, He YZ, Pan Y (2013) Enhanced hardness and fracture toughness of the laser-solidified FeCoNiCrCuTiMoAlSiB_{0.5} high-entropy alloy by martensite strengthening. *Scr Mater* 69(4):342–345. doi:[10.1016/j.scriptamat.2013.05.020](https://doi.org/10.1016/j.scriptamat.2013.05.020)
19. Zhang H, He YZ, Pan Y, Zhai PL (2011) Phase selection, microstructure and properties of laser rapidly solidified FeCoNiCrAl₂Si coating. *Intermetallics* 19(8):1130–1135. doi:[10.1016/j.intermet.2011.03.017](https://doi.org/10.1016/j.intermet.2011.03.017)
20. Qiu XW, Zhang YP, Liu CG (2014) Effect of Ti content on structure and properties of Al₂CrFeNiCoCuTi_x high-entropy alloy coatings. *J Alloys Compd* 585(2):282–286. doi:[10.1016/j.jallcom.2013.09.083](https://doi.org/10.1016/j.jallcom.2013.09.083)
21. Li MX, He YZ, Sun GX (2004) Microstructure and wear resistance of laser clad cobalt-based alloy multi-layer coatings. *Appl Surf Sci* 230(1–4):201–206. doi:[10.1016/j.apsusc.2004.02.030](https://doi.org/10.1016/j.apsusc.2004.02.030)
22. Zhang SH, Li MX, Cho TY, Yoon JH, Lee CG, He YZ (2008) Laser clad Ni-base alloy added nano- and micron-size CeO₂ composites. *Opt Laser Technol* 40(5):716–722. doi:[10.1016/j.optlastec.2007.10.007](https://doi.org/10.1016/j.optlastec.2007.10.007)

23. Qiu XW, Liu CG (2013) Microstructure and properties of Al₂CrFeCoCuTiNi_x high-entropy alloys prepared by laser cladding, *J Alloy Comp* 553(3), 216-220. doi:[10.1016/j.jallcom.2012.11.100](https://doi.org/10.1016/j.jallcom.2012.11.100)
24. Zhang H, He YZ, Pan Y, Guo S (2014) Thermally stable laser cladded CoCrCuFeNi high-entropy alloy coating with low stacking fault energy, *J Alloy Comp* 600(7): 210-214. doi:[10.1016/j.jallcom.2014.02.121](https://doi.org/10.1016/j.jallcom.2014.02.121)
25. Yue TM, Zhang H (2014) Laser cladding of FeCoNiCrAlCu_{0.5} high-entropy alloys on AZ31 Mg-alloy substrates, *Mater Res Innov* 588(S2): 588-592. doi:[10.1179/1432891714Z.000000000530](https://doi.org/10.1179/1432891714Z.000000000530)
26. Huang C, Zhang YZ, Shen JY, Vilar R (2011) Thermal stability and oxidation resistance of laser clad TiVCrAlSi high entropy alloy coatings on Ti-6Al-4V alloy, *Surf Coat Technol* 206 (6): 1389-1395. doi:[10.1016/j.surfcoat.2011.08.063](https://doi.org/10.1016/j.surfcoat.2011.08.063)
27. Benjamin JS (1970) Dispersion strengthened superalloys by mechanical alloying. *Metall Trans* 1(10):2943–2951. doi:[10.1007/BF03037835](https://doi.org/10.1007/BF03037835)
28. Benjamin JS (1976) Mechanical alloying. *Sci Am* 234(5):40–48. doi:[10.1038/scientificamerican0576-40](https://doi.org/10.1038/scientificamerican0576-40)
29. Koch CC (1991) In: Cahn RW (ed) Processing of metals and alloys, materials science and technology – a comprehensive treatment, vol 15. VCH, Weinheim, pp 193–245
30. Surayananarayana C (2004) Mechanical alloying and milling. Marcel Dekker, New York
31. Davis RM, Koch CC (1987) Mechanical alloying of brittle components: silicon and germanium. *Scr Metall* 121(3):305–310. doi:[10.1016/0036-9748\(87\)90218-3](https://doi.org/10.1016/0036-9748(87)90218-3)
32. Koch CC, Cavin OB, McKamey CG, Scarbrough JO (1983) Preparation of amorphous Ni₆₀Nb₄₀ by mechanical alloying. *Appl Phys Lett* 43:1017–1019. doi:[10.1063/1.94213](https://doi.org/10.1063/1.94213)
33. Schwartz RB, Petrich RR, Saw CK (1985) The synthesis of amorphous Ni-Ti alloy powers by mechanical alloying. *J Non-Cryst Solids* 76(2–3):281–302. doi:[10.1016/0022-3093\(85\)90005-5](https://doi.org/10.1016/0022-3093(85)90005-5)
34. Varalakshmi S (2008) Synthesis and characterization of nanocrystalline high entropy alloys by mechanical alloying. Ph.D. Thesis, Department of Metallurgical and Materials Engineering, Indian Institute of Technology, Madras
35. Varalakshmi S, Kamaraj M, Murty BS (2008) Synthesis and characterization of nanocrystalline AlFeTiCrZnCu high entropy solid solution by mechanical alloying. *J Alloys Compd* 460 (1–2):253–257. doi:[10.1016/j.jallcom.2007.05.104](https://doi.org/10.1016/j.jallcom.2007.05.104)
36. Varalakshmi S, Kamaraj M, Murty BS (2010) Processing and properties of nanocrystalline CuNiCoZnAlTi high entropy alloys by mechanical alloying. *Mater Sci Eng A* 527 (4–5):1027–1030. doi:[10.1016/j.msea.2009.09.019](https://doi.org/10.1016/j.msea.2009.09.019)
37. Varalakshmi S, Appa Rao G, Kamaraj M, Murty BS (2010) Hot consolidation and mechanical properties of nanocrystalline equiatomic AlFeTiCrZnCu high entropy alloy after mechanical alloying. *J Mater Sci* 45(19):5158–5163. doi:[10.1007/s10853-010-4246-5](https://doi.org/10.1007/s10853-010-4246-5)
38. Chen YL, Hu YH, Tsai CW, Hsieh CA, Kao SW, Yeh JW, Chin TS, Chen SK (2009) Alloying behavior of binary to octonary alloys based on Cu-Ni-Al-Co-Cr-Fe-Ti-Mo during mechanical alloying. *J Alloys Compd* 477(1–2):696–705. doi:[10.1016/j.jallcom.2008.10.111](https://doi.org/10.1016/j.jallcom.2008.10.111)
39. Zhang KB, Fu ZY, Zhang JY, Shi J, Wang WM, Wang H, Wang YC, Zhang QJ (2009) Nanocrystalline CoCrFeNiCuAl high-entropy solid solution synthesized by mechanical alloying. *J Alloys Compd* 485(1–2):L31–L34. doi:[10.1016/j.jallcom.2009.05.144](https://doi.org/10.1016/j.jallcom.2009.05.144)
40. Praveen S, Murty BS, Kottada RS (2012) Alloying behavior in multi-component AlCoCrCuFe and high entropy alloys. *Mater Sci Eng A* 534:83–89. doi:[10.1016/j.msea.2011.11.044](https://doi.org/10.1016/j.msea.2011.11.044)
41. Tariq NH, Naeem M, Hasan BA, Akhter JI, Siddique M (2013) Effect of W and Zr on structural, thermal and magnetic properties of AlCoCrCuFeNi high entropy alloy. *J Alloys Compd* 556:79–85. doi:[10.1016/j.jallcom.2012.12.095](https://doi.org/10.1016/j.jallcom.2012.12.095)
42. Sriharitha R, Murty BS, Kottada RS (2013) Phase formation in mechanically alloyed Al_xCoCrCuFeNi ($x = 0.45, 1, 2.5, 5\text{ mol}$) high entropy alloys. *Intermetallics* 32:119–126. doi:[10.1016/j.intermet.2012.08.015](https://doi.org/10.1016/j.intermet.2012.08.015)

43. Fu ZQ, Chen WP, Fang SC, Li XM (2014) Effect of Cr addition on the alloying behavior, microstructure and mechanical properties of twinned CoFeNiAl_{0.5}Ti_{0.5} alloy. *Mater Sci Eng A* 597:204–211. doi:[10.1016/j.msea.2013.12.096](https://doi.org/10.1016/j.msea.2013.12.096)
44. Praveen S, Murty BS, Kottada RS (2013) Phase evolution and densification behavior of nanocrystalline multicomponent high entropy alloys during spark plasma sintering. *J Miner, Met Mater Soc* 65(12):1797–1804. doi:[10.1007/s11837-013-0759-0](https://doi.org/10.1007/s11837-013-0759-0)
45. Zaddach AJ, Niu C, Koch CC, Irving DL (2013) Mechanical properties and stacking fault energies of NiFeCrCoMn high-entropy alloy. *J Miner, Met Mater Soc* 65(12):1780–1789. doi:[10.1007/s11837-013-0771-4](https://doi.org/10.1007/s11837-013-0771-4)
46. http://en.wikipedia.org/wiki/Sputter_deposition
47. Tasi MH, Yeh JW, Gan JY (2008) Diffusion barrier properties of AlMoNbSiTaTiZr high-entropy alloy layer between copper and silicon. *Thin Solid Films* 516:5527–5530. doi:[10.1016/j.tsf.2007.07.109](https://doi.org/10.1016/j.tsf.2007.07.109)
48. Chang HW, Huang PK, Yeh JW, Davison A, Tsau CH, Yang CC (2008) Influence of substrate bias, deposition temperature, and post-deposition annealing on the structure and properties of multi-principal-component (AlCrMoSiTi)N coatings. *Surf Coat Technol* 202:3360–3366. doi:[10.1016/j.surfcoat.2007.12.014](https://doi.org/10.1016/j.surfcoat.2007.12.014)
49. Dolique V, Thomann AL, Brault P, Tessier Y, Gillon P (2009) Complex structure/composition relationship in thin films of AlCoCrCuFeNi high entropy alloy. *Mater Chem Phys* 117:142–147. doi:[10.1016/j.matchemphys.2009.05.025](https://doi.org/10.1016/j.matchemphys.2009.05.025)
50. Dolique V, Thomann AL, Brault P, Tessier Y, Gillon P (2010) Thermal stability of AlCoCrCuFeNi high entropy alloy thin films studied by in-situ XRD analysis. *Surf Coat Technol* 204:1989–1992. doi:[10.1016/j.surfcoat.2009.12.006](https://doi.org/10.1016/j.surfcoat.2009.12.006)
51. Cheng KH, Lai CH, Lin SJ, Yeh JW (2011) Structural and mechanical properties of multi-element (AlCrMoTaTiZr)N_x coatings by reactive magnetron sputtering. *Thin Solid Films* 519:3185–3190. doi:[10.1016/j.tsf.2010.11.034](https://doi.org/10.1016/j.tsf.2010.11.034)
52. http://groups.ist.utl.pt/rschwarz/rschwarzgroup_files/PLD_files/PLD.htm
53. George SM (2010) Atomic layer deposition: An overview, *Chem Rev*, 110: 111–131. doi:[10.1021/cr900056b](https://doi.org/10.1021/cr900056b).
54. <http://newenergyandfuel.com/http://newenergyandfuel.com/2010/09/13/on-the-path-to-full-spectrum-photovoltaic-solar-cells/>
55. Zhang Y, Lu ZP, Ma SG, Liaw PK, Cheng YQ, Gao MC (2014) Guidelines in predicting phase formation of high-entropy alloys. *MRS Commun* 4:57–62. doi:[10.1557/mrc.2014.11](https://doi.org/10.1557/mrc.2014.11)
56. Singh S, Wanderka N, Murty BS, Glatzel U, Banhart J (2011) Decomposition in multi-component AlCoCrCuFeNi high-entropy alloy. *Acta Mater* 59(1):182–190. doi:[10.1016/j.actamat.2010.09.023](https://doi.org/10.1016/j.actamat.2010.09.023)
57. Lucas MS, Wilks GB, Mauger L, Munoz JA, Senkov ON, Michel E, Horwath J, Semiatin SL, Stone MB, Abernathy DL, Karapetrova E (2012) Absence of long-range chemical ordering in equimolar FeCoCrNi. *Appl Phys Lett* 100(25):251907–251904. <http://dx.doi.org/10.1063/1.4730327>

Chapter 6

Mechanical Properties of High-Entropy Alloys

Haoyan Diao, Xie Xie, Fei Sun, Karin A. Dahmen, and Peter K. Liaw

Abstract This chapter reviews mechanical properties of high-entropy alloys (HEAs) in the fields of hardness, compression, tension, serration behavior, fatigue, and nanoindentation. It shows that the hardness of HEAs varies widely from 140 to 900 HV, highly depending on the alloy systems and related processing methods. The effects of annealing treatment, alloying, and structure on the hardness are discussed. The hardness at high temperatures is also summarized. For compression tests, several parameters of materials, such as Young's modulus, compressive yield strength, elastic strain, and plastic strain, are determined and discussed. Various loading conditions, such as temperatures, Al contents, strain rates, sample sizes, and aging/annealing effects, are reported to have influence on the microstructural evolution during compression deformation. Microcompression experiments have been performed on HEAs. Even though the study of tensile properties of HEAs is limited to few alloy systems, the effects of structures, grain sizes, alloying elements, and processing parameters on the yielding stress, ductility, and shape of the stress-strain curve, and fracture behavior are discussed. The characteristic elastic behavior is studied by in situ neutron-diffraction techniques during tension. A mean-field theory (MFT) successfully predicts the slip-avalanche and serration statistics observed in recent simulations of plastic deformation of HEAs. Four-point-bending-fatigue tests are conducted on the $\text{Al}_{0.5}\text{CoCrCuFeNi}$ HEA at various applied loads and reveal that fatigue properties of HEAs could be generally better, compared with conventional alloys and bulk metallic glasses. Nanoindentation studies on the incipient plasticity and creep behavior are discussed. The future work related to mechanical properties of HEAs is suggested at the end.

H. Diao • X. Xie • P.K. Liaw (✉)

Department of Materials Science and Engineering, The University of Tennessee,
Knoxville, TN 37996, USA

e-mail: pliaw@utk.edu

F. Sun • K.A. Dahmen

Department of Physics, University of Illinois at Urbana-Champaign,
1110 West Green Street, Urbana, IL 61801, USA

e-mail: dahmen@illinois.edu

Keywords Mechanical properties • Hardness • Compression • Tension • Serration • Fatigue • Nanoindentation • Mean-field theory • Temperature effect • Alloying effect • Microstructure • Nanostructure • Face-centered cubic (FCC) • Body-centered cubic (BCC) • Solid solution • Single phase • Multiphase • High-entropy alloys (HEAs)

6.1 Introduction

Mechanical properties of high-entropy alloys (HEAs) are widely studied in the field of hardness [1–51], compression [2, 3, 52, 53], tension [15, 48, 49, 54–61], serration [62–72], fatigue [20, 45, 73], and nanoindentation [8, 74–76] since 2004. Even though HEAs have a wide range of mechanical properties, many HEAs have been reported to have promising properties, such as high hardness values [3, 4, 6, 7, 9, 10, 13, 17, 22, 29, 31, 40, 51], high yielding strengths [22, 50, 77, 78], large ductility [54, 57, 61], excellent fatigue resistance [45, 73], and good fracture toughness [20, 79]. In this chapter, we will review the effects of compositions, annealing treatments, alloying-element contents, temperatures, strain rates, sample sizes, and lattice-structure types on the mechanical behavior and related microstructural evolution of HEAs in the sections relating to hardness, compression, tension, fatigue, and nanoindentation, respectively. Besides experimental studies, a mean-field theory (MFT) model successfully predicts the slip avalanche and serration statistics observed in recent simulations of plastic deformation of HEAs [58, 62–72]. Based on former studies, future work related to mechanical properties of HEAs is proposed at the end of this chapter.

6.2 Hardness

Hardness is one of the most convenient ways to describe the mechanical properties of metallic materials [80]. Vickers hardness testing can be done quickly and efficiently, without the need for a large volume of sample materials. For some thin-film HEAs, the yield stress of thin films cannot be measured directly, but microhardness tests can easily be done with high precision. HEAs exhibit hardness values varying widely from 140 to 900 HV, depending on the alloy systems and related processing methods [2–4, 6, 9–15, 17, 19–22, 28–31, 38–42, 47–50]. The hardness values of the 20 most studied HEAs, compared with conventional alloys, are shown in Fig. 6.1. The hardness changes widely in each alloy system. Taking the AlCoCrCuFeNi [2, 3, 5, 54, 81–85] alloy system, for example, the hardness values vary from 154 to 658 HV, which are strongly dependent on the exact chemical compositions, fabrication methods, and following heat-treatment processes. The hardness values of several alloy systems, such as AlCrFeMnNi and AlCrFeMoNi, are generally higher than conventional ferrous and nonferrous alloys

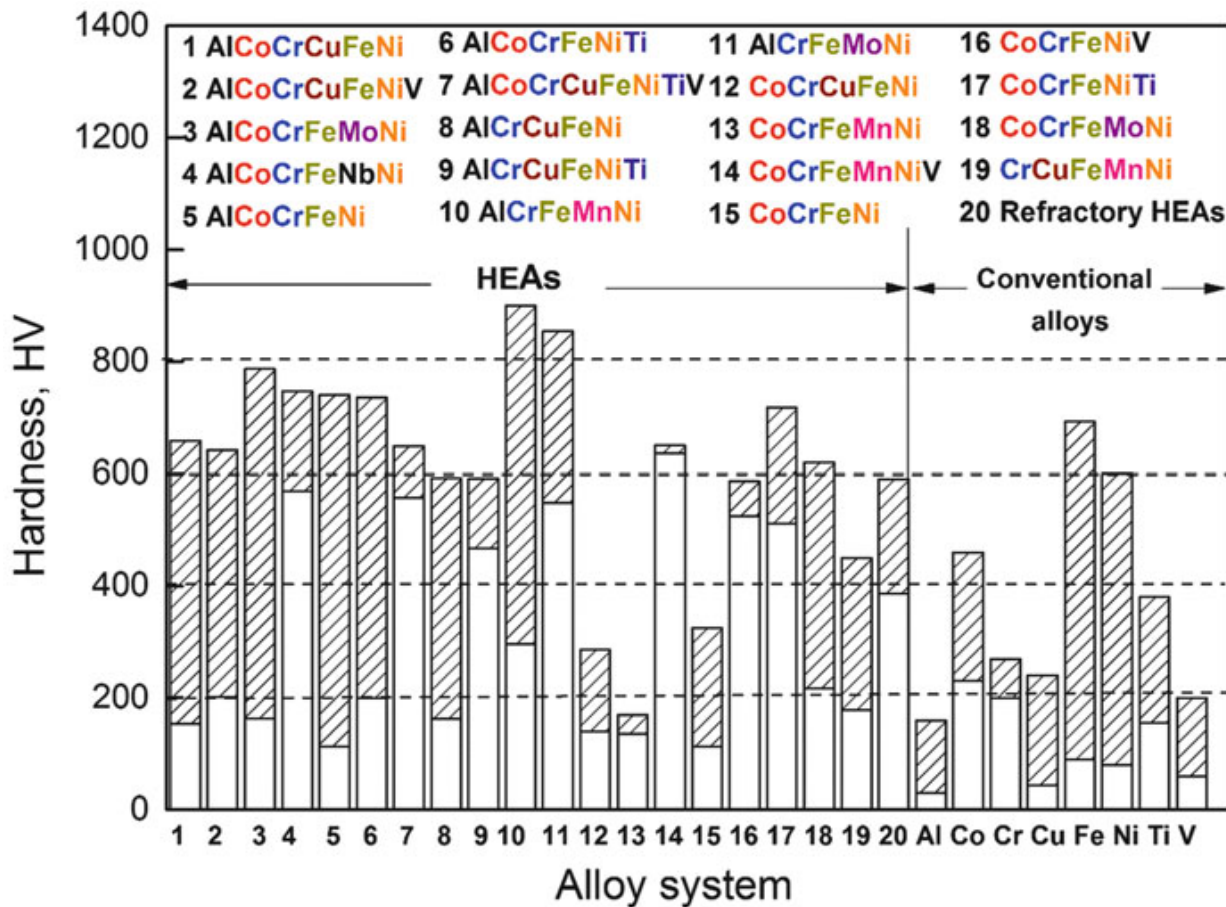


Fig. 6.1 Hardness values of 20 most studied HEAs, compared with conventional alloys, such as Al-, Co-, Cr-, Cu-, Fe-, Ni-, Ti-, and V-based alloys, using data from Refs. [2–4, 6, 9–15, 17, 19–22, 28–31, 38–42, 47–50, 81–85]. The hatched region shows the hardness range of each alloy system. For example, the hardness of AlCoCrCuFeNi varies from 154 to 658 HV

in Fig. 6.1. However, the hardness values of the as-cast HEAs mainly with the face-centered cubic (FCC) phase (i.e., CoCrFeNi, CoCrCuFeNi, and CoCrFeMnNi) are generally low at room temperature [12], but those containing appreciable amounts of Al and Ti are generally high due to the formation of stronger second phases. The average hardness values of refractory HEAs mainly with the body-centered cubic (BCC) phase are relatively high, e.g., 390 HV, 454 HV, 535 HV, 591 HV, and 500 HV for HfNbTaTiZrTi, MoNbTaW, MoNbTaVW, AlMo_{0.5}NbTa_{0.5}TiZr, and Al_{0.4}Hf_{0.6}NbTaTiZr alloys, respectively [13, 21, 50]. Thus, the selection of the alloy system, adjusting the composition ratio within an alloy system, and the choice of alloy-processing methods are critical in determining the alloy hardness of HEAs.

6.2.1 Annealing Treatment

Based on the effect of the annealing treatment on the hardness, HEAs are divided into two groups: (a) strong aging hardening (red lines) and (b) weak aging hardening (black lines), shown in Fig. 6.2.

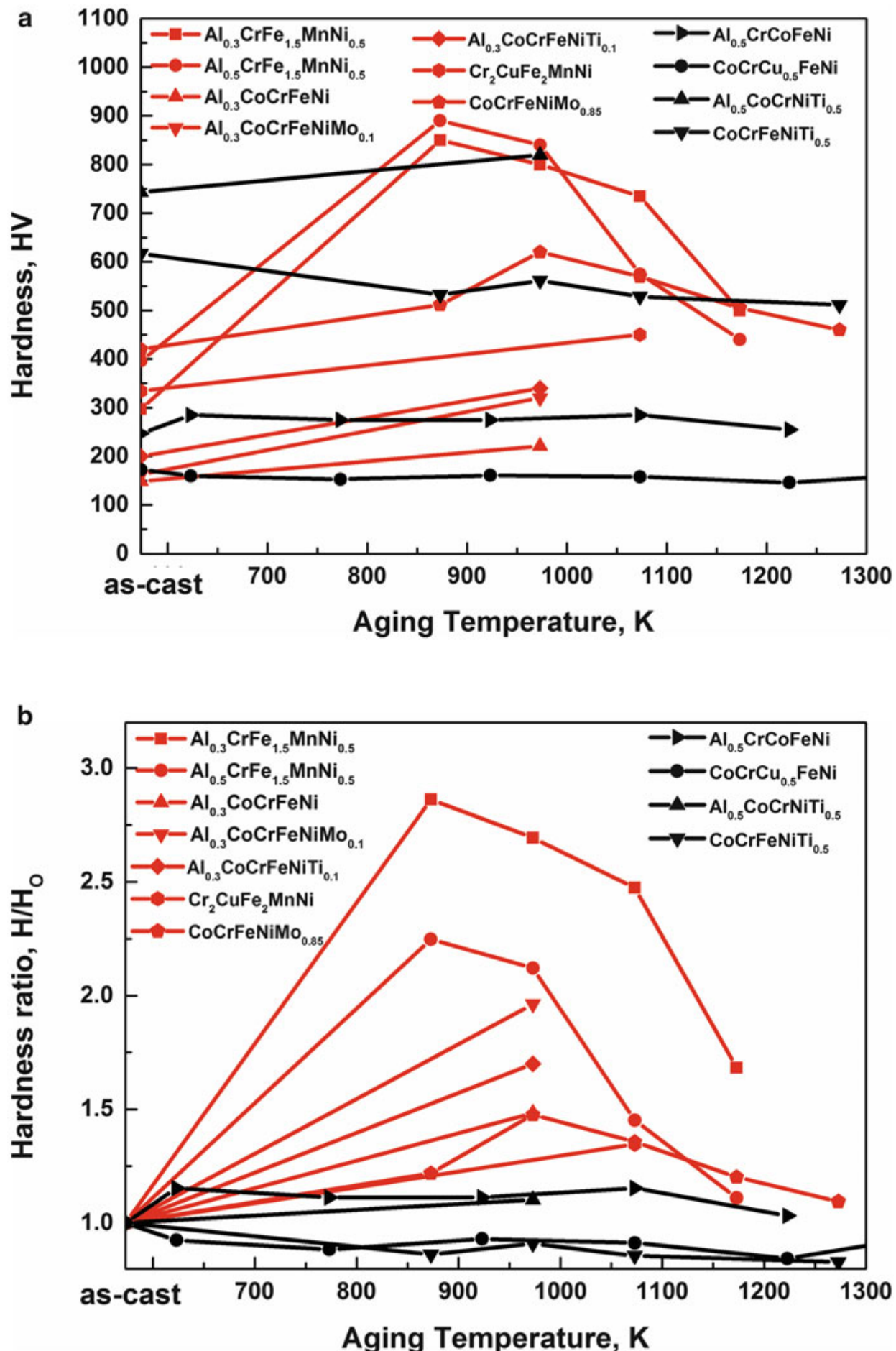


Fig. 6.2 Annealing effects on the hardness of HEAs, using data from Refs. [9, 12, 14, 19, 28, 40, 42, 47]. (a) Hardness values and (b) hardness ratio, hardness/original hardness (H/H_0)

Strong high-temperature aging hardening happens in several alloy systems, such as $\text{Al}_x\text{CrFe}_{1.5}\text{MnNi}_{0.5}$ ($x = 0.3$ and 0.5) [9], three FCC-structured HEAs ($\text{Al}_{0.3}\text{CoCrFeNi}$, $\text{Al}_{0.3}\text{CoCrFeNiMo}_{0.1}$, and $\text{Al}_{0.3}\text{CoCrFeNiTi}_{0.1}$) [14], $\text{Cr}_2\text{CuFe}_2\text{MnNi}$ [28], and $\text{CoCrFeNiMo}_{0.85}$ [42], shown by red lines in Fig. 6.2. This strong high-temperature age-hardening phenomenon is seldom found in conventional alloys. The age-hardening behavior is attributed to the formation of precipitates, for example, a ρ ($\text{Cr}_5\text{Fe}_6\text{Mn}_8$) phase in the $\text{Al}_x\text{CrFe}_{1.5}\text{MnNi}_{0.5}$ ($x = 0.3$ and 0.5) alloy, a (Ni, Al)-rich B2 phase in the $\text{Al}_{0.3}\text{CoCrFeNi}$ alloy, the dual precipitates of a (Ni, Al)-rich phase and a (Cr, Mo) (Co, Fe, Ni) σ phase in the $\text{Al}_{0.3}\text{CoCrFeNiMo}_{0.1}$ alloy, and a (Ni, Co, Ti)-rich B2 phase in the $\text{Al}_{0.3}\text{CoCrFeNiTi}_{0.1}$ alloy [9, 14]. However, when the temperature is above 900 K, the hardness of the $\text{Al}_x\text{CrFe}_{1.5}\text{MnNi}_{0.5}$ ($x = 0.3$ and 0.5) alloy decreases. The reason is mainly related to the larger grain size and softening of the second phases [9].

If there is no new precipitation during the annealing process, annealing plays a slight role in increasing hardness of HEAs. This situation happens in the $\text{Al}_{0.5}\text{CoCrFeNi}$, $\text{CoCrCu}_{0.5}\text{FeNi}$, $\text{Al}_{0.5}\text{CoCrNiTi}_{0.5}$, and $\text{CoCrFeNiTi}_{0.5}$ samples [12, 19, 40, 47], shown by black lines in Fig. 6.2.

6.2.2 Alloying Effects

The alloying ratio plays an important role on the structure and mechanical properties of HEAs, which draws much attention to HEAs in the area of metallurgy. In this section, we will summarize the effect of the Al, B, Co, Cr, Mo, Nb, Ni, and V on the mechanical properties of the single-phase HEAs and multiphase HEAs, respectively.

None of the reported equiatomic multicomponent bulk alloys of light transitions metals with Al are single-phase solid solutions. Their common feature is the eutectic type of the interaction between the components [2, 23, 86]. For the systems, $\text{Al}_x\text{CoCrCuFeNi}$ [2], $\text{Al}_x\text{CoCrFeMnNi}$ [60], $\text{Al}_x\text{CoCrFeNi}_2$ [38], and $\text{Al}_x\text{CoCuFeNi}$ [87, 88], single-phase HEAs with a FCC structure type form with very low Al contents ($x \leq 0.5$). In the FCC single-phase region ($x \leq 0.5$) (marked by gray squares in Fig. 6.3), the increase of hardness mainly results from substitutional solid-solution strengthening.

The effects of aluminum concentrations on the hardness values of the $\text{Al}_x\text{CoCrCuFeNi}$ [2, 3, 43, 60], $\text{Al}_x\text{CoCrFeNi}_2$ [38], $\text{Al}_x\text{CoCrFeNi}$ [11, 30], $\text{Al}_x\text{CoCrFeMo}_{0.5}\text{Ni}$ [39], and $\text{Al}_x\text{CoCrFeNiTi}$ [31] alloys are summarized in Fig. 6.3. From Fig. 6.3, we can see that the hardness of the alloys generally increases, as the aluminum ratio increases in the $\text{Al}_x\text{CoCrCuFeNi}$, $\text{Al}_x\text{CoCrFeNi}_2$, and $\text{Al}_x\text{CoCrFeNi}$ alloys. The aluminum contribution to the hardness increase of multiphase HEAs was related to a solution-hardening mechanism, a precipitation-strengthening effect, and a nanocomposite-strengthening effect [2, 11, 30, 38]. The origins of such effects can go back to lattice-strain energies and electronic bonds [43]. For $\text{Al}_x\text{CoCrFeMo}_{0.5}\text{Ni}$ and $\text{Al}_x\text{CoCrFeNiTi}$, the trend is different, that is, the

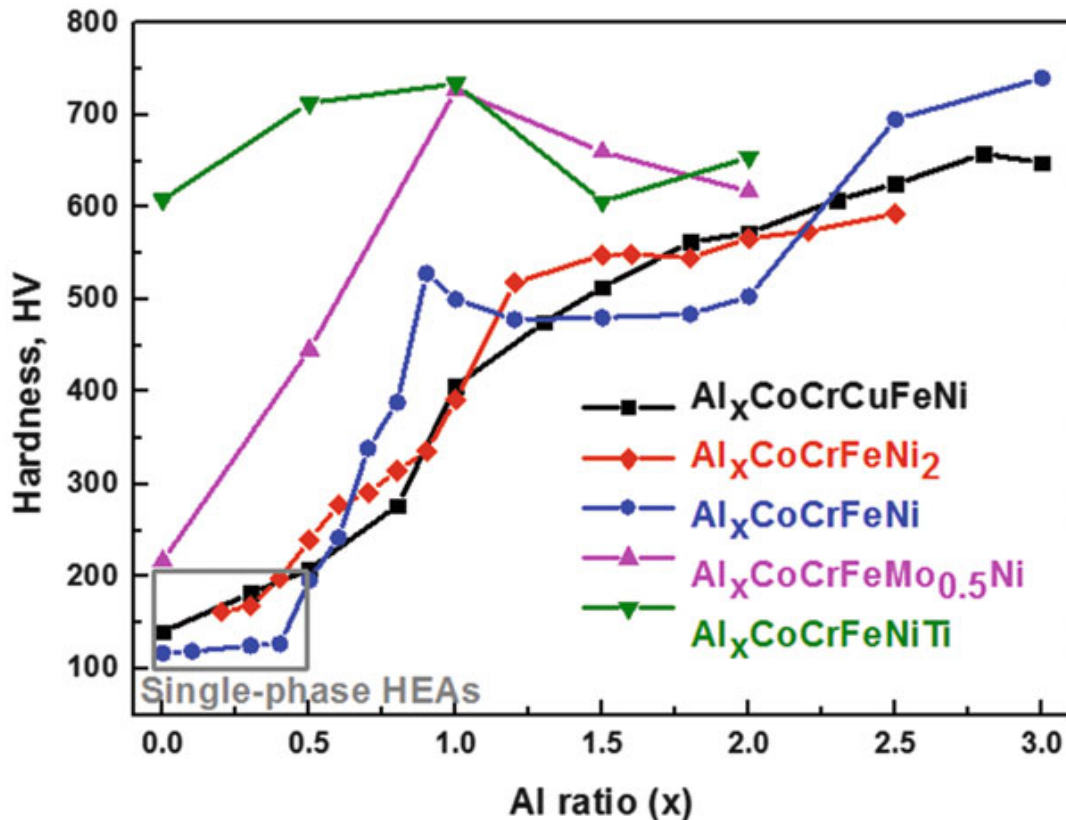


Fig. 6.3 Vickers hardness of the $\text{Al}_x\text{CoCrCuFeNi}$, $\text{Al}_x\text{CoCrFeNi}_2$, $\text{Al}_x\text{CrCuFeNi}_2$, $\text{Al}_x\text{CoCrFeMo}_{0.5}\text{Ni}$, and $\text{Al}_x\text{CoCrFeNiTi}$ alloy systems with different aluminum contents (x values in molar ratio), using data from Refs. [2, 3, 11, 30, 31, 38, 39, 43, 60]. The single-phase HEAs are marked by a gray square

hardness increases, when the atomic ratio of aluminum is lower than 1.0, while the hardness decreases, when the aluminum atomic ratio is higher than 1.0. This trend can be explained by phase compositions and microstructures. In the as-cast Al_0 alloy, the FCC solid solution was confirmed as the main phase, while the $\text{Al}_{1.0}$ alloy is mainly composed of the $(\alpha\text{-Fe}, \text{Cr})$ -based BCC solid solution, which is stronger than the FCC counterpart [31, 39]. The hardness decreases, as the aluminum ratio is higher than 1.0, resulting from the brittleness of the formed BCC phase.

The effect of B/Ni/V/Co/Cr/Nb/Mo on the hardness values of HEAs is summarized in Fig. 6.4. The alloys, $\text{AlB}_x\text{MnNiTi}$, possess high hardness. The hardness increases from 740 to 779 HV, as the boron atomic ratio increases from 0 to 0.5, which could be induced by the aberrance of the crystal lattice [6]. The effect of vanadium addition on hardness is well studied in $\text{Al}_{0.5}\text{CoCrCuFeNiV}_x$ and AlCoCrFeNiV_x . For $\text{Al}_{0.5}\text{CoCrCuFeNiV}_x$, in the range of $x < 0.4$ and $x > 1.2$, solution hardening in FCC and BCC phases seems small with the addition of more vanadium. In the range of $0.4 < x < 1.0$, with more vanadium addition, the hardness value rapidly increases and peaks (640 HV) at $x = 1.0$. The increased volume fractions of the BCC phase and the σ -phase precipitation are the main reason [4]. The hardness of as-cast AlCrFeCuNi_x HEAs is constant, around 490 HV, when x is in the range of 0.6 to 1.0. But the hardness decreases markedly, when x is in the range of 1.0 to 1.4, which results from the decrease of the proportion of the CrFe-rich BCC phase [24, 26]. The hardness of AlCrFeNiMo_x ($x = 0, 0.2, 0.5, 0.8$,

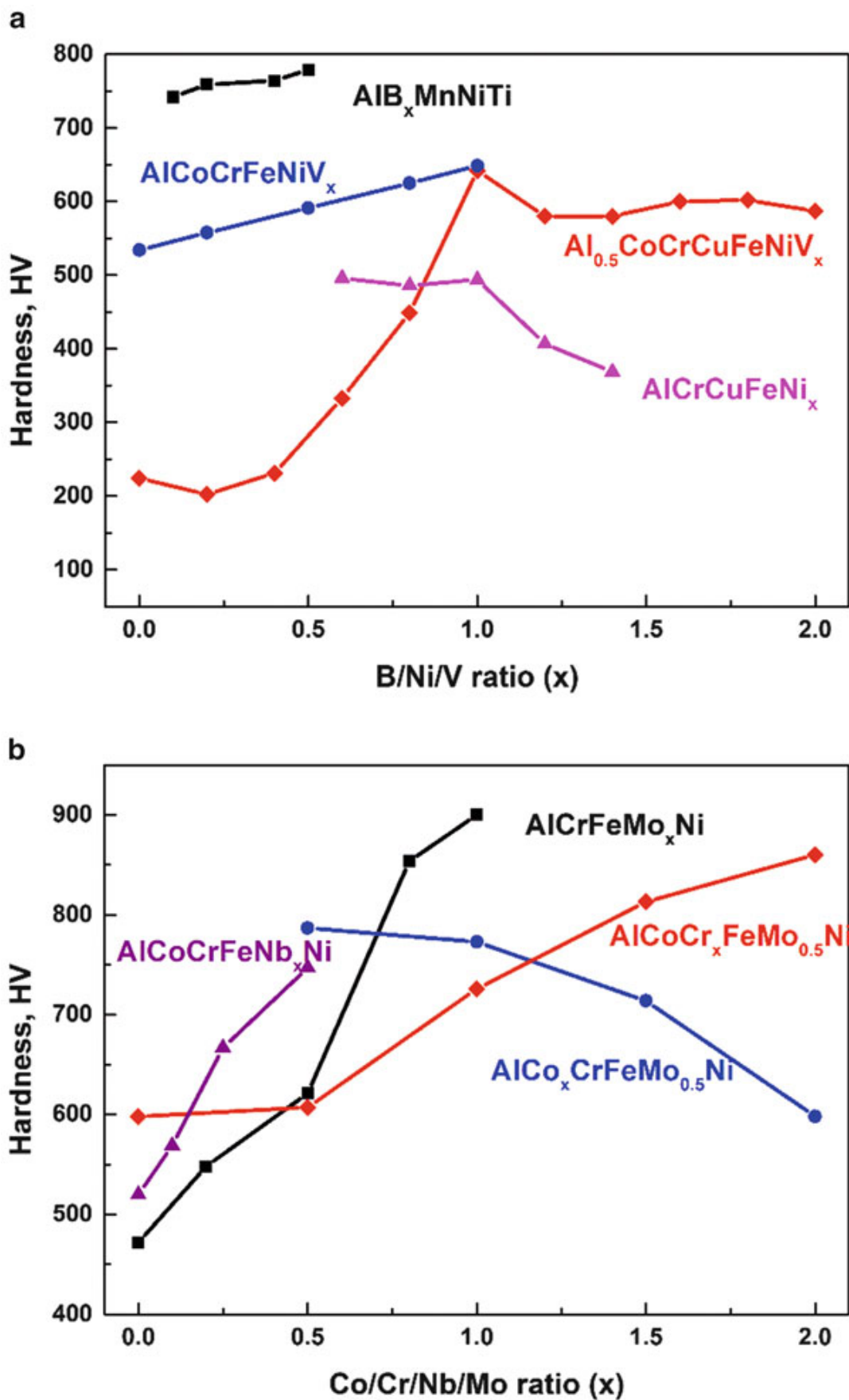


Fig. 6.4 Vickers hardness of the (a) AlMnNiTiB_x , $\text{Al}_{0.5}\text{CoCrCuFeNiV}_x$, AlCoCrFeNiV_x , AlCrFeCuNi_x , and (b) AlCrFeNiMo_x , $\text{AlCo}_x\text{CrFeMo}_{0.5}\text{Ni}$, $\text{AlCoCr}_x\text{FeMo}_{0.5}\text{Ni}$, and AlCoCrFeNiNb_x alloy systems with different B/V/Ni/Mo/Co/Cr/Nb contents (x values in molar ratio), using data from Refs. [4, 6, 10, 18, 24–26, 35]

and 1.0) increased obviously from 472.4 to 911.5 HV with the addition of the Mo element, which is due to the solution-strengthening behavior and the transformation from the CrFe-type solid solution to the CrFeMo-type σ phase [35]. $\text{AlCo}_x\text{CrFeMo}_{0.5}\text{Ni}$ HEAs are superior over the $\text{Al}_x\text{CoCrCuFeNi}$ HEAs, which is attributable to the high-volume fraction of the σ phase. With the increase of Co from 0.5 to 2.0, the hardness decreases from 800 to 600 HV [10]. For the $\text{AlCoCr}_x\text{FeMo}_{0.5}\text{Ni}$, the alloy hardness increases from 601 HV at $x=0$ to 867 HV at $x=2.0$, as a result of increasing the amount of the hard σ phase [18]. The Vickers hardness of AlCoCrFeNiNb_x [25] has an approximately linear increase with increasing the Nb content.

6.2.3 Structure Effects

There are many factors determining the hardness values of FCC and BCC phases. It is known that the FCC structure has slip planes with the closest packing, while the BCC structure has no true close-packed slip planes. Thus, the critical stress for slip in the FCC structure is basically smaller than the BCC structure. In addition, stronger interatomic bonding would have higher Young's modulus and, thus, higher strength. The solution-hardening effect is also more pronounced for metals with higher modulus. The BCC phase is stronger than the FCC phase in several alloy systems, such as $\text{Al}_x\text{CoCrCuFeNi}$ [2, 3], $\text{Al}_{0.5}\text{CoCrCuFeNiV}_x$ [4], and $\text{Al}_x\text{CoCrFeNi}$ [8], which can be explained with the basic structure factor and solution-hardening mechanism [2–5]. The hardness, H , and volume fractions of FCC and BCC phases in the transition region of the $\text{Al}_x\text{CoCrFeNi}$ system can be calculated as follows [7]:

$$H = aH_{\text{FCC}} + (1 - a)H_{\text{BCC}} \quad (6.1)$$

where H_{FCC} and H_{BCC} are the average hardness values of single FCC and BCC phases, respectively. a is the volume fraction of the FCC phase, and $(1 - a)$ is that of the BCC phase.

Microstructures affect the hardness of HEAs too. For example, dendritic and interdendritic areas in HEAs have different microhardnesses. Take the CoCrFeMnNi -related system, for example. The dendritic and interdendritic hardnesses are 30 HV and 109 HV for CoCrFeMnNi , 105 HV and 41 HV for CoCrFeMnNbNi , and 103 HV and 29 HV for CoCrFeMnNiV , respectively [1]. This trend can be explained by the composition segregation and the hardness nature of related pure metals.

6.2.4 Hot Hardness

Some HEAs own high hot hardness and have the potential in high-temperature applications. The $\text{AlCo}_x\text{CrFeMo}_{0.5}\text{Ni}$ ($x=0.5, 1.0, 1.5$, and 2.0) alloys exhibit the high hot hardness of about 740 HV at 300 K, 660 HV at 600 K, and 340 HV at

1,273 K [10]. The softening coefficients of pure metals, such as Mo, Ni, Cr, Si, and Fe [10], are two orders of magnitudes larger than those of $\text{AlCo}_x\text{CrFeMo}_{0.5}\text{Ni}$ alloys, indicating that alloying indeed has a tremendous effect on lowering the softening coefficient. It suggests that the σ phase is the main strengthener at high temperatures [10]. $\text{AlCoCr}_x\text{FeMo}_{0.5}\text{Ni}$ ($x=0, 0.5, 1, 1.5$, and 2) alloys [18] and $\text{Al}_x\text{CoCrFeNi}$ alloys [51] have respective hardness values at high temperatures, shown in Fig. 6.5.

The hot hardness as a function of temperature can be represented, using the following equation suggested by Westbrook [89]:

$$H = A \exp(-BT) \quad (6.2)$$

The constant, A , is called the intrinsic hardness or the value of hardness at 0 K, i.e., extrapolated hardness at the absolute zero temperature, and B is called the softening coefficient or thermal coefficient of hardness. There are two sets of constants, A and B , in low-temperature and high-temperature regions of $\text{AlCoCr}_x\text{FeMo}_{0.5}\text{Ni}$ ($x=0, 0.5, 1, 1.5$, and 2), respectively, suggesting a change in the deformation mechanisms. In the high-temperature region, smaller B means higher resistance to softening. The transition between low-temperature and high-temperature regions may occur at one temperature or over a range of temperatures. In most metals and alloys, the transition temperature is known to occur at about $0.5 T_m$, where T_m is the melting point.

6.3 Compressive Properties

6.3.1 Compressive Stress–Strain Curves

Compression experiments have been extensively performed to study the mechanical properties of HEAs [2, 3, 35, 49, 53, 90–102]. From the stress–strain curve, several parameters of materials can be determined, including Young’s modulus (E), compressive yield strength (σ_y), compressive strength (σ_{\max}), elastic strain (ε_e), plastic strain (ε_p), etc. The reported values determined from compression tests for different kinds of HEAs are summarized in Table 6.1.

Various loading conditions can affect the mechanical behavior of HEAs in compression tests. Yeh et al. [2] first reported that the temperature, strain rate, and Al content cause variations in the compressive yield strength for $\text{Al}_x\text{CoCrCuFeNi}$. The investigation of elemental addition is then followed, and the alloying effect has been characterized, such as the addition of Al [3, 50, 53, 90–94], Ti [95–97], Cu [98], Y [99], Si [94, 100], Mo [35, 103], C [102], Nb [25, 104], Ni [26], V [44, 104], and Cr [105]. The temperature effect also draws great attention, since it’s essential to characterize materials properties for applications under extreme temperatures, such as aerospace and nuclear fields. Recently, compressive behavior at cryogenic and elevated temperatures has been studied

Fig. 6.5 Hot hardness (H) as a function of temperature (T) for (a) $\text{Al}_x\text{CoCrFeNi}$, (b) $\text{AlCoCr}_x\text{FeMo}_{0.5}\text{Ni}$, and (c) $\text{AlCo}_x\text{CrFeMo}_{0.5}\text{Ni}$ alloys, using data from Refs. [10, 18, 51]

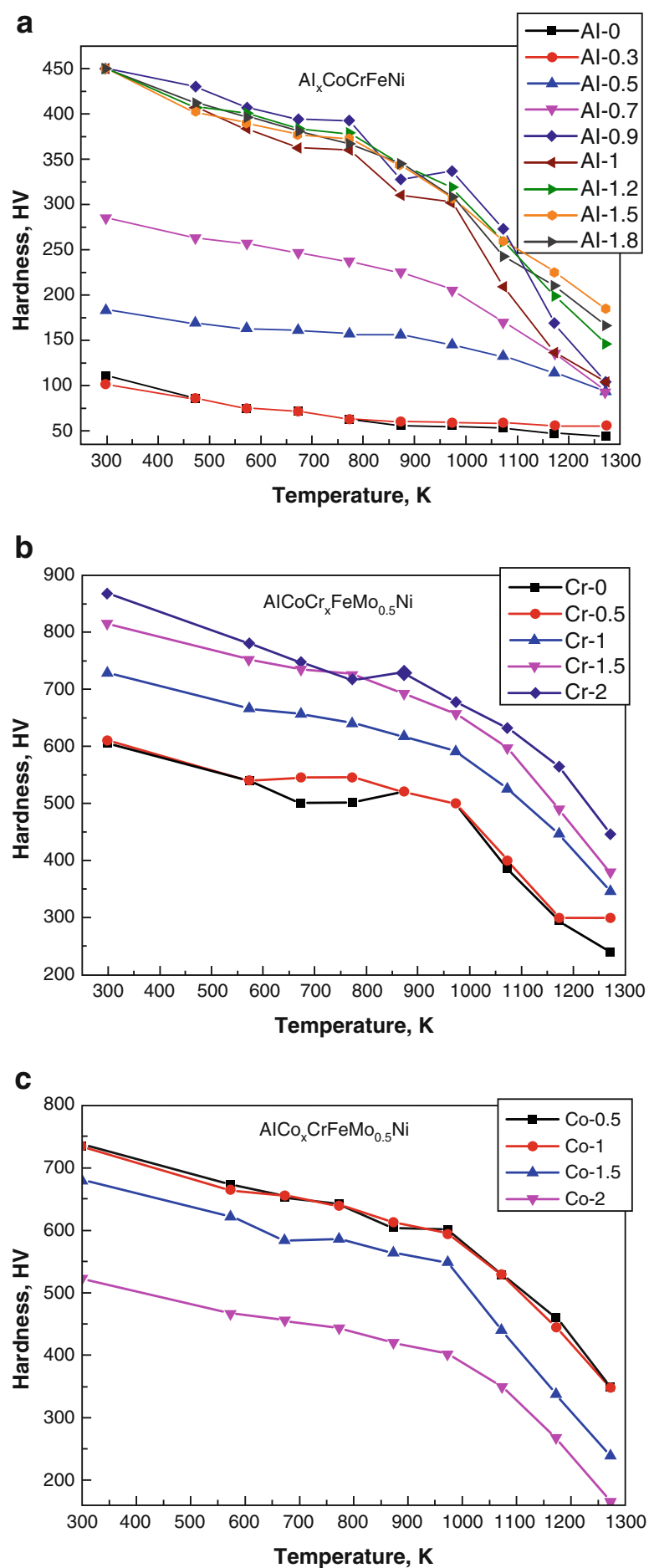


Table 6.1 Room-temperature compressive properties of HEAs

Composition	$\dot{\varepsilon}$ (s^{-1})	E (GPa)	σ_y (MPa)	σ_{max} (MPa)	ε_p (%)	S (mm)	Ref.
AlC ₀ CoCrFeNi	1×10^{-4}	125.1	1,138	∞	∞	$\varnothing 5 \times 10$	[102]
AlC _{0.1} CoCrFeNi	,	213.2	957	2,550	10.52	,	[102]
AlC _{0.2} CoCrFeNi	,	150.9	906	2,386	8.68	,	[102]
AlC _{0.3} CoCrFeNi	,	137.2	867	2,178	7.82	,	[102]
AlC _{0.4} CoCrFeNi	,	156.1	1,056	2,375	6.67	,	[102]
AlC _{0.5} CoCrFeNi	,	180.8	1,060	2,250	5.6	,	[102]
AlC _{1.0} CoCrFeNi	,	75.1	1,251	2,166	7.04	,	[102]
AlC _{1.5} CoCrFeNi	,	72.5	1,255	2,083	5.54	,	[102]
AlCoCrFeNiSi ₀	1×10^{-4}	—	1,110	∞	∞	$\varnothing 5 \times 8$	[100]
AlCoCrFeNiSi _{0.2}	,	—	1,265	2,173	13.76	,	[100]
AlCoCrFeNiSi _{0.4}	,	—	1,481	2,444	13.38	,	[100]
AlCoCrFeNiSi _{0.6}	,	—	1,834	2,195	2.56	,	[100]
AlCoCrFeNiSi _{0.8}	,	—	2,179	2,664	1.77	,	[100]
AlCoCrFeNiSi _{1.0}	,	—	2,411	2,950	1.17	,	[100]
Al ₀ CoCrFeNiTi	4.167×10^{-3}	134.6	—	2,020	9	$\varnothing 4 \times 10$	[91]
Al _{0.5} CoCrFeNiTi	,	106.8	—	1,600	9.9	,	[91]
Al _{1.0} CoCrFeNiTi	,	147.6	—	2,280	6.4	,	[91]
Al _{1.5} CoCrFeNiTi	,	133.4	—	2,110	9.8	,	[91]
Al _{2.0} CoCrFeNiTi	,	93.5	—	1,030	5.2	,	[91]
AlCoCrFeNiTi ₀	1.67×10^{-3}	—	1,250.96	2,004.23	32.7	$\varnothing 3 \times 5$	[115]
AlCoCrFeNiTi ₀	1×10^{-4}	127	1,500	2,830	26.9	$\varnothing 5 \times 10$	[96]
AlCoCrFeNiTi _{0.5}	,	177.7	2,260	3,140	23.3	,	[96]
AlCoCrFeNiTi _{1.0}	,	90.1	1,860	2,580	8.8	,	[96]
AlCoCrFeNiTi _{1.5}	,	159.8	2,220	2,720	5.3	,	[96]
AlCrCoCuFeNi	1.67×10^{-3}	—	1,147	1,560	21 [#]	$\varnothing 3 \times 5$	[116]

(continued)

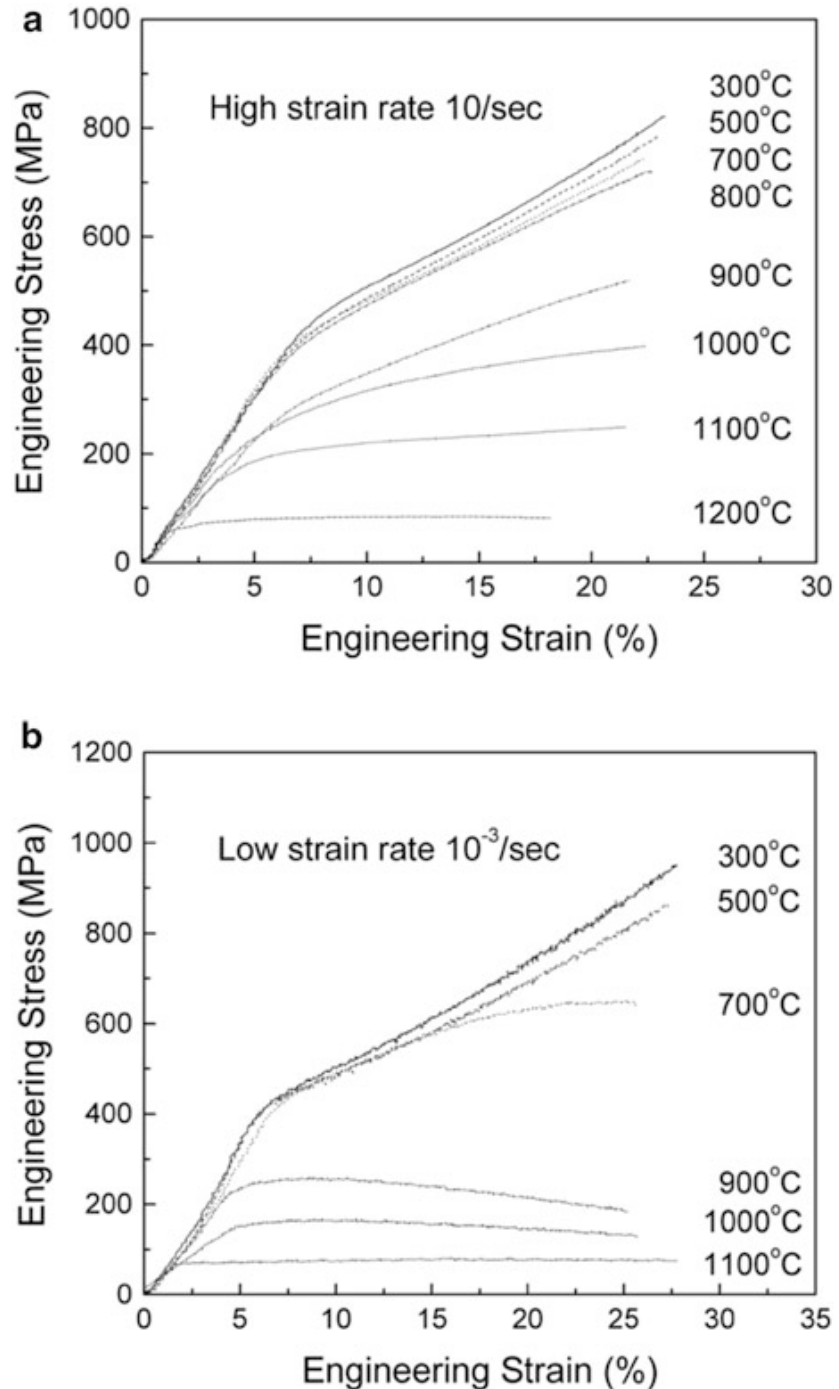
Table 6.1 (continued)

Composition	$\dot{\varepsilon}$ (s^{-1})	E (GPa)	σ_y (MPa)	σ_{max} (MPa)	ε_p (%)	S (mm)	Ref.
Al ₀ CoCrCuFeNi	,	—	237	∞	∞	,	[116]
AlCoCrCuFeMo ₀ Ni	2×10^{-4}	—	1,300	2,270	9.9	$\emptyset 5 \times 10$	[103]
AlCoCrCuFeMo _{0.2} Ni	,	—	1,420	2,240	3.5	,	[103]
AlCoCrCuFeMo _{0.4} Ni	,	—	1,690	2,660	1.5	,	[103]
AlCoCrCuFeMo _{0.6} Ni	,	—	1,880	2,820	1.4	,	[103]
AlCoCrCuFeMo _{0.8} Ni	,	—	1,920	2,640	1.2	,	[103]
AlCoCrCuFeMo _{1.0} Ni	,	—	1,750	2,600	1.1	,	[103]
AlCoCrFeNb ₀ Ni	2×10^{-4}	—	1,373	3,531	24.5	$\emptyset 5 \times 10$	[25]
AlCoCrFeNb _{0.1} Ni	,	—	1,641	3,285	17.2	,	[25]
AlCoCrFeNb _{0.25} Ni	,	—	1,959	3,008	10.5	,	[25]
AlCoCrFeNb _{0.5} Ni	,	—	2,473	3,170	4.1	,	[25]
Al ₀ CoCrCu ₁ FeNiTi _{0.5}	1×10^{-4}	92.73	700	1,650	28.7	$\emptyset 5 \times 10$	[90]
Al _{0.25} CoCrCu _{0.75} FeNiTi _{0.5}	,	102.85	750	1,970	38.5	,	[90]
Al _{0.5} CoCrCu _{0.5} FeNiTi _{0.5}	,	160.54	1,580	2,389	17.4	,	[90]
Al _{0.75} CoCrCu _{0.25} FeNiTi _{0.5}	,	164.14	1,900	2,697	12	,	[90]
AlCoCrCu _{0.25} FeNiTi _{0.5}	1×10^{-4}	110.46	1,994	2,460	9.05	$\emptyset 5 \times 10$	[98]
AlCoCrCu _{0.5} FeNiTi _{0.5}	,	107.8	1,984	2,374	6.04	,	[98]
AlCrCoCuFeNi	1.67×10^{-3}	—	1,303	2,081	24 [#]	$\emptyset 3 \times 5$	[117]
AlCrCoCuFeMnNi	,	—	1,005	1,480	15 [#]	,	[117]
AlCrCoCuFeNiTi	,	—	1,234	1,356	9 [#]	,	[117]
AlCrCoCuFeNiV	,	—	1,469	1,970	16 [#]	,	[117]

AlCoCrCuNiTiY ₀	-	35.545	-	1,495	7.68	$5 \times 5 \times 10$	[99]
AlCoCrCuNiTiY _{0.5}	-	35.815	-	1,024.5	3.07	"	[99]
AlCoCrCuNiTiY _{0.8}	-	37.69	-	1,324.5	4.73	"	[99]
AlCoCrCuNiTiY _{1.0}	-	36.855	-	1,192	3.54	"	[99]
Al ₀ (CoCrCuFeMnNiTiV) ₁₀₀	1×10^{-4}	74.247	1,312	0	$\emptyset 5 \times 10$	[53]	
Al _{11.1} (CoCrCuFeMnNiTiV) _{88.9}	,	164.087	1,862	2,431	0.95	"	[53]
Al ₂₀ (CoCrCuFeMnNiTiV) ₈₀	,	190.086	1,465	2,016	2.35	"	[53]
Al ₄₀ (CoCrCuFeMnNiTiV) ₆₀	,	163.208	1,461	1,461	0	"	[53]
CoCrCuFeNiTi ₀	1×10^{-4}	55.6	230	∞	$\emptyset 5$	[95]	
CoCrCuFeNiTi _{0.5}	,	98.6	700	1,650	21.6	"	[95]
CoCrCuFeNiTi _{0.8}	,	128.3	1,042	1,848	2.11	"	[95]
CoCrCuFeNiTi _{1.0}	,	76.5	1,272	1,272	0	"	[95]

Strain rate, $\dot{\varepsilon}$; Young's modulus, E ; yield strength, σ_y ; compressive strength, σ_{max} ; plastic strain, ε_p ; sample size, S ; symbol -, blank; symbol " , same as above; symbol # fracture strain instead of plastic strain; and symbol ∞ , not fractured

Fig. 6.6 Compressive stress-strain curves of $\text{Al}_{0.5}\text{CoCrCuFeNi}$ at different temperatures and strain rates of (a) 10/s and (b) $10^{-3}/\text{s}$ [3]



[3, 22, 50, 72, 78, 106–110], and the temperature-dependent behavior was investigated. Besides, the strain rate [3, 108], sample size [111], and aging/annealing effects [16, 49, 81, 93, 112, 113] are also reported to have dramatic influence on the microstructural evolution during compression deformation. For instance, Fig. 6.6 presents the typical compressive stress-strain curves of HEAs [3]. It's obvious that HEAs behave differently at various temperatures and strain rates. With a closer look at the plastic region, serration behavior can only be found in specific temperature and strain-rate regimes, which is at temperatures of 873, 973, 1,073, and 1,173 K and a strain rate of $10^{-3}/\text{s}$ in Fig. 6.6. This trend implies that diverse deformation mechanisms may exist. The effects of temperature, strain rate, and sample size on compressive behavior are discussed in detail in the following subsections.

6.3.2 Fracture Morphology

A characteristic fractography provides an efficient way to study the ductility of materials. Based on the understanding of conventional alloys, the fracture surfaces of HEAs can be categorized to be ductile and brittle fracture as well. The following example exhibits the effect of Cu addition on the compressive fracture surfaces at room temperature [98]. As shown in Fig. 6.7a, b, a high density of dimple-like structures can be observed on the fracture surfaces of $\text{Cu}_0\text{AlCoCrFeNiTi}_{0.5}$. A dimple-like structure is related to the microvoid coalescence or aggregation [118], which is a typical feature of ductile fracture. As the content of Cu increases, the dimple-like structures gradually decrease, and instead, tear edges and cleavage steps

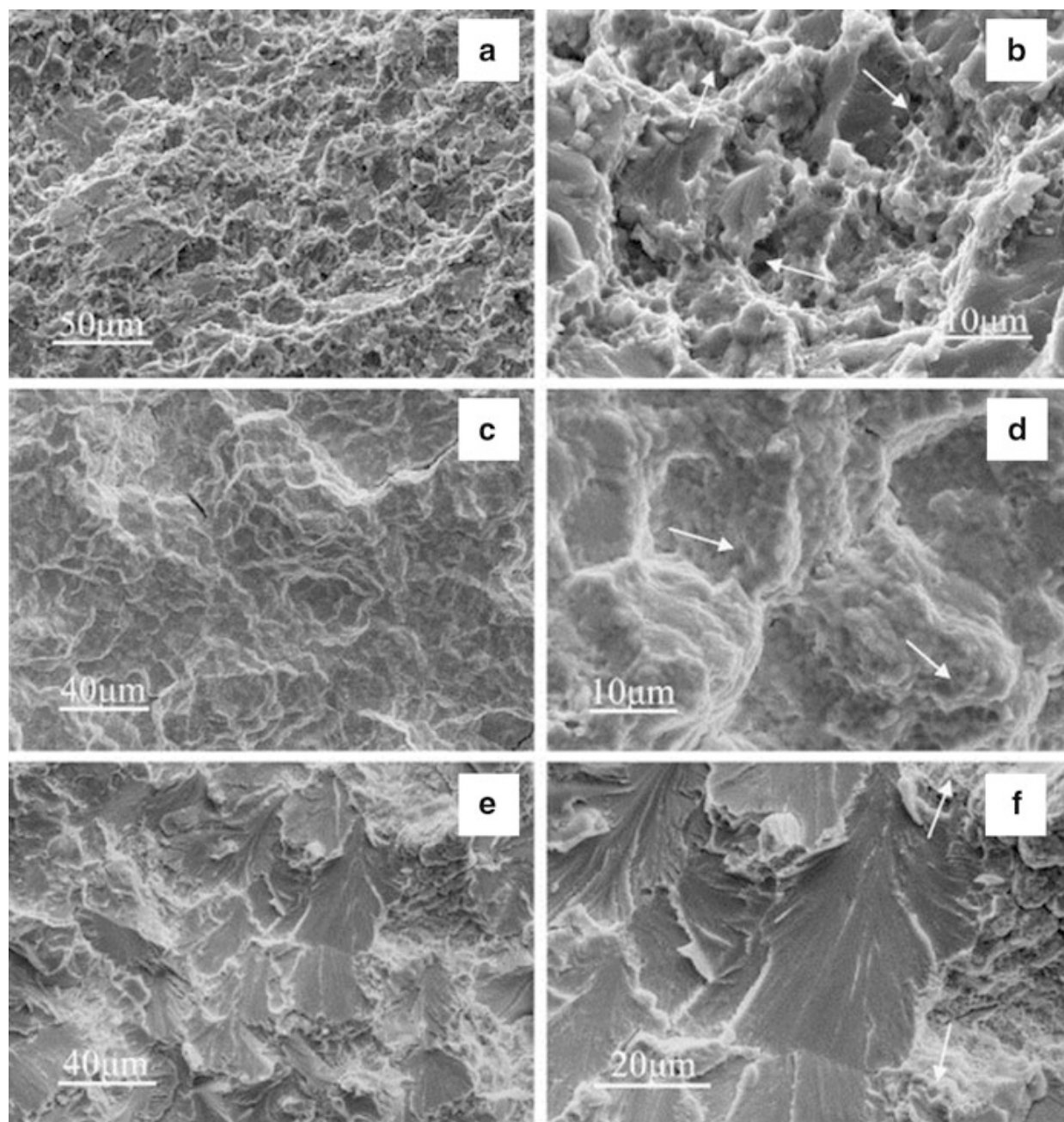


Fig. 6.7 Compressive fracture surfaces of as-cast $\text{AlCoCrCu}_x\text{FeNiTi}_{0.5}$ alloys, (a, b) $x = 0$, (c, d) $x = 0.25$, (e, f) $x = 0.5$ [98]

begin to appear, as denoted by the white arrow in Fig. 6.7c, d, which is caused by the coordinated operation of dislocations and microvoids. The combination of both features (tear edges and cleavage steps) can be classified as the quasi-cleavage fracture [93, 98], which lies in-between brittle and ductile fracture modes. With a further addition of Cu, planar facets and riverlike patterns can be identified in Fig. 6.7e, f, which is the typical cleavage fracture morphology, and cleavage fracture usually leads to brittle behavior. The analysis of the fracture morphology agrees very well with the corresponding stress–strain curves [98], which shows a plastic strain of 9.05 % for AlCoCrCu_{0.25}FeNiTi_{0.5}, 6.04 % for AlCoCrCu_{0.5}FeNiTi_{0.5}, and 21.6 % for AlCoCrFeNiTi_{0.5}, respectively (listed in Table 6.1).

6.3.3 Temperature Effects

Besides the multicomponent systems (e.g., Al-Co-Cr-Cu-Fe-Ni), refractory HEAs are also developed for high-temperature applications [22, 50, 78, 108, 109]. With the addition of refractory elements, the mechanical behavior of HEAs at elevated temperatures has been improved, compared to traditional alloys. The compressive behavior of MoNbTaW at elevated temperatures is described in Fig. 6.8a [78]. All curves exhibit significant plasticity. The yield strength decreases, as temperature increases. Microstructural examinations indicate that localized shear and cracking dominate the deformation behavior at lower temperatures (873–1,273 K), while grain-boundary sliding and voids formation should be responsible for the fracture at higher temperatures.

The compressive behavior of Al_{0.5}CoCrCuFeNi at cryogenic temperatures was also studied [72, 106, 107]. In Fig. 6.8b, interestingly, the stress–strain curves present obvious transition from a serrated flow at lower temperature (4.2–7.5 K) to non-serrated flow at higher temperatures (30–300 K), which indicates a significant change in the deformation mechanism. In addition, the sharp sawlike type of serrations could serve as a probe for microstructural evolution. Work hardening is also observed at all listed temperatures. Structural characterization at cryogenic temperatures is, thus, needed to clarify the reason.

The yield strengths at various temperatures are replotted in Fig. 6.8c using data from Table 6.2, for the comparison between HEAs and conventional alloys. The advantage for HEAs is evident over traditional alloys. For example, the MoNbTaW and MoNbTaVW have better yield strengths than Inconel 718 and Haynes 230 conventional alloys when the temperature is above 1,273 K. When the temperature is below 1,073 K, the AlMo_{0.5}NbTa_{0.5}TiZr, Al_{0.4}Hf_{0.6}NbTaTiZr, CrMo_{0.5}NbTa_{0.5}TiZr, and CrNbTiVZr have better yield strengths than Inconel 718 and Haynes 230.

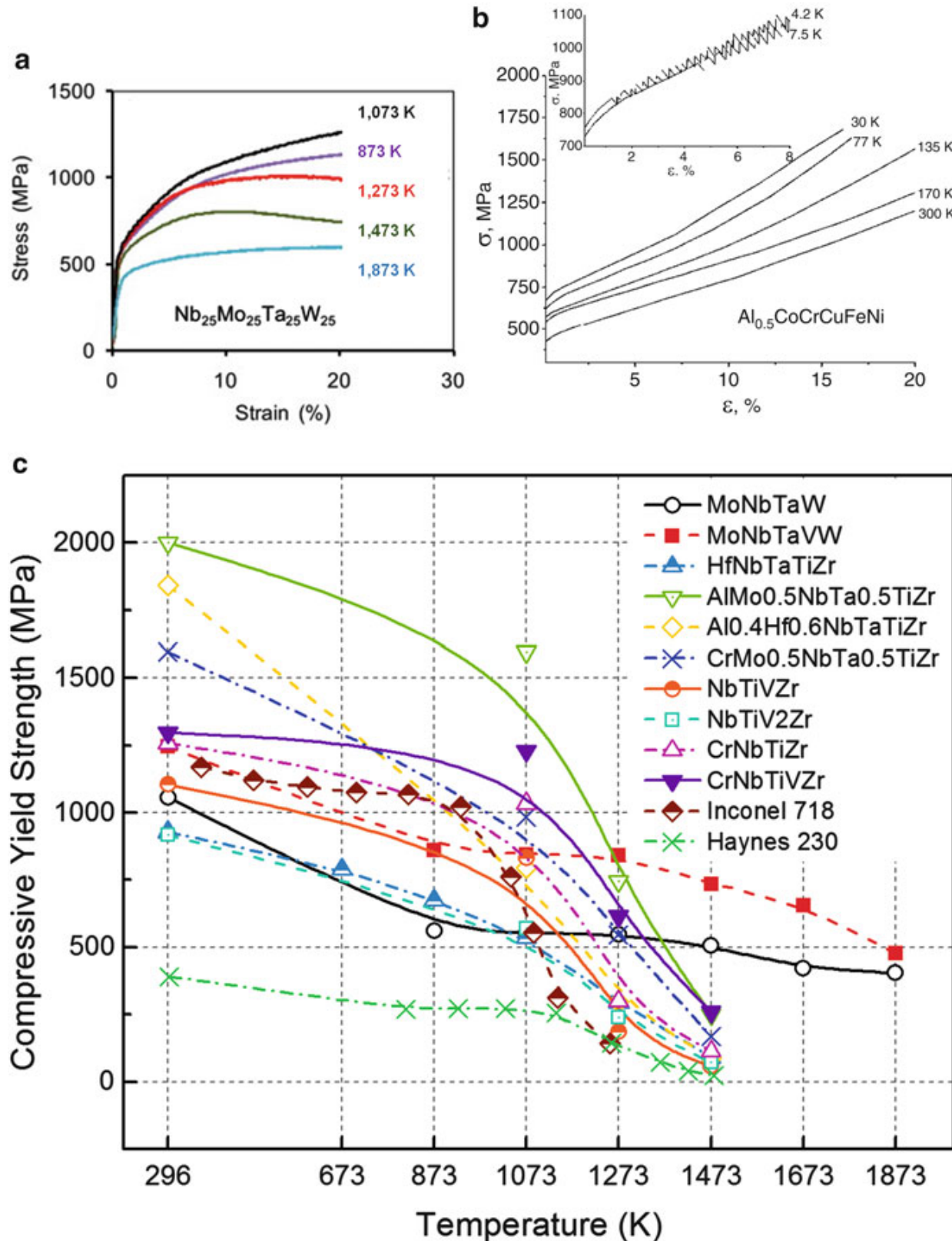


Fig. 6.8 (a) The compressive behavior of MoNbTaW at elevated temperatures [78], (b) compressive behavior of $\text{Al}_{0.5}\text{CoCrCuFeNi}$ at cryogenic temperatures [72, 106], and (c) temperature dependence of compressive yield strength for HEAs and conventional alloys, replotted using data from Table 6.2 [22, 50, 78, 108, 109]

Table 6.2 Elevated-temperature compressive behavior of refractory HEAs

Composition	<i>T</i> (K)	$\dot{\varepsilon}$ (s^{-1})	<i>E</i> (GPa)	σ_y (MPa)	σ_p (MPa)	ε_f (%)	<i>S</i> (mm)	Ref.
MoNbTaW	296	1×10^{-3}	220 ± 20	1,058	1,211	1.5 [#]	$\emptyset 3.6 \times 5.4$	[78]
	873	"	-	561	∞	∞	"	[78]
	1,073	"	-	552	∞	∞	"	[78]
	1,273	"	-	548	1,008	16 [#]	"	[78]
	1,473	"	-	506	803	12 [#]	"	[78]
	1,673	"	-	421	467	9 [#]	"	[78]
	1,873	"	-	405	600	27 [#]	"	[78]
	296	1×10^{-3}	180 ± 15	1,246	1,087	1.7	$\emptyset 3.6 \times 5.4$	[78]
MoNbTaVW	873	"	-	862	1,597	13	"	[78]
	1,073	"	-	846	1,509	17	"	[78]
	1,273	"	-	842	1,370	19	"	[78]
	1,473	"	-	735	802	7.5	"	[78]
	1,673	"	-	656	∞	∞	"	[78]
	1,873	"	-	477	∞	∞	"	[78]
	296	1×10^{-3}	-	929	-	-	$\emptyset 3.8 \times 5.7$	[108]
	673	"	-	790	-	-	"	[108]
HfNbTaTiZr	873	"	-	675	-	-	"	[108]
	1,273	"	-	295	-	-	"	[108]
	1,473	"	-	92	-	-	"	[108]
	1,073	1×10^{-1}	-	285	-	-	"	[108]
	"	1×10^{-2}	-	475	-	-	"	[108]
	"	1×10^{-3}	-	535	-	-	"	[108]
	"	1×10^{-4}	-	543	-	-	"	[108]
	"	1×10^{-5}	-	550	-	-	"	[108]
AlMo _{0.5} NbTa _{0.5} TiZr	296	1×10^{-3}	178.6	2,000	2,368	10	$4.7 \times 4.7 \times 7.7$	[50]
	1,073	"	80	1,597	1,810	11	"	[50]
	1,273	"	36	745	772	>50	"	[50]
	1,473	"	27	250	275	>50	"	[50]

Al_{0.4}Hf_{0.6}NbTaTiZr	296	1×10^{-3}	78.1	1,841	2,269	10	$4.7 \times 4.7 \times 7.7$	[50]
1,073	,	48.8	796	834	>50	,	,	[50]
1,273	,	23.3	298	455	>50	,	,	[50]
1,473	,	—	89	135	>50	,	,	[50]
CrMo_{0.5}NbTa_{0.5}TiZr	296	1×10^{-3}	—	1,595	2,046	5.0	$4.7 \times 4.7 \times 7.7$	[22]
1,073	,	—	983	1,100	5.5	,	,	[22]
1,273	,	—	546	630	∞	,	,	[22]
1,473	,	—	170	190	∞	,	,	[22]
NbTiVZr	298	1×10^{-3}	80	1,105	—	>50	$4.7 \times 4.7 \times 7.7$	[109]
873	,	—	834	—	>50	,	,	[109]
1,073	,	—	187	—	>50	,	,	[109]
1,273	,	—	58	—	>50	,	,	[109]
NbTiV₂Zr	298	1×10^{-3}	98	918	—	>50	$4.7 \times 4.7 \times 7.7$	[109]
873	,	—	571	—	>50	,	,	[109]
1,073	,	—	240	—	>50	,	,	[109]
1,273	,	—	72	—	>50	,	,	[109]
CrNbTiZr	298	1×10^{-3}	120	1,260	—	6	$4.7 \times 4.7 \times 7.7$	[109]
873	,	—	1,035	—	>50	,	,	[109]
1,073	,	—	300	—	>50	,	,	[109]
1,273	,	—	115	—	>50	,	,	[109]
CrNbTiVZr	298	1×10^{-3}	100	1,298	—	3	$4.7 \times 4.7 \times 7.7$	[109]
873	,	—	1,230	—	>50	,	,	[109]
1,073	,	—	615	—	>50	,	,	[109]
1,273	,	—	259	—	>50	,	,	[109]

Temperature, T ; strain rate, $\dot{\epsilon}$; Young's modulus, E ; yield strength, σ_y ; peak stress, σ_p ; plastic strain, ε_p ; sample size, S ; symbol —, blank; symbol —, same as above; symbol #, plastic strain instead of fracture strain; and symbol ∞ , not fractured

6.3.4 Strain-Rate Effects

Loading rate has a major effect on the response time of materials during deformation and further on the mechanical performance. For HfNbTaTiZr, it's evident that at high strain rates ($>10^{-3}/\text{s}$), deformation strengthening dominates, and the plastic flow keeps on increasing in the compression experiment at a temperature of 1,073 K, as shown in Fig. 6.9a [108]. In contrast, strain softening occurs after

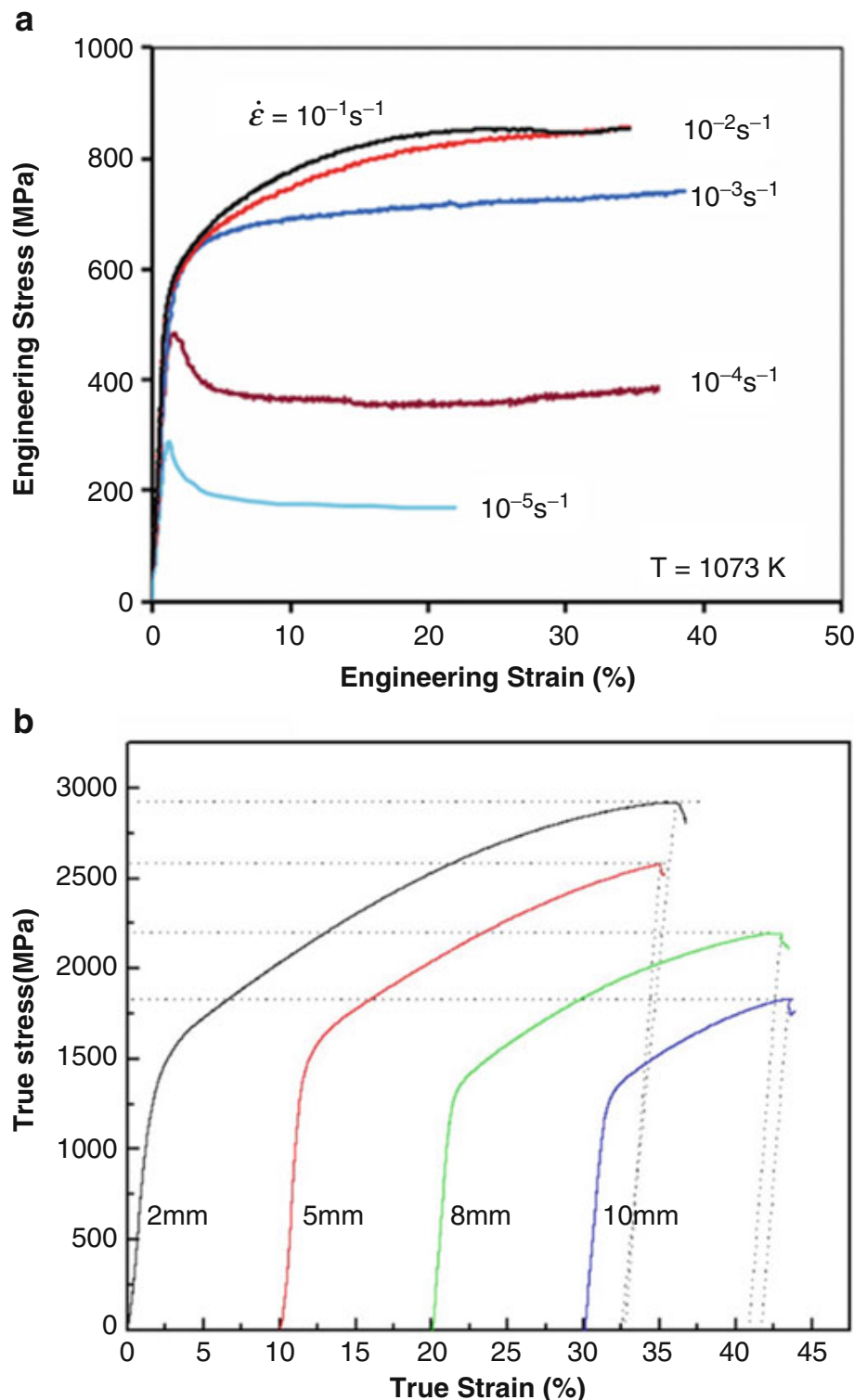


Fig. 6.9 (a) Strain-rate effect on the compressive stress–strain curve of HfNbTaTiZr at $T = 1,073 \text{ K}$ [108], and (b) sample-size effect on the compressive stress–strain curve of AlCoCrFeNi at room temperature [111]

yielding, followed up with a steady state for low strain rates of $10^{-4}/\text{s}$ and $10^{-5}/\text{s}$, which indicate an alternative deformation mechanism. Indeed, by scanning electron microscopy (SEM) characterization, extensive wedge-like cavities assemble at grain boundaries with strain rates of $10^{-3}/\text{s}$ and $10^{-2}/\text{s}$, suggesting that the pure dislocation mobility and diffusion activity are not sufficient to accommodate the deformation and relieve stress concentration around sliding grain boundaries. With higher magnification, fine recrystallized grains/particles can be found along grain boundaries, indicating the presence of the high internal stress and high-density dislocations, which may contribute to the formation of the grain-boundary cavitation. However, when the strain rate slows down to $10^{-4}/\text{s}$ and $10^{-5}/\text{s}$, only small round cavities exist, implying that the operation of dislocations and diffusion are sufficient to accommodate the deformation process.

6.3.5 Sample-Size Effects

Sample-size effects could be remarkable, since they may affect the cooling rate during solidification. As well known for bulk metallic glasses (BMGs), sample size dramatically influences their plastic behavior [114, 119, 120], due to the cooling rate and crystallization. Similarly, HEAs also show the sample-size effect on the compressive behavior to some extent. Figure 6.9b depicts the stress-strain curve of samples with diameters of 2, 5, 8, and 10 mm, respectively [111]. The yield strength decreases slightly, as the sample size increases, and the plasticity increases dramatically with decreasing the specimen size. That's to say, smaller HEA samples exhibit both higher strength and larger plasticity.

The SEM characterization [111] indicates that samples of 2 and 5 mm in diameter present similar single-phase morphologies, in contrast to the typical cast dendritic structures for larger samples. Furthermore, the energy-dispersive analysis implies that for samples of 2 and 5 mm in diameter, the elements within grains distribute homogeneously. However, for the other two samples of 8 and 10 mm in diameter, Cr segregated to the interdendritic regions, and a compound containing Ni and Cr may form during solidification, which could result in the decrease of yield strength [111].

6.3.6 Microcompression

It has been found that metallic alloys behave in a different way at the submicron scale, compared to their bulk counterpart [98, 121–126]: (1) the yield strength rises significantly, (2) plastic deformation proceeds as intermittent strain bursts, and (3) the special creep behavior occurs during high-load holding. Especially for (2), the strain burst refers to serration behavior. The previous work has demonstrated

that the distribution of strain bursts follows a power-law scaling behavior [123, 125] or a tuned critical behavior [69].

Microcompression experiments have also been conducted on HEAs [127, 128]. Figure 6.10 shows the scanning electron microscopy (SEM) images of the compressed MoNbTaW HEA pillars with different sizes and corresponding stress-strain curves. The [316] orientation is selected to obtain the single-slip system. Figure 6.10a, b clearly reveals the single-slip bands on the pillars of larger sizes, while multiple slips can be found in Fig. 6.10c, d with smaller-sized pillars, which may contribute to strain hardening. The stress-strain curves in Fig. 6.10e exhibit that smaller pillars possess larger yield strengths and larger strain bursts with higher frequency as well, which may result from more activation and interaction of multiple slips. These results verified that the above statements (1) and (2) also apply in HEAs.

6.4 Tensile Properties

Compared to hardness and compression tests, tensile experiments are sensitive to detect the embrittlement. For the HEA samples with a dendritic structure and some shrinkage pores, tensile tests are more suitable to reveal the mechanical properties in the stressed state which is frequently encountered in practical applications.

The study of tensile properties of HEAs is limited to few alloy systems [15, 48, 49, 54–61]. Tsai et al. are the first to study the tensile properties of HEAs [15]. Until now, all reported tensile properties of HEAs are analyzed. Promising results have been found in HEAs. The effects of structures and grain sizes on the shapes of stress-strain curves [59, 60], temperature effects on yielding stress [15, 54], Al/Sn/Mn/V alloying effects on yield stress and ductility [49, 55, 60], and fracture behavior [15] are summarized in this part.

6.4.1 Stress–Strain Curves

The shapes of stress–strain curves are highly affected by the structure of HEAs. Typical tensile stress–strain curves of $\text{Al}_x\text{CoCrFeMnNi}$ HEAs are shown in Fig. 6.11. In the single-phase FCC region (represented by Al0, Al4, Al7, and Al8), alloys behaved like a solid solution with relatively low strengths but extended ductility. In the mixed structure region (FCC + BCC phases, represented by Al9, Al10, and Al11), alloys behaved like a composite with a sharp increase in strength but reduced ductility. In the single-phase BCC region, alloys became extremely brittle [60].

The shapes of stress–strain curves also are affected by the grain size of HEAs. The tensile stress–strain curves of CoCrFeMnNi alloys with three different grain sizes (4.4 μm , 50 μm , and 155 μm) are compared (Fig. 6.12). Fine-grained materials

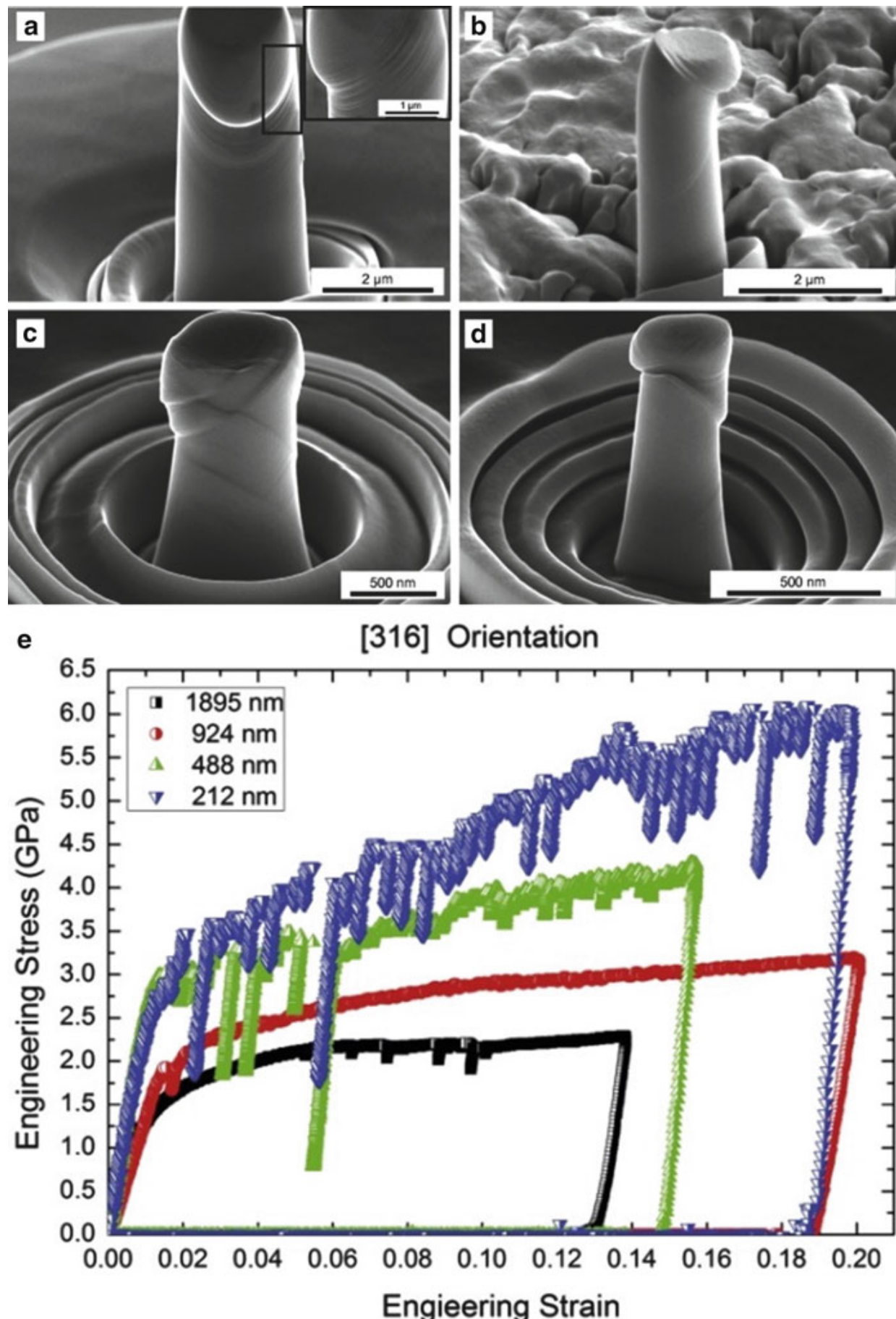


Fig. 6.10 SEM images of post-compressed [316]-oriented MoNbTaW HEA pillars with diameters of (a) 2 μm , (b) 1 μm , (c) 500 nm, (d) 250 nm, and (e) corresponding stress–strain curves [127]

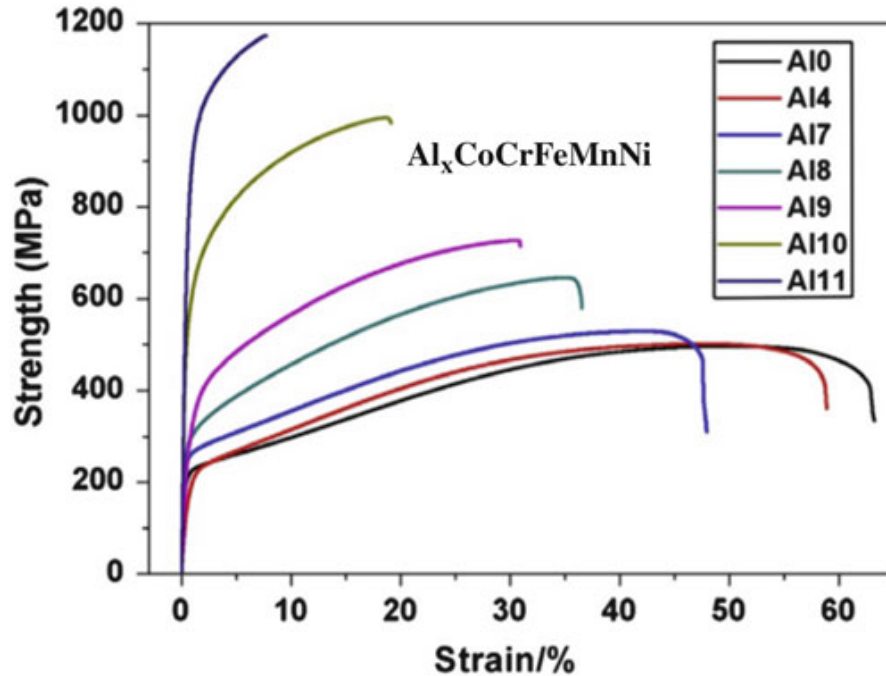


Fig. 6.11 Engineering tensile stress–strain curves of the as-cast $\text{Al}_x(\text{CoCrFeMnNi})_{100-x}$ (denoted as Al_x , where x is the atomic percent of Al) alloys at room temperature [60]

have higher strength than coarse-grained materials. Small load drops after yielding were observed in the fine-grained materials, while the stress–strain curves of the coarse-grained materials show neither well-defined yield points nor load drops after yielding [59]. For the fine-grained and coarse-grained materials, serration behavior happens at the temperature of 673 K (Fig. 6.12).

6.4.2 Yield Strength and Ductility

By summarizing all published tensile data of HEAs [15, 48, 49, 54–61], it reveals that the HEAs display both yield strength and ductility at room temperature with a wide range, shown in Fig. 6.13. The tensile yield stresses of AlCoCrCuFeNi and $\text{Al}_{0.5}\text{CoCrCuFeNi}$ are superior to Ti-6Al-4 V and Inconel 713. The CoCrFeNi has the better ductility than conventional alloys, such as 304 stainless steels, Ti-6Al-4 V, Inconel 713, and 5083 Al. The temperature effect on tensile properties is studied in the $\text{Al}_{0.5}\text{CoCrCuFeNi}$ [15] and CoCrFeMnNi [59] systems. As shown in Fig. 6.14, the yield stress decreases as the temperature increases. For the single-phase CoCrFeMnNi [129], the mechanisms of temperature effects on the yield stress are revealed.

The curves in Fig. 6.14 can be well fitted in the form:

$$\sigma_y(T) = \sigma_a \exp\left(\frac{-T}{C}\right) + \sigma_b \quad (6.3)$$

where σ_a , C , and σ_b are fitting constant.

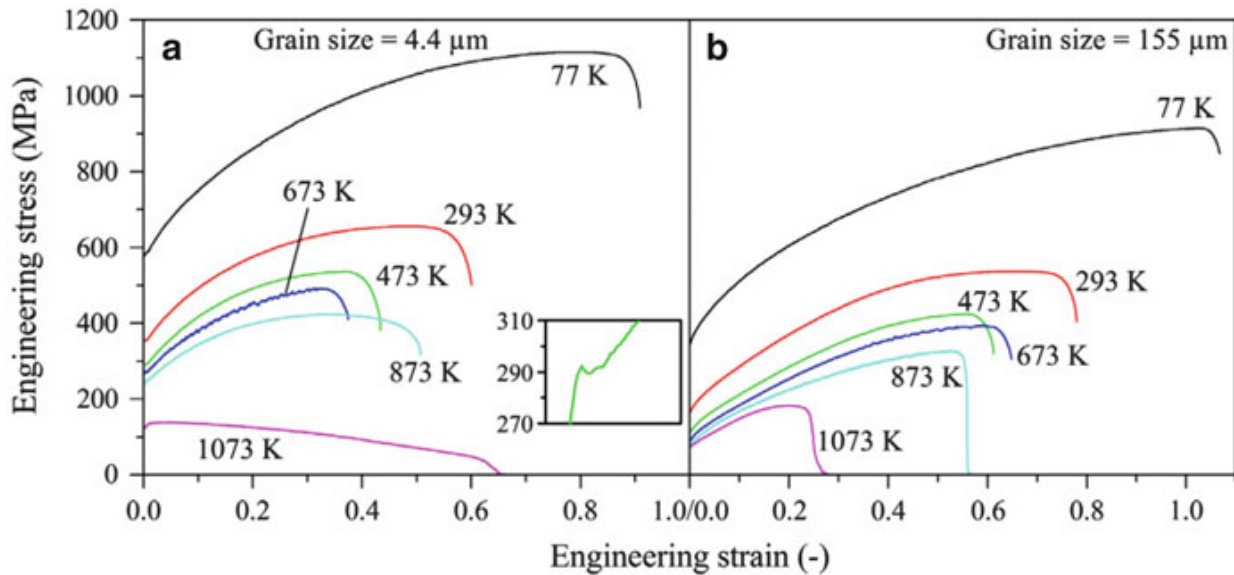


Fig. 6.12 Representative engineering stress–strain curves of the CoCrFeMnNi alloy at the six testing temperatures for the (a) fine-grained (grain size of 4.4 μm) and (b) coarse-grained (grain size of 155 μm) materials. The inset in (a) shows a small load drop after yielding for a fine-grained sample that was tested at 473 K [59]

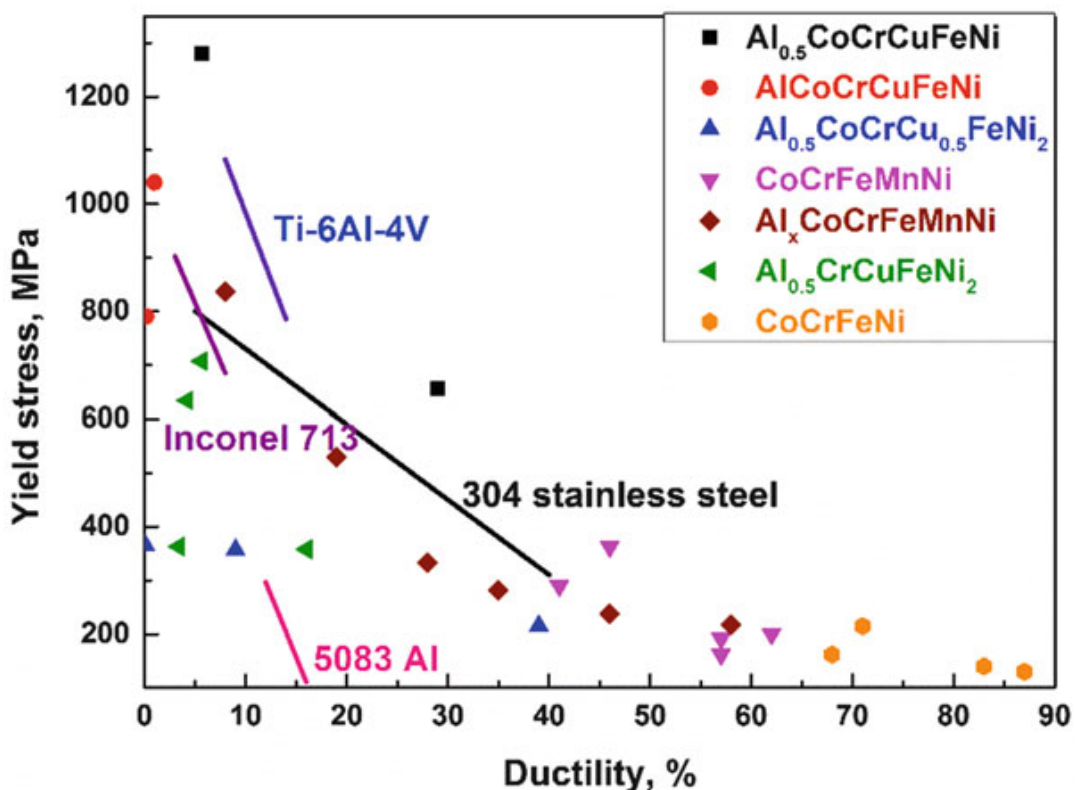


Fig. 6.13 Tensile yield stress versus ductility of most studied HEAs at room temperature, compared with conventional alloys, e.g., 304 stainless steel, Ti-6Al-4 V, Inconel 713, and 5083 Al, using data from Refs. [15, 48, 49, 54–61]

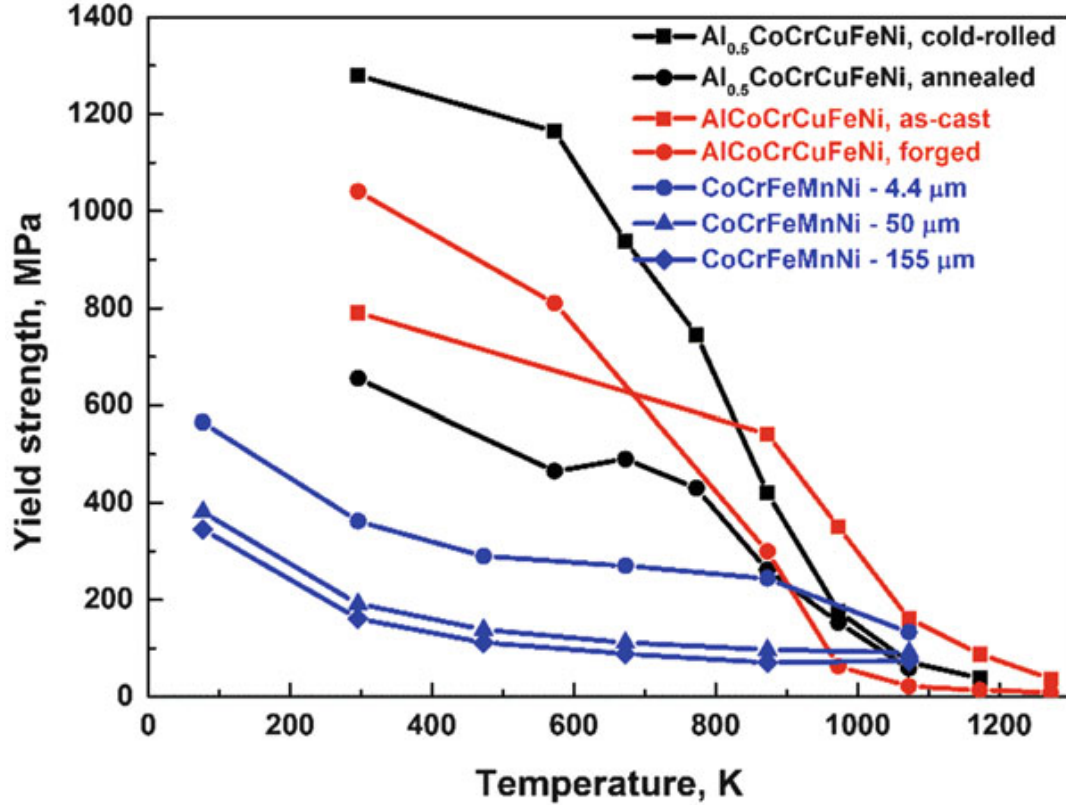


Fig. 6.14 Tensile yield stress as a function of temperature for three kinds of most studied HEAs, using data from Refs. [15, 59, 129]

The Peierls lattice friction, σ_p , is chosen to reveal the deformation mechanisms of CoCrFeMnNi [129]:

$$\sigma_p = \frac{2G}{1-\nu} \exp\left(\frac{-2\pi\omega}{b}\right) \quad (6.4)$$

where G is the shear modulus, ν is Poisson's ratio, ω is the dislocation width, and b is the magnitude of the Burgers vector.

The dependence of dislocation width, ω , on temperature has been approximated:

$$\omega = \omega_0(1 + \alpha T) \quad (6.5)$$

where α is a small positive constant, and ω_0 is the dislocation width at 0 K. Combining the above two equations yields

$$\sigma_p = \frac{2G}{1-\nu} \exp\left(\frac{-2\pi\omega_0}{b}\right) \exp\left(\frac{-2\pi\omega_0}{b} \alpha T\right) \quad (6.6)$$

Equating the temperature-dependent part of Eq. (6.3) with that of Eq. (6.6) yields

$$\sigma_a = \sigma_p(0) = \frac{2G}{1-\nu} \exp\left(\frac{-2\pi\omega_0}{b}\right) \quad (6.7)$$

and

$$C = \frac{b}{2\pi\omega_0\alpha} \quad (6.8)$$

Thus, for the single-phase CoCrFeMnNi HEAs, the calculated Peierls stress at 0 K, $\sigma_p(0)$, has the best match with the fitted σ_a values when $\omega_0 = b$. For pure Ni, the match is better when $\omega_0 = 1.5 b$. These results show that the dislocations in single-phase HEAs are narrower than in pure FCC metals. In addition, the temperature dependence of the yield strength of single-phase HEAs may be due to thermally induced changes in the dislocation width that, in turn, produce a temperature dependence of the Peierls stress [129].

The CoCrFeMnNi and CoCrFeNi alloys exhibit a strong temperature-dependent decrease in strength with increasing temperature from 77 to 1,273 K and a relatively weak strain-rate dependence (at 10^{-3} and 10^{-1} s $^{-1}$) [57].

Besides test conditions (temperatures and strain rates), the processing method has a great impact on the ductility of HEAs. The AlCoCrCuFeNi alloy was more ductile and strong after hot working than in the as-cast condition [15, 54]. The strengthening and toughening characteristics are mainly due to its small grain size (around 1.5 μ m). Very interestingly, the hot-worked AlCoCrCuFeNi alloy showed a superplastic-like behavior in the temperature range of 1,073–1,273 K. The tensile elongation was above 400 % and reached 860 % at 1,273 K [54].

6.4.3 Deformation Mechanisms

Tension tests, associated with neutron diffraction, transmission electron microscopy (TEM), and so on, are effective techniques for revealing the deformation mechanisms of HEAs. Even though the local atomic stress can be studied by the pair distribution function (PDF) [130], no paper studies the local atomic stress under loading.

To reveal the elastic deformation mechanism of HEAs, the lattice structural evolution of CoCrFeMnNi is investigated by in situ tensile deformation with neutron diffraction [131]. The lattice strain during loading can be calculated from the shift of a diffraction peak position as

$$\varepsilon_{hkl} = \frac{d_{hkl} - d_{hkl,0}}{d_{hkl,0}} \quad (6.9)$$

where d_{hkl} is the d spacing determined from the hkl reflection for a given load, and $d_{hkl,0}$ refers to the value for zero load. The lattice-strain revolution during deformation of CoCrFeMnNi is shown in Fig. 6.15. Strong elastic anisotropy exists, i.e., the lattice-strain change is strongly dependent on the grain orientations. Among them, the {200} grains have the largest elastic strain along the loading direction.

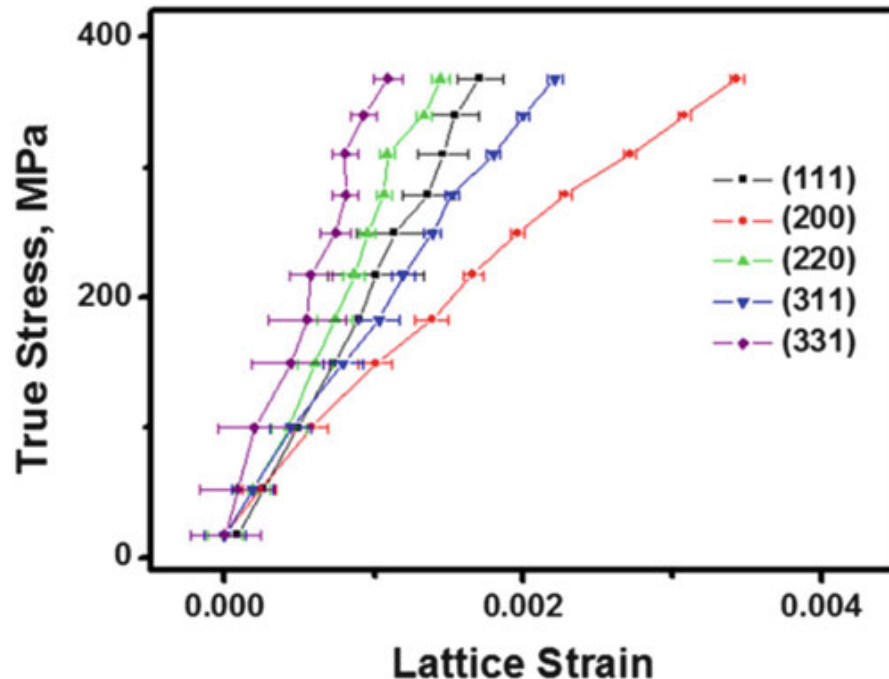


Fig. 6.15 Lattice-strain evolution of CoCrFeMnNi as a function of applied stress [131]

Elastic moduli and constants of different planes are determined to be $E_{111} = 222.6$ GPa, $E_{100} = 112.2$ GPa, $C_{11} = 172.1$ GPa, $C_{12} = 107.5$ GPa, and $C_{44} = 92.0$ GPa. These elastic trends and constants show that the elastic anisotropy behavior of the CoCrFeMnNi is close to that of its FCC component, pure Ni [131, 132].

To reveal the plastic deformation mechanism of HEAs, TEM is used to characterize the microstructure of HEAs after tension tests. The TEM results of CoCrFeMnNi reveal that initial plasticity, up to tensile strains of about 2 %, occurs exclusively by the planar glide of (110) dislocations on $\langle 111 \rangle$ planes at room temperature [57]. At higher strains, with room temperature and above, slip became more homogeneous and cell structures developed. This dislocation motion is similar to the normal FCC metals. However, at a low temperature, 77 K, extensive deformation twinning is observed in the specimen deformed to a plastic strain of 20.2 %, which is not common in normal FCC metals. This deformation-induced twinning, by providing an additional deformation mode, likely contributes to the observed increase in ductility at low temperatures [57].

6.4.4 Fracture

The fracture surfaces of HEAs are routinely used to determine the cause of failure in engineering structures and develop theoretical models of crack-growth behavior. Compared with fractures after compression, the fractures after tension own different features [15, 54, 55, 58]. The fracture mode of $\text{Al}_{0.5}\text{CoCrCuFeNi}$ transfers from the brittle to ductile types, as the temperature increases, shown in Fig. 6.16.

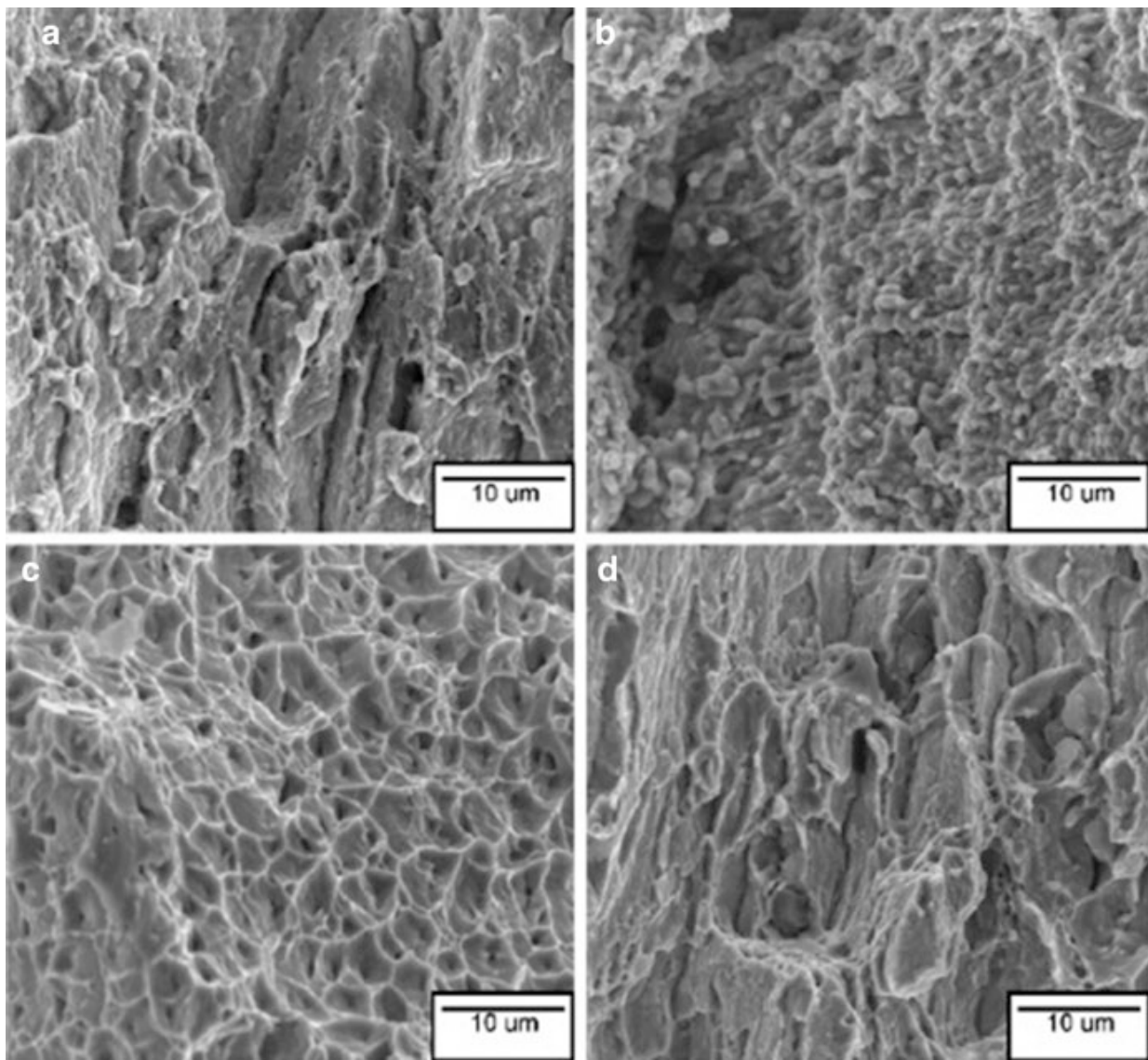


Fig. 6.16 Fracture surfaces of as-rolled Al_{0.5}CoCrCuFeNi tensile-tested samples at different temperatures: (a) room temperature, (b) 773 K, (c) 873 K, and (d) 1,073 K [15]

The fracture surfaces of Al_{0.5}CoCrCuFeNi undergo shear rupture at room temperature (Fig. 6.16a), ductile one at 873 K (Fig. 6.16c), and greater ductility with larger dimples at 1,073 K (Fig. 6.16d) [15]. At a certain temperature, HEAs exhibit a mixed type of brittle and ductile fracture. Taking AlCoCrCuFeNi, for example, the fracture morphology at 873 K is a mixed mode of brittle and ductile fractures [54]. The brittle fracture is reflected by the presence of flat facets with characteristic river-pattern markings inside large dimples, while the ductile fracture is reflected in numerous dimples of different diameters surrounding the flat facets [54]. The alloying also affects the fracture mode. For CoCuFeNiSn_x, a ductile fracture for the CoCuFeNiSn_{0.05} alloy and a cleavage fracture for the CoCuFeNiSn_{0.2} alloy were observed [55].

6.4.5 Comparison Among Hardness, Compression, and Tension Properties

Since few papers report the mechanical properties of HEAs using both hardness and tension techniques, we choose one material, $\text{Al}_{0.5}\text{CoCrCuFeNi}$ [15], fabricated by two methods, and compare both the hardness and tension properties, as shown in Fig. 6.17.

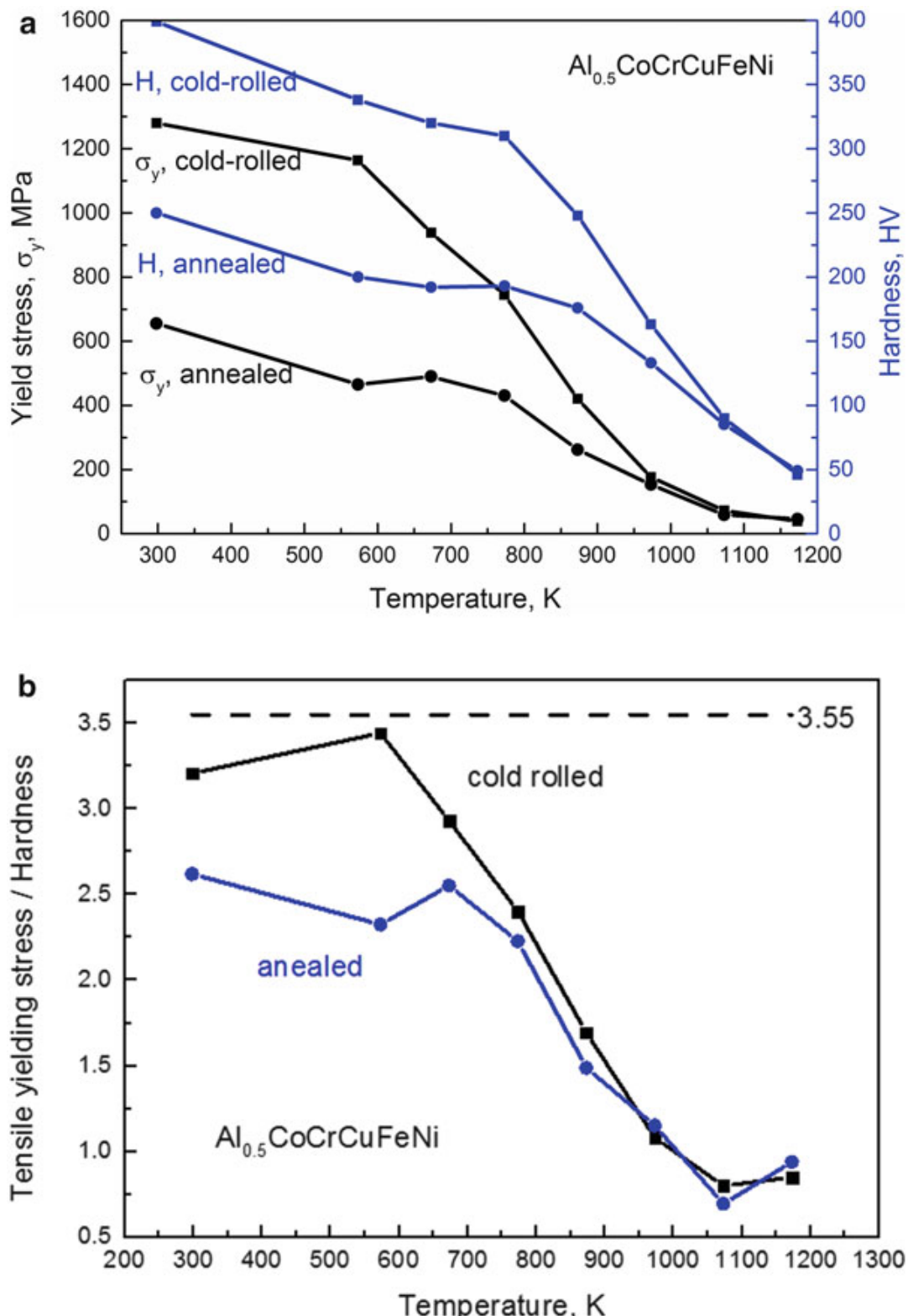


Fig. 6.17 The relationship between hardness and tensile yielding stress as a function of temperature using data from Ref. [15]. (a) Yielding stress and hardness and (b) the ratio of tensile yielding stress over hardness as a function of temperature of the annealed and cold-rolled $\text{Al}_{0.5}\text{CoCrCuFeNi}$

As described by Tabor [80] originally, during indentation, the pressure, P , normal to the surface of the indenter tip can be calculated as

$$P = 2k(1 + \pi/2) \quad (6.10)$$

Plastic deformation during indentation occurs, when the Huber–von Mises criterion is satisfied, which in the two-dimensional case occurs when the maximum shear stress reaches a critical value, k :

$$2k = 1.15\sigma_y \quad (6.11)$$

For a Vickers indenter,

$$H_v = \frac{\text{Load}}{\text{Contact Area}} = 0.927P \quad (6.12)$$

Combining Eqs. (6.10, 6.11, and 6.12) gives

$$\sigma_y = 0.364H_v \quad (6.13)$$

with σ_y and H_v in kg/mm². Alternatively,

$$\sigma_y = 3.55H_v \quad (6.14)$$

with σ_y in MPa and H_v in kg/mm².

In Fig. 6.17b, for both cold-rolled and annealed samples, the ratios of tensile yielding stress versus hardness are lower than the constant, 3.55, predicted by Tabor, no matter how high the temperature is. However, the constants are very similar in magnitude.

Compressive yielding stress is the stress state caused by an applied load that acts to reduce the length of the material along the axis of the applied load, while the tensile yielding stress is the stress state caused by an applied load that tends to elongate the material along the axis of the applied load. The compressive strength of HEAs is generally higher than their tensile strength. For example, the compressive and tensile yielding stresses at room temperature are 460 MPa and 360 MPa of Al_{0.5}CoCrCuFeNi [82], respectively. That is generally because materials loaded in tension are susceptible to stress concentrations, such as material defects or abrupt changes in geometry.

6.5 Modeling of Serration Behavior

A simple mean-field theory (MFT) model successfully predicts the slip-avalanche statistics [66, 72] observed in many recent simulations of plastic deformation [58, 68, 72, 133–141]. This analytic model has the advantage that as simple as it is and as few ingredients as it has, the model is able to give exact quantitative predictions of avalanche dynamics [66]. According to the MFT model [66]:

1. A slowly sheared material undergoes a local slip, when the local stress at a weak spot exceeds the local threshold stress, or failure stress. A local slip stops, and the weak spot resticks, when the local stress is reduced to a lower arrest stress, or sticking stress.
2. The stress released by a microscopic slip at one weak spot may trigger other weak spots to slip as well, and the process may go on and result in a macroscopically large slip avalanche.
3. The material is sheared slowly enough to prevent the slip avalanches from overlapping in time, so that each avalanche has enough time to finish before the next avalanche initiates.
4. Each weak spot in the slowly sheared material interacts with every other weak spot equally strong. In other words, the interactions between the weak spots do not decay with distance.

The MFT model predicts avalanche statistics for two boundary conditions, a slowly increasing stress applied to the boundaries, or a small strain rate imposed at the boundaries [66]. Here we present a brief review of the discrete version of the MFT model for the slowly increasing stress boundary condition. This discrete version treats the slowly sheared material as a system with N lattice points. Under the applied stress, F , that is below but close to the failure stress, F_c , the local stress at a lattice point, l , is [66, 142]

$$\tau_l = J/N \sum_m (u_m - u_l) + F \quad (6.15)$$

When the local stress, τ_l , exceeds the local threshold stress at the weak spot, l , the spot slips by Δu_l , and releases a stress of the amount, $2G\Delta u_l$, where $G \sim J$ is the elastic shear modulus. The stress released by this microscopic slip at one weak spot is equally redistributed to other weak spots of the material, which may trigger new slips. These new slips further increase the stress at other weak spots and may cause more slips. The process may continue and lead to a macroscopically large slip avalanche. A slip avalanche stops, when the local stress is lower than the current local threshold stress at each weak spot of the material. The current local threshold stress may be different from the initial local threshold stress at the beginning of the slip avalanche due to weakening or strengthening [66].

Next we present some of the main MFT model predictions [66] in the absence of weakening effects:

1. For a small stress bin around the failure stress, F_c , the probability distribution, $D(s, F_c)$, of avalanche sizes, s , obeys a universal power law, $D(s, F_c) \sim 1/s^\tau$, and the model predicts that the universal exponent of $\tau = 1.5$.
2. For small stress bins around the stress, F , the maximum avalanche size is related to the stress by $s_{\max} \sim (F_c - F)^{-1/\sigma}$, and the model predicts that the universal cutoff exponent is $\sigma = 0.5$.
3. For the distribution, $D(s, F)$, of avalanche sizes, s , observed in a small stress bin around F , the model predicts that

$$D(s, F) \sim 1/s^\tau \mathbb{D} \left[s \cdot (F_c - F)^{1/\sigma} \right] \quad (6.16)$$

where $\tau = 1.5$ and $\sigma = 0.5$, and $D(x) \sim A \exp(-Bx)$ is a universal scaling function. The values of A and B depend on the material details. When the number of avalanches is small, the stress-integrated form, $D_{\text{int}}(s) \sim \int_0^{F_c} D(s, F) dF \sim 1/s^{\tau+\sigma}$, can be more useful. In addition, using the complementary cumulative distribution, $C(s)$, instead of the probability density distribution, $D(s)$, may also improve the statistics for a small number of avalanches. Here $C(s)$ is defined as $\int_s^\infty D(s) ds$, i.e., $C(s)$ gives the probability of finding an avalanche larger than s .

4. The model predicts that the local slope, G_e of the stress-strain curve, scales as

$$G_e \sim 1/\langle s \rangle \sim (F_c - F)^{(2-\tau)/\sigma} \sim (F_c - F) \quad (6.17)$$

where $\langle s \rangle$ is the mean avalanche size for a small stress bin around the stress, F .

5. For the loading condition of a small imposed strain rate, Γ , the model predicts that

$$S_{\max} \sim \Gamma^{-\lambda} \quad (6.18)$$

$$D(s, \Gamma) \sim 1/s^\tau K(s \cdot \Gamma^\lambda) \quad (6.19)$$

where $\tau = 1.5$ and $\lambda = 2$ according to the analytical predictions, and the universal scaling function, K , is quickly decaying.

Widom scaling collapses can be used to test these predictions [143]. For example, in order to test $D(s, F) \sim 1/s^\tau D[s \cdot (F_c - F)^{1/\sigma}]$, or equivalently $D(s, F)s^\tau \sim D[s \cdot (F_c - F)^{1/\sigma}]$, one plots $D(s, F)s^\tau$ on the y axis and $s \cdot (F_c - F)^{1/\sigma}$ as the x -axis. Next the values for F_c , τ , and σ are tuned until the distributions, $D(s, F)$, for different, F , lay on top of each other. Figure 6.18 shows the Widom-scaling collapse of four $C(s)$ curves with different stresses for Mo nanopillars [69]. The corresponding experimental setup and the stress-strain curves are shown in Fig. 6.19 [69].

Recent studies indicate that the above MFT model could be applied to HEAs [72]. Figures 6.20, 6.21, and 6.22 show the complementary cumulative distribution functions of the stress-drop sizes for three kinds of HEAs at different temperatures and strain rates [72]. It's clear that the temperature dramatically affects the distribution of stress-drop sizes. In some specific temperature ranges, the stress-drop size will decrease as the temperature increases, which is true for the $\text{Al}_{0.5}\text{CoCrCuFeNi}$ HEA from 7 to 9 K (Fig. 6.20), for the MoNbTaW HEA from 298 to 873 K (Fig. 6.21), and for the $\text{Al}_5\text{Cr}_{12}\text{Fe}_{35}\text{Mn}_{28}\text{Ni}_{20}$ HEA from 573 to 673 K (Fig. 6.22). The experimental results agree well with the MFT model prediction that the slip avalanches are expected to become smaller for larger in these specific ranges of temperature [52, 58, 68, 72]. An recent extension of the MFT for the

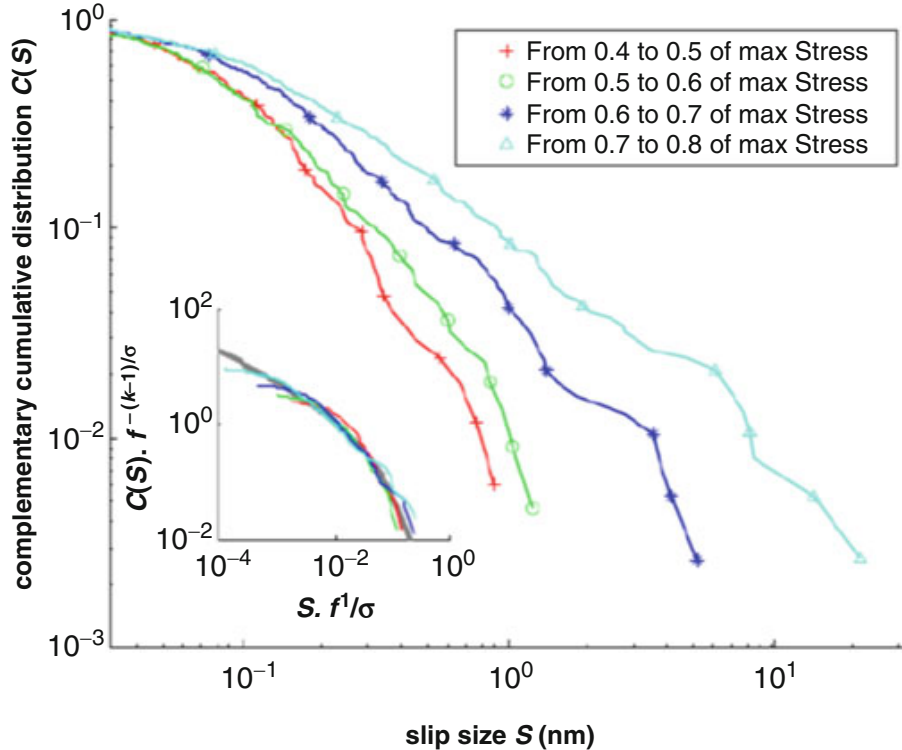


Fig. 6.18 The main figure shows $C(s)$ curves for slips in stress intervals around different applied stress values, τ . The avalanche events are obtained from compression experiments on seven 800-nm-diameter Mo nanopillars at a nominal displacement rate of 0.1 nm/s. The avalanche events are all normalized according to their respective maximum stress. The insert shows the Widom-scaling collapse of the $C(s)$ curves, and $f = (\tau_c - \tau)/\tau_c - c'$, where the adjustable parameter, $c' = 0.14$, compensates for the finite system size. The scaling exponents, $\kappa = 1.5$ and $\sigma = 0.5$, agree with MFT predictions. The gray function is the scaling function, $g(x) \equiv \int_x^\infty e^{-At} t^{-\kappa} dt$, also predicted by the MFT model [69]

serration behavior of HEAs shows that in other temperature ranges the dependence of the average avalanche size on the temperature can be even non monotonic, reaching a maximum within a special temperature range that depends on the applied strain rate.

In addition, the MFT model [66, 68, 69, 72] could also be related to the deformation mechanism for HEAs, including the dislocation motion and deformation twinning. In high-temperature ranges, i.e., the cases of MoNbTaW and Al₅Cr₁₂Fe₃₅Mn₂₈Ni₂₀ HEAs in the above discussion, the thermal vibration energy of pinning solute atoms should be considered at high temperatures. Since HEAs are regarded as solid solutions, each constituent element can be a solute atom. As temperature increases, the pinning effect of solutes around dislocations becomes smaller because solute atoms tend to shake away from their low-energy sites for pinning as the thermal vibration energy increases [62], which will lead to a decrease for the slip size. In contrast, in the cryogenic-temperature range, i.e., the case of the Al_{0.5}CoCrCuFeNi HEA in the present study, twinning may likely be responsible for the deformation process [67], since higher temperatures make it more difficult for deformation twins to be induced. Therefore, slip size will be decreased, as temperature increases since the twinning process is more restricted. However, it should be

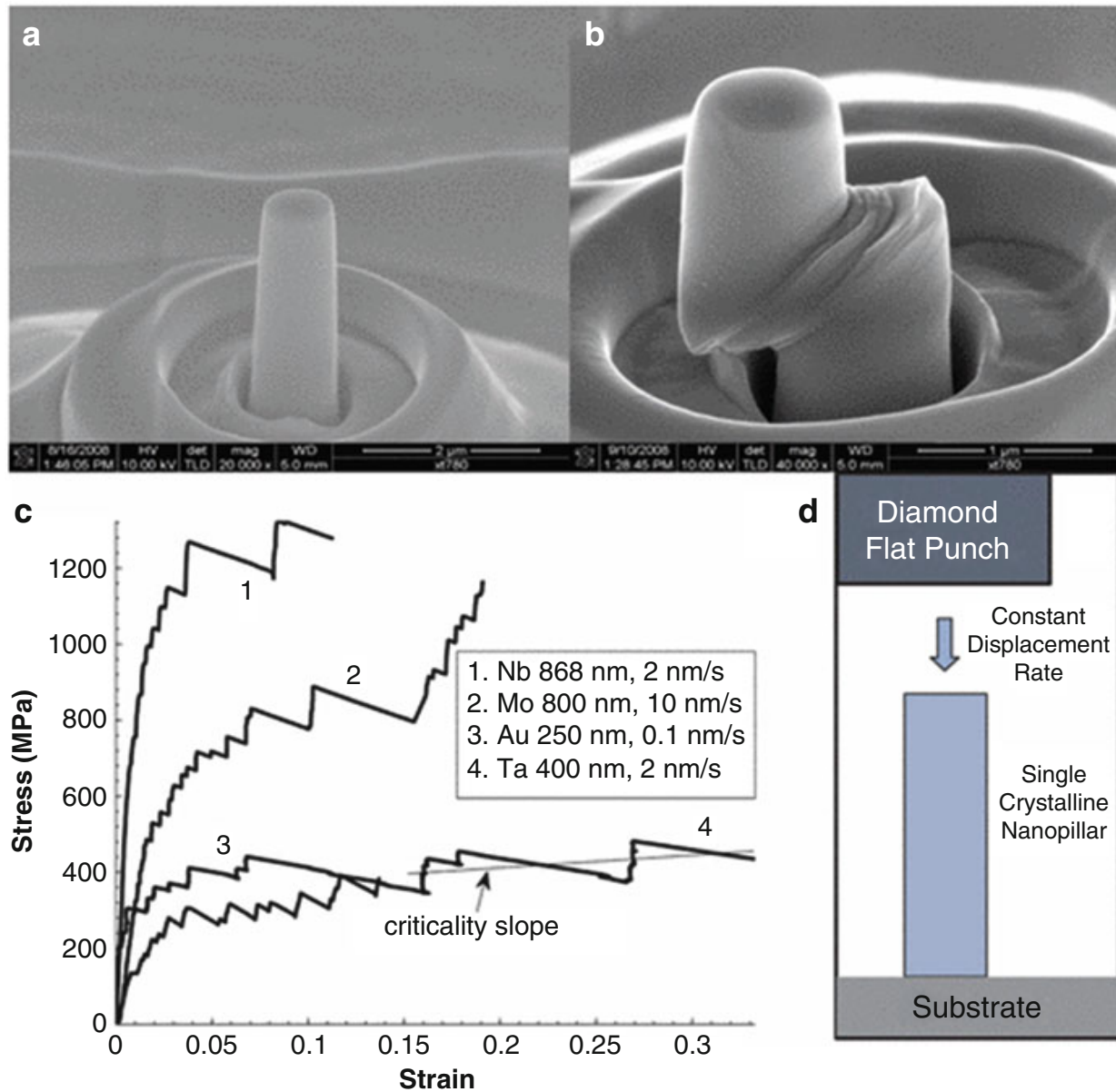


Fig. 6.19 (a) SEM image of an Nb pillar at 52° tilt before compression. (b) SEM image of the same pillar after compression and the final slip-avalanche event, with the slip data at the largest strains excluded. (c) Stress–strain curves for different metals compressed at different displacement rates. Curve 1 corresponds to the Nb pillar in (a, b). The criticality slope line is fit to estimate the slope of curve 4 near the failure stress. (d) The compression test setup [69]

noted that the above two proposed deformation mechanisms may not be only limited or separated in the specific temperature ranges as discussed. For different solid-solution systems, for instance, the twinning process may overwhelm the dislocation process and dominate in the high-temperature range, or the combination of both mechanisms may exist at the same time. Thus, more detailed studies for the temperature effects are needed. Other possible reasons may also exist, like phase-transformation-induced changes in the deformation mechanism. In summary, the experimental results of the decreasing trend for the slip size at higher temperature match well with the trend predicted by the MFT model, suggesting that the study of serration behavior may improve the understanding of the deformation process of HEAs or even for new HEA materials, which can also be used to compare with the Portevin–Le Chatelier (PLC) effect in conventional alloys [63–65, 70, 71].

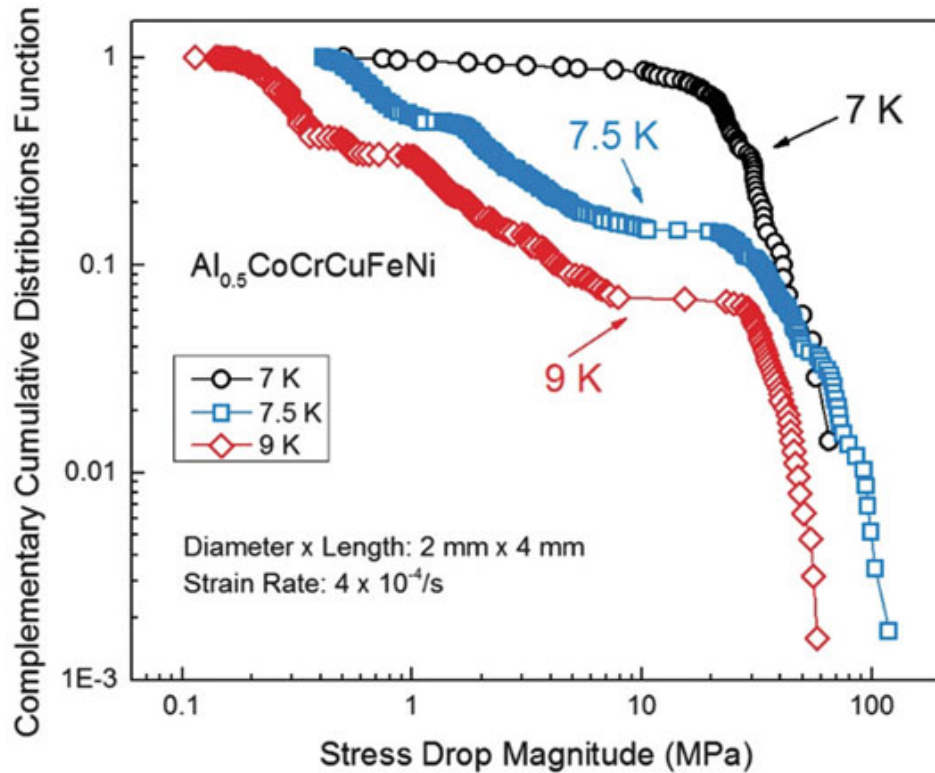


Fig. 6.20 Serration events for $\text{Al}_{0.5}\text{CoCrCuFeNi}$ in compression experiments under a constant strain rate of $4 \times 10^{-4}/\text{s}$. Serration events in samples compressed at temperatures around 7 K occur in broad ranges of magnitudes, compared to events in samples compressed at 7.5 and 9 K [72]

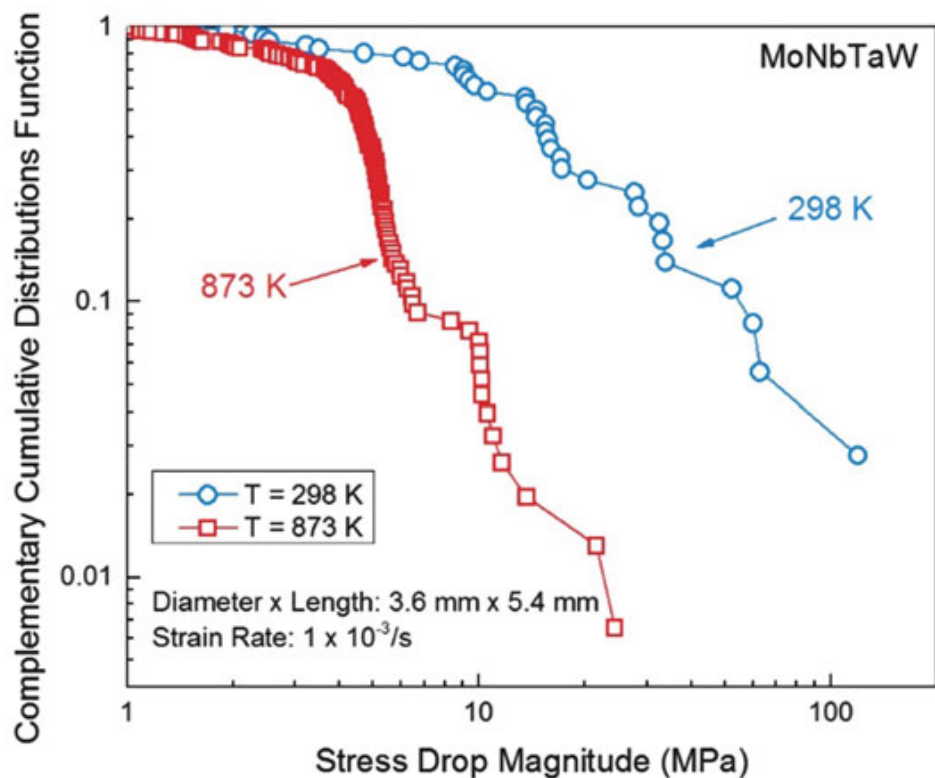


Fig. 6.21 Serration events for MoNbTaW in compression experiments under a constant strain rate of $1 \times 10^{-3}/\text{s}$. Heating the sample from room temperature to 873 K severely diminishes the characteristic size of the serrations [72]

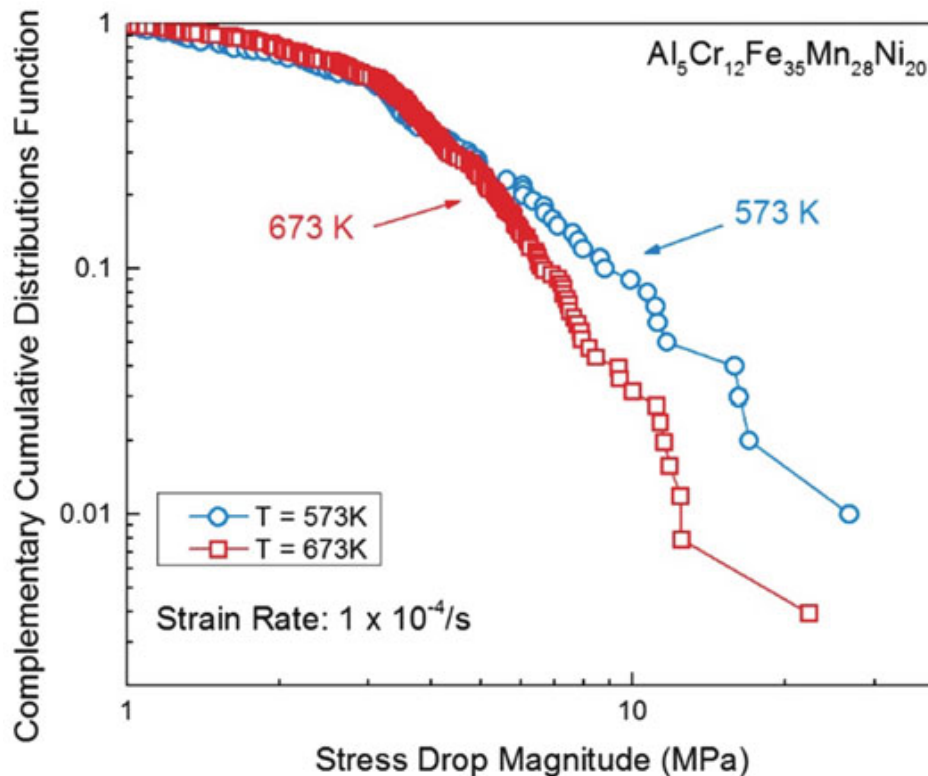


Fig. 6.22 Serration events for $\text{Al}_5\text{Cr}_{12}\text{Fe}_{35}\text{Mn}_{28}\text{Ni}_{20}$ in tension experiments under a constant strain rate of $1 \times 10^{-4}/\text{s}$. This alloy was tested in its as-homogenized state; alloys that were cold-rolled after homogenization did not exhibit serration behavior. The effect of temperature is shown here; higher temperatures curb the distribution of serration magnitudes [72]

6.6 Fatigue Properties

6.6.1 Stress–Life (S–N) Curve

Fatigue behavior of materials is extremely important for industrial and engineering applications. For the $\text{Al}_{0.5}\text{CoCrCuFeNi}$ HEA, four-point-bending tests have been conducted at various applied loads [73]. The maximum stress, σ , on the tensile surface within the span of the two outer pins can be calculated, using

$$\sigma = \frac{3P(S_o - S_i)}{2BW^2} \quad (6.20)$$

where P is the applied load, S_o is the outer span length, S_i is the inner span length, B is the thickness, and W is the height.

The stress range versus the number of cycles to failure (S–N) curve is plotted in Fig. 6.23a, marked by red and blue points. The points are scattered within stress range of 600–1,200 MPa. Even at the largest stress range above 1,100 MPa, the fatigue life still scatters from 35,000 to 450,000 cycles. One possible reason could be the defects introduced during the casting and rolling process, such as aluminum oxide particles. Figure 6.23b shows these particles in the energy-dispersive X-ray spectroscopy (EDS) analysis, which contain around 50 % oxygen. These defects

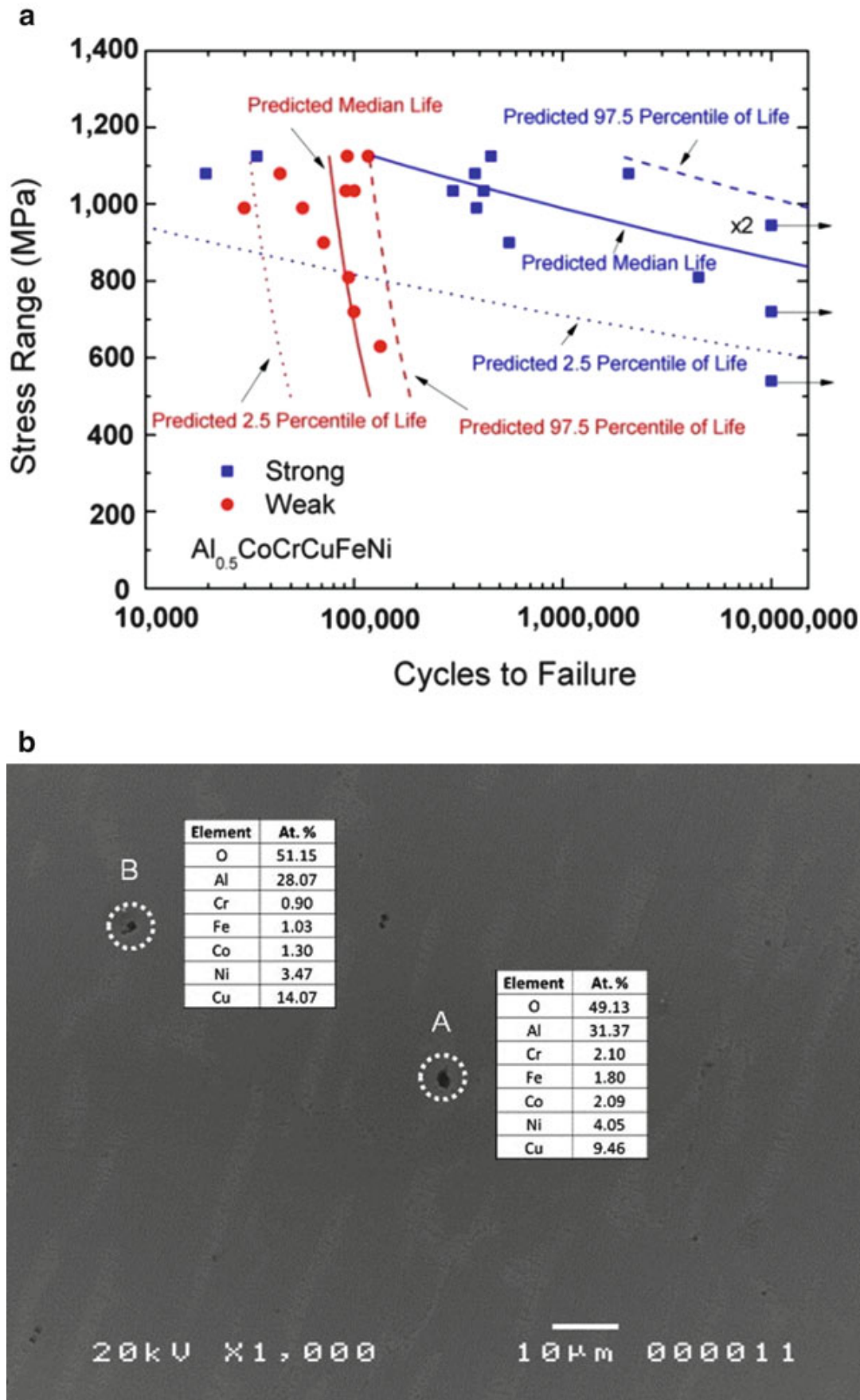


Fig. 6.23 (a) S-N curve (all red and blue points) of the $\text{Al}_{0.5}\text{CoCrCuFeNi}$ HEA in four-point-bending-fatigue tests and (b) SEM images with EDS analyses of the aluminum oxide particles [73]

may serve as nucleation sites for microcracks and shorten the fatigue life of HEA samples.

The fatigue tests reach 10^7 cycles at three stress levels, which indicates that the endurance limit is roughly estimated to be 540–945 MPa. Actually, by combining the characterization of microstructure and the predictive model, the estimation of endurance limit becomes more specific, a value of 858 MPa, as described in Sect. 6.7.3.

6.6.2 Fractography

Figure 6.24 shows the fractography of fatigued samples at a stress range of 900 MPa after 555,235 cycles [73]. In general, crack initiation occurred from defects at the surface, or the corner of the sample, where the stress highly concentrates. As indicated in Fig. 6.24a, b, the initiation sites locate at the microcracks, and typical fatigue regions (initiation, propagation, and fracture regions) can be recognized, as marked by red arrows. Within the fatigue-propagation region, characteristic striations can be identified, indicating the crack-growth direction, which is generally perpendicular to the striation direction in Fig. 6.24c. The dimple-like final fracture surface implies a ductile fracture, as shown in Fig. 6.24d.

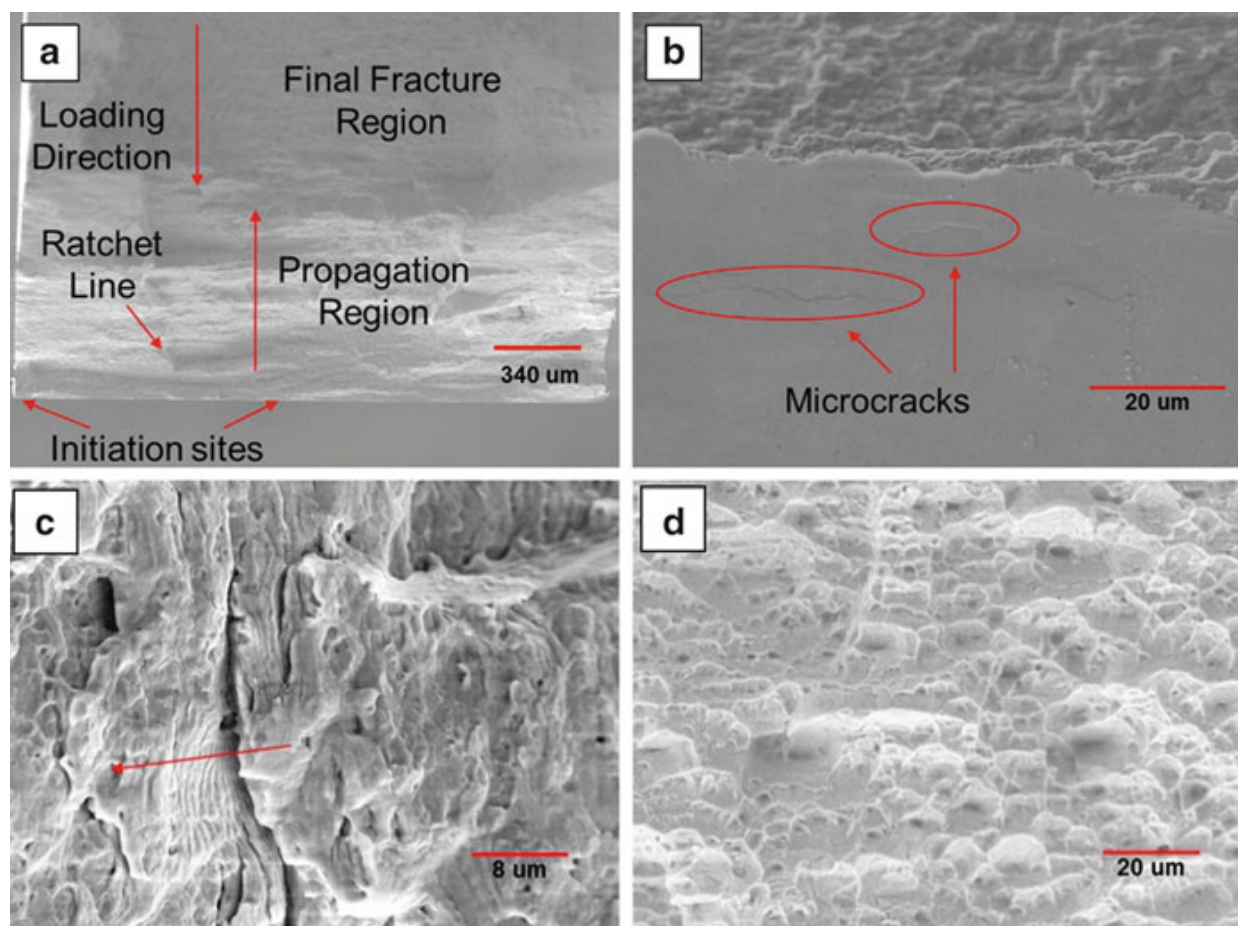


Fig. 6.24 (a) SEM images of fracture surfaces of a fatigued sample at a stress range of 900 MPa after 555,235 cycles, (b) microcracks found at the surface before the fatigue test, (c) fatigue striations in the crack-propagation region, and (d) dimples in the final fracture region [73]

6.6.3 Weibull Mixture Predictive Model for Fatigue Life

From the S–N plot in Fig. 6.23a, the data points seem to be not homogeneous and distribute into two groups. One can be denoted as a strong group, indicating samples with fewer fabrication defects, and the other is marked as a weak group. Therefore, the Weibull mixture predictive model is selected to predict the fatigue life instead of the Weibull model. The probability density function (PDF) and the cumulative distribution function (CDF) of the Weibull mixture model are given [73]:

$$\begin{aligned} f(N|p, \alpha_s, \beta_s, \alpha_w, \beta_w) &= p \frac{\beta_w}{\alpha_w} \left(\frac{N}{\alpha_w} \right)^{\beta_w - 1} \exp \left[- \left(\frac{N}{\alpha_w} \right)^{\beta_w} \right] \\ &\quad + (1 - p) \frac{\beta_s}{\alpha_s} \left(\frac{N}{\alpha_s} \right)^{\beta_s - 1} \exp \left[- \left(\frac{N}{\alpha_s} \right)^{\beta_s} \right] \end{aligned} \quad (6.21)$$

$$\begin{aligned} F(N|p, \alpha_s, \beta_s, \alpha_w, \beta_w) &= p \left\{ 1 - \exp \left[- \left(\frac{N}{\alpha_w} \right)^{\beta_w} \right] \right\} \\ &\quad + (1 - p) \left\{ 1 - \exp \left[- \left(\frac{N}{\alpha_s} \right)^{\beta_s} \right] \right\} \end{aligned} \quad (6.22)$$

where N is the cycles to failure, subscripts w and s denote the weak and strong groups, p is the fraction of samples belonging to the weak group, and the Weibull parameters, α_s and α_w , are assumed to be dependent on the stress, S , according to

$$\log(\alpha_w) = \gamma_{w,0} + \gamma_{w,1} \log(S) \quad (6.23)$$

$$\log(\alpha_s) = \gamma_{s,0} + \gamma_{s,1} \log(S) \quad (6.24)$$

So the model has seven unknown parameters in total, $p, \gamma_{s,0}, \gamma_{s,1}, \beta_s, \gamma_{w,0}, \gamma_{w,1}$, and β_w , which can be estimated by the maximum likelihood method [144]:

$$L(p, \gamma_{s,0}, \gamma_{s,1}, \beta_s, \gamma_{w,0}, \gamma_{w,1}, \beta_w) = \prod_{i=1}^m f(N_i)^{\delta_i} (1 - F(N_i))^{1-\delta_i} \quad (6.25)$$

Then the observed fatigue data can be clustered into the two groups. Therefore, the p -quantile fatigue lives of the strong group and the weak group are predicted by

$$N_{p,w}(S) = \exp[\gamma_{w,0} + \gamma_{w,1} \log(S)] [-\log(1 - p)]^{1/\beta_w} \quad (6.26)$$

$$N_{p,s}(S) = \exp[\gamma_{s,0} + \gamma_{s,1} \log(S)] [-\log(1 - p)]^{1/\beta_s} \quad (6.27)$$

More details of the model can be found elsewhere [73]. The predicted two groups are described in Fig. 6.23a using red and blue lines. The median life of the strong group exceeds 10^7 cycles when the applied stress was less than 858 MPa, which can be used as the estimation of the endurance limit.

6.6.4 Comparison with Conventional Alloys

The $\text{Al}_{0.5}\text{CoCrCuFeNi}$ HEA shows promising fatigue resistance, when compared to other conventional alloys and bulk metallic glasses (BMGs). With respect to the fatigue ratio of the stress range divided by the ultimate tensile strength (UTS), HEAs span from the lower bound comparable to IN 625 superalloy to the higher bound surpassing all the other alloys listed in Fig. 6.25a. The fluctuation is mainly introduced by the casting defects in the HEA. Figure 6.25b shows that the endurance limit increases linearly with ultimate tension strength (UTS), with a slope of being approximately equal to 0.5 for most materials, HEAs exceed this ratio, with an upper bound of 0.7. All these results indicate that HEAs are promising candidate materials in the structures requiring the fatigue resistance for future applications.

6.7 Nanoindentation

6.7.1 Nanoindentation and Modeling

Over the past years, nanoindentation was utilized as a powerful tool to determine the hardness and elastic modulus of HEA coatings, prepared by reactive magnetron sputtering [145–152] or by the transferred arc-cladding process [153], and the hardness or elastic modulus profile was successfully obtained. Recently, the investigation using nanoindentation for the bi-phase (FCC and BCC) bulk AlCrCuFeNi_2 alloy was reported [75], and the contact modulus and hardness were compared for these two phases. Besides the room-temperature indentation, the deformation behavior at elevated temperatures has also been studied [74], with emphasis on the incipient plasticity, and vacancy-mediated heterogeneous dislocation nucleation is deduced through modeling. To understand the nanoindentation deformation and results, we first review several equations for general purpose [74].

Before the first pop-in in the load–displacement (P – h) curve, the deformation can be regarded as elastic, and the Hertzian elastic theory [154] could be used to describe the elastic-loading curve:

$$P = \frac{4}{3}E_r R^{1/2} h^{3/2} \quad (6.28)$$

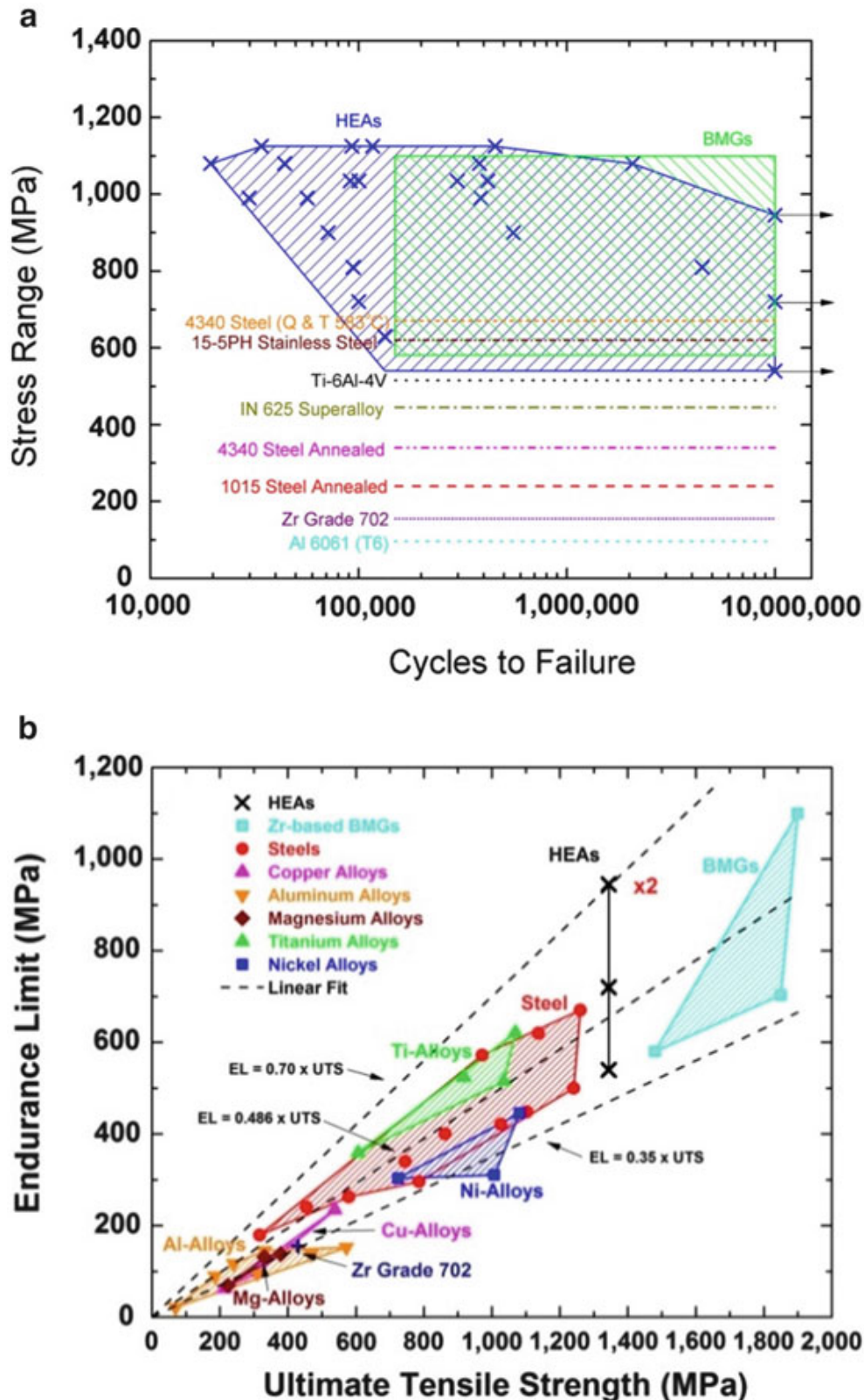


Fig. 6.25 Fatigue behavior including (a) fatigue ratio [stress range/ultimate tensile strength (UTS)] versus cycles to failure and (b) endurance limits versus UTS, comparing the $\text{Al}_{0.5}\text{CoCrCuFeNi}$ HEA, other conventional alloys, and BMGs [73]

where P is the applied load, R is the tip radius of the indenter, h is the penetration depth, and E_r is the reduced modulus of the indenter-sample combination and can be calculated as

$$\frac{1}{E_r} = \frac{1 - v_i^2}{E_i} + \frac{1 - v_s^2}{E_s} \quad (6.29)$$

where v_i and E_i are Poisson's ratio and Young's modulus of the indenter and v_s and E_s are Poisson's ratio and Young's modulus of the sample, respectively. Then the mean pressure at pop-in, P_m , and maximum shear stress, τ_{\max} , can be derived from [155]

$$P_m = \left(\frac{6PE_r^2}{\pi^3 R^2} \right)^{1/3} \quad (6.30)$$

$$\tau_{\max} = 0.31P_m \quad (6.31)$$

The cumulative probability, $F(P)$, of the indentation pop-in load, P , is given by

$$\ln[-\ln(1 - F)] = \alpha P^{1/3} + \beta \quad (6.32)$$

where β is a weak function of the pop-in load, P , and α is correlated to the activation volume, V :

$$V = \frac{\pi}{0.47} \left(\frac{3R}{4E_r} \right)^{2/3} kT\alpha \quad (6.33)$$

In addition, the relationship between the temperature and pop-in load at a specific $F(P)$ is [156]

$$P^{1/3} = \gamma kT + \frac{\pi}{0.47} \left(\frac{3R}{4E_r} \right)^{2/3} \frac{H}{V} \quad (6.34)$$

where γ is a complex function, and H is the activation enthalpy.

6.7.2 Elevated-Temperature Nanoindentation

As described in Fig. 6.26a, the typical P-h shows the pop-in behavior at different temperatures, T . Through Hertzian fitting, Eq. (6.28), the reduced modulus at different T , $E_r(T)$, can be obtained. As the temperature increases, a significant decrease in the pop-in load, $P(T)$, can be observed. Thus, from Eq. (6.31), the maximum shear stress, $\tau_{\max}(T)$, is calculated from $P(T)$, and its relationship with temperature is plotted in Fig. 6.26b. It's obvious that $\tau_{\max}(T)$ and T are linearly correlated.

To obtain the activation volume, V , and activation enthalpy, H , two more fitting steps are needed. Using Eq. (6.32), the parameter, α , can be acquired by fitting the

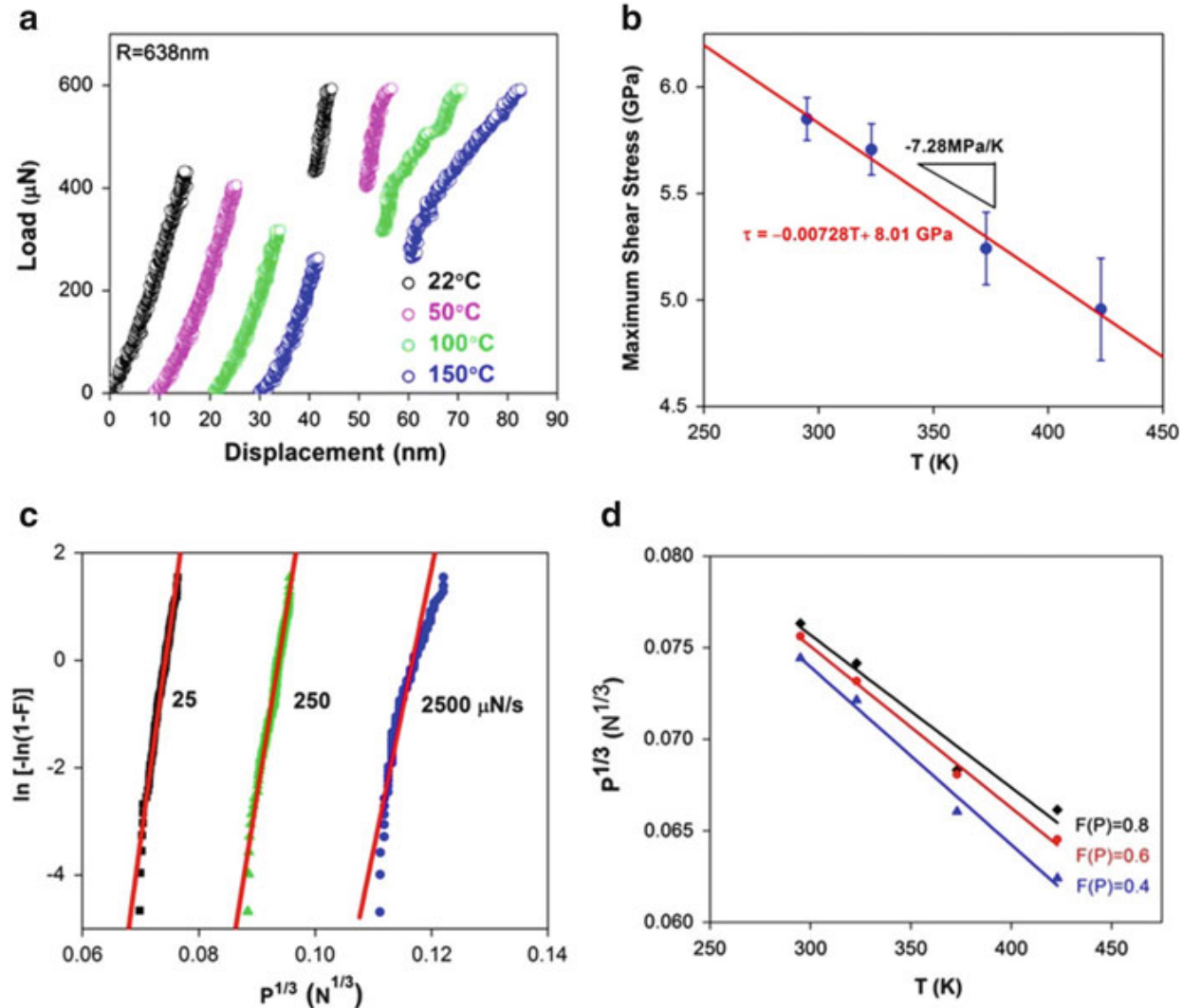


Fig. 6.26 (a) Typical P-h curves of CoCrFeMnNi at temperatures of 295, 323, 373 and 423 K, (b) maximum shear stress versus temperature, (c) extracting the activation volume from the experimental data, and (d) extracting the activation enthalpy for the pop-in [74]

slope of $\ln[-\ln(1-F)]$ versus $P^{1/3}$, as shown in Fig. 6.26c. Then by combining with Eq. (6.33), V is readily derived. By fitting $P^{1/3}$ versus T using Eq. (6.34), as plotted in Fig. 6.26d, the intercept value determines H/V , and, thus, H is obtained. The possibilities of the homogeneous dislocation nucleation and vacancy-mediated heterogeneous dislocation nucleation were then discussed [74], but only the values from the latter fall into the range of experimental values. These results improve the understanding of mechanisms for the onset of plasticity in HEAs.

6.7.3 Indentation and Nanoindentation Creep

Conventional creep tests have not been reported in the area of HEAs. Only two papers using indentation tests to study the creep behavior of HEAs have been reported [51, 76]. The indentation creep has been defined as a time-dependent motion of a hard indenter into a solid under a constant load for a long time, i.e.,

an elongated hard test. The indentation-creep experiments were done for $\text{Al}_x\text{CoCrFeNi}$ ($x=0.3, 0.5, 0.7, 0.9$, and 1.5) in the temperature range of 773–1,173 K using a load 1 kgf for dwell times of 5, 10, and 30s [51]. The creep behavior is strongly dependent on the crystal structure of HEAs. For the single-phase FCC $\text{Al}_{0.3}\text{CoCrFeNi}$ alloy, hot hardness resists without large changes for all experimental temperatures in the time range of 30s. Hence, no obvious creep occurs in single-phase FCC HEAs, even at high temperatures, which suggests that the main deformation mechanism is slip. The situation is different for the multiphase $\text{Al}_x\text{CoCrFeNi}$ ($x=0.5, 0.7, 0.9$, and 1.5) HEAs. The variations of hot hardness as a function of dwell time are negligible below 873 K, while the hot hardness decreases with increasing the dwell time above 873 K. It confirms that the creep happens for multiphase HEAs above a certain temperature (e.g., 873 K for $\text{Al}_x\text{CoCrFeNi}$, $x=0.5, 0.7, 0.9$, and 1.5).

Nanoindentation is also used to characterize the initial transient creep stage in CoFeNi by Wang et al. [76] by the viscoelastic fitting theory. The CoFeNi is a single-phase FCC HEA [157]. The displacement curve for the initial creep stage can be described by an empirical law [158]:

$$h(t) = h_i + \beta(t - t_i)^m + kt \quad (6.35)$$

where β , m , and k are fitting parameters. The fitting protocol in Eq. (6.35) is found to produce very good fits for the CoFeNi HEA at a constant load of 4,000 μN , shown in Fig. 6.27. Unlike conventional alloys, a crossover point where the slope changes in the initial creep stage is found in CoFeNi HEA (Fig. 6.27). Further studies show that the value of the crossover point increases with increasing holding time at the same constant load (Fig. 6.28a) and with the increase of the holding stress at constant holding time (Fig. 6.28b).

A hypothesis is proposed for the crossover point in the initial creep stage from the viewpoint of the dislocation migration beneath the indenter [76]. The formation

Fig. 6.27 Crossover behavior in the displacement-time curve in the initial creep stage of CoFeNi [76]

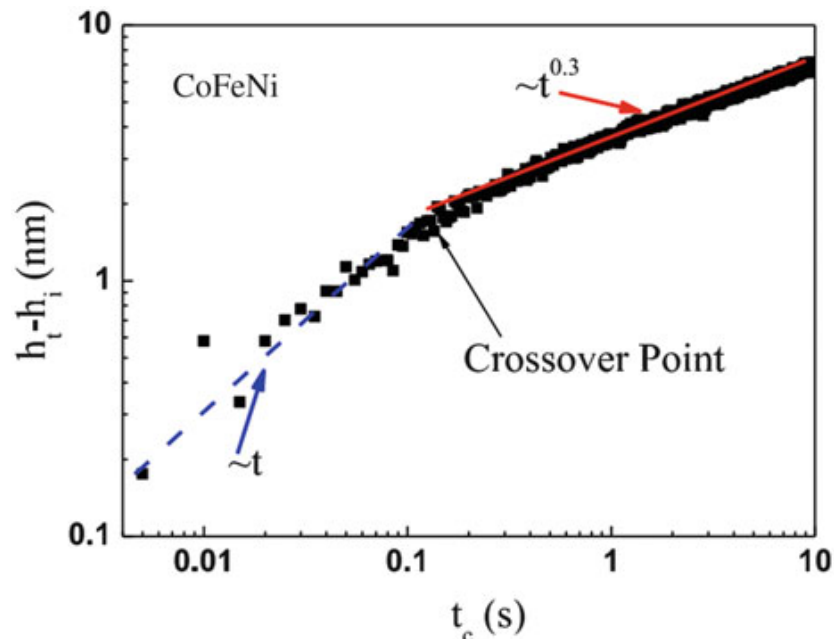
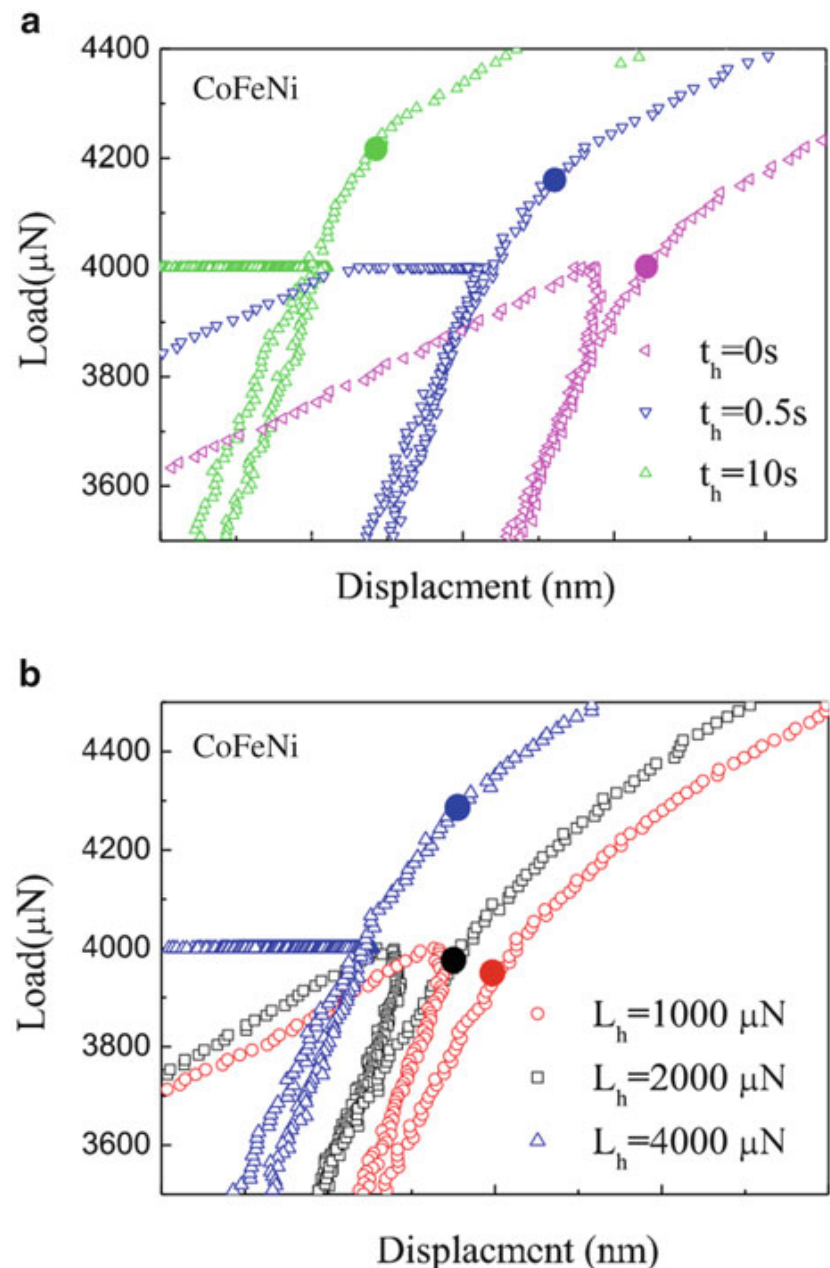


Fig. 6.28 Hardening effect in the initial creep of CoFeNi. (a) the holding-time-dependent yielding point, (b) the holding-load-dependent yielding point [76]



of the dislocation cells corresponds to the crossover behavior. Before the crossover point, the separated dislocation entanglement leads to the work-hardening effect. After the crossover point, the work-hardening effect is saturated, and the residual dislocations migrate into the domain boundary of the dislocation cell, which determines the viscous behavior [76].

6.8 Conclusions

This chapter reviews the mechanical properties of HEAs in the fields of hardness, compression, tension, serration behavior, fatigue, and nanoindentation. It shows that the hardness of HEAs varies widely from 140 to 900 HV, highly dependent on the alloy systems and related processing methods. The effects of alloying,

annealing treatment, and structure on the hardness are discussed. The trend of hot hardness is also summarized. Various loading conditions, such as temperatures, Al contents, strain rates, sample sizes, and microcompression, are related to the microstructural evolution during compression deformation. The effects of structures, grain sizes, alloying elements, and processing parameters on the tensile yielding stress, ductility, shape of tensile stress-strain curves, and fracture after tension tests are discussed. A MFT model successfully predicting the slip avalanche and serration statistics observed in recent simulations of the plastic deformation of HEAs is presented. The fatigue study under four-point-bending tests conducted on the $\text{Al}_{0.5}\text{CoCrCuFeNi}$ HEA is revealed to demonstrate that fatigue properties of HEAs are generally better, compared with conventional alloys. Nanoindentation studies on the incipient plasticity and creep behavior are discussed.

6.9 Future Work

Although extensive work has been done in exploring the mechanical behavior of HEAs, we should continue to describe and explore mechanical properties in depth.

1. The effects of heat treatment and processing on mechanical behavior have to be optimized to develop HEAs with desirable microstructures and mechanical properties.
2. More work should be focused on the high-temperature mechanical properties, such as hot hardness, hot compression, and hot tension tests.
3. Compared to hardness and compression experiments, limited work on the tensile properties of HEAs has been done. We should do tensile tests at room and high temperatures with different strain rates, which will lead a guide to the broader application of HEAs.
4. Fatigue experiments should be conducted in more alloy systems. Besides high-cycle fatigue, low-cycle-fatigue and fatigue-crack-growth behavior should be included to fully describe the fatigue performance of HEAs.
5. The indenter and nanoindenter are used to successfully describe the creep behavior of HEAs successfully on a small scale. However, we should conduct conventional creep studies on larger scales.
6. The theoretical work relating microstructural features to mechanical performance needs to be explored. Serration behavior of HEAs should be intensively studied and understood, which shed light on deformation mechanisms. The studies of tension and compression behavior have to be conducted to understand the anisotropic behavior of HEAs. Moreover, the serration characteristics of the tension and compression behavior have to be investigated to fully comprehend the deformation mechanisms. It would be great to see if there are effects of creep and fatigue damage on serration features with a hope of predicting creep and fatigue life through modeling serration characteristics.

7. Advanced characterization techniques [159, 160], such as in situ neutron and synchrotron diffraction, SEM, transmission electron microscopy (TEM), atomic probe microscopy (APT), and so on, are needed to reveal the deformation mechanisms of HEAs at the level of atomic stresses or dislocations.

Acknowledgment The authors very much appreciate Dr. Michael C. Gao's kind and excellent comments on this book chapter. HYD and PKL would like to acknowledge the Department of Energy (DOE), Office of Fossil Energy, National Energy Technology Laboratory (DE-FE-0008855 and DE-FE-0024054), with Mr. V. Cedro and Mr. R. Dunst as program managers. XX, FS, KAD, and PKL thank the support from the project of DE-FE-0011194 with the program manager, Dr. J. Mullen. PKL very much appreciates the support of the US Army Research Office project (W911NF-13-1-0438) with the program manager, Drs. D. Stepp and S. Mathaudhu, and the National Science Foundation (CMMI-1100080) with the program director, Dr. C. Cooper.

References

1. Cantor B, Chang ITH, Knight P, Vincent AJB (2004) Microstructural development in equiatomic multicomponent alloys. *Mater Sci Eng A* 375–377:213–218. doi:[10.1016/j.msea.2003.10.257](https://doi.org/10.1016/j.msea.2003.10.257)
2. Yeh JW, Chen SK, Lin SJ, Gan JY, Chin TS, Shun TT, Tsau CH, Chang SY (2004) Nanostructured high-entropy alloys with multiple principal elements: novel alloy design concepts and outcomes. *Adv Eng Mater* 6(5):299–303. doi:[10.1002/adem.200300567](https://doi.org/10.1002/adem.200300567)
3. Tong C-J, Chen M-R, Yeh J-W, Lin S-J, Chen S-K, Shun T-T, Chang S-Y (2005) Mechanical performance of the $\text{Al}_x\text{CoCrCuFeNi}$ high-entropy alloy system with multiprincipal elements. *Metall Mater Trans A* 36(5):1263–1271. doi:[10.1007/s11661-005-0218-9](https://doi.org/10.1007/s11661-005-0218-9)
4. Chen M-R, Lin S-J, Yeh J-W, Chuang M-H, Chen S-K, Huang Y-S (2006) Effect of vanadium addition on the microstructure, hardness, and wear resistance of $\text{Al}_{0.5}\text{CoCrCuFeNi}$ high-entropy alloy. *Metall Mater Trans A* 37(5):1363–1369. doi:[10.1007/s11661-006-0081-3](https://doi.org/10.1007/s11661-006-0081-3)
5. Tung C-C, Yeh J-W, Shun T-t, Chen S-K, Huang Y-S, Chen H-C (2007) On the elemental effect of AlCoCrCuFeNi high-entropy alloy system. *Mater Lett* 61(1):1–5. doi:[10.1016/j.matlet.2006.03.140](https://doi.org/10.1016/j.matlet.2006.03.140)
6. Li C, Li JC, Zhao M, Zhang L, Jiang Q (2008) Microstructure and properties of AlTiNiMnB_x high entropy alloys. *Mater Sci Technol* 24(3):376–378. doi:[10.1179/174328408x275964](https://doi.org/10.1179/174328408x275964)
7. Kao Y-F, Chen T-J, Chen S-K, Yeh J-W (2009) Microstructure and mechanical property of as-cast, –homogenized, and -deformed $\text{Al}_x\text{CoCrFeNi}$ ($0 \leq x \leq 2$) high-entropy alloys. *J Alloys Compd* 488(1):57–64. doi:[10.1016/j.jallcom.2009.08.090](https://doi.org/10.1016/j.jallcom.2009.08.090)
8. Yu PF, Cheng H, Zhang LJ, Zhang H, Jing Q, Ma MZ, Liaw PK, Li G, Liu RP (2016) Effects of high pressure torsion on microstructures and properties of an $\text{Al}_{0.1}\text{CoCrFeNi}$ high-entropy alloy. *Mater Sci Eng A* 655:283–291, doi:<http://dx.doi.org/10.1016/j.msea.2015.12.085>
9. Chen S-T, Tang W-Y, Kuo Y-F, Chen S-Y, Tsau C-H, Shun T-T, Yeh J-W (2010) Microstructure and properties of age-hardenable $\text{Al}_x\text{CrFe}_{1.5}\text{MnNi}_{0.5}$ alloys. *Mater Sci Eng A* 527 (21–22):5818–5825. doi:[10.1016/j.msea.2010.05.052](https://doi.org/10.1016/j.msea.2010.05.052)
10. Hsu C-Y, Wang W-R, Tang W-Y, Chen S-K, Yeh J-W (2010) Microstructure and mechanical properties of New $\text{AlCo}_x\text{CrFeMo}_{0.5}\text{Ni}$ high-entropy alloys. *Adv Eng Mater* 12(1–2):44–49. doi:[10.1002/adem.200900171](https://doi.org/10.1002/adem.200900171)
11. Li C, Li JC, Zhao M, Jiang Q (2010) Effect of aluminum contents on microstructure and properties of $\text{Al}_x\text{CoCrFeNi}$ alloys. *J Alloys Compd* 504:S515–S518. doi:[10.1016/j.jallcom.2010.03.111](https://doi.org/10.1016/j.jallcom.2010.03.111)

12. Lin C-M, Tsai H-L, Bor H-Y (2010) Effect of aging treatment on microstructure and properties of high-entropy Cu_{0.5}CoCrFeNi alloy. *Intermetallics* 18(6):1244–1250. doi:[10.1016/j.intermet.2010.03.030](https://doi.org/10.1016/j.intermet.2010.03.030)
13. Senkov O, Wilks G, Miracle D, Chuang C, Liaw P (2010) Refractory high-entropy alloys. *Intermetallics* 18(9):1758–1765
14. Shun T-T, Hung C-H, Lee C-F (2010) The effects of secondary elemental Mo or Ti addition in Al_{0.3}CoCrFeNi high-entropy alloy on age hardening at 700°C. *J Alloys Compd* 495 (1):55–58. doi:[10.1016/j.jallcom.2010.02.032](https://doi.org/10.1016/j.jallcom.2010.02.032)
15. Tsai C-W, Tsai M-H, Yeh J-W, Yang C-C (2010) Effect of temperature on mechanical properties of Al_{0.5}CoCrCuFeNi wrought alloy. *J Alloys Compd* 490(1–2):160–165. doi:[10.1016/j.jallcom.2009.10.088](https://doi.org/10.1016/j.jallcom.2009.10.088)
16. Zhang KB, Fu ZY, Zhang JY, Shi J, Wang WM, Wang H, Wang YC, Zhang QJ (2010) Annealing on the structure and properties evolution of the CoCrFeNiCuAl high-entropy alloy. *J Alloys Compd* 502(2):295–299. doi:[10.1016/j.jallcom.2009.11.104](https://doi.org/10.1016/j.jallcom.2009.11.104)
17. Chuang M-H, Tsai M-H, Wang W-R, Lin S-J, Yeh J-W (2011) Microstructure and wear behavior of Al_xCo_{1.5}CrFeNi_{1.5}Ti_y high-entropy alloys. *Acta Mater* 59(16):6308–6317. doi:[10.1016/j.actamat.2011.06.041](https://doi.org/10.1016/j.actamat.2011.06.041)
18. Hsu C-Y, Juan C-C, Wang W-R, Sheu T-S, Yeh J-W, Chen S-K (2011) On the superior hot hardness and softening resistance of AlCoCr_xFeMo_{0.5}Ni high-entropy alloys. *Mater Sci Eng A* 528(10–11):3581–3588. doi:[10.1016/j.msea.2011.01.072](https://doi.org/10.1016/j.msea.2011.01.072)
19. Lin CM, Tsai HL (2011) Evolution of microstructure, hardness, and corrosion properties of high-entropy Al_{0.5}CoCrFeNi alloy. *Intermetallics* 19(3):288–294. doi:[10.1016/j.intermet.2010.10.008](https://doi.org/10.1016/j.intermet.2010.10.008)
20. Seifi M, Li D, Yong Z, Liaw PK, Lewandowski JJ (2015) Fracture toughness and fatigue crack growth behavior of as-cast high-entropy alloys. *JOM* 67(10):2288–2295. doi:[10.1007/s11837-015-1563-9](https://doi.org/10.1007/s11837-015-1563-9)
21. Senkov ON, Scott JM, Senkova SV, Miracle DB, Woodward CF (2011) Microstructure and room temperature properties of a high-entropy TaNbHfZrTi alloy. *J Alloys Compd* 509 (20):6043–6048. doi:[10.1016/j.jallcom.2011.02.171](https://doi.org/10.1016/j.jallcom.2011.02.171)
22. Senkov ON, Woodward CF (2011) Microstructure and properties of a refractory NbCrMo_{0.5}Ta_{0.5}TiZr alloy. *Mater Sci Eng A-Struct* 529:311–320. doi:[10.1016/j.msea.2011.09.033](https://doi.org/10.1016/j.msea.2011.09.033)
23. Singh S, Wanderka N, Murty BS, Glatzel U, Banhart J (2011) Decomposition in multi-component AlCoCrCuFeNi high-entropy alloy. *Acta Mater* 59(1):182–190. doi:[10.1016/j.actamat.2010.09.023](https://doi.org/10.1016/j.actamat.2010.09.023)
24. Jinhong P, Ye P, Hui Z, Lu Z (2012) Microstructure and properties of AlCrFeCuNi_x ($0.6 \leq x \leq 1.4$) high-entropy alloys. *Mater Sci Eng A* 534:228–233. doi:[10.1016/j.msea.2011.11.063](https://doi.org/10.1016/j.msea.2011.11.063)
25. Ma SG, Zhang Y (2012) Effect of Nb addition on the microstructure and properties of AlCoCrFeNi high-entropy alloy. *Mater Sci Eng A* 532:480–486. doi:[10.1016/j.msea.2011.10.110](https://doi.org/10.1016/j.msea.2011.10.110)
26. Pi JH, Pan Y, Zhang H, Zhang L (2012) Microstructure and properties of AlCrFeCuNi_x ($0.6 \leq x \leq 1.4$) high-entropy alloys. *Mater Sci Eng A-Struct* 534:228–233. doi:[10.1016/j.msea.2011.11.063](https://doi.org/10.1016/j.msea.2011.11.063)
27. Praveen S, Murty BS, Kottada RS (2012) Alloying behavior in multi-component AlCoCrCuFe and NiCoCrCuFe high entropy alloys. *Mater Sci Eng A* 534:83–89. doi:[10.1016/j.msea.2011.11.044](https://doi.org/10.1016/j.msea.2011.11.044)
28. Ren B, Liu ZX, Cai B, Wang MX, Shi L (2012) Aging behavior of a CuCr₂Fe₂NiMn high-entropy alloy. *Mater Des* 33:121–126. doi:[10.1016/j.matdes.2011.07.005](https://doi.org/10.1016/j.matdes.2011.07.005)
29. Tsao LC, Chen CS, Chu CP (2012) Age hardening reaction of the Al_{0.3}CrFe_{1.5}MnNi_{0.5} high entropy alloy. *Mater Des* 36:854–858. doi:[10.1016/j.matdes.2011.04.067](https://doi.org/10.1016/j.matdes.2011.04.067)

30. Wang W-R, Wang W-L, Wang S-C, Tsai Y-C, Lai C-H, Yeh J-W (2012) Effects of Al addition on the microstructure and mechanical property of $\text{Al}_x\text{CoCrFeNi}$ high-entropy alloys. *Intermetallics* 26:44–51. doi:[10.1016/j.intermet.2012.03.005](https://doi.org/10.1016/j.intermet.2012.03.005)
31. Zhang K, Fu Z (2012) Effects of annealing treatment on properties of CoCrFeNiTiAl_x multi-component alloys. *Intermetallics* 28:34–39. doi:[10.1016/j.intermet.2012.03.059](https://doi.org/10.1016/j.intermet.2012.03.059)
32. Zhuang YX, Liu WJ, Chen ZY, Xue HD, He JC (2012) Effect of elemental interaction on microstructure and mechanical properties of FeCoNiCuAl alloys. *Mater Sci Eng A* 556:395–399. doi:[10.1016/j.msea.2012.07.003](https://doi.org/10.1016/j.msea.2012.07.003)
33. Chen W, Fu Z, Fang S, Wang Y, Xiao H, Zhu D (2013) Processing, microstructure and properties of $\text{Al}_{0.6}\text{CoNiFeTi}_{0.4}$ high entropy alloy with nanoscale twins. *Mater Sci Eng A* 565:439–444. doi:[10.1016/j.msea.2012.12.072](https://doi.org/10.1016/j.msea.2012.12.072)
34. Chen W, Fu Z, Fang S, Xiao H, Zhu D (2013) Alloying behavior, microstructure and mechanical properties in a $\text{FeNiCrCo}_{0.3}\text{Al}_{0.7}$ high entropy alloy. *Mater Des* 51:854–860. doi:[10.1016/j.matdes.2013.04.061](https://doi.org/10.1016/j.matdes.2013.04.061)
35. Dong Y, Lu Y, Kong J, Zhang J, Li T (2013) Microstructure and mechanical properties of multi-component AlCrFeNiMo_x high-entropy alloys. *J Alloys Compd* 573:96–101. doi:[10.1016/j.jallcom.2013.03.253](https://doi.org/10.1016/j.jallcom.2013.03.253)
36. Fu Z, Chen W, Fang S, Zhang D, Xiao H, Zhu D (2013) Alloying behavior and deformation twinning in a $\text{CoNiFeCrAl}_{0.6}\text{Ti}_{0.4}$ high entropy alloy processed by spark plasma sintering. *J Alloys Compd* 553:316–323. doi:[10.1016/j.jallcom.2012.11.146](https://doi.org/10.1016/j.jallcom.2012.11.146)
37. Fu Z, Chen W, Xiao H, Zhou L, Zhu D, Yang S (2013) Fabrication and properties of nanocrystalline $\text{Co}_{0.5}\text{FeNiCrTi}_{0.5}$ high entropy alloy by MA–SPS technique. *Mater Des* 44:535–539. doi:[10.1016/j.matdes.2012.08.048](https://doi.org/10.1016/j.matdes.2012.08.048)
38. Guo S, Ng C, Liu CT (2013) Anomalous solidification microstructures in Co-free $\text{Al}_x\text{CrCuFeNi}_2$ high-entropy alloys. *J Alloys Compd* 557:77–81. doi:[10.1016/j.jallcom.2013.01.007](https://doi.org/10.1016/j.jallcom.2013.01.007)
39. Hsu C-Y, Juan C-C, Sheu T-S, Chen S-K, Yeh J-W (2013) Effect of aluminum content on microstructure and mechanical properties of $\text{Al}_x\text{CoCrFeMo}_{0.5}\text{Ni}$ high-entropy alloys. *JOM* 65(12):1840–1847. doi:[10.1007/s11837-013-0753-6](https://doi.org/10.1007/s11837-013-0753-6)
40. Lee C-F, Shun T-T (2013) Age hardening of the $\text{Al}_{0.5}\text{CoCrNiTi}_{0.5}$ high-entropy alloy. *Metall Mater Trans A* 45(1):191–195. doi:[10.1007/s11661-013-1931-4](https://doi.org/10.1007/s11661-013-1931-4)
41. Qiu X-W (2013) Microstructure and properties of AlCrFeNiCoCu high entropy alloy prepared by powder metallurgy. *J Alloys Compd* 555:246–249. doi:[10.1016/j.jallcom.2012.12.071](https://doi.org/10.1016/j.jallcom.2012.12.071)
42. Shun T-T, Chang L-Y, Shiu M-H (2013) Age-hardening of the $\text{CoCrFeNiMo}_{0.85}$ high-entropy alloy. *Mater Charact* 81:92–96. doi:[10.1016/j.matchar.2013.04.012](https://doi.org/10.1016/j.matchar.2013.04.012)
43. Tang Z, Gao MC, Diao H, Yang T, Liu J, Zuo T, Zhang Y, Lu Z, Cheng Y, Zhang Y, Dahmen KA, Liaw PK, Egami T (2013) Aluminum alloying effects on lattice types, microstructures, and mechanical behavior of high-entropy alloys systems. *JOM* 65(12):1848–1858. doi:[10.1007/s11837-013-0776-z](https://doi.org/10.1007/s11837-013-0776-z)
44. Dong Y, Zhou K, Lu Y, Gao X, Wang T, Li T (2014) Effect of vanadium addition on the microstructure and properties of AlCoCrFeNi high entropy alloy. *Mater Des* 57:67–72. doi:[10.1016/j.matdes.2013.12.048](https://doi.org/10.1016/j.matdes.2013.12.048)
45. Tang Z, Yuan T, Tsai C-W, Yeh J-W, Lundin CD, Liaw PK (2015) Fatigue behavior of a wrought $\text{Al}_{0.5}\text{CoCrCuFeNi}$ two-phase high-entropy alloy. *Acta Mater* 99:247–258, doi:<http://dx.doi.org/10.1016/j.actamat.2015.07.004>
46. Ji W, Fu Z, Wang W, Wang H, Zhang J, Wang Y, Zhang F (2014) Mechanical alloying synthesis and spark plasma sintering consolidation of CoCrFeNiAl high-entropy alloy. *J Alloys Compd* 589:61–66. doi:[10.1016/j.jallcom.2013.11.146](https://doi.org/10.1016/j.jallcom.2013.11.146)
47. Jiang L, Lu Y, Dong Y, Wang T, Cao Z, Li T (2014) Annealing effects on the microstructure and properties of bulk high-entropy $\text{CoCrFeNiTi}_{0.5}$ alloy casting ingot. *Intermetallics* 44:37–43. doi:[10.1016/j.intermet.2013.08.016](https://doi.org/10.1016/j.intermet.2013.08.016)

48. Ng C, Guo S, Luan J, Wang Q, Lu J, Shi S, Liu CT (2014) Phase stability and tensile properties of Co-free $\text{Al}_{0.5}\text{CrCuFeNi}_2$ high-entropy alloys. *J Alloys Compd* 584:530–537. doi:[10.1016/j.jallcom.2013.09.105](https://doi.org/10.1016/j.jallcom.2013.09.105)
49. Salishchev GA, Tikhonovsky MA, Shaysultanov DG, Stepanov ND, Kuznetsov AV, Kolodiy IV, Tortika AS, Senkov ON (2014) Effect of Mn and V on structure and mechanical properties of high-entropy alloys based on CoCrFeNi system. *J Alloys Compd* 591:11–21. doi:[10.1016/j.jallcom.2013.12.210](https://doi.org/10.1016/j.jallcom.2013.12.210)
50. Senkov ON, Senkova SV, Woodward C (2014) Effect of aluminum on the microstructure and properties of two refractory high-entropy alloys. *Acta Mater* 68:214–228. doi:[10.1016/j.actamat.2014.01.029](https://doi.org/10.1016/j.actamat.2014.01.029)
51. Wang W-R, Wang W-L, Yeh J-W (2014) Phases, microstructure and mechanical properties of $\text{Al}_x\text{CoCrFeNi}$ high-entropy alloys at elevated temperatures. *J Alloys Compd* 589:143–152. doi:[10.1016/j.jallcom.2013.11.084](https://doi.org/10.1016/j.jallcom.2013.11.084)
52. Zhang Y, Zuo TT, Tang Z, Gao MC, Dahmen KA, Liaw PK, Lu ZP (2014) Microstructures and properties of high-entropy alloys. *Prog Mater Sci* 61:1–93. doi:[10.1016/j.pmatsci.2013.10.001](https://doi.org/10.1016/j.pmatsci.2013.10.001)
53. Zhou YJ, Zhang Y, Wang YL, Chen GL (2007) Microstructure and compressive properties of multicomponent $\text{Al}_x(\text{TiVCrMnFeCoNiCu})_{100-x}$ high-entropy alloys. *Mater Sci Eng A-Struct* 454:260–265. doi:[10.1016/j.msea.2006.11.049](https://doi.org/10.1016/j.msea.2006.11.049)
54. Kuznetsov AV, Shaysultanov DG, Stepanov ND, Salishchev GA, Senkov ON (2012) Tensile properties of an AlCrCuNiFeCo high-entropy alloy in as-cast and wrought conditions. *Mater Sci Eng A* 533:107–118. doi:[10.1016/j.msea.2011.11.045](https://doi.org/10.1016/j.msea.2011.11.045)
55. Liu L, Zhu JB, Zhang C, Li JC, Jiang Q (2012) Microstructure and the properties of FeCoCuNiSn_x high entropy alloys. *Mater Sci Eng A* 548:64–68. doi:[10.1016/j.msea.2012.03.080](https://doi.org/10.1016/j.msea.2012.03.080)
56. Daoud HM, Manzoni A, Völkl R, Wanderka N, Glatzel U (2013) Microstructure and tensile behavior of $\text{Al}_{18}\text{Co}_{17}\text{Cr}_{17}\text{Cu}_8\text{Fe}_{17}\text{Ni}_{33}$ (at.%) high-entropy alloy. *JOM* 65(12):1805–1814. doi:[10.1007/s11837-013-0756-3](https://doi.org/10.1007/s11837-013-0756-3)
57. Gali A, George EP (2013) Tensile properties of high- and medium-entropy alloys. *Intermetallics* 39:74–78. doi:[10.1016/j.intermet.2013.03.018](https://doi.org/10.1016/j.intermet.2013.03.018)
58. Carroll R, Lee C, Tsai C-W, Yeh J-W, Antonaglia J, Brinkman BAW, LeBlanc M, Xie X, Chen S, Liaw PK, Dahmen KA (2015) Experiments and model for serration statistics in low-entropy, medium-entropy, and high-entropy alloys. *Sci Rep* 5:16997. doi:[10.1038/srep16997](https://doi.org/10.1038/srep16997)
59. Otto F, Dlouhý A, Somsen C, Bei H, Eggeler G, George EP (2013) The influences of temperature and microstructure on the tensile properties of a CoCrFeMnNi high-entropy alloy. *Acta Mater* 61(15):5743–5755. doi:[10.1016/j.actamat.2013.06.018](https://doi.org/10.1016/j.actamat.2013.06.018)
60. He JY, Liu WH, Wang H, Wu Y, Liu XJ, Nieh TG, Lu ZP (2014) Effects of Al addition on structural evolution and tensile properties of the FeCoNiCrMn high-entropy alloy system. *Acta Mater* 62:105–113. doi:[10.1016/j.actamat.2013.09.037](https://doi.org/10.1016/j.actamat.2013.09.037)
61. Yao MJ, Pradeep KG, Tasan CC, Raabe D (2014) A novel, single phase, non-equiautomic FeMnNiCoCr high-entropy alloy with exceptional phase stability and tensile ductility. *Scr Mater* 72–73:5–8. doi:[10.1016/j.scriptamat.2013.09.030](https://doi.org/10.1016/j.scriptamat.2013.09.030)
62. Cottrell AH, Bilby BA (1949) Dislocation theory of yielding and strain ageing of iron. *Proc Phys Soc Sect A* 62(1):49
63. Venkadesan S, Phaniraj C, Sivaprasad PV, Rodriguez P (1992) Activation energy for serrated flow in a $15\text{Cr}5\text{NiTi}$ -modified austenitic stainless steel. *Acta Metallurgica et Materialia* 40 (3):569–580, [http://dx.doi.org/10.1016/0956-7151\(92\)90406-5](http://dx.doi.org/10.1016/0956-7151(92)90406-5)
64. Clausen AH, Børvik T, Hopperstad OS, Benallal A (2004) Flow and fracture characteristics of aluminium alloy AA5083-H116 as function of strain rate, temperature and triaxiality. *Mater Sci Eng A* 364(1–2):260–272, <http://dx.doi.org/10.1016/j.msea.2003.08.027>
65. Shankar V, Valsan M, Rao KB, Mannan SL (2004) Effects of temperature and strain rate on tensile properties and activation energy for dynamic strain aging in alloy 625. *Metall Mater Trans A* 35(10):3129–3139. doi:[10.1007/s11661-004-0057-0](https://doi.org/10.1007/s11661-004-0057-0)

66. Dahmen KA, Ben-Zion Y, Uhl JT (2009) Micromechanical model for deformation in solids with universal predictions for stress–strain curves and slip avalanches. *Phys Rev Lett* 102(17):175501
67. Tsai C-W, Chen Y-L, Tsai M-H, Yeh J-W, Shun T-T, Chen S-K (2009) Deformation and annealing behaviors of high-entropy alloy Al_{0.5}CoCrCuFeNi. *J Alloys Compd Journal of Alloys and Compounds* 486(1–2):427–435, <http://dx.doi.org/10.1016/j.jallcom.2009.06.182>
68. Chan PY, Tsekenis G, Dantzig J, Dahmen KA, Goldenfeld N (2010) Plasticity and dislocation dynamics in a phase field crystal model. *Phys Rev Lett* 105(1):015502
69. Friedman N, Jennings AT, Tsekenis G, Kim J-Y, Tao M, Uhl JT, Greer JR, Dahmen KA (2012) Statistics of dislocation slip avalanches in nanosized single crystals show tuned critical behavior predicted by a simple mean field model. *Phys Rev Lett* 109(9):095507
70. Sakthivel T, Laha K, Nandagopal M, Chandravathi KS, Parameswaran P, Panneer Selvi S, Mathew MD, Mannan SK (2012) Effect of temperature and strain rate on serrated flow behaviour of Hastelloy X. *Mater Sci Eng A* 534:580–587, <http://dx.doi.org/10.1016/j.msea.2011.12.011>
71. Wu D, Chen RS, Han EH (2012) Serrated flow and tensile properties of a Mg–Gd–Zn alloy. *Mater Sci Eng A* 532:267–274, <http://dx.doi.org/10.1016/j.msea.2011.10.090>
72. Antonaglia J, Xie X, Tang Z, Tsai CW, Qiao JW, Zhang Y, Laktionova MO, Tabachnikova ED, Yeh JW, Senkov ON, Gao MC, Uhl JT, Liaw PK, Dahmen KA (2014) Temperature effects on deformation and serration behavior of high-entropy alloys (HEAs). *JOM* 66(10):2002–2008. doi:[10.1007/s11837-014-1130-9](https://doi.org/10.1007/s11837-014-1130-9)
73. Hemphill MA, Yuan T, Wang GY, Yeh JW, Tsai CW, Chuang A, Liaw PK (2012) Fatigue behavior of Al_{0.5}CoCrCuFeNi high entropy alloys. *Acta Mater* 60(16):5723–5734. doi:[10.1016/j.actamat.2012.06.046](https://doi.org/10.1016/j.actamat.2012.06.046)
74. Zhu C, Lu ZP, Nieh TG (2013) Incipient plasticity and dislocation nucleation of FeCoCrNiMn high-entropy alloy. *Acta Mater* 61(8):2993–3001. doi:[10.1016/j.actamat.2013.01.059](https://doi.org/10.1016/j.actamat.2013.01.059)
75. Sun Y, Zhao G, Wen X, Qiao J, Yang F (2014) Nanoindentation deformation of a bi-phase AlCrCuFeNi₂ alloy. *J Alloys Compd* 608:49–53. doi:[10.1016/j.jallcom.2014.04.127](https://doi.org/10.1016/j.jallcom.2014.04.127)
76. Wang Z, Guo S, Wang Q, Liu Z, Wang J, Yang Y, Liu CT (2014) Nanoindentation characterized initial creep behavior of a high-entropy-based alloy CoFeNi. *Intermetallics* 53:183–186. doi:[10.1016/j.intermet.2014.05.007](https://doi.org/10.1016/j.intermet.2014.05.007)
77. Senkov ON, Senkova SV, Miracle DB, Woodward C (2013) Mechanical properties of low-density, refractory multi-principal element alloys of the Cr–Nb–Ti–V–Zr system. *Mater Sci Eng A* 565:51–62. doi:[10.1016/j.msea.2012.12.018](https://doi.org/10.1016/j.msea.2012.12.018)
78. Senkov ON, Wilks GB, Scott JM, Miracle DB (2011) Mechanical properties of Nb₂₅Mo₂₅Ta₂₅W₂₅ and V₂₀Nb₂₀Mo₂₀Ta₂₀W₂₀ refractory high entropy alloys. *Intermetallics* 19(5):698–706. doi:[10.1016/j.intermet.2011.01.004](https://doi.org/10.1016/j.intermet.2011.01.004)
79. Gludovatz B, Hohenwarter A, Catoor D, Chang EH, George EP, Ritchie RO (2014) A fracture-resistant high-entropy alloy for cryogenic applications. *Science* 345(6201):1153–1158. doi:[10.1126/science.1254581](https://doi.org/10.1126/science.1254581)
80. Tabor D (1951) The hardness of metals. Oxford University Press, New York
81. Wen LH, Kou HC, Li JS, Chang H, Xue XY, Zhou L (2009) Effect of aging temperature on microstructure and properties of AlCoCrCuFeNi high-entropy alloy. *Intermetallics* 17(4):266–269. doi:[10.1016/j.intermet.2008.08.012](https://doi.org/10.1016/j.intermet.2008.08.012)
82. Wang F, Zhang Y, Chen G, Davies HA (2009) Tensile and compressive mechanical behavior of a CoCrCuFeNiAl_{0.5} high entropy alloy. *Int J Mod Phys B* 23(06n07):1254–1259
83. Gómez-Esparza CD, Ochoa-Gamboa RA, Estrada-Guel I, Cabañas-Moreno JG, Barajas-Villarruel JI, Arizmendi-Morquecho A, Herrera-Ramírez JM, Martínez-Sánchez R (2011) Microstructure of NiCoAlFeCuCr multi-component systems synthesized by mechanical alloying. *J Alloys Compd* 509:S279–S283. doi:[10.1016/j.jallcom.2010.12.105](https://doi.org/10.1016/j.jallcom.2010.12.105)

84. Tsai C-W, Chen Y-L, Tsai M-H, Yeh J-W, Shun T-T, Chen S-K (2009) Deformation and annealing behaviors of high-entropy alloy $\text{Al}_{0.5}\text{CoCrCuFeNi}$. *J Alloys Compd* 486 (1–2):427–435. doi:[10.1016/j.jallcom.2009.06.182](https://doi.org/10.1016/j.jallcom.2009.06.182)
85. Liu Z, Guo S, Liu X, Ye J, Yang Y, Wang X-L, Yang L, An K, Liu CT (2011) Micromechanical characterization of casting-induced inhomogeneity in an $\text{Al}_{0.8}\text{CoCrCuFeNi}$ high-entropy alloy. *Scr Mater* 64(9):868–871. doi:[10.1016/j.scriptamat.2011.01.020](https://doi.org/10.1016/j.scriptamat.2011.01.020)
86. Shaysultanov DG, Stepanov ND, Kuznetsov AV, Salishchev GA, Senkov ON (2013) Phase composition and superplastic behavior of a wrought AlCoCrCuFeNi high-entropy alloy. *JOM* 65(12):1815–1828. doi:[10.1007/s11837-013-0754-5](https://doi.org/10.1007/s11837-013-0754-5)
87. Ma SG, Zhang SF, Gao MC, Liaw PK, Zhang Y (2013) A successful synthesis of the $\text{CoCrFeNiAl}_{0.3}$ single-crystal, high-entropy alloy by Bridgman solidification. *JOM* 65 (12):1751–1758. doi:[10.1007/s11837-013-0733-x](https://doi.org/10.1007/s11837-013-0733-x)
88. Shun T-T, Du Y-C (2009) Microstructure and tensile behaviors of FCC $\text{Al}_{0.3}\text{CoCrFeNi}$ high entropy alloy. *J Alloys Compd* 479(1–2):157–160. doi:[10.1016/j.jallcom.2008.12.088](https://doi.org/10.1016/j.jallcom.2008.12.088)
89. Westbrook JH, Conrad H (1973) The science of hardness testing and its research applications. American society for metals, Metals Park
90. Wang FJ, Zhang Y, Chen GL (2009) Atomic packing efficiency and phase transition in a high entropy alloy. *J Alloys Compd* 478(1–2):321–324. doi:[10.1016/j.jallcom.2008.11.059](https://doi.org/10.1016/j.jallcom.2008.11.059)
91. Zhang KB, Fu ZY, Zhang JY, Wang WM, Wang H, Wang YC, Zhang QJ, Shi J (2009) Microstructure and mechanical properties of CoCrFeNiTiAl_x high-entropy alloys. *Mater Sci Eng A* 508(1–2):214–219. doi:[10.1016/j.msea.2008.12.053](https://doi.org/10.1016/j.msea.2008.12.053)
92. Yang X, Zhang Y, Liaw PK (2012) Microstructure and compressive properties of NbTiVTaAl_x high entropy alloys. *Procedia Eng* 36:292–298. doi:[10.1016/j.proeng.2012.03.043](https://doi.org/10.1016/j.proeng.2012.03.043)
93. Zhang KB, Fu ZY (2012) Effects of annealing treatment on properties of CoCrFeNiTiAl_x multi-component alloys. *Intermetallics* 28:34–39. doi:[10.1016/j.intermet.2012.03.059](https://doi.org/10.1016/j.intermet.2012.03.059)
94. Zhang Y, Zuo TT, Cheng YQ, Liaw PK (2013) High-entropy alloys with high saturation magnetization, electrical resistivity, and malleability. *Sci Rep* 3:1455. doi:[10.1038/srep01455](https://doi.org/10.1038/srep01455)
95. Wang XF, Zhang Y, Qiao Y, Chen GL (2007) Novel microstructure and properties of multicomponent CoCrCuFeNiTi_x alloys. *Intermetallics* 15(3):357–362. doi:[10.1016/j.intermet.2006.08.005](https://doi.org/10.1016/j.intermet.2006.08.005)
96. Zhou YJ, Zhang Y, Wang YL, Chen GL (2007) Solid solution alloys of AlCoCrFeNiTi_x with excellent room-temperature mechanical properties. *Appl Phys Lett* 90(18):181904, <http://dx.doi.org/10.1063/1.2734517>
97. Shun TT, Chang LY, Shiu MH (2012) Microstructures and mechanical properties of multiprincipal component CoCrFeNiTi_x alloys. *Mater Sci Eng A-Struct* 556:170–174. doi:[10.1016/j.msea.2012.06.075](https://doi.org/10.1016/j.msea.2012.06.075)
98. Greer JR, De Hosson JTM (2011) Plasticity in small-sized metallic systems: intrinsic versus extrinsic size effect. *Prog Mater Sci* 56(6):654–724, doi:<http://dx.doi.org/10.1016/j.pmatsci.2011.01.005>
99. Hu ZH, Zhan YZ, Zhang GH, She J, Li CH (2010) Effect of rare earth Y addition on the microstructure and mechanical properties of high entropy AlCoCrCuNiTi alloys. *Mater Des* 31(3):1599–1602. doi:[10.1016/j.matdes.2009.09.016](https://doi.org/10.1016/j.matdes.2009.09.016)
100. Zhu JM, Fu HM, Zhang HF, Wang AM, Li H, Hu ZQ (2010) Synthesis and properties of multiprincipal component AlCoCrFeNiSi_x alloys. *Mater Sci Eng A* 527(27–28):7210–7214. doi:[10.1016/j.msea.2010.07.049](https://doi.org/10.1016/j.msea.2010.07.049)
101. Zhu JM, Zhang HF, Fu HM, Wang AM, Li H, Hu ZQ (2010) Microstructures and compressive properties of multicomponent AlCoCrCuFeNiMo_x alloys. *J Alloys Compd* 497 (1–2):52–56. doi:[10.1016/j.jallcom.2010.03.074](https://doi.org/10.1016/j.jallcom.2010.03.074)
102. Zhu JM, Fu HM, Zhang HF, Wang AM, Li H, Hu ZQ (2011) Microstructure and compressive properties of multiprincipal component AlCoCrFeNiC_x alloys. *J Alloys Compd* 509 (8):3476–3480. doi:[10.1016/j.jallcom.2010.10.047](https://doi.org/10.1016/j.jallcom.2010.10.047)

103. Zhu JM, Zhang HF, Fu HM, Wang AM, Li H, Hu ZQ (2010) Microstructures and compressive properties of multicomponent AlCoCrCuFeNiMo_x alloys. *J Alloys Compd* 497 (1–2):52–56. doi:[10.1016/j.jallcom.2010.03.074](https://doi.org/10.1016/j.jallcom.2010.03.074)
104. Zhang Y, Yang X, Liaw PK (2012) Alloy design and properties optimization of high-entropy alloys. *JOM* 64(7):830–838. doi:[10.1007/s11837-012-0366-5](https://doi.org/10.1007/s11837-012-0366-5)
105. Li AM, Ma D, Zheng QF (2014) Effect of Cr on microstructure and properties of a series of AlTiCr_xFeCoNiCu high-entropy alloys. *J Mater Eng Perform* 23(4):1197–1203. doi:[10.1007/s11665-014-0871-5](https://doi.org/10.1007/s11665-014-0871-5)
106. Laktionova MO, Tabachnikova ED, Tang Z, Antonaglia J, Dahmen KA, Liaw PK (2012) Low temperature mechanical behavior of the Al_{0.5}CoCrCuFeNi high-entropy alloy. *Materials Science and Technology*, Pittsburgh
107. Laktionova MA, Tabachnikova ED, Tang Z, Liaw PK (2013) Mechanical properties of the high-entropy alloy Al_{0.5}CoCrCuFeNi at temperatures of 4.2–300 K. *Low Temp Phys* 39 (7):630–632, <http://dx.doi.org/10.1063/1.4813688>
108. Senkov ON, Scott JM, Senkova SV, Meisenkothen F, Miracle DB, Woodward CF (2012) Microstructure and elevated temperature properties of a refractory TaNbHfZrTi alloy. *J Mater Sci* 47(9):4062–4074. doi:[10.1007/s10853-012-6260-2](https://doi.org/10.1007/s10853-012-6260-2)
109. Senkov ON, Senkova SV, Miracle DB, Woodward C (2013) Mechanical properties of low-density, refractory multi-principal element alloys of the Cr-Nb-Ti-V-Zr system. *Mater Sci Eng A-Struct* 565:51–62. doi:[10.1016/j.msea.2012.12.018](https://doi.org/10.1016/j.msea.2012.12.018)
110. Qiao JW, Ma SG, Huang EW, Chuang CP, Liaw PK, Zhang Y (2011) Microstructural characteristics and mechanical behaviors of AlCoCrFeNi high-entropy alloys at ambient and cryogenic temperatures. In: Wang RM, Wu Y, Wu XF (eds) *Materials science forum*. Elsevier, Philadelphia, PA. pp 419–425. doi:[10.4028/www.scientific.net/MSF.688.419](https://doi.org/10.4028/www.scientific.net/MSF.688.419)
111. Wang FJ, Zhang Y, Chen GL, Davies HA (2009) Cooling rate and size effect on the microstructure and mechanical properties of AlCoCrFeNi high entropy alloy. *J Eng Mater Technol* 131(3):034501. doi:[10.1115/1.3120387](https://doi.org/10.1115/1.3120387)
112. Sheng HF, Gong M, Peng LM (2013) Microstructural characterization and mechanical properties of an Al_{0.5}CoCrFeCuNi high-entropy alloy in as-cast and heat-treated/quenched conditions. *Mater Sci Eng A* 567:14–20. doi:[10.1016/j.msea.2013.01.006](https://doi.org/10.1016/j.msea.2013.01.006)
113. Zhuang YX, Xue HD, Chen ZY, Hu ZY, He JC (2013) Effect of annealing treatment on microstructures and mechanical properties of FeCoNiCuAl high entropy alloys. *Mater Sci Eng A* 572:30–35. doi:[10.1016/j.msea.2013.01.081](https://doi.org/10.1016/j.msea.2013.01.081)
114. Liu FX, Liaw PK, Wang GY, Chiang CL, Smith DA, Rack PD, Chu JP, Buchanan RA (2006) Specimen-geometry effects on mechanical behavior of metallic glasses. *Intermetallics* 14(8–9):1014–1018, doi:<http://dx.doi.org/10.1016/j.intermet.2006.01.043>
115. Wang YP, Li BS, Ren MX, Yang C, Fu HZ (2008) Microstructure and compressive properties of AlCrFeCoNi high entropy alloy. *Mater Sci Eng A-Struct* 491(1–2):154–158. doi:[10.1016/j.msea.2008.01.064](https://doi.org/10.1016/j.msea.2008.01.064)
116. Wang YP, Li BS, Fu HZ (2009) Solid solution or intermetallics in a high-entropy alloy. *Adv Eng Mater* 11(8):641–644. doi:[10.1002/adem.200900057](https://doi.org/10.1002/adem.200900057)
117. Li BS, Wang YR, Ren MX, Yang C, Fu HZ (2008) Effects of Mn, Ti and V on the microstructure and properties of AlCrFeCoNiCu high entropy alloy. *Mater Sci Eng A-Struct* 498(1–2):482–486. doi:[10.1016/j.msea.2008.08.025](https://doi.org/10.1016/j.msea.2008.08.025)
118. Tawancy HM, Ul-Hamid A, Abbas NM (2004) *Practical engineering failure analysis*. Marcel Dekker, New York
119. Gu XJ, Poon SJ, Shiflet GJ, Lewandowski JJ (2010) Compressive plasticity and toughness of a Ti-based bulk metallic glass. *Acta Mater* 58(5):1708–1720. doi:[10.1016/j.actamat.2009.11.013](https://doi.org/10.1016/j.actamat.2009.11.013)
120. Han Z, Wu WF, Li Y, Wei YJ, Gao HJ (2009) An instability index of shear band for plasticity in metallic glasses. *Acta Mater* 57(5):1367–1372, <http://dx.doi.org/10.1016/j.actamat.2008.11.018>

121. Ng KS, Ngan AHW (2008) Stochastic nature of plasticity of aluminum micro-pillars. *Acta Mater* 56(8):1712–1720, <http://dx.doi.org/10.1016/j.actamat.2007.12.016>
122. Uchic MD, Dimiduk DM, Florando JN, Nix WD (2004) Sample dimensions influence strength and crystal plasticity. *Science* 305(5686):986–989. doi:[10.1126/science.1098993](https://doi.org/10.1126/science.1098993)
123. Dimiduk DM, Uchic MD, Parthasarathy TA (2005) Size-affected single-slip behavior of pure nickel microcrystals. *Acta Mater* 53(15):4065–4077, <http://dx.doi.org/10.1016/j.actamat.2005.05.023>
124. Shade PA, Wheeler R, Choi YS, Uchic MD, Dimiduk DM, Fraser HL (2009) A combined experimental and simulation study to examine lateral constraint effects on microcompression of single-slip oriented single crystals. *Acta Mater* 57(15):4580–4587, <http://dx.doi.org/10.1016/j.actamat.2009.06.029>
125. Dimiduk DM, Woodward C, LeSar R, Uchic MD (2006) Scale-free intermittent flow in crystal plasticity. *Science* 312(5777):1188–1190. doi:[10.1126/science.1123889](https://doi.org/10.1126/science.1123889)
126. Greer JR, Oliver WC, Nix WD (2005) Size dependence of mechanical properties of gold at the micron scale in the absence of strain gradients. *Acta Mater* 53(6):1821–1830, <http://dx.doi.org/10.1016/j.actamat.2004.12.031>
127. Zou Y, Maiti S, Steurer W, Spolenak R (2014) Size-dependent plasticity in an Nb₂₅Mo₂₅Ta₂₅W₂₅ refractory high-entropy alloy. *Acta Mater* 65:85–97. doi:[10.1016/j.actamat.2013.11.049](https://doi.org/10.1016/j.actamat.2013.11.049)
128. Liu ZY, Guo S, Liu XJ, Ye JC, Yang Y, Wang XL, Yang L, An K, Liu CT (2011) Micromechanical characterization of casting-induced inhomogeneity in an Al_{0.8}CoCrCuFeNi high-entropy alloy. *Scr Mater* 64(9):868–871. doi:[10.1016/j.scriptamat.2011.01.020](https://doi.org/10.1016/j.scriptamat.2011.01.020)
129. Wu Z, Bei H, Pharr GM, George EP (2014) Temperature dependence of the mechanical properties of equiatomic solid solution alloys with face-centered cubic crystal structures. *Acta Mater* 81:428–441. doi:[10.1016/j.actamat.2014.08.026](https://doi.org/10.1016/j.actamat.2014.08.026)
130. Guo W, Dmowski W, Noh JY, Rack P, Liaw PK, Egami T (2013) Local atomic structure of a high-entropy alloy: an x-ray and neutron scattering study. *Metall Mater Trans A* 44A (5):1994–1997. doi:[10.1007/s11661-012-1474-0](https://doi.org/10.1007/s11661-012-1474-0)
131. Wu Y, Liu WH, Wang XL, Ma D, Stoica AD, Nieh TG, He ZB, Lu ZP (2014) In-situ neutron diffraction study of deformation behavior of a multi-component high-entropy alloy. *Appl Phys Lett* 104(5):051910. doi:[10.1063/1.4863748](https://doi.org/10.1063/1.4863748)
132. Huang EW, Yu D, Yeh J-W, Lee C, An K, Tu S-Y (2015) A study of lattice elasticity from low entropy metals to medium and high entropy alloys. *Scripta Mater* 101:32–35, <http://dx.doi.org/10.1016/j.scriptamat.2015.01.011>
133. Miguel MC, Vespignani A, Zapperi S, Weiss J, Grasso J-R (2001) Intermittent dislocation flow in viscoplastic deformation. *Nature* 410(6829):667–671, http://www.nature.com/nature/journal/v410/n6829/supplinfo/410667a0_S1.html
134. Zaiser M, Marmo B, Moretti P (2005) The yielding transition in crystal plasticity – discrete dislocations and continuum models. Paper presented at the International Conference on Statistical Mechanics of Plasticity and Related Instabilities, Indian Institute of Science, Bangalore, India
135. Miguel MC, Vespignani A, Zapperi S, Weiss J, Grasso J-R (2001) Complexity in dislocation dynamics: model. *Mater Sci Eng A* 309–310:324–327
136. Laurson L, Alava MJ (2006) 1/f noise and avalanche scaling in plastic deformation. *Phys Rev E Stat Nonlin Soft Matter Phys* 74(6 Pt 2):066106
137. Csikor FF, Motz C, Weygand D, Zaiser M, Zapperi S (2007) Dislocation avalanches, strain bursts, and the problem of plastic forming at the micrometer scale. *Science* 318:251–254
138. Ispanovity PD, Groma I, Gyorgyi G, Csikor FF, Weygand D (2010) Submicron plasticity: yield stress, dislocation avalanches, and velocity distribution. *Phys Rev Lett* 105(8):085503
139. Tsekenis G, Goldenfeld N, Dahmen KA (2011) Dislocations jam at any density. *Phys Rev Lett* 106(10):105501
140. Tsekenis G, Uhl J, Goldenfeld N, Dahmen K (2013) Determination of the universality class of crystal plasticity. *EPL (Europhysics Letters)* 101(3):36003

141. Koslowski M (2007) Scaling laws in plastic deformation. *Philos Mag* 87(8–9):1175–1184. doi:[10.1080/14786430600854962](https://doi.org/10.1080/14786430600854962)
142. Dahmen K, Ertaş D, Ben-Zion Y (1998) Gutenberg-Richter and characteristic earthquake behavior in SimpleMmean-field models of heterogeneous faults. *Phys Rev E Stat Nonlin Soft Matter Phys* 58(2):1494–1501
143. Sethna JP, Dahmen KA, Myers CR (2001) Crackling noise. *Nature* 410(6825):242–250
144. Meeker WQ, Escobar LA (1998) Statistical methods for reliability data, vol 314. Wiley, New York
145. Lai CH, Lin SJ, Yeh JW, Davison A (2006) Effect of substrate bias on the structure and properties of multi-element (AlCrTaTiZr)N coatings. *J Phys D-Appl Phys* 39(21):4628–4633. doi:[10.1088/0022-3727/39/21/019](https://doi.org/10.1088/0022-3727/39/21/019)
146. Chang HW, Huang PK, Davison A, Yeh JW, Tsau CH, Yang CC (2008) Nitride films deposited from an equimolar Al-Cr-Mo-Si-Ti alloy target by reactive direct current magnetron sputtering. *Thin Solid Films* 516(18):6402–6408. doi:[10.1016/j.tsf.2008.01.019](https://doi.org/10.1016/j.tsf.2008.01.019)
147. Chang HW, Huang PK, Yeh JW, Davison A, Tsau CH, Yang CC (2008) Influence of substrate bias, deposition temperature and post-deposition annealing on the structure and properties of multi-principal-component (AlCrMoSiTi)N coatings. *Surf Coat Technol* 202(14):3360–3366. doi:[10.1016/j.surfcoat.2007.12.014](https://doi.org/10.1016/j.surfcoat.2007.12.014)
148. Huang PK, Yeh JW (2009) Effects of substrate temperature and post-annealing on microstructure and properties of (AlCrNbSiTiV)N coatings. *Thin Solid Films* 518(1):180–184. doi:[10.1016/j.tsf.2009.06.020](https://doi.org/10.1016/j.tsf.2009.06.020)
149. Lin M-I, Tsai M-H, Shen W-J, Yeh J-W (2010) Evolution of structure and properties of multi-component (AlCrTaTiZr)O_x films. *Thin Solid Films* 518(10):2732–2737. doi:[10.1016/j.tsf.2009.10.142](https://doi.org/10.1016/j.tsf.2009.10.142)
150. Chang ZC, Liang SC, Han S (2011) Effect of microstructure on the nanomechanical properties of TiVCrZrAl nitride films deposited by magnetron sputtering. *Nucl Instrum Meth B* 269(18):1973–1976. doi:[10.1016/j.nimb.2011.05.027](https://doi.org/10.1016/j.nimb.2011.05.027)
151. Feng XG, Tang GZ, Gu L, Ma XX, Sun MR, Wang LQ (2012) Preparation and characterization of TaNbTiW multi-element alloy films. *Appl Surf Sci* 261:447–453. doi:[10.1016/j.apsusc.2012.08.030](https://doi.org/10.1016/j.apsusc.2012.08.030)
152. Wu ZF, Wang XD, Cao QP, Zhao GH, Li JX, Zhang DX, Zhu JJ, Jiang JZ (2014) Microstructure characterization of Al_xCoCrCuFeNi (x = 0 and 2.5) high-entropy alloy films. *J Alloys Compd* 609:137–142. doi:[10.1016/j.jallcom.2014.04.094](https://doi.org/10.1016/j.jallcom.2014.04.094)
153. Cheng JB, Liang XB, Wang ZH, Xu BS (2013) Formation and mechanical properties of CoNiCuFeCr high-entropy alloys coatings prepared by plasma transferred arc cladding process. *Plasma Chem Plasma Proc* 33(5):979–992. doi:[10.1007/s11090-013-9469-1](https://doi.org/10.1007/s11090-013-9469-1)
154. Hertz H (1896) Miscellaneous papers. Macmillan, New York
155. Johnson KL, Johnson KL (1985) Contact mechanics. Cambridge University Press, New York
156. Mason J, Lund A, Schuh C (2006) Determining the activation energy and volume for the onset of plasticity during nanoindentation. *Phys Rev B* 73(5):054102
157. Wu Z, Bei H, Otto F, Pharr GM, George EP (2014) Recovery, recrystallization, grain growth and phase stability of a family of FCC-structured multi-component equiatomic solid solution alloys. *Intermetallics* 46:131–140. doi:[10.1016/j.intermet.2013.10.024](https://doi.org/10.1016/j.intermet.2013.10.024)
158. Li H, Ngan AHW (2004) Size effects of nanoindentation creep. *J Mater Res* 19(2):513–522. doi:[10.1557/jmr.2004.19.2.513](https://doi.org/10.1557/jmr.2004.19.2.513)
159. Santodonato LJ, Zhang Y, Feygenson M, Parish CM, Gao MC, Weber RJ, Neufeind JC, Tang Z, Liaw PK (2015) Deviation from high-entropy configurations in the atomic distributions of a multi-principal-element alloy. *Nat Commun* 6:5964. doi:[10.1038/ncomms6964](https://doi.org/10.1038/ncomms6964)
160. Gao MC, Yeh JW, Liaw PK, Zhang Y (eds) (2016) High-entropy alloys: fundamentals and applications, 1st edn. Springer International Publishing, Cham, Switzerland. doi:[10.1007/978-3-319-27013-5](https://doi.org/10.1007/978-3-319-27013-5)

Chapter 7

Functional Properties

Jien-Wei Yeh, Swe-Kai Chen, Han C. Shih, Yong Zhang, and Ting Ting Zuo

Abstract This chapter reviews various functional properties of HEAs: electrical properties (including superconducting), magnetic properties, electrochemical properties, and hydrogen storage properties. Interesting phenomena and potentially promising properties better than those of conventional alloys have been observed. These indicate that HEAs provide attractive functional properties to be explored and developed from both academic and application-oriented viewpoints. In this chapter, compositions, process parameters, and microstructure will be correlated with functional properties to give a better understanding.

Keywords Electrical property • Magnetic property • Electrochemical property • Hydrogen storage property • High-entropy alloys (HEAs)

7.1 Introduction

More and more researches are conducted on functional properties of HEAs and HE-related materials because there are many promising possibilities for academic studies and industrial applications. The functional properties include electrical,

J.-W. Yeh (✉)

Department of Materials Science and Engineering, National Tsing Hua University,
Hsinchu, Taiwan 30013, Republic of China

e-mail: jwye@mx.nthu.edu.tw

S.-K. Chen

Center for Nanotechnology, Materials Science, and Microsystems,
National Tsing Hua University, Hsinchu, Taiwan 30013, Republic of China
e-mail: skchen@mx.nthu.edu.tw

H.C. Shih

Institute of Nanomaterials, Chinese Culture University, Taipei,
Taiwan 11114, Republic of China
e-mail: hchih@mx.nthu.edu.tw

Y. Zhang • T.T. Zuo

State Key Laboratory for Advanced Metals and Materials, University of Science
and Technology Beijing, Beijing 100083, People's Republic of China
e-mail: drzhangy@ustb.edu.cn; zuott1986.520@163.com

thermal, magnetic, electrochemical, hydrogen storage, diffusion barrier, irradiation resistance, and catalytic properties. Besides these, more functional properties could be also developed to enhance practical performances such as biomedical, antibacteria, electromagnetic interference (EMI) shielding, anti-fingerprint, anti-sticky, hydrophilic, and hydrophobic properties. As discussed on “cocktail effect” in Sect. 3.1.4, it is known that the overall properties of HEAs are from the overall contribution of the constituent phases by the effect of phase shape, phase distribution, phase boundaries, and properties of each phase. Because each phase is a multielement solid solution and can be regarded as atomic-scale composites, its properties not only come from the basic properties of elements by the mixture rule but also from the mutual interactions among all the elements and from the severe lattice distortion. The most distinct feature not pronounced in conventional alloys is the “severe lattice distortion” effect since all atoms are solutes and have their local lattice distortion in the whole-solute matrix as discussed in Sects. 3.1.2 and 3.3. This effect not only influences the plastic deformation and annealing behaviors, but also the behaviors of electrons, phonons, dipoles, and incident beams. Therefore, the additional special properties are mainly originated from the same lattice distortion although the extent of their influences and the degree of equations are different from each other due to their different mechanisms interacted with lattice distortion. The mechanisms or theoretical models are thus scientifically interesting topics to be revealed and to be utilized in the future. This chapter selects several important functional properties to review in consideration of their breadth and popularity. These reviews might provide a good basis for future research and development.

7.2 Electrical Properties of HEAs

7.2.1 Normal Conducting Behaviors

The first systematic study on electrical properties of HEAs was conducted on the $\text{Al}_x\text{CoCrFeNi}$ (denoted as H- x herein below) alloys with the variation of Al content ($0 \leq x \leq 2$) [1]. The samples were prepared with arc melting and subsequent homogenization treatment at 1100 °C for 24 h. Figure 7.1 shows the electrical resistivity in the temperature range from 4 to 400 K and also the effect of Al content on electrical conductivity [1]. The electrical resistivity of each alloy is approximately a linear function of temperature with a small positive slope in the range of 298–400 K except H-1 ($x=1$) alloy has a larger slope. Figure 7.1b shows the electrical resistivity of three homogenized alloys with $x=1$, 1.5, and 2 (H-1, H-2, and H-3) in the range of 4–400 K. The curves in 4–298 K and those in 298–400 K were measured with two apparatus. In the temperature range of 100–298 K, the three alloys also display a linear increase of resistivity with temperature. However, their slopes might not be the same as that in 298–400 K. The resistivity levels are generally higher as compared to that ($1 \sim 100 \mu\Omega \text{ cm}$) of conventional alloys.

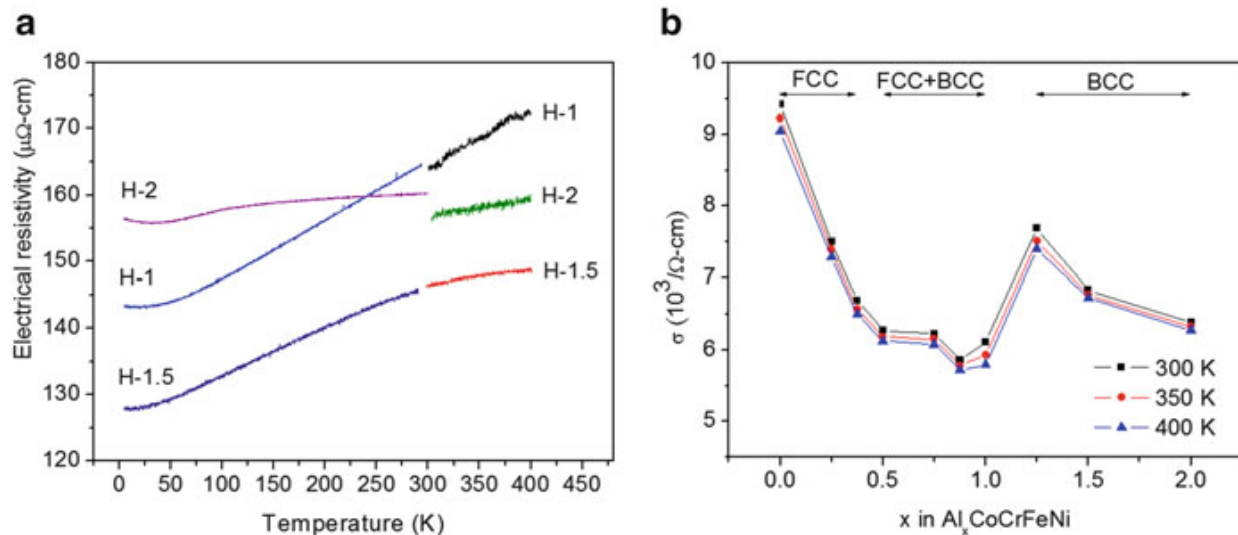


Fig. 7.1 (a) Electrical resistivity of three homogenized H-x alloys with $x = 1, 1.5$, and 2 (H-1, H-1.5, and H-2) in the range of 4–400 K (the curves in 4–298 K and those in 298–400 K were measured with two apparatus), and (b) electrical conductivity as a function of x at 300, 350, and 400 K [1]

The high-level electrical resistivity is mainly attributable to the severe lattice distortion in the whole-solute matrix of constituent phases since lattice distortion could cause intense electron scattering and reduce the free electron mobility. In each phase, the structure could be regarded as a pseudo-unitary lattice (PUL) with highly concentrated point defects or distorted lattice sites [2]. Furthermore, the thermal vibration effect causing electron scattering becomes relatively smaller as compared with severe lattice distortion effect. This makes the alloy to have a low temperature coefficient of resistivity (TCR). The variation of electrical conductivity with x can be divided into three distinct ranges which clearly relate with constituent phases: single face-centered cubic (FCC) in $0 \leq x \leq 0.375$, single body-centered cubic (BCC) in $1.25 \leq x \leq 2$, and duplex FCC/BCC in $0.5 \leq x \leq 1$. The electrical conductivity decreases with increasing x in single-phase FCC or single-phase BCC region and has a lower level in the duplex FCC/BCC phase region. These could be explained because larger additions of large-sized Al atoms would cause more severe lattice distortion and electron scattering no matter it is FCC or BCC. Besides, the interface between FCC and BCC phases would increase free electron scattering when electrons pass through interface. As for the higher conductivity level of BCC phase than FCC phase compared by extrapolating the curve of FCC to higher Al content, the reason is that the more open BCC structure has larger mean free path for electron than the close-packed FCC structure [2].

The resistivity at 4.2 K (ρ_0), resistivity at 300 K (ρ_{300}), residual resistivity ratio (RRR, ρ_0/ρ_{300}), and temperature coefficient of resistivity (TCR, $\rho_{300} - \rho_{150})/\rho_{150}$ of as-cast $\text{Al}_{0.2}\text{CoCrFeNi}$ alloys (C- x) and 75 %-cold-rolled $\text{Al}_{0.875}\text{CoCrFeNi}$ alloys (D- x) were reported and also compared [3]. The ranges of the ρ_0 values of alloys C- x , H- x , and D- x are 111.06–196.49, 93.78–162.77, and 120.48–162.05 $\mu\Omega\text{ cm}$, respectively. It suggests that homogenization could lower the resistivity but deformation increases the resistivity, even higher than that of as-cast state. The former

would relate with the significant elimination of phase boundaries by homogenization, whereas the latter relates with increased dislocations and/or twins by deformation. The RRR values range from 1.03 to 1.27. In addition, the alloys generally have low TCR, and the H-2 alloy has the lowest TCR, 82.5 ppm/K. All these results show the low-temperature sensitivity of HEAs, which have been explained above. The resistivity versus temperature curve was also fitted by $\rho(T) = \rho_0 + A \ln(T) + BT^2 + CT^3 + DT$, where ρ_0 stands for the residual resistivity at 4.2 K. Fitted coefficients A , B , C , and D are coefficients of Kondo-like, magnetic, low-temperature and high-temperature phonon terms, respectively. In 4.2–66 K, the fitting could be simplified by using $\rho(T) = \rho_0 + A \ln(T) + BT^2 + CT^3$, whereas in 100–300 K the fitting could be well with $\rho(T) = \rho_0 + A \ln(T) + BT^2 + DT$. The variations of these coefficients were discussed with their physical meaning [3]. The Hall effect measurements were also done in alloys H-0.25 (FCC), H-0.50 (FCC + BCC), H-0.75 (FCC + BCC), H-1.00 (FCC + BCC), and H-1.25 (BCC) [3]. The results demonstrate that carrier density in H-x alloys is around $10^{22–23} \text{ cm}^{-3}$ which is similar to that in conventional alloys. However, the H-x alloys has lower carrier mobility, $0.40–2.61 \text{ cm}^2 \text{ V}^{-1} \text{ s}^{-1}$, than conventional alloys. This finding is very important to illustrate that the high resistivity is mainly due to severe lattice distortion in HEAs than conventional alloys.

To further reduce TCR, Chen et al. modified H-2 alloy, i.e., Al₂CoCrFeNi, by tuning Al content and found that Al_{2.08}CoCrFeNi alloy has a very low TCR [4]. The crystal structure of this alloy is a mixture of B2 (ordered BCC) and BCC solid solutions. The values of electrical resistivity of as-cast Al_{2.08}CoCrFeNi at 4.2 and 300 K are 117.24 and 119.90 $\mu\Omega \text{ cm}$, respectively, and only differ by 2.66 $\mu\Omega \text{ cm}$, as shown in Fig. 7.2a. Its RRR is 1.02. The wide-range averaged TCR of as-cast Al_{2.08}CoCrFeNi from 4.2 to 360 K is 72 ppm/K. This is quite unusual as compared to traditional low-TCR alloys (<100 ppm/K) that have low TCR in a narrow range of temperatures, e.g., some 50 K or so, such as the commercial Manganin shown in Fig. 7.2b. Except for the 4.2–50 K range where there is a Kondo-like phenomenon,

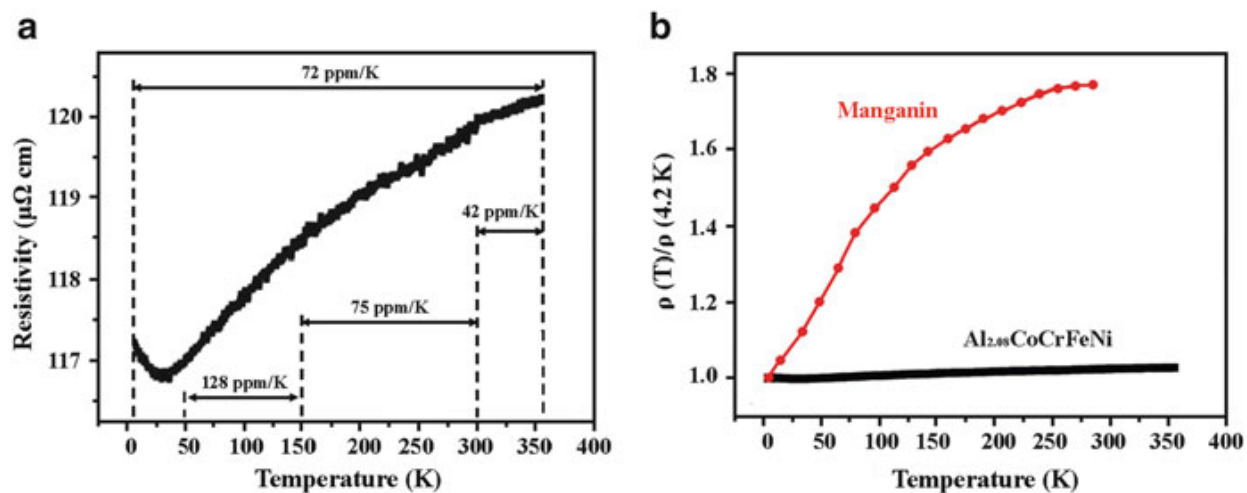


Fig. 7.2 (a) $\rho(T)$ curve of Al_{2.08}CoCrFeNi showing TCR in different temperature regions (a minimum at about 30 K showing a Kondo-like effect). (b) normalized $\rho(T)/\rho(4.2 \text{ K})$, curve for Manganin and Al_{2.08}CoCrFeNi (Inserted enlarged curve for the latter alloy [4])

the values of TCR in 50–150, 150–300, and 300–360 K are 128, 75, and 42 ppm/K, respectively. It is clear that TCR decreases as temperature increases. From the curve shape, it is reasonable to predict that the TCR value may be even lower at temperatures higher than 360 K. From the above data and unique features of the whole-solute matrix with severe lattice distortion, many HEAs and their coatings can be expected to have low TCR or extremely low TCR. Thus, potential applications of HEAs in precision resistors in broad temperature range are plentiful by nature.

In summary, current understanding of the electrical properties of HEAs is mainly based on the $\text{Al}_x\text{CoCrFeNi}$ alloys. These alloys have resistivities ranging from 120 to 175 $\mu\Omega \text{ cm}$ between 4.2 and 400 K. Another example is the $\text{FeCoNi}(\text{AlSi})_x$ alloys, whose resistivities are between 70 and 270 $\mu\Omega \text{ cm}$ [5]. As pointed out in a previous review [6], these values are higher than that of many conventional alloys. The resistivities of the $\text{Al}_x\text{CoCrFeNi}$ alloys increase with temperature, but the TCR is pretty small. Some alloys can have very small TCR values over a wide temperature range.

7.2.2 Superconducting Behaviors

Cheap and accessible superconductors with a high critical temperature (T_c), a high critical current density (J_c), and critical magnetic field (H_c) will bring a large revolution in many aspects and promote our civilization level. A traditional alloy or the material concept in composition seems to be difficult to get a breakthrough of T_c either in metal systems and nonmetallic systems. As a result, HEAs and HE-related materials have been investigated to find the possibility of better superconductors, such as room-temperature superconductors.

Chen et al. have explored the possibility on HEAs since 2011 [7–9] and have found the superconducting behavior is also possible in HEAs, and the critical temperature T_c could be higher than that predicted by the rule of mixture. Moreover, the results suggest that the T_c is not necessarily reduced by the whole-solute matrix. Table 7.1 lists the T_c values of as-cast and as-homogenized equal-atomic NbTaTiZr , GeNbTaTiZr , HfNbTaTiZr , NbSiTaTiVZr , GeNbSiTaTiZr , and GeNbTaTiVZr [7–9]. For the as-cast samples, H_{c1} is within 100–400 Oe, while H_{c2} exceeds 1 T, except GeNbTaTiVZr which shows a small H_{c2} of 6 kOe [7]. For the as-homogenized samples, H_{c1} varies from 80 to 660 Oe, while H_{c2} ranges from 1.50 to 3.29 T. J_c is in the range of 10^4 – 10^5 A/cm^2 [8]. In addition, $\text{Nb}_{45-64}\text{Zr}_{18-30}\text{Ti}_{8-20}\text{Hf}_{1-6}\text{Ta}_{5-8}\text{Ge}_{1-5}\text{V}_5$ (in at.%) alloys have a maximum T_c of 10.59 K, with an average T_c of 8.54 K. H_{c1} is from 400 Oe to 7000 Oe, and H_{c2} from 4.38 to 9.25 T with J_c being from 1×10^4 to $1.5 \times 10^6 \text{ A/cm}^2$ [9].

Although the abovementioned high-entropy alloys have multiple phases, the superconducting phase of these alloys comes from a BCC random solid solution. The fact that such kinds of random solid solutions have superconducting behavior is meaningful for academic and application investigation.

Table 7.1 Superconducting critical temperatures obtained by electrical resistivity and magnetic measurements for NbTaTiZr-based HEAs [7–9]

Alloys	$T_{c,R}$ (K)	$T_{c,M}$ (K)	$T^*_{c,R}$ (K)	$T^*_{c,M}$ (K)
M	8.98/8.28	7.98	8.27	7.97
GeM	9.16	8.61	—	—
HfM	7.93/7.12	6.30	6.69	6.40
SiVM	4.99	4.73	—	—
GeSiM	8.10	5.49	—	—
GeVM	9.10	6.34	—	—
FeM	7.12	—	6.75	5.77
HfVM	5.09	—	4.96	4.93

Note: M = NbTaTiZr, $T_{c,R}$ critical temperatures for as-cast alloys tested by resistivity measurements, $T_{c,M}$ critical temperatures for as-cast alloys by magnetism measurements at an applied magnetic field of 1 kOe, $T^*_{c,R}$ critical temperatures for as-homogenized alloys by resistivity measurements, and $T^*_{c,M}$ critical temperatures for as-homogenized alloys by magnetism measurements at an applied magnetic field of 0.1 kOe

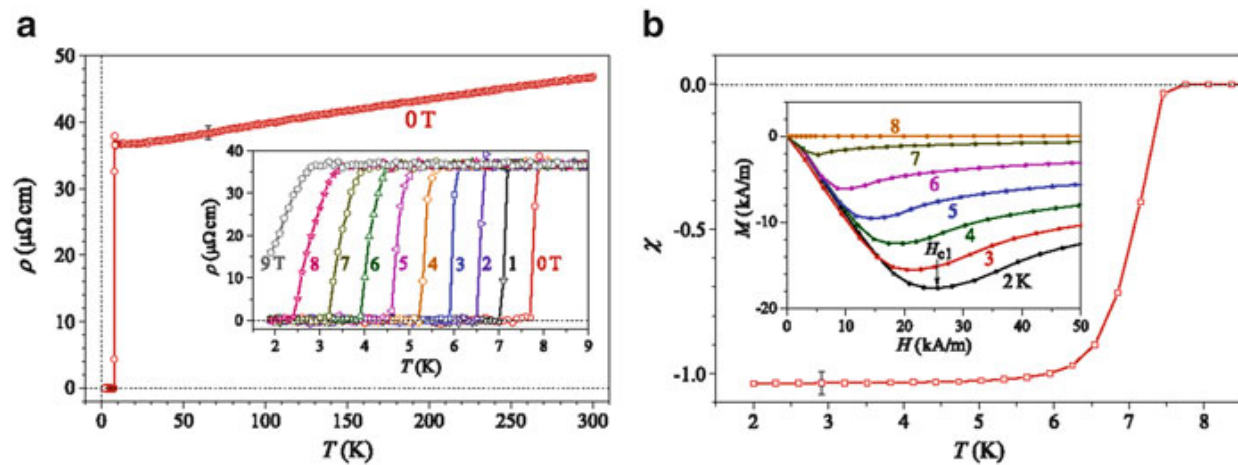


Fig. 7.3 (a) Electrical resistivity in zero magnetic field between 300 and 2 K. Magnetic field dependence of the resistivity in the region of the superconducting transition for fields up to 9 T is shown in the inset. (b) The magnetic susceptibility $\chi = M/H$ under zero-field-cooling condition in a 5 mT field in the region of the superconducting transition. The inset shows isothermal magnetization $M(H)$ in the low-field range at temperatures between 2 and 8 K. The arrow denotes the lower critical field H_{c1} at $T = 2$ K [10]

At similar time, P. Koželj et al. reported that a BCC $Ta_{34}Nb_{33}Hf_8Zr_{14}Ti_{11}$ (in at. %) HEA has a lattice parameter $a = 3.36 \text{ \AA}$ which is very close to that predicted by Vegard's law [10]. It suggests a possible random mixing of the five elements on the BCC lattice which is distorted due to the difference among constituent elements as stated in Chap. 3. In addition, they showed the measurements of the electrical resistivity, the magnetization, and magnetic susceptibility, and the specific heat and revealed that this $Ta_{34}Nb_{33}Hf_8Zr_{14}Ti_{11}$ HEA is a type II superconductor with a transition temperature $T_c \approx 7.3$ K, an upper critical field $\mu_0 H_{c2} \approx 8.2$ T, a lower critical field $\mu_0 H_{c1} \approx 32$ mT, and an energy gap in the electronic density of states (DOS) at the Fermi level of $2\Delta \approx 2.2$ meV. Figure 7.3a shows electrical resistivity

variation in zero magnetic field between 300 and 2 K and also the resistivity in the region of the superconducting transition under magnetic field up to 9 T. Figure 7.3b shows a strong diamagnetic response due to the Meissner effect below about 8 K, and the susceptibility corrected for the demagnetization factor assumes almost the ideal diamagnetic value $\chi = -1$ intrinsic to a superconductor. The isothermal magnetization $M(H)$ curves between 2 and 8 K in the low-field range up to $H = 50$ kA/m are also shown in the inset. Close to the origin, the $M(H)$ relation is linear with the slope -1 , whereas at higher fields, the $M(H)$ curves show a minimum and then approach the weakly paramagnetic value of the normal state, which is a typical behavior of type II superconductors. The field value in the minimum was taken as a measure of the lower critical field H_{c1} . At 2 K, the lower critical field amounts to $\mu_0 H_{c1} \approx 32$ mT.

By the evaluation of different criteria using parameters of the superconducting state, they concluded that the investigated HEA is close to a BCS-type phonon-mediated superconductor in the weak electron–phonon coupling limit.

7.3 Magnetic Properties of HEAs

Since the composition of FCC HEAs often contain the excessive metallic elements which include the ferromagnetic Fe, Co, and Ni, the magnetic properties of these alloys have been investigated. Among all the studied alloys, the ternary equi-atomic FeCoNi alloy which possesses the uniform polycrystalline microstructure has a higher saturation magnetization (M_s) of 1047 emu/cc and a lower coercivity [11]. Any addition of paramagnetic or ferromagnetic elements will lower the saturation magnetization, since the saturation magnetization is primarily determined by the composition and atomic-level structures. For example, the addition of 25 % anti-ferromagnetic Cr to CoFeNi alloy makes CoCrFeNi alloy paramagnetic [12]. However, CoCrFeNi alloying with Pd (FeCoCrNiPd, FeCoCrNiPd₂) can increase the magnetic moment and Curie temperature in the FCC phase. Control of the Curie temperature with Pd additions may make these alloys useful for magnetic refrigeration applications near room temperature [12].

The most widely studied AlCoCrCuFeNi HEA has been reported possessing ferromagnetic behavior. The as-cast and as-annealed AlCoCrCuFeNi HEAs possess high saturated magnetization and undergo a ferromagnetic transition as shown in Fig. 7.4 [13]. The M_s can decrease from 38.178 to 16.082 emu/g, and its coercivity can be reduced from 45 to 15 Oe after annealing which is assumed to be related with the structure coarsening and phase transformation [13]. For detailed study, Singh et al. [14] investigate the microstructure of AlCoCrCuFeNi HEA in three different states, namely, splat-quenched, as-cast, and as-aged at 600 °C for 2 h after casting. The results indicate the spinodal decomposition of Cr-Fe-Co-rich regions into Fe-Co-rich and Cr-rich domains. The splat-quenched alloy shows softer magnetic behavior than the as-cast and as-aged alloys, which is attributed to the initial stage of decomposition. The as-aged alloy exhibits a higher saturation magnetization, coercivity, and remanence ratio than the as-cast alloy due to a

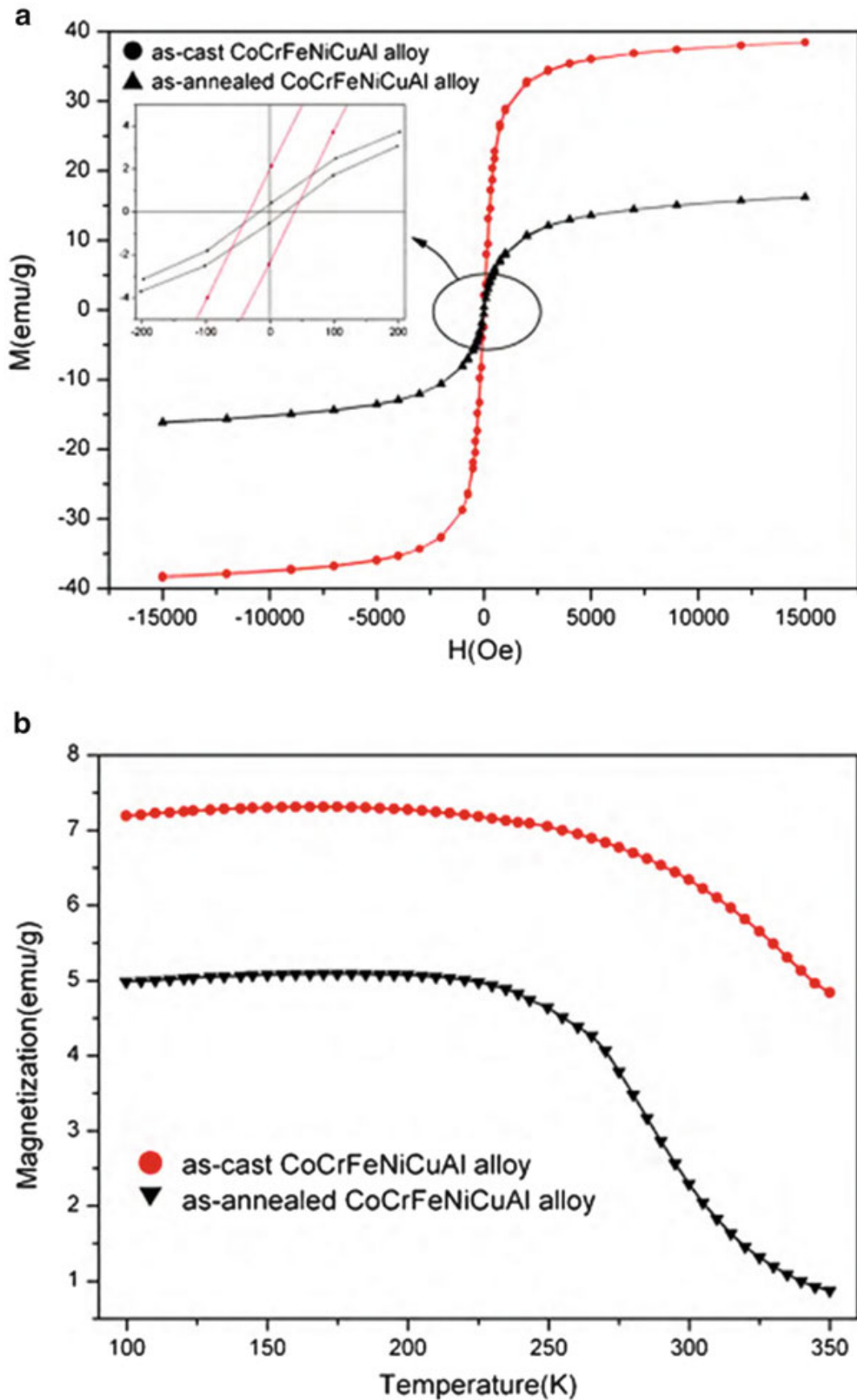


Fig. 7.4 Magnetization curves of as-cast and as-annealed AlCoCrCuFeNi HEAs: (a) the hysteresis loops and (b) the temperature dependence of magnetization ($M(T)$) curves while cooling the alloys at 200 Oe [13]

higher degree of decomposition in Cr-Fe-Co-rich regions. Thus, the ferromagnetic behavior of the AlCoCrCuFeNi HEA is correlated with the spinodal decomposition of Cr-Fe-Co-rich regions into ferromagnetic Fe-Co-rich domains and anti-ferromagnetic Cr-rich domains.

Chou et al. also studied the magnetic behavior of Cu-free $\text{Al}_{0.2-2.0}\text{CoCrFeNi}$ (denoted as H- x) alloys in homogenized condition [1]. All the H- x alloys are ferromagnetic at low temperatures (5 and 50 K). Additionally, the saturation magnetization (M_s) of alloys H-1.25 ($x = 1.25$) and H-2.0 exceeds that of alloys H-0 and H-0.25, indicating that at low temperatures, the BCC phase has higher M_s value than the FCC phase. At room temperature (300 K), alloys H-0.5, H-1.25, and H-2.0 remain ferromagnetic, while alloys H-0, H-0.25, and H-0.75 are paramagnetic. In the FCC/BCC duplex region, the saturation magnetization (M_s) of each phase at 5 K was estimated by linear superposition of BCC contribution and FCC contribution, and the volume fractions of each phase at $x = 0.5$ and 0.75. The estimated results are $M_{s,\text{FCC}} = 167.78 \text{ emu cm}^{-3}$ and $M_{s,\text{BCC}} = 54.79 \text{ emu cm}^{-3}$. The reason for $M_{s,\text{BCC}} < M_{s,\text{FCC}}$ is ascribed to the existence of Al,Ni-rich phase formed by spinodal decomposition from disordered BCC phase. It is well known that the Al,Ni-rich phase in Alnico magnets exhibits weak ferromagnetism. The M_s value declines as x increases in the ranges $0 \leq x \leq 0.25$ and $1.25 \leq x \leq 2.0$. The M_s and magnetic susceptibility values of alloy H-0 are smaller than those of alloy H-0.25, implying that Al reduces the ferromagnetism of the FCC phase alloys ($0 \leq x \leq 0.25$). On the other hand, the M_s value of H-2.0 is smaller than that of H-1.25 because H-2.0 alloy is mainly an Al,Ni-rich ordered BCC phase, whereas H-1.25 alloy has lesser B2 phase but more disordered BCC phase. In summary, the addition of Al reduces the ferromagnetism of single-FCC and single-BCC H- x alloys. In single-BCC phase, the reduction is due to the higher volume fraction of Al,Ni-rich B2 phase at a higher Al content.

By substituting Nb for Cu, the $\text{AlCoCrFeNb}_x\text{Ni}$ ($x = 0, 0.1, 0.25, 0.5$, and 0.75) HEAs studied by Ma [15] exhibit ferrimagnetic properties, since their permeability (χ) is in the range of $2.0 \times 10^{-2} - 3.0 \times 10^{-3}$ which is in the definition range of ferromagnetism, as shown in Fig. 7.5.

Recently, Zhang [5] reported a new class of $\text{FeCoNi}(\text{AlSi})_x$ ($0 \leq x \leq 0.8$ in molar ratio) HEAs by investigating the magnetic, electrical, and mechanical properties with the observed atomic-level and micro-scale structures. It was found that the saturation magnetization is primarily determined by the composition and atomic-level structures. With increasing Al and Si contents, M_s largely decreases as shown in Fig. 7.6. Different from the saturation magnetization, coercivity is sensitive to microstructures, such as grain size and phase boundary. With the compositional and structural changes, the optimal balance of magnetic, electrical, and mechanical properties is achieved at $x = 0.2$, for which the combination of saturation magnetization (1.15 T), coercivity (1400 A/m), electrical resistivity (69.5 $\mu\Omega \text{ cm}$), yield strength (342 MPa), and strain without fracture (50 %) makes the alloy an excellent soft-magnetic material.

Wang et al. [16] prepared equi-atomic AlBFeNiSi and AlBFeNbNiSi HEAs using the method of mechanical alloying and investigated the magnetic properties. They pointed out that the as-milled AlBFeNbNiSi powders are soft magnetic with

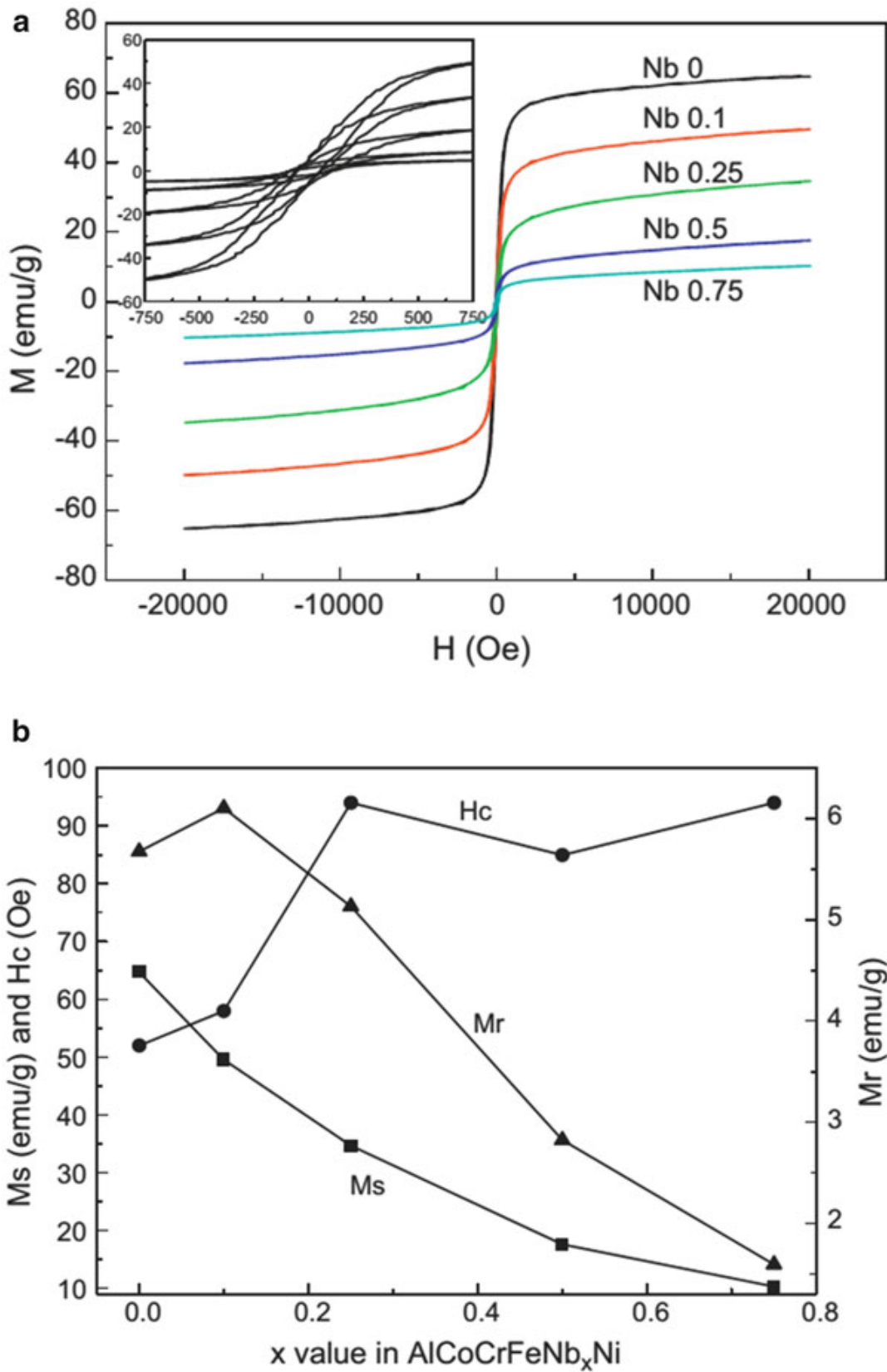


Fig. 7.5 (a) Magnetization curves of the AlCoCrFeNb_xNi alloys ($x = 0, 0.1, 0.25, 0.5, \text{ and } 0.75$). (b) the corresponding saturation magnetizations M_s , residual magnetizations M_r , and coercive forces H_c [15]

low coercivity. The saturation magnetization of the as-milled AlBFeNbNiSi powders decreases with prolonging of the milling time and shows the lowest value when the amorphous HEA are formed, as presented in Fig. 7.7. This suggests that the as-milled products with solid solution phases show the better soft-magnetic

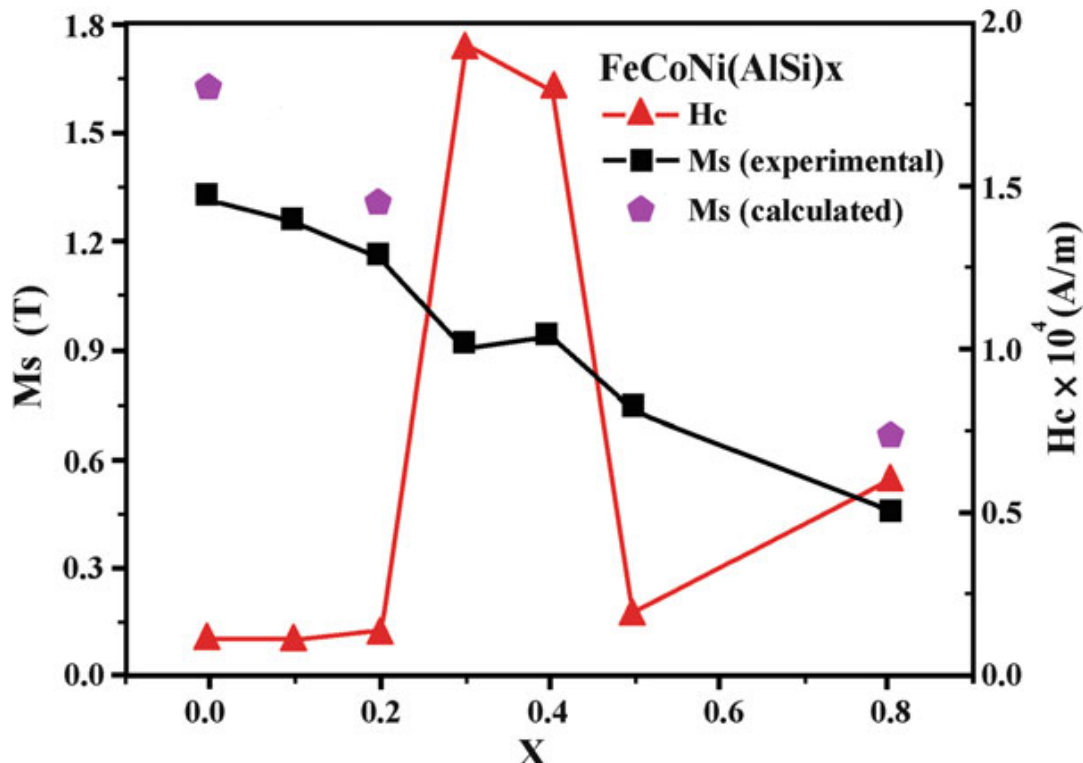


Fig. 7.6 Magnetic properties of $\text{FeCoNi}(\text{AlSi})_x$ ($x = 0, 0.1, 0.2, 0.3, 0.4, 0.5, \text{ and } 0.8$) alloys. H_c and M_s represent the coercivity and saturation magnetization, respectively [5]

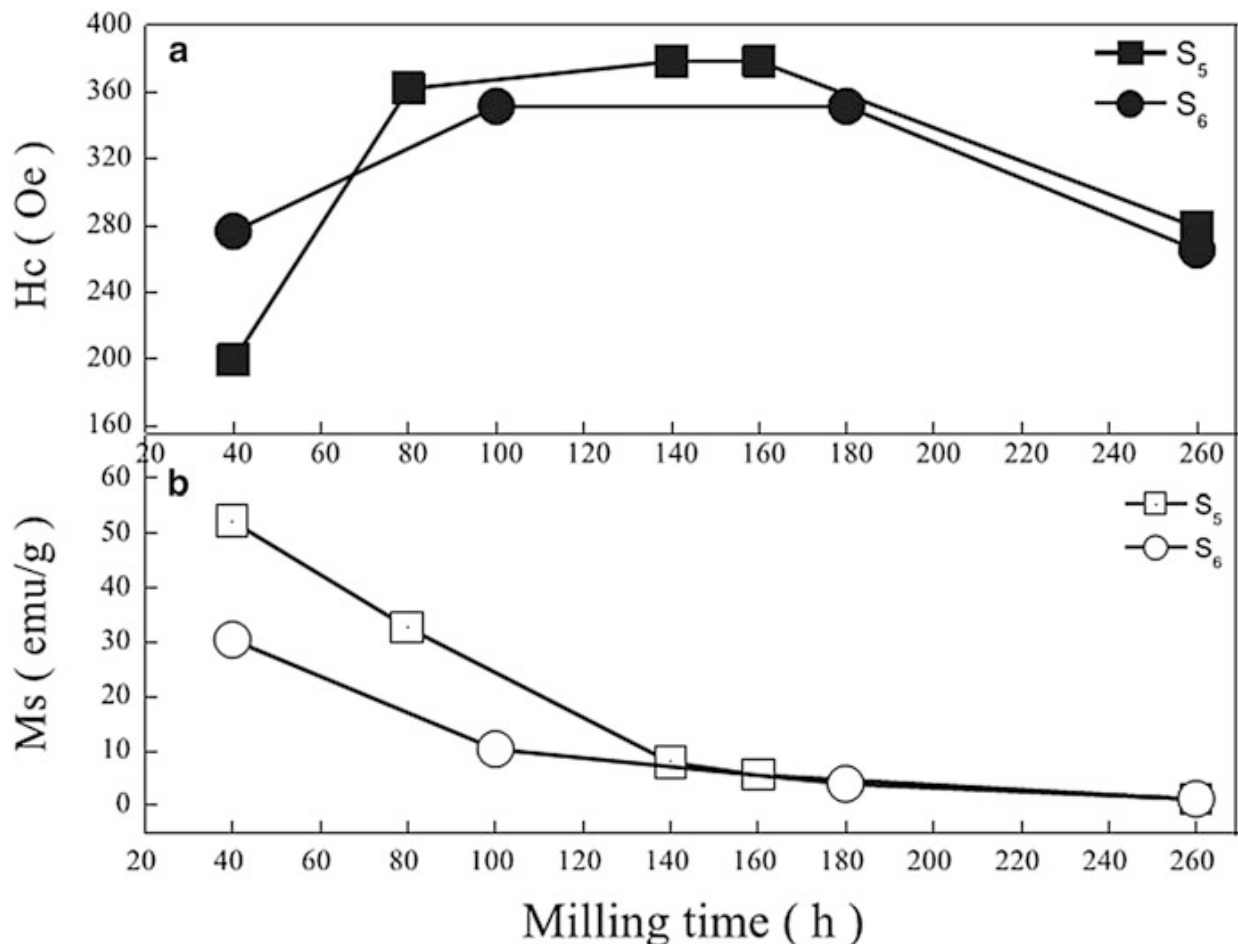


Fig. 7.7 Magnetic properties of the as-milled AlBFeNiSi (S5) and AlBFeNbNiSi (S6) powders after different milling times [16]

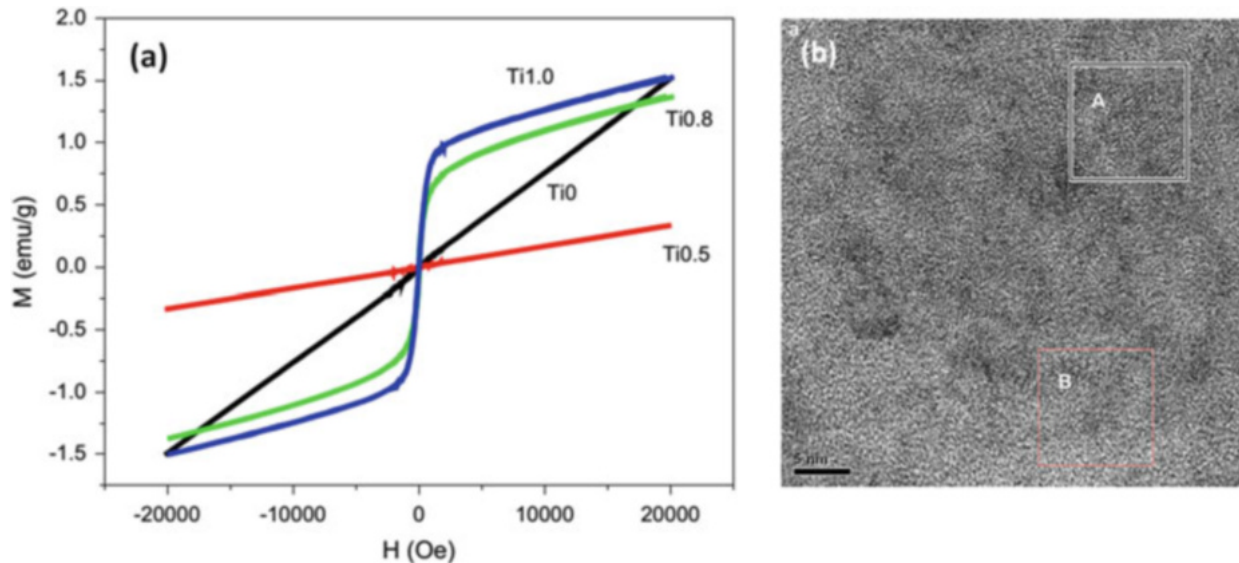


Fig. 7.8 (a) Magnetization curves of the CoCrCuFeNiTi_x alloys ($x = 0, 0.5, 0.8$, and 1) showing a transition from the paramagnetism ($x = 0$ and 0.5) to superparamagnetism ($x = 0.8$ and 1) [15]. (b) High-resolution transmission electron microscopy (HRTEM) image of nanoparticles embedded in the amorphous phase in CoCrCuFeNiTi alloy (*region A*, nanoparticles, *region B*, amorphous matrix) [15]

properties than those with fully amorphous phases. The Nb addition does not improve the soft-magnetic properties of the AlBFeNiSi HEAs. Rather, both amorphous HEAs have similar soft-magnetic properties after a long milling time.

Figure 7.8a shows the magnetization curves of the CoCrCuFeNiTi_x alloys [17]. Both CoCrCuFeNi and $\text{CoCrCuFeNiTi}_{0.5}$ exhibit typical paramagnetism, and the saturation magnetizations are 1.505 and 0.333 emu/g, respectively, under 20,000 Oe magnetic field, while the alloys of $\text{CoCrCuFeNiTi}_{0.8}$ and CoCrCuFeNiTi have likely superparamagnetic curves with the saturation magnetizations of 1.368 and 1.511 emu/g, respectively. This paramagnetism is due to the nano-precipitations in the alloys as shown in Fig. 7.8b.

Generally speaking, the more the contents of magnetic elements (Fe, Co, and Ni), the higher is the saturation magnetization. However, the amount and distribution of anti-ferromagnetic Cr can have significant effect. The saturation magnetization is usually below 500 emu/cc, unless the concentration of magnetic elements is very high. Coercivity is affected by factors such as microstructure and grain size. Most reported HEAs have coercivities less than 100 Oe [6], while some have higher values ranging from 250 to about 400 Oe.

7.4 Electrochemical Properties of HEAs

7.4.1 Electrochemical Kinetics

A structural part in engineering applications often encounters corrosive environment with different kinds of attacking chemical species. The lifetime is often determined by its corrosion resistance to the environment. In the multi-principal

element composition of HEAs, it is noted that Cr, Ni, Co, and Ti are positive to enhance corrosion resistance in acid solutions. Mo might inhibit pitting corrosion in Cl^- -containing solutions. On the other hand, Al, Cu, and Mn often display negative effect. However, microstructure and the interaction among constituent elements might alter the intuitive prediction. Therefore, it is important to conduct actual experimental study of electrochemical behaviors of different HEAs with different processing.

Anodic Process The polarization curves of the alloy $\text{AlCoCrCu}_{0.5}\text{FeNiSi}$ in comparison with the 304 stainless steel (ss) demonstrate a mixed control in 1 N H_2SO_4 (pH 0.5) and an anodic control in 1 N NaCl (pH 6.5), as presented in Figs. 7.9 [18] and 7.10 [19]. The corrosion potential (E_{corr}) increases significantly at temperatures >40 °C, while 304 ss is not that sensitive to the same temperature range and therefore maintains a constant extent of passivity (ΔE). The prominent kinetic factors shown on the anodic polarization curve are the critical current density for passivation (i_{crit}) and the passive current density (i_{pass}); both are temperature-dependent. The corrosion rate, e.g., $\mu\text{g}/\text{mm}^2$, in terms of corrosion current density (i_{corr}) according to Faraday's laws of electrolysis increases with temperature, too. The 304 ss corrodes more readily than the HEA. For instance, in 1 N H_2SO_4 (70 °C), the i_{corr} for 304 ss is measured as $10.5 \times 10^{-4} \text{ A/cm}^2$ at $E_{\text{corr}} - 0.41 V_{\text{SHE}}$ while for the HEA is $1.91 \times 10^{-4} \text{ A/cm}^2$ at $E_{\text{corr}} - 0.31 V_{\text{SHE}}$ (V_{SHE} : the potential relative to the standard hydrogen electrode) [19, 20]. The activation energy (Q) for anodic dissolution in 1 N H_2SO_4 is 94.1 kJ/mole for the HEA and 220 kJ/mole for the 304 ss according to the Arrhenius plot of $i_{\text{corr}} = A \exp(-Q/RT)$. The lower Q value of the HEA should be due to the buildup of a defect-free passivity which results from the higher anodic current density as comparing with the Q value for the 304 ss or even with the pure iron in the H_2SO_4 solution [19, 20]. The lower corrosion rate at E_{corr} may account for the higher hydrogen overvoltage, η on the alloy $\text{AlCoCrCu}_{0.5}\text{FeNiSi}$ surface which is caused by the Al content in this particular HEA $\text{AlCoCrCu}_{0.5}\text{FeNiSi}$. Literature has shown that the value of η for Al can be as high as 0.70 V in 2 N H_2SO_4 at an applied current density of 1 mA/cm² [21–23].

Anodic polarization shows that HEA is more resistant to general corrosion than 304 ss at room temperature in chloride at 0.1 and 1 N and in acidic environments at 0.1 and 1 M concentrations. Figure 7.9 shows comparisons between $\text{AlCoCrCu}_{0.5}\text{FeNiSi}$ and 304 ss in 0.1 M NaCl solution, based on the anodic polarization measurements, indicating a higher pitting potential (E_{pit}) of HEA (~0.6 V_{SHE}) than that of 304 ss (~0.4 V_{SHE}) and a lower corrosion rate (i_{corr}) of HEA (~0.5 $\mu\text{A}/\text{cm}^2$) than that of 304 ss (~2 $\mu\text{A}/\text{cm}^2$) [22, 23].

Metallic corrosion takes place mainly on the anodic reaction. Alloying and processing effects on the aqueous corrosion behavior of the HEA systems in 3.5 wt.% NaCl solution exhibit a lower i_{corr} (0.03 $\mu\text{A}/\text{cm}^2$) and higher E_{pit} (0.55 V_{SHE}) for the Al, Cu-free CoCrFeNi. However, lower values of i_{corr} and higher values of E_{pit} can be enhanced by heat treatments, e.g., on the Al-free $\text{CoCrCu}_{0.5}\text{FeNi}$ and Cu-free $\text{Al}_{0.5}\text{CoCrFeNi}$ alloys. For example, a lowest i_{corr}

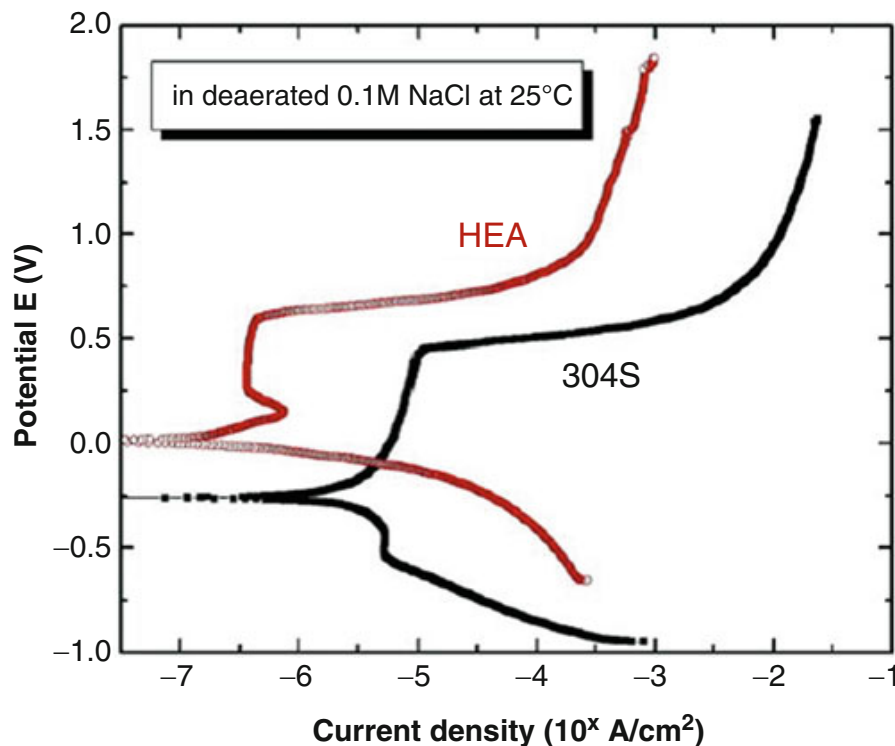


Fig. 7.9 Comparisons of the anodic polarization curves for $\text{AlCoCrCu}_{0.5}\text{FeNiSi}$ HEA and 304 ss in 0.1 M NaCl at room temperature ($\sim 25^\circ\text{C}$) [18]

($0.01 \mu\text{A}/\text{cm}^2$) for the Cu-containing $\text{CoCrCu}_{0.5}\text{FeNi}$ can be obtained through the heat treating at $1250^\circ\text{C}/24\text{ h}$, while a highest E_{pit} ($0.96 \text{ V}_{\text{SHE}}$) for the Al-containing $\text{Al}_{0.5}\text{CoCrFeNi}$ has been achieved through the heat treating at $650^\circ\text{C}/24\text{ h}$ [24].

Cathodic Process The cathodic process of the alloy $\text{AlCoCrCu}_{0.5}\text{FeNiSi}$ comprises the production of hydrogen ($2\text{H}_2\text{O} + 2\text{e}^- \rightarrow \text{H}_2 + 2\text{OH}^-$), reduction of dissolved oxygen ($\text{O}_2 + 2\text{H}_2\text{O} + 4\text{e}^- \rightarrow 4\text{OH}^-$), and various metallic ions (M^{n+}) derived from the alloy $\text{AlCoCrCu}_{0.5}\text{FeNiSi}$. Infinite concentration polarization is approached when $[\text{M}^{n+}]_s$ approaches zero at the alloy surface; the corresponding current density producing this limiting lower value of M^{n+} is the limiting current density, i_L . In the case of the deposition of M^{n+} , the potential moves to that for hydrogen evolution, and hydrogen gas is liberated together with the simultaneous plating out of M^{n+} . The limiting current density (i_L) is approximated by the relation: $i_L = 0.02 nc$ [20], where n is the number of equivalent and c is the concentration of discharging ions, i.e., M^{n+} , H^+ , OH^- in mole/liter, and i_L is increased with the increasing solution temperature. For this particular HEA $\text{AlCoCrCu}_{0.5}\text{FeNiSi}$, values of i_L are $\sim 12 \mu\text{A}/\text{cm}^2$ at 30°C and $100 \mu\text{A}/\text{cm}^2$ at 70°C , indicating that the higher valence ions, i.e., M^{n+} , in addition to the single valence ion of H^+ or OH^- , prevail at higher solution temperatures. The cathodic Tafel constant β_c can be evaluated by taking the slope of the linear region near E_{corr} on the cathodic polarization curve. It is interesting to note that the β_c for the 304 ss ($-0.150 \text{ V}/\text{decade}$ at 70°C) increases with the increasing temperature since β_c is proportional to the RT/F , where R is the gas constant and F is the Faraday constant, but decreases for the alloy $\text{AlCoCrCu}_{0.5}\text{FeNiSi}$ ($-0.108 \text{ V}/\text{decade}$ at 70°C) [19, 20, 22]. The reason for this is not clear, but it may be related to the material properties,

such as microstructure, chemical composition, and above all the entropy of the HEA system.

Polarization and Corrosion Rates The alloy composition on the surface is found very similar to the bulk HEA as confirmed by X-ray diffraction (XRD) and energy dispersive X-ray spectroscopy (EDS) [19]. Both anodic and cathodic equilibrium potentials of the HEA in 1 N H₂SO₄ (pH 0.5) and in 1 N NaCl (pH 6.2) can be calculated according to the Nernst equation; they are $-0.841 V_{\text{SHE}}$ for the anodic equilibrium (E_a) and $+0.330 V_{\text{SHE}}$ for the cathodic equilibrium (E_c) and slightly increasing with the temperature, as shown in Fig. 7.10. The measured E_{corr} , which is the potential resulting from the short-circuited galvanic cells on the alloy surface, lies between the equilibrium potentials of E_a and E_c . A mixed control is observed in 1 N H₂SO₄ solution, implying that the alloy AlCoCrCu_{0.5}FeNiSi exhibits a similar degree of the polarization between the anode (E_a) and cathode (E_c). However, an anodic control dominates the both alloys in 1 N NaCl solution; that is to say, much more polarization takes place on the anode than on the cathode (Fig. 7.10). In particular, this alloy AlCoCrCu_{0.5}FeNiSi exhibits a wide passive region ($\Delta E \geq 1.2$ V) and a passive current density (i_{pass}) of $\sim 2 \times 10^{-4} \text{ A/cm}^2$ in 288 °C water containing 0.01 N Na₂SO₄ [25]. A low weight loss of $\sim 4.5 \mu\text{g/mm}^2$ is obtained after immersion for 12 weeks [25, 26]. Besides showing the good corrosion resistance, the AlCoCrCu_{0.5}FeNiSi alloy presents a high tensile fracture strength and elongation of 2660 MPa and 2.01 %, respectively, in the air, and only a slightly lower performance, 2000 MPa and 1.49 %, in an autoclave water of 288 °C [27]. The finding of the HEA Cu_{0.5}AlCoCrFeNiSi with good corrosion resistance and mechanical strength is encouraging for the possible application as structural materials in high-temperature aqueous environments, e.g., in boiling water reactor (BWR).

Based on the data of the Tafel slopes, i.e., β_a , β_c , and the given equilibrium potentials (Fig. 7.10), it is possible to evaluate the exchange current density, i_0 , or the current density equivalent to the equal forward and reverse reactions at the electrode at equilibrium according to the Tafel equation, $\eta = \beta \log (i_{\text{corr}}/i_0)$. The larger the i_0 and the smaller the β , the smaller is the corresponding overvoltage, η . The effect of Al can effectively decrease the i_0 ($0.064 \mu\text{A/cm}^2$) as compared with the Al-free Al_xCoCrFeNi ($0.43 \mu\text{A/cm}^2$). A lower hydrogen overvoltage is thus observed for the Al-free Al_xCoCrFeNi in aqueous environments.

7.4.2 Alloying for Corrosion Resistance

Effect of Boron Boron added to the alloy is known to improve the wear resistance. Anodic polarization studies demonstrate that the E_{corr} of the B-free alloy Al_{0.5}CoCrCuFeNi ($-0.094 V_{\text{SHE}}$) is more noble, i.e., higher reduction potential than that of the 304 ss ($-0.165 V_{\text{SHE}}$), and the corresponding i_{corr} ($3.19 \mu\text{A/cm}^2$) is lower than that of the 304 ss ($33.2 \mu\text{A/cm}^2$) in 1 N H₂SO₄ solution [28]. Clearly, this

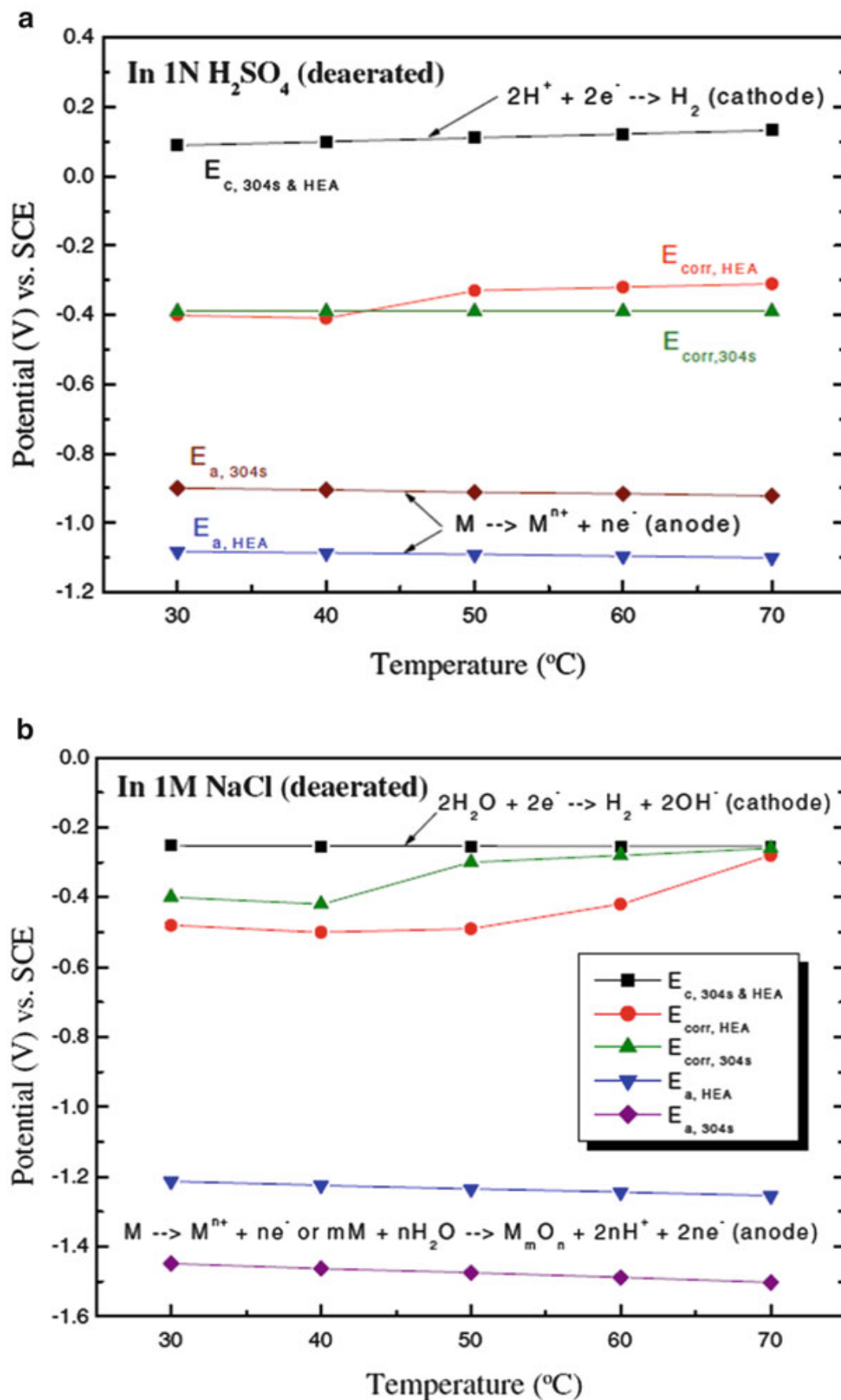


Fig. 7.10 The measured E_{corr} in relation with the calculated equilibrium potentials, E_a and E_c , for the alloy AlCoCrCu_{0.5}FeNiSi assuming $[\text{M}^{n+}] = 10^{-6}$ in solutions: (a) 1 N H_2SO_4 , pH = 0.5, and (b) 1 N NaCl , pH = 6.2 [19]

B-free alloy $\text{Al}_{0.5}\text{CoCrCuFeNi}$ is more resistant to general corrosion than the 304 ss. Cyclic polarization curves [29] indicate that these B-containing alloys $\text{Al}_{0.5}\text{CoCrCuFeNiB}_x$ are not susceptible to pitting corrosion in 1 N H_2SO_4 solution, and the corresponding values of E_{corr} and i_{corr} vary in range from -115 to -159 mV_{SHE} and from 787 to $2848 \mu\text{A}/\text{cm}^2$, respectively, responding to the boron contents up to 1 mole ($x = 1$). It is apparent that boron is detrimental to the corrosion resistance because of the stringy precipitates of Cr, Fe boride phases as revealed from X-ray photoelectron spectroscopy (XPS) analyses of alloy $\text{Al}_{0.5}\text{CoCrCuFeNiB}_{0.6}$ after anodic polarization in 1 N H_2SO_4 solution [28]. Results from electrochemical impedance spectroscopy (EIS) indicate that the polarization resistance (R_p) of the B-free $\text{Al}_{0.5}\text{CoCrCuFeNi}$ alloy ($2500 \Omega \text{ cm}^2$) considerably exceeds that of the B-containing alloy, e.g., $\text{Al}_{0.5}\text{CoCrCuFeNiB}_{0.6}$ ($900 \Omega \text{ cm}^2$), again indicating that the alloying of boron impairs the corrosion resistance.

Adding metalloid such as boron to the alloy $\text{Al}_{0.5}\text{CoCrCuFeNi}$ should increase the hardness and wear resistance through the formation of borides. However, potentiodynamic polarization curves show that the alloys $\text{Al}_{0.5}\text{CoCrCuFeNiB}_x$ are less corrosion resistant to general corrosion than the B-free alloys in 0.5 N H_2SO_4 solution [28]. Some electrochemical parameters of the $\text{Al}_{0.5}\text{CoCrCuFeNiB}_x$ alloys in 1 N H_2SO_4 solution are listed in Table 7.2 [28, 29]. The passive range, ΔE of B_0- and $B_{0.2}-$ alloys, is 273 and 256 mV, respectively. However, the passive range of the $B_{0.6}-$ and $B_{1.0}-$ alloys narrows first and finally disappears, resuming to an active dissolution accounting for the presence of boron contents. The analyzed results from Nyquist plot indicate that the alloys $\text{Al}_{0.5}\text{CoCrCuFeNiB}_x$ in 1 N H_2SO_4 possess (1) the Cr content on the surface, but outside the CrB_2 precipitate is depleted and not sufficient for the passivation, (2) the galvanic corrosion occurs along the edge of CrB_2 precipitates, and (3) the polarization resistance (R_p) reduces as the metalloid, boron being alloyed. Microstructure of the alloy $\text{Al}_{0.5}\text{CoCrCuFeNiB}_x$ system under investigation is composed of a mixture of disordered BCC and FCC phases and borides [28].

Effect of Aluminum Effect of the aluminum content in the alloy $\text{Al}_x\text{CrFe}_{1.5}\text{MnNi}_{0.5}$ system on the corrosion behavior is prominent in aqueous environments. Both polarization and EIS of the alloys $\text{Al}_x\text{CrFe}_{1.5}\text{MnNi}_{0.5}$, obtained in 0.5 M H_2SO_4 mixed with varying NaCl solutions, clearly reveal a decreasing pitting resistance as the alloying Al content increases [30]. This alloy system,

Table 7.2 Electrochemical properties of $\text{Al}_{0.5}\text{CoCrCuFeNiB}_x$ in 1 N H_2SO_4 according to the cyclic polarization [28, 29]

Designation	E_{corr}	E_{pit}	ΔE	E_{rp}	i_{corr}	R_p
	(mV _{SHE})	(mV _{SHE})	(mV)	(mV _{SHE})	($\mu\text{A}/\text{cm}^2$)	($\Omega \text{ cm}^2$)
$\text{Al}_{0.5}\text{CoCrCuFeNi}$	-115	233	273	290	787	6652
$\text{Al}_{0.5}\text{CoCrCuFeNiB}_{0.2}$	-121	215	256	266	1025	2763
$\text{Al}_{0.5}\text{CoCrCuFeNi B}_{0.6}$	-148	~0	~0	82	2626	1872
$\text{Al}_{0.5}\text{CoCrCuFeNi B}_{1.0}$	-159	~0	~0	-103	2848	1081

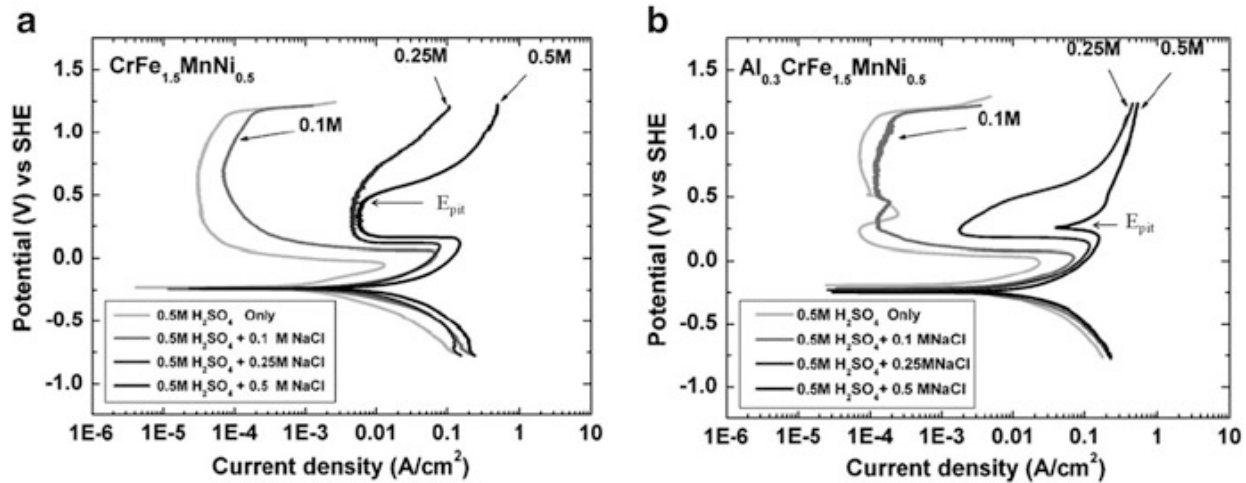


Fig. 7.11 Potentiodynamic polarization curves for (a) CrFe_{1.5}MnNi_{0.5} and (b) Al_{0.3}CrFe_{1.5}MnNi_{0.5} alloys in 0.5 M H₂SO₄ mixed with varying NaCl solutions, both showing a shift of transpassive potential for oxygen evolution (1.2 V_{SHE}) toward much active potentials for pitting corrosion, e.g., 0.45 V_{SHE} for Al-free CrFe_{1.5}MnNi_{0.5} and 0.25 V_{SHE} for Al-bearing Al_{0.3}CrFe_{1.5}MnNi_{0.5} [30]

Al_xCrFe_{1.5}MnNi_{0.5}, demonstrates a wide passive range ($\Delta E \geq 1.2$ V) in 0.5 M H₂SO₄ solution, which covers the potential range of the stability of H₂O ($\Delta E = 1.23$ V) [31], as shown in Fig. 7.11. The current peak at 0.3 V_{SHE} is likely due to the formation of Al₂O₃·3H₂O as one of the constituents that composes the passive film ($E_{\text{Al}/\text{Al}_2\text{O}_3} \sim 0.3$ V_{SHE}) [30, 31].

Potentiodynamic polarization curves obtained in 0.5 M H₂SO₄ mixed with varying, e.g., NaCl, solutions exhibit a shift of transpassive potential for oxygen evolution at 1.2 V_{SHE} toward to a much active potential for pitting corrosion. The E_{pit} depends on the Cl⁻ ion concentration and also on the Al contents of the alloy Al_xCrFe_{1.5}MnNi. For instance, both Al-free and Al-bearing alloys of CrFe_{1.5}MnNi_{0.5} tend to show a distinct passive range (ΔE) of about 1.2 V with an oxygen evolution at 1.15 V_{SHE} which drops to a much active value of 0.45 V_{SHE} for the Al-free CrFe_{1.5}MnNi_{0.5} and to an even more active potential of 0.25 V_{SHE} for the Al-bearing Al_{0.3}CrFe_{1.5}MnNi_{0.5} responding to the increasing Cl⁻ ion to values ≥ 0.25 M NaCl solution, together with the dissolving of the current peak of the $E_{\text{Al}/\text{Al}_2\text{O}_3}$ reaction at 30 V_{SHE} that could degenerate the intact passive film, as illustrated in Fig. 7.12.

Similar polarization curves for the Al_xCrFe_{1.5}MnNi_{0.5} alloys show a much narrow passive region ($\Delta E \leq 0.3$ V) in 1 N NaCl solution and clearly reveal a decreasing pitting resistance with the increasing aluminum contents in HEA as the electrochemical properties presented in Table 7.3 [30]. For the Al-containing Al_{0.3}- and Al_{0.5}CrFe_{1.5}MnNi_{0.5} alloys, the Nyquist plot has two capacitive loops, which are typically related to the presence of an electrical double layer and an adsorption layer [30].

Effect of Molybdenum The addition of molybdenum is widely recognized for its beneficial effect on the corrosion resistance of the stainless steels and has been

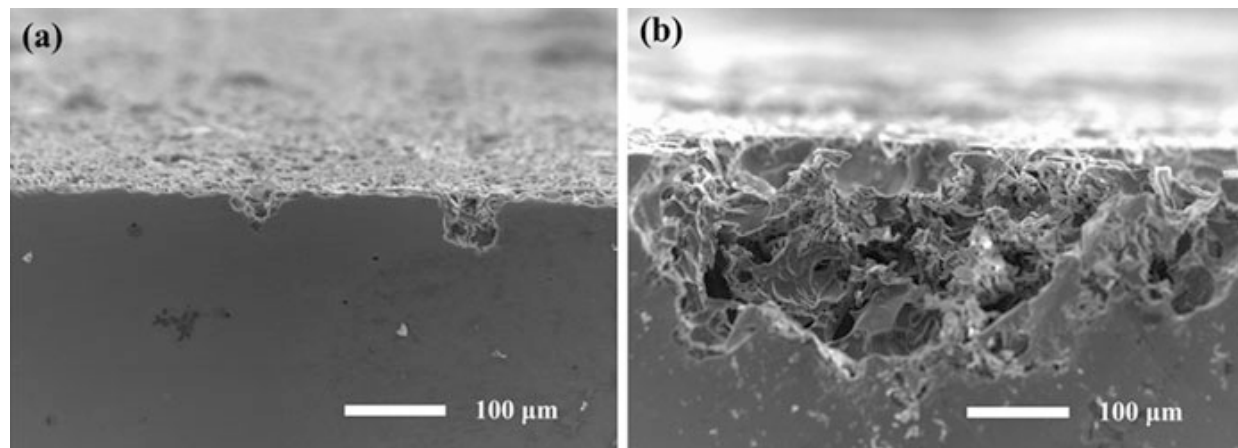


Fig. 7.12 Scanning electron microscope (SEM) micrographs of the alloy (a) $\text{CrFe}_{1.5}\text{MnNi}_{0.5}$, and (b) $\text{Al}_{0.3}\text{CrFe}_{1.5}\text{MnNi}_{0.5}$ showing that the Al-containing HEA apparently reduces the pitting resistance in 0.5 M H_2SO_4 mixed with 0.25 N NaCl solution [30]

Table 7.3 Electrochemical parameters of the alloy $\text{Al}_x\text{CrFe}_{1.5}\text{MnNi}_{0.5}$ in 0.5 N H_2SO_4 solution [30]

Designation	E_{corr} (mV _{SHE})	i_{corr} (A/cm ²)	i_{crit} (A/cm ²)	E_{pp} (mV _{SHE})	i_{pass} (A/cm ²)	ΔE (mV)
$\text{Al}_0\text{CrFe}_{1.5}\text{MnNi}_{0.5}$	-229	6.86×10^{-4}	1.26×10^{-2}	-55	3.14×10^{-5}	1227
$\text{Al}_{0.3}\text{CrFe}_{1.5}\text{MnNi}_{0.5}$	-194	2.39×10^{-3}	2.36×10^{-2}	-12	7.39×10^{-5}	1176
$\text{Al}_{0.5}\text{CrFe}_{1.5}\text{MnNi}_{0.5}$	-206	5.08×10^{-3}	5.54×10^{-2}	47	6.82×10^{-5}	1114
304 stainless steel	-186	7.45×10^{-5}	8.19×10^{-4}	-22	8.05×10^{-5}	1178

studied extensively in the past [32–34]. The anodic polarization curves of the $\text{Co}_{1.5}\text{CrFeNi}_{1.5}\text{Mo}_x$ alloy in acids exhibit an active-passive transition, an extensive passive region, and $\Delta E \geq 1.2$ V, which is consistent with the stability of H_2O . The corrosion current density, in the $\text{Co}_{1.5}\text{CrFeNi}_{1.5}\text{Ti}_{0.5}\text{Mo}_{0.1}$ alloy, is lower than that in the $\text{Co}_{1.5}\text{CrFeNi}_{1.5}\text{Ti}_{0.5}$ alloy, which may be attributed to the simultaneous presence of lower Cr and slightly higher Mo content (1.8 at.%) in the $\text{Co}_{1.5}\text{CrFeNi}_{1.5}\text{Ti}_{0.5}\text{Mo}_{0.1}$ alloy. As the Mo content increases from 0.5 to 0.8 in molar ratio in the HEAs, the interdendrite phase of the $\text{Co}_{1.5}\text{CrFeNi}_{1.5}\text{Ti}_{0.5}\text{Mo}_x$ alloys is a Cr- and Mo-rich σ phase, and the dendrite is a Cr- and Mo-depleted phase. As 316 L ss plate has failed due to the presence of σ phase, which is deleterious to corrosion performance of the stainless steels in H_2SO_4 solution, the $\text{Co}_{1.5}\text{CrFeNi}_{1.5}\text{Ti}_{0.5}\text{Mo}_x$ ($x = 0.5, 0.8$) alloys possessed the lower corrosion current density in comparison with the Mo-free alloy [35]. On the other hand, the Mo-free $\text{Co}_{1.5}\text{CrFeTi}_{1.5}$ alloy tends to pit in Cl^- environments by showing a narrower range of passive potentials. However, the Mo-containing $\text{Co}_{1.5}\text{CrFeNi}_{1.5}\text{Ti}_{0.5}\text{Mo}_x$ alloys are quite pitting resistant in chloride-containing environments, accounting for the MoO_4^{2-} ions on the passive surface which is cation selective, thus repelling the incorporation of anions such as Cl^- , Br^- , etc., and this passive film is generally believed to repair itself [35, 36]. The corrosion data of the alloy $\text{Co}_{1.5}\text{CrFeNi}_{1.5}\text{Ti}_{0.5}\text{Mo}_x$ system in deaerated 0.5 M H_2SO_4 and in deaerated 1 M

Table 7.4 Electrochemical parameters of the $\text{Co}_{1.5}\text{CrFeNi}_{1.5}\text{Ti}_{0.5}\text{Mo}_x$ alloys in deaerated 0.5 M H_2SO_4 [35]

Designation	E_{corr} (mV _{SHE})	i_{corr} ($\mu\text{A}/\text{cm}^2$)	i_{pass} ($\mu\text{A}/\text{cm}^2$)	E_{pit} (mV _{SHE})	ΔE (mV)
Mo_0	-92	30	9	1089	1130
$\text{Mo}_{0.1}$	-71	78	9	1089	1112
$\text{Mo}_{0.5}$	-64	72	11	1089	1109
$\text{Mo}_{0.8}$	-70	69	22	1089	1109

Table 7.5 Electrochemical parameters of the $\text{Co}_{1.5}\text{CrFeNi}_{1.5}\text{Ti}_{0.5}\text{Mo}_x$ alloys in deaerated 1 M NaCl [35]

Designation	E_{corr} (mV _{SHE})	i_{corr} ($\mu\text{A}/\text{cm}^2$)	i_{pass} ($\mu\text{A}/\text{cm}^2$)	E_{pit} (mV _{SHE})	ΔE (mV)
Mo_0	-443	0.57	1.46	338	557
$\text{Mo}_{0.1}$	-381	0.13	3.80	1214	1429
$\text{Mo}_{0.5}$	-493	0.20	4.10	1164	1383
$\text{Mo}_{0.8}$	-551	0.41	5.11	1182	1371

NaCl solutions have been summarized in Tables 7.4 and 7.5. XPS analysis indicates the existence of Cr_2O_3 and MoO_2 in the passive film with the respective equilibrium of $\text{CrO}_4^{2-}/\text{Cr}_2\text{O}_3$ ($E_0 = 1.31$ V) and $\text{MoO}_4^{2-}/\text{MoO}_2$ ($E_0 = 0.606$ V) is quite similar to the potentials within the passive range [31]. In alkaline environments, e.g., 1 N NaOH, the corrosion resistance deteriorates with the increasing Mo content, because of the formation of the Cr-rich σ phase, which reduces the critical composition of Cr for the passivation [35, 37].

Effect of Copper Cu tends to segregate as clusters, forming Cu-deficient dendrites and Cu-rich interdendrites during solidification due to its weaker bonding energies with Fe, Co, Ni, and Cr [19] as in the alloy $\text{Al}_{0.5}\text{CoCrCuFeNi}$. Galvanic corrosion between the composite phases also occurs in $\text{CoCrCu}_x\text{FeNi}$ in 3.5 wt.% NaCl solution at room temperature for 30 days. The localized corrosion was found along the Cu-rich interdendrites in both alloys $\text{Cu}_{0.5}$ HEA and $\text{Cu}_{1.0}$ HEA, but not in the Cu-free CoCrFeNi dendrite. In general, CoCrFeNi alloy is easier to be passivated and thus more corrosion resistant than the alloys $\text{CoCr Cu}_{0.5}\text{FeNi}$ and CoCrCuFeNi in 3.5 wt.% NaCl solution [19, 38]. Hot corrosion of the alloys $\text{Al}_{0.5}\text{CoCrCuFeNiB}_x$ may occur in the absence of liquid electrolyte. A solid reaction product film or scale forms on the metal surface through which the metal and the environment must encounter in order for the reaction to continue. The elimination of Cu-rich regions from B-free $\text{Al}_{0.5}\text{CoCrCuFeNiB}_0$ alloy would greatly improve the corrosion resistance [19, 28, 39]. Corrosion data collected during exposure of syngas containing 0.1–1 % H_2S at 500 °C showing multiphase Cu-rich regions in the low B-containing HEAs were vulnerable to the corrosion attack. $\text{Cu}_{1.96}\text{S}$ was the primary sulfide in the external corrosion scale on the low-B HEAs, whereas $\text{FeCo}_4\text{Ni}_4\text{S}_8$ on the high-B HEAs [39].

7.4.3 Corrosion Protection

Anodizing Anodizing within the passive potential, the corresponding current declines exponentially with the anodizing time which leads to the growth of the multicomponent anodized film in 15 % H₂SO₄ solution. XPS analysis proves the existence of Al and Cr oxide films as the major components resulting from the anodizing of the Al-containing alloy Al_{0.3}CrFe_{1.5}MnNi_{0.5}. The current transient of the chronoamperometric curve indicates that the Al-free alloy CrFe_{1.5}MnNi_{0.5} is susceptible to localized corrosion. However, such curve is not observed in the case of the Al-containing alloy, such as Al_{0.3}CrFe_{1.5}MnNi_{0.5}, which is smooth and effectively protective against the pitting corrosion, as shown in Fig. 7.13 [23, 40, 41]. The polarization impedance (R_p) before the anodizing Al_xCrFe_{1.5}MnNi_{0.5} increases with the alloying aluminum content, which is also notably lower than that of the 304 ss. The anodized Al_xCrFe_{1.5}MnNi_{0.5} alloys have shown a higher corrosion resistance against pitting than the untreated ones. It is also apparent to

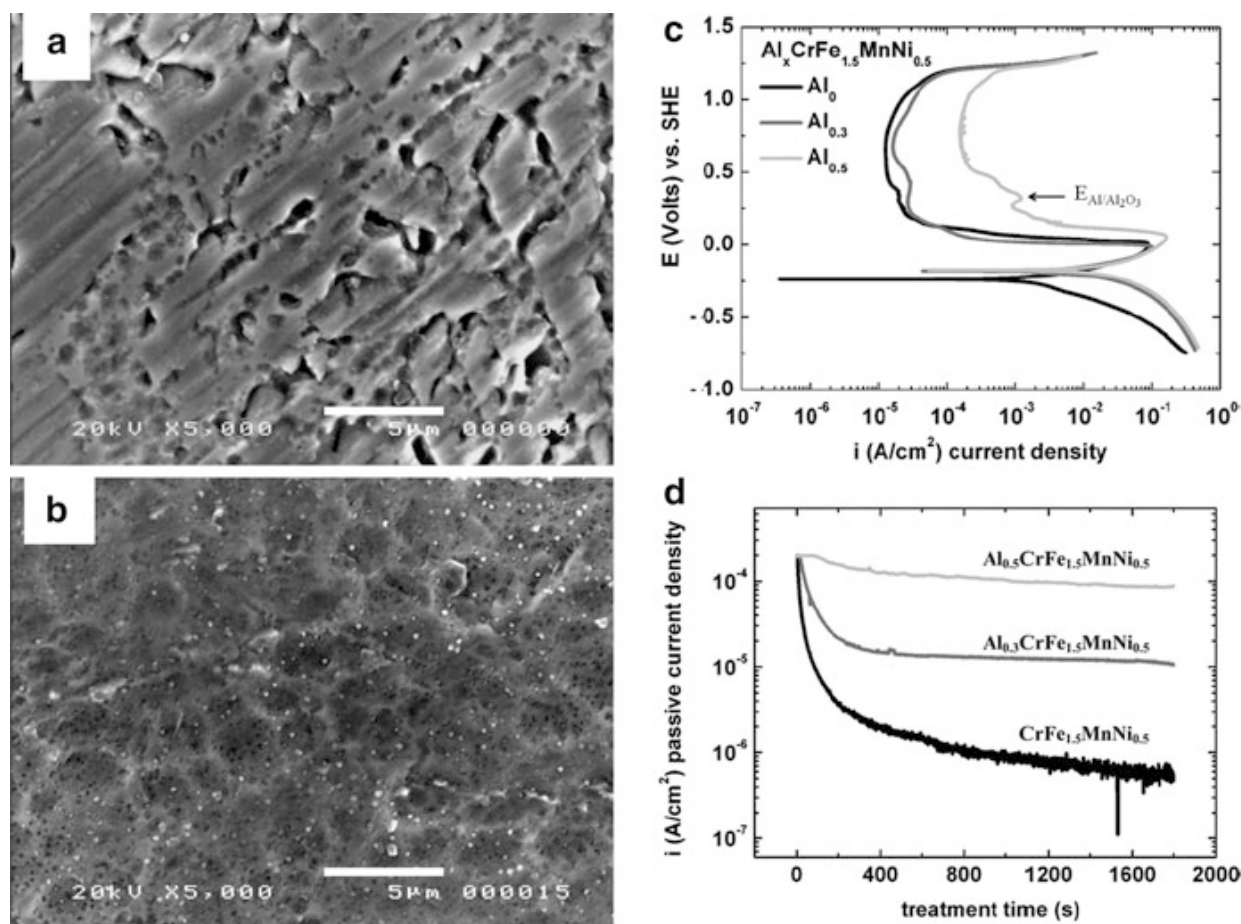


Fig. 7.13 SEM images of (a) CrFe_{1.5}MnNi_{0.5}, (b) Al_{0.3}CrFe_{1.5}MnNi_{0.5} alloys subject to anodic treatment at a passive potential of 0.7 V_{SHE} in 15 % H₂SO₄ solution, (c) anodic polarization curves for alloy Al_xCrFe_{1.5}MnNi_{0.5} in 15 % H₂SO₄ solution, showing an oxygen evolution potential at 1.2 V_{SHE} with a varying passive current density, i_{pass} (15–200 μ A/cm²) as the aluminum contents increase from Al₀– to Al_{0.5}CrFe_{1.5}MnNi_{0.5}, and (d) chronoamperometric curves for Al_xCrFe_{1.5}MnNi_{0.5} ($x = 0, 0.3$, and 0.5) alloys at a constant potential of 0.7 V_{SHE} in 15 % H₂SO₄ solution [40, 41]

show the difference in surface morphology after the anodizing in the presence with 0.25 N NaCl, as shown in Fig. 7.12 [41].

Inhibiting Critical pitting temperature (CPT) [18, 42–44] is the lowest temperature on the test surface at which stable propagating pitting occurs under specified test conditions. CPT determined by ASTM G48-03 and ASTM G150-99 is suitable for ranking the susceptibility of stainless steels and other alloys like HEAs. It is well known that Cl^- ions break down passivity or prevent its formation in Fe, Cr, Ni, Co, and the stainless steel, because Cl^- ion penetrates the oxide film through pores or defects easier than do other ions, e.g., SO_4^{2-} , or Cl^- may colloidally disperse the oxide film and increase its permeability. In other words, adsorbed chloride ions increase the exchange current, i.e., (decrease overvoltage, η) for anodic dissolution of the metal. The inhibiting effect of the SO_4^{2-} ions on the pitting potential (E_{pit}) and critical pitting temperature (CPT) of the alloy $\text{Co}_{1.5}\text{CrFeNi}_{1.5}\text{Ti}_{0.5}\text{Mo}_{0.1}$ results from the chloride solutions [32, 45, 46]. The values of CPT for the alloy in 0.1, 0.5, and to 1 N NaCl solution are 70, 65, and 60 °C, respectively; CPT apparently decreases with the increasing $[\text{Cl}^-]$ [47]. The values of E_{pit} vary linearly with the logarithm of chloride concentrations; they are $E_{\text{pit}} \text{ (mV)} = 551 - 295\log[\text{Cl}^-]$ at 70 °C, and $E_{\text{pit}} = 470 - 353\log[\text{Cl}^-]$ at 80 °C. The addition of SO_4^{2-} ions to chloride solutions has therefore the inhibiting effect on both E_{pit} and CPT [32], as shown in Figs. 7.11 and 7.13. The anodic polarization of this HEA exhibits an S-shape active-passive feature followed by transpassive corrosion which is normally beyond the stability of H_2O . Adding NaCl to the sulfate solution, the transpassive potential ($E_{\text{tr}} \cong 1.2 \text{ V}_{\text{SHE}}$) would shrink to a lower potential required for the pitting occurrence. Figure 7.11 shows that the increase in Cl^- salt shifts the pitting potential to more active values. Adding sulfate to the chloride-containing solution would cause not only an increased potential against the pitting but also an increased CPT [32] for pit nucleation and growth. In addition to sulfate ions, other anodic inhibitors such as NO_3^- , NbO_4^{-2} , ClO_4^- , $\text{C}_2\text{H}_3\text{OO}^-$, and $\text{C}_7\text{H}_5\text{O}_2^-$ are also found to be effective in the Cl^- solutions for inhibiting the pitting corrosion [32].

Effect of Heat Treatment Heat treatments are often adopted in processing the inhomogeneities of the cast and cold-worked structures to achieve peak hardness and enhanced mechanical properties in the growth of precipitates. Whenever phases in an alloy constitute the electrodes of local-action cells, their removal appreciably improves corrosion resistance. Between the separated phases, numerous galvanic couples form; the type and intensity of the corrosion depend on the electrochemical natures of each individual phase and the relative physical size.

The microstructure of the as-cast $\text{Al}_{0.5}\text{CoCrFeNi}$ comprises an FCC solid solution matrix and Al,Ni-rich phases. At aging temperatures between 350 and 950 °C, the alloy microstructure comprises an FCC + BCC solid solution and various forms of Al(Ni, Co, Cr, Fe) phases. Both the as-cast and aged $\text{Al}_{0.5}\text{CoCrFeNi}$ are considerably corroded in 3.5 wt.% NaCl solution because of segregation of the Al,Ni-rich precipitate in the FCC matrix [24, 48]. Electrochemical parameters of the Cu-bearing alloy $\text{Cu}_{0.5}\text{CoCrFeNi}$ after various aging temperatures tested in

3.5 wt.% NaCl at 25 °C show all of the as-cast and heat-treated specimens possessing i_{corr} in the range of 2.03×10^{-9} to $4.58 \times 10^{-8} \text{ Acm}^{-2}$ at E_{corr} varying from -0.28 to $-0.41 \text{ V}_{\text{SCE}}$ ($V_{\text{SHE}} (\text{Volt}) = V_{\text{SCE}} + 0.241$) in response to the aging temperature from 350 to 1350 °C; E_{pit} falls in a range between 0.07 and 0.05 V_{SCE} . The copper segregation in this particular HEA as a result of aging forms a nonprotective passive film where the Cl^- ions preferentially attack the sensitivity zone at a significantly different potential from the Cu-rich phase. The formation of a Cu-rich phase and a Cr-rich phase with different potentials in the alloy $\text{Cu}_{0.5}\text{CoCrFeNi}$ can lead to preferential galvanic corrosion [49, 50].

Effect of Work The HEA $\text{Al}_5\text{Cr}_{12}\text{Fe}_{35}\text{Mn}_{28}\text{Ni}_{20}$ is hardenable and can be worked up to 60 % from its cast structure. An extensive passivity ($\Delta E \geq 1.2 \text{ V}$) has been observed with a passive current density ($5 \mu\text{A}/\text{cm}^2$) which only slightly increases with the increasing cold work, as observed in 1 N H_2SO_4 solution. The corrosion current density (i_{corr}) falls in the range of $\sim 10 \mu\text{A}/\text{cm}^2$ that makes this alloy $\text{Al}_5\text{Cr}_{12}\text{Fe}_{35}\text{Mn}_{28}\text{Ni}_{20}$ an efficient anode for the production of oxygen, since the oxygen overvoltage is negligibly small as observed in this particular HEA, i.e., the potential for oxygen evolution is almost right on the equilibrium potential, 1.23 V for the O_2/OH^- reaction [51]. For pure iron in the similar environment, oxygen is not evolved until the potential exceeds the equilibrium value by several tenth of a volt. A few shallow pits resulting from the underlying cast structure appear and seem independent of the degree of cold work [51]. However, in Cl^- -containing environments, cold work can effectively promote the pitting potential toward noble direction. Cold work on this HEA can electrochemically transform the pitting corrosion into more or less a uniform corrosion. In NaCl solution, the anodic polarization curve shows an unequivocal E_{pit} at 0.15 V_{SHE} , $i_{\text{pass}} \sim 1 \mu\text{A}/\text{cm}^2$, and the pit size and its distribution decrease as the cold work increases [51].

Coating for Protection The field of HEA coating is new, and some of the recent studies have reported fabrication of HEA coatings by various methods like magnetron sputtering, electrolytic spark process, plasma arc cladding, and also by laser processing [52]. It is more intuitive to use HEA as coating than bulk so as to take advantage of the properties possessed by these alloys. High-entropy alloy coatings synthesized on aluminum 1100 substrate by laser surface engineering have shown an enhanced corrosion resistance for the coatings in neutral NaCl solutions. The AlFeCrCoNi-based system processed with a double layer/ 25 J mm^{-2} experienced minimal or no pitting corrosion due to the minimum compositional dilution and uniform distribution of the HEA in the coating. This system has shown an excellent corrosion resistance because the presence of corrosion resistant elements Ni, Cr, and Co and lower Al contents have been reported to be beneficial [24, 52]. For instance, a lowest corrosion current density, i_{corr} of $0.3 \mu\text{A}/\text{cm}^2$ at E_{corr} of $-730 \text{ mV}_{\text{SCE}}$, has been achieved using 25 J mm^{-2} for the AlCoCrFeNi-coated aluminum 1100.

7.5 Hydrogen Storage Properties of HEAs

The greenhouse effect is principally caused by the emission of CO₂. Various green energies without CO₂ emission such as hydrogen, solar, and wind power have been widely explored. Hydrogen energy is effective and convenient, but the storage of hydrogen is an important issue because of the flammability and explosion danger of hydrogen. Among various techniques of hydrogen storage, metal hydride has been regarded as an excellent hydrogen storage material because of its safety, low cost, high storage capacity per volume, and high absorption/desorption reversibility. LaNi₅, an important metal hydride, has been commercialized. However, it contains rare earth La and also expensive Ni. As a result, other cheap metal hydride systems having at least similar performance are highly demanded. The increase in the number of components in hydrogen-storing alloys has recently become a major developing direction in improvement of the hydrogen storage properties especially hydrogen absorption, hydrogen desorption, and life cycle. Moreover, HEAs have been explored in order to develop those potential compositions satisfying hydrogen storage requirements [53, 54].

The first HEA system designed for hydrogen storage alloys is based on equimolar CoFeMnTiVZr reported by Kao et al. [2]. The CoFeMnTiVZr HEA has a single AB₂ C14 structure (an ordered HCP structure) in which Ti and Zr are thought to occupy the A sites while Co, Fe, Mn, and V to occupy the B sites. The substitution of different elements with similar atomic size and chemical properties due to a high-entropy effect in the alloy system lowers the total free energy. A single C14 Laves phase is present in CoFeMnTi_{0.5–2.5}VZr, CoFeMnTiV_{0.4–3.0}Zr, and CoFeMnTiVZr_{0.4–3.0} alloys before and after pressure-composition isotherm (PCI) tests. Therefore, the absorption and desorption of hydrogen and the hydrogen storage properties of such CoFeMnTi_xV_yZr_z alloys can be improved by varying greatly the Ti, V, and Zr contents without changing the C14 crystal structure. The factor that dominates the maximum hydrogen storage capacity (H/M)_{max} is the affinity between the alloy elements and hydrogen. Since Ti and Zr are involved in hydrogen absorption in CoFeMnTi_xVZr (denoted as Ti_x) and CoFeMnTiVZr_z (denoted as Zr_z) alloys, the results show that (H/M)_{max} increases with x and z in the ranges $0.5 \leq x \leq 2$ and $0.4 \leq z \leq 2.3$, respectively. The maximum H_2 absorption is 1.8 wt.% for CoFeMnTi₂VZr alloy at ambient temperature. Figure 7.14 shows the PCI curve for CoFeMnTiV_yZr (denoted as V_y) alloy at 25 °C. This confirms that the additions of Ti and Zr promote the absorption of hydrogen. The decrease in (H/M)_{max} in alloys Ti_{2–2.5} and Zr_{2.3–3.0} is attributed to the serious segregation of Ti and Zr.

The kinetics of hydrogen absorption of Ti_x, V_y, and Zr_z alloys at 25 and 80 °C, as well as the time required for these alloys to absorb 90 % of their absorption capacity, $t_{0.9}$, were measured and determined. The $t_{0.9}$ parameter is a convenient indicator for the estimation of the hydrogen absorption kinetics of alloys. Figure 7.15 shows the absorption kinetic curve at 25 °C for Zr_z alloys. The time of $t_{0.9}$ is less than 60 s.

Fig. 7.14 PCI curves for CoFeMnTiV_yZr (V_y) alloys at 25 °C [2]

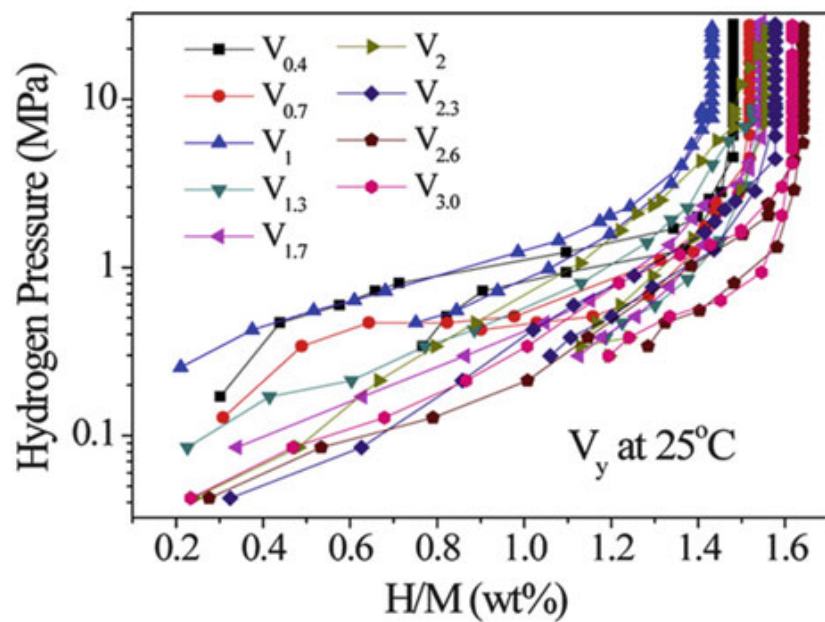
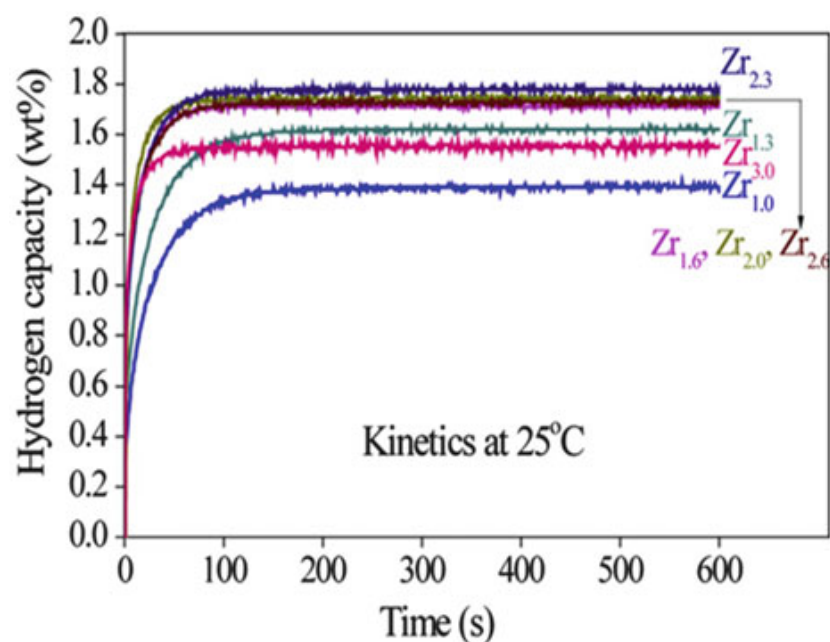


Fig. 7.15 Absorption kinetics curves for CoFeMnTiVZrz (Zrz) alloy at 25 °C [2]



After hydrogen desorption, a large amount of hydrogen is retained in alloys Zrz because of the strong bonding between Zr and H. According to PCI tests, the factor that dominates $t_{0.9}$ and the plateau pressure is the size of the interstitial sites that are associated with the lattice constants. Adding Zr or Ti enlarges the interstitial sites of the alloys and expands the lattice with lower compressive atomic stress. Therefore, the $t_{0.9}$ values and plateau pressures of alloys Zrz and Ti_x decrease as z and x increase.

From the average formation enthalpy ΔH_{cal} of various hydrides t (H/atom)_{max} is found to be a linear function of ΔH_{cal} in A₂B and AB₅ alloy systems as shown in Fig. 7.16 [2]. Although it is nonlinear, for AB and AB₂ (including Ti_x, V_y, and Zrz) systems, (H/atom)_{max} is still strongly related to ΔH_{cal} for Ti_x, V_y, and Zrz. By varying the relative content of the three elements or adding other elements while keeping the single C14 structure, many new metal hydrides with high-hydrogen storage potential might be explored.

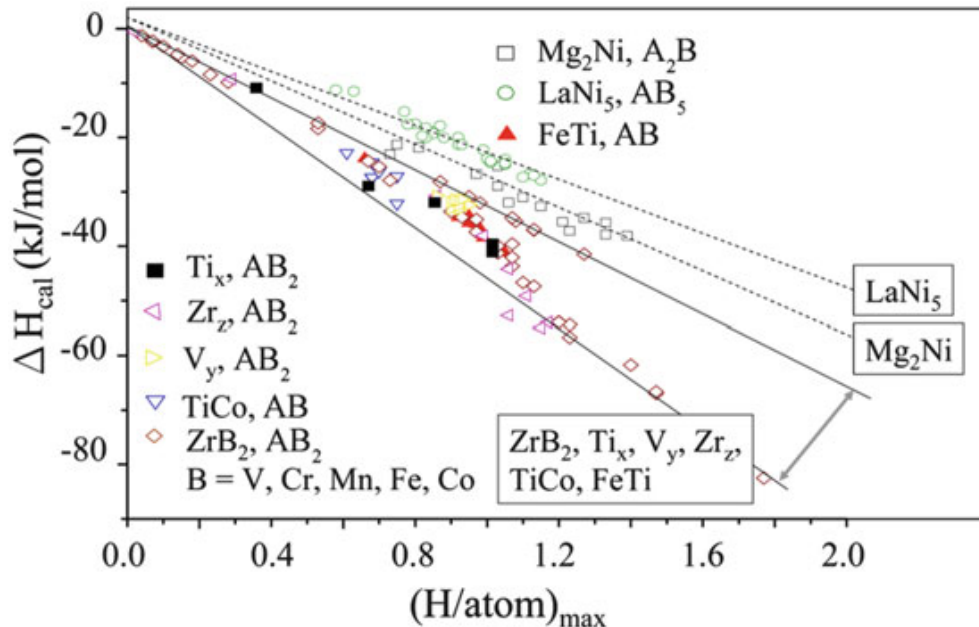


Fig. 7.16 $(H/\text{atom})_{\text{max}}$ versus ΔH_{cal} curves for Mg_2Ni (A_2B type), LaNi_5 (AB_5 type); TiFe and TiCo (AB type); and ZrB_2 , Ti_x , V_y , and Zr_z (AB_2 type) [2]

Although only a very small number of HEAs has been studied for functional properties, many interesting and sometimes unique results have been reported. For example, the $\text{Al}_{2.08}\text{CoCrFeNi}$ alloy has extremely low TCR over a wide temperature range [4]. This alloy could be used as precision resistor. The $\text{FeCoNi}(\text{AlSi})_{0.2}$ alloy has a good combination of properties, making it a potential soft-magnetic material [5]. In terms of corrosion resistance, some HEAs show better performances than 304 ss or even 316 ss. The hydrogen storage properties also appear encouraging. Other directions for functional applications [6] include but are not limited to nuclear (radiation resistant) materials, electronic materials such as diffusion barriers, electromagnetic-shielding materials, thermoelectric materials, and functional coatings.

7.6 Conclusions and Perspectives

From the review and discussion on various functional properties of HEAs including electrical properties (including superconducting), magnetic properties, electrochemical properties, and hydrogen storage properties, we can conclude that HEAs and HEA-related materials could provide a wide range of data for each property depending on composition and processing. Among them, some have been proven to have comparable properties with respect to conventional materials. Furthermore, interesting phenomena and potentially promising properties better than those of conventional alloys are also observed. Basic properties of components, interactions between components, multielement and even whole-solute matrix, phase and interface morphologies influence physical, chemical, and electrochemical properties. Their correlations and interplays will supplement the underlying principles of

materials science. More researches are needed in the future. HEAs and HEA-related materials with attractive functional properties deserve to be explored and developed from both academic and application-oriented viewpoints.

Acknowledgments J.W.Y, S.K.C, H.C.S, Y.Z, and T.T.Z. would like to thank Dr. Michael C. Gao for his great patience to provide review comments and suggestions from himself and invited experts. They also thank Professor Shou-Yi Chang for his final editing of this chapter with all revisions.

References

1. Chou HP, Chang YS, Chen SK, Yeh JW (2009) Microstructure, thermophysical and electrical properties in $\text{Al}_x\text{CoCrFeNi}$ ($0 \leq x \leq 2$) high-entropy alloys. *Mater Sci Eng B* 163:184–189
2. Kao YF, Chen SK, Sheu JH, Lin JT, Lin WE, Yeh JW, Lin SJ, Liou TH, Wang CW (2010) Hydrogen storage properties of multi-principal-component $\text{CoFeMnTi}_x\text{V}_y\text{Zr}_z$ alloys. *Int J Hydrogen Energy* 35:9046–9059
3. Kao YF, Chen SK, Chen TJ, Chua PC, Yeh JW, Lin SJ (2011) Electrical, magnetic, and hall properties of $\text{Al}_x\text{CoCrFeNi}$ high-entropy alloys. *J Alloys Compd* 509:1607–1614
4. Chen SK, Kao YF (2012) Near-constant resistivity in 4.2–360 K in a B2 $\text{Al}_{2.08}\text{CoCrFeNi}$. *AIP Adv* 2(012111):1–5
5. Zhang Y, Zuo TT, Cheng YQ, Liaw PK (2013) High-entropy alloys with high saturation magnetization, electrical resistivity, and malleability. *Sci Rep* 3(01455):1–7
6. Tsai MH (2013) Physical properties of high entropy alloys. *Entropy* 15:5338–5345
7. Tsaur DG, Chen SK (2012) Nb-containing superconductive high-entropy alloys. Master thesis, Chinese Culture University
8. Wu KY, Chen SK (2013) Superconductivity in NbTaTiZr-based high-entropy alloys. Master thesis, Chinese Culture University
9. Liu TH, Chen SK (2014) Superconductivity in NbZrTi-bearing multi-element alloys. Master thesis, Chinese Culture University
10. Koželj P, Vrtnik S, Jelen A, Jazbec S, Jagličić Z, Maiti S, Feuerbacher M, Steurer W, Dolinšek J (2014) Discovery of a superconducting high-entropy alloy. *Phys Rev Lett* 113(107001):1–5
11. Zhang Y, Zuo TT, Tang Z, Gao MC, Dahmen KA, Liaw PK, Lu ZP (2014) Microstructures and properties of high-entropy alloys. *Prog Mater Sci* 61:1–93
12. Lucas MS, Mauger L, Munoz JA, Xiao Y, Sheets AO, Semiatin SL, Horwath J, Turgut Z (2011) Magnetic and vibrational properties of high-entropy alloys. *J Appl Phys* 109 (7):07E307–07E307-3
13. Zhang KB, Fu ZY, Zhang JY, Shi J, Wang WM, Wang H, Wang YC, Zhang QJ (2010) Annealing on the structure and properties evolution of the CoCrFeNiCuAl high-entropy alloy. *J Alloys Compd* 502(2):295–299
14. Singh S, Wanderka N, Kiefer K, Siemensmeyer K, Banhart J (2011) Effect of decomposition of the Cr-Fe-Co rich phase of AlCoCrCuFeNi high entropy alloy on magnetic properties. *Ultramicroscopy* 111(6):619–622
15. Ma SG, Zhang Y (2012) Effect of Nb addition on the microstructure and properties of AlCoCrFeNi high-entropy alloy. *Mater Sci Eng A* 532:480–486
16. Wang J, Zheng Z, Xu J, Wang Y (2014) Microstructure and magnetic properties of mechanically alloyed FeSiBAlNi (Nb) high entropy alloys. *J Magn Magn Mater* 355:58–64
17. Wang XF, Zhang Y, Qiao Y, Chen GL (2007) Novel microstructure and properties of multicomponent CoCrCuFeNiTi_x alloys. *Intermetallics* 15:357–362

18. Chen YY, Duval T, Hung UD, Yeh JW, Shih HC (2005) Microstructure and electrochemical properties of high entropy alloys – a comparison with type-304 stainless steel. *Corros Sci* 47(9):2257–2279
19. Chen YY, Hong UT, Shih HC, Yeh JW, Duval T (2005) Electrochemical kinetics of the high entropy alloys in aqueous environments – a comparison with type 304 stainless steel. *Corros Sci* 47(11):2679–2699
20. Vetter KJ (1961) Theoretical kinetics: theoretical and experimental aspects. Academic Press Inc, New York, pp 104–120
21. Frangini S, Cristofaro ND, Lascovich J, Mignone A (1993) On the passivation characteristics of a β -FeAl intermetallic compound in sulphate solutions. *Corros Sci* 35:153–159
22. Kao YF, Lee TD, Chen SK, Chang YS (2010) Electrochemical passive properties of $\text{Al}_x\text{CoCrFeNi}$ ($x = 0, 0.25, 0.50, 1.00$) alloys in sulfuric acids. *Corros Sci* 52:1026–1034
23. Cristofaro ND, Frangini S, Mignone A (1996) Passivity and passivity breakdown on a β -FeAl intermetallic compound in sulphate and chloride containing solutions. *Corros Sci* 38:307–315
24. Tang Z, Huang L, He W, Liaw PK (2014) Alloying and processing effects on the aqueous corrosion behavior of high-entropy alloys. *Entropy* 16:895–911
25. Chen YY, Hong UT, Yeh JW, Shih HC (2006) Selected corrosion behaviors of a $\text{Cu}_{0.5}\text{NiAlCoCrFeSi}$ bulk glassy alloy in 288 degrees C high-purity water. *Scr Mater* 54(12):1997–2001
26. Chen YY, Duval T, Hong UT, Yeh JW, Shih HC, Wang LH, Oung JC (2007) Corrosion properties of a novel bulk $\text{Cu}_{0.5}\text{NiAlCoCrFeSi}$ glassy alloy in 288 degrees C high-purity water. *Mater Lett* 61(13):2692–2696
27. Chen YY, Hong UT, Yeh JW, Shih HC (2005) Mechanical properties of a bulk $\text{Cu}_{0.5}\text{NiAlCoCrFeSi}$ glassy alloy in 288 degrees C high-purity water. *Appl Phys Lett* 87(26):261918
28. Lee CP, Chen YY, Hsu CY, Yeh JW, Shih HC (2007) The effect of boron on the corrosion resistance of the high entropy alloys $\text{Al}_{0.5}\text{CoCrCuFeNiB}_x$. *J Electrochem Soc* 154(8):C424–C430
29. ASTM committee, Standard method G61-86, Annual book of ASTM standards (1998) vol. 3.02. ASTM, Philadelphia, p 254
30. Lee CP, Chang CC, Chen YY, Yeh JW, Shih HC (2008) Effect of the aluminium content of $\text{Al}_x\text{CrFe}_{1.5}\text{MnNi}_{0.5}$ high-entropy alloys on the corrosion behaviour in aqueous environments. *Corros Sci* 50(7):2053–2060
31. Pourbaix M (1974) Atlas of electrochemical equilibria in aqueous solutions. NACE, Houston
32. Chou YL, Yeh JW, Shih HC (2011) Effect of inhibitors on the critical pitting temperature of the high-entropy alloy $\text{Co}_{1.5}\text{CrFeNi}_{1.5}\text{Ti}_{0.5}\text{Mo}_{0.1}$. *J Electrochem Soc* 158:C246–C251
33. Chou YL, Yeh JW, Shih HC (2011) Pitting corrosion of $\text{Co}_{1.5}\text{CrFeNi}_{1.5}\text{Ti}_{0.5}\text{Mo}_{0.1}$ in chloride-containing nitrate solutions. *Corrosion* 67:065003
34. Sigimoto K, Sawada Y (1977) The role of molybdenum additions to austenitic stainless steels in the inhibition of pitting in acid chloride solutions. *Corros Sci* 17:425–445
35. Chou YL, Yeh JW, Shih HC (2010) The effect of molybdenum on the corrosion behavior of the high-entropy alloys $\text{Co}_{1.5}\text{CrFeNi}_{1.5}\text{Ti}_{0.5}\text{Mo}_x$ in aqueous environments. *Corros Sci* 52(8):2571–2581
36. Ogura K, Ohama T (1984) Pit formation in the cathodic polarisation of passive iron. IV: Repair mechanism by molybdate, chromate and tungstate. *Corrosion* 40:47–51
37. Szklarska-Smialowska Z (1986) Pitting corrosion of metals. NACE, Houston
38. Hsu YJ, Chiang WC, Wu JK (2005) Corrosion behavior of FeCoNiCrCu_x high-entropy alloys in 3.5% sodium chloride solution. *Mater Chem Phys* 92:112–117
39. Doğan ÖN, Nielsen BC, Hawk JA (2013) Elevated-temperature corrosion of $\text{CoCrCuFeNiAl}_{0.5}\text{B}_x$ high-entropy alloys in simulated syngas containing H_2S . *Oxid Metals* 80(1–2):177–190
40. Lee CP, Chen YY, Hsu CY, Yeh JW, Shih HC (2008) enhancing pitting corrosion resistance of $\text{Al}_x\text{CrFe}_{1.5}\text{MnNi}_{0.5}$ high-entropy alloys by anodic treatment in sulfuric acid. *Thin Solid Film* 517:1301–1305

41. Lee CP, Shih HC (2008) Corrosion behavior and anodizing treatment of the high-entropy alloys $\text{Al}_{0.5}\text{CoCrCuFeNiB}_x$ ($x = 0, 0.2, 0.6, 1.0$) and $\text{Al}_x\text{CrFe}_{1.5}\text{MnNi}_{0.5}$ ($x = 0, 0.3, 0.5$). Doctor thesis, National Tsing Hua University
42. Brigham RJ, Tozer EW (1973) Temperature as a pitting criterion. *Corrosion* 29:33–36
43. Salinas-Bravo VM, Newman RC (1994) An alternative method to determine CPT of stainless steels in ferric chloride solution. *Corros Sci* 36:67–77
44. Huang PK, Yeh JW, Shun TT, Chen SK (2004) Multi-principal-element alloys with improved oxidation and wear resistance for thermal spray coating. *Adv Eng Mater* 6:74
45. DeBarry DW (1993) In: Reviews on corrosion inhibitor science and technology. Raman A, Labine P (eds). NACE, Houston, p II-19-1
46. Castle JE, Qiu JH (1990) The application of ICP-MS and XPS to studies of ion selectivity during passivation of stainless steels. *J Electrochem Soc* 137:2031–2038
47. Burstein GT, Souto RM (1995) Observations of localised instability of passive titanium in chloride solution. *Electrochim Acta* 40:1881–1888
48. Lin CM, Tasi HL (2011) Evolution of microstructure, hardness, and corrosion properties of high-entropy $\text{Al}_{0.5}\text{CoCrFeNi}$ alloy. *Intermetallics* 19:288–294
49. Lin CM, Tasi HL, Bor HY (2010) Effect of aging treatment on microstructure and properties of high-entropy $\text{Cu}_{0.5}\text{CoCrFeNi}$ alloy. *Intermetallics* 18:1244–1250
50. Lin CM, Tasi HL (2011) Effect of aging treatment on microstructure and properties of high-entropy $\text{FeCoNiCrCu}_{0.5}$ alloy. *Mater Chem Phys* 28:50–56
51. Lin SY, Shih HC (2011) Studies on electrochemical corrosion properties of high-entropy alloy: $\text{Al5Cr12Fe35Mn28Ni20}$. Master Thesis. Chinese Culture University
52. Shon YK, Joshi SS, Katakam S, Rajamure RS, Dahotre NB (2015) Laser additive synthesis of high entropy alloy coating on aluminum: corrosion behavior. *Mater Lett* 142:122–125
53. Lin JT, Chen SK (2007) Design and study on the hydrogen-storage 4- to 7-element high-entropy alloys based on composition of TiVFe. Master's thesis, National Tsing Hua University
54. Sheu JH, Chen SK (2008) Hydrogen storage in $\text{CoCrFeMnTiV}_x\text{Zr}_y$ ($0.4 \leq x, y \leq 3$) high-entropy alloys. Master's thesis, National Tsing Hua University

Chapter 8

Prediction of Structure and Phase Transformations

Michael Widom

Abstract This chapter introduces calculational methods that can be used for ab initio structure prediction in multicomponent alloy systems, with an emphasis on concepts relevant to high-entropy alloys. Specifically, we will address density functional-based calculation of $T = 0\text{ K}$ total energies. Extension to finite temperature will use cluster expansions for the energies to obtain the chemical substitution entropy that characterizes the high-entropy alloy family. Additional contributions such as vibrational and electronic entropies will be included as needed. We describe molecular dynamics and Monte Carlo simulation methods and the types of information that can be obtained from them. Example applications include three high-entropy alloy families, Cr-Mo-Nb-V, Nb-Ti-V-Zr, and Mo-Nb-Ta-W, and their binary and ternary subsystems.

Keywords First principles • Density functional theory (DFT) • Hybrid Monte Carlo/molecular dynamics (MC/MD) • Entropy sources • Configurational entropy • Vibrational entropy • Electronic entropy • Helmholtz free energies • Phonon vibration • Cluster expansion • Phase stability • Phase transformations • Pair distribution function • Density of states • Temperature effect • Body-centered cubic (BCC) • High-entropy alloys (HEAs)

8.1 Introduction

High-entropy alloys form when multiple chemical species intermix freely on a simple underlying crystal lattice, forming a thermodynamically stable single phase. However, most mixtures of chemical species will not form a high-entropy alloy. Instead, the mixtures separate into multiple distinct phases, and some of these phases might be complex crystal structures. Thermodynamic states of mixtures as functions of chemical composition and temperature are recorded in phase diagrams. While the stable crystal structures of almost all pure elements are known, as are the phase diagrams and crystal structures of most binary intermetallics, many ternary

M. Widom (✉)

Department of Physics, Carnegie Mellon University, Pittsburgh, PA, USA

e-mail: widom@cmu.edu

phase diagrams have not been determined, and almost no quaternary or higher phase diagrams are known. The discovery of high-entropy alloys provides an opportunity to make progress on this scientific frontier.

This chapter outlines how basic physical principles can be used to predict the formation and stability of high-entropy alloys. Conceptually, the approach is straightforward. Every thermodynamic phase α has a Gibbs free energy G_α that depends on composition and temperature. We must calculate the free energies of different phases or combinations of phases and find the minimum. In practice, we use quantum mechanics to calculate the total energy of specific crystal structures of interest, yielding the zero temperature limit of free energy. We then extend the free energy to finite temperature by using methods of statistical mechanics to include a variety of sources of entropy. Examples will be given drawn from mixtures of refractory elements. We will discuss certain binary compounds in detail and then move on to ternaries and finally quaternaries. The concepts and procedures described here generalize directly to non-refractory metals and to quinary and higher-order alloy systems, although these lie outside the scope of this chapter.

Our approach differs from an alternative and highly successful method known as CALPHAD (see Chap. 12) for calculation of phase diagrams. CALPHAD uses databases of thermodynamic information based on experimental measurements (when available) supplemented by numerical interpolation schemes to fill in unknown territory. Ultimately, CALPHAD should be merged with first principles total energy calculations to exploit the relative advantages of each. First principles excel at prediction of low-temperature stability, obtaining enthalpies that while not exact are simply unavailable from experiment. CALPHAD excels at modeling of transition temperatures and phase diagram topology, as these are often determined experimentally with high reliability.

To illustrate these methods, we discuss in detail three overlapping examples of four-component alloy systems consisting of refractory metals. We examine Mo-Nb-Ta-W, which is known to readily form a stable high-entropy alloy [36]; Nb-Ti-V-Zr, which exhibits fine-grained second-phase precipitation [35]; and Cr-Mo-Nb-V, which has not been considered experimentally to date, but which we predict should be stable at high temperature and decompose at low temperature. Understanding the quaternary alloy system requires, in addition, understanding all four ternary and all six binary subsystems. Indeed, our calculations confirm or shed new light on several experimentally known phase diagrams in addition to making some new predictions.

8.2 Total Energy Calculation, $T = 0\text{ K}$

Our goal in this section is to predict the $T = 0\text{ K}$ limit of alloy phase diagrams by calculating the total energy of potential ground-state structures and finding the minimum. Two major and distinct challenges arise immediately: (1) how to calculate the energy of a given crystal structure and (2) how to choose candidate

structures whose energies should be determined. The first problem has a conceptually simple, though technically challenging, answer. We will apply known laws of quantum mechanics that directly provide the desired quantity. The calculation will be made tractable through the use of well-established approximations of density functional theory [28]. The second problem has no obvious solution. Although at a given composition there should be a unique minimum energy structure, we know of no method to predict what it will be. Since there are infinitely many conceivable structures, we cannot calculate all possibilities. Rather, we will make a finite number of plausible guesses, based on a combination of physical intuition, chemical analogy, and computer-assisted search. This latter approach will exploit the fact that high-entropy alloy families tend to form simple crystal lattices so that a cluster expansion of the total energy can accelerate our search for the ground state.

8.2.1 Density Functional Theory

Quantum mechanics tells us that the ground-state energy of a system of interacting particles is the lowest eigenvalue of the system Hamiltonian. The Hamiltonian is an operator that expresses the total energy by adding together the kinetic and potential energies. For bulk matter, we may separate atoms into positively charged nuclei, which are sufficiently massive that they may be treated as fixed point charges, and negatively charged electrons, whose mass is sufficiently low that they must be described through a position-dependent many-body wave function that is the eigenvector of the Hamiltonian. Electrons interact with each other and with the nuclei through the Coulomb potential. The eigenvalue equation to be solved is the Schrodinger equation of the system,

$$H\Psi^{(N)}(\mathbf{r}_1, \dots, \mathbf{r}_N) = E\Psi^{(N)}(\mathbf{r}_1, \dots, \mathbf{r}_N), \quad (8.1)$$

with $\Psi^{(N)}$ the many-body wave function.

The resulting interacting many-body problem, though well posed, is computationally intractable owing to the high dimensionality of the Hilbert space in which the many-electron wave function must be expressed. Hohenberg and Kohn [16] argued the many-body calculation could be replaced with the simpler problem of finding the electron density $\rho(r)$ that minimizes a total energy functional $E[\rho(r)]$. Kohn and Sham [23] reexpressed this minimization problem as a coupled set of single-electron Schrodinger equations that can be solved individually (but self-consistently):

$$\left(\frac{-\hbar^2}{2m} \nabla_{\mathbf{r}}^2 + V_e(\mathbf{r}) + \int d\mathbf{r}' \frac{\rho(\mathbf{r}')}{|\mathbf{r} - \mathbf{r}'|} + V_{xc}[\rho(\mathbf{r})] \right) \psi_i(\mathbf{r}) = \varepsilon_i \psi_i(\mathbf{r}). \quad (8.2)$$

The terms on the left-hand side represent, respectively, the single-electron kinetic energy, the “external potential” (electron-ion coupling), electron-electron interactions, and the “exchange-correlation potential.” The equations for the single-particle wave functions ψ_i are coupled through the electron density

$$\rho(\mathbf{r}) = \sum_{i=1}^N |\psi_i(\mathbf{r})|^2. \quad (8.3)$$

Although the replacement can be exact in principle, in practice the exact form of Eq. (8.2) is unknown, as it collects difficult to calculate effects of electron exchange and correlation into the unknown exchange-correlation potential $V_{xc}[\rho(r)]$ that is a functional of the electron density. The exchange-correlation functional can be approximated to accuracy sufficient for our present purposes using the familiar local density approximation [4] (LDA) that replaces the exchange-correlation functional with the value of the exchange-correlation potential of a uniform electron gas whose density matches the local value of $\rho(r)$ or using the generalized gradient approximation [32] (GGA) that supplements the local density approximation with corrections dependent on the gradient of the density at the same point.

For the examples given in this chapter, we solve the equations of density functional theory using a program known as VASP [24, 25]. This program exploits translational symmetry of crystal structures to express the single-electron wave functions in a plane wave basis (i.e., a Fourier series). To ensure convergence of total energies, we use dense k -point grids and truncate the basis at plane wave energy of 400 eV, significantly higher than the VASP defaults. We select the Perdew-Burke-Ernzerhof generalized gradient approximation [32] and also make an approximation that treats atomic core electrons approximately based on a variant of pseudopotential known as the projector augmented wave method [3, 26].

No simpler approach is feasible for total energy calculation of high-entropy alloys. Popular approaches such as pair potentials, embedded atom potentials, and similar empirical forms can be useful for modeling pure elements and even some binary compounds. Unfortunately, these approximations contain adjustable parameters whose number proliferates with each additional chemical species, making them impossible to fit accurately as the number of chemical species increases. In contrast, the complexity and accuracy of density functional theory is relatively independent of the number of species present. The greatest utility of empirical potentials would be the study of abstract model systems whose properties can be defined for theoretical and computational convenience rather than realism.

8.2.2 *Ground-State Prediction*

The lowest-energy structure is known as the ground state and is the stable form of matter in the limit $T \rightarrow 0$ K. Note that we adopt the absolute Kelvin scale of temperature throughout this chapter. Owing to the third law of thermodynamics

(vanishing entropy), this structure is essentially unique for a given composition and pressure. Since we fix the pressure (generally at $P = 0$, which approximates atmospheric pressure), our energy is actually an “enthalpy”

$$H = \min_V [E(V) + PV], \quad (8.4)$$

and the corresponding free energy at finite temperature is the Gibbs free energy

$$G(T, P) = H - TS. \quad (8.5)$$

We need a notation for crystal structures. Among many possible schemes, we adopt the Pearson notation as especially convenient. The Pearson notation consists of lowercase letters a, m, o, t, h , and c indicating, respectively, asymmetric, monoclinic, orthorhombic, tetragonal, hexagonal, or cubic; an uppercase letter *PRFICBA* indicating primitive, rhombohedral, or some type of centering; and a number indicating the number of atomic sites per unit cell. For example, $hP2$ indicates HCP, while $cI2$ indicates BCC. Because many different compounds can form the same crystal structure, and vice versa, we will append the Pearson symbol to the compound name to reduce ambiguity. Thus, Cr.cI2 and Nb.cI2 are BCC chromium and niobium, while $\text{Cr}_2\text{Nb.cF24}$ and $\text{Cr}_2\text{Nb.hP12}$ are Laves phases (specific types of tetrahedrally close-packed Frank-Kasper phases), with $hP12$ being Strukturbericht C14 (prototype MgZn_2) and $cF24$ being Strukturbericht C15 (prototype Cu_2Mg).

The difficulty is finding the unique minimum enthalpy structure, because there are infinitely many conceivable arrangements among which we must find the minimum. Fortunately, we often have experimental hints, as well as chemical and physical intuition and computer algorithms, that allow us to focus our search on a limited set of possibilities. By employing such constraints, we risk the possibility that we exclude the true ground state and will always be confronted with an associated uncertainty in our predictions.

For most pure elements, experimentalists voice little doubt about the stable form at low temperature and atmospheric pressure, and DFT calculations generally agree this form is the lowest in energy among competing possibilities [29] (elemental boron is a notable exception [43]). In many cases, the elements undergo allotropic transitions to alternative structures as temperature rises. Notably, among the refractory metals in the Sc and Ti columns of the periodic table (groups IIIA and IVA), the ground-state structure is a high-density, close-packed (FCC or HCP) structure. At higher temperatures, the structure transforms to a lower-density, loosely packed BCC structure. The mechanism for this transformation is the entropy of thermal vibrations, as will be explained in detail in Sect. 8.3.2.

Moving from pure elements to compounds introduces a composition variable x that is one-dimensional in the case of a binary compound but multidimensional in general. Many compounds exist as a pure phase at a precise value or over a limited range of compositions x . The thermodynamic state at composition x between

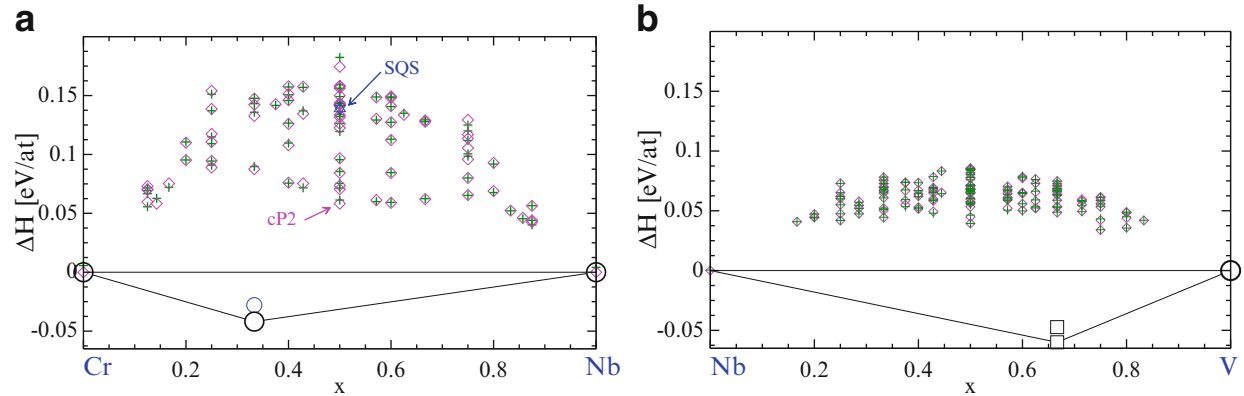


Fig. 8.1 Enthalpies of formation in the (a) Cr-Nb and (b) Nb-V binary alloy systems. Plotting symbols use *thick circles* for known low-temperature stable phases, *thin circles* for known high-temperature phases, *squares* for hypothetical structures, *diamonds* for representative structures of the BCC solid solution, and plus signs for cluster expansion fits

two pure phases of composition $x_\alpha < x < x_\beta$ consists of a mixture of the two phases α and β . Figure 8.1a, which plots enthalpies of formation (enthalpy difference ΔH between the compound at composition x and the pure elements at compositions 0 and 1) of various structures containing elements Cr and Nb, illustrates the point. In this figure, $\Delta H < 0$ indicates structures whose enthalpy is lower than a mixture of pure crystalline Cr and Nb. Here, we find two negative enthalpy compounds, both at composition Cr_2Nb . At compositions with Nb content less than $x = 1/3$, the ground state corresponds to a mixture of two coexisting crystals, one of pure Cr.cI2 and the other of pure $\text{Cr}_2\text{Nb}.c\text{F}24$. The enthalpy of formation of this mixture lies along the tie-line joining the enthalpy of formation of $\text{Cr}_2\text{Nb}.c\text{F}24$ to Cr.cI2. Similarly, at compositions $x > 1/3$, the ground state consists of $\text{Cr}_2\text{Nb}.c\text{F}24$ coexisting with Nb.cI2.

The vertices Cr.cI2, $\text{Cr}_2\text{Nb}.c\text{F}24$, and Nb.cI2, together with the line segments joining them, constitute the convex hull of a scatter plot of formation enthalpy ΔH vs. composition x . This convex hull forms the sequence of predicted ground states as a function of composition. The structure $\text{Cr}_2\text{Nb}.h\text{P}12$ has a negative enthalpy of formation, indicating it is favorable to form from pure elements, but it lies above the convex hull by an amount $\Delta E = 0.01 \text{ eV/atom}$, indicating it is thermodynamically unstable relative to the ground state. Indeed, the hP12 variant of Cr_2Nb is reported to be a high-temperature stable phase.

We have neglected compositional variability of the stable phases, treating them as “line compounds” of fixed stoichiometry and thus ruling out, for example, solubility of Cr in Nb. This is appropriate in the limit of low temperature, but at elevated temperature the scatter plot of discrete enthalpies must be replaced by a set of Gibbs free energy functions $\{G_\alpha(T, P, x)\}$. For N chemical species, the composition variable x lies within a simplex of dimension $N - 1$. The convex hull of this set forms the sequence of predicted stable phases, consisting of continuously variable composition whenever the free energy is minimized by a single phase α , separated by coexistence regions where the free energy is minimized by a combination of phases. In this latter case the convex hull is simultaneously tangent to the

Gibbs functions of the coexisting phases, with the condition of tangency implying equality of chemical potentials of each chemical species in all coexisting phases [5]. A lever rule relates the mole fractions of the coexisting phases and their individual compositions $\{x_\alpha\}$ to the global average composition x .

Also visible in Fig. 8.1a are a variety of hypothetical crystal structures formed by decorating sites of a BCC lattice with Cr and Nb atoms in various specific repeating patterns. We shall refer to these structures as representative structures of the BCC solid solution. Keep in mind that the true solid solution is infinite in size and contains within it every possible finite representative structure. One specific such structure, known as a special quasirandom structure [46] (SQS, see Chap. 10), is chosen because its correlation functions closely match an idealized perfectly random distribution of Cr and Nb among the BCC lattice sites. The SQS can be considered as a realization of the disordered structure represented by the coherent potential approximation (CPA, see Chap. 9). Another structure, which is the most ordered possible arrangement of two species on a BCC lattice, is cP2 (Strukturbericht B2, prototype CsCl) which places one species at cube vertices and the other species at cube centers. All of these decorated BCC lattices have positive enthalpy of formation indicating their formation is unfavorable at low temperature, although it is possible that some source of entropy could stabilize them at high temperature.

For convenience, we give here some representative energies of SQS and cP2 structures in three quaternary alloy families that we will focus on in this chapter, in addition to their binary and ternary subsystems.

Our ground-state prediction remains tentative because it includes only finitely many trial structures. There is no guarantee that the experiment has found *all* the relevant structures, as it can be quite difficult to ensure the experimental samples remain in thermodynamic equilibrium, especially at low temperatures where atomic diffusion vanishes. A variety of alternative methods exist that aid in the exploration of potential ground states. Probably the most powerful, in the sense that the odds of success are high, is invoking chemical and geometrical analogy [29]. Another method for generating trial structures is known as genetic or evolutionary algorithms [12, 34]. This method generates random trials and then explores combinations of successful attempts to create new trials. While it has enjoyed some successes, its efficiency in general remains to be proven. Other methods include basin hopping [40] and minima hopping [13], which jump between nearby potential energy minima. A final method, the cluster expansion, proves quite effective for high-entropy alloys, as we discuss below in Sect. 8.2.3.

Among the columns of the periodic table starting with Ti, V, and Cr, the reported structures include the hP2, cl2, cF24, and hP12 structures previously discussed. However, not every structure occurs in every combination of elements. An example of discovery by chemical analogy is illustrated in Fig. 8.1b, where we examine the same structures (cF24, hP12, and BCC-based structures) for Nb-V as we did previously for Cr-Nb. Here, we use square plotting symbols to indicate that cF24 and hP12 are hypothetical structures, proposed on the basis of chemical analogy. Although they have not been reported to occur experimentally, there is a clear

energetic preference for $\text{NbV}_2\text{hP12}$, well outside the expected errors of DFT formation enthalpies, which are typically a few meV/atom. In Sects. 8.3.1 and 8.3.2, we suggest an explanation for this discrepancy.

Noting that hP12 and cF24 are Laves (Frank-Kasper, F-K) phases characterized by tetrahedral close packing into specific clusters related to icosahedra, we invoke geometric analogy to investigate two other F-K structures, of Pearson types cP8 (A15) and hR13 (μ). We place the smaller Cr atoms at low-coordination sites, while the larger Nb atoms occupy higher-coordination sites. We find that the μ phase slightly outperforms the decorated BCC lattices, but in fact neither of these alternative F-K structures produce a new ground state for Cr-Nb, in agreement with experiment.

8.2.3 Cluster Expansion

Because the high-entropy alloys distribute multiple chemical species among sites of a common crystal lattice, we can use the underlying lattice structure to our advantage. The idea [6, 9, 45] is to represent the chemical species at each lattice site i with a variable σ_i (here for simplicity we take $\sigma_i = \pm 1$ for the case of two species) and then expand the energy in a series of pair, three-body, and higher interactions,

$$E(\sigma_1, \dots, \sigma_n) = \sum_{i,j} J_{ij} \sigma_i \sigma_j + \sum_{i,j,k} J_{ijk} \sigma_i \sigma_j \sigma_k + \dots \quad (8.6)$$

The cluster interaction coefficients J can be fit to a database of DFT energies. Although the variables are assigned to lattice sites, it is important to note that the coefficients can be fit to *relaxed* energies, so that displacements off the ideal sites caused by size and chemical variation can be included. Given a cluster expansion, it becomes quick and easy to estimate the energies of thousands of trial structures, and then the best predictions can be checked with higher precision with a full DFT calculation. A convenient implementation of this method named the Alloy-Theoretic Automated Toolkit [41, 42] (ATAT) has been placed in the public domain. This is the method that was used to generate the trial BCC decorations of Cr-Nb and Nb-V shown in Fig. 8.1.

The cluster expansion can be extended to multicomponent systems. Figure 8.2 illustrates the case of the Cr-Nb-V ternary. Conveniently, the databases of BCC energies for the three binaries (Cr-Nb, Nb-V, and Cr-V) can be reused as the starting point for the full ternary. In this figure, only the predicted lowest-energy structure is shown at each composition tested. The series of stable Cr-V binaries based on various patterns of chemical order on the BCC lattice (diamonds) demonstrate that formation enthalpies in the Cr-V binary are negative [10, 11]. The stable $(\text{Cr},\text{V})_2\text{Nb}$ sequence has structure cF24, except for V_2Nb which is hP12. Based on these data, we predict that at low temperature any ternary combination of

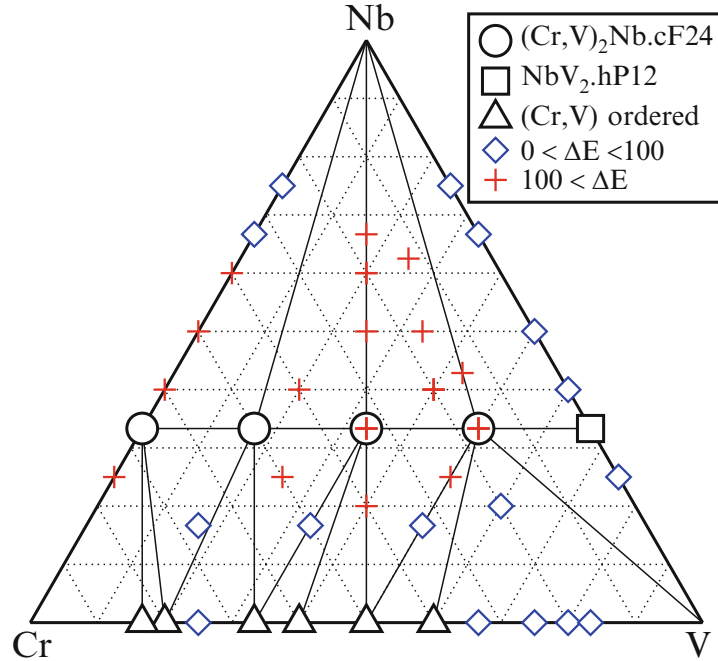


Fig. 8.2 Convex hull of the enthalpy of formation in the Cr-Nb-V alloy system. Predicted stable phases (convex hull vertices) are shown in *black*. Convex hull vertices are connected by tie-lines and by triangular tie-planes corresponding, respectively, to two- and three-phase coexistence regions. Structures above the convex hull by $\Delta E < 100$ meV/atom are shown as *blue diamonds*, while higher-energy structures are shown as *red crosses*

Cr-Nb-V will decompose into a mixture of cF24 or hP12 together with pure elemental or binary BCC-based structures. In the following, we use the cluster expansion to predict the behavior at high temperature.

8.3 Extension to Finite Temperature

In order to predict the phase behavior at high temperature, we combine the quantum-based energetics with principles of statistical mechanics and thermodynamics. Our discussion will be easiest if we neglect thermal expansion. At constant volume, the relevant free energy is the Helmholtz free energy $F(V, T)$, which differs from the Gibbs free energy by the Legendre transform

$$G(T, P) = \min_V [F(V, T) + PV], \quad (8.7)$$

similar to the relationship (Eq. 8.4) of energy and enthalpy. The Helmholtz free energy is given by the logarithm of the canonical partition function

$$F = -k_B T \ln Q, \quad (8.8)$$

where the partition function

$$Q = \frac{1}{N!} \left(\frac{2\pi m k_B}{h^2} \right)^{3N/2} Z \quad (8.9)$$

factorizes into a contribution from the momenta times a configuration integral

$$Z = \int_V \prod_{i=1}^N d\mathbf{r}_i e^{-E(\mathbf{r}_1, \dots, \mathbf{r}_N)/k_B T}. \quad (8.10)$$

The integrand in Eq. (8.10) is known as the Boltzmann factor and is proportional to the probability of a given set of positions $(\mathbf{r}_1, \dots, \mathbf{r}_N)$. In the following, we shall drop the momentum factors, as they are universal to all ordinary matter and hence thermodynamically irrelevant.

Evaluation of the configuration integral Z is our main task. The position-dependent energies $E(\mathbf{r}_1, \dots, \mathbf{r}_N)$ will be obtained from DFT. However, evaluation of the integral requires many evaluations of E , each of which is very time consuming. We will take advantage of the exponential dependence of the Boltzmann factor to make further approximations.

In crystalline solids, atoms typically vibrate within small distances of their equilibrium positions. Indeed, the character of the energy landscape is such that it possesses a collection of local minima with approximately quadratic variation in the vicinity of each minimum. Each local minimum corresponds to a discrete arrangement of atoms that we shall refer to as a “configuration,” while the small continuous displacements consist of mixtures of vibrational phonon modes. Temporarily restricting our attention to a single configuration Γ , we may evaluate the configuration integral $Z(\Gamma)$ by integrating over a neighborhood of Γ . In accordance with Eq. (8.8), we define the free energy of the configuration Γ as the logarithm $F(\Gamma) = -kT \ln Z(\Gamma)$, which we separate into the energy $E(\Gamma)$ of the discrete configuration Γ plus the vibrational free energy $F_v(\Gamma) = E(\Gamma) + F_v(\Gamma)$. Alternatively, we may factorize the configuration integral into separate contributions from the energy of the configuration $E(\Gamma)$ and the vibrational free energy $F_v(\Gamma)$,

$$Z(\Gamma) = e^{-E(\Gamma)/k_B T} e^{-F_v(\Gamma)/k_B T}. \quad (8.11)$$

Since the Boltzmann factor nearly vanishes far from the discrete configurations, the entire configurational integral can be approximated as a sum of integrals around each configuration. If we were to find that F_v depended only weakly on Γ , then in view of the factorization expressed in Eq. (8.11), we could pull a common factor out of the sum,

$$Z \approx \sum_{\Gamma} Z(\Gamma) \approx \left(\sum_{\Gamma} e^{-E(\Gamma)/k_B T} \right) e^{-F_v/k_B T} \equiv e^{-F_c/k_B T} e^{-F_v/k_B T} \quad (8.12)$$

where we define $F_c = k_B T \ln Z_c$ with $Z_c = \sum_T e^{-E(T)/k_B T}$ as the partition function of the discrete configurational degrees of freedom. Finally, we note the separation of the free energy into a discrete configurational part and a contribution from the continuous vibrations, $F = -k_B T \ln Z = F_c + F_v$.

The preceding discussion assumed the integration in Eq. (8.10) was carried out at fixed volume V , and hence the resulting free energy was a Helmholtz free energy $F(N, V, T)$. Additionally, integrating over the volume, including a factor $\exp(-PV/k_B T)$ in the integrand, takes us to a constant pressure ensemble, where the corresponding free energy is a Gibbs free energy $G(N, P, T)$. Equivalently, we could perform the Legendre transform in Eq. (8.7). The decomposition into discrete configurational and continuous vibrational contributions follows as above, resulting in the decomposition $G = G_c + G_v$.

8.3.1 Example: Configurational Free Energy

As an example of configurational free energy, consider the case of Nb-V. As seen in Fig. 8.1b, the representative structures of the BCC solid solution are all positive in energy, implying immiscibility, in seeming contradiction to the experimentally assessed phase diagram [37] which shows a continuous solid solution. However, the assessed phase diagram only goes down to $T = 2173$ K. Indeed, experiments generally cannot achieve true equilibrium at temperatures far below their melting temperature. Meanwhile, the ideal solid solution possesses $k \ln(2)$ of entropy suggesting entropic stabilization relative to phase separation at temperature $T = 0.063 \text{ eV}/k_B \ln(2) = 1055$ K, where we take the SQS energy from Table 8.1 as a characteristic value. However, the actual energy and entropy of the solid solution cannot be estimated as simply as suggested in this paragraph. Short-range

Table 8.1 Representative formation enthalpies in the Cr-Mo-Nb-V quaternary and its subsystems. Units are meV/atom. Equiatomic SQSs include a 16-atom structure for binaries [20], a 36-atom structure for ternaries [19], and a 16-atom structure for quaternary that has vanishing first and second neighbor correlations. Binary cP2 structure is CsCl-type (cP2). cF24 structures place smaller atoms on 16d sites and larger atoms on 8a (*is based on hP12,[†]has composition Cr₂MoNbV₂, and ternaries are equiatomic). Melting temperatures (units are K) are experimental minimum solidus temperatures for binaries, and averages are given for ternaries and quaternary

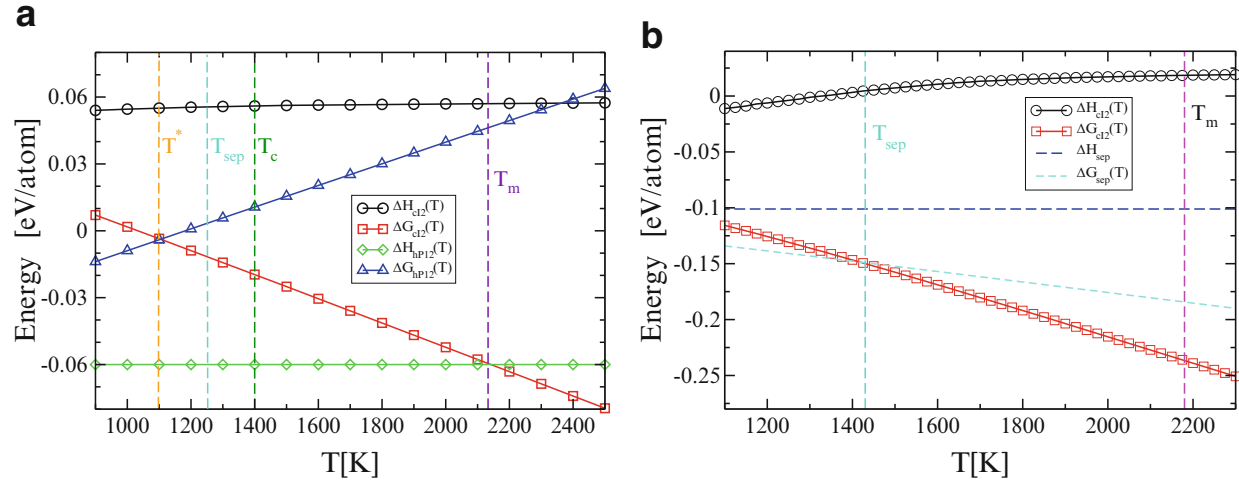


Fig. 8.3 (a) Thermodynamics of NbV₂. Enthalpy and configurational free energy of BCC (cI2) solid solutions are obtained from Monte Carlo simulations. Free energy ΔG_{hP12} of NbV₂ includes vibrational free energy from Eq. (8.14). T_m 's are experimental melting temperatures. T_c is predicted critical temperature of Nb-V, while T_{sep} is phase separation temperature of the BCC phase and T^* is predicted temperature for stability of NbV₂.hP12. (b) Thermodynamics of CrMoNbV. Notation as in (a)

correlations in chemical occupation, related to the actual chemical interactions among constituents, will tend to reduce both the energy and entropy.

Monte Carlo simulation can properly deal with these correlations, by sampling all possible configurations weighted by their Boltzmann factors which favor energetically favorable structures. Figure 8.3 illustrates results obtained using the emc2 Monte Carlo program of the ATAT [41] in conjunction with energies defined by the cluster expansion obtained using the maps program [42]. We take as our initial condition a disordered arrangement of Nb and V on a $6 \times 6 \times 6$ BCC supercell, with global stoichiometry NbV₂. The ideal entropy of $S/k_B = (1/3) \ln(3) + (2/3)\ln(3/2) = \ln 1.89$ is slightly less than ln 2 owing to the stoichiometry being non-equiautomic. Together with the initial energy of 0.058 eV/atom, this entropy determines the free energy at high temperatures. At fixed temperature T , we attempt to swap positions between pairs of atoms of differing species, always accepting the swap if it lowers the total energy and accepting with probability $\exp(-\Delta E/k_B T)$ if it raises the energy. The mean energy at temperature T provides the configurational contribution to the enthalpy, H_c , while thermodynamic integration provides the relative configurational free energy G_c between nearby temperatures. Note that the slope of $G_{\text{cI2}}(T)$ goes asymptotically to ln 1.89 at high temperature. Note also that we may perform Monte Carlo at any desired temperature, including above the actual melting temperature, because we are simulating a lattice gas model with discrete configurations.

An alternative Monte Carlo method [41] attempts to swap the chemical identity of individual atoms, rather than interchanging positions of atom pairs. Since the total number of atoms is preserved, but not the global stoichiometry, this simulation occurs in the semi-grand ensemble. The ATAT program phb uses this method to identify the boundaries of coexisting phases. When applied to the case of Nb-V, this

method confirms the existence of a low-temperature miscibility gap, which closes in a critical point at temperature $T_c = 1400$ K, far below the melting point. The phase boundary passes through stoichiometry NbV_2 at an even lower temperature, $T_{\text{sep}} = 1250$ K. It is thus no surprise that experiments fail to identify phase separation in Nb-V, as this is predicted to occur far below the melting temperature which ranges from 2133 K close to NbV_2 up to 2742 K depending on composition, and hence equilibration will prove difficult. Similar conclusions were reached in an independent study [33].

According to the DFT-calculated enthalpies, an additional competitor to the solid solution, other than phase separation, is formation of the predicted $\text{NbV}_2.\text{hP12}$ complex intermetallic, whose enthalpy of formation of -0.060 eV/atom lies on the convex hull implying stability in the limit of $T \rightarrow 0$ K. Since the tetrahedral close packing exhibits sites of differing coordination numbers that favor specific chemical species, we assume this phase possesses no appreciable configurational entropy, and hence its configurational Gibbs free energy is simply given by its formation enthalpy, as indicated in Fig. 8.3. Notice that the solid solution free energy crosses the hP12 enthalpy at a temperature that happens to be close to the melting temperature. Accordingly, if vibrational free energy were to be neglected, hP12 would be expected to be the stable phase from T_m on down at composition NbV_2 . The fact that NbV_2 has not been observed experimentally suggests that we must consider vibrational free energy, as we do in Sect. 8.3.2.

The reader may wonder why the solid solution beats $\text{NbV}_2.\text{hP12}$, but not $\text{Cr}_2\text{Nb}.\text{cF24}$, since the formation enthalpy of $\text{NbV}_2.\text{hP12}$ is even greater in magnitude than for $\text{Cr}_2\text{Nb}.\text{cF24}$. However, as can be seen in Fig. 8.1, the range of representative solid solution structure energies in Cr-Nb nearly double those in Nb-V. The Monte Carlo simulated critical temperature of $T_c = 2950$ K lies far above the melting point $T_m = 1893$ K. Although Cr exhibits 25 % solubility in Nb, at higher Cr contractions, the solid solution is unstable to the formation of $\text{Cr}_2\text{Nb}.\text{cF24}$. Thus, we understand the high-temperature Cr-Nb-V ternary phase diagram [40], which consists of BCC solid solutions along the Cr-V and Nb-V binary edges, while $\text{Cr}_2\text{Nb}.\text{cF24}$ is stable as a binary and extends stably far into the interior of the ternary composition space.

8.3.2 Example: Vibrational Free Energy

The configurational integral Z in Eq. (8.10) restricted to the region of configuration space $nbd(\Gamma)$ surrounding the specific configuration Γ becomes

$$Z(c) = \int_{nbd(\Gamma)} \prod_{i=1}^N d\mathbf{r}_i e^{-E(\mathbf{r}_1, \dots, \mathbf{r}_N)/k_B T}, \quad (8.13)$$

and the free energy is $F(\Gamma) = -k_B T \ln Z(\Gamma)$. Provided that E varies quadratically in the vicinity of the local minimum Γ , the integrand becomes a Gaussian that can be integrated analytically. The resulting vibrational free energy is

$$F_v = k_B T \int g(\omega) \ln[2\sinh(\hbar\omega/2k_B T)] d\omega \quad (8.14)$$

where $g(\omega)$ is the vibrational (phonon) density of states. In the limit of $T \rightarrow 0$, we find F_v consists entirely of the zero point energy of the harmonic phonon modes, while at elevated temperatures F_v grows negative. The form of this equation reveals that an excess of low-frequency modes makes F_v grow negative rapidly, owing to a high vibrational entropy. We will restrict our discussion in this chapter to the harmonic approximation, whose validity diminishes at elevated temperature. The *quasiharmonic* approximation is a mild generalization that takes into account the volume dependence of vibrational frequencies (Grüneisen parameters) and thus incorporates anharmonic effects leading to thermal expansion.

To compute the phonon spectrum, we use the force constant method [27]. The force constants give the forces on one atom due to a displacement of another via the second derivative of total energy $\partial^2 U / \partial \mathbf{R}_i \partial \mathbf{R}_j$, which can be evaluated from density functional perturbation theory within VASP. We convert this to a dynamical matrix $\mathbf{D}(\mathbf{k})$ by weighting the rows and columns by inverse atomic masses and then Fourier transforming at wavevector \mathbf{k} . Eigenvalues of the dynamical matrix are phonon frequencies $\omega(\mathbf{k})$, which can be converted into a density of states $g(\omega)$ by integrating over the Brillouin zone,

$$g(\omega) = \int_{\text{BZ}} \delta(\omega - \omega(\mathbf{k})) d^3\mathbf{k}. \quad (8.15)$$

In practice, we choose to sample the frequencies on a dense grid in \mathbf{k} -space and then smear the distribution to approximate g . This procedure must be performed in a cell of sufficient size that all important interatomic force constants are represented.

As a concrete example, consider the problem of stability of V₂Zr.cF24. The assessed phase diagram shows this phase as stable from low temperature up to 1592 K. However, DFT calculations (Table 8.2) suggest a formation enthalpy of

Table 8.2 Representative formation enthalpies in the Nb-Ti-V-Zr quaternary and its subsystems. Other details as in Table 8.1

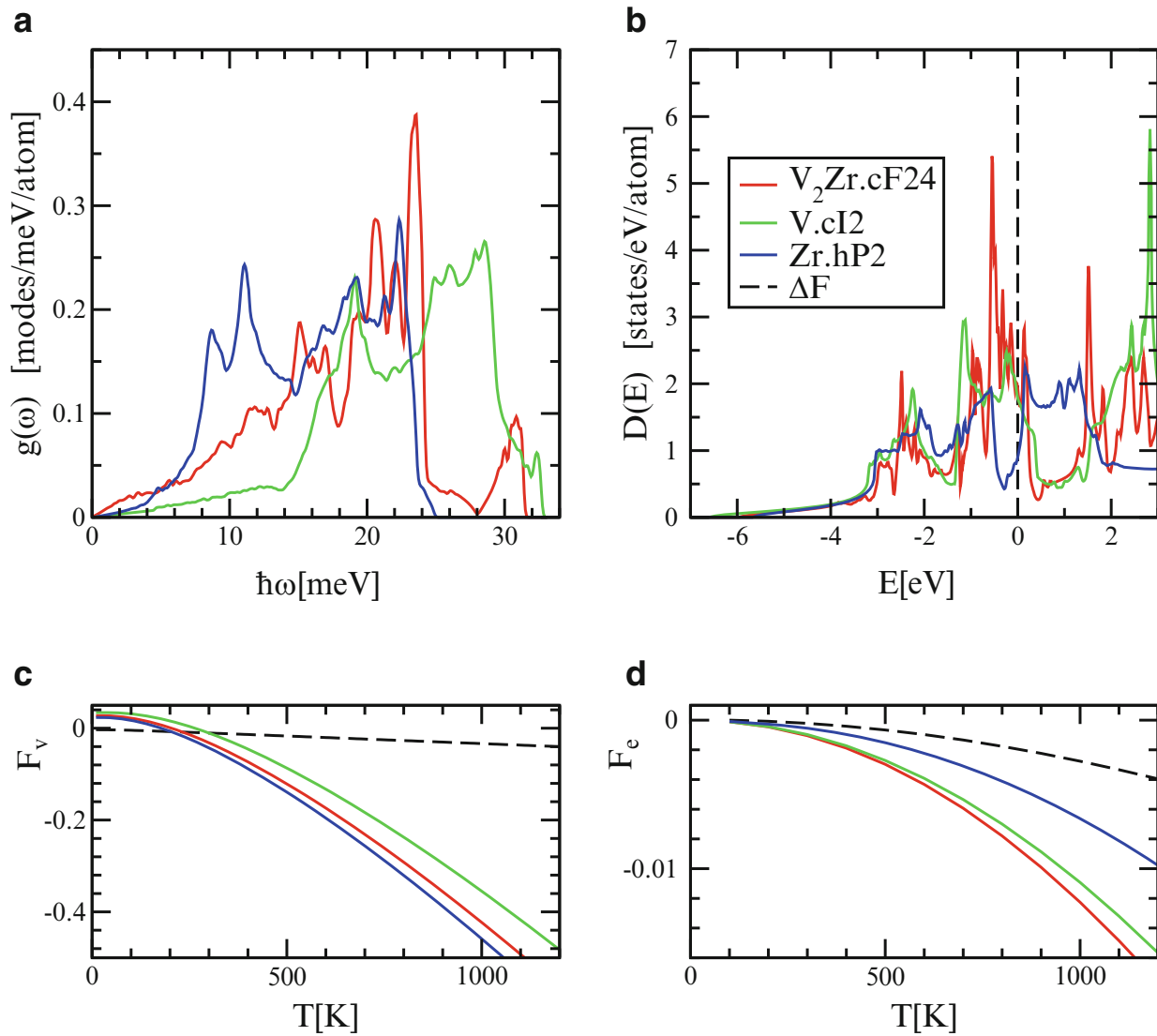


Fig. 8.4 (a) Vibrational density of states in the V-Zr alloy system; (b) electronic density of states (E is relative to the Fermi level E_F); (c) and (d) corresponding free energies

+43 meV/atom, indicating the state is unstable at low temperature. Probably this phase is actually stable only at high temperatures where it is formed and simply remains metastable at low temperature. We need to find a source of entropy that can lower the free energy of the compound relative to that of the competing elements. Substitutional entropy is unlikely, as the two atomic species play distinct roles in this tetrahedrally close-packed structure. The small V atoms center CN = 12 icosahedra, while the larger Zr atoms center CN = 16 polyhedra.

Figure 8.4 compares the vibrational densities of states of the $V_2Zr.cF24$ compound with those of the pure elemental states $V.cI2$ and $Zr.hP2$. Owing to its large mass, Zr exhibits lower-frequency modes and hence more negative vibrational free energy, than the lower mass V, with V_2Zr falling in between. Although individual vibrational free energies are large, their *differences* are small and comparable to the discrete configurational free energy. Combining the favorable vibrational free energy with the unfavorable formation enthalpy,

$\Delta H + \Delta F_v$, we find that the V_2Zr compound is unstable to separation into pure elements below $T^* = 1290$ K, but is stable above this temperature. One factor contributing to the vibrational entropy of $V_2Zr.cF24$ is the low-frequency modes below 5 meV/atom. These reside predominantly on V atoms (counterintuitively, given the low V mass) and appear related to an unusually long V-Zr bond length in this structure.

Note that Zr undergoes an allotropic transition from its low-temperature α (hP2) form to high-temperature β (cI2) at $T = 1136$ K, which is lower than the $T = 1290$ K at which we just predicted $V_2Zr.cF24$ becomes stable. Hence, we should have compared with the free energy of $Zr.cI2$ rather than hP2. Unfortunately, $Zr.cI2$ is mechanically unstable, leading to phonon modes with imaginary frequencies ω . Equation (8.14) cannot be used to calculate the vibrational free energy, requiring more sophisticated approaches [2, 7]. Alternatively, we can look up the NIST-JANAF [31] table to find that the entropy jump at the α/β transition amounts to 3.7×10^{-5} eV/atom/K. Including this additional stability of β raises the predicted stability temperature of $V_2Zr.cF24$ to $T = 1380$ K.

As a second example, recall the mysterious absence of $NbV_2.hP12$ from the experimental phase diagram despite its favorable enthalpy (Figs. 8.1b and 8.3a). Vibrational free energy provides the explanation. As a representative of the BCC solid solution, we choose a specific structure of Pearson type tI6 and presume that its vibrational free energy is representative of the entire ensemble. Indeed, we find that the G_v of tI6 matches the composition-weighted G_v of pure $Nb.cI2$ and $V.cI2$ to within 2 meV/atom over the entire temperature range of interest (too low to be worth including in Fig. 8.3), despite the individual values reaching approximately -1.2 eV/atom at T_m , justifying our neglect of the structure dependence within the solid solution. In striking contrast, the frequency spectrum of hP12 is shifted to high frequencies relative to BCC, owing to the tetrahedral close packing of the Laves phase contrasting with the loose packing of BCC. Consequently, the vibrational free energy of hP12 greatly exceeds the pure elemental reference points, ΔF_v is *positive*, leading to the upward slope of ΔG in Fig. 8.3, causing the free energy of hP12 to cross with the solid solution at $T^* = 1100$ K. We predict that the BCC solid solution is thermodynamically stable from melting at $T_m = 2133$ K down to the critical point for phase separation at $T_c = 1400$ K. The hP12 Laves phase gains stability at a slightly lower temperature $T^* = 1100$ K and remains stable down to $T = 0$ K. The low temperature at which hP12 gains stability inhibits its formation experimentally.

Notice that the enthalpically favorable $NbV_2.hP12$ was *destabilized* by F_v , while the enthalpically *unfavorable* $V_2Zr.cF24$ was *stabilized*. Strong bonding, which lowers ΔH , increases vibrational frequencies ω , in turn raising F_v .

8.3.3 Electronic Free Energy

Excitations of the electron gas contribute entropy to an associated electronic free energy $F_e(T)$. Excitations are described by the Fermi-Dirac occupation function

$$f_T(E) = \frac{1}{1 + \exp[(E - \mu)/k_B T]} \quad (8.16)$$

representing the occupation probability f of states of energy E at temperature T given electron chemical potential μ . This function interpolates from full occupation ($f=1$) for states below μ to complete vacancy ($f=0$) for states above, with intermediate values restricted to energies within a few $k_B T$ of the chemical potential, which thus approaches the Fermi energy E_F at low T .

In combination with the electronic density of states, $D(E)$, obtained from first principles calculations, we can evaluate the electronic band energy and entropy,

$$\begin{aligned} U(T) &= \int D(E)(E - E_F)(f_T(E) - f_0(E))dE \\ S(T) &= -k \int D(E)[f_T(E)\ln f_T(E) + (1 - f_T(E))\ln(1 - f_T(E))]dE, \end{aligned} \quad (8.17)$$

and set $F_e(T) = U(T) - TS(T)$. Since low-temperature excitations are restricted to the vicinity of E_F , the results are approximately proportional to the density of states at the Fermi level [22],

$$U(T) \approx \frac{\pi^2}{6} D(E_F) k^2 T^2, \quad S(T) \approx \frac{\pi^2}{3} D(E_F) k^2 T, \quad F_e(T) \approx -\frac{\pi^2}{6} D(E_F) k^2 T^2. \quad (8.18)$$

The resulting quadratic variations are evident in Fig. 8.4, with coefficients proportional to $D(E_F)$. The electronic free energy difference yields a few meV/atom of additional stability to V₂Zr.cF24, bringing its temperature of instability down to $T^* = 1180$ K. Notice that the individual electronic free energies are much smaller than the vibrational free energies, but the tendency toward cancelation is less pronounced, so the electronic contribution remains important.

8.4 Monte Carlo and Molecular Dynamics Simulation

Molecular dynamics is well suited to reproduce the small-amplitude oscillations of atoms in the vicinity of crystal lattice sites. At low temperatures, the probability for an atom crossing the barrier from one lattice site to another is prohibitively low and will rarely occur on the time scale of a molecular dynamics run. In contrast, Monte Carlo swaps of atomic species on different sites occur with a probability $P = \exp(-\Delta E/k_B T)$ related to the net energy difference $\Delta E = E_{\text{swap}} - E_{\text{ini}}$ of swapped and initial configurations, independently of the energy barrier separating

Table 8.3 Representative formation enthalpies in the Mo-Nb-Ta-W quaternary and its subsystems. Other details as in Table 8.1

Mo-Nb-Ta-W alloy system									
Binary	SQS	cP2	T_m	Ternary	SQS	T_m	Quaternary	SQS	T_m
Mo-Nb	-71	-106	2742	Mo-Nb-Ta	-70	2793	Mo-Nb-Ta-W	-73	2885
Mo-Ta	-110	-186	2896	Mo-Nb-W	-58	2793			
Mo-W	-0.4	-10	2896	Mo-Ta-W	-97	3028			
Nb-Ta	-4	1	2742	Nb-Ta-W	-33	2926			
Nb-W	-34	-25	2742						
Ta-W	-67	-94	3293						

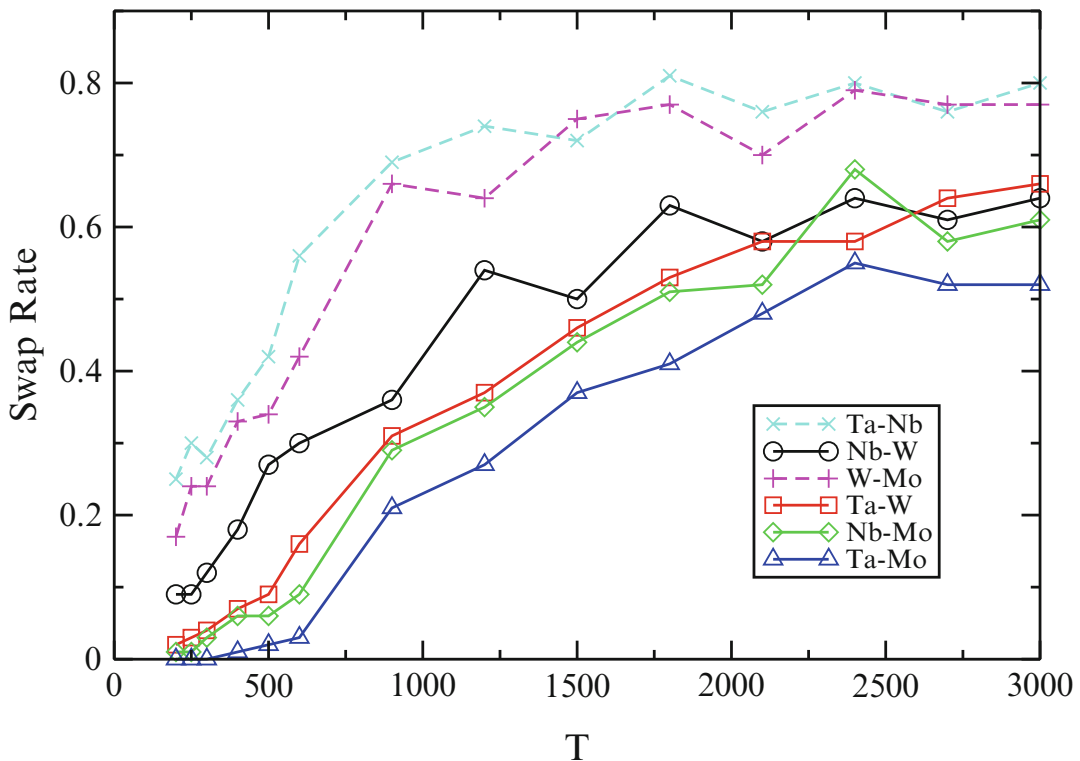


Fig. 8.5 Monte Carlo acceptance rates (ratio of accepted to attempted species swaps) for each species pair vs. temperature. Note correlation of high acceptance rate with low enthalpy values in Table 8.3

the states. Since some of the pairwise interactions are quite low (see, e.g., Mo-W, Nb-Ta, and Nb-W in Table 8.3), we expect that some Monte Carlo species swaps will be accepted even at low temperatures.

We implement this computationally by alternating molecular dynamics with Monte Carlo swaps [44], each performed from first principles using VASP. In the runs described below, we perform 10 MD steps of 1 f. per time step, between each attempted species swap. As illustrated in Fig. 8.5 for Mo-Nb-Ta-W, swaps are frequently accepted with reasonably high probability at moderate and high temperatures, indicating that the Monte Carlo achieves our goal of sampling the full configurational ensemble in the solid state. The same species swaps will almost never be observed via molecular dynamics. The utility of various hybrid MC/MD methods with empirical interaction potentials has been reviewed recently [31].

Swaps with the greatest size contrast (e.g., Ta-Mo and Nb-Mo) occur most infrequently and are nearly absent at low temperatures, while the intermediate-size swaps (Nb-W) occur occasionally and the most similar size swaps (e.g., Ta-Nb and W-Mo) occur with high probability even at the lowest temperatures. We conclude that at low temperature the system behaves nearly as a pseudobinary, consisting of the chromium group (group 5, here Ta and Nb) and the vanadium group (group 6, here W and Mo) as two effective species.

8.4.1 Pair Correlation Functions

Pair correlation functions describe the relative positional preferences of different atomic species. Their Fourier transforms yield the diffraction pattern, which is an important experimental probe of structure. Although crystalline solids are anisotropic, here we shall consider only the radial distribution function which measures the magnitudes of interatomic separations. The radial distribution function governs the angle-averaged (i.e., powder) diffraction pattern. For chemical species α and β , we define

$$g_{\alpha\beta}(r) = \frac{1}{N_\alpha N_\beta} \sum_{i=1}^{N_\alpha} \sum_{j=1}^{N_\beta} \langle \delta(|\mathbf{r}_{ij}| - r) \rangle. \quad (8.19)$$

In practice, a small amount of smearing is required to regularize the δ -functions.

Given a pair distribution function, the associated structure factor is

$$\tilde{h}_{\alpha\beta}(Q) = \int d\mathbf{r} e^{-i\mathbf{k}\cdot\mathbf{r}} (g_{\alpha\beta}(r) - 1), \quad (8.20)$$

and the total structure factor becomes

$$S(Q) = 1 + \sum_{\alpha\beta} c_\alpha f_\alpha c_\beta f_\beta \tilde{h}(\mathbf{Q}), \quad (8.21)$$

where c_α is the concentration of species α . Here, f_α is the form factor, which is approximately equal to the atomic number $f_\alpha = Z_\alpha$ for x-rays or to the scattering length $f_\alpha = b_\alpha$ for neutrons.

8.4.2 Route to the Entropy

Monitoring configuration statistics can yield estimates for the entropy. If the actual atomic positions can be mapped uniquely to nearby ideal lattice sites, then statistics on the occupation of each lattice site can be accumulated, along with statistics of various locally defined multisite clusters. Cluster variation methods [1, 8, 9, 21]

have been developed as analytical approximations for the calculation of free energy given a model Hamiltonian. The general idea is to represent both the energy and the entropy, separately, as functions of the clusters. As the cluster size grows, the approximate free energy converges toward the exact value.

The simplest of these methods takes individual atomic sites as one-point clusters. Given N sites containing $N_\alpha = x_\alpha N$ atoms of species α , where α runs from 1 to m and x_α is the concentration of species α , counting the distinct occupations of sites (one-point clusters) yields the total number of configurations $g(N_\alpha) = \prod_\alpha N_\alpha! / N!$. Neglecting correlations among sites, the total entropy takes its maximal value

$$S(N_\alpha)/k_B = \ln g = \ln N - \sum_\alpha \ln N_\alpha!. \quad (8.22)$$

Making the Stirling approximation, $\ln N! \approx N \ln N$, yields the entropy per site in the thermodynamic limit,

$$\sigma(x_\alpha) = \frac{-k}{N} S(N_\alpha) \approx -k \sum_\alpha x_\alpha \ln x_\alpha. \quad (8.23)$$

For an equiatomic composition of N species, so that $x_\alpha = 1/N$, this immediately yields the usual $S/k_B = \ln(N)$ entropy. Alternatively, we may take Eq. (8.23) as the local entropy density at any specific site. In this case, if individual sites exhibit a preference for specific elements (e.g., with the onset of chemical order), the values of x_α differ from $1/N$, and the entropy is reduced.

Moving to two-point clusters (nearest-neighbor bonds) improves accuracy of the entropy as it corrects for the onset of short-range order. Guggenheim [10] calculated the number of configurations $g(N_\alpha, N_{\alpha\beta})$, where $N_{\alpha\beta}$ denotes the average number of β neighbors of atoms of chemical species α on a regular lattice of coordination number z . In the absence of correlations, we expect $N_{\alpha\beta} = N_{\alpha\beta}^* \equiv N_\alpha N_\beta / N$ and the actual number of configurations to equal $g(\{N_\alpha\})$. In the presence of correlations, the reduced number of configurations is

$$g(N_\alpha, N_{\alpha\beta}) = g(N_\alpha) \prod_\alpha \frac{(zN_\alpha/2 - \sum_{\gamma \neq \alpha} N_{\alpha\gamma}^*)!}{(zN_\alpha/2 - \sum_{\gamma \neq \alpha} N_{\alpha\gamma})!} \prod_{\alpha \neq \beta} \frac{N_{\alpha\beta}^*! 2^{N_{\alpha\beta}}}{N_{\alpha\beta}! 2^{N_{\alpha\beta}^*}}. \quad (8.24)$$

The multiplicative factors in Eq. (8.24) reduce the entropy due to deviations of the bond frequencies $N_{\alpha\beta}$ from their uncorrelated values $N_{\alpha\beta}^*$. As in the case of the single-site cluster, this can be turned into a local entropy density

$$\sigma(N_\alpha, N_{\alpha\beta}) = k \ln g(N_\alpha, N_{\alpha\beta}). \quad (8.25)$$

Owing to the two-point correlations, the global averages are nontrivial, in contrast to the single-point case. They can be either evaluated by Monte Carlo simulation or estimated using the quasichemical approximation [14]. This method can be extended to more complex clusters, for example, the tetrahedron approximations for BCC [1] and FCC [21] lattices.

8.5 Structure and Thermodynamic Modeling of High-Entropy Alloys

So far this chapter developed basic techniques that can in principle be applied to high-entropy alloys, though the specific examples mainly concentrated on binary and ternary alloy systems. We now turn our attention to quaternary high-entropy alloys, with a focus on BCC refractory metals, as example applications of the above methods.

The properties of the periodic table imply that metals whose positions are adjacent left/right or above/below tend to have similar size, valence, and electronegativity and hence substitute with relative ease for one another. Valency generally is constant within a column and differs by 1 between adjacent columns. Electronegativity correlates strongly with atomic volume, being low for large atoms and high for small atoms. The majority of elements in the known high-entropy alloys lie in proximity to each other on the periodic table, presumably exploiting the similarity in physical properties to increase their configurational entropy.

This observation motivates our choice to draw examples from 2×2 “squares” of the periodic table, that is, groups of four elements that lie on vertices of a unit square consisting of two adjacent elements of a row together with the two elements that lie directly below. In such a square, the largest element will lie at the bottom left corner, while the smallest is at the upper right corner. We shall call this the *positive* diagonal, while the top left to bottom right, which has smaller size contrast, will be called the *negative* diagonal.

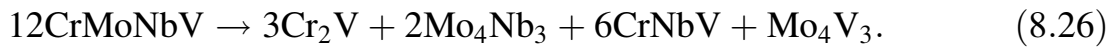
8.5.1 Cr-Mo-Nb-V

Having previously discussed the binaries Cr-Nb and Nb-V in addition to the ternary Cr-Nb-V, we add a fourth element, Mo, to complete a 2×2 square consisting of the first two elements in the (V) column (namely, V and Nb) and the first two elements of the adjacent (Cr) column (namely, Cr and Mo). We extended our ATAT models of the binary and ternary subsystems to the full quaternary, running maps until the internal database extends to at least 8 atoms/unit cell and the true and predicted ground states agree. Despite the SQS being at positive enthalpy, as listed in Table 8.1, maps was able to identify an equiatomic structure of negative enthalpy,

– 6 meV/atom. This lowest-energy structure, which has Pearson type oI8, arranges the four chemical species on the BCC lattice in such a manner that each unit cell has 24 near-neighbor pairs between columns (i.e., V-Cr, V-Mo, Nb-Cr, or Nb-Mo) and only 8 near-neighbor pairs within columns (i.e., V-V, V-Nb, Nb-Nb, Cr-Cr, Cr-Mo, or Mo-Mo). It thus exploits the preference for atoms of differing sizes and electronegativity to be nearest neighbors [44]. In general, the enthalpies of the cP2 structures lie below the SQS enthalpies (see Table 8.1), because cP2 and similar ordered structures can exploit preferred local chemical environments.

Despite the existence of negative enthalpy BCC representative structures, our DFT total energies predict that the ground state of equiatomic CrMoNbV consists of phase separation into four coexisting phases, raising questions concerning the possible existence of a high-entropy alloy of this composition. No experimental report exists to date.

Relative free energies of the BCC solid solution and the competing Laves phase are illustrated in Fig. 8.3b. The free energy of the solid solution was evaluated from Monte Carlo using memc2 (the multicomponent version of emc2 [41]), similarly to the case of NbV₂ discussed previously in Sect. 8.3.1. A by-product of the simulation is the ability to predict the entropy, in the present case by thermodynamic integration from a high-temperature reference state. Assuming maximal entropy of ln(4) at $T = 3000$ K, we obtain a nearly ideal $S/k_B = \ln(3.82)$ at T_m . The coexisting phases consist of three BCC-based structures, Cr₂V.tI6, Mo₄Nb₃.tI14, and Mo₄V₃.hR7, together with the Laves phase CrNbV.cF24, yielding the balanced equation



Taking the composition-weighted average of their enthalpies of formation predicts a ground-state enthalpy of – 101 meV/atom. We convert this into a finite-temperature free energy by assuming ideal entropy of mixing at appropriate compositions for the three BCC-based structures, together with assumed Cr-V disorder in the Laves phase. As the entropies of all four competing phases are less than ln(2), the combination loses out to the high-entropy alloy at high temperature, with phase separation expected only below $T_{sep} = 1430$ K. There is considerable uncertainty in the precise separation temperature owing to several factors: we used the ideal entropy of mixing rather than the cluster expansion to evaluate the configurational entropies of the competing phases; we have neglected vibrational entropy throughout; some other combination of phases may exist whose enthalpy is less favorable but that has higher entropy. Indeed, we have treated the competing phases as “line compounds” of fixed stoichiometry, which is appropriate only in the limit of low temperature as discussed previously in Sect. 8.2.2. At high temperature, the competing phases most likely contain all four chemical species, exploiting the higher entropy at the cost of slightly increased enthalpy to lower their combined free energies. Thus, we must regard the calculated T_{sep} as a lower bound on the actual temperature of phase separation.

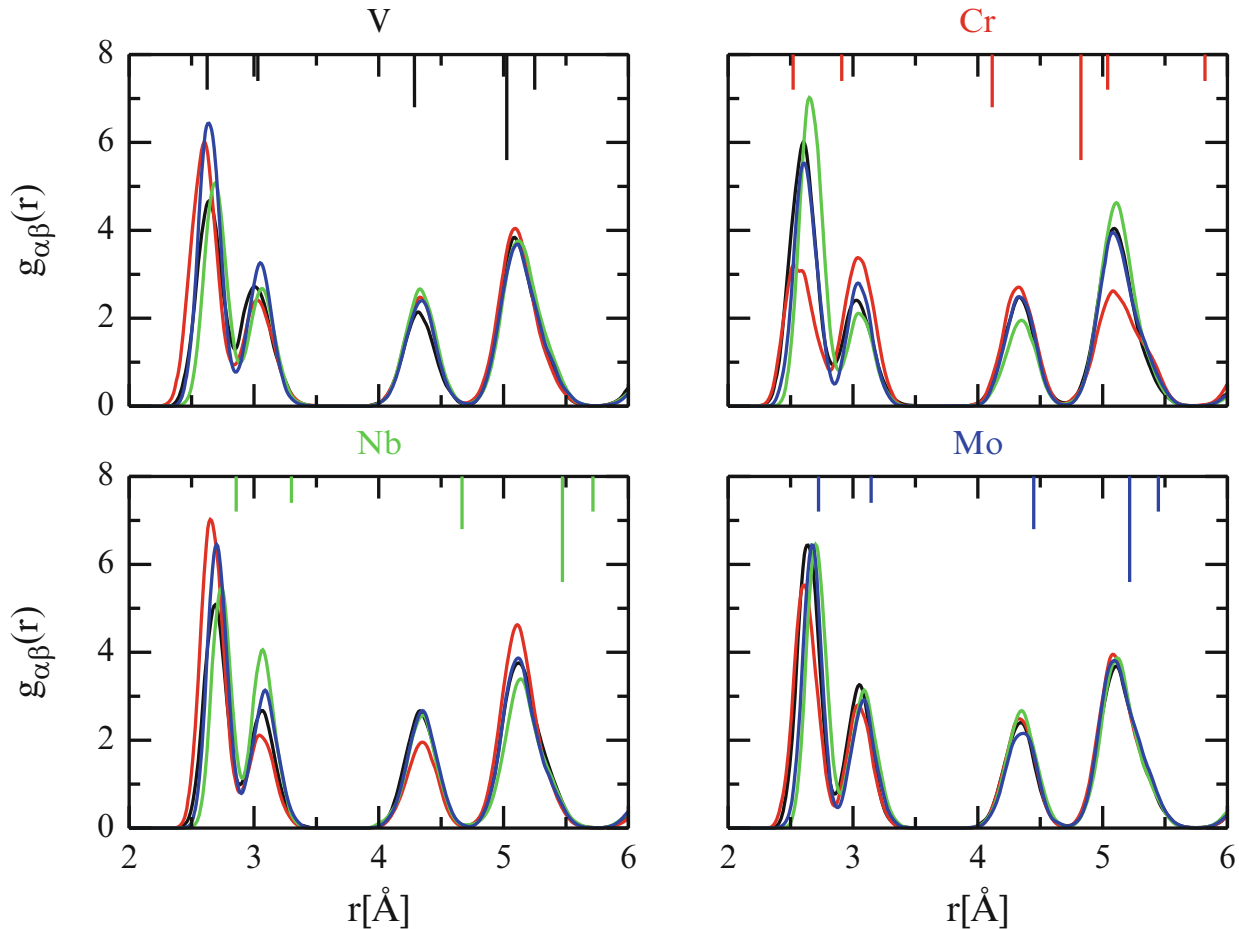


Fig. 8.6 Pair distribution functions of Cr-Mo-Nb-V at $T = 300\text{ K}$ quenched from 1200 K . Each panel shows the four partial pair correlation functions for the element named above. The partials are color-coded, e.g., under V the *black curve* is V-V and the *red curve* is V-Cr. Bars at top indicate the corresponding correlations in the pure BCC element, e.g., V has 8 neighbors at $r = 2.6\text{ \AA}$, 6 at 3.0, 12 at 4.3, 24 at 5.0, and 8 at 5.3

MC/MD simulation results are shown in Fig. 8.6. Here, we carry out the MC/MD simulation at $T = 1200\text{ K}$, a temperature sufficiently high that chemical short-range order might be in equilibrium even in experiment. We then quench the system to $T = 300\text{ K}$ and anneal under conventional molecular dynamics, where atomic diffusion is frozen out. Thus, we freeze in short-range order typical of the high annealing temperature, in an attempt to mimic the actual experiment. The figure illustrates the four partial pair correlations for each of the four constituent elements, arranged on the page according to their positions on the periodic table. The BCC structure is clearly evident, with the well-defined 8:6 split of nearest- and next-nearest-neighbor peaks as well as well-defined further neighbor peaks. Also evident is the strong preference for intercolumn neighbors, with Cr and Mo forming the strongest near-neighbor peaks of V and Nb and vice versa.

Swap rates reported in Table 8.4 give insight into respective roles of different elements, with the swap rates being largest for elements that are most similar in size (the nearest off-diagonal) and becoming progressively smaller as the size contrast grows more extreme, finally nearly vanishing for the pair Nb-Cr which constitutes the positive diagonal of the square as defined above. This table also gives the near-neighbor bond counts corresponding to the near-neighbor peaks in Fig. 8.6. We may

Table 8.4 Monte Carlo swap rates and bond statistics for Cr-Mo-Nb-V quaternary at $T = 1200\text{ K}$. Bond counts $N_{\alpha,\beta}$ count number of β -type neighbors of atom type α , where α labels rows and β labels columns. Elements are arranged in order of decreasing BCC lattice constant

$\alpha \backslash \beta$	Swap				Bonds			
	Nb	Mo	V	Cr	Nb	Mo	V	Cr
Nb		0.48	0.24	0.05	1.73	2.05	1.71	2.51
Mo			0.49	0.23	2.00	1.90	2.14	1.96
V				0.43	1.86	2.21	1.79	2.14
Cr					2.41	1.84	2.36	1.39

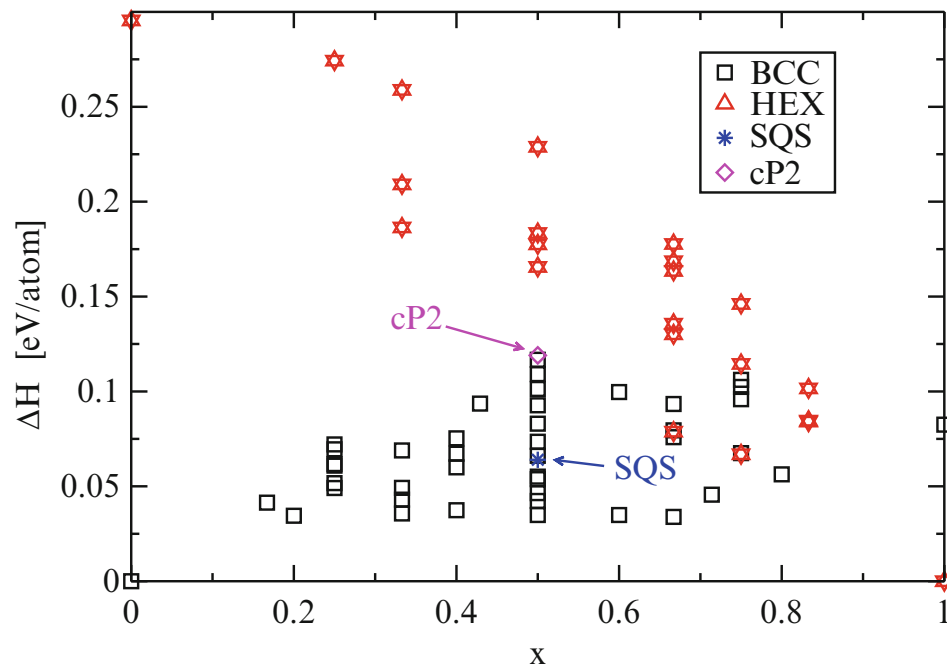


Fig. 8.7 Enthalpy of formation in the Nb-Zr alloy system. Squares indicate representative structures of the BCC solid solution. SQS and cP2 are marked with special symbols. Hexagonal stars indicate HCP

use these bond counts in the formula Eq.(8.24) to evaluate the entropy at $T = 1200\text{ K}$, which leads to $S/k_B = \ln(3.82)$, identical to the value obtained at T_m from memc2.

8.5.2 Nb-Ti-V-Zr

Our next square consists of the first two rows of the (Ti) column, namely, Ti and Zr, together with the first two rows of the (V) column. This new compound provides an interesting example because Ti and Zr are HCP at low temperature but BCC at high temperature as a result of the lower enthalpy of HCP competing with the higher vibrational entropy of BCC (HCP is close-packed, while BCC is loose-packed). Meanwhile, Nb and V are BCC at all temperatures. Can compounds formed from the (Ti) and (V) columns form HCP solid solutions, or must they form BCC? Figure 8.7 provides a hint.

Application of the ATAT cluster expansion to predict low-energy states of both BCC and HCP Nb-Zr alloys suggests complete phase separation into coexisting Nb.cI2 and Zr.hP2 in agreement with experiment at low temperature. However, in Fig. 8.7, we see a large number of individual BCC configurations with energies of order 0.05 eV/atom. Clearly, energy and configurational entropy favor a BCC solid solution over HCP at all but the most Zr-rich compositions. Applying emc2 within the BCC solid solution, we identify a critical point for phase separation into Nb-rich and Zr-rich BCC phases at $T_c = 1250$ K and at a composition of 30 % Zr. Experimentally, the critical point lies at $T_c = 1258$ K and at a composition of 40 % Zr. Extending the cluster expansion to the quaternary fails to identify additional low-temperature structures. The NbTiVZr quaternary is expected to decompose at low temperatures as



Figure 8.8 shows the quaternary pair correlation functions obtained from MC/MD. Notice that in contrast to the case of CrMoNbV just discussed, here the 8:6 split of nearest- and next-nearest-neighbor peaks is hardly evident, despite the longer-range correlations beyond 4 Å remaining intact. This reflects the inherent mechanical instability of BCC-based structures containing Zr and Ti. A side effect is that the energies of the SQS structures in Table 8.2 generally lie *below* the

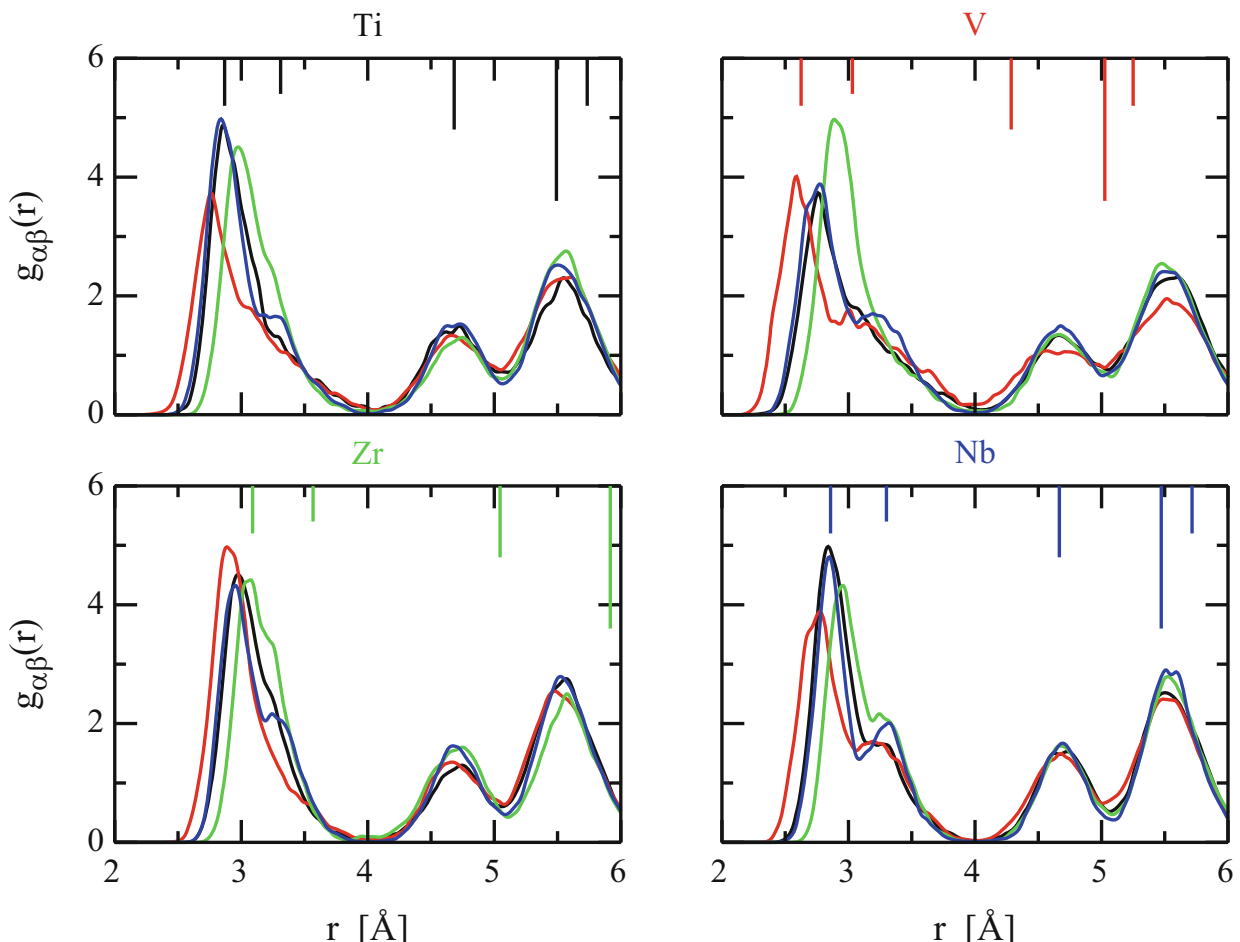


Fig. 8.8 Pair distribution functions of Nb-Ti-V-Zr at $T = 1200$ K quenched to $T = 300$ K. Layout and conventions as in Fig. 8.6

Table 8.5 Monte Carlo swap rates and bond counts for Nb-Ti-V-Zr quaternary. Elements are arranged in order of decreasing BCC lattice constant

$\alpha \backslash \beta$	Swap				Bonds			
	Zr	Ti	Nb	V	Zr	Ti	Nb	V
Zr		0.32	0.29	0.07	1.60	2.03	1.96	2.41
Ti			0.59	0.39	1.96	2.10	2.10	1.83
Nb				0.34	1.98	2.27	1.98	1.89
V					2.57	1.59	1.96	1.88

energies of the cP2 structure, because the high symmetry of cP2 prevents lattice distortion. A similar severe distortion in the local BCC structure was seen experimentally in the HfNbZr ternary HEA [15]. Indeed, the BCC lattice is more visible in the V and Nb partials than in those containing Ti and Zr. Notice further that the strongest near-neighbor correlation is between Zr and V, which lie along the positive diagonal of the square, while the partials of Ti and Nb are roughly similar, as is normal for the negative diagonal. This is further reflected in the Monte Carlo swap rates in Table 8.5, where Zr and V are almost unable to swap positions owing to their strong size contrast, while Ti and Nb swap easily. Applying the Guggenheim formulas to compute the $T=1200\text{ K}$ entropy yields $S/k_{\text{B}} = \ln(3.89)$, slightly greater than was observed in the case of CrMoNbV.

8.5.3 Mo-Nb-Ta-W

As a final example, we choose a square from the bottom two rows of the (V) and (Cr) columns, namely, Nb and Ta and Mo and W. As previously shown [44] and reproduced in Table 8.3, the enthalpies of formation in this alloy system are significantly negative between columns and nearly zero within columns. Thus, strong chemical order is anticipated, with the possibility of forming an ordered structure such as cP2 at low temperature, with the pair of elements from each column occupying its own sublattice. However, the very high melting temperature makes this phase difficult to observe experimentally. A mean field analysis of this transition [18] indicated a transition with a critical temperature of $T_c = 1600\text{ K}$, although subsequent Monte Carlo simulations place it at 1280 K [17] (mean field theory typically overestimates transition temperatures). Thermodynamics of the ternary subsystem Mo-Ta-W was investigated using combined ab initio and CALPHAD methods [39].

The cluster interaction model produced by maps predicts the equiatomic ground-state structure is a coexistence of two BCC-based phases, $\text{Mo}_2\text{NbTa}_2\text{W}_2$. hR7 and pure elemental Nb.cI2, yielding the balanced equation



Taking the composition-weighted average of the ground-state enthalpy of formation yields enthalpy of -126 meV/atom . Monte Carlo simulation using memc2 yields the entropy at T_m as $S/k_{\text{B}} = \ln 3.93$.

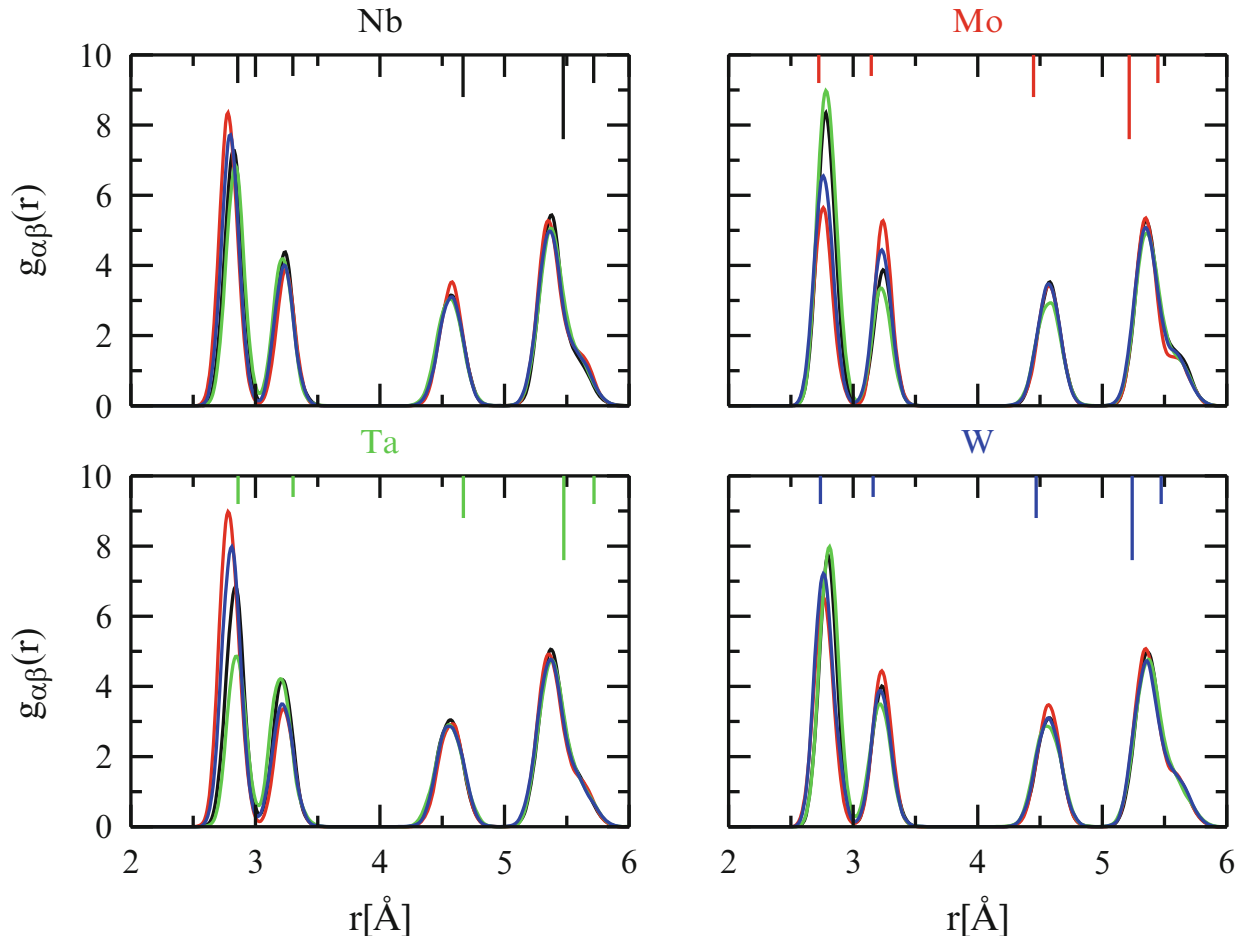


Fig. 8.9 Pair distribution functions of Mo-Nb-Ta-W at $T=1200\text{ K}$ quenched to $T=300\text{ K}$. Layout and conventions as in Fig. 8.6

Table 8.6 Monte Carlo swap rates and bond counts for Mo-Nb-Ta-W quaternary. Elements are arranged in order of decreasing BCC lattice constant

$\alpha \backslash \beta$	Swap				Bonds			
	Ta	Nb	W	Mo	Ta	Nb	W	Mo
Ta		0.74	0.37	0.27	1.39	1.90	2.20	2.51
Nb			0.54	0.35	1.84	1.95	2.11	2.10
W				0.64	2.18	1.93	1.99	1.90
Mo					2.59	2.22	1.70	1.49

MC/MD pair correlation functions shown in Fig. 8.9 reveal very strong BCC-like order including the 8:6 nearest- to next-nearest-neighbor split. As in the two previously examined cases, there is a pronounced preference for nearest-neighbor pairs along the positive diagonal (Ta and Mo), while the partials for pairs along the negative diagonal (Nb and W) generally resemble each other. The effect is also seen in the swap rates reported in Table 8.6, with the pair along the positive diagonal swapping at far lower frequency than the pair along the negative diagonal. In keeping with the nearly zero interaction on pairs within columns, we notice very high swap rates for these pairs (Nb with Ta and Mo with W).

Applying the Guggenheim formulas, we estimate the entropy at $T=1200\text{ K}$ as $S/k_B = \ln(3.82)$, again similar to the value obtained for CrMoNbV. Full temperature dependence of the entropy is plotted in Fig. 8.5 and can be seen to decrease

significantly only below 1200 K. Given the existence of a ground state at nearly the equiatomic composition, we can say that MoNbTaW is an essentially perfect high-entropy alloy that remains stable at all temperatures, with only minor shift in composition. At the same time, the entropy does vanish in this low-temperature limit, with the growth of short-range chemical order, notably an increase in intercolumn bonds.

Vibrational and electronic densities of states and the resulting free energies are presented in Fig. 8.10. Notice that the relative vibrational free energy ΔF_v is positive, owing to the relatively high vibrational frequencies, and likewise the relative electronic free energy ΔF_e is positive because of the relatively low density of states at the Fermi level. Because these have been derived at fixed volume V , the free energies are Helmholtz free energies; hence, thermodynamics yields the entropy by simple differentiation, $S = -\partial F/\partial T$, so we see that electronic and vibrational contributions actually *reduce* the entropy.

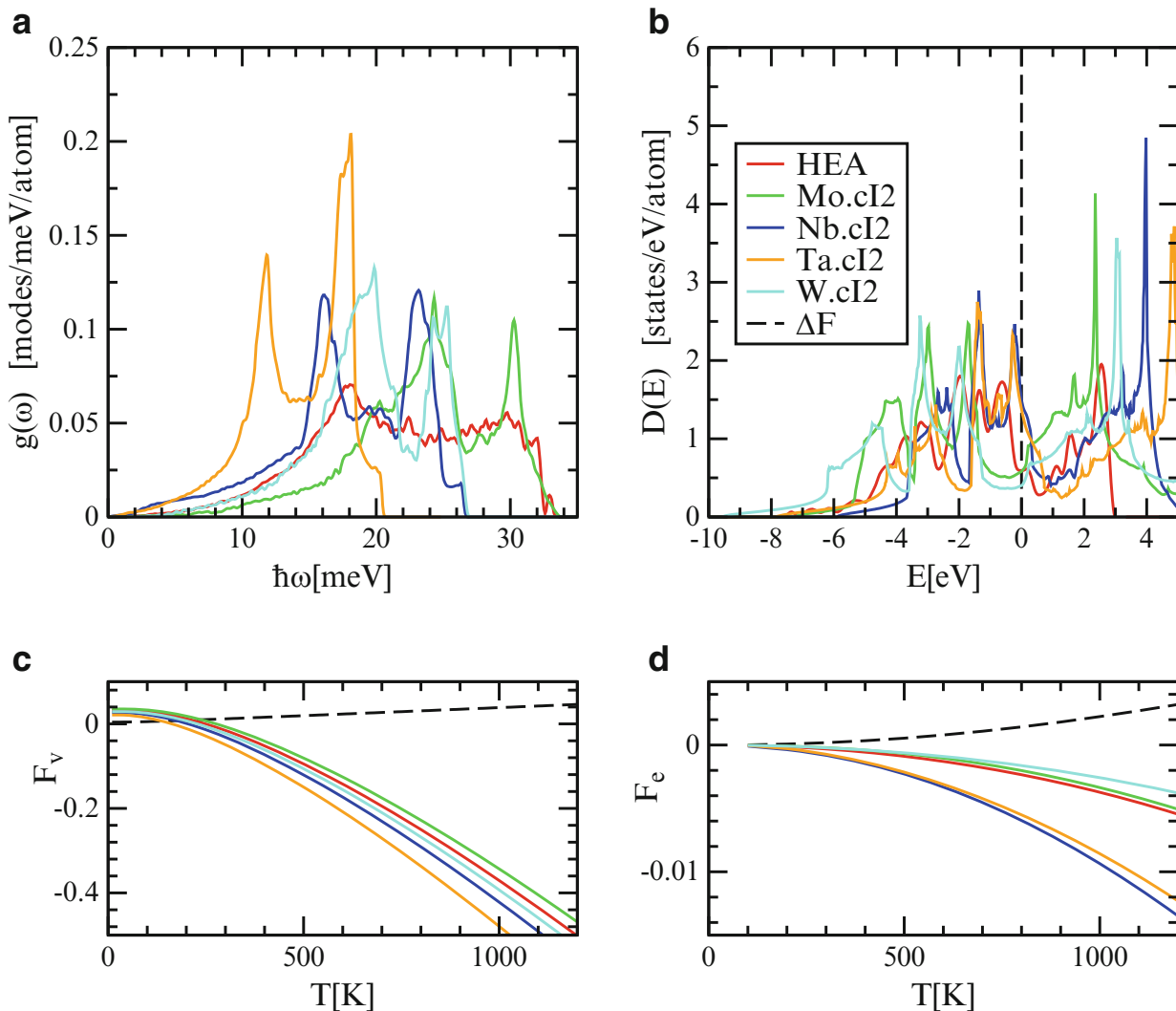


Fig. 8.10 (a) Vibrational density of states in the MoNbTaW HEA; (b) electronic density of states (E is relative to Fermi level E_F); (c) and (d) are corresponding free energies

8.6 Conclusion

This chapter provides a brief introduction to first principles approaches to free energy and phase stability calculation, with application to three high-entropy alloy-forming quaternary compounds. We describe and apply a variety of methods including the cluster expansion of total energy as implemented in the ATAT in Sect. 8.2.3, vibrational and electronic free energy calculation in Sects. 8.3.2 and 8.3.3, and a hybrid Monte Carlo/molecular dynamics method in Sect. 8.4 that is specifically efficient for systems such as HEAs where chemical substitution proliferates. Later chapters cover some additional first principles methods in detail, the coherent potential approximation (CPA) in Chap. 9 and special quasirandom structures (SQSs) in Chap. 10, as well as application of the MC/MD method to liquids in Chaps. 11 and 13. The thermodynamic data calculated using the present methods can be a guide to the refinement of CALPHAD-type thermodynamic databases such as employed in Chap. 12, which eventually provide the rigorous basis for formation rules such as those described in Chap. 2.

Although the intent was tutorial, this chapter reports several new results, illustrating the potential for new discovery in this emerging field of research. Two specific results challenge or shed new light on assessed binary phase diagrams. Namely, we propose that the continuous BCC solid solution in Nb-V is replaced by a previously unknown C14 Laves phase, $\text{NbV}_2.\text{hP12}$, below $T^* = 1100$ K, and we explain the occurrence of the C15 Laves phase $\text{V}_2\text{Zr.cF24}$, despite its unfavorable enthalpy of formation, as a result of vibrational and electronic entropy above $T^* = 1180$ K, while predicting it becomes thermodynamically unstable below this temperature. Through the use of cluster expansions of total energy, we predicted the existence of low-temperature stable quaternaries in the Mo-Nb-Ta-W alloy system. These new structures are specific ordered arrangements of species close to sites of the underlying BCC lattice. In the case of Cr-Mo-Nb-V, we found that all BCC-based quaternary structures were destabilized at low temperature by competing binaries and ternaries, but we predict this compound forms a high-entropy alloy that is stable above the temperature $T_{\text{sep}} = 1430$ K. Because Ti and Zr prefer HCP structures at low temperatures, there are likewise no BCC-based ground states in the quaternary Nb-Ti-V-Zr, so this HEA is also unstable at low temperature. Indeed, we show through MC/MD simulations that the Nb-Ti-V-Zr HEA exhibits strong deviations from ideal lattice sites even while preserving the long-range BCC structure.

To conclude this chapter, we present all contributions to the entropy for the quaternary Mo-Nb-Ta-W. The discrete configurational entropy is evaluated from Eq. (8.25), while the vibrational and electronic free energies were obtained from the free energies illustrated in Fig. 8.10 by differentiation, $S = -\partial F(V, T)/\partial T$. The corresponding entropies are shown in Fig. 8.11. For this particular compound, the vibrational and electronic entropies turn out to be *negative* relative to a mixture of pure elements. Notice that the electronic contribution is relatively small, while

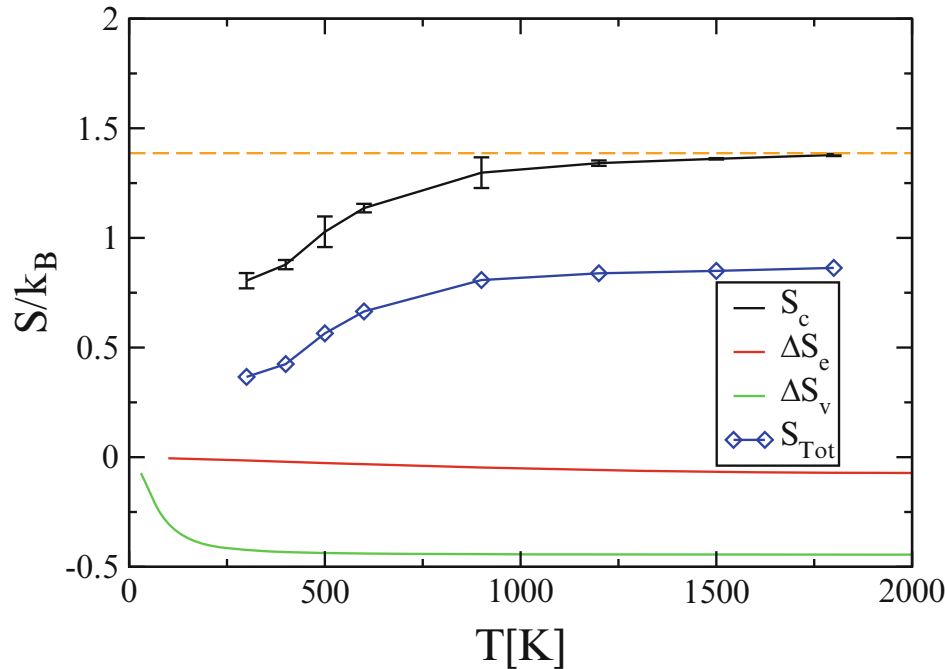


Fig. 8.11 Configurational, vibrational, and electronic contributions to the total entropy S_{Tot} . Configurational entropy calculated according to the Guggenheim approximation Eqs. (8.24) and (8.25). Vibrational and electronic contributions come from Eqs. (8.14) and (8.18), respectively

the vibrational contribution is significant, but still less than the configurational part, validating the claim that high-entropy alloys are dominated by their configurational entropy of mixing.

Acknowledgements M.W. thanks Will Huhn, Michael C. Gao, Axel van de Walle, Walter Steurer, Volker Blum, Peter Liaw, Malcolm Stocks and Takeshi Egami for useful discussions. M.W. acknowledges financial support from the DOE under grant DE-SC0014506.

References

1. Ackermann H, Inden G, Kikuchi R (1989) Tetrahedron approximation of the cluster variation method for B.C.C. alloys. *Acta Metall* 37:1–7
2. Antolin N, Restrepo OD, Windl W (2012) Fast free-energy calculations for unstable high-temperature phases. *Phys Rev B* 86:054119
3. Blochl PE (1994) Projector augmented-wave method. *Phys Rev B* 50:17953–17979
4. Ceperley DM, Alder BJ (1980) Ground state of the electron gas by a stochastic method. *Phys Rev Lett* 45:566–569
5. DeHoff R (2006) Thermodynamics in materials science. CRC Press, Hoboken
6. Ducastelle F (1991) Order and phase stability in alloys. Elsevier, Amsterdam/New York
7. Errea I, Calandra M, Mauri F (2014) Anharmonic free energies and phonon dispersions from the stochastic self-consistent harmonic approximation: application to platinum and palladium hydrides. *Phys Rev B* 89:064302
8. de Fontaine D (1979) Configurational thermodynamics of solid solutions. In: Ehrenreich H, Turnbull D (eds) Solid state physics, vol 34. Academic, New York, pp 73–274
9. de Fontaine D (1994) Cluster approach to order-disorder transformations in alloys. In: Ehrenreich H, DTurnbull (eds) Solid state physics, vol 47. Academic, San Diego, pp 33–176

10. Gao M, Dogan O, King P, Rollett A, Widom M (2008) First principles design of ductile refractory alloys. *J Metals* 60:61–65
11. Gao M, Suzuki Y, Schweiger H, Dogan O, Hawk J, Widom M (2013) Phase stability and elastic properties of Cr-V alloys. *J Phys Condens Matter* 25:075402
12. Glass CW, Oganov AR, Hansen N (2006) USPEX – evolutionary crystal structure prediction. *Comput Phys Commun* 175:713–720
13. Goedecker S (2004) Minima hopping: An efficient search method for the global minimum of the potential energy surface of complex molecular systems. *J Chem Phys* 120:9911–9917
14. Guggenheim EA (1944) Statistical thermodynamics of mixtures with non-zero energies of mixing. *Proc R Soc Lond A* 183:213–227
15. Guo W, Dmowski W, Noh JY, Rack P, Liaw PK, Egami T (2013) Local atomic structure of a high-entropy alloy: an x-ray and neutron scattering study. *Metall Mater Trans A* 44:1994–1997
16. Hohenberg P, Kohn W (1964) Inhomogeneous electron gas. *Phys Rev* 136(3B):864–871
17. Huhn WP (2014) Thermodynamics from first principles: Prediction of phase diagrams and materials properties using density functional theory. PhD thesis, Carnegie Mellon University
18. Huhn WP, Widom M (2013) Prediction of A2 to B2 phase transition in the high entropy alloy MoNbTaW. *JOM* 65:1772–1779
19. Jiang C (2009) First-principles study of ternary BCC alloys using special quasi-random structures. *Acta Mater* 57:4716–4726
20. Jiang C, Wolverton C, Sofo J, Chen LQ, Liu ZK (2004) First-principles study of binary BCC alloys using special quasirandom structures. *Phys Rev B* 69:214202
21. Kikuchi R (1974) Superposition approximation and natural iteration calculation in cluster variation method. *J Chem Phys* 60:1071–1080
22. Kittel C (2005) Introduction to solid state physics. Wiley, Hoboken
23. Kohn W, Sham LJ (1965) Self-consistent equations including exchange and correlation effects. *Phys Rev* 140:1133–1138
24. Kresse G, Furthmüller J (1996) Efficient iterative schemes for ab initio total-energy calculations using a plane-wave basis set. *Phys Rev B* 54:11169–11186
25. Kresse G, Hafner J (1993) Ab initio molecular dynamics for liquid metals. *Phys Rev B* 47: RC558–RC561
26. Kresse G, Joubert D (1999) From ultrasoft pseudopotentials to the projector augmented-wave method. *Phys Rev B* 59:1758–1775
27. Kresse G, Furthmüller J, Hafner J (1995) Ab initio force constant approach to phonon dispersion relations of diamond and graphite. *Europhys Lett* 32:729–734
28. Martin R (2008) Electronic structure: basic theory and practical methods. Cambridge University Press, Cambridge
29. Mihalkovič M, Widom M (2004) Ab-initio cohesive energies of fe-based glass-forming alloys. *Phys Rev B* 70:144107
30. Neyts EC, Bogaerts A (2013) Combining molecular dynamics with monte carlo simulations: implementations and applications. *Theor Chem Acc* 132:1–12
31. NIST (2013) Janaf thermochemical tables. <http://kinetics.nist.gov/janaf>
32. Perdew JP, Burke K, Ernzerhof M (1996) Generalized gradient approximation made simple. *Phys Rev Lett* 77:3865–3868
33. Ravi C, Panigrahi BK, Valsakumar MC, van de Walle A (2012) First-principles calculation of phase equilibrium of V-Nb, V-Ta, and Nb-Ta alloys. *Phys Rev B* 85:054202
34. Revard BC, Tipton WW, Hennig RG (2014) Structure and stability prediction of compounds with evolutionary algorithms. *Top Curr Chem* 345:181–222
35. Senkov O, Senkova S, Woodward C, Miracle D (2013) Low-density, refractory multi-principal element alloys of the CrNbTiZr system: Microstructure and phase analysis. *Acta Mater* 61:1545–1557
36. Senkova O, Wilks G, Miracle D, Chuang C, Liaw P (2010) Refractory high-entropy alloys. *Intermetallics* 18:1758–1765
37. Smith JF, Carlson ON (1990) Nb-V (niobium-vanadium). In: Massalski TB (ed) Binary alloy phase diagrams, 2nd edn. ASM, Materials Park, pp 2779–2782

38. Takasugi T, Yoshida M, Hanada S (1995) Microstructure and high-temperature deformation of the c15 NbCr₂-based laves intermetallics in Nb-Cr-V alloy system. *J Mat Res* 10:2463–2470
39. Turchi P, Drchal V, Kudrnovsky J, Colinet C, Kaufman L, Liu ZK (2005) Application of ab initio and CALPHAD thermodynamics to Mo-Ta-W alloys. *Phys Rev B* 71:094206
40. Wales DJ, Doye JPK (1997) Global optimization by basin-hopping and the lowest energy structures of Lennard-Jones clusters containing up to 110 atoms. *J Phys Chem A* 101:5111–5116
41. van de Walle A, Asta M (2002) Self-driven lattice-model monte carlo simulations of alloy thermodynamic properties and phase diagrams. *Modelling Simul Mater Sci Eng* 10:521
42. van de Walle A, Ceder G (2002) Automating first-principles phase diagram calculations. *J Phase Equil* 23:348
43. Widom M, Mihalkovic M (2008) Symmetry-broken crystal structure of elemental boron at low temperature. *Phys Rev B* 77:064113
44. Widom M, Huhn W, Maiti S, Steurer W (2013) Hybrid monte carlo/molecular dynamics simulation of a refractory metal high entropy alloy. *Mat Met Trans A* 45:196–200
45. Zunger A (1994) First principles statistical mechanics of semiconductor alloys and intermetallic compounds. In: Turchi PE, Gonis A (eds) NATO ASI on statics and dynamics of alloy phase transformation, vol 319. Plenum, New York, p 361–419
46. Zunger A, Wei SH, Ferreira LG, Bernard JE (1990) Special quasirandom structures. *Phys Rev Lett* 65:353–356

Chapter 9

Applications of Coherent Potential Approximation to HEAs

Fuyang Tian, Yang Wang, Douglas L. Irving, and Levente Vitos

Abstract This chapter details the coherent potential approximation (CPA) to describe the chemically and magnetically disordered phases for systems of arbitrary number of components. Two widely used CPA implementations, namely, the exact muffin-tin orbitals (EMTO) and the Korringa–Kohn–Rostoker (KKR) methods, are briefly reviewed. Applications to predict lattice stability, electronic and magnetic structure, elasticity properties, and stacking fault energies of single-phase HEAs are presented.

Keywords Coherent potential application (CPA) • Korringa–Kohn–Rostoker (KKR) • Exact muffin-tin orbitals (EMTO) • Density functional theory (DFT) • Magnetism • Electronic structure • Elasticity • Elastic constants • Stacking fault energy • Disordered solid solution • High-entropy alloys (HEAs)

F. Tian (✉)

Institute for Applied Physics, University of Science and Technology Beijing,
Beijing 100083, China

Applied Materials Physics, Department of Materials Science and Engineering,
Royal Institute of Technology, Stockholm SE-100 44, Sweden
e-mail: fuyang@ustb.edu.cn

Y. Wang (✉)

Pittsburgh Supercomputing Center, 300 South Craig Street, Pittsburgh, PA 15213, USA
e-mail: ywg@psc.edu

D.L. Irving

Department of Materials Science and Engineering, North Carolina
State University, Raleigh, NC 27695, USA
e-mail: dli@ncsu.edu

L. Vitos

Applied Materials Physics, Department of Materials Science and Engineering,
Royal Institute of Technology, Stockholm SE-100 44, Sweden

Division of Materials Theory, Department of Physics and Astronomy,
Uppsala University, Box 516, Uppsala SE-75120, Sweden

Wigner Research Centre for Physics, Institute for Solid State Physics
and Optics, P.O. Box 49, Budapest H-1525, Hungary
e-mail: levente@kth.se

9.1 The Coherent Potential Approximation

Ab initio density functional theory (DFT) [1, 2], as a powerful ground state theory, has been widely applied to investigate the structural and electronic properties of solids. In the case of the random solid solutions modeling, the coherent potential approximation (CPA) represents the most efficient alloy theory for the electronic structure calculations in multicomponent random solid solutions. The CPA was introduced by Soven [3] for the electronic structure problem and by Taylor [4] for phonons in random alloys. Later, Győrffy [5] formulated the CPA in the framework of the multiple scattering theory using the Green function technique.

The CPA is based on the assumption that the alloy may be replaced by an ordered effective medium, the parameters of which are determined self-consistently. The impurity problem is treated within the single-site approximation. This means that one single impurity is placed in an effective medium and no information is provided about the individual potential and charge density beyond the sphere or polyhedral around this impurity. Below, we illustrate the principal idea of the CPA within the conventional muffin-tin formalism.

We consider a substitutional alloy $A_aB_bC_c\dots$, where A, B, C, ... are the randomly distributed atoms on an underlying crystal lattice and a, b, c, \dots stand for the corresponding atomic fractions. The system is characterized by the Green function g_{alloy} and the alloy potential P_{alloy} . In a real alloy, for a selected type of atom, P_{alloy} shows small variations due to the different local chemical environments. There are two main approximations within the CPA. First, it is assumed that the local potentials around a certain type of atom from the alloy are the same, i.e., the effect of local environments is neglected. These local potentials are described by the functions P_A, P_B, P_C, \dots . Second, the system is replaced by a monoatomic setup described by the site-independent coherent potential \tilde{P} . In terms of Green functions, one approximates the real Green function g_{alloy} by a coherent Green function \tilde{g} . For each alloy component $i = A, B, C, \dots$, a single-site Green function g_i is introduced.

The main steps to construct the CPA effective medium are as follows. First, the coherent Green function is calculated from the coherent potential using an electronic structure method. Within a multiple scattering method, we have

$$\tilde{g} = [S - \tilde{P}]^{-1}, \quad (9.1)$$

where S denotes the structure constant matrix describing the underlying lattice [6–9]. Next, the Green functions of the alloy components, g_i , are determined by substituting the coherent potential of the CPA medium by the real atomic potentials P_i . Mathematically, this condition is expressed via the real-space Dyson equation

$$g_i = \tilde{g} + \tilde{g} (P_i - \tilde{P}) g_i \quad (9.2)$$

for each $i = A, B, C, \dots$. Finally, the average of the individual Green functions should reproduce the single-site part of the coherent Green function, i.e.,

$$\tilde{g} = ag_A + ag_B + cg_C + \dots \quad (9.3)$$

Equations (9.1, 9.2, and 9.3) are solved iteratively, and the output \tilde{g} and g_i s are used to determine the electronic structure, charge density, and total energy of the random alloy. According to the single-site impurity equation (9.2), the impurity Green function g_i describes the single impurity (one single atom) with potential P_i as embedded in the effective medium specified by the coherent potential \tilde{P} .

Nowadays, the CPA has become a state-of-the-art technique for electronic structure calculations in random alloys. Numerous applications have shown that within this approximation, one can calculate lattice parameter, bulk modulus, mixing enthalpy, etc., with an accuracy similar to that obtained for ordered solids. At the same time, the CPA, being a single-site approximation to the impurity problem, has intrinsic limitations. For instance, within the CPA, one cannot take into account the short-range order effects. Moreover, systems with large-size mismatch between the alloy components are difficult to describe because of the sizable local lattice relaxations. More specifically, the average lattice dilation is well captured by CPA but not the element-specific local displacements of the lattice sites.

Probably, the most important failure of the existing CPA methods happens in the case of anisotropic lattice distortions in random alloys. This problem has erroneously been attributed to the inherent single-site approximation. However, one should bear in mind that certain limitations of the CPA are not directly related to the approximation itself. Rather, they originate from additional approximations introduced by particular DFT implementations. The most common electronic structure calculation methods used in combination with the CPA are based on the Atomic Sphere Approximation (ASA). The associated shape approximation turned out to be insufficient for the accurate description of the behavior of the total energy upon anisotropic lattice distortions. Thus, one cannot calculate, for example, elastic constants in random alloys or relax the axial ratio in alloys with a tetragonal, hexagonal, or lower symmetry. In addition, such DFT methods do not give a proper description of the open structures or structural energy differences between structures with different packing fractions, to the extent that even the energy difference between the bcc and fcc structures of the late transition metals is often incorrectly described. However, a recent reformulation of the CPA [10–12] demonstrates that this approximation implemented within the framework of the exact muffin-tin orbitals (EMTO) method, in contrast to several previous implementations, is suitable to reproduce the structural energy differences and energy changes related to small lattice distortions in random alloys with high accuracy.

In addition to the CPA, the virtual crystal approximation (VCA), the cluster expansion method, and the supercell approach [13], in particular, the so-called special quasi-random structure (SQS) [14], are often used to study random alloys. Recently, the SQS was employed in describing the CoCrFeMnNi high-entropy

alloys [15]. However, today, the SQS calculations for the paramagnetic state are still very cumbersome. The reader is referred to Chap. 10 for more details about SQS. Another important method to describe atomic structure of HEAs is through hybrid Monte Carlo/Molecular Dynamic (MCMD) simulations as detailed in Chap. 8. The advantages of SQS and MCMD are that they allow atomic relaxation and render reliable prediction of temperature-dependent thermodynamic properties. On the other hand, due to the constraint associated with the supercell, they cannot account for small compositional changes as discussed, for example, in Ref. [15]. A brief comparison among the above methods in treating HEAs is presented in Chap. 10 in this book.

In the present chapter, we describe two widely used CPA implementations, namely, the EMTO-CPA and the Korringa–Kohn–Rostoker (KKR)-CPA methods, and demonstrate them through several recent applications. The structure of the chapter is as follows: in Sect. 9.2, we review the main features of the EMTO-CPA method relevant for the HEAs and in Sect. 9.3, we assess it using supercell calculations. In Sects. 9.4 and 9.5, we present results obtained for 3d and refractory HEAs, respectively. Section 9.6 puts forward a first attempt to determine the stacking fault energies of HEAs using a combined experimental–theoretical effort. Finally, the KKR-CPA method is introduced and demonstrated in Sects. 9.7 and 9.8. The chapter ends with brief conclusions.

9.2 The EMTO-CPA Method

The EMTO theory belongs to the third-generation muffin-tin approximation family. This theory is an improved KKR method, which uses large overlapping muffin-tin potential spheres which can describe the exact one-electron potential rather accurately. In the calculation of the total energy, the EMTO method employs the Full Charge Density (FCD) technique, which not only improves the calculation efficiency but also ensures total energies with accuracy similar to that of the full-potential methods [12]. For numerical details of the present EMTO-CPA calculations, see Refs. [16–18].

It should be mentioned that most of the present EMTO-CPA calculations of the 3d HEAs are based on the paramagnetic state. We employed the disordered local magnetic moment (DLM) [19] picture to describe the paramagnetic state of these HEAs. According to that model, an alloy component M of concentration m is presented by its spin-up (\uparrow) and spin-down (\downarrow) counterparts assumed to be distributed randomly on the underlying sublattice, i.e., each magnetic alloy component is treated as $M_m \rightarrow M_{m/2}^{\uparrow} M_{m/2}^{\downarrow}$. For example, CoCrFeNi is described as a quasi-eight-component random solid solution, viz., $Co_{0.125}^{\uparrow} Co_{0.125}^{\downarrow} Cr_{0.125}^{\uparrow} Cr_{0.125}^{\downarrow} Fe_{0.125}^{\uparrow} Fe_{0.125}^{\downarrow} Ni_{0.125}^{\uparrow} Ni_{0.125}^{\downarrow}$.

9.3 Assessing the EMTO-CPA Method for HEAs

In order to assess the performance of EMTO-CPA in the case of HEAs, we select CoCrFeNi and set up a simple supercell (SC) with fcc underlying lattice. To mimic a homogeneous solid solution, we distribute the four alloying elements so that they are neighbors to each other within a conventional fcc unit cell, as shown in Fig. 9.1. We notice that CoCrFeNi is found to show no tendency for long-range chemical ordering [20]. Taking into account that the long-range order has a rather small effect on the elastic properties of alloys [21], it seems to be reasonable to assume that one may directly compare the result from CPA with the SC results calculated for the present ordered structure. In this test, ferromagnetic order was assumed in both CPA and SC calculations. Table 9.1 lists the results obtained from the above SC method and those calculated for the corresponding $\text{Co}_{0.25}\text{Cr}_{0.25}\text{Fe}_{0.25}\text{Ni}_{0.25}$ (equivalent to CoCrFeNi) random solid solution using the single-site CPA as

Fig. 9.1 The simple supercell (SC) used to model the CoCrFeNi high-entropy alloy

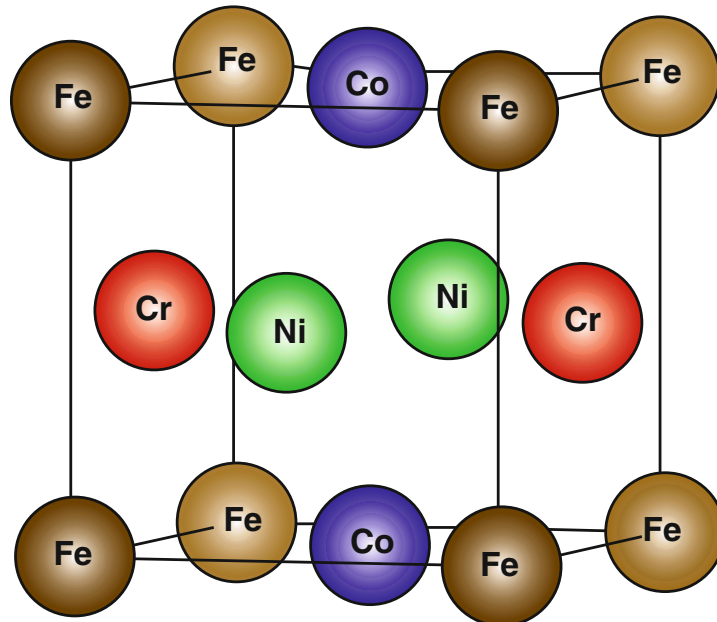


Table 9.1 Theoretical bulk parameters for fcc CoCrFeNi HEA calculated using the CPA and SC (see text) methods

Method	w	B	c_{11}	c_{12}	c_{14}	c'
CPA	2.607	207	271.0	175.0	189.3	48.0
SC	2.601	208	257.1	183.5	193.9	36.8
	A_Z	$(c_{12}-c_{44})$	G	E	ν	A_{VR}
CPA	3.9	-14.3	110	280	0.275	0.21
SC	5.2	-10.4	101	262	0.290	0.29

All data are from Ref. [16]. The Wigner–Seitz radius from experiment is 2.632 Bohr [22]. Listed are the equilibrium Wigner–Seitz radius w (Bohr); the bulk modulus B (GPa); three independent elastic constants c_{11} , c_{12} , c_{44} , and $c' = (c_{11} - c_{12})/2$ (GPa); the Zener anisotropy A_Z ; the Cauchy pressure $(c_{12} - c_{44})$ (GPa); the shear modulus G (GPa); the Young modulus E (GPa); the Poisson ratio ν ; and the polycrystalline elastic anisotropy ratio A_{VR} .

implemented in EMTO. More DFT calculations on the effect of the SC size to the energy and elastic properties of HEAs are presented in Chap. 10.

The average SC equilibrium Wigner–Seitz (WS) radius is 2.601 Bohr, which is rather close to 2.607 Bohr obtained for solid solution via CPA. The agreement between the SC (207 GPa) and CPA (208 GPa) bulk moduli is also excellent. For all theoretical parameters, we find a good consistency between the CPA and SC results. In particular, the three cubic elastic constants, c_{11} , c_{12} and c_{44} , obtained with the two methods differ on the average by ~4 %. The larger relative differences in the Zener anisotropy (c_{44}/c') and the Cauchy pressure ($c_{12}-c_{44}$) are still acceptable, especially if we consider that the present SC is the simplest periodic approximant of the four-component random alloy considered in the CPA calculations. The good agreement seen for the shear and Young's modulus (G and E), Poisson ratio (ν), and polycrystalline anisotropy ratio A_{VR} indicates that the CPA is an efficient and accurate method to investigate the bulk properties of these multicomponent alloys.

In order to further assess the performance of the calculations derived from the mean-field CPA, we construct two $2 \times 2 \times 2$ cubic supercells shown in Fig. 9.2. The supercell formed by the bcc (fcc) unit cells is treated as simple cubic (body-centered cubic), where we introduce one (two) Al atom per 16 (32) atomic sites. All other sites are occupied by an equimolar four-component CoCrFeNi alloy. We note that similar partially ordered solid solution has been reported in $\text{Al}_{0.3}\text{CoCrFeNi}$ HEA [23]. The present supercells have the molar ratio $\text{Al}_1\text{Co}_{15/4}\text{Cr}_{15/4}\text{Fe}_{15/4}\text{Ni}_{15/4}$, corresponding to $\text{Al}_{0.2667}\text{CoCrFeNi}$ HEA. The Wigner–Seitz radii obtained for these supercells are 2.620 Bohr for fcc and 2.634 Bohr for bcc, which are practically the same as those obtained in the corresponding CPA calculations (2.620 Bohr for fcc and 2.635 for bcc). The corresponding bulk moduli are 197 and 193 GPa for the fcc and bcc supercells, respectively, which are also close to the CPA results (198 GPa for fcc and 193 GPa for bcc).

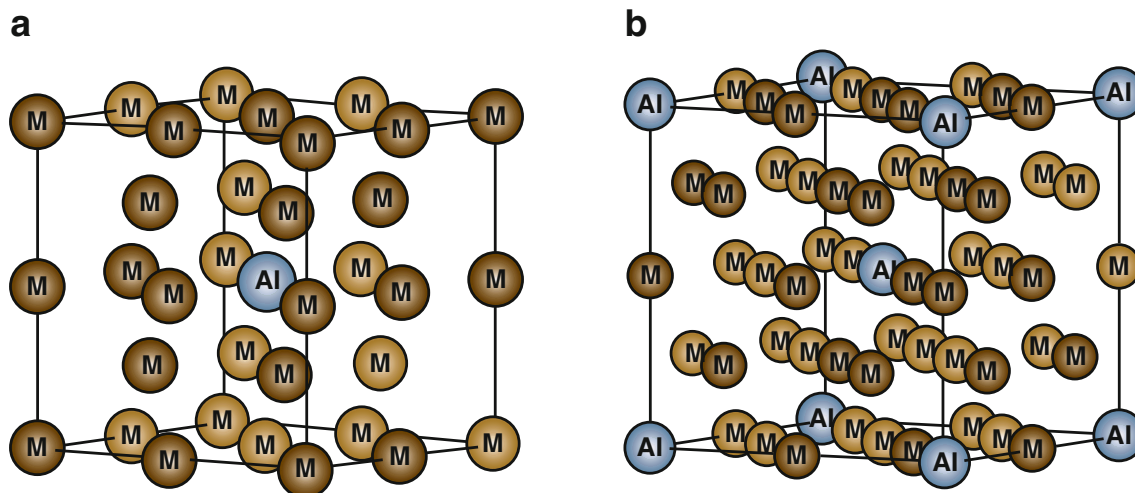


Fig. 9.2 Schematic plot of the $2 \times 2 \times 2$ bcc supercell (a) and the $2 \times 2 \times 2$ fcc supercell (b) for $\text{Al}_{0.2667}\text{CoCrFeNi}$ HEA. Label M represents an equimolar four-component CoCrFeNi alloy, and label Al is aluminum at the center or vertex sites

9.4 EMTO-CPA Applications to 3d HEAs

9.4.1 Equilibrium Volumes

In Table 9.2, we compare the EMTO-CPA Wigner–Seitz (WS) radii calculated for CoCrFeNi, CoCrCuFeNi, CoCrFeMnNi, and CoCrFeNiTi with available experimental values measured by x-ray diffraction. Using the Wigner–Seitz radii for the alloy constituents, we may estimate the equilibrium volume of the HEAs via Vegard’s rule. In Table 9.2, \bar{w}_t stands for the estimated volume based on the previous PBE-level theoretical data, and \bar{w}_e the one obtained from the experimental data. It is found that the calculated average WS radii are smaller than the averaged experimental data. The calculated WS radii are also slightly smaller than the experimental values except for CoCrFeNiTi (we notice that the as-cast CoCrFeNiTi is not a single fcc structure, but the main fcc matrix with two minor phases [27]). The connection between the WS radius and the lattice parameter a is $a^3 = 2 \cdot \frac{4}{3} \pi w^3$ ($a^3 = 4 \cdot \frac{4}{3} \pi w^3$) for bcc (fcc) structure.

9.4.2 Magnetic Properties

Figure 9.3 shows the local magnetic moments (\uparrow or \downarrow) versus the Wigner–Seitz radius for the magnetic sublattices in paramagnetic CoCrCuFeNi, CoCrFeNi, and CoCrFeNiTi high-entropy alloys. According to the calculations, the local magnetic moments vanish on the Cu, Ni, and Ti sites for all volumes and thus, they are not shown in Fig. 9.3. We should note that thermal effects would eventually induce local magnetic moments on the Ni sites as well at finite temperature. Such longitudinal spin fluctuations have been neglected in the present study. For all alloys, Fe possesses a significant ($\sim 1.8\text{--}2.0 \mu_B$) local magnetic moment around the equilibrium volume. Cobalt remains nonmagnetic in CoCrFeNi and CoCrFeNiTi but shows a small ($\sim 0.6 \mu_B$) magnetic moment for CoCrCuFeNi.

We plot the paramagnetic total density of state (DOS) and partial density of state (pDOS) for CoCrCuFeNi, CoCrFeNi, and CoCrFeNiTi in Fig. 9.4. For all alloys, Fe has a moderate pDOS peak located very close to the Fermi level (E_F). It is found that the size of the DOS at E_F ($D_{Fe}(E_F)$) is the largest among all pDOS at E_F , followed by $D_{Co}(E_F)$ and $D_{Cr}(E_F)$. This distinct Fe peak at E_F leads to magnetic instability in Fe sublattice. Indeed, as shown in Fig. 9.4, the spin-polarized pDOS of Fe has two separate peaks: one above the Fermi level and one below the Fermi level. These two Fe peaks hybridize with the Cr and Co peaks, respectively. As a result of the magnetic splitting, the total $D(E_F)$ drops significantly in all three alloys.

Table 9.2 Theoretical and experimental Wigner–Seitz radii (Bohr) for CoCrFeNi, CoCrFeMnNi, CoCrCuFeNi, and CoCrFeNiTi_x [22, 24–26]

HEAs	<i>w</i>	<i>w_e</i>	<i>bar{w}_t</i>	<i>bar{w}_e</i>	<i>c₁₁</i>	<i>c₁₂</i>	<i>c₄₄</i>	<i>c'</i>	<i>E</i>	<i>E</i> (Expt.)
CoCrFeNi	2.607	2.632	2.623	2.642	271.0	175.0	189.3	48.0	280.0	—
CoCrFeMnNi	2.609	2.651	—	—	245.1	148.9	191.5	48.1	275.9	157
CoCrCuNiFe	2.628	2.643	2.636	2.647	227.8	154.6	165.3	36.6	234.0	55.6
CoCrFeNiTi	2.682	2.650	2.706	2.724	184.5	170.9	127.0	6.8	130.3	134
CoCrCuFeNiTi _{0.1}	2.635	—	2.644	2.655	219.7	152.6	160.2	33.5	223.1	—
CoCrCuFeNiTi _{0.2}	2.643	—	2.652	2.663	213.6	152.1	155.1	30.5	231.1	—
CoCrCuFeNiTi _{0.3}	2.651	—	2.659	2.670	209.6	151.9	154.6	28.9	205.9	—
CoCrCuFeNiTi _{0.4}	2.655	—	2.666	2.677	207.6	151.7	150.8	27.9	200.4	—
CoCrCuFeNiTi _{0.5}	2.663	—	2.673	2.684	198.4	151.0	142.7	23.7	187.1	98.6
CoCrCuFeNiTi _{1.0}	2.694	—	2.703	2.715	174.3	148.6	125.0	12.8	145.4	76.5

Data taken from Ref. [16]

w and *w_e* are those predicted in EMTO-CPA calculations and the available experiments, respectively. *bar{w}_t* and *bar{w}_e* represent the alloys' Wigner–Seitz radii as estimated from Ref. [12], according to Vegard's rule

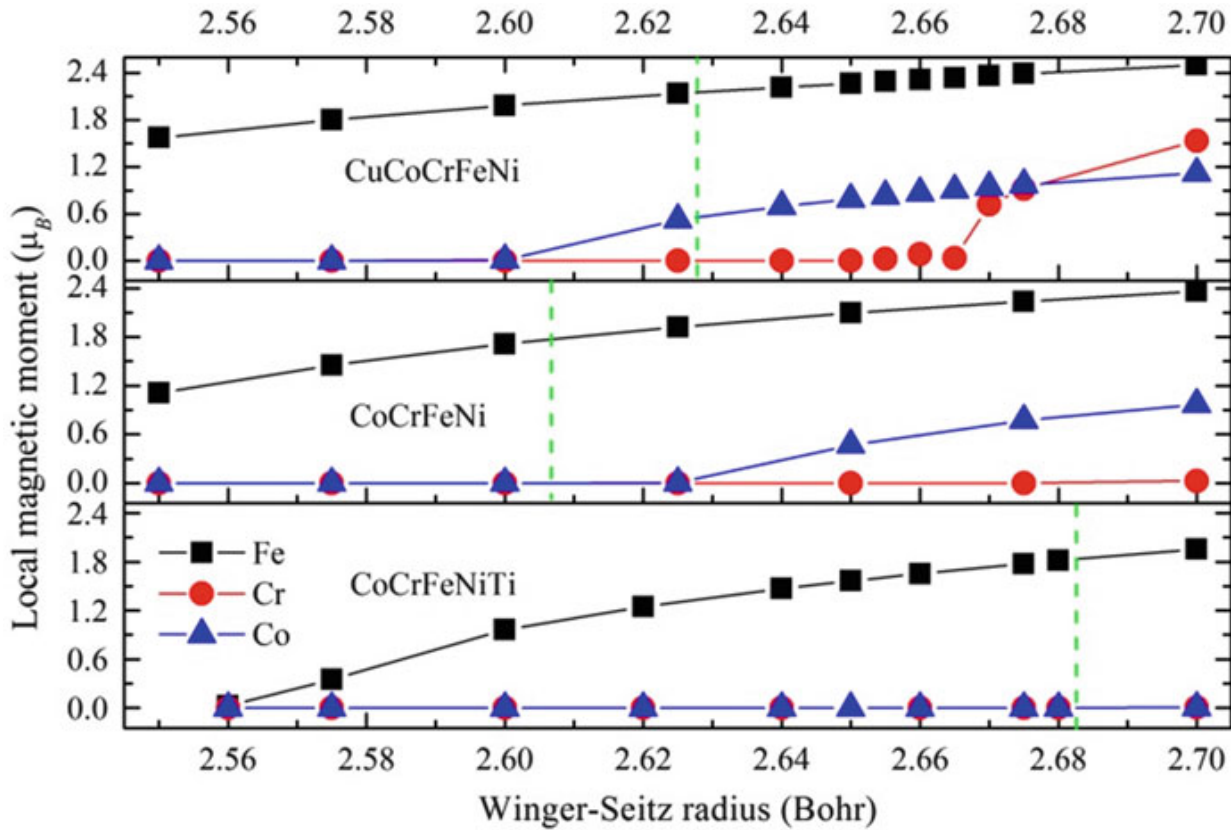


Fig. 9.3 Local magnetic moments of Co, Cr, and Fe in paramagnetic fcc CuCoCrFeNi, CoCrCuFeNi, and CoCrFeNiTi alloys as a function of the WS radius. For each HEA, the vertical (green) line stands for the calculated equilibrium SW radius (Data taken from Ref. [16])

9.4.3 Elastic Properties of 3d HEAs

The three cubic elastic constants c_{11} , c_{12} , c_{44} and c' of CoCrFeNi, CoCrFeMnNi, CoCrCuFeNi_x, and CoCrFeNiTi are listed in Table 9.2. The elastic constants and elastic moduli for CoCrCuFeNiTi_x are also plotted in Fig. 9.5 as a function of Ti content. As seen from Table 9.2, all 3d HEAs considered here are mechanically stable. Titanium decreases the tetragonal elastic constant c' both in CoCrFeNiTi and CoCrCuFeNiTi_x, as compared to that of CoCrFeNi. This indicates that Ti decreases the mechanical stability of the fcc phase, which is in line with the expectation based on the effective number of d electrons.

Theory predicts a moderate elastic anisotropy and small negative Cauchy pressure for CoCrFeNi. We recall that negative ($c_{12}-c_{44}$) has been associated with the covalent nature of the metallic bond and is characteristic to brittle alloys. In the absence of any experimental data, we compare the present results calculated for paramagnetic CoCrFeNi with those obtained for paramagnetic austenitic stainless steel alloys composed of ~18 % Cr, ~8 % Ni, and balance Fe [28]. The three cubic elastic constants reported for this stainless steel are $c_{11}=208.6$ GPa, $c_{12}=143.5$ GPa, and $c_{44}=132.8$ GPa, which yield 4.07 for the Zener anisotropy ratio and 10.7 GPa for the Cauchy pressure. Therefore, compared to the austenitic stainless steels, the paramagnetic CoCrFeNi is predicted to be more brittle. Equimolar Cu addition to CoCrFeNi is found to increase slightly the Cauchy pressure

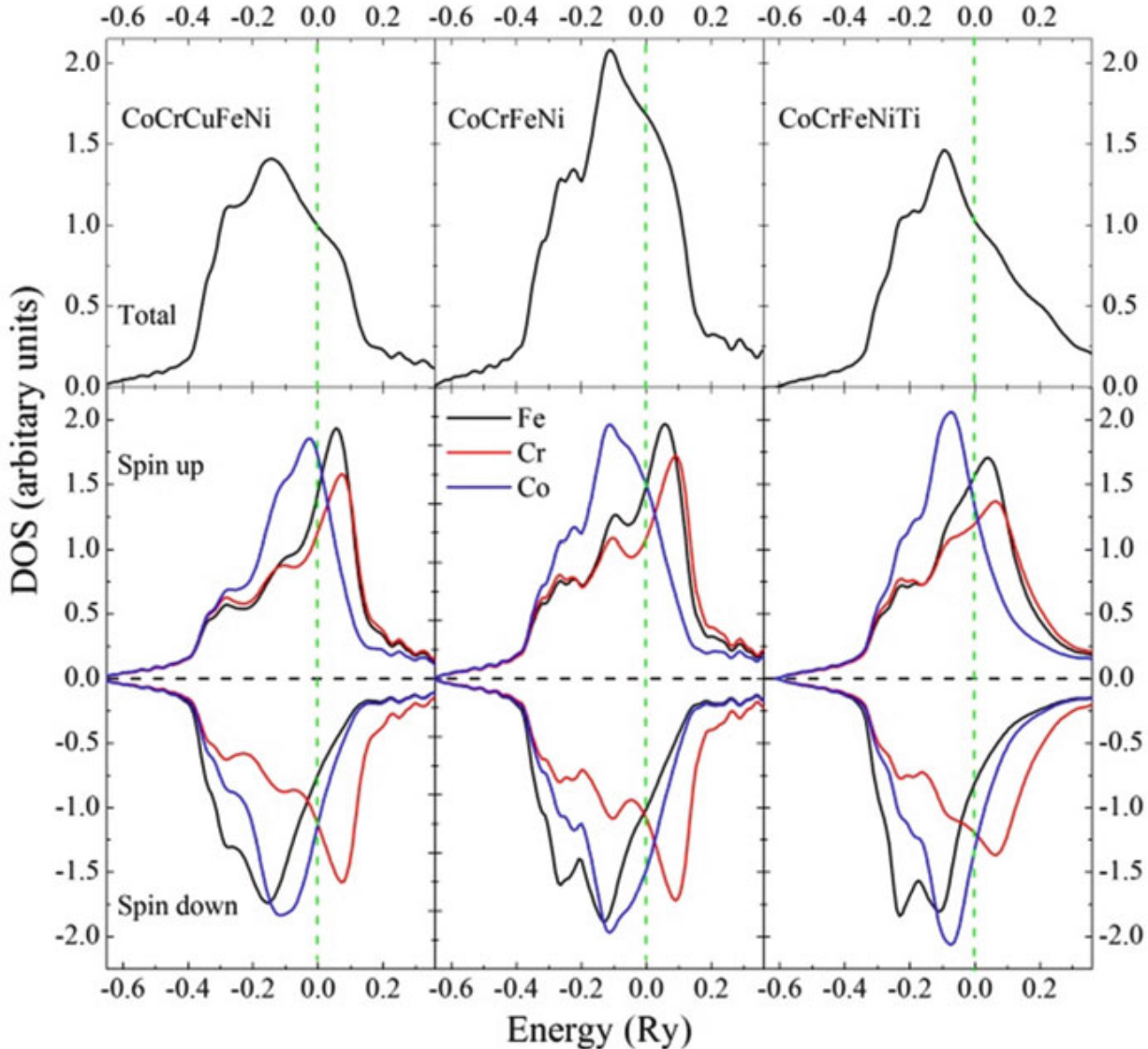


Fig. 9.4 Total (*upper panels*) and Co, Cr, and Fe partial (*lower panels*) density of states (pDOS) for the paramagnetic fcc CoCrCuFeNi, CoCrFeNi, and CoCrFeNiTi HEAs. In the lower panels, only the Co, Cr, and Fe partial densities of state are shown (Ni, Cu, and Ti are no local magnetic moments). Apart from the sign (spin up versus spin down) difference, the partial densities of states for Co, Cr, and Fe are identical to those shown in the figure (Data taken from Ref. [16])

from -14.3 GPa obtained for CoCrFeNi to -10.7 GPa calculated for CoCrCuFeNi. For reference, fcc Ir has Cauchy pressure of -13 GPa and undergoes both transgranular and intergranular fracture.

Before continuing our discussion, we mention that the validity of the correlation between brittle–ductile behavior and the Cauchy pressure has not yet been confirmed in the case of HEAs, so the above theoretical prediction regarding the brittleness of CoCrFeNi should be treated with precautions. On the other hand, we should recall that the present calculations correspond to static conditions (0 K), which substantially underestimates the equilibrium volume of the alloy. Computing the elastic parameters close to the experimental volume (i.e., accounting for the lattice expansion) leads to positive Cauchy pressures for both CoCrFeNi and CoCrFeMnNi [15]. Employing the Vienna ab initio simulation packages (VASP) in combination with special quasi-random structure (SQS) yields somewhat

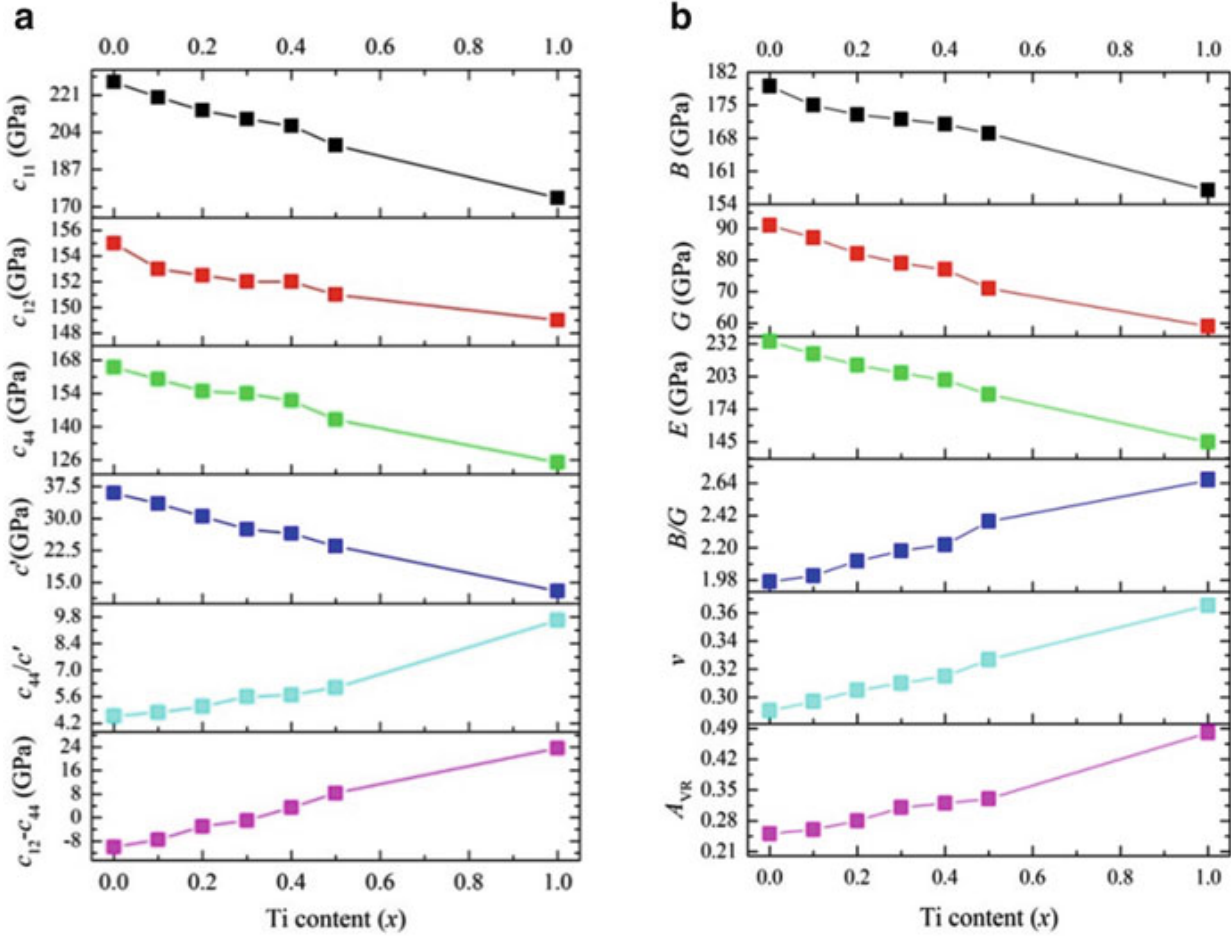


Fig. 9.5 Panel (a): Three independent elastic constants c_{11} , c_{12} , and c_{44} as well as c' ($(c_{11}-c_{12})/2$), c_{44}/c' , and $(c_{12}-c_{44})$ for CoCrCuFeNiTi_x ($x = 0-0.5, 1.0$) HEAs. Panel (b): Polycrystalline elastic moduli B , G , and E as well as B/G , v , and A_{VR} for CoCrCuFeNiTi_x ($x = 0-0.5, 1.0$) HEAs (All data are from Ref. [16])

different elastic parameters as compared to EMTO-CPA and positive (negative) Cauchy pressure for CoCrFeNi (CoCrFeMnNi) [15]. Research focusing on the above trends and differences is in progress. In the rest of this chapter, the discussions related to the brittle–ductile behavior of HEAs should be considered in the mirror of the above results.

Titanium is found to change the CoCrFeNi host into a more ductile but strongly anisotropic material. Equimolar fcc CoCrFeNiTi has $c_{44}/c' = 18.7$ and $(c_{12}-c_{44}) = 43.9$ GPa. Such high anisotropy ratio is rather unusual. For comparison, the Zener anisotropy of paramagnetic bcc and fcc Fe was found to be around 8.6 and 3.6, respectively. Considering the change of the Cauchy pressure upon equimolar doping, we may conclude that although Cu also improves the ductility of the 3d HEAs, Ti makes it especially ductile. Indeed, as seen in the case of CoCrCuFeNiTi_x , Ti can substantially increase the Cauchy pressure of the host alloy. It gradually increases the metallic character of the bonds turning the static (0 K) Cauchy pressure positive somewhere between $x = 0.3$ and $x = 0.4$. We find that all elastic parameters of CoCrCuFeNiTi_x change monotonously with the amount of Ti in Fig. 9.5b. According to the present theoretical calculations, the bulk parameters of single-crystal $\text{CoCrCuFeNiTi}_{0.5}$ HEAs, which are still believed to be

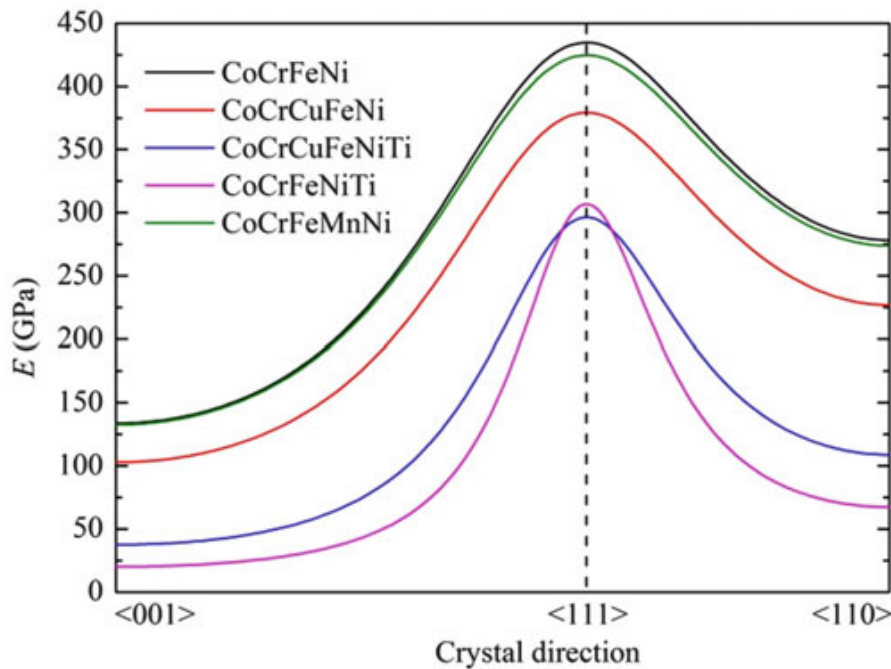


Fig. 9.6 Theoretical Young's modulus for five HEAs (CoCrFeNi, CoCrCuFeNi, CoCrCuFeNiTi, CoCrFeNiTi, and CoCrFeMnNi) as a function of direction including the three main cubic directions

single-phase alloys, are surprisingly close to those reported for the Cr_{0.18}Fe_{0.74}Ni_{0.08} austenitic stainless steel alloy [28].

Next, we compare the theoretical results with the available experimental data. It is particularly surprising that for CoCrCuFeNi, our Young's modulus of 234 GPa is about four times larger than 55.6 GPa found in experiment [24]. This alloy shows relatively low anisotropy and thus, the uncertainty associated with the Voigt–Reuss–Hill averaging is expected to be small. Furthermore, as shown in Fig. 9.6, the Young's modulus of a single-crystal CoCrCuFeNi changes between 102.79 GPa obtained for the <001> direction and 379.18 GPa calculated for the <111> direction. Therefore, even for a highly textured material, theory would predict the lowest E to be around 100 GPa, which is still almost double of the experimental value. For the two Ti-containing CoCrCuFeNiTi_{0.5} and CoCrCuFeNiTi alloys, the calculated Young's moduli differ from the reported experimental values by ~90 %. On the other hand, the agreement between theory and experiment is almost perfect for CoCrFeNiTi. Such good agreement is rather unexpected since for this alloy, we obtained very large anisotropy ratio. The single-crystal Young's modulus of CoCrFeNiTi changes significantly with direction (Fig. 9.6), the lowest value being close to 20 GPa (for <001> direction) and the largest around 307 GPa (for <111> direction). One should also point out that the recent experiments show that CoCrFeNiTi is not a single fcc phase alloy [27]. Finally, we note that the paramagnetic CoCrFeNi and CoCrFeMnNi HEAs have very close Young's moduli E as a function of direction.

Regarding the difference between the theoretical and experimental Young's moduli for CoCrCuFeNi, one possible reason is that all present calculations were carried out at static conditions (0 K) while the experimental measurements were

performed at room temperature. In addition, our calculations assumed an ideal solid solution phase with fcc underlying lattice in contrast to the real alloys having complex microstructure. For instance, in CoCrCuFeNi, Cu segregation to the interdendrite region was observed. More extensive experimental as well as theoretical studies are necessary to understand the large deviation between the theoretical and experimental Young's modulus for these important category of engineering materials.

9.4.4 The fcc–bcc Phase Transformation in Al-Doped 3d HEAs

In Fig. 9.7, we show the theoretical equilibrium volume (V) and structural energy difference $\Delta E = E_t(\text{bcc}) - E_t(\text{fcc})$ for the $\text{Al}_x\text{CoCrFeNi}$ alloys as a function of Al content. Experimental volumes are available for the single fcc phase for $x \leq 0.5$ and for single bcc phase for $x \geq 0.9$ [29–31]. Aluminum addition is found to increase the equilibrium volume of the solid solution, which is consistent with the fact that w of Al is larger than those of the other alloy components. Using a cubic spline fit for the calculated energy points, we find that the structural energy difference between ideal bcc and fcc lattices vanishes at $x = 1.11$ Al fraction.

Because of the large atomic volume of Al, the interatomic distance between Al and the other elements is larger than the average bulk value. We estimated the size

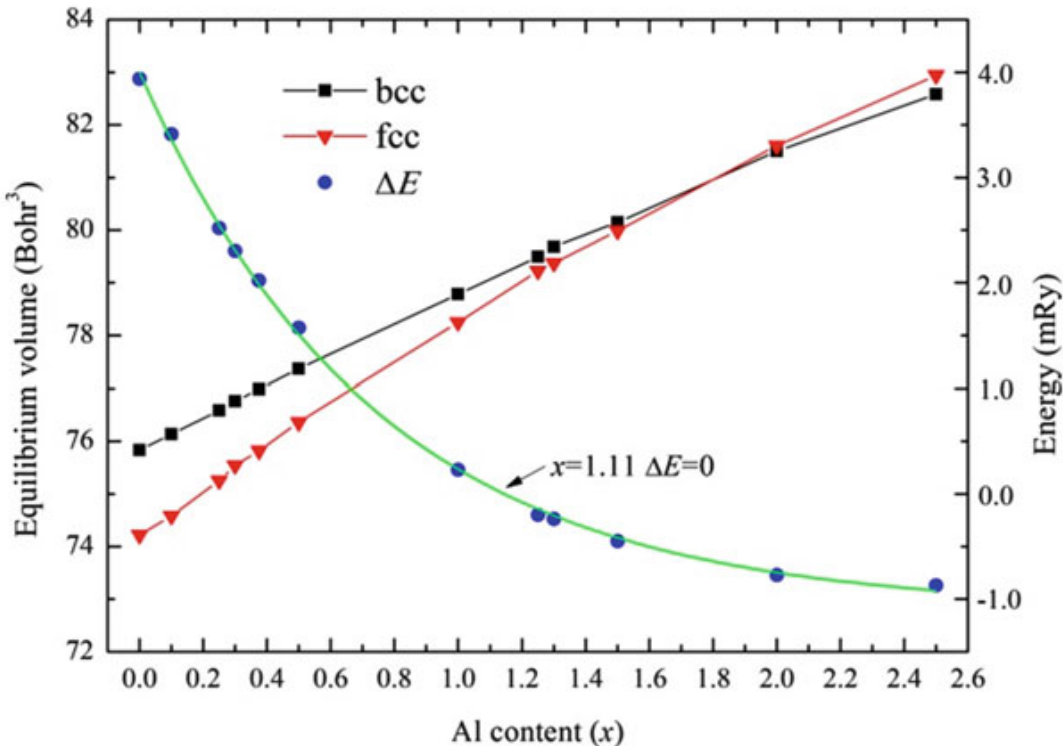


Fig. 9.7 Theoretical fcc and bcc equilibrium volumes and structural energy difference for $\text{Al}_x\text{CoCrFeNi}$ ($x = 0$ –2.5) HEAs

of the local lattice relaxation (LLR) around the Al atoms in $\text{Al}_x\text{CoCrFeNi}$ alloys by making use of the above $2 \times 2 \times 2$ supercells, each of them containing one single Al atom. We relaxed the first 12 nearest neighbor CoCrFeNi sites in the fcc supercell and the first eight nearest neighbor CoCrFeNi sites in the bcc supercell. For the energy gain upon the LLR, we obtained $\delta E_{\text{bcc}} = 0.17$ mRy and $\delta E_{\text{fcc}} = 0.32$ mRy. The larger relaxation effect in the fcc lattice is in line with our previous observation that the bcc lattice can accommodate the large substitutional Al more easily than the fcc lattice. Then, we consider $\Delta E' \equiv x(\delta E_{\text{bcc}} - \delta E_{\text{fcc}})$ as the measure of the LLR effect on the structural energy difference per Al fraction. Adding $\Delta E'$ to ΔE , we obtain that the total structural energy difference vanishes around $x = 1.2$, i.e., at only slightly larger Al content than the one predicted from the total energies obtained for rigid underlying lattices.

Two phases arrive at equilibrium when their Gibbs free energies become equal. Here, we consider the $\text{Al}_x\text{CoCrFeNi}$ system as a pseudo-binary $\text{Al}_y(\text{CoCrFeNi})_{1-y}$ alloy (with $y = x/(4+x)$) and compute the relative formation energy according to $\Delta G^\alpha(y) = G^\alpha(y) - (1-2y)G^{\text{fcc}}(0) - 2yG^{\text{fcc}}(0.5)$, where α stands for fcc or bcc and $G^\alpha(y)$ is the Gibbs free energy per atom for $\text{Al}_y(\text{CoCrFeNi})_{1-y}$ in the α phase. This is approximated as $G^\alpha(y) \sim E^\alpha(y) - TS_{\text{mix}}(y) - TS_{\text{mag}}^\alpha(y)$, where $E^\alpha(y)$ is the total energy per atom for $\text{Al}_y(\text{CoCrFeNi})_{1-y}$ in the α phase and T is the temperature. The two entropy terms are estimated within the mean-field approximation. Namely,

the mixture entropy of ideal solutions is $S_{\text{mix}} = -k_B \sum_{i=1}^5 c_i \ln c_i$, and the magnetic

entropy $S_{\text{mag}} = k_B \sum_{i=1}^5 c_i \ln(1 + \mu_i)$, where c_i is the concentration and μ_i the mag-

netic moment of the i th alloying element. Accordingly, all chemical and magnetic short-range order effects and the longitudinal spin fluctuations are neglected (i.e., for each alloy composition, we assume constant local magnetic moments with temperature). The above phenomenological approximation for the magnetic entropy was previously used to estimate the free energy of paramagnetic Fe and Fe-based alloys having non-integer magnetic moments.

The present Gibbs free energies at different temperature are plotted in Fig. 9.8. According to the rule of common tangent line, we find that at room temperature, $\text{Al}_x\text{CoCrFeNi}$ has single fcc phase for $x \leq 0.597$ ($y \leq 0.130$), single bcc phase for $x \geq 1.229$ ($y \geq 0.235$), and two phases (duplex) between the above limits. In terms of valence electron concentration, the present theory predicts that at 300 K, the fcc phase is stable for valence electronic concentration (VEC) ≥ 7.57 and the bcc one for VEC ≤ 7.04 . These theoretical solubility limits should be compared to 8.0 and 6.87 estimated by Guo et al. and 7.67–7.88 and 7.06–7.29 observed in experiments [32].

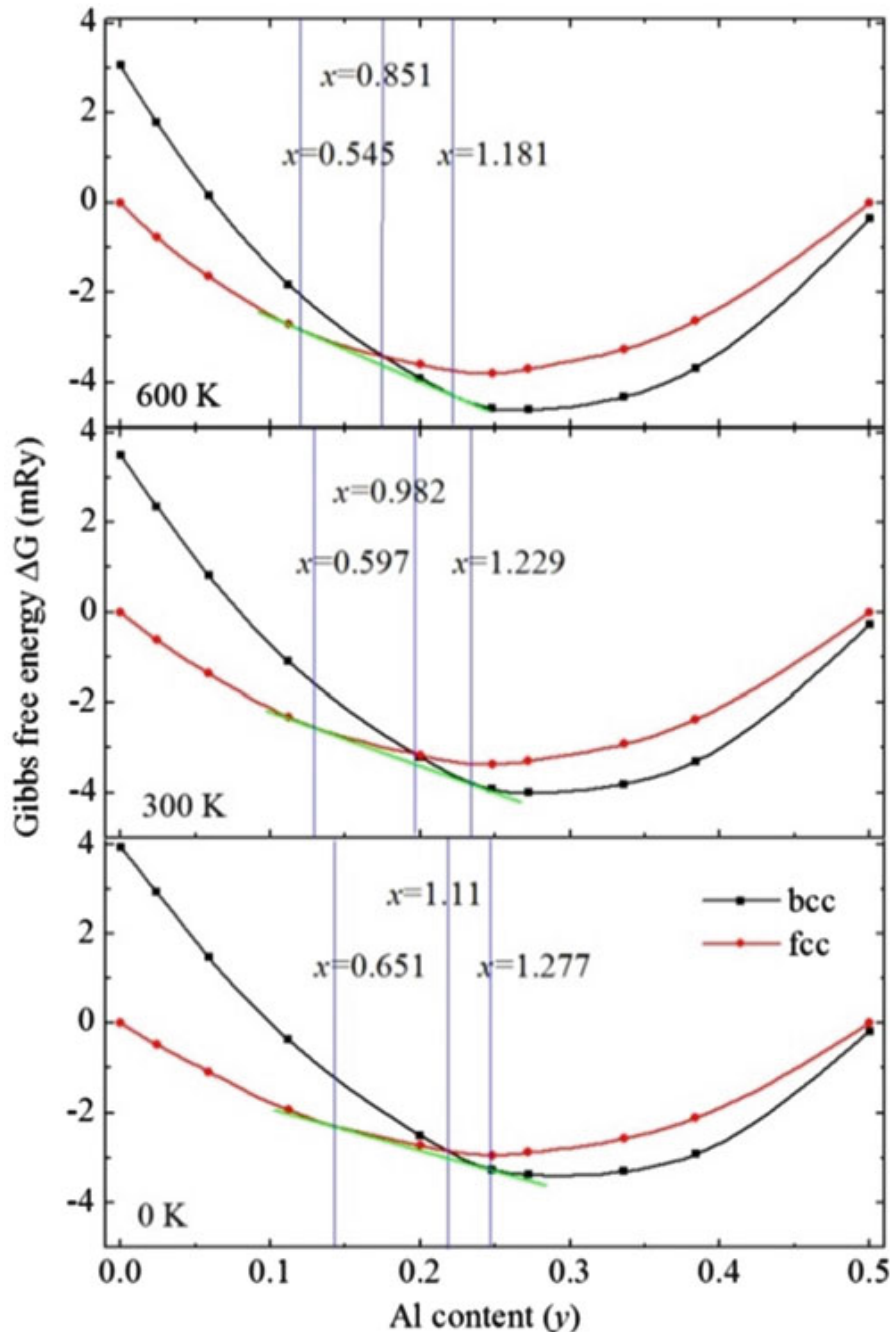


Fig. 9.8 The Gibbs free energies as a function of the content of Al for bcc and fcc $\text{Al}_y(\text{CoCrFeNi})_{1-y}$ ($y = 0\text{--}0.5$) at $T = 0, 300$, and 600 K . Note that $y = x/(4+x)$, where x is the atomic fraction of Al in $\text{Al}_x\text{CoCrFeNi}$ HEAs (All data are from Ref. [17])

9.4.5 Elastic Properties of Al-Doped 3d HEAs

The calculated elastic parameters of $\text{Al}_x\text{CoCrFeNi}$ HEAs are listed in Table 9.3. We notice that the elastic parameters obtained for the fcc and bcc phases around $x = 1$ are surprisingly close to each other. When considering the fcc or bcc structure separately, it is found that the three cubic elastic constants (c_{ij}) and the polycrystal elastic moduli (B , G , and E) decrease with increasing Al content. However, the Cauchy pressure ($c_{12}-c_{44}$), the two anisotropy ratios (A_Z and A_{VR}), the Poisson's ratio (ν), and the B/G ratio increase with x in the fcc phase.

Table 9.3 Wigner–Seitz radius w (Bohr), three cubic elastic constants ($c_{ij}, c' = (c_{11}-c_{12})/2, A_z = c_{44}/c'$), Cauchy pressure ($c_{12}-c_{44}$), and polycrystalline elastic moduli (B, G, E, A_{VR} , ν , and B/G) for fcc and bcc $\text{Al}_x\text{CoCrFeNi}$ HEAs as a function of the content of Al

x	Phase	w	c_{11}	c_{12}	c_{44}	c'	A_z	$(c_{12}-c_{44})$	B	G	E	ν	A_{VR}	B/G
0.0	fcc	2.607	271	175	189	48.0	3.94	-14.3	207	110	280	0.275	0.209	1.88
0.3	fcc	2.622	246	171	177	37.3	4.75	-6.12	196	96	248	0.289	0.262	2.04
0.5	fcc	2.632	233	169	171	32.2	5.29	-2.13	190	89	231	0.297	0.295	2.13
1.0	fcc	2.654	214	167	158	23.5	6.85	9.00	183	76	201	0.317	0.369	2.40
1.0	bcc	2.659	214	160	152	27.2	6.72	7.84	178	78	204	0.309	0.311	2.29
1.3	bcc	2.670	208	151	150	28.1	5.59	0.80	170	78	203	0.301	0.298	2.17
1.5	bcc	2.675	205	148	149	28.5	5.34	-1.66	167	78	202	0.297	0.293	2.13
2.0	bcc	2.690	197	140	147	28.3	5.26	-6.56	159	77	199	0.291	0.289	2.06

All data are from Ref. [17]

The unit is GPa except for the dimensionless A_Z, A_{VR} , ν , and B/G

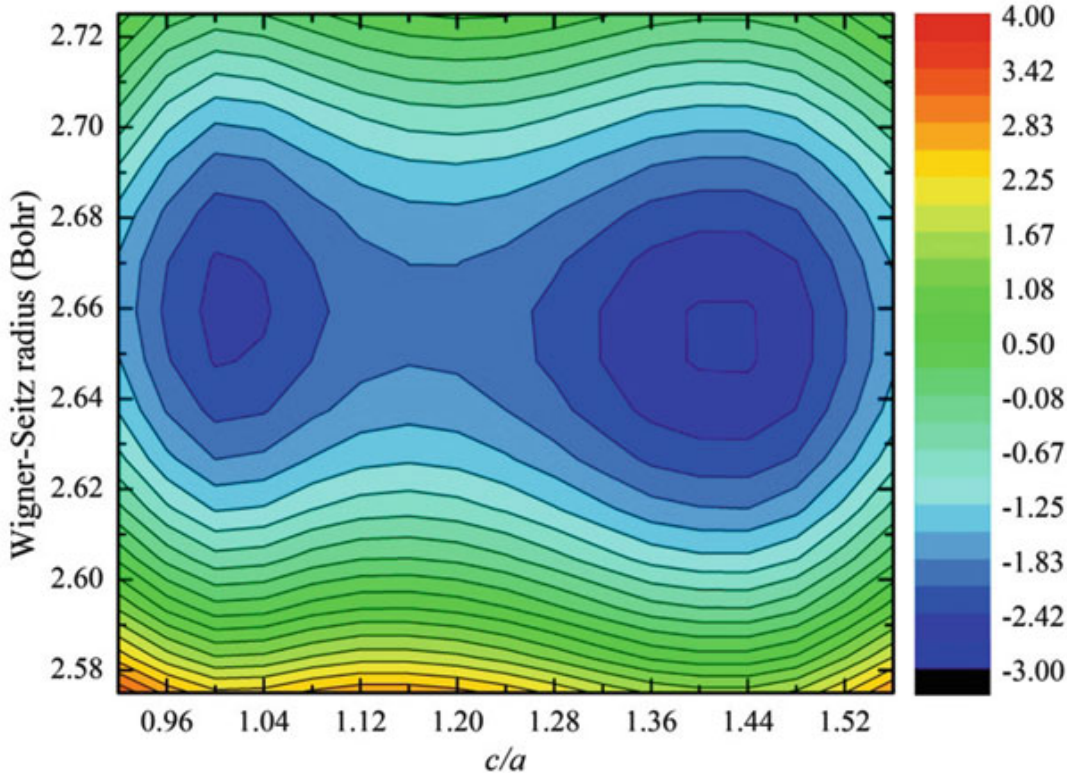


Fig. 9.9 Energy contour (mRy) for paramagnetic AlCoCrFeNi as a function of the tetragonal ratio (c/a) and the Wigner–Seitz radius (Bohr) (Data taken from Ref. [17])

From Table 9.3, we find that the somewhat different impact of Al on the elastic parameters of fcc and bcc AlCoCrFeNi leads to local maxima in $(c_{12} - c_{44})$, ν , and B/G with increase of Al content. According to the calculated trend of $c'(x)$, Al strongly reduces the dynamical stability of the fcc lattice and slightly increases that of the bcc lattice. At the same time, Al stabilizes thermodynamically the bcc structure relative to the fcc one (Fig. 9.8). Combining these two effects, we obtain that around the duplex region ($x = 0.597\text{--}1.229$), the $\text{Al}_x\text{CoCrFeNi}$ system has two very similar distinct local minima within the Bain configurational space (described by c/a and volume) with a clear barrier between them (Fig. 9.9). One local minimum corresponds to the bcc phase ($c/a = 1$) and another to the fcc phase ($c/a = \sqrt{2}$). This situation is rather unusual for elemental cubic transition metals and their alloys, for which the thermodynamically unstable cubic structure is usually also dynamically unstable.

According to Pugh, materials with B/G ratio above 1.75 are ductile. For isotropic materials, the Pugh criteria for ductility imply $\mu > 0.26$, which has been confirmed for bulk metallic glasses [33]. In the case of $\text{Al}_x\text{CoCrFeNi}$, alloys close to $x = 1$ in both phases have large positive Cauchy pressure, and large B/G and μ , indicating strong metallic character and enhanced ductility for these systems. Our calculated Young's moduli are very close for the fcc (201 GPa) and bcc (204 GPa) AlCoCrFeNi. The single-crystal Young's modulus changes from 70 to 370 GPa (77–355 GPa) for the fcc (bcc) AlCoCrFeNi along the different crystallographic directions. We note that the reported experimental value of 127 GPa [34] is within the range of our calculations.

9.5 Refractory HEAs

9.5.1 Structural Properties

For NbTiVZr and MoNbTiV_xZr ($x = 0\text{--}1.5$), the EMTO-CPA theory predicts the bcc structure to be the most stable one among the three close-packed lattices, namely, fcc, bcc, and hcp. The corresponding equilibrium Wigner–Seitz radii and total energy difference compared to bcc structure are listed in Table 9.4. The theoretical predictions are fully supported by experiments. At this point, we should note that local lattice relaxation (neglected in the present study) could slightly alter the structural energy difference. According to our previous estimation of the influence of the lattice relaxation on the bcc–fcc energy difference [17], the effect of relaxation is well below the energy differences from Table 9.4.

Experimentally, the HEAs composed of refractory elements were found to have a single bcc structure. It should be noted that the present refractory elements Ti, Zr, V, Nb, and Mo all adopt a bcc crystal structure below their melting temperature, but Ti and Zr are stable in the hcp phase at ambient conditions (the allotropic transition from hcp to bcc happens at temperatures of 1155 K and 1136 K for Ti and Zr, respectively).

We show the calculated equilibrium WS radii for bcc NbTiVZr and MoNbTiV_xZr ($x = 0\text{--}1.50$) HEAs in Table 9.5. The only experimental equilibrium radius we could find in the literature is 3.094 Bohr [35] reported for NbTiVZr. To further assess the theoretical volumes predicted for the present HEAs, we make use of Vegard’s rule and estimate the mean equilibrium WS radii for alloys using those of the alloy components. First, we study the atomic radius of the refractory elements. For the Wigner–Seitz radius of bcc Ti and Zr at 0 K, we extrapolate the high-temperature data assuming a linear thermal expansion, i.e., $w(T) = w(0 \text{ K})(1 + \alpha T)$, where $w(0 \text{ K})$ is the WS radius at 0 K and $w(T)$ at temperature T and α is the linear thermal expansion coefficient. Using the experimental values

Table 9.4 Theoretical Wigner–Seitz radius w (Bohr) for HEAs with bcc, fcc, and hcp structures, respectively

HEAs	w_{bcc}	ΔH_{bcc}	w_{fcc}	ΔH_{fcc}	w_{hcp}	ΔH_{hcp}
NbTiVZr	3.054	10.94	3.083	33.23	3.085	34.60
MoNbTiZr	3.075	1.289	3.107	13.65	3.107	14.76
MoNbTiV _{0.25} Zr	3.060	-12.99	3.092	9.394	3.092	11.10
MoNbTiV _{0.50} Zr	3.046	-0.956	3.078	21.66	3.078	23.45
MoNbTiV _{0.75} Zr	3.033	-2.098	3.065	20.55	3.066	22.54
MoNbTiV _{1.00} Zr	3.023	5.728	3.055	28.07	3.054	29.65
MoNbTiV _{1.25} Zr	3.011	12.73	3.044	35.50	3.045	37.51
MoNbTiV _{1.50} Zr	3.002	23.36	3.034	46.29	3.035	48.43

All data are from Ref. [18]

The formation enthalpy ΔH of bcc, fcc, and hcp phases (kJ/mol) is relative to that of the bcc structure

Table 9.5 Wigner–Seitz radius w (Bohr), bulk modulus B (GPa), and elastic constants c_{11} , c_{12} , c_{44} , and c' (GPa) for NbTiVZr and MoNbTiV_xZr ($x=0\text{--}1.5$) HEAs

HEAs	w_t	\bar{w}_t	\bar{w}_e	B	c_{11}	c_{12}	c_{44}	c'
NbTiVZr	3.054	3.057	3.062	118.6	166.4	94.7	53.8	35.9
MoNbTiZr	3.075	3.100	3.090	137.3	209.9	101.0	52.6	54.4
MoNbTiV _{0.25} Zr	3.060	3.083	3.074	137.4	211.0	100.6	52.1	55.7
MoNbTiV _{0.50} Zr	3.046	3.068	3.059	137.6	212.2	100.3	51.6	55.9
MoNbTiV _{0.75} Zr	3.033	3.054	3.046	138.0	213.2	100.3	51.2	56.4
MoNbTiV _{1.00} Zr	3.023	3.042	3.035	138.5	213.7	100.7	50.9	56.5
MoNbTiV _{1.25} Zr	3.011	3.031	3.024	140.6	218.0	101.9	50.0	58.0
MoNbTiV _{1.50} Zr	3.002	3.022	3.015	141.2	219.3	102.2	49.8	58.5
Mo _{0.8} NbTiZr	3.085	3.114	3.099	132.2	199.0	98.7	52.8	50.1
Mo _{0.8} NbTiV _{0.2} Zr	3.071	3.098	3.085	132.9	200.8	99.0	52.5	50.9
Mo _{0.9} NbTiZr	3.080	3.111	3.094	134.4	204.3	99.5	52.6	52.5
Mo _{0.8} NbTiV _{0.5} Zr	3.054	3.101	3.066	134.6	203.7	100.0	51.9	51.9

All data are from Ref. [18]

w_t represents the EMTO-CPA Wigner–Seitz radius and \bar{w}_t (\bar{w}_e) stands for the average Wigner–Seitz radii of the HEAs estimated from EMTO calculated (experimental or extrapolated) radius of bcc refractory elements (those for Ti, Zr, and Hf were extrapolated to 0 K), according to Vegard’s rule

$w_{\text{Ti}}(1155 \text{ K}) = 3.077 \text{ Bohr}$ and $w_{\text{Zr}}(1140 \text{ K}) = 3.358 \text{ Bohr}$ together with the reported thermal expansion coefficients for bcc Ti ($10.9 \times 10^{-6} \text{ K}^{-1}$) and Zr ($9 \times 10^{-6} \text{ K}^{-1}$) [36], we get 3.039 Bohr and 3.324 Bohr for $w(0 \text{ K})$ of the hypothetical bcc Ti and Zr, respectively. For bcc V, Nb, and Mo, the Wigner–Seitz radii at 0 K were extrapolated by fitting the selected lattice parameters in Ref.[37]. Considering the quoted estimated values in Table 9.5, we conclude that the present theory correctly describes the equilibrium properties of all five refractory elements.

It is interesting to note that for all HEAs considered here, the calculated equilibrium WS radius w_t is slightly smaller than \bar{w}_t . Hence, all alloys show a small but systematic negative deviation relative to Vegard’s rule. Similar to CoCrCuFeNiTi_x, the WS radius of MoNbTiV_xZr has a linear change as a function of the content of Vanadium x ($x=0\text{--}1.50$).

9.5.2 Electronic Structure

In the following, we discuss the electronic structure of the refractory HEAs. The total and partial DOSs for the NbTiVZr, MoNbTiZr, and MoNbTiVZr HEAs are shown in the middle and lower panels of Fig. 9.10, respectively. Although the chemical disorder smears out most of the structure characteristic to the elemental DOSs (upper panels), a weak peak survives in the vicinity of the Fermi level for all three alloys (middle panels). This peak is located at the Fermi level for NbTiVZr

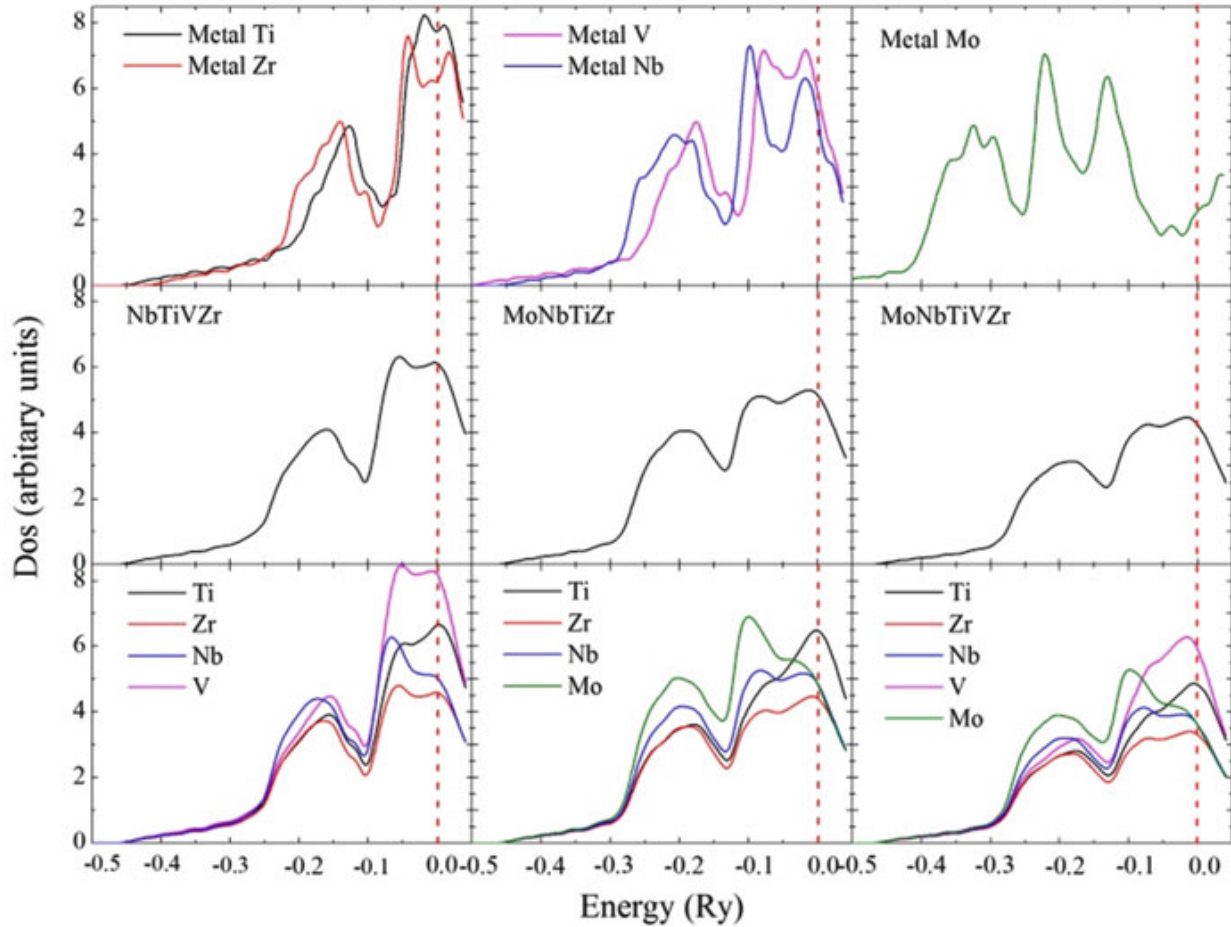


Fig. 9.10 Density of state (DOS) of bcc Ti, Zr, V, Nb, and Mo refractory metals (*upper panels*); total (*middle panels*) and partial (*lower panels*) DOS for bcc NbTiVZr, MoNbTiZr, and MoNbTiVZr high-entropy alloys. The vertical dashed lines stand for the positions of the Fermi level (All data are from Ref. [18])

and shifted toward the descending zone when equimolar Mo replaces V or is added to the alloy. This feature may explain why NbTiVZr has smaller dynamical stability against tetragonal deformation (smaller c') as compared to the other alloys (Table 9.5). We should notice that the aforementioned lattice distortion mechanism is expected to be less effective in HEAs due to the disorder-driven smearing of the DOS. Monitoring the total DOS curves (Fig. 9.10), one may conclude that the two Mo-containing HEAs should exhibit similar anomalous temperature dependence as found in V and Nb metals [38]. These theoretical predictions need to be verified by future theoretical and experimental analysis.

The partial DOSs (Fig. 9.10, lower panels) are somewhat different from the DOSs of the elemental metals (upper panels). In all three cases, Ti and Zr contribute with a peak to the DOS at the Fermi level. The partial DOSs resemble the pure metal DOSs the most in NbTiVZr. Here, the small charge redistribution between the alloy components shifts slightly the peaks in V and Nb partial DOSs close to E_F , resulting in the global peak seen in the total DOS (left middle panel). The partial DOS of Mo is strongly altered compared to that of pure Mo. However, the presence of Mo makes the V and Nb partial DOSs more V- and Nb-like, respectively (having E_F in the descending zone). That is the reason why the Mo-containing alloys are mechanically more stable than the Mo-free NbTiVZr alloy.

9.5.3 Elastic Properties

The three cubic elastic constants c_{11} , c_{12} , and c_{44} and the tetragonal shear modulus c' are listed in Table 9.6. All HEAs considered here are predicted to be mechanically stable. Adding equimolar V to MoNbTiZr-based alloy produces small changes in the elastic parameters. The weak increase of the tetragonal elastic constant c' with V content in MoNbTiV_xZr alloys indicates that V slightly enhances the elastic stability of the bcc phase against tetragonal deformation. At the same time, V addition decreases c_{44} , resulting in a small increases of the elastic anisotropy. In Table 9.6, we also list the theoretical elastic constants, the Zener anisotropy A_Z , and Cauchy pressure ($c_{12}-c_{44}$) (GPa), as well as polycrystalline elastic moduli (B , G , E , v , B/G , A_{VR}) and VEC of the present refractory HEAs. One can see that the ductility is slightly enhanced with increasing V content. However, these changes are too small and the quoted correlation between the elastic parameters and ductility too vague to be able to draw more solid conclusions here.

The VEC has often been used to classify the single solid solution phases (bcc, fcc, or mixture of bcc and fcc). According to the experimental findings, HEAs prefer to form bcc solid solution when $VEC < 7.55$. This correlation is fully supported by the present theory and former experiments. In addition to the phase stability, the VEC should also reflect the changes of the metallic bonds and thus the changes of the polycrystalline elastic moduli. Indeed, as shown in Fig. 9.11, we find a correlation between the bulk and shear moduli of MoNbTiV_xZr and the VEC. The increase in the VEC with V content (we should remember that HEAs are equimolar systems) is followed by an increase (slightly decrease) of the bulk (shear) modulus. The opposite trends in B and G explain the enhanced ductility of MoNbTiV_xZr for large x values.

Table 9.6 The Cauchy pressure ($c_{12}-c_{44}$) (GPa) and Zener anisotropy A_Z (c_{44}/c'); polycrystalline elastic moduli G and E (GPa) and Poisson's ratio v ; the B/G ratio, elastic anisotropy ratio A_{VR} , and VEC for selected refractory HEAs

HEAs	$c_{12}-c_{44}$	A_Z	G	E	v	B/G	A_{VR}	VEC
NbTiVZr	41.0	1.500	45.70	121.1	0.33	2.60	0.0196	4.50
MoNbTiZr	48.4	0.966	53.33	141.7	0.33	2.58	0.0001	4.75
MoNbTiV _{0.25} Zr	48.6	0.944	53.31	141.6	0.33	2.58	0.0004	4.76
MoNbTiV _{0.50} Zr	48.7	0.923	53.30	141.7	0.33	2.58	0.0008	4.78
MoNbTiV _{0.75} Zr	49.1	0.908	53.25	141.5	0.33	2.59	0.0011	4.79
MoNbTiV _{1.00} Zr	49.8	0.900	53.17	141.1	0.33	2.61	0.0014	4.80
MoNbTiV _{1.25} Zr	51.9	0.861	53.09	141.4	0.33	2.65	0.0027	4.81
MoNbTiV _{1.50} Zr	52.1	0.850	53.10	141.6	0.33	2.66	0.0032	4.82
Mo _{0.8} NbTiZr	45.9	1.054	51.71	137.2	0.33	2.57	0.0003	4.68
Mo _{0.8} NbTiV _{0.2} Zr	46.5	1.031	51.82	137.6	0.33	2.57	0.0001	4.70
Mo _{0.9} NbTiZr	46.8	1.004	52.56	139.5	0.33	2.56	0	4.72
Mo _{0.8} NbTiV _{0.5} Zr	48.1	1.000	51.88	137.9	0.33	2.59	0	4.72

All data are from Ref. [18]

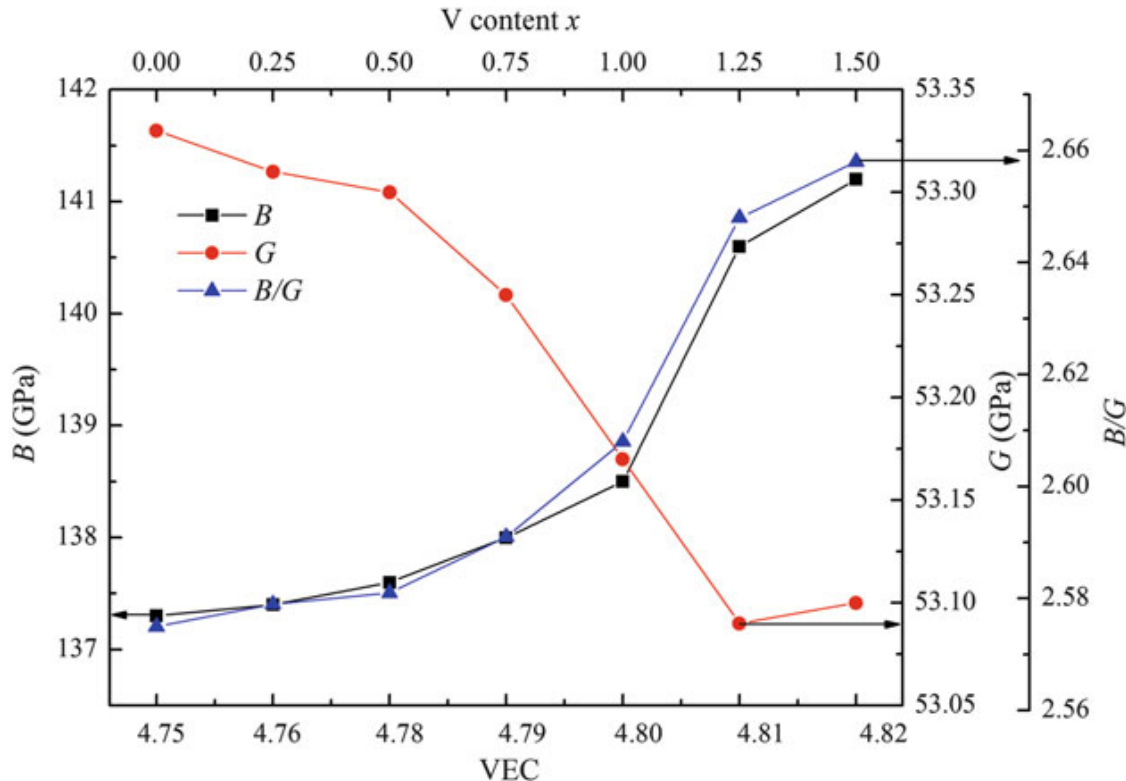


Fig. 9.11 Correlation between the bulk moduli B and shear moduli G and Pugh ratio B/G of $\text{MoNbTiV}_x\text{Zr}$ ($x = 0\text{--}1.5$) and VEC (All data are from Ref. [18])

In order to illustrate the effect of alloying on the elastic anisotropy of refractory HEAs, in Fig. 9.12, we plot the three-dimensional E for NbTiVZr , MoNbTiZr , and MoNbTiVZr . Here, E is the Young's modulus along $[\text{hlk}]$ crystallographic direction. For NbTiVZr alloy, the E exhibits rather strong orientation dependence, so this system may be regarded as being anisotropic. The largest value of E is 140.2 GPa realized along the $[111]$ direction, whereas the smallest value of 97.7 GPa belongs to the $[100]$ direction.

In contrast to the Mo-free alloy, the Mo-containing alloys seem to be almost isotropic. Namely, their three-dimensional E shown in Fig. 9.12 have almost spherical shapes. The Young's modulus changes between 136.0 and 149.2 GPa for MoNbTiVZr and between 139.9 and 144.3 GPa for MoNbTiZr . Previous theoretical calculations predicted nearly isotropic surface energies for bcc Mo and, as a consequence, spherically shaped nanoparticles for this metal.

For a fully isotropic material, the tetragonal shear modulus $c' = (c_{11} - c_{12})$ equals the cubic shear modulus c_{44} , so we have $A_Z = 1$ and $A_{VR} = 0$. The latter condition reflects the fact that all statistical averaging methods (in the present case, the Voigt and Reuss methods) lead to the same polycrystalline shear modulus. According to our calculations, V slightly enhances the anisotropy of $\text{MoNbTiV}_x\text{Zr}$, whereas equimolar Mo addition to NbTiVZr turns the alloy almost isotropic. Based on this information, we propose that one can optimize the content of Mo and V in $\text{Mo}_y\text{NbTiV}_x\text{Zr}$ so that the resulting alloy is fully isotropic. We demonstrate this by performing calculations for $\text{Mo}_y\text{NbTiV}_x\text{Zr}$ as a function of x and y (keeping the Ti, Zr, and Nb atomic fractions to 1). Some of the results of this additional study are

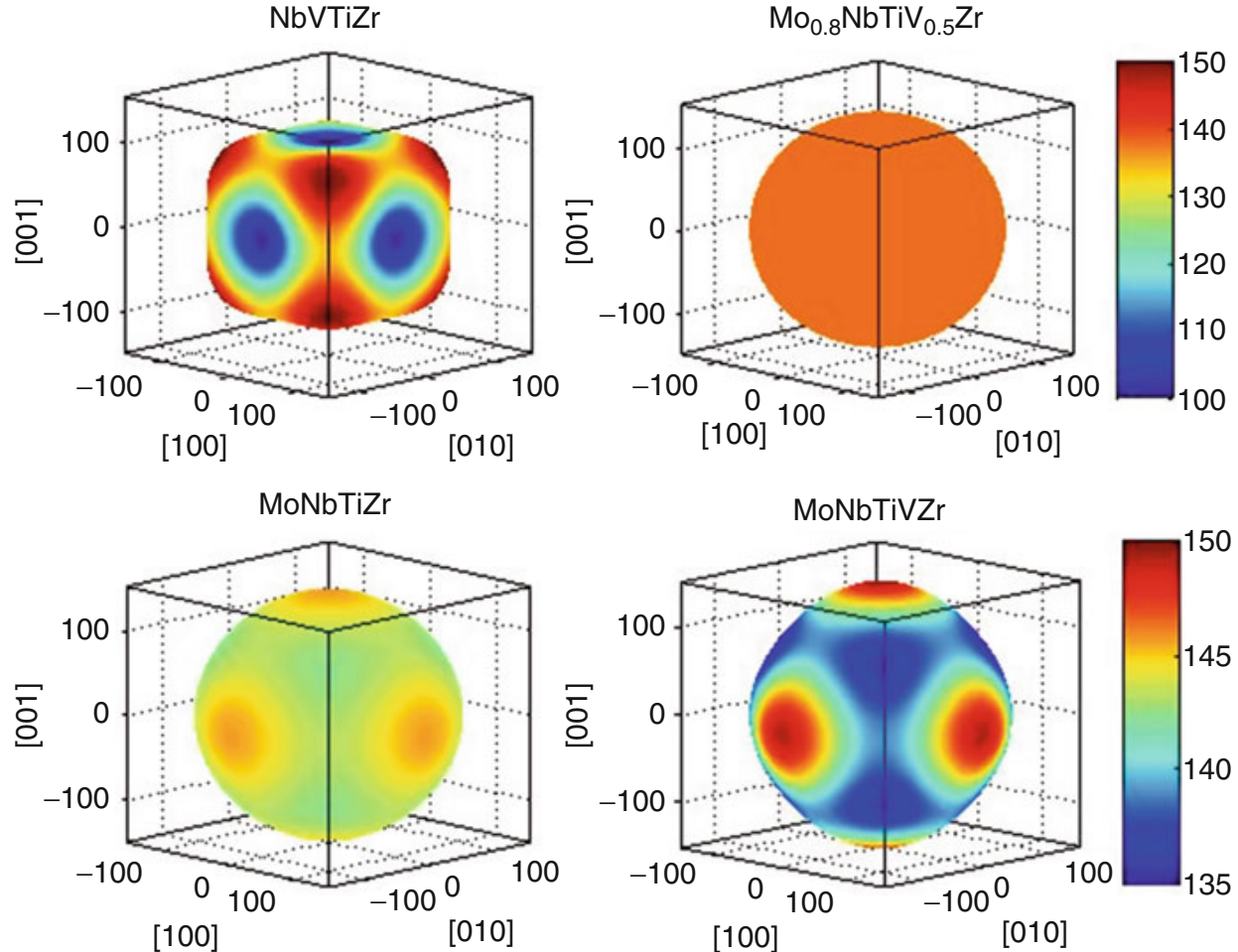


Fig. 9.12 Characteristic surfaces of the Young's modulus E for NbTiVZr , MoNbTiZr , MoNbTiVZr , and $\text{Mo}_{0.8}\text{NbTiV}_{0.5}\text{Zr}$. The values on the color scale and on the axes are in GPa. Note that the same color bar applies to NbTiVZr and $\text{Mo}_{0.8}\text{NbTiV}_{0.5}\text{Zr}$ and another to MoNbTiZr and MoNbTiVZr

shown in the lower part of Table 9.6. We find that $\text{Mo}_y\text{NbTiV}_x\text{Zr}$ becomes almost perfectly isotropic for $(x, y) = (0, 0.9)$ or $(x, y) = (0.5, 0.8)$. The Young's modulus for $\text{Mo}_{0.8}\text{NbTiV}_{0.5}\text{Zr}$ is shown in Fig. 9.12.

Very interestingly, for both isotropic $\text{Mo}_{0.9}\text{NbTiZr}$ and $\text{Mo}_{0.8}\text{NbTiV}_{0.5}\text{Zr}$ HEAs, the VEC is about 4.72. On this ground, we suggest that $\text{VEC} \sim 4.72$ (valid within the present approximations) is an important criterion for the isotropic HEAs. For comparison, Li et al. predicted that the Ti–V alloys (Gum Metals) become elastically isotropic for $\text{VEC} \sim 4.7$ [39].

In addition to the above cases, we used the EMTO-CPA method to calculate some other equimolar refractory HEAs reported in experiments. Table 9.7 lists the Wigner–Seitz radii, elastic constants, and polycrystalline elastic moduli as well as VEC of the HfNbTiXZr ($X = \text{V}, \text{Cr}, \text{Ta}$), MoNbTaW , MoNbTaVW , as well as HfNbTiZr and HfNbZr refractory HEAs. Like before, we used Vegard's law to estimate the WS radius of the solid solution, i.e., w_{mix} . Our ab initio predictions are slightly smaller than w_{mix} for these seven refractory HEAs. Hence, all alloys show a small but systematic positive deviation relative to Vegard's rule. We note that for all HEAs considered here, the calculated lattice parameter w_t is slightly larger than the experiments w_e , except for HfNbTiZr and CrHfNbTiZr . It is very likely that this

Table 9.7 Wigner–Seitz radius w (Bohr) and elastic properties of refractory HEAs

HEAs	w_t	w_{mix}	w_e	B	c_{11}	c_{12}	c_{44}	c'
HfNbTiVZr	3.160	3.171	3.145	126.6	149.5	115.1	55.0	17.2
CrHfNbTiZr	3.132	3.140	3.186	117.2	153.1	99.3	49.2	26.9
HfNbTaTiZr	3.212	3.235	3.163	136.3	160.2	124.4	62.4	17.9
MoNbTaW	3.037	3.067	2.985	261.6	413.5	185.6	69.0	114
MoNbTaVW	3.003	3.017	2.957	245.1	380.8	177.3	61.2	102
HfNbTiZr	3.253	3.187	3.270	116.0	125.9	111.1	61.2	7.4
HfNbZr	3.311	3.332	3.240	113.2	127.5	106.1	57.1	10.7
VEC	c_{44}/c'	$c_{12}-c_{44}$	G	E	ν	B/G	A_{VR}	
HfNbTiVZr	4.4	3.200	60.1	34.6	95.0	0.375	3.663	0.154
CrHfNbTiZr	4.6	1.827	50.1	38.6	104.4	0.352	3.034	0.043
HfNbTaTiZr	4.4	3.491	62.0	37.9	104.1	0.373	3.596	0.176
MoNbTaW	5.5	0.605	116.6	84.4	228.7	0.354	3.097	0.030
MoNbTaVW	5.4	0.602	116.1	75.1	204.5	0.361	3.263	0.031
HfNbTiZr	4.25	8.263	49.8	27.7	77.0	0.389	4.189	0.434
HfNbZr	4.33	5.351	49.01	29.74	81.89	0.379	3.815	0.298

Date taken from Ref. [40]

w_t , w_{mix} , and w_e stand for the theoretical, estimated (using Vegard's rule) and experimental Wigner–Seitz radii, respectively. Cubic elastic constants c_{11} , c_{12} , c_{44} , and $(c_{12}-c_{44})$ (GPa), the Poisson ratio ν , and the Pugh ratio B/G

deviation is due to the employed frozen-core approximation, which is known to yield somewhat larger lattice parameters as compared to all-electron calculations.

The seven refractory HEAs listed in Table 9.7 are predicted to be mechanically stable according to the dynamical stability conditions $c_{44} > 0$, $c_{11} > |c_{12}|$, and $c_{11} + 2c_{12} > 0$. For the HfNbTiXZr ($X = V, Cr, Ta$) refractory HEAs, the polycrystalline elastic moduli are very similar. It is found that V has a small effect on B , G , and E of MoNbTaW alloys.

The experimental Young's modulus is 128 (112) GPa for HfNbTiVZr (CrHfNbTiZr), whereas the ab initio E is 95 (104.4) GPa. We should note that $Hf_{20}Nb_{20}Ti_{20}V_{20}Zr_{20}$ is almost a single bcc phase, whereas CrHfNbTiZr consists of a mixture of bcc and Laves phases. The theoretical results are expected to be valid for the completely random and homogeneous bcc solid solutions.

The calculated large positive Cauchy pressure ($c_{12} - c_{14}$) suggests that these refractory HEAs have strong metallic character and enhanced ductility. Keeping in mind our previous discussion from Sect. 9.4.3, we find that all values in Table 9.7 would indicate enhanced ductility for these refractory alloys. Good ductility has indeed been reported for the single-phase HfNbTaTiZr alloy, while limited ductility at room temperature and extensive compressive plasticity above 873 K has been found for the single-phase MoNbTaW and MoNbTaVW alloys. The reduced ductility of CrHfNbTiZr alloy may result from the precipitation of Laves phase.

9.6 Stacking Fault Energy of HEAs

It has been established in this chapter that EMTO-CPA is a valuable tool to make independent predictions on the structure and properties of HEAs. Beyond independent calculation of properties of HEAs, this method can also be coupled to available experimental measurements to aid in the extraction of physical properties. Here, we review a recent example of the extraction of the stacking fault energy (SFE) from multicomponent alloys, including HEAs, using this combined approach.

Determination of SFEs is important in alloy design because it indicates the predominant plastic deformation mechanism to be expected in the alloys. High SFE materials tend to deform via a dislocation glide mechanism with little splitting into partial dislocations, while lower SFEs more readily split into partial dislocation pairs and the stacking fault widths tend to increase as the SFE is reduced. Solid solution alloying has been one route to engineer lower SFE alloys experimentally, typically successful in Cu- or Mg- based where a wide range of solid solubility is achievable. Although successful, these materials have not retained sufficient strength to suit all potential applications. HEAs, however, provide a unique opportunity to tune the SFE as they form as solid solutions on fcc lattices in materials typically known for having higher strength and over a wider compositional range. The ability to extract trends in SFE from new alloys is essential as these provide a means of evaluating success of experiment and also provide for comparison with independent predictive simulation.

One route to assess the SFE experimentally is accomplished through x-ray diffraction (XRD) measurements. However, this approach is only possible if elastic properties of the alloy are known ahead of the measurement. If this is not the case, first principles methods, such as EMTO+CPA, can play a valuable role of assessing the elastic constants of alloy as a function of their components and concentrations and make the extraction of SFEs possible. From XRD (and EMTO+CPA), the SFE is calculated by use of Eq. 9.4 for fcc materials

$$\gamma = \frac{6.6}{\pi\sqrt{3}} \cdot \underbrace{G_{(111)} \left(\frac{2c_{44}}{c_{11} - c_{12}} \right)^{-0.37}}_{\text{Theory}} \cdot \underbrace{\frac{a_o \varepsilon^2}{\alpha}}_{\text{Experiment}} \quad (9.4)$$

In this expression, theoretical calculations provide values for the shear modulus in (111) determined from the elastic constants, $G_{(111)}$, and the Zener elastic anisotropy determined from the independent elastic constants for fcc (i.e., c_{11} , c_{12} , and c_{44}), and experiment provides information on the lattice parameter (a_o), mean square microstrain (ε^2), and the stacking fault probability (α). The microstrain can be extracted by fitting XRD peaks with a Lorentzian function. The width of these fitted peaks yields the microstrain through the procedure of Williamson and Hall [41] and can be converted to the mean square microstrain through the procedure of Klug and Alexander [42]. The stacking fault probability can be extracted by use of the PM2K software package [43]. The elastic constants can be extracted through fits to both equations of state as well as quadratic fits to volume conserving orthorhombic strains to the unit cell [12].

Using the XRD together with EMTO-CPA approach, Zaddach et al. recently explored the SFE in equiatomic alloys as a function of the number of components up to five-component HEAs [15]. The SFEs presented in this work are plotted in Fig. 9.13. Each equiatomic alloy was found to be a single-phase random solid solution on the fcc lattice. The data in Fig. 9.13 shows a clear trend of a reduction in the SFE with the number of components.

Although the SFEs were able to be reduced as a function of the number of components, the lowest achievable value still exceeds those of conventional low SFE Cu alloys, which have been shown to exhibit an SFE in the range of 7–14 mJ/m² depending on composition [44–46]. To further explore the ability to tune the SFE, Zaddach et al. relaxed the equiatomic constraint and explored non-equiatomic compositions for the five-component HEA. The authors added and removed Cr at the expense of Ni, a typical high SFE material, and found that higher Cr content alloys further reduced the SFE while retaining the single-phase solid solution fcc structure. Ultimately, the authors found the Cr₂₆Co₂₀Fe₂₀Mn₂₀Ni₁₄ non-equiatomic HEA, with the subscripts representing atomic percent with unlabeled values fixed at 20 at. %, to have an SFE slightly less than 4 mJ/m², which is below current reported values of Cu-based alloys.

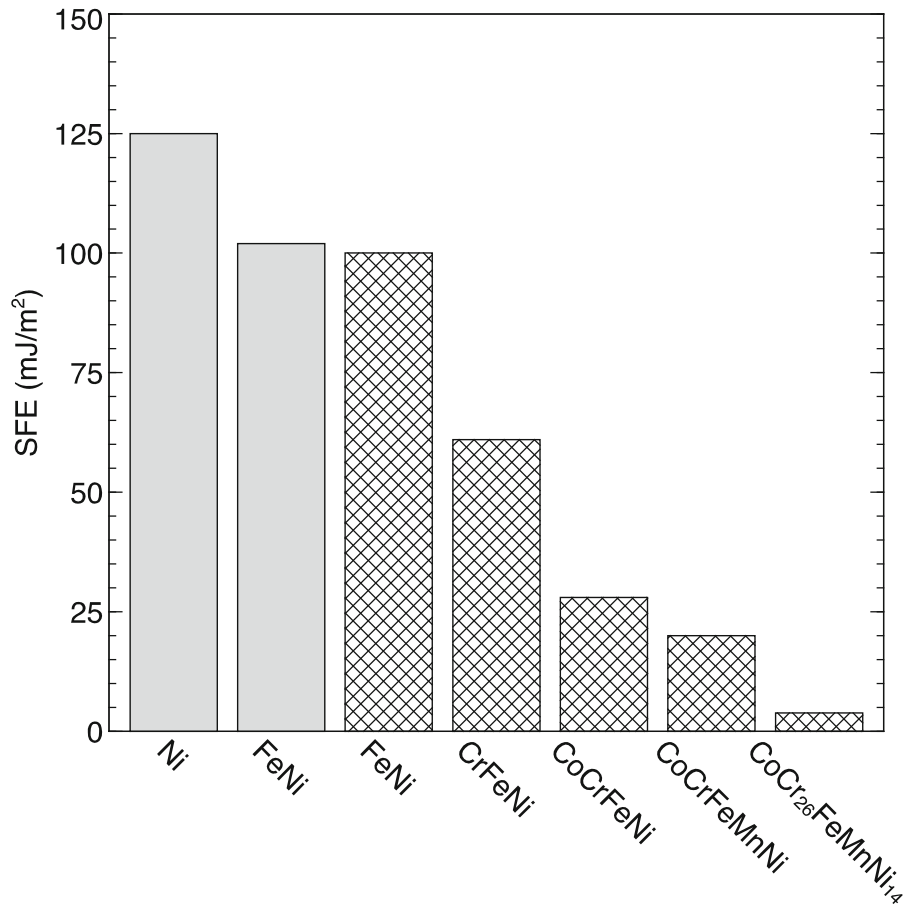


Fig. 9.13 Stacking fault energy for elements and alloys. Alloys without subscripts are equiatomic, while alloys with subscripts are given in atomic percent. The all gray values are from the literature, while the bar graphs with the patterned fill came from Ref. [15] using the combined XRD + EMTO approach discussed in this section (All data are taken from Ref. [15])

9.7 The KKR-CPA Method

In the previous sections, we have discussed theoretical studies of HEAs of four and five elements using EMTO-CPA. In this section, we present a KKR-CPA approach to the ab initio electronic structure calculation for $\text{Al}_x\text{CrCoCuFeNi}$. In its conventional implementation, the KKR-CPA takes muffin-tin approximation, in which the one-electron potential in DFT is assumed to be spherically symmetric within a nonoverlapping “muffin-tin” sphere centered at each atom and constant in the interstitial region. In contrast, the EMTO-CPA method uses the optimized overlapping muffin-tin potential, in order to employ the “best possible” spherical representation of the one-electron potential. The KKR-CPA method is based on the multiple scattering theory, where the single-site scattering and the scattering path matrices are of fundamental interest. On the other hand, the EMTO-CPA method is based on muffin-tin orbitals theory. Because of these differences, the CPA mediums in these two methods are somewhat different. For the completeness of this chapter, we present here the basic theoretical features of the KKR-CPA method adopting the usual multiple scattering terminology.

The KKR-CPA method uses Green’s function technique within the framework of multiple scattering theory and is uniquely designed for the theoretical

investigation of random alloys from the first principles. In multiple scattering theory, the Green function in the vicinity of an impurity “ i ” at site 1, embedded in the host with atoms “C”, is given by [47, 48]

$$g_i(\vec{r}, \vec{r}'; \varepsilon) = \sum_{L, L'} Z_L^i(\vec{r}_<; \varepsilon) [\underline{\tau}_i^{11}(\varepsilon)]_{LL'} Z_L^{i\bullet}(\vec{r}_<; \varepsilon) - \sum_L Z_L^i(\vec{r}_<; \varepsilon) J_L^{i\bullet}(\vec{r}_>; \varepsilon), \quad (9.5)$$

where $r_< = \min(r, r')$ and $r_> = \max(r, r')$, L and L' are the index of the combination of angular momentum and magnetic quantum numbers l and m , and $Z_L^i(\vec{r}; \varepsilon)$ and $J_L^i(\vec{r}; \varepsilon)$ are regular and irregular solutions, respectively, of single atom “ i ” with appropriate boundary condition at the origin and at the bounding sphere of the atomic cell. The symbol “•” in the superscript of the single-site solutions implies that complex conjugate is applied to the complex spherical harmonic function in the boundary condition. The scattering path matrix [49], $\underline{\tau}_i^{11}(\varepsilon)$, describes multiple scattering processes, starting from and ending at site 1 and is given by [5]

$$\underline{\tau}_i^{11}(\varepsilon) = [\underline{\tau}_C^{11}(\varepsilon)(\underline{t}_i^{-1}(\varepsilon) - \underline{t}_C^{-1}(\varepsilon)) + 1]^{-1} \underline{\tau}_C^{11}(\varepsilon), \quad (9.6)$$

where $\underline{t}_i(\varepsilon)$ and $\underline{t}_C(\varepsilon)$ are the t -matrix of atoms i and C, respectively. If the host atoms are on a periodic lattice, the scattering path matrix can be calculated using Brillouin zone (BZ) integration technique as follows:

$$\underline{\tau}_C^{11}(\varepsilon) = \frac{1}{\Omega_{BZ}} \int_{\Omega_{BZ}} [\underline{t}_C^{-1}(\varepsilon) - \underline{S}(\vec{k}; \varepsilon)] d^3 \vec{k}, \quad (9.7)$$

where Ω_{BZ} is the BZ volume and $\underline{S}(\vec{k}; \varepsilon)$ is the KKR structure constant matrix.

For a random alloy made of N atomic species with contents c_i , $i = 1, 2, \dots, N$, the CPA condition is such that the average of $\underline{\tau}_i^{11}(\varepsilon)$ is the scattering path matrix $\underline{\tau}_C^{11}(\varepsilon)$ of the CPA medium, in which the “host” atom is described by $\underline{t}_C(\varepsilon)$. In practice, it is useful to define following matrices [50]

$$\underline{X}_i(\varepsilon) = -[\underline{\tau}_C^{11}(\varepsilon) + (\underline{t}_i^{-1}(\varepsilon) - \underline{t}_C^{-1}(\varepsilon))^{-1}]^{-1}, \text{ and } \underline{X}_C(\varepsilon) = \sum_{i=1}^N c_i \underline{X}_i(\varepsilon), \quad (9.8)$$

and it is easy to verify that the CPA condition gives rise to $\underline{X}_C(\varepsilon) = 0$. To solve for $\underline{t}_C(\varepsilon)$, one may start with an initial guess of $\underline{t}_C(\varepsilon)$, $\underline{t}_C^{(1)}(\varepsilon) = \sum_{i=1}^N c_i \underline{t}_i(\varepsilon)$, and obtain $\underline{\tau}_C^{11,(1)}(\varepsilon)$ and $\underline{X}_C^{(1)}(\varepsilon)$ using (9.7) and (9.8), respectively. A better guess of $\underline{t}_C(\varepsilon)$ can be obtained from the previous one by using

$$\underline{t}_C^{(n+1), -1}(\varepsilon) = \underline{t}_C^{(n), -1}(\varepsilon) - \underline{X}_C^{(n)}(\varepsilon) \left[1 + \underline{\tau}_C^{11, (n)}(\varepsilon) \underline{X}_C^{(n)}(\varepsilon) \right]^{-1}. \quad (9.9)$$

This recursive procedure is iterated until the convergence is obtained. Once the CPA medium $\underline{t}_C(\varepsilon)$ is determined, one is able to calculate $\tau_i^{11}(\varepsilon)$ and then the Green function. If the system is in ferromagnetic state, the calculations described above are carried out for each spin channel, which means there are CPA mediums for spin up and spin down, respectively. The configurationally averaged electron density $\rho(\vec{r})$ and density of state $n(\varepsilon)$ associated with each spin channel are given by the imaginary part of the averaged Green function as follows:

$$\rho(\vec{r}) = -\frac{1}{\pi} \text{Im} \sum_{i=1}^N c_i \int_{\varepsilon_B}^{\varepsilon_F} g_i(\vec{r}, \vec{r}; \varepsilon) d\varepsilon, \text{ and } n(\varepsilon) = -\frac{1}{\pi} \text{Im} \sum_{i=1}^N \int_{\Omega} g_i(\vec{r}, \vec{r}; \varepsilon) d^3 \vec{r}, \quad (9.10)$$

where Ω is atomic cell volume, and the energy integration is usually carried out along a contour, in the upper half of complex energy plane, from the bottom of the valence bands ε_B to the Fermi energy ε_F .

Despite the fact that all of KKR-CPA calculations carried out so far have been using the muffin-tin approximation, which is a reasonable approximation for most metallic alloys, the formalism of the KKR-CPA method shown above is valid in general. A full-potential KKR-CPA method is currently under development by one of the authors.

9.8 Application of the KKR-CPA Approach

To investigate the phase stability and the mechanical and magnetic properties of $\text{Al}_x\text{CoCrCuFeNi}$ high-entropy alloys, we performed ab initio, spin-polarized, electronic structure calculation using KKR-CPA method described above. Like many other HEAs, this category of six-element alloys exhibits a combination of good material properties, including high hardness, high compressive strength, and excellent resistance to softening, corrosion, oxidation, and wearing, especially at elevated temperatures [51]. It has also been reported that this category of alloys shows ferromagnetic behavior [52]. In the KKR-CPA calculation, we chose von Barth-Hedin LSDA potential [53] and applied the muffin-tin approximation to the potential. The angular momentum quantum number cutoff was chosen to be $l_{\max} = 3$, for which the size of the scattering matrices is 16×16 . We used an adaptive method for the Brillouin zone integration and used 30 Gaussian points for the integration of the Green function along the energy contour. To determine the equilibrium state, we ran the calculation for both fcc and bcc structures for x up to 0.3.

Table 9.8 The calculated energetic, mechanical, and magnetic properties of $\text{Al}_x\text{CoCrCuFeNi}$ high-entropy alloys

x	B		ΔE	w		M	
	fcc	bcc		fcc	bcc	fcc	bcc
0.00	156.921	219.264	-0.029	2.588	2.589	0.485	0.684
0.30	184.483	196.348	-0.023	2.601	2.599	0.440	0.627
0.80	175.083	156.453	-0.020	2.623	2.616	0.400	0.540
0.50	188.643	178.334	-0.023	2.611	2.602	0.422	0.589
3.00	170.852	207.826	0.024	2.685	2.692	0.262	0.360

Bulk modulus B (GPa), the energy difference between fcc and bcc structures $\Delta E = E(\text{fcc}) - E(\text{bcc})$ (eV/atom), Wigner–Seitz radius w (Bohr), and magnetic moment M (μ_B) are obtained using KKR-CPA method

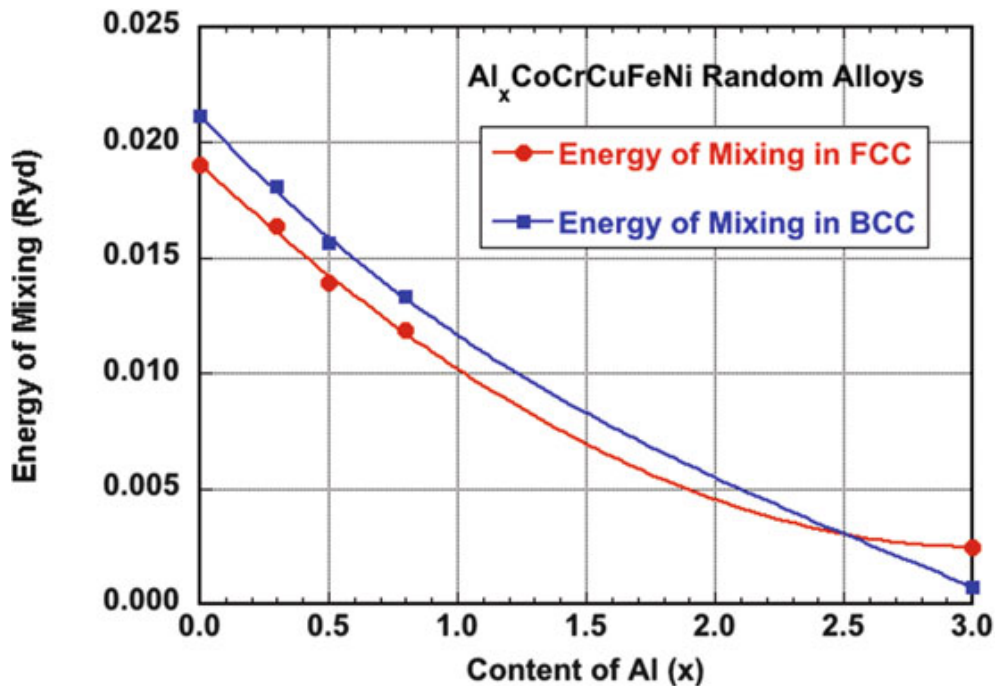


Fig. 9.14 The calculated enthalpy of mixing of $\text{Al}_x\text{CoCrCuFeNi}$ high-entropy alloys in fcc (solid circle) and bcc (solid square) structures. The data are obtained using KKR-CPA method

The computational results are summarized in Table 9.8 in which the bulk modulus and the lattice constant are obtained by fitting the calculated average total energy versus the atomic volume to the Murnaghan equation of state. The sizable average magnetic moment shows that the alloys are ferromagnetic for $x \leq 0.3$. The average magnetic moment in the bcc structure is found to be higher than that in fcc. While Cu and Al appear to be nonmagnetic in both fcc and bcc structures, Cr exhibits antiferromagnetism, but its moment in bcc is few times smaller than in fcc. For the fcc phase ($x < 2.5$), $\text{Al}_x\text{CoCrCuFeNi}$ shows significant positive enthalpy of mixing as shown in Fig. 9.14.

9.9 Conclusions

In this chapter, we have introduced two CPA-based ab initio approaches, EMTO-CPA and KKR-CPA, to the theoretical study of HEAs. We have investigated 3d HEAs with magnetic elements both in paramagnetic and in ferromagnetic states. For paramagnetic alloys, Fe remains magnetic due to its local moment nature, while most of the other alloy components are essentially in the nonmagnetic state. For ferromagnetic alloys, Cr moment appears to be antiferromagnetic or suppressed at small Wigner–Seitz radius, which may be related to the fact that we are only considering the collinear magnetic states in the spin-polarized calculations.

It is found that all the 3d HEAs under investigation are mechanically stable. As a base alloy, CoCrFeNi is found to be brittle at static conditions (0 K). However, when the calculations are performed at room temperature volume, CoCrFeNi is predicted to be ductile, in line with the observations. This finding highlights the importance of thermal effect in the case of HEAs. By adding Cu or Ti to CoCrFeNi, the material becomes more ductile. On the other hand, addition of Al to CoCrFeNi or CoCrCuFeNi is found to increase the equilibrium volume of the solid solution and reduce the dynamical stability of the fcc lattice, and as the Al content increases, the alloy undergoes phase changes from single fcc phase to fcc–bcc duplex phase and to single bcc phase.

We have investigated HEAs with refractory elements. These HEAs show large positive Cauchy pressure which suggests strong metallic character and enhanced ductility. We also found that Mo tends to enhance the isotropic elasticity while V tends to enhance the anisotropy. It is therefore possible to optimize the content of Mo and V in MoNbTiVZr so that the resulting alloy is fully isotropic.

The stacking fault energy of CoCrFeNi-based alloys has been studied using a combined theoretical–experimental approach. We have demonstrated that non-equiautomic HEAs offer additional degrees of freedom for a precise optimization of the deformation mechanism controlling the plasticity of this promising class of engineering alloys.

Acknowledgment Work were supported by the National Natural Science Foundation of China (NSFC) with the Grant No. 51401014, the National Basic Research Development Program of China with No. 2011CB606401, the Swedish Research Council, the European Research Council, and the Hungarian Scientific Research Fund (research project OTKA 84078 and 109570).

References

1. Hohenberg P, Kohn W (1964) Inhomogeneous electron gas. *Phys Rev* 136(3B):B864–B871
2. Kohn W, Sham LJ (1965) Self-consistent equations including exchange and correlation effects. *Phys Rev* 140(4A):A1133–A1138
3. Soven P (1967) Coherent-potential model of substitutional disordered alloys. *Phys Rev* 156 (3):809

4. Taylor DW (1967) Vibrational properties of imperfect crystals with large defect concentrations. *Phys Rev* 156(3):1017
5. Gyorffy BL (1972) Coherent-potential approximation for a nonoverlapping-muffin-tin-potential model of random substitutional alloys. *Phys Rev B* 5(6)
6. Korringa J (1947) On the calculation of the energy of a Bloch wave in a metal. *Phys Chem Chem Phys* 13(6–7):392–400, doi:[http://dx.doi.org/10.1016/0031-8914\(47\)90013-X](http://dx.doi.org/10.1016/0031-8914(47)90013-X)
7. Kohn W, Rostoker N (1954) Solution of the Schrödinger equation in periodic lattices with an application to metallic lithium. *Phys Rev* 94(5):1111–1120
8. Skriver HL (1984) The LMTO method. Springer, Berlin/Heidelberg/New York/Tokyo
9. Andersen OK (1975) Linear methods in band theory. *Phys Rev B* 12(8):3060–3083
10. Vitos L (2001) Total-energy method based on the exact muffin-tin orbitals theory. *Phys Rev B* 64(1):014107
11. Vitos L, Abrikosov IA, Johansson B (2001) Anisotropic lattice distortions in random alloys from first-principles theory. *Phys Rev Lett* 87(15):156401
12. Vitos L (2007) The EMTO Method and Applications in Computational Quantum Mechanics for Materials Engineers (Springer-Verlag, London)
13. Gyorffy BL, Stocks GM (1983) Concentration waves and fermi surfaces in random metallic alloys. *Phys Rev Lett* 50(5):374–377
14. Zunger A, Wei SH, Ferreira L, Bernard J (1990) Special quasirandom structures. *Phys Rev Lett* 65(3):353–356. doi:[10.1103/PhysRevLett.65.353](https://doi.org/10.1103/PhysRevLett.65.353)
15. Zaddach AJ, Niu C, Koch CC, Irving DL (2013) Mechanical properties and stacking fault energies of NiFeCrCoMn high-entropy alloy. *JOM* 65(12):1780–1789. doi:[10.1007/s11837-013-0771-4](https://doi.org/10.1007/s11837-013-0771-4)
16. Tian F, Varga L, Chen N, Delczeg L, Vitos L (2013) Ab initio investigation of high-entropy alloys of 3d elements. *Physical Review B* 87(7); 075144–075151. doi:[10.1103/PhysRevB.87.075144](https://doi.org/10.1103/PhysRevB.87.075144)
17. Tian F, Delczeg L, Chen N, Varga LK, Shen J, Vitos L (2013) Structural stability of NiCoFeCrAl_x high-entropy alloy from ab initio theory. *Physical Review B* 88(8); 085128–085132. doi:[10.1103/PhysRevB.88.085128](https://doi.org/10.1103/PhysRevB.88.085128)
18. Tian F, Varga LK, Chen N, Shen J, Vitos L (2014) Ab initio design of elastically isotropic TiZrNbMoV_x high-entropy alloys. *J Alloys Compd* 599:19–25. doi:[10.1016/j.jallcom.2014.01.237](https://doi.org/10.1016/j.jallcom.2014.01.237)
19. Pinski FJ, Staunton J, Gyorffy BL, Johnson DD, Stocks GM (1986) Ferromagnetism versus antiferromagnetism in face-centered-cubic iron. *Phys Rev Lett* 56(19):2096–2099
20. Lucas MS, Wilks GB, Mauger L, Muñoz JA, Senkov ON, Michel E, Horwath J, Semiatin SL, Stone MB, Abernathy DL, Karapetrova E (2012) Absence of long-range chemical ordering in equimolar FeCoCrNi. *Appl Phys Lett* 100(25):251907. doi:[10.1063/1.4730327](https://doi.org/10.1063/1.4730327)
21. Delczeg-Czirjak EK, Nurmi E, Kokko K, Vitos L (2011) Effect of long-range order on elastic properties of Pd0.5Ag0.5 alloy from first principles. *Phys Rev B* 84(9); 094205–094210. doi:[10.1103/PhysRevB.84.094205](https://doi.org/10.1103/PhysRevB.84.094205)
22. Lucas MS, Mauger L, Muñoz JA, Xiao Y, Sheets AO, Semiatin SL, Horwath J, Turgut Z (2011) Magnetic and vibrational properties of high-entropy alloys. *J Appl Phys* 109 (7):07E307. doi:[10.1063/1.3538936](https://doi.org/10.1063/1.3538936)
23. Shun T-T, Hung C-H, Lee C-F (2010) Formation of ordered/disordered nanoparticles in FCC high entropy alloys. *J Alloys Compd* 493(1–2):105–109, doi:<http://dx.doi.org/10.1016/j.jallcom.2009.12.071>
24. Wang XF, Zhang Y, Qiao Y, Chen GL (2007) Novel microstructure and properties of multicomponent CoCrCuFeNiTi_x alloys. *Intermetallics* 15(3):357–362. doi:[10.1016/j.intermet.2006.08.005](https://doi.org/10.1016/j.intermet.2006.08.005)
25. Zhang KB, Fu ZY, Zhang JY, Wang WM, Wang H, Wang YC, Zhang QJ, Shi J (2009) Microstructure and mechanical properties of CoCrFeNiTiAl_x high-entropy alloys. *Mater Sci Eng A* 508(1–2):214–219. doi:[10.1016/j.msea.2008.12.053](https://doi.org/10.1016/j.msea.2008.12.053)

26. Wu Y, Liu WH, Wang XL, Ma D, Stoica AD, Nieh TG, He ZB, Lu ZP (2014) In-situ neutron diffraction study of deformation behavior of a multi-component high-entropy alloy. *Appl Phys Lett* 104(5):051910. doi:[10.1063/1.4863748](https://doi.org/10.1063/1.4863748)
27. Zhang K, Fu Z (2012) Effects of annealing treatment on phase composition and microstructure of CoCrFeNiTiAl_x high-entropy alloys. *Intermetallics* 22:24–32. doi:[10.1016/j.intermet.2011.10.010](https://doi.org/10.1016/j.intermet.2011.10.010)
28. Vitos L, Korzhavyi PA, Johansson B (2003) Stainless steel optimization from quantum mechanical calculations. *Nat Mater* 2(4)
29. Kao Y-F, Chen T-J, Chen S-K, Yeh J-W (2009) Microstructure and mechanical property of as-cast, -homogenized, and -deformed Al_xCoCrFeNi ($0 \leq x \leq 2$) high-entropy alloys. *J Alloys Compd* 488(1):57–64. doi:[10.1016/j.jallcom.2009.08.090](https://doi.org/10.1016/j.jallcom.2009.08.090)
30. Chou H-P, Chang Y-S, Chen S-K, Yeh J-W (2009) Microstructure, thermophysical and electrical properties in Al_xCoCrFeNi ($0 \leq x \leq 2$) high-entropy alloys. *Mater Sci Eng B* 163 (3):184–189. doi:[10.1016/j.mseb.2009.05.024](https://doi.org/10.1016/j.mseb.2009.05.024)
31. Wang W-R, Wang W-L, Wang S-C, Tsai Y-C, Lai C-H, Yeh J-W (2012) Effects of Al addition on the microstructure and mechanical property of Al_xCoCrFeNi high-entropy alloys. *Intermetallics* 26:44–51. doi:[10.1016/j.intermet.2012.03.005](https://doi.org/10.1016/j.intermet.2012.03.005)
32. Guo S, Ng C, Lu J, Liu CT (2011) Effect of valence electron concentration on stability of fcc or bcc phase in high entropy alloys. *J Appl Phys* 109(10):103505. doi:[10.1063/1.3587228](https://doi.org/10.1063/1.3587228)
33. Gu XJ, McDermott AG, Poon SJ, Shiflet GJ (2006) Critical Poisson's ratio for plasticity in Fe–Mo–C–B–Ln bulk amorphous steel. *Appl Phys Lett* 88(21):211905. doi:[10.1063/1.2206149](https://doi.org/10.1063/1.2206149)
34. Zhou YJ, Zhang Y, Wang YL, Chen GL (2007) Solid solution alloys of AlCoCrFeNiTi_[sub x] with excellent room-temperature mechanical properties. *Appl Phys Lett* 90(18):181904. doi:[10.1063/1.2734517](https://doi.org/10.1063/1.2734517)
35. Senkov ON, Senkova SV, Woodward C, Miracle DB (2013) Low-density, refractory multi-principal element alloys of the Cr–Nb–Ti–V–Zr system: microstructure and phase analysis. *Acta Mater* 61(5):1545–1557. doi:[10.1016/j.actamat.2012.11.032](https://doi.org/10.1016/j.actamat.2012.11.032)
36. Massalski TB, Okamoto H, Subramanian PR, Kacprzak L (1990) Binary alloy phase diagram, 2nd edn. ASM International, Materials Park
37. Wang K, Reeber RR (1998) The role of defects on thermophysical properties: thermal expansion of V, Nb, Ta, Mo and W. *Mater Sci Eng Struct Mater Prop Microstruct Process* 23:101–137
38. Ramos de Debiaggi S, de Koning M, Monti AM (2006) Theoretical study of the thermodynamic and kinetic properties of self-interstitials in aluminum and nickel. *Phys Rev B* 73 (10):104103
39. Li T, Morris JW, Nagasako N, Kuramoto S, Chrzan DC (2007) “Ideal” engineering alloys. *Phys Rev Lett* 98(10):105503
40. Fazakas É, Zadorozhnyy V, Varga LK, Inoue A, Louzguine-Luzgin DV, Tian F, Vitos L (2014) Experimental and theoretical study of Ti₂₀Zr₂₀Hf₂₀Nb₂₀X₂₀ (X = V or Cr) refractory high-entropy alloys. *Int J Refract Met Hard Mater* 47:131–138. doi:[10.1016/j.ijrmhm.2014.07.009](https://doi.org/10.1016/j.ijrmhm.2014.07.009)
41. Williamson G, Hall W (1953) X-ray line broadening from filed aluminium and wolfram. *Acta Metall* 1(1):22–31
42. Alexander LE, Klug HP (1974) X-ray diffraction procedures for polycrystalline and amorphous materials, 2nd edn. Wiley, New York
43. Leoni M, Confente T, Scardi P (2006) PM2K: a flexible program implementing whole powder pattern modelling. *Z Kristallogr Suppl* 23:249–254
44. Denanot M, Villain J (1971) The stacking fault energy in Cu-Al-Zn alloys. *Physica Status Solidi (a)* 8(2):K125–K127
45. Schramm R, Reed R (1975) Stacking fault energies of seven commercial austenitic stainless steels. *Metallurg Transact A* 6(7):1345–1351

46. Gong Y, Wen C, Li Y, Wu X, Cheng L, Han X, Zhu X (2013) Simultaneously enhanced strength and ductility of Cu-xGe alloys through manipulating the stacking fault energy (SFE). *Mater Sci Eng A* 569:144–149
47. Faulkner JS, Stocks GM (1980) Calculating properties with the coherent-potential approximation. *Phys Rev B* 21(8):3222–3244
48. Rusanu A, Stocks GM, Wang Y, Faulkner JS (2011) Green's functions in full-potential multiple-scattering theory. *Phys Rev B* 84(3):035102
49. Gyorffy BL, Stott MJ (1973) Theory of soft X-ray emission from alloys. In: Fabian DJ, Watson LM (eds) *Proceedings of the international conference on band structure and spectroscopy of metals and alloys*. Academic, New York
50. Mills R, Gray LJ, Kaplan T (1983) Analytic approximation for random muffin-tin alloys. *Phys Rev B* 27(6):3252–3262
51. Tong CJ, Chen MR, Chen SK, Yeh JW, Shun TT, Lin SJ, Chang SY (2005) Mechanical performance of the Al_xCoCrCuFeNi high-entropy alloy system with multiprincipal elements. *Metallurg Mater Transact Phys Metallurgy Mater Sci* 36A:1263–1271
52. Zhang KB, Fu ZY, Zhang JY, Shi J, Wang WM, Wang H, Wang YC, Zhang QJ (2010) Annealing on the structure and properties evolution of the CoCrFeNiCuAl high-entropy alloy. *J Alloys Compd* 502(2):295–299, doi:<http://dx.doi.org/10.1016/j.jallcom.2009.11.104>
53. von Barth U, Hedin L (1972) A local exchange-correlation potential for the spin polarized case. *J Phys C: Solid State Phys* 5(13):1629–1642. doi:[10.1088/0022-3719/5/13/012](https://doi.org/10.1088/0022-3719/5/13/012)

Chapter 10

Applications of Special Quasi-random Structures to High-Entropy Alloys

Michael C. Gao, Changning Niu, Chao Jiang, and Douglas L. Irving

Abstract Special quasi-random structures (SQSs) are an important tool in modeling disordered alloys with atomic resolution. This chapter first presents the framework and the tools available to generate SQS for high-entropy alloys (HEAs). Examples of SQS in 4- and 5-component equiatomic alloys with face-centered cubic (FCC), hexagonal close-packed (HCP), and body-centered cubic (BCC) crystal structures, which are central to HEAs, are provided with different SQS cell sizes. Using SQS, the phase stability of known single-phase HEAs is examined, and the vibrational, electronic, and mechanical properties are predicted. Finally, the chapter compares the strength and limitations of SQS with hybrid Monte Carlo/molecular dynamics (MC/MD) simulations and coherent potential approximation (CPA) as introduced in prior chapters. First-principles calculations on selected single-phase HEAs show that the vibrational entropy of mixing is small, and the electronic entropy of mixing is truly negligible. Excellent agreement in the electronic density of states of HEAs was observed using SQS versus MC/MD. The accuracy of these SQS models is sensitive to the size of the cell, and larger cells produce more reliable results.

Keywords Special quasi-random structures (SQSs) • Hybrid Monte Carlo/molecular dynamics (MC/MD) • Coherent potential application (CPA) • Density functional theory (DFT) • First principles • Magnetism • Electronic structure • Elasticity • Elastic constants • Stacking fault energy • Density of state • Entropy sources • Configurational entropy • Vibrational entropy • Electronic entropy • Excess entropy • Phonon vibration • Phase stability • Pair distribution function

M.C. Gao (✉)

National Energy Technology Laboratory/AECOM, Albany, OR 97321, USA
e-mail: michael.gao@netl.doe.gov

C. Niu • D.L. Irving

Department of Materials Science and Engineering, North Carolina State University, Raleigh, NC 27695, USA
e-mail: cniu@ncsu.edu; dlirving@ncsu.edu

C. Jiang

Thermo-Calc Software, Pittsburgh, PA 15317, USA
e-mail: chao@thermocalc.com

- Face-centered cubic (FCC)
- Hexagonal close-packed (HCP)
- Body-centered cubic (BCC)
- Cell size effect
- Disordered solid solution
- High-entropy alloys (HEAs)

10.1 Introduction

Within the framework of density functional theory (DFT), periodic boundary conditions are applied to an atomic unit (or primitive) cell consisting of a limited number of atoms in order to simulate the bulk state of a material. Such calculations are straightforward for perfectly ordered structures. However, as many materials (e.g., Ni-based superalloys) are multicomponent in nature, the existence of substitutional disorder can make DFT calculations difficult. The same computational difficulty also exists in the DFT modeling of compounds with partially occupied sites. Intuitively, to model a random solid solution, one can arbitrarily distribute the solute and solvent atoms on the lattice sites of a large supercell and then obtain the averaged energy and properties from a large number of lattices of varying site distributions of atoms. Obviously this brute-force approach would therefore be computationally too expensive for DFT calculations.

The concept of SQS [1, 2] is to build a special periodic structure with a small number of atoms per unit cell whose correlation functions for the first few nearest-neighbor shells are as close to those of a target random alloy as possible such that the periodicity errors only exist between more distant neighbors. Because interactions between distant neighbors generally contribute much less to the system energy than between near neighbors, an SQS can be regarded as the best possible periodic unit cell representing a given random alloy. However, caution should be paid to ionic crystals for which distant-neighbor interactions may still be important under a given unit cell size constraint. To date, the SQS approach has been successfully applied to predict the formation energies [3], elastic properties [3–5], bond length distributions [6], density of states [6], and band gaps and optical properties [7, 8] of a wide range of materials with substitutional disorder, including semiconductors [7], oxides [8], and metallic alloys including high-entropy alloys [5].

10.2 Generation of SQS for High-Entropy Alloys

To date, SQSs have been mainly applied to model random binary [9–11] and ternary alloys [12, 13] in the literature. In the case of HEAs, SQS has some limitations that one needs to consider. Three major questions need to be answered to obtain an SQS for HEAs. The first is to determine the cell size of the desired SQS model – is it large enough to allow exploring desired compositions with sufficient

accuracy and small enough to allow DFT calculations within current hardware limitations? The second is to decide the criteria of clusters used in the calculations of correlation functions. Namely, what is the maximum distance for pairs and triplets that are considered as being important in generating SQS? Is it always preferred to use strict criteria? The third is to determine when to stop the generation of SQS. Ideally the generation of SQS will stop automatically after finding the perfect SQS model that satisfies our search criteria. However, it is likely that a perfect SQS of an HEA can never be found due to limited supercell size, in which case one needs to manually stop the generation of SQS and use the best SQS model that is obtained.

There are two methods to generate SQSs. The first one is to exhaustively generate all possible supercells for a given cell size and then pick the one that best mimics the correlation functions of the random alloy. The second method is to perform Monte Carlo simulations to search for the best SQS. The two methods have been, respectively, implemented in the *gensqs* and *mcsqs* codes within the Alloy Theoretic Automated Toolkit (ATAT) developed by Axel van de Walle and coworkers [14, 15]. ATAT's main codes include a code to construct cluster expansions from first principles to calculate the energy of a substitutional alloy as a function of its configuration and a code to perform Monte Carlo simulation of lattice models in order to compute thermodynamic properties of alloys starting from a cluster expansion [14, 15]. While the *gensqs* code can only be used to generate smaller SQS, the *mcsqs* code [16] is more powerful and can be used to generate large SQS containing hundreds of atoms per unit cell. The full functionalities of ATAT can be found in the official manual [17].

Only quaternary and quinary equiatomic SQSs for HEAs with various cell sizes to mimic disordered face-centered cubic (FCC), hexagonal close-packed (HCP), and body-centered cubic (BCC) lattices are provided in this chapter, and one can generate other SQS for HEAs with more components using ATAT. In the generation of both the 16- and 24-atom fcc quaternary SQS, only pair correlation functions up to the third nearest shell are considered. Based on the present authors' experience, it usually takes more than a few days to obtain an optimal SQS for HEAs with small correlation function mismatch. The generation of BCC and HCP SQS models uses similar settings. In all cases, triplets are not considered because chemical complexity of these models significantly raises the difficulty of finding a usable SQS. In fact, the generated best SQS by adding triplets within the first nearest shell may have larger correlation function mismatch values than the one considering only pairs.

In addition to the small SQS discussed above, larger SQS have also been developed for 4- and 5-component HEAs using the *mcsqs* code, although their generation needs much longer time than the small SQS due to combinatorial explosion. As a general rule, the larger the SQS cell is, the better it can reproduce the correlation functions of a random alloy. A convergence test on the energy versus the SQS cell size may be desirable to determine the optimal cell size for the sake of computational efficiency.

10.3 Quaternary and Quinary HEA SQS

SQSSs for quaternary and quinary random solid solution HEAs at equal molar ratio for FCC, BCC, and HCP are generated using a variety of cell sizes, namely, the number of atoms in SQS ranging from 16 to 250 atoms. The unrelaxed lattice vector and atomic position in the obtained SQS models for equal molar quaternary and quinary HEAs in FCC, BCC, and HCP structures are listed in Tables 10.1, 10.2, and 10.3, respectively. The crystal structures of quaternary (quinary) SQS are shown in Fig. 10.1 (Fig. 10.2).

Table 10.1 Quaternary ABCD SQS: 16-/24-atom FCC/HCP [5] and 64-atom FCC/BCC/HCP [18]

64-atom FCC	64-atom HCP	64-atom BCC
Lattice vectors $\begin{pmatrix} 0 & 2 & 2 \\ 2 & 0 & 2 \\ 2 & 2 & 0 \end{pmatrix}$	Lattice vectors $\begin{pmatrix} 4 & 0 & 0 \\ -2 & 3.4641 & 0 \\ 0 & 0 & 3.266 \end{pmatrix}$	Lattice vectors $\begin{pmatrix} -2 & -2 & 2 \\ 2 & -2 & -2 \\ 2 & 2 & 2 \end{pmatrix}$
Atom positions	Atom positions	Atom positions
0.00 0.00 0.50 Å	0.000000 0.000000 0.500000 Å	0.00 0.00 0.50 Å
0.00 0.25 0.25 Å	0.000000 0.250000 0.000000 Å	0.00 0.50 0.00 Å
0.00 0.50 0.25 Å	0.000000 0.750000 0.500000 Å	0.25 0.00 0.75 Å
0.00 0.75 0.25 Å	0.250000 0.000000 0.000000 Å	0.25 0.25 0.50 Å
0.00 0.75 0.75 Å	0.250000 0.250000 0.000000 Å	0.25 0.25 0.75 Å
0.25 0.00 0.25 Å	0.500000 0.250000 0.500000 Å	0.25 0.50 0.50 Å
0.25 0.25 0.00 Å	0.500000 0.500000 0.500000 Å	0.50 0.00 0.00 Å
0.25 0.25 0.50 Å	0.500000 0.750000 0.000000 Å	0.50 0.25 0.00 Å
0.25 0.50 0.50 Å	0.750000 0.000000 0.500000 Å	0.50 0.50 0.25 Å
0.25 0.75 0.25 Å	0.750000 0.750000 0.500000 Å	0.50 0.75 0.00 Å
0.50 0.00 0.50 Å	0.166667 0.083333 0.750000 Å	0.50 0.75 0.25 Å
0.50 0.75 0.00 Å	0.166667 0.833333 0.250000 Å	0.75 0.00 0.75 Å
0.75 0.00 0.00 Å	0.416667 0.833333 0.750000 Å	0.75 0.50 0.50 Å
0.75 0.00 0.25 Å	0.666667 0.333333 0.750000 Å	0.75 0.75 0.25 Å
0.75 0.00 0.50 Å	0.666667 0.583333 0.750000 Å	0.75 0.75 0.50 Å
0.75 0.75 0.25 Å	0.916667 0.833333 0.750000 Å	0.75 0.75 0.75 Å
0.00 0.00 0.25 B	0.000000 0.000000 0.000000 B	0.00 0.00 0.00 B
0.00 0.00 0.75 B	0.000000 0.250000 0.500000 B	0.00 0.25 0.00 B
0.00 0.25 0.00 B	0.250000 0.750000 0.000000 B	0.00 0.25 0.50 B
0.00 0.50 0.75 B	0.500000 0.500000 0.000000 B	0.00 0.50 0.25 B
0.00 0.75 0.00 B	0.500000 0.750000 0.500000 B	0.00 0.50 0.75 B
0.00 0.75 0.50 B	0.750000 0.250000 0.500000 B	0.25 0.25 0.00 B
0.25 0.00 0.50 B	0.166667 0.833333 0.750000 B	0.25 0.50 0.25 B
0.50 0.00 0.75 B	0.416667 0.083333 0.250000 B	0.25 0.75 0.25 B
0.50 0.25 0.75 B	0.416667 0.833333 0.250000 B	0.25 0.75 0.50 B
0.50 0.50 0.00 B	0.666667 0.083333 0.250000 B	0.25 0.75 0.75 B
0.75 0.00 0.75 B	0.666667 0.833333 0.750000 B	0.50 0.00 0.75 B
0.75 0.25 0.00 B	0.666667 0.333333 0.250000 B	0.50 0.50 0.00 B
0.75 0.25 0.50 B	0.666667 0.583333 0.250000 B	0.50 0.50 0.50 B
0.75 0.50 0.50 B	0.666667 0.833333 0.750000 B	0.50 0.50 0.75 B
0.75 0.50 0.75 B	0.916667 0.083333 0.250000 B	0.75 0.25 0.00 B

(continued)

Table 10.1 (continued)

64-atom FCC	64-atom HCP	64-atom BCC
0.75 0.75 0.75 B	0.916667 0.333333 0.250000 B	0.75 0.50 0.00 B
0.00 0.25 0.50 C	0.000000 0.500000 0.000000 C	0.00 0.00 0.25 C
0.00 0.25 0.75 C	0.000000 0.750000 0.000000 C	0.00 0.00 0.75 C
0.00 0.50 0.00 C	0.250000 0.500000 0.000000 C	0.00 0.25 0.25 C
0.00 0.50 0.50 C	0.250000 0.750000 0.500000 C	0.00 0.75 0.00 C
0.25 0.00 0.00 C	0.500000 0.000000 0.500000 C	0.00 0.75 0.25 C
0.25 0.25 0.25 C	0.500000 0.250000 0.000000 C	0.00 0.75 0.75 C
0.25 0.50 0.25 C	0.750000 0.500000 0.500000 C	0.25 0.00 0.00 C
0.25 0.75 0.00 C	0.750000 0.750000 0.000000 C	0.25 0.25 0.25 C
0.50 0.00 0.25 C	0.166667 0.333333 0.750000 C	0.25 0.50 0.75 C
0.50 0.25 0.00 C	0.166667 0.583333 0.750000 C	0.50 0.75 0.50 C
0.50 0.50 0.25 C	0.416667 0.333333 0.750000 C	0.75 0.00 0.00 C
0.50 0.50 0.50 C	0.416667 0.583333 0.250000 C	0.75 0.00 0.25 C
0.50 0.50 0.75 C	0.416667 0.583333 0.750000 C	0.75 0.00 0.50 C
0.75 0.25 0.25 C	0.666667 0.833333 0.250000 C	0.75 0.25 0.25 C
0.75 0.25 0.75 C	0.916667 0.333333 0.750000 C	0.75 0.25 0.50 C
0.75 0.50 0.25 C	0.916667 0.583333 0.250000 C	0.75 0.25 0.75 C
0.00 0.00 0.00 D	0.000000 0.500000 0.500000 D	0.00 0.25 0.75 D
0.25 0.00 0.75 D	0.250000 0.000000 0.500000 D	0.00 0.50 0.50 D
0.25 0.25 0.75 D	0.250000 0.250000 0.500000 D	0.00 0.75 0.50 D
0.25 0.50 0.00 D	0.250000 0.500000 0.500000 D	0.25 0.00 0.25 D
0.25 0.50 0.75 D	0.500000 0.000000 0.000000 D	0.25 0.00 0.50 D
0.25 0.75 0.50 D	0.750000 0.000000 0.000000 D	0.25 0.50 0.00 D
0.25 0.75 0.75 D	0.750000 0.250000 0.000000 D	0.25 0.75 0.00 D
0.50 0.00 0.00 D	0.750000 0.500000 0.000000 D	0.50 0.00 0.25 D
0.50 0.25 0.25 D	0.166667 0.083333 0.250000 D	0.50 0.00 0.50 D
0.50 0.25 0.50 D	0.166667 0.333333 0.250000 D	0.50 0.25 0.25 D
0.50 0.75 0.25 D	0.166667 0.583333 0.250000 D	0.50 0.25 0.50 D
0.50 0.75 0.50 D	0.416667 0.083333 0.750000 D	0.50 0.25 0.75 D
0.50 0.75 0.75 D	0.416667 0.333333 0.250000 D	0.50 0.75 0.75 D
0.75 0.50 0.00 D	0.916667 0.083333 0.750000 D	0.75 0.50 0.25 D
0.75 0.75 0.00 D	0.916667 0.583333 0.750000 D	0.75 0.50 0.75 D
0.75 0.75 0.50 D	0.916667 0.833333 0.250000 D	0.75 0.75 0.00 D
16-atom FCC	16-atom HCP	
Lattice vectors	Lattice vectors	
$\begin{pmatrix} -1 & -0.5 & -1.5 \\ -1 & 1.5 & 0.5 \\ 1 & 0.5 & -0.5 \end{pmatrix}$	$\begin{pmatrix} 1.5 & 0.866 & 3.266 \\ 0.5 & -0.866 & 3.266 \\ 2 & 0 & 0 \end{pmatrix}$	
Atom positions	Atom positions	
0.875 0.625 1.0 A	0.500000 0.500000 1.000000 A	
0.875 0.125 0.5 A	0.291666 0.958333 0.041667 A	
0.125 0.875 0.5 A	0.791666 0.458333 0.041667 A	
1.000 0.500 0.5 A	0.041666 0.708333 0.791667 A	
0.625 0.875 1.0 B	0.500000 0.500000 0.500000 B	
0.750 0.750 0.5 B	0.750000 0.750000 0.250000 B	
0.625 0.375 0.5 B	0.541666 0.208333 0.291667 B	
0.375 0.625 0.5 B	0.041666 0.708333 0.291667 B	
0.750 0.250 1.0 C	1.000000 1.000000 1.000000 C	
0.500 0.500 1.0 C	1.000000 1.000000 0.500000 C	

(continued)

Table 10.1 (continued)

64-atom FCC	64-atom HCP	64-atom BCC
0.125 0.375 1.0 C	0.750000 0.750000 0.750000 C	
0.250 0.250 0.5 C	0.291666 0.958333 0.541667 C	
0.250 0.750 1.0 D	0.250000 0.250000 0.250000 D	
0.375 0.125 1.0 D	0.250000 0.250000 0.750000 D	
1.000 1.000 1.0 D	0.541666 0.208333 0.791667 D	
0.500 1.000 0.5 D	0.791666 0.458333 0.541667 D	
24-atom FCC [5]	24-atom HCP [5]	
Lattice vectors $\begin{pmatrix} 0.5 & -0.5 & -1 \\ -1.5 & -1.5 & 0 \\ -1.5 & 1.5 & -1 \end{pmatrix}$	Lattice vectors $\begin{pmatrix} -2 & -1.732 & 1.633 \\ -2 & 1.732 & 1.633 \\ -1 & 0 & -1.633 \end{pmatrix}$	
Atom positions	Atom positions	
1.00 0.83333333 0.50 A	1.00 0.833333 0.50 A	
0.50 0.50000000 1.00 A	0.50 0.500000 1.00 A	
1.00 0.33333333 1.00 A	1.00 0.333333 1.00 A	
0.25 0.33333333 0.75 A	0.25 0.333333 0.75 A	
0.75 0.33333333 0.25 A	0.75 0.333333 0.25 A	
0.25 0.16666667 0.25 A	0.25 0.166667 0.25 A	
0.50 0.83333333 1.00 B	0.50 0.833333 1.00 B	
0.75 0.66666667 0.25 B	0.75 0.666667 0.25 B	
0.50 0.33333333 0.50 B	0.50 0.333333 0.50 B	
0.50 0.16666667 1.00 B	0.50 0.166667 1.00 B	
1.00 1.00000000 1.00 B	1.00 1.000000 1.00 B	
0.75 0.16666667 0.75 B	0.75 0.166667 0.75 B	
1.00 0.66666667 1.00 C	1.00 0.666667 1.00 C	
0.25 0.66666667 0.75 C	0.25 0.666667 0.75 C	
0.50 0.66666667 0.50 C	0.50 0.666667 0.50 C	
1.00 0.50000000 0.50 C	1.00 0.500000 0.50 C	
0.25 0.50000000 0.25 C	0.25 0.500000 0.25 C	
0.25 1.00000000 0.75 C	0.25 1.000000 0.75 C	
0.25 0.83333333 0.25 D	0.25 0.833333 0.25 D	
0.75 0.83333333 0.75 D	0.75 0.833333 0.75 D	
0.75 0.50000000 0.75 D	0.75 0.500000 0.75 D	
1.00 0.16666667 0.50 D	1.00 0.166667 0.50 D	
0.50 1.00000000 0.50 D	0.50 1.000000 0.50 D	
0.75 1.00000000 0.25 D	0.75 1.000000 0.25 D	

Lattice vectors and atomic positions (in fractional coordinates) are given for the unrelaxed lattices

Table 10.2 Quinary ABCDE SQS: 20-atom FCC/HCP [5], 125-atom FCC/BCC [18], and 160-atom HCP [18]

125-atom FCC	125-atom BCC	160-atom HCP
Lattice vectors $\begin{pmatrix} 0 & 2.5 & 2.5 \\ 2.5 & 0 & 2.5 \\ 2.5 & 2.5 & 0 \end{pmatrix}$	Lattice vectors $\begin{pmatrix} -2.5 & -2.5 & 2.5 \\ 2.5 & -2.5 & -2.5 \\ 2.5 & 2.5 & 2.5 \end{pmatrix}$	Lattice vectors $\begin{pmatrix} 4 & 0 & 0 \\ -2 & 3.4641 & 0 \\ 0 & 0 & 8.165 \end{pmatrix}$
Atom positions 0.2 0.8 0.4 Å	Atom positions 0.2 0.4 0.4 Å	Atom positions 0.000000 0.500000 0.400000 Å

(continued)

Table 10.2 (continued)

125-atom FCC	125-atom BCC	160-atom HCP
0.6 0.0 0.2 A	0.4 0.4 0.2 A	0.000000 0.500000 0.600000 A
0.6 0.4 0.8 A	0.6 0.4 0.8 A	0.000000 0.500000 0.800000 A
0.8 0.0 0.2 A	0.0 0.2 0.0 A	0.000000 0.750000 0.600000 A
0.0 0.8 0.8 A	0.0 0.6 0.4 A	0.250000 0.000000 0.200000 A
0.2 0.6 0.6 A	0.4 0.0 0.8 A	0.250000 0.000000 0.400000 A
0.4 0.0 0.4 A	0.8 0.8 0.8 A	0.250000 0.000000 0.800000 A
0.4 0.6 0.6 A	0.0 0.2 0.4 A	0.250000 0.250000 0.600000 A
0.6 0.4 0.4 A	0.0 0.6 0.2 A	0.250000 0.500000 0.600000 A
0.6 0.6 0.2 A	0.2 0.4 0.2 A	0.500000 0.250000 0.000000 A
0.8 0.8 0.4 A	0.4 0.2 0.6 A	0.500000 0.500000 0.200000 A
0.4 0.0 0.8 A	0.6 0.2 0.6 A	0.500000 0.500000 0.400000 A
0.4 0.2 0.6 A	0.8 0.6 0.4 A	0.750000 0.000000 0.000000 A
0.4 0.6 0.0 A	0.0 0.8 0.6 A	0.750000 0.000000 0.600000 A
0.6 0.6 0.0 A	0.2 0.0 0.0 A	0.750000 0.250000 0.600000 A
0.8 0.4 0.2 A	0.2 0.8 0.0 A	0.750000 0.500000 0.400000 A
0.0 0.4 0.4 A	0.4 0.0 0.6 A	0.750000 0.500000 0.600000 A
0.2 0.0 0.0 A	0.4 0.6 0.6 A	0.166667 0.083333 0.900000 A
0.6 0.2 0.2 A	0.8 0.4 0.8 A	0.166667 0.333333 0.700000 A
0.2 0.4 0.6 A	0.8 0.6 0.2 A	0.166667 0.583333 0.300000 A
0.2 0.8 0.6 A	0.0 0.0 0.6 A	0.166667 0.583333 0.700000 A
0.4 0.6 0.4 A	0.0 0.0 0.8 A	0.166667 0.833333 0.900000 A
0.6 0.0 0.0 A	0.2 0.6 0.6 A	0.416667 0.083333 0.100000 A
0.8 0.2 0.0 A	0.6 0.6 0.2 A	0.416667 0.333333 0.100000 A
0.8 0.2 0.8 A	0.8 0.0 0.4 A	0.416667 0.833333 0.900000 A
0.2 0.0 0.8 B	0.2 0.8 0.8 B	0.666667 0.333333 0.100000 A
0.4 0.4 0.8 B	0.4 0.4 0.0 B	0.666667 0.333333 0.700000 A
0.8 0.2 0.4 B	0.4 0.8 0.8 B	0.666667 0.833333 0.500000 A
0.8 0.4 0.8 B	0.6 0.2 0.2 B	0.666667 0.833333 0.700000 A
0.0 0.8 0.0 B	0.6 0.2 0.4 B	0.916667 0.083333 0.300000 A
0.2 0.4 0.4 B	0.6 0.2 0.8 B	0.916667 0.083333 0.500000 A
0.4 0.6 0.2 B	0.6 0.6 0.6 B	0.916667 0.833333 0.500000 A
0.6 0.6 0.8 B	0.6 0.8 0.8 B	0.000000 0.000000 0.400000 B
0.6 0.8 0.8 B	0.0 0.6 0.0 B	0.000000 0.500000 0.200000 B
0.8 0.0 0.0 B	0.2 0.0 0.4 B	0.250000 0.500000 0.800000 B
0.8 0.2 0.2 B	0.4 0.2 0.0 B	0.250000 0.750000 0.000000 B
0.2 0.0 0.6 B	0.4 0.2 0.2 B	0.500000 0.000000 0.000000 B
0.4 0.0 0.2 B	0.4 0.8 0.2 B	0.500000 0.000000 0.400000 B
0.4 0.8 0.2 B	0.6 0.8 0.6 B	0.500000 0.000000 0.600000 B
0.6 0.0 0.6 B	0.8 0.4 0.2 B	0.500000 0.250000 0.600000 B
0.6 0.6 0.6 B	0.2 0.4 0.6 B	0.500000 0.500000 0.000000 B
0.6 0.8 0.6 B	0.6 0.6 0.4 B	0.500000 0.500000 0.800000 B
0.0 0.6 0.8 B	0.8 0.8 0.2 B	0.500000 0.750000 0.200000 B
0.2 0.6 0.2 B	0.2 0.2 0.6 B	0.500000 0.750000 0.400000 B
0.4 0.0 0.6 B	0.4 0.0 0.0 B	0.750000 0.000000 0.400000 B
0.4 0.2 0.0 B	0.4 0.4 0.4 B	0.750000 0.250000 0.400000 B
0.6 0.2 0.0 B	0.0 0.2 0.6 B	0.750000 0.500000 0.200000 B
0.8 0.6 0.8 B	0.4 0.2 0.8 B	0.750000 0.750000 0.600000 B
0.0 0.6 0.6 B	0.6 0.4 0.6 B	0.750000 0.750000 0.800000 B
0.2 0.2 0.0 B	0.8 0.4 0.6 B	0.166667 0.083333 0.100000 B

(continued)

Table 10.2 (continued)

125-atom FCC	125-atom BCC	160-atom HCP
0.0 0.0 0.8 C	0.0 0.6 0.8 C	0.166667 0.333333 0.300000 B
0.2 0.2 0.2 C	0.2 0.2 0.8 C	0.166667 0.333333 0.500000 B
0.2 0.2 0.8 C	0.4 0.6 0.4 C	0.166667 0.583333 0.100000 B
0.2 0.8 0.2 C	0.8 0.2 0.0 C	0.166667 0.833333 0.100000 B
0.4 0.0 0.0 C	0.0 0.6 0.6 C	0.416667 0.083333 0.500000 B
0.8 0.4 0.6 C	0.2 0.2 0.0 C	0.416667 0.333333 0.900000 B
0.0 0.2 0.0 C	0.6 0.0 0.0 C	0.416667 0.583333 0.100000 B
0.4 0.2 0.2 C	0.8 0.2 0.4 C	0.416667 0.583333 0.900000 B
0.8 0.8 0.8 C	0.8 0.8 0.4 C	0.666667 0.333333 0.300000 B
0.0 0.2 0.2 C	0.0 0.4 0.0 C	0.666667 0.583333 0.100000 B
0.0 0.6 0.4 C	0.0 0.4 0.6 C	0.916667 0.083333 0.900000 B
0.2 0.6 0.4 C	0.2 0.6 0.2 C	0.916667 0.333333 0.300000 B
0.4 0.8 0.8 C	0.4 0.6 0.2 C	0.916667 0.333333 0.700000 B
0.6 0.8 0.4 C	0.4 0.8 0.4 C	0.916667 0.583333 0.700000 B
0.8 0.6 0.0 C	0.6 0.4 0.0 C	0.000000 0.000000 0.600000 C
0.8 0.6 0.2 C	0.2 0.0 0.6 C	0.000000 0.250000 0.400000 C
0.8 0.6 0.4 C	0.2 0.2 0.2 C	0.000000 0.750000 0.800000 C
0.0 0.2 0.8 C	0.6 0.8 0.2 C	0.250000 0.500000 0.000000 C
0.6 0.4 0.2 C	0.8 0.8 0.6 C	0.250000 0.750000 0.200000 C
0.0 0.0 0.4 C	0.0 0.2 0.2 C	0.250000 0.750000 0.600000 C
0.0 0.2 0.4 C	0.0 0.4 0.8 C	0.250000 0.750000 0.800000 C
0.0 0.4 0.2 C	0.4 0.6 0.0 C	0.500000 0.250000 0.400000 C
0.0 0.6 0.0 C	0.4 0.8 0.0 C	0.500000 0.500000 0.600000 C
0.4 0.8 0.0 C	0.6 0.0 0.4 C	0.500000 0.750000 0.000000 C
0.6 0.4 0.0 C	0.8 0.4 0.4 C	0.750000 0.000000 0.800000 C
0.0 0.4 0.6 D	0.0 0.0 0.2 D	0.750000 0.250000 0.000000 C
0.0 0.8 0.4 D	0.2 0.6 0.0 D	0.166667 0.083333 0.700000 C
0.6 0.2 0.4 D	0.4 0.0 0.2 D	0.166667 0.333333 0.900000 C
0.6 0.2 0.8 D	0.8 0.4 0.0 D	0.166667 0.583333 0.500000 C
0.6 0.4 0.6 D	0.8 0.6 0.0 D	0.166667 0.583333 0.900000 C
0.6 0.8 0.0 D	0.0 0.4 0.2 D	0.416667 0.083333 0.300000 C
0.8 0.4 0.0 D	0.0 0.8 0.4 D	0.416667 0.583333 0.700000 C
0.8 0.6 0.6 D	0.4 0.4 0.6 D	0.416667 0.833333 0.500000 C
0.0 0.0 0.0 D	0.6 0.0 0.8 D	0.666667 0.083333 0.500000 C
0.0 0.2 0.6 D	0.8 0.0 0.8 D	0.666667 0.083333 0.900000 C
0.0 0.4 0.0 D	0.6 0.4 0.2 D	0.666667 0.333333 0.500000 C
0.0 0.4 0.8 D	0.6 0.6 0.8 D	0.666667 0.333333 0.900000 C
0.0 0.8 0.2 D	0.8 0.2 0.8 D	0.666667 0.583333 0.500000 C
0.8 0.0 0.4 D	0.0 0.0 0.0 D	0.666667 0.833333 0.100000 C
0.8 0.8 0.2 D	0.2 0.0 0.2 D	0.916667 0.083333 0.100000 C
0.4 0.4 0.4 D	0.2 0.2 0.4 D	0.916667 0.333333 0.100000 C
0.2 0.0 0.4 D	0.2 0.4 0.0 D	0.916667 0.333333 0.900000 C
0.2 0.6 0.0 D	0.2 0.4 0.8 D	0.916667 0.583333 0.300000 C
0.4 0.8 0.4 D	0.2 0.8 0.2 D	0.916667 0.583333 0.900000 C
0.8 0.0 0.6 D	0.8 0.8 0.0 D	0.916667 0.833333 0.300000 C
0.0 0.6 0.2 D	0.2 0.6 0.8 D	0.916667 0.833333 0.700000 C
0.4 0.4 0.2 D	0.2 0.8 0.4 D	0.000000 0.000000 0.000000 D
0.4 0.4 0.6 D	0.2 0.8 0.6 D	0.000000 0.250000 0.600000 D
0.6 0.0 0.8 D	0.6 0.2 0.0 D	0.000000 0.500000 0.000000 D
0.6 0.2 0.6 D	0.6 0.8 0.4 D	0.000000 0.750000 0.000000 D

(continued)

Table 10.2 (continued)

125-atom FCC	125-atom BCC	160-atom HCP
0.0 0.0 0.6 E	0.4 0.4 0.8 E	0.250000 0.250000 0.000000 D
0.2 0.2 0.6 E	0.6 0.0 0.2 E	0.250000 0.250000 0.200000 D
0.4 0.6 0.8 E	0.6 0.4 0.4 E	0.250000 0.250000 0.800000 D
0.0 0.0 0.2 E	0.8 0.0 0.2 E	0.250000 0.750000 0.400000 D
0.2 0.2 0.4 E	0.8 0.6 0.6 E	0.500000 0.000000 0.200000 D
0.2 0.4 0.8 E	0.0 0.8 0.2 E	0.500000 0.000000 0.800000 D
0.2 0.8 0.0 E	0.8 0.0 0.0 E	0.500000 0.250000 0.200000 D
0.4 0.2 0.8 E	0.8 0.0 0.6 E	0.750000 0.000000 0.200000 D
0.8 0.2 0.6 E	0.8 0.6 0.8 E	0.750000 0.250000 0.200000 D
0.2 0.0 0.2 E	0.0 0.4 0.4 E	0.750000 0.250000 0.800000 D
0.2 0.4 0.2 E	0.0 0.8 0.0 E	0.750000 0.500000 0.000000 D
0.2 0.6 0.8 E	0.0 0.8 0.8 E	0.750000 0.750000 0.400000 D
0.2 0.8 0.8 E	0.2 0.0 0.8 E	0.166667 0.083333 0.300000 D
0.4 0.2 0.4 E	0.2 0.6 0.4 E	0.166667 0.333333 0.100000 D
0.4 0.4 0.0 E	0.4 0.2 0.4 E	0.166667 0.833333 0.300000 D
0.4 0.8 0.6 E	0.6 0.0 0.6 E	0.166667 0.833333 0.700000 D
0.6 0.0 0.4 E	0.0 0.0 0.4 E	0.416667 0.083333 0.700000 D
0.6 0.8 0.2 E	0.4 0.6 0.8 E	0.416667 0.083333 0.900000 D
0.8 0.8 0.6 E	0.6 0.8 0.0 E	0.416667 0.333333 0.500000 D
0.0 0.8 0.6 E	0.8 0.2 0.6 E	0.416667 0.583333 0.500000 D
0.2 0.4 0.0 E	0.0 0.2 0.8 E	0.416667 0.833333 0.100000 D
0.6 0.6 0.4 E	0.4 0.0 0.4 E	0.416667 0.833333 0.300000 D
0.8 0.0 0.8 E	0.4 0.8 0.6 E	0.416667 0.833333 0.700000 D
0.8 0.4 0.4 E	0.6 0.6 0.0 E	0.666667 0.083333 0.300000 D
0.8 0.8 0.0 E	0.8 0.2 0.2 E	0.666667 0.583333 0.700000 D
20-atom FCC [5]		
Lattice vectors		
$\begin{pmatrix} 0.5 & 2.0 & -0.5 \\ 0.5 & -0.5 & 2.0 \\ 1.0 & -0.5 & -0.5 \end{pmatrix}$		
Atom positions		
0.15 0.35 0.25 A	1.000000 1.000000 0.50 A	0.916667 0.583333 0.100000 D
0.40 0.60 1.00 A	0.200000 0.200000 0.70 A	0.916667 0.833333 0.100000 D
0.55 0.95 0.25 A	0.400000 0.400000 0.90 A	0.000000 0.000000 0.200000 E
0.45 0.05 0.75 A	1.000000 1.000000 1.00 A	0.000000 0.000000 0.800000 E
0.20 0.80 1.00 B	0.200000 0.200000 0.20 B	0.000000 0.250000 0.000000 E
0.05 0.45 0.75 B	0.400000 0.400000 0.40 B	0.000000 0.250000 0.200000 E
0.60 0.40 1.00 B	0.600000 0.600000 0.60 B	0.000000 0.500000 0.200000 E
0.95 0.55 0.25 B	0.800000 0.800000 0.80 B	0.000000 0.500000 0.400000 E
0.65 0.85 0.75 C	0.600000 0.600000 0.10 C	0.250000 0.250000 0.800000 E
0.80 0.20 1.00 C	0.800000 0.800000 0.30 C	0.250000 0.500000 0.600000 E
0.85 0.65 0.75 C	0.766666 0.433333 0.35 C	0.250000 0.500000 0.400000 E
0.90 0.10 0.50 C	0.966666 0.633333 0.55 C	0.500000 0.250000 0.800000 E
0.35 0.15 0.25 D	0.166666 0.833333 0.75 D	0.500000 0.500000 0.000000 E
0.50 0.50 0.50 D	0.766666 0.433333 0.85 D	0.750000 0.750000 0.200000 E
0.75 0.75 0.25 D	0.966666 0.633333 0.05 D	0.166667 0.083333 0.500000 E
0.70 0.30 0.50 D	0.166666 0.833333 0.25 D	0.166667 0.833333 0.500000 E
0.10 0.90 0.50 E	0.366666 0.033333 0.45 E	0.416667 0.333333 0.300000 E

(continued)

Table 10.2 (continued)

125-atom FCC	125-atom BCC	160-atom HCP
1.00 1.00 1.00 E	0.566666 0.233333 0.65 E	0.416667 0.333333 0.700000 E
0.30 0.70 0.50 E	0.366666 0.033333 0.95 E	0.416667 0.583333 0.300000 E
0.25 0.25 0.75 E	0.566666 0.233333 0.15 E	0.666667 0.083333 0.100000 E
		0.666667 0.083333 0.700000 E
		0.666667 0.583333 0.300000 E
		0.666667 0.583333 0.900000 E
		0.666667 0.833333 0.300000 E
		0.666667 0.833333 0.900000 E
		0.916667 0.083333 0.700000 E
		0.916667 0.583333 0.500000 E
		0.916667 0.833333 0.900000 E

Lattice vectors and atomic positions (in fractional coordinates) are given for the unrelaxed lattices

Table 10.3 250-atom quinary ABCDE SQS in FCC/BCC/HCP structures [18]

250-atom FCC	250-atom BCC	250-atom HCP
Lattice vectors $\begin{pmatrix} 0 & -2.5 & 2.5 \\ 0 & 2.5 & 2.5 \\ -5 & 0 & 0 \end{pmatrix}$	Lattice vector $\begin{pmatrix} 5 & 0 & 0 \\ 0 & 5 & 0 \\ 0 & 0 & 5 \end{pmatrix}$	Lattice vectors $\begin{pmatrix} 5 & 0 & 0 \\ -2.5 & 4.33 & 0 \\ 0 & 0 & 8.165 \end{pmatrix}$
Atom positions	Atom positions	Atom positions
0.1 0.5 0.9 A	0.0 0.0 0.2 A	0.000000 0.000000 0.200000 A
0.3 0.5 0.1 A	0.0 0.4 0.0 A	0.000000 0.000000 0.800000 A
0.5 0.7 0.9 A	0.0 0.6 0.6 A	0.000000 0.600000 0.600000 A
0.7 0.5 0.1 A	0.0 0.8 0.8 A	0.000000 0.600000 0.800000 A
0.9 0.1 0.1 A	0.2 0.0 0.2 A	0.200000 0.200000 0.400000 A
0.9 0.7 0.1 A	0.2 0.0 0.6 A	0.200000 0.600000 0.000000 A
0.2 0.4 0.6 A	0.2 0.2 0.0 A	0.200000 0.600000 0.200000 A
0.6 0.6 0.4 A	0.2 0.2 0.2 A	0.200000 0.600000 0.400000 A
1.0 0.6 0.2 A	0.2 0.2 0.4 A	0.200000 0.800000 0.200000 A
0.1 0.7 0.9 A	0.2 0.6 0.2 A	0.400000 0.000000 0.200000 A
0.1 0.9 0.5 A	0.2 0.6 0.4 A	0.400000 0.000000 0.600000 A
0.5 0.3 0.9 A	0.2 0.8 0.2 A	0.400000 0.000000 0.800000 A
0.5 0.7 0.1 A	0.4 0.0 0.0 A	0.400000 0.200000 0.200000 A
0.7 0.5 0.3 A	0.4 0.0 0.2 A	0.400000 0.400000 0.600000 A
0.8 1.0 0.4 A	0.4 0.2 0.8 A	0.400000 0.600000 0.000000 A
1.0 0.2 0.6 A	0.4 0.4 0.0 A	0.400000 0.600000 0.200000 A
0.1 0.3 0.7 A	0.6 0.0 0.2 A	0.400000 0.600000 0.800000 A
0.1 0.9 0.9 A	0.6 0.0 0.8 A	0.600000 0.200000 0.600000 A
0.5 0.3 0.5 A	0.6 0.2 0.8 A	0.600000 0.400000 0.600000 A
0.5 0.9 0.5 A	0.6 0.4 0.2 A	0.600000 0.600000 0.200000 A
0.9 0.9 0.5 A	0.6 0.6 0.8 A	0.800000 0.200000 0.400000 A
0.2 0.4 0.2 A	0.8 0.0 0.8 A	0.133333 0.066667 0.500000 A
0.4 0.2 0.6 A	0.8 0.4 0.0 A	0.133333 0.066667 0.700000 A
0.4 0.4 1.0 A	0.8 0.6 0.4 A	0.133333 0.266667 0.900000 A
0.4 0.8 0.2 A	0.8 0.8 0.0 A	0.133333 0.466667 0.500000 A
0.8 0.4 0.2 A	0.8 0.8 0.6 A	0.133333 0.866667 0.300000 A
0.8 0.4 0.8 A	0.8 0.8 0.8 A	0.133333 0.866667 0.700000 A

(continued)

Table 10.3 (continued)

250-atom FCC	250-atom BCC	250-atom HCP
1.0 0.2 0.2 A	0.1 0.3 0.9 A	0.333333 0.066667 0.700000 A
1.0 0.2 0.8 A	0.1 0.5 0.1 A	0.333333 0.466667 0.300000 A
0.1 0.3 0.5 A	0.1 0.5 0.3 A	0.333333 0.666667 0.100000 A
0.3 0.1 0.7 A	0.1 0.5 0.9 A	0.333333 0.866667 0.100000 A
0.3 0.5 0.7 A	0.1 0.7 0.1 A	0.333333 0.866667 0.700000 A
0.5 0.1 0.5 A	0.1 0.9 0.3 A	0.533333 0.066667 0.500000 A
0.5 0.7 0.3 A	0.3 0.1 0.5 A	0.533333 0.266667 0.900000 A
0.9 0.9 0.1 A	0.3 0.3 0.9 A	0.533333 0.466667 0.700000 A
0.4 0.2 0.8 A	0.5 0.1 0.7 A	0.533333 0.466667 0.900000 A
0.6 0.4 0.8 A	0.5 0.3 0.3 A	0.533333 0.666667 0.300000 A
0.6 0.6 0.8 A	0.5 0.3 0.9 A	0.533333 0.666667 0.700000 A
1.0 0.8 0.8 A	0.5 0.7 0.1 A	0.533333 0.866667 0.700000 A
0.1 0.1 0.5 A	0.5 0.7 0.5 A	0.733333 0.266667 0.900000 A
0.1 0.3 0.3 A	0.5 0.9 0.3 A	0.733333 0.466667 0.300000 A
0.3 0.3 0.3 A	0.7 0.3 0.9 A	0.733333 0.666667 0.300000 A
0.9 0.3 0.7 A	0.7 0.5 0.9 A	0.733333 0.866667 0.700000 A
0.4 0.4 0.4 A	0.7 0.9 0.1 A	0.933333 0.066667 0.100000 A
0.4 0.8 0.4 A	0.7 0.9 0.9 A	0.933333 0.266667 0.500000 A
0.6 0.2 0.6 A	0.9 0.1 0.5 A	0.933333 0.466667 0.900000 A
0.6 0.4 0.2 A	0.9 0.3 0.1 A	0.933333 0.666667 0.500000 A
0.6 1.0 0.2 A	0.9 0.3 0.3 A	0.933333 0.666667 0.700000 A
0.8 1.0 0.2 A	0.9 0.7 0.1 A	0.933333 0.866667 0.500000 A
1.0 0.6 0.6 A	0.9 0.9 0.3 A	0.933333 0.866667 0.900000 A
0.1 0.1 0.9 B	0.0 0.0 0.0 B	0.000000 0.400000 0.200000 B
0.3 0.7 0.5 B	0.0 0.0 0.4 B	0.000000 0.400000 0.400000 B
0.3 0.9 0.7 B	0.0 0.2 0.4 B	0.000000 0.800000 0.400000 B
0.5 0.3 0.7 B	0.0 0.8 0.6 B	0.000000 0.800000 0.600000 B
0.5 0.9 0.9 B	0.2 0.4 0.6 B	0.200000 0.000000 0.200000 B
0.7 0.9 0.5 B	0.2 0.8 0.4 B	0.200000 0.000000 0.800000 B
0.9 0.5 0.1 B	0.2 0.8 0.6 B	0.200000 0.400000 0.400000 B
0.2 0.6 0.6 B	0.4 0.2 0.2 B	0.200000 0.400000 0.600000 B
0.6 0.2 0.4 B	0.4 0.2 0.6 B	0.200000 0.400000 0.800000 B
0.8 0.2 1.0 B	0.4 0.4 0.4 B	0.200000 0.800000 0.400000 B
1.0 1.0 0.2 B	0.4 0.4 0.8 B	0.400000 0.000000 0.000000 B
0.1 0.9 0.3 B	0.4 0.6 0.2 B	0.400000 0.400000 0.000000 B
0.3 0.9 0.1 B	0.4 0.6 0.4 B	0.400000 0.400000 0.200000 B
0.4 0.2 0.2 B	0.4 0.6 0.8 B	0.400000 0.600000 0.400000 B
0.4 0.2 0.4 B	0.4 0.8 0.2 B	0.400000 0.800000 0.400000 B
0.4 0.4 0.2 B	0.6 0.4 0.0 B	0.600000 0.000000 0.200000 B
0.4 0.8 0.6 B	0.6 0.4 0.6 B	0.600000 0.200000 0.400000 B
0.6 0.2 0.8 B	0.6 0.4 0.8 B	0.600000 0.600000 0.000000 B
0.8 0.2 0.2 B	0.6 0.6 0.0 B	0.600000 0.600000 0.600000 B
0.1 0.3 0.1 B	0.8 0.0 0.2 B	0.600000 0.800000 0.600000 B
0.2 1.0 0.4 B	0.8 0.4 0.2 B	0.800000 0.000000 0.000000 B
0.4 0.6 0.2 B	0.8 0.4 0.4 B	0.800000 0.000000 0.600000 B
0.4 0.6 1.0 B	0.8 0.4 0.8 B	0.800000 0.400000 0.400000 B
0.4 1.0 0.4 B	0.8 0.8 0.2 B	0.800000 0.600000 0.600000 B
0.6 0.4 0.4 B	0.8 0.8 0.4 B	0.800000 0.800000 0.200000 B
0.6 0.8 1.0 B	0.1 0.1 0.5 B	0.800000 0.800000 0.600000 B

(continued)

Table 10.3 (continued)

250-atom FCC	250-atom BCC	250-atom HCP
0.8 0.4 1.0 B	0.1 0.3 0.1 B	0.133333 0.066667 0.900000 B
0.8 0.6 0.2 B	0.1 0.7 0.5 B	0.133333 0.266667 0.100000 B
0.3 0.1 0.9 B	0.1 0.9 0.1 B	0.133333 0.266667 0.300000 B
0.3 0.7 0.1 B	0.3 0.3 0.1 B	0.133333 0.266667 0.700000 B
0.5 0.1 0.7 B	0.3 0.3 0.3 B	0.133333 0.466667 0.100000 B
0.5 0.3 0.1 B	0.3 0.3 0.7 B	0.133333 0.866667 0.500000 B
0.7 0.7 0.7 B	0.3 0.5 0.9 B	0.333333 0.066667 0.300000 B
0.7 0.7 0.9 B	0.3 0.7 0.1 B	0.333333 0.266667 0.900000 B
0.7 0.9 0.9 B	0.3 0.9 0.1 B	0.333333 0.466667 0.700000 B
0.9 0.1 0.3 B	0.3 0.9 0.5 B	0.533333 0.066667 0.100000 B
0.2 0.8 0.6 B	0.3 0.9 0.7 B	0.533333 0.066667 0.700000 B
0.2 1.0 0.6 B	0.3 0.9 0.9 B	0.533333 0.266667 0.100000 B
0.4 1.0 0.8 B	0.5 0.3 0.1 B	0.533333 0.466667 0.100000 B
0.6 0.6 1.0 B	0.5 0.3 0.5 B	0.533333 0.466667 0.500000 B
0.8 0.4 0.4 B	0.5 0.5 0.7 B	0.533333 0.666667 0.900000 B
1.0 0.8 1.0 B	0.5 0.9 0.7 B	0.533333 0.866667 0.100000 B
0.3 0.5 0.3 B	0.7 0.5 0.5 B	0.533333 0.866667 0.300000 B
0.3 0.9 0.3 B	0.7 0.7 0.5 B	0.533333 0.866667 0.500000 B
0.3 0.9 0.9 B	0.9 0.1 0.7 B	0.533333 0.866667 0.900000 B
0.5 0.9 0.1 B	0.9 0.3 0.9 B	0.733333 0.066667 0.700000 B
0.9 0.1 0.5 B	0.9 0.5 0.7 B	0.733333 0.266667 0.300000 B
0.4 0.8 0.8 B	0.9 0.7 0.5 B	0.733333 0.266667 0.700000 B
1.0 0.8 0.4 B	0.9 0.7 0.7 B	0.933333 0.066667 0.900000 B
1.0 1.0 0.8 B	0.9 0.9 0.5 B	0.933333 0.266667 0.300000 B
0.1 0.9 0.7 C	0.0 0.2 0.6 C	0.000000 0.000000 0.000000 C
0.3 0.5 0.5 C	0.2 0.0 0.0 C	0.000000 0.000000 0.600000 C
0.5 0.5 0.9 C	0.2 0.0 0.4 C	0.000000 0.200000 0.200000 C
0.7 0.5 0.5 C	0.2 0.0 0.8 C	0.000000 0.600000 0.000000 C
0.7 0.7 0.3 C	0.2 0.4 0.2 C	0.000000 0.600000 0.400000 C
0.9 0.1 0.7 C	0.2 0.4 0.8 C	0.000000 0.800000 0.200000 C
0.9 0.1 0.9 C	0.4 0.0 0.8 C	0.000000 0.800000 0.800000 C
0.2 0.6 0.4 C	0.4 0.6 0.0 C	0.200000 0.000000 0.000000 C
1.0 0.4 0.6 C	0.4 0.8 0.4 C	0.200000 0.000000 0.600000 C
0.1 0.3 0.9 C	0.4 0.8 0.6 C	0.200000 0.200000 0.000000 C
0.1 0.7 0.7 C	0.4 0.8 0.8 C	0.200000 0.200000 0.800000 C
0.3 0.3 0.9 C	0.6 0.0 0.6 C	0.200000 0.400000 0.000000 C
0.5 0.7 0.5 C	0.6 0.2 0.6 C	0.200000 0.600000 0.800000 C
0.7 0.9 0.1 C	0.6 0.6 0.6 C	0.200000 0.800000 0.800000 C
0.2 0.8 0.8 C	0.6 0.8 0.2 C	0.400000 0.200000 0.400000 C
0.4 1.0 1.0 C	0.6 0.8 0.8 C	0.400000 0.200000 0.800000 C
0.6 0.2 0.2 C	0.8 0.0 0.0 C	0.400000 0.400000 0.400000 C
0.6 0.8 0.6 C	0.8 0.0 0.4 C	0.400000 0.400000 0.800000 C
0.6 1.0 0.4 C	0.8 0.0 0.6 C	0.400000 0.800000 0.200000 C
1.0 0.4 0.2 C	0.8 0.2 0.6 C	0.400000 0.800000 0.800000 C
0.5 0.1 0.3 C	0.1 0.1 0.9 C	0.600000 0.000000 0.000000 C
0.7 0.5 0.9 C	0.1 0.3 0.3 C	0.600000 0.200000 0.800000 C
0.9 0.7 0.5 C	0.1 0.3 0.7 C	0.600000 0.400000 0.400000 C
0.2 0.4 0.4 C	0.1 0.7 0.7 C	0.800000 0.200000 0.200000 C
0.4 0.2 1.0 C	0.3 0.1 0.7 C	0.800000 0.400000 0.200000 C
0.6 0.2 1.0 C	0.3 0.1 0.9 C	0.800000 0.600000 0.000000 C

(continued)

Table 10.3 (continued)

250-atom FCC	250-atom BCC	250-atom HCP
0.6 1.0 0.8 C	0.3 0.5 0.1 C	0.800000 0.600000 0.800000 C
0.8 0.2 0.8 C	0.3 0.7 0.5 C	0.800000 0.800000 0.800000 C
0.8 0.8 0.6 C	0.3 0.7 0.7 C	0.133333 0.266667 0.500000 C
0.8 1.0 1.0 C	0.3 0.7 0.9 C	0.133333 0.866667 0.100000 C
1.0 0.2 0.4 C	0.3 0.9 0.3 C	0.133333 0.866667 0.900000 C
0.3 0.1 0.5 C	0.5 0.1 0.3 C	0.333333 0.066667 0.900000 C
0.7 0.3 0.3 C	0.5 0.1 0.9 C	0.333333 0.266667 0.300000 C
0.2 0.6 0.2 C	0.5 0.3 0.7 C	0.333333 0.266667 0.700000 C
0.6 0.4 1.0 C	0.5 0.7 0.9 C	0.333333 0.666667 0.700000 C
0.6 0.6 0.6 C	0.5 0.9 0.1 C	0.333333 0.666667 0.900000 C
0.6 0.8 0.4 C	0.7 0.1 0.9 C	0.533333 0.266667 0.500000 C
0.8 0.2 0.6 C	0.7 0.3 0.3 C	0.533333 0.666667 0.100000 C
1.0 1.0 0.4 C	0.7 0.5 0.1 C	0.533333 0.666667 0.500000 C
1.0 1.0 1.0 C	0.7 0.5 0.3 C	0.733333 0.066667 0.300000 C
0.3 0.7 0.7 C	0.7 0.7 0.3 C	0.733333 0.066667 0.500000 C
0.5 0.1 0.1 C	0.7 0.7 0.7 C	0.733333 0.266667 0.500000 C
0.5 0.5 0.1 C	0.7 0.9 0.3 C	0.733333 0.466667 0.900000 C
0.7 0.1 0.7 C	0.7 0.9 0.5 C	0.733333 0.666667 0.100000 C
0.9 0.3 0.5 C	0.9 0.1 0.9 C	0.733333 0.666667 0.500000 C
0.9 0.9 0.9 C	0.9 0.3 0.5 C	0.733333 0.666667 0.700000 C
0.2 0.6 0.8 C	0.9 0.5 0.3 C	0.933333 0.066667 0.300000 C
0.2 0.8 0.4 C	0.9 0.5 0.9 C	0.933333 0.266667 0.100000 C
0.6 0.8 0.2 C	0.9 0.9 0.7 C	0.933333 0.466667 0.100000 C
1.0 0.4 0.4 C	0.9 0.9 0.9 C	0.933333 0.866667 0.300000 C
0.5 0.5 0.3 D	0.0 0.0 0.8 D	0.000000 0.000000 0.400000 D
0.7 0.3 0.1 D	0.0 0.4 0.4 D	0.000000 0.200000 0.800000 D
0.2 0.2 0.4 D	0.0 0.4 0.6 D	0.000000 0.400000 0.000000 D
0.4 0.6 0.4 D	0.0 0.6 0.2 D	0.000000 0.400000 0.800000 D
0.8 0.2 0.4 D	0.0 0.6 0.8 D	0.200000 0.200000 0.600000 D
0.8 0.6 0.8 D	0.0 0.8 0.4 D	0.200000 0.600000 0.600000 D
0.8 0.8 0.2 D	0.2 0.2 0.8 D	0.200000 0.800000 0.000000 D
0.8 1.0 0.8 D	0.2 0.4 0.4 D	0.200000 0.800000 0.600000 D
1.0 0.4 1.0 D	0.2 0.6 0.6 D	0.400000 0.000000 0.400000 D
1.0 0.6 1.0 D	0.2 0.6 0.8 D	0.400000 0.200000 0.000000 D
1.0 0.8 0.6 D	0.2 0.8 0.0 D	0.400000 0.200000 0.600000 D
0.1 0.1 0.1 D	0.4 0.0 0.4 D	0.400000 0.600000 0.600000 D
0.1 0.5 0.3 D	0.4 0.2 0.0 D	0.400000 0.800000 0.000000 D
0.3 0.7 0.9 D	0.4 0.2 0.4 D	0.600000 0.000000 0.600000 D
0.7 0.1 0.1 D	0.4 0.6 0.6 D	0.600000 0.000000 0.800000 D
0.7 0.1 0.9 D	0.4 0.8 0.0 D	0.600000 0.200000 0.000000 D
0.9 0.5 0.9 D	0.6 0.2 0.2 D	0.600000 0.200000 0.200000 D
0.2 0.6 1.0 D	0.6 0.2 0.4 D	0.600000 0.400000 0.000000 D
0.2 1.0 0.8 D	0.8 0.2 0.0 D	0.600000 0.400000 0.200000 D
0.4 0.4 0.8 D	0.8 0.2 0.2 D	0.600000 0.600000 0.400000 D
1.0 0.8 0.2 D	0.8 0.4 0.6 D	0.600000 0.800000 0.400000 D
0.3 0.1 0.3 D	0.8 0.6 0.6 D	0.600000 0.800000 0.800000 D
0.5 0.5 0.7 D	0.1 0.1 0.1 D	0.800000 0.000000 0.400000 D
0.7 0.3 0.5 D	0.1 0.1 0.3 D	0.800000 0.000000 0.800000 D
0.7 0.7 0.5 D	0.1 0.5 0.5 D	0.800000 0.400000 0.000000 D
0.9 0.5 0.7 D	0.1 0.5 0.7 D	0.800000 0.400000 0.600000 D

(continued)

Table 10.3 (continued)

250-atom FCC	250-atom BCC	250-atom HCP
0.9 0.7 0.7 D	0.1 0.9 0.9 D	0.800000 0.600000 0.400000 D
0.9 0.7 0.9 D	0.3 0.1 0.1 D	0.800000 0.800000 0.000000 D
0.6 0.6 0.2 D	0.3 0.1 0.3 D	0.133333 0.066667 0.100000 D
0.8 1.0 0.6 D	0.3 0.3 0.5 D	0.133333 0.666667 0.100000 D
1.0 0.4 0.8 D	0.3 0.5 0.3 D	0.133333 0.666667 0.500000 D
0.1 0.1 0.3 D	0.3 0.5 0.7 D	0.333333 0.266667 0.100000 D
0.3 0.3 0.5 D	0.3 0.7 0.3 D	0.333333 0.266667 0.500000 D
0.7 0.7 0.1 D	0.5 0.1 0.5 D	0.333333 0.466667 0.900000 D
0.9 0.5 0.5 D	0.5 0.5 0.1 D	0.333333 0.866667 0.500000 D
0.9 0.7 0.3 D	0.5 0.7 0.3 D	0.333333 0.866667 0.900000 D
0.2 0.8 0.2 D	0.5 0.7 0.7 D	0.533333 0.066667 0.300000 D
0.2 1.0 0.2 D	0.5 0.9 0.5 D	0.533333 0.066667 0.900000 D
0.2 1.0 1.0 D	0.7 0.1 0.3 D	0.533333 0.266667 0.300000 D
0.4 1.0 0.6 D	0.7 0.1 0.7 D	0.733333 0.066667 0.900000 D
0.8 0.8 1.0 D	0.7 0.3 0.1 D	0.733333 0.466667 0.500000 D
1.0 1.0 0.6 D	0.7 0.7 0.1 D	0.733333 0.466667 0.700000 D
0.1 0.5 0.5 D	0.7 0.7 0.9 D	0.733333 0.866667 0.100000 D
0.1 0.7 0.5 D	0.7 0.9 0.7 D	0.733333 0.866667 0.300000 D
0.7 0.1 0.3 D	0.9 0.1 0.1 D	0.733333 0.866667 0.900000 D
0.9 0.3 0.3 D	0.9 0.1 0.3 D	0.933333 0.066667 0.700000 D
0.9 0.5 0.3 D	0.9 0.3 0.7 D	0.933333 0.466667 0.500000 D
0.8 0.4 0.6 D	0.9 0.5 0.1 D	0.933333 0.666667 0.100000 D
0.8 0.6 1.0 D	0.9 0.5 0.5 D	0.933333 0.666667 0.900000 D
0.8 0.8 0.8 D	0.9 0.9 0.1 D	0.933333 0.866667 0.700000 D
0.1 0.1 0.7 E	0.0 0.0 0.6 E	0.000000 0.200000 0.000000 E
0.1 0.9 0.1 E	0.0 0.2 0.0 E	0.000000 0.200000 0.400000 E
0.3 0.5 0.9 E	0.0 0.2 0.2 E	0.000000 0.200000 0.600000 E
0.3 0.9 0.5 E	0.0 0.2 0.8 E	0.000000 0.400000 0.600000 E
0.7 0.9 0.3 E	0.0 0.4 0.2 E	0.000000 0.600000 0.200000 E
0.2 0.2 0.6 E	0.0 0.4 0.8 E	0.000000 0.800000 0.000000 E
0.2 0.4 0.8 E	0.0 0.6 0.0 E	0.200000 0.000000 0.400000 E
0.2 0.4 1.0 E	0.0 0.6 0.4 E	0.200000 0.200000 0.200000 E
0.2 0.8 1.0 E	0.0 0.8 0.0 E	0.200000 0.400000 0.200000 E
1.0 0.6 0.8 E	0.0 0.8 0.2 E	0.400000 0.800000 0.600000 E
0.1 0.7 0.1 E	0.2 0.2 0.6 E	0.600000 0.000000 0.400000 E
0.5 0.3 0.3 E	0.2 0.4 0.0 E	0.600000 0.400000 0.800000 E
0.5 0.7 0.7 E	0.2 0.6 0.0 E	0.600000 0.600000 0.800000 E
0.5 0.9 0.3 E	0.2 0.8 0.8 E	0.600000 0.800000 0.000000 E
0.7 0.3 0.9 E	0.4 0.0 0.6 E	0.600000 0.800000 0.200000 E
0.7 0.5 0.7 E	0.4 0.4 0.2 E	0.800000 0.000000 0.200000 E
0.2 0.2 0.8 E	0.4 0.4 0.6 E	0.800000 0.200000 0.000000 E
0.2 0.2 1.0 E	0.6 0.0 0.0 E	0.800000 0.200000 0.600000 E
0.4 0.6 0.6 E	0.6 0.0 0.4 E	0.800000 0.200000 0.800000 E
0.4 0.8 1.0 E	0.6 0.2 0.0 E	0.800000 0.400000 0.800000 E
0.4 1.0 0.2 E	0.6 0.4 0.4 E	0.800000 0.600000 0.200000 E
0.6 1.0 0.6 E	0.6 0.6 0.2 E	0.800000 0.800000 0.400000 E
0.6 1.0 1.0 E	0.6 0.6 0.4 E	0.133333 0.066667 0.300000 E
0.8 0.6 0.4 E	0.6 0.8 0.0 E	0.133333 0.466667 0.300000 E
0.1 0.5 0.1 E	0.6 0.8 0.4 E	0.133333 0.466667 0.700000 E
0.1 0.7 0.3 E	0.6 0.8 0.6 E	0.133333 0.466667 0.900000 E

(continued)

Table 10.3 (continued)

250-atom FCC	250-atom BCC	250-atom HCP
0.3 0.3 0.1 E	0.8 0.2 0.4 E	0.133333 0.666667 0.300000 E
0.3 0.7 0.3 E	0.8 0.2 0.8 E	0.133333 0.666667 0.700000 E
0.7 0.9 0.7 E	0.8 0.6 0.0 E	0.133333 0.666667 0.900000 E
0.9 0.3 0.9 E	0.8 0.6 0.2 E	0.333333 0.066667 0.100000 E
0.8 0.6 0.6 E	0.8 0.6 0.8 E	0.333333 0.066667 0.500000 E
0.3 0.1 0.1 E	0.1 0.1 0.7 E	0.333333 0.466667 0.100000 E
0.5 0.5 0.5 E	0.1 0.3 0.5 E	0.333333 0.466667 0.500000 E
0.7 0.3 0.7 E	0.1 0.7 0.3 E	0.333333 0.666667 0.300000 E
0.9 0.3 0.1 E	0.1 0.7 0.9 E	0.333333 0.666667 0.500000 E
0.2 0.2 0.2 E	0.1 0.9 0.5 E	0.333333 0.866667 0.300000 E
1.0 0.6 0.4 E	0.1 0.9 0.7 E	0.533333 0.266667 0.700000 E
0.1 0.5 0.7 E	0.3 0.5 0.5 E	0.533333 0.466667 0.300000 E
0.3 0.3 0.7 E	0.5 0.1 0.1 E	0.733333 0.066667 0.100000 E
0.5 0.1 0.9 E	0.5 0.5 0.3 E	0.733333 0.266667 0.100000 E
0.5 0.9 0.7 E	0.5 0.5 0.5 E	0.733333 0.466667 0.100000 E
0.7 0.1 0.5 E	0.5 0.5 0.9 E	0.733333 0.666667 0.900000 E
0.9 0.9 0.3 E	0.5 0.9 0.9 E	0.733333 0.866667 0.500000 E
0.9 0.9 0.7 E	0.7 0.1 0.1 E	0.933333 0.066667 0.500000 E
0.4 0.4 0.6 E	0.7 0.1 0.5 E	0.933333 0.266667 0.700000 E
0.4 0.6 0.8 E	0.7 0.3 0.5 E	0.933333 0.266667 0.900000 E
0.6 0.4 0.6 E	0.7 0.3 0.7 E	0.933333 0.466667 0.300000 E
0.6 0.8 0.8 E	0.7 0.5 0.7 E	0.933333 0.466667 0.700000 E
0.8 0.8 0.4 E	0.9 0.7 0.3 E	0.933333 0.666667 0.300000 E
1.0 0.2 1.0 E	0.9 0.7 0.9 E	0.933333 0.866667 0.100000 E

Lattice vectors and atomic positions (in fractional coordinates) are given for the unrelaxed lattices

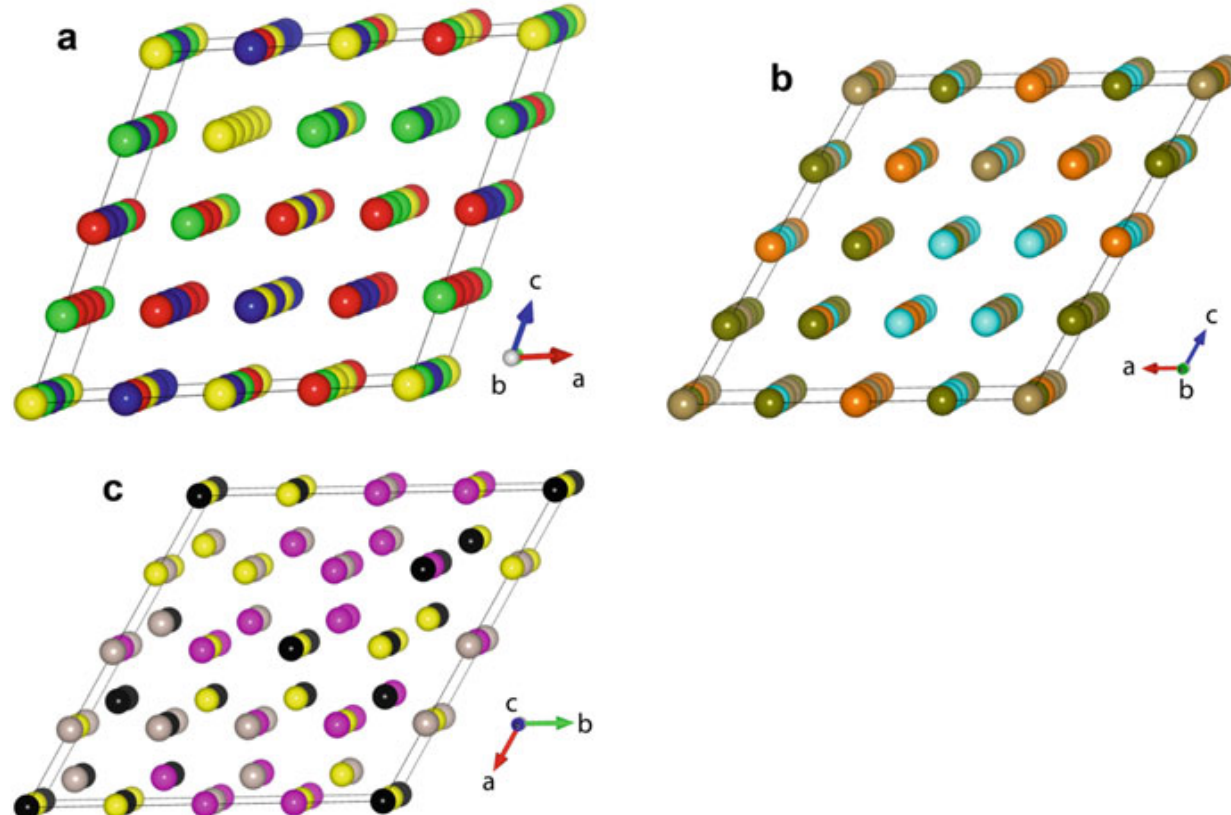


Fig. 10.1 The input unrelaxed atomic structures of 64-atom quaternary SQS [18] for (a) FCC, (b) BCC, and (c) HCP lattices in equal molar compositions. One color represents one element

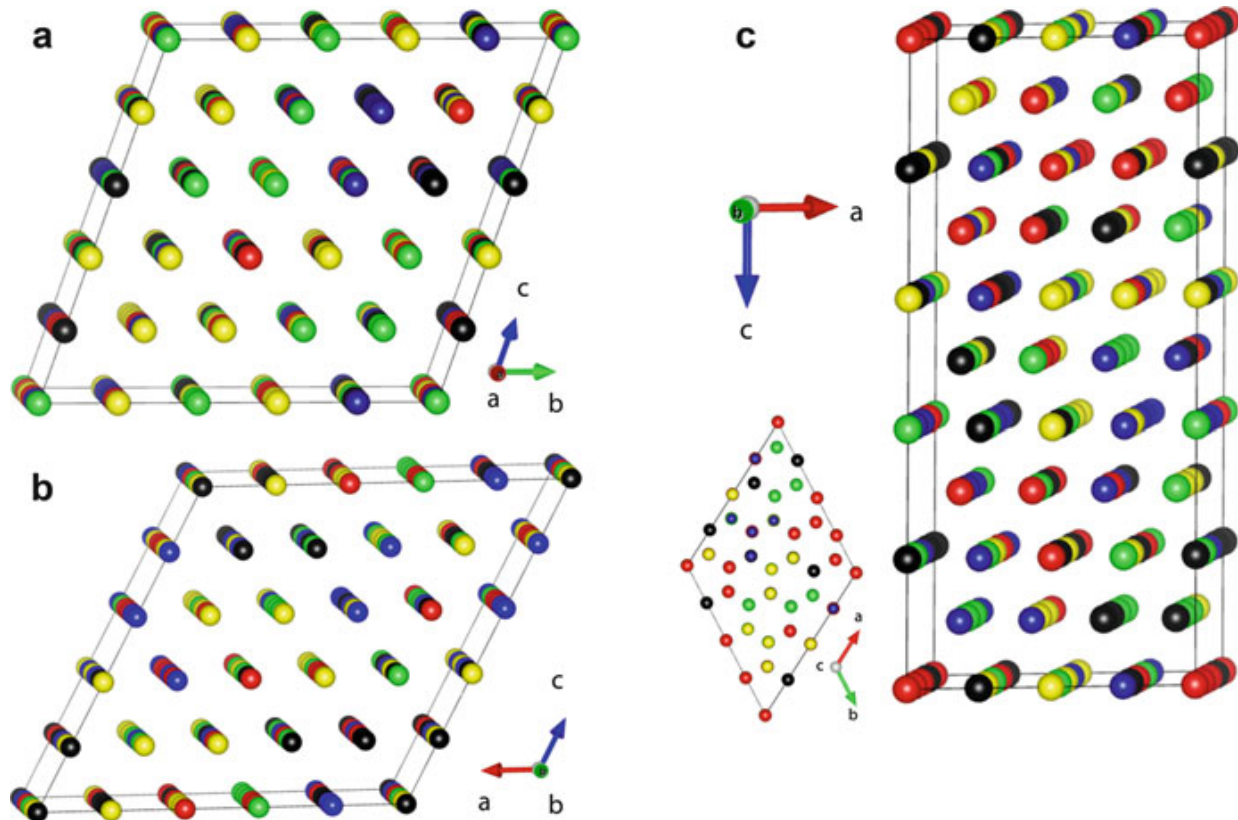


Fig. 10.2 The unrelaxed atomic structures of quinary SQS [18] for (a) 125-atom FCC, (b) 125-atom BCC, and (c) 160-atom HCP lattices in equal molar compositions

10.4 Applications of SQS

Building up the appropriate atomic structure for HEAs is the first step toward reliable predicting of materials properties of HEAs based on DFT methods, including thermodynamic, kinetic, electronic, vibrational, and magnetic properties. Considering the infancy of present HEA research, reports on SQS and its applications to HEAs in the literature have been very limited [5, 18]. This section presents the applications of those SQS presented in the prior section to several model single-phase HEAs, including their phase stability at zero temperature, phonon vibrational properties, electronic entropy and free energies, and mechanical properties.

All the calculations were performed using VASP (Vienna ab initio simulation package) [19, 20], a plane-wave pseudo-potential software. Projector-augmented wave (PAW) potentials [21] were used as supplied with VASP and the Perdew-Burke-Ernzerhof [22] gradient approximation for the exchange-correlation functional. All structures (both lattice parameters and atomic coordinates) were fully relaxed under zero pressure until the energy convergence reached 1 meV/atom. Collinear magnetism was considered for compositions that contain magnetic elements such as Co, Cr, Fe, Mn, and Ni, and three typical magnetisms (ferromagnetism, antiferromagnetic, and ferrimagnetic) as well as nonmagnetic state are all tested in order to identify the lowest energy state for each composition. Note that only a limited number of magnetic configurations for antiferromagnetism and ferrimagnetism per composition were examined due to computational facility limitations.

10.4.1 Phase Stability at T = 0 K

To date there have been no experimental reports on the enthalpies of formation (ΔH_f) of HEAs in the literature, and thus providing such data is crucial to the materials science community, for example, in establishing the HEA formation rules as detailed in Chap. 2. Previous studies on the HEA formation rules (e.g., [23]) have used the enthalpy of mixing in liquid using the semiempirical Miedema model [24].

ΔH_f is calculated by subtracting the composition-weighted total energies of the constituent elements from the total energy of the compound after full relaxation of the structure at zero temperature. In the example of a quaternary compound with an arbitrary formula of $A_mB_nC_oD_p$ (here m , n , o , and p represent the molar ratio of each element), ΔH_f was determined by

$$\Delta H_{f(A_mB_nC_oD_p)} = E_{A_mB_nC_oD_p} - \frac{1}{m+n+o+p} (mE_A + nE_B + oE_C + pE_D) \quad (10.1)$$

where $E_{A_mB_nC_oD_p}$, E_A , E_B , E_C , and E_D are the total energy of compound $A_mB_nC_oD_p$, element A, B, C, and D, respectively. These energies are direct output from VASP calculations without manipulation. A similar equation was used to calculate ΔH_f for quinary alloys. The calculated enthalpy of formation and lattice parameters of most reported single-phase equimolar HEAs are listed in Table 10.4. For simplicity, the zero-point energy is neglected in the present study, which might be important in other cases.

The agreement in lattice parameter between calculations and experiments where available is excellent. For CoCrFeNi and CoCrFeMnNi, the energies in both FCC and HCP structures are provided since they are important for stacking fault energy calculations. For other alloys, only the energy of the experimentally observed stable structure is calculated. Comparison in the energy between the FCC and HCP structures also provides a benchmark test on the accuracy of the SQS generated. At zero temperature, the ground state structure is HCP, BCC, BCC, and FCC for element Co, Cr, Fe, and Ni, respectively. For CoCrFeNi and CoCrFeMnNi, the FCC phase is the stable structure observed above room temperature. The present study demonstrated that the formation enthalpies are sensitive to the SQS cell size and that the energy difference between the FCC and HCP structures is very small (Table 10.4 and Fig. 10.3). For small cells (16-, 20-, and 24-atom SQS), the calculations incorrectly predict that the HCP phase is stable. For large cells (64 and more atoms), the calculations predict that the FCC phase is stable, in agreement with experimental observation. However, it is worth noting that the energy is expected to fluctuate with respect to both the atomic position of SQS and the magnetism setting. The degree of their fluctuations depends on the alloy composition, as addressed in Sect. 10.5 of this chapter. For those SQS of large cell sizes (≥ 64 atoms), exhaustive examination of all possible magnetic configuration in each SQS shown in Fig. 10.3 represents a formidable task, and thus only several representative magnetic states were examined and the lowest energy was used.

Table 10.4 Calculated enthalpy of formation [ΔH_f , kJ/mol] and lattice parameters [Å] using SQS

Alloy	No. atoms	Phases	ΔH_f	Lat. para.
			FCC	a (FCC/BCC) $a, c, c/a$ (HCP)
CoCrFeNi	16	FCC	+7.562	3.546
		HCP	+6.308	2.507, 4.061, 1.62
	24	FCC	+7.103	3.543
		HCP	+6.501	2.515, 4.036, 1.61
	64	FCC	+6.897	3.548; 3.575 [5]
		HCP	+7.145	2.506, 4.056, 1.62
CoCrFeMnNi	20	FCC	+8.434	3.536
		HCP	+7.855	2.500, 4.043, 1.62
	125	FCC	+7.065	3.559; 3.597 [5]
	160	HCP	+7.323	2.503, 4.014, 1.6
	250	FCC	+7.581	3.529
		HCP	+7.703	2.5, 4.027, 1.61
CoCrMnNi	64	FCC	+7.593	3.544
CoFeMnNi	64		+3.903	3.512
MoNbTaW	64	BCC	-7.313	3.237; 3.2134 [25]
MoNbTaVW	125		-4.272	3.188; 3.1832 [25]
	250		-3.852	3.200
HfNbTaTiZr	125		+8.353	3.403; 3.404 [26]
	250		+7.946	3.411
CoOsReRu	64	HCP	+3.846	2.7, 4.282, 1.59
ErGdHoTbY	160		+0.130	3.625, 5.641, 1.56
	250		+0.090	3.624, 5.641, 1.56
DyGdLuTbY	160		-0.003	3.618, 5.631, 1.56; 3.64, 5.73, 1.57 [27]
DyGdLuTbTm	160		-0.079	3.601, 5.602, 1.56; 3.59, 5.65, 1.57 [27]

The experimental lattice parameters where available are also included. The second column denotes the number of atoms in the SQS cell

The data for 16-, 20- and 24-atom cells were taken from [5] and the rest from [18]

The cell size dependence of the total energy of SQS can be understood from the underlying atomic structure. It is expected that a larger SQS cell represents better the disordered structure of HEAs. The pair distribution function (PDF) of relaxed FCC CoCrFeNi in 16-, 20-, and 64-atom SQS is illustrated in Fig. 10.4. For clarity, only the first nearest-neighbor PDF is shown. It is apparent that with increasing SQS cell size, both the pair distance and the intensity evolve toward equality. Note the 108-atom structure using the hybrid Monte Carlo/molecular dynamics (MC/MD) simulations exhibits clear preference in the Co-Ni and Cr-Ni pairs over Fe-Fe pair, in contrast to the three SQS models. In all cases, the Cr-Cr pair has the lowest probability (Fig. 10.4) than other pairs for FCC CoCrFeNi, suggesting that Cr prefers to bond with other elements.

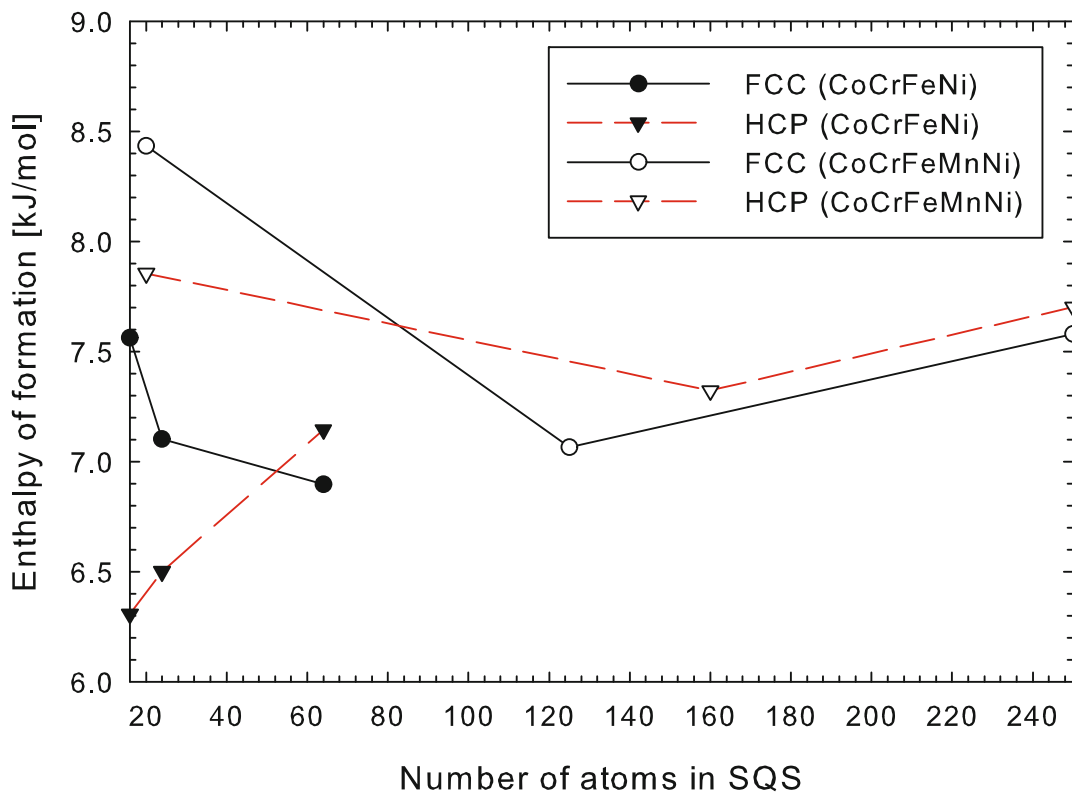


Fig. 10.3 Effect of SQS cell size on the lattice stability of CoCrFeNi and CoCrFeMnNi at zero temperature [18]. The calculations were done on a randomly chosen configuration of the lattice type

The PDFs for FCC CoCrFeMnNi in 20-, 125- and 250-atom SQS are shown in Fig. 10.5. The Cr-Cr pair distribution improves substantially than the case of CoCrFeNi, but the Cr-Mn pair distribution is far from ideal in the 20-atom cell and becomes much better in the 125- and especially 250-atom cells. Note that the Cr-Cr pair has the lowest probability in the 250-atom cell. The cell size sensitivity of the structure may contribute partially to the calculated energy fluctuation shown in Fig. 10.3 and Table 10.4.

10.4.2 Vibrational and Electronic Entropies

Besides the configurational entropy in HEAs, other entropy sources need to be quantified, including vibrational entropy, magnetic entropy, and electronic entropy [28], depending on the composition and structure of the materials. Although the Boltzmann equation of entropy ($S^{\text{conf}} = k_B \ln \Omega$, where k_B is the Boltzmann constant and Ω is the number of configurations) has been widely used to calculate the configurational entropy, Ω can strongly depend on temperature. For a solid solution, as the temperature decreases, atomic ordering or separation intensifies, which reduces the configurational entropy. At zero temperature, all entropy sources vanish. Such examples are shown in refractory HEAs by Widom et al. [29] using MC/MD simulations, as detailed in Chap. 8. In this subsection, the vibrational

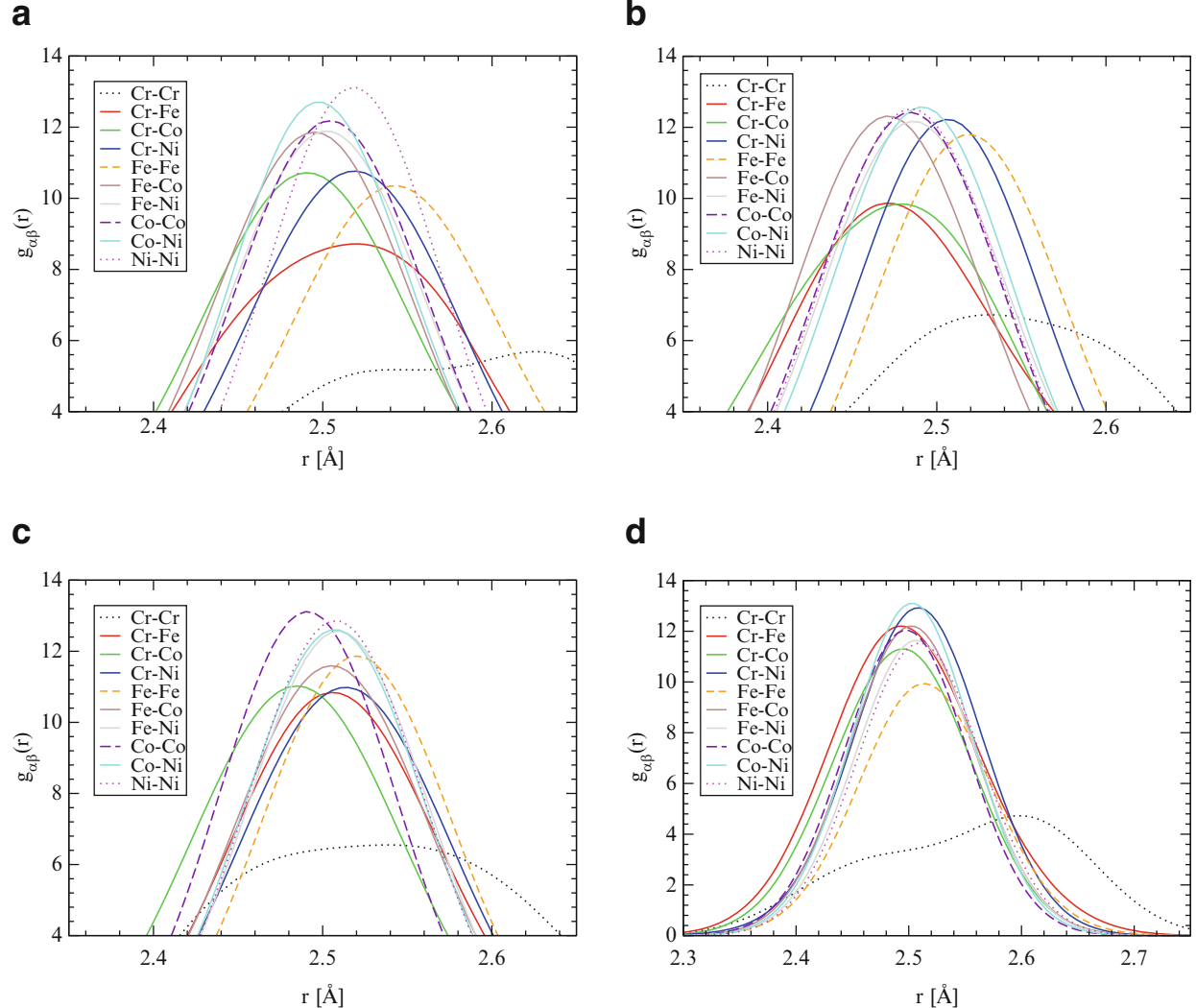


Fig. 10.4 Comparison in the first nearest-neighbor pair distribution function of FCC CoCrFeNi in (a) 16-, (b) 20-, and (c) 64-atom SQS models and (d) 108-atom MC/MD model after full relaxation at zero temperature

entropies of three single-phase HEAs are presented, namely, FCC CoCrFeNi, BCC MoNbTaW, and HCP CoOsReRu using the SQS presented in this chapter. CoOsReRu was predicted by Gao and Alman based on phase diagrams [30].

Phonon frequencies of the SQS were calculated in the harmonic approximation by diagonalizing the dynamical matrix based on the interatomic force constants reported by VASP. The vibrational free energy (f_{vib}) was then calculated by integrating the vibrational density of states $g(\omega)$ using the following equation:

$$f_{\text{vib}}(T) = k_B T \int g(\omega) \ln \left[2 \sinh \left(\frac{\hbar \omega}{2k_B T} \right) \right] d\omega \quad (10.2)$$

where k_B is the Boltzmann constant, \hbar is the reduced Planck constant, and T is the absolute temperature. The vibrational entropy (S_{ph}) is calculated by

$$S_{\text{ph}}(V, T) = 3k_B \int_0^\infty n_{\text{ph}} [(f_{\text{BE}} + 1) \ln(f_{\text{BE}} + 1) - f_{\text{BE}} \ln f_{\text{BE}}] d\varepsilon \quad (10.3)$$

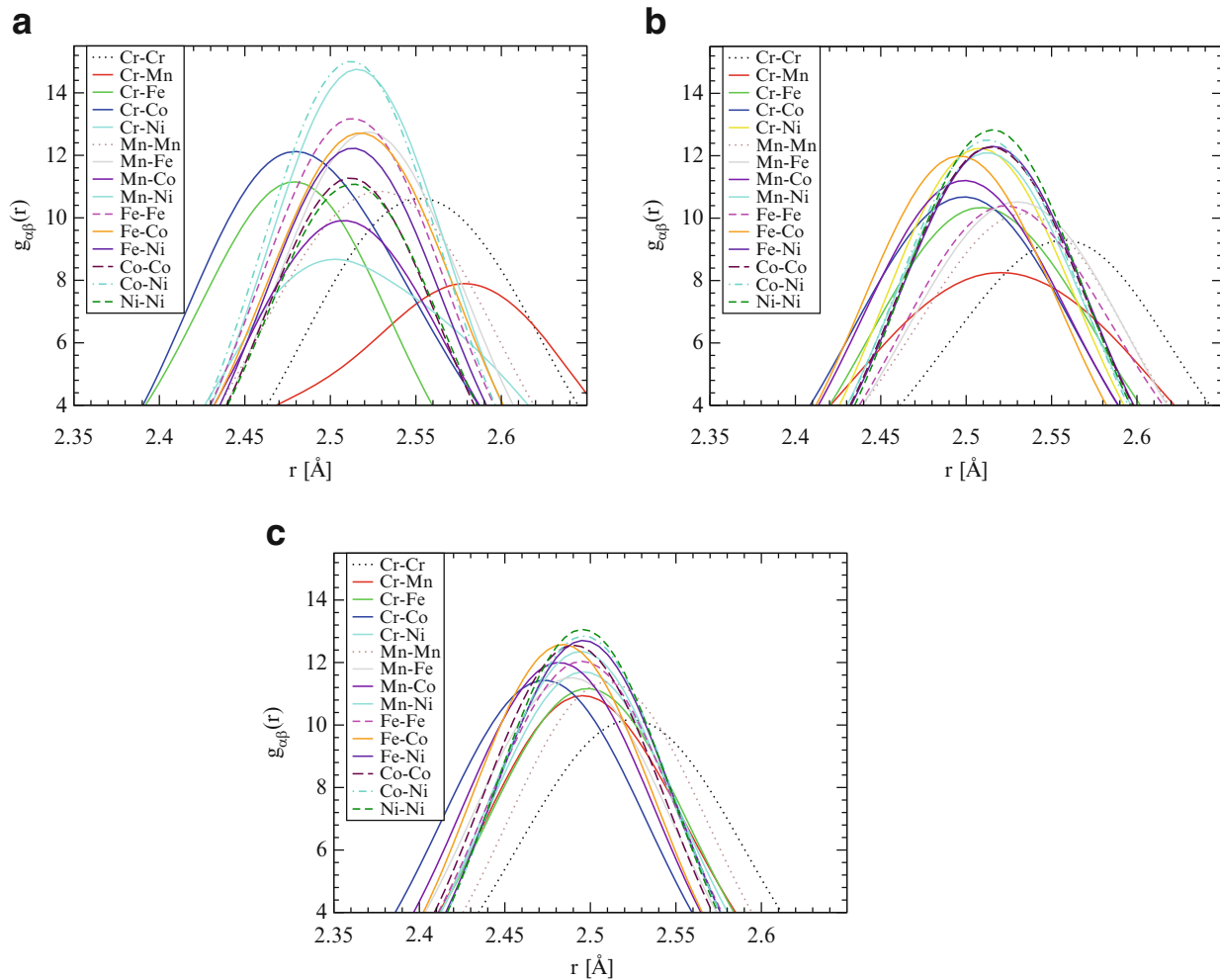


Fig. 10.5 Comparison in the first nearest-neighbor pair distribution function of FCC CoCrFeMnNi in (a) 20-, (b) 125-, and (c) 250-atom SQS models after full relaxation at zero temperature

where n_{ph} is the phonon density of states, and f_{BE} is the Bose-Einstein distribution function. At high temperatures, the electronic entropy due to electron excitation across the Fermi level needs to be considered, and the equations to determine the electronic entropy and free energy are described in Eqs. 8.17 and 8.18.

Figure 10.6 compares the calculated phonon density of states (DOS) and heat capacity at constant volume (C_v). At low energies (less than 10 meV), the phonon DOS is comparable for FCC CoCrFeNi and BCC MoNbTaW; both are larger than HCP CoOsReRu. In contrast, the heat capacity C_v appears to be very similar for all three alloys although it is slightly larger for CoOsReRu and MoNbTaW than CoCrFeNi at $T \leq 400$ K.

The calculated vibrational entropy, electronic entropy, and their corresponding Helmholtz free energy are shown in Fig. 10.7. The vibrational entropy is similar for BCC MoNbTaW and HCP CoOsReRu, while it is smaller for FCC CoCrFeNi. It is zero at zero temperature and increases rapidly with increasing temperature. At room temperature, it is already more than twice the ideal configurational entropy that is shown by the dashed line in Fig. 10.7a. In contrast, the electronic entropy is small for all three compositions even at high temperatures (Fig. 10.7b).

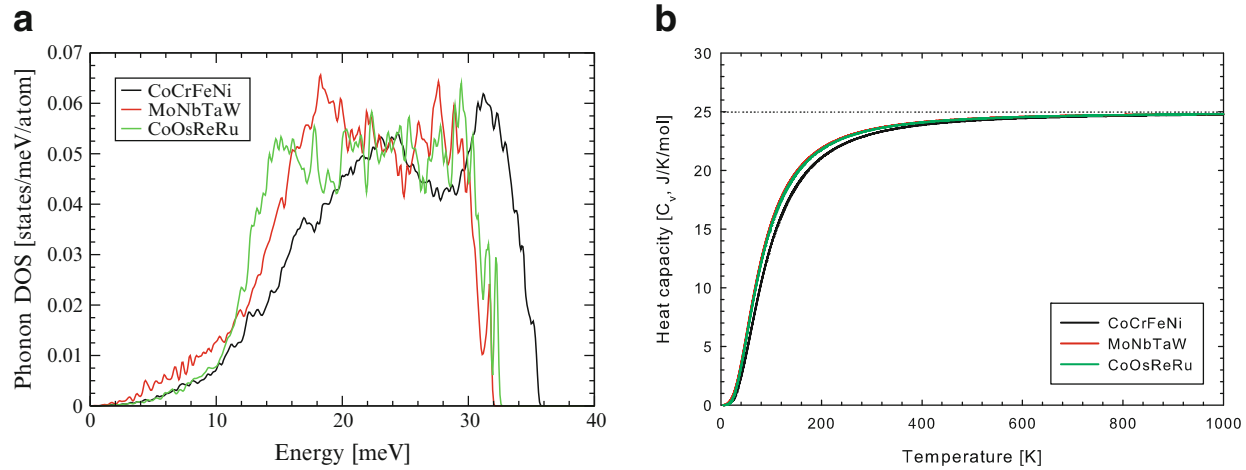


Fig. 10.6 Calculated vibrational DOS and constant-volume heat capacity of FCC CoCrFeNi, BCC MoNbTaW, and HCP CoOsReRu using 64-atom SQS

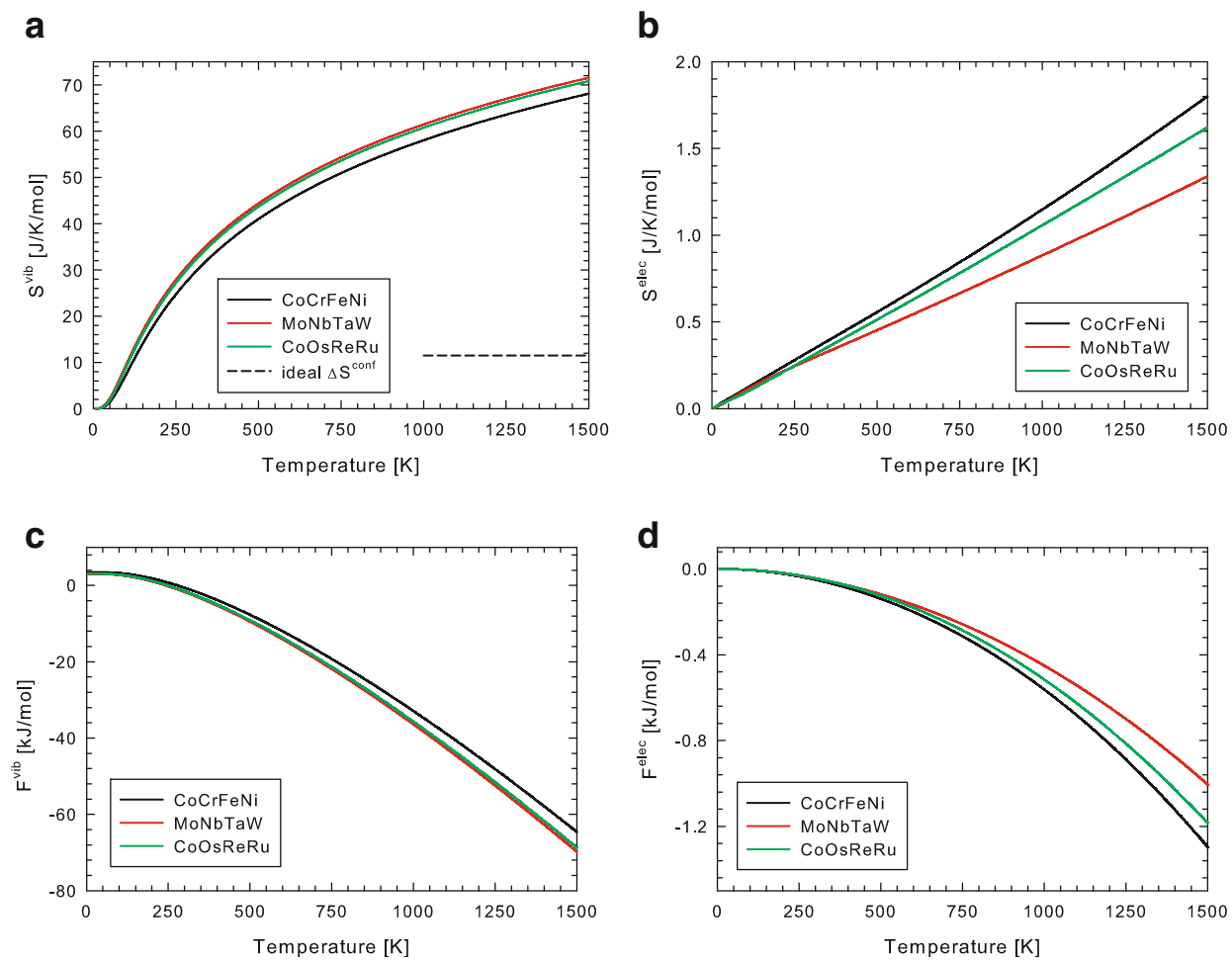


Fig. 10.7 Calculated (a) vibrational entropy, (b) electronic entropy, (c) vibrational Helmholtz free energy, and (d) electronic Helmholtz free energy of FCC CoCrFeNi, BCC MoNbTaW, and HCP CoOsReRu using 64-atom SQS

Accordingly, it is expected that, at finite temperatures, vibrational free energy dominates compared to configurational free energy and electronic free energy (Fig. 10.7c, d).

To determine the mixing behavior of the alloy, the property of the constituent elements need to be subtracted. The vibrational entropy of mixing ($\Delta S_{\text{mix}}^{\text{vib}}$) and vibrational Helmholtz free energy of mixing ($\Delta F_{\text{mix}}^{\text{vib}}$) of an HEA are calculated by

$$\Delta S_{\text{mix}}^{\text{vib}} = S_{\text{HEA}}^{\text{vib}} - \sum_{i=1}^N x_i S_i^{\text{vib}} \quad (10.4)$$

$$\Delta F_{\text{mix}}^{\text{vib}} = F_{\text{HEA}}^{\text{vib}} - \sum_{i=1}^N x_i F_i^{\text{vib}} \quad (10.5)$$

where $S_{\text{HEA}}^{\text{vib}}$ ($F_{\text{HEA}}^{\text{vib}}$) is the vibrational entropy (Helmholtz free energy) of the HEA, S_i^{vib} (F_i^{vib}) is the vibrational entropy (Helmholtz free energy) of the i th element, x_i is the molar composition of the i th element, and N is the total number of elements in the HEA. The electronic entropy of mixing ($\Delta S_{\text{mix}}^{\text{elec}}$) and electronic free energy of mixing ($\Delta F_{\text{mix}}^{\text{elec}}$) of an HEA are calculated in a similar fashion:

$$\Delta S_{\text{mix}}^{\text{elec}} = S_{\text{HEA}}^{\text{elec}} - \sum_{i=1}^N x_i S_i^{\text{elec}} \quad (10.6)$$

$$\Delta F_{\text{mix}}^{\text{elec}} = F_{\text{HEA}}^{\text{elec}} - \sum_{i=1}^N x_i F_i^{\text{elec}} \quad (10.7)$$

where $S_{\text{HEA}}^{\text{elec}}$ ($F_{\text{HEA}}^{\text{elec}}$) is the electronic entropy (free energy) of the HEA, and S_i^{elec} (F_i^{elec}) is the electronic entropy (free energy) of the i th element.

The corresponding vibrational entropy (free energy) of mixing and electronic entropy (free energy) of mixing for CoCrFeNi, MoNbTaW, and CoOsReRu are shown in Fig. 10.8 using Eqs. 10.4, 10.5, 10.6, and 10.7. The calculations predict that, at $T \geq \sim 400$ K, the vibrational entropies of mixing for all three alloys approach a constant value, namely, +2.8, -3.6, and -0.4 J/K/mol for FCC CoCrFeNi, BCC MoNbTaW, and HCP CoOsReRu, respectively. In other words, lattice phonon vibration increases the total entropy in FCC CoCrFeNi in contrast to BCC MoNbTaW. The magnitude of the vibrational free energy of mixing is small at low temperatures but scales up rapidly with increasing temperature for CoCrFeNi and MoNbTaW. Both $\Delta S_{\text{mix}}^{\text{vib}}$ and $\Delta F_{\text{mix}}^{\text{vib}}$ are negligible for CoOsReRu. On the other hand, the electronic entropy of mixing is all truly negligible for all three alloys.

The total entropy and entropy of mixing for selected single-phase HEAs are also examined using the CALPHAD (acronym of calculation of phase diagrams) approach, as presented in Chap. 12. The CALPHAD calculations predict that the

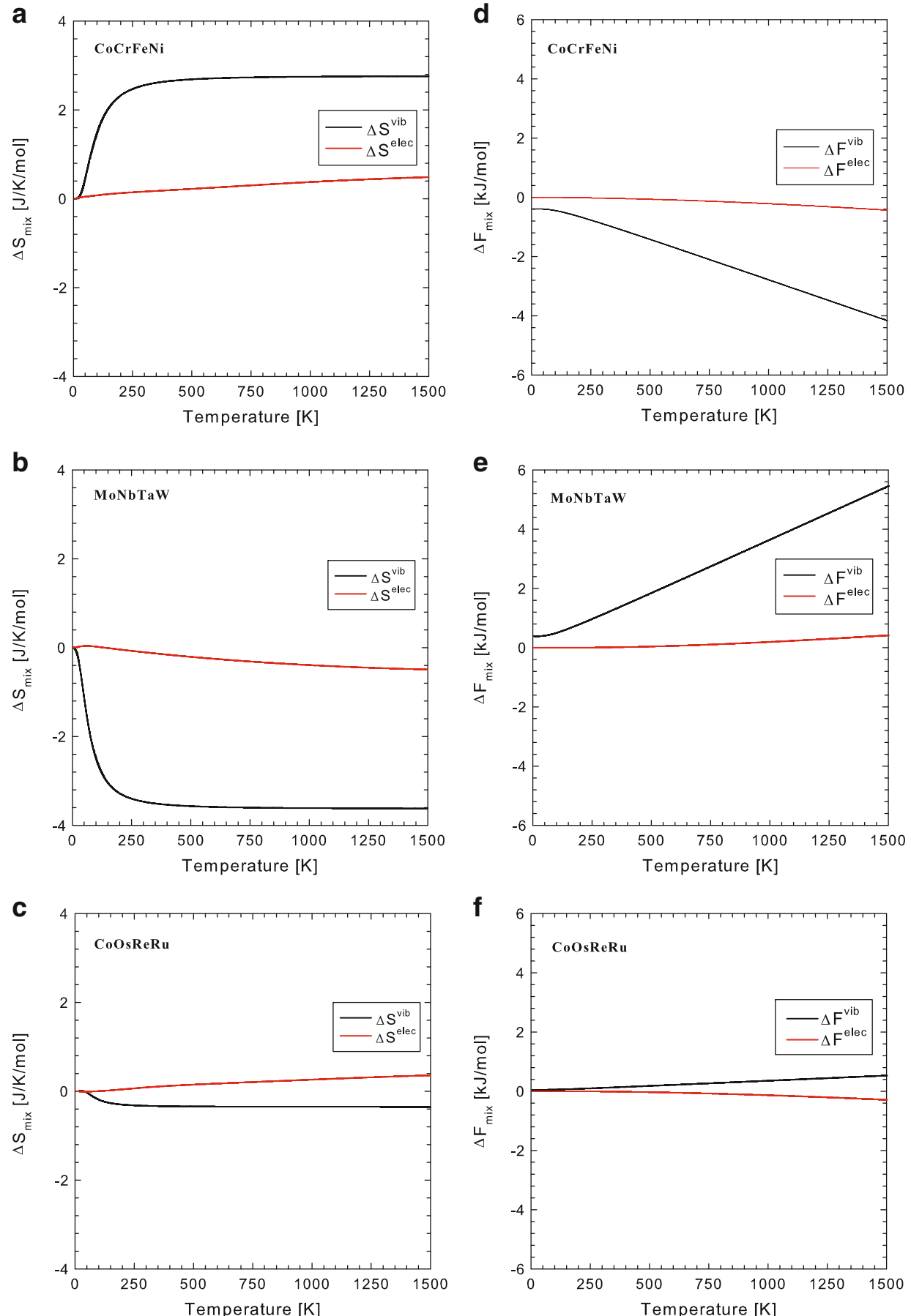


Fig. 10.8 Calculated (a–c) vibrational and electronic entropies of mixing and (d–f) vibrational and electronic Helmholtz free energies of mixing for FCC CoCrFeNi, BCC MoNbTaW, and HCP CoOsReRu using 64-atom SQS

excess entropy, which is the total entropy subtracted by the ideal configurational entropy, is +2.5 J/K/mol for FCC CoCrFeNi and +1.3 J/K/mol for CoCrFeNiMn at 1000 °C. The present DFT calculations suggest that the positive vibrational entropy of mixing (+2.8 J/K/mol) in CoCrFeNi mainly accounts for the positive excess entropy.

To account for anharmonic phonon effect at high temperatures, quasi-harmonic approximation can be a reasonable choice to start with in order to improve the accuracy of lattice phonon vibration and more importantly to predict the coefficient of thermal expansion. It is assumed that the magnetic entropy due to magnetic spin fluctuation in reported FCC HEAs (such as CoCrFeNi and CoCrFeMnNi) is small because the magnetic ordering temperature is well below room temperature [31, 32].

10.4.3 Mechanical Properties

The elastic properties of any crystal can be calculated using the basic elastic stress-strain relationship:

$$\sigma_i = \sum_{j=1}^6 C_{ij} \varepsilon_j \quad (10.8)$$

where σ_i , ε_j , and C_{ij} are the elastic stress, strain, and tensor in the Voigt notation, respectively. C_{ij} can be derived from this relation by performing six finite distortions of the lattice as implemented in VASP [3, 33]. Although the atoms are on an FCC (or BCC, HCP) lattice, the chemical distribution in small SQS cells may lead to an anisotropic environment and, thus, more scattering in the predicted elastic constants. For larger SQS cells, the chemical distribution will be better represented and should approach the real material. Therefore, in using a smaller SQS, one route to overcome this issue is to use an averaging scheme [3] to obtain single-crystal C_{11} , C_{12} , and C_{44} for cubic structures:

$$\begin{aligned} C_{11} &= \frac{C_{11} + C_{22} + C_{33}}{3} |_{\text{SQS}} \\ C_{12} &= \frac{C_{12} + C_{23} + C_{13}}{3} |_{\text{SQS}} \\ C_{44} &= \frac{C_{44} + C_{55} + C_{66}}{3} |_{\text{SQS}} \end{aligned} \quad (10.9)$$

Alternatively, the total energy approach [5, 34–36] can be used by performing pressure-volume equation of states (EOS) and applying a volume-conserving orthorhombic and monoclinic deformation to solve for C_{11} , C_{12} , and C_{44} obtained for a single cell without averaging. The bulk modulus here was obtained by fitting the energy-volume data to the Birch-Murnaghan equation of state, designated as

B_{EOS} , to differentiate it from the bulk modulus (B) calculated from stress-strain relation $B = (C_{11} + 2C_{12})/3$, although the bulk modulus obtained from both methods should be equal within computing errors. The original manuscript [5] used the Murnaghan equation of state. Tetragonal shear modulus ($C' = (C_{11} - C_{12})/2$) can be obtained by fitting the energies to $E = E_0 + 2VC'\delta^2$ by applying volume-conserving orthorhombic strain to the base lattice [5, 34–36]:

$$I + \varepsilon_o = \begin{pmatrix} 1 + \delta & 0 & 0 \\ 0 & 1 - \delta & 0 \\ 0 & 0 & \frac{1}{(1 - \delta^2)} \end{pmatrix} \quad (10.10)$$

where δ is strain, I is the identity matrix, and ε_o is the strain tensor.

The elastic constant C_{44} can be obtained by fitting the energies to $E = E_0 + 2V C_{44} \delta^2$ equation by applying the monoclinic strain (δ) to the base lattice [5, 34–36]:

$$I + \varepsilon_m = \begin{pmatrix} 1 & 0 & 0 \\ \delta & 1 & 0 \\ 0 & 0 & \frac{1}{(1 - \delta^2)} \end{pmatrix} \quad (10.11)$$

Polycrystalline elastic properties can be derived using the elastic constants and the Voigt-Reuss (V-R) averaging method – the polycrystalline bulk modulus of an isotropic crystal is the same as its single crystalline bulk modulus, while the shear modulus (G) can be estimated as an average of the upper (G_V) and lower (G_R) bounds given by [3, 35, 36]

$$\begin{aligned} G_V &= \frac{(C_{11} - C_{12} + 3C_{44})}{5} \\ G_R &= \frac{5(C_{11} - C_{12})C_{44}}{4C_{44} + 3(C_{11} - C_{12})} \end{aligned} \quad (10.12)$$

Poisson's ratio (ν) and Young's modulus (E) can be derived from the bulk modulus (B) and the shear modulus (G):

$$\nu = \frac{3B - 2G}{2(3B + G)}; \quad E = \frac{9BG}{3B + G} \quad (10.13)$$

The calculated elastic properties for CoCrFeNi and CoCrFeMnNi using smaller cell SQS are listed in Table 10.5. The disagreement in C_{ij} and polycrystalline properties (B , G , E , and ν) for both alloys is obvious among three methods, EMTO-CPA, stress-strain relation, and total energy approach. Note that the total energy approach using the Birch-Murnaghan approach leads to a more physical Poisson's

Table 10.5 Calculated lattice parameter [a , Å] elastic properties of CoCrFeNi and CoCrFeMnNi: Poisson's ratio [ν], Young's modulus [E , GPa], bulk modulus [B , GPa], and elastic constants [C_{ij} , GPa] from EMTO-CPA and VASP-SQS

	Structure	a	ν	G	E	B_{EOS}	B	C_{11}	C_{12}	C_{44}	Method
CoCrFeNi	SQS-16	3.552	0.248	88.3	220.2		145.4	210.7	113.2	131.9	Stress [18]
	SQS-24	3.543	0.311	74.4	195		171.6	227.1	143.8	109.6	Energy [5]
	SQS-24	3.551	0.275	85.6	218.2		161.5	224.1	131.8	130.5	Stress [18]
	EMTO-CPA	3.582	0.319	85.2	225		208.6	259.2	183.3	146.3	[5]
CoCrFeMnNi	SQS-20	3.536	0.250	96.4	241.1	160.2		229.3	125.6	146.0	Energy
	SQS-20	3.545	0.261	95.6	241.1	167.5	168.1	243.0	134.2	141.1	Stress [18]
	EMTO-CPA	3.600	0.313	78.8	207		184.5	229.7	161.9	138.2	[5]

The bulk modulus B_{EOS} obtained from the pressure-volume equation of state (EOS) is also listed

ratio for the quinary CoCrFeMnNi HEA than that published [5] using the Murnaghan approach. This is not surprising as the Murnaghan equation of state is more sensitive to strain ranges used in energy vs. volume fits. Note that different treatments of magnetic properties between EMTO-CPA and VASP-SQS may partially account for the observed discrepancy. The EMTO-CPA calculations are done with disordered local moment (DLM) approximation for the paramagnetic state in an attempt to represent the real alloy. Further ferromagnetic calculation using EMTO-CPA predicts lower total energy at 0 K and elastic constants in closer agreement to the VASP calculations despite that the CPA method lacks atomic relaxation. Besides, the difference in the setup of the calculations between those three methods among research groups may attribute to difference in energy and elastic properties.

The Poisson's ratio predicted using the stress-strain approach on 24-atom CoCrFeNi and 20-atom CoCrFeMnNi is 0.275 and 0.261, respectively. These values seem to be contradictory to the experimentally observed extraordinary ductility in CoCrFeMnNi [37]. However, alloy ductility is an extremely complicated issue since it is sensitive to both intrinsic (alloy chemistry) and extrinsic (processing, temperature, impurities, microstructure, etc.) factors. Intuitively one may not expect both alloys to be intrinsically ductile given such high concentration of brittle elements of Cr and Mn. On the other hand, experiments showed that extraordinarily high density of nano-twinning may be partially responsible for the unusually large ductility in CoCrFeMnNi [37] especially at low temperatures while other factors may deserve further investigation.

Generally speaking, a low stacking fault energy improves ductility of an alloy. The stacking fault energy in an FCC alloy is the energy expense required to remove a close-packed plane from the ABC stacking of the FCC lattice. Ideally the stacking fault energy of HEAs can be independently predicted by DFT calculations. Due to the compositional complexity in HEAs, direct calculation of stacking fault energy of HEAs is a daunting task. Instead, Zaddach et al. [5] managed to combine mechanical properties from DFT and stacking fault probability measurements to obtain the stacking fault energies of CoCrFeNi and CoCrFeMnNi HEAs. The stacking fault energy was calculated in this case as

$$\gamma = \frac{K_{111}\omega_0 G_{(111)} a_0 A^{-0.37}}{\pi\sqrt{3}} \cdot \frac{\varepsilon^2}{\alpha} \quad (10.14)$$

where $K_{111}\omega_0$ is assumed to be a constant (i.e., 6.6) for all FCC crystals, $G_{(111)}$ is the shear modulus in the (111) plane, a_0 is the lattice parameter, $A = 2C_{44}/(C_{11} - C_{12})$, ε^2 is the mean square microstrain, and α is the measured stacking fault probability. The experimentally measured values of ε^2/α for various FeNi, CrFeNi, CoCrFeNi, and CoCrFeMnNi alloys are reported [5]. Using the elastic constants from Table 10.5 (only those using the total energy approach), the stacking fault energies of equiatomic CoCrFeNi and CoCrFeMnNi are calculated (Table 10.6). Compared to EMTO-CPA, VASP-SQS produces very close results for the quaternary CoCrFeNi HEAs but larger for the quinary CoCrFeMnNi HEAs. From these

Table 10.6 Stacking fault energies (SFE) of FCC CoCrFeNi and CoCrFeMnNi [5]

Material	Input source	SFE (mJ/m^2)
CoCrFeNi	VASP (SQS-24, energy) [5]	27.8
	VASP (SQS-16, stress) [18]	32.7
	VASP (SQS-24, stress) [18]	31.3
	EMTO [5]	27.8
CoCrFeMnNi	VASP (SQS-20, energy) [5] ^a	26.4
	VASP (SQS-20, stress) [18]	27.2
	VASP (SQS-20, energy) ^b	26.4
	EMTO [5]	19.0

These SFEs are average values of the three points for CoCrFeNi and two points for CoCrFeMnNi

^aThe Murnaghan equation of states was used

^bThe Birch-Murnaghan equation of states was used

calculations, one may reach the conclusion that VASP calculations with small SQS (20–24 atoms) may lead to less accurate elastic properties of the random solid solution HEAs. Convergence of the calculated property will be very sensitive to the property of interest within the VASP + SQS method. As noted by von Pezold et al., high-quality elastic constants are obtained for a binary Al-Ti alloy from a small 32-atom SQS [11]. In this approach, the elastic constants were averaged over different permutations of the strain of the tensors presented in Eqs. 10.8 and 10.9 to better account for the chemical distributions in the bulk. This approach could also be done to improve the convergence of the small VASP-SQS cells presented here. Fluctuations in the measured stacking fault energy were observed with respect to the measurements, suggesting possible existence of chemical and/or structural inhomogeneity of the samples.

10.5 Comparison with Other Methods and Future Work

So far three methods to model the structure of HEAs have been introduced, MC/MD in Chap. 8, CPA in Chap. 9, and SQS in this chapter. They all capture the atomic structure of HEAs one way or the other and can be used to predict the basic structure information including the lattice parameters, thermodynamic properties including enthalpy of formation, the elastic properties such as elastic constants C_{ij} and bulk moduli, electronic structure properties such as the density of states (DOS), and the magnetic properties such as the atomic magnetic moment. Compared to MC/MD and CPA, one striking advantage of SQS is its capability to capture the random solid solution in a “physical” crystal lattice with ease.

The MC/MD simulations are computationally intense, and they require a user to have the skills in both molecular dynamics and Monte Carlo simulations. The interpretation of the results is also nontrivial. On the other hand, due to the single-site approximation used for CPA, it cannot include short-range order effects. Additionally, CPA has limitations for systems with large size mismatch, and, most

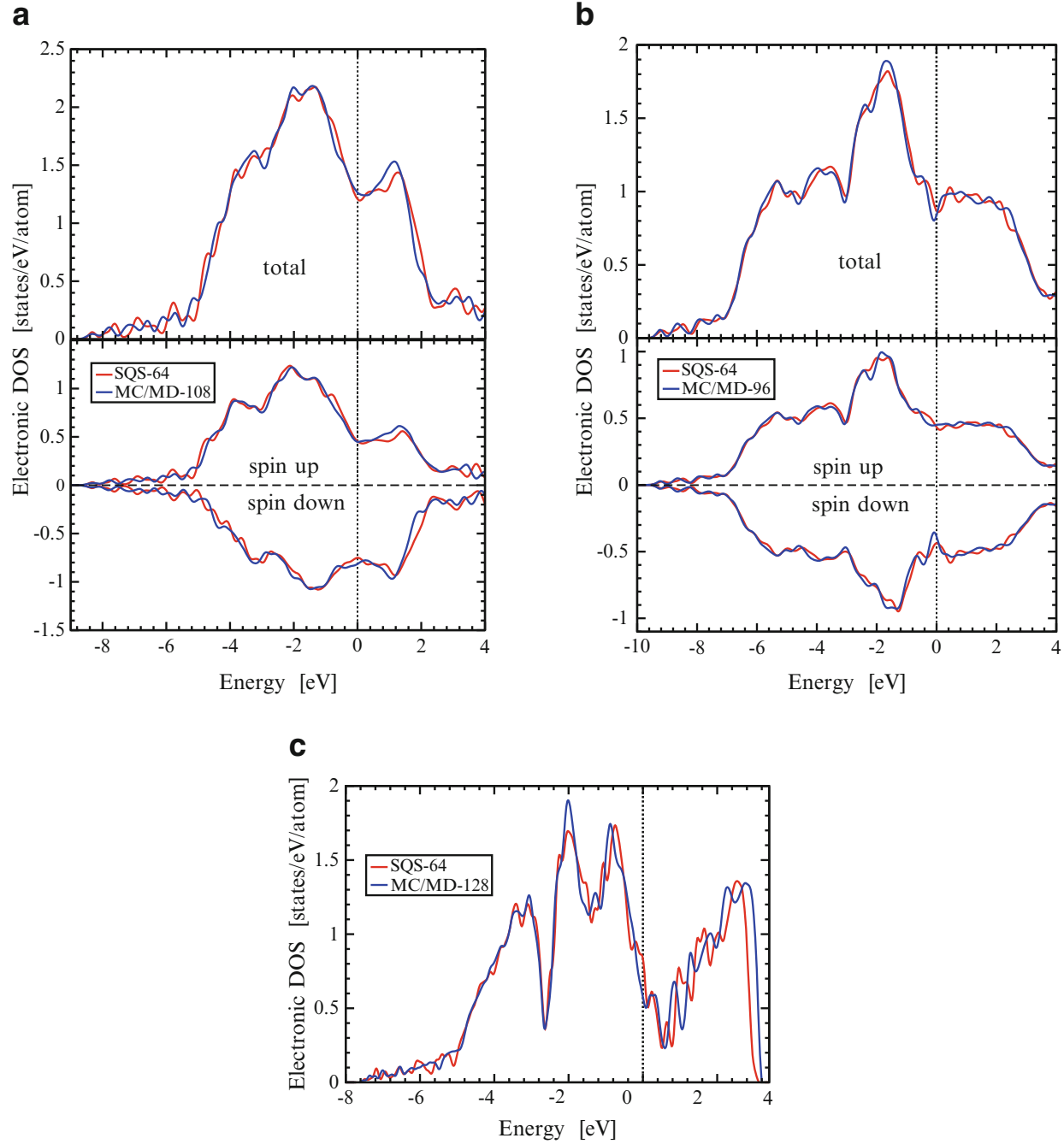


Fig. 10.9 Comparison [18] of the electronic DOS of (a) FCC CoCrFeNi, (b) HCP CoOsReRu, and (c) BCC MoNbTaW generated from SQS and MC/MD methods

importantly, neglects anisotropic lattice distortions. Moreover, lattice phonon calculations based on CPA approximation can be a formidable obstacle. SQS, being an atomic model, can overcome these shortcomings to large degrees. Local chemical environment, including short-range order effects, can be easily investigated with an SQS. In this subsection, we first compare the electronic structure and PDF of selected HEAs predicted from SQS and MC/MD and then discuss some drawbacks of SQS.

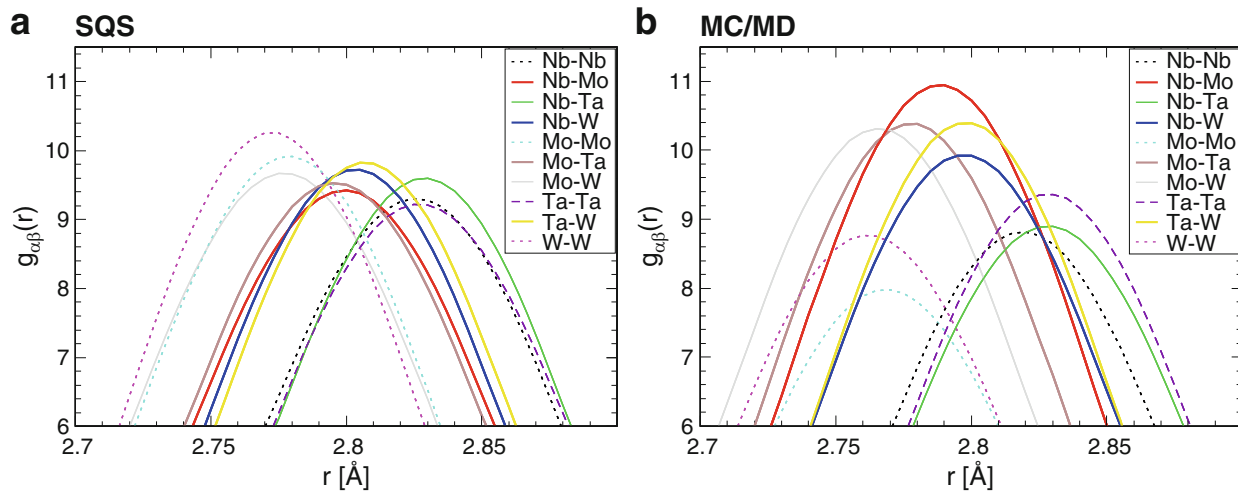


Fig. 10.10 Comparison of the BCC MoNbTaW structure generated from (a) 64-atom SQS and (b) 128-atom MC/MD [18]

10.5.1 Electronic Structure

The MC/MD structures for CoCrFeNi, CoOsReRu, and MoNbTaW were generated using a 108-, 96-, and 128-atom supercell after a total of 50, 40, and 10 ps MC/MD simulations at $T = 1473, 2173$, and 1673 K, respectively, followed by full relaxation at zero temperature. The comparison in the electronic DOS is illustrated in Fig. 10.9 [18]. The overall agreement is excellent for both CoCrFeNi and CoOsReRu, and the Fermi level is located at the local pseudo-gap. It is noteworthy that the predicted electronic DOS for CoCrFeNi (Fig. 10.9a) differs greatly from that generated using CPA (Fig. 9.4). For MoNbTaW, SQS produces a slightly higher DOS at the Fermi level than MC/MD, and this could be because a much larger cell was used for MC/MD.

10.5.2 Atomic Structure

The SQS method also has its own limitations compared to other atomic models. The hypothesis of SQS is to assume its completely random solid solution in the first few nearest-neighbor interaction, and thus preferred interatomic interaction may be absent. An example is shown in Fig. 10.10a for BCC MoNbTaW: the intensity of various atomic pairs in the first nearest neighbor fluctuates within a small range of 9.2–10.2 [18]. However, real alloys most often exhibit more or less short-range ordering or clustering depending on the composition and especially the temperature. In comparison with MC/MD as detailed in Chap. 8, the SQS lacks the variation of atomic positions, and thus, potentially, the preferred atomic pair interaction in certain alloys may not be captured. Previous MC/MD simulations by Widom et al. [29] have shown preferred interatomic interaction between Nb/Ta and Mo/W in MoNbTaW, as shown in Fig. 10.10b. Nonetheless, for single-phase HEAs that are close to ideal random mixing behavior especially at high temperature

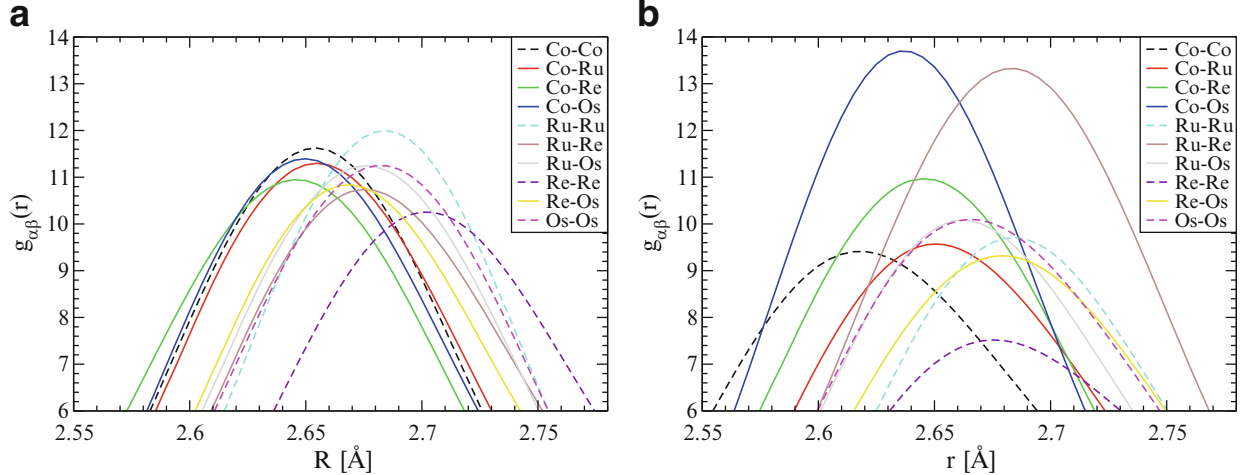


Fig. 10.11 Comparison of the HCP CoOsReRu structure generated from (a) SQS and (b) MC/MD [18]

(relative to their melting points), SQS can be a quick and near-perfect choice for the structure prediction. Furthermore, one always can apply the MC/MD procedure to SQS to obtain more realistic atomic structure as a function of temperature.

The subtle difference in PDF generated from SQS versus MC/MD is also observed in CoOSReRu as shown in Fig. 10.11. The distribution in the nearest-neighbor pairs is much more uniform in SQS, while clear preference in the Co-Os and Re-Ru pairs against the Re-Re pair is present in the MC/MD structure. Similar observation in PDF of CoCrFeNi is presented in Fig. 10.4.

10.5.3 Sensitivity to Atomic Positions

The second drawback of SQS for HEAs is that the total number of atomic configurations for a structure is fairly large (e.g., permutation in the atomic position between A/B/C/D/E elements in a quinary alloy), and thus potentially there is uncertainty in the energy of those configurations especially for anisotropic lattices (e.g., HCP) or compositions for which no small ordering (e.g., magnetic or chemical) exists. For an equal molar HEAs, the total number of atomic configurations are 24, 120, 720, 5040, and 40320 for quaternary, quinary, senary, septenary, and octonary alloys, respectively. To examine this uncertainty, the enthalpy of formation of FCC CoCrFeNi, HCP CoOsReRu, and BCC MoNbTaW versus their atomic configurations are plotted in Fig. 10.12. The results demonstrate that CoOsReRu (MoNbTaW) is most (least) sensitive to the atomic configuration. The amplitude in the variation of ΔH_f value (i.e., $|\Delta H_f^{\max} - \Delta H_f^{\min}|$) is 1.7, 0.8, and 0.3 kJ/mole for CoOsReRu, CoCrFeNi, and MoNbTaW, respectively, and the corresponding simple averaged enthalpies of formation are 2.724 ± 0.49 , 8.354 ± 0.266 , and -7.407 ± 0.069 kJ/mol, respectively. The sensitivity to the atomic configuration is presumably determined by the anisotropy of

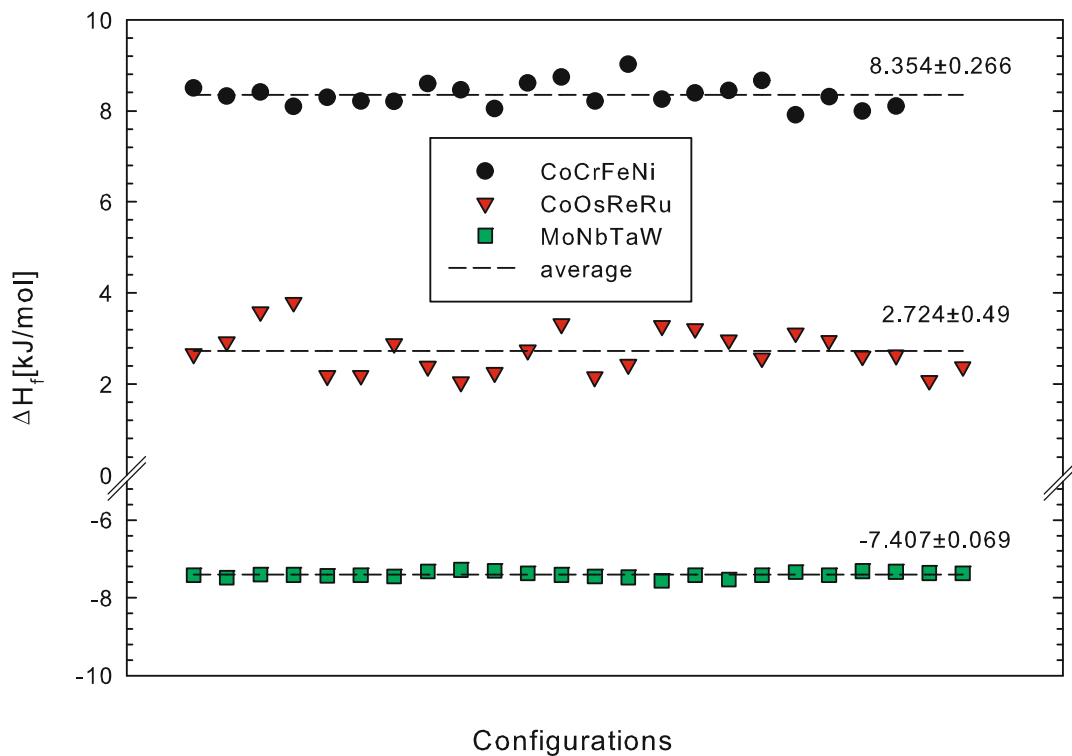


Fig. 10.12 Enthalpy of formation (ΔH_f) as a function of atomic configurations of the quaternary BCC MoNbTaW and HCP CoOsReRu SQS

the lattice and the chemical similarity of the constituent elements in terms of electronegativity, valence electron concentration, crystal structure, and atomic size. It is further assumed that this sensitivity decreases with increasing the SQS cell size.

10.5.4 Other Issues

The third drawback of the SQS method lies in its limitation to a few “special” compositions such as $A_{1/3}BCDE$, $ABCDE$, and $A_{2/3}BCDE$, while the CPA technique is capable of exploring any composition of an alloy with any components. In addition, both MC/MD and SQS suffer from cumbersome handling of magnetic materials especially in the paramagnetic state. They are computationally more expensive than CPA by many orders of magnitude. For those SQS of large cell sizes, calculation of elastic properties especially for magnetic compositions is a difficult task because of the limitation of computing capabilities.

10.6 Conclusions

In summary, this chapter provided SQS models for quaternary and quinary equimolar HEAs and detailed applications of SQS to predict the thermodynamic, vibrational, electronic, and mechanical properties of selected single-phase HEAs. Comparison between SQS, MC/MD, and CPA is provided. The following conclusions were drawn:

1. Quaternary and quinary SQS models are generated for disordered FCC, BCC, and HCP equimolar HEAs using ATAT package. The lattice vector and atomic positions are provided for the 16-, 20-, 24-, 64-, 125-, and 250-atom cell sizes.
2. The accuracy of these SQS models is sensitive to the cell size, and larger cells produce more reliable results. For CoCrFeNi and CoCrFeMnNi, larger supercells (≥ 64 atoms) predict that FCC structures are more stable than HCP, in agreement with experiments. The enthalpy of formation and lattice parameters of known single-phase HEAs are calculated.
3. At room temperature, the vibrational entropy of HEAs studied is more than twice the ideal configurational entropy. However, the vibrational entropy of mixing is very small. At $T > 400$ K, the calculated vibrational entropy of mixing is +2.8, -3.6, and -0.3 J/K/mol for FCC CoCrFeNi, BCC MoNbTaW, and HCP CoOsReRu, respectively. The calculated positive vibrational entropy of mixing for CoCrFeNi agrees with a positive excess entropy of +2.5 J/K/mol predicted from CALPHAD as presented in Chap. 12.
4. The electronic entropy is very small, and the electronic entropy of mixing is truly negligible for FCC CoCrFeNi, BCC MoNbTaW, and HCP CoOsReRu.
5. The agreement in the electronic density of states is excellent using 64-atom SQS versus MC/MD for FCC CoCrFeNi, BCC MoNbTaW, and HCP CoOsReRu.
6. MC/MD is more capable to reveal chemical ordering than SQS.

Acknowledgments MCG acknowledges the financial support by the Cross-Cutting Technologies Program at the National Energy Technology Laboratory (NETL) – Strategic Center for Coal, managed by Robert Romanosky (technology manager) and Charles Miller (technology monitor). The research was executed through NETL’s Office of Research and Development’s Innovative Process Technologies (IPT) Field Work Proposal under the RES contract DE-FE-0004000. MCG thanks Mike Widom, Dan Sorescu, Jeffrey Hawk, David Alman, and Bryan Morreale for inspiring discussion on HEAs. CN and DLI acknowledge the support from the National Science Foundation under grant DMR-1104930 and also fruitful conversations with Carl Koch, Alex Zaddach, Levente Vitos, Gus Hart, Malcolm Stocks, Stefano Curtarolo, Elizabeth Dickey, James LeBeau, Ramón Collazo, and Donald W. Brenner.

Disclaimer This chapter authored by M.C.G. was funded by the Department of Energy, National Energy Technology Laboratory, an agency of the United States Government, through a support contract with AECOM. Neither the United States Government nor any agency thereof, nor any of their employees, nor AECOM, nor any of their employees, makes any warranty, expressed or implied, or assumes any legal liability or responsibility for the accuracy, completeness, or usefulness of any information, apparatus, product, or process disclosed, or represents that its use would not infringe privately owned rights. Reference herein to any

specific commercial product, process, or service by trade name, trademark, manufacturer, or otherwise, does not necessarily constitute or imply its endorsement, recommendation, or favoring by the United States Government or any agency thereof. The views and opinions of authors expressed herein do not necessarily state or reflect those of the United States Government or any agency thereof.

References

1. Zunger A, Wei SH, Ferreira LG, Bernard JE (1990) Special quasirandom structures. *Phys Rev Lett* 65(3):353–356. doi:[10.1103/PhysRevLett.65.353](https://doi.org/10.1103/PhysRevLett.65.353)
2. Wei SH, Ferreira LG, Bernard JE, Zunger A (1990) Electronic properties of random alloys: special quasirandom structures. *Phys Rev B* 42(15):9622–9649. doi:[10.1103/PhysRevB.42.9622](https://doi.org/10.1103/PhysRevB.42.9622)
3. Gao MC, Suzuki Y, Schweiger H, Doğan ÖN, Hawk J, Widom M (2013) Phase stability and elastic properties of Cr-V alloys. *J Phys Cond Matter* 25:075402. doi:[10.1088/0953-8984/25/7/075402](https://doi.org/10.1088/0953-8984/25/7/075402)
4. Tasnádi F, Odén M, Abrikosov IA (2012) *Ab initio* elastic tensor of cubic $Ti_{0.5}Al_{0.5}N$ alloys: dependence of elastic constants on size and shape of the supercell model and their convergence. *Phys Rev B* 85(14):144112. doi:[10.1103/PhysRevB.85.144112](https://doi.org/10.1103/PhysRevB.85.144112)
5. Zaddach AJ, Niu C, Koch CC, Irving DL (2013) Mechanical properties and stacking fault energies of NiFeCrCoMn high-entropy alloy. *JOM* 65(12):1780–1789. doi:[10.1007/s11837-013-0771-4](https://doi.org/10.1007/s11837-013-0771-4)
6. Lu ZW, Wei SH, Zunger A (1992) Electronic-structure of ordered and disordered Cu_3Au and Cu_3Pd . *Phys Rev B* 45(18):10314–10330. doi:[10.1103/PhysRevB.45.10314](https://doi.org/10.1103/PhysRevB.45.10314)
7. Wei SH, Zunger A (1995) Band offsets and optical bowings of chalcopyrites and Zn-based II-VI alloys. *J Appl Phys* 78(6):3846–3856. doi:[10.1063/1.359901](https://doi.org/10.1063/1.359901)
8. Jiang C, Stanek CR, Sickafus KE, Uberuaga BP (2009) First-principles prediction of disordering tendencies in pyrochlore oxides. *Phys Rev B* 79(10):104203. doi:[10.1103/PhysRevB.79.104203](https://doi.org/10.1103/PhysRevB.79.104203)
9. Jiang C, Wolverton C, Sofo J, Chen LQ, Liu ZK (2004) First-principles study of binary bcc alloys using special quasirandom structures. *Phys Rev B* 69(21):214202, doi:<http://dx.doi.org/10.1103/PhysRevB.69.214202>
10. Shin D, Arroyave R, Liu ZK, Van de Walle A (2006) Thermodynamic properties of binary hcp solution phases from special quasirandom structures. *Phys Rev B* 74(2):024204, doi:<http://dx.doi.org/10.1103/PhysRevB.74.024204>
11. von Pezold J, Dick A, Friak M, Neugebauer J (2010) Generation and performance of special quasirandom structures for studying the elastic properties of random alloys: application to Al-Ti. *Phys Rev B* 81(9):094203. doi:[10.1103/PhysRevB.81.094203](https://doi.org/10.1103/PhysRevB.81.094203)
12. Shin DW, Liu ZK (2008) Enthalpy of mixing for ternary fcc solid solutions from special quasirandom structures. *CALPHAD* 32(1):74–81. doi:[10.1016/j.calphad.2007.09.002](https://doi.org/10.1016/j.calphad.2007.09.002)
13. Jiang C (2009) First-principles study of ternary bcc alloys using special quasi-random structures. *Acta Mater* 57(16):4716–4726. doi:[10.1016/j.actamat.2009.06.026](https://doi.org/10.1016/j.actamat.2009.06.026)
14. van de Walle A, Asta M, Ceder G (2002) The alloy theoretic automated toolkit: a user guide. *CALPHAD* 26(4):539–553. doi:[10.1016/S0364-5916\(02\)80006-2](https://doi.org/10.1016/S0364-5916(02)80006-2)
15. van de Walle A (2009) Multicomponent multisublattice alloys, nonconfigurational entropy and other additions to the alloy theoretic automated toolkit. *CALPHAD* 33(2):266–278. doi:[10.1016/j.calphad.2008.12.005](https://doi.org/10.1016/j.calphad.2008.12.005)
16. van de Walle A, Tiwary P, de Jong M, Olmsted DL, Asta M, Dick A, Shin D, Wang Y, Chen LQ, Liu ZK (2013) Efficient stochastic generation of special quasirandom structures. *CALPHAD* 42:13–18. doi:[10.1016/j.calphad.2013.06.006](https://doi.org/10.1016/j.calphad.2013.06.006)

17. van de Walle A Alloy Theoretic Automated Toolkit (ATAT) Home Page. <http://www.brown.edu/Departments/Engineering/Labs/avdw/atat/>
18. Gao MC, Jiang C, Widom M (2014) Unpublished work
19. Kresse G, Hafner J (1993) Ab initio molecular dynamics for liquid metals. *Phys Rev B* 47:558–561, doi:<http://dx.doi.org/10.1103/PhysRevB.47.558>
20. Kresse G, Furthmüller J (1996) Efficient iterative schemes for ab initio total-energy calculations using a plane-wave basis set. *Phys Rev B* 54:11169–11186, doi:<http://dx.doi.org/10.1103/PhysRevB.54.11169>
21. Blochl PE (1994) Projector augmented-wave method. *Phys Rev B* 50(24):17953, doi:<http://dx.doi.org/10.1103/PhysRevB.50.17953>
22. Perdew JP, Burke K, Ernzerhof M (1996) Generalized gradient approximation made simple. *Phys Rev Lett* 77:3865–3868, doi:<http://dx.doi.org/10.1103/PhysRevLett.77.3865>
23. Zhang Y, Zhou YJ, Lin JP, Chen GL, Liaw PK (2008) Solid-solution phase formation rules for multi-component alloys. *Adv Eng Mat* 10(6):534–538. doi:[10.1002/adem.200700240](https://doi.org/10.1002/adem.200700240)
24. Miedema AR, de Boer FR, Boom R (1977) Model predictions for the enthalpy of formation of transition metal alloys. *CALPHAD* 1(4):341–359. doi:[10.1016/0364-5916\(77\)90011-6](https://doi.org/10.1016/0364-5916(77)90011-6)
25. Senkov ON, Wilks GB, Miracle DB, Chuang CP, Liaw PK (2010) Refractory high-entropy alloys. *Intermetallics* 18(9):1758–1765. doi:[10.1016/j.intermet.2010.05.014](https://doi.org/10.1016/j.intermet.2010.05.014)
26. Senkov ON, Scott JM, Senkova SV, Miracle DB, Woodward CF (2011) Microstructure and room temperature properties of a high-entropy TaNbHfZrTi alloy. *J Alloys Comp* 509 (20):6043–6048. doi:[10.1016/j.jallcom.2011.02.171](https://doi.org/10.1016/j.jallcom.2011.02.171)
27. Takeuchi A, Amiya K, Wada T, Yubuta K, Zhang W (2014) High-entropy alloys with hexagonal close-packed structure designed by equi-atomic alloy strategy and binary phase diagrams. *JOM* 66(10):1984–1992. doi:[10.1007/s11837-014-1085-x](https://doi.org/10.1007/s11837-014-1085-x)
28. Zhang Y, Zuo TT, Tang Z, Gao MC, Dahmen KA, Liaw PK, Lu ZP (2014) Microstructures and properties of high-entropy alloys. *Prog Mat Sci* 61:1–93. doi:[10.1016/j.pmatsci.2013.10.001](https://doi.org/10.1016/j.pmatsci.2013.10.001)
29. Widom M, Huhn WP, Maiti S, Steurer W (2014) Hybrid Monte Carlo/molecular dynamics simulation of a refractory metal high entropy alloy. *Metall Mater Trans A* 45A(1):196–200. doi:[10.1007/s11661-013-2000-8](https://doi.org/10.1007/s11661-013-2000-8)
30. Gao MC, Alman DE (2013) Searching for next single-phase high-entropy alloy compositions. *Entropy* 15:4504–4519. doi:[10.3390/e15104504](https://doi.org/10.3390/e15104504)
31. Lucas MS, Mauger L, Munoz JA, Xiao Y, Sheets AO, Semiatin SL, Horwath J, Turgut Z (2011) Magnetic and vibrational properties of high-entropy alloys. *J Appl Phys* 109 (7):07E307. doi:[10.1063/1.3538936](https://doi.org/10.1063/1.3538936)
32. Lucas MS, Belyea D, Bauer C, Bryant N, Michel E, Turgut Z, Leontsev SO, Horwath J, Semiatin SL, McHenry ME, Miller CW (2013) Thermomagnetic analysis of FeCoCr_xNi alloys: Magnetic entropy of high-entropy alloys. *J Appl Phys* 113(17):17A923. doi:[10.1063/1.4798340](https://doi.org/10.1063/1.4798340)
33. Le Page Y, Saxe P (2002) Symmetry-general least-squares extraction of elastic data for strained materials from ab initio calculations of stress. *Phy Rev B* 65:104104, doi:<http://dx.doi.org/10.1103/PhysRevB.65.104104>
34. Mehl MJ, Osburn JE, Papaconstantopoulos DA, Klein BM (1990) Structural properties of ordered high-melting-temperature intermetallic alloys from first-principles total-energy calculations. *Phys Rev B* 41(15):10311–10323, doi:<http://dx.doi.org/10.1103/PhysRevB.41.10311>
35. Vitos L (2007) Computational quantum mechanics for materials engineers: the EMTO method and applications. *Eng Mater Proc* Springer London. doi:[10.1007/978-1-84628-951-4](https://doi.org/10.1007/978-1-84628-951-4)
36. Gao MC, Dogan ON, King P, Rollett AD, Widom M (2008) The first-principles design of ductile refractory alloys. *JOM* 60(7):61–65. doi:[10.1007/s11837-008-0092-1](https://doi.org/10.1007/s11837-008-0092-1)
37. Otto F, Dlouhy A, Somsen C, Bei H, Eggeler G, George EP (2013) The influences of temperature and microstructure on the tensile properties of a CoCrFeMnNi high-entropy alloy. *Acta Mater* 61(15):5743–5755. doi:[10.1016/j.actamat.2013.06.018](https://doi.org/10.1016/j.actamat.2013.06.018)

Chapter 11

Design of High-Entropy Alloys

Michael C. Gao

Abstract Identifying single-phase high-entropy alloys is extremely important to understanding HEA formation and their intrinsic properties, but lack of effective guidelines has hindered their discovery. As a result, to date the total number of single-phase HEAs is still very limited. This chapter overviews five major methodologies that may assist in HEA design, including CALPHAD modeling, experimental phase diagrams inspection, empirical parameters criteria, density functional theory calculations, and *ab initio* molecular dynamics simulations. Strength and weakness of these methodologies are discussed. Experimentally reported equimolar single-phase HEAs are reviewed, and a variety of new compositions with the face-centered cubic (FCC), body-centered cubic (BCC), and hexagonal closed-packed (HCP) structures predicted from modeling and phase diagram inspection are provided.

Keywords Single-phase • Multiphase • Bulk metallic glasses • Enthalpy of mixing • Entropy of mixing • Atomic size difference • Electronegativity difference • Hume-Rothery rules • Empirical rules • CALPHAD • Phase diagram inspection • Disordered solid solution • Solubility • Phase diagrams • First-principles • Density functional theory (DFT) • Ab initio molecular dynamics simulations (AIMD) • Face-centered cubic (FCC) • Hexagonal closed-packed (HCP) • Body-centered cubic (BCC) • Phase stability • Alloy design • High-entropy alloys (HEAs)

11.1 Introduction

The research on high-entropy alloys (HEAs) is still at its infancy stage as summarized in Chap. 1 since the first publications by Yeh [1] and Cantor [2] independently in 2004. The two definitions for HEAs by Yeh, as detailed in Chap. 1, are very broad and include wide ranges of microstructure. To date the majority of HEAs published in research papers contain more than one phase in the microstructure (in the as-cast state or after annealing) as compiled in Chap. 2 and elsewhere [3–6],

M.C. Gao (✉)

National Energy Technology Laboratory/AECOM, Albany, OR 97321, USA

e-mail: michael.gao@netl.doe.gov

Table 11.1 Single-phase HEA compositions confirmed by experiments

Alloys	Structure	References
CoCrFeNi	FCC	[9]
CoFeMnNi	FCC	[7, 10]
CoCrMnNi	FCC	[10]
CoFeNiPd	FCC	[28]
CoCrFeMnNi	FCC	[2]
CoCrFeNiPd	FCC	[11]
$\text{Al}_{20}\text{Li}_{20}\text{Mg}_{10}\text{Sc}_{20}\text{Ti}_{30}$	FCC	[27]
AlNbTiV	BCC	[29]
HfNbTiZr	BCC	[16]
MoNbTaW	BCC	[12, 13]
NbTaTiV	BCC	[14]
NbTiVZr	BCC	[15]
AlCrMoTiW	BCC	[18]
AlNbTaTiV	BCC	[14]
HfNbTaTiZr	BCC	[17]
HfNbTiVZr	BCC	[30]
MoNbTaVW	BCC	[12, 13]
MoNbTaTiV	BCC	[20]
MoNbTiVZr	BCC	[19]
NbReTaTiV	BCC	[20]
MoNbReTaW	BCC	[20]
CrMoNbTaVW	BCC	[21]
HfNbTaTiVZr	BCC	[22]
MoNbTaTiVW	BCC	[23]
MoNbReTaVW	BCC	[20]
MoNbReTaTiVW	BCC	[20]
CoFeReRu	HCP	[8]
MoPdRhRu	HCP	[31]
DyGdHoTbY	HCP	[25]
DyGdLuTbTm	HCP	[25]
DyGdLuTbY	HCP	[32]
$\text{Al}_{20}\text{Li}_{20}\text{Mg}_{10}\text{Sc}_{20}\text{Ti}_{30}$	HCP	[27]

and the total number of single-phase solid solution HEAs is still very limited mainly due to lack of effective searching guidelines as pointed out by Gao et al. [7, 8]. Table 11.1 summarizes experimentally reported single-phase HEAs in equimolar compositions with the face-centered cubic (FCC), body-centered cubic (BCC), and hexagonal closed-packed (HCP) structures. The FCC alloys are mostly based on CoCrFeMnNi [2] and its subsystems and derivatives [7, 9–11]. The BCC alloys are based on refractory metals in quaternary [12–16], quinary [12–14, 17–20], senary [20–23], and septenary [20] compositions. Zhang et al. [3] first suggested formation of HCP HEAs among rare earth (RE) elements, because these RE elements have extremely similar atomic size, electronegativity, and chemistry,

and they form isomorphous or extended solid solution in HCP structure according to their binary phase diagrams [24]. Indeed, formation of RE HCP HEAs was later confirmed in DyGdLuTbY [25], DyGdLuTbTm [25], and DyGdHoTbY [26]. HCP HEAs based on transition metals are experimentally confirmed in CoFeReRu [8] and predicted in CoOsReRu [7]. Youssef et al. [27] reported polymorphous transformation in $\text{Al}_{20}\text{Li}_{20}\text{Mg}_{10}\text{Sc}_{20}\text{Ti}_{30}$ from the FCC to HCP structure by annealing at 500 °C for 1 h, but whether the FCC and HCP phases are thermodynamically stable requires further investigation.

Since the “virtual” variations in non-equimolar compositions for any HEA system can be countless, especially for those HEAs where isomorphous solid solution forms (e.g., $\text{Hf}_x\text{NbTaTiVZr}$, $\text{HfNb}_x\text{TaTiVZr}$, $\text{HfNbTa}_x\text{TiVZr}$, $\text{HfNbTaTi}_x\text{VZr}$, and HfNbTaTiVZr_x [22]), this chapter mainly focuses on equimolar compositions that are most representative of their alloying systems. This is not to say that those non-equimolar compositions are not important. As a matter of fact, the maximum entropy of mixing of a solid solution may not necessarily occur at the equimolar compositions, since most alloys may deviate more, or less, from ideal mixing, as shown in Co-Cr-Fe-Mn-Ni (see Chap. 12), Mo-Nb-Ta-Ti-V-W (see Chap. 12), Al-Cr-Cu-Fe-Ni [33], and Hf-Nb-Ta-Ti-V-Zr systems [22].

The empirical rules on single-phase solid solution HEA formation are reviewed in Chap. 2 from the consideration of topological, thermodynamic, and physical parameters including atomic size difference (δ) [34], enthalpy of mixing (ΔH_{mix}) [34], valence electron concentration (VEC) [35], Ω -parameter [4], and electronegativity difference (χ) [36]. Out of those parameters, ΔH_{mix} and δ carry the most significance, and it has been regarded [4] that $15 \leq \Delta H_{\text{mix}}^{\text{liq}} \leq +5$ kJ/mol, $\Omega \geq 1$ and $\delta \leq 6.6\%$ would favor forming disordered solid solution HEAs. However, the ΔH_{mix} values taken from the empirical Miedema model [37], as proposed in Reference [34], are for liquid state regardless of the crystal structure of the solid solution phase. Furthermore, these empirical rules do not address any competing phases against the solid solution phase. As a result, it is not surprising to observe that these rules fail sometimes. For example, AlLiMgSnZn has $\Delta H_{\text{mix}} = -6.08$ kJ/mol, $\delta = 5.52\%$, $\Omega = 1.56$, VEC = 5.4, and $\Delta\chi = 0.33$, but more than four phases formed in the alloy [38]. Multiphases were observed in HfMoNbTaTiVWZr [39] although it has $\Delta H_{\text{mix}} = -2.9$ kJ/mol, $\delta = 5.49\%$, $\Omega = 15.7$, and $\Delta\chi = 0.36$. Note that lattice topological instability [40], a single-parameter (ϕ) [6], and an intrinsic residual strain model [5] have also been proposed recently to address single-phase solid solution formation.

On the other hand, Gao and Alman [7] proposed an effective searching strategy by combining experimental phase diagram inspection, CALPHAD (acronym of CALculation of PHase Diagram) modeling and *ab initio* molecular dynamics (AIMD) simulations. Accelerating HEA design using CALPHAD approach has been addressed in literature by Zhang et al. [23, 41, 42], Gao et al. [8, 22], and Senkov et al. [43]. Very recently, Troparevsky et al. [30] proposed a simple model that compares the ideal configurational entropy of equimolar solid solution with the enthalpy of formation of the most stable binary compound in the alloy

system, which are taken from first-principles density functional theory (DFT) in literature.

This chapter overviews and compares these major methodologies pertaining to the design of single-phase HEAs. Theoretical background on DFT and its applications to HEAs are presented in Chaps. 8, 9, and 10, while the detailed methodology in CALPHAD and its database development are presented in Chap. 12. A variety of model-predicted equimolar compositions with FCC, BCC, and HCP structures are suggested. This chapter concludes by comparing the strength and weakness of these methodologies and outlook for future development for more robust screening approaches. Note that composite HEAs are very important in balancing material properties for many challenging applications, and the readers are referred to Chap. 6 and Refs. [44–46] for details.

11.2 CALPHAD Modeling

The essence of CALPHAD method is to develop a reliable thermodynamic database that consists of self-consistent descriptions of Gibbs energy for each phase in the system in interest using semiempirical equations as a function of temperature and composition based on reliable experimental data and accurate DFT results. Once the database has been developed, then it can be used to predict phase diagrams and thermodynamic properties of this system. Therefore, CALPHAD can be regarded as the most direct approach to design HEAs [8, 22, 23, 41–43].

Previously, Otto et al. [47] studied phase stability in six alloys CoCrFeMnNi, CoCrCuFeMn, CoCrMnNiV, CoFeMnMoNi, CoFeMnNiV, and CrFeMnNiTi, and they found that a single-phase FCC solid solution formed only in CoCrFeMnNi, while the other five alloys consisted of more than one phase after annealing at 1000 °C or 800 °C. Using TCNI7 database that covers all the edge binaries and some ternaries of these alloys (except that TTNI8 database was used for CoCrCuFeMn and CoFeMnNiV), the experimental observation by Otto et al. is qualitatively reproduced by the CALPHAD calculations as shown in Fig. 11.1. A single FCC phase was predicted only in CoCrFeMnNi by both databases. An FCC matrix phase and minor μ phase were correctly predicted in CoFeMnMoNi, and complex microstructure of four phases were predicted in CrFeMnNiTi. For CoFeMnNiV, the FCC phase was predicted to be stable over a narrow temperature range, and minor σ phase forms at lower temperatures. It seems that both databases underestimate the thermal stability of the σ phase in the systems since it was observed in CoCrCuFeMn and CoCrMnNiV by Otto et al. [47]. This also indicates that both databases require further improvement especially on descriptions on all ternary systems.

Aiming to design solid solution alloys with three to six principal components that have a useable temperature ≥ 1000 °C, density $< 10 \text{ g} \cdot \text{cm}^{-3}$, Young's modulus $\geq 100 \text{ GPa}$, and cost $\leq \$200$ per kg, Senkov et al. [43] carried out CALPHAD calculations using various thermodynamic databases developed by CompuTherm [48].

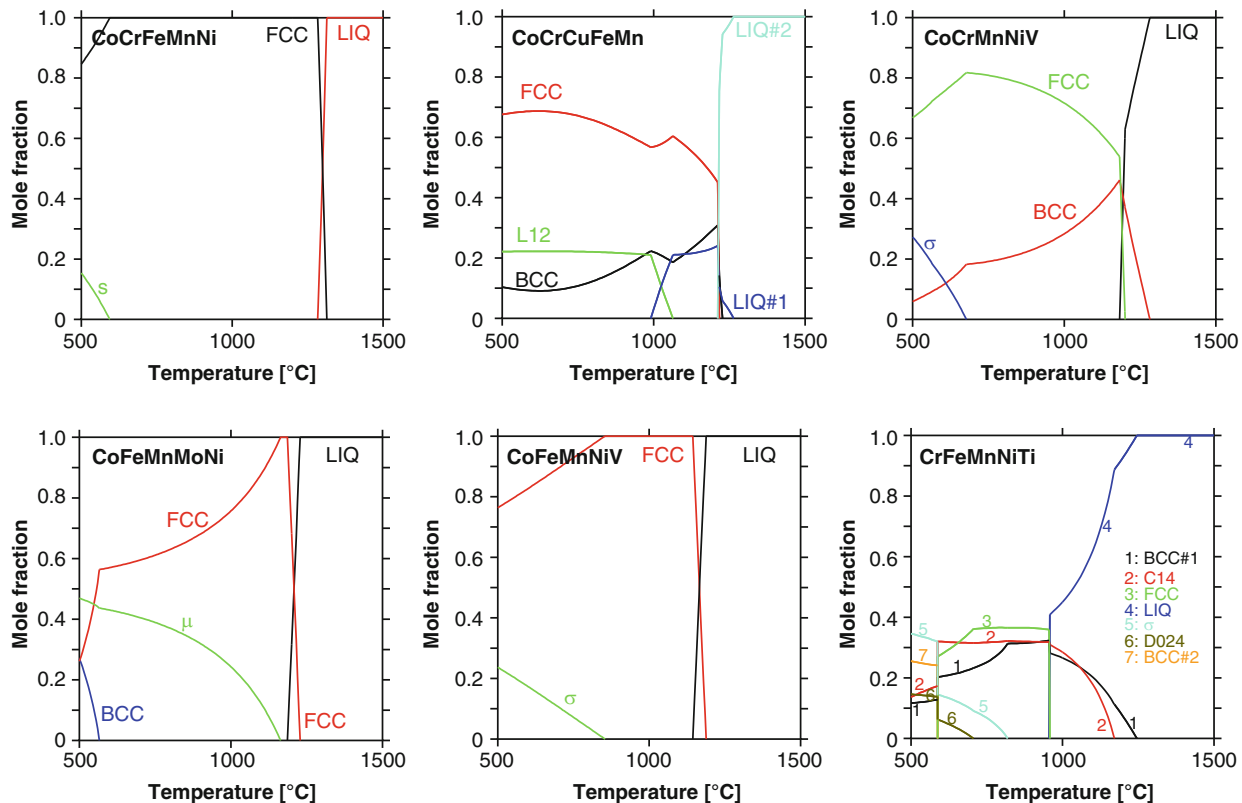


Fig. 11.1 Calculated equilibrium phase mole fraction versus temperature for CoCrFeMnNi, CoCrCuFeMn, CoCrMnNiV, CoFeMnMoNi, CoFeMnNiV, and CrFeMnNiTi that were experimentally studied by Otto et al. [47]

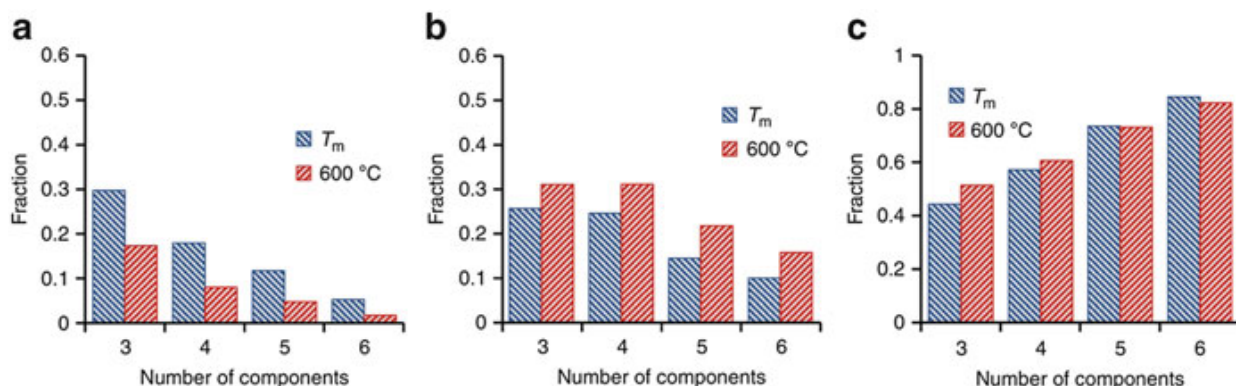


Fig. 11.2 Distributions of multi-principal element alloys by categories. Fractions of (a) SS phases, (b) IM phases, and (c) (SS + IM) phases equimolar alloys in 3- to 6-component alloy systems at solidus temperature (T_m) and 600 °C [43]

They categorized the results into solid solution (SS) phases, intermetallic (IM) phases, and SS + IM phases. They found that, with increasing the number of principal components, the fraction of SS phases decrease, while the fraction of SS + IM increases, as shown in Fig. 11.2. This suggests that although increasing the number of principal components (N) increases the maximum configurational entropy of SS phases by $R \ln(N)$ (where R is ideal gas constant), it also lowers the enthalpy of competing intermetallics, thus favoring formation of composites of SS and IM phases.

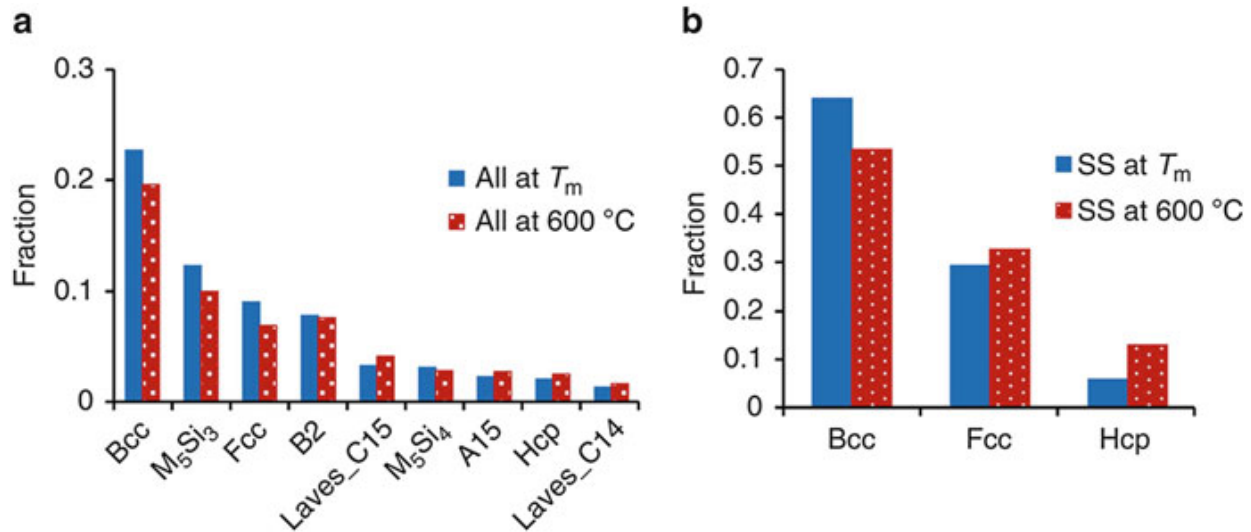


Fig. 11.3 Fractions of different phases in (a) all alloys and (b) solid solution alloys [43]

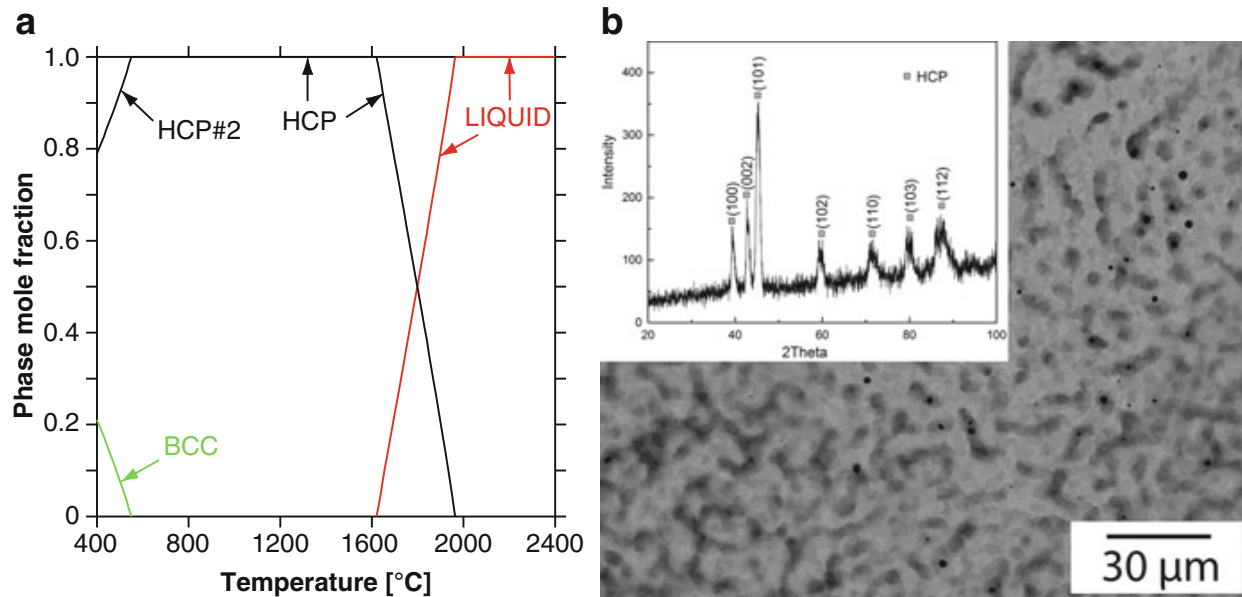


Fig. 11.4 (a) Equilibrium phase mole fraction versus temperature and (b) SEM micrograph and XRD plot for as-cast CoFeReRu [8]

The distribution (in fraction) of different phases at solidus temperature and 600 °C are shown in Fig. 11.3. The top four most frequently observed phases in descending order are BCC, M_5Si_3 , FCC, and B2 (CsCl-type) phases. In terms of solid solution phases, BCC structure dominates over FCC and HCP structures.

To design HCP HEAs, Gao et al. [8] designed CoFeReRu, CoPtReRu, CoCrReRu, and CoCrFeReRu using TCNI7 database, and a single HCP phase in as-cast CoFeReRu was verified using X-ray diffraction (XRD) and scanning electron microscopy (SEM) as shown in Fig. 11.4. Assisted by CALPHAD modeling using TCNI7 database, Gao and coworkers have also successfully designed several senary refractory HEAs including CrMoNbTaVW [21], HfNbTaTiVZr [22], and MoNbTaTiVW [23], and a single-phase BCC solid solution was experimentally confirmed in these alloys in the as-cast state. Other BCC HEAs they

designed using CALPHAD modeling as well as empirical parameters include HfMoNbTiZr, HfMoTaTiZr, NbTaTiVZr, HfMoNbTaTiZr, HfMoTaTiVZr, and MoNbTaTiVZr [39].

One important reason for the successful application of TCNI7 database to refractory BCC HEA design lies in the fact that there are few stable compounds in the vast majority of their binaries and ternaries for those nine refractory metals (Cr, Hf, Mo, Nb, Ta, Ti, V, W, and Zr); although the database only covers all the edge binaries. However, optimization of all constituent ternary systems will absolutely enhance the reliability of the database, and thus the success rate of HEA screening using the database. Typical optimization for ternaries involve introducing ternary interaction parameters, fitting the phase boundaries between BCC, HCP, Laves, and other phases, and reproducing experimental liquidus surface, etc. Note that attention also needs to be paid to the energies of those hypothetical compounds that are required for the sake of database compatibility (see Chap. 12 for details).

To ascertain whether an alloy would form single-phase solid solution in the as-cast state, one can perform nonequilibrium solidification simulation using the Scheil-Gulliver models [49, 50]. The Scheil simulation predicts formation of a single BCC phase during the entire solidification in MoNbTaTiVW (see Fig. 12.19 in Chap. 12) and sequential formation of multiphase in $\text{Al}_x\text{CoCrFeNi}$ ($x \geq 0.8$, see Fig. 12.17 in Chap. 12). Alternatively, one can also make an educated guess by examining the temperature range (ΔT) over which the solid solution phase is stable from the plot of equilibrium phase mole fraction versus temperature (e.g. Figs. 11.1 and 11.4a). Experience reveals that $\Delta T \geq \sim 0.3T_{\text{sol}}$ (where T_{sol} stands for solidus temperature at which the solid solution phase is the primary crystallization phase) typically favors a single-phase solid solution in the as-cast state. Since chemical segregation inevitably exists in the as-cast dendritic structure due to constitutional undercooling and nonequilibrium solidification path (see Chap. 5 for details on manufacturing routes), proper homogenization and/or thermomechanical treatment at higher temperature will be required to obtain equiaxed grain microstructure and achieve acceptable chemical homogeneity.

The single-phase HEA compositions predicted using CALPHAD modeling by Senkov [43], Gao et al. [7, 8], and this work are compiled in Table 11.2, but future experiments are required to verify the microstructure of these compositions. As pointed out in Chap. 12, most commercial CALPHAD databases are developed for traditional alloys that are based on single principal element (e.g., Al-, Mg-, Fe-, Ni-, or Ti-based alloys, etc.), and they are most accurate for the compositions located at the corner rich in the principal element. As a result, caution should be paid when extrapolating the compositions to the center of a multicomponent phase diagram.

To achieve accurate results, the databases should at least cover all the constituent binary and ternary systems because the descriptions for higher-order compositions are routinely obtained by extrapolation from the lower-order systems. Therefore, one should not overestimate the CALPHAD prediction when the database does not cover all the constituent binaries or ternaries. For example, experiments show

Table 11.2 Single-phase HEA compositions predicted by modeling and phase diagram inspection

Alloys	Structure	References
CuMnNiZn	FCC	This study
CuNiPdPt	FCC	[7]
CoFeIrOsRh	* ^a	[30]
CoIrNiOsRh	* ^a	[30]
CoIrNiRhPd	* ^a	[30]
CoIrOsPtRh	* ^a	[30]
CuNiPdPtRh	FCC	[7]
IrNiOsPtRh	* ^a	[30]
IrOsPtRhRu	* ^a	[30]
NiOsPtRhRu	* ^a	[30]
CoCrFeMnNiOs	* ^a	[30]
CoCrFeNiOsRh	* ^a	[30]
CoCrFeNiOsRe	* ^a	[30]
CoFeIrNiOsRh	* ^a	[30]
CoFeIrNiRhPd	* ^a	[30]
CoIrNiOsPtRh	* ^a	[30]
CoIrNiRhPdPt	* ^a	[30]
IrNiOsPtRhRu	* ^a	[30]
CoCrFeMnNiOsRh	* ^a	[30]
CoCrFeMnOsReRh	* ^a	[30]
CoCrFeMnNiOsRe	* ^a	[30]
CoCrFeNiOsReRh	* ^a	[30]
CoCrFeNiReRhPd	* ^a	[30]
CoCrMnNiOsReRh	* ^a	[30]
CoCrMnNiOsReW	* ^a	[30]
CoFeMnNiOsReRh	* ^a	[30]
CoIrFeMnNiOsRh	* ^a	[30]
CrMnNiOsReRuW	* ^a	[30]
CoFeMnOsReZn	* ^a	[30]
AlCrFeMn	BCC	[43]
AlCrFeMo	BCC	[43]
AlCrFeV	BCC	[43]
AlCrMnMo	BCC	[43]
AlCrMnTi	BCC	[43]
AlCrMnV	BCC	[43]
AlCrMoV	BCC	[43]
AlCrVW	BCC	[43]
AlFeMnV	BCC	[43]
AlFeMoV	BCC	[43]
AlFeTiV	BCC	[43]
AlMnTiV	BCC	[43]
AlMoNbV	BCC	[43]

(continued)

Table 11.2 (continued)

Alloys	Structure	References
AlNbVW	BCC	[43]
BaCaEuSr	BCC	This work
BaCaEuYb	BCC	This work
BaEuSrYb	BCC	This work
BaCaEuYb	BCC	This work
CaEuSrYb	BCC	This work
CrFeMnV	BCC	[43]
CrFeTiV	BCC	[43]
CrMnTiV	BCC	[43]
CrMoNbV	BCC	[43]
CrMoTiV	BCC	[43]
FeMoTiV	BCC	[43]
MoNbReTa	BCC	This work
MoNbReTi	BCC	This work
MoNbReV	BCC	This work
MoNbTaTi	BCC	This work
MoNbTaV	BCC	This work
MoNbTiV	BCC	[43], this work
MoNbTiW	BCC	This work
MoNbVW	BCC	This work
MoReTaTi	BCC	This work
MoReTaV	BCC	This work
MoReTaW	BCC	This work
MoReTiV	BCC	This work
MoReTiW	BCC	This work
MoReVW	BCC	This work
MoTiVW	BCC	This work
NbReTaTi	BCC	This work
NbReTaV	BCC	This work
NbReTaW	BCC	This work
NbReTiV	BCC	This work
NbReTiW	BCC	This work
NbReVW	BCC	This work
NbTaTiW	BCC	This work
NbTaVW	BCC	This work
NbTiVW	BCC	This work
ReTaTiV	BCC	This work
ReTaTiW	BCC	This work
ReTaVW	BCC	This work
ReTiVW	BCC	This work
TaTiVW	BCC	This work
BaCaEuSrYb	BCC	This work

(continued)

Table 11.2 (continued)

Alloys	Structure	References
AlCrFeMnV	BCC	[43]
AlCrFeMoV	BCC	[43]
AlCrMnTiV	BCC	[43]
AlCrNbVW	BCC	[43]
HfMoNbTiZr	BCC	[39]
HfMoTaTiZr	BCC	[39]
MoNbTaTiW	BCC	[20], this work
MoNbReTiW	BCC	[20], this work
MoNbTiVW	BCC	[20], this work
MoNbReTaTi	BCC	[20], this work
MoNbReTaV	BCC	[20], this work
MoNbReTiV	BCC	[20], this work
MoNbReVW	BCC	[20], this work
MoReTaTiV	BCC	[20], this work
MoReTaTiW	BCC	[20], this work
MoReTaVW	BCC	[20], this work
MoReTiVW	BCC	[20], this work
MoTaTiVW	BCC	[20], this work
NbReTaTiW	BCC	[20], this work
NbReTaVW	BCC	[20], this work
NbReTaTiV	BCC	This work
NbReTiVW	BCC	[20], this work
NbTaTiVW	BCC	[20], this work
NbTaTiVZr	BCC	[39]
ReTaTiVW	BCC	[20], this work
AlCrMoNbVW	BCC	[43]
HfMoNbTaTiZr	BCC	[39]
HfMoTaTiVZr	BCC	[39]
MoNbReTaTiV	BCC	[20], this work
MoNbReTaTiW	BCC	[20], this work
MoNbReTaVW	BCC	This work
MoNbReTiVW	BCC	[20], this work
MoNbTaTiVZr	BCC	[39]
MoReTaTiVW	BCC	[20], this work
NbReTaTiVW	BCC	[20], this work
CoCrReRu	HCP	[8]
CoOsReRu	HCP	[7, 8]
CoPtReRu	HCP	[8]
CrIrMoRh	HCP	[8]
CrIrRhW	HCP	[8]
CrMoOsRu	HCP	[8]
CrOsRuW	HCP	[8]

(continued)

Table 11.2 (continued)

Alloys	Structure	References
CoPtReRu	HCP	[8]
IrMoPdRu	HCP	[8]
IrMoRhW	HCP	[8]
IrMoPtRu	HCP	[8]
MoOsRuW	HCP	[8]
MoPdRhRu	HCP	[8]
MoPtRhRu	HCP	[8]
CoCrFeReRu	HCP	[8]
CoFeOsReRu	HCP	[8]
CoIrOsReRu	HCP	[8]
CoNiOsReRu	HCP	[8]
CoOsPdReRu	HCP	[8]
CoOsPtReRu	HCP	[8]
CoOsReRhRu	HCP	[8]
CoOsReRuTc	HCP	[8]
CrIrMoRhW	HCP	[8]
CrMoOsRuW	HCP	[8]
MoPdRhRuTc	HCP	[51]
210 quaternary RE* ^b	HCP	[8]
378 quinary RE* ^b	HCP	[8]
210 senary RE* ^b	HCP	[8]
120 septenary RE* ^b	HCP	[8]
45 octonary RE* ^b	HCP	[8]
10 ennead RE* ^b	HCP	[8]
1 decadal RE* ^b	HCP	[8]
CeNdPmPr	DHCP	[8]
CeLaPmPr	DHCP	[8]
CeLaNdPr	DHCP	[8]
CeLaNdPm	DHCP	[8]
LaNdPmPr	DHCP	[8]
CeLaNdPmPr	DHCP	[8]

*^aThe crystal structures of these compositions were not suggested in Ref. [30], although the majority of them likely prefer an FCC structure

*^bThese numbers represent the total number of equimolar compositions for quaternary, quinary, senary, septenary, octonary, ennead, and decadal systems, respectively, which comprises arbitrary selection of RE elements from the Dy-Er-Gd-Ho-Lu-Sc-Sm-Tb-Tm-Y system [8]

multiphase formation in CoReRuV instead of single HCP phase predicted by TCNI7 database [8]. Experimental study on AlNbTaTiV by Yang et al. [14] shows appearance of a single-phase BCC solid solution in the as-cast state, but TCNI7 database predicts formation of BCC and σ phase. These disagreements demonstrate the importance of the reliability of the thermodynamic database.

11.3 Phase Diagram Inspection

Phase diagram inspection becomes especially important if necessary CALPHAD databases are not available or are not sufficiently accurate (e.g., they do not cover all edge binaries or ternaries). Inspection of phase diagrams of those single-phase HEAs listed in Table 11.1 reveals some common important characteristics among their systems [7]: They either exhibit isomorphous solid solution (e.g., Nb-Mo-Ta-W, Hf-Nb-Ta-Ti-Zr), or the terminal solubilities are quite large (e.g., Co-Fe-Mn-Ni) in their constituent binaries and ternaries. The key of phase diagram inspection is to look for wide solubilities (i.e., compositional homogeneity range of the solid solution phase in interest). In order to search for lightweight HEAs for aerospace applications, Cotton et al. [52] exclusively used terminal solubility in binary phase diagrams as an important parameter in their screening. Mainly there are three types of solid solutions in a phase diagram as shown in Fig. 11.5, which carry most significance in HEA

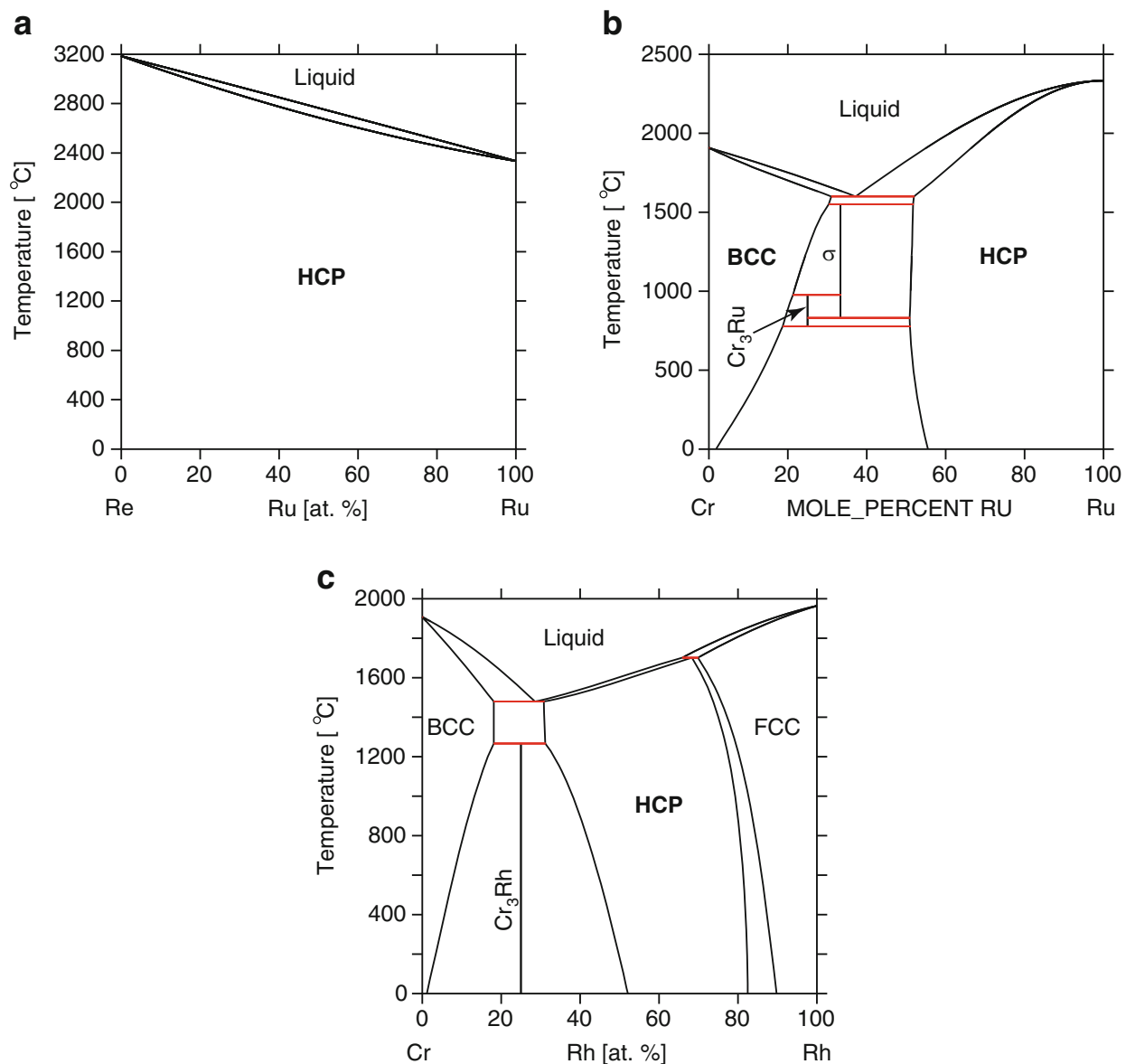


Fig. 11.5 Example experimental binary phase diagrams [53] that show isomorphous HCP solid solution in Re-Ru, large terminal HCP and BCC solubilities in Cr-Ru, and large homogeneity range of an intermediate HCP phase in Cr-Rh binary

formation: (a) isomorphous solid solution (e.g., Re-Ru), (b) extended terminal solid solubility (e.g., BCC and HCP in Cr-Ru binaries), and (c) intermediate solid solution (e.g., HCP phase in Cr-Rh binary).

11.3.1 Exclusively Isomorphous Solid Solution in All Edge Binaries

Phase diagram inspection is actually a powerful screening tool, since it allows immediate HEA design without need of other input. For example, one may expect single-phase BCC solid solution formation for quaternary, quinary, and senary alloys at equimolar compositions within Mo-Nb-Ta-Ti-V-W system, since all the edge binaries exhibit isomorphous BCC solid solution. As a result, the total number of equimolar HEA compositions of this system amount to 22:

$$C_6^4 + C_6^5 + C_6^6 = 15 + 6 + 1 = 22. \quad (11.1)$$

Previously, Gao et al. [7] suggested formation of single-phase HCP solid solution in CoOsReRu, since all six constituent binaries form isomorphous HCP solid solution. Another example of HCP HEAs is based on rare earth elements Dy, Er, Gd, Ho, Lu, Sc, Sm, Tb, Tm, and Y, as proposed by Gao et al. [8]. These RE elements all have stable HCP structure, and they form isomorphous HCP solid solution in their binaries. As a result, the total number of equimolar HEA compositions of this system equals 974, as determined as follows:

$$\begin{aligned} C_{10}^4 + C_{10}^5 + C_{10}^6 + C_{10}^7 + C_{10}^8 + C_{10}^9 + C_{10}^{10} \\ = 210 + 378 + 210 + 120 + 45 + 10 + 1. \end{aligned} \quad (11.2)$$

The individual items in Eq. (11.2) represent the total number of compositions for quaternary, quinary, senary, septenary, octonary, ennead, and decadal systems, respectively. Since several of these elements transform to the BCC structure at very high temperatures before melting, some of the proposed HEAs may require subsequent annealing in the HCP phase field in order to decompose the primary BCC phase, if any should exist.

Phase diagram inspection also suggests that isomorphous double HCP (DHCP) solid solution may form among La, Ce, Pr, Nd, and Pm that all have a stable DHCP structure at lower temperatures [24]. As a result, single-phase DHCP solid solution is expected to form in CeLaNdPmPr, CeNdPmPr, CeLaPmPr, CeLaNdPr, CeLaNdPm, and LaNdPmPr. FCC solid solution was proposed in CuNiPdPt and CuNiPdPtRh [7]; since isomorphous solid solution forms in all six edge binaries of Cu-Ni-Pd-Pt system, and Rh also forms isomorphous solid solution with Cu, Ni, Pd, and Pt, respectively. Another example of phase diagram inspection is BaCaEuSrYb and its subsystem alloys (namely BaCaEuSr, BaCaEuYb, BaEuSrYb, BaCaEuYb,

and CaEuSrYb) in which a single-phase BCC solid solution may form since isomorphous BCC solid solution forms in all edge binaries where available. Although Eu-Sr and Sr-Yb binary phase diagrams are not available in literature, it is expected that they may resemble Ca/Ba-Eu and Ca/Ba-Yb binaries, respectively.

11.3.2 Combination of Isomorphous Solid Solution and Large Terminal Solubility

Even though most binary phase diagrams do not exhibit aforementioned isomorphous solid solution, combination of isomorphous solid solution and large terminal solubility in lower-order systems also favor solid solution formation in higher-order systems. For example, for the well-studied CoCrFeMnNi alloy, Co-Fe, Co-Ni, Fe-Mn, Fe-Ni, and Mn-Ni binaries exhibit isomorphous FCC solid solution, while Co-Cr, Co-Mn, and Cr-Ni show large FCC terminal solubilities. As a result, FCC solid solution forms in CoCrFeMnNi despite of existence of stable σ phase in Co-Cr and Cr-Mn and absence of stable FCC solid solution in Cr-Mn. Likewise, FCC solid solution may form in CuMnNiZn, since isomorphous FCC solid solution exists in Cu-Mn, Cu-Ni, and Mn-Ni, while Zn solubilities in Cu, FCC γ -Mn, and Ni are very large.

Once single-phase HEA compositions are identified based on exclusively isomorphous solid solution as described in Sect. 11.3.1, then new alloys can be designed by substituting one element by a new element (or add a new element) that exhibit extended terminal solubility with majority of the elements in the base alloy. For example, one may consider Mo-Nb-Re-Ta-Ti-V-W system, since Mo, Nb, Ta, Ti, V, and W all have substantially large solubility for Re. Accordingly, the total number of equimolar HEA compositions within this system could reach

$$C_7^4 + C_7^5 + C_7^6 + C_7^7 = 35 + 21 + 7 + 1 = 64 . \quad (11.3)$$

11.3.3 Intermediate Phases with Wide Compositional Homogeneity Range

Formation of HCP MoPdRhRu HEA [31] belongs to the case of intermediate phase with large homogeneity in the middle of their binary phase diagrams (e.g., $Mo_{0.46}Pd_{0.54}$ in Mo-Pd, $Mo_{0.4}Rh_{0.6}$ in Mo-Rh, and $Mo_{0.63}Ru_{0.37}$ in Mo-Ru). Chemical similarity between Pd and Pt and between Rh and Ir suggests that it is possible to form several HCP solid solutions that are variants of MoPdRhRu, e.g., MoPtRhRu, MoIrPtRu, MoIrPtRhRu, and MoIrPdPtRhRu. Intermediate HCP

phase with wide compositional homogeneity also forms between the group (Cr,Mo,W) and the group (Ir,Rh) [24]; therefore, Gao et al. [8] proposed compositions that may favor forming HCP HEAs: CrIrMoRh, CrIrRhW, IrMoRhW, (Cr,Mo,W)_{0.5}(IrRh)_{0.5}, and CrIrMoRhW.

In summary, phase diagram inspection offers useful information on solid solution versus intermetallic compounds and can help quickly select of elements that are important for the solid solution phase in interest. Isomorphous solid solution, large terminal solubilities, and intermediate phases of wide homogeneity are the most important features that one should pay attention to during HEA design or screening activities. These features in edge binaries and ternaries are listed in descending order of importance pertaining to HEA formation:

1. Isomorphous solid solution in all edge binaries
2. Isomorphous solid solution in most ternary isothermal and isopleth sections
3. Isomorphous solid solution in most edge binaries + large terminal solubility in some edge binaries (e.g., 20 \geq at%) + absence of stable compounds or complete immiscibility in the solid state
4. Isomorphous solid solution in some binaries + large terminal solubility in most edge binaries (e.g., 20 \geq at%) + compounds that are not too stable + absence of complete immiscibility in the solid state
5. Intermediate solid solution phases with wide compositional homogeneity in the middle of phase diagrams for the majority of the constituent binaries and ternaries

11.4 Empirical Parameters

To date, the most widely studied empirical parameters are ΔH_{mix} , δ , VEC, $\Delta\chi$, and Ω -parameter. Praveen et al. [54] studied the phase evolution in AlCoCrCuFe and CoCrCuFeNi HEAs after mechanical alloying and spark plasma sintering. The ΔH_{mix} (δ) values are -2.56 (4.99 %) kJ/mol and 3.20 (1.07 %) kJ/mol for AlCoCrCuFe and CoCrCuFeNi, respectively. They concluded that configurational entropy is not sufficient to suppress the formation of Cu-rich FCC and σ phases, and they emphasized the role of enthalpy of mixing in analyzing phase stability of HEAs. Singh and Subramaniam [55] studied phase formation in CoFeNi, CrFeNi, CoCrFeNi, CuCoFeNi, AlCrFeNi, and AlCuCoFeNi after annealing 24 h at 850°C and found that only FCC solid solution forms in CoFeNi and CoCrFeNi, while more than one phase appear in other alloys. They concluded that ΔH_{mix} and δ can be thought of as the most important parameters determining the formation of disordered solid solutions, while the role of Ω -parameter is not clear in their examples.

Very recently, Gao et al. [39] studied these empirical parameters and thermodynamic properties for 16 refractory HEAs. The thermodynamic properties were calculated using TCNI7 database via CALPHAD method. Figure 11.6 compares $\Delta H_{\text{mix}}^{\text{liq}}$, $\Delta H_{\text{mix}}^{\text{BCC}}$, and Ω -parameter using the Miedema model via the Takeuchi table

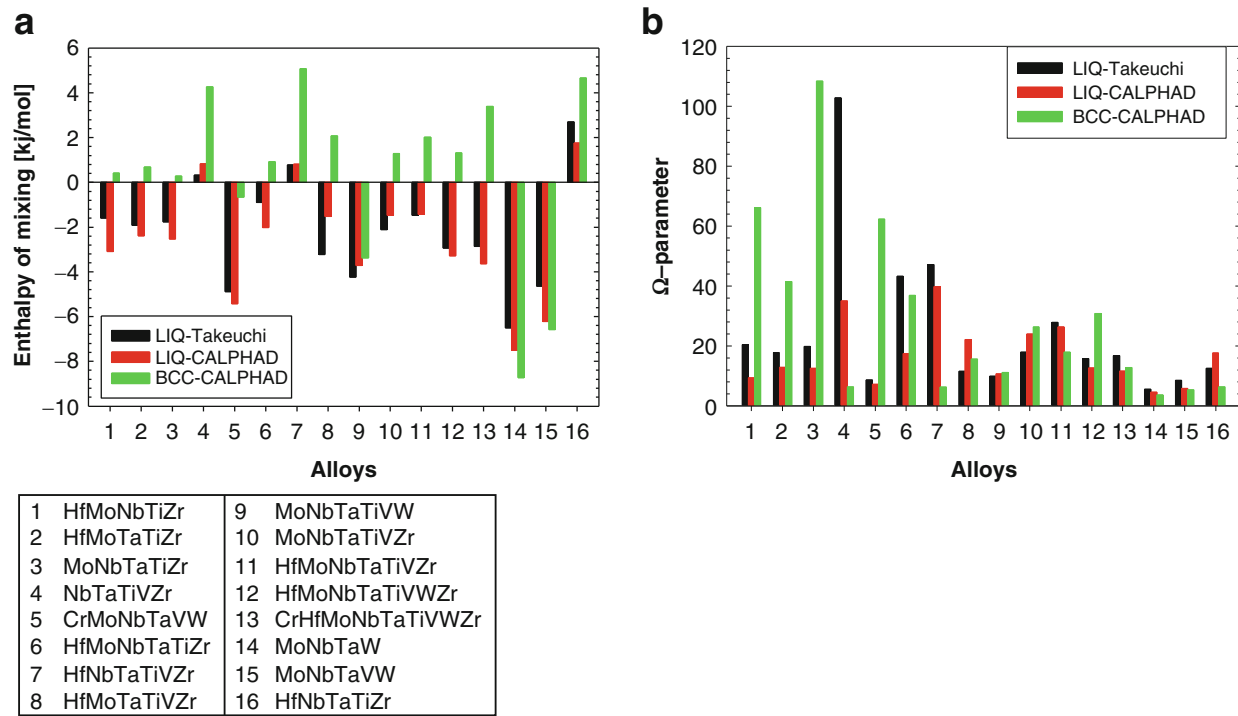


Fig. 11.6 Comparison in (a) enthalpy of mixing, and (b) Ω -parameter for the liquid and BCC phases for 16 equimolar refractory alloys [39]. Both the empirical data taken from Takeuchi table [56] and CALPHAD modeling are shown [39]

[56] and CALPHAD prediction. Overall, the agreement in $\Delta H_{\text{mix}}^{\text{liq}}$ is very good using the Takeuchi table [56] and CALPHAD, yielding negative values except for NbTaTiVZr, HfNbTaTiVZr, and HfNbTaTiZr, where the HCP metals constitute ≥ 50 at%. However, both the sign and absolute value of $\Delta H_{\text{mix}}^{\text{BCC}}$ are not necessarily in accord with $\Delta H_{\text{mix}}^{\text{liq}}$: For example, nine alloys exhibit opposite sign while seven alloys show significant contrast in their absolute values. Nonetheless, both Miedema model and CALPHAD calculations predict that MoNbTaW possesses the most negative values of both $\Delta H_{\text{mix}}^{\text{liq}}$ and $\Delta H_{\text{mix}}^{\text{BCC}}$. HfNbTaTiZr is predicted to have the most positive $\Delta H_{\text{mix}}^{\text{liq}}$, while HfNbTaTiVZr has the most positive $\Delta H_{\text{mix}}^{\text{BCC}}$.

The calculated Ω -parameters (Fig. 11.6b) are all relatively large (e.g., $\Omega \geq 4.5$ if $\Delta H_{\text{mix}}^{\text{liq}}$ is used, and $\Omega \geq 3.6$ if $\Delta H_{\text{mix}}^{\text{BCC}}$ is used), and surprisingly multiphase compositions of HfMoNbTaTiVZr, HfMoNbTaTiVWZr, and CrHfMoNb-TaTiVWZr show larger values than MoNbTaW, which has the lowest Ω -parameter because it has the most negative enthalpy of mixing. Furthermore, Ω -parameter shows much more pronounced contrast between liquid and BCC phases for several alloys. In short, the Ω -parameter does not differentiate single-phase HEAs from multiphase HEAs at least in this set of alloys, although it exhibits better function in prior studies to separate disordered solid solution from composites and bulk metallic glasses [4, 19].

The relationships of $\Delta H_{\text{mix}}^{\text{liq}}$, Ω , and $\Delta \chi$ with respect to δ for all sixteen alloys are shown in Fig. 11.7. Single-phase BCC solid solution is predicted and/or experimentally verified in all alloys except HfMoNbTaTiVZr, HfMoNbTaTiVWZr, and CrHfMoNbTaTiVWZr. However, these plots cannot clearly separate these three

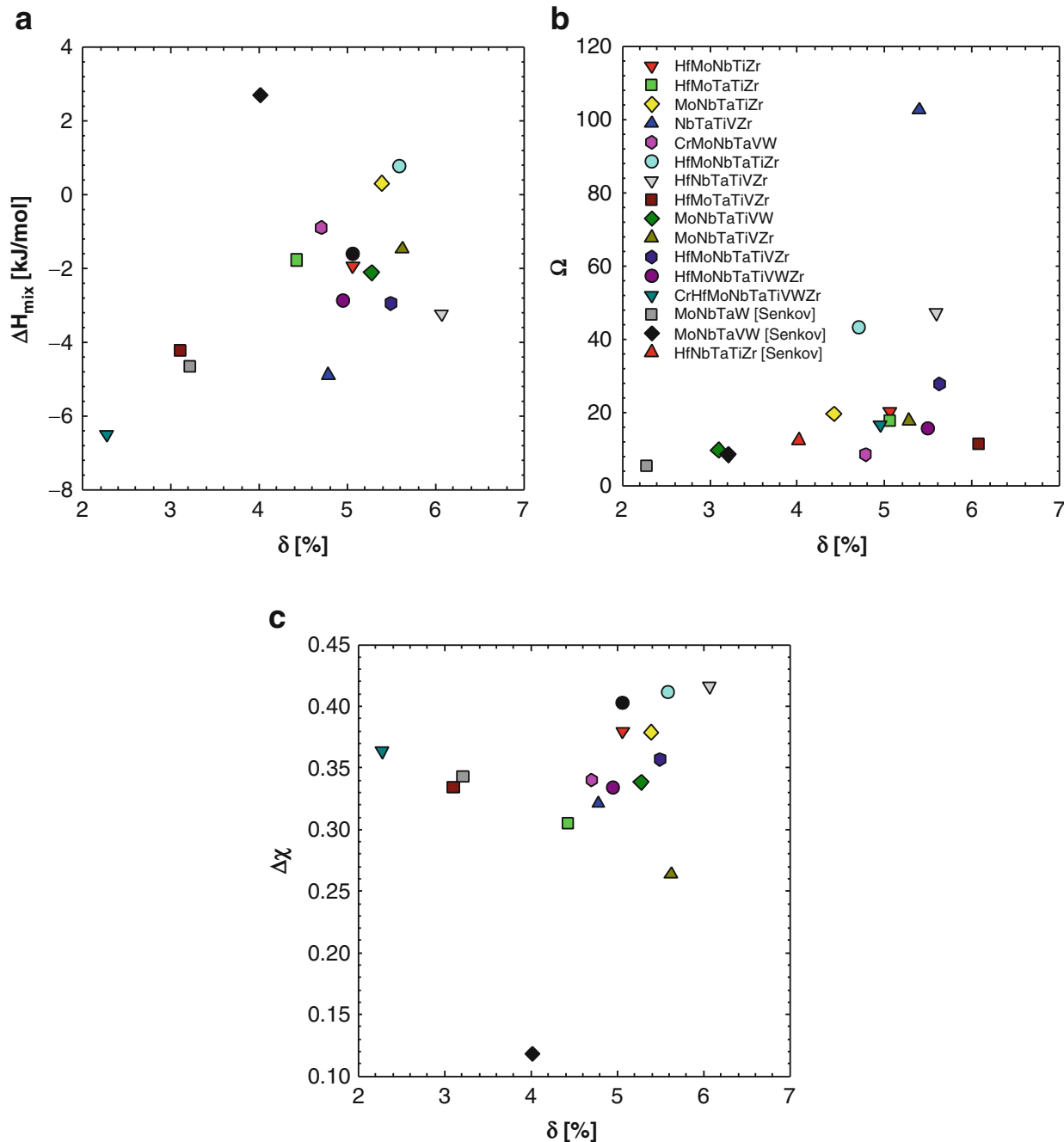
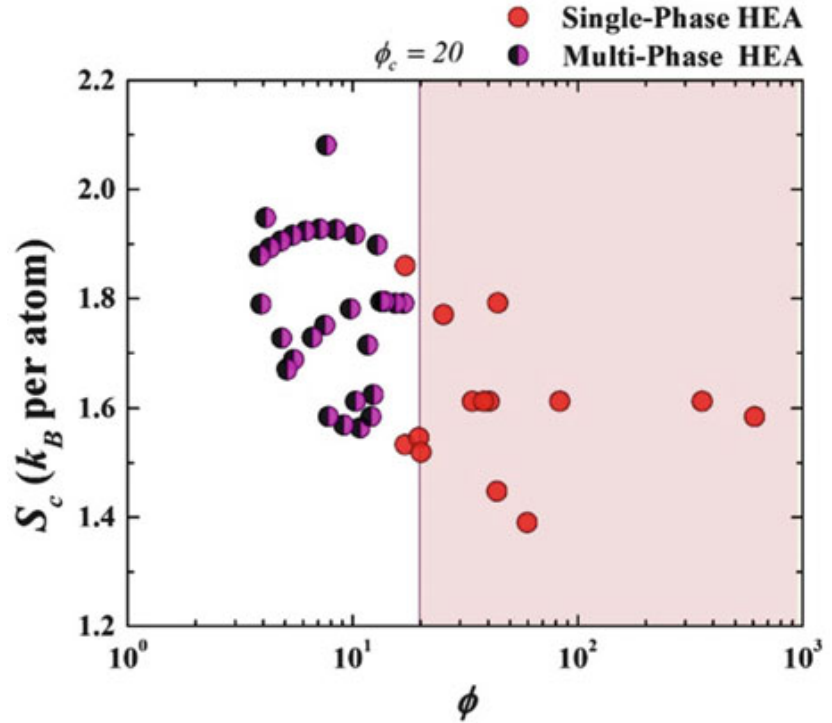


Fig. 11.7 Calculated empirical parameters: (a) $\Delta H_{\text{mix}}^{\text{liq}}$ from Miedema model, (b) Ω , and (c) $\Delta \chi$ with respect to δ [39]. Note that single-phase BCC solid solution is predicted and/or experimentally verified in all alloys except HfMoNbTaTiVZr, HfMoNbTaTiVWZr, and CrHfMoNbTaTiVWZr

multiphase alloys from the rest of the 13 solid solution alloys. This result together with prior studies [47, 54, 55] demonstrate that (1) configurational entropy does not always dominate and (2) these existing empirical parameters are not conclusive in terms of disordered solid solution formation.

It is worth mentioning two newly proposed parameters may be of importance in HEA design, a single-parameter (ϕ) [6] and intrinsic residual strain model via the root mean square (RMS) residual strain $\langle \epsilon^2 \rangle^{1/2}$ [5]. These two parameters nicely separate the single-phase HEAs from multiphase alloys. The single-parameter ϕ was originally defined by Ye et al. [6] as

Fig. 11.8 The plot of configurational entropy (S_c) versus ϕ for single-phase and multiphase HEAs [6]



$$\phi = \frac{-R \sum_{i=1}^N x_i \ln x_i - \left| \sum_{i \neq j} 4H_{ij}x_i x_j \right| / T_m}{|S_E|} \quad (11.4)$$

where N is the total number of components in the solid solution, x_i (x_j) is the mole fraction of component i (j), R is the ideal gas constant, T_m is the estimated melting point, H_{ij} is the enthalpy of mixing in liquid at equimolar composition estimated using Miedema model [56], and S_E is the excess entropy estimated using a hard ball model that considers overall packing efficiency as a function of composition, atomic diameter, and number density [57]. The ϕ -parameter that combines ideal configurational entropy, excess entropy, and enthalpy of mixing nicely separates single-phase HEAs from multiphase alloys, as shown in Fig. 11.8. The main difference between the ϕ -parameter [6] and the Ω -parameter [4, 19] lies in that the former considers excess entropy. It should be pointed out that the excess entropy value and accordingly ϕ -parameter may vary depending on the model used, and the readers can refer to Chaps. 8, 10, and 12 for guidance on obtaining the excess entropy using CALPHAD and DFT methods.

The models used to calculate the RMS residual strain $\langle \varepsilon^2 \rangle^{1/2}$ are detailed in Reference [5] and will not be repeated here. Figure 11.9 shows that the single-phase HEAs, multiphase alloys, and amorphous alloys are nicely separated by RMS residual strain. Single-phase HEAs are favored when $\langle \varepsilon^2 \rangle^{1/2}$ is less than 0.05, while amorphous alloys form when $\langle \varepsilon^2 \rangle^{1/2}$ is greater than 0.08. Multiphase alloys form in between these values.

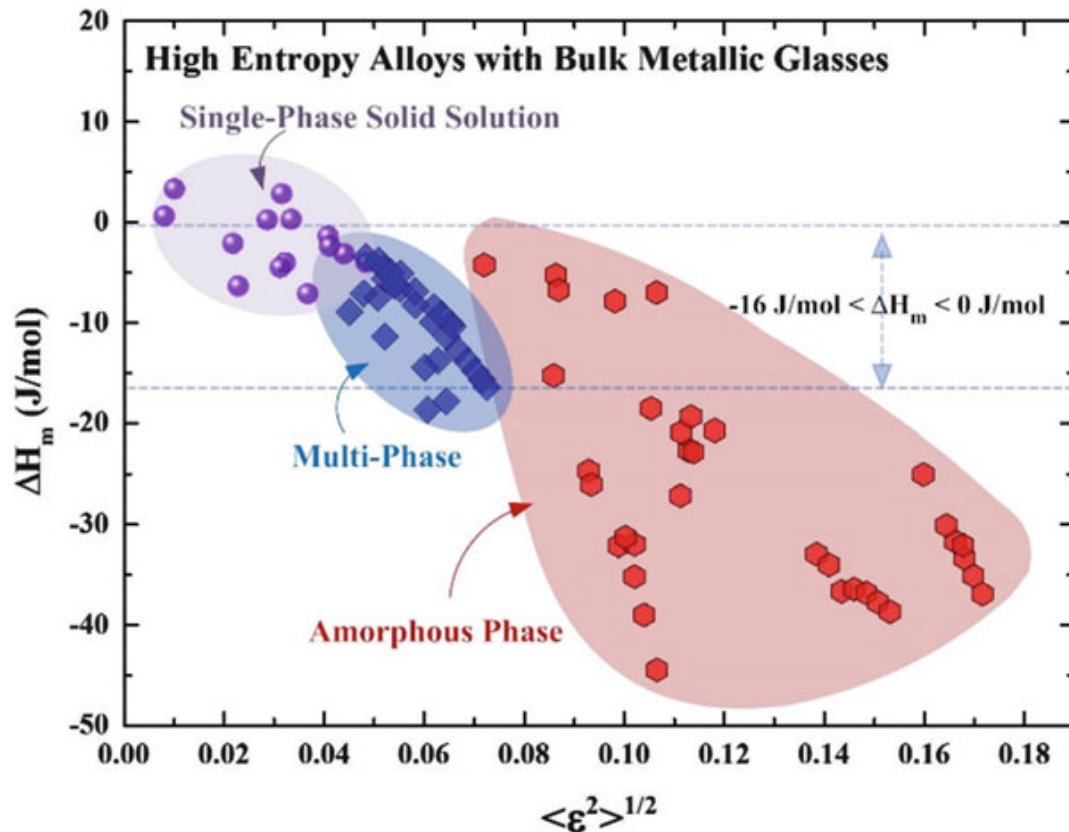


Fig. 11.9 The plot of the heat of mixing versus the root mean square residual strain for single-phase HEAs, multiphase alloys, and amorphous alloys [5]

11.5 DFT Calculations

The empirical rules use the enthalpy of mixing of the liquid phase, and thus questions arise: How will the enthalpy of formation of HEAs vary with respect to their crystal structures? How will this in turn impact those existing empirical rules? Using the special quasi-random structure (SQS) to represent the solid solution (details are provided in Chap. 10), the enthalpy of formation (ΔH_f) of representative equimolar single-phase HEAs as well as five multiphase compositions studied by Otto et al. [47] were calculated. The results are shown in Fig. 11.10. For those single-phase HEAs, the FCC and HCP HEAs have positive ΔH_f , while ΔH_f varies between -8 and $+8$ kJ/mol for BCC HEAs. Regarding the atomic size difference (δ), it is the smallest for FCC alloys ($\leq 1\%$). Alternatively, it varies from 1 to 4% for HCP and from 2 to 4% for BCC alloys.

As for the composite alloys, CoCrCuFeMn has a very large positive ΔH_f of $+16$ kJ/mol, while CrFeMnNiTi has slightly larger δ of 6.2% . On the other hand, the other three composites (CoFeMnNiV, CoCrMnNiV, and CoFeMnMoNi) have ΔH_f and δ values that are similar to those single-phase HEAs, and they satisfy the empirical ΔH - δ rules. Binary phase diagram information [24] reveals that V forms very stable σ phase in Co-V, Fe-V, Mn-V, and Ni-V systems. Consequently, presence of σ phase in an FCC matrix in CoFeMnNiV was observed even after annealing at 1000°C for 3 days. Apparently for these three composite alloys, the

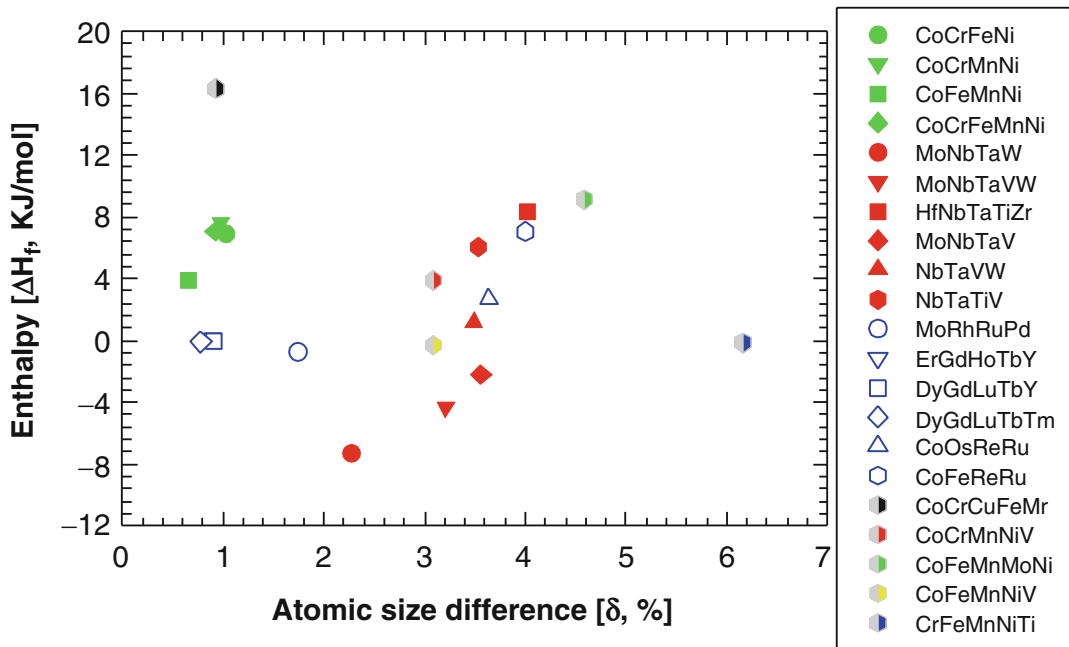


Fig. 11.10 DFT calculated enthalpy of formation of various single-phase HEAs in FCC (green-filled symbols) [2, 7, 9, 10], BCC (red-filled symbols) [12, 13, 17], and HCP (blue open symbols) [25] structures and five alloys that exhibit more than one phase (hybrid-filled symbols)

enthalpy of the competing compound phases outweighs the configurational entropy of the solid solution phase.

In short, even with accurate enthalpy data from DFT calculations, the ΔH - δ rule [34] does not always work especially for systems where very stable intermetallic compounds form in the majority of the edge binaries. Apparently, more strict screening rules are required, which involve the competing phases. Computational identification of stable compounds in 4-, 5-, and higher-order systems through DFT calculations is computationally formidable [58–61], and including the temperature effect will make the computation even more difficult (see Chap. 8 for details). In order to circumvent the computing difficulty, Troparevsky et al. [30] proposed using the most stable binary compound predicted at $T = 0$ K to represent the competing intermetallic phase and argued that equimolar single-phase HEA would form if the following criterion is satisfied:

$$-RT_{\text{crit}} \sum_{i=1}^N x_i \ln x_i \geq |\{H_{ij}\}|_{\max} \quad (11.5)$$

where T_{crit} refers to a critical temperature that can be set according to target applications, e.g., $T_{\text{crit}} = (0.55 \sim 0.6)T_m$ (where T_m is the estimated melting point of the alloy). $|\{H_{ij}\}|_{\max}$ refers to the absolute enthalpy value of the most stable binary compound in the system. Troparevsky [30] applied this model to those six alloys studied by Otto et al. [47] and found that only CoCrFeMnNi satisfies Eq. (11.5), forming single-phase solid solution, while the other five alloys do not comply with Eq. (11.5) and multiple phases form as a result (see Fig. 11.11). They further applied this model as a screening tool and suggested a series of new

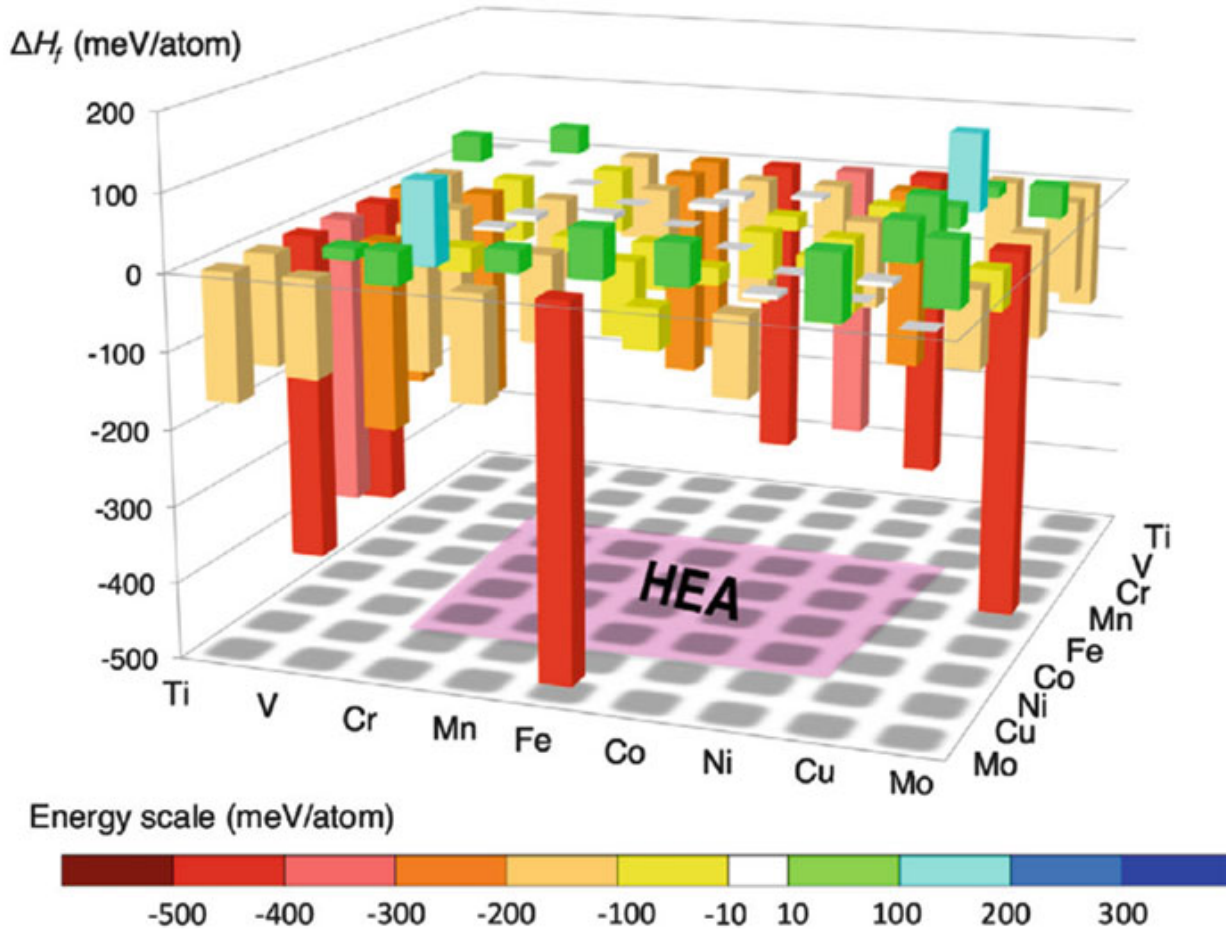


Fig. 11.11 Graphical representation [30] of the enthalpies of formation of the binary compounds from DFT calculations for the alloys studied in Ref. [47]. Marked “HEA” represents CoCrFeMnNi

single-phase HEA compositions in five to seven component systems as compiled in Table 11.2.

This approach allows straightforward computer screening, since phase stability of all the binary transition metal binary systems at zero temperature have been studied using DFT methods and the enthalpy data of binary compounds are available in literature. However, a noticeable drawback of this approach is that it severely underestimates the total number of possible equimolar single-phase HEA compositions. For example, those equimolar compositions containing Al and Ti or Al and Nb that are experimentally verified in Table 11.1 do not satisfy Eq. 11.5. Since the most stable Al-Ti binary compound has an enthalpy of formation of -428 meV/at [30], it would require an equimolar alloy of 50 components at $T \geq 1000^\circ\text{C}$ in order to compensate for the enthalpy effect! In addition, the model used does not predict the crystal structure of those compositions that satisfy Eq. (11.5), and thus, additional computational work is still required to determine the phase stability of each composition with respect to FCC, BCC, and HCP structures.

Furthermore, discrepancy has been observed in phase formation in several quinary BCC composition between model prediction by Troparevsky et al. [30] and CALPHAD prediction using TCNI7 database. CALPHAD calculations predict multiphase formation in MoNbTaWZr and MoNbTaVZr and single-phase solid

solution formation in HfMoNbTaW, HfMoNbTaV, and HfMoNbTaTi. However, Troparevsky et al. [30] predicted single BCC phase formation in the former two alloys and multiple phase formation in the latter three alloys. As a result, these five compositions are not listed in Table 11.2, and future experimental verification is needed to clarify the discrepancy.

11.6 AIMD Simulations

Identifying all the competing intermetallic phases against the solid solution phase in a multicomponent system is a daunting task if the phase diagram is not available. For example, in Chap. 8, Widom illustrates a DFT approach to predict phase stability of three quaternary refractory HEA systems [58–60]. The tendency to form intermetallic compounds during solidification is strongly correlated to the interatomic bond strength; i.e., the stronger the bond, the greater is the tendency to form compounds. Computing the bond strength of all possible compounds in a HEA system is not trivial, since they are crystal structure dependent. However, AIMD simulations in the liquid state can reveal useful information about the preferred interatomic bonding that may impact formation of disordered solid solution during solidification [3, 7, 62] while tremendously reducing computational effort. Previous AIMD simulations [3, 7, 62] show that preferred bond pairs of AlNi, CrFe, and CuCu in liquid Al_{1.25}CoCrCuFeNi may serve as precursors to nucleating B2, BCC, and FCC phases, respectively, during solidification. By comparing the partial pair distribution function (PDF) among single-phase HEAs, multiphase HEAs, and high-entropy bulk metallic glasses, Zhang et al. [3, 7, 62] proposed that a liquid structure that lacks strong elemental segregation, or potent short-range order, will promote the formation of disordered solid solutions during solidification. Another significant advantage of AIMD simulations is that there is no need for developing empirical interaction potentials compared to classical MD simulations.

Previously, Gao and coworkers ran AIMD simulations on single-phase solid solution HEAs (e.g., HfNbTaTiZr [3, 7], HfNbTaTiVZr [22], GdDyLuTbY [8], CoOsReRu [8], and MoPdRhRu [8]), multiphase alloy Al_{1.3}CoCrCuFeNi [3, 7, 62], and high-entropy bulk metallic glass-forming alloys (i.e., CuNiPPdPt [3, 7] and AlErDyNiTb, CuHfNiTiZr, and BeCuNiTiZr (see Chap. 13)). All the AIMD simulations were performed using acronym of Vienna Ab Initio Simulation Package (VASP) in a canonical ensemble, i.e., constant mole, volume, and temperature, with atomic-configuration relaxation and temperature controlled by a Nose-Hoover thermostat [63]. PAW potentials [64] and the revised Perdew-Burke-Ernzerhof [65] gradient approximation to the exchange-correlation functional were used.

The partial PDF gives information about the probability of interatomic bond formation by measuring the intensity of near-neighbor pairs against the total random distribution. Partial PDF (g_{ab}) was calculated using

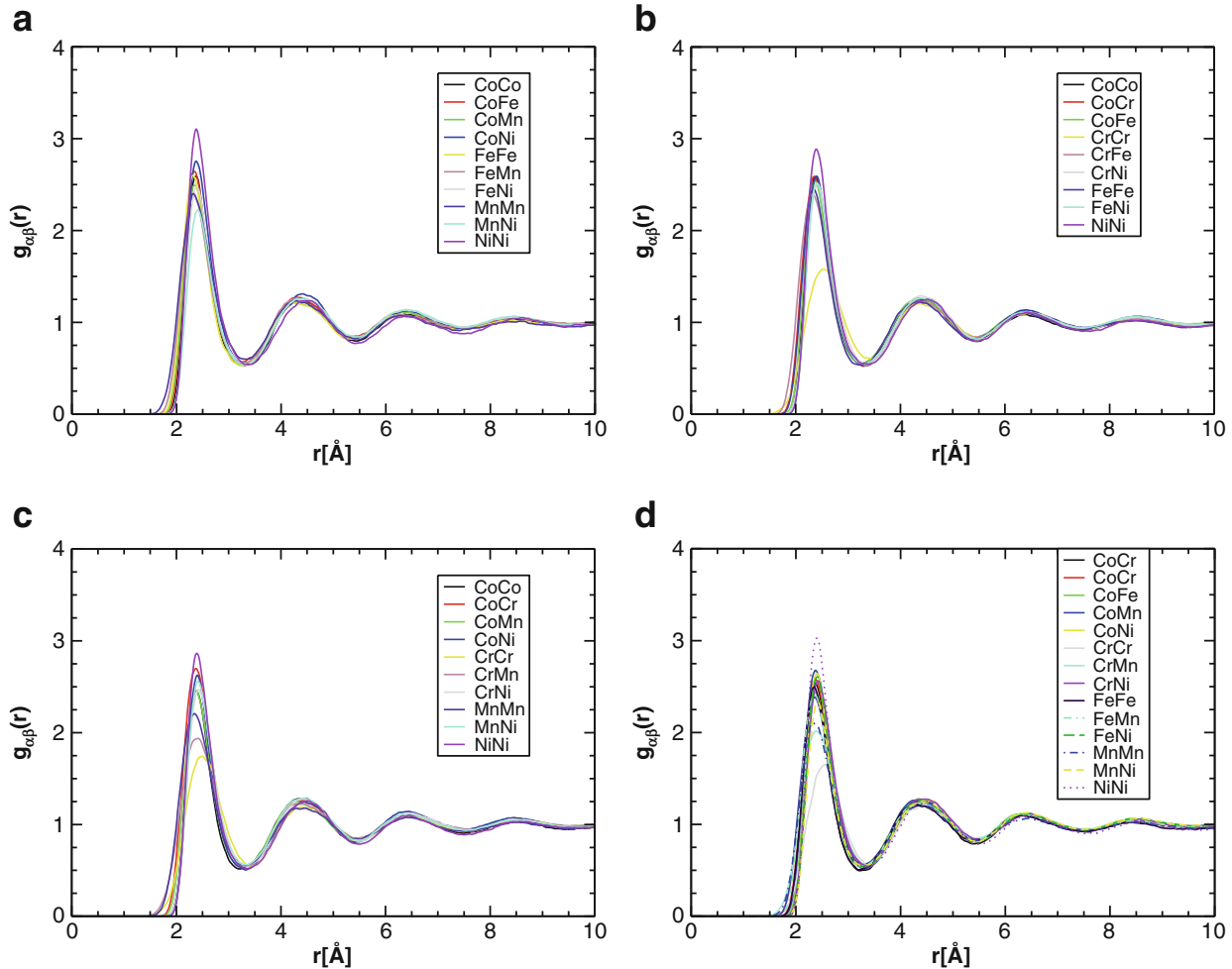


Fig. 11.12 AIMD simulated partial PDF of FCC HEAs: **(a)** CoFeMnNi, **(b)** CoCrFeNi, **(c)** CoCrMnNi, and **(d)** CoCrFeMnNi at $T = 1800\text{ }^{\circ}\text{C}$

$$g_{ab}(r) = \frac{V}{N_a N_b} \frac{1}{4\pi r^2} \sum_{i=1}^{N_a} \sum_{j=1}^{N_b} \langle \delta(|r_{ij}| - r) \rangle \quad (11.6)$$

where V is the volume of the super cell, N_a and N_b are the number of element a and b, $|r_{ij}|$ is the distance between element a and b, and the bracket $\langle \rangle$ denotes the time average of different configurations.

The partial PDF of four FCC HEAs in liquid at $1800\text{ }^{\circ}\text{C}$ is shown in Fig. 11.12. The peak intensity of the first-nearest-neighbor (FNN) pairs are all comparable except CrCr pair. That the CrCr pair has the lowest peak intensity indicates that Cr prefers to bond with other elements rather than itself. In other words, Cr prefers not to segregate in the liquid, and this is consistent with the atomic structures in CoCrFeNi and CoCrFeMnNi in the solid state as predicted using DFT methods (see Chap. 10 for details). The NiNi pair has slightly higher peak intensity than other pairs (Fig. 11.12).

The partial PDFs of two BCC HEAs (i.e., MoNbTaVW and HfNbTaTiZr) in liquid are shown in Fig. 11.13. For MoNbTaVW, the MoTa and TaW pairs have slightly higher FNN peak intensity than the other. For HfNbTaTiZr, the FNN peak

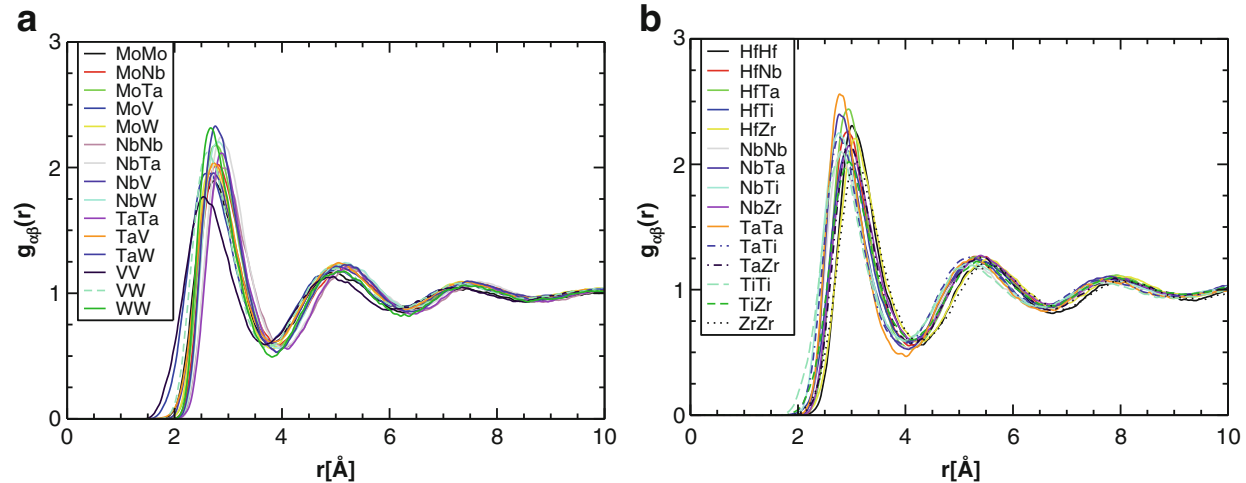


Fig. 11.13 AIMD-simulated partial correlation functions of BCC HEAs: **(a)** MoNbTaVW at $T = 3100\text{ }^{\circ}\text{C}$ and **(b)** HfNbTaTiZr at $T = 2500\text{ }^{\circ}\text{C}$

intensities are comparable for all pairs, although the intensity for TaTa, HfTa, and NbTa pairs are slightly higher than the other pairs (Fig. 11.13).

Figure 11.14 compares the partial PDFs of three representative HCP HEAs, namely DyGdLuTbY, CoOsReRu, and MoPdRhRu, in liquid. Both DyGdLuTbY and CoOsReRu alloys exhibit isomorphous HCP solid solution in their constituent binary phase diagrams. As expected, all the partial PDFs for DyGdLuTbY have little variation in the FNN peak intensity and pair distance. As for CoOsReRu, the FNN peak intensities seem very uniform except that g_{CoCo} and g_{ReRe} are slightly lower. MoPdRhRu comprises transition metal elements that form intermediate HCP phases with large compositional homogeneity in the middle of Mo-M ($\text{M} = \text{Pd}, \text{Rh}, \text{Ru}$) binaries. The FNN peak intensities of partial PDFs of liquid MoPdRhRu are also comparable for all pairs except the MoMo pair. The peak value of g_{MoMo} is noticeably lower than the other pairs, suggesting that Mo prefers to bond with Pd, Rh, or Ru rather than itself, which is consistent with the corresponding binary phase diagrams. The AIMD simulation results suggest the lack of strong chemical order or segregation in DyGdLuTbY and CoOsReRu, while Mo prefers to bond with other elements in MoPdRhRu (Fig. 11.14).

In contrast to the aforementioned partial PDFs for single-phase HEAs, noticeable preference in pair correlations can be seen in AlCoCrFeNi and $\text{Al}_{1.25}\text{CoCrCuFeNi}$ at $1800\text{ }^{\circ}\text{C}$ as shown in Fig. 11.15. For AlCoCrFeNi, the most preferred pair is AlNi followed by AlCo and CrFe. The least-favored interaction is the CrNi pair followed by the FeNi and AlAl pairs. For $\text{Al}_{1.25}\text{CoCrCuFeNi}$, the preferred pair correlations are CrFe, AlNi, and CuCu, and the least favored one is CrCu pair followed by the CuFe and AlAl pairs. These results suggest the existence of preferred short-range ordering of AlNi, CoCr, and CrFe pairs in the liquid for both alloys, while Cu has the strong tendency for segregation in $\text{Al}_{1.25}\text{CoCrCuFeNi}$. These predicted structural features at the atomic scale in the liquid are consistent with experimental observation of formation of B2-NiAl [62, 66] and (Cr-Co-Fe)-rich BCC phase [62, 67] during solidification in both alloys and Cu-rich FCC

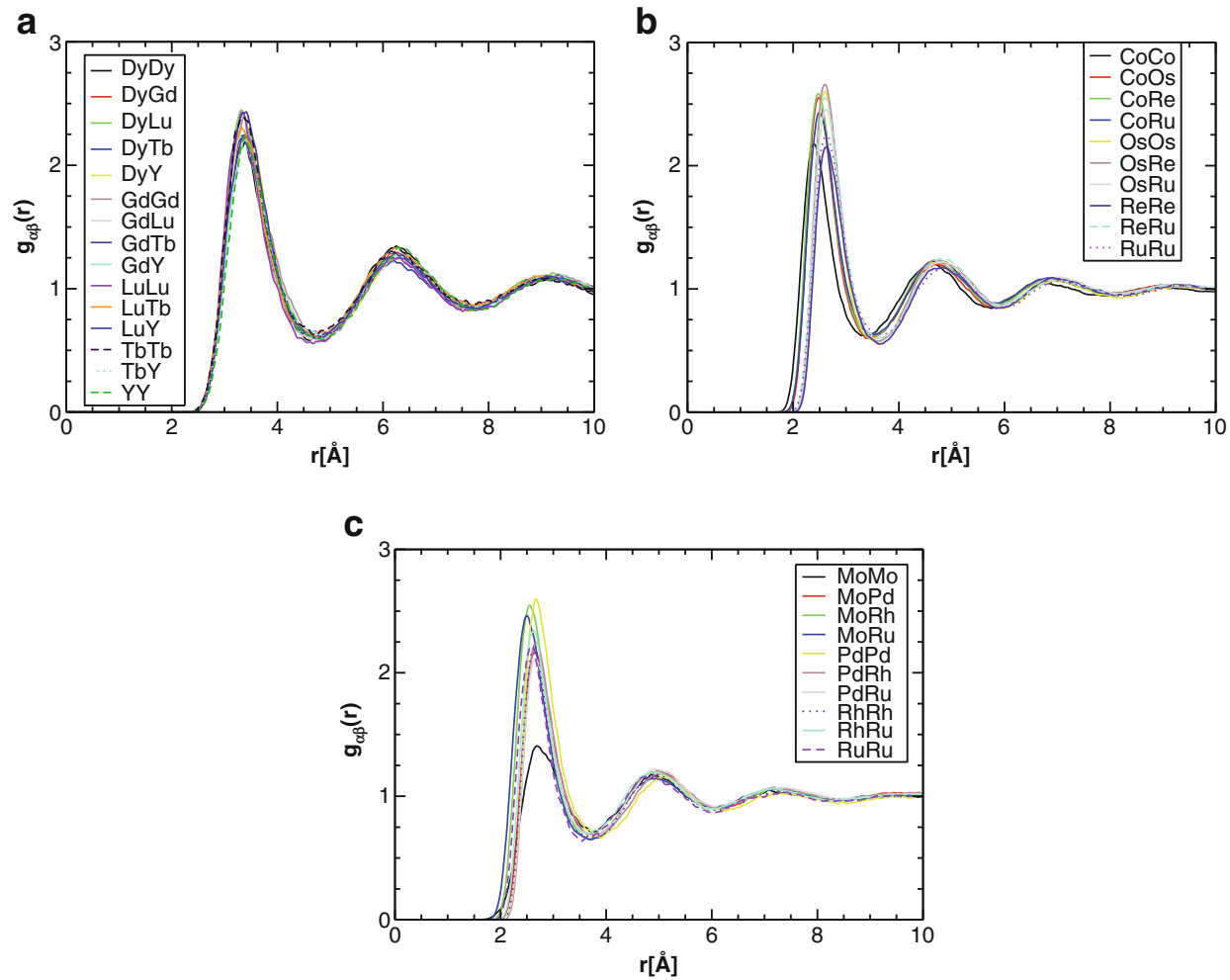


Fig. 11.14 Partial PDFs predicted from AIMD simulations for (a) GdDyLuTbY at 1800 °C, (b) CoOsReRu at 2800 °C, and (c) MoPdRhRu at 2800 °C [8]

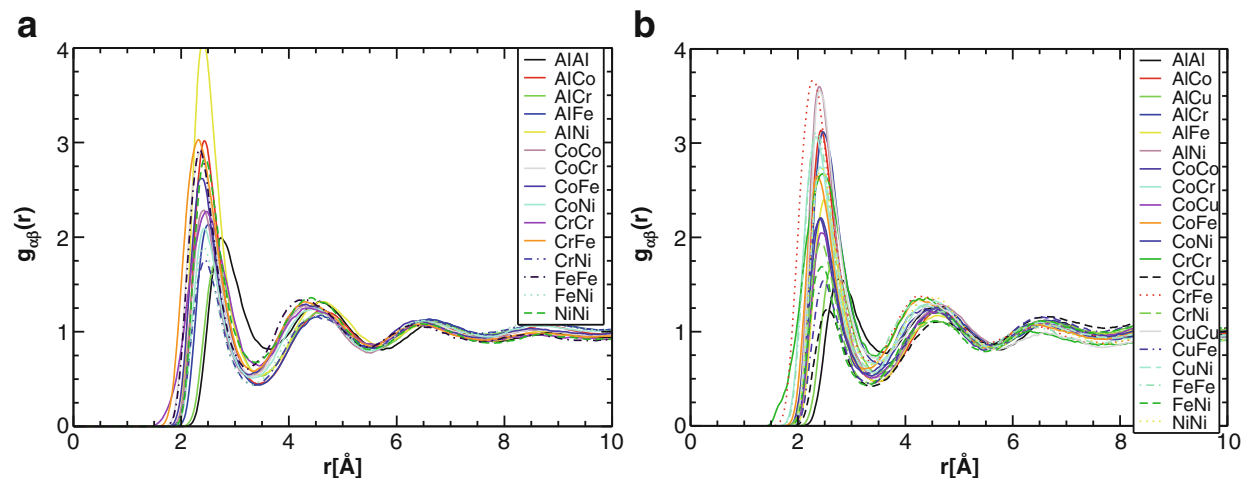


Fig. 11.15 AIMD simulated partial PDFs of (a) AlCoCrFeNi and (b) Al_{1.25}CoCrCuFeNi at $T = 1800$ °C

phases [62, 66, 68] for Al_{1.25}CoCrCuFeNi. An earlier experimental study by Tong et al. [68] also confirmed Cu segregation in all seven Al_xCoCrCuFeNi ($x \leq 3$) HEAs studied, showing that the Cu content can be as high as 78.5 at% in the interdendritic regions in the as-solidified state (Fig. 11.15).

11.7 Summary and Outlook

This chapter presents various methodologies that can be used to design single-phase HEAs, including CALPHAD modeling, phase diagram inspection, empirical parameters, DFT calculation, and AIMD simulation. Existing equimolar single-phase HEAs are reviewed and new compositions are suggested using these methodologies. Despite their apparent difference in length scale and approach, these five methodologies point to some common guidelines in HEA design. Diminishing enthalpy of mixing (i.e., close to zero), low atomic size difference, high configurational entropy ($\geq 1.5R$), and the lack of very stable intermetallic compounds in the majority of the binaries favor formation of disordered solid solution phases in a multicomponent alloy system. However, diminishing enthalpy of mixing in liquid does not necessarily accompany absence of very stable intermetallic compounds, and this basically explains why these existing empirical rules (involving ΔS , ΔH , δ , $\Delta\chi$, and Ω -parameter) may not always work. However, the recently proposed single ϕ -parameter and the root mean square residual strain show great promise in separating single-phase HEAs from multiphase alloys and bulk metallic glasses and are worth further exploiting using more physically grounded methods such as DFT.

The five methodologies addressed in this chapter have their own strengths and weaknesses. CALPHAD modeling can be regarded as the most direct method for alloy design, since it involves global minimization of Gibbs free energy of the system as a function of temperature and composition, but it suffers from insufficiently reliable databases that covers all edge binaries and ternaries for HEA systems. Inspection of experimental binary and ternary phase diagrams can provide useful guidance on proper combination of elements in forming solid solutions and is a powerful screening tool that looks for isomorphous solid solution, large terminal solubility, and intermediate phases of large homogeneity range. Some striking examples include the large number of single HCP phase (974) HEAs in Dy-Er-Gd-Ho-Lu-Sc-Sm-Tb-Tm-Y system and single BCC phase (64) HEAs in Mo-Nb-Re-Ta-Ti-V-W system in equimolar composition. However, it is not known exactly how the edge binaries/ternaries will extend into higher-order systems or whether there are other possible intermetallic compounds in higher-order systems. To date there is only a fraction of ternary phase diagrams that have been experimentally studied.

The DFT screening method through Eq. (11.5) makes screening possible using DFT-calculated enthalpy data of binary compounds available in literature, but this approach severely underestimates the total number of single-phase HEAs. More robust screening tools based on DFT methods are still to be developed. While AIMD simulations in the liquid can be used to indirectly correlate solid solution phase formation, the predicted atomic structures in the liquid are useful in quickly identifying the intensity of short-range order/segregation (if present in the system). Thus, AIMD simulations provide complementary information to supplement CALPHAD modeling and phase diagram inspection. Direct AIMD simulations of

phase transformations in the solid state remains as a significant hurdle due to computing limitation on the one hand and trapping of atoms at low-potential-energy sites on the other hand. As such, hybrid Monte Carlo/molecular dynamics simulations (see Chaps. 8 and 10 for details) may be very useful in quickly achieving the equilibrium state.

Acknowledgements M.C.G. acknowledges the financial support by the Cross-Cutting Technologies Program at the National Energy Technology Laboratory (NETL) – Strategic Center for Coal, managed by Robert Romanosky (Technology Manager) and Charles Miller (Technology Monitor). The Research was executed through NETL’s Office of Research and Development’s Innovative Process Technologies (IPT) Field Work Proposal under the RES contract DE-FE-0004000. M.C.G. wish to thank Mike Widom, Ömer N. Doğan, Shemgnin Guo, Junwei Qiao, Dan Sorescu, Jeffrey A. Hawk, Bryan Morreale, and David E. Alman for discussions on the HEA topic.

Disclaimer This chapter authored by M.C.G. was funded by the Department of Energy, National Energy Technology Laboratory, an agency of the United States Government, through a support contract with AECOM. Neither the United States Government nor any agency thereof, nor any of their employees, nor AECOM, nor any of their employees, makes any warranty, expressed or implied, or assumes any legal liability or responsibility for the accuracy, completeness, or usefulness of any information, apparatus, product, or process disclosed, or represents that its use would not infringe privately owned rights. Reference herein to any specific commercial product, process, or service by trade name, trademark, manufacturer, or otherwise, does not necessarily constitute or imply its endorsement, recommendation, or favoring by the United States Government or any agency thereof. The views and opinions of authors expressed herein do not necessarily state or reflect those of the United States Government or any agency thereof.

References

1. Yeh JW, Chen SK, Lin SJ, Gan JY, Chin TS, Shun TT, Tsau CH, Chang SY (2004) Nanostructured high-entropy alloys with multiple principal elements: novel alloy design concepts and outcomes. *Adv Eng Mat* 6(5):299–303. doi:[10.1002/adem.200300567](https://doi.org/10.1002/adem.200300567)
2. Cantor B, Chang ITH, Knight P, Vincent AJB (2004) Microstructural development in equiatomic multicomponent alloys. *Mat Sci Eng A* 375–377:213–218. doi:[10.1016/j.msea.2003.10.257](https://doi.org/10.1016/j.msea.2003.10.257)
3. Zhang Y, Zuo TT, Tang Z, Gao MC, Dahmen KA, Liaw PK, Lu ZP (2014) Microstructures and properties of high-entropy alloys. *Prog Mat Sci* 61:1–93. doi:[10.1016/j.pmatsci.2013.10.001](https://doi.org/10.1016/j.pmatsci.2013.10.001)
4. Zhang Y, Lu ZP, Ma SG, Liaw PK, Tang Z, Cheng YQ, Gao MC (2014) Guidelines in predicting phase formation of high-entropy alloys. *MRS Commun* 4(2):57–62. doi:[10.1557/mrc.2014.11](https://doi.org/10.1557/mrc.2014.11)
5. Ye YF, Liu CT, Yang Y (2015) A geometric model for intrinsic residual strain and phase stability in high entropy alloys. *Acta Mater* 94:152–161. doi:[10.1016/j.actamat.2015.04.051](https://doi.org/10.1016/j.actamat.2015.04.051)
6. Ye YF, Wang Q, Lu J, Liu CT, Yang Y (2015) Design of high entropy alloys: a single-parameter thermodynamic rule. *Scr Mater* 104:53–55. doi:[10.1016/j.scriptamat.2015.03.023](https://doi.org/10.1016/j.scriptamat.2015.03.023)
7. Gao MC, Alman DE (2013) Searching for next single-phase high-entropy alloy compositions. *Entropy* 15:4504–4519. doi:[10.3390/e15104504](https://doi.org/10.3390/e15104504)
8. Gao MC, Zhang B, Guo SM, Qiao JW, Hawk JA (2016) High-entropy alloys in hexagonal close packed structure. *Metall Mater Trans A* (in press). doi:[10.1007/s11661-015-3091-1](https://doi.org/10.1007/s11661-015-3091-1)
9. Lucas MS, Wilks GB, Mauger L, Munoz JA, Senkov ON, Michel E, Horwath J, Semiatin SL, Stone MB, Abernathy DL, Karapetrova E (2012) Absence of long-range chemical ordering in

- equimolar FeCoCrNi. *Appl Phys Lett* 100(25):251907–251904. doi:<http://dx.doi.org/10.1063/1.4730327>
- 10. Wu Z, Bei H, Otto F, Pharr GM, George EP (2014) Recovery, recrystallization, grain growth and phase stability of a family of FCC-structured multi-component equiatomic solid solution alloys. *Intermetallics* 46:131–140. doi:[10.1016/j.intermet.2013.10.024](https://doi.org/10.1016/j.intermet.2013.10.024)
 - 11. Lucas MS, Mauger L, Munoz JA, Xiao Y, Sheets AO, Semiatin SL, Horwath J, Turgut Z (2011) Magnetic and vibrational properties of high-entropy alloys. *J Appl Phys* 109(7) 07E307. doi:[10.1063/1.3538936](https://doi.org/10.1063/1.3538936)
 - 12. Senkov ON, Wilks GB, Miracle DB, Chuang CP, Liaw PK (2010) Refractory high-entropy alloys. *Intermetallics* 18(9):1758–1765. doi:[10.1016/j.intermet.2010.05.014](https://doi.org/10.1016/j.intermet.2010.05.014)
 - 13. Senkov ON, Wilks GB, Scott JM, Miracle DB (2011) Mechanical properties of Nb₂₅Mo₂₅Ta₂₅W₂₅ and V₂₀Nb₂₀Mo₂₀Ta₂₀W₂₀ refractory high entropy alloys. *Intermetallics* 19(5):698–706. doi:[10.1016/j.intermet.2011.01.004](https://doi.org/10.1016/j.intermet.2011.01.004)
 - 14. Yang X, Zhang Y, Liaw PK (2012) Microstructure and compressive properties of NbTiVTaAl_x high entropy alloys. *Iumrs International Conference in Asia* 36:292–298. doi:[10.1016/j.proeng.2012.03.043](https://doi.org/10.1016/j.proeng.2012.03.043)
 - 15. Senkov ON, Senkova SV, Miracle DB, Woodward C (2013) Mechanical properties of low-density, refractory multi-principal element alloys of the Cr-Nb-Ti-V-Zr system. *Mater Sci Eng A Struct Mater Prop Microstruct Proc* 565:51–62. doi:[10.1016/j.msea.2012.12.018](https://doi.org/10.1016/j.msea.2012.12.018)
 - 16. Wu YD, Cai YH, Wang T, Si JJ, Zhu J, Wang YD, Hui XD (2014) A refractory Hf₂₅Nb₂₅Ti₂₅Zr₂₅ high-entropy alloy with excellent structural stability and tensile properties. *Mater Lett* 130:277–280. doi:[10.1016/j.matlet.2014.05.134](https://doi.org/10.1016/j.matlet.2014.05.134)
 - 17. Senkov ON, Scott JM, Senkova SV, Miracle DB, Woodward CF (2011) Microstructure and room temperature properties of a high-entropy TaNbHfZrTi alloy. *J Alloys Compd* 509 (20):6043–6048. doi:[10.1016/j.jallcom.2011.02.171](https://doi.org/10.1016/j.jallcom.2011.02.171)
 - 18. Gorr B, Azim M, Christ HJ, Mueller T, Schliephake D, Heilmair M (2015) Phase equilibria, microstructure, and high temperature oxidation resistance of novel refractory high-entropy alloys. *J Alloys Compd* 624:270–278. doi:[10.1016/j.jallcom.2014.11.012](https://doi.org/10.1016/j.jallcom.2014.11.012)
 - 19. Zhang Y, Yang X, Liaw PK (2012) Alloy design and properties optimization of high-entropy alloys. *JOM* 64(7):830–838. doi:[10.1007/s11837-012-0366-5](https://doi.org/10.1007/s11837-012-0366-5)
 - 20. Bei H (2013) Multi-component solid solution alloys having high mixing entropy. USA Patent US 2013/0108502 A1, 2 May 2013
 - 21. Zhang B, Gao MC, Zhang Y, Guo SM (2016) Senary refractory high-entropy alloy Cr_xMoNbTaVW. *CALPHAD* 51:193–201
 - 22. Gao MC, Zhang B, Yang S, Guo SM (2016) Senary refractory high-entropy alloy HfNbTaTiVZr. *Metall Mater Trans A* (in press). doi:[10.1007/s11661-015-3105-z](https://doi.org/10.1007/s11661-015-3105-z)
 - 23. Zhang B, Gao MC, Zhang Y, Yang S, Guo SM (2015) Senary refractory high-entropy alloy MoNbTaTiVW. *Mat Sci Tech* 31:1207–1213. doi:[10.1179/1743284715Y.0000000031](https://doi.org/10.1179/1743284715Y.0000000031)
 - 24. Okamoto H (2000) Desk handbook: phase diagrams for binary alloys. ASM International, Materials Park, OH 44073
 - 25. Takeuchi A, Amiya K, Wada T, Yubuta K, Zhang W (2014) High-entropy alloys with hexagonal close-packed structure designed by equi-atomic alloy strategy and binary phase diagrams. *JOM* 66(10):1984–1992. doi:[10.1007/s11837-014-1085-x](https://doi.org/10.1007/s11837-014-1085-x)
 - 26. Feuerbacher M, Heidemann M, Thomas C (2014) Hexagonal high-entropy alloys. *Mat Res Lett*. doi:[10.1080/21663831.2014.951493](https://doi.org/10.1080/21663831.2014.951493)
 - 27. Youssefa KM, Zaddach AJ, Niu C, Irving DL, Koch CC (2015) A novel low-density, high-hardness, high-entropy alloy with close-packed single-phase nanocrystalline structures. *Mater Res Lett* 3(2):95–99. doi:<http://dx.doi.org/10.1080/21663831.2014.985855>
 - 28. Kozak R, Alla Sologubenko A, Steurer W (2014) Single-phase high-entropy alloys –an overview. *Z Kristallogr* 230(1):55–68. doi:[10.1515/zkri-2014-1739](https://doi.org/10.1515/zkri-2014-1739)
 - 29. Stepanov ND, Shaysultanov DG, Salishchev GA, Tikhonovsky MA (2015) Structure and mechanical properties of a light-weight AlNbTiV high entropy alloy. *Mater Lett* 142:153–155. doi:[10.1016/j.matlet.2014.11.162](https://doi.org/10.1016/j.matlet.2014.11.162)

30. Troparevsky MC, Morris JR, Kent PRC, Lupini AR, Stocks GM (2015) Criteria for predicting the formation of single-phase high-entropy alloys. *Phys Rev X* 5(1):011041. doi:[10.1103/PhysRevX.5.011041](https://doi.org/10.1103/PhysRevX.5.011041)
31. Paschoal JOA, Kleykamp H, Thummller F (1983) Phase-equilibria in the quaternary molybdenum-ruthenium-rhodium-palladium system. *Z Metallkd* 74(10):652–664
32. Feuerbacher M, Heidelmann M, Thomas C (2014) Hexagonal high-entropy alloys. *Mater Res Lett* 3:1–6. doi:[10.1080/21663831.2014.951493](https://doi.org/10.1080/21663831.2014.951493)
33. Yong L, Ma SG, Gao MC, Zhang C, Zhang T, Yang H, Wang Z, Qiao JW (2015) Tribological properties of AlCrCuFeNi₂ high-entropy alloy in different conditions. *Metall Mater Trans A* (in press). doi: [10.1007/s11661-016-3396-8](https://doi.org/10.1007/s11661-016-3396-8)
34. Zhang Y, Zhou YJ, Lin JP, Chen GL, Liaw PK (2008) Solid-solution phase formation rules for multi-component alloys. *Adv Eng Mat* 10(6):534–538. doi:[10.1002/adem.200700240](https://doi.org/10.1002/adem.200700240)
35. Guo S, Ng C, Lu J, Liu CT (2011) Effect of valence electron concentration on stability of fcc or bcc phase in high entropy alloys. *J Appl Phys* 109(10):103505. doi:[10.1063/1.3587228](https://doi.org/10.1063/1.3587228)
36. Poletti MG, Battezzati L (2014) Electronic and thermodynamic criteria for the occurrence of high entropy alloys in metallic systems. *Acta Mater* 75:297–306. doi:[10.1016/j.actamat.2014.04.033](https://doi.org/10.1016/j.actamat.2014.04.033)
37. Miedema AR, de Boer FR, Boom R (1977) Model predictions for the enthalpy of formation of transition metal alloys. *CALPHAD* 1(4):341–359. doi:[10.1016/0364-5916\(77\)90011-6](https://doi.org/10.1016/0364-5916(77)90011-6)
38. Yang X, Chen SY, Cotton JD, Zhang Y (2014) Phase stability of Low-density, multiprincipal component alloys containing aluminum, magnesium, and lithium. *JOM* 66(10):2009–2020. doi:[10.1007/s11837-014-1059-z](https://doi.org/10.1007/s11837-014-1059-z)
39. Gao MC, Carney CS, Doğan ÖN, Jablonksi PD, Hawk JA, Alman DE (2015) Design of refractory high-entropy alloys. *JOM* 67(11):2653–2669. doi:[10.1007/s11837-015-1617-z](https://doi.org/10.1007/s11837-015-1617-z)
40. Guo S, Ng C, Wang ZJ, Liu CT (2014) Solid solutioning in equiatomic alloys: limit set by topological instability. *J Alloys Compd* 583:410–413. doi:[10.1016/j.jallcom.2013.08.213](https://doi.org/10.1016/j.jallcom.2013.08.213)
41. Zhang F, Zhang C, Chen SL, Zhu J, Cao WS, Kattner UR (2014) An understanding of high entropy alloys from phase diagram calculations. *CALPHAD* 45:1–10
42. Zhang C, Zhang F, Chen SL, Cao WS (2012) Computational thermodynamics aided high-entropy alloy design. *JOM* 64(7):839–845. doi:[10.1007/s11837-012-0365-6](https://doi.org/10.1007/s11837-012-0365-6)
43. Senkov ON, Miller JD, Miracle DB, Woodward C (2015) Accelerated exploration of multi-principal element alloys with solid solution phases. *Nature Commun* 6(1–10):6529. doi:[10.1038/ncomms7529](https://doi.org/10.1038/ncomms7529)
44. Lu Y, Dong Y, Guo S, Jiang L, Kang H, Wang T, Wen B, Wang Z, Jie J, Cao Z, Ruan H, Li T (2014) A promising new class of high-temperature alloys: eutectic high-entropy alloys. *Sci Rep* 4:1–5. doi:[10.1038/srep06200](https://doi.org/10.1038/srep06200)
45. Liu S, Gao MC, Liaw PK, Zhang Y (2015) Microstructures and mechanical properties of AlxCrFeNiTi_{0.25} alloys. *J Alloys Compd* 619:610–615. doi:<http://dx.doi.org/10.1016/j.jallcom.2014.09.073>
46. Miracle DB, Miller JD, Senkov ON, Woodward C, Uchic MD, Tiley J (2014) Exploration and development of high entropy alloys for structural applications. *Entropy* 16:494–525
47. Otto F, Yang Y, Bei H, George EP (2013) Relative effects of enthalpy and entropy on the phase stability of equiatomic high-entropy alloys. *Acta Mater* 61:2628–2638. doi:[10.1016/j.actamat.2013.01.042](https://doi.org/10.1016/j.actamat.2013.01.042)
48. Pandat™ Thermodynamic Calculations and Kinetic Simulations. CompuTherm LLC, Madison, WI 53719, USA. <http://www.computherm.com>
49. Scheil E (1942) Comments on the layer crystal formation. *Z Metallkd* 34:70–72
50. Gulliver GH (1913) The quantitative effect of rapid cooling upon the constitution of binary alloys. *J Ins Met* 9:120–157
51. Middleburgh SC, King DM, Lumpkin GR (2015) Atomic scale modelling of hexagonal structured metallic fission product alloys. *R Soc Open Sci* 2:140292. doi:<http://dx.doi.org/10.1098/rsos.140292>

52. Cotton JD (2014) Forget entropy: an informatics approach to identifying useful complex alloy compositions, presentation at Compositionally complex alloys workshop, Munich, Germany, July 16–18, 2014
53. ASM Alloy Phase Diagram Database. <http://www1.asminternational.org/asmenterprise/apd/>
54. Praveen S, Murty BS, Kottada RS (2012) Alloying behavior in multi-component AlCoCrCuFe and NiCoCrCuFe high entropy alloys. *Mat Sci Eng A* 534:83–89. doi:[10.1016/j.msea.2011.11.044](https://doi.org/10.1016/j.msea.2011.11.044)
55. Singh AK, Subramaniam A (2014) On the formation of disordered solid solutions in multi-component alloys. *J Alloys Compd* 587:113–119. doi:[10.1016/j.jallcom.2013.10.133](https://doi.org/10.1016/j.jallcom.2013.10.133)
56. Takeuchi A, Inoue A (2005) Classification of bulk metallic glasses by atomic size difference, heat of mixing and period of constituent elements and its application to characterization of the main alloying element. *Mater Trans* 46(12):2817–2829. doi:[10.2320/matertrans.46.2817](https://doi.org/10.2320/matertrans.46.2817)
57. Ye YF, Wang Q, Lu J, Liu CT, Yang Y (2015) The generalized thermodynamic rule for phase selection in multicomponent alloys. *Intermetallics* 59:75–80. doi:[10.1016/j.intermet.2014.12.011](https://doi.org/10.1016/j.intermet.2014.12.011)
58. Mihalkovič M, Widom M (2004) Ab initio calculations of cohesive energies of Fe-based glass-forming alloys. *Phys Rev B* 70(14):144107. doi:[10.1103/PhysRevB.70.144107](https://doi.org/10.1103/PhysRevB.70.144107)
59. Widom M, Huhn WP, Maiti S, Steurer W (2014) Hybrid Monte Carlo/molecular dynamics simulation of a refractory metal high entropy alloy. *Metall Mater Trans A* 45A(1):196–200. doi:[10.1007/s11661-013-2000-8](https://doi.org/10.1007/s11661-013-2000-8)
60. Huhn WP, Widom M, Cheung AM, Shiflet GJ, Poon SJ, Lewandowski J (2014) First-principles calculation of elastic moduli of early-late transition metal alloys. *Phys Rev B* 89(10). doi:[10.1103/PhysRevB.89.104103](https://doi.org/10.1103/PhysRevB.89.104103)
61. Ganesh P, Widom M (2008) Ab initio simulations of geometrical frustration in supercooled liquid Fe and Fe-based metallic glass. *Phys Rev B* 77(1):014205. doi:[10.1103/PhysRevB.77.014205](https://doi.org/10.1103/PhysRevB.77.014205)
62. Santodonato LJ, Zhang Y, Feygenson M, Parish CM, Gao MC, Weber RJK, Neufeind JC, Tang Z, Liaw PK (2015) Deviation from high-entropy configurations in the atomic distributions of a multi-principal-element alloy. *Nature Commun* 6:5964. doi:[10.1038/ncomms6964](https://doi.org/10.1038/ncomms6964)
63. Nose S (1984) A unified formulation of the constant temperature molecular-dynamics methods. *J Chem Phys* 81(1):511–519
64. Blochl PE (1994) Projector augmented-wave method. *Phys Rev B* 50(24):17953. doi:<http://dx.doi.org/10.1103/PhysRevB.50.17953>
65. Perdew JP, Ruzsinszky A, Csonka GI, Vydrov OA, Scuseria GE, Constantin LA, Zhou XL, Burke K (2008) Restoring the density-gradient expansion for exchange in solids and surfaces. *Phys Rev Lett* 100(13):136406. doi:[10.1103/PhysRevLett.100.136406](https://doi.org/10.1103/PhysRevLett.100.136406)
66. Singh S, Wanderka N, Murty BS, Glatzel U, Banhart J (2011) Decomposition in multi-component AlCoCrCuFeNi high-entropy alloy. *Acta Mater* 59(1):182–190. doi:[10.1016/j.actamat.2010.09.023](https://doi.org/10.1016/j.actamat.2010.09.023)
67. Singh S, Wanderka N, Kiefer K, Siemensmeyer K, Banhart J (2011) Effect of decomposition of the Cr-Fe-Co rich phase of AlCoCrCuFeNi high entropy alloy on magnetic properties. *Ultramicroscopy* 111(6):619–622. doi:[10.1016/j.ultramic.2010.12.001](https://doi.org/10.1016/j.ultramic.2010.12.001)
68. Tong CJ, Chen YL, Chen SK, Yeh JW, Shun TT, Tsau CH, Lin SJ, Chang SY (2005) Microstructure characterization of $Al_xCoCrCuFeNi$ high-entropy alloy system with multiprincipal elements. *Metall Mat Trans A* 36A(4):881–893. doi:[10.1007/s11661-005-0283-0](https://doi.org/10.1007/s11661-005-0283-0)

Chapter 12

CALPHAD Modeling of High-Entropy Alloys

Chuan Zhang and Michael C. Gao

Abstract Phase diagrams are the key to understanding of high-entropy alloy formation. This chapter first presents the basics of CALPHAD (acronym of Calculation of Phase Diagrams) methodology and then details the procedures used in developing self-consistent thermodynamic databases tailored for HEA systems. A self-consistent thermodynamic database (PanHEA) has been developed for the Al-Co-Cr-Fe-Ni system that covers the complete compositional ranges for all its constituent binaries and ternaries, and it will be useful for future HEA design and processing optimization. HEA formation from the thermodynamic point of view is then illustrated for three HEA systems using TCNI7 database: FCC-forming Co-Cr-Fe-Mn-Ni, FCC- and BCC-forming Al-Co-Cr-Fe-Ni, and BCC-forming Mo-Nb-Ta-Ti-V-W systems. The FCC system shows large positive excess entropy while the BCC system shows small negative excess entropy, and these results are consistent with their vibrational entropies of mixing predicted from first-principle calculations presented in Chap. 10 “Applications of Special Quasi-random Structures to High-Entropy Alloys.” Addition of Al to CoCrFeNi stabilizes the BCC phase via the dominating enthalpy effect. The present study demonstrates that configurational entropy does not always dominate, and enthalpy and competing phases need to be considered in terms of phase stability. Applications of CALPHAD to high-entropy alloy design and microstructure development are then presented for the case of several alloys and satisfactory agreement between modeling calculations and experimental results is observed. Various isotherms and isopleths of the Al-Co-Cr-Fe-Ni system are predicted. Future perspectives on CALPHAD development including short-range ordering and kinetic database development pertaining to HEAs conclude this chapter.

Keywords Single phase • Multiphase • Enthalpy of mixing • Entropy of mixing • Gibbs energy of mixing • Excess entropy • CALPHAD • Phase diagrams

C. Zhang (✉)
CompuTherm, LLC, Madison, WI 53719, USA
e-mail: chuan.zhang@computherm.com

M.C. Gao
National Energy Technology Laboratory/AECOM, Albany, OR 97321, USA
e-mail: Michael.Gao@netl.doe.gov

- Thermodynamic databases • Kinetics • Phase transformations • Solidification
- Disordered solid solution • Solubility • Face-centered cubic (FCC) • Hexagonal close packed (HCP) • Body-centered cubic (BCC) • Phase stability • Alloy design
- High-entropy alloys (HEAs)

12.1 Introduction

The core of the high-entropy alloy (HEA) [1, 2] concept is the ideal configurational entropy maximization in solid solution alloys with multi-principal elements in equimolar composition. This is in contrast to the traditional alloy design, which is usually based on one or at most two key elements. However, to date the vast majority of alloys with multi-principal elements reported in the literature contain multiple phases, while only those carefully chosen compositions can form single-phase solid solution [3]. Arbitrary mixing of elements from the periodic table does not render formation of single-phase solid solution but composite structures. For example, Cantor et al. [4] investigated 20- and 16-component alloys in equimolar ratios and found that both alloys contained multiple phases and were brittle in the as-cast ingot and melt-spin ribbon forms. Although they fabricated a single-phase FCC alloy of CoCrFeMnNi with success, their attempt to add additional 1–4 elements all failed. Otto et al. [5] investigated five quinary alloys based on the composition of CoCrFeMnNi by replacing one element at a time using a chemically similar element, but again all five new alloys consisted of more than one phase in the as-cast state. These experiments demonstrated that the configurational entropy does not, at least not always, play a dominant role in the determination of phase stability and therefore the microstructure of an alloy.

On the other hand, establishing universal rules for HEA formation is not trivial, which involve a number of empirical parameters, including atomic size difference, enthalpy, and valence electron concentration (VEC), as detailed in Chap. 2. In spite of the usefulness of these empirical rules, they may not be able to convincingly explain the experiments by Cantor [4], Otto [5], and others. In fact, the most intuitive way of representing the phase stability in a material is by its phase diagram [6–8]. Thus one rational key to understanding of HEA formation may be phase diagrams as pointed by Zhang et al. [9, 10] and Gao and Alman [3].

Phase diagrams are typically determined using equilibration experiments followed by thermal analysis and phase identification using diffraction and microscopy techniques and thus can be costly and time consuming especially for the higher-order systems. The CALPHAD method [11, 12] makes it possible to obtain multicomponent phase diagrams not only for basic materials research in related areas such as solidification and solid state transformation but also for alloy design and processing development and improvement. It is based on the well-known thermodynamic law that a system reaches its equilibrium when it attains the lowest Gibbs energy at a given composition, temperature, and pressure. Provided that the Gibbs energy (as a function of pressure, temperature, and composition) is known

for the individual phases, then it is possible to calculate the equilibrium state of the system by an energy minimization procedure.

One important advantage of the CALPHAD method is to enable predicting higher-order phase diagrams via extrapolation from its constituent lower-order systems, such as binary and ternary systems. This is especially useful for commercial alloy systems, which are normally multicomponent systems and lack sufficient experimental data. For example, Haynes 282 has ~57 wt.% Ni with addition of alloying elements of Cr, Co, Mo, Ti, Al, Fe, Mn, Si, C, and B in various amounts. Stainless steel 316 contains alloying elements of Cr, Ni, Mo, Mn, C, and N with Fe as the dominant element. Prediction of multicomponent phase diagrams can in turn reduce the number of experiments required to determine the complete phase diagram in the space of temperature, composition, and pressure if compared with a complete trial-and-error approach. The application of CALPHAD method requires both computational software and thermodynamic databases. Over the past three decades, several commercial software packages, such as PandatTM [13], Thermo-Calc [14], FactSage [15], etc., have become available. The demand for consistent multicomponent thermodynamic databases has grown steadily. Two databases are used mainly in this chapter: PanHEA [13] and TCNI7 [14]. The PanHEA contains all constituent binary and ternary descriptions for the Al-Co-Cr-Cu-Fe-Mn-Ni while TCNI7 contains all binary and limited ternary systems that are important to Ni-based alloys.

In this chapter, we first provide a concise description on the CALPHAD methodology, followed by the optimization procedure tailored for HEA systems. Then we demonstrate thermodynamic analysis on HEA formation in the well-known quinary Co-Cr-Fe-Mn-Ni FCC HEA system. The σ phase becomes unstable with increasing the number of components in the system. The mixing behavior in the Gibbs free energy, enthalpy, and entropy among key phases are analyzed and the excess entropy is highlighted. A contrasting example is then introduced by adding Al to the Co-Cr-Fe-Ni system, which destabilizes the FCC solid solution while stabilizes the BCC phase. Similar thermodynamic analysis is then applied to the BCC Mo-Nb-Ta-Ti-V-W senary HEA system to illustrate how the C15 Laves phase is destabilized by the entropy of BCC phase. Applications of CALPHAD modeling to the microstructure evolution of several HEA systems are then presented. We conclude by presenting outlooks on CALPHAD modeling of HEAs such as addressing short-range ordering and developing mobility databases, followed by conclusions.

12.2 CALPHAD Methodologies

The CALPHAD method [11] adopts a phenomenological methodology to obtain a self-consistent thermodynamic description of a multicomponent system as shown in Fig. 12.1. The term “thermodynamic database” means that the parameters for the Gibbs energies of a large number of binary and ternary systems have been

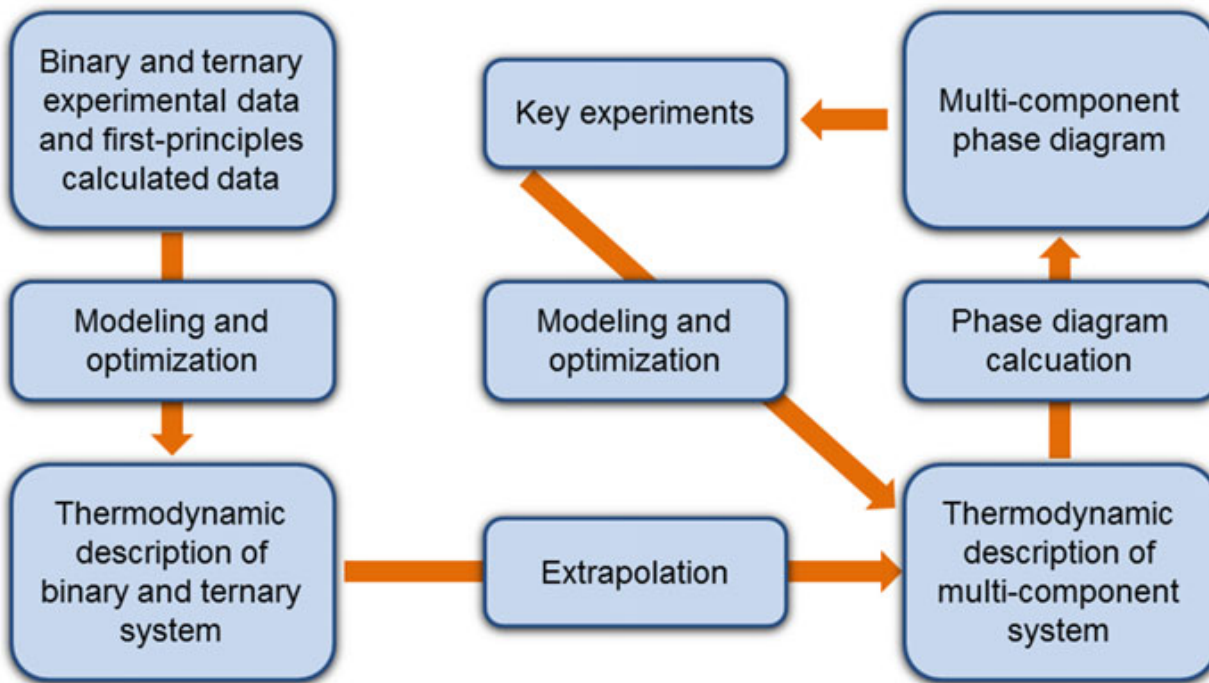


Fig. 12.1 The CALPHAD or phenomenological approach used to obtain a thermodynamic description of a multicomponent system

assembled that are important for the intended compositional ranges. The first step in developing a thermodynamic database of a multicomponent system is to collect the thermochemistry and phase equilibrium data from the literature for the lower-order systems, normally binaries and ternaries. However, if such data are not available, it becomes necessary to design and carry out experiments. In this regard, the thermodynamic data obtained from first-principles calculations will be useful to supplement experimental data. The model parameters of the phases involved are then determined through the optimization procedure. Care is always taken to ensure that the parameters of these Gibbs energies are physically realistic instead of relying purely on the optimization [7]. This is particularly important if available experimental data are very limited.

Once reliable thermodynamic descriptions of lower-order constituent systems, usually binaries and ternaries, are obtained, the higher-order thermodynamic database can be achieved via extrapolation as the first step [16]. In fact, extensive experience has shown that a reliable description of a quaternary system can be obtained from those of the lower-order systems. However, if there is a new quaternary phase form, then one needs to provide its Gibbs free energy description that is consistent with the database through the optimization procedure. However, readjustment of the binary and ternary systems may be required if the agreement between the as-extrapolated and experimental phase diagrams is not satisfactory. Especially high attention needs to be paid to the Gibbs energy descriptions of “hypothetical” phases that are unstable or metastable within some of the constituent binaries and/or ternaries, and more discussions are given in Sect. 12.5.

Traditionally, a multicomponent thermodynamic database for a specific material system, such as Al alloys, steels, or Ni-base superalloys, focuses only on the

key-element-rich corner. However, a thermodynamic database applicable to HEAs needs to cover its whole composition range since the composition of a HEA is located in the center of the multidimension composition space. This requires much more effort to develop the HEA thermodynamic database than the traditional alloying system with the same number of components. Proper thermodynamic models need to be selected in order to describe the Gibbs energies of all the phases involved in the HEA system.

12.2.1 Elements

The Gibbs energy of the pure element i , with a certain structure φ , referred to the enthalpy of its standard state at room temperature, is described as a function of temperature by the following equation:

$${}^0G_i^\varphi(T) = a + bT + cT \ln T + dT^2 + eT^3 + fT^{-1} + gT^7 + hT^{-9} \quad (12.1)$$

The values of the coefficients $a \dots h$ are taken from Dinsdale [17].

For elements that display a magnetic ordering, such as Ni, an additional term ${}^{\text{mag}}G_m^\varphi$ is added to the molar Gibbs energy on the right hand side of Eq. (12.1):

$${}^{\text{mag}}G_m^\varphi = RT \ln(\beta^* + 1)f\left(\frac{T}{T^*}\right) \quad (12.2)$$

where T^* is the critical temperature for magnetic ordering and β^* is the average magnetic moment per atom of the element expressed in Bohr magnetons. Values of the coefficient β^* and the expression of function f are also taken from Dinsdale [17].

12.2.2 Substitutional Solution Model

The most common substitutional solution phases in HEA systems are liquid, BCC, FCC, and HCP. All components in each substitutional solution phase are equivalently distributed in the phase, regardless of the number of components in the solution, whereas deviation from it is described by the excess free energy. The molar Gibbs energy of a substitutional solid solution phase (φ) is described as

$$G_m^\varphi = {}^{\text{ref}}G_m^\varphi + {}^{\text{id}}G_m^\varphi + {}^{\text{ex}}G_m^\varphi + {}^{\text{mag}}G_m^\varphi \quad (12.3)$$

The term ${}^{\text{ref}}G_m^\varphi$ defines a reference, which is

$${}^{\text{ref}}G_m^\varphi = \sum_i x_i \cdot {}^0G_m^\varphi \quad (12.4)$$

where x_i is the mole fraction of element i and the quantity ${}^0G_i^\varphi$ is the molar Gibbs energy of the element i with the structure φ . The term ${}^{\text{ex}}G_m^\varphi$ describes the excess free energy of the phase in the nonmagnetic state, and an additional term ${}^{\text{mag}}G_m^\varphi$ is required to describe the excess due to magnetic contribution of the alloy.

The term ${}^{\text{id}}G_m^\varphi$ is related to the molar ideal configurational entropy, which is

$${}^{\text{id}}G_m^\varphi = RT \sum_i x_i \ln x_i \quad (12.5)$$

and the nonmagnetic excess Gibbs energy ${}^{\text{ex}}G_m^\varphi$ for a quinary system is

$${}^{\text{ex}}G_m^\varphi = \sum_{i \neq j} x_i x_j L_{i,j}^\varphi + \sum_{i \neq j \neq k} x_i x_j x_k L_{i,j,k}^\varphi + \sum_{i \neq j \neq k \neq l} x_i x_j x_k x_l L_{i,j,k,l}^\varphi + x_i x_j x_k x_l x_m L_{i,j,k,l,m}^\varphi \quad (12.6)$$

The three summations are done over all components and account for binary, ternary, and quaternary excess free energy contributions in the nonmagnetic state, respectively. The terms $L_{i,j}^\varphi$, $L_{i,j,k}^\varphi$, $L_{i,j,k,l}^\varphi$, and $L_{i,j,k,l,m}^\varphi$ are the interaction parameters from the constituent binary, ternary, and quinary, respectively.

The binary interaction parameter $L_{i,j}^\varphi$, which can be described by polynomials which are most commonly the Redlich-Kister polynomial [18] with temperature-dependent coefficients, is as follows:

$$L_{i,j}^\varphi = \sum_{\nu=0}^n {}^\nu L_{i,j}^\varphi (x_i - x_j)^\nu \quad (12.7)$$

$${}^\nu L_{i,j}^\varphi = {}^\nu a_{i,j}^\varphi + {}^\nu b_{i,j}^\varphi T + {}^\nu c_{i,j}^\varphi T \ln(T) + \dots \quad (12.8)$$

The coefficients ${}^\nu a_{i,j}^\varphi$, ${}^\nu b_{i,j}^\varphi$, ${}^\nu c_{i,j}^\varphi$, etc., are the parameters to be optimized.

The ternary interaction parameter $L_{i,j,k}^\varphi$ is expressed by

$$L_{i,j,k}^\varphi = v_i L_i^\varphi + v_j L_j^\varphi + v_k L_k^\varphi \quad (12.9)$$

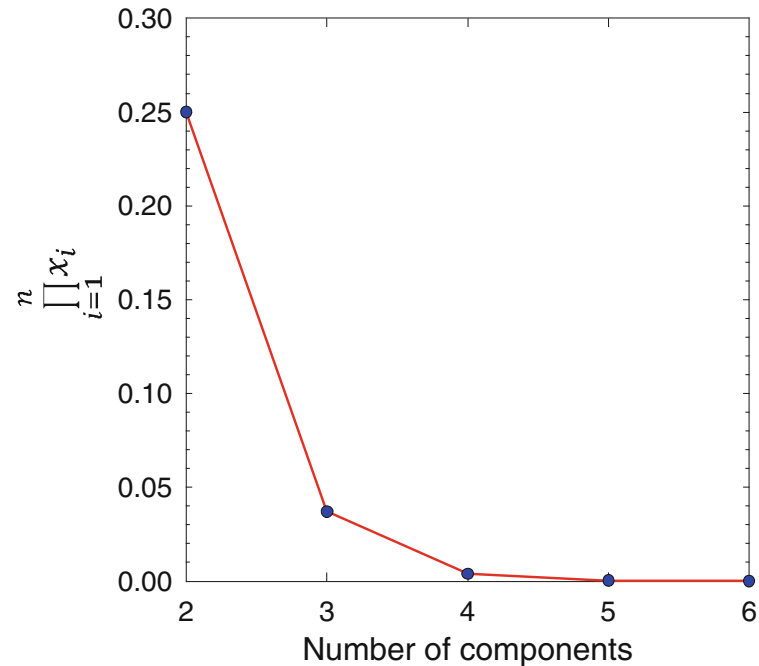
where $v_i = x_i - \frac{1-x_i-x_j-x_k}{3}$, $v_j = x_j - \frac{1-x_i-x_j-x_k}{3}$, and $v_k = x_k - \frac{1-x_i-x_j-x_k}{3}$,

and L_i^φ , L_j^φ , and L_k^φ represent the interaction on the Gibbs energy surface in the three corners of the ternary system, respectively.

The term ${}^{\text{mag}}G_m^\varphi$ applies only if the solution phase exhibits magnetic ordering and is described similarly as Eq. (12.2). The compositional dependence of the critical ordering temperature (T_m^*) and magnetic moment (β_m^*) is expressed by

$$T_m^* = \sum_i x_i T_i^* + {}^{\text{ex}}T_m^* \quad (12.10)$$

Fig. 12.2 Product of equimolar compositions versus the number of components



$$\beta_m^* = \sum_i x_i \beta_i^* + {}^{\text{ex}}\beta_m^* \quad (12.11)$$

Both the excess term of ${}^{\text{ex}}T_m^*$ and ${}^{\text{ex}}\beta_m^*$ are represented by an equation similar to Eqs. (12.7 and 12.8).

It should be noted that quaternary and quinary excess terms as shown in Eq. (12.6) are very rarely used. They play a less significant role compared to binary and ternary interaction parameters, because the product of the molar compositions (i.e., $x_i x_j x_k x_l$ for quaternary, $x_i x_j x_k x_l x_m$ for quinary, etc.) become negligible for quaternary and quinary systems. This effect is demonstrated in Fig. 12.2 for compositions in equimolar ratio in 2- to 6-component systems.

12.2.3 Stoichiometric Compound Model

The intermetallic phases with zero or negligible homogeneity range are usually described by the stoichiometric compound model. The Gibbs energy of a binary stoichiometric compound A_pB_q , G_m^φ , is described as a function of temperature only:

$$G_m^\varphi = \sum_i x_i {}^0G_i^\varphi + \Delta_f G(A_pB_q) \quad (12.12)$$

where x_i is the mole fraction of component i and ${}^0G_i^\varphi$ represents the Gibbs energy of component i with the φ structure; $\Delta_f G(A_pB_q)$, which is normally a function of temperature (Eq. 12.1), represents the Gibbs energy of formation of the stoichiometric compound. If $\Delta_f G(A_pB_q)$ is a linear function of temperature,

$$\Delta_f G(A_pB_q) = \Delta_f H(A_pB_q) - T \cdot \Delta_f S(A_pB_q) \quad (12.13)$$

where $\Delta_f H(A_pB_q)$ and $\Delta_f S(A_pB_q)$ are the enthalpy and entropy of formation of the stoichiometric compound, respectively. Equations (12.12 and 12.13) can be readily extended to a multicomponent stoichiometric compound phase.

12.2.4 Compound Energy Formalism (CEF)

An ordered intermediate phase can be described by a variety of sublattice models, such as the compound energy formalism [19, 20] and the bond energy model [21, 22]. In these models, the Gibbs energy is a function of the sublattice species concentrations and temperature. For example, the B2 phase in the PanHEA database is described using a two-sublattice model $(\text{Al}, \text{Co}, \text{Cr}, \text{Fe}, \text{Ni})_1 : (\text{Co}, \text{Cr}, \text{Fe}, \text{Ni}, \text{Va})_1$, and the σ phase is described using a three-sublattice model $(\text{Al}, \text{Co}, \text{Fe}, \text{Ni})_8(\text{Cr})_4(\text{Al}, \text{Co}, \text{Cr}, \text{Fe}, \text{Ni})_{18}$. For a clear demonstration, here we only show the Gibbs energy of a binary ordered phase described by a two-sublattice compound energy formalism $(A, B)_p : (A, B)_q$:

$$\begin{aligned} G_m^\phi = & \sum_{i=A, B} \sum_{j=A, B} y_i^I y_j^{\text{II}} G_{i:j}^\phi + RT \left[p \sum_{i=A, B} y_i^I \ln y_i^I + q \sum_{i=A, B} y_i^{\text{II}} \ln y_i^{\text{II}} \right] \\ & + \sum_{j=A, B} y_A^I y_B^I y_j^{\text{II}} \sum_v (y_A^I - y_B^I)^v L_{A, B:j}^v + \sum_{i=A, B} y_i^I y_A^{\text{II}} y_B^{\text{II}} \sum_v (y_A^{\text{II}} - y_B^{\text{II}})^v L_{i:A, B}^v \\ & + y_A^I y_B^I y_A^{\text{II}} y_B^{\text{II}} L_{A, B:A, B} \end{aligned} \quad (12.14)$$

where y_i^I and y_i^{II} are the species concentrations of component i in the first and second sublattices, respectively. Note that a comma is usually used to separate species in the same sublattice, while a colon sign is used to separate species belonging to different sublattices for the Gibbs energy expression such as in Eq. (12.14). The first term on the right hand of the equation represents the reference state with the mechanical mixture of the stable or hypothetical compounds: A, A_pB_q , B_pA_q and B. $G_{i:j}^\phi$ is the Gibbs energy of the stoichiometric compound $i_p j_q$ with the ϕ structure. The value of $G_{i:j}^\phi$ can be obtained experimentally if $i_p j_q$ is a stable compound or by the optimization. If the $i_p j_q$ phases are unstable or metastable in their binary/ternary systems, then it is extremely difficult to measure their thermodynamic properties experimentally, and accordingly a physics-based optimization of these phases becomes challenging. In this regard, their thermodynamic properties predicted from first-principles density functional theory (DFT) can be important and used as input to the optimization procedure [23–27].

The second term in Eq. (12.14) is the ideal mixing Gibbs energy which corresponds to the random mixing of species on the first and second sublattices. The last three terms are the excess Gibbs energies of mixing. The “L” parameters in these

terms are the model parameters whose values are to be optimized using the experimental phase equilibrium and thermodynamic data. $L_{A,B:j}^v$ and $L_{i:A,B}^v$ are the so-called “regular interaction” parameters and represent the next nearest neighbor interactions between constituents A and B in one sublattice when the other sublattice is occupied by A and B, respectively. $L_{A,B:A,B}$ is the so-called reciprocal parameter and represents the interactions between constituents A and B in both sublattices simultaneously. More discussion of the reciprocal parameter within the CEF model will be given in detail at Sect. 12.5.1. The compound energy formalism can be applied to phases in a multicomponent system by considering the interactions from all the constituent binaries. Additional ternary and higher-order interaction terms may also be added to the excess Gibbs energy term in a similar fashion to Eq. (12.14).

For the $(A,B)_8(B)_4(A,B)_{18}$ model, there are elements mixing in the first and third sublattices except the second sublattice. Therefore, the total mixing entropy results only from the first and third sublattices. The Gibbs energy of this phase can be expressed as follows:

$$\begin{aligned} G_m^\varphi = & y_A^I y_A^{III} {}^0G_{A:B:A} + y_A^I y_B^{III} {}^0G_{A:B:B} + y_B^I y_A^{III} {}^0G_{B:B:A} + y_B^I y_B^{III} {}^0G_{B:B:B} \\ & + 8RT[y_A^I \ln(y_A^I) + y_B^I \ln(y_B^I)] + 18RT[y_A^{III} \ln(y_A^{III}) + y_B^{III} \ln(y_B^{III})] + {}^{ex}G_m^\varphi \end{aligned} \quad (12.15)$$

$${}^0G_{i:B:j}^\varphi = 8{}^0G_i^\varphi + 4{}^0G_B^\varphi + 18{}^0G_j^\varphi \quad (12.16)$$

${}^{ex}G_m^\varphi$ is the excess energy in the nonmagnetic state and can be described as

$${}^{ex}G_m^\varphi = \sum_{k=A,B} y_i^I y_j^I y_k^{III} \sum_n L_{i,j:B:k}^n \left(y_i^I - y_j^I \right)^n + \sum_{k=A,B} y_k^I y_i^{III} y_j^{III} \sum_n L_{k:B:i,j}^n \left(y_i^{III} - y_j^{III} \right)^n \quad (12.17)$$

where n is the order to interaction parameters, such as 0, 1, 2...

Note that the magnetic contribution to the Gibbs free energy of phases described by the CEF model can use Eq. (12.2) as well.

12.2.5 Optimization

The optimization is the processing to ultimately obtain the parameters of the Gibbs energy function of each phase, which will make the thermodynamic description account for the known experimental data but also be able to extrapolate beyond the ranges of temperature and composition where data are available. This is achieved when proper thermodynamic models are used for the phases in question. Needless to say, the broad thermodynamic knowledge of the user who performs the

optimization also matters. The following steps are general guidelines for the thermodynamic optimization of HEA systems using the CALPHAD approach [28]:

- (a) Collect all published thermodynamic databases for the constituent binary and ternary systems, and then evaluate the reliability of and compatibility among these databases.
- (b) Select the proper thermodynamic models based on crystallographic information for all phases in the system.
- (c) For a system whose database is not available or requires re-optimization, first collect and categorize the thermodynamic and phase equilibrium data. In principle any kind of experimental datum that is explicitly or implicitly linked to the Gibbs energy can be used as input for optimization. For those “hypothetical” phases, obtaining the thermodynamic data from DFT calculations can be a viable option.
- (d) Evaluate the collected data critically by essentially eliminating bad and contradictory data. Critical evaluation requires considerable expertise in phase diagrams and some familiarity with different experimental techniques. It is important to consider the details such as the technique used, the phases present, the purity of the samples, the experimental conditions, the quantities measured and their reliability, etc. Frequently, difficulties occur during the optimization primarily due to poorly evaluated experimental data such as contradictory data or theoretically unacceptable data as the inputs! However, contradictions between different types of data, for example, phase diagram data and thermochemical data, may only be revealed during the optimization process.
- (e) Assign the proper starting values for the computerized thermodynamic optimization of phase diagrams. This is important because if bad starting values are used for the parameters to be optimized, the nonlinear equations may not yield any solution. Accordingly, it is more practical to begin the optimization with a “minimal” data set, comprising only a few vital experimental data. Including too many experimental data in the very beginning stage of the optimization may prove unwieldy. In the case of binary systems, for example, it is often sufficient to use a well-defined three-phase invariant-phase equilibrium, a congruent transformation, and the enthalpy of formation of the compound undergoing the congruent transformation.
- (f) After completing optimization of all necessary binary and ternary systems over the entire compositional ranges, try calculations on HEAs, and then compare the calculation results with experimental data where available. Readjust the descriptions of those critical phases (especially those hypothetical ones) until satisfaction is reached.

These procedures have been exercised to develop the Al-Co-Cr-Fe-Ni database using PandatTM [13], and a satisfactory agreement has been obtained for most of the reliable experimental data for all the constituent 10 binaries and 10 ternaries of this important HEA system. Upon report of new experimental data on this system, improvement on the database will be continued. This database is part of the

PanHEA database. Since there are no quaternary or quinary compounds reported in this system, the phase diagrams and thermodynamic properties for this quinary and its five quaternary systems can be obtained via extrapolation [16] within the whole compositional ranges. Comparisons of CALPHAD predictions using the PanHEA database with experimental data will be presented and discussed in detail in Sect. 12.4 of this chapter.

12.3 Thermodynamic Analysis of HEA Formation

From the physical standpoint of view, those empirical parameters, such as the difference in atomic size difference, VEC and electronegativity, etc., should be reflected at least partially in the free energy of the system. The essence of phase stability concerns energy competition among phases, and thus it is of fundamental importance to study and analyze the Gibbs free energies of individual phases in the system. For a disordered solid solution phase (φ), the mixing properties refer to the thermodynamic quantities that can be obtained via excluding the mechanical mixing parts. For example, the Gibbs energy of mixing $\Delta G_{\text{mix}}^{\varphi}$ can be determined by excluding the term of ${}^{\text{ref}}G_m^{\varphi}$ in Eq. (12.3); therefore, we have

$$\Delta G_{\text{mix}}^{\varphi} = {}^{\text{id}}G_m^{\varphi} + {}^{\text{ex}}G_m^{\varphi} + {}^{\text{mag}}G_m^{\varphi} = \Delta H_{\text{mix}}^{\varphi} - T\Delta S_{\text{mix}}^{\varphi} \quad (12.18)$$

where $\Delta H_{\text{mix}}^{\varphi}$ and $\Delta S_{\text{mix}}^{\varphi}$ are the enthalpy of mixing and entropy of mixing, respectively, and they are determined by

$$\Delta H_{\text{mix}}^{\varphi} = H_m^{\varphi} - \sum_i x_i H_i^{\varphi} \quad (12.19)$$

$$\Delta S_{\text{mix}}^{\varphi} = S_m^{\varphi} - \sum_i x_i S_i^{\varphi} \quad (12.20)$$

H_m^{φ} (S_m^{φ}) is the total enthalpy (entropy) of the alloy, and H_i^{φ} (S_i^{φ}) is enthalpy (entropy) of each component with the structure φ . The total excess entropy of the alloy including the magnetic contribution is determined by

$${}^{\text{ex}}S_m^{\varphi} = S_m^{\varphi} + R \sum_i x_i \ln x_i \quad (12.21)$$

The total excess Gibbs free energy (the terms ${}^{\text{ex}}G_m^{\varphi} + {}^{\text{mag}}G_m^{\varphi}$) includes all other contributions except *ideal* configurational entropy, such as vibrational free energy of mixing, magnetic free energy of mixing, electronic entropy of mixing, and destruction of configurational entropy due to presence of short-range chemical ordering/clustering. As a result, itemizing these contributions individually from CALPHAD method can be a daunting task. However, this can be carried out using predictive DFT calculations as detailed in Chaps. 8 and 10.

In the following, we present three case studies to illustrate the evolution of the Gibbs energy, enthalpy, and entropy as a function of system size and alloy composition. They are the FCC-forming Co-Cr-Fe-Mn-Ni, FCC- and BCC-forming Al-Co-Cr-Fe-Ni, and BCC-forming Mo-Nb-Ta-Ti-V-W systems. The TCNI7 database is used for consistency and its sublattice model for the σ phase allows extension to the entire compositional range. Note that TCNI7 uses a single phase description for both disordered and ordered contributions for the FCC and BCC phases, and no attempt was made to differentiate these contributions in the presentation in this section. It is also expected that more accurate results on the phase diagrams of these systems will be obtained once the thermodynamic descriptions for all the constituent ternaries are included in the database in the future.

12.3.1 FCC Co-Cr-Fe-Mn-Ni HEA System

To date, the Co-Cr-Fe-Mn-Ni system is the only FCC HEA system that has ever been studied extensively. The major phases in the solid state that compete against FCC solid solution include BCC solid solution, σ phase, and HCP solid solution phase. The σ phase originates from the Co-Cr binary system (see Fig. 12.3a) with a complex tetragonal crystal structure (Pearson symbol tP30, space group P4₂/mnm), but it has a range of solubility for other transition metals [29]. Using the TCNI7 database, the binary Co-Cr and pseudo-binary CoFe-Cr, CoFeNi-Cr, and CoFeMnNi-Cr phase diagrams are plotted in Fig. 12.3. By increasing the number of components of the system, the σ phase field shrinks and finally becomes unstable in the vertical section of the quinary system. However, the phase field of the FCC phase is the broadest in the quaternary section (e.g., the largest Cr solubility and the highest thermal stability) despite that the ideal configurational entropy is the highest in the quinary system. This suggests that other factors (e.g., enthalpy, competing phases such as liquid and BCC, etc.) may outweigh the configurational entropy of the FCC phase.

Phase stability concerns free energy competition among all phases in a system using the same reference states. For the four systems shown in Fig. 12.3, the sigma (σ), BCC, and HCP phases occur in equilibrium with the FCC solid solution phase, and thus the thermodynamic properties including the Gibbs free energy, enthalpy, and entropy for all these four phases are examined at a series of temperatures with varying Cr contents. For clarity, only the results for binary Co-Cr and pseudo-binary (CoFeMnNi)-Cr systems at $T = 1000$ °C are shown in Fig. 12.4. Note that the TCNI7 database adopts a sublattice model of $(\text{Co,Cr,Fe,Mn,Ni})_{10}(\text{Co,Cr,Fe,Mn,Ni})_4(\text{Co,Cr,Fe,Mn,Ni})_{16}$ for the σ phase in this quinary system, which differs from the one introduced in Sect. 12.2.4 used in the PanHEA database. For binary systems, the tie lines for two-phase regions lie within the Gibbs energy – composition plane and the common-tangent-line method can be used to determine the phase equilibrium

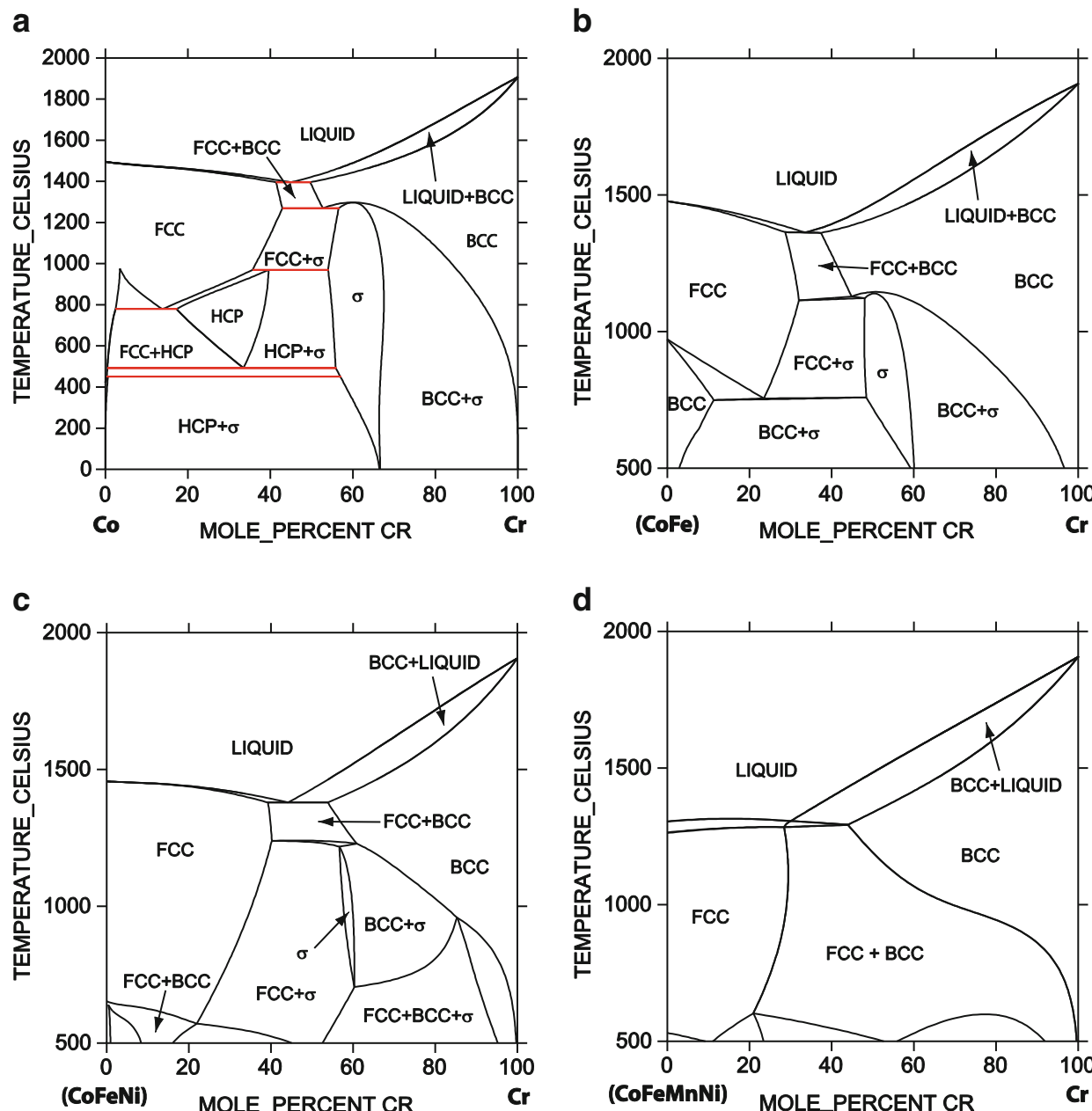


Fig. 12.3 (a) Co-Cr binary and pseudo-binary, (b) CoFe-Cr, (c) CoFeNi-Cr, and (d) CoFeMnNi-Cr phase diagrams calculated using TCNI7 database. The major phase fields are labeled

(i.e., equilibrium phases and their compositions). For example, the common tangent lines shown in Fig. 12.4a clearly define two two-phase regions of FCC + σ and σ + BCC, respectively. For multicomponent systems, the equilibrium phase compositions for regions of two or more phases are determined by the common-tangent-plane method. However, most often the tie lines determined by the common-tangent-plane method for multicomponent system and thus the equilibrium phase compositions may lie out of the two-dimensional (2D) Gibbs energy – composition plane (such as the case of $\text{CoCr}_x\text{FeMnNi}$ as shown in Fig. 12.4d–f). Consequently, thermodynamic analysis within the 2D plane for these scenarios is only meaningful for the single-phase regions and should not be used for global phase equilibrium determination for regions of coexisting phases.

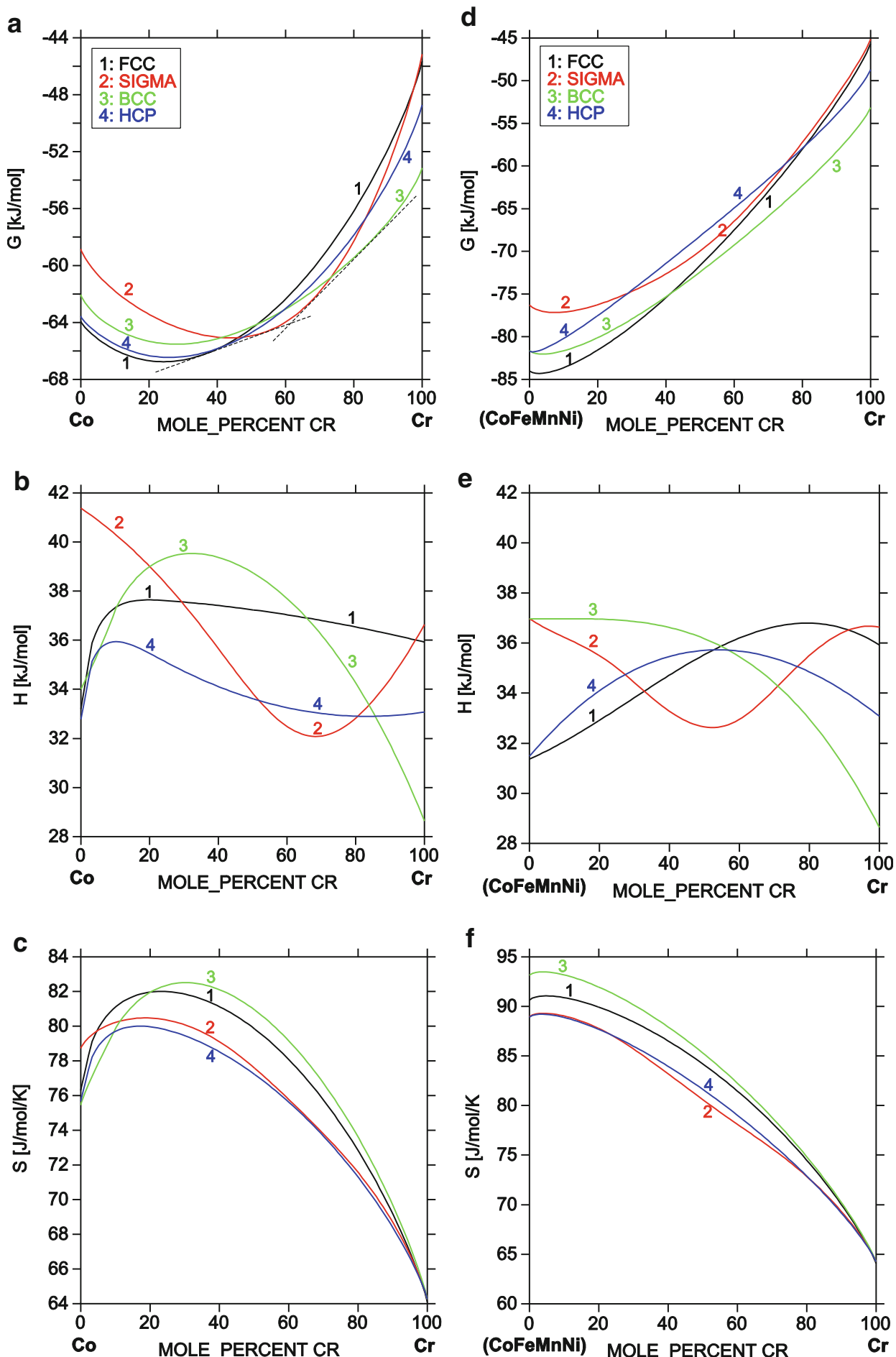


Fig. 12.4 Calculated thermodynamic properties of the FCC, σ , BCC, and HCP phases (labeled as 1–4, respectively, in the plot) for (a–c) binary Co–Cr and (d–f) pseudo-binary (CoFeMnNi)–Cr systems: (a, d) the Gibbs free energy, (b, e) enthalpy, and (c, f) entropy as a function of Cr contents at $T = 1000\text{ }^{\circ}\text{C}$. The reference states are the stable structure of the pure elements at $P = 1\text{ atm}$ and $T = 25.15\text{ }^{\circ}\text{C}$. The *dashed lines* in (a) denote the tie lines (or common tangent lines), which define the two-phase region where the chemical potential of the component is equal in both phases. The tie line is out of the 2D plane in (d)

Nonetheless, the analysis on the compositional dependence of the thermodynamic properties within the 2D plane still offers enriched information on their magnitude and the trend among various phases over the entire compositional ranges for multicomponent systems. Figure 12.3 shows that the effect of number of components on each individual phase varies, and both FCC and BCC phases become much more stable than the σ and HCP phases in the quinary system, compared to the binary system. The stabilization effect actually comes from both enthalpy and entropy contributions. Addition of Fe, Mn, and Ni to CoCr lowers the total enthalpy (i.e., making it more negative) for all phases except the HCP phase. In terms of entropy, the BCC phase has the highest entropy followed by the FCC phase in $\text{CoCr}_x\text{FeMnNi}$, but yet the FCC phase has lower energy for alloys containing up to 40 at.% Cr. The results suggest that both enthalpy and entropy need to be considered for phase stability analysis.

The mixing behavior in the Gibbs energy, enthalpy, and entropy of the FCC phase in these systems is presented in Fig. 12.5. ΔG_{mix} decreases monotonically for the whole composition range with increasing the number of components in the system (Fig. 12.5a). This is due to both lowering ΔH_{mix} and increasing ΔS_{mix} . Figure 12.5b shows that ΔH_{mix} decreases and eventually becomes negative for $\text{CoCr}_x\text{FeMnNi}$ (with less than 40 at.% Cr). Achieving a more negative ΔH_{mix} implies formation of stronger bonds among elements. At 20 at.% Cr, the decrease in ΔH_{mix} is about 6.5 kJ/mol for the quinary compared to the binary alloy, while the increase in ΔS_{mix} is about 7 J/K/mol that corresponds to an energy of $7 \times 1273 = 8911 \text{ J/mol} \approx 9 \text{ kJ/mol}$ at 1000 °C.

Figure 12.5c shows that, for all four systems studied, they deviate notably from ideal mixing by exhibiting positive excess entropy. Especially, the mixing entropy, ΔS_{mix} , for the binary FCC CoCr alloy already exceeds the maximum ideal configurational entropy of a ternary system. The predicted positive excess entropy is +3.9, +2.9, +2.5, and +1.3 J/K/mol for FCC CoCr, CoCrFe, CoCrFeNi, and CoCrFeMnNi, respectively. Furthermore, the maximum ΔS_{mix} occurs at Cr = 44.2, 35.3, 35.9, and 22.8 at.% for 2-, 3-, 4-, and 5-component systems, respectively. The deviation of these compositions from their maximum ideal configurational entropy case is not big except for the quaternary CoCr_xFeNi system, which is $x = 35.9 \text{ at.\%} - 25 \text{ at.\%} = 10.9 \text{ at.\%}$. The deviation in the composition of the maximum entropy and the presence of large positive excess entropy suggest the presence of other entropy contributions besides the configurational entropy. As a matter of fact, Gao et al. (see Chap. 10) predicted a positive vibrational entropy of mixing of +2.8 J/K/mol for FCC CoCrFeNi using DFT methods, agreeing well with the calculated positive excess entropy of +2.5 J/K/mol using TCNI7 database. However, DFT calculations on the vibrational, magnetic, electronic, and configurational entropies for CoCr, CoCrFe, and CoCrFeMnNi will be desirable to verify the calculated positive excess entropies using TCNI7.

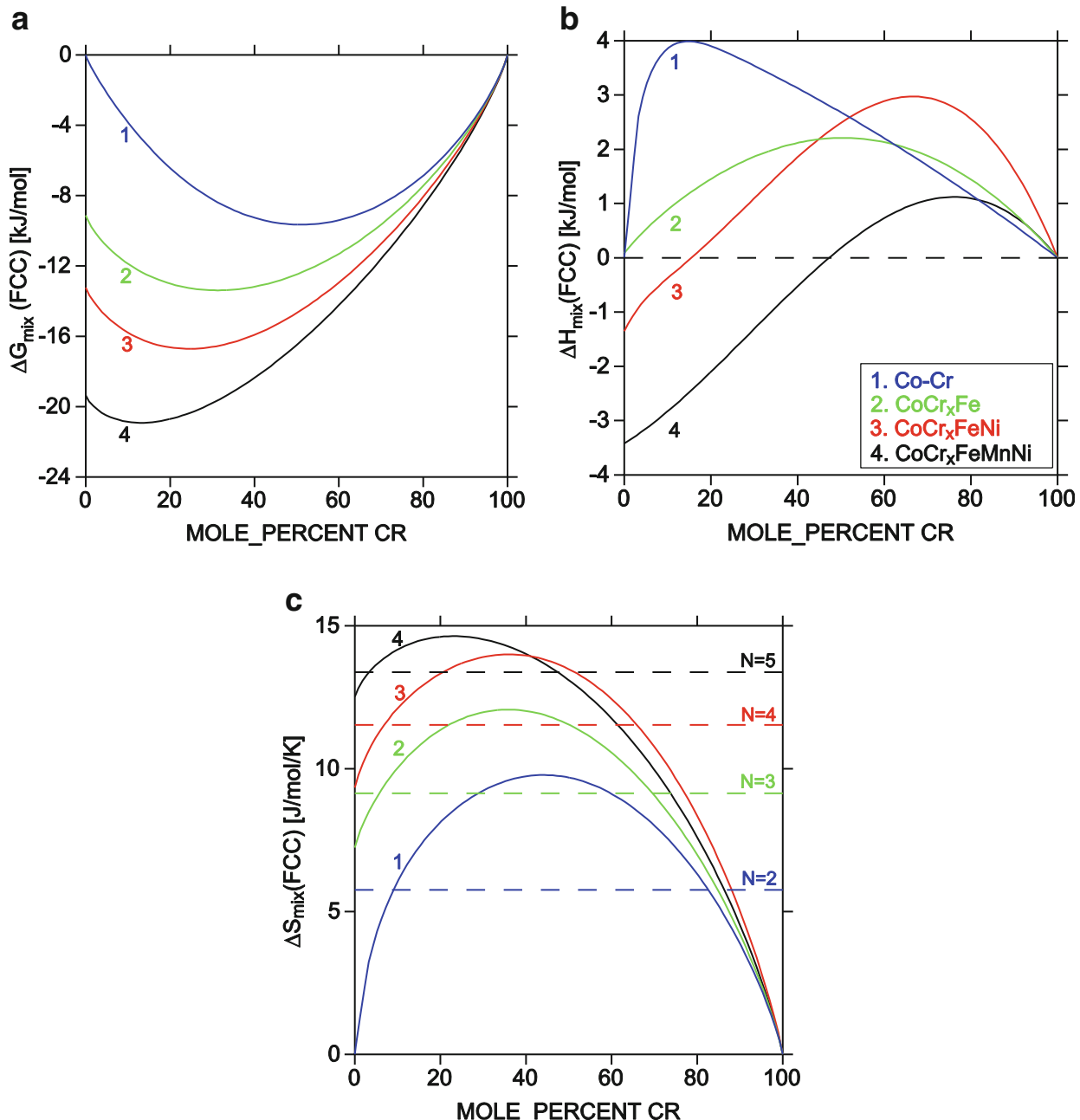


Fig. 12.5 Calculated mixing properties of the FCC phase at $T = 1000$ °C: (a) the Gibbs free energy of mixing, (b) enthalpy of mixing, and (c) entropy of mixing of CoCr_x , CoCr_xFe , CoCr_xFeNi , and $\text{CoCr}_x\text{FeMnNi}$ as a function of Cr contents. The reference states are FCC at $T = 1000$ °C. The *dashed lines* in (c) denote the *maximum configurational entropy of mixing*, and N signifies the total number of components

12.3.2 HEA Formation of $\text{Al}_x\text{CoCrFeNi}$ in Comparison to $\text{CoCrFeMn}_x\text{Ni}$

The thermodynamic analysis of the Co-Cr-Fe-Mn-Ni system presented above demonstrates the importance of both enthalpy and entropy in terms of phase stability. In the next example, we compare the mixing behavior of thermodynamic properties of solid solution phases of FCC, BCC, and HCP in $\text{CoCrFeMn}_x\text{Ni}$ and $\text{Al}_x\text{CoCrFeNi}$ as shown in Fig. 12.6. For $\text{CoCrFeMn}_x\text{Ni}$, the FCC phase has the lowest ΔG_{mix} followed by the BCC and then HCP phases (Fig. 12.6a). Addition of

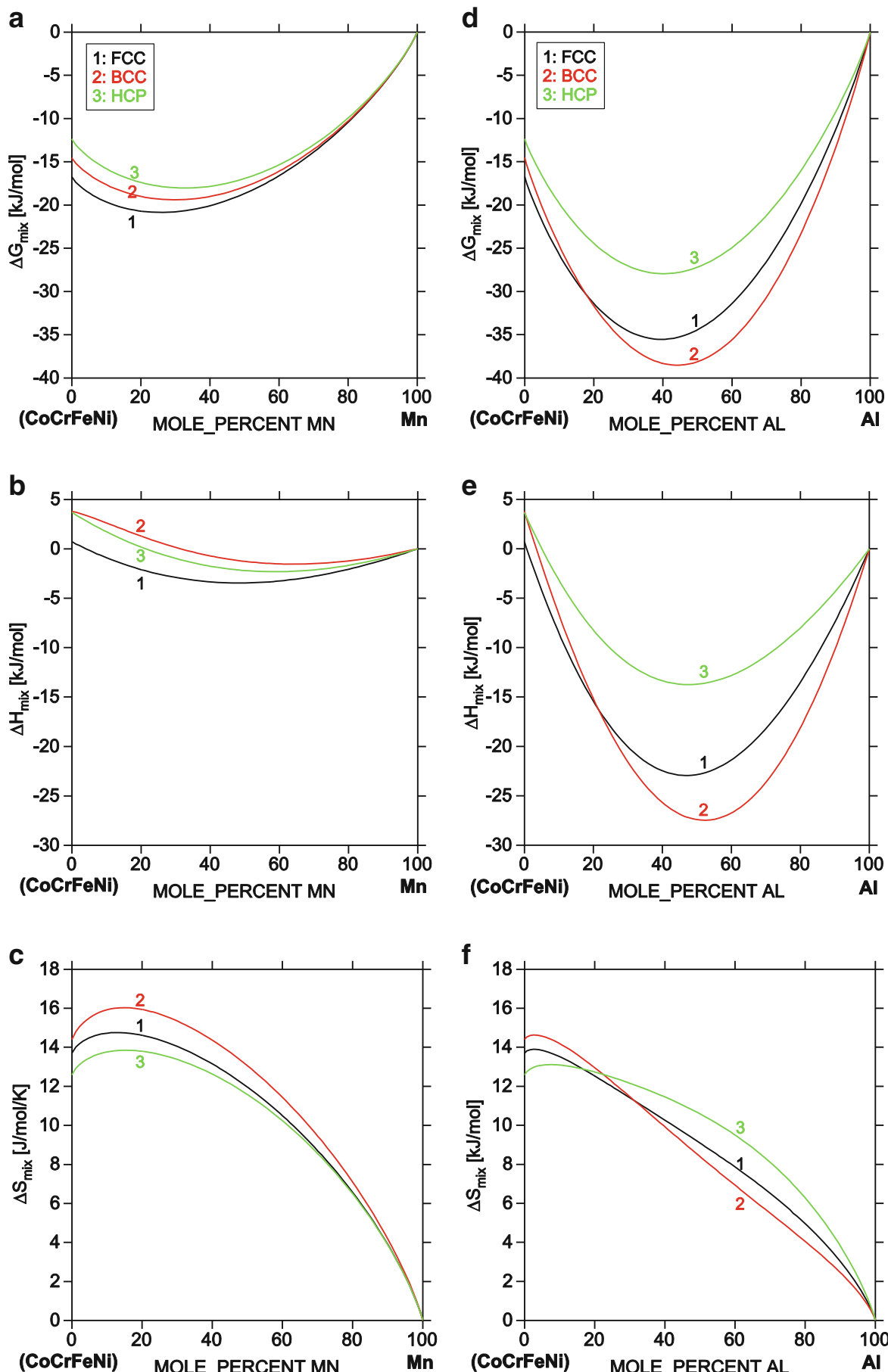


Fig. 12.6 Calculated thermodynamic properties of FCC, BCC, and HCP phases (labeled as 1–3, respectively, in the plot) for (a–c) $\text{CoCrFeMn}_x\text{Ni}$ and (d–f) $\text{Al}_x\text{CoCrFeNi}$ alloys: (a, d) the Gibbs free energy of mixing, (b, e) enthalpy of mixing, and (c, f) entropy of mixing as a function of Mn or Al contents at $T = 1000^\circ\text{C}$. The reference states are FCC, BCC, and HCP at $T = 1000^\circ\text{C}$

Mn to CoCrFeNi lowers ΔH_{mix} for all three phases by a small amount (<5 kJ/mol), and clearly the FCC phase has the lowest ΔH_{mix} (Fig. 12.6b). Similar to the case of $\text{CoCr}_x\text{FeMnNi}$, the BCC phase has the highest ΔS_{mix} , but the difference among these 3 solution phases is quite small (Fig. 12.6c). In addition, it is noteworthy that the maximum entropy occurs at 13.2 at.% Mn for the FCC phase, 12.2 at.% Mn for the BCC phase, and 13.2 at.% Mn for the HCP phase, deviating substantially from the equimolar composition (i.e., 20 at.%). The examples of both $\text{CoCr}_x\text{FeMnNi}$ and $\text{CoCrFeMn}_x\text{Ni}$ demonstrate that even for solid solution phases in the same system, enthalpy of mixing is as important as entropy of mixing.

In contrast to the case of $\text{CoCrFeMn}_x\text{Ni}$, addition of Al to CoCrFeNi changes its thermodynamics dramatically as shown in Fig. 12.6d–f. The ΔG_{mix} and ΔH_{mix} curves of the FCC and BCC phases cross at about 20 at.% Al; at higher Al contents, the BCC phase has lower ΔG_{mix} and ΔH_{mix} than the FCC phase. The entropy curves of the FCC and BCC phases cross at about 30 at.% Al but they are fairly close for the entire composition ranges. Clearly the stabilization of the BCC phase from Al addition is dictated by the enthalpy effect rather than the entropy effect. Compared to $\text{CoCrFeMn}_x\text{Ni}$, the maximum ΔS_{mix} is apparently smaller for all phases in $\text{Al}_x\text{CoFeMnNi}$, and it occurs for both FCC and BCC phases at less than 5 at.% Al for $\text{Al}_x\text{CoFeMnNi}$ and then drops rapidly with increasing Al contents.

12.3.3 BCC Mo-Nb-Ta-Ti-V-W HEA System

Formation of single-phase senary BCC HEA MoNbTaTiVW is reported in a very recent study [30] following the HEA search strategy [3]. For this senary system, formation of isomorphous BCC solid solution is observed in all 15 edge binary systems [29]. Most of the solid solutions cover extremely wide ranges of temperatures, except the Ta-V system where C15 TaV_2 Lave phase is stable from room temperature up to 1300 °C [29]. Using DFT methods, Widom predicts formation of stable C15 NbV_2 at low temperatures in the Nb-V binary system as presented in Chap. 8 [31]. In this subsection, we perform phase diagram calculations and present thermodynamic analysis of BCC HEA formation against the C15 phase. The TCNI7 database is used since it has complete descriptions for all binaries of this senary system. The sublattice model adopted for the C15 phase is (Mo,Nb,Ta,Ti,V,W)₂(Mo,Nb,Ta,Ti,V,W) in the TCNI7 database.

Figure 12.7 illustrates the calculated phase diagrams for the binary Ta-V and pseudo-binary systems of MoTa-V, MoTaW-V, MoNbTaW-V, and MoNbTaTiW-V. For the equimolar compositions, the temperature range within which the BCC phase is stable increases from binary to ternary, quaternary, and quinary and then starts to decrease for the senary system. This is understandable since Ti has the lowest melting point, and the melting point of the constituent elements in the descending order is 3422 (W), 3017 (Ta), 2623 (Mo), 2477 (Nb), 1910 (V), and 1668 °C (Ti). It is often observed that the liquidus temperature of substitutional solid solution alloys is high if the constituent elements have high melting points.

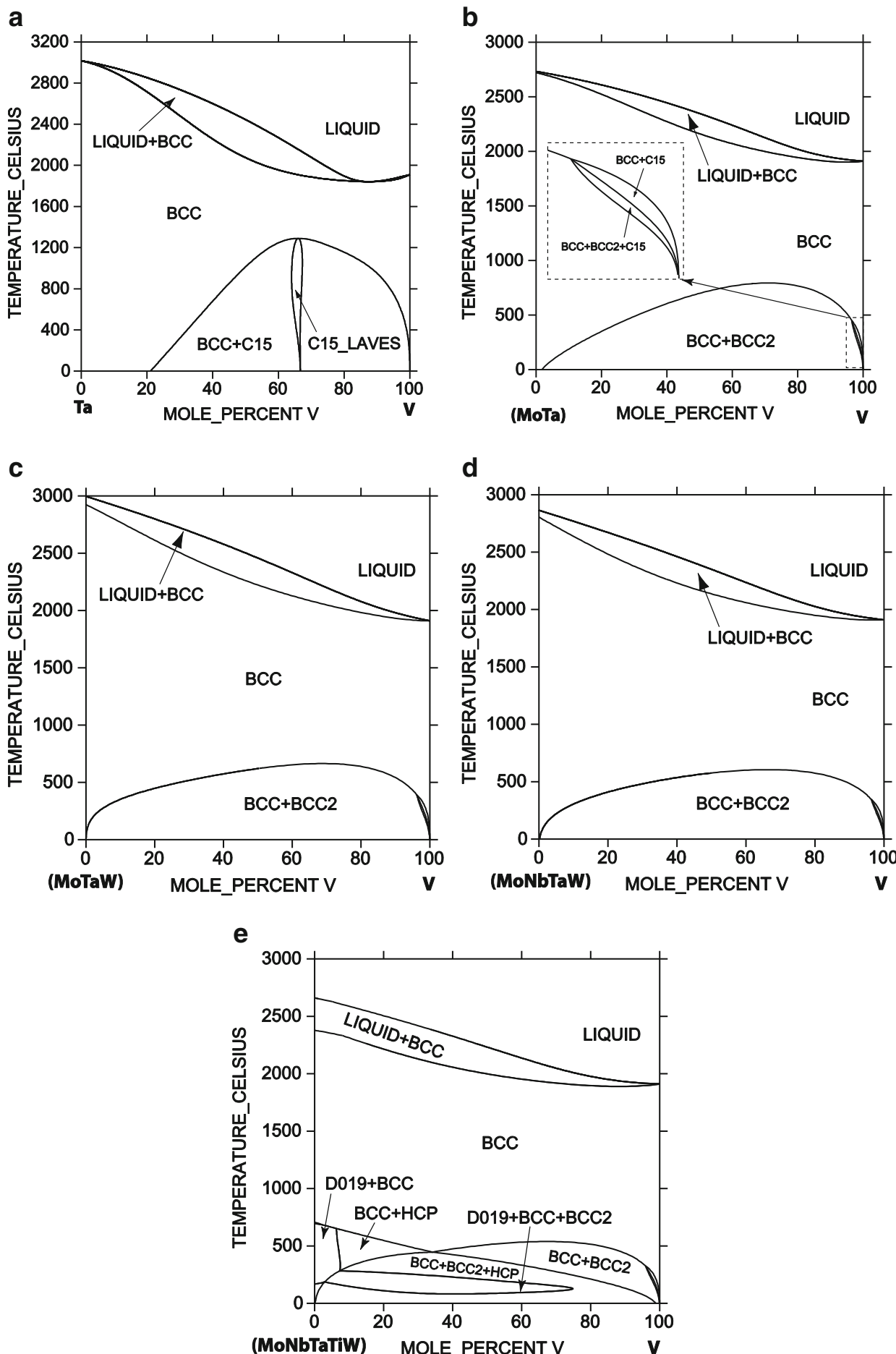


Fig. 12.7 (a) Ta-V binary and pseudo-binary (b) (MoTa)-V, (c) (MoNbTa)-V, (d) (MoNbTaW)-V, (e) (MoNbTaTiW)-V phase diagrams calculated using TCNI7 database. The major phase fields are labeled

In other words, one needs to avoid addition of elements that have too low melting points while they are chemically similar, if high melting points and high strength are important for the applications. Although the senary BCC phase has the highest configurational entropy, its phase field is smaller than in the quaternary and quinary systems. This again demonstrates that the configurational entropy of a phase may not always dominate its phase stability and other factors such as competing phases and enthalpy need to be considered. This conclusion is consistent with the phase diagram and thermodynamic analysis of the Co-Cr-Fe-Mn-Ni and Al-Co-Cr-Fe-Ni systems presented in Sects. 12.3.1 and 12.3.2.

Next we analyze the underlying thermodynamic quantities for these systems. The comparison in the Gibbs energy, enthalpy, and entropy between the binary and the senary systems at $T = 1000\text{ }^{\circ}\text{C}$ is shown in Fig. 12.8 for the BCC, C15, and HCP phases. The C15 phase is stable in Ta-V (Fig. 12.8a), but becomes unstable in the senary (Fig. 12.8d). The trend in the enthalpy is similar between the binary and the senary. Both systems have a minimum in the enthalpy curve for the C15 phase, which occurs at ~65 at.% V (50 at.%V) for the binary (senary). The destabilization of the C15 phase in the senary is mainly due to the contrasting trend in entropy for C15 and competing BCC and HCP phases. Note that the entropy for the C15 phase is fairly close to that of the BCC phases except for small ranges in the vicinity of 60 at.% V in Ta-V binary, and both are much higher than the entropy of the HCP phase. This is somewhat counterintuitive considering the intermetallic nature of the C15 phase; therefore, further theoretical and experimental study on the entropy sources of the C15, BCC, and HCP phases in Ta-V is needed. However, the HCP phase is unstable in Ta-V, so experimental measurement of its thermodynamic properties will be extremely difficult.

In contrast to the Ta-V binary system, the reduction of entropy for the C15 phase in the senary system is obvious and the entropy has a minimum in the vicinity of 52.2 at.% V (Fig. 12.8f). The reduction corresponds well to the enthalpy profile (Fig. 12.8e), suggesting potent chemical ordering in the compound results in the sharp decrease in its entropy. For the senary system at 52.2 at.% V, the entropy of the C15 phase is by 27 J/K/mol (i.e., $S_{\text{BCC}} - S_{\text{C15}}$) lower than that of the BCC phase and outweighs the enthalpy gain of 5.1 kJ/mol (i.e., $H_{\text{BCC}} - H_{\text{C15}}$). In other words, entropy effect clearly outweighs the enthalpy effect by almost 7 times, which is responsible for destabilization of C15 phase in the senary system at $T = 1000\text{ }^{\circ}\text{C}$.

The thermodynamic mixing properties of the BCC phase are shown in Fig. 12.9. The combination of monotonic increase in entropy and complex change in enthalpy causes the ΔG_{mix} to become significantly lower in higher-order systems than the binary system. But the lowering trend in ΔG_{mix} is not monotonic, and it is in descending order: binary \gg ternary $>$ quaternary $>$ senary $>$ quinary (Fig. 12.9a). In other words, the quinary system has the lowest ΔG_{mix} over the whole composition range. The results indicate that more components may not always result in the lower Gibbs energy of mixing. Figure 12.9b shows that the decrease in ΔH_{mix} is not monotonic with respect to the number of components in the system. At < 20 at.% V, the ΔH_{mix} varies in descending order from binary $>$ senary $>$ quaternary $>$ quinary $>$ ternary (i.e., ternary has the most negative ΔH_{mix}). Between 20 and 50 at.% V, the order becomes

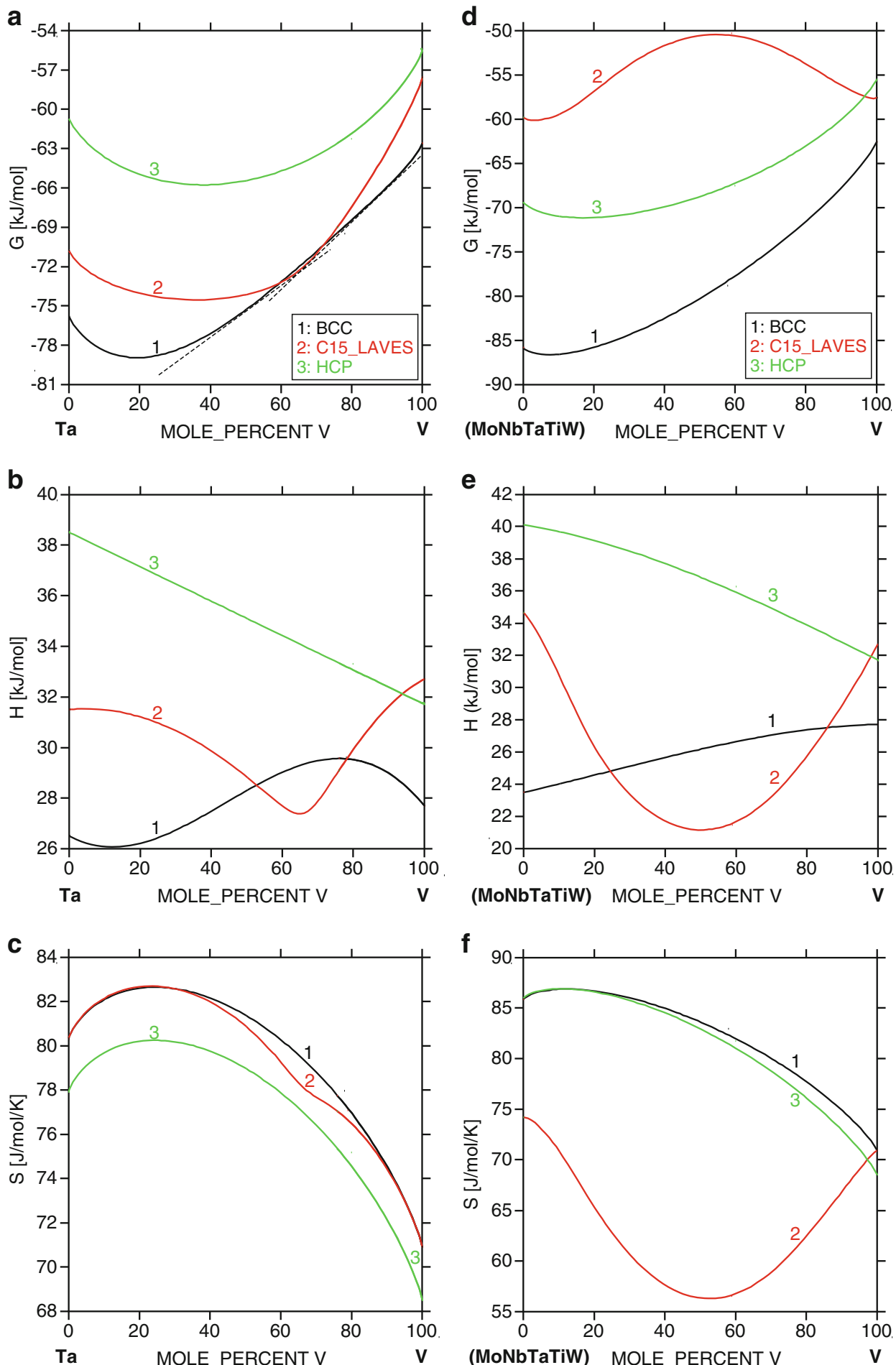


Fig. 12.8 Calculated thermodynamic properties of BCC, C15, and HCP phases (labeled as 1–3, respectively, in the plot) for (a–c) binary Ta–V and (d–f) pseudo-binary (MoNbTaTiW)–V systems: (a, d) the Gibbs free energy, (b, e) enthalpy, and (c, f) entropy as a function of V contents at $T = 1000$ °C. The reference states are the stable structure of the pure elements at $P = 1$ atm and $T = 25.15$ °C. The *dashed lines* in (a) denote the common tangent lines, which define the two-phase regions

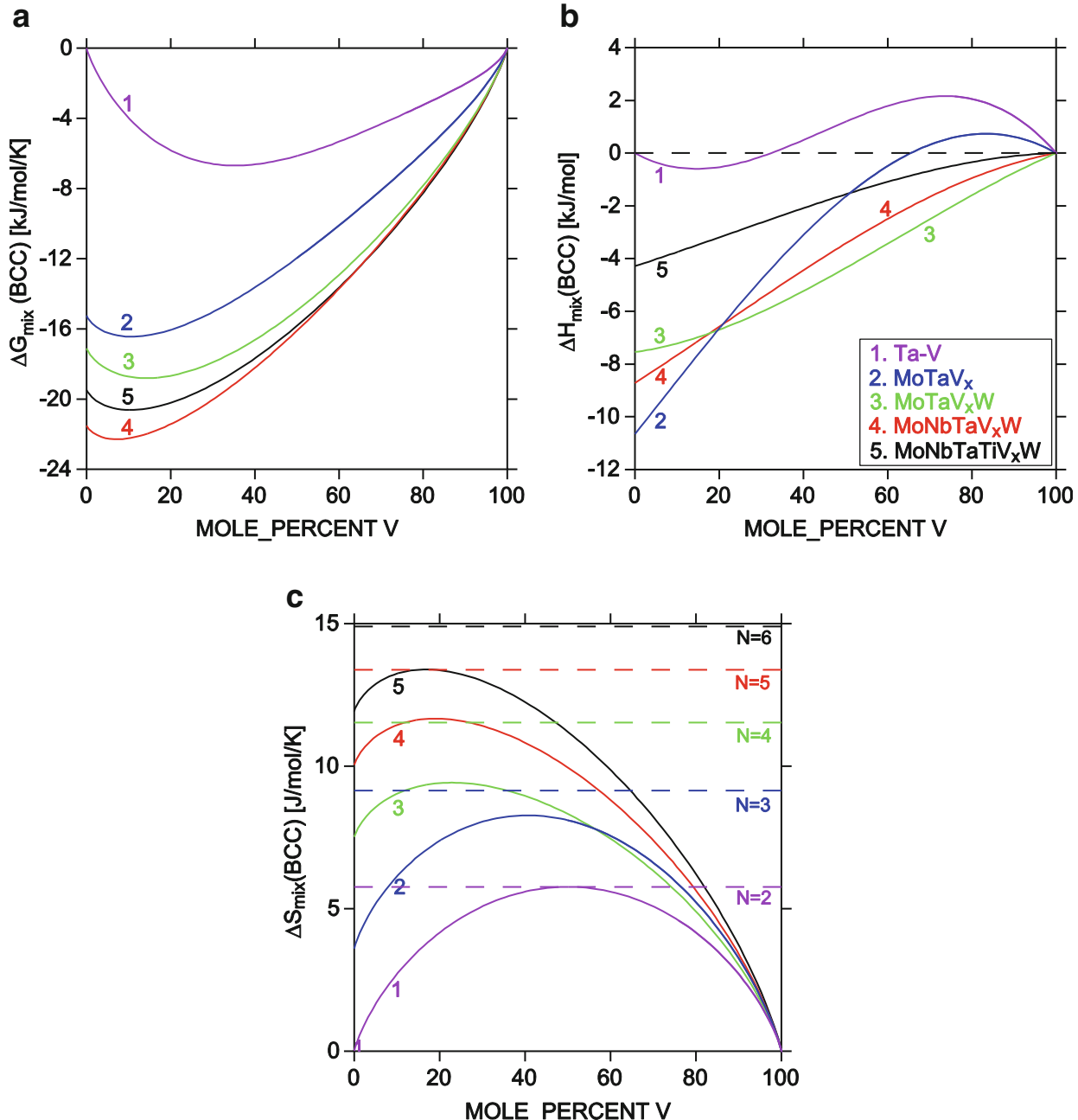


Fig. 12.9 Calculated mixing properties of the BCC phase at $T = 1000$ °C: (a) the Gibbs free energy of mixing, (b) enthalpy of mixing, and (c) entropy of mixing of TaV_x , MoTaV_x , MoTaV_xW , and $\text{MoNbTaTiV}_x\text{W}$ as a function of V contents. The reference state is the BCC phase at $P = 1$ atm and $T = 1000$ °C. The *dashed lines* in (c) denote the *maximum configurational entropy* of mixing and N signifies the total number of components

binary > senary > ternary > quinary > quaternary. For alloys > 50 at.% V, the order becomes binary > ternary > senary > quinary > quaternary. Figure 12.9c shows that the entropy of mixing in $\text{Ta}-\text{V}$ binary follows ideal mixing in entropy and the maximum entropy of mixing equals the maximum configurational entropy at 50 % V. With increasing of the number of components in the system, ΔS_{mix} increases as expected, but the solution deviates from the ideal solution, and the excess entropy becomes negative. The calculated excess entropy is 0.0, -0.9, -2.1, -1.7, and -1.5 J/K/mol for TaV , MoTaV , MoTaVW , MoNbTaVW , and MoNbTaTiVW , respectively. Note that

DFT calculations predict a negative vibrational entropy of mixing of -3.6 J/K/mol for MoNbTaW (see Chap. 10). The deviation in the composition that has the maximum entropy of mixing from the ideal mixing case is very small though.

12.4 Computational Thermodynamics-Aided HEA Design

The expression “computational thermodynamics” is frequently used in place of “calculation of phase diagrams.” This reflects the fact that the phase diagram is only a portion of the information that can be obtained from these calculations [32]. As a valuable tool, the applications of the computational thermodynamics to alloy design and development in various systems have been well established for decades [7, 33–35]. In recent years, hundreds of research papers on HEAs have been published (see Chap. 1). However, very few studies employed the computational thermodynamic approach for aiding the HEA development [3, 9, 10, 36–38]. As mentioned previously, the phase diagram is the crucial key to understanding of HEA formation. Phase diagrams contain succinct information about the thermodynamic properties of stable phases in equilibrium. In previous Sect. 12.3, we illustrated the understanding of HEA formation from the thermodynamic standpoint of view and analyzed the effects of different alloying elements on the thermodynamic properties, such as the Gibbs energy, enthalpy, and entropy. In this section, we first present experimental validation of PanHEA database by comparing model calculations and experimental results in several case studies. They are the phase relation as a function of Al contents as reflected in the $\text{Al}_x\text{CoCrFeNi}$ isopleth, phase evolution in $\text{Al}_{0.3}\text{CoCrFeNi}$ and $\text{Al}_{0.875}\text{CoCrFeNi}$, and equilibration study in $\text{Al}_{0.7}\text{CoCrFeNi}$. Then applications to other phase diagram calculations and modeling solidification are presented.

12.4.1 Phase Diagrams of the Al-Co-Cr-Fe-Ni System

12.4.1.1 Isopleth of $\text{Al}_x\text{CoCrFeNi}$

The $\text{Al}_x\text{CoCrFeNi}$ system has been one of the most thoroughly studied HEAs to date [39–46]. The effects of Al addition on the microstructure, mechanical properties, thermophysical properties, and magnetic and electrical properties have been systematically investigated. Figure 12.10 shows the calculated vertical section of the $\text{Al}_x\text{CoCrFeNi}$ with x varying between 0 and 2 using the PanHEA database [13]. This figure clearly demonstrates that the phase relation is very sensitive to Al contents in $\text{Al}_x\text{CoCrFeNi}$. It is seen that when $x < 0.78$, the primary solidified phase is FCC, and when $x > 0.78$, B2 solidifies first. Figure 12.10 also indicates that single-phase FCC will only be developed if Al ratio is kept small, while BCC and/or B2 phases will be developed if higher Al ratio is used, and a mixture of

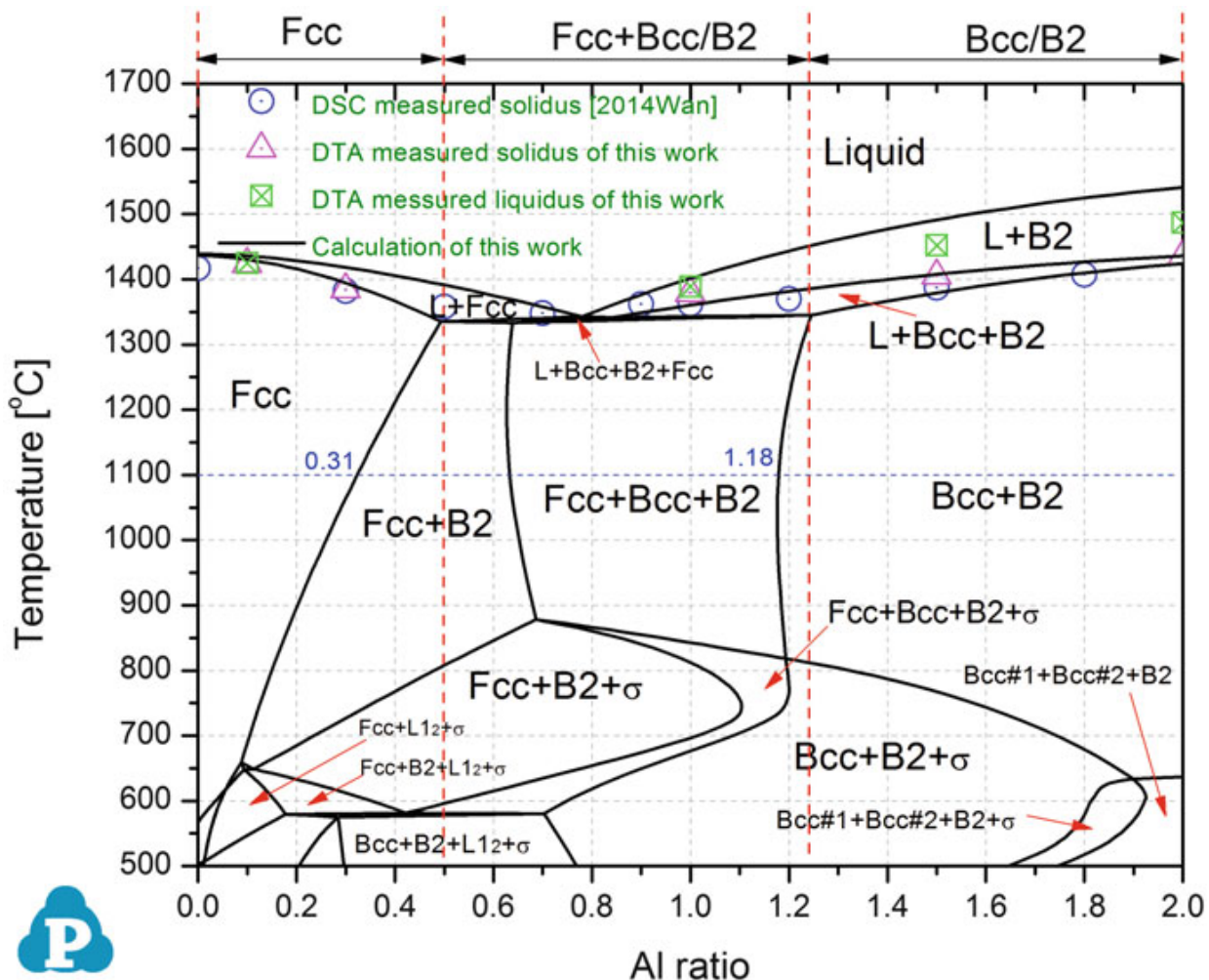


Fig. 12.10 Calculated isopleth of the $\text{Al}_x\text{CoCrFeNi}$ alloys with $x=0 \sim 2$ using our current thermodynamic description with DSC/DTA experimental data

FCC + BCC phases and/or B2 phase should form in between. This is exactly what was observed by many experimental studies on $\text{Al}_x\text{CoCrFeNi}$ alloys [39–46]. In addition, Kao et al. [39] characterized the structural evolution of the homogenized $\text{Al}_x\text{CoCrFeNi}$ HEAs at 1100 °C for 24 h. Their experimental results indicated that the FCC + BCC and/or B2 multiphase region is at $0.3 < x < 1.17$, while our CALPHAD predictions show that the same region is at $0.31 < x < 1.18$, as revealed by the horizontal line at 1100 °C in Fig. 12.10.

The liquidus and solidus temperatures of structural alloys are important to determine their working temperatures, and good agreement in these temperatures with experimental data is demonstrated in Fig. 12.10. The solidus temperatures were measured by Wang et al. [42] using differential scanning calorimetry (DSC), while the liquidus temperatures of four $\text{Al}_x\text{CoCrFeNi}$ alloys (with $x = 0.1, 1, 1.5$, and 2) were measured by the present authors and their collaborator using differential thermal analysis (DTA) at 10 °C/min for both heating and cooling cycles between room temperature and 1600 °C.

12.4.1.2 Phase Evolution in $\text{Al}_{0.3}\text{CoCrFeNi}$ and $\text{Al}_{0.875}\text{CoCrFeNi}$

To reveal the phase evolution in an alloy as a function of temperature, one can draw a vertical line in the isopleth (as shown in Fig. 12.10). However, unless the isopleth is a true quasi-binary section where all tie lines are in the plane of the section, the relative phase fractions cannot be obtained from such a section. Next we show in Fig. 12.11 two examples of 1D equilibrium thermodynamic calculation for fixed compositions of $\text{Al}_{0.3}\text{CoCrFeNi}$ and $\text{Al}_{0.875}\text{CoCrFeNi}$ and compare them with available experimental results.

Figure 12.11 predicts that the majority phase in $\text{Al}_{0.3}\text{CoCrFeNi}$ at elevated temperatures is FCC, and the B2 phase forms below the solvus temperature 1060 °C. Shu et al. [46] investigated the microstructure and tensile behaviors of the $\text{Al}_{0.3}\text{CoCrFeNi}$ HEA. They found the as-cast structure of this alloy is FCC and the B2 phase precipitates out when aged at 900 °C for 72 h. The tensile strength of this alloy after heat treatment was significantly improved. Although the results of ref. [46] were not used for the development of our Al-Co-Cr-Fe-Ni database, our prediction agrees with their experimental observation.

Chou et al. [47] investigated the phase transformation of $\text{Al}_{0.875}\text{CoCrFeNi}$ alloys at low temperatures using DTA and high-temperature X-ray diffraction (HTXRD). The precipitation of the σ phase was observed only at temperatures higher than 600 °C. Our CALPHAD calculation (shown in Fig. 12.11b) predicts that the σ phase forms in the temperature range of 375–860 °C (highlighted in the blue area). The main reason why Chou et al. [47] did not observe the σ phase below 600 °C could be the sluggish kinetics of σ formation at such low temperatures. Formation of complex σ phase involves typical nucleation and growth process, for which long-range diffusion is a rate-controlling factor at low temperatures. It is known that the kinetics of σ formation is very sluggish such as in the high-Cr steels [48]. Secondly, the heating rates used in typical DTA and HTXRD experiments usually do not

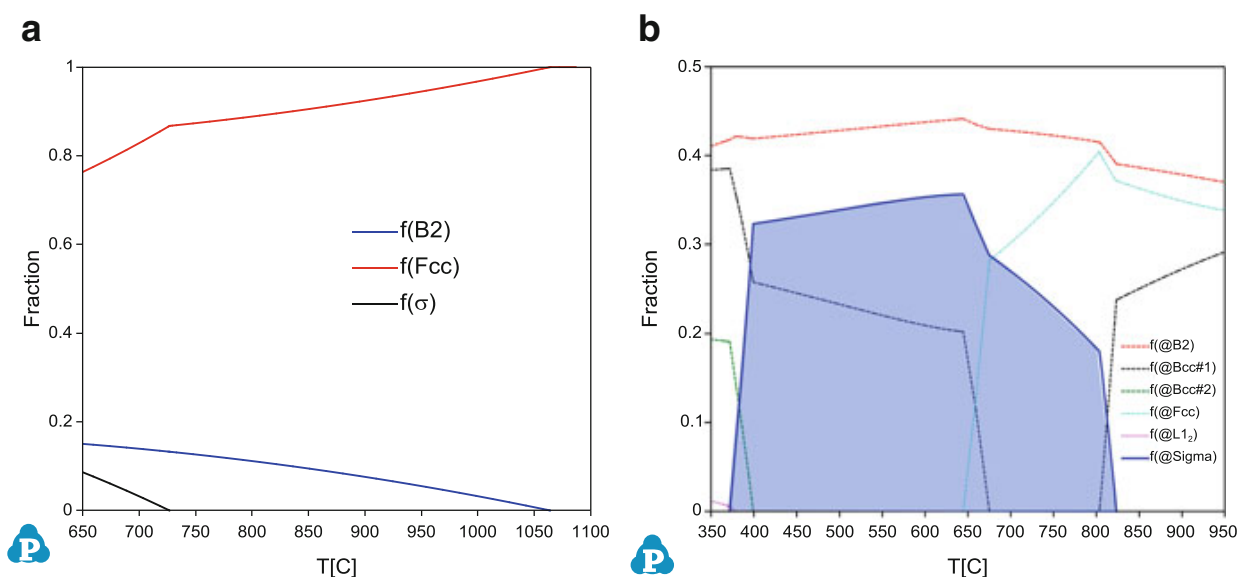


Fig. 12.11 1D equilibrium calculations of the (a) $\text{Al}_{0.3}\text{CoCrFeNi}$ and (b) $\text{Al}_{0.875}\text{CoCrFeNi}$ high-entropy alloys. The *shaded* region in (b) signifies the temperature range where σ phase forms

allow thermodynamic equilibration at low temperatures because of slow atomic diffusivity that follows an Arrhenius relationship with temperature. Future thermal equilibration experiments at 400–550 °C will be desirable to further validate the present CALPHAD predictions.

12.4.1.3 Phase Evolution in $\text{Al}_{0.7}\text{CoCrFeNi}$

It is possible that phase equilibria were not reached in previous experiments on $\text{Al}_x\text{CoCrFeNi}$ alloys [39–46] since the annealing times were not long enough. Therefore, the present authors and their collaborators annealed an alloy $\text{Al}_{0.7}\text{CoCrFeNi}$ at 1250 °C for 1000 h to ensure that the equilibrium state was reached. The alloy was prepared using arc melter from constituent elements of purity greater than 99 wt.% in a vacuum of at least 0.01 torr under a Ti-gettered argon atmosphere. The sample was remelted several times to improve its homogeneity. The obtained button was about 300 g in weight and 10 mm in thickness. The final composition of the alloy is confirmed through quantitative analysis by inductively coupled plasma optical emission spectrometers (ICP-OESs), which is very close to the nominal composition. The as-cast alloy was then cut into cuboid and wrapped by Ta foil before being sealed in the quartz tube with backfilled argon atmosphere. The encapsulated sample was placed in a box furnace at 1250 °C for 1000 h and then water-quenched at the end of the heat treatment. The identification of phases within the heat-treated sample was carried out by using a high-energy synchrotron X-ray diffraction (XRD), scanning electron microscopy (SEM) including energy-dispersive X-ray spectroscopy (EDS) and orientation image mapping (OIM), electron backscatter diffraction (EBSD), as well as atom probe tomography (ATP).

The 1D equilibrium calculation for $\text{Al}_{0.7}\text{CoCrFeNi}$ (see Fig. 12.12) shows that there is no single-solid-phase region. The FCC phase coexists with both the disordered BCC and ordered B2 phases at elevated temperatures ($850 < T < 1340$ °C). The σ phase precipitates out from the FCC phase at lower temperatures (< 850 °C). At 1250 °C as indicated by the green dashed line, the majority phase is FCC at about 64 % mole percent. The amount of the BCC and B2 phases are comparable (~20 % for each phase).

The microstructure of the equilibrated $\text{Al}_{0.7}\text{CoCrFeNi}$ alloy is shown in Fig. 12.13a. It contains two distinct phases (gray and dark). The phase identification results using XRD and SEM/EDS indicate that the gray phase is FCC and the dark one is BCC. The EBSD phase mapping shows in Fig. 12.13b and the measured phase fraction of the FCC is about 67 %, which agrees with our thermodynamic prediction 64 %. Note that the XRD and EBSD may not be able to distinguish the disordered BCC and ordered B2 phases due to their similarity on crystal structure. In order to clarify this issue, the high-accuracy atom probe investigation was performed at Oak Ridge National Laboratory (ORNL). Figure 12.14 shows the detected elemental distributions within different phases. Figure 12.14a shows that each element uniformly distributes within the FCC phase, which confirms the red

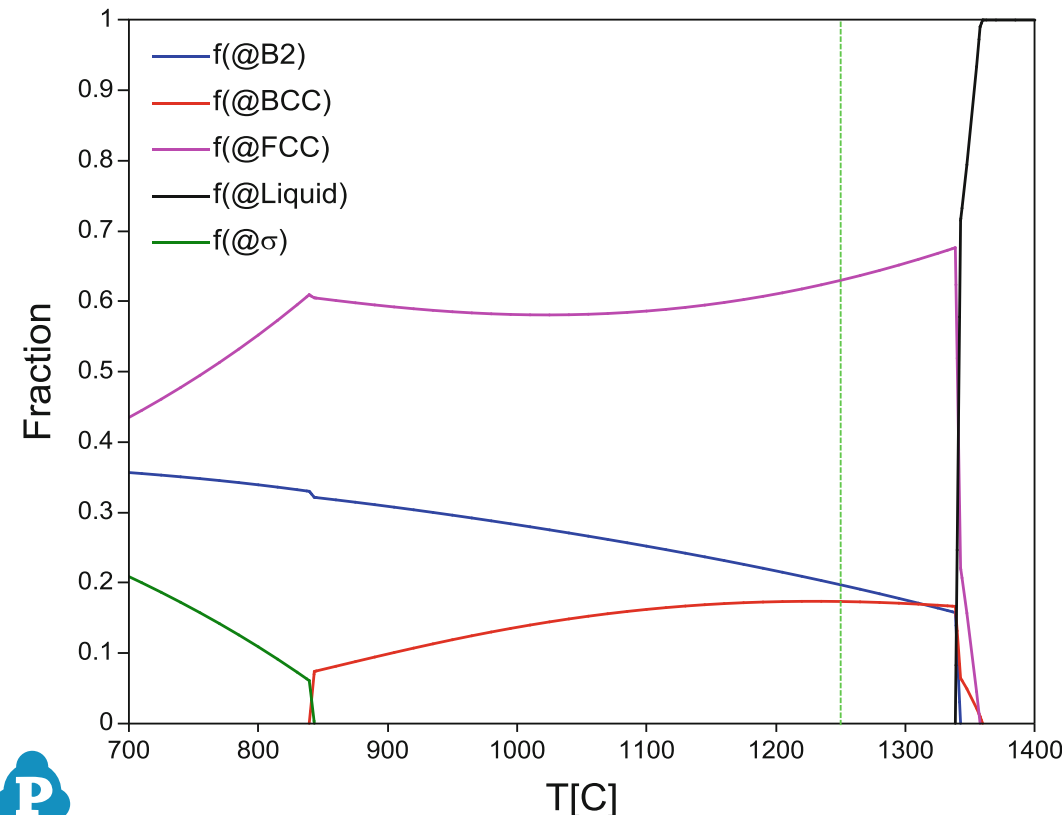


Fig. 12.12 Equilibrium calculation of the $\text{Al}_{0.7}\text{CoCrFeNi}$ HEA using the PanHEA database

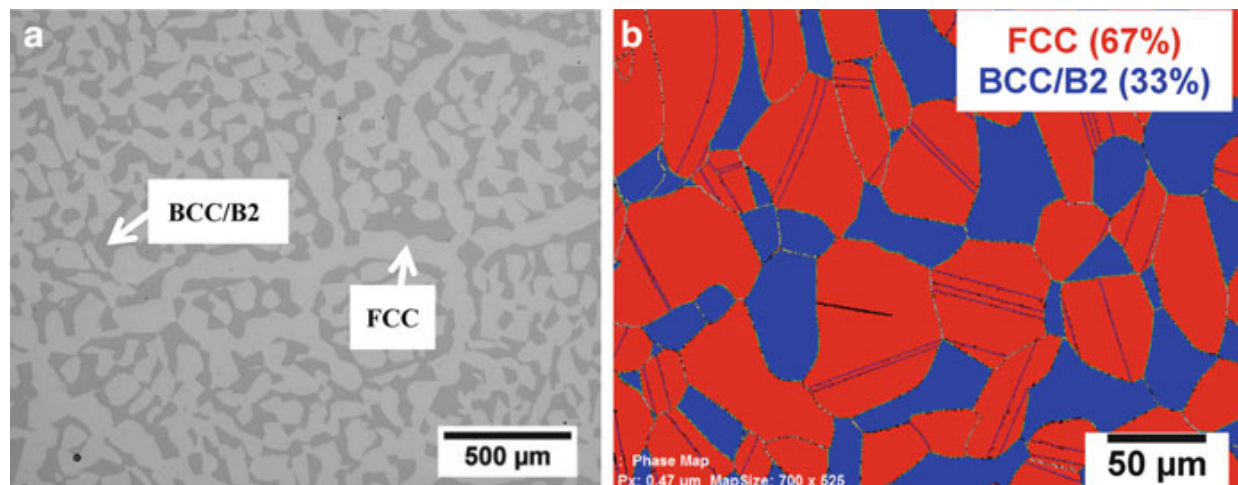


Fig. 12.13 Microstructure of $\text{Al}_{0.7}\text{CoCrFeNi}$ HEA annealed at $1250\text{ }^{\circ}\text{C}$ for 1000 h (a) SEM; (b) EBSD

phase region within Fig. 12.14b is a single solid solution phase. Conversely, Fig. 12.14b shows obvious elemental segregation within the blue-phase region. As shown in Fig. 12.14b–f, there are two concentration-rich regions: one is the NiAl rich and the other one is the CrFe rich. Coupling with our XRD results, they are confirmed to be the NiAl-rich B2 and CoCrFe-rich BCC phases individually, which validates the reliability of our thermodynamic prediction. On the basis of our current APT results (as shown in Fig. 12.14), the BCC and B2 phases are

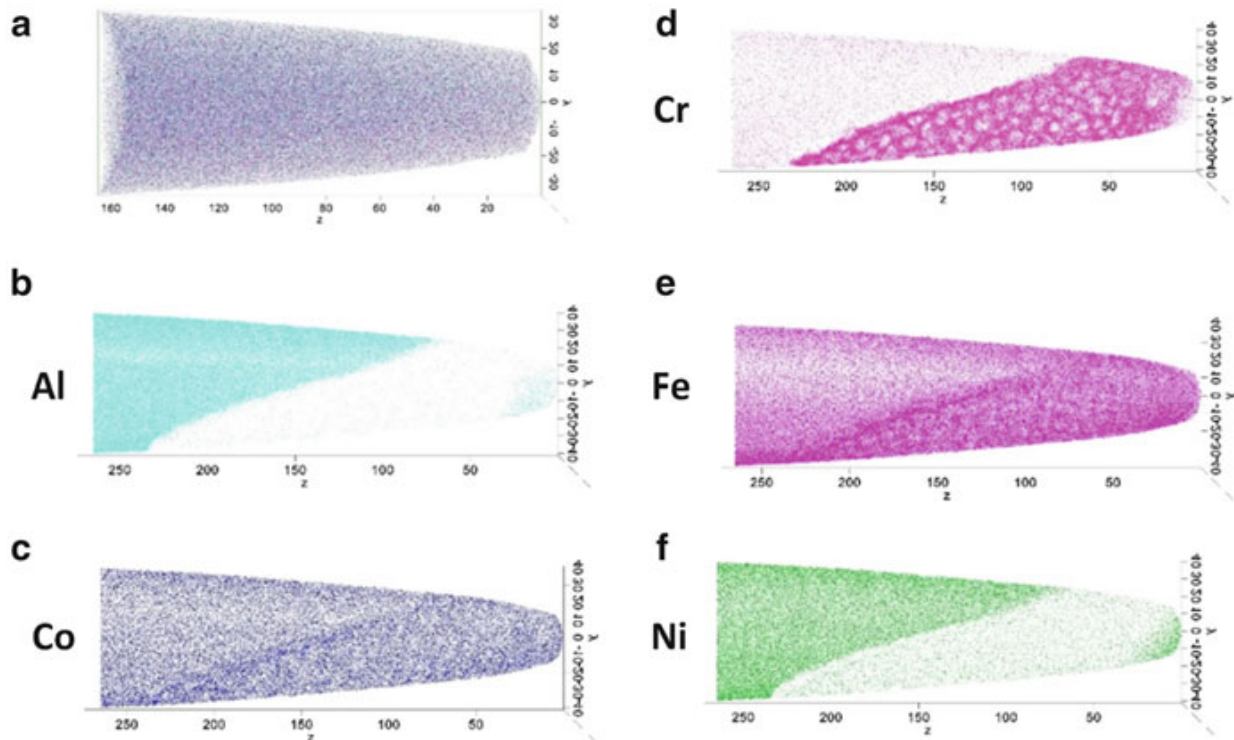


Fig. 12.14 Concentration mapping using the atom probe tomography, (a) all elements distribution within the FCC phase region; (b–f) distribution of each component within the BCC-based phase region

Table 12.1 Calculated chemical composition of stable phases in comparison with experimental measurements for the $\text{Al}_{0.7}\text{CoCrFeNi}$ alloy equilibrated at $1250\text{ }^{\circ}\text{C}$ for 1000 h

Phases	Composition (at.%)									
	Al		Co		Cr		Fe		Ni	
	Cal.	Exp.	Cal.	Exp.	Cal.	Exp.	Cal.	Exp.	Cal.	Exp.
FCC	9.54	10.2	23.95	22.7	22.32	23.1	24.69	23.6	19.50	20.1
BCC	8.68	5.1	21.14	21.1	34.59	37.1	27.14	27.2	8.45	9.5
B2	37.5	35.8	12.86	15.6	6.23	4.4	5.21	7.8	38.2	36.4

concomitant. Small NiAl-rich B2 particles were found in the vicinity of the CrFe-rich BCC phase region.

The chemical compositions for the FCC, BCC, and B2 phases in $\text{Al}_{0.7}\text{CoCrFeNi}$ at $1000\text{ }^{\circ}\text{C}$ calculated from PanHEA are listed in Table 12.1, and the agreement with experimental measurements is good. Note that a previous study by Liu et al. [49] also shows good agreement in the chemical composition of the BCC and B2 phases in $\text{Al}_{0.5}\text{CrFeNiTi}_{0.25}$ between CALPHAD prediction and TEM measurements.

In summary, taking into account the uncertainties from both experimentation and thermodynamic calculation, the agreement in phase diagrams between CALPHAD modeling using the PanHEA database and the available experiments for the Al-Co-Cr-Fe-Ni system is considered acceptable overall.

12.4.1.4 Phase Diagram Predictions

Taking advantage of computational thermodynamics, more phase diagrams of the Al-Co-Cr-Fe-Ni system are calculated using the current PanHEA database for better understanding the compositional and temperature effects on the microstructure of HEAs in the Al-Co-Cr-Fe-Ni system. Figure 12.15 shows how the calculated isothermal section at 1000 °C evolves with respect to the alloy system. For the Cr-Fe-Ni ternary system, FCC solid solution phase dominates at low Cr contents and BCC is stable at the Cr-rich region. With the addition of Al to the Cr-Fe-Ni system, the order BCC structure (i.e., B2) forms and the phase field of BCC + B2 dominates. The ordered FCC structure (i.e., Fcc_L1₂) only forms at the Ni-rich corner.

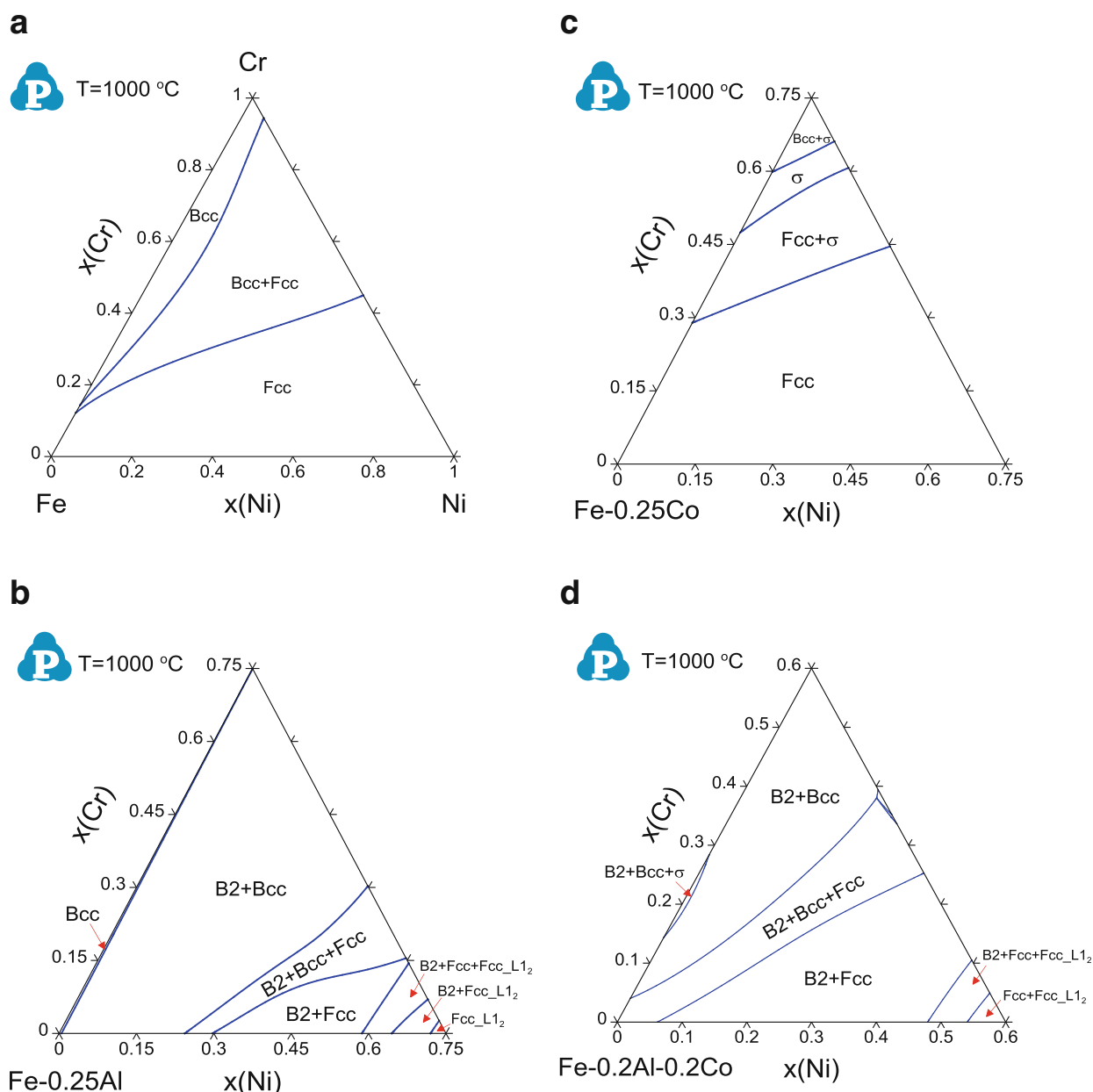


Fig. 12.15 Calculated 1000 °C isothermal sections for (a) Cr-Fe-Ni, (b) Cr-Fe-Ni-0.25Al, (c) Cr-Fe-Ni-0.25Co, and (d) Cr-Fe-Ni-0.2Al-0.2Co systems using our current thermodynamic database

(The terms Ll_2 and Fcc_Ll_2 are used interchangeably in this chapter.) With the addition of Co to the Cr-Fe-Ni system, FCC solid solution phase dominates, and it has much larger Cr solubility than that in the ternary Cr-Fe-Ni system. Note that the σ phase forms at the Cr-rich corner since the σ phase is stable in both the Cr-Fe and Co-Cr binary systems. Especially for the Co-Cr system, the σ phase can be stable up to 1283 °C. Thus Co has the side effect of stabilizing the σ phase although it is a potent FCC stabilizer for the Al-Co-Cr-Fe-Ni system. With the additions of both Al and Co, the phase relationships (Fig. 12.15d) are similar to those obtained when adding Al only (Fig. 12.15b). These findings indicate that Al has a stronger effect than Co on the stability of solution phases within the Al-Co-Cr-Fe-Ni system. This is due to the remarkable enthalpy lowering of the BCC phase with Al addition as shown in Sect. 12.3. Nonetheless, the phase field of BCC + B2 in Cr-Fe-Ni-0.2Al-0.2Co is much smaller than Cr-Fe-Ni-0.25Al.

Previous examples have shown the effect of Al addition on the FCC/BCC phase transition since it impacts tremendously the microstructure and mechanical properties of various HEA systems [50]. It will be interesting to fully understand the effect of other alloying elements in this regard, and such examples are shown in Fig. 12.16 for the isopleths of $Al_xCo_{1.5}CrFeNi$, $Al_xCoCr_{1.5}FeNi$, $Al_xCoCrFe_{1.5}Ni$, and $Al_xCoCrFeNi_{1.5}$ with $x = 0 \sim 2$. Figure 12.16a indicates that the higher Co ratio has insignificant effect on the BCC/FCC phase transformation, compared to $Al_xCoCrFeNi$ (Fig. 12.10). Higher Cr ratio (Fig. 12.16b) stabilizes the disordered BCC phase against both ordered B2 and FCC. It has been found that both Al and Cr are stabilizers of the BCC-based structure [45, 51], which is consistent with our thermodynamic calculations. In addition, our calculations also indicate that Al stabilizes both BCC and B2 phases, yet more in favor of B2 phase, while Cr stabilizes BCC phase but destabilizes B2 phase. The isopleth with higher Fe ratio shown in Fig. 12.16c indicates that Fe can also stabilize the BCC phase especially at elevated temperatures. But the BCC stabilizing effect of Fe is much weaker than that of Al and Cr. Figure 12.16d shows the higher ratio of Ni stabilizes the FCC phase to higher Al ratio.

12.4.1.5 Modeling Solidification

As demonstrated in Figs. 12.10, 12.11, 12.12, 12.13, 12.14, 12.15, and 12.16, the phases within under the equilibrium conditions can be directly predicted on the basis of thermodynamic calculations at constant compositions or constant temperatures. While in some cases, the HEAs were obtained in the as-cast conditions, which are not in thermodynamic equilibrium. The as-cast microstructure of HEAs, such as the degree of the microsegregation and the types and amounts of the secondary phases, will significantly impact the mechanical properties of the solidified alloys. Thus, accurate prediction of the solidification paths and microsegregation of multicomponent alloys under a given solidification condition is important in optimizing the composition and processing parameters in developing new HEAs. Based on the CALPHAD approach, two crude models are

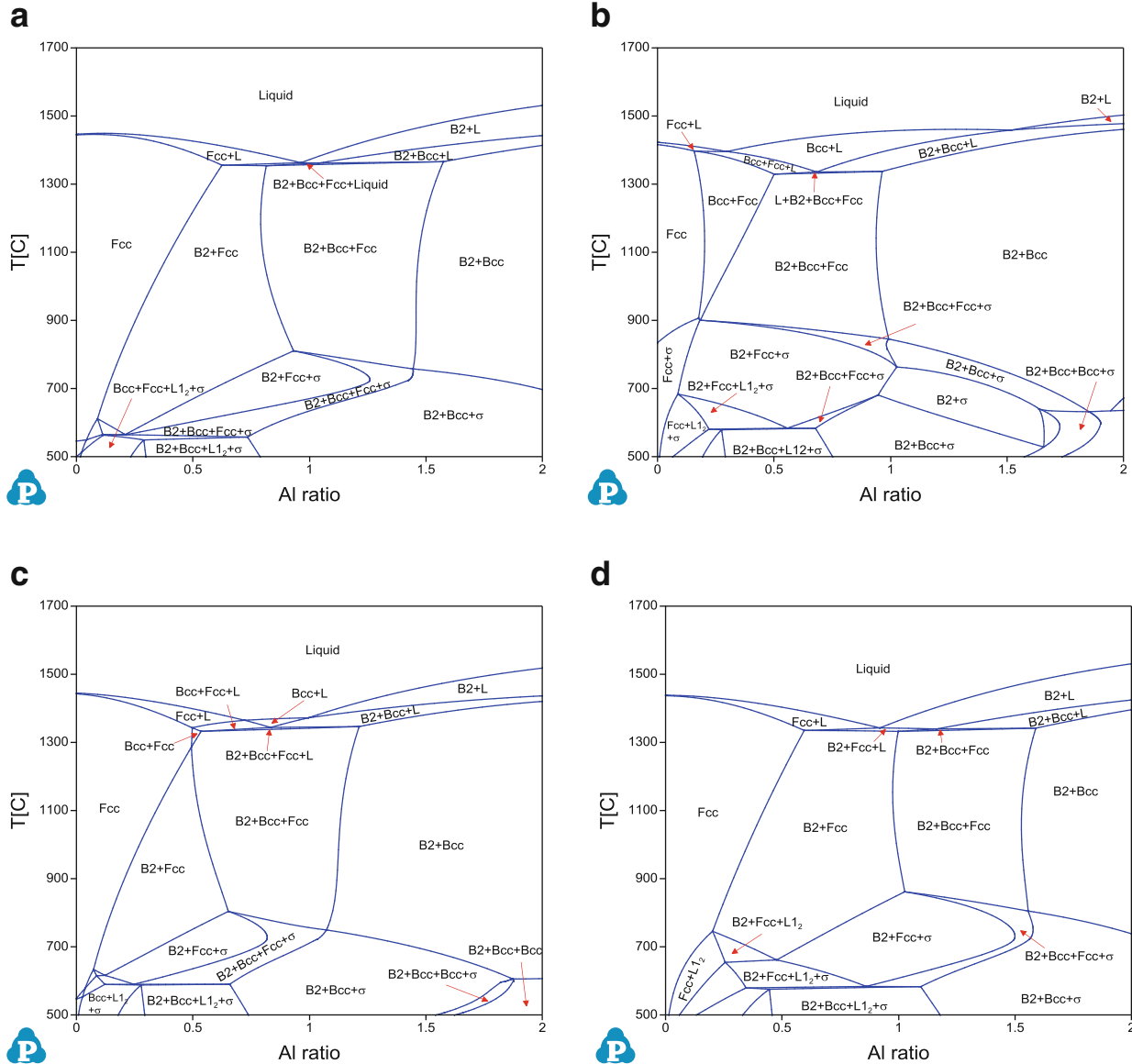


Fig. 12.16 Calculated isopleths of (a) $\text{Al}_x\text{Co}_{1.5}\text{CrFeNi}$, (b) $\text{Al}_x\text{CoCr}_{1.5}\text{FeNi}$, (c) $\text{Al}_x\text{CoCrFe}_{1.5}\text{Ni}$, and (d) $\text{Al}_x\text{CoCrFeNi}_{1.5}$ with $x = 0 \sim 2$ using PanHEA thermodynamic database

commonly employed to simulate the solidification process in simple and efficient ways without evoking kinetic calculations: equilibrium (lever-rule) and non-equilibrium (Scheil-Gulliver) models [52, 53]. They both assume complete solute mixing in the liquid. For the solid, the lever-rule model assumes the solute diffusion is infinity, while the Scheil-Gulliver model assumes no solute diffusion within the solid. These two models describe the two extreme cases of solidification. Most HEAs usually are made via the drop-casting or arc-melting techniques with relatively high cooling rates; thus we can employ the Scheil-Gulliver model as presented next.

Kao et al. [40] also did systematic microstructure investigations of the as-cast $\text{Al}_x\text{CoCrFeNi}$ HEAs with various Al contents. Based on their experimental observation of microstructure dependence on the Al content, they found that it is single-phase FCC when $x < 0.45$ and BCC/B2 when $x > 0.88$. The FCC + BCC/B2 duplex structure was seen when the Al ratio is in the midrange, i.e., $0.45 < x < 0.88$. Figure 12.17a shows the simulated solidification paths of the $\text{Al}_x\text{CoCrFeNi}$ HEAs

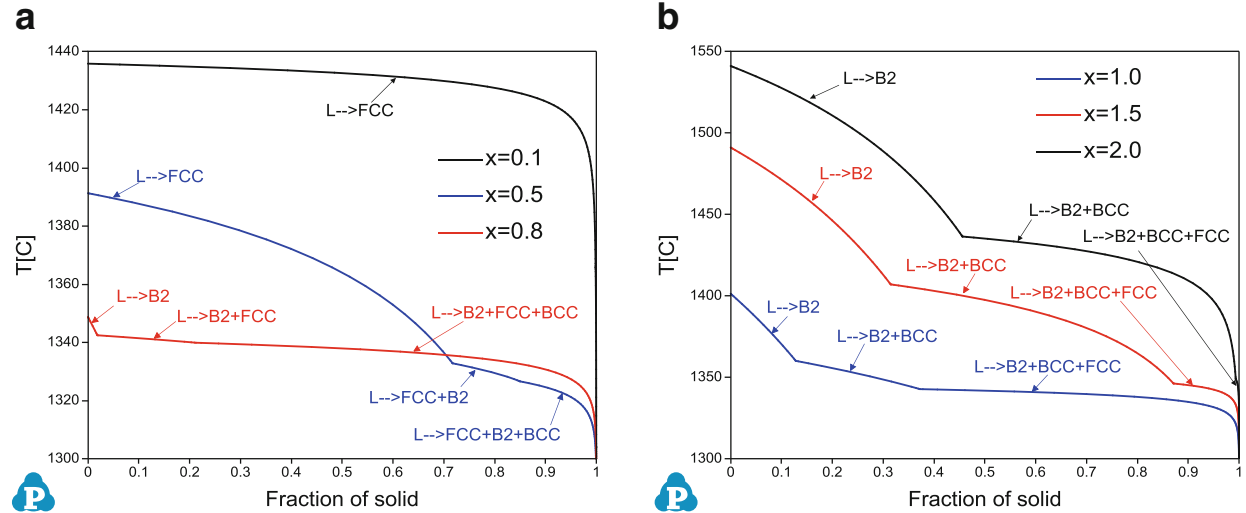


Fig. 12.17 Calculated solidification paths of the $\text{Al}_x\text{CoCrFeNi}$ alloys with $x=0 \sim 2$ using our current thermodynamic description and the Scheil-Gulliver model

with $x = 0.1, 0.5$, and 0.8 using the Scheil-Gulliver model. Following the black line shown in Fig. 12.17a, the solidification path of the $\text{Al}_{0.1}\text{CoCrFeNi}$ alloy can be directly forecast, which is $\text{liquid} \rightarrow \text{liquid} + \text{FCC} \rightarrow \text{liquid} + \text{FCC} + \text{BCC} \rightarrow \text{liquid} + \text{FCC} + \text{BCC} + \text{B}2 \rightarrow \text{FCC} + \text{BCC} + \text{B}2$. It indicates that the $\text{FCC} + \text{BCC}/\text{B}2$ structure solidified together from liquid even for $x = 0.1$. However, 99.8 % of the liquid forms the primary FCC phase, and the total amount of BCC + B2 formed from the calculation is only 0.2 %, which is hardly seen even if it does exist. When $x = 0.5$, the calculated solidification path is the same as for $\text{Al}_{0.1}\text{CoCrFeNi}$. It is seen from the blue line of Fig. 12.17a that 28 % liquid is still there to form FCC + BCC/B2 duplex structure when $x = 0.5$. The simulation shows that the total mole fraction of BCC + B2 that may form in this case is 8.7 %, which is sufficient to be observed in the microstructure. The simulation for $x = 0.8$ shows very interesting features (red line in Fig. 12.17a). The calculated solidification path is $\text{liquid} \rightarrow \text{liquid} + \text{B}2 \rightarrow \text{liquid} + \text{FCC} + \text{B}2 \rightarrow \text{liquid} + \text{FCC} + \text{BCC} + \text{B}2 \rightarrow \text{FCC} + \text{BCC} + \text{B}2$. The primary solidified phase is $\text{B}2$ (total 1.8 %), while 98.2 % liquid is to form the mixture of $\text{B}2 + \text{BCC} + \text{FCC}$. The solidification of this alloy finishes in a narrow temperature range, from 1342 to 1294 $^{\circ}\text{C}$. This composition is close to the so-called deep eutectic point and may develop into an amorphous structure upon very high cooling rates [35].

Figure 12.17b shows the simulated solidification paths for $x > 0.8$ of the $\text{Al}_x\text{CoCrFeNi}$ alloys, which indicate that the primary solidified phase is $\text{B}2$. According to our simulations, their solidification paths are the same: $\text{liquid} \rightarrow \text{liquid} + \text{B}2 \rightarrow \text{Liquid} + \text{B}2 + \text{BCC} \rightarrow \text{Liquid} + \text{FCC} + \text{BCC} + \text{B}2 \rightarrow \text{FCC} + \text{BCC} + \text{B}2$. When $x = 1.0$, only 12.8 % of the liquid is consumed to form the primary $\text{B}2$ and the next 8.4 % of liquid forms BCC-base phases (both BCC and $\text{B}2$). Then the rest of liquid forms FCC + BCC/B2 structures. It should also be pointed out that, when $x > 1.0$, the simulation shows that the BCC structure is a mixture of ordered $\text{B}2$ and disordered BCC, which is consistent with many published experimental results [39, 45, 47]. The simulation shows that FCC phase

should appear even when $x = 2$, while in reality it may not be observed due to its insignificant amount (0.3 %). As is seen, with the increasing of x , the amount of liquid left for the $L \rightarrow B2 + BCC + FCC$ reaction becomes smaller, and the solidification temperature range becomes narrower. Both factors make it difficult to observe the FCC phase in the as-solidified microstructure under high cooling rate.

Using the Al-Co-Cr-Fe-Ni quinary system as an example, we show how to apply proper thermodynamic calculations to understand the experimental results and guide HEA design. It should be pointed out that the alloy properties are determined by their microstructures that depend on not only the alloy chemistry but also processing and heat treatment. Most of the HEAs were usually prepared by arc melting and then drop casting, which tend to maintain the structure of primary solidified phase. However, in case if the equilibrium phase is not the disordered solid solution phase, then other phases will form upon annealing at high temperatures for long enough time. The alloy with the FCC structure shows good ductility but low strength while the B2-type intermetallic compounds generally show excellent strength but low ductility. Therefore, it is expected that a composite of FCC matrix with B2 precipitates may provide the optimal balance in strength and ductility such as $Al_{0.3}CoCrFeNi$. It is expected that similar microstructure could also be obtained in $Al_xCo_{1.5}CrFeNi$, $Al_xCoCrFe_{1.5}Ni$, and $Al_xCoCrFeNi_{1.5}$ with wider ranges of x values based on the phase diagram information shown in Fig. 12.16.

12.4.2 Phase Diagrams of Al-Cr-Cu-Fe-Ni System

Previously the microstructures of the as-cast $Al_xCrCuFeNi_2$ alloys ($x = 0.2 \sim 2.5$) were investigated by Guo et al. [54]. They showed that only the FCC solid solution was detected when $x \leq 0.7$ and that the BCC disordered solid solution started to be detected at $x = 0.8$ by XRD. Formation of ordered BCC (the B2 phase) started to form at $x = 0.9$ seen from those superlattice diffraction peaks from the XRD. At $x \geq 1.8$, FCC solid solutions could not be detected, suggesting this phase either no longer exists or its amount was tiny. Based on the as-cast microstructures of $Al_xCrCuFeNi_2$ alloys, it was concluded that $Al_{1.2}CrCuFeNi_2$ is a eutectic composition.

The calculated isopleth using the PanHEA database is shown in Fig. 12.18. The agreement with Guo et al.'s experiments [54] is very good. As illustrated in Fig. 12.18, with $x \leq 0.6 \sim 0.74$ at the temperature range of 1100–1150 °C, only FCC phase exists. With increasing Al ratio, the BCC-typed phases (ordered B2 and/or disordered BCC) form and the amount of FCC phase decreases. At $x \approx 1.1$, the calculated liquidus temperature reaches a local minimum implying that the eutectic point is in the vicinity of this composition. When $x \geq 1.8$, the FCC amount becomes negligible. This indicates that our thermodynamic calculation can well describe the experimental observation [54], which give us great confidence on our

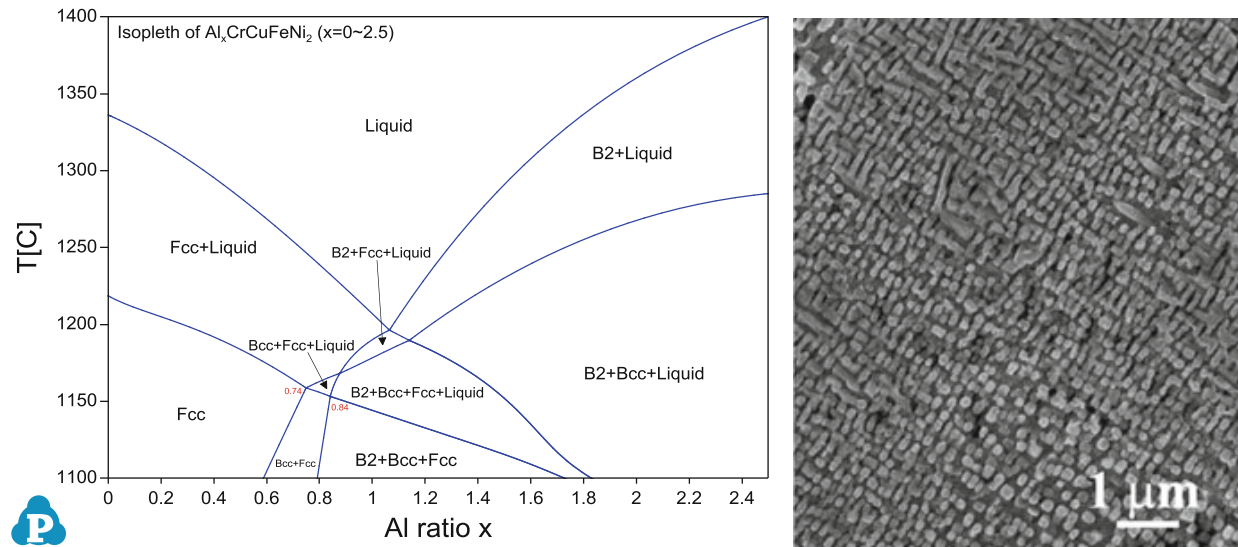


Fig. 12.18 Calculated isopleth of $\text{Al}_x\text{CrCuFeNi}_2$ ($x=0 \sim 2.5$) [55] (The SEM picture is reproduced from [54])

thermodynamic database capabilities to assist alloy design in the Al-Cr-Cu-Fe-Ni system.

12.4.3 Phase Diagrams of Mo-Nb-Ta-Ti-V-W System

The phase diagrams and thermodynamic properties of the Mo-Nb-Ta-Ti-V-W system were presented in the Sect. (12.3.3). Here we present the phase composition evolution during non-equilibrium solidification in an alloy with nominal composition of MoNbTaTiVW in comparison with experiments, as shown in Fig. 12.19. The non-equilibrium solidification simulated using the Scheil-Gulliver model indicates the formation of a single-phase BCC structure in the as-cast state. The simulations predict a liquidus temperature of 2533 °C, equilibrium solidus temperature 2246 °C [30], and a (non-equilibrium) solidus temperature of 1661 °C. The simulations also predict that elements of high melting points are depleted in the liquid in descending order W > Ta > Mo > Nb while it is enriched with Ti and V. At the very beginning of solidification, BCC phase is enriched in W followed by Ta but is depleted of V and Ti, while Mo and Nb seem to be close to the nominal composition. Therefore, due to the continuous cooling in a non-equilibrium path during typical arc-melting process for ingot preparation, compositional fluctuation in wide ranges especially for W, Ta, Ti, and V is anticipated in the as-cast alloy. The predicted micro-segregation behavior actually agrees well with experimental measurement using SEM-EDX as shown in Fig. 12.19d. The dendrites form first during solidification and are truly enriched in W followed by Ta, while the interdendritic regions form at lower temperatures and are enriched in Ti, V, and Nb. The distribution of Mo seems fairly uniform, and there is small Nb segregation to the interdendritic

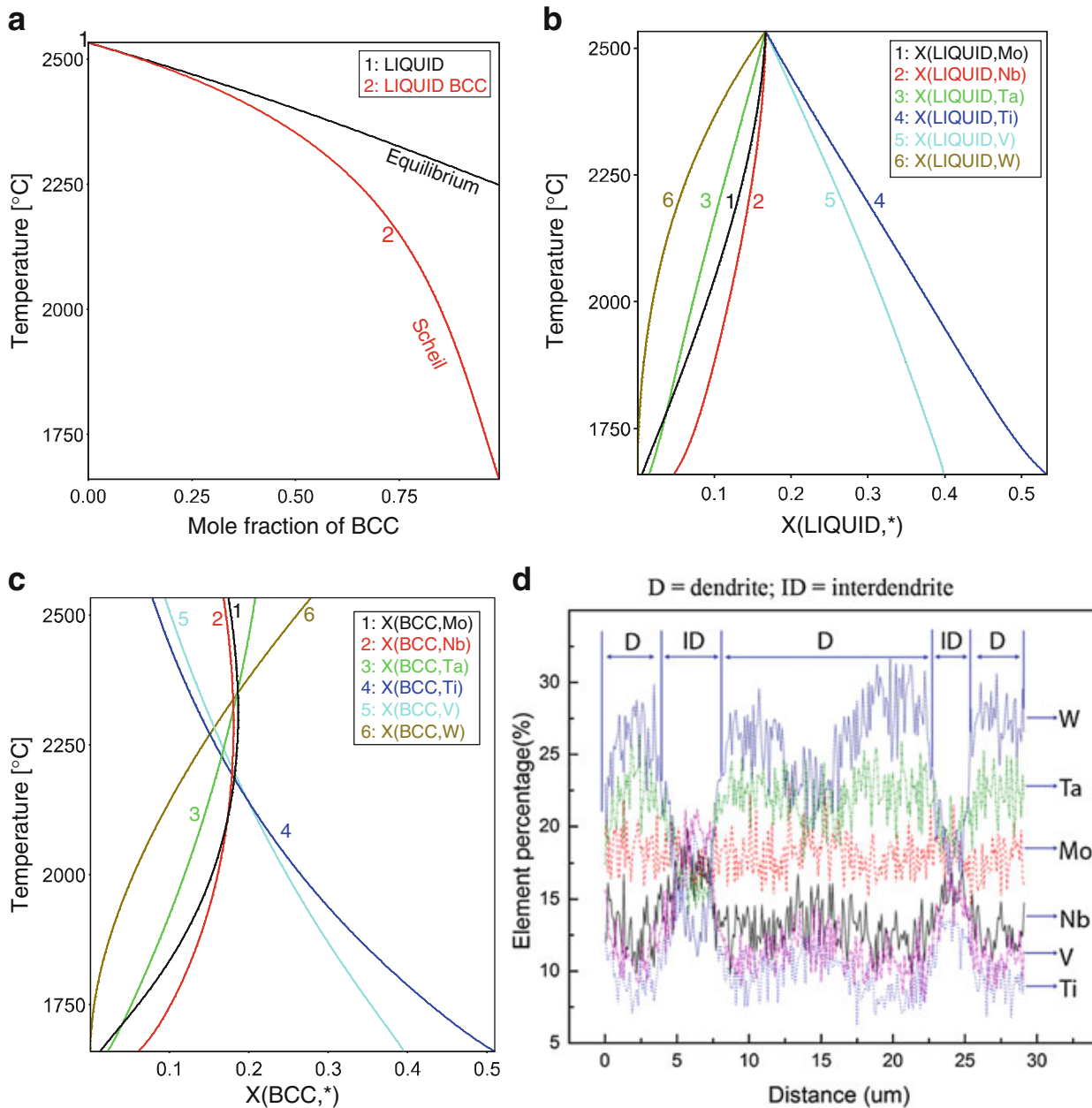


Fig. 12.19 Non-equilibrium solidification using the Scheil-Gulliver model: (a) mole fraction of solids, (b) liquid composition, and (c) BCC phase composition. (d) Composition profile across dendrites and interdendrites (Reproduced from Ref. [30])

regions. It is expected that the agreement can be improved if atomic diffusion can be considered in the simulation provided that the mobility database is available.

12.5 Outlook

The CALPHAD approach adopts a semiempirical methodology and the coefficients of many interaction parameters may not have true physical meaning. The thermodynamic database development using the CALPHAD method critically relies on the availability of reliable experimental data on phase diagrams and

thermochemistry of phases. Extrapolation of binaries and ternaries into higher-order systems may not always guarantee satisfactory agreement with experiments, especially if there are stable quaternary and/or quinary compounds. When using thermodynamic databases for HEA design, the user needs to consider the following key issues:

1. How reliable are the binary and ternary descriptions? Do they cover the entire composition and temperature ranges?
2. Are the Gibbs energy descriptions for those “hypothetical” phases and pure elements physically reasonable? For example, the competing phases against FCC in Al-Co-Cr-Cu-Fe-Mn-Ni-Ti include σ , BCC, B2, and HCP phases, but σ phase is not stable for those binary systems containing Al or Cu. Similar questions arise for those BCC HEA systems based on refractory metals. The Laves phases (C14, C15, and C36) are only stable in certain binaries (e.g., Cr with Ti, Zr, Hf, Nb, Ta; Mo/W with Hf/Zr; etc.) and not stable in many others (e.g., Cr with V/Mo/W, Ti with V/Nb/Ta/Mo/Ta, etc.). But the Gibbs energies for these hypothetical/unstable compounds are still needed for a self-consistent database development (see Eqs. 12.13 and 12.14). It is not sufficient to select the Gibbs energy descriptions that will make those hypothetical phases unstable, but whether they are physically meaningful remains a big question. Without doubts, the energies of these hypothetical phases will impact the phase stability for multicomponent systems such as HEAs and thus the rationale of these data cannot be ignored during CALPHAD database development.
3. Since HEAs are still at their infancy stage, there are few experimental data dedicated to their phase equilibrium and thermochemistry data. This makes direct validation of thermodynamic databases very difficult.

With recent progress in first-principles DFT calculations, the enthalpy of formation [23–27, 56] and even the Gibbs free energy of compounds can be predicated without experimental input. The application of these data to the hypothetical compounds in binary and ternary systems is particularly important for developing physically meaningful databases for HEA systems.

Due to the prevalence in partially disordered solid solution and partially ordered intermetallics in HEA systems as pointed out by Santodonato et al. [57] who studied the solidification behavior in $\text{Al}_{1.3}\text{CoCrCuFeNi}$, it will be important to quantify the true configurational entropy and then other entropy sources in HEAs within the CALPHAD framework. Developing kinetic databases using the CALPHAD method is equally important as developing thermodynamic databases, which will allow users to simulate more realistic solidification behavior and phase transformations kinetics. The following subsections provide brief discussions along these directions.

12.5.1 Impact of Chemical Ordering on Entropy

The term “order” in metallurgical parlance denotes the presence of crystallinity as opposed to an amorphous arrangement of atoms. Orderliness over distance comparable to interatomic distances is called short-range order (SRO), whereas orderliness repeated over infinitely great distances is called long-range order (LRO). LRO distinguishes a crystalline solid solution in which the atomic species, two or more, reside on distinct sublattices. SRO distinguishes a solid in which atoms of one species have more nearest neighbors of the other species than would be found if environments were entirely random [58]. The disordered solution and LRO have been well handled in the CALPHAD assessments by thermodynamic models [59].

In thermodynamics, entropy is defined as a measure of the disorder in the arrangements of atoms in a system. According to the third law of thermodynamics [60], the crystalline phases have the perfect “ordered” structures and the entropy is zero at absolute zero temperature. In order to reveal the temperature effect on the entropy of HEAs, the total entropy and entropy of mixing of BCC, FCC, and HCP phases in the compositions of CoCr, CoCrFe, CoCrFeMn, and CoCrFeMnNi are calculated and are presented in this subsection. The same crystal structure as the according phase of each component is used as the reference state. For example, thermodynamic properties of pure Co and Cr in the BCC structure are used as their reference states to calculate the entropy mixing of BCC CoCr phase.

Figure 12.20a shows the declining trend in the total entropy of BCC phase with decreasing temperature, obeying the third law of thermodynamics. Note that the inflection point on each line of Fig. 12.20a is due to the BCC phase separation: $BCC = BCC\#1 + BCC\#2$. The second inflection point for the CoCrFeMnNi system at lower temperature is according to the reaction of $BCC = BCC\#1 + BCC\#2 + BCC\#3$. The calculated mixing entropy (ΔS_{mix}) of each alloy using Eq. 12.19 is shown in Fig. 12.20b. It indicates that the ΔS_{mix} slightly increases with decreasing temperature till the vicinity of 565 °C (CoCr binary) and then drops quickly at

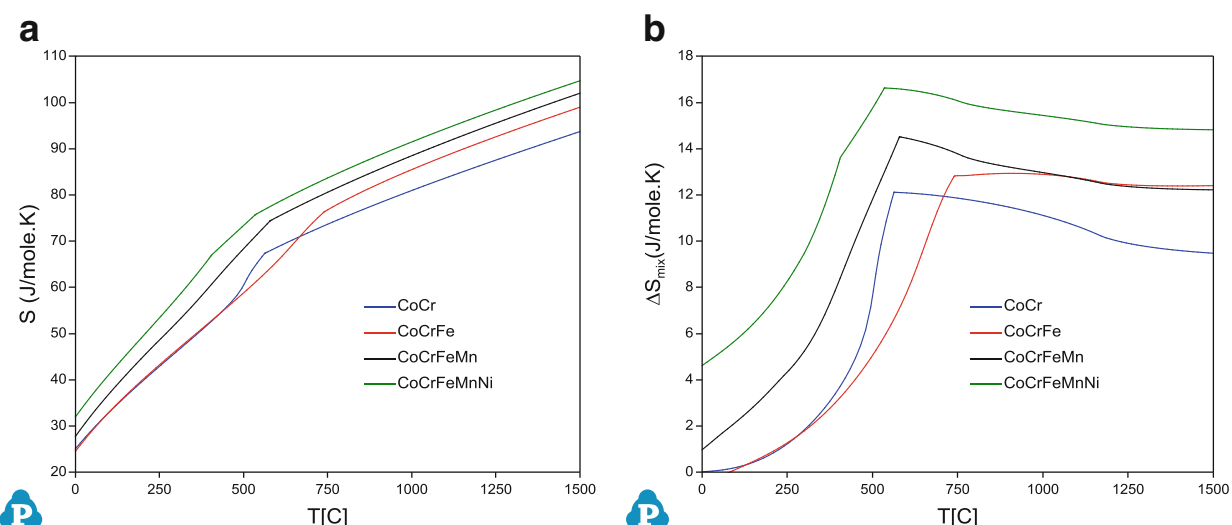


Fig. 12.20 Calculated entropies for the BCC phase within different systems at the equi-atomic ratio: (a) total entropy; (b) entropy of mixing

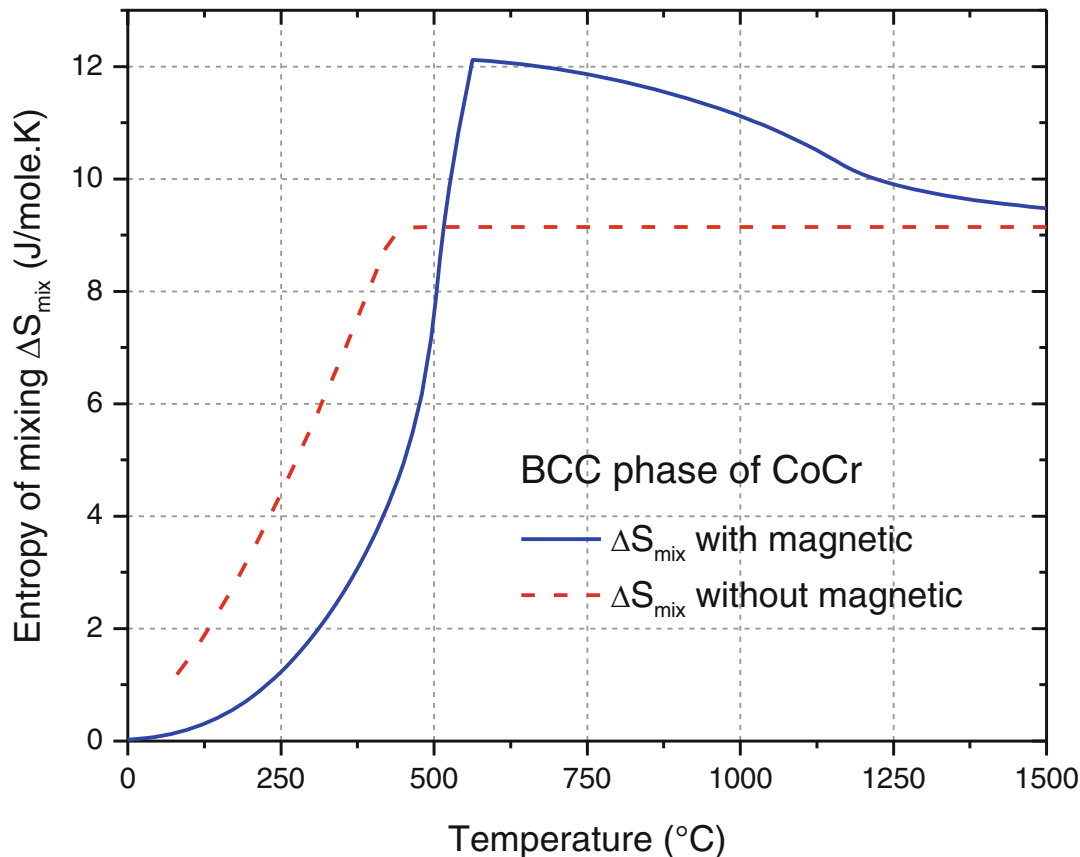


Fig. 12.21 Comparison of the calculated mixing entropy of the BCC phase of the CoCr alloy with/without magnetic contribution

lower temperatures when phase separation occurs. It is understandable that the phase separation will make the system less disordering; thus ΔS_{mix} decreases with decreasing temperature. However, the trend of ΔS_{mix} vs. temperature before the phase separation occurs seems very counterintuitive, so we compare ΔS_{mix} for BCC CoCr with and without considering the magnetic contributions. The results are shown in Fig. 12.21 and clearly indicate that the magnetic contribution causes the slight increase of ΔS_{mix} when the temperature decreases. On the other hand, without considering the magnetic contribution, the entropy of mixing is constant for $T \geq 450$ °C, and this means that SRO is not considered in the database. Note that very similar trends are found for both the total entropies and entropies of mixing of CoCr, CoCrFe, CoCrFeMn, and CoCrFeMnNi alloys in FCC and HCP structures as shown in Fig. 12.22.

SRO not only exists in the solid (see Chap. 10 for examples) but also liquid (see Chap. 11 for details and refs. [2, 3]) states of HEAs. The configurational entropy of a solid solution phase should decrease as the temperature decreases as shown in BCC MoNbTaW in Chap. 8. Therefore, for a more physical modeling of the configurational entropy in HEA system using CALPHAD approach, one needs to consider proper treatment of SRO. However, the lack of explicit SRO has been recognized as one of the major expression shortcomings to consider the order/disorder phase transformation using the CALPHAD approach. The Bragg-William-Gorsky (BWG) approximation [61] was the first model used to calculate the ordered prototype FCC phase diagrams [62]. But it shows large discrepancies with the real

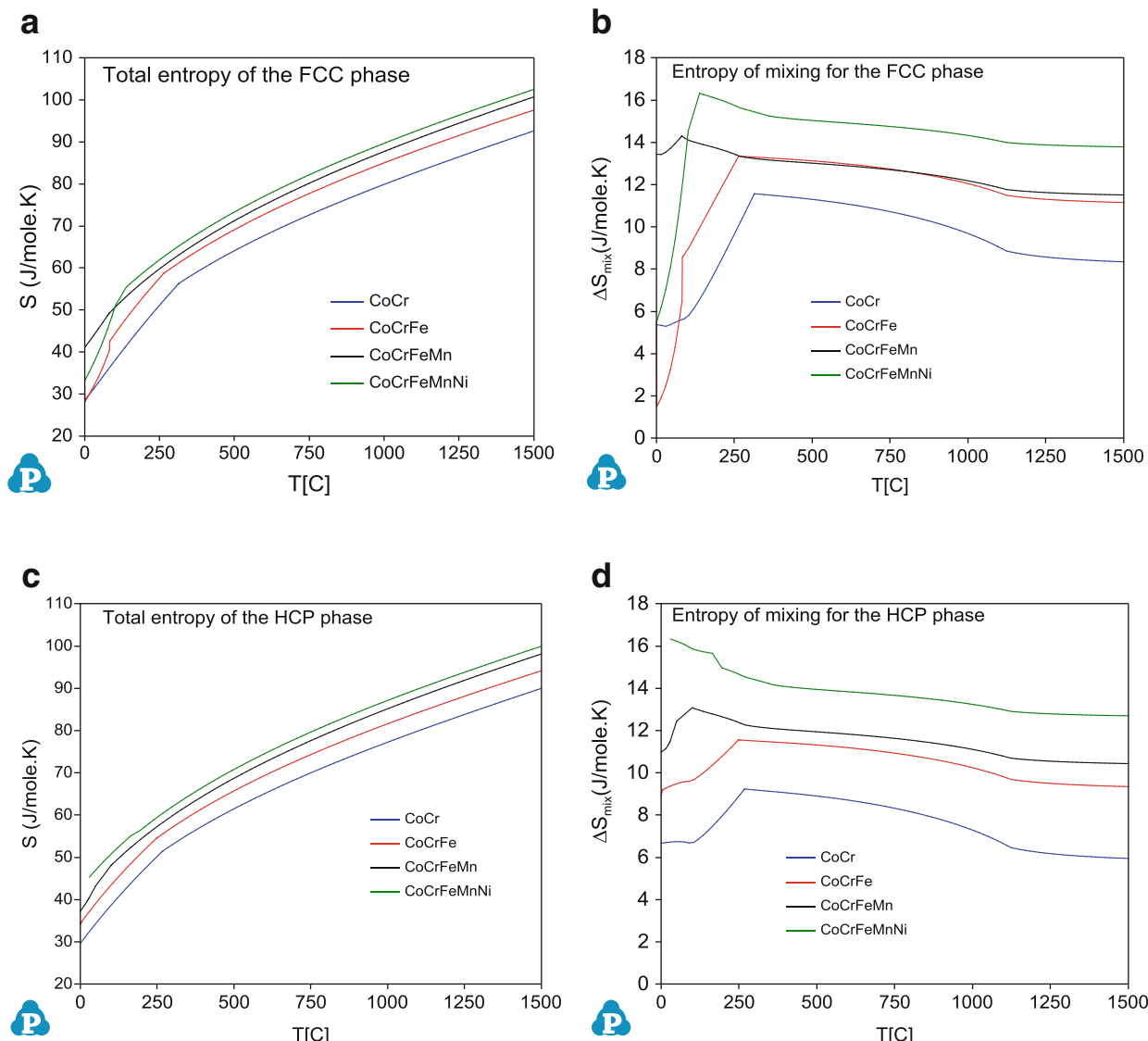


Fig. 12.22 Calculated entropies for the FCC and HCP phases within different systems at the equiatomic ratio: (a) total entropy of FCC phase; (b) mixing entropy of FCC phase; (c) total entropy of HCP phase; (d) mixing entropy of HCP phase

order phase diagrams because of the neglect of the SRO contributions in either the ordered (within a sublattice) or disordered phases. Currently, several models have been developed and gradually improved to describe the effect of SRO. The cluster variation method (CVM) [63] and Monte Carlo (MC) techniques [64] were developed by using the improved approximations of the Ising model to consider the SRO contribution and reproduced the main features of the experimental phase diagrams. However, thermodynamic modeling using CVM and MC is mainly in binary systems due to their complexity of model parameters and heavy computationally expensive for multicomponent systems. The CEF model has been widely used for several years to model chemical ordering in alloys. In this model, the LRO is described by sublattices and the SRO contribution to the Gibbs energy is approximated by the means of the quasi-chemical pair approximation. In the framework of the CEF, the SRO for the phase with both two sublattices and four sublattices has been explicitly expressed by Sundman et al. [65, 66]. In this context cluster/site approximation (CSA) approach is the simplest thermodynamic model capable of producing quantitative ordered phase diagrams. It permits only sharing corners but

not faces and edges and can be used to describe both LRO and SRO, which drastically reduces the number of variables and increases the computational efficiency especially for multicomponent systems. The CSA first introduced by Fowler [67] for treating atom/molecule equilibria was found suitable in describing the thermodynamics of the FCC phases by Oates et al. [68]. The CSA model is implemented in the PandatTM software [13] and has been successfully used to describe the phase stability of the FCC and HCP phase diagrams [69–72]. At present, the CSA model is limited to these phase diagrams.

12.5.2 Kinetics Modeling of HEAs

The materials presented hitherto focus on developing thermodynamic databases for HEA systems and their applications to phase diagrams and alloy design and processing via the CALPHAD approach. In addition, the CALPHAD method can be extended to model atomic mobilities and diffusivities as well. Using the method as described in ref. [73], a compatible mobility database with the current PanHEA thermodynamic database has been developed. The self-, impurity, and chemical diffusivities of each component within the liquid, BCC, FCC, and B2 phases were included. By combining the thermodynamic and mobility databases, kinetic reactions during solidification and subsequent heat treatment processes can then be

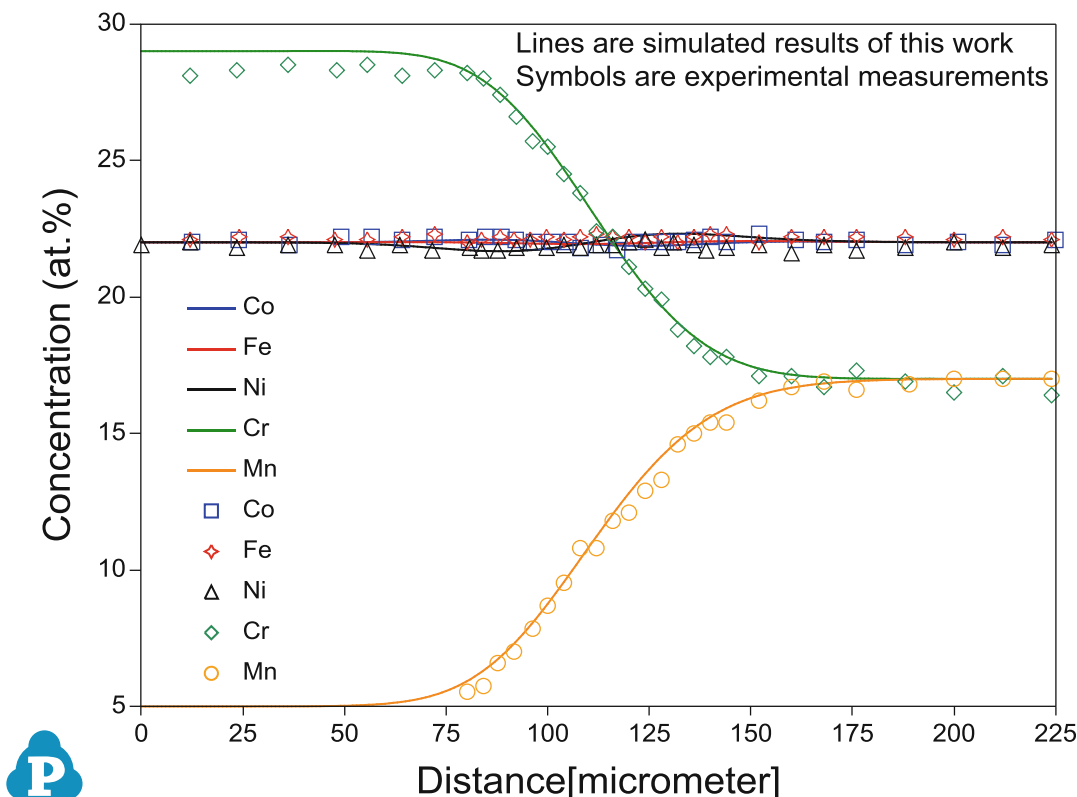


Fig. 12.23 Simulated concentration profiles for Co-Cr-Fe-Mn-Ni diffusion couple at 1000 °C in comparison with experimental results by Tsai et al. [74]

simulated. The mobility data for Liquid, BCC, FCC, and B2 phases are available in current PanHEA database, which enables us to carry out diffusion simulations.

Simulated concentration profiles for Co-Cr-Fe-Mn-Ni diffusion couple at 1000 oC in comparison with experimental results by Tsai et al. [74] are superimposed in the same figure for comparison. It shows that our simulated results are in good agreement with the experimental measurements (Fig. 12.23).

12.6 Conclusions

The application of the CALPHAD method to HEAs is presented in this chapter, and strategies in developing thermodynamic databases for HEA systems are illustrated. Analysis of the Gibbs free energy, enthalpy, and entropy of key phases of Co-Cr-Fe-Mn-Ni, Al-Co-Cr-Fe-Ni, and Mo-Nb-Ta-Ti-V-W systems is carried out using PanHEA and TCNI7 databases. Applications of these databases to assist HEA design in terms of phase diagrams and microstructure evolution during solidifications are shown for several HEA systems. The following conclusions are reached:

1. The thermodynamic database for the Al-Co-Cr-Fe-Ni system was developed based on the available experimental data and is included in the PanHEA database. The optimization covers all 10 binaries and 10 ternaries. Various phase diagrams were predicted using this database, which may be useful for future HEA design and processing. Acceptable agreement between model calculations and experiments is observed in various alloys such as $\text{Al}_{0.3}\text{CoCrFeNi}$, $\text{Al}_{0.7}\text{CoCrFeNi}$, $\text{Al}_{0.875}\text{CoCrFeNi}$, and $\text{Al}_x\text{CrCuFeNi}_2$.
2. Thermodynamic analysis using the TCNI7 database predicts positive excess entropy of +3.9, +2.9, +2.5, and +1.3 J/K/mol for FCC CoCr, CoCrFe, CoCrFeNi, and CoCrFeMnNi, respectively. The CALPHAD-predicted excess entropy for CoCrFeNi agrees well with the positive vibrational entropy of mixing of +2.8 J/K/mol predicted by DFT calculations (see Chap. 10). Furthermore, the maximum ΔS_{mix} occurs at Cr = 44.2 %, 35.3 %, 35.9 %, and 22.8 % for 2-, 3-, 4-, and 5-component systems, respectively, which deviate noticeably from the equimolar compositions.
3. Thermodynamic analysis using the TCNI7 database predicts small negative excess entropy of -0.9, -2.1, -1.7, and -1.5 J/K/mol for MoTaV, MoTaVW, MoNbTaVW, and MoNbTaTiVW, respectively.
4. Addition of Al to CoCrFeNi stabilizes the BCC phase significantly because of the dominating enthalpy effect. The maximum ΔS_{mix} for both FCC and BCC phases occur at less than 5 % Al and then drop rapidly with further increasing Al contents.
5. More principal elements in HEAs may not necessarily result in broader phase field of the solution phase. This is because the enthalpy factors as well as competing phases cannot be ignored when addressing phase stability. For example, the FCC phase field in CoCrFeNi is broader than in CoCrFeMnNi, and the

BCC phase field in MoNbTaTiVW is smaller than in MoNbTaW and MoNbTaVW.

6. Outlook to address short-range ordering and develop mobility database are discussed.

Acknowledgments M.C.G. acknowledges the financial support by the Crosscutting Technology Research Program at the National Energy Technology Laboratory (NETL) – Strategic Center for Coal – managed by Robert Romanosky (Technology Manager) and Charles Miller (Technology Monitor). The research was executed through NETL’s Office of Research and Development’s Innovative Process Technologies (IPT) Field Work Proposal under the RES contract DE-FE-0004000. The authors thank Prof. P.K. Liaw’s group for providing experimental support. C.Z. thanks Fan Zhang and Shuanglin Chen for inspiring discussions on CALPHAD modeling. M.C.G. thanks Mike Widom, Jeffrey A. Hawk, David E. Alman, and Bryan Morreale for their general discussion on HEAs.

Disclaimer This chapter co-authored by M.C.G. was funded by the Department of Energy, National Energy Technology Laboratory, an agency of the United States Government, through a support contract with AECOM. Neither the United States Government nor any agency thereof, nor any of their employees, nor AECOM, nor any of their employees, makes any warranty, expressed or implied, or assumes any legal liability or responsibility for the accuracy, completeness, or usefulness of any information, apparatus, product, or process disclosed, or represents that its use would not infringe privately owned rights. Reference herein to any specific commercial product, process, or service by trade name, trademark, manufacturer, or otherwise, does not necessarily constitute or imply its endorsement, recommendation, or favoring by the United States Government or any agency thereof. The views and opinions of authors expressed herein do not necessarily state or reflect those of the United States Government or any agency thereof.

References

1. Yeh JW, Chen YL, Lin SJ, Chen SK (2007) High-entropy alloys – a new era of exploitation. *Mater Sci Forum* 560:1–9. doi:[10.4028/www.scientific.net/MSF.560.1](https://doi.org/10.4028/www.scientific.net/MSF.560.1)
2. Zhang Y, Zuo TT, Tang Z, Gao MC, Dahmen KA, Liaw PK, Lu ZP (2014) Microstructures and properties of high-entropy alloys. *Prog Mater Sci* 61:1–93. doi:[10.1016/j.pmatsci.2013.10.001](https://doi.org/10.1016/j.pmatsci.2013.10.001)
3. Gao MC, Alman DE (2013) Searching for next single-phase high-entropy alloy compositions. *Entropy* 15:4504–4519. doi:[10.3390/e15104504](https://doi.org/10.3390/e15104504)
4. Cantor B, Chang ITH, Knight P, Vincent AJB (2004) Microstructural development in equiatomic multicomponent alloys. *Mater Sci Eng A* 375–377:213–218. doi:[10.1016/j.msea.2003.10.257](https://doi.org/10.1016/j.msea.2003.10.257)
5. Otto F, Yang Y, Bei H, George EP (2013) Relative effects of enthalpy and entropy on the phase stability of equiatomic high-entropy alloys. *Acta Mater* 61:2628–2638. doi:[10.1016/j.actamat.2013.01.042](https://doi.org/10.1016/j.actamat.2013.01.042)
6. Ohtania H, Ishida K (1998) Application of the CALPHAD method to material design. *Thermochimica Acta* 314:69–77. doi:[10.1016/S0040-6031\(97\)00457-7](https://doi.org/10.1016/S0040-6031(97)00457-7)
7. Chang YA, Chen SL, Zhang F, Yan XY, Xie FY, Schmid-Fetzer R, Oates WA (2004) Phase diagram calculation: past, present and future. *Prog Mater Sci* 49:313–345. doi:[10.1016/S0079-6425\(03\)00025-2](https://doi.org/10.1016/S0079-6425(03)00025-2)
8. Olson GB, Kuehmann CJ (2014) Materials genomics: from CALPHAD to flight. *Scr Mater* 70:25–30. doi:[10.1016/j.scriptamat.2013.08.032](https://doi.org/10.1016/j.scriptamat.2013.08.032)
9. Zhang C, Zhang F, Chen S, Cao W (2012) Computational thermodynamics aided high-entropy alloy design. *JOM* 64(7):839–845. doi:[10.1007/s11837-012-0365-6](https://doi.org/10.1007/s11837-012-0365-6)

10. Zhang F, Zhang C, Chen S, Zhu J, Cao W, Kattner UR (2014) An understanding of high entropy alloys from phase diagram calculations. *Calphad* 45:1–10. doi:[10.1016/j.calphad.2013.10.006](https://doi.org/10.1016/j.calphad.2013.10.006)
11. Kaufman L, Bernstein H (1970) Computer calculation of phase diagrams. Academic, New York
12. Hillert M (1968) Phase transformations. ASM, Cleveland
13. PandatTM Thermodynamic Calculations and Kinetic Simulations. CompuTherm LLC, Madison, WI, USA – 53719
14. Thermo-Calc thermodynamic equilibrium calculations. Thermo-Calc Software, Stockholm, Sweden
15. FactSage Thermochemical Software. Montreal, Canada
16. Chou KC, Chang YA (1989) A study of ternary geometrical models. *Berichte der Bunsengesellschaft für physikalische Chemie* 93(6):735–741. doi:[10.1002/bbpc.19890930615](https://doi.org/10.1002/bbpc.19890930615)
17. Dinsdale AT (1991) SGTE data for pure elements. *Calphad* 15(4):317–425. doi:[10.1016/0364-5916\(91\)90030-N](https://doi.org/10.1016/0364-5916(91)90030-N)
18. Redlich O, Kister AT (1948) Algebraic representation of thermodynamic properties and the classification of solutions. *Ind Eng Chem* 40:345–348. doi:[10.1021/ie50458a036](https://doi.org/10.1021/ie50458a036)
19. Ansara I (1979) Comparison of methods for thermodynamic calculation of phase diagrams. *Int Met Rev* 24(1):20–53. doi:<http://dx.doi.org/10.1179/imtr.1979.24.1.20>
20. Anderson JO, Guillermet AF, Hillert M, Jason B, Sundman B (1986) A compound-energy model of ordering in a phase with sites of different coordination numbers. *Acta Metall* 34 (3):437–445. doi:[10.1016/0001-6160\(86\)90079-9](https://doi.org/10.1016/0001-6160(86)90079-9)
21. Oates WA, Wenzl H (1992) The bond energy model for ordering in a phase with sites of different coordination numbers. *Calphad* 16(1):73–78. doi:[10.1016/0364-5916\(92\)90040-5](https://doi.org/10.1016/0364-5916(92)90040-5)
22. Chen SL, Kao CR, Chang YA (1995) A generalized quasi-chemical model for ordered multi-component, multi-sublattice intermetallic compounds with anti-structure defects. *Intermetallics* 3(3):233–242. doi:[10.1016/0966-9795\(95\)98934-z](https://doi.org/10.1016/0966-9795(95)98934-z)
23. Gao MC, Unlu N, Shiflet GJ, Mihalkovic M, Widom M (2005) Reassessment of Al-Ce and Al-Nd binary systems supported by critical experiments and first-principles energy calculations. *Metall Mater Trans A Phys Metall Mater Sci* 36A(12):3269–3279. doi:[10.1007/s11661-005-0001-y](https://doi.org/10.1007/s11661-005-0001-y)
24. Gao MC, Rollett AD, Widom M (2006) First-principles calculation of lattice stability of C15-M₂R and their hypothetical C15 variants (M = Al, Co, Ni; R = Ca, Ce, Nd, Y). *Calphad Comput Coupling Phase Diagrams Thermochem* 30(3):341–348. doi:[10.1016/j.calphad.2005.12.005](https://doi.org/10.1016/j.calphad.2005.12.005)
25. Gao MC, Rollett AD, Widom M (2007) The lattice stability of aluminum-rare earth binary systems: a first principles approach. *Phys Rev B* 75:174120. doi:<http://dx.doi.org/10.1103/PhysRevB.75.174120>
26. Mihalkovic M, Widom M (2004) Ab initio calculations of cohesive energies of Fe-based glass-forming alloys. *Phys Rev B* 70(14):144107. doi:[10.1103/PhysRevB.70.144107](https://doi.org/10.1103/PhysRevB.70.144107)
27. Gao MC, Suzuki Y, Schweiger H, Dogan ON, Hawk J, Widom M (2013) Phase stability and elastic properties of Cr-V alloys. *J Phys Condensed Matter* 25(7):075402. doi:[10.1088/0953-8984/25/7/075402](https://doi.org/10.1088/0953-8984/25/7/075402)
28. Kumar KCH, Wollants P (2001) Some guidelines for thermodynamic optimisation of phase diagrams. *J Alloys Compd* 320(2):189–198. doi:[10.1016/S0925-8388\(00\)01491-2](https://doi.org/10.1016/S0925-8388(00)01491-2)
29. Ishida K, Nishizawa T (1990) Co-Cr phase diagram, vol 3, Alloy phase diagrams. ASM International, Materials Park
30. Zhang B, Zhang Y, Gao MC, Yang S, Guo SM (2015) Senary refractory high-entropy alloy MoNbTaTiVW. *Mat Sci Tech* 31(10):1207–1213. doi:[10.1179/1743284715Y.0000000031](https://doi.org/10.1179/1743284715Y.0000000031)
31. Widom M (2015) Prediction of structure and phase transformations. In: Gao MC, Yeh JW, Liaw PK, Zhang Y (eds) High entropy alloys: fundamentals and applications. Springer, Cham
32. Kattner UR (1997) The thermodynamic modeling of multicomponent phase equilibria. *JOM* 49(12):14–19. doi:[10.1007/s11837-997-0024-5](https://doi.org/10.1007/s11837-997-0024-5)

33. Schmid-Fetzer R, Grobner J (2001) Focused development of magnesium alloys using the calphad approach. *Adv Eng Mater* 3(12):947–961. doi:[10.1002/1527-2648\(200112\)3:12<947::AID-ADEM947>3.0.CO;2-P](https://doi.org/10.1002/1527-2648(200112)3:12<947::AID-ADEM947>3.0.CO;2-P)
34. Saunders N, Fahrmann M, Small CJ (2000) The application of CALPHAD to Ni-based superalloys. *Superalloys*. TMS (The Minerals, Metals & Materials Society). In “Superalloys 2000” eds. K. A. Green, T. M. Pollock and R. D. Kissinger (TMS, Warrendale, 2000), 803–811
35. Chang YA (2006) Phase diagram calculations in teaching, research, and industry. *Metall Mater Trans A* 37(2):273–305. doi:[10.1007/s11661-006-0001-6](https://doi.org/10.1007/s11661-006-0001-6)
36. Hsieh KC, Yu CF, Hsieh WT, Chiang WR, Ku JS, Lai JH, Tu CP, Yang CC (2009) The microstructure and phase equilibrium of new high performance high-entropy alloys. *J Alloys Compd* 483(1–2):209–212. doi:[10.1016/j.jallcom.2008.08.118](https://doi.org/10.1016/j.jallcom.2008.08.118)
37. Miracle DB, Miller JD, Senkov ON, Woodward C, Uchic MD, Tiley J (2014) Exploration and development of high entropy alloys for structural applications. *Entropy* 16(1):494–525. doi:[10.3390/e16010494](https://doi.org/10.3390/e16010494)
38. Senkov ON, Zhang F, Miller JD (2013) Phase composition of a CrMo_{0.5}NbTa_{0.5}TiZr high entropy alloy: comparison of experimental and simulated data. *Entropy* 15(9):3796–3809. doi:[10.3390/e15093796](https://doi.org/10.3390/e15093796)
39. Kao YF, Chen TJ, Chen SK, Yeh JW (2009) Microstructure and mechanical property of as-cast, -homogenized, and -deformed Al_xCoCrFeNi ($0 \leq x \leq 2$) high-entropy alloys. *J Alloys Compd* 488:57–64. doi:[10.1016/j.jallcom.2009.08.090](https://doi.org/10.1016/j.jallcom.2009.08.090)
40. Kao YF, Chen SK, Chen TJ, Chu PC, Yeh JW, Lin SJ (2011) Electrical, magnetic, and hall properties of Al_xCoCrFeNi high-entropy alloys. *J Alloys Compd* 509(5):1607–1614. doi:[10.1016/j.jallcom.2010.10.210](https://doi.org/10.1016/j.jallcom.2010.10.210)
41. Lin CM, Tsai HL (2011) Evolution of microstructure, hardness, and corrosion properties of high-entropy Al_{0.5}CoCrFeNi alloy. *Intermetallics* 19(3):288–294. doi:[10.1016/j.intermet.2010.10.008](https://doi.org/10.1016/j.intermet.2010.10.008)
42. Wang WR, Wang WL, Yeh JW (2014) Phases, microstructure and mechanical properties of Al_xCoCrFeNi high-entropy alloys at elevated temperatures. *J Alloys Compd* 589:143–152. doi:[10.1016/j.jallcom.2013.11.084](https://doi.org/10.1016/j.jallcom.2013.11.084)
43. Li C, Li JC, Zhao M, Jiang Q (2010) Effect of aluminum contents on microstructure and properties of Al_xCoCrFeNi alloys. *J Alloys Compd* 504:S515–S518. doi:[10.1016/j.jallcom.2010.03.111](https://doi.org/10.1016/j.jallcom.2010.03.111)
44. Wang WR, Wang WL, Wang SC, Tsai YC, Lai CH, Yeh JW (2012) Effects of Al addition on the microstructure and mechanical property of Al_xCoCrFeNi high-entropy alloys. *Intermetallics* 26:44–51. doi:[10.1016/j.intermet.2012.03.005](https://doi.org/10.1016/j.intermet.2012.03.005)
45. Li C, Zhao M, Li JC, Jiang Q (2008) B2 structure of high-entropy alloys with addition of Al. *J Appl Phys* 104:113504–113506. doi:<http://dx.doi.org/10.1063/1.3032900>
46. Shun TT, Du YC (2009) Microstructure and tensile behaviors of FCC Al_{0.3}CoCrFeNi high entropy alloy. *J Alloys Compd* 479(1–2):157–160. doi:[10.1016/j.jallcom.2008.12.088](https://doi.org/10.1016/j.jallcom.2008.12.088)
47. Chou HP, Chang YS, Chen SK, Yeh JW (2009) Microstructure, thermophysical and electrical properties in Al_xCoCrFeNi ($0 \leq x \leq 2$) high-entropy alloys. *Mater Sci Eng B* 163(3):184–189. doi:[10.1016/j.mseb.2009.05.024](https://doi.org/10.1016/j.mseb.2009.05.024)
48. Vitek JM, David SA (1986) The sigma phase transformation in austenitic stainless steels. *Weld Res Suppl* 65:106–111
49. Liu S, Gao MC, Liaw PK, Zhang Y (2015) Microstructures and mechanical properties of AlxCrFeNiTi0.25 alloys. *J Alloys Compd* 619:610–615. doi:<http://dx.doi.org/10.1016/j.jallcom.2014.09.073>
50. Tang Z, Gao MC, Diao HY, Yang T, Liu J, Zuo T, Zhang Y, Lu Z, Cheng Y, Zhang Y, Dahmen KA, Liaw PK, Egami T (2013) Aluminum alloying effects on lattice types, microstructures, and mechanical behavior of high-entropy alloys systems. *JOM* 65(12):1848–1858. doi:[10.1007/s11837-013-0776-z](https://doi.org/10.1007/s11837-013-0776-z)

51. Tung CT, Yeh JW, Shun TT, Chen SK, Huang YS, Cheng HC (2007) On the elemental effect of AlCoCrCuFeNi high-entropy alloy system. *Mater Lett* 61(1):1–5. doi:[10.1016/j.matlet.2006.03.140](https://doi.org/10.1016/j.matlet.2006.03.140)
52. Scheil E (1942) *Z Metallkd* 34:70–72
53. Gulliver GH (1913) The quantitative effect of rapid cooling upon the constitution of binary alloys. *J Ins Met* 9:120–157
54. Guo S, Ng C, Liu CT (2013) Anomalous solidification microstructures in Co-free AlxCrCuFeNi₂ high-entropy alloys. *J Alloys Compd* 557:77–81. doi:[10.1016/j.jallcom.2013.01.007](https://doi.org/10.1016/j.jallcom.2013.01.007)
55. Liu Y, Ma SG, Gao MC, Zhang C, Zhang T, Yang H, Wang ZH, Qiao JW (2016) Tribological properties of AlCrCuFeNi₂ high-entropy alloy in different conditions. *Metallurgical and Materials Transactions A* (in press). doi:[10.1007/s11661-016-3396-8](https://doi.org/10.1007/s11661-016-3396-8)
56. Ghosh G, Asta M (2005) First-principles calculation of structural energetics of Al-TM (TM = Ti, Zr, Hf) intermetallics. *Acta Mater* 53(11):3225–3252. doi:[10.1016/j.actamat.2005.03.028](https://doi.org/10.1016/j.actamat.2005.03.028)
57. Santodonato LJ, Zhang Y, Feygenson M, Parish CM, Gao MC, Weber RJK, Neufeind JC, Tang Z, Liaw PK (2015) Deviation from high-entropy configurations in the atomic distributions of a multi-principal-element alloy. *Nat Commun* 6:5964. doi:[10.1038/ncomms6964](https://doi.org/10.1038/ncomms6964)
58. Cahn RW (1991) Mechanisms and kinetics in ordering and disordering. In: Yavari AR (ed) *Ordering and disordering in alloys*. Elsevier Science Publishers LTD, Grenoble, pp 3–12
59. Lukas HL, Fries SG, Sundman B (2007) Computational thermodynamics – the Calphad method. Cambridge University Press, New York, doi:www.cambridge.org/9780521868112
60. Greven A, Keller G, Warnerke G (2003) Entropy, Princeton series in applied mathematics. Princeton University Press, Princeton
61. Grosky W (1928) X-ray analysis of transformations in the alloy Cu Au. *Zeitschrift für Physik* 50(1–2):64–81. doi:[10.1007/BF01328593](https://doi.org/10.1007/BF01328593)
62. Shockley W (1938) Theory of order for the copper gold alloy system. *J Chem Phys* 6 (3):130–144. doi:[10.1063/1.1750214](https://doi.org/10.1063/1.1750214)
63. deFontaine D, Kikuchi R (1978) Fundamental calculations of phase diagrams using the cluster variation method, vol 2, Applications of phase diagrams in metallurgy and ceramics. NBS, National Bureau of Standards, Gaithersburg
64. Ackermann H, Crusius S, Inden G (1986) On the ordering of face-centered-cubic alloys with nearest neighbour interactions. *Acta Metall* 34(12):2311–2321. doi:[10.1016/0001-6160\(86\)90134-3](https://doi.org/10.1016/0001-6160(86)90134-3)
65. Sundman B, Fries SG, Oates WA (1998) A thermodynamic assessment of the Au-Cu system. *Calphad* 22(3):335–354. doi:[10.1016/S0364-5916\(98\)00034-0](https://doi.org/10.1016/S0364-5916(98)00034-0)
66. Abe T, Sundman B (2003) A description of the effect of short range ordering in the compound energy formalism. *Calphad* 27(4):403–408. doi:[10.1016/j.calphad.2004.01.005](https://doi.org/10.1016/j.calphad.2004.01.005)
67. Fowler RH (1938) Statistical mechanics, 2nd edn. Cambridge University Press, Cambridge
68. Oates WA, Wenzl H (1996) The cluster/site approximation for multicomponent solutions – a practical alternative to the cluster variation method. *Scr Mater* 35(5):623–627. doi:[10.1016/1359-6462\(96\)00198-4](https://doi.org/10.1016/1359-6462(96)00198-4)
69. Cao W, Zhu J, Yang Y, Zhang F, Chen S, Oates WA, Chang YA (2005) Application of the cluster/site approximation to fcc phases in Ni-Al-Cr system. *Acta Mater* 53(15):4189–4197. doi:[10.1016/j.actamat.2005.05.016](https://doi.org/10.1016/j.actamat.2005.05.016)
70. Zhang C, Zhu J, Bengtson A, Morgan D, Zhang F, Cao W-S, Chang YA (2008) Modeling of phase stability of the fcc phases in the Ni-Ir-Al system using the cluster/site approximation method coupling with first-principles calculations. *Acta Mater* 56(11):2576–2584. doi:[10.1016/j.actamat.2008.01.056](https://doi.org/10.1016/j.actamat.2008.01.056)
71. Zhang C, Zhu J, Bengtson A, Morgan D, Zhang F, Yang Y, Chang YA (2008) Thermodynamic modeling of the Cr-Pt binary system using the cluster/site approximation coupling with first-principles energetics calculation. *Acta Mater* 56(19):5796–5803. doi:[10.1016/j.actamat.2008.07.057](https://doi.org/10.1016/j.actamat.2008.07.057)

72. Zhang F, Chang YA, Du Y, Chen S-L, Oates WA (2003) Application of the cluster-site approximation (CSA) model to the f.c.c. phase in the Ni–Al system. *Acta Mater* 51(1):207–216. doi:[10.1016/S1359-6454\(02\)00392-0](https://doi.org/10.1016/S1359-6454(02)00392-0)
73. Campbell CE, Boettinger WJ, Kattner UR (2002) Development of a diffusion mobility database for Ni-base superalloys. *Acta Mater* 50(4):775–792. doi:[10.1016/S1359-6454\(01\)00383-4](https://doi.org/10.1016/S1359-6454(01)00383-4)
74. Tsai K-Y, Tsai M-H, Yeh J-W (2013) Sluggish diffusion in Co–Cr–Fe–Mn–Ni high-entropy alloys. *Acta Mater* 61(13):4887–4897. doi:[10.1016/j.actamat.2013.04.058](https://doi.org/10.1016/j.actamat.2013.04.058)

Chapter 13

High-Entropy Metallic Glasses

Akira Takeuchi, Michael C. Gao, Junwei Qiao, and Michael Widom

Abstract This chapter applies the concept of high entropy to metallic glasses (MGs), in particular, to those in a bulk shape: bulk metallic glasses (BMGs). The resultant target materials in this chapter are mainly high-entropy bulk metallic glasses (HE-BMGs), which have recently been developed as alloys with characteristics of both high-entropy alloys (HEAs) and BMGs. The contents in this chapter start by introducing historic background of HE-BMGs and by summarizing the differences between HEAs and BMGs. Then, the fundamental properties of representative HE-BMGs found to date are described mainly in terms of thermodynamic and mechanical behaviors. Besides the experiments, the latest computational approach for clarifying the features of HE-BMGs is described based on the results using *ab initio* molecular dynamics simulations for the atomic structure, chemical interaction, and diffusivity in this unique class of materials. The current status and future prospects of the HE-BMGs by utilizing their unique features are outlined for their future applications.

Keywords Bulk metallic glasses (BMGs) • Amorphous • Glass-forming ability • Multiphase • Enthalpy of mixing • Entropy of mixing • Atomic size difference • Phase diagrams • Thermodynamics • Kinetics • Phase transformations • Solidification • Phase stability • *ab initio* molecular dynamics simulations (AIMD) • Diffusion constants • High-entropy alloys (HEAs)

A. Takeuchi (✉)

Institute for Materials Research, Tohoku University, Sendai 980-8577, Japan
e-mail: takeuchi@imr.tohoku.ac.jp

M.C. Gao

National Energy Technology Lab/AECOM, Albany, OR 97321-2198, USA
e-mail: michael.gao@contr.netl.doe.gov; michael.gao@netl.doe.gov

J. Qiao

College of Materials Science and Engineering, Taiyuan University of Technology,
Taiyuan 030024, China
e-mail: qiaojunwei@gmail.com

M. Widom

Department of Physics, Carnegie Mellon University, Pittsburgh, PA, USA
e-mail: widom@cmu.edu

13.1 Introduction

In this chapter, the focus is put on the formation mechanisms, mechanical properties, and atomic structure of metallic glasses (MGs) that are associated with high-entropy alloys (HEAs) [1, 2]. In particular, descriptions principally include MGs in a bulk form named bulk metallic glasses (BMGs), with a compositional feature of HEAs: high-entropy bulk metallic glasses (HE-BMGs) [3]. The HE-BMGs are mathematical intersection of sets of bulk metallic glasses (BMGs) and HEAs. Specifically, HE-BMGs possess both features of MGs with sample dimensions of a couple of millimeter or more and of HEAs for exact or near equi-atomic composition. In fact, BMGs and HEAs possess different crystallographic structures, BMGs as well as MGs and HEAs, respectively, and are formed into a glassy and a crystalline phase. However, HE-BMGs that have been recently discovered have academically contributed in a major way to widening the definition of HEAs from crystalline solid solutions only to whole solid solutions including a glassy phase. Furthermore, new BMGs as well as MGs have been developed by utilizing the unique nature of HEAs. Thus, HE-BMGs play a role in leading HEAs and BMGs toward their future research orientations.

This introduction starts with describing similarities and differences in characteristics of BMGs and HEAs, leading to the resultant HE-BMGs with characteristics of both HEAs and BMGs. Subsequent sections in this chapter deal with the alloy design of HE-BMGs, followed by individual characteristics of the HE-BMGs found to date.

13.1.1 *Differences Between BMGs and HEAs*

It has long been believed that the BMGs differ from HEAs because of the many different characteristics between these alloys. For instance, BMGs differ from HEAs in terms of (1) crystallographic structure, (2) thermodynamic state, and (3) compositional feature. First, BMGs are defined as bulk-shaped noncrystalline metallic solids that exhibit the so-called glass transition temperature (T_g). Conversely, HEAs are crystalline materials. Although some HEAs can be fabricated into a noncrystalline structure in thin film form, this thin-film HE-MG will not be covered in this chapter. Secondly, the BMGs are formed into a non-equilibrium state through quenching at a cooling rate of the order of $\sim 10^3$ K/s or slower by avoiding nucleation and growth of crystalline phases during solidification. On the other hand, the HEAs are thermodynamically stable, and so far HEAs in bcc and fcc structures [4] are frequently reported, and those in hcp structures [5–8] have very recently been suggested or reported. Thirdly, the BMGs possess one or two principal elements from Zr, La, Fe, Mg, Pd, Cu, and Ca [9], whereas there is no dominating element in HEAs with equal molar ratio among elements. These fundamental differences between BMGs and HEAs have promoted their separate development since the early 1990s.

13.1.2 *Historical Background of HE-BMGs and Derivation of HE-BMGs from BMGs*

The widely accepted belief regarding the differences between BMGs and HEAs mentioned above, however, has been broken due to the appearance of new alloys that have both the features of HEAs for their composition and those of metallic glasses for their noncrystalline structure. These new alloys are regarded as HE-BMGs or high-entropy bulk glassy alloys. At present, several HE-BMGs have been found in sequence, since the first report in 2002 in a Cu₂₀Hf₂₀Ni₂₀Ti₂₀Zr₂₀ alloy [10]. These HE-BMGs found to date are summarized in Table 13.1, together with representative BMGs that include the prototypical ones for HE-BMGs. The Cu₂₀Hf₂₀Ni₂₀Ti₂₀Zr₂₀ alloy is the first HE-BMG fabricated by referring to the “confusion principle” proposed by Greer in 1993 [11]. Specifically, Greer argued that the confusion principle works for glass formation in such a way that the more elements involved, the lower the chance that the alloy can select viable crystal structures and the greater the chance of glass formation. In contrast, Cantor et al. [12] reported in 2004 that “the confusion principle does not apply, and other factors are more important in promoting glass formation,” based on experimental results that glassy structures are not formed by casting or melt spinning of late-transition metal-rich equi-atomic multicomponent alloys. After these arguments, researchers overlooked HE-BMGs for years.

However, the subsequent HE-BMGs have been found in sequence in 2011 in a Ca₂₀(Li_{0.55}Mg_{0.45})₂₀Sr₂₀Yb₂₀Zn₂₀ alloy [13] and a Cu₂₀Ni₂₀P₂₀Pd₂₀Pt₂₀ alloy [14], and the two alloys [15] related to the Ca-(Li,Mg)-Sr-Yb-Zn of Ca₂₀Mg₂₀Sr₂₀Yb₂₀Zn₂₀ and Ca₂₀Cu₁₀Mg₂₀Sr₂₀Yb₂₀Zn₁₀ [13], and an Al₂₀Er₂₀Dy₂₀Ni₂₀Tb₂₀ alloy [15]. Here, Ca₂₀Mg₂₀Sr₂₀Yb₂₀Zn₂₀ has been studied for biomedical applications [16]. Furthermore, Be₂₀Cu₂₀Ni₂₀Ti₂₀Zr₂₀ [17] and Be_{16.7}Cu_{16.7}Ni_{16.7}Hf_{16.7}Ti_{16.7}Zr_{16.7} [18] alloys have very recently been reported as the latest HE-BMGs. These findings of HE-BMGs are achieved by selecting five or more principal alloying elements in equal molar ratio but still forming BMG. As frequently applied to MGs and BMGs, the HE-BMGs can be classified into two sets of metal–metal and metal–metalloid, depending on whether or not the alloys include metalloid elements, such as B, C, Si, P, and Ge. The HE-BMGs in metal–metalloid type have only been found in Cu₂₀Ni₂₀P₂₀Pd₂₀Pt₂₀ alloy. The lineups of HE-BMGs are shown in Table 13.1. The constituent elements of the HE-BMGs are mixtures of early- and late-transition metals, s-block elements, metalloids, lanthanides, and p-block metallic elements. These combinations of constituent elements indicate that classification of BMGs [9] can be used as a guide for finding out unprecedented BMGs as well as HE-BMGs.

Some of the HE-BMGs mentioned above resemble prototypical BMGs in their constituent elements and compositions. As usual in alloy development, the elements in the same group in the periodic table or those with similar chemical properties are added or substituted in order to search for new alloys. Taking

Table 13.1 HE-BMGs found to date and representative BMGs that include the prototypical ones for HE-BMGs for their maximum sample thickness (d_c) and year published

No.	Alloy	d_c/mm	Year published	References
HE-BMG-1	$\text{Cu}_{20}\text{Hf}_{20}\text{Ni}_{20}\text{Ti}_{20}\text{Zr}_{20}$	1.5	2002	[10]
HE-BMG-2	$\text{Ca}_{20}(\text{Li}_{0.55}\text{Mg}_{0.45})_{20}\text{Sr}_{20}\text{Yb}_{20}\text{Zn}_{20}$	3	2011	[13]
HE-BMG-3	$\text{Cu}_{20}\text{Ni}_{20}\text{P}_{20}\text{Pd}_{20}\text{Pt}_{20}$	10	2011	[14]
HE-BMG-4	$\text{Ca}_{20}\text{Mg}_{20}\text{Sr}_{20}\text{Yb}_{20}\text{Zn}_{20}$	$2 \times 5 \text{ mm}^2$ (sheet sample)	2011	[15]
HE-BMG-5	$\text{Ca}_{20}\text{Cu}_{10}\text{Mg}_{20}\text{Sr}_{20}\text{Yb}_{20}\text{Zn}_{10}$	5	2011	[15]
HE-BMG-6	$\text{Al}_{20}\text{Er}_{20}\text{Dy}_{20}\text{Ni}_{20}\text{Tb}_{20}$	2	2011	[15]
HE-MGB-7	$\text{Be}_{20}\text{Cu}_{20}\text{Ni}_{20}\text{Ti}_{20}\text{Zr}_{20}$	3	2013	[17]
HE-BMG-8	$\text{Be}_{16.7}\text{Cu}_{16.7}\text{Ni}_{16.7}\text{Hf}_{16.7}\text{Ti}_{16.7}\text{Zr}_{16.7}$	>15	2014	[18]
BMG-01	$\text{Pd}_{40}\text{Cu}_{30}\text{Ni}_{10}\text{P}_{20}$	72	1997	[21]
BMG-02	$\text{Zr}_{41.2}\text{Ti}_{13.9}\text{Cu}_{12.5}\text{Ni}_{10}\text{Be}_{22.5}$ (Vit1)	>50	1996	[20]
BMG-03	$\text{Pd}_{35}\text{Pt}_{15}\text{Cu}_{30}\text{P}_{20}$	30	2005	[22]
BMG-04	$\text{Zr}_{55}\text{Al}_{10}\text{Ni}_5\text{Cu}_{30}$	30	1996	[23]
BMG-05	$\text{Mg}_{59.5}\text{Cu}_{22.9}\text{Ag}_{6.6}\text{Gd}_{11}$	27	2007	[24]
BMG-06	$\text{Mg}_{54}\text{Cu}_{26.5}\text{Ag}_{8.5}\text{Gd}_{11}$	25	2005	[25]
BMG-07	$\text{Zr}_{48}\text{Cu}_{36}\text{Ag}_8\text{Al}_8$	25	2008	[26]
BMG-08	$\text{Pd}_{40}\text{Ni}_{40}\text{P}_{20}$	25	1996	[19]
BMG-09	$\text{Y}_{36}\text{Sc}_{20}\text{Al}_{24}\text{Co}_{20}$	25	2003	[27]
BMG-10	$(\text{La}_{0.7}\text{Ce}_{0.3})_{65}\text{Co}_{25}\text{Al}_{10}$	25	2007	[28]
BMG-11	$\text{La}_{62}(\text{Cu}_{5/6}\text{Ag}_{1/6})_{14}\text{Ni}_5\text{Co}_5\text{Al}_{14}$	>20	2006	[29]
BMG-12	$\text{Zr}_{57}\text{Ti}_5\text{Cu}_{20}\text{Ni}_8\text{Al}_{10}$	20	1997	[30]
BMG-13	$\text{Pt}_{42.5}\text{Cu}_{27}\text{Ni}_{9.5}\text{P}_{21}$	20	2004	[31]
BMG-14	$(\text{Fe}_{0.8}\text{Co}_{0.2})_{48}\text{Cr}_{15}\text{Mo}_{14}\text{C}_{15}\text{B}_6\text{Tm}_2$	18	2008	[32]
BMG-15	$\text{Pt}_{60}\text{Cu}_{16}\text{Ni}_2\text{P}_{22}$	16	2004	[31]
BMG-16	$\text{Mg}_{54}\text{Cu}_{28}\text{Ag}_7\text{Y}_{11}$	16	2005	[25]
BMG-17	$\text{Ca}_{65}\text{Mg}_{15}\text{Zn}_{20}$	>15	2004	[33]
BMG-18	$\text{Zr}_{58.5}\text{Nb}_{2.8}\text{Cu}_{15.6}\text{Ni}_{12.8}\text{Al}_{10.3}$	15	1998	[34]
BMG-19	$\text{Ni}_{50}\text{Pd}_{30}\text{P}_{20}$	21	2009	[35]
BMG-20	$\text{Pd}_{40}\text{Ni}_{40}\text{Si}_4\text{P}_{16}$	20	2011	[36]
BMG-21	$\text{Zr}_{61}\text{Ti}_2\text{Nb}_2\text{Al}_{7.5}\text{Ni}_{10}\text{Cu}_{17.5}$	20	2009	[37]
BMG-22	$\text{Zr}_{60}\text{Ti}_2\text{Nb}_2\text{Al}_{7.5}\text{Ni}_{10}\text{Cu}_{18.5}$	20	2009	[37]
BMG-23	$\text{Ti}_{40}\text{Zr}_{25}\text{Cu}_{12}\text{Ni}_3\text{Be}_{20}$	14	2005	[38]
BMG-24	$\text{Fe}_{48}\text{Cr}_{15}\text{Mo}_{14}\text{Er}_2\text{C}_{15}\text{B}_6$	12	2004	[39]

The HE-BMGs from Nos. 1 to 8 are sorted according to the year published, whereas the BMGs with d_c over 10 mm from Nos. 1 to 24 are in the order of d_c .

HE-BMGs for example, $\text{Cu}_{20}\text{Ni}_{20}\text{P}_{20}\text{Pd}_{20}\text{Pt}_{20}$ and $\text{Be}_{20}\text{Cu}_{20}\text{Ni}_{20}\text{Ti}_{20}\text{Zr}_{20}$ HE-BMGs, respectively, were developed by referring to $\text{Pd}_{40}\text{Ni}_{40}\text{P}_{20}$ [14, 19] and $\text{Zr}_{41.2}\text{Ti}_{13.9}\text{Cu}_{12.5}\text{Ni}_{10}\text{Be}_{22.5}$ [20] BMGs, by modifying the compositions of the constituent elements to meet the equi-atomicity.

13.1.3 Similarities Between BMGs and HEAs in Their Alloy Designs

Interestingly, some of the BMGs and HEAs have been developed under the same alloy design principles, including the following factors:

1. The number of elements (N)
2. Atomic size mismatch (difference in atomic size)
3. Heat of mixing (mixing enthalpy, ΔH_{mix})

The details of the three factors for the development of BMGs and HEAs are described as follows. The BMGs are usually restricted to $N \geq 3$, excepting a couple of binary BMG alloys, such as Cu-Zr [40, 41] and Ni-Nb [42], whereas HEAs have $N \geq 5$, together with an additional restriction requiring equi-atomic or near equi-atomic composition. The second and third factor for BMGs are simply described as 12 % or more specifically mismatch and negative heat of mixing, respectively [43]. On the other hand, the second and third factor for HEAs are more complicated than BMGs and are associated with values of parameter (δ) and ΔH_{mix} in a δ - ΔH_{mix} diagram [44], to form zone S for disordered and zone S' for ordered HEAs as detailed in Chap. 2 of this book. Here, it should be noted that the order and disorder mentioned above refer to chemical species (elements), and not the atomistic positions in crystallography. In addition, zones for BMGs are also indicated as zone Bs in the δ - ΔH_{mix} diagram.

Furthermore, a new parameter (Ω) comprising average melting temperature multiplied by configurational entropy and divided by mixing enthalpy has been proposed to form δ - Ω diagrams [45] for predicting HEAs as well as BMGs. The details of these criteria for HEAs are described in Chap. 2 in this book. As mentioned above, all three factors in the alloy design for HEAs and BMGs deal with numerical and thermodynamic quantities, enabling alloy design of HEAs as well as BMGs. Here, it should be noted that there are several ways to calculate the values of ΔH_{mix} , such as thermodynamic method based on CALPHAD [46] as described in Chap. 12 of this book as well as electronic density functional theory as described in Chaps. 8, 9, 10, and 11 of this book. Besides, Miedema's empirical method [47] is also widely utilized for evaluating ΔH_{mix} for BMGs as well as HEAs. The exact data on ΔH_{mix} for 2628 atomic pairs from combination of 73 elements that are available in Miedema's model taken 2 at a time (${}_{73}C_2$) at equi-atomic binary alloy composition are provided in the authors' previous work [9].

Classifications of BMGs as well as MGs were reported since 1980s by Hafner [48], Masumoto [49], and Inoue [43] and Takeuchi and Inoue [9, 50]. Inoue [43] has summarized the BMGs with five groups comprising (1) Zr and La based, (2) Fe-ETM based, (3) Fe (Al, Ga) based, (4) Mg based, and (5) Pd and Pt based where ETM stands for early-transition metals, and the following two supplemental groups have been added later by Takeuchi and Inoue [9, 50]: (6) LTM (late-transition metals)-based and (7) Ca-based BMGs. The classifications by Takeuchi

and Inoue [9] were made basically by taking into account the subgroups of ETM, Ln, LTM, BM, and IIA corresponding to early-transition, lanthanide, late-transition, group IIIB–IVB, and group IIA metals, respectively. On the other hand, the latest classification of BMGs proposed by Takeuchi and Inoue [50] was based on four subgroups of s, d_{EF}, d_{LP}, and p from s-, d-, f-, and p-block elements on the periodic table that correspond to s-block elements, early-transition metals and lanthanides, late-transition metals and p-block metallic elements, and metalloids in p-block. These classifications provide a hint to discover unknown HE-BMGs. The HE-BMGs have been found by referring to and modifying the components and compositions of the BMGs. Takeuchi and Inoue [50] eventually succeeded in obtaining a universal trend of BMG formation on the basis of the regular tetrahedral composition diagram comprising s, d_{EF}, d_{LP}, and p. It appears that a compositional band connects BMGs on the surface of the regular tetrahedral composition diagram.

The guiding principle of the alloy design for HE-BMGs has two stages. First, one should find out the prototypical alloy compositions from the early studies of BMGs. Second, one should approximate the compositions of the prototypical BMGs by taking into account the chemical similarities in elements, such as the same group of the periodic table. Table 13.2 [51] summarizes the relationships between the representative BMGs and the corresponding HE-BMGs found to date summarized by class, subgroups, as well as the relative atomic size for BMGs, s–d_{EF}–d_{LP}–p description, and corresponding HE-BMGs.

$\text{Al}_{20}\text{Er}_{20}\text{Dy}_{20}\text{Ni}_{20}\text{Tb}_{20}$ and $\text{Be}_{20}\text{Cu}_{20}\text{Ni}_{20}\text{Ti}_{20}\text{Zr}_{20}$ are chemically near $\text{La}_{60}\text{Al}_{15}\text{Ni}_{20}$ [52, 55], $\text{Ca}_{20}\text{Mg}_{20}\text{Sr}_{20}\text{Yb}_{20}\text{Zn}_{20}$ between $\text{Mg}_{50}\text{Ni}_{30}\text{La}_{20}$ [56] and $\text{Mg}_{65}\text{Cu}_{25}\text{Y}_{10}$ [57], $\text{Cu}_{20}\text{Ni}_{20}\text{P}_{20}\text{Pd}_{20}\text{Pt}_{20}$ near $\text{Pd}_{40}\text{Ni}_{40}\text{P}_{20}$ [19, 58], and $\text{Cu}_{20}\text{Hf}_{20}\text{Ni}_{20}\text{Ti}_{20}\text{Zr}_{20}$ near $\text{Cu}_{23}\text{Ni}_{11}\text{Fe}_7\text{Ti}_{52}\text{Mo}_7$ [59]. These HE-BMGs surely possess exact or near equi-atomicity, but chemical similarity among the constituent elements reduces HE-BMGs to conventional BMGs.

13.2 HE-BMGs, Relevant Alloys and Their Characteristics

This subsection deals with three types of alloys: $\text{Cu}_{20}\text{Ni}_{20}\text{P}_{20}\text{Pd}_{20}\text{Pt}_{20}$ -, $\text{Be}_{20}\text{Cu}_{20}\text{Ni}_{20}\text{Ti}_{20}\text{Zr}_{20}$ -, and $\text{Ca}_{20}\text{Mg}_{20}\text{Sr}_{20}\text{Yb}_{20}\text{Zn}_{20}$ -based HE-BMGs. The thermodynamic properties are mainly explained for the $\text{Cu}_{20}\text{Ni}_{20}\text{P}_{20}\text{Pd}_{20}\text{Pt}_{20}$ HE-BMG and its relevant HEAs. The mechanical properties are explained for $\text{Be}_{20}\text{Cu}_{20}\text{Ni}_{20}\text{Ti}_{20}\text{Zr}_{20}$ - and $\text{Ca}_{20}\text{Mg}_{20}\text{Sr}_{20}\text{Yb}_{20}\text{Zn}_{20}$ -based HE-BMGs that belong to the metal–metal type comprising metallic elements only, while the $\text{Cu}_{20}\text{Ni}_{20}\text{P}_{20}\text{Pd}_{20}\text{Pt}_{20}$ HE-BMG from metal–metalloid type including metalloid elements from B, C, Si P, and Ge is eliminated for its mechanical properties due to the brittle nature inherent to the inclusion of the metalloid elements.

Table 13.2 Relationships between seven classes of BMGs and HE-BMGs

Class	Subgroup				Representative BMGs	References	s-d _{Ef} -d _{Lp} -p description	Corresponding HE-BMGs	References
	s	d _{Ef}	d _{Lp}	p					
I	M	<u>L</u>	S	—	La ₆₀ Al ₁₅ Ni ₂₅	[52]	(d _{Ef}) ₆₀ s ₁₅ (d _{Lp}) ₂₅	Al ₂₀ Er ₂₀ Dy ₂₀ Ni ₂₀ Tb ₂₀	[15]
	S	<u>L</u>	M	—	Zr _{41.2} Ti _{13.9} Cu _{12.5} Ni ₁₀ Be _{22.5}	[20]	(d _{Ef}) ₅₅ (d _{Lp}) _{22.5} s _{22.5}	Be ₂₀ Cu ₂₀ Ni ₂₀ Ti ₂₀ Zr ₂₀	[17]
II	—	<u>L</u>	<u>M</u>	S	(Fe _{0.8} Co _{0.2}) ₄₈ Cr ₁₅ Mo ₁₄ Tm ₂ C ₁₅ B ₆	[32]	(d _{Lp}) ₄₈ (d _{Ef}) ₃₁ P ₂₁	—	—
	L	—	<u>M</u>	S	Fe ₇₃ Al ₅ Ga ₂ P _{1.1} C ₅ B ₄	[53]	(d _{Lp}) ₇₃ P ₂₀	—	—
IV	<u>M</u>	L	S	—	Mg _{59.5} Cu _{22.9} Ag _{6.6} Gd ₁₁	[25]	s _{59.5} (d _{Lp}) _{29.5} (d _{Ef}) ₁₁	Ca ₂₀ Mg ₂₀ Sr ₂₀ Yb ₂₀ Zn ₂₀	[15]
	—	—	<u>L</u>	S	Pd ₄₀ Ni ₄₀ P ₂₀	[19]	(d _{Lp}) ₈₀ P ₂₀	Cu ₂₀ Ni ₂₀ P ₂₀ Pd ₂₀ Pt ₂₀	[14]
V	—	—	<u>L</u>	S	Pd ₄₀ Cu ₃₀ Ni ₁₀ P ₂₀	[21]	—	—	—
	—	L	<u>S</u>	—	Cu ₆₀ Zr ₃₀ Ti ₁₀	[52]	(d _{Lp}) ₆₀ (d _{Ef}) ₄₀	—	—
VI-I	—	<u>L</u>	S	—	—	—	(d _{Ef}) ₆₀ (d _{Lp}) ₄₀	Cu ₂₀ Hf ₂₀ Ni ₂₀ Ti ₂₀ Zr ₂₀	[10]
	<u>L</u>	—	S	—	Ca ₆₅ Mg ₁₅ Zn ₂₀	[33]	s ₈₀ (d _{Lp}) ₂₀	—	—

Reproduced with permission from Ref. [51]

The letters “L, M, and S” indicate the relative atomic size (large, medium, or small) of the constituent elements. The bold and underlined letter in each class indicates the main constituent element. It should be noted that C-VI-I is not the result of classification of BMGs, but is shown for comparison for Cu₂₀Hf₂₀Ni₂₀Ti₂₀Zr₂₀ HE-BMG. The BMGs do not list their constituents alphabetically, but in an empirical way to show the principal element d_{Ef} early-transition metals from d-block, d_{Lp} late-transition metals from d-block and lanthanides from f-block, p metalloid elements in p-block, s-block elements where Al and Sn are supposed to belong to either s or d_{Lp} depending on the other constituent elements

13.2.1 $\text{Cu}_{20}\text{Ni}_{20}\text{P}_{20}\text{Pd}_{20}\text{Pt}_{20}$ HE-BMG and Relevant Alloys

Of the HE-BMGs found to date, the $\text{Cu}_{20}\text{Ni}_{20}\text{P}_{20}\text{Pd}_{20}\text{Pt}_{20}$ [14] as well as $\text{Be}_{16.7}\text{Cu}_{16.7}\text{Ni}_{16.7}\text{Hf}_{16.7}\text{Ti}_{16.7}\text{Zr}_{16.7}$ [18] HE-BMGs exhibit sample dimensions reaching a centimeter. The outer appearance and the XRD profile taken from a cross-sectional area of the $\text{Cu}_{20}\text{Ni}_{20}\text{P}_{20}\text{Pd}_{20}\text{Pt}_{20}$ HE-BMG are shown in Fig. 13.1.

The $\text{Cu}_{20}\text{Ni}_{20}\text{P}_{20}\text{Pd}_{20}\text{Pt}_{20}$ HE-BMG was designed from a prototypical BMG of $\text{Pd}_{40}\text{Ni}_{40}\text{P}_{20}$ with $d_c = 25$ mm [19] by replacing half moles of Pd with Pt and those of Ni with Cu. These replacements, ironically, degrade glass-forming ability (GFA), resulting in decreasing d_c from 25 for the $\text{Pd}_{40}\text{Ni}_{40}\text{P}_{20}$ BMG to 10 mm for the $\text{Cu}_{20}\text{Ni}_{20}\text{P}_{20}\text{Pd}_{20}\text{Pt}_{20}$ HE-BMG. The degrading GFA indicates that the best BMG compositions are not always the ones for HEAs. Another peculiar feature of the $\text{Cu}_{20}\text{Ni}_{20}\text{P}_{20}\text{Pd}_{20}\text{Pt}_{20}$ HE-BMG is seen for the reduced glass transition temperature (T_g/T_1), which is evaluated by glass transition temperature (T_g) normalized with liquidus temperature (T_1). It is widely accepted that $T_g/T_1 \geq 0.6$ is a condition for an alloy with a high GFA. The value of T_g/T_1 of the $\text{Cu}_{20}\text{Ni}_{20}\text{P}_{20}\text{Pd}_{20}\text{Pt}_{20}$ HE-BMG is as high as 0.71, which is the highest value among BMGs with $d_c \geq 10$ mm, but it seemingly contradicts the low $d_c = 10$ mm. Including T_g/T_1 , 12 GFA parameters in all have been proposed to evaluate GFA where the features of each parameter are well summarized in literature [60]. The representative GFA parameters include T_g/T_1 , supercooled liquid region ($\Delta T_x = T_x - T_g$) exhibiting the temperature interval between onset temperature of crystallization (T_x) and T_g , γ parameter defined by $T_x/(T_g + T_1)$. However, these GFA parameters exhibit a critical issue that there is no absolutely reliable GFA parameter that makes it possible to evaluate GFA universally over different kinds of BMGs with different compositions. Accordingly, the 12 GFA parameters each preferentially characterize BMG families with specific base elements. For instance, the evaluation of GFA with T_g/T_1 provides the best fit for Co-based BMGs [60]. In this sense, the GFA parameters fall into utter confusion. The existence of preferential base element for each GFA parameter prevents description of HE-BMGs with

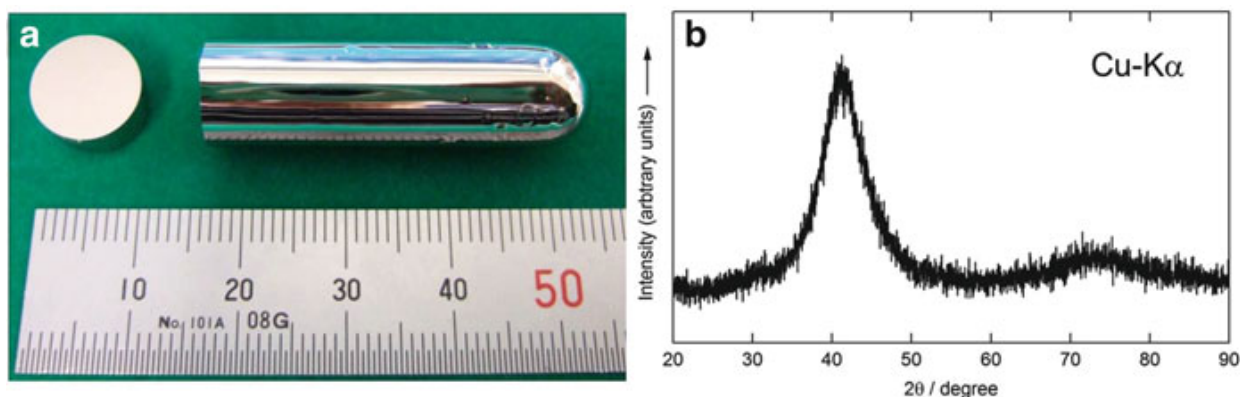


Fig. 13.1 (a) Outer appearance and (b) XRD profile taken from the cross-sectional area of $\text{Cu}_{20}\text{Ni}_{20}\text{P}_{20}\text{Pd}_{20}\text{Pt}_{20}$ HE-BMG with a diameter of 10 mm (Reproduced with permission from Ref. [14])

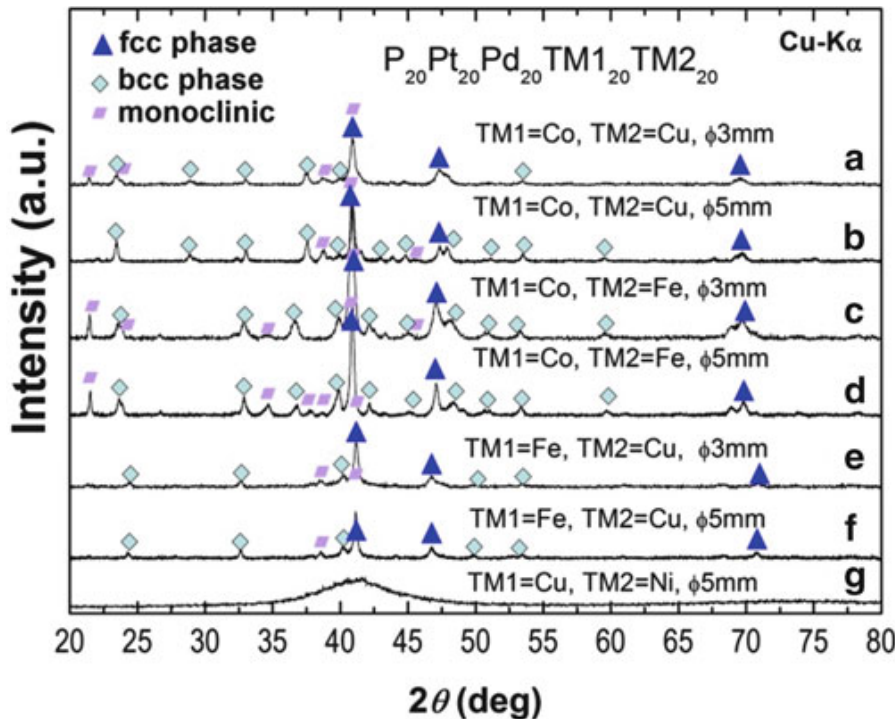
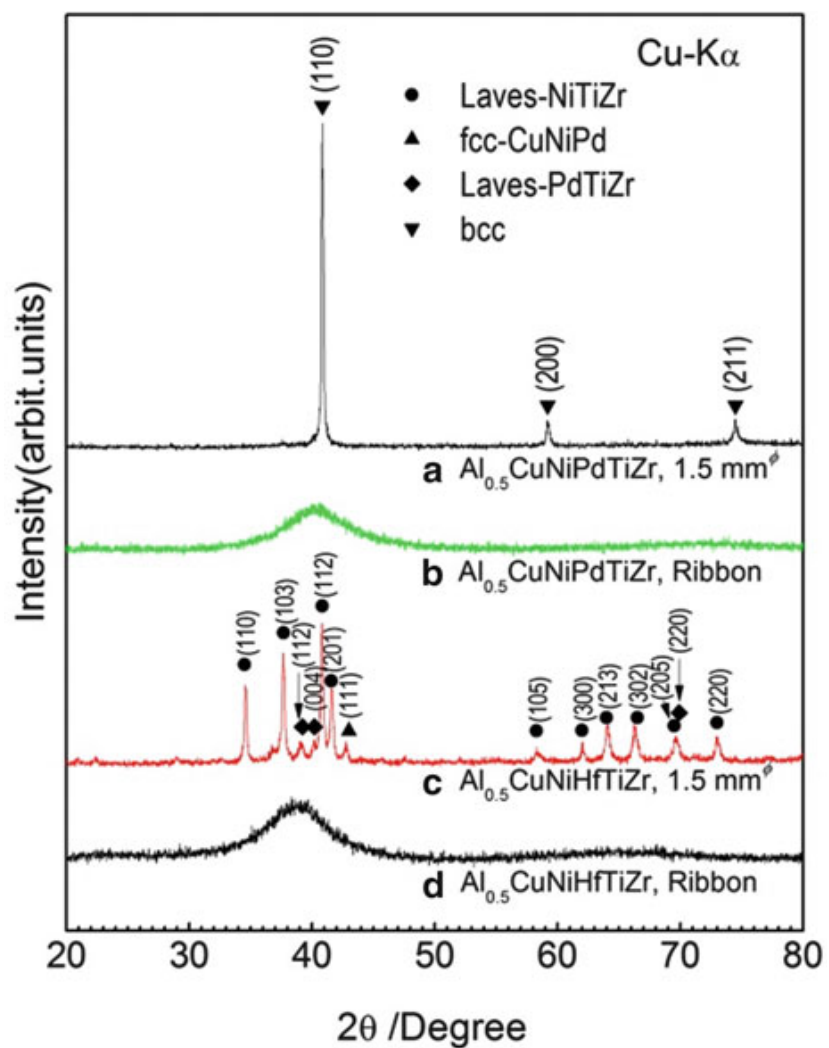


Fig. 13.2 XRD profiles of $P_{20}Pd_{20}Pt_{20}TM_{120}TM_{220}$ cylindrical alloys cast into diameters of 3 and 5 mm [61]

no principal elements and raises a question on the utility of presently known GFA parameters. Further study of the GFA parameters is required in the near future.

In a process of fabricating the $Cu_{20}Ni_{20}P_{20}Pd_{20}Pt_{20}$ HE-BMG, other possible combinations were examined by fixing Pd, Pt, and P and changing LTM_s from Cu and Ni, and it was found that the $P_{20}Pd_{20}Pt_{20}TM_{120}TM_{220}$ alloys form into a glassy phase only by $(TM_1, TM_2) = (Cu, Ni)$ as shown in Fig. 13.2 [61]. Besides, Takeuchi et al. examined three types of alloys with ETM₆₀LTM₄₀, ETM₅₀LTM₅₀, and ETM₄₀LTM₆₀ alloys, such as (a) $Hf_{20}Ni_{20}Pd_{20}Ti_{20}Zr_{20}$, (b) $Cu_{16.7}Ni_{16.7}Hf_{16.7}Pd_{16.7}Ti_{16.7}Zr_{16.7}$, and (c) $Cu_{20}Ni_{20}Pd_{20}Ti_{20}Zr_{20}$ alloy ribbons, and found that the $Cu_{20}Ni_{20}Pd_{20}Ti_{20}Zr_{20}$ alloy from ETM₄₀LTM₆₀ type can be a candidate for HE-BMGs because of formation of a glassy phase in the ribbon specimen. However, it was impossible to obtain $Cu_{20}Ni_{20}Pd_{20}Ti_{20}Zr_{20}$ HE-BMGs even with a sample diameter as small as 1 mm. Instead, it was found that that half mole of addition of Al ($Al_{0.5}$) to an ETM₄₀LTM₆₀ type, $Al_{0.5}CuNiPdTzr$ alloy, is formed into an HEA with bcc structure when prepared by a cylindrical shape with a diameter of 1.5 mm as shown in Fig. 13.3 [62]. It should be noted in Fig. 13.3 that $Al_{0.5}CuNiPdTzr$ alloy resulted in failure to obtain HEAs, although $Cu_{20}Hf_{20}Ni_{20}Ti_{20}Zr_{20}$ alloy is an HE-BMG [10]. The XRD profiles in Fig. 13.3 indicate that the $Al_{0.5}$ addition, which works efficiently to obtain HEA, does not always work well for enhancing GFA. In any case, the $Al_{0.5}CuNiPdTzr$ alloy exhibits unique forming ability to be into a glassy phase as well as crystalline HEA depending on the sample size and the cooling rate. Thus, it is considered that $Al_{0.5}CuNiPdTzr$ alloy can be a high-entropy metallic glass to bridge HEAs and MGs (BMGs) scientifically.

Fig. 13.3 XRD profiles of (a) and (b) $\text{Al}_{0.5}\text{CuNiPdTiZr}$ and (c) and (d) $\text{Al}_{0.5}\text{CuNiHfTiZr}$ alloys formed into (a) and (c) cylindrical specimens with 1.5 mm in diameter and (b) and (d) ribbons (Reproduced with permission from Ref. [62])



The possible reason for the peculiar characteristics of the $\text{Al}_{0.5}\text{CuNiPdTiZr}$ alloy to appear in two different phases, either glassy or bcc depending on the cooling rate, is considered with a schematically illustrated continuous cooling transformation (CCT) diagram shown in Fig. 13.4. A C-curve for a bcc phase is drawn at a high temperature range in Fig. 13.4. This is due to allotropic transformation of pure Ti and Zr [63] as well as a widely accepted fact that the bcc structure is often the high-temperature structure of a metal that has a close-packed structure at lower temperature [63]. Thus, the authors [63] think that the allotropic transformation of pure Ti and Zr could provide a symptom of the $\text{Al}_{0.5}\text{CuNiPdTiZr}$ alloy to be formed into a bcc phase at high temperatures. One such symptom would be provided as formulae of nucleation sites or embryos. In casting the alloy in the process (2) in Fig. 13.4, the alloy remains a bcc phase because of limited diffusions of atoms at a medium cooling rate (R). On the other hand, a glassy phase is obtained in the process (1) at a high R , whereas a bcc phase may transform into stable phases at a low R in the process (3). In addition to Ti and Zr, it should be noted that Al can be regarded as a bcc former in HEAs [64], supporting the presence of a bcc phase at a high temperature.

The peculiarity of the $\text{Al}_{0.5}\text{CuNiPdTiZr}$ HEA can be seen in Table 13.3 for the values of δ and ΔH_{mix} for the $\text{Cu}_{20}\text{Ni}_{20}\text{Pd}_{20}\text{Ti}_{20}\text{Zr}_{20}$, $\text{Al}_{0.5}\text{CuNiPdTiZr}$, and $\text{Al}_{0.5}\text{CuNiHfTiZr}$ alloys. The δ - ΔH_{mix} values were calculated using the equations

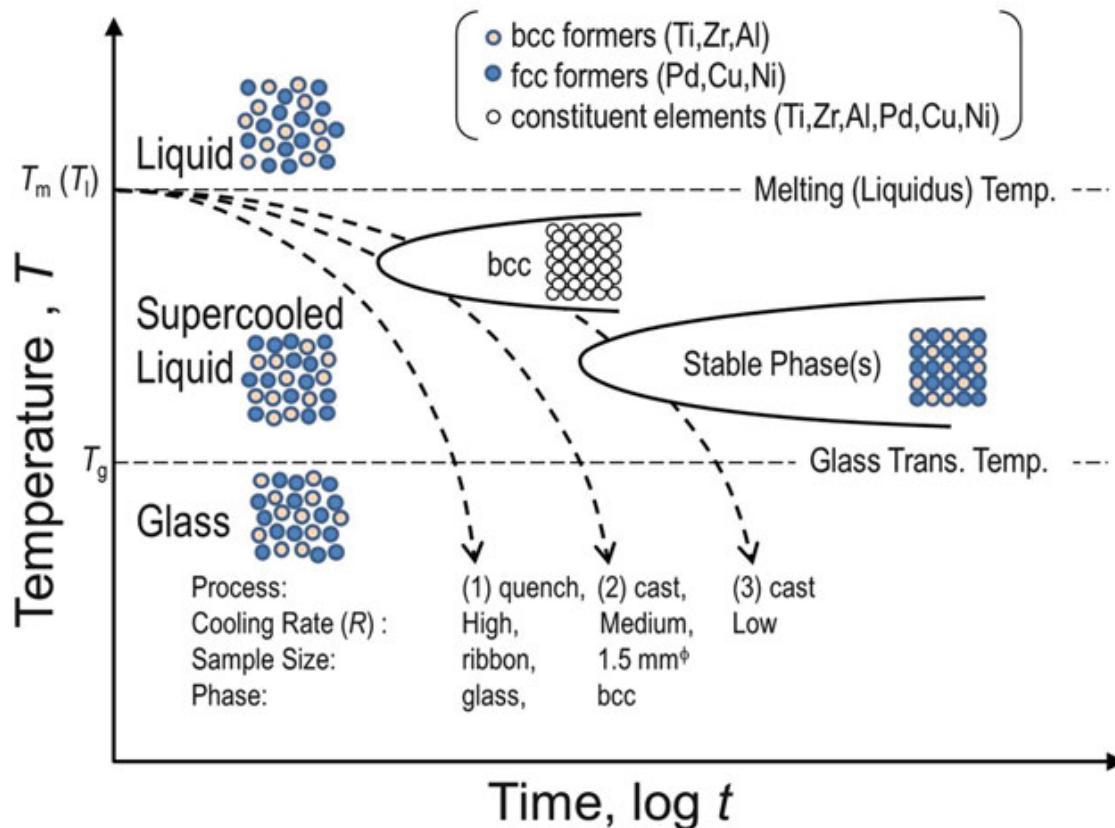


Fig. 13.4 A schematic illustration of the continuous cooling transformation (CCT) diagram of the $\text{Al}_{0.5}\text{CuNiPdTiZr}$ alloy with different processes (1) to (3). Atomic arrangements in 2 dimensions for phases of liquid, supercooled liquid, glass, bcc, and stable phases are given to demonstrate the statuses of atomic bonding of the $\text{Al}_{0.5}\text{CuNiPdTiZr}$ alloy for bcc (Ti, Zr, and Al) and fcc (Pd, Cu, and Ni) formers. The atomic arrangements exhibit a tendency that the bcc and fcc formers are separately percolated in an atomistic level in liquid, supercooled liquid, glassy and stable crystalline phases statistically. The bcc and fcc formers occupy the sites in the bcc structure randomly where the bcc structure is drawn as a hypothetical layered structure intentionally to distinguish it from the stable phase(s) (Reproduced with permission from Ref. [62])

Table 13.3 Mixing enthalpy (ΔH_{mix}), Delta parameter (δ), phases in the forms of ribbon and 1.5 mm rod specimens and reference of the HEAs

	$\Delta H_{\text{mix}}/\text{kJ mol}^{-1}$	δ	Phase in a form of ribbon/(1.0)* 1.5 mm rod
$\text{Cu}_{20}\text{Ni}_{20}\text{Pd}_{20}\text{Ti}_{20}\text{Zr}_{20}$	-45.1	9.2	Glass/(fcc + hcp + Laves + unknown)*
$\text{Cu}_{20}\text{Hf}_{20}\text{Ni}_{20}\text{Ti}_{20}\text{Zr}_{20}$	-27.4	10.3	Glass/glass
$\text{Al}_{0.5}\text{CuNiPdTiZr}$	-46.7	8.8	Glass/bcc
$\text{Al}_{0.5}\text{CuNiHfTiZr}$	-31.6	9.9	Glass/(fcc + Laves)

*Only this case ($\text{Cu}_{20}\text{Ni}_{20}\text{Pd}_{20}\text{Ti}_{20}\text{Zr}_{20}$), the sample diameter is 1.0 mm while that of the others are 1.5 mm . Reproduced with permission from Ref. [62]

presented in Chap. 2 in this book. It is also important that $\text{Al}_{0.5}\text{CuNiPdTiZr}$ HEA is located in a less dense area in the δ - ΔH_{mix} diagram covered by the ternary amorphous alloys [44]. These features of the $\text{Al}_{0.5}\text{CuNiPdTiZr}$ HEA encourage us to search for new HEAs by referring to the δ - ΔH_{mix} diagram.

The $\text{Cu}_{20}\text{Ni}_{20}\text{Pd}_{20}\text{Pt}_{20}$ HE-BMG exhibits poor mechanical properties. In short, it is mechanically brittle. This is expected from the fact that some of the BMGs belonging to metal–metalloid type are brittle in the as-cast state. It is

possible that local atomic arrangements of HE-BMGs are associated with those of intermetallic compounds. Other treatments can worsen the brittleness including structural relaxation and crystallization upon annealing.

13.2.2 $Be_{20}Cu_{20}Ni_{20}Ti_{20}Zr_{20}$ HE-BMG and Its Mechanical Properties

One can list the $Be_{20}Cu_{20}Ni_{20}Ti_{20}Zr_{20}$ HE-BMG as a representative HE-BMG of metal–metal type based on the prototypical BMG $Zr_{41.2}Ti_{13.9}Cu_{12.5}Ni_{10}Be_{22.5}$ (Vit1) [20]. The $Be_{20}Cu_{20}Ni_{20}Ti_{20}Zr_{20}$ HE-BMG was prepared by arc melting the mixture of the pure Zr, Ti, Be, Cu, and Ni in a water-cooled Cu crucible under a Ti-gettered high purity argon atmosphere. Rodlike samples with a diameter of 3 mm and a length of about 70 mm were obtained. Figure 13.5 shows the SEM of the $Be_{20}Cu_{20}Ni_{20}Ti_{20}Zr_{20}$ high-entropy alloys (HEAs). The contrast is featureless, indicating an amorphous structure for the present alloy. Thermodynamic characteristics of the $Be_{20}Cu_{20}Ni_{20}Ti_{20}Zr_{20}$ HE-BMG were reported as follows: $T_g = 683$ K and $T_x = 729$ K. High thermal stability and strength is attributed to the high-entropy (equal atomic) nature of this HE-BMG as well as an increase in Ni concentration. After annealing under vacuum at 813 K for 1 h, three

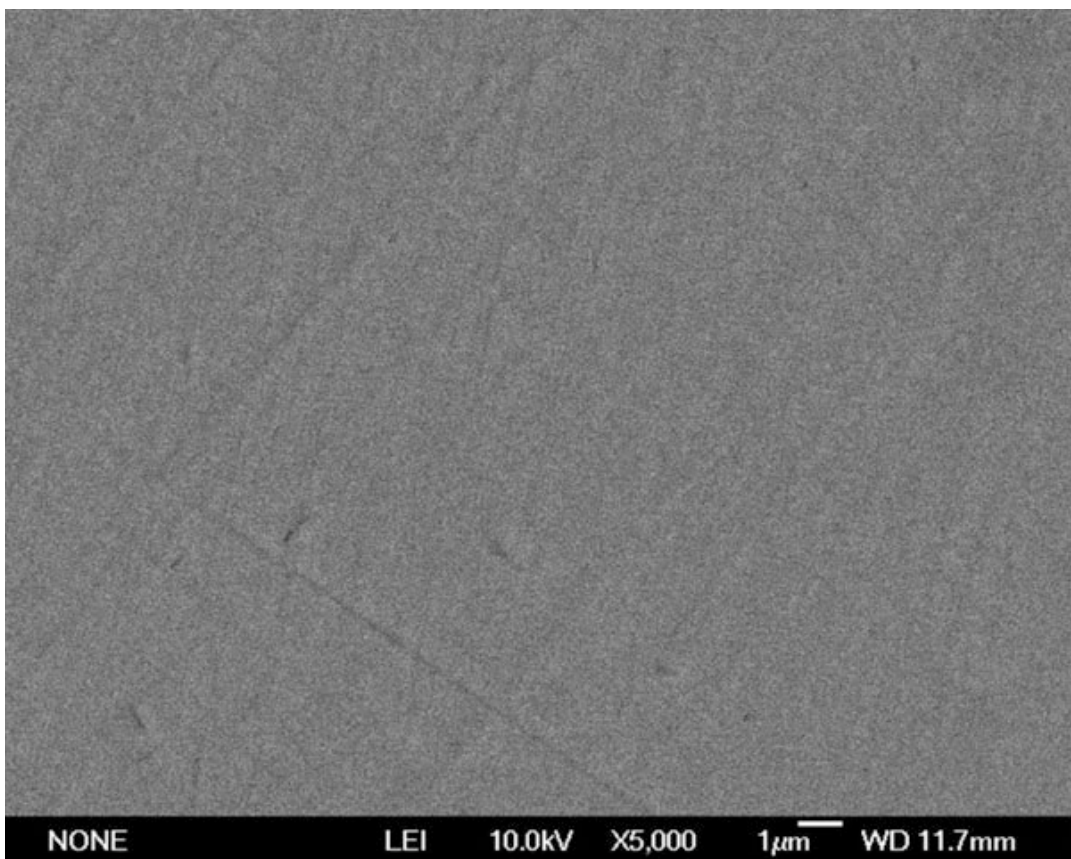


Fig. 13.5 SEM of $Be_{20}Cu_{20}Ni_{20}Ti_{20}Zr_{20}$ HEA

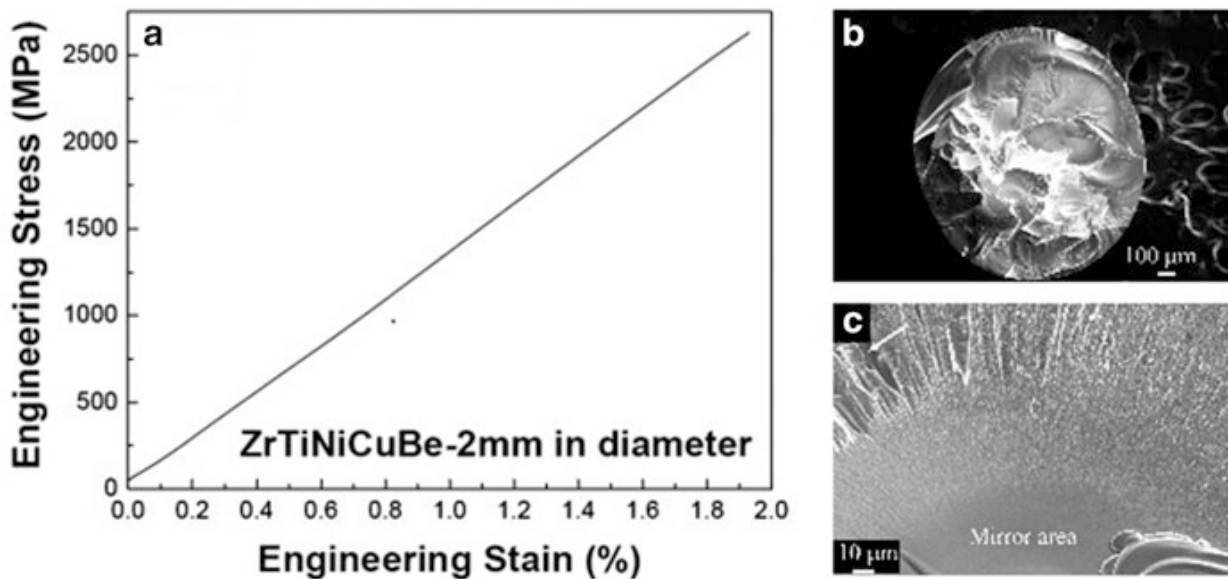


Fig. 13.6 (a) The engineering stress–strain curve of $\text{Be}_{20}\text{Cu}_{20}\text{Ni}_{20}\text{Ti}_{20}\text{Zr}_{20}$ and (b, c) presents the fractographies of the current amorphous HEA

phases including fcc, bcc solid solutions together with Ni_7Zr_2 intermetallic phase precipitated.

Examples of the uniaxial compressive tests are shown in Fig. 13.6 that were performed on 6-mm-long sections cut from the 2-mm-diameter cylinders using the MTS 809 material testing machine at room temperature (RT) with a strain rate of $2 \times 10^{-4} \text{ s}^{-1}$. For the compression testing, the samples were sandwiched between two WC platens, and two blades were mechanically fixed on the side surface of the WC platens. Figure 13.6a exhibits the engineering stress–strain curve of $\text{Be}_{20}\text{Cu}_{20}\text{Ni}_{20}\text{Ti}_{20}\text{Zr}_{20}$ at RT. This HEA has a brittle fracture, and no plasticity can be observed from Fig. 13.6a. It is noted that it exhibits the maximum strength of about 2600 MPa and elastic limit of about 1.9 %. Figure 13.6b presents the fractographies of the current amorphous HEA. From Fig. 13.6b, it is seen that multiple facets are dominant features, suggesting that more fracture energy is needed to convert to surface energy during fracture. A high magnification of a localized fracture surface is shown in Fig. 13.6c revealing a radiating pattern. In the front of this pattern, profuse molten liquids could be found, associated with shear adiabatic heating. Besides, a mirror area is present in the core of the radiating pattern.

In contrast to Zr-based BMGs, the $\text{Be}_{20}\text{Cu}_{20}\text{Ni}_{20}\text{Ti}_{20}\text{Zr}_{20}$ HE-BMG exhibits a brittle behavior, although the fracture strength is as high as over 2000 MPa. In part, this brittle nature is due to the precipitation of Ni_7Zr_2 intermetallic phase besides the conventional simple solid solutions with fcc and bcc structures. The brittle nature of the $\text{Be}_{20}\text{Cu}_{20}\text{Ni}_{20}\text{Ti}_{20}\text{Zr}_{20}$ HE-BMG is supported by the value of $\Delta H_{\text{mix}} = -30.24 \text{ kJ/mol}$ estimated from Miedema's model, which is extremely large and negative relative to that for conventional HEAs. The large and negative nature of ΔH_{mix} suggests the tendency to form intermetallic compounds which leads to the brittle nature of the alloy.

13.2.3 $\text{Ca}_{20}\text{Mg}_{20}\text{Sr}_{20}\text{Yb}_{20}\text{Zn}_{20}$ -Based HE-BMGs and Their Unique Mechanical Properties

This subsection describes the peculiar mechanical properties of $\text{Ca}_{20}\text{Mg}_{20}\text{Sr}_{20}\text{Yb}_{20}\text{Zn}_{20}$ -based HE-BMGs. In principle, crystalline and glassy alloys reveal different mechanical properties when subjected to forces [63]. The appearance of different mechanical properties is caused by some factors, such as chemical bonding, macroscopic morphology with and without grain boundaries and dislocations as a result of the atomic arrangements, and so on. These factors determine the properties of materials. Among various properties, mechanical properties are the most sensitive to the inhomogeneity included in the materials where the inclusions here are represented by defects, cracks, secondary phases, pores, and so on. The key phenomenon to determine the mechanical properties of materials can be a stress concentration generated at the sharp corners and edges by the inclusions, such as dislocations and cracks for crystalline and glassy alloys, respectively.

In principle, HE-BMGs behave as a glassy material in mechanical tests. As is similar to oxide and other glassy materials, HE-BMGs with a macroscopic dense random packing structure without long-range atomic periodicity exhibit the brittleness in mechanical tests at room temperature. This brittle nature of HE-BMGs originates from the absence of dislocations inherent to crystalline alloys, and thus, crack propagations via shear band formation and propagation lead to fracture without exhibiting plastic deformation. In contrast to the crystalline alloys with dislocations that release the stress concentrations by their movements by forming networks with resultant macroscopic deformations, in glassy alloys, stress concentration takes place at the points of inclusions, leading to crack propagation and resultant fracture. As a result, the stress-strain curves of glassy materials in tensile test are very brittle or exhibit a strain (ε) of $\sim 0.2\%$, which is extremely smaller than ductile metallic crystalline alloys with ε reaching a couple of tens % or more. As an exceptional case, some glassy alloys, such as $\text{Cu}_{60}\text{Zr}_{30}\text{Ti}_{10}$ BMG [54], exhibit plastic deformation at room temperature, but its deformation can be observed in compression tests only. The comparison of representative features of glassy alloys with crystalline alloys is summarized as follows: (1) relatively higher tensile strength and lower Young's modulus and (2) absence of distinct plastic elongation at room temperature due to inhomogeneous deformation modes. Here, one can see the relatively low Young's modulus of HE-BMG in Fig. 13.7 [13].

In general, the latter feature of glassy alloys in mechanical tests makes it difficult to utilize the glassy alloys as structural materials. In contrast, glassy alloys exhibit advantageous aspects at relatively high temperature near T_g , which can be widely accepted as viscous flow. The viscous flow of glassy materials takes place as a result of a homogeneous deformation mode at a temperature range called the supercooled liquid region ΔT_x defined as the temperature interval between T_g and T_x . Thus, HE-BMGs as well as BMGs with extremely low T_g provide us an opportunity to overcome the brittle nature in mechanical tests. An example can be seen in $\text{Ca}_{20}\text{Mg}_{20}\text{Sr}_{20}\text{Yb}_{20}\text{Zn}_{20}$ -based HE-BMGs tested at RT in Fig. 13.8 [13]. The latest results of HE-BMGs regarding mechanical properties including the ones in Figs. 13.7 and 13.8 are also summarized in Ref. [65].

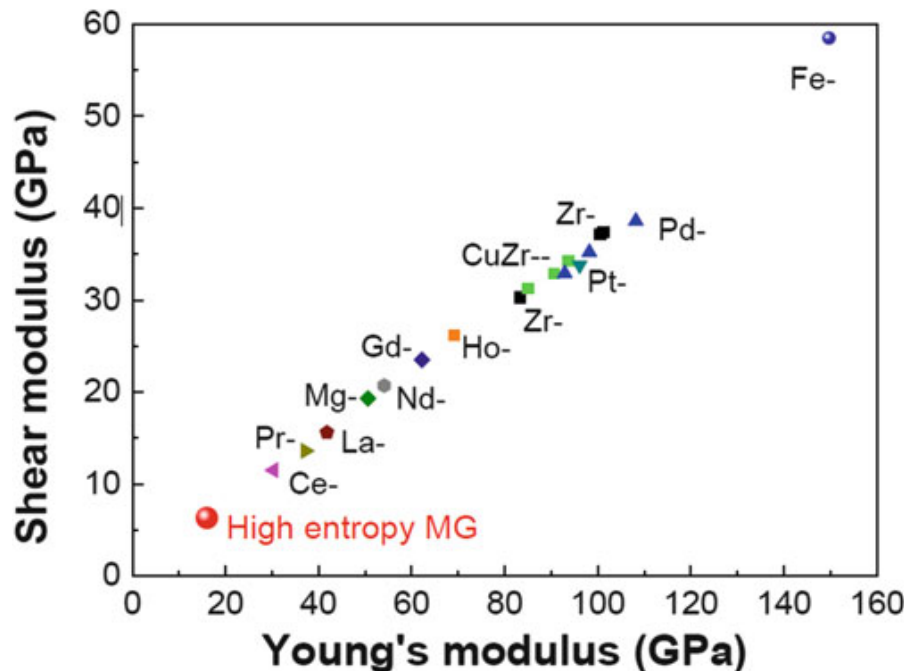


Fig. 13.7 The comparison of Young's modulus and shear modulus of a series of MGs. The $\text{Ca}_{20}(\text{Li}_{0.55}\text{Mg}_{0.45})_{20}\text{Sr}_{20}\text{Yb}_{20}\text{Zn}_{20}$ BMG has the smallest elastic constant among other typical BMGs (Reproduced with permission from Ref. [13])

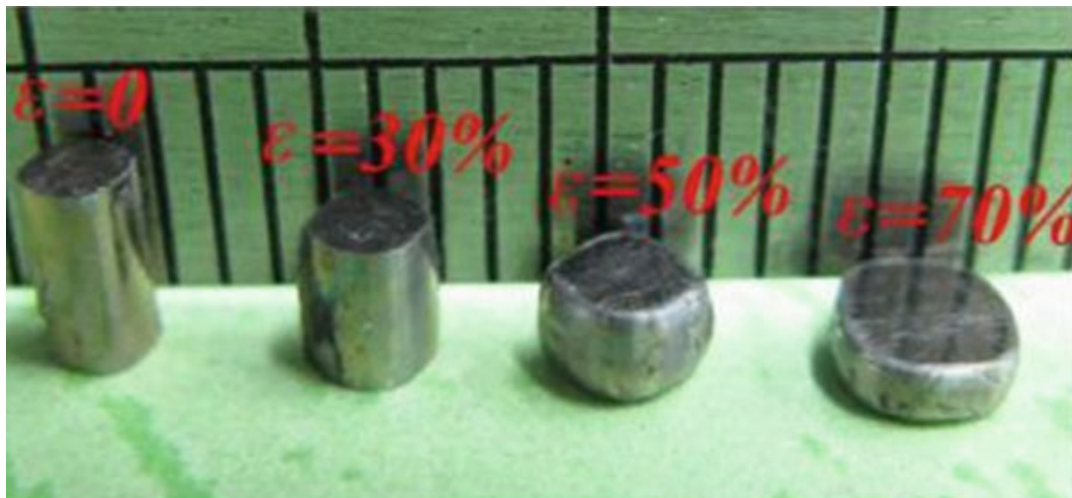


Fig. 13.8 The photo image of the compressed $\text{Ca}_{20}(\text{Li}_{0.55}\text{Mg}_{0.45})_{20}\text{Sr}_{20}\text{Yb}_{20}\text{Zn}_{20}$ HE-BMG, which can be compressed up to 70 % of its original height without shear banding and cracking [13] (Reproduced with permission from Ref. [13])

13.2.4 Factors Affecting the Mechanical Properties of HE-BMGs

This subsection focuses on two factors that would affect the mechanical properties of HE-BMGs. The first one are the types of HE-BMGs, MGs, and BMGs: metal–metal and metal–metalloid types. In principle, metal–metalloid type MGs and BMGs only tend to be more brittle than metal–metal type ones [66] because of the presence of covalent-like atomic bonding between the metal and the metalloid

and easiness in promoting chemically induced structural relaxation as well as topological ones. The second one is the values of ΔH_{mix} [67], which indicate the tendency of forming glassy and intermetallic phases. Generally, HE-BMGs as well as MGs possess larger and more negative ΔH_{mix} and larger δ than HEAs in the δ - ΔH_{mix} diagram [44]. In reality, the values of ΔH_{mix} are approximately in the range of 0 to -10 kJ/mol, which forms zone S in the δ - ΔH_{mix} diagram. On the other hand, $\text{Be}_{20}\text{Cu}_{20}\text{Ni}_{20}\text{Ti}_{20}\text{Zr}_{20}$ HE-BMG has $\Delta H_{\text{mix}} = -30.24$ kJ/mol and $\text{Cu}_{20}\text{Ni}_{20}\text{P}_{20}\text{Pd}_{20}\text{Pt}_{20}$ HE-BMG has $\Delta H_{\text{mix}} = -25$ kJ/mol, which are considerably larger and negative than those for HEAs. However, $\text{Ca}_{20}\text{Mg}_{20}\text{Sr}_{20}\text{Yb}_{20}\text{Zn}_{20}$ -based HE-BMGs have $\Delta H_{\text{mix}} = -10$ to -12 kJ/mol, which are within the ΔH_{mix} range of those crystalline HEAs. This feature of ΔH_{mix} of the HE-BMGs could determine the mechanical properties for ductility or brittleness to some extent. The values of ΔH_{mix} are closely related to the interatomic interaction and bonding in the alloys, which are explained in the next subsection by showing the results of *ab initio* molecular dynamics (AIMD) simulations for model HE-BMGs.

13.2.5 AIMD Simulations

The atomic structures of model HE-BMG alloys including $\text{Cu}_{20}\text{Ni}_{20}\text{P}_{20}\text{Pd}_{20}\text{Pt}_{20}$, $\text{Al}_{20}\text{Er}_{20}\text{Dy}_{20}\text{Ni}_{20}\text{Tb}_{20}$, $\text{Cu}_{20}\text{Hf}_{20}\text{Ni}_{20}\text{Ti}_{20}\text{Zr}_{20}$, and $\text{Be}_{20}\text{Cu}_{20}\text{Ni}_{20}\text{Ti}_{20}\text{Zr}_{20}$ were studied using canonical ensemble (NVT) AIMD simulations at $T = 1400$ K [68]. A cell of 200 atoms was used except 100 for $\text{Cu}_{20}\text{Ni}_{20}\text{P}_{20}\text{Pd}_{20}\text{Pt}_{20}$, and the data were collected over 50 ps. The calculated partial pair distribution functions (PDF) are presented in Fig. 13.9. As is similar to the classification of BMGs described in Sect. 13.1.3, we group chemically similar elements as a “single element.” In the case of CuNiPPdPt, we group Ni, Pd, and Pt as “N” for “nickel group.” The partial CuN PDF was obtained by averaging over CuNi, CuPd, and CuPt pairs and likewise for partial PDFs over NN and PN pairs. Clearly, P binds more strongly to the nickel group than to Cu. This follows expectation, as the enthalpies of formation of P with the Ni group are approximately four times larger than with Cu. Equally dramatic is the absence of a P-P near neighbor peak, reflecting the strong preference of P to surround itself with metal atoms. A complete presentation of the partial PDFs of $\text{Cu}_{20}\text{Ni}_{20}\text{P}_{20}\text{Pd}_{20}\text{Pt}_{20}$ at $T = 1200$ K was shown in Ref. [7].

It is well known that the rare earth lanthanide series consists of chemically similar elements, because the strongly localized 4f electrons hardly participate in chemical bonding. Hence, the RX ($R = \text{Er}, \text{Dy}, \text{Tb}; X = \text{Al}, \text{Ni}$) correlations exhibit little dependence on rare earth element “R” in $\text{Al}_{20}\text{Dy}_{20}\text{Er}_{20}\text{Ni}_{20}\text{Tb}_{20}$, and we choose to average the correlation functions over the R elements. The strongest correlations occur between chemically dissimilar pairs of elements. Hence, the rare earths strongly bind both Al and Ni, while the Al–Ni correlation is also strong, consistent with the strong compound formation and chemical ordering prevalent in solid Al–Ni alloys. The preference for binding with unlike elements leads to strong reductions in the strength of the nearest-neighbor Al–Al and Ni–Ni peaks.

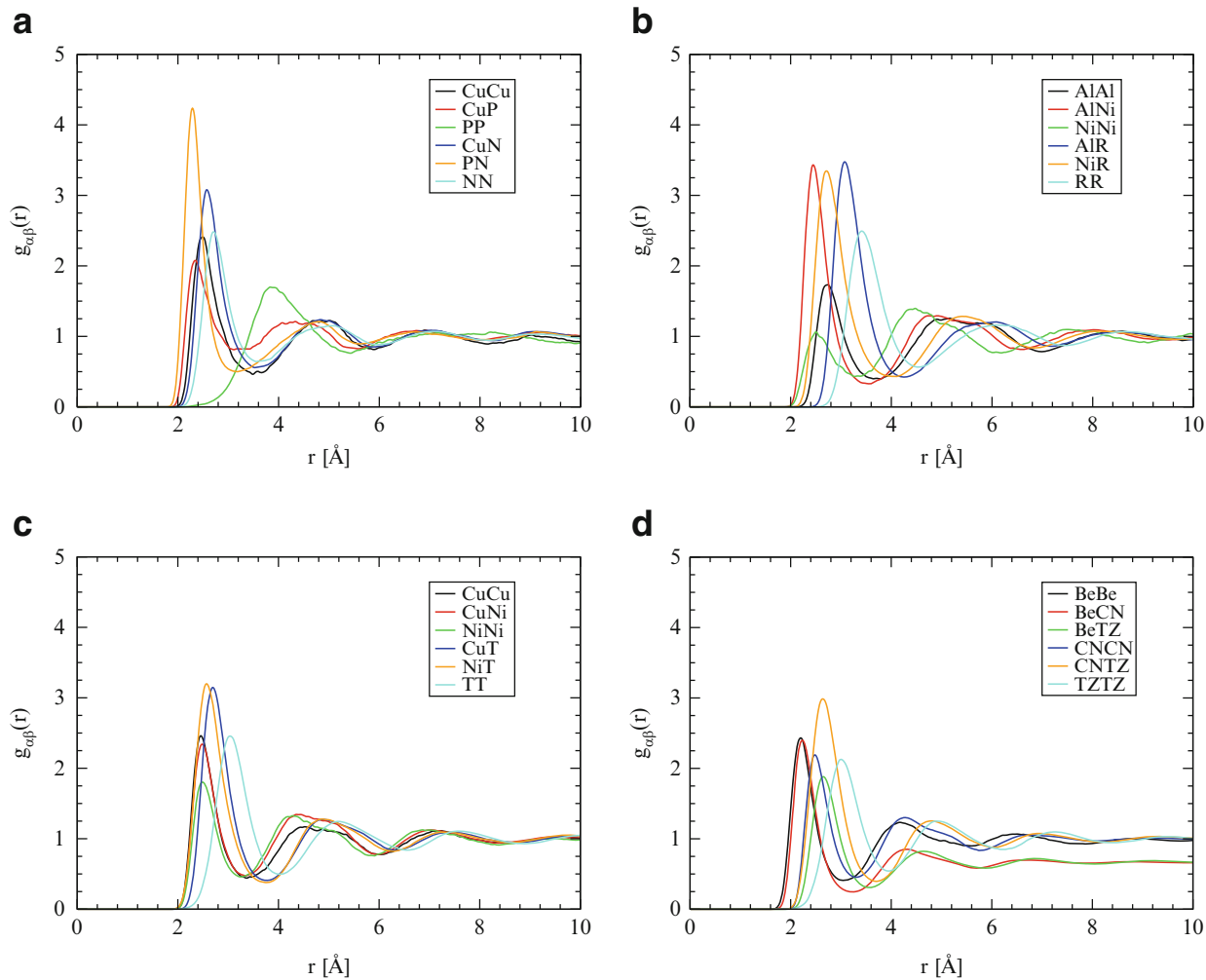


Fig. 13.9 Calculated partial PDF pertaining to Ni in (a) $\text{Cu}_{20}\text{Ni}_{20}\text{P}_{20}\text{Pd}_{20}\text{Pt}_{20}$ (where N = Ni, Pd, Pt) (b) $\text{Al}_{20}\text{Er}_{20}\text{Dy}_{20}\text{Ni}_{20}\text{Tb}_{20}$ (where R = Dy, Er, Tb), (c) $\text{Cu}_{20}\text{Hf}_{20}\text{Ni}_{20}\text{Ti}_{20}\text{Zr}_{20}$ (where T = Hf, Ti, Zr), and (d) $\text{Be}_{20}\text{Cu}_{20}\text{Ni}_{20}\text{Ti}_{20}\text{Zr}_{20}$ (where TZ = Ti, Zr, and CN = Cu, Ni) [68]

The Ti group shares a common valence of 4^+ and a relatively large radius and low electronegativity since they are positioned early in the transition metal rows. Hence, we group these elements under the label “T” and average their correlation functions. This group binds strongly to both of the strongly electronegative and relatively small late-transition metals Cu and Ni. The relative sizes of atoms are evident in the positions of the peaks, starting with the late–late pairs at the shortest distances, followed by late–early pairs, and finally early–early.

For the last compound, $\text{Be}_{20}\text{Cu}_{20}\text{Ni}_{20}\text{Ti}_{20}\text{Zr}_{20}$, we separately group the early-transition metals Ti and Zr (label “TZ”) and the late-transition metals Ni and Cu (label “CN”). A hierarchy of sizes is apparent, in the order Be, CN, TZ. The strongest binding occurs between CN and TZ, again reflecting their large electronegativity difference, with Be intermediate in both electronegativity and in binding strength to CN and to TZ.

The diffusion constants were obtained by plotting the mean square displacement (MSD) versus time. The plot is fairly linear for all species, and the obtained diffusion constants are shown in Fig. 13.10 and Table 13.4 [68]. With the smallest atomic size, P has the slowest diffusivity at $T = 1400$ K due to strong chemical

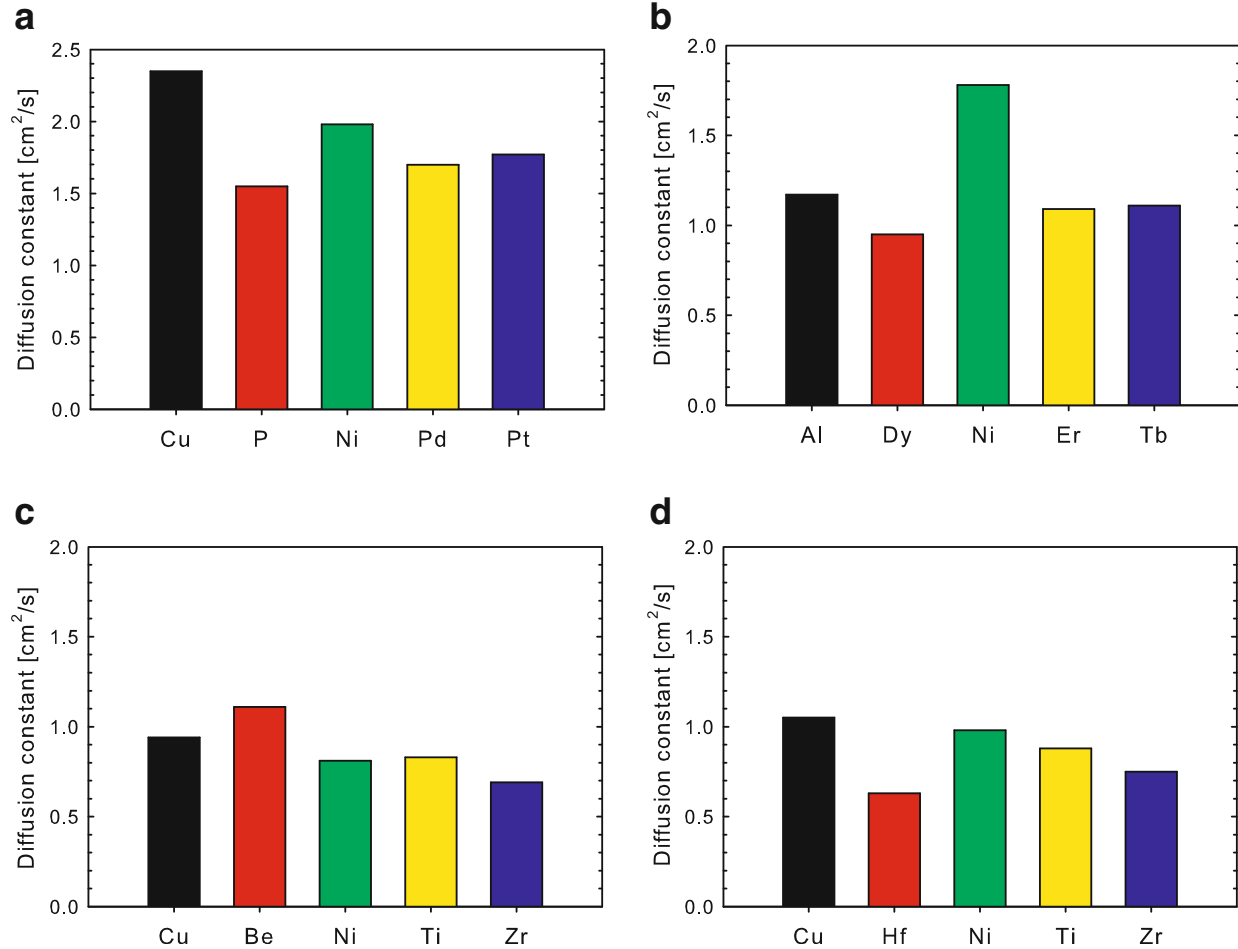


Fig. 13.10 Diffusion constants obtained from MSD plots for (a) Cu₂₀Ni₂₀P₂₀Pd₂₀Pt₂₀, (b) Al₂₀Er₂₀Dy₂₀Ni₂₀Tb₂₀, (c) Be₂₀Cu₂₀Ni₂₀Ti₂₀Zr₂₀, and (d) Cu₂₀Hf₂₀Ni₂₀Ti₂₀Zr₂₀ from AIMD simulations at $T = 1400$ K [68]

Table 13.4 Diffusion constants [10^{-5} cm²/s] at $T = 1400$ K obtained from AIMD simulations [68]

	Cu	Ni	P	Pd	Pt
Cu ₂₀ Ni ₂₀ P ₂₀ Pd ₂₀ Pt ₂₀	2.35	1.98	1.55	1.70	1.77
Al ₂₀ Er ₂₀ Dy ₂₀ Ni ₂₀ Tb ₂₀	Al	Er	Dy	Ni	Tb
	1.17	1.09	0.95	1.78	1.11
Be ₂₀ Cu ₂₀ Ni ₂₀ Ti ₂₀ Zr ₂₀	Be	Cu	Ni	Ti	Zr
	1.11	0.94	0.81	0.83	0.69
Cu ₂₀ Hf ₂₀ Ni ₂₀ Ti ₂₀ Zr ₂₀	Cu	Hf	Ni	Ti	Zr
	1.05	0.63	0.98	0.88	0.75

bonding between P and metallic elements. For the rest three alloys, the atomic diffusivity largely is inversely correlated to their atomic size, namely, element of large atomic radii diffuses slowly. Note that atomic diffusivity is also system sensitive. The diffusivity of Ni in Cu₂₀Ni₂₀P₂₀Pd₂₀Pt₂₀ is nearly twice that in Be₂₀Cu₂₀Ni₂₀Ti₂₀Zr₂₀.

The glass structure of Cu₂₀Ni₂₀P₂₀Pd₂₀Pt₂₀ was obtained by quenching the liquid at $T = 1200$ K to 500 K at a cooling rate of 8.75×10^{13} K/s followed by full relaxation at $T = 0$ K [68]. The resulting partial PDF and atomic structure are shown in Fig. 13.11. In consistent with liquid simulation, the PNi pair ordering has the highest probability at shortest bond length.

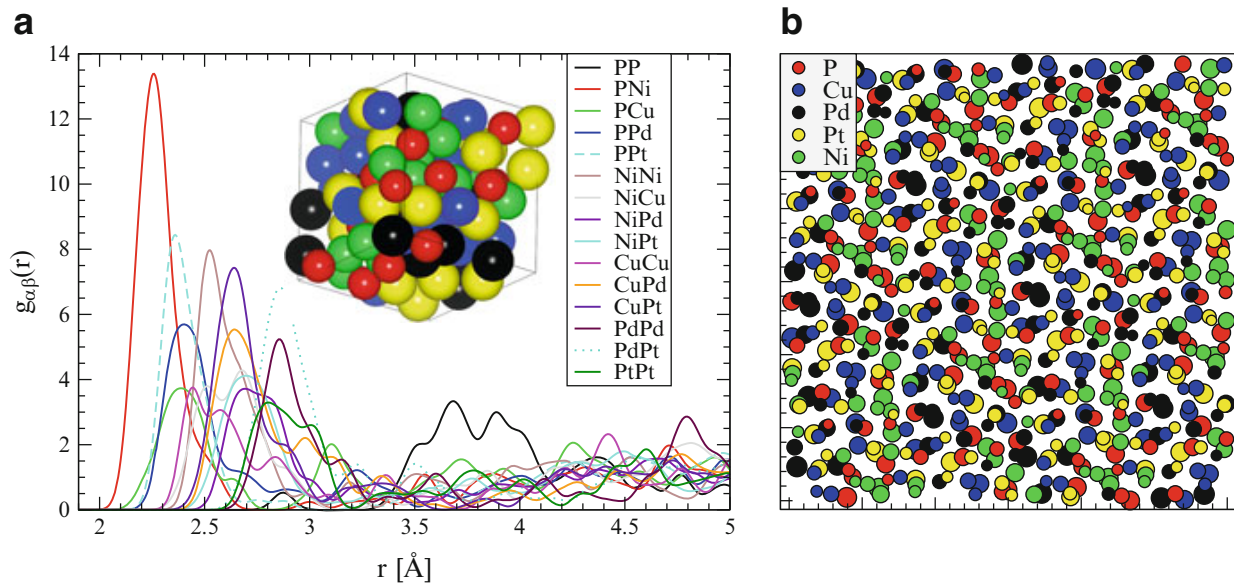


Fig. 13.11 Partial PDF of $\text{Cu}_{20}\text{Ni}_{20}\text{P}_{20}\text{Pd}_{20}\text{Pt}_{20}$ glass and the cross section along [100] projection [68]

13.3 Expected Applications of HE-BMGs

A recent report on the application of products of BMGs [3] focused on the mechanical properties of BMGs for Zr-, Ti-based, and Fe-based alloys where the former two are metal–metal and the last one is metal–metalloid type. Of these three alloys, there is little prospect to discover new HE-BMGs as magnetic alloys comprising iron-group elements because of the limited selection of metal and metalloid elements with approximate composition of $(\text{metal})_{80}(\text{metalloid})_{20}$. Exceptionally, it has recently been reported [69] that alloys comprising iron-group element and metalloids with compositions of $\text{Al}_{x/2}\text{CoFeNiSi}_{x/2}$ ($0 \leq x \leq 0.8$) can be formed into HEAs as soft magnetic alloys, but the magnetization of these soft magnetic HEAs is restricted to around $1.3 T$ due to the limited content of iron-group elements. Thus, it is expected that new HE-BMGs belonging to metal–metal type could be used as materials in the application fields where the BMGs have already reached to date. The expected applications depend on the characteristics of porous behavior, imprintability in nanoscale, and so forth which all are achieved by utilizing the viscous behavior of BMGs. In fact, it was reported that the $\text{Ca}_{20}(\text{Li}_{0.55}\text{Mg}_{0.45})_{20}\text{Sr}_{20}\text{Yb}_{20}\text{Zn}_{20}$ alloy was applied to imprinted material [13]. Besides, low Young's modulus can also be utilized for applications of HE-BMGs where it was previously applied to head materials of golf clubs made of Zr-based BMGs [43]. In addition to the unique mechanical properties of HE-BMGs, HE-BMGs as well as BMGs can be used as coating materials [3] by utilizing the glassy nature of the alloys that do not contain defects. It is expected that HE-BMGs will find both similar and new applications by making the most of the unique properties inherent to glassy materials.

13.4 Conclusions

High-entropy BMGs have been successfully produced by substituting chemically similar elements to known BMG. For example, the Cu₂₀Ni₂₀P₂₀Pd₂₀Pt₂₀ and Be₂₀Cu₂₀Ni₂₀Ti₂₀Zr₂₀ HE-BMGs are derived from the prototypical BMGs of Pd₄₀Ni₄₀P₂₀ and Zr_{41.2}Ti_{13.9}Cu_{12.5}Ni₁₀Be_{22.5}, respectively. However, the glass-forming ability of HE-BMG to date is significantly poorer than conventional BMG. These HE-BMGs exhibit brittle nature inherited from the glass materials. Their enthalpies of mixing (ΔH_{mix}) are much more negative than the threshold in forming crystalline HEAs, suggesting a preference to form intermetallic compounds. Besides, inclusion of metalloid elements in the Cu₂₀Ni₂₀P₂₀Pd₂₀Pt₂₀ HE-BMG may intensify its brittle characteristics. In sharp contrast, Ca₂₀Mg₂₀Sr₂₀Yb₂₀Zn₂₀-based HE-BMGs are ductile and are characterized by peculiar mechanical properties exceeding those of the HEAs and BMGs. An extremely low glass transition temperature near RT of the Ca₂₀Mg₂₀Sr₂₀Yb₂₀Zn₂₀-based HE-BMGs leads to extremely large deformation at RT, which cannot be achieved by any other BMGs. Unlike single-phase HEAs, AIMD simulations reveal preferred near-neighbor interaction in these HE-BMGs, showing strong tendency in forming intermetallic compounds. The current and upcoming HE-BMGs have a potential to be used as application products which have been accomplished by BMGs. In addition, it is possible that HE-BMGs have a potential to open a new research field by utilizing the unique properties of HEAs and BMGs in the near future.

Acknowledgments A.T. acknowledges Japan Society for the Promotion of Science (JSPS) for financial support: Grants-in-Aid for Scientific Research (B) with a program title of “Fabrication of High-Entropy Bulk Metallic Glasses based on Confusion Principle, Clarification of their Properties and their Application” (grant number 24360284). M.C.G. acknowledges the financial support by the Cross-Cutting Technologies Program at the National Energy Technology Laboratory (NETL) – Strategic Center for Coal, managed by Robert Romanosky (Technology Manager) and Charles Miller (Technology Monitor). The Research was executed through NETL’s Office of Research and Development’s Innovative Process Technologies (IPT) Field Work Proposal under the RES contract DE-FE-0004000. M.W. acknowledges support from the DOE under grant DE-SC0014506.

Disclaimer This chapter co-authored by M.C.G. was funded by the Department of Energy, National Energy Technology Laboratory, an agency of the United States Government, through a support contract with AECOM. Neither the United States Government nor any agency thereof, nor any of their employees, nor AECOM, nor any of their employees, makes any warranty, expressed or implied, or assumes any legal liability or responsibility for the accuracy, completeness, or usefulness of any information, apparatus, product, or process disclosed, or represents that its use would not infringe privately owned rights. Reference herein to any specific commercial product, process, or service by trade name, trademark, manufacturer, or otherwise, does not necessarily constitute or imply its endorsement, recommendation, or favoring by the United States Government or any agency thereof. The views and opinions of authors expressed herein do not necessarily state or reflect those of the United States Government or any agency thereof.

References

1. Yeh JW, Chen SK, Lin SJ, Gan JY, Chin TS, Shun TT, Tsau CH, Chang SY (2004) Nanostructured high-entropy alloys with multiple principal elements: novel alloy design concepts and outcomes. *Adv Eng Mater* 6(5):299–303. doi:[10.1002/adem.200300567](https://doi.org/10.1002/adem.200300567)
2. Yeh JW (2006) Recent progress in high-entropy alloys. *Annales De Chimie-Science Des Materiaux* 31(6):633–648. doi:[10.3166/acsm.31.633-648](https://doi.org/10.3166/acsm.31.633-648)
3. Inoue A, Takeuchi A (2011) Recent development and application products of bulk glassy alloys. *Acta Mater* 59(6):2243–2267. doi:[10.1016/j.actamat.2010.11.027](https://doi.org/10.1016/j.actamat.2010.11.027)
4. Murty BS, Yeh J-W, Ranganathan S (2014) High-entropy alloys. Butterworth-Heinemann, London
5. Takeuchi A, Amiya K, Wada T, Yubuta K, Zhang W (2014) High-entropy alloys with a hexagonal close-packed structure designed by equi-atomic alloy strategy and binary phase diagrams. *JOM* 66(10):1984–1992. doi:[10.1007/s11837-014-1085-x](https://doi.org/10.1007/s11837-014-1085-x)
6. Feuerbacher M, Heidemann M, Thomas C (2015) Hexagonal high-entropy alloys. *Mater Res Lett* 3(1):1–6. doi:[10.1080/21663831.2014.951493](https://doi.org/10.1080/21663831.2014.951493)
7. Zhang Y, Zuo TT, Tang Z, Gao MC, Dahmen KA, Liaw PK, Lu ZP (2014) Microstructures and properties of high-entropy alloys. *Prog Mater Sci* 61:1–93. doi:[10.1016/j.pmatsci.2013.10.001](https://doi.org/10.1016/j.pmatsci.2013.10.001)
8. Gao MC, Alman DE (2013) Searching for next single-phase high-entropy alloy compositions. *Entropy* 15:4504–4519. doi:[10.3390/e15104504](https://doi.org/10.3390/e15104504)
9. Takeuchi A, Inoue A (2005) Classification of bulk metallic glasses by atomic size difference, heat of mixing and period of constituent elements and its application to characterization of the main alloying element. *Mater Trans* 46(12):2817–2829. doi:[10.2320/matertrans.46.2817](https://doi.org/10.2320/matertrans.46.2817)
10. Ma LQ, Wang LM, Zhang T, Inoue A (2002) Bulk glass formation of Ti-Zr-Hf-Cu-M (M = Fe, Co, Ni) alloys. *Mater Trans* 43(2):277–280. doi:[10.2320/matertrans.43.277](https://doi.org/10.2320/matertrans.43.277)
11. Greer AL (1993) Materials science – confusion by design. *Nature* 366(6453):303–304. doi:[10.1038/366303a0](https://doi.org/10.1038/366303a0)
12. Cantor B, Chang ITH, Knight P, Vincent AJB (2004) Microstructural development in equiatomic multicomponent alloys. *Mater Sci Eng A Struct Mater Proper Microstruct Proc* 375:213–218. doi:[10.1016/j.msea.2003.10.257](https://doi.org/10.1016/j.msea.2003.10.257)
13. Zhao K, Xia XX, Bai HY, Zhao DQ, Wang WH (2011) Room temperature homogeneous flow in a bulk metallic glass with low glass transition temperature. *Appl Phys Lett* 98(14):141913-1–141913-3. doi:[10.1063/1.3575562](https://doi.org/10.1063/1.3575562)
14. Takeuchi A, Chen N, Wada T, Yokoyama Y, Kato H, Inoue A, Yeh JW (2011) $Pd_{20}Pt_{20}Cu_{20}Ni_{20}P_{20}$ high-entropy alloy as a bulk metallic glass in the centimeter. *Intermetallics* 19(10):1546–1554. doi:[10.1016/j.intermet.2011.05.030](https://doi.org/10.1016/j.intermet.2011.05.030)
15. Gao XQ, Zhao K, Ke HB, Ding DW, Wang WH, Bai HY (2011) High mixing entropy bulk metallic glasses. *J Non Cryst Solids* 357(21):3557–3560. doi:[10.1016/j.jnoncrysol.2011.07.016](https://doi.org/10.1016/j.jnoncrysol.2011.07.016)
16. Li HF, Xie XH, Zhao K, Wang YB, Zheng YF, Wang WH, Qin L (2013) In vitro and in vivo studies on biodegradable $CaMgZnSrYb$ high-entropy bulk metallic glass. *Acta Biomater* 9(10):8561–8573. doi:[10.1016/j.actbio.2013.01.029](https://doi.org/10.1016/j.actbio.2013.01.029)
17. Ding HY, Yao KF (2013) High entropy $Ti_{20}Zr_{20}Cu_{20}Ni_{20}Be_{20}$ bulk metallic glass. *J Non Cryst Solids* 364:9–12. doi:[10.1016/j.matlet.2014.03.185](https://doi.org/10.1016/j.matlet.2014.03.185)
18. Ding HY, Shao Y, Gong P, Li JF, Yao KF (2014) A senary $TiZrHfCuNiBe$ high entropy bulk metallic glass with large glass-forming ability. *Mater Lett* 125:151–153. doi:[10.1016/j.matlet.2014.03.185](https://doi.org/10.1016/j.matlet.2014.03.185)
19. He Y, Schwarz RB, Archuleta JI (1996) Bulk glass formation in the Pd-Ni-P system. *Appl Phys Lett* 69(13):1861–1863. doi:[10.1063/1.117458](https://doi.org/10.1063/1.117458)
20. Johnson WL (1996) Fundamental aspects of bulk metallic glass formation in multicomponent alloys. *Metastab Mech Alloyed Nanocryst Mater Pts 1 and 2* 225:35–49

21. Inoue A, Nishiyama N, Kimura H (1997) Preparation and thermal stability of bulk amorphous Pd₄₀Cu₃₀Ni₁₀P₂₀ alloy cylinder of 72 mm in diameter. Mater Trans JIM 38(2):179–183. doi:[10.2320/matertrans1989.38.179](https://doi.org/10.2320/matertrans1989.38.179)
22. Nishiyama N, Takenaka K, Wada T, Kimura H, Inoue A (2005) Undercooling behavior and critical cooling rate of Pd-Pt-Cu-P alloy. Mater Trans 46(12):2807–2810. doi:[10.2320/matertrans.46.2807](https://doi.org/10.2320/matertrans.46.2807)
23. Inoue A, Zhang T (1996) Fabrication of bulk glassy Zr₅₅Al₁₀Ni₅Cu₃₀ alloy of 30 mm in diameter by a suction casting method. Mater Trans JIM 37(2):185–187. doi:[10.2320/matertrans1989.37.185](https://doi.org/10.2320/matertrans1989.37.185)
24. Zheng Q, Xu J, Ma E (2007) High glass-forming ability correlated with fragility of Mg-Cu (Ag)-Gd alloys. J Appl Phys 102(11):113519-1–113519-5. doi:[10.1063/1.2821755](https://doi.org/10.1063/1.2821755)
25. Ma H, Shi LL, Xu J, Li Y, Ma E (2005) Discovering inch-diameter metallic glasses in three-dimensional composition space. Appl Phys Lett 87(18):181915-1–181915-3. doi:[10.1063/1.2126794](https://doi.org/10.1063/1.2126794)
26. Zhang W, Zhang QS, Qin CL, Inoue A (2008) Synthesis and properties of Cu-Zr-Ag-Al glassy alloys with high glass-forming ability. Mater Sci Eng B Adv Funct Solid State Mater 148 (1–3):92–96. doi:[10.1016/j.mseb.2007.09.064](https://doi.org/10.1016/j.mseb.2007.09.064)
27. Guo FQ, Poon SJ, Shiflet GJ (2003) Metallic glass ingots based on yttrium. Appl Phys Lett 83 (13):2575–2577. doi:[10.1063/1.1614420](https://doi.org/10.1063/1.1614420)
28. Li R, Pang SJ, Ma CL, Zhang T (2007) Influence of similar atom substitution on glass formation in (La-Ce)-Al-Co bulk metallic glasses. Acta Mater 55(11):3719–3726. doi:[10.1016/j.actamat.2007.02.026](https://doi.org/10.1016/j.actamat.2007.02.026)
29. Jiang QK, Zhang GQ, Chen LY, Wu JZ, Zhang HG, Jiang JZ (2006) Glass formability, thermal stability and mechanical properties of La-based bulk metallic glasses. J Alloys Compd 424 (1–2):183–186. doi:[10.1016/j.jallcom.2006.07.109](https://doi.org/10.1016/j.jallcom.2006.07.109)
30. Xing LQ, Ochin P (1997) Bulk glass formation in the Zr-Ti-Al-Cu-Ni system. J Mater Sci Lett 16(15):1277–1280. doi:[10.1023/A:1018574808365](https://doi.org/10.1023/A:1018574808365)
31. Schroers J, Johnson WL (2004) Highly processable bulk metallic glass-forming alloys in the Pt-Co-Ni-Cu-P system. Appl Phys Lett 84(18):3666–3668. doi:[10.1063/1.1738945](https://doi.org/10.1063/1.1738945)
32. Amiya K, Inoue A (2008) Fe-(Cr, Mo)-(C, B)-Tm bulk metallic glasses with high strength and high glass-forming ability. Rev Adv Mater Sci 18(1):27–29
33. Park ES, Kim DH (2004) Formation of Ca-Mg-Zn bulk glassy alloy by casting into cone-shaped copper mold. J Mater Res 19(3):685–688. doi:[10.1557/jmr.2004.19.3.685](https://doi.org/10.1557/jmr.2004.19.3.685)
34. Busch R, Masuhr A, Bakke E, Johnson WL (1998) Bulk metallic glass formation from strong liquids. Mech Alloyed Metastab Nanocryst Mater Part 2 269(2):547–552
35. Zeng YQ, Nishiyama N, Yamamoto T, Inoue A (2009) Ni-rich bulk metallic glasses with high glass-forming ability and good metallic properties. Mater Trans 50(10):2441–2445. doi:[10.2320/matertrans.MRA2008453](https://doi.org/10.2320/matertrans.MRA2008453)
36. Chen N, Yang HA, Caron A, Chen PC, Lin YC, Louguine-Luzgin DV, Yao KF, Esashi M, Inoue A (2011) Glass-forming ability and thermoplastic formability of a Pd₄₀Ni₄₀Si₄P₁₆ glassy alloy. J Mater Sci 46(7):2091–2096. doi:[10.1007/s10853-010-5043-x](https://doi.org/10.1007/s10853-010-5043-x)
37. Inoue A, Zhang QS, Zhang W, Yubuta K, Son KS, Wang XM (2009) Formation, thermal stability and mechanical properties of bulk glassy alloys with a diameter of 20 mm in Zr-(Ti, Nb)-Al-Ni-Cu system. Mater Trans 50(2):388–394. doi:[10.2320/matertrans.MER2008179](https://doi.org/10.2320/matertrans.MER2008179)
38. Guo FQ, Wang HJ, Poon SJ, Shiflet GJ (2005) Ductile titanium-based glassy alloy ingots. Appl Phys Lett 86(9):091907-1–091907-3. doi:[10.1063/1.1872214](https://doi.org/10.1063/1.1872214)
39. Ponnambalam V, Poon SJ, Shiflet GJ (2004) Fe-based bulk metallic glasses with diameter thickness larger than one centimeter. J Mater Res 19(5):1320–1323. doi:[10.1557/jmr.2004.0176](https://doi.org/10.1557/jmr.2004.0176)
40. Wang D, Li Y, Sun BB, Sui ML, Lu K, Ma E (2004) Bulk metallic glass formation in the binary Cu-Zr system. Appl Phys Lett 84(20): 4029–4031. doi:[10.1063/1.1751219](https://doi.org/10.1063/1.1751219)
41. Xu DH, Lohwongwatana B, Duan G, Johnson WL, Garland C (2004) Bulk metallic glass formation in binary Cu-rich alloy series - Cu100-xZrx (x=34, 36 38.2, 40 at.%) and mechanical

- properties of bulk Cu₆₄Zr₃₆ glass. *Acta Mater* 52(9):2621–2624. doi:10.1016/j.actamat.2004.02.009
42. Xia L, Li WH, Fang SS, Wei BC, Dong YD (2006) Binary Ni-Nb bulk metallic glasses. *J Appl Phys* 99(2). doi:10.1063/1.2158130
43. Inoue A (2000) Stabilization of metallic supercooled liquid and bulk amorphous alloys. *Acta Mater* 48(1):279–306. doi:10.1016/S1359-6454(99)00300-6
44. Zhang Y, Zhou YJ, Lin JP, Chen GL, Liaw PK (2008) Solid-solution phase formation rules for multi-component alloys. *Adv Eng Mater* 10(6):534–538. doi:10.1002/adem.200700240
45. Yang X, Zhang Y (2012) Prediction of high-entropy stabilized solid-solution in multi-component alloys. *Mater Chem Phys* 132(2–3):233–238. doi:10.1016/j.matchemphys.2011.11.021
46. Saunders N, Miodownik AP, Dinsdale AT (1988) Metastable lattice stabilities for the elements. *Calphad Comput Coupling Phase Diagrams Thermochem* 12(4):351–374. doi:10.1016/0364-5916(88)90038-7
47. de Boer FR, Boom R, Mattens WCM, Miedema AR, Nissen AK (1988) Cohesion in metals: transition metal alloys, vol 1, Cohesion and structure. North Holland Physics Publishing, a division of Elsevier Science Publishers B.V, The Netherlands
48. Hafner J (1980) Theory of the formation of metallic glasses. *Phys Rev B* 21(2):406–426. doi:10.1103/PhysRevB.21.406
49. Masumoto T (1982) Present status and prospects of rapidly quenched metals. In: Masumoto T, Suzuki K (eds) The 4th international conference on rapidly quenched metals. The Japan Institute of Metals, Sendai, pp 1–5
50. Takeuchi A, Murty BS, Hasegawa M, Ranganathan S, Inoue A (2007) Analysis of bulk metallic glass formation using a tetrahedron composition diagram that consists of constituent classes based on blocks of elements in the periodic table. *Mater Trans* 48(6):1304–1312. doi:10.2320/matertrans.MF200604
51. Takeuchi A, Amiya K, Wada T, Yubuta K, Zhang W, Makino A (2014) Alloy designs of high-entropy crystalline and bulk glassy alloys by evaluating mixing enthalpy and delta parameter for quinary to decimal equi-atomic alloys. *Mater Trans* 55(1):165–170. doi:10.2320/matertrans.M2013352
52. Inoue A, Zhang T, Masumoto T (1990) Production of amorphous cylinder and sheet of La₅₅Al₂₅Ni₂₀ alloy by a metallic mold casting method. *Mater Trans JIM* 31(5):425–428. doi:10.2320/matertrans1989.31.425
53. Inoue A, Shinohara Y, Gook JS (1995) Thermal and magnetic properties of bulk Fe-based glassy alloys prepared by copper mold casting. *Mater Trans JIM* 36(12):1427–1433. doi:10.2320/matertrans1989.36.1427
54. Inoue A, Zhang W, Zhang T, Kurosaka K (2001) High-strength Cu-based bulk glassy alloys in Cu-Zr-Ti and Cu-Hf-Ti ternary systems. *Acta Mater* 49(14):2645–2652. doi:10.1016/S1359-6454(01)00181-1
55. Inoue A, Zhang T, Masumoto T (1989) Al-La-Ni amorphous-alloys with a wide supercooled liquid region. *Mater Trans JIM* 30(12):965–972. doi:10.2320/matertrans1989.30.965
56. Inoue A, Kohinata M, Tsai AP, Masumoto T (1989) Mg-Ni-La amorphous-alloys with a wide supercooled liquid region. *Mater Trans JIM* 30(5):378–381. doi:10.2320/matertrans1989.30.378
57. Inoue A, Kato A, Zhang T, Kim SG, Masumoto T (1991) Mg-Cu-Y amorphous-alloys with high mechanical strengths produced by a metallic mold casting method. *Mater Trans JIM* 32(7):609–616. doi:10.2320/matertrans1989.32.609
58. Kui HW, Greer AL, Turnbull D (1984) Formation of bulk metallic-glass by fluxing. *Appl Phys Lett* 45(6):615–616. doi:10.1063/1.95330
59. Nishiyama N, Amiya K, Inoue A (2004) Bulk metallic glasses for industrial products. *Mater Trans* 45(4):1245–1250. Elsevier Ltd. (Published online) doi:10.2320/matertrans.45.1245
60. Suryanarayana C, Inoue A (2011) Bulk metallic glasses. CRC Press, Boca Raton

61. Takeuchi A, Chen N, Wada T, Zhang W, Yokoyama Y, Inoue A, Yeh JW (2011) Alloy design for high-entropy bulk glassy alloys. In: IUMRS international conference in Asia (Procedia Engineering). Procedia Engineering, pp 226–235. doi:[10.1016/j.proeng.2012.03.035](https://doi.org/10.1016/j.proeng.2012.03.035)
62. Takeuchi A, Wang JQ, Chen N, Zhang W, Yokoyama Y, Yubuta K, Zhu SL (2013) $\text{Al}_{0.5}\text{TiZrPdCuNi}$ high-entropy (H-E) alloy developed through $\text{Ti}_{20}\text{Zr}_{20}\text{Pd}_{20}\text{Cu}_{20}\text{Ni}_{20}$ H-E glassy alloy comprising inter-transition metals. Mater Trans 54(5):776–782. doi:[10.2320/matertrans.M2012370](https://doi.org/10.2320/matertrans.M2012370)
63. Understanding Solids (2004) The science of materials. Wiley, West Sussex
64. Guo S, Ng C, Lu J, Liu CT (2011) Effect of valence electron concentration on stability of fcc or bcc phase in high entropy alloys. J Appl Phys 109(10)103505-1–103505-5. doi:[10.1063/1.3587228](https://doi.org/10.1063/1.3587228)
65. Wang WH (2014) High-entropy metallic glasses. JOM. 66(10):2067–2077: doi:[10.1007/s11837-014-1002-3](https://doi.org/10.1007/s11837-014-1002-3)
66. Chen HS (1980) Glassy metals. Rep Prog Phys 43(4):353–432. doi:[10.1088/0034-4885/43/4/001](https://doi.org/10.1088/0034-4885/43/4/001)
67. Takeuchi A, Amiya K, Wada T, Yubuta K, Zhang W, Makino A (2013) Entropies in alloy design for high-entropy and bulk glassy alloys. Entropy 15(9):3810–3821. doi:[10.3390/e15093810](https://doi.org/10.3390/e15093810)
68. Gao MC, Widom M (2015) On the structural, electronic, thermodynamic, and elastic properties of high-entropy metallic glasses: a first-principles study (Unpublished work)
69. Zhang Y, Zuo TT, Cheng YQ, Liaw PK (2013) High-entropy alloys with high saturation magnetization, electrical resistivity, and malleability. Sci Rep 3:1455-1–1455-7. doi:[10.1038/srep01455](https://doi.org/10.1038/srep01455)

Chapter 14

High-Entropy Coatings

Jien-Wei Yeh, Su-Jien Lin, Ming-Hung Tsai, and Shou-Yi Chang

Abstract High-entropy alloys (HEAs) can be deposited on substrates as thick or thin alloy films for protection against wear, corrosion, and heat, and for function enhancement and decorative purposes. In addition, various HEA nitride coatings based on HEAs can be easily deposited using reactive coating technology by allowing the atoms or ions from the targets to react with N₂-containing Ar flow during deposition. Similarly, HEA carbides, oxides, and carbonitrides could be deposited under CH₄-containing, O₂-containing, and CH₄ + N₂-containing Ar flow, respectively. Such HEA ceramic coatings also show the four core effects observed in HEAs: high-entropy, sluggish diffusion, severe lattice distortion, and cocktail effects. The structure is, in general, much simpler than expected. Amorphous, nanocrystalline, and nanocomposite films are often obtained. The properties of HEA coatings or HEA ceramic coatings can be outstanding, and these coatings have great potential for various applications if proper compositions and deposition parameters are used.

Keywords High-entropy alloy coating • High-entropy alloy nitride coating • High-entropy alloy carbide coating • Amorphous coating • Nanocomposite coating

14.1 Introduction

Surface coating is an effective method to improve the performance, durability, and decorativeness of materials. For cutting tools, a protective surface layer with superior mechanical behavior and thermal stability can maintain the functionality of tools even under severe conditions and prolong lifetime. Protective coatings for

J.-W. Yeh (✉) • S.-J. Lin • S.-Y. Chang

Department of Materials Science and Engineering, National Tsing Hua University,
Hsinchu, Taiwan 30013, Republic of China

e-mail: jwyeh@mx.nthu.edu.tw; sjlin@mx.nthu.edu.tw; changs@mx.nthu.edu.tw

M.-H. Tsai

Department of Materials Science and Engineering, National Chung Hsing University,
Taichung, Taiwan 40227, Republic of China

e-mail: mhtsai@nchhu.edu.tw

tools and dies that have high hardness, low friction coefficient, good adhesion to the substrate, and high oxidation and wear resistance have been pursued in the last decades. Similarly, superior chemical resistance is a requirement for coatings used in corrosive environments. Modern requirements for surface coatings also include better diffusion barrier, biomedical, antibacterial, EMI shielding, anti-fingerprint, nonstick, and hydrophilic/hydrophobic properties.

Since the 1980s, transition metal nitrides have been commonly used to provide wear protection to component surfaces in many industrial applications [1]. Among binary nitride systems, titanium nitride (TiN) has been the most widely used material for machining and cutting tools because of its excellent mechanical properties and corrosion resistance. In the 1990s, titanium aluminum nitride ($Ti_{1-x}Al_xN$) hard coatings were also developed to improve the hardness and stability of TiN films for higher-speed machining [2]. It has been reported that aluminum addition in TiN films increases its oxidation resistance from 500 to 800 °C, which is attributed to a protective aluminum-rich oxide layer formed on the film surface. Adding elements such as chromium or zirconium to form a ternary system ($Ti_{1-x}Cr_xN$ or $Ti_{1-x}Zr_xN$) was also found to enhance its performance and capability [3]. It has been demonstrated that alloying appropriate elements into a binary nitride coating is an effective way to modify the coating properties. However, most studies on coatings are still limited to ternary or quaternary systems. In 2004 and 2005, Chen et al. deposited two multi-element nitride films with more than five elements (not including nitrogen) from HEA targets for the first time [4, 5]. Subsequently, more and more studies on HEA and HEA-based coatings have been performed and reported because of their high potential for achieving outstanding properties.

Thin-film-coating processes mainly include electroless plating, electroplating, physical vapor deposition (PVD), and chemical vapor deposition (CVD). However, because of the difference in the reduction potentials among different metal ions, it is difficult to produce coatings with homogenous HEA compositions using electroless plating or electroplating. Similarly, CVD using different precursors simultaneously is also difficult for HEA and HEA-based coatings. In addition, achieving simultaneous evaporation of different elements for HEA coatings by the evaporation method (a kind of PVD) is also not easy because of their different melting and boiling temperatures and the need for separate crucibles for different elements. On the contrary, PVD techniques including cathode arc deposition, ion plating, and magnetron sputtering are feasible for fabricating HEA and HEA-based coatings with desired properties, because different elements in the targets can be sputtered simultaneously through application of high-energy processes such as arc and ion bombardments until the steady state is obtained. Thus, such PVD methods can easily achieve the desired compositions.

By using suitable reaction gases, HEA ceramic coatings can be obtained. HEA nitride (HEAN) coating can be deposited by allowing the atoms or ions from a single HEA target (or a segmented target fabricated by combining several pieces with different compositions) to react with N_2 -containing Ar during deposition. Similarly, HEA carbides (HEACs) can be deposited in the presence of CH_4 -containing Ar or co-deposited with a graphite target, HEA oxides (HEAOs) in the

presence of O₂-containing Ar, and HEA carbonitrides (HEACNs) in the presence of CH₄ + N₂-containing Ar.

On the other hand, thermal spray methods including flame spraying, plasma spraying, detonation spraying, wire arc spraying, and high velocity oxy-fuel coating spraying (HVOF) are used to deposit thick layers ranging from 20 μm to several millimeters. Cladding methods using laser, electron beam, plasma, or arc welding can be used to produce thick surface layers for surface modifications. As a result, most studies on coatings have been conducted on HEA coatings deposited by using the sputtering, thermal spray, arc, and cladding methods and on HEA-based coatings such as HEANs and HEACs deposited using a sputtering method. This chapter will mainly review the research progress in the area of surface coatings based on the HEA concept. Fabrication routes of traditional liquid solidification and mechanical alloying for bulk HEAs, and laser cladding and PVD techniques for HEAs and HEA-based surface coating, are reviewed in Chap. 5 of this book.

14.2 HEA Coatings

HEA coatings have been fabricated by different techniques including thermal spraying, gas tungsten arc welding (GTAW), laser cladding, and sputtering. These coatings have been tested for applications such as protective surface coatings and diffusion barriers. Because HEA coatings have a small thickness and are formed via rapid solidification such as thermal spraying and laser cladding, or via vapor deposition such as sputtering, they would suffer a high cooling rate which increases the nucleation rate to yield small grain size and tends to inhibit phase separation to cause a supersaturated state. However, this cooling rate effect also occurs in conventional alloy coatings. Despite this, it should be noted that sluggish diffusion effect of HEAs could strengthen the effects from high cooling rate because multicomponents are involved during deposition. That means the efficiency of microstructure refining and second-phase inhibition is much stronger than conventional alloy coatings under similar cooling rate. Furthermore, sluggish diffusion of HEA coatings generally reduces the coarsening rate of grains and phases and retards the crystallization of amorphous structure at high temperatures. Besides these, high entropy and severe lattice distortion effects also affect microstructure and properties of HEA coatings in different aspects, which could bring advantages for special applications.

14.2.1 Thermal-Sprayed Coatings

Protective surface coatings can significantly improve the wear, erosion, corrosion, and oxidation resistance of a component. The first work done in this regard is thermally sprayed AlCrFeMo_{0.5}NiSiTi and AlCoCrFeMo_{0.5}NiSiTi alloys for

producing a protective layer with a thickness of around 200 μm on a substrate [1]. The powders for the spray process were prepared by crushing arc-melted alloy ingots and then ball milling the crushed particles into finer powders. Both coatings are composed of a primary BCC phase, but there are also other unknown phases present. The coatings exhibit a lamellar structure typical of thermal-sprayed coatings. The hardness of the as-sprayed AlCrFeMo_{0.5}NiSiTi and AlCoCrFe-Mo_{0.5}NiSiTi coatings is around 525 and 485 HV, respectively, because of the supersaturated concentration of solutes in the matrix. Both coatings harden significantly at high temperature because of the precipitation of the Cr-silicide phase. For example, the hardness of both coatings is around 925 HV after heat treatment at 800 °C for 1 h. Both coatings exhibit superior abrasion wear resistance, as shown in Fig. 14.1. Despite the apparently lower hardness of the as-sprayed coatings, they show wear resistance similar to SUJ2 bearing steel (AISI 52100). Annealed coatings, owing to their higher hardness, are evidently more wear resistant than SUJ2 and SKD61 tool steel (AISI H13). For example, the wear resistance (wear distance per unit volume loss) of AlCrFeMo_{0.5}NiSiTi (18.8 m/mm³) measured using the pin-on-belt method is nearly twice that of SKD61 (10.2 m/mm³). The oxidation resistance of these coatings is also good. It is mainly attributed to the formation of a dense aluminum oxide layer on the top surface. The weight gains of AlCrFeMo_{0.5}NiSiTi and AlCoCrFeMo_{0.5}NiSiTi coatings maintained at 1100 °C for 150 h are about 8.2 and 9.2 mg/cm², respectively, and are comparable with that of commercial oxidation-resistant NiCrAlY alloys. The results demonstrate that these coatings hold great potential for components that require both oxidation resistance and wear resistance.

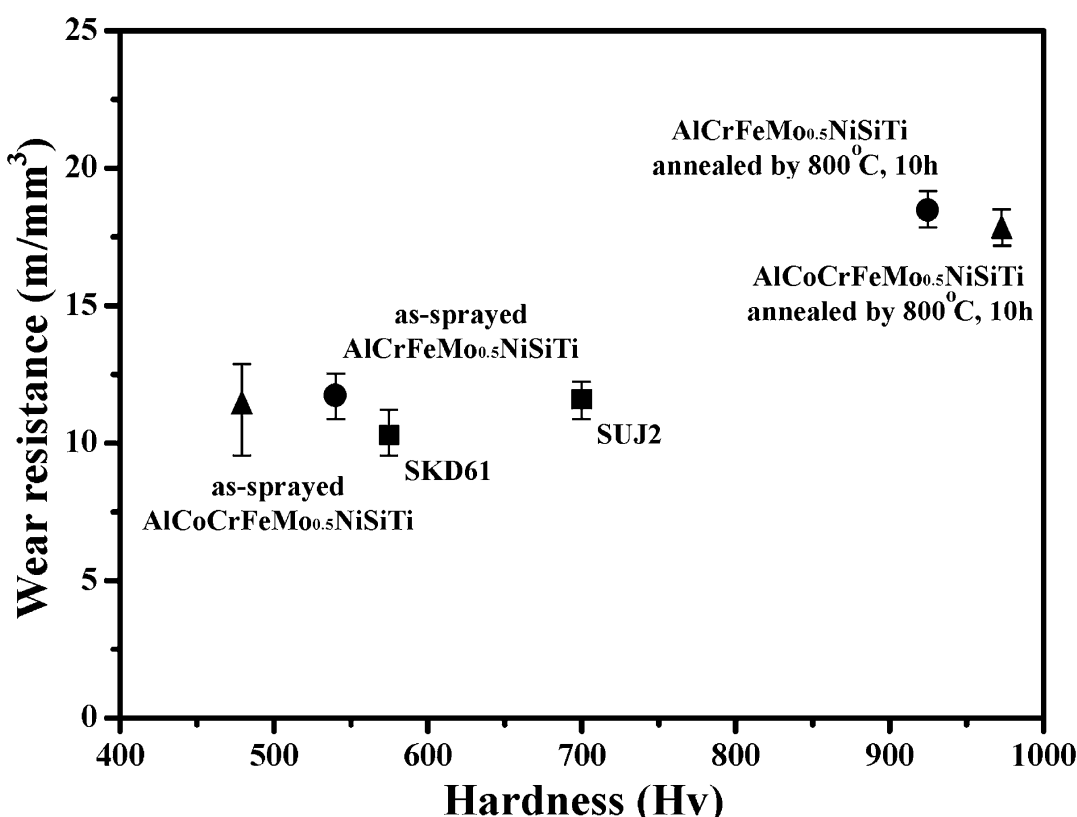


Fig. 14.1 Wear resistance and hardness of SKD61, SUJ2, and as-sprayed and annealed AlCrFeMo_{0.5}NiSiTi and AlCoCrFeMo_{0.5}NiSiTi coatings [1]

14.2.2 Claddings

Chen et al. [2] prepared Al-Co-Cr-Mo-Ni layer claddings via the GTAW technique (also known as tungsten inert gas (TIG) welding). The iron source is not from mixed elemental powder, but from the low carbon steel substrate. Therefore, the iron content changes in each cladding layer. The single layer coating (directly on top of the substrate) contains about 50 at.% Fe. The double layer coating (in which a second layer was cladded on top of the first layer using the same powder source) contains about 15.3 at.% Fe, leading to a near-equimolar senary HEA coating. Both coatings are composed of a soft Fe-rich BCC phase and a hard Mo-rich tetragonal phase. Hardness of the single layer coating is about 500 HV, and that of the double layer coating is about 800 HV. This is owing to the decreased amount of Fe in the latter that leads to a reduced amount of the soft Fe-rich BCC phase. The wear resistance of the double layer coating is more than three times better than the steel substrate.

Lin et al. studied AlCoCrNiW and AlCoCrNiSi HEA coatings that were also prepared via GTAW [3]. The AlCoCrNiW coating is composed of a W-based phase, a NiAl-based phase, and a Cr-Fe-C carbide phase. The AlCoCrNiSi coating is composed mainly of a BCC phase. Both coatings have a hardness of around 700 HV. However, the former shows significantly higher resistance than the latter. The authors explain that the higher wear resistance is due to the stronger mechanical interlocking between the complex phases and microstructure of the AlCoCrNiW clad layer.

Zhang et al. [4] fabricated AlCoCrFe₆NiSiTi coatings about 1.2 µm in thickness via laser cladding. The coating is composed of equiaxed polygonal grains surrounded by interdendritic regions. The compositions of the two regions are very similar, except that the interdendritic region is slightly rich in Ti and Si. Therefore, the XRD pattern reveals only one set of peaks corresponding to the BCC structure. The hardness of this coating is about 780 HV. In a later study, the AlCoCrFe₆NiSiTi coatings were treated at various temperatures for 5 h. Annealing at 500, 750, and 1000 °C led to the coarsening of the interdendritic region, while the Si and Ti contents in the interdendritic region evidently increased. This led to the formation of a SiTi-type phase at 1000 °C. At the highest annealing temperature (1150 °C), the (Si,Ti)-rich phase coarsened significantly such that it formed large, isolated islands embedded in the Fe-rich matrix. The formation of a SiTi₂-type phase was also observed in the XRD pattern at this annealing temperature. The hardness of the coating remains unchanged after annealing at 500 and 750 °C. However, softening was observed after annealing at 1000 and 1150 °C. The hardness decreases to 700 and 650 HV, respectively. These values indicate that the coating has very good resistance to softening.

Huang et al. tested the thermal stability and oxidation resistance of 2-mm-thick AlCrSiTiV HEA coating on Ti–6Al–4 V substrate prepared via laser cladding [5]. The as-cladded coating is composed of (Ti,V)₅Si₃ islands embedded in a BCC matrix. The coating was then annealed at various temperatures for 3 days to obtain

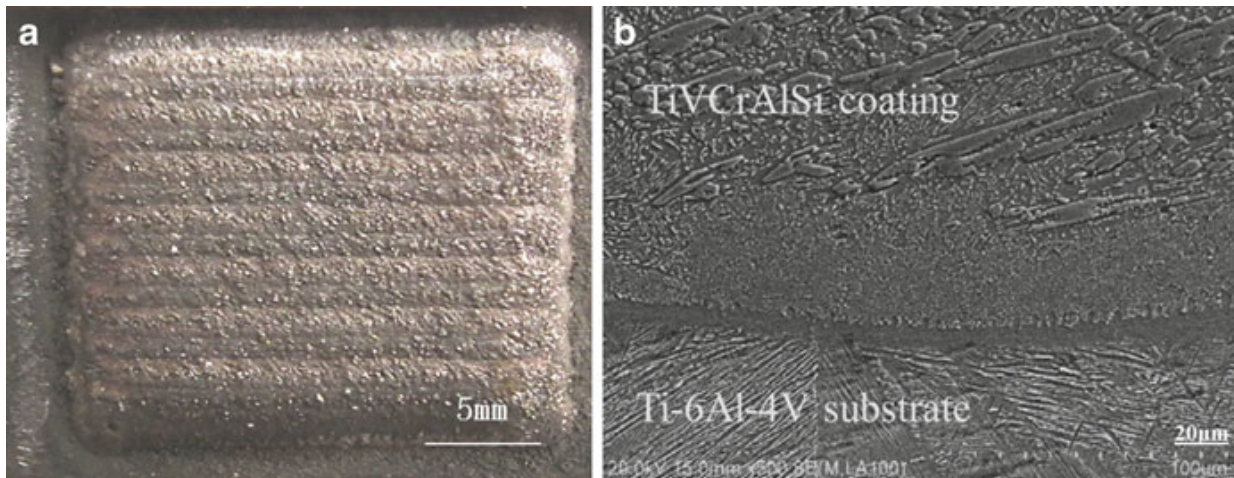


Fig. 14.2 (a) Surface morphology of the laser-clad AlCrSiTiV coating. (b) SEM micrograph of the interface between the AlCrSiTiV coating and the Ti–6Al–4 V alloy [6]

the near-equilibrium state at each temperature. It was found that the samples quenched at 900 °C or above are composed of a BCC solid solution and (Ti, V)₅Si₃, while samples quenched at $T \leq 800$ °C are composed of (Ti,V)₅Si₃, Al₈(V,Cr)₅, and a BCC solid solution. These results agree well with their calculations using the CALPHAD method. Metallographic observations and EDS analysis together revealed that the Al₈(V,Cr)₅ phase observed at 800 °C and below is located in the annealed matrix, probably because of the decomposition of the BCC phase. The weight gain after exposure to 800 °C for 50 h is about 4.2 mg/cm², which is significantly better than that of the substrate (~19.3 mg/cm²). This result shows that the coating can effectively protect the Ti–6Al–4 V alloy. The oxide scale of the coating is thin and adherent and consists of SiO₂, Cr₂O₃, TiO₂, Al₂O₃, and a small amount of V₂O₅ [5]. The dry sliding wear tests also show that the wear resistance of Ti–6Al–4 V is improved by laser cladding with AlCrSiTiV [6]. The appearance and microstructure of the cladding layer are shown in Fig. 14.2. The enhancement in the wear resistance is explained by the presence of the hard silicide phase dispersed in a relatively ductile BCC matrix, which allows sliding wear to occur in a mild oxidative regime for a wide range of testing conditions. In another report, an FCC-structured CoCrCuFeNi HEA was laser cladded on to a steel substrate [7]. It was found that both the phase constitution and the dendritic morphology of the alloy coating showed an impressive stability up to 0.7 T_m (750 °C), and a high level of hardness could be retained even after annealing at 1000 °C for 5 h.

14.2.3 Diffusion Barriers

The other important application of HEA coatings is diffusion barriers. Interlayers are very important in the interconnect structures of integrated circuits. They are also called “diffusion barriers” and are layers such as those between Cu or Al wires and dielectrics or between metal pads and solders. Robust interlayers with high thermal

stability, low electrical resistivity, and good adhesion to adjoining layers are in high demand to inhibit the rapid interdiffusion of adjacent materials (e.g., Cu and Si) and/or the formation of detrimental compounds (e.g., Cu silicides) that will lead to the early failure of microelectronic devices [8]. Refractory transition metals, such as Ti and Ta [8], and the nitrides of unitary transition metals including TiN and TaN [9], were the first materials used as diffusion barriers in interconnects, but have the drawback of polycrystalline/columnar structures with boundaries that act as fast diffusion paths. In recent years, thinner and more effective barriers have been developed, which typically consist of (1) ternary components with an amorphous structure to diminish diffusion paths, such as Ru-Ti-N and Ru-Ta-N [10–12], and (2) layered structures with interface mismatches to elongate diffusion paths, such as Ru/TaN and Ru/TaCN [13–15]. Nevertheless, more robust and ultrathin (<3 nm) barrier layers with a higher diffusion resistance are greatly demanded in the manufacturing of the next generation of integrated circuits below 20 nm.

In recent studies, HEA coatings such as AlMoNbSiTaTiVZr, NbSiTaTiZr, and AlCrRuTaTiZr alloys with a simple solid-solution amorphous structure, high thermal stability, and low electrical resistivity below $250 \mu\Omega \cdot \text{cm}$ have been developed as effective diffusion barriers [16–18]. They were deposited using a sputtering method from a single alloy target. The quinary NbSiTaTiZr with a thickness of 20 nm prevents the interdiffusion of Cu and Si at a temperature of 800°C for 30 min [17], and the senary AlCrRuTaTiZr of only 5 nm thickness shows the same extreme resistance to Cu/Si interdiffusion [18]. The senary AlCrRuTaTiZr of 500 nm thickness, which is used as a diffusion barrier and an adhesion layer, also prevents Cu pads on printed circuit boards from dissolution into the molten solders (Sn-Ag-Cu) at 250°C for 60 min. Cu plates with a thickness of 1 mm completely dissolve under these conditions. The high-endurance temperatures of HEA coatings against the interdiffusion of Cu and Si, and their dissolution in molten solders at a small film thickness, suggest their high potential as promising diffusion barriers for practical applications in microelectronic devices.

In 2014, Chang et al. elucidated a mechanism for the high resistance of HEA coatings to interdiffusion (i.e., the highly suppressed interdiffusion kinetics) from structural and thermodynamic perspectives [19]. They examined the diffusion resistance of thin solid-solution alloy films (a thickness of about 7 nm) systematically with different metallic elements, including unitary Ti, binary TiTa, ternary TiTaCr, quaternary TiTaCrZr, quinary TiTaCrZrAl, and senary TiTaCrZrAlRu. While a Cu/Si structure (without a barrier) failed because of the severe interdiffusion of Cu and Si at about 400°C , the failure temperature of the alloy barriers against interdiffusion markedly increased from 550 to 900°C when more metallic elements were incorporated, as presented in Fig. 14.3. Through unitary Ti, the diffusivity of Cu atoms reached a level as high as $4.1 \times 10^{-20} \text{ m}^2/\text{s}$ at 600°C , whereas through senary TiTaCrZrAlRu, it was only $1.6 \times 10^{-21} \text{ m}^2/\text{s}$ at 700°C and $8.0 \times 10^{-20} \text{ m}^2/\text{s}$ at 900°C . The activation energy of Cu diffusion through the alloy barriers was experimentally determined and increased with the number of added metallic elements, from 110 kJ/mol (with unitary Ti) to 163 kJ/mol (with senary TiTaCrZrAlRu), indicating the obvious suppression of interdiffusion by the

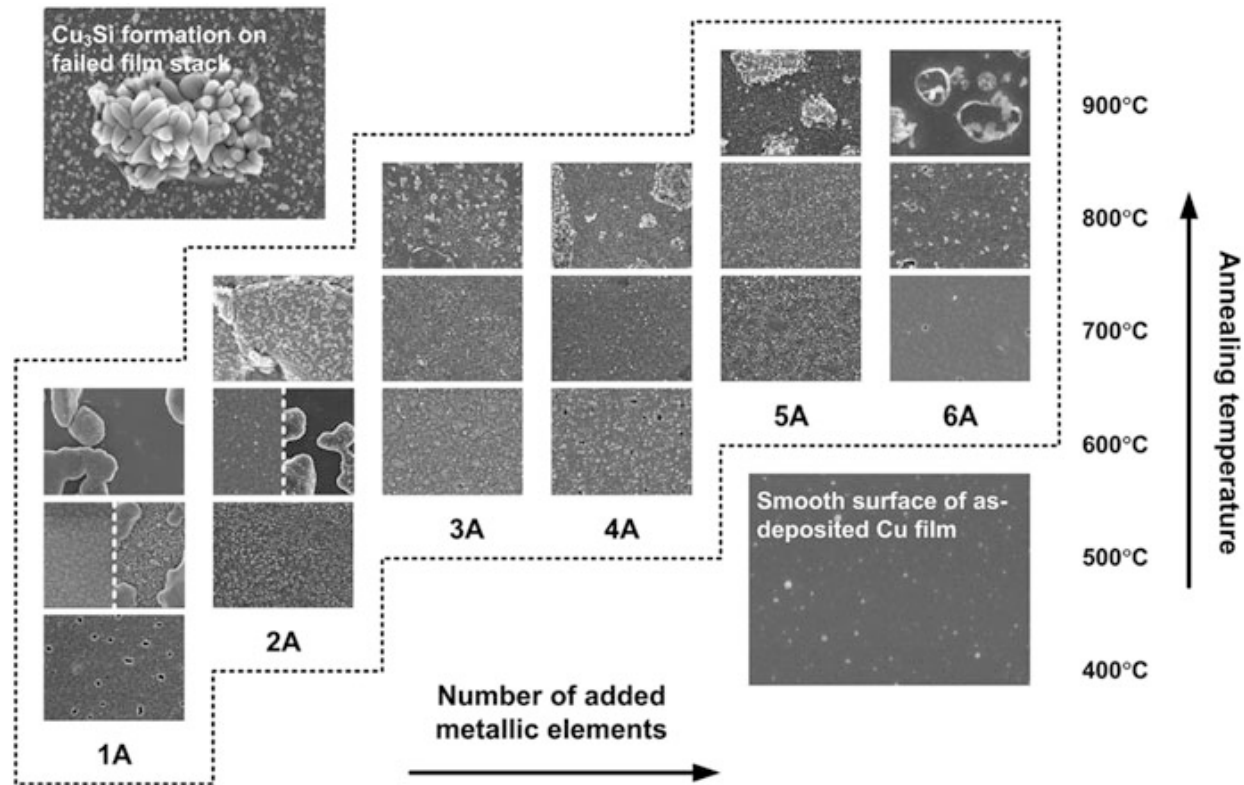


Fig. 14.3 Surface morphologies of thermally annealed Si/BarriernA/Cu film stacks in a tube furnace at different temperatures for 30 min in a N₂/H₂ reducing atmosphere (total gas flow rate of 500 sccm, H₂ flow ratio of 5 %; nA: the alloy with n elements). Dotted lines in the film indicate stacks with Barrier_{1A} at 500 °C and Barrier_{2A} at 600 °C: (left) not failed, (right) Cu film agglomeration into islands; insets: (top left) as-deposited with a typical Cu film surface, (bottom right) failed with a typical silicide formation [19]

multicomponent barriers. Chang's mechanistic analyses [19] suggest that structurally severe lattice distortions caused by different atom sizes will influence the site of vacancy formation and the direction of atom movement as well as elongate the diffusion paths. Compared to the normal (regular, isotropic) lattice structure of unitary Ti without any distortions, the lattice strain energy of senary TiTaCrZrAlRu will theoretically increase to 14.6 kJ/mol. Thermodynamically, a strengthened and anisotropic cohesion is expected to inhibit bond breaking for vacancy formation and atomic diffusion, as well as change the direction of atomic diffusion. Relative to the low cohesion energy of unitary Ti, the cohesive energy of senary TiTaCrZrAlRu will theoretically increase to 38.1 kJ/mol.

In addition, the increased packing density of atoms caused by different atom sizes, i.e., the shrinkage in free volume, is believed to diminish vacancy formation/concentration. Compared to unitary Ti with an atom-size ratio of 1, the packing density of senary TiTaCrZrAlRu will theoretically increase to a ratio of around 1.1. Combining the contributions of lattice distortion strain energy, the increase in cohesive energy, and the multiplied packing density, the theoretical (total) increase in the activation energy of Cu diffusion in senary TiTaCrZrAlRu alloy (55 kJ/mol), which is nearly equal to the measured increase (from 110 to 163 kJ/mol, i.e., 53 kJ/mol), is believed to suppress the formation of vacancies and hinder the movements of atoms, thus suppressing interdiffusion kinetics through multicomponent HEA barriers.

14.3 HEAN Coatings

High-entropy alloy nitrides (HEANs) have drawn great attention in the past decade (2004–2014). More than 30 different nitride systems have been prepared and studied, mainly by reactive DC/RF sputtering techniques. The target applications of these materials include hard protective coatings and diffusion barriers. Although nitrogen is involved to form HEANs, it is not proper to regard nitrogen as a component except the coating is still in the metallic state. A HEAN is in fact a mixture of constituent binary nitrides. Because most strong binary nitrides such as TiN, CrN, TaN, HfN, ZrN, and NbN have NaCl-type FCC structure with similar lattice constant, their mixture tends to form the solid solution of binary nitrides with the NaCl-type FCC structure mainly under high-entropy effect since overall nitrogen-metal bonding is almost the same before and after mixing. For example, the above six binary nitrides could form $(\text{Ti,Cr,Ta,Hf,Zr,Nb})_{50}\text{N}_{50}$ HEANs with NaCl-type FCC structure in which metal elements occupy Na site and nitrogen does Cl site. Besides high-entropy effect, lattice distortion and sluggish diffusion effects can also affect microstructure and properties in different aspects. As a result, proper composition design by utilizing the advantages of these effects could be helpful to obtain required properties.

14.3.1 Hard Coatings

The use of transition metal nitrides as a protective coating layer for cutting tools, dies, and molds began in the 1980s. Because of their high hardness, wear resistance, and good oxidation resistance, transition metal nitride coatings such as TiN, TiAlN, TiAlSiN, TiC, CrN, and TiCN can significantly enhance the lifetime of the parts. Because HEAs have many outstanding properties, it is anticipated that their nitride forms may also possess these advantages. Most of the reported HEANs are based on strong nitride-forming elements such as Al, Cr, Ti, Si, Ta, Zr, Hf, Nb, etc. Table 14.1 shows the structure, hardness, modulus, substrate bias, and oxidation resistance of published HEAN hard coatings under the process conditions that yield the highest hardness. It demonstrates that HEAN hard coatings with suitable composition and processing can have outstanding properties such as hardness larger than 40 GPa (minimum level for superhard coatings) and an excellent oxidation resistance, only forming 80 nm thick oxide layer after annealing at 900 °C for 2 h.

1. Phenomena relating to composition and process factors

The concentration of nitrogen in the coatings can be controlled by the nitrogen flow ratio (R_n) in the deposition gas. For HEANs based mostly on strong nitride-forming elements, an R_n of around 15 % is usually sufficient to fabricate $\text{M}_{50}\text{N}_{50}$ -type stoichiometric nitrides (M: metal, N: nitrogen, metal:nitrogen = 1:1) [20]. Higher R_n can lead to overstoichiometric nitrides, but the deviation from the 1:1 composition is usually small [20, 21]. Because many

Table 14.1 Various properties of reported HEAN films under the process conditions that yield the highest hardness

Composition	Structure	Hardness (GPa)	Modulus (GPa)	Substrate bias (V)	Oxidation condition and oxide thickness	Ref.
(Al _{0.5} CoCrCuFeNi) ₅₉ N ₄₁	Amorphous	10.4	146	-100	-	[30]
(AlCoCrCuFeMnNi) ₆₅ N ₃₅	Amorphous	11.8	-	-150	-	[30]
(AlCrNiSiTi) _{82.3} N _{17.7}	Amorphous	15.1	157	N/A	-	[31]
(AlCrMoTaTiZr) ₅₀ N ₅₀	FCC (NaCl)	40	400	N/A	-	[24]
(AlCrTaTiZr) ₅₀ N ₅₀	FCC (NaCl)	36	360	-150	-	[27]
(AlCrMoSiTi) ₆₇ N ₃₃	FCC (M ₂ N)	34.8	325	-100	-	[29]
(AlCrSiTiV) ₄₁ N ₅₉	FCC (NaCl)	31.2	300	N/A	-	[21]
(AlBCrSiTi) ₄₇ N ₅₃	Amorphous	25.1	260	N/A	-	[32]
(AlCrNbSiTiV) ₅₀ N ₅₀	FCC (NaCl)	42	350	-100	-	[28]
(AlCrMnMoNiZrB _{0.1})N _x	FCC (NaCl)	10.3	180	N/A	-	[33]
(AlCrTiVZr)N	FCC (NaCl)	15.2	204	-100	-	[34]
(AlCrTaTiZr) _{42.1} Si _{7.9} N ₅₀	Nanocomposite	34	343	N/A	330 nm, 1000 °C, 2 h	[25]
(AlMoNbSiTaTiVZr) ₅₀ N ₅₀	FCC (NaCl)	37	250	N/A	-	[23, 35]
(AlCrSiTiZr) _{77.8} N _{22.2}	Amorphous	20	228	-100	-	[36]
(Al _{29.1} Cr _{30.8} Nb _{11.2} Si _{7.7} Ti _{21.2}) ₅₀ N ₅₀	FCC (NaCl)	36.7	390	-150	80 nm, 900 °C, 2 h	[37]
(Al _{0.34} Cr _{0.22} Nb _{0.11} Si _{0.11} Ti _{0.22}) ₅₀ N ₅₀	FCC (NaCl)	36	350	-100	290 nm, 1000 °C, 2 h	[26, 38]
(HfNbTaTiZr) ₅₀ N ₅₀	FCC + compound	32.9	-	-100	-	[39]
(AlCrTaTiZr) ₅₂ N ₄₈	FCC (NaCl)	30	277	-100	-	[40]
(AlCrTaTiZr) ₄₈ C ₉ N ₄₃	Amorph. + FCC	35	279	-150	-	[41]
(AlCrMoNiTi) ₄₄ N ₅₆	FCC (NaCl)	15.5	205	N/A	-	[42]
(AlCrMoTiZr) ₃₄ N ₆₆	FCC (NaCl)	19.6	236	N/A	-	[42]
(Hf _{33.7} Nb ₁₅ Ti _{18.5} V _{5.64} Zr _{13.5}) _{86.3} N _{13.7}	FCC (NaCl)	58	-	-200	-	[43]
(HfCrTiVZr) ₅₅ N ₄₅	FCC (NaCl)	31.2	305	-100	280 nm, 600 °C, 2 h	[44]

binary stoichiometric nitrides have NaCl-type FCC structure (e.g., TaN, TiN, ZrN, CrN, NbN, HfN, VN), near-stoichiometric HEANs that are composed mainly of these elements also have a NaCl-type FCC structure. These HEANs can be considered as a solid solution of these binary nitrides. Huang et al. annealed (AlCrNbSiTiV)N at 1000 °C for 5 h and observed the annealed coating using TEM [22]. No evidence of phase separation was found. The highest hardness is usually achieved when R_n is around 40–50 %.

Another important process parameter is the applied substrate bias. Substrate bias hardly affects the composition of stoichiometric nitrides, but it significantly changes the microstructure and properties of the coatings. From Table 14.1, it can be seen that without substrate bias, the as-deposited coatings have scattered hardness values (between 11 and 40 GPa) depending on the bonding strength, density, grain size, and residual stress [20, 21, 23–26]. In general, HEAN shows a solution hardening effect because different-sized atoms occupying the Na sites cause lattice distortion. An amorphous structure is softer than a crystalline structure. Insufficient nitrogen content results in reduced number of strong Me-N bonds and lower hardness. Incorporation of weaker nitride formers such as Mn, Ni, and Cu decreases overall hardness. In addition, increased density, decreased grain size (but not down to below the critical grain size which begins to activate significant grain boundary sliding, and thus, softening in relation to the inverse Hall–Petch relation), and higher compressive residual stress are useful for improving hardness.

When deposited with suitable bias, crystalline HEANs based on strong nitride-forming elements in general have hardness values between 30 and 40 GPa, which are higher than the layers deposited without any bias. The guaranteed high hardness level obtained by suitable bias voltage is due to ion bombardment under the acceleration caused by bias voltage. Because of this ion bombardment, the structure of the coatings evolves from typical coarse columnar grains to a fine fibrous structure and further to a dense, featureless structure that eventually eliminates the voids between the columns and densifies the coatings. A more detailed explanation is that ion bombardment causes a stronger re-sputtering effect that suppresses the rate of grain growth and thus conversely increases the nucleation rate. Thus, further grain refinement and higher hardness are obtained. Moreover, the ion bombardment effect can introduce excess interstitial atoms into the lattice. This results in a compressive residual stress in the coatings and increases their hardness. In general, a bias voltage of –100 to –150 V can improve the hardness of the coatings best [27–29].

2. Deformation behavior of HEAN films

Mechanical properties play an important role in determining the mechanical performance of protective films. Thus, studies on the deformation behavior will provide a better understanding of their performance. The deformation behaviors of HEAN were examined recently by Chang and Lin et al. using (AlCrTaTiZr)N_{0.7}, (AlCrTaTiZr)N_{0.9}C_{0.2}, and (AlCrTaTiZr)N_{1.07}Si_{0.15} coatings with good mechanical properties [40, 41, 45, 46]. A localized mechanical deformation was typically introduced on the coatings by high-load indentations, and the

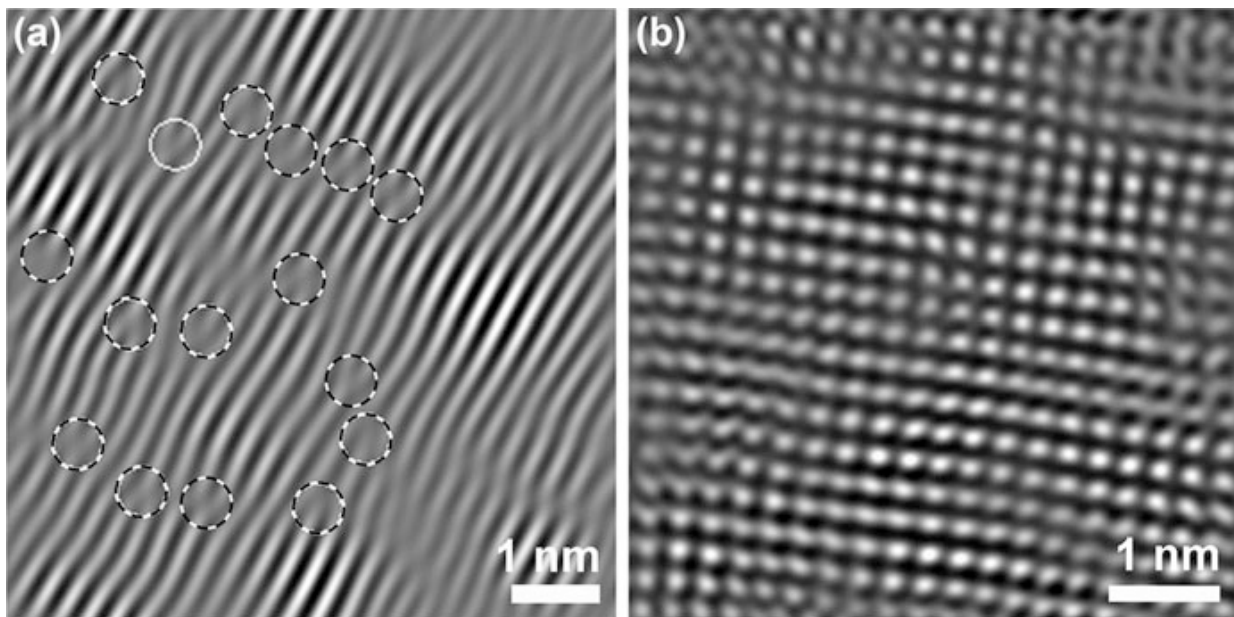


Fig. 14.4 TEM analyses of deformed $(\text{AlCrTaTiZr})\text{N}_{1.07}\text{Si}_{0.15}$ coating: (a) under an indent, *solid circles*: complete dislocations; *dashed circles*: partial dislocations; (b) around a crack [45]

deformed regions under the indent marks were cut by a focused ion beam (at an ultralow current) and observed in an electron microscope. In contrast to the formation and extension of shear bands during the deformation of metallic AlCrTaTiZr HEA coating with an amorphous structure, the deformation of crystalline HEAN nanocomposite coatings is mainly mediated by dislocation activities, with a large number of dislocation clusters observed [40]. However, rather than high-angle complete dislocations, which are the dominant deformation media of conventional crystalline materials, most stacking faults and extended partial dislocations are formed in deformed HEAN coatings, as shown in Fig. 14.4a, possibly because of their large lattice distortions and high strain energy [41, 45]. The stacking faults and partial dislocations are believed to distribute and slide along low-angle domain boundaries and to dominate the deformation of HEAN coatings. Under high indentation stresses, a greater number of waved lattices were formed compared to the original distorted lattices of nondeformed regions, revealing the further development of lattice distortions. However, it was found that in the regions where stress was released just adjacent to cracks, a near-perfectly ordered lattice structure without distortions, stacking faults, or dislocations was observed, as shown in Fig. 14.4b [41, 45]. It has been suggested that as the coatings crack, the high strain energy that has been stored in the form of lattice distortions or established under the indentations is for the recovery of regularly ordered lattices through the reversible low-angle partial dislocations and/or low-energy stacking faults along near-parallel domain boundaries.

3. Oxidation resistance and mechanism of HEAN films

Oxidation resistance of the protective films is also an important property for better performance. The current trend in machining is to minimize the use of cutting fluid in order to save cost, protect the environment, and avoid possible health hazards to workers. However, high-speed cutting without cutting fluid can

lead to excessive heat at the tool-chip interface. Therefore, oxidation resistance becomes a critical issue. Conventionally, improvement in oxidation resistance is achieved mainly by alloying. For example, alloying of Al can increase the oxidation resistance in TiN or TiSiN coatings [47–49]. HEANs have shown great potential in this regard. For example, the $(\text{AlCrTaTiZr})\text{Si}_{7.9}\text{N}_{50.9}$ coating develops an oxide layer of only 330 nm after annealing at 1000 °C for 2 h in air [25]. The oxide layer can be roughly divided into two layers, and the top layer is a dense protective layer, rich in Al and Cr. The second layer is also composed of oxides without nitrogen but has a different composition from the top layer. Besides the formation of the Al- and Cr-rich protective layers, the high oxidation resistance is also attributed to the abundant amount of amorphous SiN_x segregated at the grain boundaries. These amorphous structures can effectively block the diffusion of oxygen and are thus beneficial for antioxidative properties. In 2013, Hsieh et al. reported the oxidation properties of $(\text{Al}_{23.1}\text{Cr}_{30.8}\text{Nb}_{7.7}\text{Si}_{7.7}\text{Ti}_{30.7})\text{N}_{50}$ and $(\text{Al}_{29.1}\text{Cr}_{30.8}\text{Nb}_{11.2}\text{Si}_{7.7}\text{Ti}_{21.2})\text{N}_{50}$ coatings [37]. They exhibited a high hardness of 36–37 GPa and good oxidation resistance. After annealing at 900 °C for 2 h in air, the surface oxide layer on the $(\text{Al}_{23.1}\text{Cr}_{30.8}\text{Nb}_{7.7}\text{Si}_{7.7}\text{Ti}_{30.7})\text{N}_{50}$ is only 100 nm thick, and that on $(\text{Al}_{29.1}\text{Cr}_{30.8}\text{Nb}_{11.2}\text{Si}_{7.7}\text{Ti}_{21.2})\text{N}_{50}$ is only 80 nm thick. These values are truly remarkable. For example, advanced antioxidative $\text{Al}_{0.53}\text{Si}_{0.2}\text{Ti}_{0.27}\text{N}$ coatings have a 100 nm thick oxide layer after annealing at 850 °C for only 1 h [48], and the oxide scale on $\text{Al}_{0.52}\text{Ti}_{0.43}\text{Cr}_{0.03}\text{Y}_{0.02}\text{N}$ coatings is 400 nm thick after annealing at 950 °C for 1 h [50].

Shen et al. investigated the oxidation behavior and structure of oxide scales on the $(\text{Al}_{0.34}\text{Cr}_{0.22}\text{Nb}_{0.11}\text{Si}_{0.11}\text{Ti}_{0.22})_{50}\text{N}_{50}$ coating [38]. This coating exhibits excellent resistance to oxidation. The thickness of the oxide scale after air annealing at 900 °C for 50 h is merely 290 nm. The weight gain during continuous thermal ramping to 1300 °C was merely 0.015 mg/cm². These values are among the best known in nitrides. Detailed TEM investigation was carried out on the oxide scale of this coating, as shown in Fig. 14.5. Eight individual layers were distinguished (Fig. 14.5a). EDS results (Fig. 14.5b) reveal that these eight layers are all oxides. Below these oxides, the nitride coatings remain unreacted, as shown in Fig. 14.5c. The first layer of the oxide is an Al-rich layer. High-resolution TEM analysis (Fig. 14.5d) indicates that its structure is identical to $\alpha\text{-Al}_2\text{O}_3$. Layer 2 is an Al- and Cr-rich oxide layer and contains nanograins about 5–8 nm in diameter (Fig. 14.5e). These grains are surrounded by a thin amorphous layer about 2–5 nm thick. Layers 3–8 exhibit alternating light and dark contrast. Further inspection reveals that the light layers (3, 5, and 7) have an amorphous structure, while the dark layers (4, 6, and 8) are composed of nanograins 5–10 nm in size. Fig. 14.5f shows the typical microstructure in layers 3–8. In some areas, the lighter regions can even penetrate the dark layers, suggesting that the amorphous phase forms a continuous network in layers 3–8. EDS results show that the light regions are Al and Si rich, while the dark layers are Ti, Nb, and Cr rich. The excellent oxidation resistance of the $(\text{Al}_{0.34}\text{Cr}_{0.22}\text{Nb}_{0.11}\text{Si}_{0.11}\text{Ti}_{0.22})_{50}\text{N}_{50}$ coatings is attributable to the formation of the dense surface $\alpha\text{-Al}_2\text{O}_3$ layer, and the rich amorphous networks of these structures effectively hinder the inward diffusion of oxygen and, thus, significantly enhance the oxidation resistance.

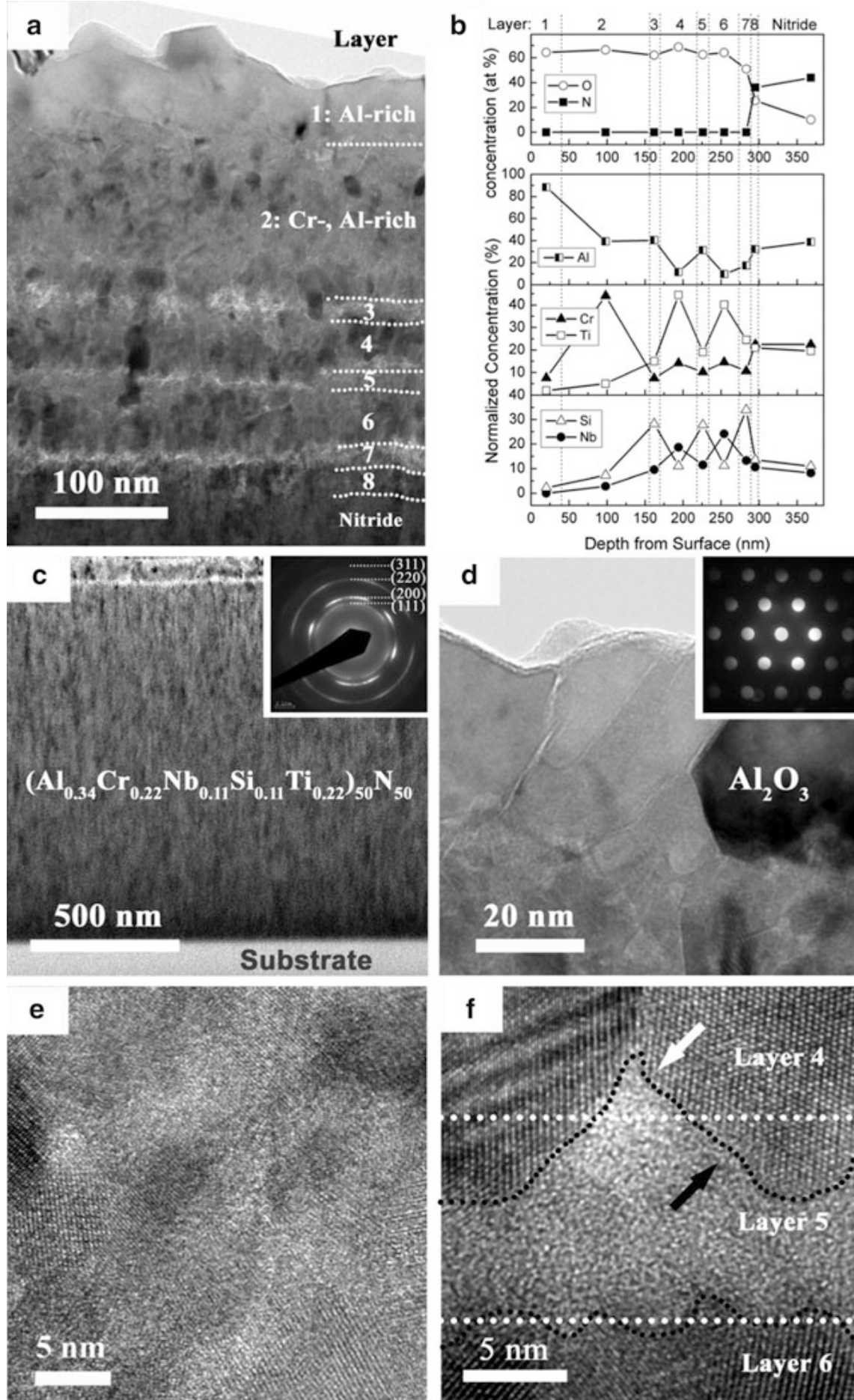


Fig. 14.5 (a) Cross-sectional TEM micrograph of the oxide scale on $(\text{Al}_{0.34}\text{Cr}_{0.22}\text{Nb}_{0.11}\text{Si}_{0.11}\text{Ti}_{0.22})_{50}\text{N}_{50}$ coating after annealing at 900 °C for 50 h. (b) EDS results of the oxide layers in (a). (c) TEM image and diffraction pattern of the un-oxidized nitride film underneath the oxide layer. (d) TEM micrograph and nanobeam electron diffraction pattern of $\alpha\text{-Al}_2\text{O}_3$ oxide particles at surface. (e) HRTEM image of layer 2 (Cr rich). (f) HRTEM image of layers 4–6 in (a) [38]

14.3.2 Diffusion Barriers

Another important potential application of HEAN thin films is as diffusion barriers in microelectronics, i.e., a thin film to prevent rapid interdiffusion and reaction of Cu and Si. Similar applications of HEA thin films for diffusion barriers have been reviewed in Sect. 14.2.3. Although HEAN thin films may have disadvantages such as high electrical resistivity and low interface adhesion, they can show outstanding thermal stability, which is crucial to diffusion barriers because of their strong metal-nitrogen bonding [35, 51–55]. The first study in this regard uses a 70 nm thick amorphous HEAN, $(\text{AlMoNbSiTaTiVZr})_{50}\text{N}_{50}$. This nitride film successfully prevents the reaction between Si and Cu at 850 °C for 30 min [35]. Later, an $(\text{AlCrTaTiZr})\text{N}$ film with a thickness of 10 nm was developed and was found to endure Cu/Si interdiffusion at 900 °C for 30 min [52]. To further enhance the diffusion resistance of HEAN barriers at an even lower thickness as well as decrease the electrical resistivity and improve their adhesion to Cu, Ru was added and the N content was reduced so as to form $(\text{AlCrRuTaTiZr})\text{N}_{0.5}$ with senary metallic elements. Merely a 5 nm thick film could achieve resistance to a temperature of 800 °C after annealing for 30 min [53]. Furthermore, the stacked structures of HEAN and HEA films could enhance performance. Bi-layered $(\text{AlCrTaTiZr})\text{N}_x/\text{AlCrTaTiZr}$ (10/5 nm thick) could be achieved after annealing at 900 °C for 30 min [54]. A quaternary-layered $(\text{AlCrRuTaTiZr})\text{N}_{0.5}/\text{AlCrRuTaTiZr}/(\text{AlCrRuTaTiZr})\text{N}_{0.5}/\text{AlCrRuTaTiZr}$ (each layer 1 nm thick) film could be achieved after annealing at 800–900 °C for 30 min, as shown in Fig. 14.6 [55]. The latter, with an ultralow thickness of only 4 nm has a lower electrical resistivity and better interfacial adhesion than individual HEAN films, but exhibits

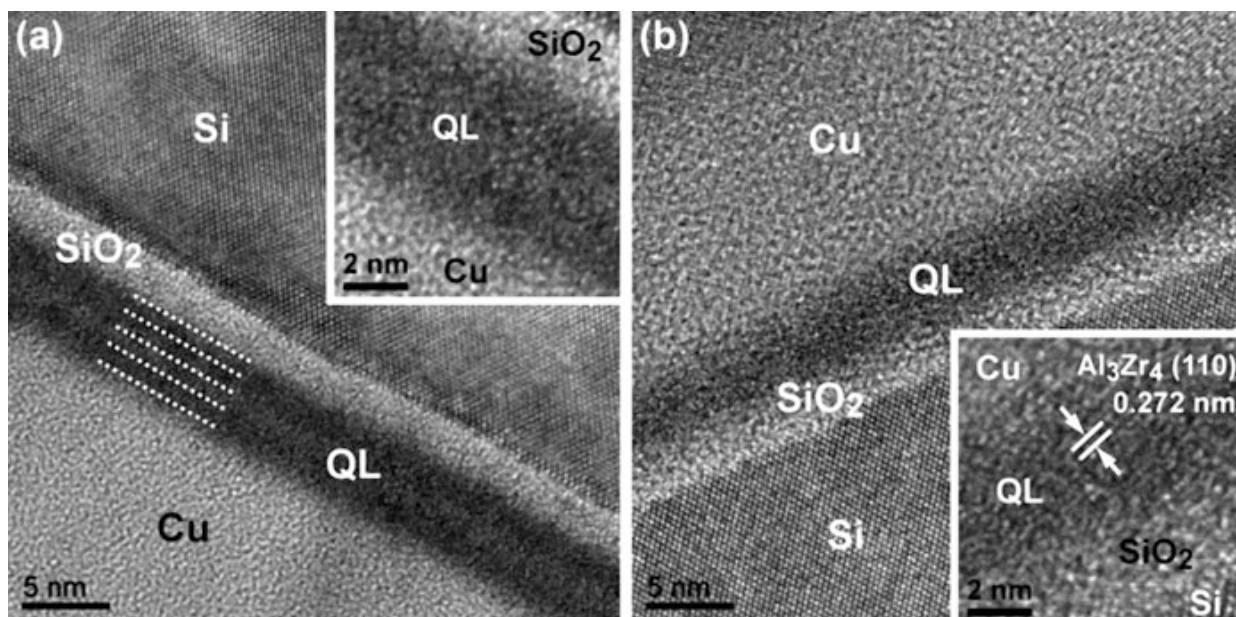


Fig. 14.6 TEM images of (a) as-deposited and (b) 800 °C-annealed Si/QL/Cu film, where QL represents the stacked structure of quaternary-layered diffusion barrier of $(\text{AlCrRuTaTiZr})\text{N}_{0.5}/\text{AlCrRuTaTiZr}/(\text{AlCrRuTaTiZr})\text{N}_{0.5}/\text{AlCrRuTaTiZr}$; inset: magnified image around QL barrier [55]

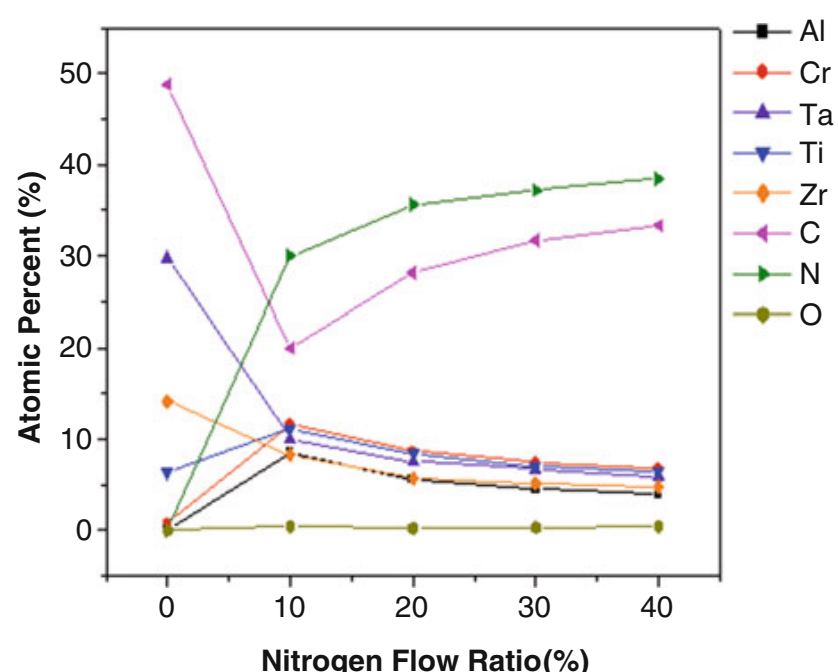
the same excellent resistance to Cu/Si interdiffusion at 800–900 °C. This can possibly be attributed to not only severe lattice distortions and strengthened cohesion but also large interface mismatches [19, 55]. All these results demonstrate that the high-stability HEAN barriers would perform well for much longer durations in the thermal cycles of IC manufacturing (300–400 °C) and operation (100–200 °C), which suggests their high potential for practical applications in microelectronic devices.

14.4 Other HEA-Based Coatings

14.4.1 Low-Friction Hard Coatings

Similar to HEAN coatings, HEA carbides (HEACs) can be deposited using CH₄-containing Ar or co-deposited with a graphite target, HEA oxides (HEAOs) using O₂-containing Ar, and HEA carbonitrides (HEACNs) using CH₄ + N₂-containing Ar. For HEAC and HEACN films, Lin et al. first used two targets, AlCrTaTiZr and graphite, to co-deposit the films on Si substrates at 350 °C and under a bias voltage of –100 V [56–58]. By fixing the sputtering power at 100 W and 250 W, and controlling the nitrogen flow ratio, N₂/(Ar + N₂), the film composition could be varied from (Ta,Ti,Zr)₅₀C₅₀ to (Al,Cr,Ta,Ti,Zr)₃₀C₃₂N₃₈, respectively, as shown in Fig. 14.7. The negligible concentrations of Al and Cr in the carbide film are due to their weak bonding with carbon in vacuum, whereas their appreciable concentrations in the carbonitride film are due to their strong bonding with nitrogen. The two films have nanohardness values of 39 GPa and 24 GPa and friction coefficients of 0.43 and 0.29, respectively. As a comparison, these values for (Al,Cr,Ta,Ti,Zr)₅₀N₅₀ are 31 GPa and 0.80, respectively. By using the ball-on-disk method

Fig. 14.7 EPMA chemical composition variation of HEACN films with nitrogen flow ratio, N₂/(Ar + N₂). Two targets, AlCrTaTiZr and graphite, were used to co-deposit the films on Si substrate at 350 °C and under a bias of –100 V



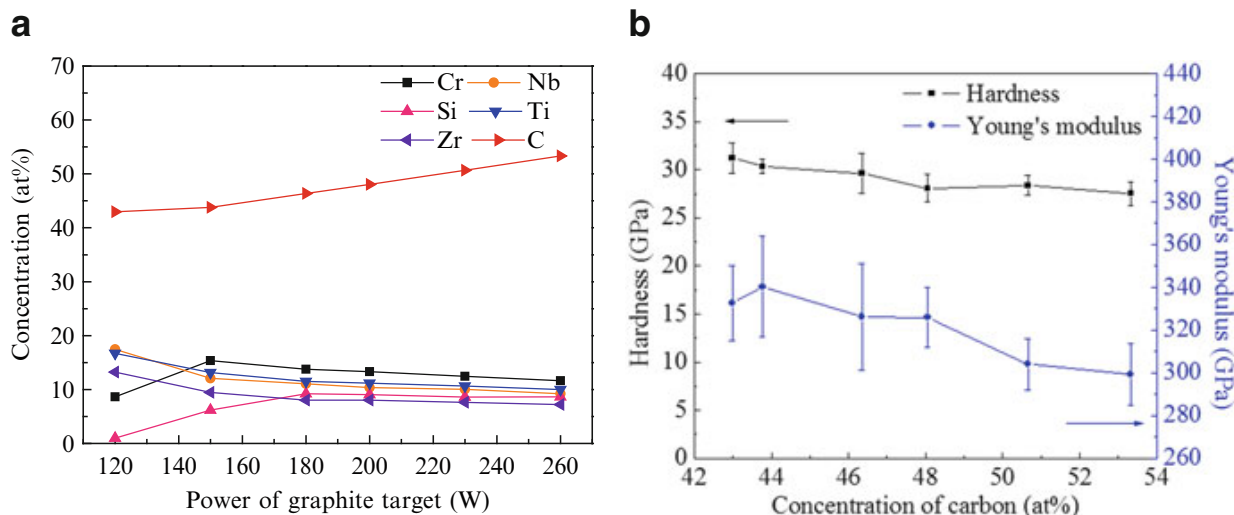


Fig. 14.8 (a) EPMA chemical composition variation of HEAC films with the power applied to the graphite target. Two targets, CrNbSiTiZr and graphite, were used to co-deposit the films on Si substrates at 400 °C and under a bias of –100 V and (b) hardness and Young's modulus variation with carbon content

(AISI 52100 bearing-steel ball) to measure the wear resistance, (Al,Cr,Ta,Ti,Zr)₃₀C₃₂N₃₈ films display an even lower wear rate than the (Ta,Ti,Zr)₅₀C₅₀ film. The low wear rate of both films is attributed to the formation of a graphite-like substance at the wear surface, which acts as a lubricant.

HEAC coatings based on CrNbSiTiZr were developed by Lin et al. using two targets: one was equimolar CrNbSiTiZr and another was graphite [59]. Films were co-deposited from both targets on Si substrates at 400 °C and under a bias of –100 V. By fixing the sputtering power at 40 W for the alloy target and varying the power from 120 to 260 W for graphite target, they obtained a series of HEAC films with compositions shown in Fig. 14.8a. Although the HEA alloy film obtained without graphite co-sputtering is amorphous, all the HEAC films have simple NaCl-type FCC structure. Using X-ray photoelectron spectroscopy (XPS) analysis, it was determined that as the carbon content increases from 43.0 to 53.3 at.% (from 120 to 260 W), the C-C bonding of amorphous carbon increases from 1.6 to 7.7 %, based on the total number of bonds with carbon. The hardness and Young's modulus are shown in Fig. 14.8b. A small decrease in both properties with the carbon content is believed to be due to the higher proportion of amorphous carbon. Table 14.2 shows carbon content, friction coefficient, wear rate, and hardness of HEAC films obtained under different applied powers on a graphite target. A target power of 260 W gives the film a carbon content of 53.3 at.%, the lowest friction coefficient of 0.11, and the lowest wear rate of $0.45 \times 10^{-6} \text{ mm}^3/\text{N} \cdot \text{m}$. This film is obviously superior to a TiC film with similar carbon content and hardness.

Lin et al. also developed HEACs from an equimolar CrNbTaTiZr target by reaction sputtering under different CH₄/(Ar + CH₄) flow ratios of 0, 3, 7, 10, 15, and 20 % [60]. The structure is amorphous under pure Ar and becomes a simple FCC structure when the flow ratio is 7 %. Figure 14.9 shows the chemical compositions, hardness, and Young's modulus of HEAC films with different CH₄ flow ratio,

Table 14.2 Carbon content, friction coefficient, wear rate, and hardness of HEAC films obtained under different applied powers on a graphite target

Power of graphite (W)	Carbon content (at.%)	Friction coefficient	Wear rate ($10^{-6} \text{ mm}^3/\text{N} \cdot \text{m}$)	Hardness (GPa)
120	43.0	0.24	0.89 ± 0.06	31.2
150	43.8	0.29	2.94 ± 0.49	30.3
180	46.4	0.17	1.60 ± 0.21	29.6
200	48.1	0.15	1.18 ± 0.44	28.1
230	50.7	0.15	0.72 ± 0.04	28.4
260	53.3	0.11	0.45 ± 0.04	27.5
TiC	57.9	0.20	1.47 ± 0.11	28.8

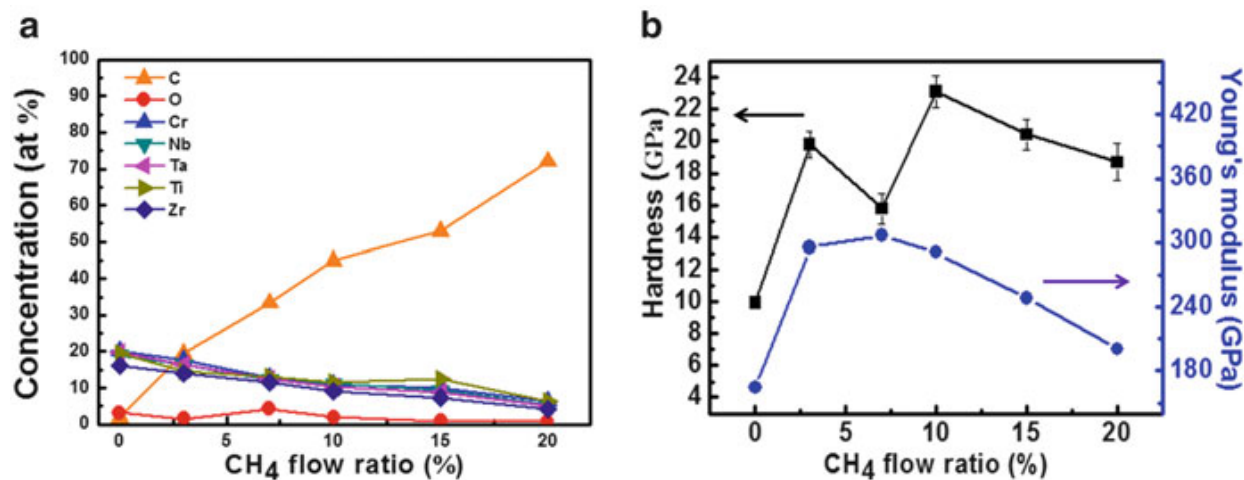


Fig. 14.9 (a) Electron probe microanalysis (EPMA) chemical composition variation and (b) hardness and Young's modulus variations with the CH₄ flow ratio for HEAC films sputtered on Si substrate without bias

which was sputtered on Si substrates without any bias. A stoichiometric carbon content can be obtained when the flow ratio is between 10 and 15 %. The hardness is about 21.5 GPa. When a bias of -100 V is applied, the carbon content of the film becomes 59.3, 70.6, and 83.4 at.% for flow ratios of 10 %, 15 %, and 20 %, respectively, and the film hardness is 33.2, 24.4, and 14.7 GPa. The ball-on-disk wear test gave friction coefficients of 0.2, 0.14, and 0.09 and wear rates of 1.21, 0.89, and $0.4 \times 10^{-6} \text{ mm}^3/\text{N} \cdot \text{m}$. All the above results demonstrate that HEAC and HEACN coatings can provide excellent wear resistance and lower the friction force for punches, dies, molds, and wear parts.

Braic et al. also studied HEAC coatings [39, 61, 62]. (AlCrNbTiY)C coatings were prepared by co-sputtering of separate, pure metallic Al, Cr, Nb, Ti, and Y targets in an Ar+CH₄ reactive atmosphere [60]. The metals in the carbide films were controlled to form an almost equiatomic ratio, whereas the carbon content varied from about 46–82 at.%. The films consisted of a mixture of carbides, intermetallic compounds, and carbon, having a proportion that depends on the CH₄/(CH₄+Ar) flow ratio. For film compositions close to stoichiometry, a single

FCC solid-solution phase was detected, whereas films with higher carbon concentrations (69–82 at.%) exhibited an amorphous structure. The film hardness (13–23 GPa) was found to depend on the carbon content. A ball-on-disk tribometer with a sapphire ball 6 mm in diameter was used to test the tribology behavior. The results show that the dry friction coefficients were in the range 0.05–0.25 and the wear resistance is good. Because of their fine microstructures, good wear resistance, and dry friction characteristics, the coatings can be considered as potential candidates for various tribological and anticorrosive applications [61]. Furthermore, (HfNbTaTiZr)C coatings were deposited on C45 and M2 steel substrates by co-sputtering of pure metallic Hf, Nb, Ta, Ti, and Zr targets in an Ar + CH₄ atmosphere [39]. The film hardness is higher than TiC by 6 GPa. The friction coefficient and wear rate of the (HfNbTaTiZr)C film were 0.15 and 0.8×10^{-6} mm³/N·m, respectively, better than that of TiC film (0.18 and 9.4×10^{-6} mm³/N·m) [39].

14.4.2 Biomedical Coatings

For biomedical applications, (HfNbTaTiZr)N and (HfNbTaTiZr)C coatings were deposited on Ti-6Al-4 V alloy by co-sputtering of Hf, Nb, Ta, Ti, and Zr metallic targets in Ar + N₂ and Ar + CH₄ reactive atmospheres, respectively [62]. All the films showed simple FCC solid-solution phases with (111) preferred orientations and crystallite sizes in the range of 7.2–13.5 nm. The highest hardness value was measured for the carbide coating with the highest carbon content, which also exhibited the best friction performance ($\mu = 0.12$) and the highest wear resistance ($K = 0.20 \times 10^{-6}$ mm³/N·m) measured using the ball-on-disk tribometer and performed in a solution of simulated body fluids (SBFs). In addition, electrochemical measurements showed that all coatings exhibited good protective properties in SBF solution. Biocompatibility tests showed that the investigated coatings did not induce any cytotoxic response due to osteoblasts, and a good morphology of the attached cells was observed. Cell viability analysis showed a very high ratio of live cells compared to dead cells for all the investigated groups. Hence, it was demonstrated that the mechanical, tribological, and anticorrosive characteristics of the biocompatible Ti-6Al-4 V alloy could be significantly improved using HEAN and HEAC coatings. They possess high hardness, low friction coefficient, and superior wear-corrosion resistance, as well as good biocompatible properties [62].

14.5 Conclusions and Perspective

In this chapter, we reviewed typical HEAs and HEA-related thick layer and thin layer coatings. They can be produced by suitable coating technologies and can provide additional functions to parts or components for improving performance

such as wear, corrosion, diffusion, and heat resistance. Thermal spray technology can deposit thick HEA layers with a thickness from tens to hundreds of micrometers and even to millimeters on substrates. Arc welding and laser welding may produce HEA cladding with a thickness over a similar range. Sputtering technology can deposit thin-film HEA coatings that are submicron to micrometers thick on substrates, and if a suitable reactive gas is used during deposition, HEAN, HEAC, HEACN, or HEAO could be deposited on substrates from HEA targets or split targets. Therefore, HEA and HEA-based ceramic coatings are easily deposited by using suitable conventional coating technologies despite the fact that many components are involved during the coating process. Most importantly, HEA and HEA-based ceramic coatings can display outstanding properties, and thus, have a potential for use in various applications. The mechanisms for the formation of crystal structure and microstructure, and for the improved properties presented in this chapter, demonstrate that HEA and HEA-based ceramic coatings also have high-entropy, lattice distortion, and sluggish diffusion effects observed in bulk HEAs and are a new attractive field providing many opportunities for developing even better coatings with improved performance and lifetime. Although not emphasized in this chapter, modern requirements for surface coatings with biomedical, antibacterial, EMI shielding, anti-fingerprint, nonstick, hydrophilic, or hydrophobic properties are also future directions for value-added development.

Acknowledgments J.W.Y, S.J.L, M.H.T, and S.Y.C. would like to thank Dr. Michael C. Gao for his patience to provide review comments and suggestions from himself and invited experts. They also acknowledge all the financial supports from Ministry of Science and Technology, Ministry of Economic Affairs, and National Tsing Hua University, R.O.C.

References

1. Huang PK, Yeh JW, Shun TT, Chen SK (2004) Multi-principal-element alloys with improved oxidation and wear resistance for thermal spray coating. *Adv Eng Mater* 6:74–78
2. Chen JH, Hua PH, Chen PN, Chang CM, Chen MC, Wu W (2008) Characteristics of multi-element alloy cladding produced by TIG process. *Mater Lett* 62:2490–2492
3. Lin YC, Cho YH (2008) Elucidating the microstructure and wear behavior for multicomponent alloy clad layers by *in situ* synthesis. *Surf Coat Technol* 202:4666–4672
4. Zhang H, Pan Y, He YZ (2011) Grain refinement and boundary misorientation transition by annealing in the laser rapid solidified 6FeNiCoCrAlTiSi multicomponent ferrous alloy coating. *Surf Coat Technol* 205:4068–4072
5. Huang C, Zhang YZ, Shen JY, Vilar R (2011) Thermal stability and oxidation resistance of laser clad TiVCrAlSi high entropy alloy coatings on Ti-6Al-4V alloy. *Surf Coat Technol* 206:1389–1395
6. Huang C, Zhang YZ, Vilar R, Shen JY (2012) Dry sliding wear behavior of laser clad TiVCrAlSi high entropy alloy coatings on Ti-6Al-4V substrate. *Mater Des* 41:338–343
7. Zhang H, He YZ, Pan Y, Guo S (2014) Thermally stable laser cladded CoCrCuFeNi high-entropy alloy coating with low stacking fault energy. *J Alloys Compd* 600:210–214
8. Kouno T, Niwa H, Yamada M (1998) Effect of TiN microstructure on diffusion barrier properties in Cu metallization. *J Electrochem Soc* 145:2164–2167

9. Alen P, Ritala M, Arstila K, Keinonen J, Leskela M (2005) Atomic layer deposition of molybdenum nitride thin films for Cu metallizations. *J Electrochem Soc* 152:G361–G366
10. Kwon SH, Kwon OK, Min JS, Kang SW (2006) Plasma-enhanced atomic layer deposition of Ru-TiN thin films for copper diffusion barrier metals. *J Electrochem Soc* 153:G578–G581
11. Chen CW, Chen JS, Jeng JS (2008) Effectiveness of Ta addition on the performance of Ru diffusion barrier in Cu metallization. *J Electrochem Soc* 155:H1003–H1008
12. Fang JS, Lin JH, Chen BY, Chin TS (2011) Ultrathin Ru-Ta-C barriers for Cu metallization. *J Electrochem Soc* 158:H97–H102
13. Leu LC, Norton DP, McElwee-White L, Anderson TJ (2008) Ir/TaN as a bilayer diffusion barrier for advanced Cu interconnects. *Appl Phys Lett* 92:111917–111917-3
14. Kim SH, Kim HT, Yim SS, Lee DJ, Kim KS, Kim HM, Kim KB, Sohn H (2008) A bilayer diffusion barrier of ALD-Ru/ALD-TaCN for direct plating of Cu. *J Electrochem Soc* 155: H589–H594
15. Xie Q, Jiang YL, Musschoot J, Deduytsche D, Detavernier C, Van Meirhaeghe RL, Van den Berghe S, Ru GP, Li BZ, Qu XP (2009) Ru thin film grown on TaN by plasma enhanced atomic layer deposition. *Thin Solid Films* 517:4689–4693
16. Tsai MH, Yeh JW, Gan JY (2008) Diffusion barrier properties of AlMoNbSiTaTiVZr high-entropy alloy layer between copper and silicon. *Thin Solid Films* 516:5527–5530
17. Tsai MH, Wang CW, Tsai CW, Shen WJ, Yeh JW, Gan JY, Wu WW (2011) Thermal stability and performance of NbSiTaTiZr high-entropy alloy barrier for copper metallization. *J Electrochem Soc* 158:H1161–H1165
18. Chang SY, Wang CY, Chen MK, Li CE (2011) Ru incorporation on marked enhancement of diffusion resistance of multi-component alloy barrier layers. *J Alloys Compd* 509:L85–L89
19. Chang SY, Li CE, Huang YC, Hsu HF, Yeh JW, Lin SJ (2014) Structural and thermodynamic factors of suppressed interdiffusion kinetics in multi-component high-entropy materials. *Sci Rep* 4:4162
20. Lai CH, Lin SJ, Yeh JW, Chang SY (2006) Preparation and characterization of AlCrTaTiZr multi-element nitride coatings. *Surf Coat Technol* 201:3275–3280
21. Lin CH, Duh JG, Yeh JW (2007) Multi-component nitride coatings derived from Ti-Al-Cr-Si-V target in RF magnetron sputter. *Surf Coat Technol* 201:6304–6308
22. Huang PK, Yeh JW (2010) Inhibition of grain coarsening up to 1000°C in (AlCrNbSiTiV)N superhard coatings. *Scr Mater* 62:105–108
23. Tsai MH, Lai CH, Yeh JW, Gan JY (2008) Effects of nitrogen flow ratio on the structure and properties of reactively sputtered $(\text{AlMoNbSiTaTiVZr})\text{N}_x$ coatings. *J Phys D Appl Phys* 41:235402
24. Cheng KH, Lai CH, Lin SJ, Yeh JW (2011) Structural and mechanical properties of multi-element $(\text{AlCrMoTaTiZr})\text{N}_x$ coatings by reactive magnetron sputtering. *Thin Solid Films* 519:3185–3190
25. Cheng KH, Tsai CW, Lin SJ, Yeh JW (2011) Effects of silicon content on the structure and mechanical properties of $(\text{AlCrTaTiZr})\text{-Si}_x\text{-N}$ coatings by reactive RF magnetron sputtering. *J Phys D Appl Phys* 44:205405
26. Shen WJ, Tsai MH, Chang YS, Yeh JW (2012) Effects of substrate bias on the structure and mechanical properties of $(\text{Al}_{1.5}\text{CrNb}_{0.5}\text{Si}_{0.5}\text{Ti})\text{N}_x$ coatings. *Thin Solid Films* 520:6183–6188
27. Lai CH, Lin SJ, Yeh JW, Davison A (2006) Effect of substrate bias on the structure and properties of multi-element (AlCrTaTiZr)N coatings. *J Phys D Appl Phys* 39:4628
28. Huang PK, Yeh JW (2009) Effects of substrate bias on structure and mechanical properties of (AlCrNbSiTiV)N coatings. *J Phys D Appl Phys* 42:115401
29. Chang HW, Huang PK, Yeh JW, Davison A, Tsau CH, Yang CC (2008) Influence of substrate bias, deposition temperature and post-deposition annealing on the structure and properties of multi-principal-component (AlCrMoSiTi)N coatings. *Surf Coat Technol* 202:3360–3366
30. Chen TK, Shun TT, Yeh JW, Wong MS (2004) Nanostructured nitride films of multi-element high-entropy alloys by reactive DC sputtering. *Surf Coat Technol* 188:188–193

31. Chen TK, Wong MS, Shun TT, Yeh JW (2005) Nanostructured nitride films of multi-element high-entropy alloys by reactive DC sputtering. *Surf Coat Technol* 200:1361–1365
32. Tsai CW, Lai SW, Cheng KH, Tsai MH, Davison A, Tsau CH, Yeh JW (2012) Strong amorphization of high-entropy AlBCrSiTi nitride film. *Thin Solid Films* 520:2613–2618
33. Ren B, Liu ZX, Shi L, Cai B, Wang MX (2011) Structure and properties of $(\text{AlCrMnMoNiZrB}_{0.1})\text{N}_x$ coatings prepared by reactive DC sputtering. *Appl Surf Sci* 257:7172–7178
34. Chang ZC, Liang SC, Han S (2011) Effect of microstructure on the nanomechanical properties of TiVCrZrAl nitride films deposited by magnetron sputtering. *Nucl Instrum Methods Phys Res, Sect B* 269:1973–1976
35. Tsai MH, Wang CW, Lai CH, Yeh JW, Gan JY (2008) Thermally stable amorphous $(\text{AlMoNbSiTaTiVZr})_{50}\text{N}_{50}$ nitride film as diffusion barrier in copper metallization. *Appl Phys Lett* 92:052109
36. Hsueh HT, Shen WJ, Tsai MH, Yeh JW (2012) Effect of nitrogen content and substrate bias on mechanical and corrosion properties of high-entropy films $(\text{AlCrSiTiZr})_{100-x}\text{N}_x$. *Surf Coat Technol* 206:4106–4112
37. Hsieh MH, Tsai MH, Shen WJ, Yeh JW (2013) Structure and properties of two Al-Cr-Nb-Si-Ti high-entropy nitride coatings. *Surf Coat Technol* 221:118–123
38. Shen WJ, Tsai MH, Tsai KY, Juan CC, Tsai CW, Yeh JW, Chang YS (2013) Superior oxidation resistance of $(\text{Al}_{0.34}\text{Cr}_{0.22}\text{Nb}_{0.11}\text{Si}_{0.11}\text{Ti}_{0.22})_{50}\text{N}_{50}$ high-entropy nitride. *J Electrochem Soc* 160:C531–C535
39. Braic V, Vladescu A, Balaceanu M, Luculescu CR, Braic M (2012) Nanostructured multi-element $(\text{TiZrNbHfTa})\text{N}$ and $(\text{TiZrNbHfTa})\text{C}$ hard coatings. *Surf Coat Technol* 211:117–121
40. Chang SY, Lin SY, Huang YC, Wu CL (2010) Mechanical properties, deformation behaviors and interface adhesion of $(\text{AlCrTaTiZr})\text{N}_x$ multi-component coatings. *Surf Coat Technol* 204:3307–3314
41. Lin SY, Chang SY, Huang YC, Shieh FS, Yeh JW (2012) Mechanical performance and nanoindenting deformation of $(\text{AlCrTaTiZr})\text{NC}_y$ multi-component coatings co-sputtered with bias. *Surf Coat Technol* 206:5096–5102
42. Ren B, Yan SQ, Zhao RF, Liu ZX (2013) Structure and properties of $(\text{AlCrMoNiTi})\text{N}_x$ and $(\text{AlCrMoZrTi})\text{N}_x$ films by reactive RF sputtering. *Surf Coat Technol* 235:776–772
43. Pogrebnyak AD, Yakushchenko IV, Abadias G, Chartier P, Bondar OV, Beresnev VM, Takeda Y, Sobol OV, Oyoshi K, Andreyev AA, Mukushev BA (2013) The effect of the deposition parameters of nitrides of high-entropy alloys $(\text{TiZrHfVNb})\text{N}$ on their structure, composition, mechanical and tribological properties. *J Superhard Mater* 35:356–368
44. Tsai DC, Chang ZC, Kuo LY, Lin TJ, Lin TN, Shieh FS (2013) Solid solution coating of $(\text{TiVCrZrHf})\text{N}$ with unusual structural evolution. *Surf Coat Technol* 217:84–87
45. Lin SY, Chang SY, Chang CJ, Huang YC (2014) Nanomechanical properties and deformation behaviors of multi-component $(\text{AlCrTaTiZr})\text{N}_x\text{Si}_y$ high-entropy coatings. *Entropy* 16:405–417
46. Veprek S (2013) Recent search for new superhard materials: go nano! *J Vac Sci Technol A* 31:050822
47. Munz WD (1986) Titanium aluminum nitride films: a new alternative to TiN coatings. *J Vac Sci Technol A* 4:2717
48. Vaz F, Rebouta L, Andritschky M, da Silva MF (1998) Oxidation resistance of $(\text{Ti, Al, Si})\text{N}$ coatings in air. *Surf Coat Technol* 98:912–917
49. PalDey S, Deevi SC (2003) Single layer and multilayer wear resistant coatings of $(\text{Ti, Al})\text{N}$: a review. *Mater Sci Eng A* 342:58–79
50. Donohue LA, Smith II, Munz WD, Petrov I, Greene JE (1997) Microstructure and oxidation-resistance of $\text{Ti}_{1-x-y-z}\text{Al}_x\text{Cr}_y\text{Y}_z\text{N}$ layers grown by combined steered-arc/unbalanced-magnetron-sputter deposition. *Surf Coat Technol* 94–95:226–231
51. Chang SY, Chen MK, Chen DS (2009) Multiprincipal-element AlCrTaTiZr-nitride nanocomposite film of extremely high thermal stability as diffusion barrier for Cu metallization. *J Electrochem Soc* 156:G37–G42

52. Chang SY, Chen DS (2009) 10-nm-thick quinary (AlCrTaTiZr)N film as effective diffusion barrier for Cu interconnects at 900°C. *Appl Phys Lett* 94:231909
53. Chang SY, Wang CY, Li CE, Huang YC (2011) 5 nm-thick (AlCrTaTiZrRu)N_{0.5} multi-component barrier layer with high diffusion resistance for Cu interconnects. *Nanosci Nanotechnol Lett* 3:289–293
54. Chang SY, Chen DS (2010) Ultra-thin (AlCrTaTiZr)N_x/AlCrTaTiZr bilayer structures of high diffusion resistance to Cu metallization. *J Electrochem Soc* 157:G154–G159
55. Chang SY, Li CE, Chiang SC, Huang YC (2012) 4-nm thick multilayer structure of multi-component (AlCrRuTaTiZr)N_x as robust diffusion barrier for Cu interconnects. *J Alloy Compd* 515:4–7
56. Gu WB, Lin SJ (2008) Study on the structure and properties of (AlCrTaTiZr)(CN) thin films. Master's thesis, Department of Materials and Science Engineering, National Tsing Hua University, Taiwan
57. Liu TW, Lin SJ (2009) Study on the microstructure and properties of multi-element carbide and carbonitride thin films. Master's thesis, Department of Materials and Science Engineering, National Tsing Hua University, Taiwan
58. Cheng KH, Liu TW, Lin SJ, Yeh JW (2009) Effect of carbon contents on the structural and mechanical properties of sputtered (AlCrTaTiZr)C_x coatings. E-MRS 2009 Fall Meeting, Warsaw, September 14–18, Paper No. 18410
59. Lin JW, Lin SJ (2010) Study on the microstructure and properties of multi-element (CrNbSiTiZr)Cx coatings. Master's thesis, Department of Materials and Science Engineering, National Tsing Hua University, Taiwan
60. Chen SH, Lin SJ (2012) The mechanical properties and microstructures of the (CrNbTaTiZr) CX coating. Master's thesis, Department of Materials and Science Engineering, National Tsing Hua University, Taiwan
61. Braic M, Braic V, Balaceanu M, Zoita CN, Vladescu A, Grigore E (2010) Characteristics of (TiAlCrNbY)C films deposited by reactive magnetron sputtering. *Surf Coat Technol* 204:2010–2014
62. Braic V, Balaceanu M, Braic M, Vladescu A, Panseri S, Russo A (2012) Characterization of multi-principal-element (TiZrNbHfTa)N and (TiZrNbHfTa)C coatings for biomedical applications. *J Mech Behav Biomed Mater* 10:197–205

Chapter 15

Potential Applications and Prospects

Jien-Wei Yeh, An-Chou Yeh, and Shou-Yi Chang

Abstract High-entropy alloys (HEAs) inherently have four core effects that enable improvement in microstructure and properties. During the course of research on HEAs, other special materials, such as high-entropy (HE) superalloys, HE refractory alloys, HE bulk metallic glasses, HE carbides, HE nitrides, and HE oxides, have also been developed. All these materials have promising potential applications, e.g., in fabricating machine components, dies and molds, corrosion-resistant parts, cutting tools, functional coatings, hard-facing, thin-film resistors, diffusion barriers, and high-temperature structural components. Greater understanding of the basic science, accumulated knowledge and experience, and effective simulation and modeling will lead to the successful development of numerous HE materials with better properties in the future. This chapter first addresses several important high-entropy materials with promising potential applications and finally forecasts the trends and prospects in their research and development.

Keywords High-entropy superalloys • High-entropy refractory alloys • High-entropy ceramics • High-entropy alloys (HEAs) • Medium-entropy alloys

15.1 Introduction

Many compositions have been designed and studied with the new alloy design concept of utilizing high mixing entropy. Among these, many special kinds of HEAs have been reported, such as high-entropy superalloys (HESAs), high-entropy refractory alloys (HERAs), and high-entropy bulk metallic glasses (HEBMGs). In addition, high-entropy ceramics (HECs), such as high-entropy carbides (HEACs), high-entropy nitrides (HEANs), and high-entropy oxides (HEAOs), have been developed. Composites, such as sintered carbide with HEA binders and cermets with HEA binders, have also recently been reported. It is very fortunate that all the processes and methods used to prepare conventional materials can be applied to

J.-W. Yeh (✉) • A.-C. Yeh • S.-Y. Chang

Department of Materials Science and Engineering, National Tsing Hua University,
Hsinchu, Taiwan 30013, Republic of China

e-mail: jwyeh@mx.nthu.edu.tw; yehac@mx.nthu.edu.tw; changsy@mx.nthu.edu.tw

HE-related materials (HEMs) as long as suitable selections are made. Moreover, different measurements, facilities, and apparatuses used to characterize conventional materials can be used similarly for HEMs as long as the intended purposes are determined. It is for this reason that scientists can easily gain access to research and develop HEMs. In addition, the combinations of compositions and processes are countless and could lead to a potentially wide range of microstructures and properties of HEMs and thus broad applications in different areas where conventional materials have been applied.

Research on HEMs not only satisfies our scientific curiosity but also leads to the development of new materials with better performance than conventional materials. Although the research on HEMs is still very limited, the studies available show evidence of their potential for applications. In this chapter, important examples from previous chapters are selected to show their promising potential applications. Based on these and other similar examples, further development could generate better HEMs for improving our life and environment. However, during the course of research, it has been found that information related to the basic science of HEMs is also very important. This not only makes the related materials science information more comprehensive but also accelerates the development of better HEMs. Finally, future trends and prospects extrapolated from the current state described in previous chapters are forecasted at the end of this chapter.

15.2 Potential Applications

15.2.1 High-Entropy Superalloys

Ni-based superalloys have made many high-temperature engineering technologies possible, especially in the aerospace, energy, and oil and gas sectors [1, 2]. These superalloys have relied on dispersion of coherent γ' precipitates in the γ matrix for excellent high-temperature mechanical properties; for example, creep deformation is typically restricted to the γ channels that lie between the precipitates of γ' . Compositions of superalloys have continued to evolve to meet demanding operation conditions [3]. The recent additions of Re and Ru to superalloys have led to improved creep strength [4–12]. However, Re and Ru additions can lead alloys to possess high density and high cost, and thus traditional alloy design methods that rely on the addition of refractory elements appear to have reached the limit. In this section, a new type of high-entropy alloy, which allows the four core effects of HEAs to be exploited for high-temperature applications, is introduced.

Novel alloy systems (density $<8.0 \text{ g/cm}^3$) based on non-equimolar $\text{Al}_x\text{Co}_{1.5}\text{CrFeNi}_{1.5}\text{Ti}_{(0.5-x)}$ containing an FCC γ matrix with a uniform dispersion of $\text{L1}_2 \gamma'$ particles have been developed [13]. Since alloy compositions are designed according to the HEA concept and their microstructures also resemble that of conventional superalloys, the term “high-entropy superalloys” (HESAs) has been

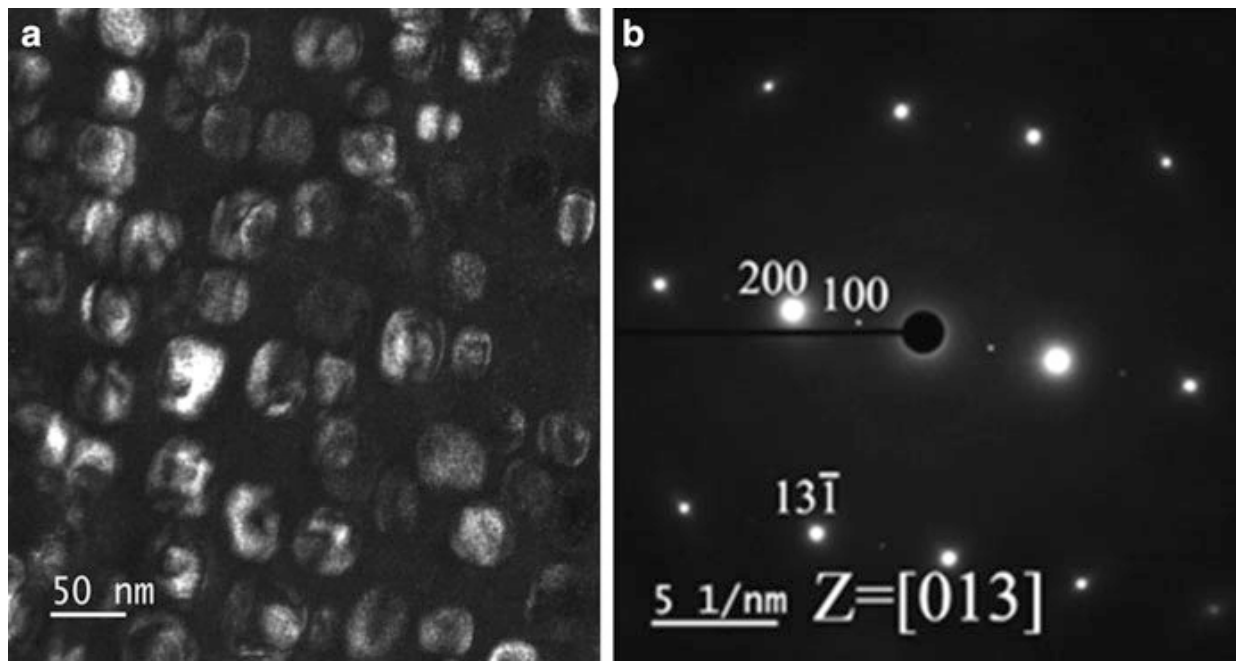


Fig. 15.1 TEM analyses on $\text{Co}_{1.5}\text{CrFeNi}_{1.5}\text{Ti}_{0.5}$ after a solution heat treatment at 1423 K for 6 h followed by precipitation aging at 1023 K for 50 h: (a) a dark field image shows γ' particles in a γ matrix, and (b) a diffraction pattern shows the superlattice reflection of γ'

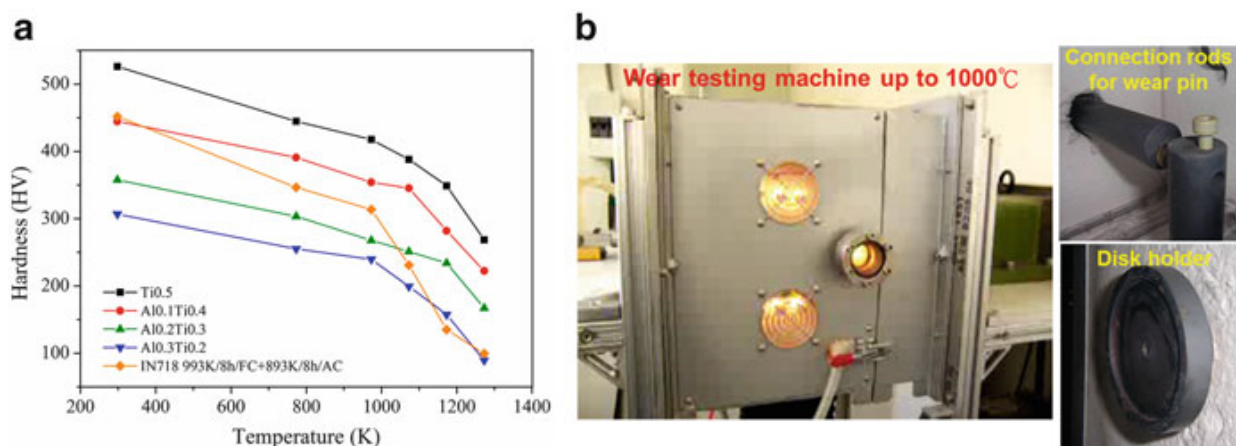


Fig. 15.2 (a) High-temperature hardness of Ti0.5 ($\text{Co}_{1.5}\text{CrFeNi}_{1.5}\text{Ti}_{0.5}$), Al0.1Ti0.4 ($\text{Al}_{0.1}\text{Co}_{1.5}\text{CrFeNi}_{1.5}\text{Ti}_{0.4}$), Al0.2Ti0.3 ($\text{Al}_{0.2}\text{Co}_{1.5}\text{CrFeNi}_{1.5}\text{Ti}_{0.3}$), and Al0.3Ti0.2 ($\text{Al}_{0.3}\text{Co}_{1.5}\text{CrFeNi}_{1.5}\text{Ti}_{0.2}$) alloys and (b) pin-on-disk wear-testing machine for testing up to 1000 °C, interior connecting rods made of cast $\text{Co}_{1.5}\text{CrFeNi}_{1.5}\text{Ti}_{0.5}$ HEA to support the wear pin and exert the applied load and disk holder to fix the alumina disk in the recess

used. After a solution heat treatment at 1423 K for 6 h followed by precipitation aging at 1023 K for 50 h, the microstructure of $\text{Co}_{1.5}\text{CrFeNi}_{1.5}\text{Ti}_{0.5}$ consists of an FCC matrix and γ' particles of 63 % by volume (Fig. 15.1) [13]. Its potential to replace conventional superalloys in high-temperature applications was illustrated in Fig. 15.2, which shows that $\text{Co}_{1.5}\text{CrFeNi}_{1.5}\text{Ti}_{0.5}$ exhibits higher hardness than IN718 from room temperature to 1273 K and has performed well in interior components of a high-temperature wear-testing machine. Furthermore, beyond 973 K, where the hardness of IN718 drops dramatically due to the transformation of γ'' into the δ phase [14], the hardness values of HESAs remain high. At 1273 K,

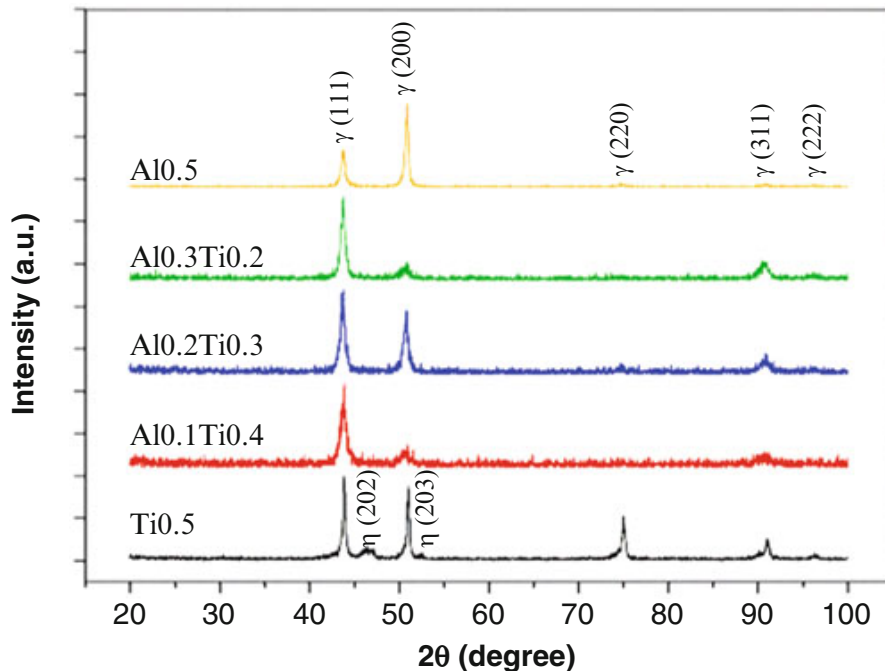


Fig. 15.3 XRD analyses of Ti0.5 ($\text{Co}_{1.5}\text{CrFeNi}_{1.5}\text{Ti}_{0.5}$), Al0.1Ti0.4 ($\text{Al}_{0.1}\text{Co}_{1.5}\text{CrFeNi}_{1.5}\text{Ti}_{0.4}$), Al0.2Ti0.3 ($\text{Al}_{0.2}\text{Co}_{1.5}\text{CrFeNi}_{1.5}\text{Ti}_{0.3}$), and Al0.3Ti0.2 ($\text{Al}_{0.3}\text{Co}_{1.5}\text{CrFeNi}_{1.5}\text{Ti}_{0.2}$) alloys after aging at 1173 K for 6 h

the hardness of $\text{Co}_{1.5}\text{CrFeNi}_{1.5}\text{Ti}_{0.5}$ is HV 280, which is almost three times that of IN718. The high-temperature strength of HESAs has been attributed to the high volume fraction of γ' precipitates. However, in $\text{Co}_{1.5}\text{CrFeNi}_{1.5}\text{Ti}_{0.5}$, the γ' phase can transform to the η phase in a sluggish manner after prolonged exposure above 1073 K, as shown in Fig. 15.3; the solvus temperature of the η phase is close to 1423 K. Although similar transformation behavior can also be observed in several superalloys, such as X-750, 740, and 706 strengthened by Ni_3Ti γ' phase, this γ' phase can transform rapidly into the detrimental η phase beyond 923 K with a solvus temperature around 1227 K [15, 16]. However, both γ' particles and the η phase in the high-entropy system possess better thermal stability, a phenomenon that may be attributed to the high-entropy composition of γ' and η , which is $(\text{Co}, \text{Fe}, \text{Ni})_3(\text{Cr}, \text{Ti})$ [13]. Interestingly, the mixing entropy of γ' in HESAs is $1.49R$ (where R is the ideal gas constant), which compares to $1.06R$ for γ' in conventional superalloys, such as CM247LC [17]; hence, lattice distortion and sluggish diffusion effects are expected to affect the properties of the ordered γ' phase, resulting in higher strength and more sluggish phase transformation. Actually, the η phase in superalloys has been utilized to control the grain size of polycrystalline superalloys during thermal mechanical processes. The presence of the η phase in $\text{Co}_{1.5}\text{CrFeNi}_{1.5}\text{Ti}_{0.5}$ may not entirely be detrimental for processing. Minor η phases in HESAs have been observed to pin the migration of grain boundaries for grain size control [18]. Hence, wrought HESAs can be developed to replace conventional superalloys, such as IN718.

To improve the high-temperature microstructural stability of $\text{Co}_{1.5}\text{CrFeNi}_{1.5}\text{Ti}_{0.5}$, partial substitution of Ti content by Al can further stabilize the γ' phase by eliminating the formation of the η phase, as shown in Fig. 15.3.

However, comparisons between $\text{Co}_{1.5}\text{CrFeNi}_{1.5}\text{Ti}_{0.5}$ and $\text{Al}_{0.3}\text{Co}_{1.5}\text{CrFeNi}_{1.5}\text{Ti}_{0.2}$ indicate that the ordering temperature of the γ' phase decreases with the mixing entropy of γ' compositions from 1.49R to 1.54R, and the γ' volume fraction also decreases from 63 to 41 %. Hence, the hardness of HESAs decreases with higher Al contents. The complete substitution of Ti by Al can result in the formation of a minor β phase instead of the γ' phase, so $\text{Al}_{0.5}\text{Co}_{1.5}\text{CrFeNi}_{1.5}$ is not considered a HESA, although its structure is mainly FCC, as shown in Fig. 15.3.

Conventional superalloys can be cast into single-crystal components to increase their resistance to high-temperature creep [1, 2]. Single-crystal casting trials have been conducted on HESAs with success using the conventional Bridgman process [19]. Previous work on casting single-crystal $\text{Co}_{1.5}\text{CrFeNi}_{1.5}\text{Ti}_{0.5}$ has shown that its elemental partitioning behaviors are similar to those of commercial superalloys. γ' -forming elements, such as Ti and Ni, tend to partition toward interdendritic regions, and Co, Cr, and Fe partition toward the dendritic region [7, 9]. The solid-liquid partitioning ratios could be an indication of the possibility of density inversion during the single-crystal casting process for superalloys, and the partition coefficients of elements in HESAs are comparable to those of typical superalloys, such as CMSX-4 and RR2000 [20, 21]. Thus, the single-crystal castability of HESA should be as good as that of the commercial superalloys with a minimal tendency to form freckle defects [22]. This work suggests that HESAs can potentially be cast into complex shapes as a single crystal, such as turbine blades.

To increase the γ' solvus temperature, an alloy design based on CALPHAD simulation has been carried out. By enlarging the mixing enthalpy relative to the mixing entropy of γ' compositions in HESAs, the γ' solvus can be increased while maintaining relatively high mixing entropy in the HESA alloy system [19]. Furthermore, high-temperature oxidation resistance can be enhanced through the cocktail effect of HEA by the formation of a continuous and protective Al_2O_3 layer, since the Cr and Ti contents in HESAs can enhance the Al activity for the rapid formation of alumina [19].

To increase the high-temperature creep strength of HESAs, alloys can be designed to control the coarsening kinetics of the γ' phase. In conventional superalloys, the directional coarsening of the γ' precipitates, known as “rafting,” is an important microstructural evolution during high-temperature creep [23–27]. It has been established that rafting occurs when superalloys are subject to loading at temperatures higher than 1173 K. In addition, numerous experimental results have shown that rafting is strongly dependent on the sign of the applied loading, lattice misfit, and the elastic constants of the γ and γ' phases [28–32]. Lattice misfit (δ) is defined by the following equation, where $a_{\gamma'}$ is the lattice parameter of the γ' phase and a_{γ} is the lattice parameter of the γ phase:

$$\delta = 2(a_{\gamma'} - a_{\gamma}) / (a_{\gamma'} + a_{\gamma})$$

When δ is negative, γ' can raft in the direction perpendicular to the stress axis, effectively hindering the climbing of dislocations and resulting in excellent creep

resistance [33]. Furthermore, the denser interfacial dislocation network in high-misfit alloys can contribute to decreasing the minimum creep strain rate, since a dense dislocation network can hinder pairs of dislocations in the γ channels from cutting through the γ/γ' interfaces [34]. Thus, HESAs can be designed to possess negative lattice misfit, which can be achieved by the addition of various γ - and γ' -forming elements, not restricted to Al, Co, Cr, Fe, Ni, and Ti. With an increasing amount of data being generated for HESAs, the alloy design of HESAs can be conducted more effectively in the future.

15.2.2 Refractory High-Entropy Alloys

Refractory high-entropy alloys (or high-entropy refractory alloys, HERAs) represent another approach to increase the temperature capability of alloys beyond that of conventional superalloys and comprise of refractory elements (melting points higher than 1650 °C in a broad sense, thus including Ti) as the principal constituent elements. The first two reports revealed that MoNbTaW and MoNbTaVW refractory HEAs possess a simple body-centered cubic (BCC) microstructure and pronounced solution hardening [35, 36]. Both alloys maintained yield strengths of 405 and 477 MPa at 1600 °C, respectively. Later, Senkov et al. reported the BCC alloy HfNbTaTiZr [37] with slightly lower yield strength than the first two refractory HEAs but excellent compression ductility exceeding 50 % and high strain hardening. Apparently, this alloy is unique in terms of its large room-temperature ductility, since most BCC alloys and ordered BCC (B2-type) intermetallic phases are brittle and tend to fracture by cleavage. In addition, this alloy also has quite high strength at elevated temperatures and thus is promising for high-temperature applications. As a result, this finding provides a good basis or reference for developing ductile BCC HEAs. By modifying the composition, other refractory HEAs with various molar ratios of the constituent elements were developed [38–47]. Among these, Senkov et al. reported four high-hardness and low-density refractory HEAs in the Cr–Nb–Ti–V–Zr system [43, 46] and two Al-containing refractory HEAs: AlMo_{0.5}NbTa_{0.5}TiZr and Al_{0.4}Hf_{0.6}NbTaTiZr [45, 46]. NbTiVZr, NbTiV₂Zr, CrNbTiZr, and CrNbTiVZr have densities of 6.52, 6.34, 6.67, and 6.57 g/cm³, respectively. Figure 15.4 compares the compression curves of these alloys from 298 to 1273 K. Some alloys reached a compression of 50 % without fracturing [43]. It is interesting to note that, although the room-temperature ductility of Cr-containing HEAs is somewhat low, their high-temperature strength is much higher than that of NbTiVZr and NbTiV₂Zr alloys. In addition, the specific strengths of CrNbTiZr and CrNbTiVZr alloys are far higher than those of most other high-temperature alloys. Among these two, the CrNbTiVZr alloy shows the most attractive properties, such as considerably improved elevated-temperature strength, reduced density, and much higher melting point. Based on this observation, a better combination of strength, ductility, and low density could be expected if compositions and microstructure are

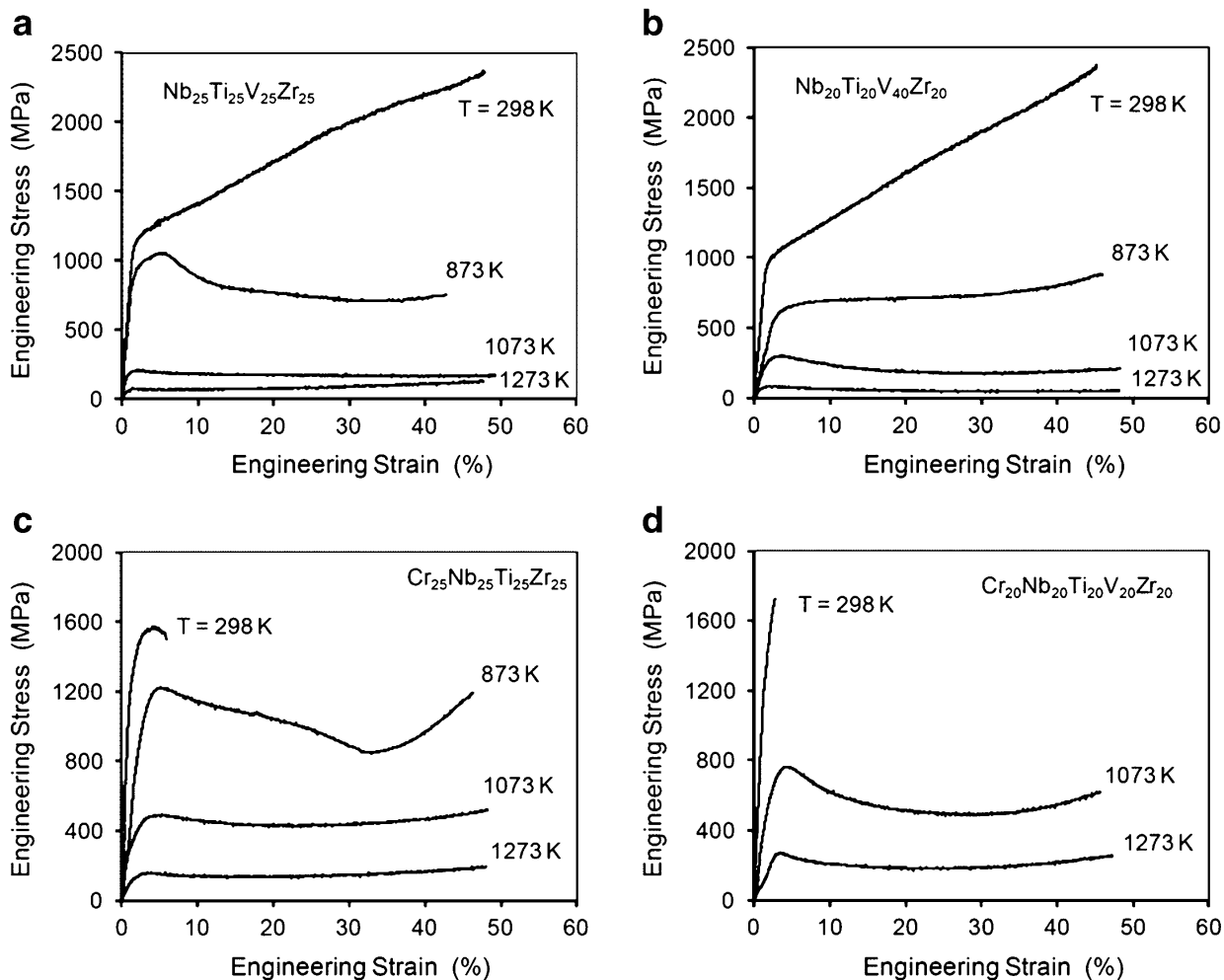


Fig. 15.4 Engineering compression stress vs. strain curves of (a) NbTiVZr, (b) NbTiV₂Zr, (c) CrNbTiZr, and (d) CrNbTiVZr alloys at $T = 298, 873, 1073$, and 1273 K [43]

properly adjusted. In the two Al-containing refractory HEAs [45, 46], it was noted that the addition of Al stabilized the BCC crystal structure and reduced the density of the refractory HEAs. The partial substitution of Hf with Al in the HfNbTaTiZr alloy was shown to reduce the density by ~9 %, increase the RT hardness by 29 %, and enhance the yield strength by 98 %. However, complete substitution of Cr with Al in the CrMo_{0.5}NbTa_{0.5}TiZr alloy reduced the alloy density by 10.1 %, increased the RT hardness and yield strength by 12 %, noticeably improved the RT ductility, and considerably increased, by more than 50 %, the high-temperature strength in the temperature range from 1073 to 1473 K. Therefore, it is clear that Al addition could have positive effects on the microstructures and properties of such refractory HEAs.

The research on HERAs mentioned above has apparently demonstrated that the alloy compositions could be further modified, which is very promising for the development of excellent HERAs for ultrahigh-temperature applications.

15.2.3 Carbides and Cermets with HEA Binders

Because suitable alloy design of HEAs has been proven to give promising properties, such as high hardness, softening resistance at high temperature, wear resistance, and corrosion resistance, some of them have been identified as good candidates for binders in cemented carbides and cermets to improve properties and reduce cost. Among these candidates, $\text{Al}_{0.5}\text{CoCrCuFeNi}$ HEA with an FCC structure has recently been reported to be a promising binder for wetting WC and inhibiting WC coarsening [48]. The sintered WC/HEA carbide displays a higher hardness-toughness level at room temperature than sintered WC/Co, as shown in Table 15.1. In addition, it has higher hot hardness. This superiority is attributed to the much finer WC grains of WC/HEA carbide. The grain size of WC can be divided into two ranges: $\sim 0.66 \mu\text{m}$ for the larger grain size and $\sim 0.15 \mu\text{m}$ for the smaller grain size. In contrast, the WC/Co composite has a larger grain size of about $9.95 \mu\text{m}$ and a smaller grain size of about $4.5 \mu\text{m}$. This refinement demonstrates that HEA binder could inhibit grain growth considerably. In addition, the hardness of WC/20 wt% $\text{Al}_{0.5}\text{CrCoCuFeNi}$ carbide is HV 300 higher than that of the WC/Co composite at 700°C , indicating that the HEA binder has good high-temperature softening resistance.

Similarly, new $\text{TiC}/\text{Co}_{1.5}\text{CrFeNi}_{1.5}\text{Ti}_{0.5}$ cermets with superior properties have been developed [49] by considering that FCC $\text{Co}_{1.5}\text{CrFeNi}_{1.5}\text{Ti}_{0.5}$ HEA (or T12), as mentioned in Sect. 15.2.1. It has higher contents of Ni, Cr, and Ti to wet TiC during liquid phase sintering and also the high hardness and toughness necessary to be a strong binder [50, 51]. The results show that $\text{TiC}/\text{Co}_{1.5}\text{CrFeNi}_{1.5}\text{Ti}_{0.5}$ ($\text{TiC} + 20\%$ T12) cermet has a much better combination of hardness and toughness than typical TiC/Ni , $\text{TiC}/\text{Ni}_{13}\text{Mo}_7$, and commercial TiC cermets, as shown in Table 15.2.

Table 15.1 Comparison of the hardness and fracture toughness of commercial WC/Co carbides and WC/ $\text{Al}_{0.5}\text{CrCoCuFeNi}$ carbide [48]

Carbides	Grade	Binder (%)	HV ₃₀	K _{IC} (MPa m ^{-1/2})
WC/ $\text{Al}_{0.5}\text{CrCoCuFeNi}$	EA	20	1413	17.4
WC/Co (commercial)	EF05	10	1900	9.1
	EF20	18	1450	13

Table 15.2 Hardness and fracture toughness of sintered $\text{TiC} + 20\%$ T12, $\text{TiC} + 20\%$ Ni, and $\text{TiC} + 20\%$ ($\text{Ni}_{13}\text{Mo}_7$). Other data are also listed for comparison [49]

Cermets	HV ₃₀	K _{IC} (MPa m ^{-1/2})
TiC + 20 %T12	1876	9.0
TiC + 20 %Ni	1372	11.8
TiC + 20 %Ni	1295	11.1
TiC + 20 %($\text{Ni}_{13}\text{Mo}_7$)	1639	8.5
Commercial TiC Cermet ^a	1685	9.1

^aThe composition in weight percentage is (TiC, WC, TaC) + 20 % (Ni, Co, Mo) in which TiC/WC/TaC = 16:2:2 and Co/Ni/Mo = 5:3:2

Given the coarsening behavior of TiC grains, the coarsening process of TiC in these three binders (HEA, Ni, and $\text{Ni}_{13}\text{Mo}_7$) was found to be diffusion-controlled. The activation energies of $\text{TiC} + 20\% \text{Co}_{1.5}\text{CrFeNi}_{1.5}\text{Ti}_{0.5}$, $\text{TiC} + 20\% \text{Ni}$, and $\text{TiC}/\text{Ni}_{13}\text{Mo}_7$ are 788.8, 265.3, and 422.4 kJ/mol, respectively. The high activation energy of the $\text{Co}_{1.5}\text{CrFeNi}_{1.5}\text{Ti}_{0.5}$ binder is attributed to its high content of carbon-strong-binding elements, cooperative diffusion, and higher packing density of multiple, different-sized atoms. The low diffusion coefficient and low surface energy of TiC grains and low solubility of Ti in the HEA liquid explain the slow coarsening of TiC grains. In brief, the two examples above show that suitable HEAs could be excellent HEA binders for WC carbides or TiC cermets.

15.2.4 HEA Hard Coatings

In 2004, the first six papers on HEAs were published [52–57]. One was on the concept of HEAs, three were on the investigation of cast bulk HEAs, and the other two papers were on thermal-spray HEA coatings and HEAN coatings [52, 57]. That is, the concept of HEAs was not only extended from bulk form to coatings but also from HEAs to HEANs in the first year of journal publication on HEAs. Through alloy designs with an aim to increase the hardness, wear resistance, and oxidation resistance of components in high-temperature applications, two alloy powders of $\text{AlCoCrFeMo}_{0.5}\text{NiSiTi}$ and $\text{AlCrFeMo}_{0.5}\text{NiSiTi}$ were prepared by arc melting, crushing, and ball milling to below 325 meshes (44 μm) and then plasma sprayed on alumina and 304 stainless steel substrates as a coating layer of about 160 μm in thickness [52]. Both alloys, in the as-deposited condition, were supersaturated with solutes in the matrix due to rapid solidification and had hardness values of HV486 and HV524, respectively, which were about one-half of their corresponding hardness values of HV933 and HV944 in the as-cast state. After aging at 500, 800, and 1000 °C, they showed significant precipitation hardening and achieved hardness levels of HV962 and HV990, respectively. Their wear resistances in the as-deposited condition were similar to those of wrought SUJ2 and SKD61 steels with much higher hardness but became superior to them by around 60 % in the 800 °C-aged condition. Furthermore, both coating layers possessed good oxidation resistance at 1000 °C and even up to 1100 °C, because their weight gains due to the formation of oxides approached a constant level after about 50–100 h. The excellent oxidation resistance is mainly attributed to the chromium oxide layer, which forms next to the top layer of titanium oxide. Therefore, thick coatings of HEAs are promising for environments where high-temperature oxidation resistance and abrasion resistance are critical, and more compositions with excellent high-temperature properties can be designed.

The first HEAN thin-film coating was deposited from a HEA target of $\text{FeCoNiCrCuAl}_{0.5}$ alloy using reactive magnetron sputtering [57]. HEA film without the incorporation of nitrogen had FCC structure and a hardness of 4.4 GPa, and the HEAN film with 41 at% N had a mixture of nanocrystalline HE nitride and

amorphous phase and a hardness of 10.4 GPa. Soon, Lai et al. reported a large improvement in hardness and achieved a level of 36 GPa for HEAN coatings by using strong nitride forming elements [58, 59], i.e., using a target of equiatomic AlCrTaTiZr to deposit nitride films. Afterward, many HEANs were developed and researched as described in Chap. 14. The main purpose of hard coatings is to protect the substrate by providing superior wear resistance and oxidation resistance to extend the lifetime of tools or molds. A lower friction coefficient is also beneficial in reducing the operation power, improving the surface quality, and lengthening lifetime. As an example to show the promising potential applications of HEAN coatings in cutting or milling tools, AlCrNbSiTiV HEAN film displays excellent thermal stability in terms of both nanostructure and superhardness [60]. It remains a simple NaCl-type FCC structure with a grain size around 12 nm, even after annealing at 1000 °C for 5 h. It also maintains a hardness level around 41 GPa up to 900 °C, as shown in Fig. 15.5. The flank wear of cutting tools coated with this HEAN coating was measured by a dry-cutting test and compared with that of tools without coating and tools with commercial TiN or TiAlN coatings [61]. Figure 15.6a shows the test with a 304 stainless steel workpiece, triangular carbide insert cutting tool, and milling machine, and Fig. 15.6b shows the flank wear depths obtained with different coatings. The comparison of flank wear depth demonstrates the significant improvement of HEAN coatings in terms of wear resistance and lifetime.

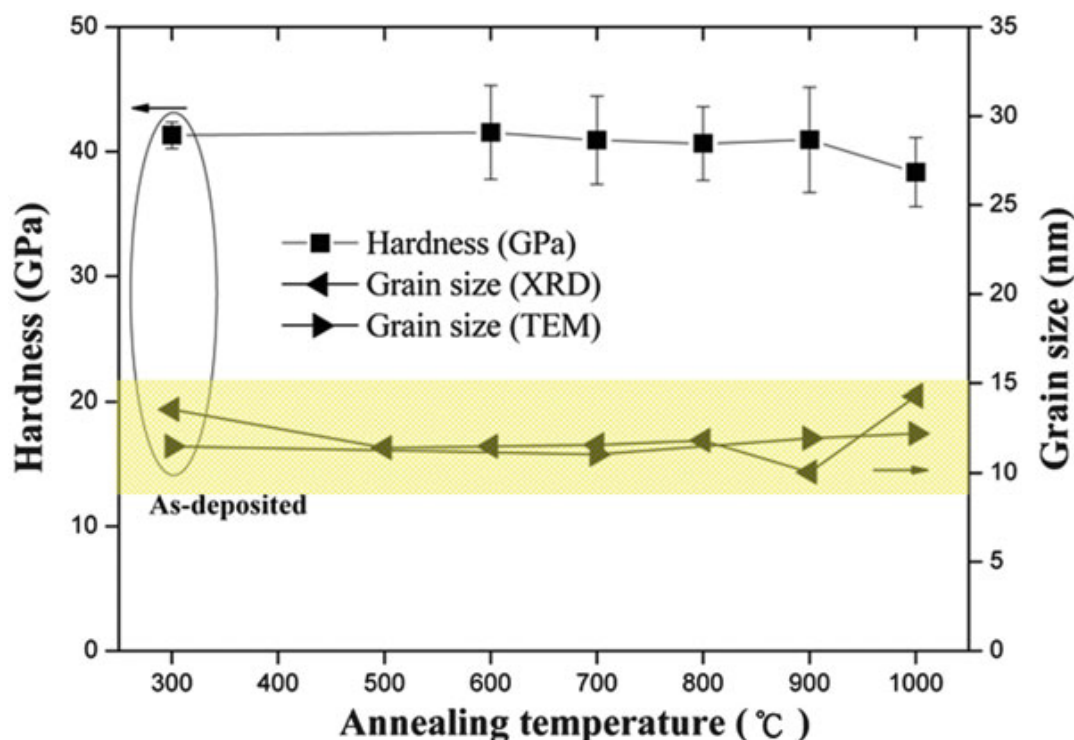


Fig. 15.5 Effect of annealing temperature on the hardness and grain sizes (according to XRD and TEM analyses) of AlCrNbSiTiV HEAN film. The samples were vacuum-sealed and annealed at each temperature for 6 h [60]

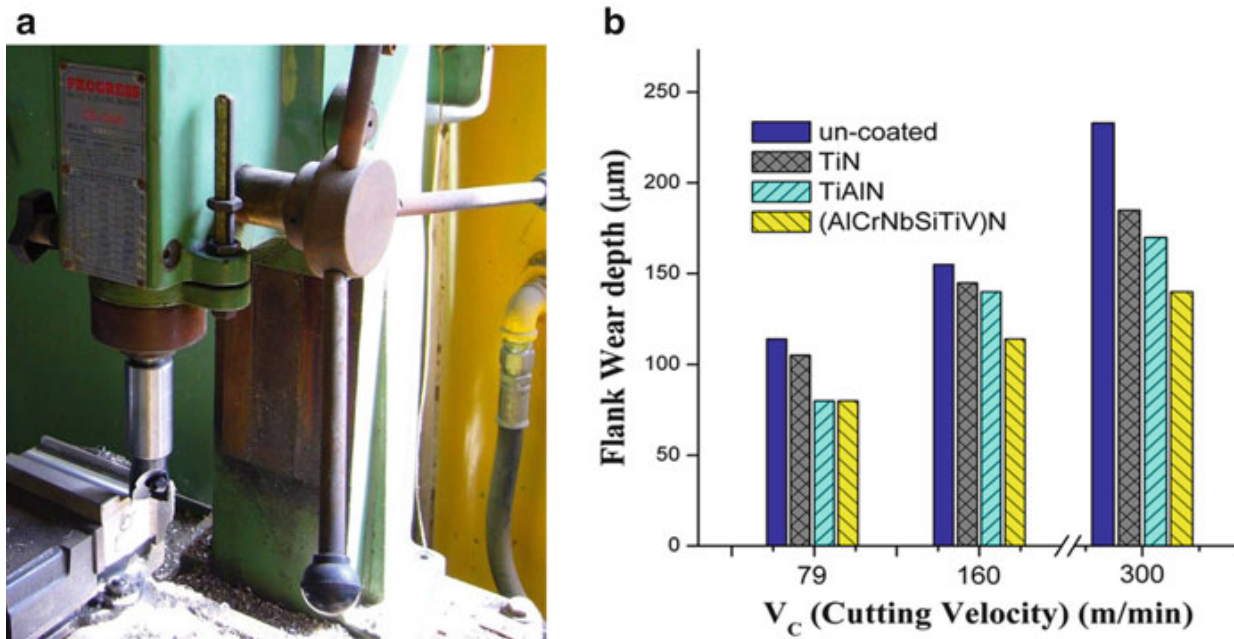


Fig. 15.6 (a) The dry-cutting test with a workpiece, triangular carbide insert cutting tool, and milling machine. (b) Flank wear depth versus cutting velocity for uncoated, TiN-coated, TiAlN-coated, and HEAN-coated insert cutting tools. Tool materials: WC/Co with a hardness of HV1516; film thickness, 1 μm ; workpiece, 304 stainless steel; depth of cut, 0.1 mm; feed rate, 0.1 mm; and total cutting length, 460 m [61]

15.2.5 HEA Diffusion Barriers

Besides being investigated as protective hard coatings that require good mechanical and tribological properties as mentioned above, HEA and HEAN coatings with high thermal stability have also been considered for applications as diffusion barriers [62]. Diffusion barriers are important interlayers, particularly in the interconnect structures of integrated circuits, e.g., between Cu wires and dielectrics or between metal pads and solders, to inhibit the rapid interdiffusion of adjacent materials (e.g., Cu and Si) or the formation of detrimental compounds (Cu silicides) that will lead to the early failure of microelectronic devices [61]. Other applications including refractory transition metals, such as Ti and Ta [63], and nitrides of unitary transition metals, including TiN and TaN [64, 65], were first practically used as diffusion barriers in interconnects in recent decades. However, they are unsuitable for next-generation interconnects due to their high solid solubility to Cu and polycrystalline/columnar structures with boundaries as fast diffusion paths. Thinner and more effective barriers have been developed in recent years, which are typically composed of (1) ternary components with an amorphous structure to diminish diffusion paths, such as Ru-Ti-N and Ru-Ta-N [66–68], and/or (2) layered structures with interface mismatches to elongate diffusion paths, such as Ru/TaN and Ru/TaCN [69–71]. Nevertheless, in the manufacturing generation of integrated circuits below 20 nm, robust and ultrathin (<3 nm) barrier layers with a much higher diffusion resistance are required.

Recent studies indicated that HEA and HEAN coatings with a simple solid solution, amorphous or nanocomposite structure, and very high thermal stability

present extreme resistance to the interdiffusion of Cu and Si [62]. Various effective HEA and HEAN coatings were then developed as suitable diffusion barriers for practical processing times within 30 min, including quinary NbSiTaTiZr (thickness, 20 nm; endurance temperature, 800 °C; endurance time, 30 min [72]) and senary AlCrRuTaTiZr (5 nm, 800 °C, 30 min [73]) alloys as well as (AlCrTaTiZr)N (10 nm, 900 °C, 30 min [74]) and (AlCrRuTaTiZr)N_{0.5} (5 nm, 800 °C, 30 min [75]) nitrides. The stacking structures of HEA and HEAN films, such as (AlCrTaTiZr)N_x/AlCrTaTiZr (10/5 nm, 900 °C, 30 min [76]) and (AlCrRuTaTiZr)N_{0.5}/AlCrRuTaTiZr/(AlCrRuTaTiZr)N_{0.5}/AlCrRuTaTiZr (4 nm, each layer 1 nm, 900 °C, 30 min [77]), have also been developed. Despite some practical demands including a low electrical resistivity, good adhesion to both metal wires (Cu or Al) and dielectrics, and high resistance to current leakage, the ultrahigh endurance temperatures (800–900 °C) of HEA and HEAN coatings against the interdiffusion of Cu and Si at a small film thickness (down to only 4–5 nm) suggest that they are promising materials for practical applications as diffusion barriers in microelectronic devices.

A mechanism for the high resistance to interdiffusion of HEA and HEAN coatings (i.e., highly suppressed interdiffusion kinetics) has been suggested by Chang et al. from structural and thermodynamic perspectives by examining the diffusion resistance of thin alloy films with different numbers of metallic elements (also refer to Sect. 14.2.3 of Chap. 14). The alloys include unitary Ti, binary TiTa, ternary TiTaCr, quaternary TiTaCrZr, quinary TiTaCrZrAl, and senary TiTaCrZrAlRu [78]. They found that the failure temperature of the barriers against interdiffusion of Cu and Si increased obviously from 550 to 900 °C as more metallic elements were incorporated. The activation energy of Cu diffusion through senary TiTaCrZrAlRu markedly increased from 110 kJ/mol (through unitary Ti) to 163 kJ/mol as well, according to measurements. Mechanistic analyses suggest that severe lattice distortion strains and a high packing density caused by different atom sizes affected the structure, and a strengthened cohesion affected the thermodynamics, which hindered the formation of vacancies and the movements of atoms, providing a total increase of 53 kJ/mole in the activation energy of substitutional Cu diffusion. This in turn suppressed interdiffusion kinetics through multicomponent HEA and HEAN barriers.

15.2.6 Irradiation-Resistant HEAs

To ensure the safe operation of nuclear reactors and maintain a sustainable energy supply, new and advanced nuclear materials are in high demand. Much effort has been exerted to develop better nuclear materials. It is important to understand their degradation under irradiation, determine their optimal operating conditions, and evaluate their lifetimes [79]. However, there is a diminishing return to improve various conventional nuclear materials that have matured in the last century. Therefore, HEAs might provide a new possibility for a larger advance in materials

for nuclear reactors. Egami et al. [79, 80] proposed that HEAs are characterized not only by high values of entropy but also by high atomic-level stresses originating from the mixing of elements with different atomic sizes. Particle irradiation on solids produces atomic displacements and thermal spikes. However, the high atomic-level stresses in HEAs facilitate amorphization upon particle irradiation, followed by local melting and recrystallization due to thermal spikes. This process leaves far fewer defects in HEAs than in conventional alloys. For this reason, they may be excellent candidates for new nuclear materials. They also conducted an electron microscopy study of Hf-Nb-Zr alloys to support this speculation and demonstrated the extremely high irradiation resistance of these alloys against electron damage. In addition, simulations of Hf-Nb-Zr alloys led to the conclusion that HEAs with atomic-level volume strain close to 0.1 are self-healing and highly irradiation resistant.

Furthermore, Egami et al. [81] reported the irradiation-induced structural changes and phase stability of CoCuCrFeNi HEAs under fast-electron irradiation by high-voltage electron microscopy. They found that FCC solid solution shows high phase stability against irradiation, and the FCC phase remained as the main constituent phase after over 40 dpa of irradiation at 298 and 773 K. This is the first study to provide experimental evidence for high phase stability in a five-component HEA against irradiation. In addition, irradiation produced minor structural changes, while grain coarsening was not observed under irradiation.

Therefore, these results demonstrate that suitable HEAs might have excellent irradiation resistance. If high-temperature strength and toughness, high oxidation resistance, and a low absorption cross section for neutrons are also achieved, such HEAs would be promising for broader applications in nuclear power plants.

15.3 Future Trends and Prospects

Although there are over 650 journal papers (by the end of 2014) on HEA and HE-related materials and more groups entering into this field, our current understanding of HEMs is just the tip of an iceberg. However, several future trends and prospects can still be forecasted based on the known literature on HEMs and materials science as reviewed in previous chapters:

1. More fundamental and basic scientific studies

Because materials science and solid-state physics are mainly based on research on conventional materials with one or two principal elements, corresponding research on HEMs will have academic value. Because HEMs can be single phase or multiphase, the best approach to understand the basic science is to investigate single-phase HEMs because a multiphase material is an aggregate of different phases. Any property or behavior is in fact the overall manifestation of all constituent phases and the phase boundaries between them. In a single-phase HEA, the phase is a solid solution with the whole-solute matrix, and many issues

in conventional physical metallurgy must be reconfirmed with the four core effects of HEAs: high-entropy, severe lattice distortion, sluggish diffusion, and cocktail effects. They must all be understood according to their mechanisms and theories, which may not be a simple extension of the properties of conventional alloys. Chapter 2 (Formation rules) and Chap. 3 (Physical metallurgy) present the preliminary understanding of these mechanisms. They include phase formation, mixing entropy, mixing enthalpy, atomic size difference, atomic-level stress, strain and energy of lattice distortion, diffusion coefficients, dislocation structure and energy, stacking fault structure and energy, grain boundary structure and energy, serration phenomenon, slip, twinning, and strengthening. More experimental results and explanations related to basic science on superplasticity, fatigue, creep, wear, corrosion, oxidation, magnetism, electrical and thermal conductivity, superconductivity, etc. can be found in Chap. 6 (Mechanical Properties of High-Entropy Alloys), Chap. 7 (Functional Properties), Chap. 13 (High-Entropy Metallic Glasses), and Chap. 14 (High-Entropy Coatings). Furthermore, direct observations and support for mechanisms and theories according to basic science are very important and can be achieved by using advanced technologies, as described in Chap. 4 (Advanced Characterization Techniques), which include high-resolution scanning transmission electron microscopy or analytical TEM, three-dimensional atom probes, and neutron scattering to characterize HEAs.

2. Further development of single-phase HEMs

Among HEAs, CoCrFeMnNi [19, 82–84], HfNbTaTiZr [37, 41], and DyGdHoTbY [85] are typical representatives for equiatomic single-phase HEAs in FCC, BCC, and HCP lattices for basic science investigations. More similar equiatomic systems will be found or designed through various means, such as CALPHAD, ab initio density functional theory calculations, hybrid Monte Carlo/molecular dynamics simulations, and combinatorial methods, as detailed in Chap. 11 (Design of High-Entropy Alloys) and Refs. [86, 87]. In addition, searching for single-phase HEA compositions with more than five principal components will be important for both theoretical understanding and technological applications.

In addition to equiatomic single-phase HEAs, non-equiatomic single-phase HEAs are also valuable for basic science since they can be compared with equiatomic single-phase HEAs to complete our understanding. It is also easier to find and prepare non-equiatomic single-phase HEAs by simply analyzing the single phase of interest in multiphase HEAs with EDS (energy-dispersive X-ray spectroscopy) and EPMA (electron probe microanalysis). It should be mentioned that both equiatomic single-phase and non-equiatomic single-phase HEAs might provide practical properties for applications. They can be further modified to improve their properties by changing the composition ratio and adding more components while maintaining a single phase or forming a second phase for precipitation strengthening or composite strengthening. In fact, conventional single-phase materials and multiphase materials have their own merits

and have been widely used in many engineering applications. This status would be similar for HEAs.

Compared to other HECs, single-phase HEANs and HEACs are much easier to obtain, especially by reactive sputtering with reacting gases, such as N₂ and CH₄, respectively. This is because many binary nitrides and binary carbides have similar NaCl-type crystal structures, and the direct formation from the vapor state, bypassing the liquid state, could also prevent phase separation during solidification.

3. More research on computational methods

Because HEMs cover many combinations of new compositions, processes, and properties, effective alloy designs and predictions by effective computational methods are very important to save time and reduce cost in material development. Chapter 8 (Prediction of Structure and Phase Transformations), Chap. 9 (Applications of Coherent Potential Approximation to High-Entropy Alloys), Chap. 10 (Applications of Special Quasi-random Structures to High-Entropy Alloys), Chap. 11 (Design of High-Entropy Alloys), and Chap. 12 (CALPHAD Modeling of High-Entropy Alloys) provide various approaches with different modeling and computer software. However, as HEMs involve multiple components and different microstructures, the complexity makes computations more difficult than those for conventional materials. Furthermore, databases of conventional materials are still far from complete for HEMs, and the calculation results and predictions using these databases may deviate significantly from the corresponding experimental results of HEMs. Therefore, there is urgent need in developing reliable and robust databases dedicated for HEMs as detailed in Chap. 12. Needless to say, advanced computing methodologies that can model dislocation-related properties in HEMs are highly desirable.

4. More research on performance challenges unattainable by traditional materials

HEMs have many opportunities to overcome the bottlenecks of conventional materials. They include room-temperature superconductors, alloys exceeding the performance and temperature capability of superalloys, and tools with very high hot hardness and long lifespan. For example, it is well known that metal-type, intermetallic-type, and oxide-type superconductors can attain a critical temperature around 10 K, 23 K, and 160 K, respectively. However, the highest record of each type of superconductor is based on a conventional design of their compositions. It is very possible to use the high-entropy concept to further promote the critical temperature. Room-temperature or near room-temperature superconductors could be realized in the future.

5. Further development of MEAs

Although conventional concentrated alloys, such as some superalloys and some BMGs, belong to the category of MEAs, there still exists a large uncharted area in MEAs. This is reasonable because MEAs are viewed differently from the high-entropy side than from the conventional low-entropy side, i.e., conventional alloys. It is very probable that the HEA concept will generate ideas in the area of MEAs. The MEAs could be Fe-based, Ni-based, Co-based, Cr-based, and Cu-based alloys and two-base, three-base, and four-base alloys. In addition to

different alloy design strategies for MEAs, it is suggested that suitable compositions of MEAs might be easily obtained from phases rich in some specific elements during the investigation of microstructures and their correlations with properties of HEAs. Similar to the fact that outstanding compositions exist in conventional alloys, it is expected that new outstanding compositions of MEAs will be discovered.

6. Assessments of existing databases to find possible applications

Because the number of papers on HEMs exceeded 650 by the end of 2014 and there is also much unpublished work, the accumulated results with promising properties have become sufficient to provide suitable assessments to find feasible applications. The gap between academic research and commercialization is often small if a mutual connection is built. It can be expected that a researcher might consider using or modifying current HEAs and HECs to fit the application requirements through this connection. According to this academic and industrial correlation model, many applications of HEMs will be generated in the future.

Acknowledgment J.W.Y, A.C.Y, and S.Y.C. would like to thank Dr. Michael C. Gao for his patience to provide review comments and suggestions from himself and invited experts. They also acknowledge all the financial supports from the Ministry of Science and Technology, Ministry of Economic Affairs, and National Tsing Hua University, R.O.C.

References

1. Sims CT, Stoloff NS, Hagel WC (1987) Superalloys II. Wiley, New York
2. Reed RC (2006) The superalloys: fundamentals and applications. Cambridge University Press, Cambridge
3. Reed RC, Tao T, Warnken N (2009) Alloys-by-design: application to nickel-based single crystal superalloys. *Acta Mater* 57:5898–5913
4. Walston S, Cetel A, MacKay R, O'Hara KS, Duhl D, Dreshfield R (2004) Joint development of a fourth generation single crystal superalloy. In: Green KA (ed) Proceedings of Superalloys 2004, (The 10th international symposium on superalloys, champion, Pennsylvania, USA). TMS (The Minerals, Metals & Materials Society), pp 15–24
5. Zhang JX, Murakumo T, Koizumi Y, Kobayashi T, Harada H, Masaki S (2002) Interfacial dislocation networks strengthening a fourth-generation single-crystal TMS138 superalloy. *Metall Mater Trans A* 33:3741–3746
6. Frasier DJ, Whetstone JR, Harris K, Erickson GL, Schwer RE (1990) Process and alloy optimization for CMSX-4 superalloy single crystal airfoil. In: High temperature materials for power engineering. Kluwer, Dordrecht, pp 1281–1300
7. Reed RC, Yeh AC, Tin S, Babu SS, Miller MK (2004) Identification of the partitioning characteristics of ruthenium in single crystal superalloys using atom probe tomography. *Scr Mater* 51:327–331
8. Yeh AC, Tin S (2005) Effects of Ru and Re additions on the high temperature flow stresses of Ni-base single crystal superalloys. *Scr Mater* 52:519–524
9. Yeh AC, Tin S (2006) Effects of Ru on the high-temperature phase stability of Ni-base single-crystal superalloys. *Metall Mater Trans A* 37:2621–2631
10. Yeh AC, Sato A, Kobayashi T, Harada H (2008) On the creep and phase stability of advanced Ni-base single crystal superalloys. *Mater Sci Eng A* 490:445–451

11. Kawagishi K, Sato A, Harada H, Yeh AC, Koizumi Y, Kobayashi T (2009) Oxidation resistant Ru containing Ni base single crystal superalloys. *Mater Sci Technol* 25:271–275
12. Kawagishi K, Yeh AC, Yokokawa T, Kobayashi T, Koizumi Y, Harada H (2012) Development of an oxidation-resistant high-strength sixth-generation single-crystal superalloy TMS-238. In: Huron ES (ed) *Proceedings of Superalloys 2012* (The 12th international symposium on superalloys). Wiley, New York, pp 189–195
13. Yeh AC, Chang YJ, Tsai CW, Wang YC, Yeh JW, Kuo CM (2014) On the solidification and phase stability of a Co-Cr-Fe-Ni-Ti high-entropy alloy. *Metall Mater Trans A* 45:184–190
14. Azadian S, Wei LY, Warren R (2004) Delta phase precipitation in Inconel 718. *Mater Charact* 53:7–16
15. Smith GD, Patel SJ (2005) The role of niobium in wrought precipitation-hardened nickel-base alloys. In: Loria EA (ed) *Proceedings of The 6th international superalloys symposium: superalloys 718, 625, 706 and derivatives 2005*, champion, Pennsylvania, USA. TMS, pp 135–154
16. Shibata T, Shudo Y, Yoshino Y (1996) Effects of aluminum, titanium and niobium on the time-temperature-precipitation behavior of alloy 706. In: Kissinger RD (ed) *Proceedings of superalloys 1996* (The 8th international symposium on superalloys, champion, Pennsylvania, USA). TMS, pp 153–162
17. Yeh AC, Yang KC, Yeh JW, Kuo CM (2014) Developing an advanced Si-bearing DS Ni-base superalloy. *J Alloys Compd* 585:614–621
18. Chang YJ, Yeh JW, Yeh AC (2014) High-entropy superalloys. Doctoral thesis in progress, National Tsing Hua University, Taiwan
19. Tsao TK, Yeh JW (2014) On high entropy effect and sluggish diffusion effect of high-entropy alloys. Doctoral thesis, National Tsing Hua University, Taiwan
20. Hobbs RA, Tin S, Rae CMF (2005) A castability model based on elemental solid–liquid partitioning in advanced nickel-base single-crystal superalloys. *Metall Mater Trans A* 36:2761–2773
21. Wills VA, McCartney DG (1991) A comparative study of solidification features in nickel-base superalloys: microstructural evolution and microsegregation. *Mater Sci Eng A* 145:223–232
22. Tin S, Pollock TM (2004) Predicting freckle formation in single crystal Ni-base superalloys. *J Mater Sci* 39:7199–7205
23. Webster GA, Sullivan CP (1967) Some of temperature cycling on the creep behaviour of nickel-base alloy. *J Inst Met* 95:138–142
24. Tien JK, Gamble RP (1972) Effects of stress coarsening on coherent particle strengthening. *Metall Trans* 3:2157–2162
25. Mackay RA, Ebert LJ (1983) The development of directional coarsening of the γ' precipitate in superalloy single crystals. *Scr Mater* 17:1217–1222
26. Ichitsubo T, Koumoto D, Hirao M, Tanaka K, Osawa M, Yokohawa T, Harada H (2003) Rafting mechanism for Ni-base superalloy under external stress: elastic or elastic-plastic phenomena? *Acta Mater* 51:4033–4044
27. Serin K, Gobenli G, Eggeler G (2004) On the influence of stress state, stress level and temperature on γ -channel widening in the single crystal superalloy CMSX-4. *Mater Sci Eng A* 387:133–137
28. Nabarro FRN, Cress CM, Kotschy P (1996) The thermodynamic driving force for rafting in superalloys. *Acta Mater* 44:3189–3198
29. Nabarro FRN (1996) Rafting in superalloys. *Metall Mater Trans A* 27:513–530
30. Laberge CA, Fratzl P, Lebowitz JL (1997) Microscopic model for directional coarsening of precipitates in alloys under external load. *Acta Mater* 45:3949–3962
31. Svoboda J, Lukas P (1996) Modelling of kinetics of directional coarsening in Ni-superalloys. *Acta Mater* 44:2557–2565
32. Tien JK, Copley SM (1971) The effect of orientation and sense of applied uniaxial stress on the morphology of coherent gamma prime precipitates in stress annealed nickel-base superalloy crystals. *Metall Trans* 2:543–553

33. Zhang JX, Wang JC, Harada H, Koizumi Y (2005) The effect of lattice misfit on the dislocation motion in superalloys during high-temperature Low-stress creep. *Acta Mater* 53:4623–4633
34. Zhang JX, Murakumo T, Harada H, Koizumi Y (2003) Dependence of creep strength on the interfacial dislocations in a fourth generation SC superalloy TMS-138. *Scr Mater* 48:287–293
35. Senkov ON, Wilks GB, Miracle DB, Chuang CP, Liaw PK (2010) Refractory high-entropy alloys. *Intermetallics* 18:1758–1765
36. Senkov ON, Wilks GB, Scott JM, Miracle DB (2011) Mechanical properties of $\text{Nb}_{25}\text{Mo}_{25}\text{Ta}_{25}\text{W}_{25}$ and $\text{V}_{20}\text{Nb}_{20}\text{Mo}_{20}\text{Ta}_{20}\text{W}_{20}$ refractory high entropy alloys. *Intermetallics* 19:698–706
37. Senkov ON, Scott JM, Senkova SV, Miracle DB, Woodward CF (2011) Microstructure and room temperature properties of a high-entropy TaNbHfZrTi alloy. *J Alloys Compd* 509:6043–6048
38. Zhu G, Liu Y, Ye JW (2014) Early high-temperature oxidation behavior of $\text{Ti}(\text{C}, \text{N})$ -based cermets with multi-component AlCoCrFeNi high-entropy alloy binder. *Int J Refract Met Hard Mater* 44:35–41
39. Zhang Y, Zuo TT, Tang Z, Gao MC, Dahmen KA, Liaw PK, Lu ZP (2014) Microstructures and properties of high-entropy alloys. *Prog Mater Sci* 61:1–93
40. Couzinié JP, Dirras G, Perrière L, Chauveau T, Leroy E, Champion Y, Guillot I (2014) Microstructure of a near-equimolar refractory high-entropy alloy. *Mater Lett* 126:285–287
41. Senkov ON, Scott JM, Senkova SV, Meisenkothen F, Miracle DB, Woodward CF (2012) Microstructure and elevated temperature properties of a refractory TaNbHfZrTi alloy. *J Mater Sci* 47:4062–4074
42. Senkov ON, Senkova S, Miracle DB, Woodward C (2013) Mechanical properties of Low-density, refractory multi-principal element alloys of the Cr-Nb-Ti-V-Zr system. *Mater Sci Eng A* 565:51–62
43. Senkov ON, Senkova S, Woodward C, Miracle DB (2013) Low-density, refractory multi-principal element alloys of the Cr-Nb-Ti-V-Zr system: microstructure and phase analysis. *Acta Mater* 61:1545–1557
44. Yang X, Zhang Y, Liaw PK (2012) Microstructure and compressive properties of NbTiVTaAl_x high entropy alloys. *Procedia Eng* 36:292–298
45. Senkov ON, Senkova SV, Woodward C (2014) Effect of aluminum on the microstructure and properties of two refractory high-entropy alloys. *Acta Mater* 68:214–228
46. Senkov ON, Woodward C, Miracle DB (2014) Microstructure and properties of aluminum-containing refractory high-entropy alloys. *JOM* 66:2030–2042
47. Zhang B, Gao MC, Zhang Y, Yang S, Guo SM (2015) Senary refractory high-entropy alloy MoNbTaTiVW . *Mater Sci Tech* 31:1207–1213
48. Chen CS, Yang CC, Chai HY, Yeh JW, Chau JLH (2014) Novel cermet material of WC/multi-element alloy. *Int J Refract Hard Met* 43:200–204
49. Lin CM, Tsai CW, Huang SM, Yang CC, Yeh JW (2014) New $\text{TiC}/\text{Co}_{1.5}\text{CrFeNi}_{1.5}\text{Ti}_{0.5}$ cermet with slow TiC coarsening during sintering. *JOM* 66:2050–2056
50. Chou YL, Yeh JW, Shih HC (2011) Effect of molybdenum on the pitting resistance of $\text{Co}_{1.5}\text{CrFeNi}_{1.5}\text{Ti}_{0.5}\text{Mo}_x$ alloys in chloride solutions. *Corrosion* 67:085002
51. Chuang MH, Tsai MH, Wang WR, Lin SJ, Yeh JW (2011) Microstructure and wear behavior of $\text{Al}_x\text{Co}_{1.5}\text{CrFeNi}_{1.5}\text{Ti}_y$ high-entropy alloys. *Acta Mater* 59:6308–6317
52. Huang PK, Yeh JW, Shun TT, Chen SK (2004) Multi-principal-element alloys with improved oxidation and wear resistance for thermal spray coating. *Adv Eng Mater* 6:74–78
53. Yeh JW, Chen SK, Lin SJ, Gan JY, Chin TS, Shun TT, Tsau CH, Chang SY (2004) Nanostructured high-entropy alloys with multiple principal elements: novel alloy design concepts and outcomes. *Adv Eng Mater* 6:299–303
54. Hsu CY, Yeh JW, Chen SK, Shun TT (2004) Wear resistance and high-temperature compression strength of Fcc $\text{CuCoNiCrA}_{10.5}\text{Fe}$ alloy with boron addition. *Metall Mater Trans A* 35:1465–1469

55. Cantor B, Chang ITH, Knight P, Vincent AJB (2004) Microstructural development in equiatomic multicomponent alloys. *Mater Sci Eng A* 375–377:213–218
56. Yeh JW, Chen SK, Gan JY, Lin SJ, Chin TS, Shun TT, Tsau CH, Chang SY (2004) Formation of simple crystal structures in Cu-Co-Ni-Cr-Al-Fe-Ti-V alloys with multiprincipal metallic elements. *Metall Mater Trans A* 35:2533–2536
57. Chen TK, Shun TT, Yeh JW, Wong MS (2004) Nanostructured nitride films of multi-element high-entropy alloys by reactive DC sputtering. *Surf Coat Technol* 188–189:193–200
58. Lai CH, Lin SJ, Yeh JW, Chang SY (2006) Preparation and characterization of AlCrTaTiZr multi-element nitride coatings. *Surf Coat Technol* 201:3275–3280
59. Lai CH, Lin SJ, Yeh JW, Davison A (2006) Effect of substrate bias on the structure and properties of multi-element (AlCrTaTiZr)N coatings. *J Phys D Appl Phys* 39:4628–4633
60. Huang PK, Yeh JW (2010) Inhibition of grain coarsening up to 1000°C in (AlCrNbSiTiV)N superhard coatings. *Scr Mater* 62:105–118
61. Huang PK, Yeh JW (2009) On high-entropy alloy and nitride coatings sputtered from AlCrNbSiTiV target. Doctoral thesis, National Tsing Hua University, Taiwan
62. Chang SY, Chen MK, Chen DS (2009) Multiprincipal-element AlCrTaTiZr-nitride nanocomposite film of extremely high thermal stability as diffusion barrier for Cu metallization. *J Electrochem Soc* 156:G37–G42
63. Kaloyerous AE, Eisenbraun E (2000) Ultrathin diffusion barriers/liners for gigascale copper metallization. *Annu Rev Mater Sci* 30:363–385
64. Kouno T, Niwa H, Yamada M (1998) Effect of TiN microstructure on diffusion barrier properties in Cu metallization. *J Electrochem Soc* 145:2164–2167
65. Alén P, Ritala M, Arstila K, Keinonen J, Leskelä M (2005) Atomic layer deposition of molybdenum nitride thin films for Cu metallizations. *J Electrochem Soc* 152:G361–G366
66. Kwon SH, Kwon OK, Min JS, Kang SW (2006) Plasma-enhanced atomic layer deposition of Ru-TiN thin films for copper diffusion barrier metals. *J Electrochem Soc* 153:G578–G584
67. Chen CW, Chen JS, Jeng JS (2008) Improvement on the diffusion barrier performance of reactively sputtered Ru-N film by incorporation of Ta. *J Electrochem Soc* 155:H438–H442
68. Fang JS, Lin JH, Chen BY, Chin TS (2011) Ultrathin Ru-Ta-C barriers for Cu metallization. *J Electrochem Soc* 158:H97–H102
69. Leu LC, Norton DP, McElwee L, Anderson TJ (2008) Ir/TaN as a bilayer diffusion barrier for advanced Cu interconnects. *Appl Phys Lett* 92:111917
70. Xie Q, Jiang YL, Musschoot J, Deduytsche D, Detavernier C, Vanmeirhaeghe R, Van den Berghe S, Ru GP, Li BZ, Qu XP (2009) Ru thin film grown on TaN by plasma enhanced atomic layer deposition. *Thin Solid Films* 517:4689–4693
71. Kim SH, Kim HT, Yim SS, Lee DJ, Kim KS, Kim HM, Kim KB, Sohn HC (2008) A bilayer diffusion barrier of ALD-Ru/ALD-TaCN for direct plating of Cu. *J Electrochem Soc* 155: H589–H594
72. Tsai MH, Wang CW, Tsai CW, Shen WJ, Yeh JW, Gan JY, Wu WW (2011) Thermal stability and performance of NbSiTaTiZr high-entropy alloy barrier for copper metallization. *J Electrochem Soc* 158:H1161–H1165
73. Chang SY, Wang CY, Chen MK, Li CE (2011) Ru incorporation on marked enhancement of diffusion resistance of multi-component alloy barrier layers. *J Alloy Compd* 509:L85–L89
74. Chang SY, Chen DS (2009) 10 nm-thick quinary (AlCrTaTiZr)N film as effective diffusion barrier for Cu interconnects at 900°C. *Appl Phys Lett* 94:231909
75. Chang SY, Wang CY, Li CE, Huang YC (2011) 5 nm-thick (AlCrTaTiZrRu)N_{0.5} multi-component barrier layer with high diffusion resistance for Cu interconnects. *Nanosci Nanotechnol Lett* 3:289–293
76. Chang SY, Chen DS (2010) Ultrathin (AlCrTaTiZr) Nx/AlCrTaTiZr bilayer structures with high diffusion resistance for Cu interconnects. *J Electrochem Soc* 157:G154–G159
77. Chang SY, Li CE, Chiang SC, Huang YC (2012) 4-nm thick multilayer structure of multi-component (AlCrRuTaTiZr)N_x as robust diffusion barrier for Cu interconnects. *J Alloy Compd* 515:4–7

78. Chang SY, Li CE, Huang YC, Hsu HF, Yeh JW, Lin SJ (2014) Structural and thermodynamic factors of suppressed interdiffusion kinetics in multi-component high-entropy materials. *Sci Rep* 4:4162
79. Egami T, Guo W, Rack PD, Nagase T (2014) Irradiation resistance of multicomponent alloys. *Metall Mater Trans A* 45:180–183
80. Nagase T, Anada S, Rack PD, Noh JH, Yasuda H, Mori H, Egami T (2013) MeV electron-irradiation-induced structural change in the BCC phase of Zr–Hf–Nb alloy with an approximately equiatomic ratio. *Intermetallics* 38:70–79
81. Nagase T, Rack PD, Noh JH, Egami T (2015) In-situ TEM observation of structural changes in nano-crystalline CoCrCuFeNi multicomponent High-Entropy Alloy (HEA) under fast electron irradiation by high voltage electron microscopy (HVEM). *Intermetallics* 59:32–42
82. Otto F, Yang Y, Bei H, George EP (2013) Relative effects of enthalpy and entropy on the phase stability of equiatomic high-entropy alloys. *Acta Mater* 61:2628–2638
83. Tsai KY, Tsai MH, Yeh JW (2013) Sluggish diffusion in Co–Cr–Fe–Mn–Ni high-entropy alloys. *Acta Mater* 61:4887–4897
84. Otto F, Dlouhy A, Somsen C, Bei H, Eggeler G, George EP (2013) The influences of temperature and microstructure on the tensile properties of a CoCrFeMnNi high-entropy alloy. *Acta Mater* 61:5743–5755
85. Feuerbacher M, Heidemann M, Thomas C (2015) Hexagonal high-entropy alloys. *Mater Res Lett* 3:1–6
86. Gao MC, Alman DE (2013) Searching for next single-phase high-entropy alloy compositions. *Entropy* 15:4504–4519. doi:[10.3390/e15104504](https://doi.org/10.3390/e15104504)
87. Gao MC, Zhang B, Guo SM, Qiao JW, Hawk JA (2015) High-entropy alloys in hexagonal close-packed structure. *Metall Mater Trans A*, doi: [10.1007/s11661-015-3091-1](https://doi.org/10.1007/s11661-015-3091-1)

Index

A

Ab initio molecular dynamics simulations (AIMD), 13, 17, 68, 371, 390–394, 460–464
Alloy design, 17, 62, 63, 72, 77, 109, 323, 394, 400, 421, 428, 431–432, 475, 476, 479, 480, 482, 483, 489, 490
Alloying effect, 83, 174, 185–189, 202
Amorphous, 5, 12, 13, 22, 25, 31–33, 40, 41, 45, 71, 72, 78, 79, 89, 165, 166, 168, 169, 174–176, 246, 248, 386, 387, 437–439, 453, 457, 460–463, 465, 467, 469, 484, 485
coating, 453, 457, 462
Atomic scale, 63, 72, 78, 83, 91, 133, 238, 392
Atomic size difference, 9, 13, 23–25, 45, 54–56, 58, 65, 67, 71, 72, 74, 79, 82, 84, 86, 103, 105, 371, 387, 394, 400, 409, 488

B

Binary alloys, 64, 66, 67, 91, 99, 272, 413, 431
BMGs. *See* Bulk metallic glasses (BMGs)
Body-centered cubic (BCC), 16, 17, 22, 26–31, 36, 37, 40–46, 53, 55–57, 64, 66–69, 75, 94, 97–101, 104, 106, 108, 116, 118–122, 129–133, 138, 140, 142, 153, 162, 163, 169, 170, 183, 186, 188, 202, 221, 239–242, 245, 253, 271–275, 277–279, 282, 287–293, 295, 301, 304, 305, 309, 311–320, 323, 327–329,

335–350, 352–357, 362–366, 370, 372, 374–382, 384, 385, 387–392, 394, 401, 403, 410–416, 418–422, 424, 425, 428, 435–437, 439, 454–456, 480, 481, 488

Bridgman method, 16

Bulk metallic glasses (BMGs), 7, 8, 11, 12, 15, 23–25, 34, 35, 55, 154, 155, 201, 221, 222, 315, 390, 394, 428–435, 437–442, 445, 446, 489

C

CALculation of PHase Diagrams (CALPHAD), 13, 17, 36, 140, 268, 292, 295, 355, 366, 371–380, 383, 384, 386, 389, 394, 399–425, 431, 456, 479, 488, 489
Cell size effect, 351
Cluster expansion, 272–275, 278, 288, 291, 295, 335
Cocktail effect, 52, 62–64, 238, 488
Coherent potential application (CPA), 17, 273, 295, 300–311, 316, 317, 321, 323–329, 358–363, 365, 366
Compression, 16, 78, 97, 98, 182, 189, 194, 200, 202, 208, 210–211, 214–216, 226, 227, 439, 440, 480, 481
Configurational entropy, 8–13, 22, 54, 65, 68, 69, 118, 169, 287, 291, 295, 296, 351, 353, 366, 371, 385, 386, 388, 400, 404, 409, 410, 413, 414, 418, 420, 431
CPA. *See* Coherent potential application (CPA)

D

- Density functional theory (DFT), 17, 36, 269–271, 274, 276, 279, 280, 288, 300, 301, 304, 325, 334, 335, 348, 357, 360, 372, 386–391, 394, 406, 408, 409, 413, 416, 421, 431, 488
 Density of states (DOS), 37, 40, 43, 135, 242, 280, 281, 283, 294, 305, 318, 327, 334, 352–354, 361–363, 366
DFT. *See* Density functional theory (DFT)
 Diffusion constants, 443, 444
 Disordered solid solution, 22, 55, 58, 140, 175, 371, 384, 385, 390, 394, 409
 DOS. *See* Density of states (DOS)

E

- e/a ratio, 37–40, 45, 46, 65
 Elastic constants, 303, 304, 307, 309, 313, 314, 317, 319, 321, 322, 324, 358–361, 497
 Elasticity, 17, 329
 Electrical property, 238–243, 262, 421
 Electrochemical property, 79, 248–259
 Electronegativity difference, 44
 Electronic entropy, 295, 348, 351–357, 366, 409
 Electronic structure, 300, 301, 317–318, 325, 327, 361–363
 Empirical rules, 23, 46, 67, 168, 371, 387, 394, 400
 EMTO. *See* Exact muffin-tin orbitals (EMTO)
 Enthalpy of mixing, 9–11, 13, 22–25, 36, 45, 54, 55, 65, 67, 79, 301, 328, 349, 371, 383, 384, 386, 387, 394, 409, 414–416, 420, 431, 437, 479, 488
 Entropy of mixing, 5, 6, 8–13, 22, 23, 25, 54, 55, 57, 60, 65–69, 72, 76, 140, 288, 296, 355, 357, 366, 371, 407, 409, 413–416, 420, 421, 475, 478, 479, 488
 Entropy sources, 16, 17, 23, 140, 351
 Exact muffin-tin orbitals (EMTO), 16, 301–316, 321, 323–325, 329, 358–361
 Excess entropy, 77, 357, 366, 386, 401, 409, 413, 420

F

- Fabrication routes, 16, 151–176, 453
 Face-centered cubic (FCC), 4, 5, 7, 17, 22, 25–31, 36, 37, 39–46, 53, 55–57, 60, 64, 66–69, 73–75, 79, 82–86, 88, 91, 93, 95–97, 99–101, 105, 106, 108, 116, 118–122, 124, 125, 129, 135, 143–146, 163, 169, 170, 175, 182, 183, 185, 186,

- 188, 202, 207, 208, 221, 225, 239, 240, 243, 245, 253, 258, 271, 287, 301, 303–305, 307–316, 319, 323, 324, 327–329, 335–357, 360–362, 364, 366, 370–372, 374, 376, 381–383, 387–392, 400–403, 410–416, 421–424, 428, 437, 439, 456, 459–461, 467, 469, 476, 477, 479, 482–484, 487, 488

Fatigue, 16, 52, 102, 124, 125, 127, 128, 182, 217–222, 226, 227, 488

FCC. *See* Face-centered cubic (FCC)

First-principles, 16, 36, 37, 43, 46, 140, 372, 402, 406

G

- Gibbs energy of mixing, 406, 409, 413, 418
 Glass-forming ability, 434

H

- Hardness, 6, 16, 35, 58, 59, 99, 100, 106–108, 160, 161, 163, 164, 167, 172, 174, 182–190, 202, 210–211, 221, 225–227, 253, 258, 327, 452, 454–456, 459–461, 463, 467–469, 477–485, 489
 HCP. *See* Hexagonal close-packed (HCP)
 HEAC coating. *See* High-entropy alloy carbide (HEAC) coating
 HEA coating. *See* High entropy alloy (HEA) coating
 HEAN coating. *See* High-entropy alloy nitride (HEAN) coating
 HECs. *See* High-entropy ceramics (HECs)
 Helmholtz free energies, 275, 277, 294, 353–356
 HERAs. *See* High-entropy refractory alloys (HERAs)
 HESAs. *See* High-entropy superalloys (HESAs)
 Hexagonal close-packed (HCP), 17, 27, 36–38, 44, 53, 55, 56, 64, 66, 75, 83, 94, 97, 100, 101, 116, 260, 271, 290, 291, 295, 316, 335–350, 352–357, 362, 364–366, 370–372, 374, 375, 378–384, 387–389, 392, 394, 403, 410, 412–416, 418, 419, 428, 437, 488
 High-entropy alloy carbide (HEAC) coating, 466–469
 High-entropy alloy (HEA) coating, 1–17, 22–25, 34–37, 39–46, 52–109, 116, 118, 120, 123, 124, 126, 127, 133, 134, 136, 138, 140, 143, 144, 146–148, 152–164,

- 166–171, 176, 181–228, 237–246, 248–263, 267–269, 273, 274, 287–296, 299–329, 333–367, 369–395, 399–425, 428, 429, 431–432, 434–439, 442, 445, 446, 452–459, 462, 465–470, 475–477, 479–490
- High-entropy alloy nitride (HEAN) coating, 452, 453, 459–466, 469, 483–486
- High-entropy ceramics (HECs), 7, 475, 489, 490
- High entropy effect, 6, 12, 52–56, 65, 66, 68–70, 260, 459
- High-entropy refractory alloys (HERAs), 475–481
- High-entropy superalloys (HESAs), 105, 475–480
- High-resolution transmission electron microscopy (HRTEM), 248, 464
- HRTEM. *See* High-resolution transmission electron microscopy (HRTEM)
- Hume-Rothery (H-R) rules, 23, 37, 38, 40, 67
- Hybrid Monte Carlo/molecular dynamics (MC/MD), 16, 17, 284, 289, 291, 293, 295, 302, 350–352, 361–366, 395
- Hydrogen storage property, 16, 260–262
- K**
- Kinetics, 13, 16, 23, 35, 42, 52, 71, 76, 91, 92, 164, 168, 248–251, 260, 261, 269, 270, 348, 423, 457, 458, 479, 486
- Korringa–Kohn–Rostoker (KKR), 302, 325–329
- L**
- Laser cladding, 152, 160–164, 176, 453, 455, 456
- Liquid melting, 152, 174
- Local strain, 147, 148
- M**
- Magnetic property, 243–248, 262, 305–307, 327, 328, 348, 360, 361
- Magnetism, 348, 349, 488
- MC/MD. *See* Hybrid Monte Carlo/molecular dynamics (MC/MD)
- Mean-field theory (MFT), 182, 211–215, 227
- MEAs. *See* Medium-entropy alloys (MEAs)
- Mechanical alloying, 12, 16, 71, 84, 152, 164–170, 174–176, 245, 383
- Mechanical properties, 16, 22, 52, 63, 68, 96, 133, 153, 174, 176, 181–228, 245, 258, 348, 357–361, 366, 432, 437, 440–442, 445, 446, 452, 461, 476
- Medium-entropy alloys (MEAs), 11, 64, 66, 489, 490
- MFT. *See* Mean-field theory (MFT)
- Micro-segregation, 153, 162
- Microstructure, 3, 6, 7, 13–16, 52, 53, 55, 62, 68, 69, 72, 88, 97, 98, 109, 116, 118, 121–124, 127, 129, 130, 133, 147, 153, 154, 158–163, 165, 169, 171, 175, 176, 186, 188, 208, 219, 227, 243, 245, 248, 249, 251, 253, 258, 311, 360, 369, 372, 375, 400, 401, 421, 423, 424, 453, 455, 456, 459, 461, 463, 469, 470, 476, 477, 480, 481, 489, 490
- Microstructure characterization, 16, 147
- Multi-component alloys, 8
- Multi-phase, 63
- Multi-principal-element alloys, 6, 22, 69
- N**
- Nanocomposite coating, 462
- Nanoindentation, 163, 164, 182, 221–227
- Nanoscale, 83, 118, 124, 131, 132, 148, 155, 162, 169, 445
- Nanostructure, 6, 7, 147, 169, 484
- Nano-twins, 127
- Neutron scattering, 16, 116, 117, 134–136, 138, 140, 141
- P**
- Pair distribution function (PDF), 116, 136, 138, 139, 147, 207, 220, 285, 289, 291, 293, 350–353, 362, 364, 390–393, 442–445
- Phase diagrams, 3, 7, 8, 12, 13, 17, 38, 53, 64, 65, 67, 69, 70, 166, 167, 267, 268, 277, 279, 280, 282, 295, 352, 355, 371, 372, 376, 380–383, 387, 390, 392, 394, 400–402, 408–411, 416, 417, 421–425 inspection, 371, 376, 380–383, 394
- Phase stability, 16, 37, 39–43, 45, 46, 72, 164, 295, 327, 348–351, 372, 383, 389, 400, 410, 413, 418, 487
- Phase transformations, 13, 16, 52, 59, 60, 64–72, 76, 243, 267–296, 311–313, 395, 423, 478, 489
- Phonon vibration, 348, 357
- Physical metallurgy, 3, 12, 16, 45, 51–109, 488

S

Serration, 94–95, 147, 182, 194, 196, 201, 204, 211–217, 226, 227, 488
 Severe lattice distortion effect, 52, 56–59, 63, 72, 78, 80, 238–241, 453, 458, 466, 488
SFE. *See* Stacking fault energy (SFE)
 Single crystal, 16, 104, 157–160, 173, 176, 309, 310, 315, 357, 358, 479
 Single phase, 10, 13, 17, 22, 57, 69, 90, 99, 124, 129–131, 140, 158, 161, 162, 166, 170, 182, 185, 201, 202, 204, 207, 225, 239, 267, 272, 310, 323, 324, 349, 352, 355, 363, 366, 370–372, 374–376, 379–382, 384–390, 394, 400, 410, 411, 416, 421, 446, 487–489
 Sluggish diffusion effect, 12, 52, 59–62, 68, 71–72, 104, 108, 174, 459, 470
 Solidification, 5, 16, 22, 24, 68, 70–72, 80, 152–158, 161–163, 165, 167, 174, 176, 201, 256, 375, 390, 392, 400, 421, 428, 453, 483, 489
 Solid solution, 3–13, 22–25, 34–38, 40–46, 53–58, 60, 63, 64, 66–69, 71, 72, 77–79, 92, 95, 96, 102–105, 108, 116, 118, 119, 124, 125, 127, 129, 130, 134, 135, 138, 140, 153, 161, 162, 165–169, 174–176, 185, 186, 188, 202, 214, 215, 238, 241, 246, 258, 272, 273, 277–279, 282, 288, 290, 291, 295, 300, 302–304, 311, 319, 321, 323, 324, 329, 334, 336, 361, 363, 370–375, 379–388, 390, 392, 394, 400, 401, 403, 409, 410, 414, 416, 425, 428, 439, 456, 457, 459, 461, 469, 487
 Solubility, 10, 53, 55, 66–68, 91, 166, 167, 272, 279, 312, 323, 380–383, 394, 410, 483, 485

Special quasi-random structures (SQS), 17,

273, 277, 280, 284, 287, 288, 290, 291, 295, 301, 302, 308, 333–367, 387, 489

Stacking fault energy (SFE), 82–87, 95–97, 100, 103–105, 170, 323–325, 329, 349, 360, 361

T

Temperature effect, 96, 189, 196–199, 202, 204, 215

Tension, 16, 36, 78, 105, 124, 127, 182, 208, 210–211, 217, 226, 227

Thermodynamics, 8, 11, 13, 16, 17, 23–35, 43, 45, 52, 54, 65, 69, 158, 174–175, 267, 268, 270–273, 276, 278, 282, 286–295, 302, 315, 335, 348, 361, 366, 371, 372, 379, 383, 400–403, 406–425, 428, 431, 438, 457, 458, 486

databases, 295, 372, 379, 401–403, 408

Thin film, 6, 12, 16, 138, 168, 171–173, 176, 182, 428, 452, 465, 470, 483

Three-dimension (3D) atom probe tomography, 13

V

Valence electron concentration (VEC), 11, 13, 25, 26, 28, 30, 32, 37–46, 65, 312, 319–322, 365, 371, 383, 400, 409

Vapor deposition, 171, 175, 453

Vibrational entropy, 280, 282, 288, 290, 351–357, 366, 413, 421